

# **5<sup>th</sup> Joint International Symposium on Deformation Monitoring**



**JISDM 2022**

## **PROCEEDINGS**

**20 - 22 June 2022**

**Polytechnic City of Innovation**

**Valencia (Spain)**



**edUPV**

Universitat Politècnica de València



**UNIVERSITAT  
POLITÈCNICA  
DE VALÈNCIA**

# **5<sup>th</sup> Joint International Symposium on Deformation Monitoring**



## **PROCEEDINGS**

**20 - 22 June 2022**

**Polytechnic City of Innovation**

**Valencia (Spain)**

## **Congresos UPV**

*Proceedings of th 5<sup>th</sup> Joint International Symposium on Deformation Monitoring - JISDM 2022*

The contents of this publication have been evaluated by the Scientific Committee which it relates and the procedure set out <http://ocs.editorial.upv.es/index.php/JISDM/JISDM2022/about/editorialPolicies>

© **Scientific Editors**

Luis García-Asenjo

José Luis Lerma

© texts: The authors

© **Publisher**

Editorial Universitat Politècnica de València, 2023

[www.lalibreria.upv.es](http://www.lalibreria.upv.es) / Ref.: 6661\_01\_01\_01

ISBN: 978-84-9048-979-6

DOI: <http://dx.doi.org/10.4995/JISDM2022.2022.16057>



*Proceedings of th 5th Joint International Symposium on Deformation Monitoring - JISDM 2022*

This book is licensed under a [Creative Commons Attribution-NonCommercial-ShareAlike 4.0 International \(CC BY-NC-SA 4.0\)](https://creativecommons.org/licenses/by-nc-sa/4.0/)

Editorial Universitat Politècnica de València

Based on a work in <http://ocs.editorial.upv.es/index.php/JISDM/JISDM2022>

## PREFACE

We had the pleasure to welcome you in Valencia for the 5th Joint International Symposium on Deformation Monitoring (JISDM 2022).

The Covid-19 pandemic interrupted our lives, professional activities and projects for almost two years, and naturally impacted the organization of this edition, which had to be postponed for two months. Fortunately, the JISDM 2022 was eventually held in person, which undoubtedly contributed to be a fruitful conference with open discussions and networking to promote high-quality deformation monitoring.

The number of participants registered was 195 from 25 different countries. As is being customary, two types of submissions were allowed, peer review and non-peer review papers, so that experts with different profiles can equally contribute to the advancement of deformation monitoring. This edition included 90 oral presentations and 18 posters with topics relate to technical, methodological, and practical advances in the field of deformation monitoring tackling landslides, debris flows and rockfalls, large engineering structures, and last but not least, tangible cultural heritage in archaeology and architecture.

We strongly acknowledge the support of the three scientific and professional commissions, FIG, IAG and ISPRS, and the time and effort devoted by the members of the Scientific Committee to review the papers. We are especially grateful to all the authors for their contributions.

We hope that you had a memorable and fruitful time during this symposium in Valencia, and that you can track the high-quality content of these proceedings.

Valencia, January 2023

Prof. Luis García-Asenjo

Prof. José Luis Lerma

*Co-chairmen of the JISDM 2022*

# INTERNATIONAL SYMPOSIUM COMMITTEE

## Congress Co-Chairs

Luis García-Asenjo

José Luis Lerma

## Scientific Committee

<i>Arnosó, José</i>	Spain	<i>Meng, Xiaolin</i>	China
<i>Baselga, Sergio</i>	Spain	<i>Neuner, Hans</i>	Austria
<i>Bastos, Luísa</i>	Portugal	<i>Niemeier, Wolfgang</i>	Germany
<i>Bolkas, Dimitrios</i>	USA	<i>Núñez-Andrés, Amparo</i>	Spain
<i>Brzezinska, Dorota</i>	USA	<i>Paffenholz, Jens-André</i>	Germany
<i>Capra, Alessandro</i>	Italy	<i>Poutanen, Markku</i>	Finland
<i>Catalão, João</i>	Portugal	<i>Prieto, Juan F.</i>	Spain
<i>Crosetto, Michele</i>	Spain	<i>Psimoulis, Panos</i>	UK
<i>Danezis, Chris</i>	Cyprus	<i>Pytharouli, Stella</i>	UK
<i>Ding, Xiaoli</i>	China	<i>Rizos, Chris</i>	Australia
<i>Eschelbach, Cornelia</i>	Germany	<i>Roman, Daniel R.</i>	USA
<i>García-Asenjo, Luis</i>	Spain	<i>Rinaudo, Fulvio</i>	Italy
<i>García-Cañada, Laura</i>	Spain	<i>Santos, Marcelo</i>	Canada
<i>Georgopoulos, Andreas</i>	Greece	<i>Scaioni, Marco</i>	Italy
<i>Gikas, Vassilis</i>	Greece	<i>Schwieger, Volker</i>	Germany
<i>Gil-Cruz, Antonio</i>	Spain	<i>Sousa, Joaquim J.</i>	Portugal
<i>Gonçalves, José</i>	Portugal	<i>Staller, Alejandra</i>	Spain
<i>Hancock, Craig</i>	UK	<i>Tari, Ergin</i>	Turkey
<i>Henriques, Maria</i>	Portugal	<i>Toth, Charles</i>	USA
<i>Kuhlmann, Heiner</i>	Germany	<i>Wieser, Andreas</i>	Switzerland
<i>Lerma, José Luis</i>	Spain	<i>Yigit, Cemal Ozer</i>	Turkey
<i>Lichti, Derek</i>	Canada	<i>Zang, Kefei</i>	Australia
<i>Lienhart, Werner</i>	Austria	<i>Zurutuza, Joaquín</i>	Spain
<i>Masiero, Andrea</i>	Italy		

## Organising Committee

*García-Asenjo, Luis*

*Lerma, José Luis*

*Anquela, Ana Belén*

*Padín, Jorge*

*Marqués, Ángel*

*Garrido, Natalia*

*Cabrelles, Miriam*

*Luján, Raquel*

*Calderón, Pedro*

*Martín, Ángel*

## Local Organiser

Universitat Politècnica de València

Department of Cartographic Engineering, Geodesy and Photogrammetry

Higher Technical School of Geodetic, Cartographic and Surveying Engineering

## Scientific & Professional Commissions

International Federation of Surveyors (FIG)

*Commission 6: Engineering Surveys*

*WG 6.1: Deformation Monitoring and Analysis.*

*Commission 5: Positioning and Measurement*



International Federation  
of Surveyors

International Association of Geodesy (IAG)

*Commission 4: Positioning and Applications*



International Association  
of Geodesy

International Society for Photogrammetry and Remote Sensing (ISPRS)

*WG III/5: Information Extraction from LiDAR Intensity Data*



Information from Imagery

## Sponsors



CÀTEDRA DE  
GEOMÀTICA  
VALENCIANA



## CONTENTS

### Peer-reviewed contributions

A feasibility study for accelerated reference point determination using close range photogrammetry.....	1
<i>Cornelia Eschelbach, Michael Lösler</i>	
Adaptive spatial discretization using reinforcement learning.....	9
<i>Jemil Avers Butt, Andreas Wieser</i>	
Bridge deformations during train passage: monitoring multiple profiles using concurrently operating MIMO-SAR sensors.....	11
<i>Andreas Baumann-Ouyang, Jemil Avers Butt, Andreas Wieser</i>	
High-precision intermode-beating EDM for mitigation of atmospheric delays .....	21
<i>Pabitra Ray, David Salido-Monzú, Andreas Wieser</i>	
2D strain rate and ground deformation modelling from continuous and survey mode GNSS data in El Hierro, Canary Islands .....	23
<i>Jose Arnosó, Umberto Riccardi, Umberto Tammara, Maite Benavent, Fuensanta G. Montesinos, Emilio Vélez</i>	
Two multi-wavelength interferometers for large-scale surveying .....	31
<i>Anni Sauthoff, Paul Köchert, Günther Prellinger, Tobias Meyer, Frank Pilarski, Stephanie Weinrich, Frank Schmaljohann, Joffray Guillory, Daniel Truong, Jakob Silbermann, Ulla Kallio, Jorma Jokela, Florian Pollinger</i>	
The European GeoMetre project – developing enhanced large-scaledimensional metrology for geodesy .....	41
<i>Florian Pollinger, Sergio Baselga, Clément Courde, Cornelia Eschelbach, Luis García-Asenjo, Pascual Garrigues, Joffray Guillory, Per Olof Hedekvist, Tuomas Helojärvi, Jorma Jokela, Ulla Kallio, Thomas Klügel, Paul Köchert, Michael Lösler, Raquel Luján, Tobias Meyer, Pavel Neyezhnikov, Damien Pesce, Marco Pisani, Markku Poutanen, Günther Prellinger, Anni Sauthoff, Jeremias Seppä, Daniel Truong, Robin Underwood, Kinga Wezka, Jean-Pierre Wallerand, Mariusz Wiśniewski</i>	
Real movement or systematic errors? – TLS-based deformation analysis of a concrete wall .....	43
<i>Berit Jost, Daniel Coopmann, Christoph Holst, Heiner Kuhlmann</i>	
Automated damage detection for port structures using machine learning algorithms in heightfields .....	45
<i>Frederic Hake, Paula Lippmann, Hamza Alkhatib, Vincent Oettel, Ingo Neumann</i>	
Supervoxel-based targetless registration and identification of stable areas for deformed point clouds .....	47
<i>Yihui Yang, Volker Schwieger</i>	
Investigation of space-continuous deformation from point clouds of structured surfaces.....	49
<i>Elisabeth Ötsch, Corinna Harmening, Hans Neuner</i>	
Permanent terrestrial LiDAR monitoring in mining, natural hazard prevention and infrastructure protection – Chances, risks, and challenges: A case study of a rockfall in Tyrol, Austria.....	51
<i>Daniel Schröder, Katharina Anders, Lukas Winiwarter, Daniel Wujanz</i>	
EDM-GNSS distance comparison at the EURO5000 calibration baseline: preliminary results.....	61
<i>Kinga Wezka, Luis García-Asenjo, Dominik Próchniewicz, Sergio Baselga, Ryszard Szpunar, Pascual Garrigues, Janusz Walo, Raquel Luján</i>	

Implementation of a fixed-location time lapse photogrammetric rock slope monitoring system in Castellfollit de la Roca, Spain .....	63
<i>Gerard Matas, Albert Prades, M. Amparo Núñez-Andrés, Felipe Buill2, Nieves Lantada</i>	
Quantification of the dependence of the results on several network adjustment applications.....	69
<i>Stéphane Durand, Michael Lösler, Mark Jones, Paul-Henri Cattin, Sébastien Guillaume, Laurent Morel</i>	
Assessing vertical terrain displacement from TLS data by applying Msplit estimation – theoretical analysis .....	79
<i>Patrycja Wyszowska, Robert Duchnowski</i>	
Point displacements during classical measurements – a practical approach to pseudo epochs between measurements.....	87
<i>Robert Duchnowski, Patrycja Wyszowska</i>	
Validation of GNSS-based reference point monitoring of the VGOS VLBI telescope at Metsähovi .....	93
<i>Ulla Kallio, Joonas Eskelinen, Jorma Jokela, Hannu Koivula, Simo Marila, Jyri Näränen, Markku Poutanen, Arttu Raja-Halli, Paavo Rouhiainen, Heli Suurmäki</i>	
Dynamic concepts to handle geodetic networks with continuous monitoring data in areas with ground movements.....	99
<i>Wolfgang Niemeier, Dieter Tengen</i>	
Accuracy improvement of mobile laser scanning point clouds using graph-based trajectory optimization.....	105
<i>Felix Esser, José Angel Moraga, Lasse Klingbeil, Heiner Kuhlmann</i>	
Assessing sandy beach width variations on intertidal time scales using permanent laser scanning .....	113
<i>Mieke Kuschnerus, Roderik Lindenbergh, Sierd de Vries</i>	
Integrated survey approaches for monitoring procedures during yard phases.....	121
<i>Awal Rahali, Eva Savina Malinverni, Roberto Pierdicca, Alessio Pierdicca, Gabriele Potenza, Matteo Lucesoli</i>	
4D point cloud analysis of the September 2020 Mediane impact on Myrtos beach in Cephalonia, Greece .....	129
<i>Emmanuel Vassilakis, Aliko Konsolaki, Stelios Petrakis, Evangelia Kotsi, Christos Fillis, Stelios Lozios, Efthymios Lekkas</i>	
GLOMON-Monitoringportal for storage, management, advanced processing and intelligent visualization of GNSS- and other sensors data .....	137
<i>Michael Schulz, Florian Schäfer, Jürgen Ruffer</i>	
Image segmentation of breakwater blocks by edge-base Hough transformation .....	143
<i>Fernando Soares, Vinicius Barbon</i>	
Crustal velocity field in Baza and Galera faults: A new estimation from GPS position time series in 2009 - 2018 time span .....	145
<i>Antonio J. Gil, M. Jesús Borque, Manuel Avilés, M. Clara de Lacy, Jesús Galindo-Zaldívar, Pedro Alfaro, F. J. García-Tortosa, Alberto Sánchez-Alzola, Iván Martín-Rojas, Iván Medina-Cascales, Patricia Ruano, Víctor Tintero, Asier Madarieta-Txurruka, Sergio Blanca, Moisés Madrigal, Fernando Chacón, Lucía Miras</i>	
Optical distance measurements at two wavelengths with air refractive index compensation .....	151
<i>Joffray Guillory, Daniel Truong, Jean-Pierre Wallerand</i>	
Preserving the heritage of world’s monuments through Structural Health Monitoring – A case study: the Garisenda Tower.....	159
<i>François-Baptiste Cartiaux, Gian Carlo Olivetti, Valeria Fort, Patrice M. Pelletier</i>	



Keypoint-based deformation monitoring using a terrestrial laser scanner from a single station: Case study of a bridge pier.....	167
<i>Tomislav Medic, Pia Ruttner, Christoph Holst, Andreas Wieser</i>	
Vibration monitoring of a bridge using 2D profile laser scanning: Lessons learned from the comparison of two spatio-temporal processing strategies .....	177
<i>Nicholas Meyer, Lorenz Schmid, Andreas Wieser, Tomislav Medic</i>	
Extraction of key geometric parameters from segmented masonry arch bridge point clouds.....	185
<i>Yixiong Jing, Brian Sheil, Sinan Acikgoz</i>	
Drill bit grading using LiDAR and imagery on the apple smart devices .....	191
<i>Fengman Jia, Derek D. Lichti, Roman Shor, Arsh Khawaja, Min Kang, Max Kepler</i>	
Two-epoch TLS deformation analysis of a double curved wooden structure using approximating B-spline surfaces and fully-populated synthetic covariance matrices .....	199
<i>Gabriel Kerekes, Jakob Raschhofer, Corinna Harmening, Hans Neuner, Volker Schwieger</i>	
Landslide monitoring using geotechnical, UAV, GNSS and MTInSAR instrumentation.....	207
<i>Nikolaos Depountis, Katerina Kavoura, Konstantinos Nikolakopoulos, George Drakatos, Panagiotis Argyrakis, Panagiotis Elias, Nikolaos Sabatakakis</i>	
Monitoring the spatiotemporal variability of beach mesoforms by analyzing Sentinel-2 images.....	215
<i>Josep E. Pardo-Pascual, Carlos Cabezas-Rabadán, Jesús Palomar-Vázquez, Alfonso Fernández-Sarriá</i>	
Design, establishment, analysis and quality control of a high-precision reference frame in Cortes de Pallás (Spain).....	223
<i>Luis García-Asenjo, Laura Martínez, Sergio Baselga, Pascual Garrigues, Raquel Luján</i>	
BIM approach applied to urban tunneling interferences .....	225
<i>Marco Trani, Silvia Longo, Monica Conti</i>	
Imaging land subsidence in the Guadalentín River Basin (SE Spain) using Advanced Differential SAR Interferometry .....	227
<i>Guadalupe Bru, Juan J. Portela, Pablo Ezquerro, M. Inés Navarro, Alejandra Staller, Marta Béjar-Pizarro, Carolina Guardiola-Albert, José A. Fernández-Merodo, Juan López-Vinielles, Roberto Tomás, Juan M. López-Sánchez</i>	
On the quality checking of persistent scatterer interferometry by spatial- temporal modelling .....	235
<i>Mohammad Omidalizarandi, Bahareh Mohammadivojdan, Hamza Alkhatib, Jens-André Paffenholz, Ingo Neumann</i>	
Towards an automated machine learning and image processing supported procedure for crack monitoring .....	237
<i>Luigi Parente, Cristina Castagnetti, Eugenia Falvo, Francesca Grassi, Francesco Mancini, Paolo Rossi, Alessandro Capra</i>	
Pathological diagnostic tool based on the combination of different disciplines. Management of the preservation of cultural heritage. Application in the structural consolidation of rock structures .....	243
<i>Jorge Juan Romo-Berlana, Manuel Sánchez-Fernández, José Juan de Sanjosé-Blasco, Fernando Berenguer-Sempere</i>	
Monitoring the production process of lightweight fibrous structures using terrestrial laser scanning .....	251
<i>Laura Balangé, Corinna Harmening, Rebeca Duque Estrada, Achim Menges, Hans Neuner, Volker Schwieger</i>	
The potential of UAV-based Laser Scanning for Deformation Monitoring – Case Study on a Water Dam.....	261
<i>Ansgar Dreier, Heiner Kuhlmann, Lasse Klingbeil</i>	

S-Wave detection using continuously operated GNSS stations: A case study of two Mw 7.1 earthquake events .....	271
<i>Vassiliki Krey, Iordanis Galanis, Vangelis Zacharis, Maria Tsakiri</i>	
Planning UAV surveys: can we rely on wind forecasts?.....	273
<i>Maria Henriques, Dora Roque</i>	
Deformation analysis in landslides NE Bulgaria using GNSS data complemented by InSAR for better interpretation results.....	279
<i>Mila Atanasova, Hristo Nikolov, Ivan Georgiev, Anton Ivanov</i>	
InSAR displacement time series post-processing to back-analyze a slope failure .....	285
<i>Dora Roque, Martino Correia, Ricardo Cabral, Steffan Davies, Tiago Cordeiro, Ana Fonseca, Paulo Barreto</i>	
Including virtual target points from laser scanning into the point-wise rigorous deformation analysis at geo-monitoring applications .....	291
<i>Lukas Raffl, Christoph Holst</i>	
MOMPA: InSAR monitoring in the Eastern Pyrenees .....	299
<i>Anna Barra, Ivan Fabregat, Anna Echeverria, Jordi Marturià, Qi Gao1, Guido Luzi, María Cuevas, Pere Buxó, Laura Trapero, Muriel Gasc, Pedro Espin, Michele Crosetto</i>	
Registering the ground deformations at the area of the archaeological site “Solnitsata” .....	305
<i>Hristo Nikolov, Mila Atanasova</i>	
First experiment of long-range panoramic images on a high-precision geodetic reference frame.....	311
<i>Peyman Javadi, José Luis Lerma, Luis García-Asenjo</i>	
Transferability of an estimation procedure for distance deviations of terrestrial laser scanners from laboratory to on-site conditions .....	319
<i>Finn Linzer, Hans-Berndt Neuner</i>	
Identifying individual rocks within laser scans for a rigorous deformation analysis of water dams.....	327
<i>Wolfgang Wiedemann, Christoph Holst</i>	
Evaluation of synthetic aperture radar interferometric techniques for monitoring of fast deformation caused by underground mining exploitation.....	335
<i>Kamila Pawłuszek-Filipiak, Maya Ilieva, Natalia Wielgocka, Krzysztof Stasch</i>	
ADATools: a set of tools for the analysis of terrain movement maps obtained with SAR Interferometry .....	343
<i>Oriol Monserrat, Anna Barra, Cristina Reyes-Carmona, María Cuevas, Marta Bejar-Pizarro, José Navarro, Roberto Tomas, Jorge Pedro Galve, Lorenzo Solari, Roberto Sarro, Rosa María Mateos, José Miguel Azañon, Gerardo Herrera, Bruno Crippa</i>	
Static and Dynamic Monitoring of the Notre Dame de Paris Cathedral.....	351
<i>Véronique Le Corvec, Patrick Lézin, François-Baptiste Cartiaux</i>	
Comparison of TLS and sUAS point clouds for monitoring embankment dams.....	359
<i>Dimitrios Bolkas, Matthew O’Banion, Jakeb Prickett, Gregory Ellsworth, Gerald Rusek, Hannah Corson</i>	
PS-InSAR and UAV technology used in the stability study of Ankang expansive soil airport .....	367
<i>Jinzhao Si, Shuangcheng Zhang, Yufen Niu</i>	
Terrestrial Laser Scanning based deformation monitoring for masonry buildings subjected to ground movements induced by underground construction.....	375
<i>Yiyan Liu, Sinan Acikgoz, Harvey Burd</i>	

Pan-European deformation monitoring: The European Ground Motion Service .....	383
<i>Michele Crosetto, Lorenzo Solari, Marek Mróz</i>	
Selected aspects of geometrical analyses of surfaces measured using terrestrial laser scanning (TLS) .....	389
<i>Janina Zaczek-Peplinska, Maria Elżbieta Kowalska, Krystian Ryczko, Cezary Sekular</i>	
Monitoring embankment dams from space using satellite radar interferometry: Case studies from RemoDams project.....	397
<i>Antonio M. Ruiz-Armenteros, José Manuel Delgado-Blasco, Matus Bakon, Francisco Lamas-Fernández, Miguel Marchamalo-Sacristán, Antonio J. Gil-Cruz, Juraj Papco, Beatriz González-Rodrigo, Milan Lazecky, Daniele Perissin, Joaquim J. Sousa</i>	
Deep machine learning in bridge structures durability analysis.....	405
<i>Karolina Tomaszekiewicz, Tomasz Owerko</i>	
Monitoring instabilities by MT-InSAR in a mesa placed town (Arjona, Guadalquivir valley, South Spain) .....	413
<i>Antonio Miguel Ruiz-Armenteros, Mario Sánchez-Gómez, José Manuel Delgado-Blasco, Matus Bakon, Ana Ruiz-Constán, Jesús Galindo-Zaldívar, Milan Lazecky, Miguel Marchamalo-Sacristán, Joaquim J. Sousa</i>	
Forecasting post-earthquake rockfall activity .....	421
<i>Michael J. Olsen, Chris Massey, Ben Leshchinsky, Joseph Wartman, Andrew Senogles</i>	
Monitoring of underwater animal forests: geometry and biometry.....	423
<i>Paolo Rossi, Cristina Castagnetti, Stefano Cattini, Giorgio Di Loro, Francesca Grassi, Luigi Parente, Sara Righi, Luigi Rovati, Roberto Simonini, Alessandro Capra</i>	
Structural analysis of monitoring results of long-span roof structures .....	431
<i>Roman Shults</i>	
Monitoring of land subsidence in the city of Recife/Brazil using Sentinel-1 SAR interferometry.....	439
<i>Wendson de Oliveira Souza, Antonio Miguel Ruiz-Armenteros, Jaime J. da Silva Pereira Cabral</i>	
Monitoring Gravitational Deformations of the Wettzell 20 m Radio Telescope's Main Reflector Using a Leica RTC360 .....	447
<i>Agnes Weinhuber, Alexander Neidhardt, Christoph Holst</i>	
High-rate real-time PPP for dynamic motion detection in vertical direction.....	455
<i>Baris Karadeniz, Mert Bezcioglu, Cemal Ozer Yigit, Ahmet Anil Dindar, Burak Akpınar</i>	
High-rate real-time single-frequency PPP for structural motion detection in horizontal directions .....	461
<i>Mert Bezcioglu, Baris Karadeniz, Cemal Ozer Yigit, Ahmet Anil Dindar, Burak Akpınar</i>	
Assessment of accuracy and performance of terrestrial laser scanner in monitoring of retaining walls.....	467
<i>Ali Algadhi, Panos Psimoulis, Athina Grizi, Luis Neves</i>	
Assessment of the accuracy of low-cost multi-GNSS receivers in monitoring bridge response .....	475
<i>Chenyu Xue, Panos Psimoulis, Qiuzhao Zhang, Xiaolin Meng</i>	
Sensitivity analysis of control networks in terms of minimal detectable displacements.....	477
<i>Krzysztof Książek, Sławomir Łapiński</i>	
Long and close-range terrestrial photogrammetry for rocky landscape deformation monitoring.....	485
<i>Miriam Cabrelles, José Luis Lerma, Luis García-Asenjo, Pascual Garrigues, Laura Martínez</i>	
A self-acting mobile robot for monitoring floor flatness.....	493
<i>Christoph Naab</i>	
Multispectral imaging for the documentation of graffiti in an urban environment .....	495
<i>Max Rahrig, José Luis Lerma</i>	

## Non-peer-reviewed contributions

Deformation monitoring with robotic total stations. Pushing the limits .....	505
<i>Josep Raventós, Enric Sans</i>	
Current State of Multi-constellation and multi-frequency Precise Point positioning .....	511
<i>Fernando Chacón, Antonio Herrera, M. Clara de Lacy</i>	
CGPS Crustal velocity field in the Iberian Peninsula .....	517
<i>Fernando Chacón, M. Clara de Lacy, Manuel Avilés, Antonio J. Gil</i>	
Classical Concepts for Deformation Monitoring - Strategies, Status and Limitations.....	523
<i>Wolfgang Niemeier</i>	
Deformation Analysis with Feature Voting.....	533
<i>Omer Bar, Gilad Even-Tzur</i>	
Dynamic monitoring of civil infrastructures with geodetic sensors .....	537
<i>Caroline Schönberger, Werner Lienhart, Thomas Moser</i>	
Analysis of the Lisbon metropolitan area using the P-SBAS service of the Geohazards Exploitation Platform .....	545
<i>Jorge P. Galve, Cristina Reyes-Carmona, Anna Barra, Marta Béjar-Pizarro, Oriol Monserrat, Ricardo Garcia Campus, Jose Luis Zezere, Paulo S. de Figueiredo Ferreira, Sara A. Figueira Damaso, Susana I. Magro Siborro, Rosa M. Mateos, José Miguel Azañón</i>	
Data fusion of MEMS accelerometer and hydrostatic leveling for structural health monitoring – the test rig investigations.....	553
<i>Leonhard Pleuger, Mario Haupt, Jens-André Paffenholz</i>	
Rockfall monitoring: comparing several strategies for surveying detached blocks and their volume, from TLS point clouds and GigaPan pictures .....	561
<i>Oriol Pedraza, Álvaro P. Aronés, Càrol Puig, Marc Janeras, Josep A. Gili</i>	
Hydrological-driven landslide in northwestern China measured by InSAR time series analysis.....	569
<i>Qianyou Fan, Shuangcheng Zhang, Yufen Niu</i>	
Soil Moisture Mapping Based on Temperature-Soil Moisture Dryness Index - a case study for the tailing dam in Brumadinho, Brazil .....	577
<i>Yu Lan, Jens-André Paffenholz</i>	
Concept for the integration of BIM and GIS data for monitoring land deformation around an ongoing infrastructure project.....	585
<i>Szymon Glinka, Tomasz Owerko</i>	
Early detection, permanent monitoring and documentation of critical locations at the surface in mining areas.....	591
<i>Alexander Kipp, Andreas Schlienkamp, Anna Ens</i>	
Geomonplus – Application for Storage, Allocation, Exchange, and Visualization of Historical and Actual 4d-Position-Data within Mining Areas.....	597
<i>Steffen Bechert, Andreas Schlienkamp, Volker Spreckels</i>	
Kalman filter for integration of GNSS and InSAR data applied for monitoring of mining deformations.....	605
<i>Damian Tondaś, Witold Rohm, Maya Ilieva, Jan Kapłon</i>	
Multi-epoch deformation analysis with geodetic datum invariance.....	613
<i>Hiddo Velsink</i>	
Continuous long-term (2016-2021) monitoring of the surface deformations in the Upper Silesian Coal Basin, Poland.....	621
<i>Maya Ilieva, Patryk Balak, Paweł Bogusławski, Piotr Polanin, Piotr Gruchlik, Andrzej Kowalski, Damian Tondaś, Krzysztof Stasch, Przemysław Tymków</i>	

A discussion on the uses of smart sensory network, cloud-computing, digital twin and artificial intelligence for the monitoring of long-span bridges .....	629
<i>Xiaolin Meng, Zejun Xiang, Yilin Xie, George Ye, Panagiotis Psimoulis, Qing Wang, Ming Yang, Yulong Ge, Shengli Wang, Jian Wang</i>	
Multisensor monitoring of ground movements over large areas to conduct the change from the active underground hard coal mining ages to the post-mining era .....	637
<i>Volker Spreckels</i>	
Set-up and application of multisensor-referencestations (MSST) for levelling, GNSS and InSAR in the former mining regions Saarland and Ruhrgebiet within Germany .....	645
<i>Volker Spreckels, Thomas Engel</i>	
Status of the new German DIN standards Project “InSAR– Radarinterferometry for the detection of ground movements” .....	653
<i>Volker Spreckels</i>	
Low-cost GNSS RTK receiver in structure monitoring under demanding conditions .....	659
<i>Przemysław Kuras, Daniel Janos, Łukasz Ortyl</i>	
Experimental assessment of the accuracy of a Ground-Based Radar Interferometer in a fully controlled laboratory environment .....	665
<i>George Piniotis, Vassilis Gikas</i>	
Steel bridge structural damage detection using Ground-Based Radar Interferometry vibration measurements and deep learning Convolutional Neural Networks .....	673
<i>George Piniotis, Vassilis Gikas</i>	

**5<sup>th</sup> Joint International Symposium on  
Deformation Monitoring**



**Peer-reviewed contributions**

# A feasibility study for accelerated reference point determination using close range photogrammetry

Cornelia Eschelbach, Michael Lösler

Frankfurt University of Applied Sciences, Faculty 1: Architecture – Civil engineering – Geomatics, Laboratory for Industrial Metrology, Nibelungenplatz 1, 60318 Frankfurt am Main, Germany,  
([cornelia.eschelbach@fb1.fra-uas.de](mailto:cornelia.eschelbach@fb1.fra-uas.de); [michael.loesler@fb1.fra-uas.de](mailto:michael.loesler@fb1.fra-uas.de))

**Key words:** *reference point determination; close range photogrammetry; bundle adjustment; satellite laser ranging; GeoMetre*

## ABSTRACT

The Global Geodetic Observing System (GGOS) aims for an accuracy of 1 mm in position concerning a global geodetic reference frame such as the International Terrestrial Reference Frame (ITRF). To derive a global frame, several space geodetic techniques are combined. The combination procedure requires the geometric relations between the invariant reference points of these techniques, the so-called local tie vectors. Each space geodetic technique defines its reference point individually, so the determination of the position of the reference point varies significantly between techniques. Within the international GeoMetre project, measurement systems and analysis strategies are developed to improve the quality of local tie vectors and, thus, the quality of the resulting global frame. The use of close range photogrammetry to determine the reference point of a telescope used for Satellite Laser Ranging (SLR) at the GGOS core station Wettzell in September 2020 is considered as a milestone in this project. This contribution deals with a novel approach for an accelerated reference point determination using close range photogrammetry. In comparison to the conventional photogrammetric approach, published so far, this new approach leads to a significant reduction in recording time. However, in case of inappropriate measurement configuration the approach also bears the risk of biased results. Most importantly, the new approach has the potential to be automated, which is one of the primary calls of GGOS for reference point determinations.

## I. INTRODUCTION

One of the mayor challenges of humankind in this century is to face the global climate change. A reliable and high accurate geodetic infrastructure is essential for modelling the system Earth to get a better understanding of global processes. For instance, the detection of the rising of the sea-level requires accuracies of the reference frame of better than  $0.5 \text{ mm a}^{-1}$  in height position on a global scale. Four space geodetic techniques form a global frame of reference points, the International Terrestrial Reference Frame. Multi-technique stations host these space geodetic techniques close to each other on a single site and, therefore, play a key role in the combination process of the space geodetic techniques. These stations provide the so-called local ties: spatial vectors including the geometric relations between the invariant reference points of the techniques.

Local ties have been identified as a critical component within the combination process (Glaser *et al.*, 2015). Generating a local tie always consists of three determination steps: deriving the reference points of each space geodetic technique at a multi-technique station, combining the reference points in a consistent local reference frame including the related dispersion matrices, and, finally, transforming the local ties into the global reference frame (Lösler *et al.*, 2022). In total,

GGOS aims for an accuracy of 1 mm for the reference points and, thus, also for the local ties.

The EURAMET project GeoMetre (2020) takes up the topic of improving the quality and reliability of global reference frames by, for instance, traceably transforming local ties to the global reference frame (Pollinger *et al.*, 2022). Also part of this research project is the further development of measurement and analysis strategies for the determination of the reference points of telescope-based space geodetic techniques. Two milestones have already been reached in this topic: a novel approach for the determination of reference points overcomes the necessity of synchronization between the measurement instrument and the telescope (Lösler *et al.*, 2018). Furthermore, close range photogrammetry has been applied to determine the reference point of an SLR telescope at the GGOS core station Wettzell (Figure 1) for the first time (Lösler *et al.*, 2021; 2022). During a measurement campaign in 2020, a first study proved the general suitability of close range photogrammetry for reference point determination. Nevertheless, the photogrammetric approach published so far is on the same level with standard methods in terms of handling and effort. This approach will be referred to as CRP approach (CRP: Close Range Photogrammetry) hereafter.



Figure 1. Satellite Observing System Wettzell at the GGOS core station Wettzell in the Bavarian Forest.

In this contribution, we present a novel photogrammetric measurement and analysis strategy, which is an advancement of the CRP approach. With this new approach, we mainly address the request to accelerate the measurement process and enable automation for data acquisition during regular telescope operation.

Section II describes the theoretical background and gives the most important formulas regarding the calculation algorithms of the bundle adjustment, the concatenated transformation and the determination of the reference point. In Section III, the measurement object and the circumstances for photogrammetry are mentioned. In addition, the measurement system and the measurement procedure are described in detail. The analysis strategy and the results are presented in Section IV. Finally, this contribution concludes with an outlook in Section V.

## II. THEORETICAL BACKGROUND

The determination of the reference point of an SLR telescope in this approach consists of three analysis steps. The first step, described in Section II A, includes the determination of photogrammetric marker positions at the turnable part of the telescope structure in different telescope positions using a bundle adjustment. Section II B gives the formulas to reorient images using a concatenated transformation. This strategy enables the combination of data of a fixed object while the camera position is moved as well as with data of a fixed camera position while the object is moved. The camera positions change during the measurement of the reference frame and of the telescope, which was oriented in eight different azimuth positions. On the other hand, fixed camera positions are used to measure the telescope in twelve further elevation positions per azimuth. Finally, in Section II C, the coordinates of all marker positions and their fully populated dispersion matrix serve as observations for the calculation of the reference point

using the algorithms developed by Lösler *et al.* (2018). Due to the concatenated transformation, this approach is hereafter called the CRP-CT approach (CRP-CT: Close Range Photogrammetry using Concatenated Transformations).

### A. Bundle adjustment

Each photogrammetric image provides the image coordinates of all visible marker positions. The image coordinates and the perspective center of the camera generate a spatial bundle of rays. Several ray bundles of several images taken from different perspectives form a stiff bundle network. The bundle adjustment orients all images and yields the interior and the exterior orientation parameters as well as the spatial coordinates of all marker positions, using the collinearity equations given by (Eq. 1):

$$\begin{pmatrix} x'_i \\ y'_i \end{pmatrix}_j = \begin{pmatrix} x'_0 \\ y'_0 \end{pmatrix} + \begin{pmatrix} x_i^* \\ y_i^* \end{pmatrix}_j + \begin{pmatrix} \Delta x'_i \\ \Delta y'_i \end{pmatrix}_j \quad (1)$$

with (Eqs. 2 and 3):

$$x_i^* = -c \frac{r_{11}(X_i - X'_0) + r_{21}(Y_i - Y'_0) + r_{31}(Z_i - Z'_0)}{r_{13}(X_i - X'_0) + r_{23}(Y_i - Y'_0) + r_{33}(Z_i - Z'_0)} \quad (2)$$

$$y_i^* = -c \frac{r_{12}(X_i - X'_0) + r_{22}(Y_i - Y'_0) + r_{32}(Z_i - Z'_0)}{r_{13}(X_i - X'_0) + r_{23}(Y_i - Y'_0) + r_{33}(Z_i - Z'_0)} \quad (3)$$

The equations serve as functional model for connecting the planar image coordinates  $(x'_i \ y'_i)^T$  with the corresponding spatial coordinates  $(X_i \ Y_i \ Z_i)^T$  of the photogrammetric targets. The principal distance  $c$ , the coordinates of the principal point  $(x'_0 \ y'_0)^T$  and the distortion parameters  $(\Delta x'_i \ \Delta y'_i)^T$  are the parameters of the so-called interior orientation of the camera. The exterior orientation includes the spatial position  $(X_0 \ Y_0 \ Z_0)^T$  of the perspective centre and the rotation matrix  $\mathbf{R}_j$ , which reads (Eq. 4):

$$\mathbf{R} = \begin{pmatrix} r_{11} & r_{21} & r_{31} \\ r_{12} & r_{22} & r_{32} \\ r_{13} & r_{23} & r_{33} \end{pmatrix} \quad (4)$$

For the spatial orientation of the camera for each image. A detailed derivation of Equations 1-4 is given by, *e. g.*, Luhmann *et al.* (2019). Seven additional independent condition equations solve the datum defect of the estimation problem. The condition equations prevent any translation, rotation or scaling of the network by transforming the adjusted network to the approximation values of the datum points (Papo, 1982). Including these equations, a Gauß-Markov model can be set up. While the image coordinates serve as observations, the interior and the exterior orientation parameters as well as the spatial coordinates of the marker positions are parameters to be estimated (Förstner and Wrobel, 2016; Luhmann *et*



*al.*, 2019). Since the parameters of the interior orientation are parameters to be estimated, this approach is known as self-calibration (Brown, 1971).

The estimated spatial coordinates of the photogrammetric markers are assigned for both the realization of a stable photogrammetric reference frame, which surrounds the measurement object, and deriving desired information about the measured object. Regarding the measurement campaign at Wettzell in 2020, the telescope was equipped with photogrammetric markers and rotated to different orientation positions. The spatial coordinates of the photogrammetric markers in different telescope positions were introduced to the calculation algorithm for the determination of the reference point of the SLR telescope (Lösler *et al.*, 2021; 2022).

During the measurement campaign further photogrammetric data were collected, which require an intermediate calculation step. In general, photogrammetric data acquisition means capturing images of an object from different positions providing as many different viewing angles as possible. Normally, the measured object remains fixed, and the camera is moved. But data acquisition also works inverted, i.e., when the camera is fixed and the measured object moves in front of the camera to take images from different viewing angles. Both strategies cannot be combined, if images contain subsets of moved and fixed photogrammetric markers. However, if, and only if, the moved marker subset is not related to the fixed reference frame via images, a contradiction-free combination by bundle adjustment is possible. Since the images of the moved object are unrelated to the fixed reference frame, the corresponding exterior orientation is determined only by the subset of photogrammetric markers at the moved object. In consequence of the unknown movement of the object, the camera is assumed to move in the opposite sense (Figure 2).

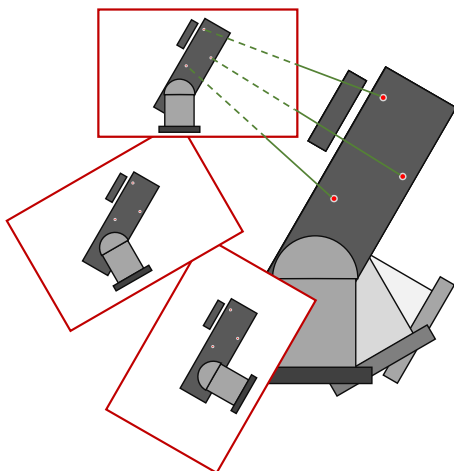


Figure 2. Estimated exterior orientations of subset images derived by the bundle adjustment; without image information concerning the fixed reference frame, the movement of an object, in this case the telescope, is interpreted as movement of the camera.

In order to provide correct spatial coordinates of the marker positions, the exterior orientations of these images, hereafter called subset images, have to be updated. In this approach, concatenated transformations relate the exterior orientations of the subset images to a reference exterior orientation referring to the fixed frame, which was obtained before the telescope rotated.

### B. Concatenated transformation

The bundle adjustment yields the exterior orientation parameters of all images and the spatial coordinates of the photogrammetric markers. Subset images, which are exclusively oriented by a consistently moved subset of photogrammetric markers, are not yet properly oriented with respect to the fixed photogrammetric reference frame. The spatial coordinates of the marker positions provided by these images have to be transformed using the exterior orientation parameters of the reference image (Figure 3).

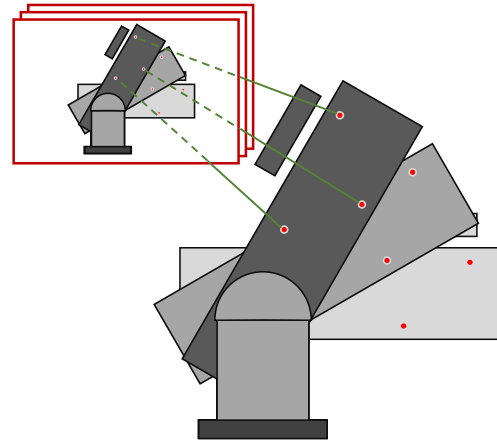


Figure 3. Re-oriented images after concatenated transformation; the rotation of the telescope is now apparent.

In fact, these exterior orientation parameters represent the true position and orientation of the camera at the time of the measurement. The set of exterior orientation parameters are combined to transform the spatial coordinates to the fixed photogrammetric reference frame. The concatenated transformation of the CRP-CT approach reads (Eq. 5):

$$\begin{pmatrix} X \\ Y \\ Z \end{pmatrix}_{\text{Ref}} = \begin{pmatrix} X_0 \\ Y_0 \\ Z_0 \end{pmatrix}_{\text{Ref}} + \mathbf{R}_{\text{Ref}}^T \mathbf{R}_S \left[ \begin{pmatrix} X \\ Y \\ Z \end{pmatrix}_S - \begin{pmatrix} X_0 \\ Y_0 \\ Z_0 \end{pmatrix}_S \right] \quad (5)$$

Where  $\mathbf{R}_{\text{Ref}}$  is the rotation matrix orienting the reference image,  $\mathbf{R}_S$  is the rotation matrix orienting the subset image. The translation vectors of the camera positions  $(X_0 \ Y_0 \ Z_0)_{\text{Ref}}^T$  and  $(X_0 \ Y_0 \ Z_0)_S^T$  belong to the reference image and to the subset image, respectively. The coordinates of an object point referring to the subset image are denoted by  $(X \ Y \ Z)_S^T$ , and  $(X \ Y \ Z)_{\text{Ref}}^T$  is the corresponding

corrected position. Thus, the transformation provides the spatial coordinates of the marker positions related to the photogrammetric reference frame. By applying the propagation of uncertainty to Equation 5, the fully populated dispersion matrix is obtained for the transformed positions. These coordinates and their dispersion serve as input data for the determination of the reference point.

### C. Reference point determination

The invariant reference point (IRP) of an SLR telescope is defined as the intersection of the azimuth axis and the elevation axis. If both axes do not intersect, the reference point is the point on the azimuth axis, which is nearest to the elevation axis. By definition, the IRP lies inaccessibly in the telescope structure and, therefore, can only be determined from targets, which are mounted at the telescope structure and measured in different telescope positions. Most commonly, polar measurement systems, *e.g.* total stations or laser trackers, provide the coordinates of the targets.

The simplest model for the calculation of biaxial telescopes like SLR or VLBI telescopes are spheres but this model is insensitive for any other telescope parameter except the position. Other approaches use circle models in different levels of complexity. When the telescope rotates around one axis while the other axis is fixed, targets at the turnable part of the telescope describe circles, which can be connected via several geometrical conditions (Eschelbach and Haas, 2003; Dawson *et al.*, 2007). Such models are rigorous but require dedicated telescope positions, and, thus, are unsuitable for a continuous reference point determination during regular telescope operations. The transformation model IRP-II presented by Lösler *et al.* (2018) overcomes the necessity of specific telescope positions, and provides the most complex set of telescope parameters.

The functional model of the IRP-II model reads (Eq. 6):

$$\mathbf{P}_{i,k} = \mathbf{P}_{\text{IRP}} + \mathbf{R}_x(\beta)\mathbf{R}_y(\alpha)\mathbf{R}_z^T(\kappa_k)\mathbf{R}_y(\gamma)\mathbf{1E} + \mathbf{R}_x(\omega_k)\mathbf{p}_i \quad (6)$$

And relates the point  $\mathbf{p}_i^T = (x_i \ y_i \ z_i)$  in a telescope fixed frame to its corresponding position  $\mathbf{P}_{i,k}^T = (X_i \ Y_i \ Z_i)$  in a fixed frame, *e.g.* the station network. The sub-indexed coordinate axes and the braced angles indicate the rotation axis and the rotation angle of the rotation matrices  $\mathbf{R}$ . Index  $k$  denotes the orientation of the telescope at the measurement time. The angles  $\omega_k$  and  $\kappa_k$  are the azimuth angle and the elevation angle, respectively. The axis offset is considered by  $\mathbf{E}^T = (0 \ e \ 0)$ . The tilt of the azimuth axis w.r.t. the  $Z$ -axis of the fixed frame is parametrized by the angles  $\alpha$ ,  $\beta$ , and  $\gamma$  is introduced to compensate for the deviation from the orthogonality of the two telescope axes. The translation vector  $\mathbf{P}_{\text{IRP}}$  is the invariant reference point.

The great advantage of IRP-II in contrast to former versions (Lösler, 2008), is that IRP-II overcomes the synchronization necessity between the measurement system and the telescope by introducing the rotation angles of the telescope as additional unknown parameters. Thereby the targets at the turnable part of the telescope can be measured during normal operations of the telescope. However, the application of the model depends on one condition: IRP-II requires at least two targets, which are observed at least partially at the same time. Photogrammetry fulfills this condition excellently, because images always contain several photogrammetric markers at the telescope. Therefore, the CRP approach as well as the CRP-CT approach presented in this contribution are suitable for data acquisition for IRP-II.

## III. MEASUREMENT SETUP

### A. Satellite Observing System Wettzell

The Geodetic Observatory Wettzell (GOW) is a GGOS core station and hosts all four space geodetic techniques. SLR telescopes measure the distances to satellites, which are equipped with retro reflectors. Therefore, an SLR telescope rotates around two axes, the azimuth axis and the elevation axis, to cover the sky. A rotatable protection dome encloses the telescope (*cf.* Figure 1). During a measurement campaign in 2020, close range photogrammetry was applied to determine the reference point of the SOS-W using the CRP approach for the first time. Further photogrammetric data was captured, the CRP approach was refined and integrated in an extended analysis procedure, which is presented for the first time and referred to as CRP-CT approach in this contribution.

### B. Measurement setup

Hexagon's Aicon DPA Industrial measurement system is chosen for the data acquisition and pre-analysis. The photogrammetry system consists of the digital camera C1, a Canon EOS 5D, which is protected by a robust and extremely stiff IP51-rated camera case, and the analysis software Aicon Studio 3D. The maximum permissible error (MPE) of a measured length between two signalized points is specified by  $15 \mu\text{m} + 15 \mu\text{m m}^{-1}$ . The typical standard deviation of a position-based measurement obtained by a bundle adjustment is stated by  $2 \mu\text{m} + 5 \mu\text{m m}^{-1}$  (Hexagon, 2019).

The DPA Industrial works with uncoded and coded circular black-and-white markers. About 225 14 bit coded markers at the dome wall and on the height level of the protecting dome establish the photogrammetric reference frame. Three certified scale bars, which are traced to the SI meter, provide the scale information for the photogrammetric reference frame, and contribute to all three coordinate components.

Furthermore, the dome wall is equipped with nine interoperable 1.5" drift nests, which magnetically support both reference markers for photogrammetric

systems and corner cube reflectors for multi-lateration coordinate measurement systems (Guillory *et al.*, 2020) and for polar measurement systems such as laser trackers or total stations (Lösler *et al.*, 2018). The interoperability facilitates the integration of the photogrammetric reference frame into the station survey network later on.

As in the CRP approach, the telescope is prepared with uncoded photogrammetric markers. The maximum distance between these markers and the elevation axis of the telescope is about 1 m and the markers cover an area of about 1 m<sup>2</sup>.

The CRP-CT approach works with additional coded markers on the telescope. Twelve coded markers are randomly attached between 14 uncoded markers (Figure 4). The coded markers at the telescope ensure a reliable orientation of the image while coded markers of the surrounding reference frame are covered and, therefore, are not captured.

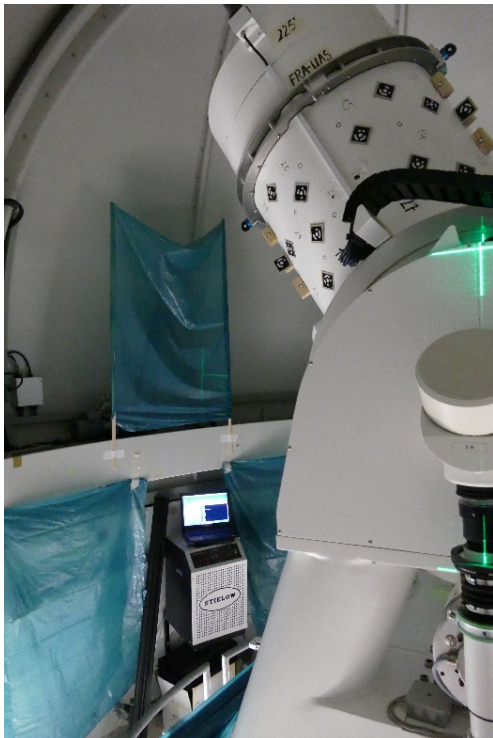


Figure 4. SLR-telescope prepared with coded and uncoded photogrammetric markers. The fixed photogrammetric reference frame in the background is covered with blue foil. The luminous green cross indicates the principal axis of the camera while the camera is fixed in the azimuthal reference position.

The telescope rotates to a specific azimuth and elevation position, which allows an excellent photogrammetric image capturing for the telescope markers in combination with the photogrammetric reference frame. The last image for this telescope position is captured from a fixed camera position, and is called the azimuthal reference image. For this camera position (Figure 5), as many telescope markers as possible have to remain visible, when the telescope rotates around the elevation axis.



Figure 5. Fixed camera position on a stable tripod for one of eight azimuthal reference positions. Photogrammetric reference points beyond the camera's field of view, for instance under the tripod, are not covered. Image acquisition is performed by remote control.

After capturing the azimuthal reference image, the photogrammetric reference frame behind the telescope is covered completely as shown in Figure 4. The telescope rotates stepwise to twelve elevation positions to cover the full range of motion of the axis, and the fixed camera captures one image per elevation position (Figure 4). Figures 4 and 5 show this scenario for elevation 225° from different perspectives. In absence of the reference frame in the background, the coded markers at the telescope exclusively define the exterior orientation of the image. From the perspective of the measurement process, the selection of the reference position of the telescope depends on two aspects: accessibility for photogrammetric measurements and a suitable position for the fixed camera. This study focuses on photogrammetric aspects; therefore, the azimuthal reference position is set to 90° elevation, which offers the widest configuration for image capturing.

To guarantee the stability of the camera position during all elevation positions referring to the azimuthal reference position, the camera is mounted on a stable tripod, and the images are captured via remote control. Once all elevation positions are measured, the cover of the photogrammetric reference frame is removed, and a new set of coded markers replaces the spent coded markers at the telescope. To avoid overlaps in the range of the point numbers, the removed coded markers must not be used again in the current experiment. The telescope rotates to the next azimuth position to continue the image capturing for the next azimuthal

reference position. In total, the telescope rotated to eight azimuth positions in combination with thirteen elevation positions in the CRP-CT approach.

Summarized, image capturing aims for three different aspects here:

- 1) For the determination of the photogrammetric reference frame, which is carried out at the beginning and at the end of an experiment.
- 2) For measuring different azimuth positions of the telescope, which will serve as azimuthal reference positions for the concatenated transformation.
- 3) For increasing the number of marker positions by further elevation positions, to cover the working range of the telescope.

The full configuration was performed independently twice, on day of year (DOY) 262 and 263 in 2020, respectively.

The effort of image capturing for the determination of the photogrammetric reference frame is identical in both the CRP and the CRP-CT approaches. The effort for acquiring the coordinates of the marker positions for different azimuth and elevation positions of the telescopes significantly differs in the two approaches. The conventional measurement of one telescope position requires approximately 20 images. For the CRP approach, all telescope positions consisting of up to six azimuth positions and seven elevation positions were measured conventionally. In the CRP-CT approach, only one elevation position per azimuth was measured conventionally, while twelve further elevation positions per azimuth were captured by one image each. The CRP-CT approach reduced the required time to less than a tenth compared to the CRP approach. Nevertheless, the time to cover the photogrammetric reference frame narrows the benefit depending on the concept of handling. For the purpose of a feasibility study, lightweight semi-transparent foil and wooden struts were sufficient (Figure 4). In total, the strategy of the CRP-CT approach at least halved the time effort for the data acquisition compared to the CRP approach or approaches using polar measurement systems with a comparable number of telescope positions.

#### IV. ANALYSIS AND RESULTS

The Aicon DPA Industrial measurement system includes the software package Aicon Studio 3D for storage management of the images, automated measurement of the image coordinates and pre-analysis to evaluate the quality and usability of the images. The bundle adjustment follows the procedure described in Section II A. The adjustment is based on the approximation values of the pre-analysis and provides the parameters of the interior orientation of the camera, the exterior orientations of the images, and the spatial coordinates of the photogrammetric markers. The datum refers to the nine markers defined by the

positions of the drift nests. Since only the standard deviations of the spatial coordinates are provided by the commercial software, the bundle adjustment was implemented in the in-house software JAiCov (2021). JAiCov reprocesses the final result from Aicon Studio 3D to obtain the fully populated dispersion matrix.

Lösler *et al.* (2021; 2022) studied the potential of close range photogrammetry for the reference point determination of an SLR telescope and presented the results of seven independent experiments applying the CRP approach at DOY 255-260 and 264 in 2020. The measurements for the CRP-CT approach were carried out in the same period at DOY 262 and 263. For the CRP-CT approach the mean standard deviations of the coordinate components of the marker positions in different telescope orientations are in the range of 0.01 mm to 0.02 mm. The values given in Table 1 are slightly smaller in comparison to the results of the experiments presented by Lösler *et al.* (2021). The reason can be found in the subset images, which participate in the solution of the bundle adjustment and refine the coordinates of the marker positions. Although they do not directly contribute to the determination of the absolute marker positions, they strengthen the geometric connection.

Table 1. Benchmark data of bundle adjustment of experiment days 262 and 263 in comparison with results for days 255, 256 and 264 given by Lösler *et al.* (2021):  $n_{obs}$  and  $n_{par}$  are the number of observations and unknowns, respectively. The mean standard deviations of the marker positions are  $\bar{\sigma}_X$ ,  $\bar{\sigma}_Y$ ,  $\bar{\sigma}_Z$  and  $\bar{\sigma}_{3D}$ . Standard deviations are given in mm.

DOY	$n_{obs}$	$n_{par}$	$\bar{\sigma}_X$	$\bar{\sigma}_Y$	$\bar{\sigma}_Z$	$\bar{\sigma}_{3D}$
255	64 367	10 015	0.03	0.03	0.02	0.05
256	82 905	13 003	0.03	0.03	0.02	0.05
262	36 763	4 828	0.02	0.02	0.01	0.03
263	44 299	5 572	0.01	0.01	0.01	0.02
264	120 005	13 663	0.02	0.02	0.01	0.03

The spatial coordinates of 112 marker positions, which belong to the eight azimuthal reference positions, were immediately used for the determination of the reference point. The marker positions derived by the subset images in different telescope positions had to be transformed to the photogrammetric reference frame using the formulas presented in Section II B. The number of transformed marker positions is 1268 at DOY 262 and 1282 at DOY 263, and does not meet the theoretical value 1344 resulting from eight azimuth and thirteen elevation positions. A small number of marker positions is missing because they were obscured by parts of the telescope structure during image acquisition or could not be measured due to a poor viewing angle. In total, for a single CRP-CT experiment 1380 and 1394 marker positions and their fully populated dispersion matrix were introduced to the reference point determination of DOY 262 and 263, respectively. For comparison, the CRP approaches of

DOY 264 provided 588 marker positions from six azimuth positions and seven elevation positions with the same number of markers at the telescope.

The calculation of the reference point of the SLR telescope followed the IRP-II model developed by Lösler *et al.* (2018) and presented in Section II C. Figure 6 depicts the results for the invariant reference point  $\mathbf{P}_{\text{IRP}}$  derived by the different photogrammetric approaches. The solutions of DOY 255 to 260 and 264 are taken from Lösler *et al.* (2022).

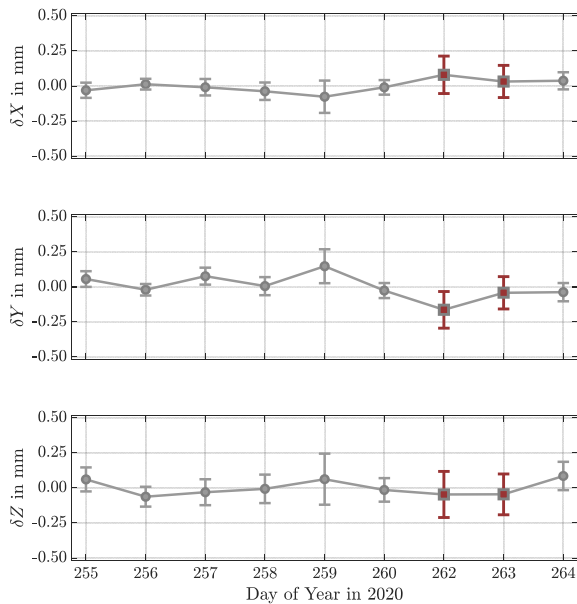


Figure 6. Results for the invariant reference point including  $3\sigma$  error bars derived by different photogrammetric approaches. The results of DOY 262 and 263 refer to the CRP-CT approach and are denoted by red squares. The results of the CRP approach are denoted by grey circle and were derived by Lösler *et al.* (2022).

The solutions of DOY 262 and 263 refer to the CRP-CT approach. They fit very well into the sequence of solutions derived by the CRP approach. The position of the reference point for nine individual experiments varies in the X-component by 0.16 mm, in the Y-component by 0.31 mm, and in the Z-component by 0.15 mm. The  $3\sigma$  confidence interval for the X-component and Y-component does not exceed 0.12 mm and 0.20 mm, respectively. The  $3\sigma$  confidence interval for the Z-component is the largest of the three components and amounts to 0.33 mm. The reason can be found in the measurement configuration for the uncoded markers at the telescope related to the surrounding reference frame. While the photogrammetric markers of the reference frame enclosed the reference point in the horizontal component, the height of the reference frame did not include all measured marker positions.

Even though the results of this photogrammetric approach fit very well into the results of the complete measurement campaign, the question of biased results in case of unfavorable recording configurations cannot be answered conclusively. A risk for biased results lies

in an unfavorable choice of the telescope's reference position, to which all elevation positions for this azimuth are related by the concatenated transformation. The configuration used in this approach does not have a noticeable negative effect on the results, especially not on the position of the reference point.

## V. CONCLUSION AND OUTLOOK

Improving the quality and reliability of local tie vectors is one of the major tasks in the EURAMET project GeoMetre. GGOS calls for an accuracy of 1 mm for the local ties, including the reference point determination of each space geodetic technique, the combination of the reference points in a consistent local reference frame, and the transformation of the local ties into the global reference frame. As many components as possible should have a high potential of automation in order to improve the acceptance of the application at multi-technique stations all over the world. Lösler *et al.* (2021; 2022) published promising results on the use of close range photogrammetry to determine the reference point at the SOS-W in Wettzell. This paper presented a modified method for using close range photogrammetry, which significantly reduces the measurement time. In this feasibility study, the measurement time was halved, while doubling the measured telescope positions. The accuracy of the position of the reference point was comparable to results derived from the observation material of polar measuring systems (Eschelbach and Haas, 2003; Lösler *et al.* 2018).

The use of close range photogrammetry also has the potential for automation. In the CRP-CT approach, the transformation parameters for the concatenated transformation were entirely obtained from the photogrammetric data. Modern total stations are equipped with on-board cameras, which provide images for a visual impression of the environment of the measurement object. The quality of the images does not yet reach the quality of a photogrammetric camera. However, first investigations to use these built-in cameras as measuring sensor show promising results (Schestauer *et al.* 2017). The combination of a total station with a high-quality built-in camera will be able to combine the advantages of polar observations and photogrammetric observations. The parameters of the exterior orientation of an image may then result from the orientation of the total station. The simultaneous measurement of polar observations to reflectors at the telescope will improve the stability of the algorithm. The number of photogrammetric markers is not relevant for the measurement time, and the measurement of a single reflector by a total station only costs seconds. Such a fast measurement configuration is suitable to eliminate the down times for surveying the reference point of VLBI and SLR telescopes during their regular operations. The application of the novel

approach presented in this contribution in combination with upcoming technological developments will reduce measurement times and effort for the reference point determination, leading to an increased deployment at multi-technique stations.

#### VI. AVAILABILITY OF DATA AND MATERIAL

All data analyzed in this investigation are available online. The data sets of the common CRP approach, *i.e.*, DOY 255-260 as well as 264, are available online at <https://doi.org/10.3390/app11062785>. The data sets of the novel CRP-CT approach, *i.e.*, DOY 262 and 263, are available at <https://doi.org/10.5281/zenodo.6482984>.

#### VII. ACKNOWLEDGEMENTS

We thank Svetlane Mähler and Dr. Stefan Riepl from the Geodetic Observatory Wettzell for their support during the fieldwork. This project 18SIB01 GeoMetre has received funding from the EMPIR programme co-financed by the Participating States and from the European Union's Horizon 2020 research and innovation programme.

#### References

- Brown, D.C. (1971). Close-Range Camera Calibration. *Photogrammetric Engineering*, 37, pp. 855–866.
- Dawson, J., P. Sarti, G. M. Johnston, and L. Vittuari (2007). Indirect approach to invariant point determination for SLR and VLBI systems: an assessment. *Journal of Geodesy*, 81(6-8), pp. 433–441. DOI: 10.1007/s00190-006-0125-x
- Eschelbach, C., and R. Haas (2003). The IVS-reference point at Onsala – high end solution for a real 3D-determination. In *Proceedings of the 16th Working Meeting on European VLBI for Geodesy and Astrometry*, Schwegmann, W., and Thorandt, V., Eds.; Bundesamt für Kartographie und Geodäsie, pp. 109–118.
- Förstner, W., and B.P. Wrobel (2016). Photogrammetric Computer Vision—Statistics, Geometry, Orientation and Reconstruction; *Geometry and Computing*, 11; Springer. DOI: 10.1007/978-3-319-11550-4
- GeoMetre (2020). *Large-Scale Dimensional Measurements for Geodesy - A Joint Research Project within the European Metrology Research Programme EMPIR*; European Commission (EC), Grant Number: 18SIB01; EURAMET e.V.: Brunswick, Germany. DOI: 10.13039/100014132
- Glaser, S., M. Fritsche, K. Sošnica, C.J. Rodríguez-Solano, K. Wang, R. Dach, U. Hugentobler, M. Rothacher, and R. Dietrich (2015). Validation of Components of Local Ties. In *REFAG 2014*; van Dam, T., Ed.; Springer; Vol. 146, pp. 21–28. DOI: 10.1007/1345\_2015\_190
- Guillory, J., D. Truong, and J.-P. Wallerand (2020). Uncertainty assessment of a prototype of multilateration coordinate measurement system. *Precision Engineering*. DOI: 10.1016/j.precisioneng.2020.08.002
- Hexagon (2019). AICON DPA Series—Unrivalled High-End Photogrammetry Systems, Datasheet; Hexagon Manufacturing Intelligence: Shenzhen, China. Available online: <https://hexagonmi.com> (accessed on 22 December 2021)
- JAIcCov (2021). Java Aicon Covariance matrix—Bundle Adjustment for Close-Range Photogrammetry. Available online: <https://github.com/applied-geodesy/bundle-adjustment> (accessed on 15 December 2021).
- Luhmann, T., S. Robson, S. Kyle, and J. Boehm (2019). *Close-Range Photogrammetry and 3D Imaging*, 3rd ed.; de Gruyter: Berlin, Germany. DOI: 10.1515/9783110607253
- Lösler, M. (2008). Reference point determination with a new mathematical model at the 20 m VLBI radio telescope in Wettzell. *Journal of Applied Geodesy*, 2(4), pp. 233–238. DOI: 10.1515/JAG.2008.026
- Lösler, M., C. Eschelbach, and T. Klügel (2022). Close Range Photogrammetry for High-Precision Reference Point Determination: A Proof of Concept at Satellite Observing System Wettzell. In *Proceedings of the 2021 IAG Symposium*; Freymueller, J.T. and Sánchez, L., Eds.; Springer. DOI: 10.1007/1345\_2022\_141
- Lösler, M., C. Eschelbach, T. Klügel, and S. Riepl (2021). ILRS Reference Point Determination using Close Range Photogrammetry. *Applied Sciences*, 11(6), 2785, 2021. DOI: 10.3390/app11062785
- Lösler, M., C. Eschelbach, and S. Riepl (2018). A Modified Approach for Automated Reference Point Determination of SLR and VLBI Telescopes. *Technisches Messen*, 85(10), pp. 616–626. DOI: 10.1515/teme-2018-0053
- Papo, H.B (1982). Free Net Analysis in Close-Range Photogrammetry. *Photogrammetric Engineering and Remote Sensing*, 48(4), pp. 571–576.
- Pollinger, F., S. Baselga, C. Courde, C. Eschelbach, L. García-Asenjo, P. Garrigues, J. Guillory, P. O. Hedekvist, T. Helojärvi, U. Kallio, T. Klügel, P Köchert, M. Lösler, R. Luján, T. Meyer, P. Neyezhmakov, D. Pesce, M. Pisani, M. Poutanen, G. Prellinger, A. Röse, J. Seppä, D. Truong, R. Underwood, K. Wezka, J.-P. Wallerand, and M. Wiśniewski (2022). The European GeoMetre project – developing enhanced large-scale dimensional metrology for geodesy. *5th Joint International Symposium on Deformation Monitoring (JISDM)*, 20-22 June 2022, Valencia, Spain.
- Schestauer, B.-J., A. Wagner, W. Wiedemann, and T. Wunderlich (2017). Tachymetrisches 6DOF-Messverfahren. In *Ingenieurvermessung 17: Beiträge zum 18. Internationalen Ingenieurvermessungskurs Graz*; Lienhart, W., Ed.; Wichmann: Offenbach, Germany, pp. 213-220.

## Adaptive spatial discretization using reinforcement learning

Jemil Avers Butt<sup>1, 2</sup>, Andreas Wieser<sup>1</sup>

<sup>1</sup>Institute of Geodesy and Photogrammetry, ETH Zürich, Stefano-Francini-Platz 5, 8093 Zurich, Switzerland, ([jemil.butt@geod.baug.ethz.ch](mailto:jemil.butt@geod.baug.ethz.ch); [andreas.wieser@geod.baug.ethz.ch](mailto:andreas.wieser@geod.baug.ethz.ch))

<sup>2</sup>Atlas optimization GmbH, Zürich, Switzerland, ([jemil.butt@atlasoptimization.ch](mailto:jemil.butt@atlasoptimization.ch))

**Key words:** *spatial discretization; monitoring; reinforcement learning; optimization; neural networks*

### ABSTRACT

A well-known challenge for deformation monitoring is the spatial discretization, *i.e.* the choice of monitoring points at which measurements are to be taken. Well-chosen monitoring points employ prior knowledge to yield a significant amount of information about a certain aspect of the monitored object. However, the choice of such a set of points is typically made to be practically expedient or left to the measurement instrument itself. We aim to derive adaptive discretization strategies that implicitly incorporate domain knowledge about the monitored object via a cycle of interaction and learning. In those strategies, previous measurements impact the locations of subsequent ones. We formulate the choice of monitoring points as a decision theoretical problem and review the framework of reinforcement learning which formalizes the problem of deriving optimal sequential decisions under uncertainty. Iterative algorithms produce solution schemes for this optimal control task. We benchmark the performance of reinforcement learning and compare its results to random, pseudorandom, and numerically designed discretization strategies on several geodetically motivated examples. Advantages, disadvantages, and practical feasibility of the approach are evaluated and reveal a significant boost in efficiency of the data collection scheme compared to classical approaches.

*This contribution was selected by the Scientific Committee for publication as an extended paper in Applied Geomatics <https://www.springer.com/journal/12518>*

## Bridge deformations during train passage: monitoring multiple profiles using concurrently operating MIMO-SAR sensors

Andreas Baumann-Ouyang<sup>1</sup>, Jemil Avers Butt<sup>1,2</sup>, Andreas Wieser<sup>1</sup>

<sup>1</sup> Institute of Geodesy and Photogrammetry, ETH Zürich, Stefano-Franscini-Platz 5, 8093 Zurich, Switzerland, ([andreas.baumann@geod.baug.ethz.ch](mailto:andreas.baumann@geod.baug.ethz.ch); [jemil.butt@geod.baug.ethz.ch](mailto:jemil.butt@geod.baug.ethz.ch); [andreas.wieser@geod.baug.ethz.ch](mailto:andreas.wieser@geod.baug.ethz.ch))

<sup>2</sup> Atlas optimization GmbH, Zürich, Switzerland, ([jemil.butt@atlasoptimization.ch](mailto:jemil.butt@atlasoptimization.ch))

**Key words:** *synthetic aperture radar (SAR); structural health monitoring (SHM); bridge monitoring; deformation; vibration*

### ABSTRACT

Sensors capable of measuring surface deformations with areal coverage and high spatial and temporal resolution are beneficial for many monitoring applications. However, such sensors are typically expensive, or their configuration cannot be adapted flexibly by the user like in case of satellite-based systems. Automotive Multiple-Input-Multiple-Output Synthetic Aperture Radar (MIMO-SAR) systems are interesting potential alternatives associated with low cost and high flexibility. In this paper, we present an experimental investigation showing the capabilities of a particular off-the-shelf, automotive radar system for structural monitoring. We analyse the accuracy of the measured line-of-sight displacements, the spatial and temporal resolution, and the impact of simultaneous coverage of the same area by two sensors of the same type. Finally, we demonstrate the MIMO-SAR system in a real-world use case measuring deformations of a railway bridge in response to dynamic load by trains passing over it. We operated two MIMO-SAR sensors simultaneously, analyse and interpret the individual interferograms and combine the data to derive the temporal and spatial distribution of vertical displacements along selected profiles. The results show that off-the-shelf automotive-grade MIMO-SAR systems can be used to quantify sub-millimetre deformations of structures and derive high-resolution time series beneficial for structural health monitoring applications.

### I. INTRODUCTION

#### A. Overview

Many natural and artificial structures are monitored to mitigate the risk of failure or fatal events, e.g. landslides (Chae *et al.*, 2017), dams (Scaioni *et al.*, 2018), or bridges (Enckell, 2011; Lienhart *et al.*, 2017, Galmarini *et al.*, 2020). A large variety of sensors with different strengths and weaknesses is being applied for deformation monitoring. Radar sensors are particularly attractive because of their areal coverage, the high sensitivity with respect to deformations, and their capability to provide useful signals in a large range of weather conditions. Terrestrial radar interferometry (TRI) can measure surface deformations with sub-millimetre precision and a temporal resolution on the level of milliseconds (Rödelsperger, 2011; Caduff *et al.*, 2015; Baumann-Ouyang *et al.*, 2021). It is therefore a technology with potential applications in structural health monitoring (SHM) as changes of the frequency response of a structure over time can be used to identify and locate potential damage (Sampaio *et al.*, 1999, Holst *et al.*, 2020). As of now, the actual application of TRI in this field is mainly limited to scientific investigations. This could change with a special type of low-cost radar systems: Multiple Input Multiple Output Synthetic Aperture Radar (MIMO-SAR) systems. These systems are currently developed

particularly for automotive applications and allow quantifying line-of-sight (LOS) displacements with 2D spatial resolution over a wide field of view (almost 180°), with high data rate (>100 Hz) and with very high precision ( $\mu\text{m}$ -level standard deviations) despite the low-cost.

MIMO-SAR systems employing frequency modulated continuous waves (FMCW) have thus been applied already for monitoring bridges (Miccinesi *et al.*, 2021; Pieraccini *et al.*, 2019; Tian *et al.*, 2019) and buildings (D'Aria *et al.*, 2019). In each of these applications, only one MIMO-SAR system at a time was used. Due to the low cost, it is also feasible to operate several MIMO-SAR systems simultaneously and covering the same object from different viewing angles. This allows (i) improving the spatial coverage, e.g. by acquiring multiple profiles, and (ii) improving the information content by deriving displacement vectors in an external coordinate frame rather than LOS displacements only. However, using FMCW radar systems with the same or similar frequencies may cause interference and degrade the resulting observations (Amar *et al.*, 2021).

In this work, we investigate the influence of using equal or different frequencies when operating two MIMO-SAR systems simultaneously with overlapping spatial coverage. We then deploy the MIMO-SAR systems for monitoring a railway bridge and derive the vertical displacements caused by trains passing over it.



We first review the principles of MIMO-SAR, then introduce the experimental devices in Section II. In Section III we investigate interference, and in Section IV we describe and analyse the bridge monitoring experiment. We conclude in Section V.

### B. Principles of MIMO-SAR

Terrestrial radar interferometry is a measurement technique used in combination with FMCW radar systems (Rödelsperger, 2011). A transmitting antenna (TXA) emits an electromagnetic wave that is reflected within illuminated scene and subsequently registered by a receiving antenna (RXA). Range resolution is a consequence of the bandwidth of the signal, angular resolution is either achieved by large rotating antennas (real aperture radar, RAR) or by small antennas radiating and receiving at different positions (synthetic aperture radar, SAR). MIMO-SAR implements the latter principle using multiple TXA and RXA in a fixed assembly.

Each pair of TXA and RXA creates one virtual antenna (VA). The TXA and RXA can be positioned in such a way that all resulting VA are arranged linearly and regularly separated, representing a uniform linear array (ULA). For such a system, we define a 3D cartesian coordinate system with its  $X^R$ -axis along the ULA, the  $Y^R$ -axis parallel to the antenna boresight direction, and the  $Z^R$ -axis complementing a right-handed system (Figure 1). The position of a scatter  $S_i$  in this coordinate systems can also be expressed in polar coordinates with:

- range  $R_i$  i.e., distance between the centre of the ULA and  $S_i$ ,
- azimuth  $\theta_i$  i.e., deflection from boresight in the  $X^R Y^R$ -plane; and
- elevation  $\varepsilon_i$  i.e., deflection from  $X^R Y^R$ -plane.

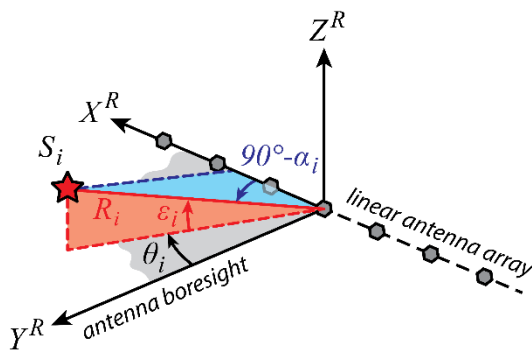


Figure 1. Definition coordinate system and angles (see text) of a MIMO-SAR system with linear antenna array.

Azimuth and elevation are commonly used to indicate angles within or from a horizontal plane. For simplicity we still use these terms herein although the  $X^R Y^R$ -plane of a MIMO-SAR sensor does not have to be horizontal and thus, in this paper, azimuth and elevation do not refer to the gravity field of the Earth.

The radar instrument is not sensitive to azimuth and elevation but instead yields the range  $R_i$  and the cross-range angle  $\alpha_i$  which is the angle between the  $Y^R Z^R$ -plane and the line-of-sight to  $S_i$ . For scatterers close to the  $X^R Y^R$ -plane, however, cross-range and azimuth are approximately equal.

The result of one measurement is the phase  $\phi$ . The outcome of one full radar acquisition is a single look complex image (SLC) i.e., a complex-valued matrix whose dimension corresponds to the number of resolution cells in range and cross-range. The complex numbers represent the amplitude and phase of the radar signal scattered back by the surfaces at the location corresponding to the respective range and cross-range. The amplitude encodes the total power scattered back to the radar instrument from the corresponding surfaces. The phase is related to the range  $R$  of the scatterer and the wavelength  $\lambda$  of the signal as (Eq. 1):

$$\phi = \frac{(2 \cdot \pi) \cdot (2 \cdot R)}{\lambda} \pmod{2\pi} \quad (1)$$

The core idea of TRI is to calculate the line-of-sight (LOS) displacement  $\Delta D_{LOS}$  of the respective surfaces between two epochs  $t_1$  and  $t_2$  from the phase measurements obtained at those epochs (Eq. 2):

$$\Delta D_{LOS} = (\phi_{t_1} - \phi_{t_2}) \cdot \frac{\lambda}{4\pi} \quad (2)$$

Depending on the instrument's configuration and data rate, this allows measuring displacements at high temporal and spatial resolution. Displacements as small as a few  $\mu\text{m}$  can be detected. Displacements larger than  $\lambda/4$  are ambiguous due to Equation 1 but can still be recovered by phase unwrapping (e.g., Yu *et al.*, 2019).

The actual displacement will typically not occur in the LOS direction. However, if the direction of displacement in relation to the radar's coordinate system is known from other sources, or if LOS measurements are made simultaneously with instruments from different locations, the LOS displacement, Equation 2, can be transformed into the actual displacement. We use the former approach in Section IV where we set up radar sensors below the bridge with the antenna array parallel to a vertical plane through the longitudinal axis of the bridge, and the antenna boresight inclined by an angle  $\nu$  above the horizon. The situation is indicated in Figure 2.

The relation between vertical displacement  $\Delta U_i$  and LOS displacement  $\Delta D_{LOS_i}$  can be derived directly from the figure in this case (Eq. 3):

$$\Delta U_i = \Delta D_{LOS_i} \cdot \sin(\nu + \alpha_i) \quad (3)$$

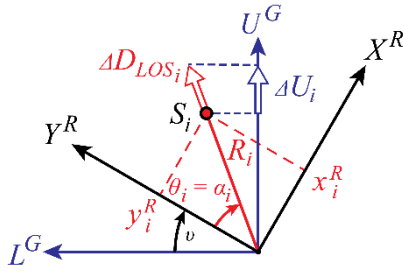


Figure 2. Relation of vertical displacement  $\Delta U_i$  and the MIMO-SAR system's LOS displacement  $\Delta D_{LOS_i}$  for a specific setup of the radar instrument and a scatterer within the instrument's  $X^R Y^R$ -plane ( $U^G$  indicates the up-direction in the local gravity field, and  $L^G$  the longitudinal axis in the horizontal plane).

## II. EXPERIMENTAL DEVICE

### A. Characteristics of the experimental Device

For our experimental investigations, we use two Texas Instruments TIDEP-01012 (Rev. E) MIMO-SAR systems (see Figure 3). Each of these devices has 12 transmitting and 16 receiving antennas arranged such as to yield  $N = 86$  virtual antennas spaced by  $\lambda/2$  in a ULA where  $\lambda$  denotes the average wavelength. The instrument's frequency range is 77 to 81 GHz, limiting the configurable bandwidth  $\Delta f$  to a maximum of 4 GHz. This implies a range and cross-range resolution of (Eqs. 3 and 4):

$$\Delta r = \frac{c}{2 \cdot \Delta f} \geq 3.75 \text{ cm} \quad (4)$$

$$\Delta \theta = \frac{2}{N \cdot \cos(\theta_k)} = \frac{1.33 \text{ deg}}{\cos(\theta)} \quad (5)$$

respectively, see (Baumann-Ouyang *et al.*, 2021) and (Rao, 2018) for details. In the configuration used herein, the systems cannot distinguish different elevations but rather integrate the signals from all scatterers within  $\pm 20$  deg elevation (corresponding to the antenna beam width) into the SLC bin corresponding to the respective azimuth and cross-range. We have so far used the system with acquisition rates of up to 400 Hz, *i.e.* obtaining up to 400 SLCs per second. Due to memory and communication bandwidth constraints the evaluation boards used herein do not allow arbitrarily long continuous data acquisition but require a break of a few seconds for data transfer after a maximum of 65'535 SLCs.

### B. Accuracy

In Baumann-Ouyang *et al.* (2021), we showed that the accuracy and the range of application of the TIDEP are affected by noise and biases. In previous investigations, we observed an empirical standard deviation of approximately  $7 \mu\text{m}$  for a time series of deformations associated to a single pixel at a distance of 20 m from the instrument and sampled at 400 Hz. Temperature variations of the onboard chips introduce scale-factor

variations of approximately 10 ppm in the initial warm-up phase. On a longer timescale, the uncertainty of the phase observations is dominated by meteorological changes—especially changes in humidity and temperature. A change of temperature by  $+2^\circ\text{C}$  or of relative humidity of  $+4\%$ , not accounted for, creates the same phase change as an actual deformation of around  $50 \mu\text{m}$  at a distance of 20 m and under standard atmospheric conditions, as can be verified using the equations given by R ueger (2002).

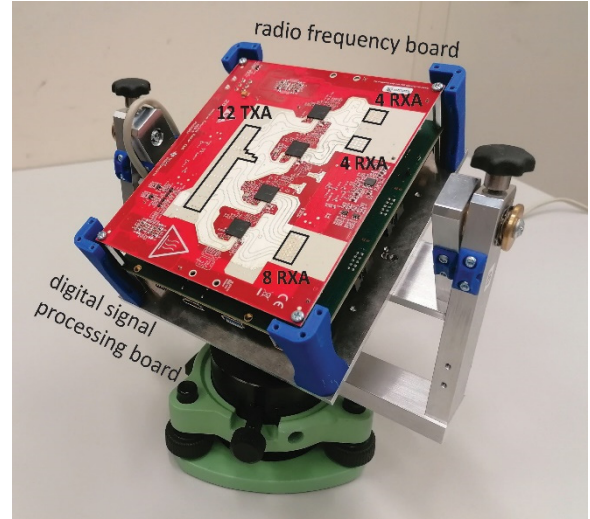


Figure 3. TIDEP-01012 (digital signal processing board, and radio frequency board with 12 TXA and 16 RXA) on custom made holder for mounting during experiments.

### C. Chirp Configuration

The TIDEP-01012 MIMO-SAR system supports a wide range of chirp configurations when operated via the native Texas Instruments mmWave Studio software and Lua scripting. For the following investigations, we used two different configurations, see Table 1, which result in a range resolution of 10 cm with a maximum unambiguous distance of 51 m.

Table 1. Chirp, timing, and analogue/digital conversion (ADC) parameters for the experiments

Parameter configuration		
	F1	F2
Centre Frequency $f_c$ [GHz]	77.95	79.95
Sweep Bandwidth $\Delta f$ [MHz]	1498.5	
Frequency Slope $s_c$ [MHz/ $\mu\text{s}$ ]	65.854	
Idle Time $T_{idle}$ [ $\mu\text{s}$ ]	3	
ADC Starting Time $T_{ADC,Start}$ [ $\mu\text{s}$ ]	3	
Ramp Duration $T_{Ramp}$ [ $\mu\text{s}$ ]	28	
Frame Duration $T_{Frame}$ [ $\mu\text{s}$ ]	372	
Samples per Chirp $N_{ADC}$ [-]	512	
ADC Sampling Frequency $f_{ADC}$ [MHz]	22.5	

Figure 4a shows a typical FMCW chirp and some of the parameters. The acquisition of an entire scene requires to consecutively emit a chirp from every TXA (Figure 4b-c) which takes a time of  $T_{Frame}$ . A subsequent acquisition can be started after a short

break of  $T_{InterFrame}$ . This break is required because of the limited onboard storage rate and needs to last between 0.3 and 1342 ms (Texas Instruments, 2020).

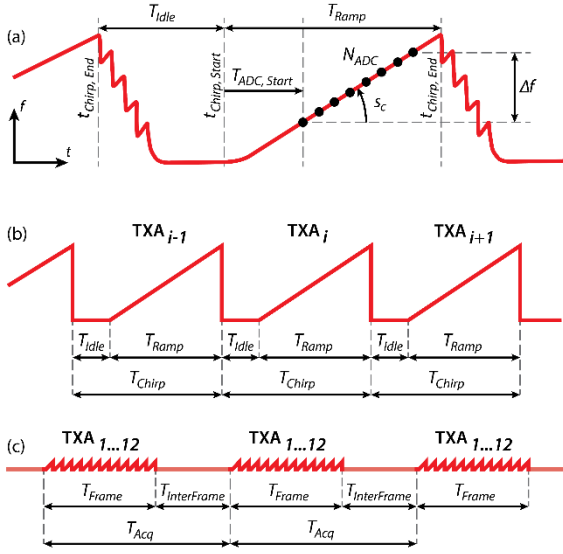


Figure 4. FMCW acquisition with associated chirp and timing parameters: (a) typical FMCW chirp; (b) simplified chirps for a series of consecutively emitting TXA; and (c) frame structure to acquire an entire dataset. Adapted from (Dham, 2020).

### III. EXPERIMENTAL INVESTIGATION OF INTERFERENCE

#### A. Interference

Using two or more sensors simultaneously allows to observe different parts of a larger structure at the same time. However, the presence of multiple radar sensors with uncoordinated transmissions at the same frequencies is known to impact the measurements negatively (Amar *et al.*, 2021) because of unwanted interference. This results from signals of one instrument being received by another instrument and mixing with that instrument's own signals. A future solution to avoid unwanted interference could be based on time synchronisation of all the devices, *e.g.* by triggering the sensors with a common timing signal like a GNSS pulse per second or a dedicated controller. With only one sensor active at a time, the available frequency bands would be used optimally. However, there is currently no synchronization solution available for the given MIMO-SAR systems. One option to avoid interference in this case is to use non-overlapping frequency bands (like configurations F1 and F2 in Table 1) which deteriorates the attainable range resolution, see Equation 4, as compared to using the whole bandwidth. An alternative is to accept the presence of interference but pseudo-randomize its temporal appearance by providing inter-frame periods much larger than the frame durations (see Figure 4) and using slightly different inter-frame periods for the different devices. In this way, the chirps emitted by the different devices will overlap only at some times and thus cause interference during short periods while not overlapping at others. The likelihood

of interferences could be further reduced by using narrower bandwidth or steeper frequency slopes and by (further) increasing the inter-frame periods at the cost of temporal and spatial resolution. While this pseudo-randomizing approach is only useful for applications where the times with interference can be detected from the results and filtering out those times does not impair the benefit of the measurement system, we will use this approach herein for the opposite purpose, *i.e.* to assure that we actually do have interference at some times.

#### B. Experimental setup

In Baumann-Ouyang *et al.* (2021), we showed that the TIDEP-01012 MIMO-SAR system can reliably detect movements of a corner cube by as few as 25  $\mu\text{m}$  in an indoor environment. We repeated the experiment in a 23 m long hallway with relatively stable atmospheric conditions to investigate the influence of two radar sensors concurrently emitting signals, herein.

The two instruments were set up next to each other facing along the hallway. A corner cube with an edge length of 40 mm was mounted on a motorised translation stage located at a distance of roughly 19 m, see Figure 5, and moved over a total distance of 2.5 mm in steps of 25  $\mu\text{m}$ , remaining stable for two seconds at each location. The experiment was carried out twice, using the same configuration (F1, see Table 1) of both radar instruments once, *i.e.*, overlapping frequencies, and different configuration (F1, F2), *i.e.*, non-overlapping frequencies, the other time.

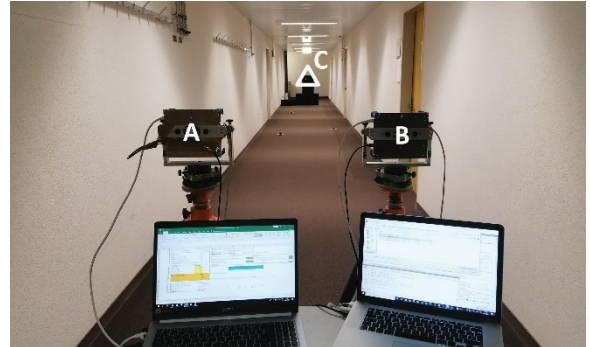


Figure 5. Measurement setup for the indoor experiment. A and B indicate the two TIDEP-01012 devices and C denotes the corner cube.

We cannot choose  $T_{InterFrame}$  short enough to assure close to 100% temporal overlap between the chirps of the two devices and using the same acquisition rate  $T_{Acq}$  for both devices would lead to a constant but unknown chirp overlap and thus amount of interference. So, we chose acquisition rates  $T_{Acq} = 1250 \mu\text{s}$  and  $T_{Acq} = 1251 \mu\text{s}$  for the two devices, respectively. This results in a complete overlap of the chirps every 1.25 s and at least a partial overlap for approximately 60% of the time, thus enabling us to investigate the effect of interference.

### C. Results and analysis

We formed interferograms and derived the cumulative displacements representing the motion of the corner cube mounted on the translation stage. Figure 6 shows excerpts of the resulting time series for device A and for times with overlapping (top) and non-overlapping frequencies (bottom) of the two, simultaneously operating devices. The RMSE of these observations are approximately  $6.4\ \mu\text{m}$  when the frequencies overlap and  $5.7\ \mu\text{m}$  when they do not. Both values are comparable to the empirical standard deviation of  $7\ \mu\text{m}$  based on earlier experiments (see Section II). Similar results are also obtained for other parts of the scene monitored during these experiments: Figure 7 shows the calculated displacements for a bin representing a rough plastered wall *i.e.*, a stable diffusive natural reflector instead of a moving corner cube. The RMSE values for these observations are  $6.5\ \mu\text{m}$  and  $5.5\ \mu\text{m}$ , respectively. Since the interference varies over time it does not show up strongly in the RMSE values, but it is visually recognizable by the distinct peaks in Figures. 6 (top) and 7 (top).

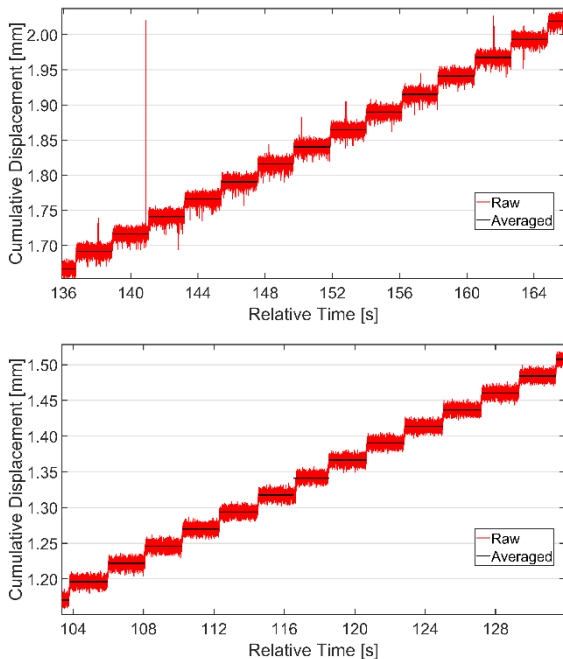


Figure 6. Cumulative displacement measurement observed by instrument A for one bin representing a corner cube for the acquisition setup with overlapping (top) and non-overlapping frequencies (bottom).

Based on this analysis, we can confirm that overlapping frequencies cause interference leading to corrupted measurements. However, with the devices used herein the impact is surprisingly small, may be reduced by filtering the displacement time series, and may even be negligible for many applications. We leave it for future work to study the interference more comprehensively and clarify whether there are circumstances where the impacts are much larger or would possibly even affect phase-unwrapping.

However, if the resulting reduced bandwidths are sufficient, it is advisable to avoid overlapping frequencies and instead use disjoint sets of frequency ranges when operating two or more radar instruments simultaneously.

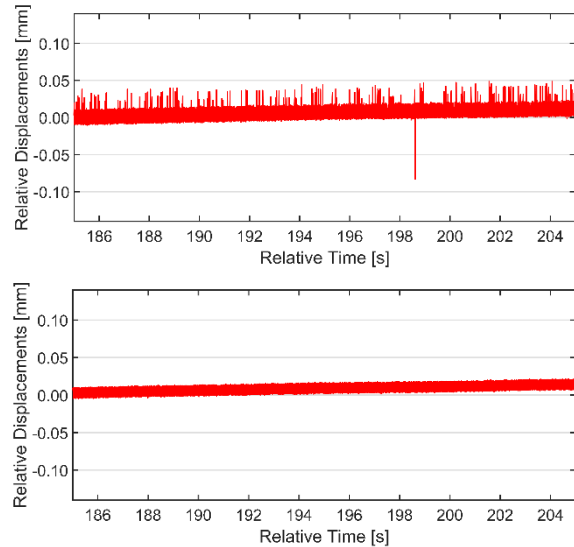


Figure 7. Cumulative displacement measurement observed by instrument A for one bin representing an area on the wall at the end of the floor for the acquisition setup with overlapping (top) and non-overlapping frequencies (bottom). In both cases, a trend caused by warm-up (Baumann-Ouyang *et al.*, 2021) is visible.

## IV. EXPERIMENTAL MONITORING APPLICATION

### A. Experimental setup

We selected a twin-track, prestressed concrete train bridge as an object for monitoring using MIMO-SAR sensors. The bridge is subject to short-term deformations at the sub-mm level with trains passing on top. Two radar instruments (A, B) were mounted on tripods below the bridge, see Figures 8 and 9. They were set up with their antenna array in a vertical plane along the bridge and the antenna boresight tilted upward with an elevation of approximately  $45^\circ$  *i.e.*, using a geometric configuration as depicted in Figure 2. The acquisition rate was set to 100 Hz and the other parameters were set for non-overlapping frequencies according to the values in Table 1.



Figure 8. Situation during the bridge monitoring experiment where A and B indicate the two TIDEP-01012 devices, P1-P3 selected areas on the upper soffit, MP and TS a metallic platform and a tram shelter, respectively.

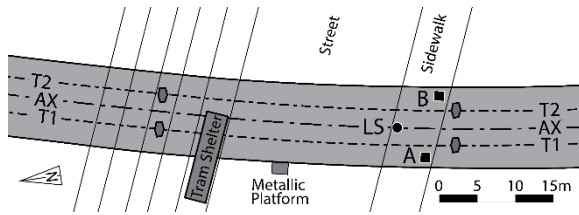


Figure 9. Map of the measurement setup for the bridge monitoring experiment where A and B indicate the locations of the two TIDEP-01012 devices, LS the location of a laser scanner, T1 and T2 the axes of the train tracks and AX the symmetry axis.

### B. Initial observations and processing

An exemplary amplitude image can be seen in Figure 10 (top). It shows the typical distribution of amplitudes for the acquisition geometry sketched in Figure 8. Metallic constructions like the tram shelter or the metallic platform on the bridge, with appropriate orientation relative to the radar instruments, produce high amplitude signal returns. Also some other surfaces yield strong signal returns, with the strongest ones being found for surfaces illuminated almost orthogonally (*i.e.*, line-of-sight perpendicular to the surface) and for surfaces locally representing corner cube like shapes.

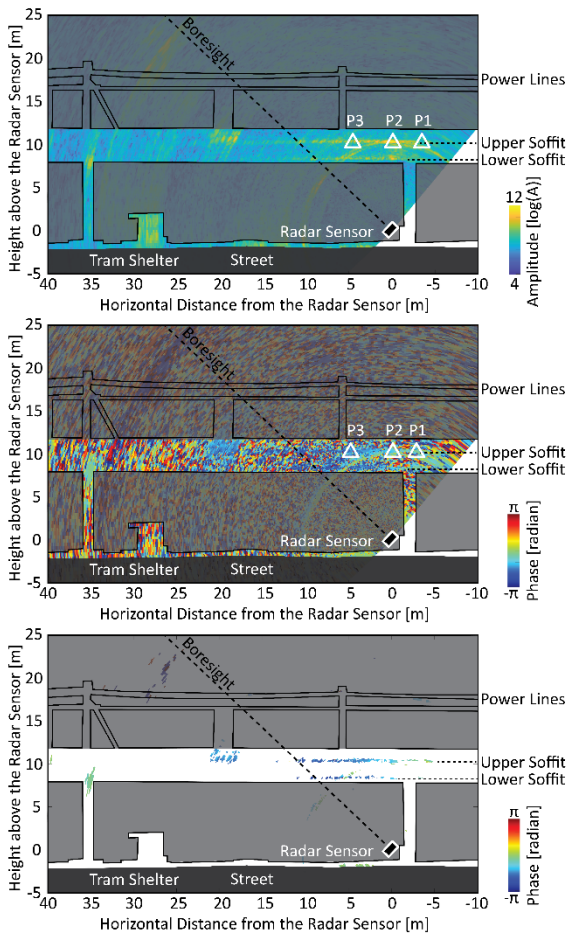


Figure 10. Image of the interferometric amplitudes (top) and phases (centre) of radar instrument A for the bridge experiment, and the bins remaining after filtering (bottom). The images are overlaid with a mask highlighting the parts of the scene visible (non-obstructed) for the instruments.

An example of an unfiltered interferometric phase image can be seen in Figure 10 (centre). This interferogram was computed from two SLCs gathered 148 seconds apart, one of them during an unloaded state and one while a train passed over the bridge. The interferogram mostly consists of random noise, because much of the scene shown in the figure is either empty space (air, not reflecting the radar signal sufficiently) or obstructed (the radar signals do not penetrate the pillars, bridge deck and other solid objects). Upon closer inspection, some small areas with little noise can be seen, e.g. a circular area at a distance of about 10 m. The same area stands out also in the amplitude image. The circle intersects with the upper soffit of the bridge; the radar signals are strongly reflected there because of the orthogonal LOS and the planar concrete surface. The circular area is a sidelobe caused by the impact of the particularly strong reflection at point P2 and the synthetic aperture data processing for cross-range resolution.

Before analysing the interferograms, areas with low amplitude and thus high phase-noise need to be excluded. We do this herein by thresholding on coherence ( $\geq 0.9$ ) after (Touzi *et al.*, 1999) and amplitude stability index ( $\geq 0.75$ ) after (Ferretti *et al.*, 2001). The result of this selection process is a relatively small set of persistent scatterers (less than 1% or 1300 of the bins from the SLCs) which are shown in Figure 10 (bottom) as points with colour corresponding to phase change.

Looking at this filtered interferogram, we can now identify the areas represented well by the radar images. A comparison with Figure 8 shows that the upper and lower soffit with an angle of incidence of less than  $45^\circ$  are observable, the metallic platform at the bridge, and the upper corner of the bridge pier at 35 m. Considering the colours with dark blue indicating a displacement of  $\pi$  rad *i.e.*, approximately 1 mm, towards the radar instrument and dark red 1 mm away, we notice a downwards displacement of the soffit and the metallic platform of roughly 0.5 mm with the train passing over the bridge. Little to no deformations is indicated at the locations of the two bridge piers at -2.5 and 35 m. These results are in accordance with the expected behaviour.

Spatial and temporal registering is required to compare or combine the acquisitions of both radar sensors. A coarse temporal registration was given by the timestamps of the computers used for data logging, and the registration was manually improved by shifting the timeseries of sensor B such that signals caused by trains passing occurred approximately simultaneously for both sensors. Better or automated temporal registration was not needed herein but could be achieved by cross-correlation using signals created by trains passing in both directions and on both tracks. The spatial registration was achieved by direct georeferencing of the radar sensors using geodetic measurements.

### C. Results and analysis

Ten trains passed over the bridge while the radar instruments were measuring. Figures 11 - 13 show the vertical displacements caused by a passing train driving on the track at the side of sensor A. The vertical displacements were calculated from the LOS displacements using Equation 3. The first figure shows the displacements-over-time for three selected bins (P1-P3, see Figures 8 and 10). For this graphic the time series have been down-sampled from 100 to 50 Hz for direct comparison with laser scanning observations (LS@P3) of P3, available from a different experiment (see Meyer *et al.*, 2022). P1 is located next to a bridge pier, and only small displacements are to be expected for this point.

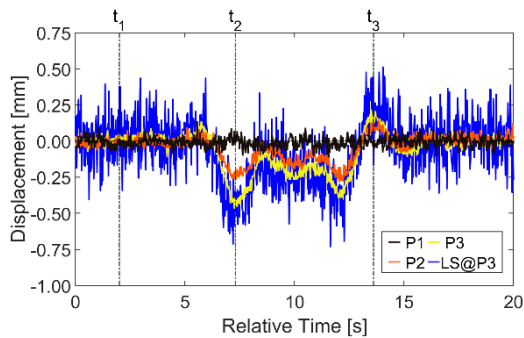


Figure 11. Displacement over time for three different positions along the bridge.

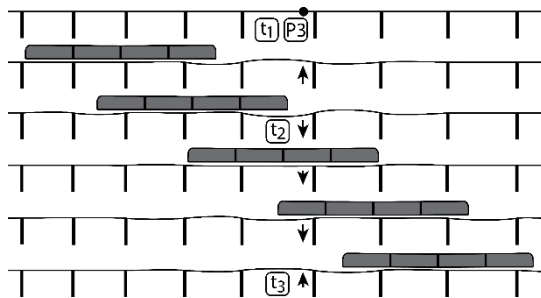


Figure 12. Deformation principle of the bridge with the example of a passing train. The arrows indicate the expected directions of deformation at P3.

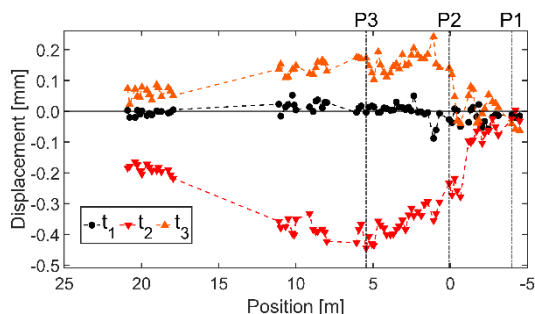


Figure 13. Displacement along the bridge as measured by instrument A for three different points in time.

Looking at Figure 11, we can see that no movements occur in the first five seconds of the time series. Afterwards, an approximately ten-second period with wave-like up- and downward movements occurs before the series stabilises again. The time series can be

explained by the deformation expected with a train running over the bridge (see Figure 12, with  $t_1$ ,  $t_2$ , and  $t_3$  corresponding to the labels in Figure 11).

The laser scanner acquisitions are significantly noisier ( $\sigma_{\text{Vertical}} = 152 \mu\text{m}$ ) than the radar acquisitions ( $\sigma_{\text{Vertical}} = 23 \mu\text{m}$ , both values are empirical standard deviations at P3 during a static period) but independently obtained with a different measurement principle and a slightly different viewing angle. The laser scanner was operated in profile mode with a temporal resolution of 0.02 s and an angular resolution of 0.08 mrad. The points acquired over a length of 5 cm along the profile were averaged and allowed calculating displacements of the area at point P3 also covered by the radar sensor and shown in Figure 11. Except for the noise levels the time series correspond to each other, and thus the laser scanning observations corroborate that the radar data yield the real surface displacements.

Looking at Figure 13, we see the deformation for bins located in parallel to the main axis of the bridge for  $t_1$ ,  $t_2$ , and  $t_3$ . The bins are not uniformly distributed along the axis as can be seen in Figure 10(bottom). Furthermore, the bridge seems not to deform symmetrically but the pattern is reasonable because when extending the trend of deformation to the left, all three series intersect at about +30 metres which coincides with the next pier.

On another occasion, two trains in opposite directions passed almost simultaneously. Figure 14 shows the displacements of the bridge at location P3 as measured by instrument A and at the opposite side of the bridge as measured by instrument B. The first train passed on track T2 (see Figure 8) on the side of instrument B and did not cause a visible torsion. The second train on the opposite track T1 (see Figure 8) caused torsion. We have also observed this with other train passages: trains passing on track T1 always caused torsion, while trains passing on track T2 did not. This can be explained by the construction of the bridge. The observed section is part of a curved line and the bridge deck is slightly inclined. The shear center lies on the symmetry axis of the bridge (Figure 9). This means that the force exerted on the bridge by a train on the inner carriageway is directed towards the shear center and thus causes a uniform lowering. In contrast, a train on the outer carriageway causes torsion because the force is not directed in the direction of the shear center.

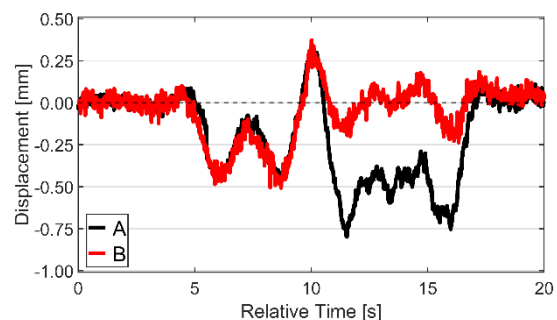


Figure 14. Displacement along the bridge as measured by instruments A and B for a cross section near P3.

## V. CONCLUSION

Automotive-grade radar systems of type MIMO-SAR are potentially very useful for structural monitoring. They allow measuring surface displacements from distances of up to several tens of meters, with quasi-continuous areal coverage, temporal resolution of up to several hundred hertz and detection of displacements larger than about 0.02 mm. In this paper, we explored the feasibility of operating two identical MIMO-SAR systems simultaneously and thus increasing the spatial coverage.

We first investigated experimentally the impact of interference by carrying out measurements concurrently using two radar instruments operating in the same frequency band, once with full frequency overlap and once with non-overlapping frequencies. Since the available devices do not allow synchronization, we chose quasi-random interference patterns by using slightly different data acquisition rates and thus temporally varying degrees of interference covering all situations from 0 to 100% signal overlap. The results showed sporadic outliers or peak-like interference patterns overall only slightly affecting the precision of the displacement time series. While filtering those may be sufficient for monitoring slow movements, using disjoint frequency ranges is preferable for data acquisition if the high data rate of the radar instrument shall be exploited.

We then applied two MIMO-SAR systems with non-overlapping frequencies to monitor the vertical displacements of different parts of a railway bridge in response to passing trains. The sub-mm displacements were clearly delivered by the interferometric data processing and conversion from line-of-sight to vertical. The standard deviation of the individual displacements (per bin within the radar image) was on the order of 20  $\mu\text{m}$ . The high-quality temporal and spatial deformation patterns provided contact-less by this low-cost measurement systems were checked for plausibility using the load situation and independent laser scans. The results corroborate the potential benefit of automotive-grade MIMO-SAR systems for structural monitoring, and the feasibility of operating such systems concurrently.

## VI. ACKNOWLEDGEMENTS

We thank Tomislav Medic, Nicholas Meyer, Robert Presl, Lorenz Schmid, and Alexander Wolf, ETH Zurich, for support during the experiments and for providing the laser scanning results, as well as Eugenio Serantoni, Swiss Federal Railways (SBB), for comments on an earlier version of this paper.

## References

- Amar, R., Alae-Kerahroodi, M., and Bahavani Shankar, M.R. (2021). FMCW-FMCW Interference Analysis in mm-Wave Radars; An indoor case study and validation by measurements. In: *21<sup>st</sup> International Radar Symposium (IRS)*, online, pp. 1-11.
- Baumann-Ouyang, A., Butt, J.A., Salido-Monzú, D., and Wieser, A. (2021). MIMO-SAR Interferometric Measurements for Structural Monitoring: Accuracy and Limitations. *Remote Sensing*, Vol. 12, No. 21: 4290.
- Caduff, R., Schlunegger, F., Kos, A., and Wiesmann, A. (2015). A review of terrestrial radar interferometry for measuring surface change in the geosciences, *Earth Surface Processes and Landforms*, Vol. 40, No. 2, pp. 208– 228.
- Chae, B.-G., Park, H.-J., Catani, F., Simoni, A., and Berti, M. (2017). Landslide prediction, monitoring and early warning: a concise review of state-of-the-art. *Geoscience Journal*, Vol. 21, No. 6, pp. 1033-1070.
- D'Aria, D., Falcone, P., Maggi, L., Cero, A., and Amoroso, G. (2019). MIMO Radar-Based System for Structural Health Monitoring and Geophysical Applications. *International Journal of Structural and Construction Engineering*, Vol. 13, No. 5, pp. 258-265.
- Dham, V. (2020). Programming Chirp Parameters in TI Radar Devices. *Application Report SWRA553A*, Texas Instruments Inc., Dallas, TX, USA.
- Enckell, M. (2011). Lessons Learned in Structural Health Monitoring of Bridges Using Advanced Sensor Technology. [Doctoral dissertation] KTH Royal Institute of Technology, Stockholm.
- Ferretti, A., Prati, C., and Rocca, F. (2001). Permanent scatterers in SAR interferometry. *IEEE Transactions on Geoscience and Remote Sensing*, Vol. 39, No. 1, pp. 8-20.
- Galmarini, A., Schmid, L., Ludin, M., and Wieser, A. (2020). Belastungsversuche zur Verifikation des Tragverhaltens. In: *20<sup>th</sup> Symposium Brückenbau*, Leipzig, Germany, pp. 114-119.
- Holst, C., Kuhlmann, H., and Neuner, H. (2020). Analyse flächenhafter Schwingungen mit 3D-Laserscanning, In: *Beiträge zum 19. Internationalen Ingenieurvermessungskurs*, Munich, Germany, pp. 149-162.
- Lienhart, W., Ehrhart, M., and Grick, M. (2017) High Frequent Total Station Measurements for the Monitoring of Bridge Vibrations. *Journal of Applied Geodesy*, Vol. 11, No. 1, pp. 1-8.
- Meyer, N., Schmid, L., Wieser, A., and Medic, T. (2022). Vibration monitoring of a bridge using 2D profile laser scanning: Lessons learned from the comparison of two spatio-temporal processing strategies. In: *5<sup>th</sup> Joint International Symposium on Deformation Monitoring (JISDM)*, Valencia, Spain.
- Miccinesi, L., Consumi, T., Beni, A., and Pieraccini, M. (2021). W-band MIMO GB-SAR for Bridge Testing/Monitoring. *Electronics*, Vol. 10, No. 18:2261.
- Pieraccini, M., Miccinesi, L., and Rojhani, N. (2019). Monitoring of Vespucci bridge in Florence, Italy using a fast real aperture radar and a MIMO radar. In: *IGARSS 2019 – 2019 IEEE International Geoscience and Remote Sensing Symposium*, Yokohama, Japan, pp. 1982-1985.
- Rao, S. (2018). MIMO Radar. *Application Report SWRA554A*, Texas Instruments Inc., Dallas, TX, USA.
- Rödelsperger, S. (2011). Real-time processing of ground based synthetic aperture radar (GB-SAR) measurements.

- [Doctoral dissertation] Technische Universität Darmstadt, Darmstadt.
- Rüeger, J.M. (2002). Refractive Index Formulae for Radio Waves. In: *Proceedings of the FIG XXII International Congress*, Washington, DC, USA, Vol. 113.
- Sampaio, R.P.C., Maia, N.M.M., and Silva, J.M.M. (1999). Damage Detection using the Frequency-Response-Function Curvature Method. *Journal of Sound and Vibration*, Vol. 226, No. 5, pp. 1029-1042.
- Scaioni, M., Marsella, M., Crosetto, M., Tornatore, V., and Wang, J. (2018). Geodetic and Remote-Sensing Sensors for Dam Deformation Monitoring. *Sensors*, Vol. 18, No. 11:3682.
- Texas Instruments (2020). mmWave Radar Interface Control Document. Texas Instruments Inc. Dallas, TX, USA.
- Tian, W., Li, Y., Hu, C., Li, Y., Wang, J., and Zeng, T. (2019). Vibration measurement method for artificial structure based on MIMO imaging radar. *IEEE Transactions on Aerospace and Electronic Systems*, Vol. 56, No. 1, pp. 749-760.
- Touzi, R., Lopes, A., Bruniquel, J., and Vachon, P.W. (1999). Coherence estimation for SAR imagery. *IEEE Transactions on Geoscience and Remote Sensing*, Vol. 37, No. 1, pp. 135-149.
- Yu, H., Lan, Y., Yuan, Z., Xu, J., and Lee, H. (2019). Phase Unwrapping in InSAR: A Review. *IEEE Geoscience and Remote Sensing Magazine*, Vol. 7, No. 1, pp. 40-58.



## High-precision intermode-beating EDM for mitigation of atmospheric delays

Pabitro Ray, David Salido-Monzú, Andreas Wieser

Institute of Geodesy and Photogrammetry (IGP), ETH Zurich, Stefano-Franscini-Platz 5, 8093 Zurich, Switzerland, ([pabitro.ray@geod.baug.ethz.ch](mailto:pabitro.ray@geod.baug.ethz.ch); [david.salido@geod.baug.ethz.ch](mailto:david.salido@geod.baug.ethz.ch); [andreas.wieser@geod.baug.ethz.ch](mailto:andreas.wieser@geod.baug.ethz.ch))

**Key words:** *optical metrology; frequency combs; supercontinuum; multiwavelength EDM; refractivity compensation*

### ABSTRACT

High-precision electro-optical distance measurement (EDM) is essential for deformation monitoring. Although sub-ppm instrumental accuracy is already feasible with state-of-the-art commercial technology, the practically attainable accuracy on distances over more than a few hundred meters is limited by uncertainties in estimating the integral refractive index along the propagation path, which often results in measurement errors of several ppm. This paper presents a new instrumental basis for high-accuracy multispectral EDM using an optical supercontinuum to enable dispersion-based inline refractivity compensation. Initial experiments performed on two spectrally filtered bands of 590 and 890 nm from the supercontinuum show measurement precision better than 0.05 mm over 50 m for an acquisition time of around 3 ms on the individual bands. This represents a comparable performance to our previously reported results on 5 cm by over a range of 3 orders of magnitude longer, which can still be improved by increasing the acquisition time. The preliminary results indicate a relative accuracy of about 0.1 mm at 50 m on each wavelength. Improvement is possible by calibration and by implementing a self-reference scheme that mitigates slow drifts caused by power-to-phase coupling. The results reported herein thus indicate that the presented approach can be further developed for achieving sub-ppm accuracy of refractivity compensated distance measurements on practically useful ranges and under outdoor conditions.

*This contribution was selected by the Scientific Committee for publication as an extended paper in the Journal of Applied Geodesy <https://www.degruyter.com/journal/key/jag/html>*

## 2D strain rate and ground deformation modelling from continuous and survey mode GNSS data in El Hierro, Canary Islands

Jose Arnosó<sup>1,2</sup>, Umberto Riccardi<sup>2,3</sup>, Umberto Tammaro<sup>4</sup>, Maite Benavent<sup>2,5</sup>,  
Fuensanta G. Montesinos<sup>2,5</sup>, Emilio Vélez<sup>1,2</sup>

<sup>1</sup> Instituto de Geociencias (CSIC-UCM). C/ Doctor Severo Ochoa 7, 28040 Madrid, Spain, ([jose.arnosó@csic.es](mailto:jose.arnosó@csic.es); [emilio.velez@csic.es](mailto:emilio.velez@csic.es))

<sup>2</sup> Research Group 'Geodesia', Universidad Complutense de Madrid, Spain

<sup>3</sup> Dipartimento di Scienze della Terra, dell'Ambiente e delle Risorse (DiSTAR), University "Federico II" of Naples, Italy, ([umbricca@unina.it](mailto:umbricca@unina.it))

<sup>4</sup> Istituto Nazionale di Geofisica e Vulcanologia Sezione, "Osservatorio Vesuviano", Naples, Italy, ([umberto.tammaro@ingv.it](mailto:umberto.tammaro@ingv.it))

<sup>5</sup> Facultad de Matemáticas, Universidad Complutense de Madrid. Plaza de Ciencias 3, 28040 Madrid, Spain, ([mbena@ucm.es](mailto:mbena@ucm.es); [fuensant@ucm.es](mailto:fuensant@ucm.es))

**Key words:** GNSS; kinematics and ground deformation; Canary Islands

### ABSTRACT

We present a study of the deformation pattern in El Hierro Island through the analysis of GNSS data from surveys carried out between 2015 and 2019 as well as continuous data. The last eruption in El Hierro occurred under the sea on the south rift, lasted from October 2011 to March 2012, and it was preceded by intense seismic activity and nearly 5 cm ground inflation. After this eruptive cycle, further magmatic intrusions were detected, from June 2012 to March 2014, associated to intense seismic swarms and inflation (about 22 cm of uplift). Nevertheless, these magmatic intrusions did not culminate in any eruption. Following these post-eruptive episodes, the seismic activity became less intense. Thus, for the period of this study, about 500 earthquakes with magnitude ranging from  $m_{bLG}$  2 to  $m_{bLG}$  3.9 were recorded, the ground deformation measured is of lower magnitude, still remaining a slight uplift trend in the GNSS stations up to 2017 and followed by a slight subsidence of about 1.5 cm between 2017-2019. Our purpose is to explain the ground displacements measured and the earthquake occurrence in terms of geodynamics and seismotectonic activity along the island, for the period 2015-2019. Firstly, we retrieved the geodetic velocities from the GNSS daily solutions. Secondly, we computed the 2D infinitesimal strain rates from the velocities through a triangular segmentation approach to map the deformation pattern along the respective GNSS surveys.

### 1. INTRODUCTION

Over the last decade, GNSS has seen enormous advances in the precision and accuracy of measurements. Time series analysis has become a widely used tool for detecting and interpreting very small and slow amplitude displacements of the Earth's surface with sub-centimetre accuracy induced by multiple geodynamic phenomena. Quantifying both in space and time the crustal deformation cycles related to volcanic and tectonic processes are currently the major challenges in tectonic geodesy. Today, continuous GNSS observations collected on permanent networks shed light on crustal movement and deformation processes at high temporal resolution. However, tackling challenging studies such as monitoring volcanoes and detecting pre-eruptive magmatic processes (*e.g.* Segall, 2010; Arnosó *et al.*, 2020) requires the reconstruction of a reliable image of the deformation field. In this case, it is necessary to bridge the spatial resolution gap through the integration of continuous and repeated GNSS

observations. In any case, either continuous or precise repeated positioning measurements provide only displacement information for a finite number of points. Therefore, in order to derive local and regional deformation models, it is necessary to apply an interpolation-oriented analysis method to obtain a continuous field. GNSS-derived strain rates have countless applications in studies aimed at comparing stress fields and rates to explain earthquake occurrence or volcano deformation (Tammaro *et al.*, 2013). Currently, there are two possible approaches to estimate strains from GNSS observations. A gridded approach, called least-squares collocation (LSC), which consists of inverting a uniform velocity field to the strain rate field or calculating strain rates in triangular or more complex segments. A very detailed description of the pros and cons of the different methods of strain retrieval can be found in (Wu *et al.*, 2011). Several papers have dealt with the study of geodynamics, tectonic and/or volcanic processes on the Canary Islands using GNSS data and different geodetic techniques, some focused on a specific island (*e.g.*

Berrocoso *et al.*, 2010; García *et al.*, 2014; Riccardi *et al.*, 2018) others on the whole archipelago (Geyer *et al.*, 2016; Arno *et al.*, 2020).

Compiling a regional seismic catalogue and analysing long time series of permanent GPS from a regional network, López *et al.* (2017) detected the first signs of geodynamic activity preceding the El Hierro eruption and subsequent episodes of magma intrusion. Later, the occurrence of six post-eruptive magmatic intrusions during 2012-2014 was studied by Domínguez-Cerdeña *et al.* (2018), and the relation between seismicity and deformation for the period 2011-2014 was recently examined by Pérez-Plaza *et al.* (2021).

Here, we present a study of the deformation pattern in El Hierro Island through the analysis of GNSS data from surveys carried out between 2015 and 2019 as well as continuous data. Our purpose is to explain the ground displacements measured and the earthquake occurrence in terms of geodynamics and seismotectonic activity along the island, for the period 2015-2019. Firstly, we retrieved the GNSS velocities from the daily solutions. Secondly, we computed the 2D infinitesimal strain rates from the velocities through a triangular segmentation approach to map the deformation pattern along the respective GNSS surveys. Our results suggest that magma movement and/or accumulation within the lower crust beneath El Hierro plays an important role in its volcanic evolution in terms of tectonic stresses.

## II. GEOLOGICAL SETTING

El Hierro Island is the youngest of the Canary Islands archipelago, and corresponds to a volcanic shield structure that includes three rift zones and superimposed volcanoes. The island rises from 4000 m below sea level to a maximum altitude of 1501 m above sea level. The rift zones associated with the typical instability of the volcanic islands, especially in its stage of growth and shield formation due to gravitational tensions, dike injections, magmatic intrusions, etc., they progressively tend to increase the possibility of giant landslides. Presently, there are three collapse scars which appear as steep cliffs or formation of arc-shaped bays, which configure a typical three-armed star morphology in the island's edifice (Figure 1). The emerged parts of the island's rifts are defined by topographic ridges, lying at 120°, corresponding to aligned dike complexes with clusters of cinder cones (Cantagrel *et al.*, 1999; Carracedo *et al.*, 2001). The ridges concentrate the Holocene volcanism, the most recent being the southern ridge. The 2011-2012 submarine eruption was the last observed in more than 500 years of historical records, and lasted for 5 months. The eruption occurred on a north-south fissure in the southern part of the rift, about 1.8 km from the coast, and built a new 220 m high underwater volcanic edifice (Martí *et al.*, 2013; López *et al.*, 2017). The eruption started on October 10<sup>th</sup> and was preceded by 3 months

of intense seismic activity, ground deformation (a maximum uplift of about 5 cm in the central El Hierro) and gas emissions. The post-eruptive phase (March 2012 to July 2014) was attached to 6 seismic swarms corresponding to magmatic intrusive events, which took place in different areas and were accompanied by rapid island uplift (2 cm/day) that revealed faster inflation processes than in the eruptive phase (Domínguez-Cerdeña *et al.*, 2018). Analysis of seismic and geodetic data suggested that the volume of magma emplaced was also bigger than during the eruptive phase (Klügel *et al.*, 2015).

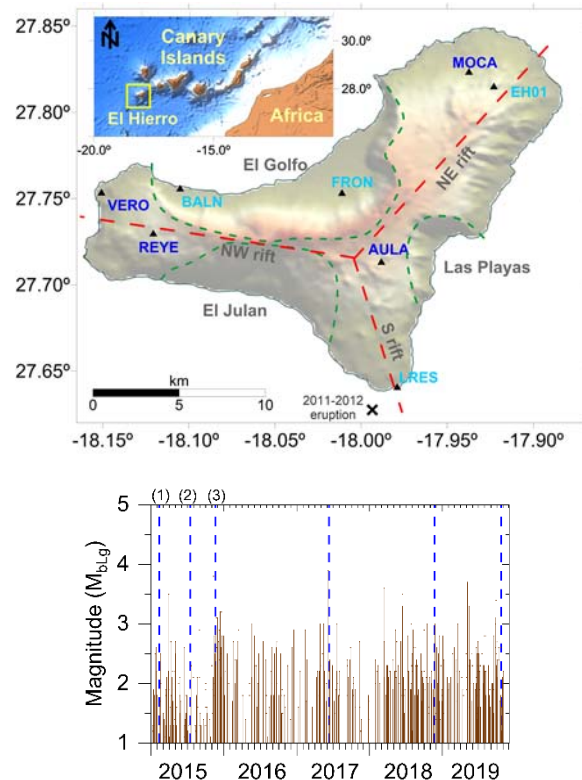


Figure 1. (Up) Relief map of El Hierro (Canary Islands) showing the triple-armed volcanic rift system (dashed red lines), as well as the embayments (green dashed lines) of El Golfo, El Julian, and Las Playas. Black triangles show the location of GNSS sites (blue colour indicate the survey sites and light blue the permanent sites). (Down) Seismicity recorded in El Hierro between 2015 – 2019. Dashed blue lines mark the time of the episodic GNSS surveys used in this study; (1), (2), (3) denote the respective surveys performed during 2015.

## III. GNSS SURVEYS AND DATA PROCESSING

El Hierro GNSS survey network consists of 8 observing sites, 4 non-permanent and 4 in continuous operating mode (Figure 1). Episodic surveys were made at the sites REYE, VERO, MOCA and AULA in 2015 (3 surveys), 2017, 2018 and 2019 using observation periods ranging from a minimum of 48 hours to a maximum of 96 hours. Additionally, we used data from the permanent GNSS site FRON during all the episodic surveys, and the permanent sites LRES, EH01 for strain calculations in the period from 2018 to 2021. The most recent GNSS

site, BALN, was included in the calculations covering the years 2019 to 2021. The stations EH01 and LRES belong to Spanish Geographical Institute (IGN), whereas FRON belong to the Cartographic Service (GRAFCAN) of the Government of Canary Islands. The station BALN is managed from the Spanish National research Council (CSIC) and the University Complutense of Madrid (UCM). Table 1 lists the geographic coordinates of the 8 observing sites.

Table 1. Example table Location and owner of the GNSS sites in El Hierro used in this study

Site	Long [°]	Lat [°]	h [m]	Owner
BALN	-18.105	27.756	55.5	CSIC-UCM
EH01	-17.923	27.815	800.9	IGN
FRON	-18.011	27.753	308.5	GRAFCAN
LRES	-17.979	27.641	51.1	IGN
MOCA	-17.937	27.823	499.5	CSIC-UCM
REYE	-18.121	27.730	768.1	CSIC-UCM
VERO	-18.151	27.754	78.6	CSIC-UCM
AULA	-17.988	27.714	984.7	CSIC-UCM

All non-permanent sites are managed by the Research Group Geodesy (UCM). The location of the sites has been selected so that they are easily accessible, satisfying suitable geometrical conditions and having homogeneous distance between sites, good satellite visibility and trying to avoid electromagnetic interferences.

We used the Canadian Spatial Reference System Precise Point Positioning (CSRS-PPP) online web service of the Natural Resources of Canada to provide the daily solutions. The service provides Precise Point Absolute Positioning (PPP) for data prior to 2018, and PPP with reliable integer ambiguity resolution for GPS (PPP-AR) from 2018 in advance (Banville, 2020). Both methods allow estimating the station coordinates for the specific epoch using accurate satellite orbit and clock information from the International GPS Service, from the absolute calibration models of the IGS antenna phase-center and from the elimination of systematic errors through the accurate modelling of various error sources, such as ionospheric and tropospheric delays, Earth tide and ocean tide loading, the latter correction uses the GOT4.10 model (Ray, 2013; 1999). For the case of PPP processing, time (P-code modulated on L1 and L2 carrier waves) and phase shift (of L1 and L2 waves) measurements are considered as observables, modeled by forming double differences of a linear free ionosphere combination. Additionally, PPP-AR processing transforms ambiguous carrier-phase observations into precise ranges using a backward run process (Tenuissen and Montenbruck, 2017). The daily GNSS solutions refer to the IGS14 realization of the ITRF2014 (Altamimi *et al.*, 2016).

For the episodic surveys, GNSS data have been processed for the entire observation period of each survey, whereas data from permanent GNSS sites were

analysed in continuous 168-hour sessions. In both cases, the data sampling interval was 30 seconds.

The analysed GNSS data set comprises a set of 3D (North, East, Up) site positions for each episodic survey, with which the velocities are determined through the respective difference between surveys. For the permanent GNSS sites, we used time series of the weekly solutions with the 3D positions. In this case, the velocities were computed through a least squares procedure to remove annual and semi-annual periodicities.

#### IV. 2D STRAIN CALCULATION

We used the horizontal velocities to compute the bi-dimensional (2D) infinitesimal strain from various sets of 3 non-co-linear GNSS stations each, forming triangles, as formulated by Jaeger *et al.* (2007) for a flat Earth. Thus, if  $u_x, u_y$  denote the components of the displacement vector, the partial derivatives along the  $x$  and  $y$  directions, at point  $(x, y)$ , represent the respective normal strains,  $\varepsilon_{xx}, \varepsilon_{yy}$ , that is (Eq. 1):

$$\varepsilon_{xx} = \frac{\partial u_x}{\partial x}, \varepsilon_{yy} = \frac{\partial u_y}{\partial y} \quad (1)$$

The other two components of the strain matrix are considered symmetrical,  $\varepsilon_{xy} = \varepsilon_{yx}$ . By setting  $i = 1, 2$ ,  $\varepsilon_1$  and  $\varepsilon_2$  define the two principal horizontal strains, which can be computed as (Eq. 2):

$$\varepsilon_i = \varepsilon_{yy} \cos^2 \theta_i + \varepsilon_{xx} \sin^2 \theta_i + \varepsilon_{xy} \sin \theta_i \cos \theta_i \quad (2)$$

where  $\theta_i =$  principal directions,  $i=1, 2$

In our analysis, we have determined the elongation/shortening (i.e., the ratio  $u/l$  in strain units,  $10^{-9}$ ;  $l$  being the undeformed baseline length) the dilatation and the principal strains for triplets of GNSS sites according to the respective differences between surveys.

Figure 2 shows the distribution of areal strain along the island with significant changes when we compare each GNSS survey with the first one carried on in 2015. The west sector of the island displays a compression pattern, which increases in magnitude as successive campaigns advance along the years. Some smaller compressive sectors come out in the central and north-eastern areas of the island during 2017 and 2018. The central and east sectors of the island evidence a dilatation pattern, which slightly varies its magnitude along the years. If we consider the maximum lapse between surveys (4.7 years) for the period 2019-2015(1), the strain pattern still remarks the two compressive-extensional regimes, the highest strain values corresponding to a dilatation regime located in the centre-east of the island.

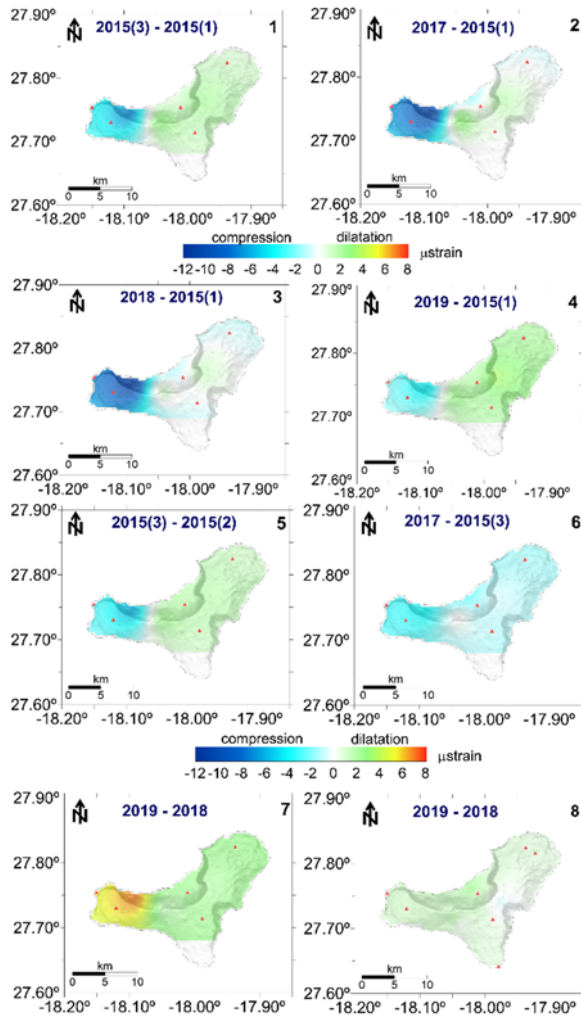


Figure 2. Contour maps of the areal strain computed as for the difference with the first survey (panels 1 to 4) and for the difference survey by survey (panels 5 to 7). The panel 8 includes the permanent GNSS sites LRES and EH01 in the calculation. Red triangles show the location of the GNSS sites.

Similarly, we have computed the areal strain based on the difference between subsequent surveys (Figure 2). The strain pattern exhibits changes in the magnitude that are not observed when the first survey is fixed as a reference. Thus, the dilatation pattern in the central and east sectors of the island vanishes during year 2017, and it moves to west and central areas during year 2018. Furthermore, the year 2018 shows a significant difference in the strain with regard to 2019 as the dilatation pattern is completely extended along the island, with the maximum values located in the westernmost area of the island.

In addition, we have calculated the 2D maximum shear strain through the angle between the positions before and after the deformation. That is (Eq. 3),

$$\varepsilon_{xy} = \frac{1}{2} \left( \frac{\partial u_x}{\partial x} + \frac{\partial u_y}{\partial y} \right) \quad (3)$$

Which in terms of the principal horizontal strains (2) is computed as  $\frac{1}{2}(\varepsilon_1 - \varepsilon_2)$ . Figure 3 shows the results for

the maximum shear strain thus calculated, which are in accordance with the surface distribution of the areal strain. This is clearly seen through the comparison of each survey with the first one of 2015. Most of the NW rift sector shows the highest shear strain values found along the island, which increase in magnitude by the middle of 2017 and subsequently towards the end of 2018.

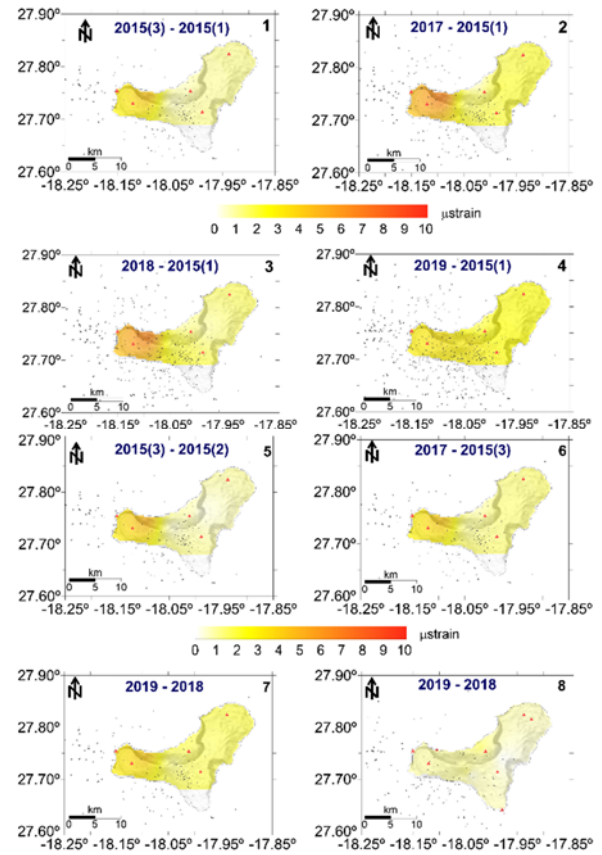


Figure 3. Same contour map as Figure 2 but for the maximum shear strain. The grey circles are the epicentres of the earthquakes ( $m_{bLG}$  1.2 to 3.9) recorded during the respective time intervals.

By including the stations LRES and EH01 for the time difference 2019-2018 (panel 8 in Figures 2 and 3), then the areal strain and the maximum shear strain evidence a lower magnitude, and specific areas located to the North and in the NW rift of the island show the greatest values. This is a consequence of the larger surface area involved in the calculation, which consequently causes the strain and maximum shear strain to be stretched.

Because there are no more than 3 permanent stations with publicly accessible data (FRON, LRES, EH01), we have installed the GNSS site named BALN at the north of the island (see Figure 1). Consequently, it is possible to form a radial GNSS geodetic network configuration to deepen into this ground deformation study. Actually, we can define three quasi-equilateral triangles covering the three-armed rift structure of the island, which favours the condition of homogeneity that is required for reliable 2D strain results (Figure 4). Such network configuration makes it possible to study the

concordance with the results from the GNSS episodic surveys, and to check for alterations in the deformation pattern to a larger scale. The results from the strain and maximum shear strain calculation encompassing 2019-2021 time interval are shown in Figure 4.

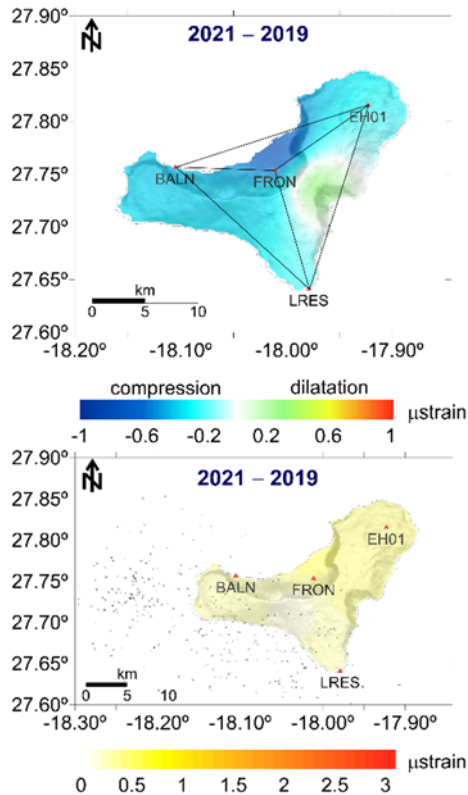


Figure 4. (Up) Areal strain computed for the difference 2021-2019 using the permanent GNSS sites LRES, EH0, FRON and the most recent site BALN. The quasi-equilateral triangles used for the segmentation approach are also indicated. (Down) Maximum shear strain computed as for the difference 2021-2019. The dots are the epicentres of the earthquakes ( $m_{bLG}$  1.2 to 3.9) recorded during the indicated time interval.

## V. DISCUSSION OF RESULTS

During the period 2015 to 2019 that follows the post-eruptive episodes identified between 2012 and 2014 (e.g., Klügel *et al.*, 2015), the seismic activity became less intense in El Hierro. About 500 earthquakes from low to moderate magnitude ( $m_{bLG}$  2 to  $m_{bLG}$  3.9) were recorded in the seismic catalogue of the Spanish IGN ([www.ign.es](http://www.ign.es)). According to our analysis of the episodic GNSS observations, the ground displacement measured is of lower magnitude, still remaining an uplift trend (from 1 to 6.5 cm) in the central and NE sector of the island and a slight subsidence (about 0.8 cm) in the W sector up to 2017. This behaviour is followed by stability in the central zone of El Hierro and a subsidence of about 3.0 cm in the NE and W rifts until the end of 2019. In addition, the time series analysis of the four continuous GNSS sites (BALN, FRON, EH01, LRES) report an average ground subsidence of about 8 mm from 2019 to 2021.

The Figure 5 summarizes the time variation of the length of the baselines computed with respect to the first survey 2015(1). As we are using data from repeated surveys (2015 to 2019), it is reasonable to assume 1 cm change in the baseline length as a limit of detectability of deformations.

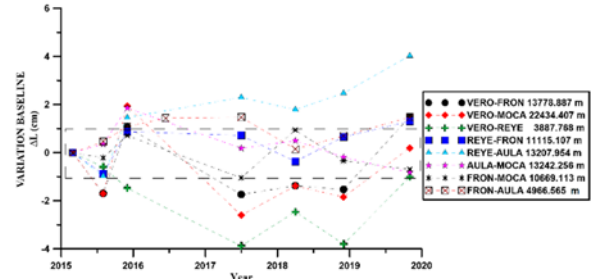


Figure 5. Time change of the baseline's length calculated for the GNSS episodic surveys carried out for the period 2015-2019. The gray rectangle visually provides an order of magnitude for the reliability of the length changes assessed from the repeated surveys.

Stations VERO and REYE (Figure 5), in the West sector, display the largest dynamics among the considered stations. The shortening in VERO-REYE might confirm that the west sector of El Hierro undergoes a compression. This is a quite obvious derivation, because the strain comes from the displacements assessed among pair of stations (baselines), namely the sides of the triangles. Otherwise, the baseline REYE-AULA (Figure 5) would confirm a dilatation in the central sector.

The strain pattern calculated through episodic GNSS points out two compressive-extensional regimes in El Hierro (Figure 2). The maximum shear strain results are in accordance with the surface distribution of the areal strain, and the NW rift of the island exhibits the highest values while the seismicity is mostly concentrated in the central and West sectors of the island (Figure 3). That fact could be a consequence of the magma accumulation and/or displacement in depth during the period of time analysed here. Indeed, seismicity recorded during this period (Figure 6) is spatially extensive and it is mostly located at 10-15 km in depth, which corresponds to the lower oceanic crust area, and 15-25 km, which corresponds to areas of different magma reservoirs during the eruption phase and other level of emplacement of sill-like magma intrusions during the post-eruptive phase (Longpré *et al.*, 2014; Klügel *et al.*, 2015). The seismicity for the period 2019-2021 is more homogeneously distributed for the depths 10-22 km and 30-40 km.

The unrest episode that preceded the last eruption in El Hierro involved a winding dyke propagation as local crustal structures and discontinuities diverted the magma pathway (e.g., Martí *et al.*, 2013; Gorbatikov *et al.*, 2013; Sainz-Maza *et al.*, 2014). A similar situation was produced during the 2012-2014 post-eruptive stage, which involved six different magmatic intrusions, as suggested by the seismicity and the ground

deformation produced as a consequence of the lateral magma movement in depth across the island's edifice (Klügel *et al.*, 2015; Domínguez-Cerdeña *et al.*, 2018). However, this has not been the case since 2015 in advance, although the strain patterns obtained in this study suggest a kind of dipole behaviour in terms of stress change for the period studied here. Such dipole structure evidences slight time changes, as suggested through the strain differences computed survey by survey (Figure 2). That is, the difference between subsequent surveys exhibits changes in the strain magnitude that are not observed when the first survey is fixed as a reference. For instance, the dilatation pattern in the central and east sectors of the island vanishes during year 2017, and it moves to west and central areas during year 2018. In addition, the year 2018 shows a significant difference in the strain with regard to 2019 as the dilatation pattern is completely extended along the island, with the maximum values located in the westernmost area of the island. The period of time analysed here points out the stress distribution inside the crust and possibly reveals the tectonic stresses across the island's edifice, as a consequence of the previous eruption and post-eruptive activity.

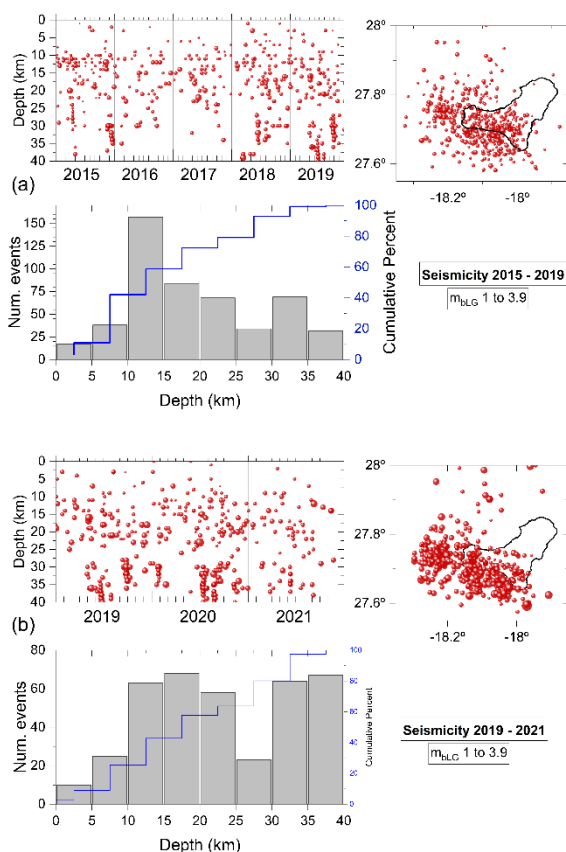


Figure 6. (a) Seismicity recorded at El Hierro Island from 2015 to 2019. Panels show the location, distribution in depth and a bar diagram with the cumulative number of earthquakes. (b) Same as (a) but for the period 2019 to 2021.

## VI. CONCLUSIONS

Based on the analysis of continuous and survey GNSS data spanning 2015-2019 time interval, we have tried to image the deformation pattern in El Hierro Island. The strain pattern retrieved from episodic GNSS surveys displays a peculiar pattern depending on how data are taken into account. A kind of dipole strain field, slightly changing over time, emerges when strain is computed from the difference between subsequent surveys, with two compressive-extensional regimes in the west and central-east sectors of the island respectively. Such a dipole structure becomes less evident when the first survey is fixed as a reference. However, considering that the dipolar field emerges from the deformation obtained from the most temporally spaced pair of surveys (2019-2015), when most of the deformation has been accumulated, we believe that in the time interval covered by the present study this is the deformation field that characterises El Hierro. The maximum shear strain field appears to be in accordance with the surface distribution of the areal strain, and the NW rift of the island exhibits the highest values, while the seismicity is mostly concentrated in the central and West sectors of the island. In fact, the crustal heterogeneity and the six post-eruptive intrusions associated with intense seismic swarms and inflation, which did not produce an eruption, but lateral magma movements could have affected the observed strain field. The reconstructed strain field could be compatible with a magma accumulation and/or displacement. The results of our study allowed us to highlight the distribution of deformation in response to tectonic stresses within the crust and the island's edifice, as a consequence of previous eruption and post-eruptive activity.

## VII. ACKNOWLEDGEMENTS

Projects PID2019-104726GB-I00 and CGL2015-63799-P of the Spanish Research Agency has supported this research. We wish to acknowledge GRAFCAN ([www.grafcan.es](http://www.grafcan.es)) of the Government of the Canary Islands for providing GNSS data from permanent station FRON. Likewise, to the Spanish IGN ([www.ign.es](http://www.ign.es)) for providing the EH01 and LRES data.

## References

- Altamimi, Z., Rebischung, P., Métivier, L., and Collilieux, X. (2016). ITRF2014: A new release of the International Terrestrial Reference Frame modeling nonlinear station motions. *Journal of Geophysical Research*, Vol., 121, pp. 6109–6131.
- Arnosó, J., U. Riccardi, M. Benavent, U. Tammaro, FG. Montesinos, I. Blanco-Montenegro, and E. Vélez (2020). Strain pattern and kinematics of the Canary Islands from GNSS time series analysis. *Remote Sensing*, Vol. 12, 3297, DOI: 10.3390/rs12203297.
- Banville, S. (2020). CSRS-PPP Version 3: Tutorial, p. 11. <https://webapp.geod.nrcan.gc.ca/geod/tools->

- ouils/sample\_doc\_filesV3/NRCan%20CSRS-PPP-v3\_Tutorial%20EN.pdf.
- Berrocoso, M., Carmona, J., Fernandez-Ros, A., Pérez-Pena, A., Ortiz, R., and García, A. (2010). Kinematic model for Tenerife Island (Canary Islands, Spain): Geodynamic interpretation in the Nubian plate context. *Journal of African Earth Sciences*, Vol. 58, pp. 721–733, DOI: 10.1016/j.jafrearsci.2010.04.007.
- Cantagrel, J.M., Arnaud, N.O., Ancochea, E., Fuster, J.M., and Huertas, M.J., (1999). Repeated debris avalanches on Tenerife and genesis of Las Cañadas caldera wall (Canary Islands). *Geology* 27, pp. 739–742.
- Carracedo, J. C., E. R. Badiola, H. Guillou, J. de la Nuez, and F. J. Perez-Torrado (2001). Geology and volcanology of La Palma and El Hierro, Western Canaries. *Estudios Geológicos*, Vol. 57, pp. 175–273.
- Domínguez-Cerdeña, I., L. García-Cañada, M.A. Benito-Saz, C. del Fresno, H. Lamolda, J. Pereda de Pablo, and C. Sánchez Sanz, (2018). On the relation between ground surface deformation and seismicity during the 2012–2014 successive magmatic intrusions at El Hierro Island. *Tectonophysics*, Vol. 744, pp. 422–437, DOI: 10.1016/j.tecto.2018.07.019.
- García, A., Fernández-Ros, A., Berrocoso, M., Marrero, J.M., Prates, G., De La Cruz-Reyna, S., and Ortiz, R. (2014). Magma displacements under insular volcanic fields, applications to eruption forecasting: El Hierro, Canary Islands, 2011–2013. *Geophysical Journal International*, Vol. 197, pp. 322–334.
- Geyer, A., Marti, J., and Villaseñor, A. (2016). First-order estimate of the Canary Islands plate-scale stress field: Implications for volcanic hazard assessment. *Tectonophysics*, Vol. 679, pp. 125–139.
- Gorbatikov, A.V., Montesinos, F.G., Arnosó, J., Benavent, M., and Tsukanov, A.A. (2013). New features in the subsurface structure model of El Hierro Island (Canaries) from low-frequency microseismic sounding: an insight into the 2011 seismo-volcanic crisis. *Surveys in Geophysics*, Vol. 34, pp. 463–489. DOI: 10.1007/s10712-013-9240-4.
- Jaeger, J.C., Cook, N.G.W., and Zimmerman, R.W. (2007). *Fundamentals of Rock Mechanics*, 4<sup>th</sup> ed. Blackwell Publishing Ltd. USA, ISBN 13: 978-0-632-05759-7.
- Klügel, A., MA. Longpré, L. García-Cañada, and J. Stix (2015). Deep intrusions, lateral magma transport and related uplift at ocean island volcanoes. *Earth and Planetary Science Letters*, Vol. 431, pp. 140–149. DOI: 10.1016/j.epsl.2015.09.031.
- Longpré, M.A., A. Klügel, A. Diehl, and J. Stix (2014). Mixing in mantle magma reservoirs prior to and during the 2011–2012 eruption at El Hierro, Canary Islands. *Geology*, Vol. 42, pp. 315–318. DOI: 10.1130/g35165.1.
- López, C., García-Cañada, L., Martí, J., and Cerdeña, I.D. (2017). Early signs of geodynamic activity before the 2011–2012 El Hierro eruption. *Journal of Geodynamics*, Vol. 104, pp. 1–14.
- Martí, J., V. Pinel, C. López, A. Geyer, R. Abella, M. Tárraga, M. J. Blanco, A. Castro, and C. Rodríguez (2013). Causes and mechanisms of El Hierro submarine eruption (2011–2012) (Canary Islands). *Journal of Geophysical Research, Solid Earth*, Vol. 118, pp. 823–839, DOI: 10.1002/jgrb.5008.
- Pérez-Plaza, S., Berrocoso, M., Rosado, B., Prates, G., and Fernández-Palacín, F. (2021). The time lag between deformation process and seismic activity in El Hierro Island during the eruptive process (2011–2014): a functional phased approach. *Earth, Planets and Space*, Vol. 73, No. 1. DOI: 10.1186/s40623-021-01514-0.
- Ray, R.D. (1999). A global ocean tide model from Topex/Poseidon altimetry: GOT99.2, NASA Tech. Memo., 209478
- Ray, R.D. (2013). Precise comparisons of bottom-pressure and altimetric ocean tides. *Journal of Geophysical Research, Oceans*, Vol. 118, pp. 4570–4584. DOI:10.1002/jgrc.20336
- Riccardi, U., Arnosó, J., Benavent, M., Vélez, E., Tammaro, U., and Montesinos, F.G. (2018). Exploring deformation scenarios in Timanfaya volcanic area (Lanzarote, Canary Islands) from GNSS and ground based geodetic observations. *Journal of Volcanology and Geothermal Research*, 357, pp. 14–24. DOI: 10.1016/j.volgeores.2018.04.009
- Sainz-Maza Aparicio, S., Arnosó Sampedro, J., Montesinos, F. G., and Marti Molist, J. (2014) *Volcanic signatures in time gravity variations during the volcanic unrest on El Hierro (Canary Islands)*. *Journal of Geophysical Research - Part B - Solid Earth*, 119 (6). pp. 5033-5051.
- Tammaro, U., DeMartino, P., Obrizzo, F., Brandi, G., D’Alessandro, A., Dolce, M. Malaspina, S., Serio, C., and Pingue, F. (2013). Somma Vesuvius volcano: Ground deformations from CGPS observations (2001–2012). *Annals of Geophysics*, Vol. 56, No. 4, 50456, DOI: 10.4401/ag-6462.
- Teunissen, P.J.G., and Montenbruck, O. (2017). *Springer Handbook of Global Navigation Satellite Systems*. Springer International Publishing, Cham. DOI: 10.1007/978-3-319-42928-1.
- Segall P. (2010). *Earthquake and volcano deformation*. Princeton University Press, pp. 432.
- Wu, Y., Jiang, Z.-S., Yang, G., Wei, W., and Liu, X. (2011). Comparison of GPS strain rate computing methods and their reliability. *Geophysical Journal International*, Vol. 185, pp. 703–717. DOI: 10.1111/j.1365-246X.2011.04976.x



## Two multi-wavelength interferometers for large-scale surveying

Anni Sauthoff<sup>1</sup>, Paul Köchert<sup>1</sup>, Günther Prellinger<sup>1</sup>, Tobias Meyer<sup>1</sup>, Frank Pilarski<sup>1</sup>,  
Stephanie Weinrich<sup>1</sup>, Frank Schmaljohann<sup>1</sup>, Joffray Guillory<sup>2</sup>, Daniel Truong<sup>2</sup>, Jakob Silbermann<sup>3</sup>,  
Ulla Kallio<sup>4</sup>, Jorma Jokela<sup>4</sup>, Florian Pollinger<sup>1</sup>

<sup>1</sup>Physikalisch-Technische Bundesanstalt (PTB), Bundesallee 100, 38116 Braunschweig, Germany, ([anni.sauthoff@ptb.de](mailto:anni.sauthoff@ptb.de); [paul.koechert@ptb.de](mailto:paul.koechert@ptb.de); [guenther.prellinger@ptb.de](mailto:guenther.prellinger@ptb.de); [tobias.meyer@ptb.de](mailto:tobias.meyer@ptb.de); [frank.pilarski@ptb.de](mailto:frank.pilarski@ptb.de); [stephanie.weinrich@ptb.de](mailto:stephanie.weinrich@ptb.de); [frank.schmaljohann@ptb.de](mailto:frank.schmaljohann@ptb.de); [florian.pollinger@ptb.de](mailto:florian.pollinger@ptb.de))

<sup>2</sup>Conservatoire National des Arts et Métiers (Cnam), Laboratoire commun de métrologie LNE-Cnam, 1 rue Gaston Boissier, 75015 Paris, France, ([joffray.guillory@cnam.fr](mailto:joffray.guillory@cnam.fr); [daniel.truong@cnam.fr](mailto:daniel.truong@cnam.fr))

<sup>3</sup>Bernhard Halle Nachfl. GmbH, Hubertusstr. 10, 12163 Berlin, Germany, ([jakob.silbermann@b-halle.de](mailto:jakob.silbermann@b-halle.de))

<sup>4</sup>Finnish Geospatial Research Institute, National Land Survey of Finland, Geodeetinrinne 2, 02430 Masala, Finland, ([ulla.kallio@nls.fi](mailto:ulla.kallio@nls.fi); [jorma.jokela@nls.fi](mailto:jorma.jokela@nls.fi))

**Key words:** *two-colour refractivity compensation; multi-wavelength interferometry; multilateration; system design; long range measurement*

### ABSTRACT

Deformation monitoring requires the detection of smallest changes, always at the limits of technical feasibility. Trying to push these limits further, we have realised two terrestrial ranging instruments: a long-range 1D electro-optic distance meter and a 3D multilateration-capable sensor system of 50 m range. The former one is intended as primary standard for the calibration of geodetic instrumentation with low uncertainty to the SI definition of the metre. The latter one is intended for monitoring larger monuments like VLBI antennas. In this contribution, we describe the technical challenges and our solutions for such instrumentation. We use the two-colour method for inline refractive index compensation. As common optical source, we developed a versatile multi-wavelength generator based on two Nd:YAG lasers stabilised by a phase-locked loop realised by Field Programmable Gate Arrays (FPGA). The 1D interferometer uses custom-designed achromatic optics and a mechanical frame optimised for form stability under field conditions. The phase demodulation system allows for maximum range flexibility from several meters up to several kilometres. The base ranging unit of the 3D multilateration system adheres to a different demodulation technique, which allows a relatively simple interferometer head design. This approach requires a sophisticated source modulation scheme limiting the applicability to distances over 15 m up to approximately 50 m in our case.

### 1. INTRODUCTION

Commercial electronic distance meters (EDM) are mainly based on amplitude modulation (Köhler, 2012). In the last years several research projects have shown that this concept has not achieved its resolution limits yet. Modern photonics and electronics enable working with radio frequencies of several Gigahertz (Guillory *et al.*, 2016). Standard deviations below 30  $\mu\text{m}$  over 5.4 km have been demonstrated (Guillory *et al.*, 2019). High modulation frequencies can also be generated making use of modern optical sources. Intermode beats of optical frequency combs make modulation frequencies of several tens to hundred Gigahertz possible (Minoshima and Matsumoto, 2000). Millimetric accuracy up to 600 m under field conditions have been demonstrated with this technique (Pollinger *et al.*, 2012). Absolute interferometry can be an alternative for highly precise distance measurements in surveying. This technique mainly developed for precision engineering relies on one or more optical interference measurements and uses the optical wavelength as a very sensitive scale for the

measurement. Unlike classical interferometry, the absolute distance is not acquired by a continuous displacement measurement in which the reflector is moved relatively over the distance to be measured, but by a sophisticated measurement strategy like frequency sweeping interferometry (FSI, *e.g.* Meiners-Hagen *et al.*, 2009) or fixed synthetic multi-wavelength interferometry. Conceptual studies have shown the enormous potential of this technique driven by optical frequency combs (van den Berg *et al.*, 2012; Coddington *et al.*, 2009) in the laboratory, but also sub-millimetric accuracy over 1.2 km measurement range in free space has already been successfully demonstrated (Wu *et al.*, 2017).

The achievable uncertainty of any optical measurement in surveying, however, is limited by the fact that the measurement is performed in air and the index of refraction needs to be properly considered. The inhomogeneity of the index of refraction parallel to the optical beam propagation direction limits the achievable uncertainty of the optical distance measurement. Elaborate sensor networks can mitigate

this problem, *e.g.* at reference baselines (Pollinger *et al.*, 2012; Neyezhnikov *et al.*, 2020). Ideally, however, the effective index of refraction is measured in the same volume as the optical beam. There are multiple approaches, based, *e.g.*, on a measurement of the speed of sound (Pisani *et al.*, 2018), or on spectroscopy (Tomberg *et al.*, 2017). We pursue the two-colour method which was originally introduced in 1965 by Bender and Owens for surveying purposes. Initial instrumental realisations (Earnshaw and Owens, 1967) climaxed in the famous commercial two-colour terrameter (Hugget and Slater, 1975; Hugget, 1981). Since knowledge of the index of refraction limits the achievable uncertainty in large-scale distance measurements today, interest in this technology has recently considerably increased again. Meiners-Hagen and Abou-Zeid provided an extended model for humid air in 2008. The two-colour method is especially interesting for broadband optical sources like optical frequency combs as they provide the necessary spectrum for this measurement technology (Minoshima and Matsumoto, 2000; Salido-Monzú and Wieser, 2018). Stabilities of  $10^{-11}$  over 500 s were demonstrated for distance measurements in the laboratory (Wu *et al.*, 2013). We demonstrated application of the two-colour method to long distance measurements (Meiners-Hagen *et al.*, 2015; Meiners-Hagen *et al.*, 2017) and to measurements over several tens of metres in industrial environments (Meiners-Hagen *et al.*, 2016). In this contribution, we describe two multi-wavelength interferometers developed for two different application scenarios in large-scale surveying. The TeleYAG-II interferometer is designed for the low-uncertainty, SI-traceable measurement of reference baselines with a range of up to 5 km. This relatively long range is relevant for the ground-based SI-traceable verification of space-geodetic techniques like Satellite-Laser-Ranging (SLR) or global navigation satellite systems (GNSS). The Absolute3D interferometer, on the other hand, is developed as an absolute interferometer for a range of several tens of meters. It is intended for multilateration-monitoring of larger critical structures like VLBI antennas. Although their fundamental physical working principles are nearly identical, the different use cases require two substantially different technical realisations. In the paper, we briefly review the fundamentals of multi-wavelength interferometry and two-colour refractive index compensation and describe the challenges for the technical and field-capable realisation of these ideas (Section II). We introduce the multi-wavelength source we developed for both systems (Section III) and then describe the two interferometer systems with an emphasis on their response to the application challenges (Sections IV and V).

## II. METHOD

### A. Two-colour method

The refractive index of air depends on the vacuum wavelengths  $\lambda$ , and the thermodynamic properties ambient pressure  $p$ , temperature  $T$ , water vapor pressure  $p_w$  and carbon dioxide contents  $x$  (*e.g.* Bönsch and Potulski, 1998). The basic concept of the two-colour method is based on the fact that the dependencies on wavelength and environmental parameters separate naturally in the typical functional model of the form (Eq. 1):

$$n(\lambda, T, p, x, p_w) - 1 = K(\lambda) \cdot D(T, p, x) - p_w g(\lambda) \quad (1)$$

with the functionals  $K(\lambda)$  representing the dispersion term,  $D(T, p, x)$  the density term, and  $g(\lambda)$  the humidity term (Meiners-Hagen *et al.*, 2017). If the optical path lengths  $d_1$  and  $d_2$  of an identical geometric distance are measured with two different wavelengths ( $\lambda_1, \lambda_2$ ), the geometric length  $l$  can be expressed by the respective vacuum wavelengths and the corresponding refractive index (Eq. 2):

$$l n_1 = d_1; \quad l n_2 = d_2. \quad (2)$$

Inserting Equation 1 leads to a system of equations which can be solved for the geometric length by (Eq. 3):

$$l = \frac{K_1 d_2 - K_2 d_1}{K_1 - K_2 + p_w (g_1 K_2 - g_2 K_1)}. \quad (3)$$

The geometric length can hence be measured without explicitly detecting most of the ambient conditions. Nevertheless, a very accurate measurement of the raw optical path lengths  $d_1$  and  $d_2$  (*i.e.* the observed distances uncorrected for the index of refraction) is required to achieve a sufficient uncertainty of the geometric length.

### B. Multi-wavelength interferometry

An ordinary counting interferometer is based on interference fringe counting while moving one reflector. When the integer order is lost, *e.g.*, due to a fast and discontinuous movement, only the fractional order of interference is obtained (phase/ $2\pi$ ). The range of unambiguity can be enlarged by using more than one wavelength. The difference between two interferometric phases  $\phi_1, \phi_2$  of two optical wavelengths can be interpreted as a differential phase (Eq. 4):

$$\phi = \phi_2 - \phi_1 \quad (4)$$

which can be interpreted as interference phase of a virtual synthetic wavelength (Eq. 5):

$$\Lambda = \frac{\lambda_1 \lambda_2}{\lambda_1 - \lambda_2}. \quad (5)$$

The synthetic wavelength  $\Lambda$  is always longer than the two optical vacuum wavelengths  $\lambda_1$  and  $\lambda_2$ . In consequence, any uncertainty of the phase measurement is multiplied by the synthetic wavelength, increasing the actual length uncertainty by a factor of  $\Lambda/\lambda$  in comparison to a classic interference measurement. Long synthetics hence imply high uncertainties. But the range of non-ambiguity is limited to half of the synthetic wavelength, comparable to the limitation of the 'scale' given by the modulation frequencies in classical EDM. Instead of working with long synthetics, the remaining ambiguity can be resolved using FSI. The interferometer phase for a given light frequency  $\nu$  is generally expressed by (Eq. 6):

$$\phi = \frac{4\pi\nu}{c}nl \quad (6)$$

with  $c$  representing the vacuum speed of light. For the variable synthetic wavelengths approach the laser frequency  $\nu$  is tuned by  $\Delta\nu$ . If the synthetic phase change  $\Delta\Phi$  is simultaneously tracked, the absolute geometric length  $l$  can be calculated by (Eq. 7):

$$l = \frac{c}{4\pi n_g} \frac{\Delta\Phi}{\Delta\nu}. \quad (7)$$

It should be noted that the target is required to stand reasonably still during such a frequency sweep for the measurement to work.

### C. Technical challenges

Although the fundamentals of dispersion-compensating multi-wavelength interferometry may seem straightforward, its implementation for geodetic purposes poses multiple technical challenges. First, the provided laser source must emit light of a high degree of coherence. Furthermore, the prerequisite for multi-wavelength interferometry is a perfect geometrical superposition of all optical beams. Otherwise, a difference in length measurement would not only attribute to the refractive index, but also to a cosine error between the different beam paths. Classical free-space beam superposition is unstable, hard to achieve and to control outside the lab. A more elegant and robust way is to combine the beam paths in a photonic crystal fibre (PCF) (Liu *et al.*, 2020). The PCF automatically ensures a perfect superposition of the optical beams and reduces the number of mirrors and therefore the time for readjustments. The emitted beam size by a PCF, however, strongly depends on the wavelength. This needs to be considered in the optics design. Moreover, all optics need to be carefully achromatically designed because the wavelengths used for dispersion compensation are usually strongly

spectrally separated. Finally, optical phases must be detected for every wavelength used and correctly assigned. This implies that the phases or respectively colours can be separated before detection. For the spectrally well-separated fundamental working wavelengths, like 532 nm and 1064 nm, this can be achieved by standard optical means like dichroitic mirrors. But for separating the two wavelengths used for the fixed synthetic wavelengths (differing in our case only by 20 GHz or about 0.1 nm) alternative electronic demodulation schemes are needed.

### III. MULTI-WAVELENGTH SOURCE

One key requirement for the realisation of a geodetic multi-wavelength measurement is hence an optical source providing light at multiple well-defined wavelengths and sufficient coherence. Furthermore, a demodulation scheme needs to be implemented. For this purpose, we developed a versatile multi-wavelength source consisting of Nd:YAG lasers (model: Innolight Prometheus 20NE) and a modulation technique that varies depending on the application scenario the respective interferometer.

The Nd:YAG lasers provide wavelengths at 1064 nm and 532 nm and an optical power of each laser of 1 W and 20 mW, respectively. The 532 nm wavelength is generated by second harmonic generation (SHG) and is intrinsically phase-stable to the 1064 nm wavelength (Wynands *et al.*, 1995). Their energy efficiency, size, lifetime, robustness, and intrinsic noise levels, render diode-pumped solid-state lasers like Nd:YAG lasers ideal for the use in multi-wavelength interferometry. The coherence length of Nd:YAG ring oscillators has been subject of investigation in prior research (Sorin *et al.*, 1990): with self-interference techniques using a delay fibre line of 100 km, coherence was still observable. Czarske *et al.* estimated in 1995 that Nd:YAG oscillators had linewidth properties to measure distances of more than 1000 km.

The design of the multi-wavelength source should be as simple as possible to cope with the uncertainties during field operation. Therefore, in contrast to numerous scientific works in the field of laser stabilisation, no measures were taken to protect the laser sources from disturbing sources. Multiple wavelengths were generated in three ways: by offset locking of the fundamental wavelengths at a beat frequency of 20 GHz using an optical phase-locked loop (OPLL), by shifting the laser frequency using acousto-optic modulators (AOMs) and by modulating the wavelength using piezo transducer (PZT).

#### A. OPLL offset lock

The setup for the OPLL is summarized in Figure 1a. Both independent laser oscillators, the so-called master and slave laser, are phase-locked using their 1064 nm outputs by the well-known offset-locking technique. The heterodyned optical signal is converted into a

microwave signal using a fibre-coupled photo detector (New Focus 1414, 25 GHz bandwidth). To precisely tune the frequency offset between both phase-locked lasers, a super high frequency (SHF) synthesizer (R&S SMA-100B) with low noise characteristics (R&S SMAB-B710; single-sideband (SSB) phase noise, typical -111 dBc at 1 kHz offset), is employed as an offset stage to down convert the 20 GHz beat signal with a mixer to an intermediate frequency of 62.5 MHz. The down-mixed signal is then sampled with a sample rate of 250 MSPS by a 14 bit analogue-to-digital-converter (ADC, ADS62P49) equipped on a transceiver board (NI-5782), which is connected to an FPGA-based controller (NI-7935R, Kintex-7-410T). The FPGA executes an I/Q demodulation algorithm to extract the phase information from the data stream with a low latency of about 1  $\mu$ s. The data processing is based on a 256 tap FIR filter with a bandwidth between 125 kHz and 10 MHz, which is adjustable to meet the boundary conditions of our two interferometer systems. We choose a minimum bandwidth of 125 kHz for TeleYAG-II measurements to optimally reject disturbances, while the bandwidth is increased to more than 4 MHz for the Absolute3D system to tolerate the frequency deviation of the modulated signals. Finally, the phase information is used to process two output signals with a cascaded PID control method. While a 16 bit fast control output (DAC5682Z, SFDR: 77 dB) is fed to the PZT actuator, a slower 20 bit (AD5791, SFDR: 100 dB) is used to precisely control the crystal temperature. To determine the wavelength instability of the offset-locked laser system, we recorded the 62.5 MHz waveform at the maximum acquisition rate of 250 MSPS over a measurement time of 4 s (Figure 1b). The 2 GB data sampled by our controller were post processed to estimate the power spectral density (method according to Welch 1967 50% overlap). It turned out that without any averaging a stability of about 2 kHz FWHM can be achieved for the 20.0625 GHz beat node, which is equivalent to a relative value of  $1 \cdot 10^{-7}$ . This corresponds to an error of  $\pm 0.75$  nm for a single 15 mm synthetic wavelength at 1064 nm for our multi-wavelength interferometers. For fixed synthetic wavelengths interferometry, we typically choose an offset frequency of 20 GHz, generating synthetic wavelengths of 14.94 mm at 1064 nm and of 7.47 mm at 532 nm. By varying the synthesizer frequency, the frequency of the slave laser can be continuously tuned in this scheme, enabling a ‘super-heterodyning’ detection mode (Dändliker *et al.*, 1988).

### B. Modulation techniques

Figure 2 summarises the different modulation techniques used for phase retrieval by the two interferometers. The TeleYAG-II interferometer uses a classical heterodyne demodulation scheme. This enables the separation of optical phases of closely adjacent optical wavelengths by lock-in techniques,

Thus, a minimal set of photo detectors is sufficient for detection (Köchert *et al.*, 2012; Yang *et al.*, 2015). For the TeleYAG-II system, we use acousto-optic modulators (AOMs) to generate eight different carrier frequencies. In addition to the relatively short synthetic wavelengths generated by the OPLL, the wavelength shift by the AOMs is also used to realise two synthetic wavelengths of 1.486 m at 1064 nm which are continuously emitted in parallel. In contrast to our previous work (Meiners-Hagen *et al.*, 2015), we use eight fibre-coupled AOMs (3x VIS, 5x NIR) to generate the carriers and to enhance the robustness of the overall system, improving field capability. After passing through the interferometer optics, the light is subject of interference and can be detected by two photo receivers for each colour which convert the optical to a voltage signal. The voltage signals contain the carrier frequencies and are fed to an in-house developed phase meter (ADC board NI-5762, 75.5-dB SNR). It is capable of extracting the phase information for each carrier. In the post-processing step, the phase information is used to unfold the multiple wavelengths to determine the absolute value of the distance measurement.

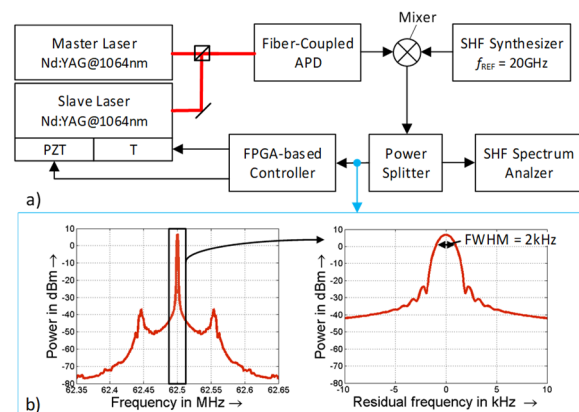


Figure 1. (a) Simplified scheme of the OPLL for locking both lasers with a frequency offset of 20 GHz. (b) Spectrum of intermediate frequency to distinguish the Full Width Half Maximum (FWHM). (T – Temperature, PZT – Piezo Transducer, SHF – Super High Frequency, APD – Avalanche Photo Diode).

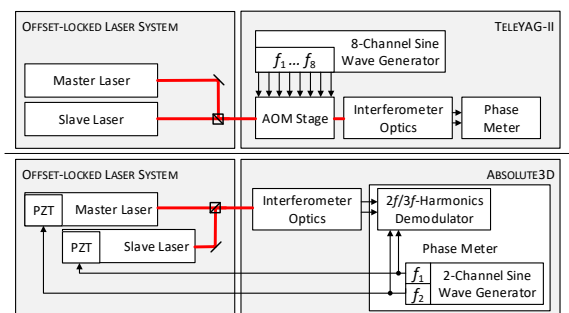


Figure 2. Scheme of the different modulation techniques.

The Absolute3D interferometer makes use of a sinusoidal modulation technique (Suzuki, 1989), enabling a more compact measurement head. The wavelengths of the master and slave lasers are phase

modulated by using the integrated piezo transducer with two independent carrier frequencies in the range of 20 kHz to 30 kHz and modulation widths of about 2.3 MHz at 1064 nm. The modulation signals are generated using the same FPGA-based electronics used to record the interference signals. The optical signals are converted into electrical signals, which are then decomposed on the FPGA in real time with respect to its second ( $2f_1$ ,  $2f_2$ ) and third order ( $3f_1$ ,  $3f_2$ ) harmonic components according to Sudarshanam and Srinivasan (1989). From the relationship between signals  $2f_1/3f_1$  and  $2f_2/3f_2$ , the phase information corresponding to the absolute distance can be determined.

#### IV. THE TELEYAG-II INTERFEROMETER

The TeleYAG-II interferometer follows the heterodyne approach used for the original TeleYAG interferometer (Meiners-Hagen *et al.*, 2015). However, we use PCFs to superpose the 532 nm and 1064 nm beams. In consequence, all optical components need to be achromatic and anti-reflection coated for both wavelengths. The system is supposed to reliably work outside. The complex optical setup and the long optical paths in the system imply a large sensitivity to thermally induced drifts. In our case, even small drifts are fatal for the measurement result as any uncertainty in the interferometric measurement is highly unfavourably scaled up due to the multi-wavelength measurement approach. We therefore very carefully designed the interferometer head for mechanical stability, using mainly invar as material with a low coefficient of thermal expansion (CTE) (Pilarski *et al.*, 2021). To monitor remaining drifts, we introduce a retractable reference mirror in the measurement path. The targeted range of 5 km is a particular challenge for the imaging optics. The two main colours of the system, 532 and 1064 nm, pass the same optics on the interferometer head. Any chromatic error would fatally propagate. In Figure 3a, the custom-designed achromatic telescope lenses of the expansion optics are depicted. The ocular consists of a lens doublet, the objective of a lens triplet. The optics design for this long-range two-colour system is non-trivial for two reasons. In general, a simple linear optics approximation cannot be used to describe the beam propagation for a confined laser beam given the inevitable extreme spot size to propagation distance ratio for distances over several hundreds of meters. We must consider that the beams do not propagate with planar wavefronts, but as Gaussian beams. In this context, the most critical aspect is the fact that Gaussian beams propagate in curved wave fronts. The most unfavourable consequence thereof is the fact, that Gaussian beams cannot be collimated in the sense of linear optics, but continuously change their beam waist over their propagation distance. This effect is usually mitigated by choosing larger initial beam waists. But in our case, even when choosing an aperture of

119 mm, after propagation over several thousands of metres, the beam waist considerably enlarges so that clipping at the aperture cannot be completely avoided (compare beam expansion between point B and C in Figure 3b). This effect is worsened by a second particularity of our optics design. As mentioned, we use a PCF to superpose the infrared and the green light. The price to pay for this perfect concentric overlap, however, is the fact that the beams emitted by the fibre vary in their spot size, depending on the optical wavelength. For the 532/1064 nm pair, the beam size almost doubles for the longer wavelength (dashed lines A in Figure 3c). Our optical system is designed so that up to approximately 1000 m measurement distance, the returning wavefront (labelled D in Figure 3c) matches almost perfectly the reference wave front in the interferometer head (A in Figure 3c). For longer distances, this match can only be imperfectly assured, possibly requiring a length-dependent correction factor. Furthermore, to realise the large beam expansion, the distance between ocular and objective lens amounts to 486 mm. To limit the extensions of the whole instrument, we chose a sandwich structure with interferometer and beam expansion being positioned on different levels (see Figure 3a). We also want to note that, like in every telescope, this distance is highly critical for the imaging properties of the expansion optics. For the TeleYAG-II system, the ocular position  $\Delta z$  (*cf.* Figure 3a) should not deviate more than 100  $\mu\text{m}$  from the optimum lens position, given by the sum of the lenses' focal lengths according to the simulation. Bigger deviations considerably deteriorate the beam collimation. As consequence, the sharp increase in beam diameter visible in Figure 3b moves to shorter and shorter distances, which quickly significantly reduces the application range. Therefore, a fine-tuneable solid-state joint was designed for ocular positioning. The absolute distance is also fixed by the low CTE material of the interferometer frame.

Figure 4 depicts a typical observation indoors over a range of approximately 26 m. The data have been recorded at a rate of 1024 data points per second for one minute. For the analysis, we require that the interference contrast in all six interferometers (two at 532 nm, four at 1064 nm) is between 25 and 99 % of the maximum of each channel. Only 52.9 % of all data sets pass this filtering process. We depict the measurement results using the high-resolution data with the shortest synthetic wavelengths at 1064 nm and 532 nm. For the power-filtered raw data, we obtain a standard deviation of 82  $\mu\text{m}$  at 1064 nm, 57  $\mu\text{m}$  at 532 nm. Averaging over 1024 data points, the standard deviation at 532 nm reduces to 11  $\mu\text{m}$ , at 1064 nm to 53  $\mu\text{m}$  only. The bad scaling properties of the 1064 nm result indicates a more fundamental problem. Currently, we revise the optical setup to facilitate the alignment of the infrared beams, hoping to improve the performance. It should also be noted that preliminary results over distances over 800 m outdoors show standard deviations of

similar magnitude, indicating that the optical system manages to preserve the fundamental performance over such long distances as desired.

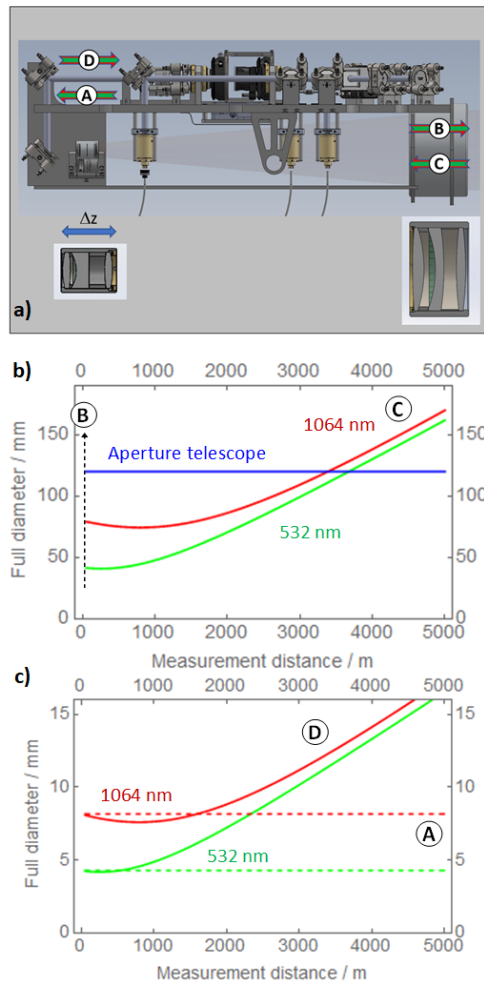


Figure 3. Beam expansion optics of the TeleYAG-II interferometer: a) Beam path in the expansion optics and cut through the achromatic telescope lenses. b) Calculated full beam diameter ( $2\omega$  beam waist) before re-entering the telescope. c) Matching of the full beam diameters ( $2\omega$  beam waist) of returned and emitted beam in the interferometer itself. The figures b) and c) are based on a configuration with  $\Delta z = 20 \mu\text{m}$ .

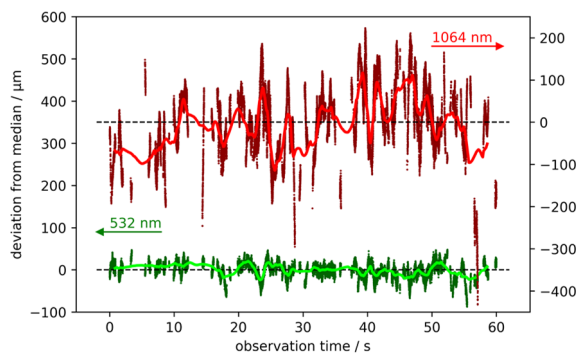


Figure 4. Typical observation data with the TeleYAG-II system over 26 m indoors. The data shows the deviation from the median value for the position data obtained from the synthetic wavelengths at 532 nm and 1064 nm. The scattered data show the power-filtered raw data, the lines indicate a moving average over 1024 data points.

## V. THE ABSOLUTE 3D INTERFEROMETER

The Absolute3D system targets a more flexible and better affordable interferometer design for shorter ranges. Thus, multiple interferometer heads can be more easily constructed. The intended applications comprise multilateration measurements requiring four heads or the intrinsic measurement of vertical temperature gradients (Röse *et al.*, 2020). Compared to the TeleYAG-II system we reduced the optical setup to a minimum complexity level at the cost of the rather complex phase detection scheme based on sinusoidal modulation. For the interferometer set up the compact Michelson design was chosen. The reduced number of optical elements in the structure means that the system can be easily readjusted in case of changes due to vibrations or environmental changes. The interferometer platforms are mounted on gimbal systems (Zaber: X-G-RST300) which enable horizontal and lateral movements (see Figure 5). The interferometer itself and its source are decoupled but connected by a single PCF only, while the TeleYAG-II system requires two PCFs. Auxiliary instrumentation needed for signal generation and analysis can be stowed in a nearby trailer.

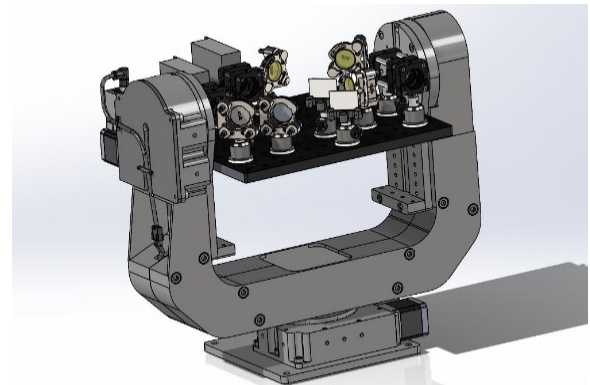


Figure 5. 3D Sketch Absolute3D on Gimbal System (model: Zaber X-G-RST300).

The length measurement consists of two partial measurements. Two Nd:YAG lasers are being used. Their laser frequency is sinusoidally modulated to enable the  $2f/3f$  detection scheme. In static operation mode, their frequency offset is fixed to 20.0625 GHz, corresponding to synthetic wavelengths of  $\Lambda_1 = 14.89 \text{ mm}$  at 1064 nm and of  $\Lambda_2 = 7.48 \text{ mm}$  at 532 nm. The flexible application scenario requires a truly absolute measurement. We realise a variable synthetic interferometry measurement within the same setup by sweeping the frequency of the slave laser. To guarantee the best optical superposition of all four laser paths, we couple them into a PCF. We use two beam splitters to superpose the two 1064 nm as well as the two 532 nm beams first. A second beam splitter in the infrared path splits the already superposed beam paths and provides the light necessary for the laser stabilization. We use a dichroic mirror to superimpose these two beams. Usually, a coupling rate of about 70%

can be achieved for each beam path. The optical system encounters similar problems regarding beam expansion and chromaticity errors as the TeleYAG-II interferometer. But since the range is limited to 50 m, a single custom-designed achromatic triplet lens collimating the beams of the PCF is sufficient. The system works with a full beam diameter of 12 mm at 1064 nm and 6 mm at 532 nm. After interference of measurement and reference beams, a dichroitic mirror separates the infrared from the visual beams. They are subsequently detected in a separate photoreceiver (Femto: HCA-S-200M-Si & HCA-S-200M-IN). All four phases of the interferometric signal are then derived by the 2f/3f lock-in technique.

In Figure 6, a typical indoor measurement of a fixed position at approx. 26 m is depicted. A sweep of 1 GHz at 1064 nm (corresponding to 2 GHz at 532 nm) with one laser was performed for a variable synthetic wavelength measurement to determine a pre-value of the geometric distance from the corresponding absolute phase change (see inset of Figure 6). We then use the phase information of the fixed synthetic wavelength measurement performed on plateau 1 (P1 in Figure 6) to refine this pre-value. This leads to a total optical distance of  $d_1 = 26.017858$  m for the 532 nm measurement and of  $d_2 = 26.017520$  m for the 1064 nm measurement. Using Equation 3 with a water vapor pressure  $p_w$  of 1188 Pa, we can now directly calculate the geometric length to  $l = 26.0107$  m. The standard deviation of the acquired geometric length amounts to 1.8 mm. Theory predicts the standard deviation of the refractivity-compensated result to scale by a factor of 21 in comparison to standard deviation of the underlying observation at 532 nm. The raw 1064 nm data shows a standard deviation of 119  $\mu\text{m}$ , the raw 532 nm data of 42  $\mu\text{m}$  which reduce to 109  $\mu\text{m}$  and 40  $\mu\text{m}$  for 1024 points (1 second) averaging (cf. Figure 6). As expected, both signals largely show a common-mode behaviour due to the environmental influences. These are then compensated by the application of Equation 3. Thus, we would expect a standard deviation of the compensated result in the order of 0.8 mm. Nevertheless, inconsistencies like subtle differences in the drift behaviour indicate additional unresolved error sources. We currently investigate probable origins. We work, e.g., on the enhanced compensation of nonlinear effects, to which sinusoidal modulation is notoriously sensitive. Ultimately, we target a measurement uncertainty of a few tenths of a millimetre for the refractivity-compensated length.

## VI. CONCLUSIONS

In this paper we discuss two multi-wavelength interferometers to achieve high accuracy measurements for different geodetic applications: one for 1D measurements distances up to 5 km, one for 3D measurements within a measurement volume of

approximately 50 m. Both systems rely on a complex versatile multi-wavelength optical source based on two Nd:YAG lasers. Their optical design and phase demodulation varies to match their use cases. In Table 1, we summarise key technical features of both systems. So far, they have not achieved the full targeted measurement capability, but show similar standard deviations and first meaningful intrinsically refractivity-compensated distance measurements could be demonstrated over relevant longer distances. In future, the systems will be further optimised and applied to geodetic measurement challenges.

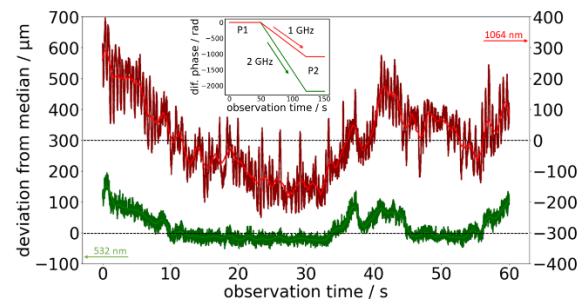


Figure 6. Typical observation data with the Absolute3D system over 26 m indoors. The data shows the deviation from the median value for the position data obtained from the synthetic wavelengths at 532 and 1064 nm. The lines indicate a moving average over 1024 data points. The inset depicts the phase hub while tuning one laser to determine the pre-value.

Table 1. Key features of the two interferometers

TeleYAG-II	Absolute3D
PCF architecture for broadband beam superposition Based on two Nd:YAG laser sources	
Frequency modulation by AOMs	Sinusoidal phase modulation by laser resonators
4 achromats	1 achromat per head
Complex optical setup (Sandwich structure)	Simple optical setup (Michelson Interferometer)
Range up to 5 km	Range 15 m to 50 m
1 head	4 optical heads
Weight ~50 kg	Weight ~20 kg (each)

## VII. ACKNOWLEDGEMENTS

This project 18SIB01 GeoMetre has received funding from the EMPIR programme co-financed by the Participating States and from the European Union's Horizon 2020 research and innovation programme. We would like to thank P. Knigge, D. Fiala, M. Wedde, and M. Peglow for technical assistance.

## References

- Bender, P. L., and Owens, J. C. (1965) Correction of optical distance measurements for the fluctuating atmospheric index of refraction. *J. Geophys. Res.* 70, pp. 2461–2.
- van den Berg, S., Persijn, S., Kok, G., Zeitouny, M., and Bhattacharya, N. (2012) Many-wavelength interferometry

- with thousands of lasers for absolute distance measurement. *Phys. Rev. Lett.* 108, 183901 (5 pp.).
- Bönsch, G., Potulski, E. (1998), Measurement of the refractive index of air and comparison with modified Edlén's formulae. *Metrologia* 35, pp. 133-9.
- Coddington, I., Swann, W. C., Nenadovic, L. and Newbury, N. R. (2009) Rapid and precise absolute distance measurements at long range. *Nat. Photonics* 3, pp. 351-6.
- Czarske, J. W., Phillipps, R., and Freitag, I. (1995) Spectral properties of diode-pumped non-planar monolithic Nd:YAG ring lasers. *Appl. Phys. B* 61, pp. 243-8.
- Dändliker, R., Thalmann, R., and Prongue, D. (1988) Two-wavelength laser interferometry using superheterodyne detection. *Opt. Lett.* 13, 339-41.
- Earnshaw, K. B., and Owens, J. C. (1967) Dual wavelength optical distance measuring instrument, which corrects for air density. *IEEE J. Quantum Electron.* 3, pp. 544-50.
- Guillory, J., Šmid, R., Garcia-Marquez, J., Truong, D. Alexandre, C., and Wallerand, J.-P. (2016) High resolution kilometeric range optical telemetry in air by radio frequency phase measurement. *Rev. Sci. Instr.* 87, 075105 (6 pp.).
- Guillory, J., Teyssendier de la Serve, M., Truong, D., Alexandre, C. and J.-P. Wallerand (2019) Uncertainty assessment of optical distance measurements at micrometer level accuracy for long-range applications. *IEEE Trans. Instrum. Meas.* 68, pp. 2260-2267.
- Hugget, G.R. and Slater, L.E. (1975) Precision electromagnetic distance measuring instrument for determining secular strain and fault movement. *Tectonophysics* 29, pp. 19-27.
- Huggett, G.R. (1981) Two-color terrameter. *Tectonophysics* 71, pp. 29-39.
- Köchert, P., Flügge, J., Weichert, C., Köning, R., and Manske, E. (2012) Phase measurement of various commercial heterodyne He-Ne-laser interferometers with stability in the picometer regime. *Meas. Sci. Technol.* 23, 074005 (6 pp.).
- Köhler, M. (2012) Distanzmessverfahren elektrooptischer Tachymeter – Stand der Trimble Technik. *avn* 119, pp. 291-304.
- Liu, Y., Röse, A., Prellinger, G., Köchert, P., Jigui, Z., and Pollinger, F. (2020) Combining Harmonic Laser Beams by Fiber Components for Refractivity-Compensating Two-Color Interferometry. *J. Light. Technol.* 38, pp. 1945-52.
- Meiners-Hagen, K., and Abou-Zeid, A. (2008) Refractive index determination in length measurement by two-colour interferometry. *Meas. Sci. Technol.* 19, 084004 (5 pp.).
- Meiners-Hagen, K., Schödel, R., Pollinger, F., and Abou-Zeid, A. (2009), Multi-Wavelength Interferometry for Length Measurements Using Diode Lasers. *Meas. Sci. Rev.* 9, pp. 16-26.
- Meiners-Hagen, K., Bosnjakovic, A., Köchert, P., and Pollinger, F. (2015) Air index compensated interferometer as a prospective novel primary standard for baseline calibrations. *Meas. Sci. Technol.* 26, 084002 (8 pp.).
- Meiners-Hagen, K., Meyer, T., Prellinger, G., Pöschel, W., Dontsov, D., and Pollinger, F. (2016). Overcoming the refractivity limit in manufacturing environment. *Opt. Express* 24, pp. 24092-104.
- Meiners-Hagen, K., Meyer, T., Mildner, J., and Pollinger, F. (2017) SI-traceable absolute distance measurement over more than 800 meters with sub-nanometer interferometry by two-color inline refractivity compensation. *Appl. Phys. Lett.* 111, 191104 (5 pp.).
- Minoshima, K., and Matsumoto, H. (2000) High-accuracy measurement of 240-m distance in an optical tunnel by use of a compact femtosecond laser. *Appl. Opt.* 39 5512-7.
- Neyezhmakov, P., Panasenkov, T., Prokopov, A., Skliarov, V., and Trevoho, I. (2020). Comparative analysis of quadrature formulas for the mean integral refractive index of air in high-precision ranging. *Modern achievements of geodesic science and industry* 39, pp. 69-73.
- Pilarski, F., Schmaljohann, F., Weinrich, S., Huismann, J., Truong, D., Meyer, T., Köchert, P., Schödel, T., and Pollinger, F. (2021). Design and manufacture of a reference interferometer for long-range distance metrology. In: Proc. Euspen's 21st International Conference & Exhibition, Virtual Conference, 7-10, June, pp. 511-512.
- Pisani, M., Astrua, M., and Zucco, M. (2018). An acoustic thermometer for air refractive index estimation in long distance interferometric measurements. *Metrologia* 55, pp. 67-74.
- Pollinger, F., Meyer, T., Beyer, J., Doloca, N. R., Schellin, W., Niemeier, W., Jokela, J., Häkli, P., Abou-Zeid, A. and Meiners-Hagen, K. (2012) The upgraded PTB 600 m baseline: a high-accuracy reference for the calibration and the development of long distance measurement devices. *Meas. Sci. Technol.* 23, 094018 (11 pp.).
- Röse, A., Liu, Y., Köchert, P., Prellinger, G., Manske, E., and Pollinger, F. (2020) Modulation-based long-range interferometry as basis for an optical two-color temperature sensor. In: Conference Proceedings - 20<sup>th</sup> International Conference & Exhibition, Geneva, CH, June 2020.
- Salido-Monzú, D., and Wieser, A. (2018) Simultaneous distance measurement at multiple wavelengths using the intermode beats from a femtosecond laser coherent supercontinuum. *Opt. Eng.* 57, 044107 (10 pp.).
- Sorin, W.V., Donald, D.K., Newton, S.A., and Nazarathy, M. (1990) Coherent FMCW reflectometry using a temperature tuned Nd:YAG ring laser. *IEEE Phot. Technol. Lett.* 2, pp. 902-4.
- Sudarshanam, V.S., and Srinivasan, K. (1989) Linear readout of dynamic phase change in a fiber optic homodyne interferometer, *Opt. Lett.* 14, pp. 140-2.
- Suzuki, T., Sasaki, O., Higuchi, K. and Maruyama, T. (1989) Real time displacement measurement in sinusoidal phase modulating interferometry, *Appl. Opt.* 28, pp. 5270-4.
- Tomberg, T., Fordell, T., Jokela, J., Merimaa, M., and Hieta, T. (2017) Spectroscopic thermometry for long-distance surveying. *Appl. Opt.* 56, pp. 239-46.
- Welch, D. (1967) The use of fast Fourier transform for the estimation of power spectra *IEEE Trans. Audio Electroacoustics* 15, pp. 70-73.
- Wu, G., Takahashi, M., Arai, K., Inaba, H., and Minoshima, K. (2013) Extremely high-accuracy correction of air refractive index using two-colour optical frequency combs. *Sci. Rep.* 3, 1894 (5 pp.).
- Wu, H., Zhao, T., Wang, Z., Zhang, K., Xue, B., Li, J., He, M., and Qu, X. (2017) Long distance measurement up to 1.2 km by electro-optic dual-comb interferometry. *Appl. Phys. Lett.* 111, 251901 (5 pp.).



- Wynands, R., Coste, O., Rembe, C., and Meschede, D. (1995) How accurate is optical second-harmonic generation? *Opt. Lett.* 20, pp. 1095-7.
- Yang, R., Pollinger, F., Meiners-Hagen, K., Krystek, M., Tan, J., and Bosse, H. (2015) Absolute distance measurement by dual-comb interferometry with multi-channel digital lock-in phase detection. *Meas. Sci. Technol.* 28, 084001 (10 pp.).

## The European GeoMetre project – developing enhanced large-scale dimensional metrology for geodesy

Florian Pollinger<sup>1</sup>, Sergio Baselga<sup>2</sup>, Clément Courde<sup>3</sup>, Cornelia Eschelbach<sup>4</sup>, Luis García-Asenjo<sup>2</sup>, Pascual Garrigues<sup>2</sup>, Joffray Guillory<sup>5</sup>, Per Olof Hedekvist<sup>6</sup>, Tuomas Helojärvi<sup>7</sup>, Jorma Jokela<sup>8</sup>, Ulla Kallio<sup>8</sup>, Thomas Klügel<sup>9</sup>, Paul Köchert<sup>1</sup>, Michael Lösler<sup>4</sup>, Raquel Luján<sup>2</sup>, Tobias Meyer<sup>1</sup>, Pavel Neyezhmakov<sup>10</sup>, Damien Pesce<sup>11</sup>, Marco Pisani<sup>12</sup>, Markku Poutanen<sup>8</sup>, Günther Prellinger<sup>1</sup>, Anni Sauthoff<sup>1</sup>, Jeremias Seppä<sup>7</sup>, Daniel Truong<sup>5</sup>, Robin Underwood<sup>13</sup>, Kinga Wezka<sup>14</sup>, Jean-Pierre Wallerand<sup>5</sup>, Mariusz Wiśniewski<sup>15</sup>

<sup>1</sup> Physikalisch-Technische Bundesanstalt (PTB), Bundesallee 100, 38116 Braunschweig, Germany, ([florian.pollinger@ptb.de](mailto:florian.pollinger@ptb.de); [paul.koechert@ptb.de](mailto:paul.koechert@ptb.de); [tobias.meyer@ptb.de](mailto:tobias.meyer@ptb.de); [guenther.prellinger@ptb.de](mailto:guenther.prellinger@ptb.de); [anni.sauthoff@ptb.de](mailto:anni.sauthoff@ptb.de))

<sup>2</sup> Departamento de Ingeniería Cartográfica, Geodesia y Fotogrametría, Universitat Politècnica de València, Camino de Vera s/n, 46022 Valencia, Spain, ([serbamo@cgf.upv.es](mailto:serbamo@cgf.upv.es); [lugarcia@cgf.upv.es](mailto:lugarcia@cgf.upv.es); [pasgarta@cgf.upv.es](mailto:pasgarta@cgf.upv.es); [ralugar@cgf.upv.es](mailto:ralugar@cgf.upv.es))

<sup>3</sup> Université Côte d'Azur, CNRS, Observatoire de la Côte d'Azur, IRD, Géoazur, 2130 Route de l'Observatoire, 06460 Caussols, France, ([clement.courde@oca.eu](mailto:clement.courde@oca.eu))

<sup>4</sup> Laboratory for Industrial Metrology, Faculty of Architecture, Civil Engineering and Geomatics, Frankfurt University of Applied Sciences, Nibelungenplatz 1, 60318 Frankfurt am Main, Germany, ([cornelia.eschelbach@fb1.fh-frankfurt.de](mailto:cornelia.eschelbach@fb1.fh-frankfurt.de); [michael.loesler@fb1.fra-uas.de](mailto:michael.loesler@fb1.fra-uas.de))

<sup>5</sup> Conservatoire National des Arts et Métiers (Cnam), Laboratoire commun de métrologie LNE-Cnam, 1 rue Gaston Boissier, 75015 Paris, France, ([joffray.guillory@cnam.fr](mailto:joffray.guillory@cnam.fr); [daniel.truong@cnam.fr](mailto:daniel.truong@cnam.fr); [jean-pierre.wallerand@cnam.fr](mailto:jean-pierre.wallerand@cnam.fr))

<sup>6</sup> RISE Research Institutes of Sweden, Box 857, 501 15 Borås, Sweden, ([per.olof.hedekvist@ri.se](mailto:per.olof.hedekvist@ri.se))

<sup>7</sup> VTT Technical Research Centre of Finland Ltd, Centre for Metrology MIKES, PO Box 1000, 02044 VTT, Finland, ([tuomashelajarvi@gmail.com](mailto:tuomashelajarvi@gmail.com); [Jeremias.Seppa@vtt.fi](mailto:Jeremias.Seppa@vtt.fi))

<sup>8</sup> Finnish Geospatial Research Institute, National Land Survey of Finland, Geodeetinrinne 2, 02430 Masala, Finland, ([jorma.jokela@nls.fi](mailto:jorma.jokela@nls.fi); [ulla.kallio@nls.fi](mailto:ulla.kallio@nls.fi); [markku.poutanen@nls.fi](mailto:markku.poutanen@nls.fi))

<sup>9</sup> Geodetic Observatory Wettzell, Federal Agency for Cartography and Geodesy, 93444 Bad Kötzing, Germany, ([Thomas.Kluegel@bkg.bund.de](mailto:Thomas.Kluegel@bkg.bund.de))

<sup>10</sup> National Scientific Center “Institute of Metrology” (NSC-IM), Mironositskaya str. 42, 61002 Kharkiv, Ukraine, ([pavel.neyezhmakov@gmail.com](mailto:pavel.neyezhmakov@gmail.com))

<sup>11</sup> Institut national de l’information géographique et forestière (IGN), 94160 Saint-Mandé, France, ([Damien.Pesce@ign.fr](mailto:Damien.Pesce@ign.fr))

<sup>12</sup> Istituto Nazionale di Ricerca Metrologica (INRIM), Strada delle Cacce, 91, 10135 Torino, Italy, ([m.pisani@inrim.it](mailto:m.pisani@inrim.it))

<sup>13</sup> National Physical Laboratory, Hampton Road, Teddington, TW11 0LW, United Kingdom, ([robin.underwood@npl.co.uk](mailto:robin.underwood@npl.co.uk))

<sup>14</sup> Faculty of Geodesy and Cartography, Warsaw University of Technology, Plac Politechniki 1, 00-661 Warsaw, Poland, ([Kinga.Wezka@pw.edu.pl](mailto:Kinga.Wezka@pw.edu.pl))

<sup>15</sup> Central Office of Measures, ul. Elektoralna 2, 00-139 Warszawa, Poland, ([m.wisniewski@gum.gov.pl](mailto:m.wisniewski@gum.gov.pl))

**Key words:** *novel distance sensor systems; multilateration systems; SI traceability; GNSS-EDM comparison; local tie metrology; air refractivity compensation; GeoMetre project*

### ABSTRACT

We provide a survey on the joint European research project “GeoMetre”, which explores novel technologies and their inclusion to existing surveying strategies to improve the traceability of geodetic reference frames to the SI definition of the metre. This work includes the development of novel distance meters with a range of up to 5 km, the realisation of optical multilateration systems for large structure monitoring at an operation distance of 50 m and beyond, and a novel strategy for GNSS-based distance determination. Different methods for refractivity compensation, based on classical sensors, on dispersion, on spectroscopic thermometry and on the speed of sound to reduce the meteorological uncertainties in precise distance measurements are developed

further and characterised. These systems are validated at and applied to the novel European standard baseline EURO5000 at the Pieniny Kippen Belt, Poland, which was completely refurbished and intensely studied in this project. We use our novel instruments for a reduced uncertainty of the scale in the surveillance networks solutions for local tie measurements at space-geodetic co-location stations. We also investigate novel approaches like close-range photogrammetry to reference point determination of space-geodetic telescopes. Finally, we also investigate the inclusion of the local gravity field to consider the deviations of the vertical in the data analysis and to reduce the uncertainty of coordinate transformations in this complex problem.

*This contribution was selected by the Scientific Committee for publication as an extended paper in Applied Geomatics <https://www.springer.com/journal/12518>*

## Real movement or systematic errors? – TLS-based deformation analysis of a concrete wall

Berit Jost<sup>1</sup>, Daniel Coopmann<sup>1</sup>, Christoph Holst<sup>2</sup>, Heiner Kuhlmann<sup>1</sup>

<sup>1</sup> University of Bonn, Nussallee 17, 53115 Bonn, Germany, ([b.jost@igg.uni-bonn.de](mailto:b.jost@igg.uni-bonn.de); [coopmann@igg.uni-bonn.de](mailto:coopmann@igg.uni-bonn.de); [heiner.kuhlmann@uni-bonn.de](mailto:heiner.kuhlmann@uni-bonn.de))

<sup>2</sup> Technical University of Munich, Arcisstraße 21, 80333 Munich, Germany, ([christoph.holst@tum.de](mailto:christoph.holst@tum.de))

**Key words:** *deformation monitoring; terrestrial laser scanner; correlations; stochastic model; point cloud comparison*

### ABSTRACT

Performing deformation analyses with high accuracy demands using terrestrial laser scanners is very challenging due to insufficient knowledge about the error budget and correlations. Terrestrial laser scans suffer from random and systematic errors that mitigate the quality of the point cloud. Even though the vast majority of systematic errors can be calibrated, remaining errors or errors that vary with time or temperature influence spatially neighbored points in the same way. Hence, correlations between the measurements exist. Considering area-based deformation analyses, these correlations have two effects: On the one hand, they reduce the effective number of measurements in the point cloud, which mainly influences the decision whether the movement is significant or not. On the other hand, correlations caused by systematic errors in the scanner can lead to a misinterpretation as a deformation of the object. Within this study, we analyze the deformation of a concrete wall (9.50 m height, 50 m width), and we develop a workflow that avoids the misinterpretation of correlated measurements as deformations of the object. Therefore, we first calibrate the scanner to reduce the influence of systematic errors. Afterwards, we use the average of two-face measurements from several scanner stations to eliminate remaining systematic errors and correlated measurements. This study demonstrates that systematic effects can lead to errors of a few millimeters that are likely to be interpreted as small deformations, and it provides a strategy to avoid misinterpretation. Hence, it is inevitable either to model or to eliminate systematic errors of the scanner while performing a precise deformation analysis with a magnitude of a few millimeters.

*This contribution was selected by the Scientific Committee for publication as an extended paper in the Journal of Applied Geodesy <https://www.degruyter.com/journal/key/jag/html>*

## Automated damage detection for port structures using machine learning algorithms in heightfields

Frederic Hake<sup>1</sup>, Paula Lippmann<sup>1</sup>, Hamza Alkhatib<sup>1</sup>, Vincent Oettel<sup>2</sup>, Ingo Neumann<sup>1</sup>

<sup>1</sup> Geodetic Institute Hannover, Leibniz University Hannover, Nienburger Straße 1, Hannover, Germany, ([hake@gih.uni-hannover.de](mailto:hake@gih.uni-hannover.de); [alkhatib@gih.uni-hannover.de](mailto:alkhatib@gih.uni-hannover.de); [neumann@gih.uni-hannover.de](mailto:neumann@gih.uni-hannover.de); [paula.lippmann@stud.uni-hannover.de](mailto:paula.lippmann@stud.uni-hannover.de))

<sup>2</sup> Institute of Concrete Construction, Leibniz University Hannover, Appelstraße 9a, Hannover, Germany, ([oettel@ifma.uni-hannover.de](mailto:oettel@ifma.uni-hannover.de))

**Key words:** *damage detection; machine-learning; laserscanning; multibeam-echosounder; infrastructure*

### ABSTRACT

The ageing infrastructure in ports requires regular inspection. This inspection is currently carried out manually by divers who sense by hand the entire underwater infrastructure. This process is cost-intensive as it requires a considerable amount of time and manpower. To overcome these difficulties, we propose to scan the above and underwater port structure with a Multi-Sensor-System (MSS), and -by a fully automated process- classify the obtained point cloud into damaged and undamaged regions. The MSS consists of a high-resolution hydro-acoustic underwater multi-beam echo-sounder, an above-water profile laser scanner, and five HDR cameras. In addition to the IMU-GPS/GNSS method known from various applications, hybrid referencing with automatically tracking total stations is used for positioning. The main research idea is based on 3D data from TLS, multi-beam or dense image matching. To that aim, we build a rasterised heightfield of the point cloud of a harbour structure by subtracting a CADbased geometry. To do this, we fit regular shapes into the point cloud and determine the distance of the points to the geometry. This latter is propagated through a Convolutional Neural Network (CNN) which detects anomalies. We make use of two methods: the VGG19 Deep Neural Network (DNN) and Local-Outlier-Factors (LOF). We tested our approach on simulated training data and evaluated it on a real-world dataset in Lübeck, Germany measured by an MSS. We showed that our approach can achieve a fully automated, reproducible, quality-controlled damage detection that can analyse the whole structure instead of the sample wise manual method with divers. We were able to achieve valuable results for our application.

*This contribution was selected by the Scientific Committee for publication as an extended paper in Applied Geomatics <https://www.springer.com/journal/12518>*

## Supervoxel-based targetless registration and identification of stable areas for deformed point clouds

Yihui Yang, Volker Schwieger

Institute of Engineering Geodesy, University of Stuttgart, Geschwister-Scholl-Str. 24D, 70174 Stuttgart, Germany, ([yihui.yang@iigs.uni-stuttgart.de](mailto:yihui.yang@iigs.uni-stuttgart.de); [volker.schwieger@iigs.uni-stuttgart.de](mailto:volker.schwieger@iigs.uni-stuttgart.de))

**Key words:** *TLS point clouds; targetless registration; stable area identification; supervoxel; ICP*

### ABSTRACT

Accurate and robust 3D point clouds registration is the crucial part of the processing chain in terrestrial laser scanning (TLS)-based deformation monitoring that has been widely investigated in the last two decades. For the scenarios without signalized targets, however, automatic and robust point cloud registration becomes more challenging, especially when significant deformations and changes exist between the sequence of scans which may cause erroneous registrations. In this contribution, a fully automatic registration algorithm for point clouds with partially unstable areas is proposed, which does not require artificial targets or extracted feature points. In this method, coarsely registered point clouds are firstly over-segmented and represented by supervoxels based on the local consistency assumption of deformed objects. A confidence interval based on an approximate assumption of the stochastic model is considered to determine the local minimum detectable deformation for the identification of stable areas. The significantly deformed supervoxels between two scans can be detected progressively by an efficient iterative process, solely retaining the stable areas to be utilized for the fine registration. The proposed registration method is demonstrated on two datasets (both with two-epoch scans): An indoor scene simulated with different kinds of changes, including rigid body movement and shape deformation, and the Nesslrinna landslide close to Obergurgl, Austria. The experimental results show that the proposed algorithm exhibits a higher registration accuracy and thus a better detection of deformations in TLS point clouds compared with the existing voxel-based method and the variants of the iterative closest point (ICP) algorithm.

*This contribution was selected by the Scientific Committee for publication as an extended paper in the Journal of Applied Geodesy <https://www.degruyter.com/journal/key/jag/html>*

## Investigation of space-continuous deformation from point clouds of structured surfaces

Elisabeth Ötsch<sup>1</sup>, Corinna Harmening<sup>2</sup>, Hans Neuner<sup>1</sup>

<sup>1</sup> Department of Geodesy and Geoinformation, TU Wien, Wiedner Hauptstraße 8-10, 1040 Wien, Austria, ([elisabeth.oetsch@tuwien.ac.at](mailto:elisabeth.oetsch@tuwien.ac.at); [hans.neuner@tuwien.ac.at](mailto:hans.neuner@tuwien.ac.at))

<sup>2</sup> Geodetic Institute, Karlsruhe Institute of Technology, Engelerstraße 7, 76131 Karlsruhe, Germany, ([corinna.harmening@kit.edu](mailto:corinna.harmening@kit.edu))

**Key words:** *B-spline surfaces; terrestrial laser scanning; segmentation; space-continuous deformation analysis; congruence model; parameter-based point cloud comparison; modelling of structured surfaces*

### ABSTRACT

One approach to estimate space-continuous deformation from point clouds is the parameter-based epochal comparison of approximating surfaces. This procedure allows a statistical assessment of the estimated deformations. Typically, holistic geometric models approximate the scanned surfaces. Regarding this, the question arises on how discontinuities of the object's surface resulting from *e.g.* single bricks or concrete blocks, influence the parameters of the approximated continuous surfaces and in further consequence the derived deformation. This issue is tackled in the following paper. B-spline surfaces are used to approximate the scanned point clouds. The approximation implies solving a Gauss-Markov-Model, thus allowing accounting for the measurement's stochastic properties as well as propagating them on the surface' control points. A parametric comparison of two B-spline surfaces can be made on the basis of these estimated control points if common parameterization of the observations is applied. This approach is advantageous with regard to the transition of the space-continuous deformation analysis to a point-based task, thus ensuring the applicability of the well-established congruence model. The influence of the structure's geometry on the surface' control points is investigated using terrestrial laser scans of a clinker façade. Points measured in the joints are eliminated using an own developed segmentation approach. This is based on a region-growing solution, which is optimized by adding preliminary information about the dimensions and orientation of individual bricks. A comparison of the results obtained from segmented as well as from unsegmented laser scans for the B-spline approximation and the subsequent deformation analysis provides information about the structure-related influence. An aqueduct arc is used as measuring object in this study. For the intended comparison, data sets, which contain possible influences due to changes of the mechanical loads, are analysed.

*This contribution was selected by the Scientific Committee for publication as an extended paper in the Journal of Applied Geodesy <https://www.degruyter.com/journal/key/jag/html>*

## Permanent terrestrial LiDAR monitoring in mining, natural hazard prevention and infrastructure protection – Chances, risks, and challenges: A case study of a rockfall in Tyrol, Austria

Daniel Schröder<sup>1,2</sup>, Katharina Anders<sup>3</sup>, Lukas Winiwarter<sup>3</sup>, Daniel Wujanz<sup>4</sup>

<sup>1</sup> DMT GmbH & Co. KG, Civil and Mining Engineering, Essen, Germany, ([daniel.schroeder@dm-group.com](mailto:daniel.schroeder@dm-group.com))

<sup>2</sup> Faculty of Geoscience, Geotechnology and Mining, University of Mining and Technology Freiberg, Germany

<sup>3</sup> Heidelberg University, 3DGeo Research Group, Germany, ([katharina.anders@uni-heidelberg.de](mailto:katharina.anders@uni-heidelberg.de); [winiwarter@uni-heidelberg.de](mailto:winiwarter@uni-heidelberg.de))

<sup>4</sup> Technet GmbH, Berlin, Germany, ([daniel.wujanz@technet-gmbh.com](mailto:daniel.wujanz@technet-gmbh.com))

**Key words:** *automated laser scanning; multitemporal 3D point cloud analysis; web-based monitoring; georeferencing; error budget; level of detection*

### ABSTRACT

The objective of this work is the development of an integrated monitoring service for the identification and evaluation of ground surface and slope movements in the context of coal mining, the prevention of natural hazards and protection of infrastructure. The focus is set on the integration of a long-range terrestrial laser scanner into a continuous monitoring system from an engineering geodetic point of view. In the Vals valley in Tyrol, a permanently installed laser scanner was successfully operated via a web portal to monitor surface processes in the area of rockfall debris on a high-mountain slope in the summers of 2020 and 2021. This paper describes the practical benefits of this permanent laser scanning installation. In addition to the potentials of automatic data acquisition, possibilities for multitemporal analysis with respect to spatio-temporally variable changes are presented, using advanced 3D change detection with Kalman filtering. The level of detection for deformation analyses therein depends on the quality of the georeferencing of the sensor and the noise within the measured point cloud. We identify and discuss temporally variable artifacts within the data based on different methods of georeferencing. Finally, we apply our change detection method on these multitemporal data to extract specific information regarding the observed geomorphologic processes.

### I. INTRODUCTION

Analysis of mass movements and of geomorphic processes in general are a key subject in the prevention of natural hazards and protection of infrastructure (Bremer *et al.*, 2019). Such events are induced by various environmental processes as drivers while their occurrence is causally linked to climate change, therefore posing an increasing risk in terms of magnitude and frequency (Huggel *et al.*, 2012). In the context of climate change and the expansion of areas of urban settlement, *e.g.* in Alpine regions, the demand for high-quality, *i.e.* spatially and temporally detailed, datasets as well as the integration in risk management as an early warning system is increasing.

Monitoring high-mountain areas is often difficult and dangerous. Remote sensing techniques are hence preferable for observation and to achieve high spatial and temporal coverage (Hermle *et al.*, 2022). The technical advancement of terrestrial laser scanning (TLS) instruments towards communication-capable, programmable multi-sensor systems, compact and robust design as well as economically attractive systems allow the installation of permanent laser scanning (PLS) systems in areas of interest, and their integration into near real time early warning systems. A major

advantage of PLS compared to measurements at selected points in time is that time series contain morphometric measures at high temporal resolution, which allow gaining a deeper insight into Earth surface processes (Eitel *et al.*, 2016). With regard to the application of PLS within an early warning system, false alarms and misinterpretations of the results due to low levels of detection (LOD) or systematic deviations must be avoided. The risk of a poorly designed system provokes a lack of acceptance by stakeholders or derivation of incorrect conclusions on observed surface changes due to the influence of systematic errors.

Past research on point cloud registration and atmospheric influences often only used data limited to a few points in time over limited periods, from few hours to several days. The results, conclusions and recommendations derived from them are only generalizable to a limited extent. In this contribution, we present data integration of a permanent TLS installation which took place in 2020 and 2021 in Vals (Tyrol, Austria), emphasizing on quality-checked point cloud data and extraction of change information. We expect to provide a better understanding of the parameters influencing the observations and subsequent change analysis, which are variable on different temporal scales over long periods. From an



engineering geodetic point of view, initial results demonstrate the need for improving the compensation of daily variations, which commonly occur in permanent TLS installations. We further present results of a change analysis using a new approach considering the full temporal domain of the 3D time series. Our results contribute to improved geoscientific monitoring using PLS by reducing uncertainty in the interpretation of processes that shape the Earth's surface.

## II. RELATED WORK

Deformation measurement in a geodetic sense (Lang, 1929) is conducted by surveying an area of interest at different epochs and identifying geometric changes based on the captured data. Despite its long existence and the development of novel sensors and algorithms, the processing chain of deformation measurement is still valid. Hence, it is recommended to carry out all steps of the following processing chain:

- Viewpoint planning (*e.g.*, Bechtold and Höfle, 2016; not elaborated in this paper),
- Data acquisition at different points in time (*cf.* Section A),
- Transformation of individual epochs into a stable reference frame (*cf.* Section B), and
- Quantification of deformation (*cf.* Section C).

### A. Permanent Laser Scanning (PLS)

PLS is being used in numerous applications for the observation of natural surface dynamics (*e.g.*, Kromer *et al.*, 2017; Vos *et al.*, 2017; Williams *et al.*, 2018; Voordendag *et al.*, 2021). The automatic acquisition from a fixed position at regular intervals, *e.g.* hourly to daily, enables capturing surface changes at a large range of spatial and temporal scales (Eitel *et al.*, 2016).

As one of the first applications of PLS, Kromer *et al.* (2017) implemented a landslide monitoring system with half-hourly data acquisition over six weeks. The resulting 3D time series contained information on slope deformation preceding the occurrence of a rockfall event. Hourly PLS of a coastal cliff was conducted by Williams *et al.*, (2019) to investigate the magnitude-frequency distribution of rockfalls, which provides information about their hazard potential.

In PLS, monitoring systems are assumed to be stable in terms of position and orientation to acquire 4D point clouds from the exact same instrument origin throughout the entire observation period. Theoretically, no further alignment of data would be required. In practice, applications of PLS have shown various effects that arise specifically in setups with high temporal acquisition frequency. In a coastal monitoring setting, Kuschnerus *et al.* (2021a) identified movement of the survey instrument, which needs to be corrected between epochs before applying point cloud comparisons for change analysis to reduce systematic errors.

Another important challenge that arises from high-frequency TLS acquisition is that variable atmospheric conditions influence the measurements at a scale which affects the detectability of changes. Variation in surface measurements linked to changing atmospheric conditions were found to strongly exceed the expected measurement accuracy in use cases of hourly coastal (Anders *et al.*, 2020; Kuschnerus *et al.*, 2021a) and glacier monitoring (Voordendag *et al.*, 2021). The influence of (changing) atmospheric refraction on long-range TLS was determined to reach decimeter scales at kilometer acquisition ranges by Friedli *et al.* (2019). How these temporally variable uncertainties and measurement error can be fully accounted for in PLS-based monitoring is subject to current research.

### B. Registration

Methods to analyze geometric changes in multitemporal point clouds are based on the assumption that individual scans are available in a common reference frame. Thus, bi- or multitemporal scans require transformation into such a frame (*cf.* Friedli and Wieser, 2016). Erroneous effects that occur in this step have an immediate and systematic impact on the quantification of deformation. Thus, all conclusions that are drawn based on the generated results are affected. Typically, parameters of a 6- or 7-parameter Helmert transformation are estimated using stable parts of the scene, and the derived transformation is subsequently applied to the whole scene (Vosselman and Maas, 2010). By using redundant computation of the parameters residuals can be quantified, and variances and covariances are available as a result for further processing.

In general, two strategies can be deployed to transform point clouds into common coordinate systems, either by georeferencing or co-registration approaches. Since deformed areas that occurred in between epochs would influence the outcome of registration, it is vital to exclude these from this process. Solutions to automatically reject deformed areas from the registration process are presented by Friedli and Wieser (2016), as well Wujanz *et al.* (2016).

### C. Quantification of surface changes

A crucial factor for the practicability of PLS-based monitoring is the ability to fully automatically derive information from the large amount of 4D topographic data and to present interpretable layers to stakeholders. For use cases of topographic monitoring, the result of these analyses can be, *e.g.* maps of change magnitude and direction, the points in time when change occurs, a time series of change for each spatial location, or other information derived from the time series (*e.g.*, Winiwarter *et al.*, 2022). In applications of natural hazards, near real time analysis may provide a warning when surface change surpass a defined threshold (*e.g.*, Kromer *et al.*, 2017).

Currently, one of the main challenges for analyzing data acquired with PLS is that, while the information content is very high, the types of changes to be extracted from the data are not known *a priori*. Recently, new methods have therefore been presented, focusing on such change analysis tasks and information extraction from 4D topographic point cloud data. Due to the fixed setup and repeated scanning from the same position some error sources can be disregarded, whereas others appear more pronounced (Kuschnerus *et al.*, 2021a). The requirement for an appropriate consideration of measurement uncertainties to separate small-scale displacements from noise is pointed out by Lague *et al.* (2013), and demonstrated by Fey and Wichmann (2017) for a rockfall area. The LOD, representing this separation threshold, is typically derived using a statistical test at a certain level of confidence.

Different methods to minimize the influence of noise in the quantification of change and to identify important change events have been developed. Among them is the multiscale model-to-model cloud comparison (M3C2, Lague *et al.*, 2013). Though the M3C2 is a strictly bitemporal point cloud distance measure, differencing of successive epochs can be employed, for example, with respect to a fixed reference epoch. The M3C2 includes a statistical significance test, where the uncertainty of the measurements is derived from the data, combined with a globally constant value representing the alignment quality (Lague *et al.*, 2013). To improve the quantification of measurement uncertainty, Winiwarter *et al.* (2021) have developed a method to integrate error propagation, which uses knowledge on the sensor's accuracy to predict the uncertainty in bitemporal point cloud distances.

To leverage the temporal domain of PLS data, the results of bitemporal surface change quantification can subsequently be processed as a time series for each location. Kromer *et al.* (2017) have used temporal averaging using a moving window to decrease uncertainty for a dense 3D time series. A similar approach has been employed by Anders *et al.* (2021), who further use the time series for the detection and spatial delineation of temporary surface changes on a sandy beach. Another approach which uses the full temporal information of hourly PLS is time series clustering, presented by Kuschnerus *et al.* (2021b) to identify characteristic change patterns on a beach.

In Winiwarter *et al.* (2022), the use of a Kalman filter is presented to reduce uncertainty through informed temporal smoothing. The smoothed time series enable to additionally output a set of physically descriptive features, such as the maximum change velocity or the acceleration. Different feature groups can then be used to create clusters, which can give additional insights when interpreting results. 4D point cloud data can hence be visualized as 2D clusters and magnitude maps,

with additional time series at selected locations, to provide the temporal information.

### III. DATA DESCRIPTION

Our test site is the Vals valley in Tyrol (Austria). A rockfall occurred in this area on 24 December 2017, leaving a large debris cone at the lower part of the Alpine slope. Though causing neither human casualties nor significant damage to buildings, a road located directly below the rockfall slope was covered with 8 m of debris and a total volume of 116,000 m<sup>3</sup> of rock was relocated (Hartl, 2019). The local authorities set up a geodetic monitoring system, consisting of a total station with 21 corresponding prisms (Model: LEICA GPR1) and geotechnical sensors (*e.g.* extensometers) distributed over the source area of the rockfall on the upper mountain slope. As no significant rock movements were detected in the acquired data, the infrastructure of the existing monitoring system was made available for research. Point cloud data of the rockfall and debris area below was recorded during three campaigns using two different RIEGL VZ-2000i laser scanners (referred to as Model A and B), which were permanently installed on a survey pillar in a shelter on the opposite slope about 800 m from the rockfall area:

- Measuring setup 1 (M1): 13 August 2020 to 08 September 2020 – bi-hourly.
- Measuring setup 2 (M2): 10 May 2021 to 17 June 2021 – tri-hourly.
- Measuring setup 3 (M3): 28 July 2021 to 17 December 2021 – tri-hourly.

The acquisition was designed for various research and development activities regarding the deployment of long-range terrestrial laser scanners within a remotely controlled, web-based monitoring system from an engineering geodetic perspective. In addition to the laser scanner, a total station (LEICA TM30), inclination sensors on the survey pillar where the scanner was mounted on (aligned to the scanner-own coordinate system; PC-IN 1-1° by POSITION CONTROL). Various meteorological sensors were installed in the shelter and around the monitored slope area.

The additional measurements can be used to verify diurnal and seasonal systematic effects on the results of surface change quantification. Furthermore, the prisms of the total station monitoring installed in the stable rock part and support different methodical approaches to verify such effects, as the RIEGL TLS instruments are able to detect these prisms as corresponding measuring points in the multitemporal scan data. During PLS acquisition, a high-resolution scan of the area was carried out with a resolution of 15 mdeg in azimuth and elevation at a pulse repetition rate of 50 kHz every 2 hours (M1) and every 3 hours (M2 and M3), respectively. As outlined in Table 1, fine-resolution scans of the prisms were acquired in-between regular scanning intervals.

Table 1. Applied sensors and their measuring frequency

Data	Sensor	Acquisition interval	Campaign
3D point cloud of rockfall area 3D point cloud of each prism	RIEGL VZ-2000i (Model A)	Meas. prog. interval of 120 min: ▪ 1 areal scan (15 min) ▪ 5 prism scans (Every 21 min)	M1
3D point cloud of rockfall area 3D point cloud of each prism	RIEGL VZ-2000i (Model B)	Meas. prog. interval of 180 min: ▪ 1 areal scan (15 min) ▪ 2 prism scans (Every hour)	M2, M3
3D meas. to each prism	LEICA TM30	Every hour	M1, M2
Inclination of the pillar	POSITION CONTROL, PC-IN1-1°	Every 15 sec	M1, M2, M3
Air temperature	WIESEMANN & THEIS (WUT),	Every 15 sec	M1, M2, M3
Air pressure	WEB THERMO-HYGROBAROMETER 57713		
Relative Humidity			
Air temperature	ELITECH TEMPERATURE-LOGGER, RC-51H	Every 15 min	M1, M2
Relative Humidity			
Global radiation	ZAMG. AC. AT METEOSTATION: SCHMIRN, BRENNER, STEINACH	Every 10 min	M1, M2
	LAMBRECHT U[SONIC]WS7	Every 15 sec	M2, M3
Air temperature			
Air pressure			
Rel. Humidity			
Wind speed			
Wind direction			
Global radiation			
Dew point			

Due to logistical constraints, the more accurate web thermo-hygrobarometers by WuT were only installed in the shelter, at the valley basin and in the lower part of the observed slope area. Elitech temperature loggers that require no additional power supply, were installed at the top of the rockslide so that no additional power supply is needed in these areas. A different scanning instrument, but of the same type and model, was deployed for the M2 and M3 acquisition periods. The remainder of this paper, *i.e.* all analyses, focus on the data acquired from 28-07-2021 to 15-11-2021 (M3).

#### IV. METHODS AND INITIAL RESULTS

##### A. Registration of 4D point clouds

The investigation of systematic long-term effects in the measurement data, a study of local effects in terms of spatial and temporal scale is initially omitted. Data from 19 prisms within the study area are analyzed for a period from 28-07-2021 to 31-10-2021. The time series of each prism is (1) reduced to a daily mean, then (2) relative changes to a global reference scan on 29-07-2021 at 13:00 are evaluated, and finally (3), in order to investigate global effects on the point cloud data, an average value for each coordinate axis in the scanner's own coordinate system (SOCS) is calculated. Figure 1 shows these time series in black color.

The assumption that the surveying pillar is stable and exempt from any movement does not apply. It is evident that the raw data varies over time and leads to non-negligible deviations. A linear drift is evident on the Y-axis and significant time-varying deviations on the Z-

axis. This supports the requirement of data referencing before multitemporal change analysis.

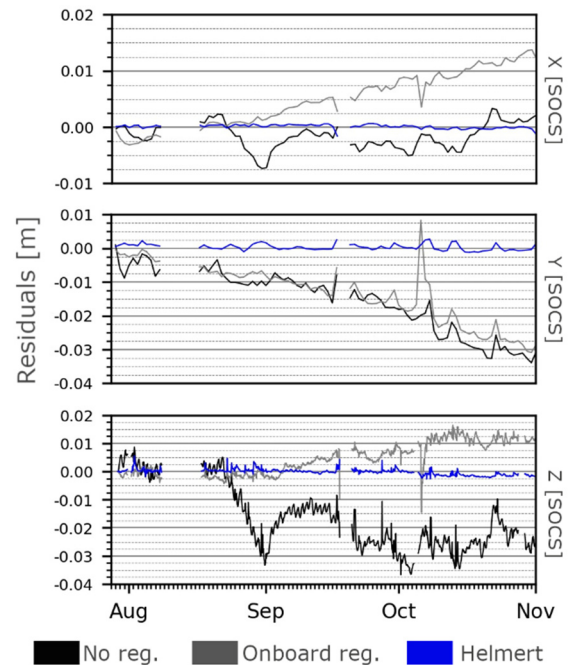


Figure 1. The comparison of different registration approaches as impact mapping: [1] No registration, [2] Onboard registration and [3] Helmert transformation.

As an initial registration procedure, onboard algorithms of the scanning device are applied. They use a simple ICP approach with the entire point cloud as input for the determination of the transformation

parameters. The distances between two corresponding point clouds are minimized for this purpose. No classification and segmentation of the point cloud is performed within this process, so that non-stable areas are included in the analysis. It is noticeable that there is almost no correction on the Y-axis since this axis runs parallel to the valley, which lacks measurement data. On the X- and Z-axes, we see a change in their signs. A visual comparison of the parameters with records of the inclination sensors (*cf.* Figure 2) allows a first conclusion that the values cannot be explained exclusively by movements of the survey pillar. Rather, when assessing the measurement data, it can be seen that the predominant part of the scene is characterized by vegetation, which increases or decreases linearly in the course of a measurement series depending on the season. The non-consideration leads to misinterpretations. An alternative approach demonstrates that the classification of stable areas in the geodetic sense remains important. The current lack of an automatable algorithm for the application of the whole point cloud can be compensated by the possibility of detection the prisms in the respective scans. Thus, a 7-parameter Helmert transformation can be applied. The procedure also offers the possibility to estimate a scale parameter as another quality criterion. A visual inspection of the transformation parameters does not indicate any systematic effects, so that this mathematical model demonstrates an adequate consideration of stable areas.

A set of impact maps (Figure 3), showcasing the effects of different transformation parameter sets on resulting point cloud distances, is derived by applying the M3C2-EP (Winiwarter *et al.*, 2021) on two point clouds, which were acquired on 28-07-2021 and 03-10-2021. For the parameterization of this numerical example, we introduce transformation parameters exclusively. The influence of registration is considered and realistic accuracy measures are disregarded. The map is generated by comparing the two scans with

respect to their differences in the transformation parameters. Without using transformation parameters, a tendency to higher values is visible, corresponding to a shift of the normally distributed deviations by 0.015 m in the mean (*cf.* Figure 3 – [1]). The application of the simplified registration algorithm of the scanner shows a normal distribution with the mean tending towards zero, but with a slight bias of -0.008 m (*cf.* Figure 3 – [2]). The transformation using 7 parameters shows a Gaussian distribution at almost zero (-0.002 m), which is the expected magnitude of differences (*cf.* Figure 3 – [3]).

#### B. Change detection using Kalman filtering for full 4D point cloud analysis

The dense time series of the 4D point clouds contains spatially and temporally detailed information on surface processes. We use data acquired every three hours over 110 days (from 28-07-2021 to 15-11-2021), yielding a total of 766 epochs. To extract and visualize information on surface changes, which occur at variable a-priori unknown locations and timespans, we apply a recent method using a Kalman filter to combine the spatial and temporal properties of 4D point clouds for change analysis, following Winiwarter *et al.* (2022). We explain this method in the following.

First, M3C2-EP (Winiwarter *et al.*, 2021) is used to calculate bitemporal surface change for each epoch, using the first epoch as reference. No filtering of changes by statistical significance is applied at this point, but uncertainty information is recorded (as suggested by Anderson, 2019). We use the following parameter settings for M3C2-EP: normal radius 5 m, projection radius 0.5 m, maximum cylinder length 3 m, core point density 0.45 pts/m<sup>2</sup>, ranging uncertainty: 0.005 m, angular uncertainty 0.0675 mrad.

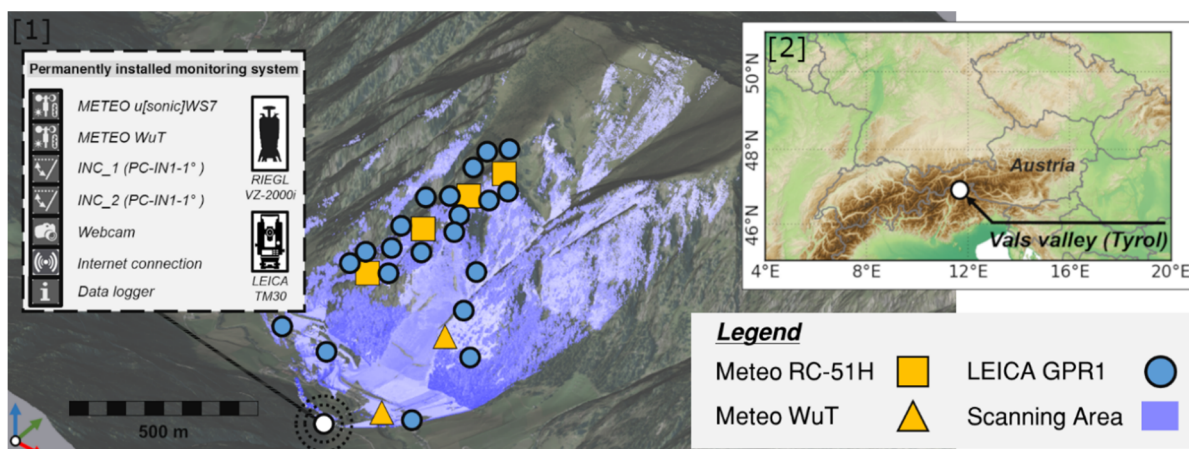


Figure 2. Figure Three-dimensional overview of the test site in the Vals Valley including applied sensor technology and overview of the geographical situation of the Vals Valley. (Data Source: Land Tirol - data.tirol.gv.at [1] and <http://ows.mundialis.de/services/service?layers=SRTM30-Colored-Hillshade> [2]).

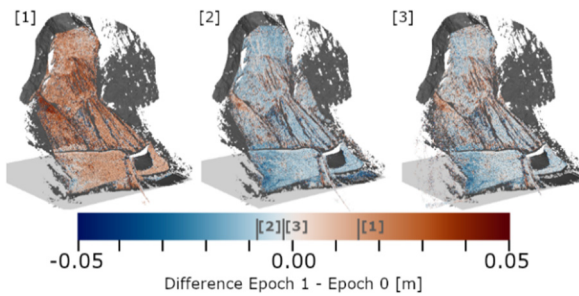


Figure 3. The comparison of different registration approaches as impact map: [1] No registration, [2] Onboard registration and [3] Helmert transformation.

We use a Kalman filter on each spatial location (*i.e.*, core point) individually to model the displacement at this location over time. A Kalman filter represents a dynamical system by a state vector, a measurement function, and a state transfer function, and requires errors in the obtained bitemporal surface change to be normally distributed. As we modelled these changes with M3C2-EP, we assume that this condition is met. In the Kalman filter, the state vector contains the parameters (in our case, the estimated displacement value, the change rate, and the acceleration at a single location) for a single point in time. From this state, a future state can then be predicted using the state transfer function, linearized to be representable by a matrix. This is referred to as the prediction step. If observations, *i.e.*, measurements are available, they can be introduced to the state in the update step. Again, a linearized model is used to represent the relation of observations and parameters. In both the predict and update steps, uncertainty is employed. The state vector itself is accompanied by a covariance matrix. In the prediction step, the uncertainty generally increases, as the last observations become less recent.

The increase of uncertainty over time due to a lack of measurements is modelled by the Kalman filter. As the behavior of the observed surface is not known prior to analysis, a piecewise (discrete) white noise model is employed, following Labbe (2021). We assume that for each time step, an uncorrelated (to the previous

change) and random change in the acceleration value may happen, where the expected value of this change is normally distributed with mean zero and a standard deviation of  $\sigma = 0.05 \text{ m/day}^2$ . Hence, the more time has passed since the last measurement, the more uncertain the model will be about its state. Our choice of  $\sigma$  was made to allow the filter to closely follow the observations, yet smoothing daily or diurnal patterns (Figure 4; *cf.* Winiwarter *et al.*, 2022).

The Kalman filter is combined with a Rauch-Tung-Striebel smoother to create a smoothed time series considering both future and previous measurements for any point in time. This also allows interpolation over data gaps. Figure 4 shows a time series for a single spatial location with the measurements, the smoother value and the respective uncertainties, together with the derived velocity and the acceleration. At the end of the measurement period (starting on 01-11-2021), snowfall occurred in Vals. The deposition and melt of this large-scale surface change show in all time series of this dataset, and induce uncertainty that is not well represented by the Kalman filter.

In Figure 5, the resulting change magnitudes (a) at the end of the 110-day period and (b) at their maximum value for each spatial location are shown. The red areas in (a) correspond to deposited material, the blue ones to eroded material. The overall orange color in (b) corresponds to snowfall in the beginning of November.

Similar values, such as the time when significant change was first recorded at each location (Figure 6) can be extracted from the time series at each location.

The erosion channels following a thunderstorm can be seen in pink, as well as anthropogenic works in the lower area of the slope. Snowfall in the first days of November is the cause for the major peak that can be seen in cyan, covering large areas. We subsequently use 20 such attributes derived for each location as feature vectors for unsupervised classification, *i.e.*, clustering, using a Gaussian Mixed Model (following Winiwarter *et al.*, 2022). The result of the clustering is shown in Figure 7, where individual change processes can be identified through visual interpretation.



Figure 4. Exemplary time series at a location with subtle, but continuous erosion. Note how data gaps are interpolated, but if they are too long, a ringing effect occurs (as seen in the days before 17-08-2021). A daily pattern can be observed, especially in the velocity and acceleration estimations. Snowfall at the end of the observation period causes large displacement values.

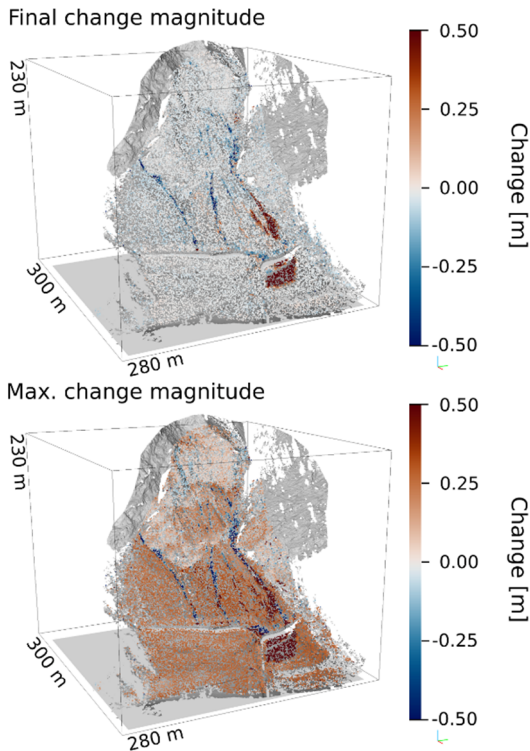


Figure 5. Resulting change magnitudes: a) Change magnitude between the first epoch and the last epoch; b) Maximum change magnitude.

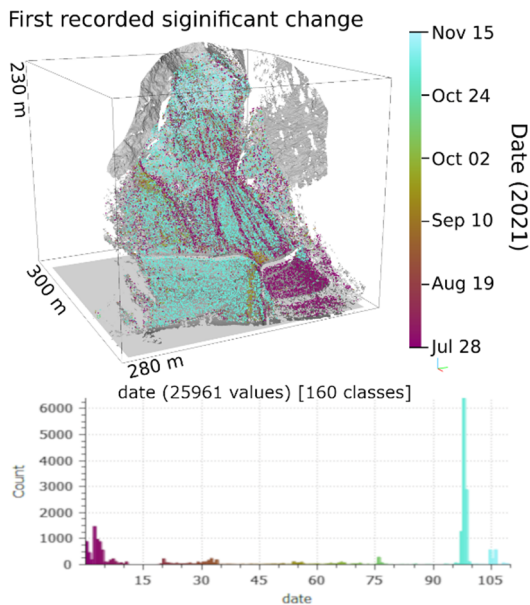


Figure 6. Date when change is larger than LOD.

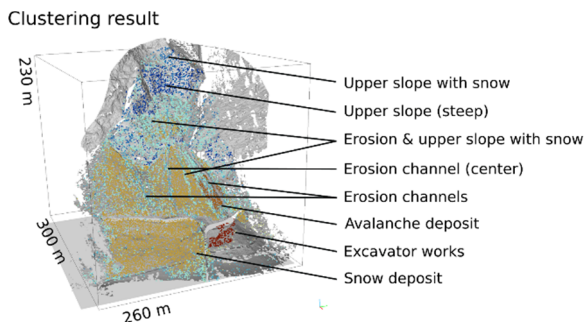


Figure 7. Result of clustering on features derived from the Kalman-filtered time series.

## V. CONCLUSION AND OUTLOOK

The use of bitemporal data from a TLS to verify surface changes is widely used and discussed. We discuss the transition to permanent installations and the acquisition of multitemporal data sets. The quality of the extracted information is directly dependent on the underlying data quality. With regard to data qualification, the focus in this paper is on different registration procedures. It becomes obvious that registration is absolutely necessary when integrating the system into an automated monitoring system with a corresponding alarm function. The level of detection (LOD) varies with the application of the different registration procedures. The simplified ICP algorithm, as used by the employed scanner instrument, is valid if the area undergoing change is small in extent compared to the whole scene. Under certain conditions (large areas covered by vegetation or other moving objects in the scene) it comes to its limits.

For example, an alarm value set at the beginning is triggered by the drift effects in the co-registration alone after a specific point in time and leads to false alarms. The use of a rigorous approach shows the necessity of segmenting and classifying the point cloud into stable and non-stable areas as described by Friedli and Wieser (2016) and Wujanz (2016). We show that data alignment is of vital importance for subsequent change quantification and analysis, even in the widely stable survey setup of permanent TLS.

We reduce the uncertainty of change analysis by employing a Kalman filter operating on M3C2 distances in the point cloud, which makes use of the full spatiotemporal information in the dataset. The consideration of uncertainty in this analysis is not purely data-based, but also uses information from the previous alignment step by means of the derived covariance in the transformation parameters. Periodically appearing deviations are evident both in the time series of measurements and of the transformation parameters.

Whereas no methods are currently available to remove periodic measurement effects, reducing uncertainty in change analysis from high-frequency TLS time series is subject to ongoing research efforts. In the course of these research activities, causal descriptions of the above-mentioned error influences will be verified and modelled. The first objective is to more efficiently design the permanent installation of terrestrial laser scanners within an integrative monitoring system in order to avoid misinterpretations and false alarms. The second objective is to achieve a higher degree of automation of the entire system. Automatic processing chains are only available in parts of the full workflow and there is no holistic software solution yet. In addition, a high level human expertise is typically necessary. Now that point cloud acquisition is highly automated, there is strong need for research and development in the individual fields of 4D point cloud

analysis within a monitoring system, with a focus on extracting change information and final quality assessment from an engineering geodetic point of view.

## VI. ACKNOWLEDGEMENTS

We would like to thank the Tyrol State Government - Department of Geoinformation for their support in conducting the experimental study. Many thanks to the Central Institute for Meteorology and Geodynamics (ZAMG) for providing the weather data. The measurement setup is supported by the European Union Research Fund for Coal and Steel [RFCS project number 800689 (2018)].

## References

- Anders, K., Lindenbergh, R. C., Vos, S. E., Mara, H., De Vries, S., and Höfle, B. (2019). High-frequency 3D geomorphic observation using hourly terrestrial laser scanning data of a sandy beach. *ISPRS Annals of the Photogrammetry, Remote Sensing and Spatial Information Sciences*, 4(2/W5), pp. 317-324.
- Anders, K., Winiwarter, L., Lindenbergh, R., Williams, J. G., Vos, S. E., and Höfle, B. (2020). 4D objects-by-change: Spatiotemporal segmentation of geomorphic surface change from LiDAR time series. *ISPRS Journal of Photogrammetry and Remote Sensing*, 159, pp. 352-363.
- Anders, K., Winiwarter, L., Mara, H., Lindenbergh, R. C., Vos, S. E., and Höfle, B. (2021). Influence of spatial and temporal resolution on time series-based coastal surface change analysis using hourly terrestrial laser scans. *ISPRS Annals of the Photogrammetry, Remote Sensing and Spatial Information Sciences*, 2, pp. 137-144.
- Anderson, S. W. (2019). Uncertainty in quantitative analyses of topographic change: error propagation and the role of thresholding. *Earth Surface Processes and Landforms*, 44(5), pp. 1015-1033.
- Bechtold, S., and Höfle, B. (2016). Helios: a Multi-Purpose LIDAR Simulation Framework for Research, Planning and Training of Laser Scanning Operations with Airborne, Ground-Based Mobile and Stationary Platforms. *ISPRS Annals of Photogrammetry, Remote Sensing & Spatial Information Sciences*, 3(3).
- Bremer, M., Zieher, T., Pfeiffer, J., Petrini-Monteferrri, F., and Wichmann, V. (2019). Monitoring der Großhangbewegung Reissenschuh (Schmirntal, Tirol) mit TLS und UAV-basiertem Laserscanning. Hanke, K.; Weinold, pp. 321-33.
- Eitel, J. U., Höfle, B., Vierling, L. A., Abellán, A., Asner, G. P., Deems, J. S., and Vierling, K. T. (2016). Beyond 3-D: The new spectrum of lidar applications for earth and ecological sciences. *Remote Sensing of Environment*, 186, pp. 372-392.
- Fey, C., and Wichmann, V. (2017). Long-range terrestrial laser scanning for geomorphological change detection in alpine terrain—handling uncertainties. *Earth Surface Processes and Landforms*, 42(5), pp. 789-802.
- Friedli, E., and Wieser, A. (2016). Identification of stable surfaces within point clouds for areal deformation monitoring. In Proc. of 3<sup>rd</sup> Joint International Symposium on Deformation Monitoring (JISDM).
- Friedli, E., Presl, R., and Wieser, A. (2019). Influence of atmospheric refraction on terrestrial laser scanning at long range. In Proceedings of the 4<sup>th</sup> Joint International Symposium on Deformation Monitoring (JISDM), Athens, Greece (pp. 15-17).
- Hartl, S. (2019). Analyse der Felslawinen Frank Slide und Vals mit Hilfe des Computercodes r. avaflow (Master thesis, Wien).
- Hermle, D., Gaeta, M., Krautblatter, M., Mazzanti, P., and Keuschnig, M. (2022). Performance Testing of Optical Flow Time Series Analyses Based on a Fast, High-Alpine Landslide. *Remote Sensing*, 14(3), 455.
- Huggel, C., Clague, J. J., and Korup, O. (2012). Is climate change responsible for changing landslide activity in high mountains?. *Earth Surface Processes and Landforms*, 37(1), pp. 77-91.
- Kromer, R. A., Abellán, A., Hutchinson, D. J., Lato, M., Chanut, M. A., Dubois, L., and Jaboyedoff, M. (2017). Automated terrestrial laser scanning with near-real-time change detection—monitoring of the Séchilienne landslide. *Earth surface dynamics*, 5(2), pp. 293-310.
- Kuschnerus, M., Schröder, D., and Lindenbergh, R. (2021a). Environmental influences on the stability of a permanently installed laser scanner. *The International Archives of Photogrammetry, Remote Sensing and Spatial Information Sciences*, 43, pp. 745-752.
- Kuschnerus, M., Lindenbergh, R., and Vos, S. (2021b). Coastal change patterns from time series clustering of permanent laser scan data. *Earth Surface Dynamics*, 9(1), pp. 89-103.
- Labbe, R. (2021). *Kalman and Bayesian Filters in Python*. Online Book: <https://github.com/rllabbe/Kalman-and-Bayesian-Filters-in-Python>.
- Lague, D., Brodu, N., and Leroux, J. (2013). Accurate 3D comparison of complex topography with terrestrial laser scanner: Application to the Rangitikei canyon (NZ). *ISPRS journal of photogrammetry and remote sensing*, 82, pp. 10-26.
- Lang, W. (1929). Deformationsmessungen an Staumauern nach den Methoden der Geodäsie: im Auftrag der Abteilung für Landestopographie des Eidgenössischen Militärdepartements. *Verlag der Abteilung für Landestopographie*.
- Voordendag, A. B., Goger, B., Klug, C., Prinz, R., Rutzinger, M., and Kaser, G. (2021). Automated and permanent long-range terrestrial laser scanning in a high mountain environment: Setup and first results. *ISPRS Annals of the Photogrammetry, Remote Sensing and Spatial Information Sciences*, 2, pp. 153-160.
- Vos, S., Lindenbergh, R., de Vries, S., Aagaard, T., Deigaard, R., and Fuhrman, D. (2017). Coastscan: Continuous monitoring of coastal change using terrestrial laser scanning. In *Proceedings of Coastal Dynamics* (Vol. 2017, p. 115).
- Vosselman, G., and Maas, H. G. (2010). *Airborne and terrestrial laser scanning*. CRC press.
- Williams, J. G., Rosser, N. J., Hardy, R. J., Brain, M. J., and Afana, A. A. (2018). Optimising 4-D surface change detection: an approach for capturing rockfall magnitude-frequency. *Earth surface dynamics*, 6(1), pp. 101-119.
- Williams, J. G., Rosser, N. J., Hardy, R. J., and Brain, M. J. (2019). The importance of monitoring interval for rockfall

- magnitude-frequency estimation. *Journal of Geophysical Research: Earth Surface*, 124(12), pp. 2841-2853.
- Winiwarter, L., Anders, K., and Höfle, B. (2021). M3C2-EP: Pushing the limits of 3D topographic point cloud change detection by error propagation. *ISPRS Journal of Photogrammetry and Remote Sensing*, 178, pp. 240-258.
- Winiwarter, L., Anders, K., Schröder, D., and Höfle, B. (2022). Full 4D Change Analysis of Topographic Point Cloud Time Series using Kalman Filtering. *Earth Surface Dynamics Discussions*, pp. 1-25.
- Wujanz, D., Krueger, D., and Neitzel, F. (2016). Identification of stable areas in unreferenced laser scans for deformation measurement. *The Photogrammetric Record*, 31(155), pp. 261-280.



## EDM-GNSS distance comparison at the EURO5000 calibration baseline: preliminary results

Kinga Wezka<sup>1</sup>, Luis García-Asenjo<sup>2</sup>, Dominik Próchniewicz<sup>1</sup>, Sergio Baselga<sup>2</sup>, Ryszard Szpunar<sup>1</sup>, Pascual Garrigues<sup>2</sup>, Janusz Walo<sup>1</sup>, Raquel Luján<sup>2</sup>

<sup>1</sup> Faculty of Geodesy and Cartography, Warsaw University of Technology, Plac Politechniki 1, 00-661 Warsaw, Poland, ([Kinga.Wezka@pw.edu.pl](mailto:Kinga.Wezka@pw.edu.pl); [Dominik.Prochniewicz@pw.edu.pl](mailto:Dominik.Prochniewicz@pw.edu.pl); [ryszard.szpunar@pw.edu.pl](mailto:ryszard.szpunar@pw.edu.pl); [janusz.walo@pw.edu.pl](mailto:janusz.walo@pw.edu.pl))

<sup>2</sup> Departamento de Ingeniería Cartográfica, Geodesia y Fotogrametría, Universitat Politècnica de València, Camino de Vera s/n, 46022 Valencia, Spain, ([lugarcia@cgf.upv.es](mailto:lugarcia@cgf.upv.es); [serbamo@cgf.upv.es](mailto:serbamo@cgf.upv.es); [pasgarta@cgf.upv.es](mailto:pasgarta@cgf.upv.es); [ralugar@cgf.upv.es](mailto:ralugar@cgf.upv.es))

**Key words:** *calibration baselines; SI traceability; GNSS-EDM comparison; air refractivity compensation*

### ABSTRACT

At the Pieniny Kippen Belt in Poland, the novel primary reference baseline EURO5000 is required as part of the European Research project GeoMetre to both validate refractivity-compensated EDM prototypes and investigate the metrological traceability of GNSS-based distances. Since the aimed uncertainty is 1 mm at 5 km ( $k=2$ ), the design, construction, and validation must be carefully prepared to fulfil the high standards of the GeoMetre field campaigns which are planned to be carried out in May 2022. This contribution describes the main features of the EURO5000 and presents the results of the preliminary validation which includes a first comparison between the results obtained by using precise currently available EDMs as well as GNSS techniques following the standard GNSS geodetic processing algorithms, on the one hand, and the improved GNSS-Based Distance Meter (GBDM+) approach developed at UPV, on the other hand. The preliminary validation presented in this contribution also permits (1) to detect potential problems in the use of the baseline such as potential geodynamic problems, atmospheric refraction or multipath limitations, (2) to produce a set of reliable results, and (3) to pave the way for the final field comparisons between the novel EDMs and the GBDM+ approach. The result of this metrological experiment may significantly contribute to overcome the limitations of current high-precision deformation monitoring applications that require their scale to be consistent with the SI-metre within 0.1 ppm in several km.

*This contribution was selected by the Scientific Committee for publication as an extended paper in the Journal of Applied Geodesy <https://www.degruyter.com/journal/key/jag/html>*

## Implementation of a fixed-location time lapse photogrammetric rock slope monitoring system in Castellfollit de la Roca, Spain

Gerard Matas<sup>1</sup>, Albert Prades<sup>2</sup>, M. Amparo Núñez-Andrés<sup>2</sup>, Felipe Buill<sup>2</sup>, Nieves Lantada<sup>1</sup>

<sup>1</sup> Department of Civil and Environmental Engineering, Universitat Politècnica de Catalunya, C/ Jordi Girona 1-3, 08034 Barcelona, Spain, ([gerard.matas@upc.edu](mailto:gerard.matas@upc.edu); [nieves.lantada@upc.edu](mailto:nieves.lantada@upc.edu))

<sup>2</sup> Department of Civil and Environmental Engineering, Universitat Politècnica de Catalunya, Av. Doctor Marañón 44-50, 08028 Barcelona, Spain, ([alberto.prades.i@upc.edu](mailto:alberto.prades.i@upc.edu); [m.amparo.nunez@upc.edu](mailto:m.amparo.nunez@upc.edu); [felipe.buill@upc.edu](mailto:felipe.buill@upc.edu))

**Key words:** rockfall; time-lapse photogrammetry; monitoring; automation

### ABSTRACT

When monitoring deformations in natural hazards such as rockfalls and landslides, the use of 3D models has become a standard. Several geomatic techniques allow the generation of these models. However, each one has its pros and cons regarding accuracy, cost, sample frequency, etc. In this contribution a fixed-location time lapse camera system for continuous rockfall monitoring using photogrammetry has been developed as an alternative to Light Detection and Ranging (LiDAR) and ground-based interferometric synthetic-aperture radar (GB-InSAR). The usage of stereo photogrammetry allows the obtention of 3D points clouds at a low cost and with a high sample frequency, essential to detect premonitory displacements. In this work the designed system consists of three digital single-lens reflex (DSLR) cameras which collect photographs of the rock slope daily controlled by a Raspberry Pi computer using the open-source library gPhoto2. Photographs are automatically uploaded to a server using 3G network for processing. This system was implemented at Castellfollit de la Roca village (Girona province, Spain), which sits on a basaltic cliff that has shown significant rockfall intensity in recent years. The 3D models obtained will allow monitoring rockfalls frequency, premonitory displacements, and calculate the erosion rate of the slope. All technical decisions taken for the design and implementation on this specific site are discussed and first results shown.

### I. INTRODUCTION

In recent years, technological improvements in remote sensing technologies led to improve the characterization and monitoring of rock slope hazards and other geomorphic processes. Most used technologies for this purpose are terrestrial laser scanning (TLS), structure from motion (SfM) photogrammetry and Ground-based Interferometric synthetic-aperture radar (GB-InSAR). These three methodologies can be used in very different situations depending on the site and the required sampling frequency. GB-InSAR achieves sub-millimeter measurements of displacements for landslides at near-real time (Atzeni *et al.*, 2015). However, the high costs of GB-InSAR systems pushed the usage of TLS and SfM as cheaper and feasible alternatives. In both cases, the systems can be classified depending on the mobility and the sampling frequency. They can be mounted on fixed locations or on moving vehicles like drones or satellites and capture information at specific time intervals in an almost continuous mode or at specific moments corresponding to field campaigns. Several authors have used SfM to monitor displacements in landslides and rockfall prone areas both using fixed location cameras (Kromer *et al.*, 2019; Blanch *et al.*, 2021) or moving cameras mounted on drones (Sarro *et al.*, 2018). In the case of laser scanners most take information from the

ground since the usage of laser scanners mounted on drones is still not common. Some authors have compared SfM with TLS and concluded that each one has its strengths that may depend on the specific study site (Núñez-Andrés *et al.*, 2019).

In the specific field of rockfall monitoring and management, the three-dimensional models obtained with all these techniques are used to identify potential rockfall sources (Albarelli *et al.*, 2021), monitoring displacements to predict future events (Janeras *et al.*, 2016) and quantifying rockfall activity for obtaining magnitude frequency curves (Williams *et al.*, 2018).

In this study we present an implementation on a fixed location set of cameras in Castellfollit de la Roca study site. The objective was to develop a system able to detect precursory displacements and monitor activity for inventorying purposes. The characteristics of the study site required placing the cameras at distances around 170 meters, which is substantially higher than in other studies (Kromer *et al.*, 2019; Blanch *et al.*, 2021).

### II. STUDY SITE

The study area is in the village of Castellfollit de la Roca (Catalunya, Spain). It is located at an altitude of 296 m and sits on a basaltic cliff that is more than 50 m high and almost one kilometer long. This basaltic cliff is the consequence of the erosive action of the rivers

Fluvià and Toronell on the volcanic remains resulting from the superposition of two lava flows that are estimated to be 217.000 and 192.000 years old, respectively. On this cliff the prism shaped disjunctions that are formed when the basalt cools slowly and at rest are present. Due to erosion these basalt towers can collapse generally following a toppling failure. Previous observations with TLS (Terrestrial Laser System) detected precursory deformation of the rockfall (Abellan *et al.*, 2009; 2011). They followed an apparent stationary stage with displacements lower than 1.64 cm/year.

Contrary to the usual rockfall risk scenario in which the element exposed at risk is under the cliff, in this case it is over the cliff. The erosion of the massif on which the town is built can put at risk the buildings that are closer to it. From all the massif a specific area to monitor was chosen considering the more active part of the cliff from previous event inventories and the closest part of the cliff to the buildings.

### III. SYSTEM DESIGN AND IMPLEMENTATION

The implementation of a fixed photogrammetric camera system depends on both the site and the nature of the phenomenon under study. There are several important factors influencing the results. On the one hand the optical characteristics of the cameras (Gance *et al.*, 2014): the resolution of the cameras, the lens used and their focal length, on the other hand factors related to the system configuration: the number of cameras, the relation base/object, *i.e.* distance among cameras, and from the camera network to the target, site access constraints and environmental constraints. On the other hand, the technical requirements if the images need to be transferred remotely: the possibility of accessing the electrical connection or not, the 3G/4G signal for internet connection, the desired monitoring interval etc. (Kromer *et al.*, 2019).

The following subsections describe the solution adopted at Castellfollit de la Roca site for rockfall monitoring using a time lapse system considering all cited factors.

#### A. System components

The objective of the system is to take pictures at a regular interval for a continuous monitoring of the studied cliff. These pictures must be sent over the internet to a storage server for further processing. Since mounted outdoors, the system must withstand inclement weather. The system was placed near a populated area and thus all components could be connected to the local power grid. This simplifies the continuous use of the system since the use of solar panels and batteries was not required. The system consists of a power management unit, a control unit, a total of three cameras.

The power management unit has an electrical transformer to filter possible electrical spikes and a

surge protection system to protect all components. It is enclosed in an IP67 cage to ensure water protection. The protected cable is directly connected to the main control unit.

The control unit (Figure 1) is in charge of controlling the cameras and sending collected pictures over a 3G network to a server. The brain of the control unit is a Raspberry Pi 4 (RPi4) microcomputer, which is capable of interfacing through USB protocol with the cameras and has a Rj45 connector for internet connectivity. To allow the usage of just one microcomputer on the system, all three cameras were directly wired to the Raspberry Pi through USB. However, since the maximum allowed cable distance for USB protocol is 10 m and the two cameras were placed at more than 30 m distance from the control unit, a USB extension through ethernet was required. A relay board connected to the RPi4 is in charge of controlling the camera power supply and thus when they are turned on or turned off. To allow multiple USB connections a USB hub was plugged into the RPi4, and finally, for internet connection a 3G router was directly connected to the Rj45 port of the RPi4.

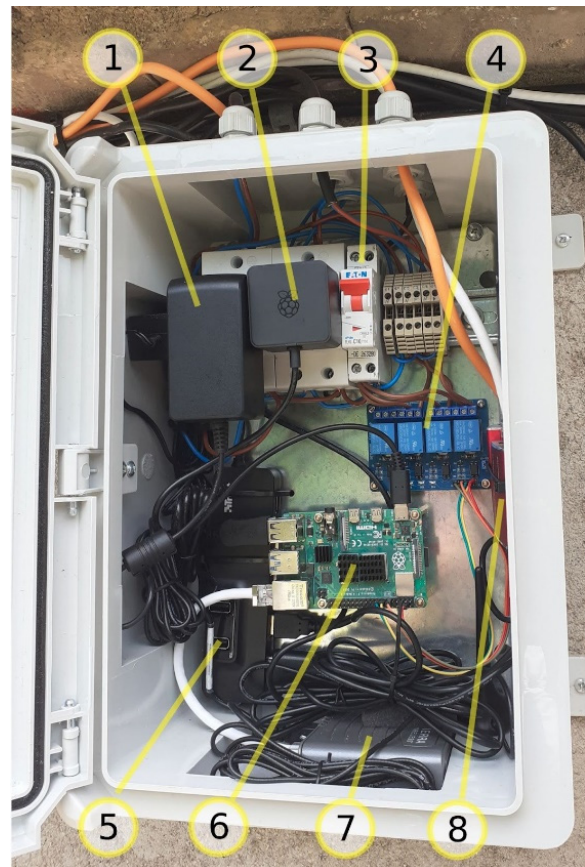


Figure 1. Control unit and its components: 1) Router power supply; 2) RPi4 Power supply; 3) Main power switch; 4) Relay board; 5) USB Hub; 6) RPi4 microcomputer; 7) 3G router; 8) USB extenders through ethernet.

Each DSLR camera is housed in a commercial protective housing used for camera trap photography. Both the camera power adapter and the USB extender receiver including its own power supply were fitted

inside the housing. Figure 2 shows the camera housing and its components. The camera that is placed next to the control unit lacks the USB extender since the distance is short enough to be covered by a single USB cable.

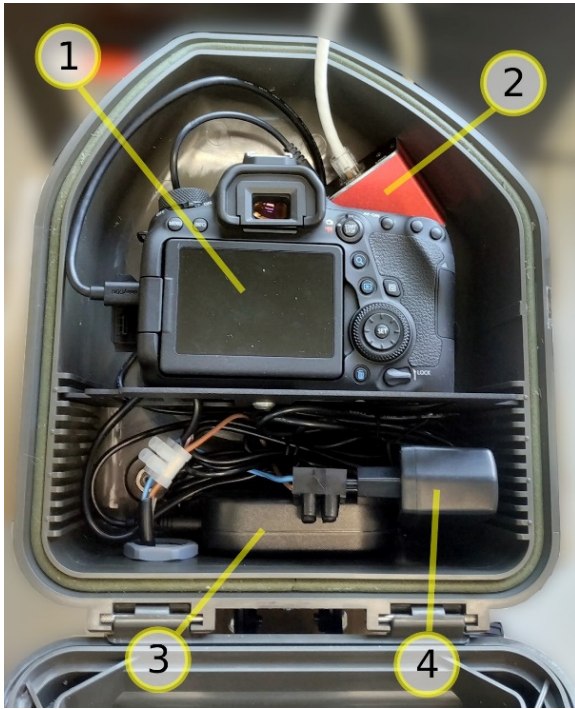


Figure 2. Single camera housing: 1) DSLR camera; 2) USB extender through ethernet receiver; 3) DSLR camera power supply; 4) USB extender power supply.

### B. System setup

The three cameras forming the system are at an average distance from the monitored area of 170 meters. This distance is greater than other similar devices (Gance *et al.*, 2014; Kromer 2019; Blanch 2021) mounted in other studios and implies a challenge when choosing the optics of the cameras. The control unit (CU) is placed next to Camera 2 (C2) and has the ability to trigger photos from all three cameras schedule based or at user request. C1, C2 and the CU were installed on the facade of an old factory, while C3 was installed on a wooden pole that supports a telecommunications cable (Figure 3). The location of the cameras allowed a 90% overlap between the central photo of C2 and C1 & C3.

### C. Cameras and lens

The geometrical constraints of the site and the required resolution condition the choice of cameras and optics. In this project, the distance from the massif to be monitored is considerable and it has been required to use telescopic optics mounted on DSLR cameras. In rockfall photogrammetric monitoring, the higher the resolution of the used camera, the smaller the volume that the system is capable of detecting. Detecting rockfalls around 0.001 m<sup>3</sup> is a key point since they can be the prelude of bigger events. With all these considerations the cameras chosen were Canon EOS 6D

Mark II, whose characteristics are CMOS sensor, aspect ratio 3:2, image format 35.9 x 24.0 mm and maximum resolution 6240 x 4160 pixels, and a focal length of 105 mm. Fixed conditions, sensibility ISO 100 and aperture f/8, are used for the photographic capture.



Figure 3. Top: Control unit next to Camera 2 (C2). Bottom: Camera 3 (C3) placed on a telecommunication wooden pole.

The capture geometry has been defined in order to achieve the best reliability in the detection of change in the basaltic columns. In this way the base distance between the cameras are 39 and 37 meters (Figure 4) with a distance to base ratio 1:5, moreover, the photographic bases were approximately parallel to the rock wall.



Figure 4. Position of the three cameras of the system (C1, C2 and C3) and the control unit (CU) with respect to the monitored area behind Castellfollit de la Roca village.

Through the scale ratio, Equation 1 and parallax equations, Equation 2, we calculate the minimum measurable displacement Equation 3.

$$E = \frac{Y}{f} = \frac{B}{p} \quad (1)$$

where  $E$  = scale factor  
 $Y$  = distance from reference to observed point  
 $B$  = the photographic base  
 $p$  = parallax,  $dp = \sqrt{2}dx$   
 $f$  = focal length (Figure 5).

$$X = x \cdot E \quad Y = f \cdot E = \frac{B \cdot f}{p} \quad Z = y \cdot E \quad (2)$$

$$dX = dx \cdot E \quad dY = \frac{Y^2}{B \cdot f} dp \quad dZ = dy \cdot E \quad (3)$$

where  $X, Y, Z$  = ground coordinates (GC)  
 $x, y$  = image coordinates  
 $dX, dY, dZ$  = estimated error in GC  
 $dx, dy, dz$  = distance from reference

In the worst-case scenario where cameras C1 or C3 fail, the photographic base will be  $B \approx 37$  m,  $f = 105$  mm,  $Y \approx 170$  m, and the appreciation,  $dx$  and  $dy$ , will stay within a range from  $\frac{1}{4}$  to  $\frac{1}{2}$  px. The measurable movements are  $dX \approx 0.3$  cm,  $dY \approx 1.5$  cm,  $dZ \approx 0.3$  cm, and  $dX \approx 0.6$  cm,  $dY \approx 3$  cm,  $dZ \approx 0.6$  cm considering an appreciation of  $\frac{1}{4}$  px and  $\frac{1}{2}$  px respectively. These values would be achieved in optimal conditions, however in the study area environmental humidity and changes in the temperature will affect the quality of the images and therefore the real values will be higher than the optimal ones.

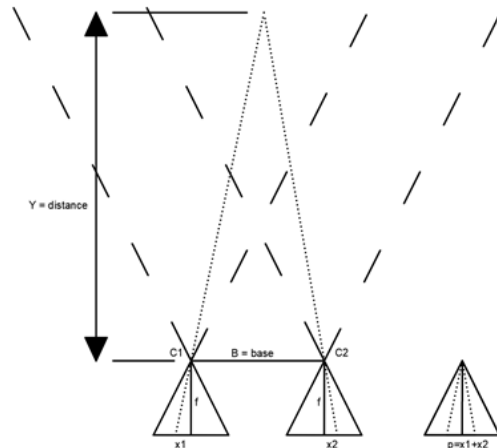


Figure 5. Coordinate system parallel to the object, X parallel to the photographic base, Y normal to this base (depth) and Z complete the normal trihedron.

#### IV. SYSTEM WORKFLOW

The microcomputer is in charge of turning on the cameras following a certain schedule. This schedule can be easily reprogrammed, for example for taking a photo every hour or for taking photos at a certain time every day. When it is time to take the pictures, the microcomputer turns on each camera one by one through the relay plate, it waits for the camera to be detected through the USB port and then prompts the device to take the picture. Once the three photographs have been taken, with all the cameras turned off, a backup copy of the three photographs is done to a USB memory and later the same photographs are sent to an intermediate server through the SFTP protocol.

The microcomputer is always turned on since everything is connected to the power grid, however it is automatically rebooted once a week. This reboot ensures that in case some part of the control software fails, up to a week of potential data could be lost.

### A. Control unit software

The microcomputer (RPI4) runs a full linux distribution, RaspberryPi OS, which is especially designed for usage on this device. The OS allows interoperability between devices through the USB protocol, the internet through RJ45 port and all access to all required libraries to manage system operations. The main control code of the system is written in Python programming language and uses the library Gphoto2 to interface and control the DSLR cameras. When this main code is called it performs the following operations:

1. Turns on the cameras using the python gpio library to control the relay board that power the cameras.
2. Asks the cameras to take pictures using the gphoto2 library.
3. Creates a backup of all the photos in the external USB memory stick.
4. Sends the photos to a server through the SFTP protocol using python sftp library.

To control when this program is triggered a linux crontab file is used which allows to specify certain triggering times during the day.

For remote control of the system it is connected to a virtual VPN provided by Zerotier service. This is required since the mobile network provider operates using a CGNAT router which masks the ip of its connected devices thus not allowing direct connection from the internet. With this virtual VPN, access to the RPI4 microcomputer is allowed through the ssh protocol as if it were connected to the local network. Having constant remote access to the system allows for tweaking of the parameters and controlling the real time performance.

### B. Data management and backups

All photos taken by the system are stored on the SD card in the RPi and on a USB stick. This allows for redundancy in case the system gets disconnected from the internet. This storage is limited and old photos must be deleted to ensure new ones have enough space. After taking and storing the photos the system sends them to an intermediate university server using SFTP. All files contained in this server are then backed up into another machine to ensure no data loss in case of a hard disk failure.

### C. Image processing

We have worked with the images in a double process. On one hand, the comparison of monoscopic images, and on the other hand the construction of the 3d model.

Since the displacement can be slow we compare the data daily, biweekly and monthly. The phases for the monoscopic imaging process are:

1. Correction of sensor movements. The cameras suffer small movements due to the wind, temperature changes etc.
2. Radiometric adjustment. However, according to Desrues *et al.*, (2019) it is not determinant.
3. Multitemporal images comparison for each camera.

## V. SYSTEM PERFORMANCE AND FIRST RESULTS

After setting up the system it has been continuously sending photographs to the server for half a year by the time of submitting this contribution. We observed that the quality of the images significantly depends on the hour at which they are taken. The sun incidence produces a blurred image because of the protective case glass. Thus, the best quality images are the ones taken at the sunset and sunrise.

The color of the basalt rock depends on the incidence of sunlight, and considerable color changes have been observed in images due to this effect.

It has been observed that the vegetation present in the study cliff is of rapid growth, making the direct comparison of images and models difficult, thus requiring a meticulous filtering process.

During this period of time the system has been working, no rockfalls have been detected on the cliff. However, the system was able to detect the presence of a bastide in a facade restoration work, as shown in Figure 6. In this figure the growth of the vegetation can also be observed (orange-red colors).

## VI. CONCLUSIONS

The implementation of time-lapse fixed position systems with DSLR cameras, using currently available open source hardware and software, has been easy and inexpensive.

These systems can work even at great distances using the right optics for the cameras. The incidence of the light on the glass of the protective cases showed a relevant sole on the quality of the images. This effect must be considered when choosing the location of the cameras when possible.

The quality of the solution is influenced not only by the optical characteristics of the camera but also dramatically by the geometry of the cameras' position. However, to select the best places to set them is not always possible.

In places like this area where there is riparian and ivy vegetation the use of vegetation mask during the image processing is essential.

Despite the difficulties, movements on the order of centimeters can be detected on the unstable boulders of the massif.

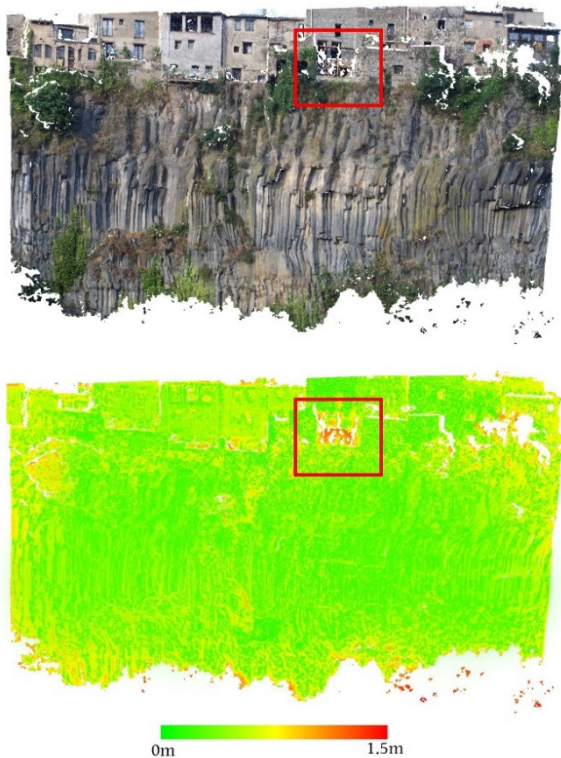


Figure 6. Cloud point comparison of two models before and after the collocation of a structure for restoring one of the buildings. Color scale shows displacement in meters.

## VII. ACKNOWLEDGEMENTS

This work has been carried within the framework of the research project Georisk “Avances en el análisis de la cuantificación del riesgo (QRA) por desprendimientos rocosos”, PID2019-103974RB-I00 funded by MCIN/AEI/10.13039/501100011033.

We want to acknowledge the ICGC team for their recommendations during the design of the system and during its implementation on the field. Also, to Vilarrasa S.L enterprise for allowing the placement of the cameras on its buildings. Finally, we appreciate all help provided by the Montagut i Oix local council.

## References

- Abellan A., Vilaplana J. M., Calvet J., García-Sellés D., and Asens E. (2011). Rockfall monitoring by Terrestrial Laser Scanning - Case study of the basaltic rock face at Castellfollit de la Roca (Catalonia, Spain). *Natural Hazards and Earth System Sciences* 11(3), pp. 829-841. DOI: 10.5194/nhess-11-829-2011
- Abellan A., Vilaplana J.M., Calvet J., and Rodriguez-Lloveras X., (2009). Detection of millimetric deformation using a terrestrial laser scanner: experiment and application to a rockfall event. *Nat. Hazards Earth Syst. Sci.*, 9, pp. 365–372. DOI: 10.5194/nhess-9-365-2009
- Albarelli, D.S.N.A., Mavrouli, O.C. and Nyktas, P. (2021). Identification of potential rockfall sources using UAV-derived point cloud. *Bull Eng Geol Environ* 80, p. 6539–6561. DOI: 10.1007/s10064-021-02306-2
- Atzeni, C., Barla, M., Pieraccini, M., and Antolini, F. (2015). Early Warning Monitoring of Natural and Engineered Slopes

with Ground-Based Synthetic-Aperture Radar. *Rock Mech. Rock Eng.*, 48, pp. 235–246.

- Blanch X., Eltner A., Guinau M. and Abellan A. (2021). Multi-Epoch and Multi-Imagery (MEMI) Photogrammetric Workflow for Enhanced Change Detection Using Time-Lapse Cameras. *Remote Sens.* 13, 1460. DOI: 10.3390/rs13081460
- Desrues, M., Malet, J.-P., Brenguier, O., Point, J., Stumpf, A., and Lorier, L. (2019). TSM—Tracing Surface Motion: A Generic Toolbox for Analyzing Ground-Based Image Time Series of Slope Deformation. *Remote Sens.*, 11, 2189. DOI: 10.3390/rs11192189
- Gance J., Malet J.-P., Dewez T., and Travelletti J. (2014). Target Detection and Tracking of moving objects for characterizing landslide displacements from time-lapse terrestrial optical images. *Engineering Geology*, 172, pp.26-40. DOI: 10.1016/j.enggeo.2014.01.003
- Janeras, M., Jara, J.A., Royán, M.J., Vilaplana, J.M., Aguasca, A., Fàbregas, X., Gili, J.A., and Buxó, P., (2016). Multi-technique approach to rockfall monitoring in the Montserrat massif (Catalonia, NE Spain), *Engineering Geology*, DOI: 10.1016/j.enggeo.2016.12.010
- Kromer, R., Walton, G., Gray, B., Lato, M., and Group, R. (2019). Development and Optimization of an Automated Fixed-Location Time Lapse Photogrammetric Rock Slope Monitoring System. *Remote Sens.*, 11, 1890. DOI: 10.3390/rs11161890
- Núñez-Andrés, M. A, Buill, F., Puig, C., Lantada, N., Prades, A., Janeras, M., and Gili, J.A. (2019). Comparison of geomatic techniques for rockfall monitoring. *4<sup>th</sup> Joint International Symposium on Deformation Monitoring (JISDM)*, 15-17 May 2019, Athens (Greece).
- Sarro, R., Riquelme, A., García-Davalillo, J.C., Mateos, R.M., Tomás, R., Pastor, J.L., Cano, M., and Herrera, G. (2018). Rockfall Simulation Based on UAV Photogrammetry Data Obtained during an Emergency Declaration: Application at a Cultural Heritage Site. *Remote Sens.*, 10, 1923. DOI: 10.3390/rs10121923
- Williams, J. G., Rosser, N. J., Hardy, R. J., Brain, M. J., and Afana, A.A. (2018). Optimising 4-D surface change detection: an approach for capturing rockfall magnitude-frequency, *Earth Surf. Dynam.*, 6, pp. 101–119, DOI: 10.5194/esurf-6-101-2018.

## Quantification of the dependence of the results on several network adjustment applications

Stéphane Durand<sup>1</sup>, Michael Lösler<sup>2</sup>, Mark Jones<sup>3</sup>, Paul-Henri Cattin<sup>4</sup>, Sébastien Guillaume<sup>4</sup>, Laurent Morel<sup>1</sup>

<sup>1</sup> Geomatics and Land Law Lab (Cnam/GeF - EA 4630), 1 boulevard Pythagore, F-72000, Le Mans, France, ([stephane.durand@lecnam.net](mailto:stephane.durand@lecnam.net); [laurent.morel@lecnam.net](mailto:laurent.morel@lecnam.net))

<sup>2</sup> Laboratory for Industrial Metrology, Frankfurt University of Applied Sciences, Nibelungenplatz 1, D-60318 Frankfurt am Main, Germany, ([michael.loesler@fb1.fra-uas.de](mailto:michael.loesler@fb1.fra-uas.de))

<sup>3</sup> Geodetic Metrology, BE Dept., European Organization for Nuclear Research (CERN), 1211 Genève, Switzerland, ([mark.jones@cern.ch](mailto:mark.jones@cern.ch))

<sup>4</sup> School of Management and Engineering Vaud (HEIG-VD), Institut Géomatique, insit – Institut d'ingénierie du territoire, Route de Cheseaux 1, 1400 Yverdon-les-Bains, Switzerland, ([paul-henri.cattin@heig-vd.ch](mailto:paul-henri.cattin@heig-vd.ch); [sebastien.guillaume@heig-vd.ch](mailto:sebastien.guillaume@heig-vd.ch))

**Key words:** *network adjustment; functional model discrepancies; generated measurements*

### ABSTRACT

The dependency of the results from a network adjustment on the application used is investigated. For that purpose, the results obtained by each tested application on several sets of simulated measurements are compared. In each simulation, only one parameter varies. We first present our comparison methodology and the method that was used to add Gaussian-like errors to theoretical measurements. We then apply it to study the impact of the side length of the network and of the ellipsoidal height difference among points in the network for several network adjustment applications: Columbus, CoMeT, Geolab, JAG3D, LGC, Move3, Star\*Net and Trinet+.

### I. INTRODUCTION

Adjusting geodetic networks is one of the most important tasks in the daily business of modern geodesists. In applied geodesy, such networks are the basis for planning landscape reorganization in, for example, urban development, operating and extending mechanical engineering facilities like particle accelerators, or the monitoring of structural facilities such as dams, bridges, or radio telescopes.

Many network adjustment applications are available today. Each user is free to use the application that best suits their own needs and preferences. In case of software replacement, for economic or practical reasons, of sending raw data to someone else, who is using different software, or for control purposes, the question of the dependency of the results on the software used (so called software effect) arises.

In the last decade, several studies have investigated this problem, using field measurements from given networks. The results from different adjustment applications are then compared, in terms of values and standard deviations for all estimated coordinates and relevant quality parameters (Lösler and Bähr, 2010; Schwiager *et al.*, 2010; Herrmann *et al.*, 2015).

In Durand *et al.* (2020) a comparison methodology to study the impact of the software on the results for applications using the Gauss-Markov model was proposed, based on the comparison of the results

obtained by each application, on the same simulated measurements. The main advantage of using generated measurements is that it allows the controlled alteration of one parameter at a time, between sets of measurements: shape or size of the network, refraction coefficient value, a priori accuracy, and so on. Thus, the generated measurements allow us to investigate the impact of each parameter.

In Durand *et al.* (2020), the comparison methodology was used to investigate the impact of the size of the network on the compatibility among the network adjustment applications developed in the authors institutions, *i.e.*, CoMeT, LGC, and Trinet+.

The main objectives of this contribution are to include more network adjustment applications in the comparisons, and to show that our methodology is relevant to better understand the impact of a particular parameter on the discrepancies between the applications.

In the first part of this contribution, we present our comparison methodology, based on the adjustment of a set of networks with simulated measurements. In the second part, we focus on the method that was used to add Gaussian-like errors to theoretical measurements fulfilling the following properties:

- 1) Adjusted coordinates are equal to the theoretical values and the computation is achieved in only one iteration step.



- 2) The estimated variance factor of unit weight is equal to the empirical one.
- 3) For a selected significance level, standardized residuals are not rejected in Baarda's test.

In the last part, we apply our comparison methodology to study the impact of two parameters on the results of the adjustment process: the side length of the network and the ellipsoidal height of the unknown point in the network.

We present and discuss the results obtained after processing the same simulated measurements with the following network adjustment applications. These are all using three-dimensional mathematical functional models, with an ellipsoidal approach, except for the LGC application where, for practical reasons, a spherical approach has been used in this instance:

1. *Columbus*, from Best-Fit computing, version 4.6.2.41 (<http://bestfit.com/>);
2. *CoMeT* (Compensation de Mesures Topographiques), from the Cnam/GeF, version 2017.02.14 (<http://comet.esgt.cnam.fr/>);
3. *Geolab*, from Bitwise Ideas Inc., version 2021.1.1 (<https://www.geolabsolutions.com/>);
4. *JAG3D* (Java Applied Geodesy 3D), using the ellipsoidal approach, version 20211123 (<https://software.applied-geodesy.org/>);
5. *LGC* (Logiciel Général de Compensation), from the CERN, version 2.03.01 (<https://move3software.com/>);
6. *Move3*, from Sweco, version 4.5.1 (<https://move3software.com/>);
7. *Star\*Net*, from MicroSurvey, version 10.0.15.974 (<https://www.microsurvey.com/products/starnet/>);
8. *Trinet+*, from the Heig-Vd, version 7.2.

## II. TEST METHODOLOGY

### A. Using simulated test networks

As in Durand *et al.* (2020), our test methodology is based on simply shaped networks, all with only one variable parameter. Each network is made up of two points (S1 and S2) with known coordinates and one point M with coordinates to be estimated. In order to build these networks, we defined a point P0 as the barycentre of all our networks, with ETRS89 Cartesian and ellipsoidal coordinates as defined in Table 1, and with no geoidal undulation with respect to the IAG GRS80 ellipsoid. To ensure compatibility with the LGC application, this P0 point has the same definition as the CERN P0 point used in the LGC application and linked to the CERN Coordinate System (CCS).

In the local astronomical system of point P0, given a side length  $d$ , the horizontal coordinates for the points of each network are computed to form an equilateral triangle, with point P0 as barycentre, point M being located north of point P0, and point S1 and S2 being located east and west of point P0, respectively, as illustrated in Figure 1.

Table 1. ETRS89 Cartesian and ellipsoidal coordinates of point P0, the barycentre of all the test networks

	ETRS89 Cartesian Coordinates	Ellipsoidal coordinates (w.r.t. IAG GRS80)
X [m]	4395400.3638	--
Y [m]	465785.0567	--
Z [m]	4583458.2260	--
Latitude [grad]	--	51.3692
Longitude [grad]	--	6.72124
Ellipsoidal height [m]	--	433.65921

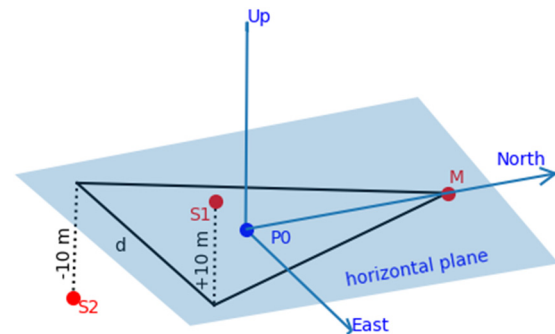


Figure 1. Common design of the test networks with side length  $d$ , in the local astronomical system of P0.

Such a simple network without peculiarities is sufficient to investigate the software effect. An application that yields different results for such a simple network design will also give different results in complex networks. However, the effect will be easier to be detected in a simple network design than in a complex one.

The local vertical coordinates of points S1, S2, and M were fixed to be respectively +10 m, -10 m, and 0 m. These local coordinates were used to compute ETRS89 geodetic Cartesian coordinates for all points in the test networks (with no deflection of the vertical for point P0 with respect to the IAG GRS80 ellipsoid).

These ETRS89 Cartesian coordinates were used to compute simulated observations between points in the networks, as the sum of a theoretical value and an error value. The theoretical value of the observation was computed using the three-dimensional mathematical functional models of the CoMeT application, with an ellipsoidal datum (IAG GRS80 ellipsoid, deflection of the vertical of zero for all points). The error value was computed in a particular way explained in part III. As illustrated in Table 2, conventional measurements, *i.e.*, horizontal direction, zenith angle, and slope distance, are made from points S1 and S2 to point M and only horizontal direction observations are included from S1 to S2 and from S2 to S1.

Table 2. Type of observations between points in the test networks

	From S1 to:	From S2 to:
Horizontal direction	M, S2	M, S1
Zenith angle	M	M
Slope Distance	M	M

Therefore, the adjustment of each network entails the estimation, using least squares, of the coordinates of point M as well as the orientation unknowns for the instrument stations at S1 and S2.

**B. Functional and stochastic parameters**

Even if all the applications involved in this study make use of three-dimensional mathematical functional models, with an ellipsoidal datum, some differences may exist both in the functional and stochastic implementations. Table 3 summarizes the main parameters used in this work to both simulate and process the measurements, in order to avoid any unwanted discrepancies in the results. We used a convergence criterion of 0.1 mm, as this is the smallest selectable value in some applications.

Table 3. Relevant functional and stochastic parameters for both simulation and processing

Parameter	Value
Refraction coefficient	None
Standard deviation (angle measurements)	0.3 mgrad
Standard deviation (slope distance)	5 mm
Convergence criterion	0.1 mm

The distance dependent part of the a priori uncertainty for slope distances is left out because their processing differs in each application. Let  $a$ , in meters, and  $b$ , in parts per million (ppm), denote the constant and distance-dependant parts respectively of the standard deviation for a slope distance  $D$  between the station and the target. As indicated in Shih (2013), there exists two interpretations of electronic distance meter accuracy specifications, based on different assumptions: the “additive” method, in which the standard deviation  $\sigma$  is computed from Equation 1, and the “propagated” one, which uses Equation 2.

$$\sigma = a + b \times 10^{-6} \times D \tag{1}$$

$$\sigma = \sqrt{a^2 + (b \times 10^{-6} \times D)^2} \tag{2}$$

Depending on the applied model and especially for long distances, different results are obtained. This effect must be taken into account when comparing adjustment applications. Table 4 indicates for each application involved in this study which approaches are implemented and used by default.

The refraction correction to zenith angle measurements is also not applied since the method used to compute this correction differs for each program or does not exist (Durand *et al.*, 2020). Let  $V_{mes}$  denote the zenith angle observation,  $V_{cor}$  the corrected value from the refraction effect, and  $k$  the coefficient of refraction.

In the LGC application, no refraction corrections are applied to zenith angle measurements - the application

was developed primarily for networks located in underground tunnels, or buildings.

Table 4. Implemented stochastic models to obtain the a priori uncertainty of a slope distance

Software	Additive approach (Equation 1)	Propagated approach (Equation 2)
Columbus	Yes	No
CoMeT	Yes	Yes (default)
Geolab	No	Yes
JAG3D	No	Yes
LGC	Yes	No
Move3	Yes	No
Star*Net	Yes (default)	Yes
Trinet+	Yes	No

As indicated in their user manuals, the Columbus and CoMeT applications apply the following formula (Eq. 3):

$$V_{cor} = V_{mes} + \frac{k \times D}{2 \times R} \tag{3}$$

In the Columbus application,  $R$  corresponds to the sum of the radius of the Earth and the ellipsoidal height at the station. In the CoMeT application,  $R$  corresponds to the semi-major axis of the selected ellipsoid.

In the Trinet+ and JAG3D applications, the correction is computed using a slightly different formula (Eq. 4):

$$V_{cor} = V_{mes} + \frac{k \times D_h}{2 \times R} \tag{4}$$

where  $D_h$  denotes the horizontal distance between points. In the JAG3D application, the Earth radius is approximated using the latitude of the barycentre P0. In the Trinet+ application,  $R$  can be selected in the range [6000, 7000] km.

The documentation of the Geolab and Move3 applications do not clearly indicate which formula is used to compute the refraction correction. Nevertheless, in these applications it is possible to output a measurement value including the refraction correction, and potentially deduce the refraction correction formula. From tests that we have conducted, it seems that the Geolab and Move3 applications use a formula very close to the one in Equation 3.

The user manual of the Star\*Net application indicates that the refraction error is computed following (Bomford, 1971). In practice, using the same notations as above, this corresponds to the formula (Eq. 5):

$$V_{cor} = V_{mes} + \frac{k \times D_h}{R} \tag{5}$$

In this representation, the largest difference is the factor 2, which means that in the Star\*Net application, the refraction coefficient,  $k$ , may not be directly comparable with those used in Equations 3 and 4. This

effect of the refraction handling must be taken into account when comparing adjustment applications.

For all applications involved in this work, known and initial coordinates for all points are entered directly as ETRS89 Cartesian or ellipsoidal (w.r.t. IAG GRS80 ellipsoid) coordinates. There are only a few exceptions. The JAG3D application does not process global Earth-fixed coordinates but supports local tangent plane coordinates. For that reason, the ETRS89 Cartesian geodetic coordinates are converted into local coordinates in the local tangent plane system of point P0 w.r.t. the IAG GRS80 ellipsoid. In the Trinet+ application, observation equations are expressed in terms of topocentric coordinates. The topocentre as well as the points in the network have to be defined using CH1903+ Cartesian coordinates and the values of the deflection of the vertical with respect to the Bessel 1841 reference ellipsoid. Thus, the ETRS89 Cartesian coordinates were converted to CH1903+ Cartesian coordinates. Starting from zero value deflection of the vertical on each point relative to the IAG GRS80 reference ellipsoid, the deflection of the vertical relative to the Bessel 1841 reference ellipsoid was computed. In the case of geodetic calculations in the LGC application, coordinates have to be entered in a CERN 2D+1 system derived from the CERN Coordinate System (CCS). Thus, the ETRS89 Cartesian coordinates of each point in each network were transformed into the Cartesian CCS system. Subsequently, the Z-coordinates were converted to ellipsoidal heights using the CERN Spherical vertical datum (Durand *et al.*, 2020) - to avoid the application of a geoid model.

### III. GENERATION OF RANDOM ERRORS

Simulated measurements are the sum of theoretical measurements and error values, which could be equal to zero, or randomly selected from a Gaussian distribution. In this work, we have developed a particular method for computing the error values, hereafter detailed.

Suppose an unknown vector  $X = (x_1, \dots, x_m)^T$  is to be estimated from observation vector  $L = (l_1, \dots, l_n)^T$ , where  $n \geq m$ . In classical least squares estimation, they are related by (Eq. 6):

$$L = f(X) + V, V \sim \mathcal{N}(0, s_0^2 Q) \quad (6)$$

where  $f$  denotes the functional relation between measurements and parameters,  $V$  the error vector,  $s_0^2$  the a priori variance factor of unit weight and  $Q$  the cofactor matrix of the observations. Equation 6 assumes the absence of systematic and gross errors. Only random errors are considered.

As indicated for example in (Casparly and Rieger, 2000), in an iterative least squares method, Equation 6 is linearized by approximation to a first-order Taylor series expansion (Eq. 7):

$$B = L - f(X_0) = A(X - X_0) + V, V \sim \mathcal{N}(0, s_0^2 Q) \quad (7)$$

where  $B = L - f(X_0)$  is the difference between the measurements and their estimated values using  $X_0$ , the initial values of the parameters. Solution of Equation 6 is computed using an iterative process on the least squares solution of Equation 7, until the adjusted estimate of Equation 7 is sufficiently close to the initial value  $X_0$  used in the last iteration step. Using matrix  $Q$  to define the norm, the least squares solution  $\hat{X}$  to Equation 7 is expressed as (Eq. 8):

$$\hat{X} - X_0 = (A^T Q^{-1} A)^{-1} A^T Q^{-1} B \quad (8)$$

At the end of the iterative process, we obtain the estimated least squares solution of Equation 7. It is thus possible to compute the vector of residuals (Eq. 9):

$$\hat{V} = B - A(\hat{X} - X_0) \quad (9)$$

And the estimated variance factor of unit weight (Eq. 10):

$$\hat{s}_0^2 = \frac{\hat{V}^T Q^{-1} \hat{V}}{n - m} \quad (10)$$

In the process of simulating measurements for a particular network, the theoretical coordinates of all points, the different measurements between the points introduced and the a priori standard deviations of the measurements are known. Let  $X_{th}$  denote the vector containing the theoretical coordinates of all points in a network, as well as initial or randomly selected values for the orientation unknowns. Let  $V_s$  denote a simulated error vector. It is possible to directly use Equation 6 to compute simulated values for the measurements (Eq. 11):

$$L_s = f(X_{th}) + V_s \quad (11)$$

The simulated error vector  $V_s$  could be obtained using several methods: a null vector (no error), randomly selected values, randomly selected values with respect to a Gaussian distribution with the a priori standard deviation of each measurement, to cite but a few.

In this study, we used a particular method to compute the error vector  $V_s$ . We wanted to compute an error vector which fulfilled the following conditions:

- (i) Vector  $V_s$  is not null, nor unique;
- (ii) If the initial coordinates for all points are the theoretical ones (which means  $X_0 = X_{th}$ ), then the adjusted coordinates are equal to the theoretical ones (which means  $\hat{X} = X_{th}$ ) and the iterative process is achieved in only one iteration step;
- (iii) The global model test used as a first step in outlier detection as described in (Casparly and

Rüeger, 2000) is not rejected regardless of the selected significance level;

- (iv) For a selected significant level  $\alpha$ , standardized residuals are not rejected in Baarda's test.

Now let  $V_s$  denote an error vector fulfilling these four conditions. From Equation 11, the measurements vector to process is  $L_s = f(X_{th}) + V_s$ . As the theoretical coordinates are used as initial values in the adjustment process, we have, for the first iteration step, as indicated in Equation 7, (Eq. 12):

$$B = L_s - f(X_{th}) = V_s \quad (12)$$

From Equation 8, the least squares solution for the first iteration step yields (Eq. 13):

$$\hat{X} - X_{th} = (A^T Q^{-1} A)^{-1} A^T Q^{-1} V_s \quad (13)$$

Condition (ii) means that  $\hat{X} - X_{th} = 0$ . The first consequence is that the vector of residuals corresponds to the simulated error vector (Eq. 14):

$$\hat{V} = (L_s - f(X_{th})) - A(\hat{X} - X_{th}) = V_s \quad (14)$$

The second consequence is that vector  $V_s$  lies in the kernel of the linear map with corresponding matrix (Eq. 15):

$$H = (A^T Q^{-1} A)^{-1} A^T Q^{-1} \quad (15)$$

As matrix  $Q$  is symmetric positive definite, it is possible to find an upper triangular matrix  $R$  such that  $Q^{-1} = R^T R$ , and to define matrix  $K$  as (Eq. 16):

$$K = (A^T Q^{-1} A)^{-1} A^T R^T \quad (16)$$

Thus, if  $V_s \in \ker(H)$  then  $y = R V_s \in \ker(K)$ . As  $K$  is a matrix of size  $n \times m$  and of rank  $m$ ,  $\ker(K)$  is of dimension  $n - m$ . Let  $\beta$  be an orthogonal basis of  $\ker(K)$ . By definition, for each vector  $z \in \mathbb{R}^{n-m}$ ,  $y = \beta z$  lies in  $\ker(K)$ . This gives us a practical way to compute an error vector that fulfils conditions (i) and (ii). We just have to randomly select a non-zero vector  $z \in \mathbb{R}^{n-m}$ , to compute an orthogonal basis  $\beta$  of  $\ker(K)$  (from the singular value decomposition (SVD) of matrix  $K$  for example), and to compute (Eq. 17):

$$V_s = R^{-1} \beta z \quad (17)$$

The third condition is related to the global model test commonly used as a first step in outlier detection. As explained, for example in (Caspary and Rüeger, 2000), its aim is to verify that the error vector is compatible with a statistical distribution of the errors according to the  $\mathcal{N}(0, s_0^2 Q)$  normal law. The statistic used for this test is, according to the definitions in Equations 9 and 10, (Eq. 18):

$$T = \frac{\hat{V}^T Q^{-1} \hat{V}}{s_0^2} = (n - m) \frac{\hat{s}_0^2}{s_0^2} \sim \chi_{n-m}^2 \quad (18)$$

After selecting a significance level  $\alpha$  for the test, and according to the  $\chi_{n-m}^2$  distribution, one has to verify that the observed test statistic  $T$  is located in the acceptance region. As the central value of the  $\chi^2$  distribution is equal to  $(n - m)$ , if the observed test statistic is equal to  $(n - m)$ , it is in the acceptance region, whatever the selected significant level.

Thus, we have to compute an error vector  $V_s$  in such a way that the corresponding observed test statistic yields  $T = n - m$ .

As vector  $V_s$  fulfils conditions (i) and (ii), it is of the form  $V_s = R^{-1} \beta z$  with  $z \in \mathbb{R}^{n-m}$  and corresponds to the vector of residuals. The observed test statistic is (Eq. 19):

$$T = \frac{V_s^T Q^{-1} V_s}{s_0^2} = \frac{z^T z}{s_0^2} \quad (19)$$

To fulfil condition (iii), we just have to compute a vector  $z \in \mathbb{R}^{n-m}$  in such a way that (Eq. 20):

$$z^T z = (n - m) s_0^2 \quad (20)$$

The fourth condition is related to the test strategy proposed by Baarda, which is commonly used to detect outliers when the residuals are normally distributed (Baarda, 1968; Caspary and Rüeger, 2000). This test assumes that the variance factor  $s_0^2$  is known and uses the standardized residual as the test statistic (Eq. 21):

$$\forall i = 1, \dots, n, \quad \hat{w}_i = \frac{\hat{v}_i}{s_0 \sqrt{q_{v_i v_i}}} \quad (21)$$

In Equation 21,  $\hat{v}_i$  denotes the  $i$ -th element of the vector of residuals  $\hat{V}$  and  $q_{v_i v_i}$  is the corresponding element  $(i, i)$  of the cofactor matrix  $Q_{\hat{V}}$  of  $\hat{V}$  defined by (Eq. 22):

$$Q_{\hat{V}} = Q - A(A^T Q^{-1} A)^{-1} A^T \quad (22)$$

Selecting a significance level  $\alpha$ , it is possible to compute the critical value  $\gamma$  of the test statistic using the normal distribution  $\mathcal{N}(0,1)$ . No gross error is detected if the absolute value of the standardized residual  $\hat{w}_i$  is less than  $\gamma$ .

Let  $G$  denote the vector of length  $n$  in which each entry  $G_i$  corresponds to (Eq. 23):

$$\forall i = 1, \dots, n, \quad G_i = s_0 \sqrt{q_{v_i v_i}} \quad (23)$$

The acceptance region of Baarda's test could be written in the following matrix formulation (Eq. 24):

$$U = \{u \in \mathbb{R}^n / -G\gamma \leq u \leq G\gamma\} \quad (24)$$

To fulfil condition (iv), the simulated error vector  $V_s$  must be included in  $U$ . As it also fulfils conditions (i) and (ii), it is computed as  $V_s = R^{-1} \beta z$ , where  $z \in \mathbb{R}^{n-m}$ , (see Equation 17). Thus, the acceptance region of Baarda's test could be written as (Eq. 25):

$$U = \{u \in \mathbb{R}^{n-m} / -G\gamma \leq R^{-1} \beta u \leq G\gamma\} \quad (25)$$

In practice, finding a simulated error vector that fulfils conditions (i) to (iv) is related to the quadratic optimization problem (Eq. 26):

$$\begin{aligned} \max_{u \in \mathbb{R}^{n-m}} \quad & \varphi(u) = u^T u \\ \text{s. t.} \quad & -G\gamma \leq R^{-1} \beta u \leq G\gamma \end{aligned} \quad (26)$$

In the general case, finding a solution of Equation 26 is a non-deterministic polynomial-time hard problem (Pardalos and Vavasis, 1991) and called a nonconvex quadratic programming problem. It can be resolved using several global optimization methods for nonconvex QP problems (Pardalos, 1991).

In practice, we do not really have to find the solution of problem (Equation 26). We just need to find  $\tilde{u} \in \mathbb{R}^{n-m}$  fulfilling conditions (i), (ii) and (iv). It is thus more suitable to use vertex enumeration methods like the ones described in (Avis and Fukuda, 1992). For the polyhedron defined in Equation 25, a point  $u \in U$  is a vertex of  $U$  if, and only if, it is the unique solution to a subset of  $n - m$  inequalities, solved as equations. The enumeration process can be stopped when we get a vertex  $\tilde{u} \in \mathbb{R}^{n-m}$  such that  $\varphi(\tilde{u}) \geq (n - m)s_0^2$ . It is also possible to continue the enumeration process in order to select another vertex with the same properties, to simulate a kind of random selection. If the enumeration process finishes, we get the solution to the QP problem in Equation 26.

Suppose now that we get a vertex  $\tilde{u} \in \mathbb{R}^{n-m}$  such that  $\varphi(\tilde{u}) \geq (n - m)s_0^2$ . Let  $S$  denote the sphere defined by (Eq. 27):

$$S = \{u \in \mathbb{R}^{n-m} / u^T u = (n - m)s_0^2\} \quad (27)$$

We may then compute a vector  $\hat{z}$  that fulfils conditions (i) to (iv) as the orthogonal projection of  $\tilde{u}$  onto the sphere defined in Equation 27. If for the solution  $\hat{u}$  of problem (Equation 26) we have  $\varphi(\hat{u}) < (n - m)s_0^2$ , then it is not possible to find a point fulfilling the four conditions and  $\hat{z}$  is the point which is closest to fulfilling condition (iv).

In our particular case, it is very easy to find the vertices of the polyhedron. As  $\beta$  is an orthogonal basis of  $\ker(K)$ ,  $\beta^T \beta$  corresponds to the identity matrix, and by setting  $\kappa = \beta^T R G \gamma$ , Equation 25 is simplified by (Eq. 28):

$$U = \{u \in \mathbb{R}^{n-m} / -\kappa \leq u \leq \kappa\} \quad (28)$$

Polyhedron  $U$  corresponds to a  $(n - m)$ -dimensional rectangle, whose  $2^{n-m}$  vertices are easy to find. For each vertex  $\tilde{u}$ , the quantity  $\varphi(\tilde{u})$  is the same and corresponds to  $\varphi(\tilde{u}) = \kappa^T \kappa$ .

In contrast to randomly selected values, the benefit of the described procedure is to control the synthetically generated observations w.r.t. the effect under investigation.

## IV. RESULTS AND DISCUSSION

### A. Criteria for comparisons

For each network under consideration, measurements were simulated using the functional mathematical models of the CoMeT application, and were processed by each network adjustment application, using the same parameters as summarized in Table 3. We obtain adjusted ETRS89 coordinates for the unknown point M, directly or after transformation (JAG3D, Trinet+, LGC). Then the local coordinates of the estimated point M in the local astronomical system of the theoretical point M are computed, allowing the computation of coordinate deviations in the local horizontal plane and the local vertical.

We also obtain quality parameters, such as residuals and estimated variance factors. The estimated variance factor can be seen as a global metric of the agreement between all the measurements in a network and the three-dimensional mathematical models used in a particular application. The method used to generate the error vector associated with simulated measurements ensures that when processed with an application that uses similar functional models, the estimated variance factor is close to one. This facilitates the comparisons as the closer the estimated variance factor is to one, the greater the similarity of CoMeT's functional models to those of the tested application.

### B. Impact of the side length of the network

This test is similar to the one proposed in Durand *et al.* (2020) and uses the same simulated measurements, which are available on a dedicated webpage<sup>1</sup>. All networks share the same shape (equilateral triangle in the horizontal plane) and the same barycentre P0, with point M located north of point P0 and side length  $d$  as the varying parameter, as shown in Figure 1. In this contribution, we focus on the results obtained by all the tested applications for side lengths varying from 30 m up to 10 km.

Figure 2 shows the estimated variance factors obtained by each adjustment application against the side length  $d$  of each network. Small deviations of the estimated variance of unit weight is usually tolerable and does not significantly affect the estimates. For all network side lengths, the estimated variance factors are coherent among all the tested applications. Small discrepancies, about 10 percent difference, are just

<sup>1</sup> <http://comet.esgt.cnam.fr/index.php?page=0801>

noticeable for the Move3 and Geolab applications, for the network with side length 30 m. All applications are in good agreement whatever the network side length. It is evident that for the Trinet+ application, for network side lengths above 2 km, the estimated variance factor tends to decrease with the network side length (*cf.* Durand *et al.*, 2020). This is coherent with the fact that the Trinet+ application was developed initially for application in an industrial context and not for large networks.

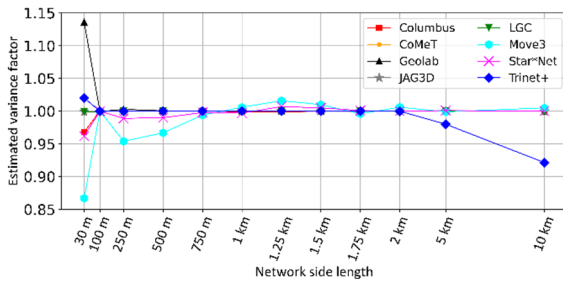


Figure 2. Estimated variance factor against network side length.

Figure 3 shows the differences, in the vertical component, between the adjusted and theoretical coordinates of point M, against network side length. In this study, a convergence criterion of 0.1 mm is used, indicated by the black dotted line, and absolute values of discrepancies less than this criterion could not be considered as significant. As shown in Figure 3, the discrepancies among the applications are negligible for network side lengths under 10 km. The only exception is the LGC application where non-negligible discrepancies exist: 2.3 mm at 5 km and 10 mm at 10 km. These discrepancies are coherent with the use of the spherical datum, the IUGG Sphere, and not the IAG GRS80 reference ellipsoid.

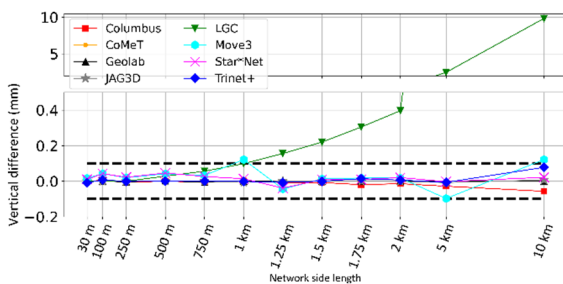


Figure 3. Differences, in millimetres, in the vertical component, between estimated and theoretical coordinates of point M, against network side length.

Figure 4 shows the horizontal distances between the adjusted and theoretical coordinates of point M against network side length. The black dotted line indicates the convergence criterion value for 2D coordinates. For the Columbus, CoMeT, JAG3D, LGC and Trinet+ applications, no discrepancies exist, showing that their three-dimensional mathematical functional models are

consistent. For Geolab, Move3 and Star\*Net, discrepancies above the convergence criterion exist, but remain very small. We observe mean discrepancies values of 0.15 mm and 0.12 mm for the Move3 and Star\*Net applications respectively. For Geolab the maximum discrepancy value is 0.19 mm for the network with side length 250 m.

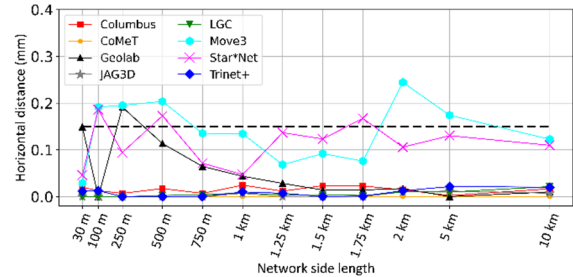


Figure 4. Horizontal distance, in millimetres, between estimated and theoretical coordinates of point M, against network side length.

### C. Impact of the ellipsoidal height of point M

In this test, the main objective is to study the impact of an ellipsoidal height difference between the points on the results obtained by each software. The starting point is the network with a side length of 500 meters, with local vertical coordinates of 0 m, +10 m and -10 m for points M, S1 and S2 respectively, corresponding to ellipsoidal heights of 433.6658 m, 443.6658 m and 423.6658 m respectively with respect to the IAG GRS80 ellipsoid.

Simulated measurements were computed for networks in which the ellipsoidal height of point M is modified by an offset varying from 30 m to 2500 m. This generates a varying ellipsoidal height difference among the points in the networks. The coordinates of the simulated networks, as well as the measurements, are available on a dedicated webpage<sup>2</sup>.

Figure 5 shows the estimated variance factors of unit weight, obtained from each adjustment application, against the offset on the ellipsoidal height of point M. Whilst the network length affects the estimated variance of unit weight slightly, a vertical variation of the network biases the variance significantly in some applications. For the Trinet+ application, the estimated variance factor increases with the offset value on the ellipsoidal height of point M, from 1.0 under 250 m, up to 1.12 at 2.5 km. For the Geolab application, we observe that for offset values above 500 m, non-negligible biases may exist, with a maximum value of 1.3 visible for an offset value of 1 km.

Figure 6 depicts the vertical difference between adjusted and theoretical coordinates of point M, against the offset on the ellipsoidal height of point M. We observe a very good agreement among all the applications, with negligible discrepancies. There are only two exceptions. For the Geolab application,

<sup>2</sup> <http://comet.esgt.cnam.fr/index.php?page=0802>

significant deviations exist, with a maximum value of 0.5 mm for the network with an offset value of 1.5 km, and a standard deviation of 0.32 mm on the discrepancy value. For the Trinet+ application, small discrepancies (less than 0.2 mm) are visible for offset values between 500 m and 1.5 km.

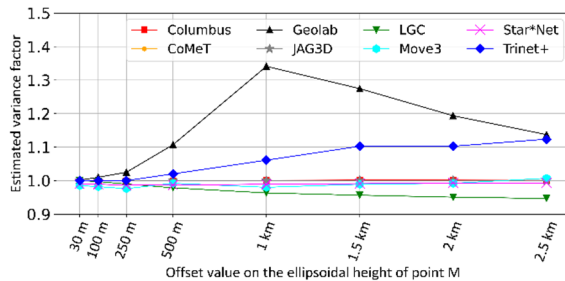


Figure 5. Estimated variance factor of unit weight against offset value on the ellipsoidal height of point M.

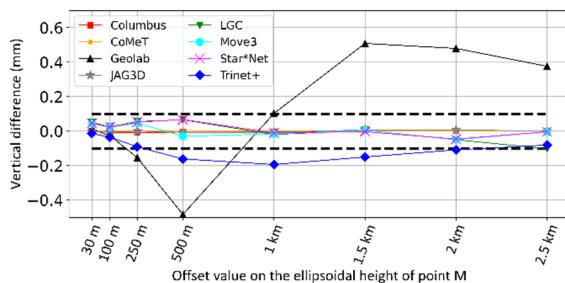


Figure 6. Differences, in millimetres, in the vertical component, between estimated and theoretical coordinates of point M, against offset value on its ellipsoidal height.

Figure 7 shows the horizontal distances, between adjusted and theoretical coordinates of point M, against the offset on the ellipsoidal height of point M. For the Columbus, CoMeT and JAG3D applications, no discrepancies exist. The Move3 and Star\*Net applications show very similar results, with small discrepancies: mean value of 0.22 mm and 0.19 mm, respectively. For the LGC and Trinet+ applications, discrepancies increase with the offset value. These go from 0 mm at 100 m to 0.3 mm at 500 m for Trinet+; and for LGC from 0.15 mm at 1.5 km to 0.4 mm at 2.5 km. Geolab is the application most affected by the variation of the offset value, with a mean discrepancy value of 1.7 mm and the maximum value of 3.3 mm for an offset value of 1.5 km.

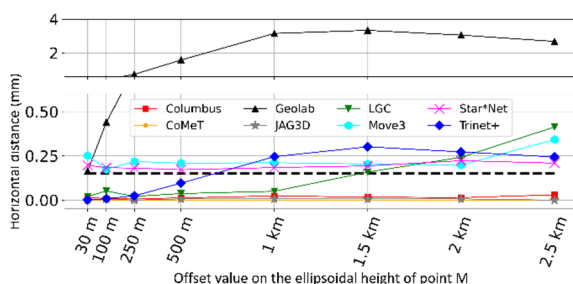


Figure 7. Horizontal distance, in millimetres, between estimated and theoretical coordinates of point M, against offset value on the ellipsoidal height of point M.

## V. CONCLUSION

This paper has investigated the dependency of network results on the adjustment application. Simulated measurements were processed with all tested applications. The main advantage of the test methodology presented is that it allows the selection and control of a single changing parameter in comparable sets of measurements. It also allows random error values, added to the theoretical measurements, to be determined to facilitate the comparison process. Both the estimated variance factors and the differences between adjusted and theoretical coordinates of the unknown point are used as metrics of the agreement between the three-dimensional mathematical models used in each of the tested applications. We apply our test methodology on several network adjustment applications, to study the impact of the network side length and of a difference in the ellipsoidal heights of the points. We show that all applications agree to the first order, but there can be non-negligible discrepancies, that have a real impact on the adjusted coordinates of up to several millimeters.

Almost identical results are obtained from Columbus, CoMet, JAG3D and Trinet+ in the horizontal network. LGC approximates the Earth by a sphere instead of an ellipsoid. For small networks, the resulting vertical deviations are well below 0.1 mm and are negligible. However, the vertical deviation depends on the network extent and, thus, becomes significant in networks larger than 1 km.

In the vertical network, the results are more heterogeneous. Geolab achieved the largest deviations in the results. Moreover, for Move3 and Star\*Net, an offset was detected in the horizontal distance, which needs further investigation. Almost identical results yield Columbus, CoMet and JAG3D.

## References

- Avis, D., and Fukuda, K. (1992). A pivoting algorithm for convex hulls and vertex enumeration of arrangements and polyhedra, *Discrete Comput. Geom.*, 8(3), pp. 295–313.
- Baarda, W. (1968). *A Testing Procedure for Use in Geodetic Networks*. Netherlands Geodetic Commission, Delft: Publications on Geodesy, 2(5).
- Bomford, G. (1971). *Geodesy*. Clarendon Press.
- Caspary, W., and Rüeger, J.M. (2000). *Concepts of network and deformation analysis*. 3rd (corrected) impression. Sydney, N.S.W.: School of Geomatic Engineering, University of New South Wales.
- Durand, S., Touzé, T., Jones, M., Guillaume, S., Henri Cattin, P., and Morel, L. (2020). Evaluation of Compatibility among Network Adjustment Software: CoMeT, LGC, and Trinet+. *Journal of Surveying Engineering*, 146(2), 04020005.
- Herrmann, C., Lösler, M., and Bähr, H. (2015). Comparison of SpatialAnalyzer and Different Adjustment Programs, in Kutterer, H. et al. (eds) *The 1st International Workshop on the Quality of Geodetic Observation and Monitoring Systems (QuGOMS'11)*. Cham: Springer, pp. 79–84.

- Lösler, M., and Bähr, H. (2010). Vergleich der Ergebnisse verschiedener Netzausgleichsprogramme, *Zippelt, K. (ed) Vernetzt und ausgeglichen.*, 3, pp. 205–214.
- Pardalos, P.M. (1991). Global optimization algorithms for linearly constrained indefinite quadratic problems, *Comput. Math. Appl.*, 21(6), 87–97.
- Pardalos, P.M., and Vavasis, S.A. (1991). Quadratic programming with one negative eigenvalue is NP-hard, *J. Glob. Optim.*, 1(1), pp. 15–22.
- Schwieger, V., Foppe, K., and Neuner, H. (2010). Qualitative Aspekte zu Softwarepaketen der Ausgleichsrechnung, in Kutterer, H. and Neuner, H. (eds) *Qualitätsmanagement geodätischer Mess- und Auswerteverfahren*, Augsburg: Wißner, 61, pp. 129–163.
- Shih, P.T.-Y., (2013). On accuracy specifications of electronic distance meter. *Survey Review* 45, pp. 281–284.



## Assessing vertical terrain displacement from TLS data by applying $M_{split}$ estimation – theoretical analysis

Patrycja Wyszowska, Robert Duchnowski

Department of Geodesy, Institute of Geodesy and Civil Engineering, Faculty of Geoengineering, University of Warmia and Mazury in Olsztyn, Oczapowskiego 1 Str. 10-719 Olsztyn, Poland, ([patrycja.wyszowska@uwm.edu.pl](mailto:patrycja.wyszowska@uwm.edu.pl); [robert.duchnowski@uwm.edu.pl](mailto:robert.duchnowski@uwm.edu.pl))

**Key words:**  $M_{split}$  estimation; terrestrial laser scanning; vertical displacement; deformation analysis; robust estimation

### ABSTRACT

Terrestrial laser scanning (TLS) is a measurement technique that has become popular in the last decades. Measurement results, usually as a point cloud, contain many points measured. When the TLS technique is used to determine terrain surface (e.g., by determining terrain profiles), one should realize that some points measured do not concern the terrain surface itself, but trees, shrubs, or generally the vegetation cover. Considering terrain surface determination, they should be regarded as outliers. Some other observations can also be outliers of different origins; for example, they might be disturbed by gross errors. We should consider such observation types when the data are processed. Two leading solutions in such a context are data cleaning and the application of robust estimation methods. Robust M-estimation is the most popular for the latter approach. As an alternative, one can also consider the application of  $M_{split}$  estimation, in which the functional model is split into two competing ones. Hence, the paper aims to analyze how  $M_{split}$  estimation can assess vertical terrain displacement based on terrain profile determination from TLS data. We consider processing data in separate sets (two measurement epochs) or one combined set, a natural approach in  $M_{split}$  estimation. The analyses based on simulated TLS data proved that the first solution seems better. Furthermore, the application of  $M_{split}$  estimation can also provide more satisfactory results than the classical methods used in such a context.

### I. INTRODUCTION

Laser scanning, as a very popular measurement technique, has found many applications in the last decades, e.g., in measuring vegetation, mining displacements, cultural heritage sites, urban environments, buildings, or other objects (Gordon and Lichti, 2007; Wang and Hsu, 2007; Spaete *et al.*, 2011; Rodríguez-González *et al.*, 2017; Crespo-Peremarch *et al.*, 2018; Matwij *et al.*, 2021). Depending on what platform a laser scanner is installed, one can distinguish airborne laser scanning (ALS), terrestrial laser scanning (TLS), or mobile laser scanning (MLS) (Kuzia, 2016). As a typical measurement result, a point cloud contains many points measured that are the basis for further processing. In this paper, we consider the determination of the terrain surface, by determining terrain profiles, from such a TLS result. One should realize some measured points do not concern the terrain surface itself but, for example, vegetation cover (trees, shrubs, etc.), small animals (e.g., birds), or other obstacles. If we focus on terrain surface determination, they should be regarded as so-called positive outliers (Matkan *et al.*, 2014; Carrilho *et al.*, 2018). Outlying observations might also have other origins, such as multipath distance ranging, leading to negative outliers. In some sense, both groups might be considered observations disturbed by gross errors. We should consider the possible occurrence of such observations

when processing TLS point clouds. Two main solutions in such a context are data cleaning or application of robust estimation methods, which are well-known in surveying engineering (Hodges and Lehmann, 1963; Baarda, 1968; Pope, 1976; Gui and Zhang, 1998; Huber and Ronchetti, 2009; Duchnowski, 2013; Ge *et al.*, 2013; Lehmann, 2013). As an alternative, one can also consider the application of  $M_{split}$  estimation. That novel development of M-estimation assumes that the functional model is split into two or more competitive ones (Wiśniewski, 2009; 2010). Such an estimation method allows us automatically isolate observation subsets and estimate their location parameters. That feature might be advisable when processing TLS point clouds that include outliers (Wyszowska *et al.*, 2021).

The paper's main aim is to analyze how  $M_{split}$  estimation can be used to assess vertical terrain displacement from estimated terrain profiles based on TLS data. We assume two measurement epochs in such a context, hence two observation sets. We compare two approaches: processing data separately (related to each measurement epoch) or in one combined set, a natural approach in  $M_{split}$  estimation. We apply two main variants of  $M_{split}$  estimation, i.e., the squared  $M_{split}$  estimation, the basic variant, and the absolute  $M_{split}$  estimation, which was introduced to be less sensitive to outliers than the first variant (Wyszowska and Duchnowski, 2019). For the sake of comparison, we also

use the following classical methods: the least-squares method, and two variants of robust M-estimation, *i.e.*, the Huber method and the Tukey method. The example M-estimation methods differ from each other in general features of the influence functions. The Tukey influence function has rejection points in contrast to the Huber method (Gui and Zhang, 1998; Ge *et al.*, 2013).

## II. GENERAL ASSUMPTIONS

While processing or adjusting geodetic observations, we usually apply the conventional linear functional model given as follows (Eq. 1):

$$\mathbf{y} = \mathbf{A}\mathbf{X} + \mathbf{v} \quad (1)$$

where  $\mathbf{y}$  = vector of observations  
 $\mathbf{A}$  = known matrix of coefficients  
 $\mathbf{X}$  = vector of parameters  
 $\mathbf{v}$  = vector of measurement errors

Assuming the same accuracy for each observation, hence the weight matrix  $\mathbf{P}$  is equal to the identity matrix, and additionally, that  $\mathbf{A}$  is full column rank, the least-squares estimator (LS)  $\hat{\mathbf{X}}_{LS}$  of the vector of parameters can be written as (Eq. 2):

$$\hat{\mathbf{X}}_{LS} = (\mathbf{A}^T \mathbf{A})^{-1} \mathbf{A}^T \mathbf{y} \quad (2)$$

Similar formula can be written for the M-estimate of the parameter vector when referring to the iteratively reweighted least squares (Eq. 3):

$$\hat{\mathbf{X}}_M = (\mathbf{A}^T \mathbf{W} \mathbf{A})^{-1} \mathbf{A}^T \mathbf{W} \mathbf{y} \quad (3)$$

where  $\mathbf{W}$  = diagonal matrix of weights for which  
 $[\mathbf{W}]_{ii} = w(\hat{v}_i)$   
 $w(\hat{v}_i)$  = weight function related to particular M-estimation variant  
 $\hat{v}_i$  = standardized error of *i*th observation  
 $[\circ]_{ii}$  = *i*th diagonal element of matrix

The form of the weight function depends on the chosen M-estimation variant. In the Huber method it holds that (*e.g.*, Yang, 1994; Ge *et al.*, 2013) (Eq. 4):

$$w_H(\hat{v}_i) = \begin{cases} 1 & \text{for } |\hat{v}_i| \leq k \\ \frac{k}{|\hat{v}_i|} & \text{for } |\hat{v}_i| > k \end{cases} \quad (4)$$

where  $k$  = positive constant, equals to 2, 2.5 or 3

In this paper, we assume the constant  $k=2$ . The Tukey weight function is given as (Gui and Zhang, 1998; Ge *et al.*, 2013) (Eq. 5):

$$w_T(\hat{v}_i) = \begin{cases} \left(1 - \frac{|\hat{v}_i|^2}{k^2}\right)^2 & \text{for } |\hat{v}_i| \leq k \\ 0 & \text{for } |\hat{v}_i| > k \end{cases} \quad (5)$$

For the unknown variance, the constant  $k$  is usually assumed equal to 6.

M-estimates of the parameter vector are determined in the iterative process. The end of the iterative process is when the estimated vector of the parameters is not changing between the iteration steps.

$M_{split}$  estimation has a different fundamental assumption. The functional model from Equation 1 is split into two competitive ones (Wiśniewski, 2009; Wyszowska and Duchnowski, 2019) (Eq. 6):

$$\mathbf{y} = \mathbf{A}\mathbf{X} + \mathbf{v} \Rightarrow \begin{cases} \mathbf{y} = \mathbf{A}\mathbf{X}_{(1)} + \mathbf{v}_{(1)} \\ \mathbf{y} = \mathbf{A}\mathbf{X}_{(2)} + \mathbf{v}_{(2)} \end{cases} \quad (6)$$

where  $\mathbf{X}_{(m)}$  = version of vector of parameters  
 $\mathbf{v}_{(m)}$  = version of vector of measurement errors  
 $m = 1$  or  $2$

The main difference between the models of Equations 2 and 6 is that we assume two versions of the parameter vector in the latter model; however, the observation vector remains the same. Thus, each observation can be described as either  $\mathbf{X}_{(1)}$  or  $\mathbf{X}_{(2)}$ . Such a situation might stem from the theoretical origin of observations as realizations of two different random variables (which differ from each other in location parameters, here  $\mathbf{X}_{(1)}$  and  $\mathbf{X}_{(2)}$ ). The observation division into two subsets is automatic, and it is performed during the estimation process.

Thus, the goal of  $M_{split}$  estimation is to estimate  $\mathbf{X}_{(1)}$  and  $\mathbf{X}_{(2)}$ . It can be done by solving the optimization problem with the following general form of the objective function (Wiśniewski, 2009) (Eq. 7):

$$\varphi(\mathbf{X}_{(1)}, \mathbf{X}_{(2)}) = \sum_{i=1}^n \rho(v_{i(1)}, v_{i(2)}) \quad (7)$$

The component functions  $\rho(v_{i(1)}, v_{i(2)})$  might have different forms depending on the estimation variant. In the case of the squared  $M_{split}$  estimation (SMS), it holds that  $\rho(v_{i(1)}, v_{i(2)}) = v_{i(1)}^2 v_{i(2)}^2$  as for the absolute  $M_{split}$  estimation (AMS)  $\rho(v_{i(1)}, v_{i(2)}) = |v_{i(1)}| |v_{i(2)}|$ . The difference between these two functions results in the general features of the  $M_{split}$  estimation variants and a scheme of the iterative process. In the case of SMS estimation, the estimates can be computed by using the

modified Newton method, the so-called traditional iterative process (Wiśniewski, 2009) (Eq. 8):

$$\begin{aligned}
 \mathbf{X}_{(1)}^j &= \mathbf{X}_{(1)}^{j-1} + d\mathbf{X}_{(1)}^j = \\
 &= \mathbf{X}_{(1)}^{j-1} - \left[ \mathbf{H}_{(1)}(\mathbf{X}_{(1)}^{j-1}, \mathbf{X}_{(2)}^{j-1}) \right]^{-1} \mathbf{g}_{(1)}(\mathbf{X}_{(1)}^{j-1}, \mathbf{X}_{(2)}^{j-1}) \\
 \mathbf{X}_{(2)}^j &= \mathbf{X}_{(2)}^{j-1} + d\mathbf{X}_{(2)}^j = \\
 &= \mathbf{X}_{(2)}^{j-1} - \left[ \mathbf{H}_{(2)}(\mathbf{X}_{(1)}^j, \mathbf{X}_{(2)}^{j-1}) \right]^{-1} \mathbf{g}_{(2)}(\mathbf{X}_{(1)}^j, \mathbf{X}_{(2)}^{j-1})
 \end{aligned} \quad (8)$$

where  $d\mathbf{X}_{(m)}$  = increment to vector of parameters

$$\mathbf{H}_{(m)}(\mathbf{X}_{(1)}, \mathbf{X}_{(2)}) = 2\mathbf{A}^T \mathbf{w}_{(m)}(\mathbf{v}_{(1)}, \mathbf{v}_{(2)}) \mathbf{A} = \text{Hessian}$$

$$\mathbf{g}_{(m)}(\mathbf{X}_{(1)}, \mathbf{X}_{(2)}) = -2\mathbf{A}^T \mathbf{w}_{(m)}(\mathbf{v}_{(1)}, \mathbf{v}_{(2)}) \mathbf{v}_{(m)} = \text{gradient}$$

$$\mathbf{w}_{(m)}(\mathbf{v}_{(1)}, \mathbf{v}_{(2)}) = \text{diag} \left[ w_{(m)}(v_{1(1)}, v_{1(2)}), \dots, w_{(m)}(v_{n(1)}, v_{n(2)}) \right]$$

$$= \text{matrix of the weight function } w_{(m)}(v_{i(1)}, v_{i(2)})$$

$$\text{diag}(\circ) = \text{diagonal matrix}$$

The weight functions stem from the functions  $\rho(v_{i(1)}, v_{i(2)})$  by holding the following relations (Wiśniewski, 2009) (Eq. 9):

$$\begin{cases} w_{(1)}(v_{i(1)}, v_{i(2)}) = \frac{\psi_{(1)}(v_{i(1)}, v_{i(2)})}{2v_{i(1)}} \\ w_{(2)}(v_{i(1)}, v_{i(2)}) = \frac{\psi_{(2)}(v_{i(1)}, v_{i(2)})}{2v_{i(2)}} \end{cases} \quad (9)$$

where the influence functions  $\psi_{(1)}(v_{i(1)}, v_{i(2)})$  and  $\psi_{(2)}(v_{i(1)}, v_{i(2)})$  are defined as (Eq. 10):

$$\begin{cases} \psi_{(1)}(v_{i(1)}, v_{i(2)}) = \frac{\partial \rho(v_{i(1)}, v_{i(2)})}{\partial v_{i(1)}} \\ \psi_{(2)}(v_{i(1)}, v_{i(2)}) = \frac{\partial \rho(v_{i(1)}, v_{i(2)})}{\partial v_{i(2)}} \end{cases} \quad (10)$$

Hence, for SMS estimation, it holds that (Eq. 11):

$$\begin{cases} w_{(1)}(v_{i(1)}, v_{i(2)}) = v_{i(2)}^2 \\ w_{(2)}(v_{i(1)}, v_{i(2)}) = v_{i(1)}^2 \end{cases} \quad (11)$$

In the case of AMS estimation, we use the parallel iterative process conducted in the following way (Wyszkowska and Duchnowski, 2019) (Eq. 12):

$$\begin{aligned}
 \mathbf{X}_{(1)}^j &= \mathbf{X}_{(1)}^{j-1} + d\mathbf{X}_{(1)}^j = \\
 &= \mathbf{X}_{(1)}^{j-1} - \left[ \mathbf{H}_{(1)}(\mathbf{X}_{(1)}^{j-1}, \mathbf{X}_{(2)}^{j-1}) \right]^{-1} \mathbf{g}_{(1)}(\mathbf{X}_{(1)}^{j-1}, \mathbf{X}_{(2)}^{j-1}) \\
 \mathbf{X}_{(2)}^j &= \mathbf{X}_{(2)}^{j-1} + d\mathbf{X}_{(2)}^j = \\
 &= \mathbf{X}_{(2)}^{j-1} - \left[ \mathbf{H}_{(2)}(\mathbf{X}_{(1)}^{j-1}, \mathbf{X}_{(2)}^{j-1}) \right]^{-1} \mathbf{g}_{(2)}(\mathbf{X}_{(1)}^{j-1}, \mathbf{X}_{(2)}^{j-1})
 \end{aligned} \quad (12)$$

The respective Hessians and gradients are computed as in Equation 7 and by applying the following weight functions resulting from Equation 9 (Wyszkowska and Duchnowski, 2019) (Eq. 13):

$$\begin{aligned}
 w_{(1)}^*(v_{i(1)}, v_{i(2)}) &= \begin{cases} \frac{|v_{i(2)}|}{2c} & \text{for } |v_{i(1)}| < c \\ \frac{|v_{i(2)}|}{2|v_{i(1)}|} & \text{for } |v_{i(1)}| \geq c \end{cases} \\
 w_{(2)}^*(v_{i(1)}, v_{i(2)}) &= \begin{cases} \frac{|v_{i(1)}|}{2c} & \text{for } |v_{i(2)}| < c \\ \frac{|v_{i(1)}|}{2|v_{i(2)}|} & \text{for } |v_{i(2)}| \geq c \end{cases}
 \end{aligned} \quad (13)$$

where  $c$  = assumed small positive constant

Both iterative processes end when the gradients are equal to zero, in other words when both estimated vectors of the parameters are not changing between the iteration steps. More information about iterative processes of  $M_{\text{split}}$  estimation can be found in (Wyszkowska and Duchnowski, 2020).

### III. NUMERICAL EXAMPLE

The methods introduced in the previous section are now applied to process simulated TLS data to determine vertical displacements of terrain.

Let us assume a terrain profile of 50 m long, which is measured at two epochs. The observation sets are simulated by taking all theoretical heights of the terrain profile at the first epoch equal to 0 m. We assume some vertical movements of the terrain, which can be described by the following heights of the terrain profile at the second epoch: 0.005 m at a distance  $D=0$  m, 0.008 m at  $D=10$  m, 0.005 m at  $D=30$  m, and 0.006 m at  $D=40$  m. It allows us to describe the complete profile in the second epoch by the third-degree polynomial with the following coefficients:  $a_{(3)} = 5.83 \cdot 10^{-7}$ ,  $a_{(2)} = -3.83 \cdot 10^{-5}$ ,  $a_{(1)} = 6.25 \cdot 10^{-4}$  and  $a_{(0)} = 5 \cdot 10^{-3}$ . Then, let us simulate 500 observations, TLS points, at each measurement epoch. The measurement errors are assumed to be normally distributed  $N(0 \text{ m}, 4 \cdot 10^{-6} \text{ m}^2)$ . We also assume that some observations might be affected by gross errors generated from the uniform distribution in the interval from 0.005 m to 0.050 m. Thus, we assume that all outliers are positive.

In this section, we consider the following variants of the observation set:

- Variant I – lack of outliers in epochs I and II.
- Variant II – 10% outliers in epochs I and II.
- Variant III – 10% outliers in epoch I, 30% outliers in epoch II.

Observation sets for these variants are presented in Figures 1-3. The top panel of each figure shows observations from the measurement epoch I; the middle panel – observations from the measurement epoch II, and the bottom panel – observations from both epochs (the combined set).

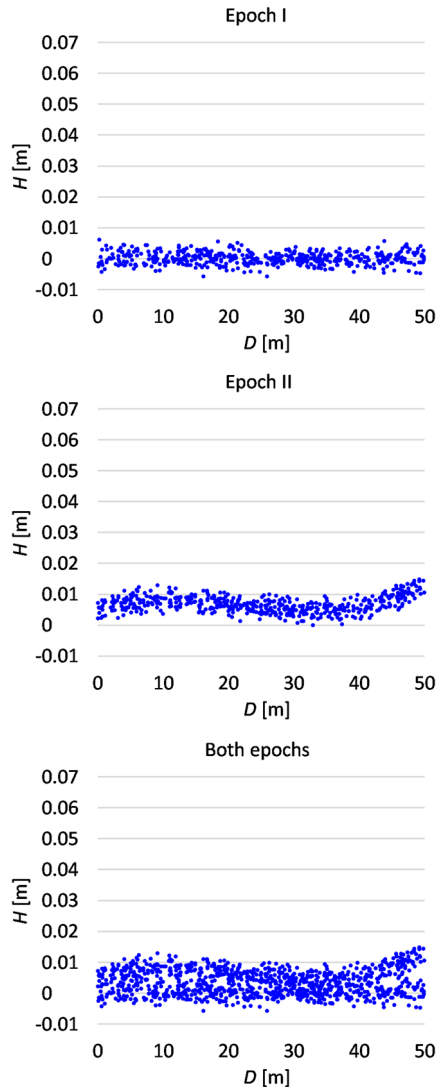


Figure 1. Observation sets for Variant I.

First, let the polynomial coefficients be estimated in each epoch separately. Then, one can compute the estimated profile heights (every meter) at each epoch. It allows us to calculate the terrain displacements obtained by subtracting the respective point heights. Note that in the case of  $M_{split}$  estimation, we always get two competitive solutions in each epoch.

Considering the terms of the case at hand (mainly, the terrain profile estimation), the polynomial in which the graph is located lower is taken as the  $M_{split}$  solution. The second solution describes the location of outliers, and here is omitted.

The results are presented in Figure 4: Variant I in the top panel, Variant II in the middle panel, and Variant III in the bottom panel. All estimation methods provide very similar and correct results for the first two variants.

It is noteworthy that even LS estimation seems to show robustness against outliers. It stems from the character of outlying observations (they are spread over the whole profile randomly and uniformly). The results obtained in each epoch, which are not presented here, are disturbed by outliers significantly; however, after subtracting results from two epochs, such an effect is eliminated, resulting in the correct estimation of terrain displacements. The significant differences between different method applications are in Variant III. LS estimation, both M-estimation variants, and SMS estimation do not cope with the different shares of outlying observations in both measurement epochs. Robust M-estimation cannot deal with 30% outliers at the second measurement epoch. Only AMS estimation provides correct results in such a case. Thus, it predominates over conventional robust M-estimation for a higher percentage of outliers. AMS estimation also provides better results than SMS estimation.

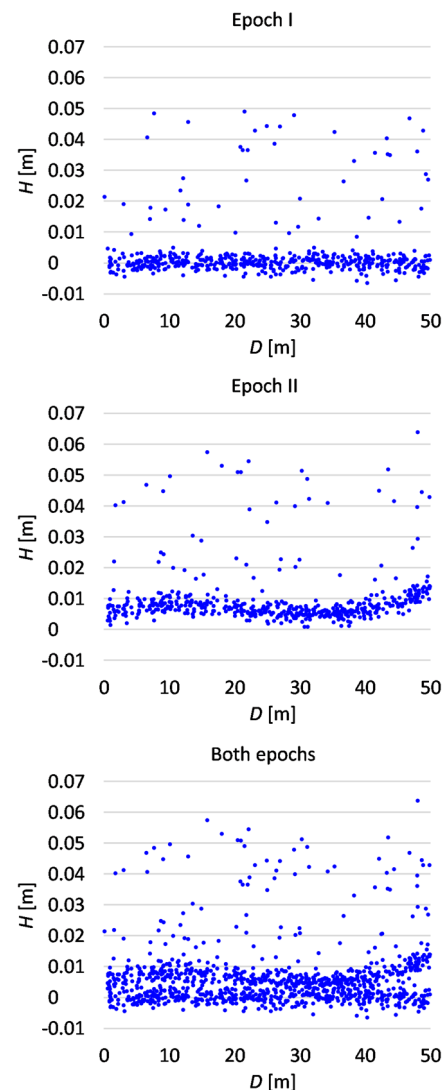


Figure 2. Observation sets for Variant II.

The graphical interpretation provides only a general comparison between the methods. The minor differences between the estimation results (especially in Variants I and II) are unnoticeable. To describe the

results more detailedly, let us assess how the estimated displacements fit into the simulated ones. The fit accuracy can be evaluated by using the root-mean-square deviation  $RMSD(\hat{H})$  in the following form (Wyszkowska *et al.*, 2021) (Eq. 14):

$$RMSD(\hat{H}) = \sqrt{\frac{\sum_{i=0}^n (\Delta\hat{H}_i - \Delta H_i)^2}{n}} \quad (14)$$

where  $\Delta\hat{H}_i$  = estimated displacements  
 $\Delta H_i$  = simulated displacements  
 $n = 51$  = number of points for which displacements are calculated for distances  $D_j = j \cdot 1 \text{ m}$  ( $j = 0, \dots, 50$ ).

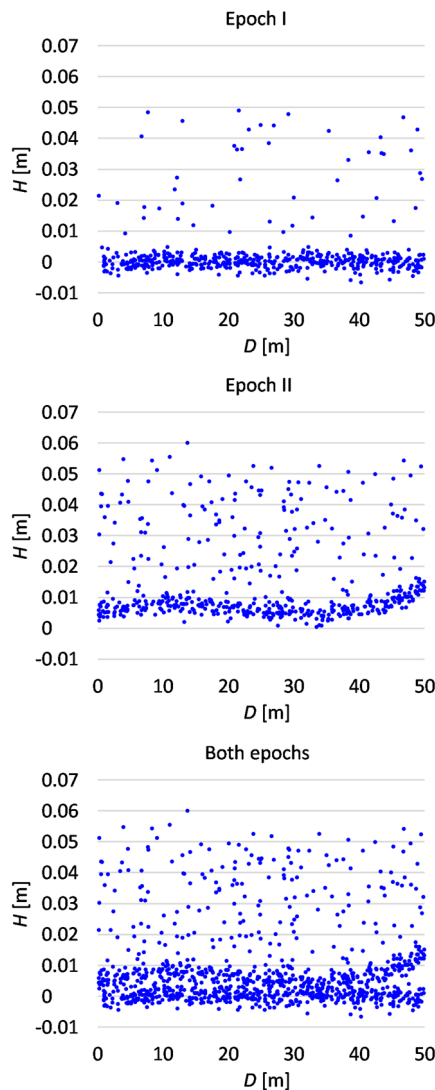


Figure 3. Observation sets for Variant III.

RMSDs for Variants I-III are presented in Table 1. When there are no outliers, LS estimation provides the best results; however, the results of robust M-estimation variants are only a little bit worse. The results of  $M_{split}$  estimation variants are also comparable

(especially for AMS estimation). LS estimation provides the least accurate outcomes in Variant II, whereas other methods give similar accuracy. In the case of Variant III, the results of AMS estimation are significantly better than the results of other variants considered. Note that robust M-estimation and SMS estimation give outcomes that are less accurate than the results of LS estimation. It means that those methods have not coped with 30% outliers in the second epoch definitively.

Table 1. RMSDs of estimated displacements [mm]

Variant	LS	Huber	Tukey	SMS	AMS
I	0.29	0.33	0.30	0.50	0.43
II	0.38	0.20	0.13	0.25	0.15
III	5.62	5.63	5.68	10.13	0.16

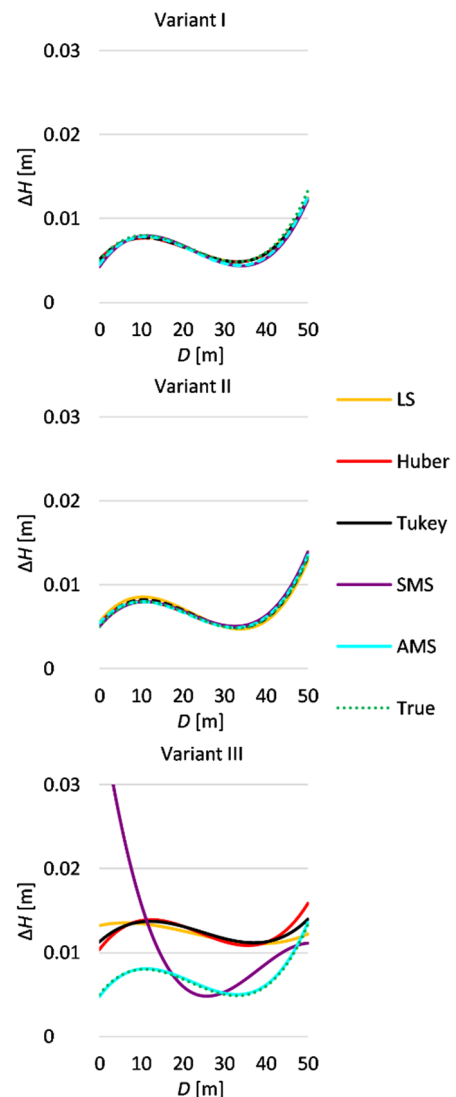


Figure 4. Estimated vertical terrain displacement (between values from two sets) for different variants.

In many practical applications of  $M_{split}$  estimation, we apply only one observation set, namely the set consisting of two (or more) observation groups. Such an approach is natural for  $M_{split}$  estimation and advisable in many surveying problems (Błaszczak-Bąk *et al.*, 2015;

Nowel, 2019; Guo *et al.*, 2020; Wyszowska *et al.*, 2021). It could also be involved in deformation analysis (Zienkiewicz, 2015; 2019). Let us use that way in the present example. Thus, we apply the combined sets (presented in the bottom panels of Figures 1-3) to obtain  $M_{split}$  estimates of the polynomial coefficients in one estimation process. The obtained competitive solutions refer to both epochs, respectively. One could evaluate the estimated terrain displacement using Equation 14. Table 2 presents RMSDs of the fit of the estimated displacements to the simulated ones.

Table 2. RMSDs of estimated displacements from the combined observation set [mm]

Variant	SMS	AMS
I	15.17	10.88
II	26.32	1.82
III	28.87	21.18

The obtained values clearly indicate that the estimation based on the combined observation sets provides much less accurate results. It might seem that SMS and AMS estimation cannot deal with outliers. However, results obtained in Variant I are also very poor. It means that the “separation” between regular observations from the first and the second epochs, respectively, is not enough to be easily detected. Thus, the estimation process is disturbed, resulting in the low accuracy of the final outcomes. Probably, if the terrain displacements were more significant (in comparison to the measurement accuracy), the  $M_{split}$  estimation would provide better results.

#### IV. CONCLUSIONS

$M_{split}$  estimation is a modern method dedicated to processing observation sets consisting of two (or more) observation groups. For that reason, it is applied to TLS, or more generally LiDAR, data processing. On the other hand, the method might also be used for deformation analysis. This paper answers the question is the method applicable in determining vertical terrain displacement from TLS data. From a theoretical point of view, there are no obstacles. It is shown that such an approach seems interesting and advisable, mainly when some outlying observations might occur. It is essential because outliers often concern TLS point clouds. Usually, observations of such a type do not result from gross errors but mismeasured points (measurement of different objects, obstacles, or surfaces that we are not interested in).

The presented example proves that  $M_{split}$  estimation, especially AMS estimation, could be an alternative to classical methods. It can cope with a higher share of outliers than robust M-estimation can. The condition is that we should have *a priori* information about the location of a line or a surface under investigation. In the case of TLS data, we almost always know which estimated line or surface (from two competitive

variants) we should choose as the final outcome. For example, here, we always choose the lower estimated line, which concerns the terrain profile for sure.

The paper also checks two approaches to processing TLS data from two epochs by applying  $M_{split}$  estimation. There is no doubt that processing observation sets from both epochs separately is a much better approach than using the combined observation set.

#### V. ACKNOWLEDGEMENTS

This research was funded by the Department of Geodesy, University of Warmia and Mazury in Olsztyn, Poland, statutory research no. 29.610.001-110.

#### References

- Baarda, W. (1968) A testing procedure for use in geodetic networks. *Publications on Geodesy Delft, Series 9*, Vol. 5.
- Błaszczak-Bąk, W., A. Janowski, W. Kamiński, and J. Rapiński (2015). Application of the  $M_{split}$  method for filtering airborne laser scanning data-sets to estimate digital terrain models. *International Journal of Remote Sensing*, Vol. 36, No. 9, pp. 2421–2437.
- Carrilho, A.C., M. Galo, and R.C. Santos (2018). Statistical outlier detection method for Airborne LiDAR data. *The International Archives of the Photogrammetry, Remote Sensing and Spatial Information Sciences*, Vol. XLII–1, pp. 87–92.
- Crespo-Peremarch, P., P. Tompalski, N.C. Coops, and L.A. Ruiz (2018). Characterizing understory vegetation in Mediterranean forests using full-waveform airborne laser scanning data. *Remote Sensing of Environment*, Vol. 217, pp. 400–413.
- Duchnowski, R. (2013). Hodges-Lehmann estimates in deformation analyses. *Journal of Geodesy*, Vol. 87, No. 10, pp. 873–884.
- Ge, Y., Y. Yuan, and N. Jia (2013). More efficient methods among commonly used robust estimation methods for GPS coordinate transformation. *Survey Review*, Vol. 45, No. 330, pp. 229–234.
- Gordon, S.J., and D.D. Lichti (2007). Modeling terrestrial laser scanner data for precise structural deformation measurement. *Journal of Surveying Engineering*, Vol. 133, No. 2, pp. 72–80.
- Gui, Q., and J. Zhang (1998). Robust biased estimation and its applications in geodetic adjustments. *Journal of Geodesy*, Vol. 72, No. 7, pp. 430–435.
- Guo, Y., Z. Li, H. He, G. Zhang, Q. Feng, and H. Yang (2020). A squared  $M_{split}$  similarity transformation method for stable points selection of deformation monitoring network. *Acta Geodaetica et Cartographica Sinica*, Vol. 49, No. 11, pp. 1419–1429.
- Hodges, J.L., and E.L. Lehmann (1963). Estimates of location based on rank tests. *Annals of Mathematical Statistics*, Vol. 34, No. 2, pp. 598–611.
- Huber, P.J., and E.M. Ronchetti (2009). *Robust statistics*. 2<sup>nd</sup> edn. John Wiley & Sons, Ltd. Hoboken, New Jersey.
- Kuzia, K. (2016). Application of airborne laser scanning in monitoring of land subsidence caused by underground mining exploitation. *Geoinformatica Polonica*, Vol. 2016, No. 15, pp. 7–13.

- Lehmann, R. (2013). On the formulation of the alternative hypothesis for geodetic outlier detection. *Journal of Geodesy*, Vol. 87, No. 4, pp. 373–386.
- Matkan, A.A., M. Hajeb, B. Mirbagheri, S. Sadeghian, and M. Ahmadi (2014). Spatial analysis for outlier removal from LiDAR data. In: *The International Archives of the Photogrammetry, Remote Sensing and Spatial Information Sciences*. WG II/1, WG II/4, ICWG II/IV, WG IV/7. The 1<sup>st</sup> ISPRS International Conference on Geospatial Information Research (Vol. XL-2/W3), 15-17 November 2014, Tehran, Iran, Copernicus GmbH, pp. 187–190.
- Matwij, W., W. Gruszczyński, E. Puniach, and P. Cwiąkała. (2021). Determination of underground mining-induced displacement field using multi-temporal TLS point cloud registration. *Measurement*, Vol. 180, Article no. 109482.
- Nowel, K. (2019). Squared  $M_{split}(q)$  S-transformation of control network deformations. *Journal of Geodesy*, Vol. 93, No. 7, pp. 1025–1044.
- Pope, A.J. (1976). The statistics of residuals and the outlier detection of outliers. *National Geodetic Survey Rockville*, NOAA Technical Report, NOS 65.
- Rodríguez-González, P., B. Jiménez Fernández-Palacios, A.L. Muñoz-Nieto, P. Arias-Sanchez, and D. Gonzalez-Aguilera (2017). Mobile LiDAR System: new possibilities for the documentation and dissemination of large cultural heritage sites. *Remote Sensing*, Vol. 9, No. 3, Article no. 189.
- Spaete, L.P., N.F. Glenn, D.R. Derryberry, T.T. Sankey, J.J. Mitchell, and S.P. Hardgree (2011). Vegetation and slope effects on accuracy of a LiDAR-derived DEM in the sagebrush steppe. *Remote Sensing Letters*, Vol. 2, No. 4, pp. 317–326.
- Wang, C., and P.H. Hsu (2007). Building detection and structure line extraction from airborne LiDAR data. *Journal of Photogrammetry and Remote Sensing*, Vol. 12, No. 4, pp. 365–379.
- Wiśniewski, Z. (2009). Estimation of parameters in a split functional model of geodetic observations ( $M_{split}$  estimation). *Journal of Geodesy*, Vol. 83, No. 2, pp. 105–120.
- Wiśniewski, Z. (2010).  $M_{split}(q)$  estimation: estimation of parameters in a multi split functional model of geodetic observations. *Journal of Geodesy*, Vol. 84, No. 6, pp. 355–372.
- Wyszkowska, P. and R. Duchnowski (2019).  $M_{split}$  estimation based on L1 norm condition. *Journal of Surveying Engineering*, Vol. 145, No. 3, Article no. 04019006.
- Wyszkowska, P. and Duchnowski, R. (2020). Iterative process of  $M_{split}(q)$  estimation. *Journal of Surveying Engineering*, Vol. 146, No. 3, Article no. 06020002.
- Wyszkowska, P., R. Duchnowski, and A. Dumalski (2021). Determination of terrain profile from TLS data by applying  $M_{split}$  estimation. *Remote Sensing*, Vol. 13, No. 1, Article no. 31.
- Yang, Y. (1994). Robust estimation for dependent observations. *Manuscripta Geodaetica*, Vol. 19, pp. 10–17.
- Zienkiewicz, M.H. (2015). Determination of vertical indicators of ground deformation in the Old and Main City of Gdansk area by applying unconventional method of robust estimation. *Acta Geodynamica et Geomaterialia*, Vol. 12, No. 3(179), pp. 249–257.
- Zienkiewicz, M.H. (2019). Deformation analysis of geodetic networks by applying  $M_{split}$  estimation with conditions binding the competitive parameters. *Journal of Surveying Engineering*, Vol. 145, No. 2, Article no. 04019001.

## Point displacements during classical measurements – a practical approach to pseudo epochs between measurements

Robert Duchnowski, Patrycja Wyszowska

Department of Geodesy, Institute of Geodesy and Civil Engineering, Faculty of Geoengineering, University of Warmia and Mazury in Olsztyn, Oczapowskiego 1 Str., 10-719 Olsztyn, Poland, ([robert.duchnowski@uwm.edu.pl](mailto:robert.duchnowski@uwm.edu.pl)); [patrycja.wyszowska@uwm.edu.pl](mailto:patrycja.wyszowska@uwm.edu.pl))

**Key words:** *displacement analysis; pseudo epochs;  $M_{split}$  estimation; robust estimation, Monte Carlo simulations*

### ABSTRACT

Various measurement techniques and data processing are applied to determine point displacements and deformation of geodetic networks or buildings. Considering classical measurements and analysis of the network deformation, we should realize that the measurements are not “immediate.” The question arises: what happens if a point (or some points) displaces between particular measurements within one epoch. In such a case, the observation set would consist of the observations before and after point displacement, and such hypothetical observation groups can be regarded as related to two (or more) pseudo epochs. The paper's main objective is to examine some estimation methods that would probably deal with such a problem, namely  $M_{split}$  estimation (in two variants, the squared and the absolute  $M_{split}$  estimation) and chosen robust methods, namely Huber's method (example M-estimation) and the Hodges-Lehmann weighted estimation (basic R-estimation). The first approach can provide two (or more) variants of the network point coordinates (here, before and after point movements), providing information about two (or more) states of the network during measurements. In contrast, the robust methods can only decrease the influence of the outliers on the computed network point coordinates. Thus, estimation results would concern only one network state in such a case. The presented empirical analyses show that the better and more realistic results are obtained by applying  $M_{split}$  estimation. Huber's method can also provide acceptable results (describing the network state at the epoch beginning) only if the number of observations conducted after the point displacements is not too high.

### I. INTRODUCTION

The displacement of the network point is determined between at least two measurement epochs. Thus, the deformation analysis is conducted between two moments in time. However, geodetic observations, namely measurements of angles, distances, or height differences, are not “immediate,” and sometimes they require some time. Such a fact concerns traditional measurements and, in some cases also, other techniques like GPS measurements. Generally, we assume that the network points are stable during the measurements of each epoch. The question arises, what if a point (or some points) displaces between measurements within one epoch. It is evident that such displacements would affect the observation set, in which some observations relate to the stage before displacements, whereas the other observations to the stage after displacements. Since all observations belong to one epoch, thus we can call such subsets observations at the first and second pseudo epoch; however, we do not know the assignment of each observation to either of the pseudo epochs in practice. This problem was mentioned in (Wiśniewski *et al.*, 2019). It is also no doubt that the existence of the pseudo epoch would also affect further computations, such as the deformation analysis between two epochs.

That would indeed happen if one applied the usual approach based on the least squares method, without any statistical tests or analyses detecting “outlying” observations (in the problem considered here, the observations of one of the pseudo epochs could be regarded as outliers). An alternative would be the application of robust estimation or other methods which can deal with such an observation set. In the first case, we can apply any robust M-estimation (Caspary *et al.*, 1990; Hekimoğlu, 1999; Xu, 2005; Nowel, 2015), or R-estimation (Hodges and Lehmann, 1963; Duchnowski, 2013; Wyszowska and Duchnowski, 2018). A method called  $M_{split}$  estimation was created to estimate the location parameters (more generally, the parameters of the split functional models) when an observation set consists of the subsets mentioned before. The method has already been applied in deformation analysis (Wiśniewski, 2009; Zienkiewicz *et al.*, 2017; Wyszowska and Duchnowski, 2019).

The paper aims to compare different approaches to the problem of pseudo epochs. The following methods will be analyzed: the least squares estimation (LS), the Huber method (an example of robust M-estimation), and the Hodges-Lehmann weighted estimation (example of R-estimation; HLW), the squared  $M_{split}$



estimation (SMS), and the absolute  $M_{\text{split}}$  estimation (AMS).

## II. EMPIRICAL ANALYSES

Let us consider the following linear model (Eq. 1):

$$\mathbf{y} = \mathbf{A}\mathbf{X} + \mathbf{v} \quad (1)$$

where  $\mathbf{y}$  = observation vector of size  $n \times 1$   
 $\mathbf{A}$  = coefficient matrix of size  $n \times r$   
 $\mathbf{X}$  = parameter vector of size  $r \times 1$   
 $\mathbf{v}$  = measurement error vector  $n \times 1$

The LS estimator  $\hat{\mathbf{X}}_{LS}$  of the parameter vector can be computed as (Eq. 2):

$$\hat{\mathbf{X}}_{LS} = (\mathbf{A}^T \mathbf{P} \mathbf{A})^{-1} \mathbf{A}^T \mathbf{P} \mathbf{y} \quad (2)$$

where  $\mathbf{P}$  = weight matrix of size  $n \times n$

Whereas the Huber estimator  $\hat{\mathbf{X}}_H$  of the parameter vector is determined in the iterative process (Eqs. 3 and 4):

$$\hat{\mathbf{X}}_H = (\mathbf{A}^T \mathbf{W} \mathbf{A})^{-1} \mathbf{A}^T \mathbf{W} \mathbf{y} \quad (3)$$

$$[\mathbf{W}]_{ii} = [\mathbf{P}]_{ii} \cdot w(\hat{v}_i) \quad (4)$$

where  $\mathbf{W}$  = diagonal matrix of weights of size  $n \times n$   
 $w(\hat{v}_i)$  = weight function related to variant of M-estimation,  $1 \leq i \leq n$   
 $\hat{v}_i$  = standardized error of  $i$ th observation  
 $[\circ]_{ii}$  =  $i$ th diagonal element of matrix

The new version of the matrix  $\mathbf{W}$  is computed in each subsequent iterative step. The general formula of the Huber weight function can be written as (Yang, 1994; Ge *et al.*, 2013) (Eq. 5):

$$w(\hat{v}_i) = \begin{cases} 1 & \text{for } |\hat{v}_i| \leq c \\ \frac{c}{|\hat{v}_i|} & \text{for } |\hat{v}_i| > c \end{cases} \quad (5)$$

where  $c$  = positive constant

Here, we assume the constant  $c=2$ , which defines the interval of the acceptable, standardized measurement errors (Gui and Zhang, 1998).

Another robust estimator which can be applied in the paper context is the Hodges-Lehmann weighted estimator of the expected value  $\hat{E}^{HLW}(X_j)$ ,  $1 \leq j \leq r$ . The general formula is as follows (Duchnowski, 2013) (Eq. 6):

$$\hat{E}^{HLW}(X_j) = \text{medw} \left( \frac{z_k + z_l}{2} \right) \quad (6)$$

where  $\text{medw}$  = weighted median operator  
 $z_k, z_l$  = elements of sample of size  $s$  ( $1 \leq k \leq s$ ,  $1 \leq l \leq s$ )

The sample mentioned is created for each parameter  $X_j$  separately. In the paper context, the sample elements are created by computing the coordinates of a particular network point by applying the raw observations and the reference point coordinates in all possible independent ways (Duchnowski, 2013, 2021).

$M_{\text{split}}$  estimation is the last method considered here. The general assumption of that estimation method is the split of the functional model (Equation 1) into two competitive ones (Wiśniewski, 2009; Wyszowska and Duchnowski, 2019) (Eq. 7):

$$\mathbf{y} = \mathbf{A}\mathbf{X} + \mathbf{v} \Rightarrow \begin{cases} \mathbf{y} = \mathbf{A}\mathbf{X}_{(1)} + \mathbf{v}_{(1)} \\ \mathbf{y} = \mathbf{A}\mathbf{X}_{(2)} + \mathbf{v}_{(2)} \end{cases} \quad (7)$$

where  $\mathbf{X}_{(m)}$  = versions of parameter vector  
 $\mathbf{v}_{(m)}$  = versions of measurement error vector  
 $m = 1$  or  $2$

We examine two  $M_{\text{split}}$  estimation variants: the squared and absolute  $M_{\text{split}}$  estimation. These two methods differ in the objective function, hence also in the influence and weight functions. The weight functions of SMS estimation are as follows (Wiśniewski, 2009) (Eq. 8):

$$\begin{cases} w_{(1)}(v_{i(1)}, v_{i(2)}) = v_{i(2)}^2 \\ w_{(2)}(v_{i(1)}, v_{i(2)}) = v_{i(1)}^2 \end{cases} \quad (8)$$

while AMS estimation refers to the following weight functions (Wyszowska and Duchnowski, 2019) (Eq. 9):

$$\begin{cases} w_{(1)}(v_{i(1)}, v_{i(2)}) = \begin{cases} -\frac{|v_{i(2)}|}{2v_{i(1)}} & \text{for } v_{i(1)} < 0 \\ \frac{|v_{i(2)}|}{2v_{i(1)}} & \text{for } v_{i(1)} > 0 \end{cases} \\ w_{(2)}(v_{i(1)}, v_{i(2)}) = \begin{cases} -\frac{|v_{i(1)}|}{2v_{i(2)}} & \text{for } v_{i(2)} < 0 \\ \frac{|v_{i(1)}|}{2v_{i(2)}} & \text{for } v_{i(2)} > 0 \end{cases} \end{cases} \quad (9)$$

The competitive  $M_{\text{split}}$  estimates, namely  $\hat{X}_{(1)}$  and  $\hat{X}_{(2)}$  of the parameter vector, are determined in the iterative process by applying the modified Newton method (Wiśniewski, 2009). Because of the difference in the

weight functions, two variants of  $M_{split}$  estimation require different computing algorithms. SMS estimation uses the traditional iterative process, while AMS estimation requires a parallel iterative process (Wyszkowska and Duchnowski, 2020). The differences between the algorithms concern the starting point and computing the estimates in subsequent iterative steps. There is one starting point in the traditional iterative process (usually LS estimates of the parameters) and two different starting points in the parallel iterative process. The algorithms are described in detail in (Wiśniewski, 2009; Wyszkowska and Duchnowski, 2019).

Considering the problem of pseudo epochs, the competitive versions of the parameter vector should reflect the point displacements. One expects one version to correspond to the point coordinates before displacement and the second after the point movement.

### III. TITLE

Let us consider a leveling network presented in Figure 1. The network consists of two reference points (fixed ones), A and B, and seven object points (points with unknown heights). The observations, namely twenty height differences, are assumed to be measured twice in one measurement epoch with the assumed standard deviation of 1 mm. Without loss of generality, we can assume that the theoretical heights of all network points are equal to 0 mm; hence, all theoretical height differences are equal to 0 mm.

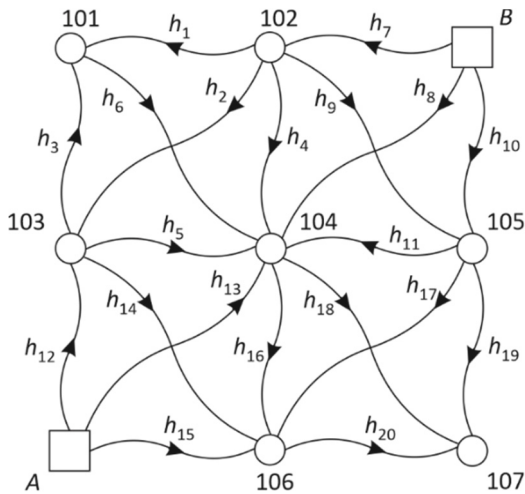


Figure 1. Simulated leveling network.

Let us assume that points 101 and 102 have moved vertically for  $\Delta H_{101} = 10$  mm,  $\Delta H_{102} = 20$  mm during the measurements. Additionally, we consider two variants: Variant I, the second measurements of the height differences  $h_1, h_3, h_7$  were measured after the point displacements; Variant II, the first measurements of the height differences  $h_3, h_7$  and the second measurements of the height differences  $h_1, h_3, h_4, h_7, h_9$  were measured after the point displacements. Two

variants help us to understand how each estimation method reacts to a different number of observations after the point displacement. One should realize that in practice, we do not know which points are displaced and which observations are performed before and after the point displacement; thus, we cannot divide observations into subsets *a priori*.

Now let us examine how such an affected observation set influences the estimation results. Assuming that the observations are normally distributed, we simulated 5000 observation sets in each variant.

#### A. Variant I

The histograms of the heights of the chosen points estimated by applying the conventional methods are presented in Figure 2.

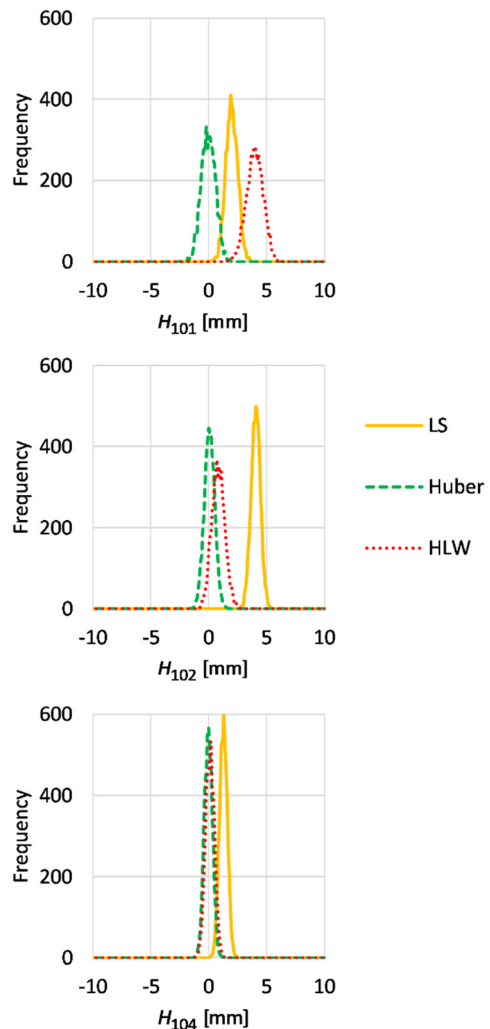


Figure 2. Histograms of estimated point heights (Variant I).

The histograms are determined for the heights of the object points that moved, namely 101 and 102, and one chosen stable point 104. The histograms obtained for the other stable points are very similar to the histogram of the point 104 height; hence they are omitted here.

The best results are obtained for the Huber method, where the height estimates are robust against outlying observations. The other robust method (HLW) does not

provide correct results, especially for point 101. It results from the location of outliers and the low breakdown point of the method in the case of a small number of observations (Duchnowski, 2011). Note that we have 6 independent ways to compute the heights of point 101, 8 ways for point 102, and 12 ways for point 104, which determines the size of the samples in Equation 6.

The histograms of the estimated heights of the same variant and points obtained for the two variants of  $M_{split}$  estimation are shown in Figure 3. Following the split functional model of Equation 7 we have two competitive solutions (the competitive estimates of the point heights).

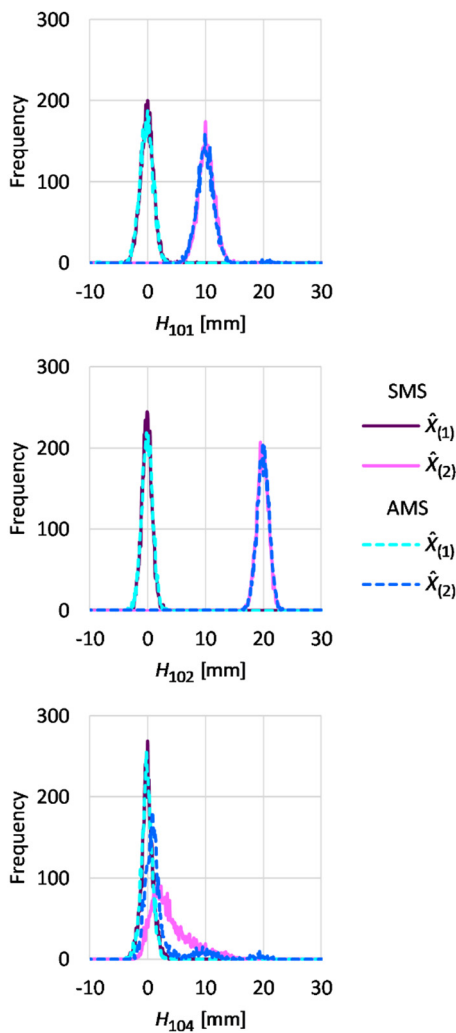


Figure 3. Histograms of estimated point heights (Variant I).

The histograms obtained for the estimated heights of points 101 and 102 show that the  $M_{split}$  estimation detects the point displacements correctly (the histograms coincide with the simulated point heights). The situation is different for the estimated height of point 104 (similar histograms are obtained for the rest of the object points). The first solutions of both variants seem correct; the histogram coincides with 0 mm. The histograms of the second solutions are generally proper; however, they seem a little bit skewed right,

especially in the case of SMS estimation. Tables 1 and 2 present some descriptive statistics from the Monte Carlo simulations to complete the comparison. The medians here describe the central tendencies of the estimates. The mean values omitted here are usually equal to the respective medians or differ from them by no more than 0.2 mm. The accuracy of the estimates is described by the root-mean-square deviation (RMSD) computed as (Eq. 10):

$$RMSD = \sqrt{\sum_{i=1}^{5000} \frac{(\hat{X}_i^{MC} - X)^2}{5000}} \quad (10)$$

where  $\hat{X}_i^{MC}$  = estimated parameter in  $i$ th simulation  
 $X$  = simulated parameter

For the conventional method, for each point  $X = 0$  mm. In the case of  $M_{split}$  estimation, for the first solution, namely  $X_{(1)}$ , it is assumed that  $X = 0$  mm, but for the second one,  $X_{(2)}$ , it holds that  $X = \Delta H_{101} = 10$  mm,  $X = \Delta H_{102} = 20$  mm or  $X = \Delta H_{104} = 0$  mm, respectively.

Table 1. Medians [mm] of the estimates of chosen object point heights from MC simulations (Variant I)

Parameter	Point 101	Point 102	Point 104
LS	2.0	4.1	1.3
Huber	0.0	0.1	0.0
HLW	4.1	0.9	0.2
SMS $\hat{X}_{(1)}$	-0.1	-0.1	0.0
SMS $\hat{X}_{(2)}$	10.1	19.9	3.0
AMS $\hat{X}_{(1)}$	-0.1	0.0	-0.1
AMS $\hat{X}_{(2)}$	10.0	20.2	1.0

Table 2. RMSDs [mm] of the estimates of chosen object point heights from MC simulations (Variant I)

Method	Point 101	Point 102	Point 104
LS	2.1	4.1	1.4
Huber	0.6	0.5	0.4
HLW	4.1	1.0	0.4
SMS $\hat{X}_{(1)}$	1.2	0.9	1.0
SMS $\hat{X}_{(2)}$	1.4	1.0	5.1
AMS $\hat{X}_{(1)}$	1.2	0.9	1.0
AMS $\hat{X}_{(2)}$	1.9	1.0	4.7

Tables confirm that the Huber method provided the correct results, and LS or HLW estimation did not. They also prove that  $M_{split}$  estimation might tell apart the first pseudo epoch from the second one. What is more, it can assess the point displacements correctly. However,  $M_{split}$  estimation provides worse assessments of  $X_{(2)}$  for the points which do not displace during the measurements (see the results obtained in the case of point 104, especially RMSD). It might result from the

small number of observations performed after the point displacements.

**B. Variant II**

In that variant, more measurements are carried out after the point displacements. The histograms of the heights of the chosen points estimated by using the conventional methods are shown in Figure 4. This time, any of the methods did not provide satisfactory results. Only histograms obtained for the height of point 104 are located close to 0 mm. It results from the fact that the most height differences between that point and the other network points were measured at the first pseudo epoch.

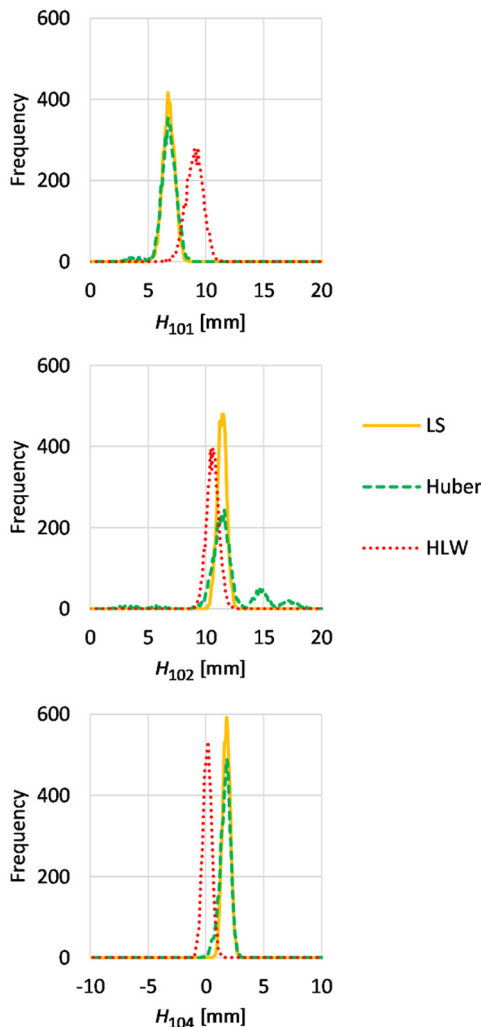


Figure 4. Histograms of estimated point heights (Variant II).

Figure 5 presents histograms of the point heights estimated by  $M_{split}$  estimation variants. The location of all the histograms is correct, and the histograms obtained for point 104 seem less skewed right than in the previous variant.

Like in the preceding subsection, we can also compare the descriptive statistics from the Monte Carlo method (Tables 3 and 4). The medians confirm the conclusions from the simple analysis of the histogram

locations. The conventional methods cannot provide the correct results, and SMS as well as AMS estimation correctly identified the pseudo epochs and assessed the point displacements. The best results, the medians closest to the theoretical values, are obtained for AMS estimation. Empirical accuracies presented in Table 4 show that  $M_{split}$  estimation can deal with pseudo epochs better than the conventional methods when the number of observations carried out after the point displacements is greater. Even the Huber method, which succeeded in Variant I, cannot manage a higher number of outlying observations.

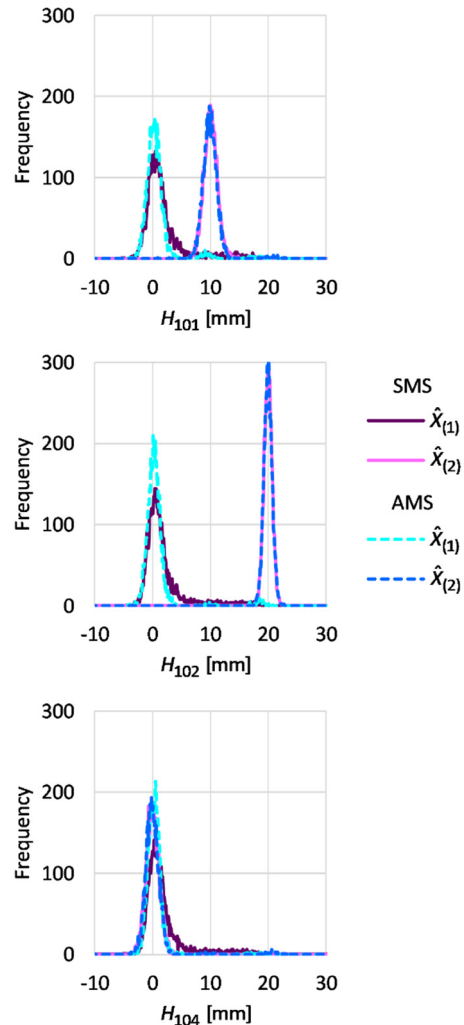


Figure 5. Histograms of estimated point heights (Variant II).

**IV. CONCLUSIONS**

The displacements of the object points during one measurement epoch, if they really happen, stay undetected at the stage of measurements. They mainly might concern large networks where the number of observations is high; hence the longer time of measurements is required. That situation might also happen in networks that were established to determine terrain surface deformations resulting, for example, from uplifts or mining damages, where the vertical

displacements might be sudden and have a relatively high magnitude.

Table 3. Medians [mm] of the estimates of chosen object point heights from MC simulations (Variant II)

Method	Point 101	Point 102	Point 104
LS	6.8	11.4	1.8
Huber	6.8	11.6	1.8
HLW	9.1	10.6	0.2
SMS $\hat{X}_{(1)}$	0.9	0.9	0.9
SMS $\hat{X}_{(2)}$	10.1	20.0	0.0
AMS $\hat{X}_{(1)}$	0.4	0.3	0.3
AMS $\hat{X}_{(2)}$	10.1	20.0	0.0

Table 4. RMSDs [mm] of the estimates of chosen object point heights from MC simulations (Variant II)

Method	Point 101	Point 102	Point 104
LS	6.9	11.4	1.9
Huber	6.8	12.2	1.8
HLW	9.1	10.7	0.4
SMS $\hat{X}_{(1)}$	3.9	3.9	3.9
SMS $\hat{X}_{(2)}$	1.2	0.7	1.4
AMS $\hat{X}_{(1)}$	2.7	3.1	2.1
AMS $\hat{X}_{(2)}$	1.7	0.7	2.7

Loss or preservation information about point displacements is the essential difference between the conventional methods and the approach based on  $M_{\text{split}}$  estimation. The example presented in the paper proves that the conventional methods might not manage with point displacement during measurements. However, the robust methods can provide correct results only when the number of outlying observations is small enough. When applying robust M-estimation, it is assumed that observations from one pseudo epoch (before or after point displacements) are regarded as outliers. We would surely lose information about point displacements by “ignoring” such a group of observations. We would also not know which pseudo epoch is described finally. By applying  $M_{\text{split}}$  estimation, one can preserve the information about point displacements and keep track of point movements during the measurement epoch. In the given example, both variants of  $M_{\text{split}}$  estimation distinguish two groups of observations. What is more, they assess the point displacements between the pseudo epochs correctly. Comparing the results obtained for  $M_{\text{split}}$  estimation variants, one can suggest applying the AMS method rather than SMS estimation in the problem addressed in the paper.

#### V. ACKNOWLEDGEMENTS

This research was funded by the Department of Geodesy, University of Warmia and Mazury in Olsztyn, Poland, statutory research no. 29.610.001-110.

#### References

- Casparly, W.F., W. Haen, and H. Borutta (1990). Deformation Analysis by Statistical Methods. *Technometrics*, Vol. 32, No. 1, pp. 49–57.
- Duchnowski, R. (2011). Robustness of strategy for testing levelling mark stability based on rank tests. *Survey Review*, Vol. 43, No. 323, pp. 687–699.
- Duchnowski, R. (2013). Hodges-Lehmann estimates in deformation analyses. *Journal of Geodesy*, Vol. 87, No. 10, pp. 873–884.
- Duchnowski, R. (2021). Vertical displacement analysis based on application of univariate model for several chosen estimation methods. In: *Proceedings of FIG e-Working Week 2021*, Netherlands, pp. 1–13.
- Ge, Y., Y. Yuan, and N. Jia (2013). More efficient methods among commonly used robust estimation methods for GPS coordinate transformation. *Survey Review*, Vol. 45, No. 330, pp. 229–234.
- Gui, Q., and J. Zhang (1998). Robust biased estimation and its applications in geodetic adjustments. *Journal of Geodesy*, Vol. 72, No. 7, pp. 430–435.
- Hekimoğlu, Ş. (1999). Robustifying conventional outlier detection procedures. *Journal of Surveying Engineering*, Vol. 125, No. 2, pp. 69–86.
- Hodges, J.L., and E.L. Lehmann (1963). Estimates of location based on rank tests. *Annals of Mathematical Statistics*, Vol. 34, No. 2, pp. 598–611.
- Nowel, K. (2015). Robust M-estimation in analysis of control network deformations: classical and new method. *Journal of Surveying Engineering*, Vol. 141, No. 4, Article no. 04015002.
- Wiśniewski, Z. (2009). Estimation of parameters in a split functional model of geodetic observations (Msplit estimation). *Journal of Geodesy*, Vol. 83, No. 2, pp. 105–120.
- Wiśniewski, Z., R. Duchnowski, and A. Dumalski (2019). Efficacy of Msplit estimation in displacement analysis. *Sensors*, Vol. 19, No. 22, Article no. 5047.
- Wyszkowska, P., and R. Duchnowski (2018). Increasing reliability of basic R-estimates in deformation analysis. In: *Proceedings of 2018 Baltic Geodetic Congress (BGC Geomatics)*, IEEE, Piscataway, NJ, pp. 241–245.
- Wyszkowska, P., and R. Duchnowski (2019). Msplit estimation based on L1 norm condition. *Journal of Surveying Engineering*, Vol. 145, No. 3, Article No. 04019006.
- Wyszkowska, P. and R. Duchnowski (2020). Iterative process of Msplit(q) estimation. *Journal of Surveying Engineering*, Vol. 146, No. 3, Article No. 06020002.
- Xu, P. (2005). Sign-constrained robust least squares, subjective breakdown point and the effect of weights of observations on robustness. *Journal of Geodesy*, Vol. 79, No. 1, pp. 146–159.
- Yang, Y. (1994). Robust estimation for dependent observations. *Manuscripta Geodaetica*, Vol. 19, pp. 10–17.
- Zienkiewicz, M.H., K. Hejbudzka, and A. Dumalski (2017). Multi split functional model of geodetic observations in deformation analyses of the Olsztyn castle. *Acta Geodynamica et Geomaterialia*, Vol. 14, No. 2(186), pp. 195–204.

## Validation of GNSS-based reference point monitoring of the VGOS VLBI telescope at Metsähovi

Ulla Kallio, Joona Eskelinen, Jorma Jokela, Hannu Koivula, Simo Marila, Jyri Näränen, Markku Poutanen, Arttu Raja-Halli, Paavo Rouhiainen, Heli Suurmäki

Finnish Geospatial Research Institute FGI, NLS, Geodeetinrinne 2, 02430 Masala, Finland, ([ulla.kallio@nls.fi](mailto:ulla.kallio@nls.fi); [joona.eskelinen@nls.fi](mailto:joona.eskelinen@nls.fi); [jorma.jokela@nls.fi](mailto:jorma.jokela@nls.fi); [hannu.koivula@nls.fi](mailto:hannu.koivula@nls.fi); [simo.marila@nls.fi](mailto:simo.marila@nls.fi); [jyri.naranen@nls.fi](mailto:jyri.naranen@nls.fi); [markku.poutanen@nls.fi](mailto:markku.poutanen@nls.fi); [arttu.raja-halli@nls.fi](mailto:arttu.raja-halli@nls.fi); [paavo.rouhiainen@nls.fi](mailto:paavo.rouhiainen@nls.fi); [heli.suurmaki@nls.fi](mailto:heli.suurmaki@nls.fi))

**Key words:** *VGOS; radio telescope; reference point; GNSS; monitoring*

### ABSTRACT

VLBI telescope reference point, the closest point in the telescope primary axis from the secondary axis, is typically determined indirectly by observation of points co-rotating with the telescope. We have previously measured telescope reference point indirectly with two GPS-antennas attached on the edge of the dish of the Aalto University Metsähovi radio telescope in 2008-2015. Now we have applied the same technique to the new VGOS-telescope of the FGI Metsähovi geodetic research station. The reference point of the VGOS antenna was estimated using post-processed trajectory coordinates of two GNSS antennas. The antennas are attached on the edge of the radio telescope dish with gimbals where a counterweight with shock absorber act as compensators to ensure zenith pointing at all telescope elevation angles. In addition, spherical prisms are attached to the structure of the telescope for tachymetric reference point determination. One purpose of this study is to evaluate the limit values and uncertainties of the compensator assembly by simulations and precise tachymeter measurements. To ensure that the compensation error is nearly constant or can be modelled, we have measured the residual tilt of the GNSS antennas with different VLBI antenna elevations. The results indicate a need to apply the corrections or to improve the compensator design. We aim to improve the counterweight and dampening so that no extra model corrections to trajectory coordinates are needed. For final assurance of our GNSS-based reference point monitoring performance, we have compared the reference point coordinates determined by simultaneous tachymetric and GNSS data. Our results and simulations showed that, with a small compensation error, the influence on reference point coordinates is marginal but the axis offset will be compromised, provided that the compensating angle bias is nearly constant. Preliminary reference point estimates show a rather good agreement of simultaneous GNSS-based and tachymetric reference points. The final results will be achieved as part of the 18SIB01 EMPIR GeoMetre project, funded from the EMPIR programme and co-financed by the Participating States and from the European Union's Horizon 2020 research and innovation programme.

### I. INTRODUCTION

The first published work using a GPS antenna on the structure of the VLBI telescope for the determination of local ties or axis offset was done by (Combrinck and Merry, 1997). At the Hartebeesthoek Radio Astronomy Observatory, the GPS antenna was attached to the apex of the radio telescope quadripod with a gimbal having the axis aligned to the antenna's nominal phase centre.

Promising results for GPS-based local ties were achieved at the observatory of Medicina in 2001-2006. Two GPS antennas with compensators were attached on the left and right sides of the telescope dish. The quality assessment, results, and comparison with tachymeter measurements were reported in Abbondanza *et al.*, (2009a; 2009b). The coordinates of rotating points were based on Bernese 5.0 processing and the local GPS network was combined with a larger one. The reference point estimation was based on 3D circle fittings. The effect of the orientation of vectors to the combination of Terrestrial Reference Frames was also studied.

At Metsähovi, Southern Finland, the first experiments with corresponding, locally designed compensators and GPS antennas on the Aalto University radio telescope were performed in 2008 (Kallio and Poutanen, 2012). In contrast to the static method in Medicina, at Metsähovi the GPS points were measured, for the first time, simultaneously with the VLBI campaign (Kallio and Poutanen, 2012). The effective detection of outliers of trajectory points was developed and a new model for reference point estimation was introduced.

Two Ashtech Dorne Margolin choke ring antennas were used in the first GPS-based local tie campaigns but they were later changed to Leica AX2012 antennas which were lighter and more suitable for the purpose. In both cases, the antennas were individually calibrated and the phase centre offset (PCO) and variation (PCV) were taken into account. In spring 2009 also the static GPS was tested with Bernese processing. The results showed that the kinematic approach was more suitable and even more precise than the static one in the Metsähovi case (Kallio and Poutanen, 2013).

The GPS-based local tie measurements were continued regularly at Metsähovi simultaneously with geodetic VLBI campaigns in 2009-2015 (Jokela *et al.*, 2016). In this case, the trajectories of GPS antennas were processed with commercial software and the PCO and PCV corrections were included in the RINEX file. The first Metsähovi system was validated in 2015 in the EMPR SIB60 campaign with simultaneous tachymeter monitoring, GPS-based monitoring, and the VLBI campaign (Kallio *et al.*, 2016) and (Jokela *et al.*, 2016).

A similar type GNSS local tie system was used at Onsala Space Observatory 20m telescope in 2013. In-house software was used, and in addition, the hydrostatic part of the tropospheric time-delay differences between the permanent GNSS station and the rotating GPS antennas with varying heights were corrected for. The mathematical model for estimating the reference point was the same as in (Kallio and Poutanen, 2012). Both static and kinematic strategies were tested and results of local tie vectors were reported (Ning *et al.*, 2015).

The new VLBI Global Observing System (VGOS) compliant telescope at Metsähovi, constructed in 2018, was equipped with two NovAtel NOV850 GNSS antennas in March 2020. Both antennas were individually calibrated. The new design of compensators includes stabilisation. The rotating points were processed with RTKlib (Takasu, 2013), and the final processing after troposphere and PCC corrections were applied in the RINEX file.

One of the activities in the 18SIB01 EMPIR GeoMetre project (GeoMetre, 2019), funded from the EMPIR programme and co-financed by the Participating States and from the European Union's Horizon 2020 research and innovation programme, was to investigate the influence of the compensator as this was not studied in the previous work. The functional or installation error of the compensation system and its influence on the reference point coordinates are discussed in Section IV. The principles of GPS processing are presented in Section V B, and validation of the GPS-based local ties is shown in Section VII.

In this paper, the acronym "GNSS" was used when discussing generally the method or if the receiver and antenna have been capable to observe GNSS. In our experiments, we used GPS-only observations and the acronym "GPS" is used.

## II. PRINCIPLE OF COMPENSATOR

The gimbal or compensator corrects the GNSS antenna to normal position with a counterweight and bearings (Figure 1) and thus compensates for the rotation of the radio telescope dish around the elevation axis. The counterweight keeps the GNSS antenna axis perpendicular to the gimbal axis and horizontal line, which is perpendicular to the gimbal axis. If the gimbal axis is collinear with the elevation axis of the telescope and the elevation axis is on the

horizontal plane (perpendicular to the plumb line), then the gimbal compensates for the elevation angle.



Figure 1. GNSS antenna on the left side of the VLBI-antenna with the compensator. The black Thorlabs plate was installed by the manufacturer of the VLBI telescope.

The rotation of the telescope around the azimuth axis changes GNSS antenna orientation and it is taken into account by applying the phase centre offsets (PCO) and phase centre variations (PCV) from the calibration tables of the GNSS antenna.

The compensator should be reliable, react quickly, and be stable. Because the angular velocity of the VGOS-telescope is rather high, maximum speed  $12^\circ/\text{s}$  in azimuth and  $6^\circ/\text{s}$  in elevation, we decided to install a damping system to stabilise the counterweight. We use a shock absorber, originally designed for snowmobiles.

A question arises, whether it would be better to let the GNSS antenna rotate with the telescope without any active compensation. If we have the GNSS antenna in a normal position when the telescope elevation is at zero, then when the telescope points to the zenith the attitude of the GNSS antenna will be rather bad for tracking signals from satellites, and probably a good quality position solution cannot be achieved.

## III. METHODS

Two methods were used to investigate the influence of compensation error on the reference point coordinates of the VLBI telescope and the uncertainties of the GNSS-based local tie vectors. The limit values of installation and functional errors of the compensator were obtained by simulation. On the other hand, real GPS observations were used for estimating the reference point and to compare the results with the simultaneous tachymeter determination.

### A. Simulation

In the simulation, the errors due to the installation and compensation are added to the "perfect" GNSS antenna coordinates. The antenna parameters are then estimated using these erroneous coordinates and compared with the results of the perfect antenna. In

addition, the random effect of compensation is included. The simulated cases are:

- Case 1: Extreme case.
- Case 2: No compensation angle basis error.
- Case 3: No installation error.
- Case 4: Basis compensation error compared to real case.
- Case 5: Only random part of compensation angle error.

The simulation parameters for installation, compensation, and random errors are listed in Table 1.

Table 1. Parameters in simulation cases. eRight is compensation angle error in the right side, eLeft the compensation angle error in the left side, ±eRand the random part of compensation, elnst error angle in installation

	eRight rad	eLeft rad	eRand rad	elnst rad
Case 1	0.175	0.175	0.035	0.050
Case 2	0	0	0.035	0.087
Case 3	0.175	0.175	0.035	0
Case 4	0.087	0.122	0.035	0.170
Case 5	0	0	0.035	0.170

#### B. Comparing the GPS local tie with the tachymeter local tie

The actual measurements were used to validate the functionality of the current installation of the compensation system. With the real GNSS trajectories, it is hard or nearly impossible to separate the contribution of error sources of GNSS measurement and processing from the contribution of compensation errors. The local tie vector based on the precise tachymeter measurements can be used as a reference for the GNSS local tie vector, especially if the measurements are performed simultaneously.

In our experiment, simultaneous measurements with GPS and tachymeter were performed on the rotating part of the telescope (Figure 2). The telescope was stopped for 40 s in each position for the tachymeter measurements. The GPS measurements were processed to the coordinates at each telescope position. The coordinates of the prisms in the tachymeter measurements were calculated in a 3D-network adjustment as a part of the local network. The reference point estimation was performed independently for both GPS and tachymeter data sets.

#### IV. ERROR SOURCES IN SIMULATION

The errors of the compensation system can be handled as an error of the functionality of the system and as installation errors of the system. Even if we had a perfect calibration table for GNSS antennas and we used it for correcting the phase observation to the antenna reference points (ARP) of the antenna, the correction would be inaccurate due to the errors in the compensator axis direction or actual angle of the

compensation. That is why we need to handle the PCC in connection with the compensation.



Figure 2. Simultaneous tachymeter and GPS local tie monitoring.

#### A. Perfect errorless case

In our perfect errorless telescope, we have two axes that are perpendicular to each other. In an az-el-type telescope, they are the azimuth axis and elevation axis. The azimuth axis is the primary axis around which the elevation axis rotates. In a perfect telescope, the axes intersect; there is no axis offset. The azimuth axis is perfectly vertical. The ARP of the GNSS antennas are attached to the compensator axis which is collinear with the elevation axis. The counterweight of the compensator turns the GNSS antenna axis to align it with the plumb line. We have a perfect model for GNSS antenna phase centre corrections (PCC) and we correct GNSS observations to the ARP without errors.

The errorless coordinates at antenna position azimuth  $\alpha$  and elevation  $\beta$  are calculated as (Kallio and Poutanen, 2012), Eq. (1).

$$X_{\alpha,\beta} = X_0 + R_{\alpha,\alpha}(E - X_0) + R_{\alpha,\alpha}R_{\beta,e}p \quad (1)$$

where  $X_{\alpha,\beta}$  = (3x1) coordinates of the point in antenna position  $\alpha, \beta$

$X_0$  = (3x1) coordinates of the reference point

$R_{\alpha,\alpha}$  = Rotation matrix around azimuth axis  $\alpha$  by angle  $\alpha$

$E$  = (3x1) Coordinates of the eccentric point in elevation axis in zero position

$R_{\beta,e}$  = Rotation matrix around elevation axis  $e$  in zero position by angle  $\beta$

$p$  = Vector from eccentric point to the prism or ARP in zero position

#### B. The direction of the compensator axis

The direction of the compensator should be collinear with the elevation axis. Inaccuracies in the installation of the compensator may cause an error in the direction of the GNSS antenna supporting axis. The misalignment of the compensator axis and thus the direction of the GNSS antenna axis change in rotation around the



elevation axis (Figure 3) even with a perfect compensator. Also the angle of the incoming signal in the GNSS antenna coordinate system changes.

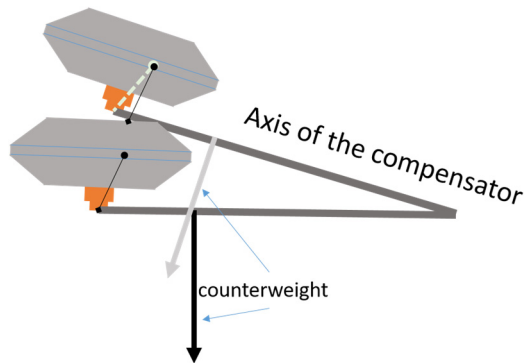


Figure 3. The misalignment of the compensator affects the elevation-dependent change in the direction of the compensator axis.

The PCC of the GNSS antenna is applied with the assumption that the antenna axis points to the zenith. The errors propagate to the estimated reference point coordinates, axis offset, and the other parameters in estimation. The direction error is systematic by nature and modelled in simulation as limit values (Table 1).

### C. Compensation angle

The compensation angle is opposite to the elevation angle. If the shock absorber or bearings work improperly, they generate an angular error (Figure 4). The GNSS antenna remains in the wrong attitude if there is a compensation angle error. Overcompensation might also occur. In the simulation example, the limit values (Table 1) for a basic constant compensation angle error are used. The possible changes to that are modelled by a random angle with uniform distribution.

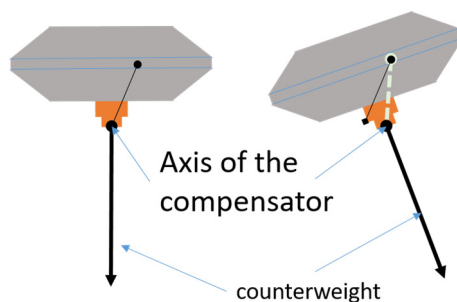


Figure 4. The GNSS antenna remains in the wrong attitude if there is a compensation angle error.

### D. PCC correction

The phase centre of the GNSS antenna changes every epoch due to the change of the elevation and azimuth of the satellites. PCC also depends on the attitude of the GNSS antenna. In our case, the VLBI telescope rotates moving the GNSS antennas with it, thus the attitude of them changes with the telescope elevation and azimuth positions. With real observations, we correct phase observations according to the antenna orientation and

the calibration table for every epoch, every frequency, and every satellite during the GNSS data processing. We do it before estimating the trajectories and generate a new RINEX-file with corrected observations. When the correction is applied it is assumed that the compensation is perfect due to rotation around the elevation axis.

We do not simulate the phase observations of GNSS but start from perfect trajectories. Thus, we need to proceed differently with PCC than in the case of real observations. We generate an error by applying the perfect correction to the incorrectly compensated case. In simulations we rotated the right and left antenna PCO vectors for L1  $[0.0002, 0.00048, 0.05192]$  m and  $[0.00024, -0.00012, 0.05147]$  m. Before the compensation (situation if no compensator is available) the GNSS antenna rotates around the elevation axis with the telescope. In compensation, it turns around the compensator axis which has an axis direction error. Moreover, the full compensation does not occur due to the shock absorber errors. Thus the GNSS antenna does not stop at the position of the perfect case. In the simulation, we calculate trajectory points with these axis directions and compensation angle errors and still apply the PCO corrections of the perfect case. After that, the generated point coordinates are the observations for reference point (RP) estimation in simulation.

## V. ACTUAL MEASUREMENTS

### A. Tachymeter measurements

Monitoring measurements of the reference point of the VLBI telescope were performed with a robot tachymeter TS50 from two concrete pillars and a 3 m steel mast near the telescope. Four prisms on the counterweight of the VLBI telescope were measured in several telescope angle positions. The timetable of tachymeter measurements was calculated before the measurement to synchronise the observations with the movement of the telescope. An in-house software controlled the automated measurements. Telescope movements were predefined in a schedule covering the antenna positions that allow visibility to the prisms. The movement of the telescope was controlled with another in-house software. The angle and distance measurements to the prisms were the observations in the 3D adjustment and their coordinates were estimated as a part of the local network in the global frame. The orientation of the network comes from the GPS network around the area. The coordinates were then used as observations in RP estimation.

The behaviour of the counterweights during the movement of the telescope was visually inspected and the directions of the counterweights of the GNSS antenna compensators were also measured with the tachymeter using prisms positioned on the counterweight.

## B. GPS measurements

The same VLBI antenna positions were simultaneously tracked with GPS and tachymeter measurements. In-house software was used to control the data logging of GNSS receivers and the movement of the telescope. In our experiment, we collected only GPS observations. GPS-only data was used since it was sufficient for this purpose and simplified the analysis. The coordinates of GNSS antennas were estimated and used as observations in RP estimation. The local tie vector was compared with the tachymetric RP.

The procedure for processing the GPS observations is as follows:

1. Processing trajectories with RTKlib (Takasu, 2013) using basic settings.
2. Calculating corrections using troposphere model GMT3 (Landskron and Böhm, 2018) for every single observation by using preliminary coordinates calculated in step 1.
3. Calculating corrections using PCO and PCV of the calibration tables and VLBI-telescope antenna positions.
4. Applying corrections to the observations.
5. Writing RINEX with corrected observations.
6. Processing trajectories with RTKlib without tropospheric corrections and PCC corrections.
7. Compiling trajectory coordinates and related VLBI antenna positions to the input files for RP estimation.
8. Estimating the RP and other related parameters.

To see the effect of the corrections on the RP coordinates, the RP estimation was performed after steps 1, 2, and 7.

## VI. RESULTS OF SIMULATION

A final simulation was performed with the extreme value 0.050 rad for the directions of the compensation axes and 0.175 rad (10°) for the basic compensation error with uniform distribution from -0.035 rad to 0.035 rad. The direction error was applied in four directions for both compensators to obtain 16 different directions in each VLBI antenna position.

The error in compensation or compensator axis direction propagates mainly in the axis offset parameter: In the extreme case, a -1 cm axis offset was obtained (Case 1 in Table 1). The height of the RP is affected in the extreme case about -1 mm. In the horizontal components, the effect was less than 0.1 mm. The numerical values of the input parameters in simulations are listed in Table 1 and the results in Table 2.

## VII. RESULTS OF REAL MEASUREMENTS

The comparison of tachymetric-based local tie and GPS-based local tie is presented in Table 3.

Table 2. Influence of compensator errors on RP

	$dN$ mm	$dE$ mm	$dU$ mm
Case 1	0.00	0.00	-0.86
Case 2	-0.01	-0.01	-0.08
Case 3	0.02	0.01	-0.88
Case 4	0.00	0.01	-0.36
Case 5	0.01	0.02	0.00

Table 3. Difference between GPS local tie and tachymeter local tie (GPS minus tachymeter)

	$dX$ [mm]	$dY$ [mm]	$dZ$ [mm]	$dN$ [mm]	$dE$ [mm]	$dU$ [mm]
Step 1	-2.69	-0.63	-3.28	+0.72	+0.53	-4.19
Step 2	-1.64	-0.24	-0.92	+0.92	+0.46	-1.59
Step 7	-0.80	-0.02	+0.56	+0.92	+0.31	+0.12

The varying height due to the change of the elevation angle of the telescope causes the difference in troposphere corrections influencing 2.6 mm in height of the RP. The full PCO and PCV corrections at the permanent GNSS point and the rover points cause a 1.6 mm change in height of the RP. The RTKlib software can read antenna calibration tables but apply only the elevation-dependent corrections. In steps 1 and 2, RTKlib was allowed to do the PCC, and for rover antennas the North and East offsets were changed to zeros in the calibration tables. In step 7 full PCC was applied with an in-house OCTAVE function before the RTKlib processing.

## VIII. COMPARISON OF SIMULATION AND REAL DATA CASES

The compensator counterweight directions were determined with tachymeter measurements. The results showed that the left side counterweight was stuck to the position differing about 0.12 rad from the plumb line and at the right side almost the same. A visual inspection confirmed this. The shock absorber inhibited the free movement of the counterweight. There is a trade-off between the dampening power of the shock absorber and the counterweight being able to settle at the plumb line quickly enough to follow the antenna movement.

Simulations and the real case observations showed equally well that the uncertainties in the compensator axis direction and compensation angle influence the axis offset parameter but not significantly the RP coordinates. The simulation was repeated with the inspected compensation error values with 0.017 rad for installation error. The result agrees with the real data case. However, the influence of the errors on the axis offset in the simulated case was more than the difference between the real case tachymeter-based and GPS-based axis offset.

## IX. DISCUSSION AND CONCLUSION

The study of the compensator system shows that sufficient installation accuracy of the compensator axis direction is rather easy to achieve. The antenna support

with bearings forms the basis of the compensation system. In addition to the compensator bearings, some kind of dampening is needed. New fast-moving VGOS telescopes and the future geodetic VLBI campaigns with short tracking times may otherwise cause undesirable swinging of the GNSS antennas.

The GNSS-based local ties give an alternative for the rather time-consuming tachymeter measurements. The concept has been confirmed first in Medicina, then at Metsähovi and Onsala, and now again at Metsähovi with the new VGOS telescope. The GPS-based local tie as a system is described comprehensively in (Abbondanza *et al.*, 2009a), (Kallio and Poutanen, 2012), and (Ning *et al.*, 2015), thus it is possible to install a similar system to new VGOS telescopes and apply necessary corrections to the GNSS observations before or during the processing.

The new compensator with the shock absorber at Metsähovi needs further development. Visual inspection and tachymeter measurements of the prisms on the counterweights show that the counterweights of the compensators remain in the tilted position due to the damping. However, the comparison of the local tie vector to the tachymeter-based local ties shows that the system otherwise works and agreement is good enough if only the reference point is considered. Further development to stabilise the quick movements of the compensator will continue.

The orientation of the GNSS-based vector depends on the satellite orbits and other uncertainty sources, affecting mainly in the vertical direction (like errors in antenna calibration tables, multipath, and errors in tropospheric corrections). Individual calibrations of GNSS antennas are necessary. The changes in the height difference between permanent and rotating antenna due to the VLBI antenna elevation positions should be taken into account when correcting for the effect of the troposphere.

## X. ACKNOWLEDGEMENTS

Ack The 18SIB01 GeoMetre project has received funding from the EMPIR programme co-financed by the Participating States and from the European Union's Horizon 2020 research and innovation programme.

MP Acknowledges the Academy of Finland grant 315722.

## References

- Abbondanza, C., M. Negusini, P. Sarti, and L. Vittuari, (2009a). VLBI-GPS eccentricity vectors at Medicina's observatory via GPS surveys: reproducibility, reliability and quality assessment of the results. Edited by H. Drewes. *International IAG symposium, Geodetic reference frames*, Munich, 9–14 O.
- Abbondanza, C., Z. Altamimi, P. Sarti, M. Negusini, and L. Vittuari, (2009b). Local effects of redundant terrestrial and GPS-based tie vectors in ITRF-like combinations. *Journal of Geodesy*, 83, 1031.

Combrinck, W. L., and C. L. Merry, (1997). Very long baseline interferometry antenna axis offset and intersection determination using GPS. *Journal of Geophysical Research* 102.

GeoMetre, (2019). Available in: <https://www.ptb.de/empir2018/geometre/home>, (accessed 13. 01. 2022).

Jokela, J., U. Kallio, H. Koivula, S. Lahtinen, and M. Poutanen, (2016). FGI's contribution in the JRP SIB60 "Metrology for Long Distance Surveying". Proceedings of the 3rd Joint International Symposium on Deformation Monitoring (JISDM) 30.3-1.4, 2016, Vienna.

Kallio, U., M. Lösler, S. Bergstrand, R. Haas, and C. Eschelbach, (2016). Automated Simultaneous Local Ties With GNSS and Robot Tachymeter. *IVS2016 proceeding*.

Kallio, U., and M. Poutanen, (2012). Can We Really Promise a mm-Accuracy for the Local Ties on a Geo-VLBI Antenna. In *Geodesy for Planet Earth*, 35–42. Springer Science Business Media.

Kallio, U., and M. Poutanen, (2013). Local Ties at Fundamental Stations. In *Reference Frames for Applications in Geosciences*, 147–152. Springer Science Business Media.

Landskron, D., and J. Böhm, (2018). VMF3/GPT3: refined discrete and empirical troposphere mapping functions. *Journal of Geodesy* 92, pp. 349–360.

Ning, T., R. Haas, and G. Elgered, (2015). Determination of the local tie vector between VLBI and GNSS reference points at Onsala using GPS measurements. *Journal of Geodesy* 89, pp. 711-723.

Takasu, T., (2013). RTKLIB ver. 2.4.2 Manual.

## Dynamic concepts to handle geodetic networks with continuous monitoring data in areas with ground movements

Wolfgang Niemeier<sup>1</sup>, Dieter Tengen<sup>2</sup>

<sup>1</sup> Institut of Geodesy and Photogrammetry, Technische Universität Braunschweig, Bienroder Weg 81, 38106 Braunschweig, Germany, ([w.niemeier@tu-bs.de](mailto:w.niemeier@tu-bs.de))

<sup>2</sup> Geotec GmbH, Heinrich-Heine-Weg 69, 30880 Laatzen, Germany, ([dieter.tengen@geotec-gmbh.de](mailto:dieter.tengen@geotec-gmbh.de))

**Key words:** *dynamic networks; time-dependent coordinate; GNSS continuous monitoring data; ground movement areas*

### ABSTRACT

Since decades the discrepancy exists that geodesists monitor changes of the earth surface resp. large engineering structures with most-modern equipment, but the results are computed and presented in a suboptimal manner: In many cases, the displacements are computed in relation to reference (datum) stations, which are not stable over a long time. Aside, the variations of an object are presented as coordinates for representative points with time stamps or with displacements rates (absolute values or velocities). Finally, nowadays often we have continuous measuring sensors and data, but there is no complete concept to treat variations continuously within the coordinate approach. In this paper at first the problems are outlined and open questions are formulated. Then some ideas are presented, how to analyse and describe coordinates in a continuous manner, taking into account the classical concepts and thinking of the surveying profession. The new ideas start with the definition of a stable reference frame over time, followed by the introduction of time dependent coordinates. A specific objective is to deliver day-by-day precise reference coordinate values for different groups, working on monitoring with their own sensors and computational concepts in the same area. These concepts are applied to an extended monitoring network of the mining authority Ruhrkohle AG (RAG), responsible for the eternal obligations that the German hard coal mining industry has left behind. This RUHR-network is located in the federal state North-Rhine-Westphalia within German, where after 300 years of coal mining larger and irregular ground movements can be expected.

### I. INTRODUCTION

Starting in the middle of the last century, the monitoring of large engineering structures, of local, regional or larger areas of the earth surface and even of small industrial objects has found more and more attention within partial disciplines of our profession.

In general the most-modern sensors are used and sophisticated methods for the evaluation and analysis of data are applied. Aside, after a long period with discontinuous monitoring, *i.e.* capturing the geometry of an object in specific campaigns or epochs, nowadays more and more continuous sensors and by this continuous data are available.

For any time-related project an adequate description of the object geometry over time is of primary importance. In section III some concepts are presented and applied, which seem to be suitable to serve for this task, *i.e.* to describe time-dependent coordinates in a dynamic environment.

But first, in section II, a fundamental problem of any long-term monitoring project is discussed, *i.e.* the setting-up and maintenance of a stable reference frame or a stable datum system. For use of a network with

permanently installed and continuously active GNSS-receivers, here innovative solutions are applied, based on developments given in Tengen *et al.* (2019), which are outlined and described in detail in Niemeier (2022).

In this paper the focus is laid on regional studies of vertical ground movements in the Ruhr Area in Germany, which has an original extension of about 7000 km<sup>2</sup>, effected by underground hardcoal mining. Now, being in the post-mining era, an area of about 140 km<sup>2</sup> is undergoing flooding of the old mines within the next years. By this an extended rising of the groundwater level have to be considered, see Spreckels (2022).

For a 3-year-period of continuous GNSS-monitoring between 2019 - 2021 for this region the developed concepts are presented and first results are depicted in this paper.

All processing and analysis steps were performed with an extended version of the established software package PANDA of GEOTEC GmbH. The data-storage concepts and the visualization are explained in the paper Schulz and Schäfer (2022).

## II. STABLE REFERENCE FRAME

As each information on displacements or deformations at time  $t_i$  has to be related to the geometry of the monitoring object at time  $t_{i-1}$ , both sets of information - and by this all data since time  $t_0$  - have to be defined within an identical reference frame. For long-term monitoring project the realization and maintenance of such a stable reference frame over time is a serious problem: Many practical monitoring projects suffer from the non-existence of a stable geodetic datum!!

### A. Cascading sensor systems for monitoring

In Figure 1 a typical example is given for the interaction of various sensors used for monitoring of a larger area.

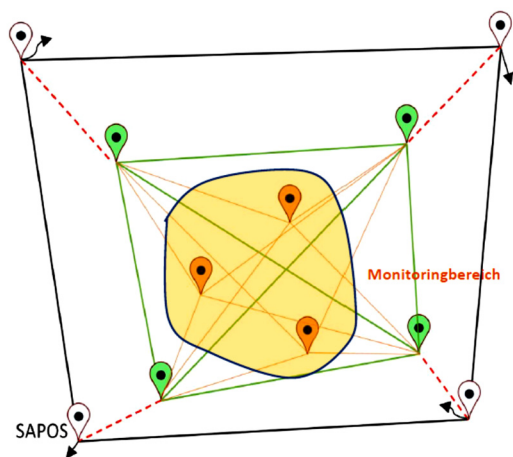


Figure 1. Cascading groups of sensors resp. networks for monitoring of larger areas (Spreckels *et al.*, 2020).

To get detailed information on the behaviour of the most critical, central section of the area, specific sensors are used like UAV, RTK-GNSS, total stations and levelling. These measurements refer to reference stations, which are close by, often in instable areas (yellow area in Figure 1).

These observations have to be related to reference stations, which are less effected by possible ground movements, *i.e.* are in a more stable zone (in green in Figure 1).

All these data have to be related to really invariant stations in geologically stable zones, here called *external reference stations*. As possible external reference stations in our area existing permanent GNSS-stations could be used, the SAPOS-stations of the state survey authorities of Germany. The RINEX-files of these stations area available free of charge and these data were processed by adequate GNSS-software, see Schäfer and Schulz (2022).

As we doubt the long-term stability of these SAPOS-stations, our statistical analysis does include the data-sets of these stations and it was found out, see section II/D, that significant movements were detects for these external stations, as well.

### B. Basic strategy to derive movement pattern

We start by applying the classical congruency test (*e.g.* Niemeier, 2008;2022), using the weekly mean GNSS-coordinate sets incl. covariance matrix as input data. By comparing the epochs one-by-one, *i.e.* the data sets of each subsequent week with the first week, we found out that after several weeks for a lot of stations, even out of the expected “stable” external reference stations, significant movements were identified.

A first possibility to account for irregular point movements is to allow for “individual points movements”, realized by enlarging the covariance information. But this tool does not help in a sufficient way.

The here selected basic strategy is depicted in Figure 2, it is the search for movement pattern within the displacement quantities after several epochs, in Figure 2 shown with epochs on an annual basis.

In theory, this strategy can be classified as *data-driven and/or behaviour-oriented*, and by this as being suboptimal, see Niemeier and Velsinck (2019). But for the surrounding we have in the RUHR area, due to 300 years of intensive coal mining, water management and city developments, no physical or mechanical model for the behaviour of the surface is known; the situation is too complicated.

In detail, the following steps are performed: If after the analysis of several epochs the group of stable reference stations is reduced, but still valid, an analysis of the movements of the unstable stations up to this time is encountered: We try to find out, whether there are linear movements (see station 1), just one outlier or jump (see station 8) or just irregular movements (see station 3).

All stations with “known” movement pattern now can remain within the group of reference stations, what has the most relevant effect that even after several epochs and detected movement pattern the number of reference stations does not reduce dramatically. The reference frame or geodetic datum is still valid for the subsequent congruency tests.

### C. Advanced strategy to analyse time series of data

For the analysis of the full data-sets of all 3 years of GNSS observations in the RUHR area we extended this concept by a detailed time series analysis of the coordinate components  $x$ ,  $y$  and  $z$  of each station.

For each component we allow:

- **Linear movements** (kinematic concept).
- **Seasonal movements** with period length of one year, to account for temperature effects or groundwater level variations.
- **Offsets**, *e.g.* known antenna changes or not yet detected offsets.

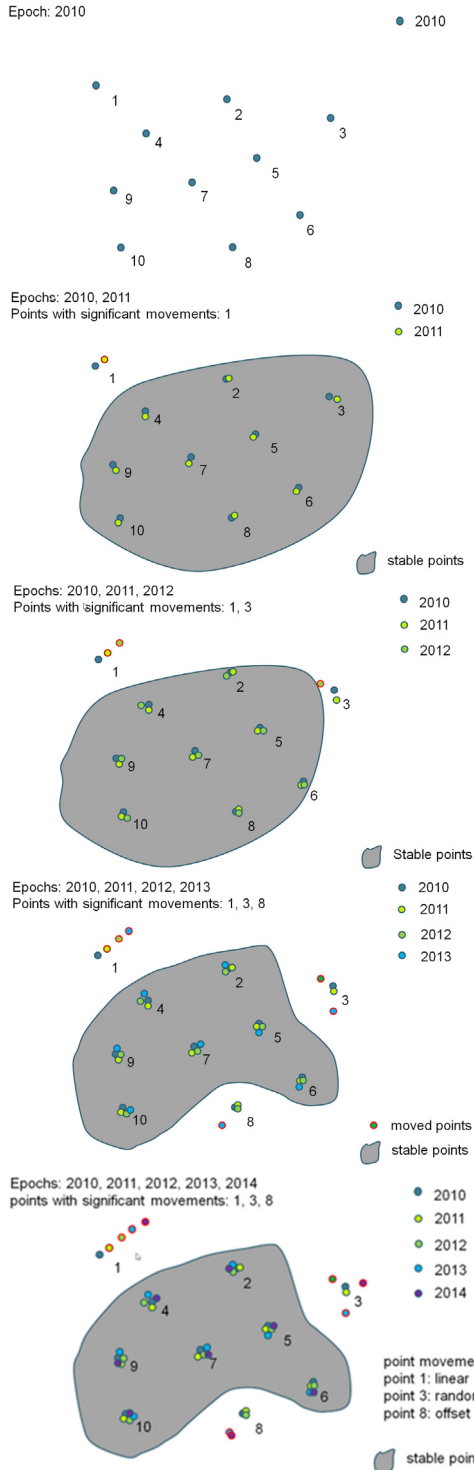


Figure 2. Strategy to derive movement pattern out of repeated coordinate sets. (Tengen *et al.*, 2019).

The formula to describe these movements is (Eq. 1):

$$f(t) = a_0 + a_1 * (t - t_0) + A * \sin\left(\frac{2\pi}{365}(t - t_0) + P\right) + o \quad (1)$$

In this formula a parameter P is included to account for seasonal shifts of the seasonal effects.

Two examples for such movement pattern, detected for reference stations of the RUHR network, are

depicted in Figure 3. Station 2594 has just an offset, but does not show seasonal or linear effects. For station 2579 all three effects are encountered.

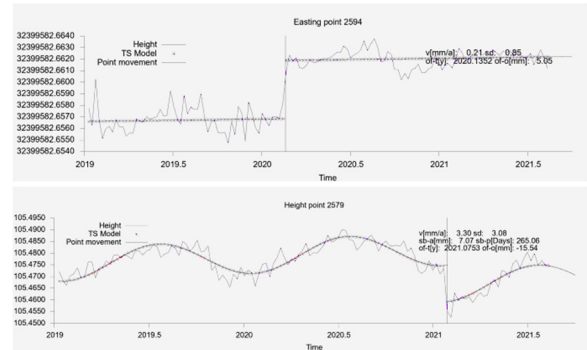


Figure 3. Movement pattern for the reference stations 2579 and 2594 with velocity, seasonal effect and offset.

It has to be mentioned that seasonal effects cannot be determined with just a few epochs of data. We need about two years of data to have valid estimates for seasonal effects. Aside the detection of offsets needs a detailed analysis of data directly before and after the variation, to be able to compute the offsets and to differentiate them from pure outliers.

#### D. Results for the RUHR network 2019 - 2021

As depicted in Figure 4, the GNSS monitoring network of the RUHR area consists of 10 SAPOS permanent stations of Geobasis NRW, the state survey authority in this region, which raw data can be downloaded online and are free of charge. These stations have 4-digit identifiers.

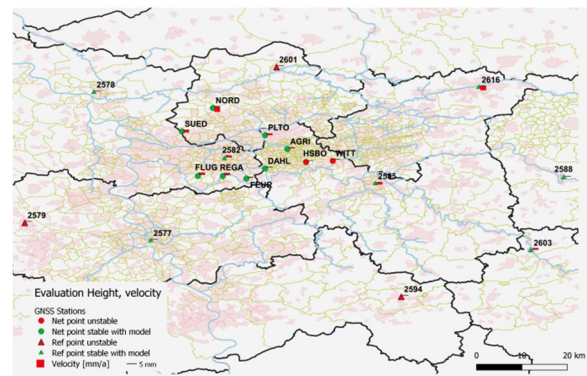


Figure 4. Linear velocities for the height component for all stations of the RUHR GNSS network.

In the central section 11 permanent GNSS-stations were installed and maintained by the mining authority Ruhrkohle AG (RAG), responsible for the eternal implications of 300 years of coal mining to this area.

In Figure 4 and 5 the achieved results after almost three years of observation are presented. It turns out that for several of the external reference stations (SAPOS) significant movements are detected. But due to our approach, most of them could maintain within the group that define the datum of the system.

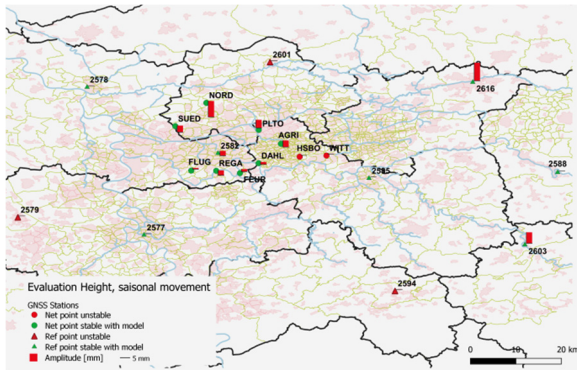


Figure 5. Amplitudes for seasonal variations in the height component for all stations of the RUHR GNSS network.

### III. TIME-VARIANT COORDINATES

#### A. Outline of the problem

Since decades within Geodesy, Geoinformatics, Surveying and Photogrammetry the concept of stable coordinates is valid, *i.e.* the geometry of an object is represented by a set of fixed coordinates. Maybe, better observations lead to more precise coordinates, but in principle is geometry of an object is considered as being invariant over time.

Coming to height systems, variations with time are more common in our disciplines. Due to new height definitions, new measuring campaigns and more sophisticated processing, there are different height systems, in Germany called “height status”, which are established from time to time and then set to be valid (official) for the next years or decades.

As outlined in Figure 6., this sequence of height fixations does not represent the real or complete behaviour of a stations resp. the surface of the earth. No one knows what happens in-between the fixations at time  $t_1, t_2, t_3$ , or how long a defined height status is really valid. Figure 6 makes it very clear that the challenge is to define a continuous “movement-model”, *i.e.* we need a new concept for a time-variant representation of heights.

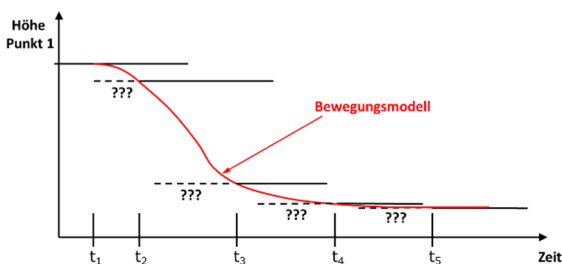


Figure 6. Height variation of a station, described by a sequence of different height values or a movement-model.

A very similar situation is given for the 3D-presentation of monitoring results of the earth surface and of large engineering structures: Either the coordinates get a time stamp or the displacement rates are added just as attributes to given (a priori) coordinates. No movement or displacement model is included in our data sets.

Modern concepts for data management, following these concepts of time-variant coordinates, can be found in Schulz and Schäfer (2022).

#### B. Coordinates on a day-by-day basis

As mentioned before, different sensors are used for monitoring and most of them give relative information, *i.e.* they have to be related to reference station near by. If we accept a variable surrounding, the coordinates of these near-by reference stations may change with time, as well, see section II/A. This makes it necessary, to keep ready coordinates on a daily basis. If we determine coordinate sets for the reference stations once a week, the daily values will be – in many cases - a prognosis, *i.e.* their quality may be reduced a bit.

In Figure 7 this situation is depicted: For image flights (airplane or UAV) and the determination of passpoints the coordinates of any reference station have to have values that are valid for the time of observation.

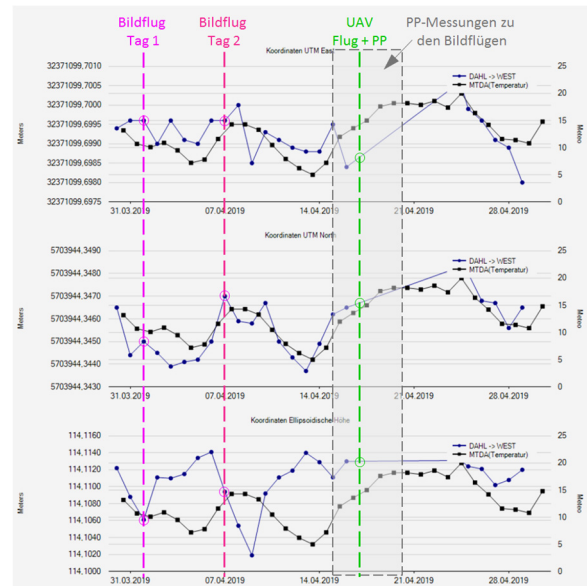


Figure 7. Different sensors, applied for monitoring, need valid coordinates for reference points on a day-by day basis (Spreckels et al., 2020).

#### C. Derivation of a movement model

For the description of movements in dynamic environment at first the KALMAN- filtering seems to be the adequate choice, see the principle in Figure 8. In the ideal case we have a physically defined movement model, which is used for the prediction of the behaviour of an object, here the coordinate component of a station.

Actual measurements allow a comparison between predicted and observed values and by this on the validity of the physical model.

Due to the complexity of the surrounding in the RUHR area, no physically justified model for the variation of geodetic stations is available. Therefore again a data driven approach is applied, which does not follow

directly the above outlined principle of KALMAN-filtering.

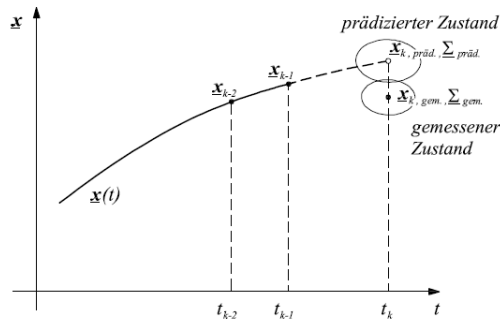


Figure 8. Principle of KALMAN-filtering for the prediction of the status of a system (e.g. Niemeier, 2008).

In Figure 9 the numerical strategy for an extrapolation of coordinates for one week is depicted. At the end of GPS-week 2020 the movements of the considered coordinate component is computed, following the approach, given in section II/C. This model - given as full red line - is used for an extrapolation up to the end of GPS-week 2021, the dashed red line.

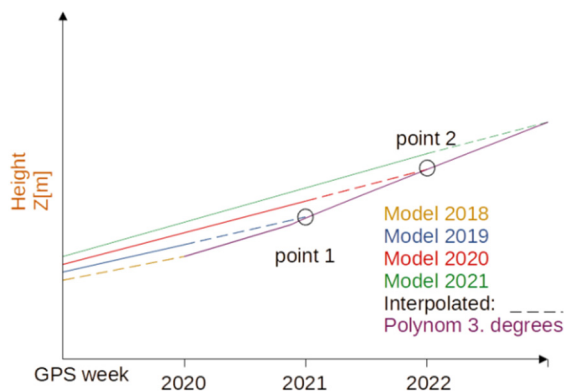


Figure 9. Extrapolation of the movements of stations, based on complete computations for each GPS-week.

For the preceding GPS-week 2019 the prediction ends at the end point of the blue line. Between the end points of each extrapolation a polynomial of grade 3 is applied to smooth the behaviour.

For coordinate of a daily basis these smoothed coordinates are used. Due to our numerical experiences, the deviations between the afterwards computed “real” coordinates and the extrapolation ones are sufficiently small, they lie in the range of about 2 mm, what can be accepted for our task.

#### D. Results for stations in RUHR area

The preceding approach is applied to all stations of the RUHR area; here just the height component is discussed. For two typical stations within the RUHR network the results are given in Figure 10. for a time span of several month in 2021.

The “Current Model” describes the behaviour with data up to this moment, while the “Optimal Model” is computed afterwards, i.e. with all available data. The

current model converges asymptotically to the optimal model. It can be seen that a sufficient approximation is achieved, even if sometimes some offsets appear.

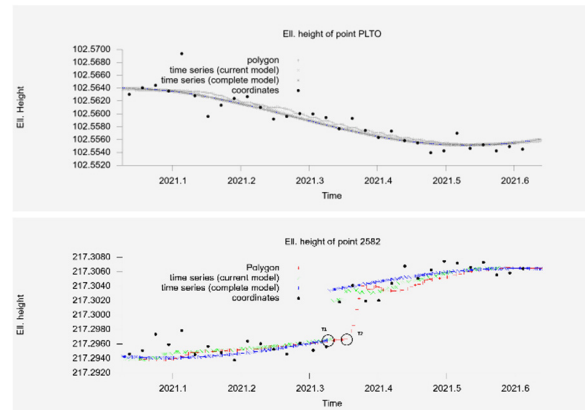


Figure 10. Approximation of the movement behaviour for height components of stations PLTO and 2582. Comparison of different computational steps.

#### IV. CONCLUSION

The here presented strategies and numerical concepts are a consequent extension of the classical deformation analysis of networks, but now applicable for continuous data.

At first, we look after a stable geodetic datum by a detailed analysis of the stability of the external reference stations. Even if some movement pattern can be encountered, in general these stations can remain within the group of datum defining stations. Of course, during the setup of each long-term monitoring project, the datum problems have to be taken into account by an adequate design resp. extension of the network.

We allow all permanent stations a linear and seasonal movements and consider offsets.

A more detailed description of displacement pattern would include reliable data on acting forces and/or external effects, an information, that was not available in the study area.

As second fundamental step we developed a concept to define and derive time-variant coordinates, which are more flexible and better suited for the approximation of continuous movements, than any other concept.

The results for the RUHR area demonstrate, that this concept really can be used for defining continuous coordinate representations, which then have to be included into the data-base concepts, what already is done by a different group, see Schulz and Schäfer (2022).

These time-variant coordinates allow the derivation of day-by-day coordinates, what is necessary to have a more consistent coordinate basis, if other sensors and methods are included in the complete monitoring task.

Finally, the here developed methods and concepts are not restricted to continuous GNSS-data. They allow the inclusion of continuous monitoring data of all applicable sensors, e.g. InSAR, UAV, total station and



levelling data. Practical work in this direction is left for the future.

## V. ACKNOWLEDGEMENTS

This research was supported by the RAG foundation, research and development project 0777 0000 “GNSS-Monitoringnetze”. We want to thank this agency and its representatives for supporting and encouraging our work during the period 2019 – 2021.

## References

- Niemeier W. (2008). Ausgleichsrechnung – Statistische Auswertemethoden. *Lehrbuch. 2. Auflage. deGruyter Verlag Berlin, 493 S.*
- Niemeier W. (2022). Classical Concepts for Deformation Monitoring - Strategies, Status and Limitations. *Proceedings JISDM 2022, Valencia.*
- Niemeier W., and Velsinck H. (2019). Strategies and methods for multi-epoch deformation analysis with geodetic networks. *Proceedings JISDM 2019, Athens.*
- Schulz, M., and Schäfer F. (2022). GLOMON-Monitoringportal for storage, management, advanced processing and intelligent visualization of GNSS- and other sensors data. *Proceedings JISDM 2022, Valencia.*
- Spreckels V., Bechert S., Schlienkamp A., Drobniowski M., Schulz M., Schäfer F., Kemkes E., Ruffer J., Niemeier W., Tengen D., Engel Th., Müller M., and Schmitt P. (2020). GNSS, Nivellement und Radar – einheitliche Multisensor-Referenzpunkte zur Überwachung von Bodenbewegungen in ehemaligen Bergbaubereichen. *In: Proceedings GeoMonitoring 2020, TU Braunschweig.*
- Spreckels V. (2022). Multisensor monitoring of ground movements over large areas to conduct the change from the active underground hardcoal mining ages to the post-mining era. *Proceedings JISDM 2022, Valencia.*
- Tengen D., Riedel A., Riedel B., Gerke M. und Niemeier W. (2019). Ableitung vertikaler Landbewegungen an der deutschen Nord- und Ostseeküste aus GNSS- und PS-Auswertungen. *In: Proceedings GeoMonitoring 2019, Uni Hannover.*

## Accuracy improvement of mobile laser scanning point clouds using graph-based trajectory optimization

Felix Esser, José Angel Moraga, Lasse Klingbeil, Heiner Kuhlmann

Institute of Geodesy and Geoinformation, University of Bonn, Nußallee 17, 53115 Bonn, Germany,  
([esser@igg.uni-bonn.de](mailto:esser@igg.uni-bonn.de); [s7jomora@uni-bonn.de](mailto:s7jomora@uni-bonn.de); [l.klingbeil@igg.uni-bonn.de](mailto:l.klingbeil@igg.uni-bonn.de); [heiner.kuhlmann@uni-bonn.de](mailto:heiner.kuhlmann@uni-bonn.de))

**Key words:** *point clouds; deformation analysis; mobile laser scanning; factor graph optimization; sensor fusion; GNSS/IMU processing*

### ABSTRACT

The detection of deformations on man-made structures such as bridges and dams are an essential task in engineering geodesy. The classical method uncovering deformations is based on geodetic networks using measurements from total stations or GNSS receivers. Another new approach is the determination of deformations based on terrestrial laser scans leading to large-scale deformation results by point cloud comparisons. In the field of geodetic engineering, mobile laser scanning systems are increasingly used for high-resolution point cloud generation in short measurement times, which leads to the idea to use these for deformation analysis. A crucial part of this measurement strategy is the estimation of the trajectory (position and orientation) of the scanner, which allows a consistent registration of the single scan lines in a global coordinate system (georeferencing). The largest limitation to the accuracy of the resulting point cloud is the accuracy of the estimated trajectory. In most applications, the estimation of position and orientation are based on the fusion of GNSS (Global Navigation Satellite System) and IMU (Inertial Measurement Unit) measurements. Systematic errors, as they often appear in GNSS measurements, are directly transferred to the georeferenced point cloud and therefore limit the potential for deformation analysis. With this paper we address the questions, if the trajectory estimation can be improved by the integration of known landmarks into the trajectory estimation procedure. Using a point cloud generated with an initial GNSS/IMU based trajectory, landmark targets can be observed in the point cloud and integrated into an updated estimate, using a factor graph-based approach. For the evaluation of a potential accuracy increase due to landmark observations, we performed measurements, comparing GNSS/IMU based results with the ones where landmarks are additionally integrated. The experiments show, that the accuracy increases especially in the heading angle, which is reflected in lower residuals to observed reference coordinates, but also in the trajectory covariances of the estimation results.

### 1. INTRODUCTION

In recent years, the method of point cloud comparisons between consecutive epochs has become increasingly popular for detecting deformations of man-made structures, such as bridges and dam walls (Neuner *et al.*, 2016; Xu *et al.*, 2018). The acquisition of these point clouds is usually realized by taking terrestrial laser scans from multiple points of view and then registering the individual scans into one. Another increasingly popular method for recording point clouds is the use of kinematic laser scanning with multi-sensor systems (MSS), (Heinz *et al.*, 2020; Eling *et al.*, 2015; Paffenholz, 2012). By estimating the position and orientation of the system for each laser observation in time, a georeferenced point cloud of the environment can be acquired. A crucial aspect in this procedure is a precise estimation of the trajectory.

An established method of trajectory estimation is the fusion of sensor information from GNSS (Global Navigation Satellite System) and IMU (Inertial Measurement Unit), where the accuracy of position and orientation depends significantly on the actual GNSS conditions. Systematic deviations in GNSS observations,

caused by multipath and non-line of sight effects due to objects in the environment of the system (Zimmermann *et al.*, 2017; Strode and Groves, 2016), are directly transferred to the point cloud due to the direct georeferencing of the 2D scan profiles. This reduces the detectability of deformations in the context of deformation analysis. For this reason, it might be beneficial to include additional absolute sensor information in the trajectory estimation process, in order to reduce systematic errors in the trajectory and the resulting point cloud. This absolute sensor information can be obtained by observing known control points in the environment, either with a camera or with a laser scanner. In this work, we analyze the usage of a profile laser scanner, which is already part of the measurement system used in context of this work.

The integration of these observations introduces challenges for the algorithmic implementation. We chose a factor graph-based approach (Dellaert, 2012; Dellaert and Kaess, 2017; Choudhary *et al.*, 2015) for the integration of this information, which also realizes a smoothing of the trajectory. This approach is closely related to SLAM algorithms such as realized in Shan *et*

*al.*, (2020) and Chang *et al.*, (2019). However, in contrast to most SLAM algorithms, we do not estimate the position of the landmarks within the process. Instead, we use the known positions to improve the estimate of the trajectory. The accuracy of the resulting point cloud (map) is improved in a second step.

We analysed the result of the method within an experiment, where we scanned an environment which contains a number of known landmark targets with our MSS. The evaluation of the accuracy improvement by observing and including landmark observations in the trajectory estimation is first performed by comparing the estimated variances of the trajectory states with and without inclusion of landmark information in the graph-based trajectory optimization algorithm. Furthermore, an evaluation of the residuals to landmark control points is performed. The rest of the paper is organized as follows: We first introduced the used sensor platform and the factor graph-based method for trajectory optimization in Section II, followed by the description of the experimental field used for evaluation. We discuss the evaluation results in Section III, closing this work by a conclusion and outlook in Section IV.

## II. MATERIALS AND METHODS

### A. Multi-Sensor System and Point Cloud Creation

The multi-sensor system used in this study is well suited for mobile laser scanning in urban areas and consists of a high-end Inertial Navigation System (INS) (IMAR iNav-FJI-SURV), a GNSS antenna (Leica AS10) and a high-precision profile laser scanner (Z+F Profiler 9012A), see Figure 1, left. In a measurement campaign, the system can be fixed to the roof of a vehicle. In order to exclude the vehicle from the field of view of the sensor, the scanner is tilted by 30°.

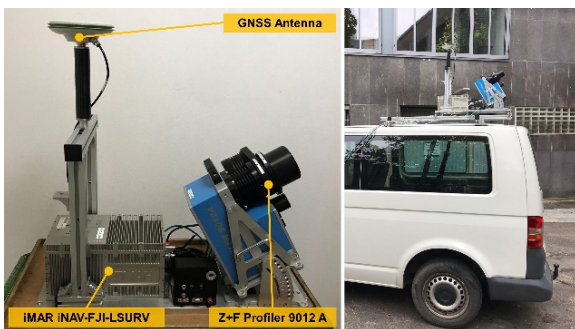


Figure 1. Multi-Sensor System with GNSS Antenna, IMU with integrated GNSS receiver and profile laser scanner.

*Right:* MSS mounted on vehicle.

The INS consist of an internal multi GNSS receiver, a fiber optic gyroscope and servo accelerometers in all three spatial axes. Data can be recorded with a rate of up to 1500 kHz. The integrated Novatel OEM628 Multi GNSS receiver provides centimeter accurate position estimates using kinematic baseline processing.

The Z+F profile laser scanner delivers up to 1 million points per second with a spatial resolution of 0.5 mm at a distance of 3 m, and a distance accuracy of less than 1 mm, as specified by the manufacturer. The scans are synchronized to the INS data using the PPS (Pulse-Per-Second) signal from the GNSS receiver.

In order to create a georeferenced point cloud, the laser scans have to be transformed using the georeferencing equation (Eq. 1):

$$\begin{bmatrix} x_g \\ y_g \\ z_g \end{bmatrix} = \begin{bmatrix} t_x \\ t_y \\ t_z \end{bmatrix} + \mathbf{R}_n^e(\theta, \psi, \phi) \begin{bmatrix} \Delta x \\ \Delta y \\ \Delta z \end{bmatrix} + \mathbf{R}_s^b(\alpha, \beta, \gamma) \begin{bmatrix} x_s \\ y_s \\ z_s \end{bmatrix} \quad (1)$$

The laser measurements  $[x_s, y_s, z_s]$  given in the sensor frame of the scanner are transformed into the body frame  $b$  using the system calibration parameters, which are the translation vector  $[\Delta x, \Delta y, \Delta z]^T$  and the rotation matrix  $\mathbf{R}_s^b$ . The subsequent transformation from the body into the global frame  $g$  requires the estimation of the trajectory parameters, which are the positions  $[t_x, t_y, t_z]^T$  and orientations  $\mathbf{R}_n^e$  (or roll, pitch and yaw angles  $\theta, \psi$  and  $\phi$ ) for each laser scanner measurement. The determination of these parameters is the main contribution in this study and will be described later.

Apart from the position and orientation states, the system calibration parameters also have a significant influence on the accuracy of the resulting point cloud. We estimated them very accurately using a plane-based approach which is described in more detail in (Heinz *et al.*, 2015).

### B. Measurements and State Definition for Trajectory Optimization

The calculation of the trajectory is based on the measured rotation rates and accelerations of the IMU, the GNSS position information processed from the baseline and the laser measurements of the profile scanner to the known landmark coordinates.

1) *GNSS:* In the trajectory estimation a loosely coupled approach is used for the integration of the GNSS information. For this reason, we performed a kinematic GNSS carrier-phase based baseline processing, using a virtual reference station from SAPOS NRW. The GNSS coordinates for each GNSS epoch  $j$  are given by  $\mathbf{z}_j^{GNSS} = \{x, y, z\}_j$  with a corresponding standard deviation.

2) *Landmark Targets:* In order to create target observations, we first compute the initial point cloud based on the trajectory estimation with GNSS and IMU observations only. In this point cloud the known landmark targets are visible which allows to manually deduce the laser scanner observation to the target centrum. The detection of the target center and corresponding observation could also be performed automatically, but is beyond the scope of this paper.

The laser observations of the target centers are first given in the sensor frame in cartesian coordinates, and then transformed into the body frame using the system calibration parameters, and finally converted into polar coordinates. This results in two angles and a distance measurement, which are called bearing  $\varphi$ ,  $\theta$  and range  $d$ . The full set of observations to  $n$  landmarks is given by  $\mathbf{z}_n^{BR} = \{\varphi, \theta, d\}_n$ . An example target resolved in the initial point cloud is visualized in Figure 2.

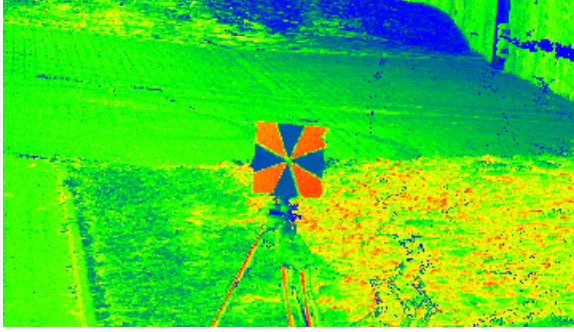


Figure 2. Example landmark target in initial point cloud, computed with GNSS / IMU trajectory.

3) *IMU*: The measured accelerations  $a$  and angular velocities  $\omega$  of the IMU  $\mathbf{z}_l^{IMU} = \{a_x, a_y, a_z, \omega_x, \omega_y, \omega_z\}_l$  are given in the IMU frame which coincides with the body frame of the system and therefore do not have to be transformed.

All sensor observations can be summarized in the set  $M = \{\mathbf{z}_j^{GNSS}, \mathbf{z}_l^{IMU}, \mathbf{z}_n^{BR}\}$  marked with the corresponding indices to distinguish between different sensor observations.

4) *States*: The state vector describing position, velocity and orientation of the system, defining one navigation system state in time, is given by  $\mathbf{x}_i = [x, y, z, v_x, v_y, v_z, \mathbf{q}_{rpy}]_i^T$ .

The position coordinates  $x, y, z$ , velocities  $v_x, v_y, v_z$  and orientation  $\mathbf{q}_{rpy}$  refer to the UTM (Universal Transverse Mercator) coordinate system in which the estimation of the states is implemented. The description of the orientation angles roll, pitch and yaw are represented by the quaternion  $\mathbf{q}_{rpy}$  and refers to the axes of the navigation frame, coinciding with the axes of UTM. Due to the dynamic evolution of the IMU bias in time (Groves, 2015), it is necessary to include

inertial sensor bias variables in the optimization in order to remove the systematic errors from the raw IMU observations. The additional six parameters for the IMU bias result in  $\mathbf{b}_q = [v_x, v_y, v_z, v_x, v_y, v_z]_q^T$ .

Summarizing the trajectory states and bias variables over the entire measurement period  $k$ , all states to be optimized result in  $\mathbf{v}_k = \{\{\mathbf{x}_i\}\{\mathbf{b}_q\}\}$ .

Since the landmark coordinates are available with very high accuracy, they are assumed to be known and are therefore not included as optimizing quantities in the set of state vectors  $\mathbf{v}_k$ .

### C. Factor Graph-Based State Optimization

We use a factor graph-based approach to optimize the trajectory state variables  $\mathbf{v}_k$ . Within the graph, nodes describe the states to be estimated. The sensor observations result in so-called factors, which contain sensor observations and state variables. By assuming zero mean gaussian noise for the sensor measurements, the factors represent error functions involving measurements and variables. The factor graph representation of variables nodes and factors for the estimation problem in this work is visualized in Figure 3. More information about concept and definitions of factors is given in (Kaess *et al.*, 2012). We introduce first the least squares optimization problem containing factors and state variables. Afterwards we define the individual factors and their error functions.

1) *Least Squares Optimization*: By setting up all error functions over the entire period for sensor measurements and defining the variable nodes, the optimization of all trajectory states can be described by the least squares problem (Eq. 2)

$$\mathbf{v}_k^* = \arg \min_{\mathbf{x}_k} \sum_j \|f^{IMU}\|_{\Sigma_{\Delta\Delta}^2}^2 + \sum_j \|f^{BIAS}\|_{\Sigma_{cc}^2}^2 + \sum_j \|f^{GNSS}\|_{\Sigma_{xx}^2}^2 + \sum_j \|f^{GNSS}\|_{\Sigma_{xx}^2}^2 \quad (2)$$

assuming zero mean gaussian noise for all sensor observations. The corresponding factor graph visualization to Equation 2 is visualized in Figure 3 and is composed of the individual factors, that we introduce in the following.

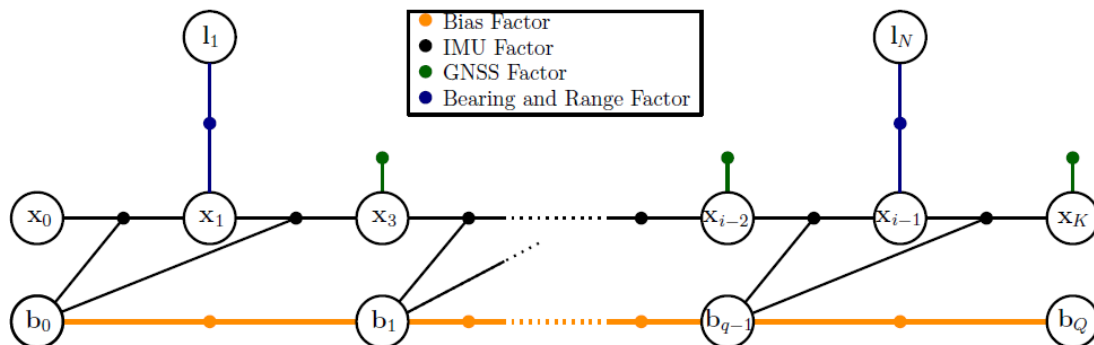


Figure 3. Full factor graph representation of the least squares problem (Equation 2).

By linearizing the individual error functions of the graph by a first order Taylor expansion, the normal equations can be set up containing all navigation states  $\mathbf{x}$  and IMU bias states  $\mathbf{b}$ . The linearization requires knowledge about approximate values for each variable node of the graph to be optimized. These are not available for the orientation parameters, since these must be updated in time by integrating the IMU observations. To solve this problem, we use the ISAM2 algorithm that incrementally builds up the graph structure and optimizes the state variables periodically in time. The algorithm is implemented in the GTSAM library, detailed information about library and ISAM2 algorithm used for optimizing the graph can be found in (Kaess *et al.*, 2011; 2012; Indelman *et al.*, 2013).

2) *Preintegrated IMU Factor*: The IMU factor is a non-linear error function involving two consecutive navigation states in time  $\mathbf{x}_{i-1}$  and  $\mathbf{x}_i$ , and the corresponding bias states  $\mathbf{b}_q$  and is defined by (Eq. 3)

$$f^{IMU}(\mathbf{x}_{i-1}, \mathbf{x}_i, \mathbf{b}_q) = err^{IMU}(\mathbf{x}_i - h(\mathbf{x}_{i-1}, \mathbf{b}_q, \Delta \mathbf{x}_{i-1 \rightarrow i})). \quad (3)$$

By preintegrating the raw IMU observations considering the estimated bias variables  $\mathbf{b}_q$ , the so-called preintegrated IMU measurements  $\Delta \mathbf{x}_{i-1 \rightarrow i}$ , related to the time interval between two defined navigation states  $\mathbf{x}_i$  and  $\mathbf{x}_{i-1}$  are obtained. The factor calculates the error of the current state  $\mathbf{x}_i$  and the predicted state by the function  $h()$  involving the previous state, bias state and preintegrated measurements and is minimized in the least-squares optimization. More information about the preintegration, including the bias variables is given in Forster (2015).

3) *IMU Bias Factor*: The evolution of the bias variables requires a model for propagation in time which is computed by a function  $g(\mathbf{b}_{q-1})$  assuming a zero-mean gaussian noise model. By the definition of this noise model with a random walk process, the bias factor results in (Eq. 4)

$$f^{BIAS}(\mathbf{b}_q, \mathbf{b}_{q-1}) = d(\mathbf{b}_q - g(\mathbf{b}_{q-1})) \quad (4)$$

The error function computes the residuals of predicted bias by  $g(\mathbf{b}_{q-1})$  and current bias state  $\mathbf{b}_q$ , minimized in the optimization. More information about the bias factor and the connection to the preintegrated IMU factor is given in (Forster *et al.*, 2016).

4) *GNSS Factor*: The GNSS factor is a so-called unary factor and is defined by the linear error function (Eq. 5)

$$f^{GNSS}(\mathbf{x}_j) = err^{GNSS}(\mathbf{z}_j^{GNSS} - h^{GNSS}(\mathbf{x}_j)) \quad (5)$$

which computes the error between the GNSS position measurement  $\mathbf{z}_j^{GNSS}$  and predicted position by the

function  $h^{GNSS}(\mathbf{x}_j)$  including the navigation state  $\mathbf{x}_j$  and the translation from body to GNSS antenna frame, the so-called lever arm.

5) *Bearing and Range Factor*: The bearing and range factor is described by the error function (Eq. 6)

$$f^{BR}(\mathbf{x}_i) = err^{BR}(\mathbf{z}_n^{BR} - \pi^{BR}(\mathbf{x}_i, \mathbf{l}_n)) \quad (6)$$

computing the error between predicted bearing and range measurement by the function  $\pi^{BR}$  depending on the current trajectory state  $\mathbf{x}_i$ , known landmark  $\mathbf{l}_n$  and laser scanner measurement  $\mathbf{z}_n^{BR}$ . Detailed information about the bearing and range factor is given by (Setterfield *et al.*, 2017; Dellaert, 2012).

6) *Sensor Noise Models*: The weighting of the sensor information within the optimization of the state variables requires the definition of noise models for the factors in Figure 2, in which the observations are included. The specified standard deviations of the individual observations, which we used for the optimization are collected in Table 1. The standard deviation of the target measurements in Table 1 refer to the coordinates in the sensor frame of the laser scanner. The standard deviations of bearing and range in the body frame are determined by a variance propagation considering the accuracy of the system calibration. The variances of the raw IMU observations are also transferred to the preintegrated IMU observations of the IMU factor by a variance propagation (Forster *et al.*, 2015).

Table 1. Sensor noise models for the individual measurements

GNSS	IMU and Bias		Target
$\sigma_x, \sigma_y, \sigma_z$ 5cm	Acceleration $\sigma_{ax}, \sigma_{ay}, \sigma_{az}$ $7.8 \cdot 10^{-5} \text{ m/s}$ Bias noise $7 \cdot 10^{-5} \text{ m/s}$	Gyroscope $\sigma_{\omega_x}, \sigma_{\omega_y}, \sigma_{\omega_z}$ $3 \cdot 10^{-7} \text{ rad/s}$ Bias noise $5 \cdot 10^{-7} \text{ rad/s}$	$\sigma_x^l, \sigma_y^l, \sigma_z^l$ 5mm

#### D. Experimental Setup for Evaluation

For recording measurements and later evaluation of our results we use an existing experimental field 20 km in west of the city of Bonn, Germany. We perform a network adjustment based on total station observations and static GNSS measurements to optimize a geodetic net with points known with an accuracy in submillimeter range in global frame.

A subset of these coordinates was used as reference coordinates for evaluation purposes, while another subset was used as observations in the trajectory estimation process. In order to transform the local network into the UTM frame, known datum points are observed which are available with a high accuracy near the location of the network. By performing a least squares network adjustment, considering the datum

information, the network point coordinates are estimated with a standard deviation below 1 mm. The distribution of network points and points defining the datum are visualized in Figure 4.

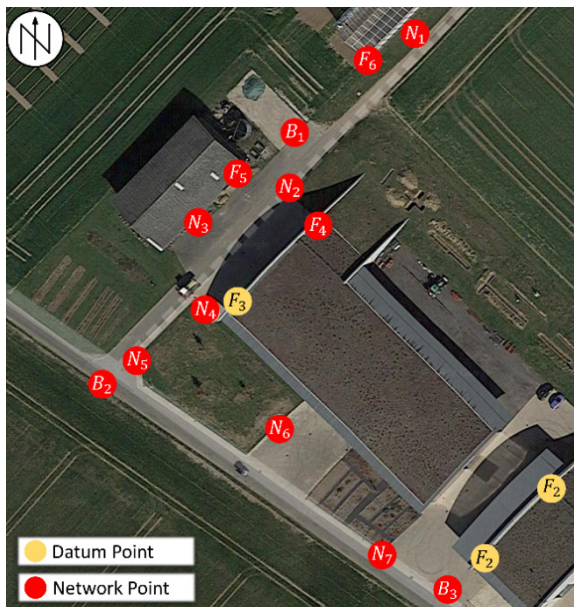


Figure 4. Resulting coordinates from network adjustment (Image Source: Google Maps, 2022).

We perform multiple measurement drives with the car setup shown in Figure 1. The start and end points of campaigns are located in the north of the measurement area and proceeds through the geodetic network in the middle part. To ensure a high resolution of the point cloud, a low velocity of the system near the landmarks of only about 10 cm/s is chosen. An example target is visualized in Figure 2.

We perform two trajectory optimizations: The first on basis of GNSS and IMU observations only and the second with additional landmark observations, in order to elaborate the accuracy improvement due to target observations. The analysis focusses on comparison of both trajectories regarding the precision gain of position and orientation. Highlighting the influence of the bearing and range factors on state estimation in more detail, the number of GNSS observations within the algorithm is reduced by the factor 20 resulting in a GNSS position update rate of 10 s. Afterwards we analyze the residuals to the subset of coordinates from the geodetic network that we did not include in the trajectory optimization.

### III. RESULTS AND DISCUSSION

#### A. Trajectory Estimates

Figure 5 shows an example trajectory estimate with included landmark observations in the trajectory estimation.

We use the target measurements to the red network points in Figure 5 to formulate the bearing and range factors, include them in the factor graph and perform the trajectory optimization. The factors are visualized in

Figure 5 as red lines connecting landmark target and corresponding trajectory state. The subsequent discussions are made on basis of the chosen trajectory part introduced within this section.

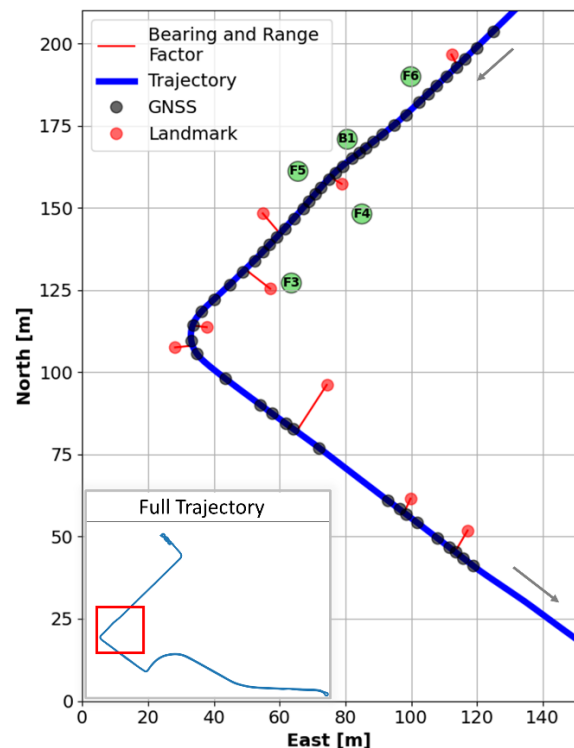


Figure 5. Trajectory state of east and north coordinate (blue), GNSS observations (black, rate: 10 s) and landmarks. Bearing and range factors (red lines) connect landmark and corresponding trajectory states.

#### B. Estimate of Trajectory Variances

The ISAM2 algorithm also provides estimated covariance information for the trajectory states, which allows the evaluation of the precision gain when including the landmark observations. For the analysis we compare the variances of the estimates based on GNSS and IMU measurements only and with the ones where additional target observations are included. The time interval of occurring landmarks and estimated standard deviations of the orientation angles roll, pitch and yaw is visualized in Figure 6. This selected interval corresponds to the trajectory part shown in Figure 5. The yaw angle is clearly improved in precision by about 50% ( $\sim 0.5^\circ$ ) over the whole section compared to the estimation without landmark information. The precision of pitch and roll angle is also improved, but less significant ( $0.01^\circ - 0.02^\circ$ ). Overall, this improvement has not only a positive effect close to the target observations, but also in between of two of them. The overall higher standard deviations in the yaw angle in both estimates compared to roll and pitch can be explained by the non-eccentric mounting of the GNSS antenna, which prevents an indirect observation of the yaw angle by the GNSS positions, resulting in higher standard deviation estimates for yaw.

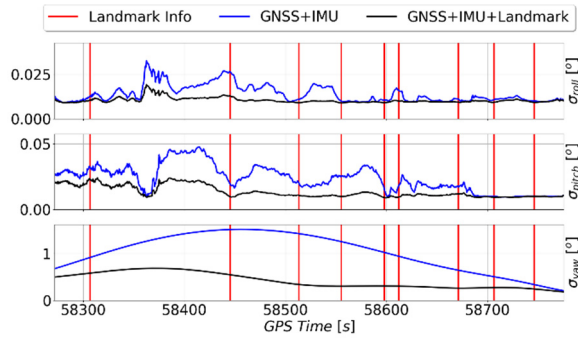


Figure 6. Estimated orientation standard deviations of roll, pitch and yaw angles, GNSS + IMU vs. GNSS + IMU + Landmark. The time interval visualized corresponds to the trajectory section from figure 5. Red lines mark times of landmark observations.

Figure 7 shows for the corresponding time interval for the estimated position standard deviations of the trajectories with and without landmark information. A GNSS position update has been used in the graph every 10 seconds.

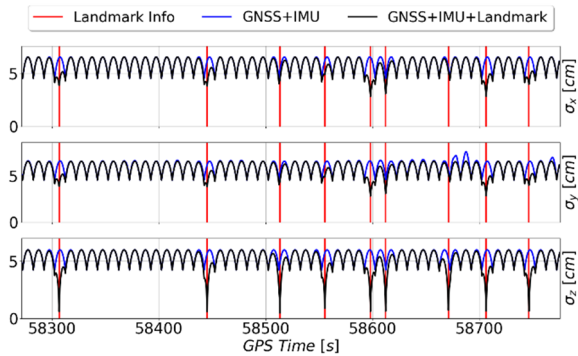


Figure 7. Estimated position standard deviations (X=east, Y=north, Z=height), GNSS + IMU vs. GNSS + IMU + Landmark. The time interval shown corresponds to the trajectory section from figure 4. Red lines mark times of landmark observations.

The arc-like increase of the standard deviations in the position in all three coordinates between two GNSS observations can be explained by the relative propagation of the variances in the IMU preintegration and is about 6 cm in the middle between two GNSS positions. GNSS coordinates are included in the estimation with a standard deviation of 5 cm which indicates a reliable variance propagation of the preintegrated IMU factor.

At the time of landmark observations, the standard deviations can be significantly decreased by about 1-2 cm in east (X) and north (Y). In the ellipsoidal height (Z) a reduction of the standard deviation to about 1 cm can be observed, see Figure 7. Compared to the precision increase of the orientation angles, the observations of landmark targets cause only a local improvement of the precision.

### C. Root Mean Squared Error

So far, we focused entirely on the increase in precision by comparing the variance estimates. In order to be able to make a statement about the point accuracy of MSS, the green reference points shown in Figure 5 are used, known with a standard deviation in the sub-millimeter range due to the network adjustment.

Using the georeferencing Equation 1, the laser scanner measurements to reference points are transformed to the UTM coordinate frame, resulting in the target center coordinates. For evaluation of the increase in accuracy, we analyze the residuals to the reference coordinates. The residuals computed with the trajectory based on GNSS and IMU measurements only and with included bearing and range factors are compared to each other.

In order to visualize the accuracy improvement due to the integration of landmark information, several trajectory estimates are performed with a decreasing number of GNSS position data in the trajectory estimation. For each estimate, the root mean squared error (RMSE) to the reference coordinates is calculated, which is defined by (Eq. 7)

$$RMSE_x = \sqrt{\frac{\sum_{i=0}^N (\hat{x} - x)^2}{N}} \quad (7)$$

in which  $x$  describes the coordinate estimated from the sensor system with the corresponding trajectory estimate and  $\hat{x}$  marks the reference coordinate from the network adjustment. The number of reference points used for RMSE computation is marked by  $N$ .

The results of the RMSE values are shown in Figure 8 for the east, north and ellipsoidal height for one measurement drive. For evaluation we performed several estimation runs and incrementally increased the time between consecutive GNSS position updates from 1 to 50 seconds.

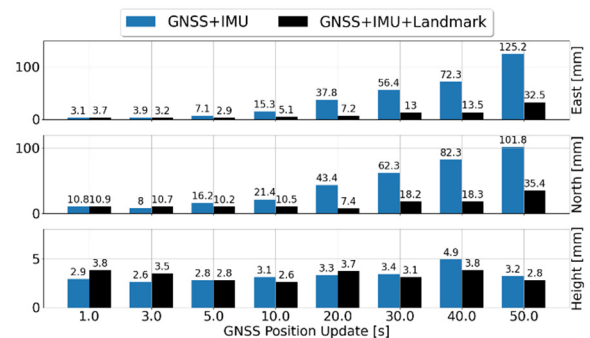


Figure 8. Root mean squared error of georeferenced control points from MSS and reference coordinates from network adjustment (Figure 5, green points). GNSS + IMU vs. GNSS + IMU + Landmark.

Comparing the RMSE values for the coordinates computed with both trajectory estimates in Figure 8 significant differences are observable. The reduction of the height RMSE when inserting landmark information is the smallest with just a few mm and can be considered as barely significant, comparing the RMSE to the estimate without landmark information. A possible reason for this non-significant influence could be the much higher accuracy in the states of the roll and pitch angles, see Figure 6.

In contrast to this observation, we see an increase in RMSE in the X, Y coordinates (north and east), especially detectable when inserting less GNSS position updates in the trajectory estimation. Comparing both estimates at a GNSS position update rate of 30 s the east RMSE can be reduced by about 40 mm, in north a reduction of over 45 mm is visible, when target observations are included into the state optimization, see Figure 8.

The significant increase can be explained by the lower yaw angle precision compared to pitch and roll, see Figure 6. Errors in the yaw angle are directly transferred to the east and north coordinates, resulting in higher errors in these coordinates, when computing the RMSE to the reference coordinates. Please note, that the result only shows one particular measurement and that the maximal achieved accuracy may vary, depending on the GNSS conditions at the particular time and location of this measurement.

#### IV. SUMMARY AND OUTLOOK

Using the graph-based approach of trajectory estimation, landmark information can be easily incorporated as bearing and range factor in the trajectory estimation.

The analysis of the accuracy gains by including landmark target information have shown a significant improvement of the yaw angle precision. A significant increase in roll and pitch angle accuracy could not be demonstrated. Improvements in position coordinates have only local effect compared to improvements of the angle variance estimates.

The analysis of the root mean squared error when comparing to known reference coordinates results in lower values for the east and north coordinates, but not for the height residuals. This is especially valid when the number of GNSS observations are decreased in the trajectory estimation procedure.

With this study we showed, that it can be beneficial for the accuracy of the trajectory estimation of a mobile mapping system, when additional information from known landmarks are included into the estimation. This is especially valid, when GNSS observations are less often available. We also presented a procedure how this can be realized, using a graph-based optimization approach. As the trajectory accuracy directly transfers to the accuracy of the resulting point cloud we can assume, that deformations can be better detected. In

an extension of the work, we will evaluate the resulting point cloud using reference information.

#### V. ACKNOWLEDGEMENTS

Funding: This work was funded by the Deutsche Forschungsgemeinschaft (DFG, German Research Foundation) under Germany's Excellence Strategy-EXC 2070-390732324.

#### References

- Chang, L., Niu, X., Liu, T., Tang, J., and Qian, C. (2019). GNSS/INS/LiDAR-SLAM integrated navigation system based on graph optimization. *Remote Sensing*, 11(9), 1009.
- Choudhary, S., Indelman, V., Christensen, H. I., and Dellaert, F. (2015, May). Information-based reduced landmark SLAM. In *2015 IEEE International Conference on Robotics and Automation (ICRA)* (pp. 4620-4627). IEEE.
- Dellaert, F. (2012). *Factor graphs and GTSAM: A hands-on introduction*. Georgia Institute of Technology.
- Dellaert, F., and Kaess, M. (2017). Factor graphs for robot perception. *Foundations and Trends® in Robotics*, 6(1-2), pp. 1-139.
- Eling, C., Klingbeil, L., and Kuhlmann, H. (2015). A direct georeferencing system for real-time position and attitude determination of lightweight UAVs. In *FIG Working Week*.
- Forster, C., Carlone, L., Dellaert, F., and Scaramuzza, D. (2016). On-manifold preintegration for real-time visual-inertial odometry. *IEEE Transactions on Robotics*, 33(1), pp. 1-21.
- Forster, C., Carlone, L., Dellaert, F., and Scaramuzza, D. (2015). On-manifold preintegration theory for fast and accurate visual-inertial navigation. *IEEE Transactions on Robotics*, 1-18.
- Groves, P. D. (2015). *Principles of GNSS, inertial, and multisensor integrated navigation systems*, [Book review]. *IEEE Aerospace and Electronic Systems Magazine*, 30(2), pp. 26-27.
- Heinz, E., Eling, C., Wieland, M., Klingbeil, L., and Kuhlmann, H. (2015). Development, calibration and evaluation of a portable and direct georeferenced laser scanning system for kinematic 3D mapping. *Journal of Applied Geodesy*, 9(4), pp. 227-243.
- Heinz, E., Eling, C., Klingbeil, L., and Kuhlmann, H. (2020). On the applicability of a scan-based mobile mapping system for monitoring the planarity and subsidence of road surfaces-Pilot study on the A44n motorway in Germany. *Journal of Applied Geodesy*, 14(1), pp. 39-54.
- Indelman, V., Williams, S., Kaess, M., and Dellaert, F. (2013). Information fusion in navigation systems via factor graph based incremental smoothing. *Robotics and Autonomous Systems*, 61(8), pp. 721-738.
- Kaess, M., Johannsson, H., Roberts, R., Ila, V., Leonard, J., and Dellaert, F. (2011, May). iSAM2: Incremental smoothing and mapping with fluid relinearization and incremental variable reordering. In *2011 IEEE International Conference on Robotics and Automation* (pp. 3281-3288). IEEE.
- Kaess, M., Johannsson, H., Roberts, R., Ila, V., Leonard, J. J., and Dellaert, F. (2012). iSAM2: Incremental smoothing and mapping using the Bayes tree. *The International Journal of Robotics Research*, 31(2), pp. 216-235.



- Neuner, H., Holst, C., and Kuhlmann, H. (2016). Overview on current modelling strategies of point clouds for deformation analysis. *Allgemeine Vermessungs-Nachrichten: AVN; Zeitschrift für alle Bereiche der Geodäsie und Geoinformation*, 123(11-12), pp. 328-339.
- Paffenholz, J. A. (2012). *Direct geo-referencing of 3D point clouds with 3D positioning sensors* (Doctoral dissertation, Hannover: Gottfried Wilhelm Leibniz Universität Hannover).
- Setterfield, T. P., Miller, D., Leonard, J. J., and Saenz-Otero, A. (2017, March). Smoothing-based estimation of an inspector satellite trajectory relative to a passive object. In *2017 IEEE Aerospace Conference* (pp. 1-11). IEEE.
- Shan, T., Englot, B., Meyers, D., Wang, W., Ratti, C., and Rus, D. (2020, October). Lio-sam: Tightly-coupled lidar inertial odometry via smoothing and mapping. In *2020 IEEE/RSJ international conference on intelligent robots and systems (IROS)* (pp. 5135-5142). IEEE.
- Strode, P. R., and Groves, P. D. (2016). GNSS multipath detection using three-frequency signal-to-noise measurements. *GPS solutions*, 20(3), pp. 399-412.
- Xu, X., Bureick, J., Yang, H., and Neumann, I. (2018). TLS-based composite structure deformation analysis validated with laser tracker. *Composite Structures*, 202, pp. 60-65.
- Zimmermann, F., Eling, C., and Kuhlmann, H. (2017). Empirical assessment of obstruction adaptive elevation masks to mitigate site-dependent effects. *GPS Solutions*, 21(4), pp. 1695-1706.

## Assessing sandy beach width variations on intertidal time scales using permanent laser scanning

Mieke Kuschnerus<sup>1</sup>, Roderik Lindenbergh<sup>1</sup>, Sierd de Vries<sup>2</sup>

<sup>1</sup> Department of Geoscience and Remote Sensing, Delft University of Technology, Stevinweg 1, 2628 CN Delft, The Netherlands, ([m.kuschnerus@tudelft.nl](mailto:m.kuschnerus@tudelft.nl); [r.c.lindenbergh@tudelft.nl](mailto:r.c.lindenbergh@tudelft.nl))

<sup>2</sup> Department of Hydraulic Engineering, Delft University of Technology, Stevinweg 1, 2628 CN Delft, The Netherlands, ([sierd.devries@tudelft.nl](mailto:sierd.devries@tudelft.nl))

**Key words:** *permanent laser scanning; long term monitoring; coastal deformation; change detection*

### ABSTRACT

Coastal zones are highly dynamic, and their topography is subject to constant deformation. These deformations are governed by sediment transports that are forced by environmental conditions of waves, tides and wind which result in topographic changes at various spatial and temporal scales. In the view of climate change and intensification of extreme weather events, it is important for coastal management to monitor the deformation and coastal topography with high accuracy. To demonstrate a novel way of deriving these deformations and of analyzing the underlying processes, we use permanent laser scanning (PLS) to monitor part of the typical urban coastal beach in Noordwijk, The Netherlands. A laser scanner permanently installed on a hotel building acquired one 3D point cloud of the sandy beach and dunes every hour, continuously, for a duration of two years. The resulting spatio-temporal data set consists of ~ 15 000 point clouds and contains the evolution of a section of the coast of ~ 1 km length at great detail. The elevation changes are observed at centimeter level, allowing to monitor even small scale and slow processes. However, this information is not readily available from the extensive data set. By deriving digital elevation models (DEMs) from each point cloud and collecting elevation data as time series per spatial grid cell, we structure the data in an efficient way. We use the DEMs to estimate two parameters describing the coastal deformation, beach width and intertidal width. We also extract the shoreline at low and high tide for a part of the data set and estimate beach width and intertidal width from them. We find that heavy storms influence the location of the shoreline and the intertidal width in particular. Ultimately, the estimated beach width and intertidal width at high temporal frequency (monthly) and with high spatial accuracy (meters) helps coastal management to improve the understanding of coastal deformation processes.

### I. INTRODUCTION

#### A. Background

Sandy coasts are very dynamic areas, undergoing constant topographic changes. Observation of specific topographic deformations in these areas are of great importance for coastal maintenance and research. The long-term development of the coast is closely followed by the establishment and analysis of so-called coastal state indicators (CSI). Examples are the width of the beach and dune volume (Davidson *et al.*, 2007; Van Koningsveld *et al.*, 2005). The importance to quantify beach width and derive optimal/acceptable values for coastal management was stressed by (Tucker *et al.*, 2019). Also, the long-term development of beach width has been related to dune evolution (Galiforni Silva *et al.*, 2019).

Different types of data are used to quantify these CSIs. Observations range from satellite data (large scale, medium to high temporal frequency) to in-situ

measurements (small scale, local, low temporal frequency/incidental). In the middle of this spectrum lays permanent laser scanning (PLS). PLS makes use of a permanently installed programmable laser scanner to observe small-scale changes (theoretically up to cm range) at high temporal frequency (up to hourly). The changes in CSIs discussed in this article are in the range of several decimetres to meter due to lower point spacing at the edges of the point clouds and high variability of the shoreline due to waves.

The resulting data set contains a large number of consecutive point clouds and thus provides a 3D representation of a section of the coast and its evolution over time. This source of information on deformations and processes is comprehensive, but the analysis of CSIs is not immediate. The subject of this research is to make information on the evolution of the coast from PLS data accessible in the form of coastal state indicators.

## B. Research Questions

In this work we are analysing the possibilities to estimate two coastal state indicators that give indications on the development of a sandy beach with permanent laser scanning, by answering the following research questions:

1. How can the width of the beach be detected automatically from laser scanning point clouds?
2. How can we detect the separation between dry beach and intertidal area?
3. How do extreme weather conditions influence these parameters?

To answer these questions, we derive digital elevation models, estimate the extent of the point clouds and locate the approximate shoreline at high tide and low tide per month.

## C. Related Work

Beach width is mentioned by (Van Koningsveld *et al.*, 2005) as a coastal state indicator, relevant for coastal management as recreational factor as well as for disaster prevention. Optimal values for recreational use were derived by (Tucker *et al.*, 2019). Definition of coastal state indicators and the observation of the coast with regular imaging from fixed positions have been studied for example by (Davidson *et al.*, 2007). Additional studies deriving coastal state indicators for the Dutch coast have been presented by (Giardino *et al.*, 2014) and (Jimenez *et al.*, 2007). The latter derived automatic methods to estimate beach visitor distribution from video images of the beach. Also, CSIs are an important tool for the Dutch Ministry of Infrastructure and Water Management to make decisions about coastal management, for example about the necessity and quantity of beach nourishments.

A long-term study on monitoring the position of the shoreline with the help of laser scanning data was performed by (Caudle *et al.*, 2019) for a part of the Texan coast in the US over a period of 13 years. (Castelle *et al.*, 2021) presented a method to monitor the long-term development of the shoreline on a part of the French coast from satellite data. Next to satellite image data they made use of wave and tide hindcast data to limit the considerable uncertainty that resulted from large tidal ranges and relatively low-resolution satellite images. Beach width is estimated from yearly JARKUS data by (Keijsers *et al.*, 2014) and related to dune development by (Galiforni Silva *et al.*, 2019). The study of (Van IJsendoorn *et al.* 2021) makes use of JARKUS data to quantify dune growth and relates it to sea level rise.

A study of the set-up of a permanent laser scanner with the same equipment as used for this research was presented by (Vos *et al.*, 2022). The resulting data set has subsequently been analysed to detect 4D objects of change (Anders *et al.*, 2020), and change pattern with

the help of k-means clustering (Kuschnerus *et al.*, 2021). The latter resulted in a separation between a cluster dominated by erosion in the intertidal area and a relatively stable cluster on the dry part of the beach.

## D. Data Set

The data set used for this research is a selection of 3D point clouds out of an hourly data set covering two years of permanent laser scanning. The data set is acquired with a RieglVZ-2000 laser scanner mounted on the balcony of Grand Hotel Huis ter Duin in Noordwijk, The Netherlands. It is overlooking a section of the coast, including an about 1km long part of dunes and beach. The coast consists of dunes and a sandy beach that is varying in size (width and height) depending on tides, wave heights and weather conditions and human (maintenance) activities.

Our study covers the period of 1<sup>st</sup> January 2020 until end of April 2020. This period includes three major storms, on 9/10 February, 17/18 February, and 22/23 February 2020.

Each point of the point cloud is represented by 3D coordinates (x,y,z-coordinates). For each point cloud the respective inclination angles (pitch and roll) of the laser scanner at the time are recorded by the internal inclination sensors of the laser scanner. These angles are used to correct each point cloud for small deviations due to changes in the tilt and orientation of the laser scanner.

We make use of tide data consisting of hourly measured water levels above NAP, collected and distributed by the Dutch Ministry of Infrastructure and Water Management (Rijkswaterstaat, 2022) at Scheveningen, a coastal city about 20 km south of Noordwijk.

## II. METHODS

The methods are presented in three parts. First, we explain the pre-processing steps that we take to prepare the data set, then we present two different methods to derive the beach width and the width of the intertidal area.

### A. Pre-processing

In a first step we loop through each point cloud of the four-months data set, get the inclination values and align the data with a simple rotation matrix based on the pitch and roll values per scan. Then we remove all points with z-coordinates larger than 20 m and x-coordinates larger than -100 m, as they are not part of the beach. Of this reduced point cloud, we generate a digital elevation model (DEM) with 1 m x 1 m regular grid parallel to the coastline taking the mean elevation of all grid cells that contain at least one point (for an overview see Figure 1).

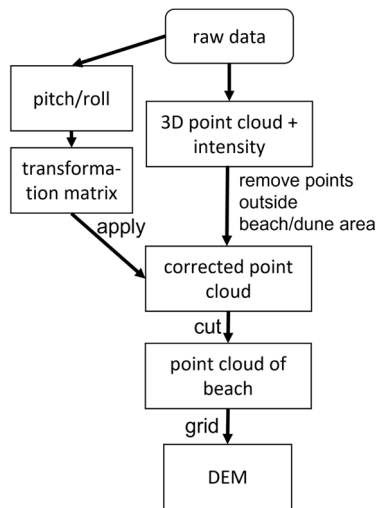


Figure 1. Schematic of pre-processing steps from raw data to DEM applied to each individual point cloud.

### B. Estimating Beach Width and Intertidal Width directly from DEMs

The waterfront is roughly perpendicular to the 0°-scan-line (see Figure 2). Further, we assume that the dune foot is constant throughout our observation period at an x-coordinate of about -145 m in the local coordinate system of the laser scanner (see Figure 2). The exact location of the border between the dunes and the beach is not covered by our data set, due to the dunes blocking the sight of the dune foot.

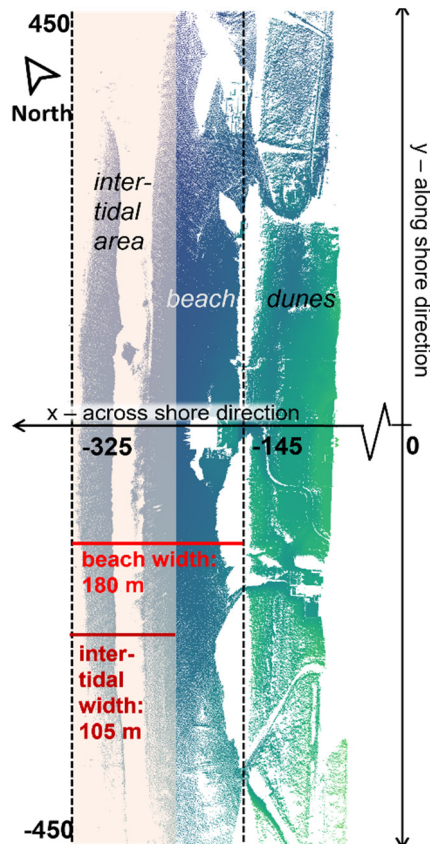


Figure 2. Point cloud of beach and dunes in Noordwijk on 01-01-2020 at 15:00, coloured with elevation. The estimated width of the beach and width of the intertidal area are shown as an example.

We define the sandy beach as the part of the beach that is more than 145 m (approximate location of the dune foot) away from the laser scanner, which means, all points of the point clouds with x-coordinate smaller than -145. The observed part of the beach is limited by the range of the laser scanner, and we discard areas with very low point density. We consider the area within 450 m along shore to the North and South of the laser scanner (*i.e.*, all points with y-coordinate:  $-450 \leq y \leq 450$ ). The dry part of the beach is the sandy beach that is never covered by high tides and therefore mostly dry, unless it is raining. The width of the beach is the distance in x-direction between the dune foot (estimated to be at -145 m in local scanner coordinate system) and the point on the beach with the lowest x-coordinate at the lowest water level during one day. This means that the beach width is determined only by the variability of the water height. The most seawards border between the water and the sandy beach at that time is the shoreline at low tide.

The shoreline at high tide is the line between water and sandy beach at the highest water level per day. The area between the low tide shoreline and the high tide shoreline is what we call the intertidal area in this article. The width of the intertidal area is the across shore distance between the highest point of the high tide shoreline and the lowest point of the low tide shoreline (see Figure 2 for an illustration).

To estimate the width of the beach and the width of the intertidal area, as well as the approximate location of the high tide shoreline, we remove all columns of the DEM with less than ten non-empty grid cells. Then we extract the lowest x-coordinate from each generated DEM. We save this minimal x-coordinate per DEM and find the smallest minimal x-coordinate and the largest minimal x-coordinate per day and save the times at which they occurred. This provides an estimate of the times of low and high tide.

By subtracting the smallest minimal x-coordinate from the location of the dune foot, we get the estimated beach width for that day. Deriving the difference between this value and the largest minimal x-coordinate per day we get an estimated width of the intertidal area. Both estimated widths are in meters resolution because of the size of the grid cells of the DEM.

To filter the results for the most reliable values, we check if the estimated smallest beach width per day and largest beach width per day match the actual low and high tides. We compare the times that the respective point clouds were taken with the tide data from (Rijkswaterstaat, 2022). If these times roughly match, *i.e.* agree within a threshold of two hours, we assume that the estimated beach width is close to the actual width of the beach at the lowest water level on that day. If the times disagree, we discard the beach width for that day. Subsequently we use the remaining points to calculate the average width of the beach and average width of the intertidal area per month.

### C. Estimating Shoreline at High and Low Tide

As an alternative method we use the data from Rijkswaterstaat to select the point cloud that resulted from a scan closest to the time of highest tide and lowest tide per day. From this selection of point clouds, we generate DEMs as described above and get the location of the shoreline as the grid cells that are at the border of the DEM in x-direction. This provides two shorelines per day, one at high tide and one at low tide. Each shoreline is then filtered for extreme outliers.

We collect all shorelines at high tide for one month and take the most landwards point for each alongshore position to derive the high tide shoreline of that month. From all shorelines at low tide, we use the most seaward point for each alongshore location to derive the low tide shoreline of that month. Then we fit a second-degree polynomial to both of these shorelines and estimate the beach width and the width of the intertidal area per month from the extremum of the fitted curves.

## III. RESULTS

The results are presented in three parts. We first analyse the estimated width of the beach and the intertidal area from the direct method. Then we present the results of the estimation of the shorelines and subsequently we compare both methods over the entire period of January to April 2020.

### A. Estimation of Beach Width

The beach width was estimated for January and February 2020 as described above and is shown in Figure 3. The beach width is varying between 150 m and 250 m and the width of the intertidal area between 50 m and 180 m for most days. The estimated times of high tide and low tide match the times from the tide data of Rijkswaterstaat on 24 days in a two-months period. This indicates that our method to find the point cloud with the largest extend of the beach is not optimal, and most likely misrepresents the estimated widths in 60 % of the cases. It can be seen clearly that the width of beach and intertidal area both vary more in February than in January.

There are many factors that influence the extend of a point cloud next to the actual water height. Weather conditions such as heavy rain and low visibility due to fog can reduce the size of the visible part of the beach. Figure 4 shows a point cloud at high tide during a storm in February 2020, we can see the large number of points resulting from reflections of the high waves.

To further investigate reasons for inaccurate beach width estimations, we plot all the high tide shorelines and all the low tide shorelines for January 2020 as shown in Figures 5 and 6. It can be seen clearly in Figure 5 that reflections from high waves especially during high tides are mistaken for parts of the beach, disturbing the estimated low tide shoreline.

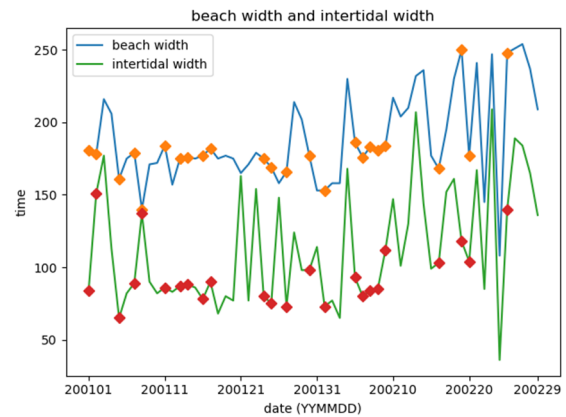


Figure 3. Width of the beach and the intertidal area estimated from the largest and smallest point clouds per day. The estimates where both high tide and low tide matches the time of the tide data from Rijkswaterstaat are marked with a diamond.

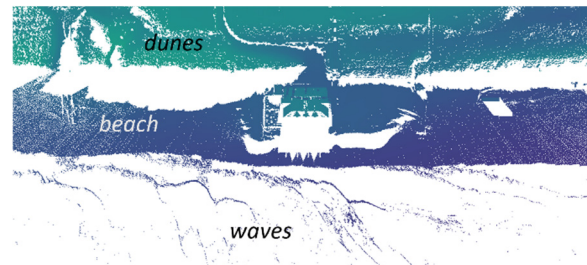


Figure 4. Point cloud at high tide on 10-02-2020 during a heavy storm. A large part of the beach is covered with water. Reflection of the waves can clearly be seen.

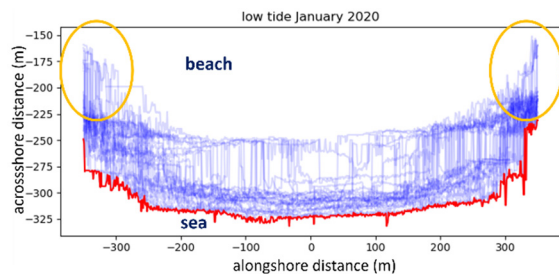


Figure 5. All estimated shorelines at high tide in January 2020 with the minimum of all lines marked in red. The outliers due to high waves are circled yellow.

In Figure 6 we clearly see the effects of the lower point density with increasing range around 400 m. This leads to an artificial border of the point cloud that is mistaken as part of the low tide shoreline.

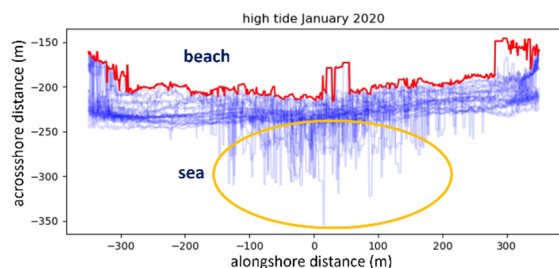


Figure 6. All estimated shorelines at low tide in January 2020 with the minimum of all lines marked in red. The areas circled in yellow show the effect of reduced point density in the point cloud around 400 m range.

## B. Comparison

We fit a curve (2<sup>nd</sup> degree polynomial) through the high and low tide shorelines and use the local minimum of this curve to derive an alternative estimate for the monthly beach and intertidal width. These are shown for January and February 2020 in Figures 7 and 8.

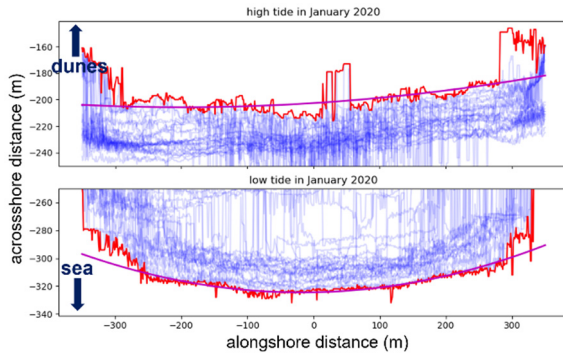


Figure 7. Curve (in purple) fitted through minimal low tide shoreline and maximal high tide shoreline for the estimation of beach width and intertidal width in January 2020.

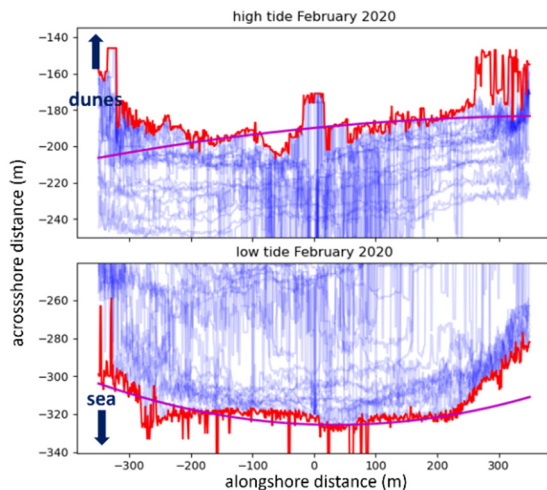


Figure 8. Curve (in purple) fitted through minimal low tide shoreline and maximal high tide shoreline for the estimation of beach width and intertidal width in February 2020.

From the estimated width as presented in Section III A, the average beach width in January 2020 is 173 m and the estimated width of the intertidal area is 92 m. From the high and low tide shorelines shown in Figure 7 we estimate the total beach width for January 2020 around 179 m and the width of the intertidal area 119 m.

For February 2020 we estimated an average beach width of 191 m, considerably larger than in January and an intertidal width of 99 m. With the high and low tide shorelines as shown in Figure 8 we derive a beach width of 180 m and an intertidal width of 137 m. We can clearly see the effect of the extreme weather here. If we take the extend of all the shorelines as an indication for the uncertainty of the monthly shoreline, there is a much higher uncertainty in February than in January. Both high and low tide shoreline are varying much more

and cannot be distinguished as easily from their location on the beach alone.

As shown in Table 1, the width estimated by both methods do not match for every month. Note that the width of the intertidal area is considerably smaller in March and April than in January and February, which we attribute to the extreme stormy weather conditions, especially in February.

Table 1. Table with estimated beach width and intertidal width from two different methods

Month	Width estimated directly from point clouds [m]		Width estimated from high and low tide shorelines	
	Beach	Intertidal	Beach	Intertidal
January 2020	173	92	179	119
February 2020	191	99	180	137
March 2020	190	103	196	141
April 2020	197	97	191	116

## IV. DISCUSSION

We present two different methods to estimate the width of the beach directly from DEMs from point clouds from PLS, by evaluating the maximal width of smallest and largest point cloud per day as well as by extracting the location of the high and low tide shoreline and comparing these.

Both methods have their draw backs. They often mistake reflections from high waves, especially at high tide, as parts of the beach leading to overestimated width, or unrealistic peaks in the high and low tide shorelines. Additionally, weather conditions like dense fog or heavy rain, limit the extend of the point clouds and therefore lead to erroneous estimations. Overall, the method of first estimating high and low tide shorelines appears more reliable than the ‘direct’ method. Additional smoothing/filtering applied to the high and low tide shorelines could even further improve the results. Further, filtering the lines with too many outliers will lead to additional improvement.

Another way to validate our estimations of beach width, is the comparison with estimations from camera images. This validation is part of the ongoing research and will be presented in future publications.

The z-coordinate or elevation of the minimal x-coordinate and the entire high and low tide shorelines has not been considered for this research. Including this additional information, could potentially improve the beach width estimation, as well as deliver more insights into the coastal change detection. The estimation of beach runup due to waves and wind setup is another open question to be considered during future analysis of the PLS data set.

As presented by (Kuschnerus *et al.*, 2021) a clustering approach was used on the time series derived from daily point clouds for a similar dataset of the coast in Kijkduin, The Netherlands. This method was applied here as well, as an example for the month of January (see Figure 9). The resulting clusters can be used to find

the border between eroding and accreting areas, which roughly corresponds with the location of the high water line. Therefore, this method, with some more refinement can potentially provide another alternative to derive the beach and intertidal width and compare with the methods presented here.

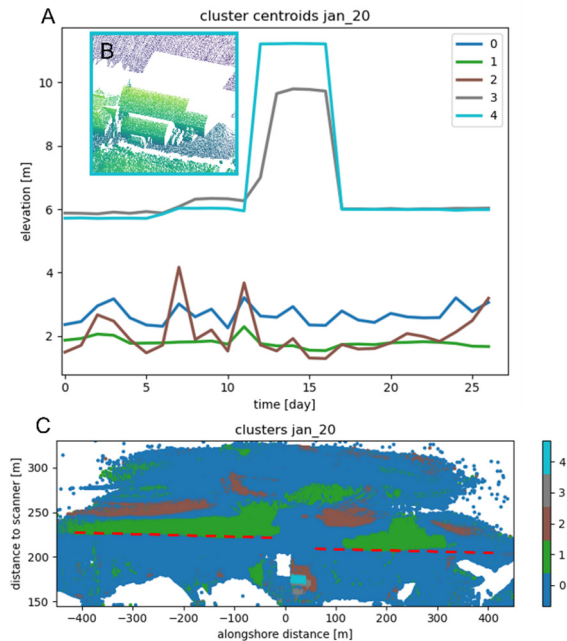


Figure 9. k-means clustering for January 2020. A: Mean time series per cluster, with peak in clusters 3 and 4, caused by tents. B: Point cloud with tents. C: Point cloud coloured by cluster with estimated border between dry beach and intertidal area shown as dashed line in red.

## V. CONCLUSION

This research presents the estimation of two CSIs: beach width and intertidal width from PLS data, to quantify the deformation of a typical coastal beach in The Netherlands. We derived two methods to estimate both CSIs from DEMs of the 4D point cloud data set. High waves and other extreme weather conditions, like fog and heavy rain lead to inexact estimations of both beach width and intertidal width. However, when considering the results for the entire month, we obtain valid estimates varying between 173 m and 197 m (beach width) and between 92 m and 141 m (intertidal width). The heavy storms in February influence the uncertainty of the estimation and render it less reliable. Future research will include the estimation of wave runoff and make use of the elevation of the shorelines to improve the estimates for beach width and intertidal width, as well as the entire coastal deformation. A possible extension of this research is the inclusion of the clustering of time series from PLS data. Ultimately, the quantification of CSIs from PLS data at high temporal frequency (monthly) and with high spatial accuracy (meters) will improve understanding of coastal deformation and support coastal management.

## VI. ACKNOWLEDGEMENTS

The authors would like to thank Grand Hotel Huis ter Duin for their cooperation. This research has been supported by the Netherlands Organization for Scientific Research (NWO, grant no. 16352) as part of the Open Technology Programme and by Rijkswaterstaat (Dutch Ministry of Infrastructure and Water Management).

## References

- Anders, K., Winiwarter, L., Lindenbergh, R., Williams, J.G., Vos, S.E., and Höfle, B. (2020). 4D objects-by-change: Spatiotemporal segmentation of geomorphic surface change from LiDAR time series. *ISPRS Journal of Photogrammetry and Remote Sensing*, 159, pp. 352–363.
- Castelle, B., Masselink, G., Scott, T., Stokes, C., Konstantinou, A., Marieu, V., and Bujan, S. (2021). Satellite-derived shoreline detection at a high-energy meso-macrotidal beach. *Geomorphology* 107707.
- Caudle, T.L., Paine, J.G., Andrews, J.R., and Saylam, K. (2019). Beach, Dune, and Nearshore Analysis of Southern Texas Gulf Coast Using Chiroptera LIDAR and Imaging System. *Journal of Coastal Research* 35, pp. 251–268
- Davidson, M., Van Koningsveld, M., de Kruijff, A., Rawson, J., Holman, R., Lamberti, A., Medina, R., Kroon, A., and Aarninkhof, S. (2007). The CoastView project: Developing video-derived Coastal State Indicators in support of coastal zone management. Coastal Engineering. *The CoastView Project: Developing coastal video monitoring systems in support of coastal zone management* 54, pp. 463–475.
- Galiforni Silva, F., Wijnberg, K.M., de Groot, A.V., and Hulscher, S.J.M.H. (2019). The effects of beach width variability on coastal dune development at decadal scales. *Geomorphology* 329, pp. 58–69.
- Giardino, A., Santinelli, G., and Vuik, V. (2014). Coastal state indicators to assess the morphological development of the Holland coast due to natural and anthropogenic pressure factors. *Ocean & Coastal Management* 87, pp. 93–101.
- Jiménez, J.A., Osorio, A., Marino-Tapia, I., Davidson, M., Medina, R., Kroon, A., Archetti, R., Ciavola, P., and Aarninkhof, S.G.J. (2007). Beach recreation planning using video-derived coastal state indicators. Coastal Engineering. *The CoastView Project: Developing coastal video monitoring systems in support of coastal zone management* 54, pp. 507–521.
- Keijsers, J. G. S., Poortinga, A., Riksen, M. J. P. M., and Maroulis, J. (2014). Spatio-Temporal Variability in Accretion and Erosion of Coastal Foredunes in the Netherlands: Regional Climate and Local Topography. *PLOS ONE* 9, e91115 (2014).
- Kuschnerus, M., Lindenbergh, R., and Vos, S. (2021). Coastal change patterns from time series clustering of permanent laser scan data. *Earth Surface Dynamics*, 9(1), pp. 89–103.
- Rijkswaterstaat, (2022). Dutch Ministry of Infrastructure and Water management. Available in url: <https://www.rijkswaterstaat.nl/water/waterdata-en-waterberichtgeving/waterdata/getij>
- Tucker, T.A., Carley, J.T., Couriel, E.D., Phillips, M.S., and Leaman, C.K. (2019). Seawalls and acceptable beach width for public amenity. *Australasian Coasts and Ports 2019*

*Conference: Future directions from 40 [degrees] S and beyond, Hobart, 10-13 September 2019, 1158.*

Van IJzendoorn, C. O., de Vries, S., Hallin, C., and Hesp, P. A. (2021). Sea level rise outpaced by vertical dune toe translation on prograding coasts. *Sci Rep* 11, 12792.

Van Koningsveld, M., Davidson, M.A., and Huntley, D.A. (2005). Matching Science with Coastal Management Needs: The Search for Appropriate Coastal State Indicators. *Journal of Coastal Research* pp. 399–411.

Vos, S., Anders, K., Kuschnerus, M., Lindenbergh, R., Höfle, B., Aarninkhof, S., and de Vries, S. (2022). A high-resolution 4D terrestrial laser scan dataset of the Kijkduin beach-dune system, *The Netherlands. Sci Data* 9, 191.



## Integrated survey approaches for monitoring procedures during yard phases

Awal Rahali<sup>1</sup>, Eva Savina Malinverni<sup>1</sup>, Roberto Pierdicca<sup>1</sup>, Alessio Pierdicca<sup>2</sup>, Gabriele Potenza<sup>3</sup>, Matteo Lucesoli<sup>4</sup>

<sup>1</sup> Dipartimento di Ingegneria Civile Edile e Architettura, Università Politecnica delle Marche, Ancona, Italy, ([a.rahali@pm.univpm.it](mailto:a.rahali@pm.univpm.it); [e.s.malinverni@staff.univpm.it](mailto:e.s.malinverni@staff.univpm.it); [r.pierdicca@staff.univpm.it](mailto:r.pierdicca@staff.univpm.it))

<sup>2</sup> Capstudio, Piazza del Plebiscito 21, Ancona, Italy, ([a.pierdicca@capstudio.eu](mailto:a.pierdicca@capstudio.eu))

<sup>3</sup> Microgeo Srl, Via Petrarca 42, Campi Bisenzio, Firenze, Italy, ([g.potenza@microgeo.it](mailto:g.potenza@microgeo.it))

<sup>4</sup> Geomax Srl, Via dell'Agricoltura 9, Falconara, Ancona, Italy, ([matteo.lucesoli@geomax-positioning.it](mailto:matteo.lucesoli@geomax-positioning.it))

**Key words:** *deformation measurements; structural monitoring; sensors; topographic survey; construction site*

### ABSTRACT

Buildings, construction sites and civil structures need an accurate, continuous, and real time monitoring system. This necessity arises to detect dangerous situations for the structures and any occupant, especially during natural or anthropogenic events such as earthquakes or delicate phases of invasive operations such as excavations for piling. During these situations, the static and dynamic conditions of a structure and everything related to it could be impaired. The analysis and evaluation of significant displacements and deformation parameters, which are fundamental for structural controls and health monitoring, can be approached following different exchangeable procedures. Among the non-destructive monitoring techniques used in recent years, such as in this research, wireless sensors, are having a remarkable development in detecting anomalies. The acquisition of significant deformation parameters is obtained starting from the traditional topographic survey by total station and using static and dynamic sensors. Monitoring equipment concerns three-axial wireless tiltmeters which allow to measure accurately any angle of inclination in the points where they are installed in order to monitor kinematic movements during yard phases. The main purpose of this experiment is to compare data collected by tiltmeters with those obtained by the robotic total station. Three-axial accelerometers are also installed to obtain the acceleration value of the different reference points. By processing the collected data, it is proved that the final results are comparable, despite using different and completely independent monitoring systems. These integrated survey approaches demonstrate the effectiveness and efficiency of designing a monitoring system based on sensors that are installed to observe changing phenomena over the time, especially during delicate phases of invasive operations, which may represent a more widespread low-cost and reliable solution.

### I. INTRODUCTION

Monitoring of the impact of the high-risk works on the environment is one of the most important elements enabling the safe implementation of projects. So, it is necessary to strengthen monitoring during the construction period, especially if it concerns the risk of structural failure of adjacent existing structures (Zhang, *et al.*, 2020). The trend of a health monitoring system started getting attention in the last decades of the previous millennium after catastrophic events, like the Japanese earthquakes, which damaged and destroyed thousands of buildings (Mita, 1999). Monitoring operations are then necessary to guarantee health and safety conditions by detecting instabilities or controlling the evolution of deformation patterns (Di Stefano *et al.*, 2020). After the most recent drastic events in Italy, such as the collapse of the Morandi Bridge in Genoa, there is a growing attention to prevention, so an increasing focus on preventive maintenance (Morgese *et al.*, 2020; Domaneschi *et al.*, 2021; Petito *et al.*, 2019). In order to

increase the investments dedicated to prevention, several Italian engineering companies are allowed to take benefits from bonuses for buildings rehabilitation. One of these is the Decreto Rilancio n. 34/2020, so-called Superbonus 110%, which aims to relaunch the building sector by favoring the anti-seismic requalification of the building heritage and favoring the economy with its advantages (Artese *et al.*, 2021). For this reason, it is possible to integrate construction works with a monitoring system that gives information on the structural performance during the various stages of work by taking advantage of the existing tax reduction. For this reason, and because of the high risk for structures and infrastructures, an elaborate monitoring system can allow a careful predictive and preventive analysis of structural damage, so as to direct the authorities towards more adequate and timely interventions. A network of sensors for the displacement and deformation's monitoring of various engineering infrastructures is a nowadays very important issue (Antunes *et al.*, 2012).

Recent Structural Health Monitoring (SHM) applications in civil infrastructures pointed out the uniqueness of each structure and the importance of long-term evaluation of the structural performance (Aktan *et al.*, 2000). Furthermore, the effectiveness of a monitoring procedure is better when it is supported by the continuity and the accessibility of performance's data collected in real time (Brownjohn *et al.*, 2008; Brownjohn *et al.*, 1998).

Given the above, the proposed monitoring system was executed by using three non-destructive techniques: i) a topographical survey, ii) wireless tiltmeters and iii) triaxial accelerometers. The first two systems were paired, in order to compare the accuracy and the reliability of the acquired data. Besides, a vibration velocity for the worksite was also derived using triaxial accelerometers, placed to complete the proposed monitoring system and with which they were evaluated for making a comparison to the reference values. Therefore, the main goal of this ecosystem is to create an interoperability framework involving these monitoring systems for data acquisition, evaluation and management, also supported by the advances provided by the Internet of Things (IoT) for the SHM solutions.

## II. OVERVIEW OF THE STUDY CASE

Starting from the necessity of a comprehensive survey of a construction site, the subject of this research work is a civil building which needs to be monitored due to its proximity to a demolition area. Specifically, we have focused on monitoring the structural performance of the building's high wall adjacent to the site (Figure 1). So, starting from the demolition works, the aim is to establish an initial situation and the subsequent presence of possible problems with the area affected by a future excavation for a pile work construction.

The absence of a dividing element or seismic joint between the monitored wall and the adjacent building that has to be demolished, it made the operation particularly critical, so a great care was taken for both structures during the demolition phase, thanks also to the monitoring system installed nearby. Observations and measurements (*e.g.* acceleration values (Figures from 2 to 5), angles of inclination (Figures 6 and 7), horizontal and vertical displacements (Figures 8 and 9) and velocity time response (Figures from 10 to 13)) were also carried out during excavation phase for the construction of the piles. So, a special attention was given to also this phase. In fact, very often, during excavation works the level of the trench bottom is lower than the existing foundation level of the adjacent structures which are therefore very sensitive to any horizontal displacements and settlements resulting from the works in progress whereby very strict restrictions in this respect are imposed (Lupieżowicz, 2021).



Figure 1. The wall to be monitored adjacent to the building to be demolished.

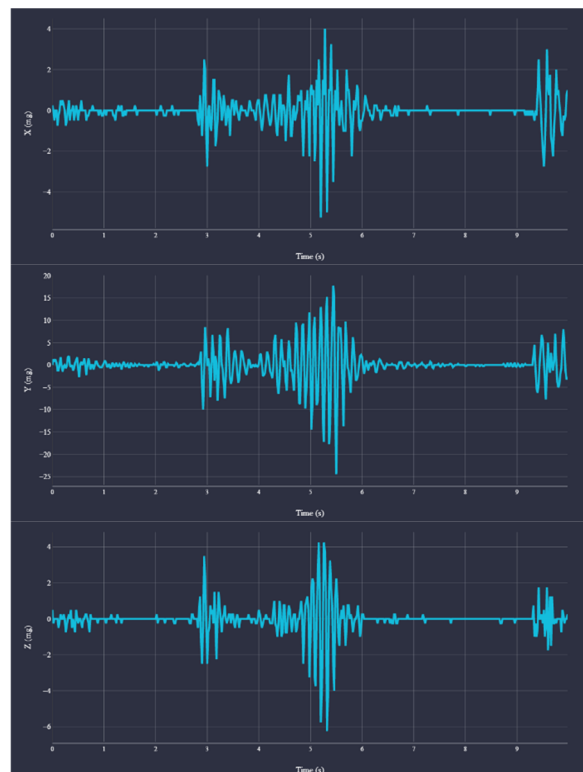


Figure 2. Acceleration Time Response during demolition phase detected by Sensor AXE-A (peak-peak 42,25 mg).

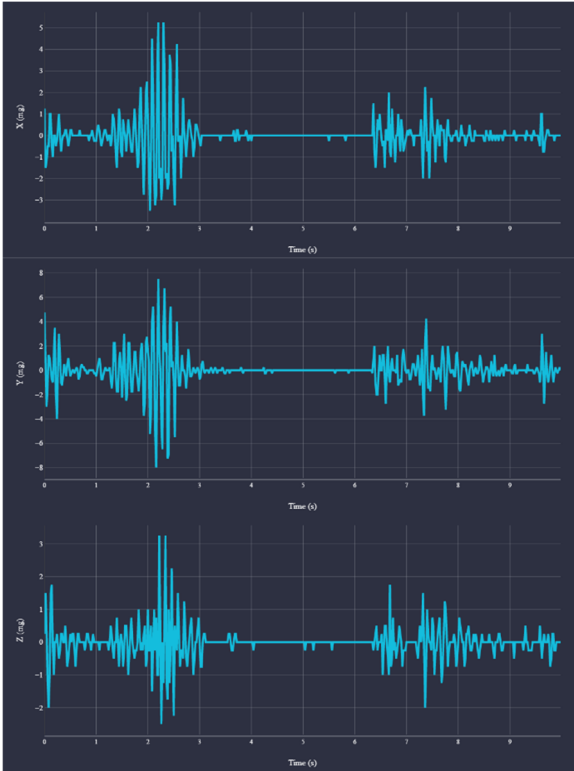


Figure 3. Acceleration Time Response during demolition phase detected by Sensor AXE-B (peak-peak 15,5 mg).

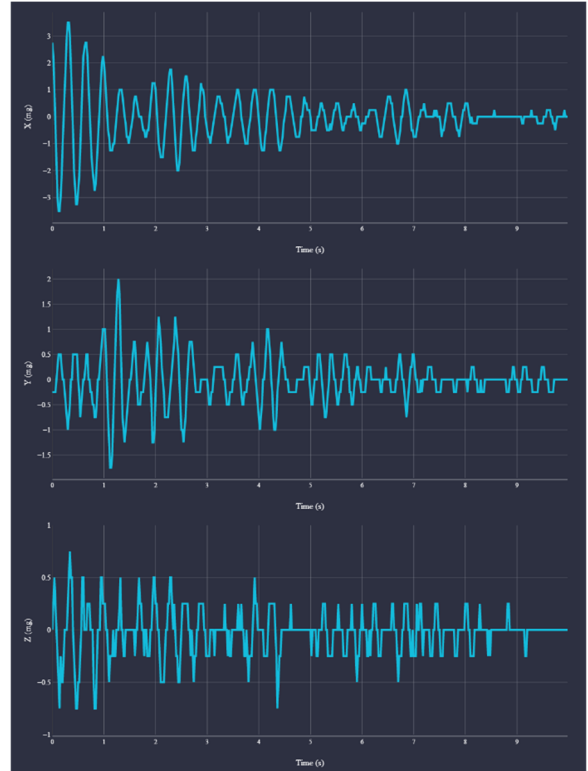


Figure 5. Acceleration Time Response during piling work construction detected by Sensor AXE-B (peak-peak 7 mg).

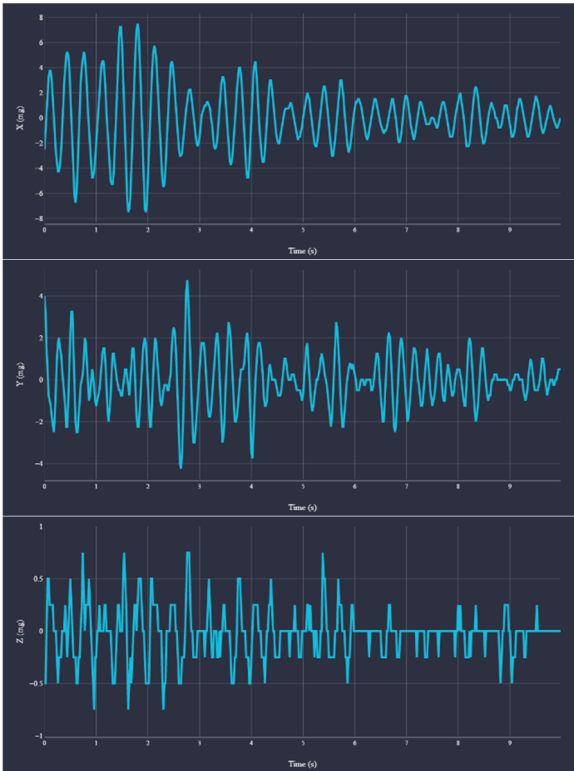


Figure 4. Acceleration Time Response during piling work construction detected by Sensor AXE-A (peak-peak 15 mg).

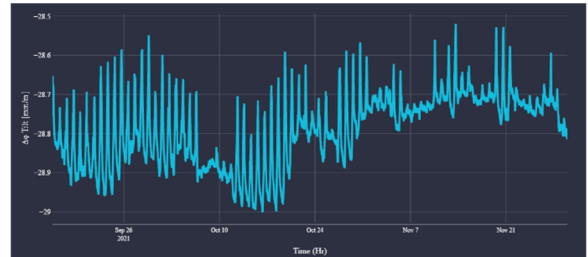


Figure 6. Trend of  $\phi$  angle detected by TILT-B sensor.

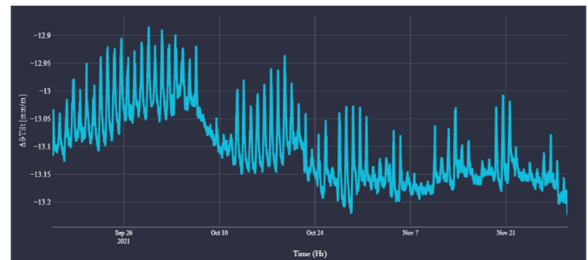


Figure 7. Trend of  $\theta$  angle detected by TILT-B sensor.

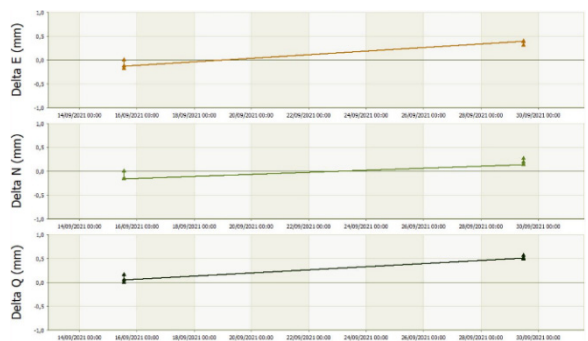


Figure 8. Prism 104A trend.

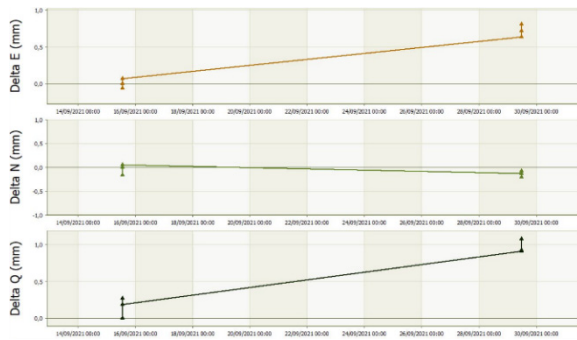


Figure 9. Prism 102B trend.

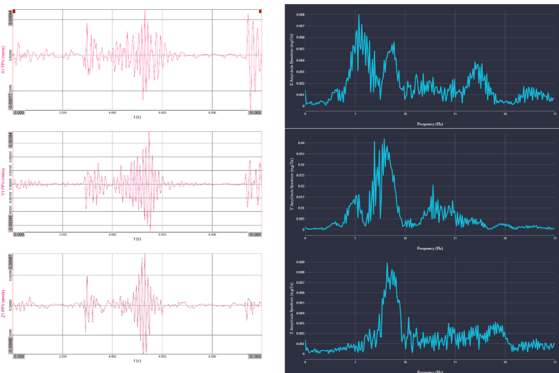


Figure 10. Velocity Time Response (left) and FFT analysis (right) of demolition detected by sensor AXE-A.

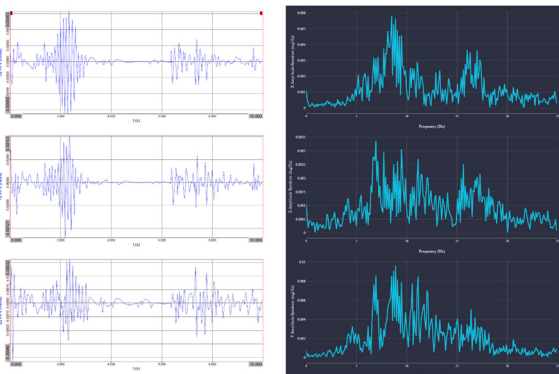


Figure 11. Velocity Time Response (left) and FFT analysis (right) of demolition detected by sensor AXE-B.

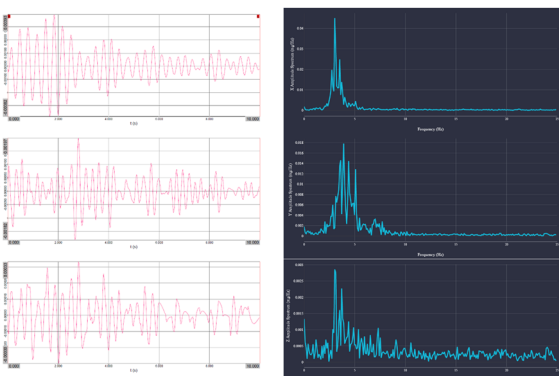


Figure 12. Velocity Time Response (left) and FFT analysis (right) of piling work construction detected by sensor AXE-A.

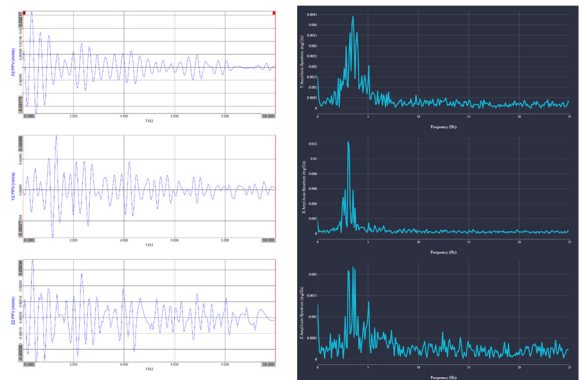


Figure 13. Velocity Time Response (left) and FFT analysis (right) of piling work construction detected by sensor AXE-B.

### III. METHODOLOGY

#### A. Wireless monitoring ecosystem

The proposed performance monitoring system (Figure 14) was installed to monitor the wall during the demolition phase of the nearby building. The sensor system is reported in the following table (Table 1).

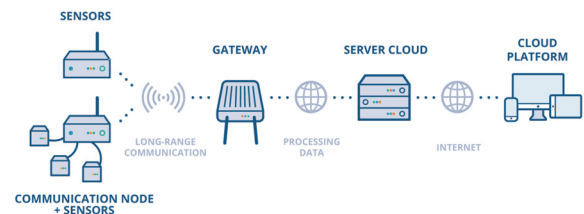


Figure 14. The wireless monitoring ecosystem.

Table 1. Sensors deployed in the monitoring system

Sensor type	Monitoring items	Nº of sensors
Accelerometer	Acceleration	2
Tiltmeter	Inclination	2
Prisms	Translations and rotations	5
Total station	Orientation and measurement	1
Total		10

All these sensors were selected to capture important information about the static and dynamic properties of the structure. The real-time data acquired from the sensors have been transmitted from the sub-stations to the Cloud Platform via gateway. This is a control unit device that is essential for receiving and sending data with which, thanks to the wide-range communication protocol LoRaWAN, it is possible to manage and communicate with all the sensors deployed.

#### B. Dynamic characterization

Performing a dynamic response characterization of the building is the typical practice to detect velocity and use its significant kinematic parameter to assess the effects of vibration on structures during construction phases (Monti *et al.*, 2013). Some velocity-based vibration criteria depends on the knowledge of the spectral energy distribution so as the frequency content. Therefore, for the purpose of calculating the

velocity, the analysis can be limited to frequencies up to 100 Hz as the most building damages falls in the frequency range from 1 Hz to 100 Hz (UNI 9916). Table 2 shows, purely as an indication, the range of interest for different types of excitations.

Table 2. Characteristic frequency ranges of vibration sources

Vibration sources	Frequency range [Hz]
Road or rail traffic	From 1 to 300
End bearing piles	From 1 to 300
Demolitions	From 1 to 100
Machines outside the building	From 1 to 300
Machines inside the building	From 1 to 300
Human activities	From 0,1 to 100
Wind	From 0,1 to 2

The analysis of the measured data should lead to determinate if the vibration level causes damages to the monitored building. There are various approaches for evaluating if the vibration levels are dangerous or not. Some criteria refer to the PCPV (Peak Component Particle Velocity), defined as the maximum modulus of one of the three orthogonal velocity components obtained by integration. However, other criteria refer to PPV (Peak Particle Velocity), defined as the maximum value of the modulus of the velocity vector obtained by integration at the control points. Different thresholds are defined in DIN 4150-3, BS 7385-1, BS 5228-4, and SN 640312a.

C. Vibration monitoring with MEMS technology

Searching for a reliable, versatile, and yet cost-effective monitoring system design, led to the use of a system equipped with MEMS (Micro Electro-Mechanical Systems) based sensors as well as accurate but low-cost triaxial accelerometers assembled by Movesolutions (www.movesolutions.it). These sensors are ideal for a monitoring system and can act as data collectors during man-made phenomena or during earthquake events. Continuous improvements in the manufacturing processes for these types of sensors, and in their technical specifications (Table 3) make them more efficient, better performing, and available at a lower cost, making structural monitoring more affordable than other off-the-shelf solutions. The wireless accelerometers transmit accurate data from the site by the LoRaWAN wireless communication protocol with a gateway. So, it is possible to view and interact with all the acquired data on the web using a Cloud Platform.

Experimental acceleration measurements with MEMS sensors were taken at two control points on the building.

Both measurement points were set up on the side of the building close to the vibration source. Accelerometer AXE-A was placed on the top floor and accelerometer AXE-B at the base of the building

(Figure 15). For both points, acceleration was measured in the vertical direction and in the other two orthogonal horizontal directions, with reference to the main axes of the building. For each event it was possible to visualize the specific vibration, analyze the trend and the amplitude of the detected peak-peak value.

Table 3. Technical specifications of the wireless sensors

	Tiltmeters	Accelerometers
Technology	MEMS	MEMS
Radio channel	LoRaWAN	LoRaWAN
Resolution	0,000015°	15bit (31,25µg)
Accuracy	0,005°	±62,5 µg
Range	±90°	±0,512g
Sample rate	-	50 Hz
Noise density	-	22,5 µg/√Hz

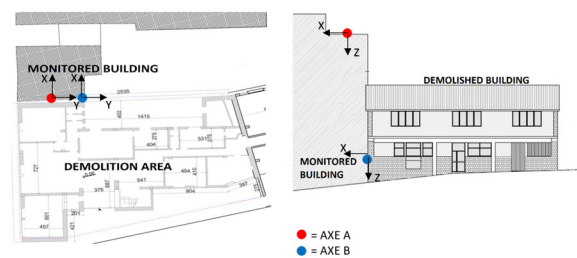


Figure 15. Accelerometers layout.

Therefore, each detected event is represented by six graphs, with reference to the three axes. Three graphs correspond to the “Time response” (Figures from 2 to 5) of each sensor then, they describe the acceleration detected by the sensors in 10 seconds of sampling.

The other three graphs correspond to the “Frequency response” (Figures from 10 to 13, on the right) of the oscillations (mg) so they are relating to the FFT (Fast Fourier Transform) algorithm which allows to highlight the spectral content of the signals coming to the sensors. So, it is possible to obtain characteristics and information of the signal perceptible in the time domain and not. The two main events which were investigated are the demolition of the adjacent building and the piling work construction.

During the demolition phase, the maximum peak-peak was detected by the sensors on the 15<sup>th</sup> of September at 15:49 p.m. and it amounted to:

- 42,25 mg for the triaxial accelerometer AXE-A.
- 15,50 mg for the triaxial accelerometer AXE-B.

During the piling work construction, the maximum peak-peak was detected by the sensors on the 29<sup>th</sup> of October at 12:53 a.m. and it amounted to:

- 15 mg for the triaxial acceleration AXE-A
- 7 mg for the triaxial accelerometer AXE-B.

In this work, it was necessary to trace the measurements taken by the accelerometers in terms of velocity. Accelerations are traced back to this kinematic quantity by integration. For this case, the integration of

the accelerometric signal was carried out in the time domain, considering the filtering on the recorded signal. A high-pass filter was used to eliminate the low-frequency noise components, after having duly verified that no significant components of the useful signal were lost with such filtering.

The aim of a vibration evaluation is to guarantee that the allowable vibration levels in the nearby building are met. So, the acceleration time series (mm/s<sup>2</sup>) recorded by the wireless triaxial sensors has been integrated over the time in order to change it in velocity ( $\Delta v = \int a dt$ ) and to evaluate the higher vibration velocity values to assess possible exceedances of the permissible limits.

**D. Inclinometer monitoring**

Displacement monitoring is an important part of the construction processes. Inclinometric control systems are designed to determine the angular displacement of structure elements. Inclinometers, tiltmeters of various designs are based on the principle of recording the deviation of a horizontal or vertical surface from the direction of the gravity vector (Glot *et al.*, 2021). Some works (Su *et al.*, 2013) show the application of inclinometric control systems equipped in high-rise structures and the key features of this monitoring system which are the simultaneous installation of all the sensors and data acquisition using the cloud platform to record initial values, and the measurement of structural settlement and displacement at different construction stages.

Wall's displacement monitoring includes horizontal and vertical displacement. For these processes we used two different technologies: a total station survey is supportive to the tiltmeter placed in two control points.

1) *Wireless tiltmeters*: tilt control devices were placed as follows. Tiltmeter TILT-A was placed on the upper end of the wall and the other tiltmeter TILT-B in the middle of the monitored wall (Figure 16).

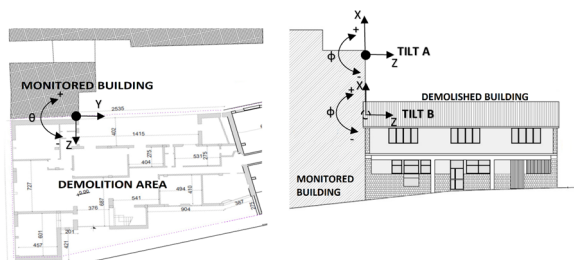


Figure 16. Tiltmeters layout.

These triaxial tiltmeters were installed to measure the variation of the static angular inclination of the monitored wall. These systems are battery powered and have a LoRaWAN wireless transmission of the MEMS previously introduced, so they too acquire data and transmit them to the Cloud platform (Figure 14).

The Tiltmeters give in output angles (Figures 6 and 7, Tables 4) that describe any variation in inclination

(Table 5) of the wall on which the devices were installed. The calculation of these angles is based on the projections of the gravity vector on the three axes of the sensor, averaged over an acquisition interval of one minute (Figure 17).

Table 4.  $\phi$  and  $\Theta$  angles detected by TILT-B sensor

	$\phi$ [mm/m]	$\Theta$ [mm/m]
15/09/2021	-28,68778	-13,07825
29/09/2021	-28,75519	-12,96675
15/10/2021	-28,84568	-13,03855
29/10/2021	-28,69111	-13,08553
15/11/2021	-28,64456	-13,09804
29/11/2021	-28,77162	-13,17783

Table 5. Variation of tilt angles  $\phi$  and  $\Theta$

	$\Delta\phi$ [mm/m]	$\Delta\Theta$ [mm/m]
$\Delta_1$	0,06741	-0,081575
$\Delta_2$	0,1579	-0,0397
$\Delta_3$	0,00333	0,00728
$\Delta_4$	-0,04322	0,01979
$\Delta_5$	0,08384	0,09958

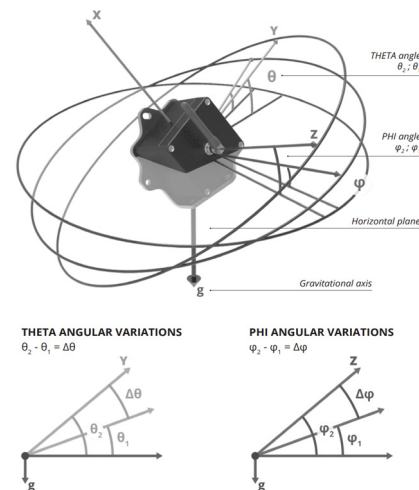


Figure 17. Phi and theta angles.

The angles provided by the device are:

- $\phi$  – Phi angle: it represents the angle between the Z axis, represented on the orientation label, and its projection on the horizontal plane.
- $\theta$  – Theta angle: it represents the angle between the Y axis, represented on the orientation label, and its projection on the horizontal plane.

2) *Topographical survey*: the topographic monitoring activity started using a Sokkia NET05AX robotic total station which was placed in a position where it could be repositioned for upcoming topographical measurements.

Three orientation prisms were installed and used to orientate the total station and two control prisms were installed to monitor translations and rotations (Figure 18).

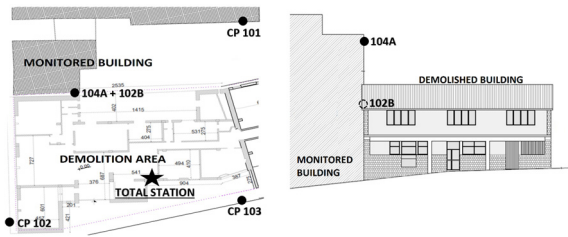


Figure 18. Topographical survey layout.

Three orientation prisms were positioned as absolute reference point to determine the coordinates of the station by inverse intersection.

The prisms were named CP101; CP102; CP103 and they were positioned facing the construction site as follows:

- CP101 on a wall of the monitored building.
- CP102 on a niche in the perimeter of the construction site area.
- CP103 on the jersey barrier enclosing the area.

Once the coordinates of the station were calculated, the measurements were carried out on two control prisms on the building's wall to be monitored, positioned below the triaxial tiltmeters.

The prisms were respectively named 104A and 102B were positioned as follows:

- 104A on the wall under the triaxial inclinometer TILT-A.
- 102B on the wall under the triaxial inclinometer TILT-B (Figure 19).

Topographical measurements started with the zero-measurement acquisition which was consisting of the average of three layers acquired in straight line mode and conjugated on the horizontal, vertical, and inclined distance angles. The measurements are aimed at verifying any elevation ( $\Delta Q$ ) and planimetric displacements ( $\Delta N$ ,  $\Delta E$ ). From data processing software (Polifemo, [www.geopro.it](http://www.geopro.it)) it was possible to extrapolate the raw measurements relative to the prisms measured (Figures 8 and 9).



Figure 19. Prism 102B positioned under the TILT-B sensor.

#### IV. DISCUSSION AND RESULTS

During both demolition operation and the pile work construction, the acceleration was measured and afterward the velocity was obtained so PPV was calculated. Accelerations and PPV are within the permissible limits according to DIN 4150. Velocity time history and the corresponding FFT analysis are shown hereafter in the following Figures (from 10 to 13).

Regarding to the monitoring of the inclination angles, the elevations and planimetric displacement measured by the two inclinometric proposed systems (total station and sensors) the measured data show that they are in the order of tenth of a millimeter. For this reason, the displacement measured are within the accuracy of the robotic total station or the positioning of the prisms which should be rotated in order to recreate a perfect perpendicularity. Since these measurements are correlated to the total station's accuracy, the comparison between the two systems don't reveal any discrepancies or particular problems. This is also due to the fact that the measurements taken over a very short observation period are not sufficient for the estimation of any trends or drifts. On the other hand, it may be interesting to pay attention to the correlation revealed between the measurements of the angle of inclination and the temperature (Figure 20). In Figure 20 it is possible to clearly see fluctuations in the tilt values consistent with daily changes in the temperature. In fact, the temperature strongly influences the changes in the measured inclination (Glot *et al.*, 2021).

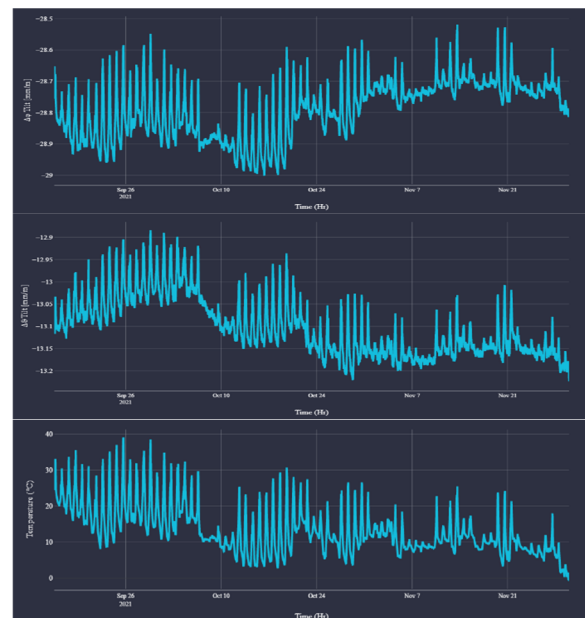


Figure 20. Correlation between the angle alteration and temperature trend.

#### V. CONCLUSIONS

Starting from the identification of the velocity based on the vibrations produced during the yard phases, the different approaches for evaluating the effects of vibration produced were highlighted. Specifically in this

work we monitored a demolition phase and the successive excavation for pile work construction, with the installation of a wireless system network. This long-term monitoring may help the definition of any damage, fortunately absent in this case study, which were caused by different vibration levels referring to one of the mentioned criteria. The combination of the dynamic characterization with a static one, by using tiltmeters sensors and topographical measurements, provides a comprehensive overview of the site's health from the beginning of the works through the subsequent various phases. The efficiency of the system, the validity of the measured data and the widespread low-cost sensors solution, made this integrated system a valid approach to be taken into account and to support to all construction phases.

### References

- Aktan, A. E., Catbas, F. N., Grimmelsman, K. A., and Tsikos, C. J. (2000). Issues in infrastructure health monitoring for management. *Journal of Engineering Mechanics*, 126(7), pp. 711-724.
- Antunes, P., Lima, H., Varum, H., and André, P. (2012). Optical fiber sensors for static and dynamic health monitoring of civil engineering infrastructures: Abode wall case study. *Measurement*, 45(7), pp. 1695-1705.
- Artese, S., De Ruggiero, M., Salvo, F., and Zinno, R. (2021). Economic Convenience Judgments among Seismic Risk Mitigation Measures and Regulatory and Fiscal Provisions: The Italian Case. *Sustainability*, 13(6), 3269.
- Brownjohn, J. M., and Pan, T. C. (2008). Identifying loading and response mechanisms from ten years of performance monitoring of a tall building. *Journal of performance of constructed facilities*, 22(1), pp. 24-34.
- Brownjohn, J. M. W., Pan, T. C., and Cheong, H. K. (1998). Dynamic response of republic plaza, singapore. *Structural Engineer*, 76, pp. 221-226.
- BS 5228-4:1992 Noise and vibration control on construction and open sites – Code of practice for noise and vibration control applicable to piling operations.
- BS 7385-1, Evaluation and measurement for vibration in buildings - Part 1: Guide for measurement of Vibrations and evaluation of their effects on buildings.
- DIN 4150-3, Structural vibration – Part 3: Effects of vibration on structures.
- Di Stefano, F., Cabrelles, M., García-Asenjo, L., Lerma, J. L., Malinvernì, E. S., Baselga, S., and Pierdicca, R. (2020). Evaluation of Long-Range Mobile Mapping System (MMS) and Close-Range Photogrammetry for Deformation Monitoring. A Case Study of Cortes de Pallás in Valencia (Spain). *Applied Sciences*, 10(19), 6831.
- Domaneschi, M., Cimellaro, G. P., Ansari, F., and Morgese, M. (2021). Safety of existing infrastructures: The collapse of the Morandi bridge in Genoa. In *Bridge Maintenance, Safety, Management, Life-Cycle Sustainability and Innovations* (pp. 1499-1506). CRC Press.
- Glott, I., Shardakov, I., Shestakov, A., Tsvetkov, R., and Gusev, G. (2021). Inclinometer-Based Long-Term Monitoring of the Headframe of Salt Mine Shaft. In *Journal of Physics: Conference Series* (Vol. 1945, No. 1, p. 012009). IOP Publishing.
- ISO 4866, Mechanical vibration and shock - Vibration of buildings - Guidelines for the measurement of vibrations and evaluation of their effects on buildings.
- Lupieżowicz, M. (2021). Monitoring the Impact of the Large Building Investments on the Neighborhood. *Applied Sciences*, 11(14), 6537.
- Mita, A. (1999). Emerging needs in Japan for health monitoring technologies in civil and building structures. In *Proc. Second International Workshop on Structural Health Monitoring* (pp. 56-67).
- Monti, G., Fumagalli, F., Marano, G. C., Quaranta, G., Rea, R., and Nazzaro, B. (2013). Effects of ambient vibrations on heritage buildings: overview and wireless dynamic monitoring application. In *Proceedings of the 3rd International Workshop "Dynamic Interaction of Soil and Structures-Dynamic Interaction between Soil, Monuments and Built Environment"*.
- Morgese, M., Ansari, F., Domaneschi, M., and Cimellaro, G. P. (2020). Post-collapse analysis of Morandi's Polcevera viaduct in Genoa Italy. *Journal of Civil Structural Health Monitoring*, 10(1), pp. 69-85.
- Petito, V., Leotta, M., and Ribaudo, M. (2019). Improving the Performance of Road Network Analysis: The Morandi Bridge Case Study. In *GISTAM* (pp. 259-266).
- SN 640312 a, Effet des ébranlements sur les constructions.
- Su, J. Z., Xia, Y., Chen, L., Zhao, X., Zhang, Q. L., Xu, Y. L., and Chen, A. R. (2013). Long-term structural performance monitoring system for the Shanghai Tower. *Journal of civil structural health monitoring*, 3(1), pp. 49-61.
- UNI 9916, Criteri di misura e valutazione degli effetti delle vibrazioni sugli edifici.
- Zhang, Z., Huang, M., and Wu, B. (2020). Risk Analysis and Control Factors Based on Excavation of a Large Underground Subway Station under Construction. *Symmetry*, 12(10), 1629.



## 4D point cloud analysis of the September 2020 Mediane impact on Myrtos beach in Cephalonia, Greece

Emmanuel Vassilakis, Aliko Konsolaki, Stelios Petrakis, Evangelia Kotsi, Christos Fillis, Stelios Lozios, Efthymios Lekkas

National and Kapodistrian University of Athens, Zographou, Greece, ([evasilak@geol.uoa.gr](mailto:evasilak@geol.uoa.gr); [alidikons@geol.uoa.gr](mailto:alidikons@geol.uoa.gr); [spetrakis@geol.uoa.gr](mailto:spetrakis@geol.uoa.gr); [ekotsi@geol.uoa.gr](mailto:ekotsi@geol.uoa.gr); [chfillis@geol.uoa.gr](mailto:chfillis@geol.uoa.gr); [slozios@geol.uoa.gr](mailto:slozios@geol.uoa.gr); [elekkas@geol.uoa.gr](mailto:elekkas@geol.uoa.gr))

**Key words:** *mudflow; photogrammetry; landslide; coastal management; Unmanned Aerial Systems*

### ABSTRACT

The coastal area of Myrtos beach, is a very popular Natura protected area at the Northern part of Cephalonia Island, in W. Greece, which suffered severe damages during the Mediane named after “Ianos”, that affected the Greek territory in September 2020. Most of the steep slope area, which hosts the road that leads to the beach area itself were extensively covered by debris due to mudflows, interrupting aggressively the road connection with the inland network. The use of Unmanned Aerial Systems proved to be an ideal way of mapping quite small areas, with limited access to road networks. The generation of ultra-high resolution spatial products seems to be optimal for mapping and quantifying mass movements that cover areas ranging from less than one square kilometer up to few square kilometers. The aim of such a multi-temporal study, which is described herein, contains aerial image data collection and analysis, before and after the catastrophic event. It is leading to the quantification of the surface topographic changes, by generating a time series of point clouds, after creating several terrain models along with ortho-photo-mosaics, based on Structure-from-Motion photogrammetric techniques. The digital comparison of the co-registered photogrammetric products showed that significant surface alterations have taken place due to the 2020 Mediane. The diachronic point clouds led to the detection and quantification of elevation changes, mainly at the central part of the area of interest, whereas the elevation values of the point clouds were found rather altered, before and after “Ianos”, either positively (deposition) or negatively (erosion), delineating the areas that suffered surface changes.

### I. INTRODUCTION

During the recent years, the demands on very high-resolution topography data are constantly increasing, leading to the generation of ultra-high density point clouds, which are used for the construction of Digital Surface Models (DSMs) and Ortho-photo-mosaics. Structure-from-motion (SfM) photogrammetry and multi-view stereo (MVS) have given the scientific community the opportunity to generate 3D topographic and morphological data derived from data based on the use of Unmanned Aerial Systems (UAS), with pixel sizes that reach even few millimeters. Moreover, the opportunity to use time as the fourth dimension, provide the capability to detect topographic changes at a very high resolution and accuracy.

One of the main issues regarding the topographic change detection, is the requisiteness of very accurate georeferencing. There are several methods to achieve accurate positioning, such as Ground Control Point (GCP) based georeferencing method (James *et al.*, 2017), direct georeferencing method (Zhang *et al.*, 2019) and a post-processing georeferencing method with the use of ‘pseudo-GCPs’ (Peppas *et al.*, 2018). The latter, seems to be adequate for the work that is described in this manuscript, since the meantime between the two periods of data acquisition (July 2020 – October 2020, before and after the Ianos Mediane)

is too short and the uncovered terrain characteristics of the wider area remain relatively stable and clear.

The area of interest was photographed twice by a large number of overlapping aerial images. As generally accepted, a sequence of a relatively low-cost UAS time series dataset can provide useful support for the delineation of the earth’s surface structures and specifically for the study of gravitational processes evolution (Niethammer *et al.*, 2012; Liu *et al.*, 2015). Furthermore, landslide monitoring within the framework of multi-temporal UAS data acquisition is a method that could produce accurate results after careful data collection and photogrammetric processing (Turner *et al.*, 2015; Rossi *et al.*, 2018; Seier *et al.*, 2018).

The purpose of multi-temporal UAS data collection and analysis is to create a series of DSMs along with ortho-photo-mosaics (Westoby *et al.*, 2012; Granshaw, 2018; Mauri *et al.*, 2021), to quantify the surface topographic changes.

High-resolution images acquired by a small but accurately located UAS may support the definition of not only the identification of the actual margins of a studied landslide phenomenon but also the identification and mapping of the main geomorphological features (Fiorucci *et al.*, 2018; Karantanellis *et al.*, 2019), either based on the classic

methodologies or by using more sophisticated and automated state-of-the-art techniques (Karantanellis *et al.*, 2020).

## II. SITE AND MEDICANE DESCRIPTION

The area of Myrtos beach, is a popular 800 m long coastal area, sited in the northern part of Cephalonia Island (Figure 1) and protected by Natura 2000 network. The beach is rather small (average width of 50 m) and is located under a rather steep slope, consisting of loose highly tectonised rocks, which in turn have produced a thick surface layer consisted of large amounts of cobbles and boulders.



Figure 1. The Natura 2000 protected Myrtos beach is located at the NW coastline of Cephalonia Island. See at the bottom index map its location in the context of Greece and Europe, respectively.

In the past few years, the area has suffered extended landslides, rockfalls and mudflows (Mavroulis *et al.*, 2022), and therefore informative «danger» plates have been placed along the beach for the protection of the visitors.

In September 2020, the Medicane “Ianos” has affected Greece, causing damages in several territories across the country. The area mostly affected by Ianos was the Ionian Island complex and more specifically the island of Cephalonia. The road network leading to the Myrtos beach parking lot was entirely covered by soil material, which was originally constituting the surface layer of the basement rocks at the uphill areas (Figure 2). Many thousands of tons of detached soil material were found deposited across the slopes that

surround the beach, altering the environment and its morphology.



Figure 2. The infrastructure suffered extensive destructions caused by material relocation which resulted severe damage due to erosional phenomena and mudflows.

The weather conditions were rather extreme during the Medicane phenomenon as a rainfall and wind mixture produced severe damages. According to the nearest meteorological station, located on Ithaki Island, the total rainfall during the two-day event of 17-18/09/2020 reached 227.4 mm, whilst the average wind speed for the same period was 21 km/h, with wind gusts of the order of 90 km/h (~10 Beauforts).

## III. DATA AND METHODS

The first -out of two- flight survey was carried out before the Medicane and more specifically on July 18<sup>th</sup>, 2020, using a commercial multi-rotary UAS, which carries a Global Navigation Satellite System (GNSS) antenna with the ability of Real Time Kinematics (RTK) processing. The same equipment was used also at the post-Medicane survey, which was carried out on October 6<sup>th</sup>, 2020. The earliest survey was planned during a research project, whereas the latest survey was intentionally scheduled for acquiring comparable data, in terms of micro-topographical change detection.

Although the same flight properties were used (path, elevation, camera angle etc.), the total number of the acquired photographs was slightly different at the two surveys (Table 1) and we presume that the satellite geometry during the flights, which in turn affects the UAS camera positioning, as well as the weather (wind direction and amplitude) factor, play important roles on the amount of data, but at the bottom line there is no significant change at the overall methodology. Therefore, it took several pre-surveying flights, for planning the flying strategy to cover in a safe and satisfactory way the entire study area, due to the steep topography of the slopes surrounding the beach (Figure 3).

A DJI Phantom 4 RTK UAS had to be operated at a maximum of 385 m above sea level (ASL), after it was launched from a suitable take off area located at a beach view balcony located at 330 m ASL (Figure 4). The covered area was about 1.2 km<sup>2</sup>.

Table 1. Flight and processing information

	July 2020	October 2020
Flying Altitude	375 m	383 m
Images	595	451
Overlap	70%	70%
Dense Point Cloud	~77 million	~74 million
Camera Location RMSE	1.5 m	0.009 m



Figure 3. South-Westwards view of Myrtyos beach, which is covered by transferred material after the Ianos Medicanne.



Figure 4. The DJI Phantom 4 RTK UAS at the take-off area.

The on-board GNSS receiver, antenna, and an inertial measurement unit (IMU) calculate the absolute camera positions and altitudes directly with high accuracy measurements (Klingbeil *et al.*, 2017; Grayson *et al.*, 2018).

The preflight planning included the setup of the flight routes and elevation above the take-off area, the image acquisition angle, the front, and side overlap between the successive aerial photographs, the UAS speed during the flight, as well as the camera function details. Additionally, setting up the connectivity with the GNSS base station network is also a crucial point for taking advantage of the RTK ability and consequently increase the positioning accuracy during the data acquisition

phase, even if the error would be largely minimized during the photogrammetric processing phase.

The quality of the camera (FC6310R, 20Mpx, 8.8 mm focal length) does not require the UAS to stop at waypoints for taking oriented photographs for avoiding motion blur in images due to possible short-term compensating UAS movements and therefore excluding many of them at the quality control phase during the processing was not necessary.

A serious effort to keep the Ground Sampling Distance (GSD) as low as possible was made but the site topography conditions did not allow to succeed values better than 6-8 cm, at the areas with severe damages, which was rather satisfactory for the specific use of the final products.

The imagery was acquired with the camera set at an off-nadir position and this 90° angle was steady due to the UAS built-in gimbal. The flight plan was set for keeping an image overlap of 70% forward and 70% side as this was calculated by the flight mission software.

The photogrammetric processing was carried out twice, for the pre- and post-Medicane periods. It was based on the Structure-from-Motion (SfM) approach and implemented using the commercial software Agisoft Metashape Professional (1.7.5 build 13229). The processing requires the alignment of the aerial images and the creation of a sparse point cloud, followed by a regular mesh generation, which was used at both flight projects.

The differentiation between the two projects comes right afterwards at the processing workflow and it has to do with the co-registration of the results of the two periods (before and after the Medicanne damages) and the need for higher precision of both outcomes. Several techniques, each one with its pros and cons, are used for the determination of surface deformation features as well as for the calculation of changes within the prone area covered by mudflows accompanied by volumetric differences from the multi-temporal DSMs (Rossi *et al.*, 2018).

Therefore we chose the post-Medicane survey as the reference project since the non-destructed areas could be identified at both projects and used as tie-points between them. This is a very important barrier that needs to be overcome for creating a successive multi-temporal image after co-registering the final products very accurately (Vassilakis *et al.*, 2020).

We chose the Network RTK (NRTK) approach for georeferencing the latest survey as this is a rather accurate and less time-consuming data acquisition technique but connectivity problems during the flight led us to adopt the Post Processing Kinematics (PPK) approach during the processing, by including GNSS permanent stations' RINEX data within the procedure (Panagiotopoulou *et al.*, 2020). The succeeded accuracy was more than satisfactory, reaching horizontal and vertical errors of the order of 0.009 m yielding a very reliable dataset from the geolocation point of view.

The procedure continued with generating a dense point cloud, therefore creating much finer topographic details. At a later step a texturing was also applied before generating the final ortho-image as well as the DSM (Mancini *et al.*, 2013). Even though the NRTK approach was also chosen for the earliest survey too, the need for co-registration led us to also use GCPs within the processing. By applying this technique we managed to succeed the highest precision between the two projects by picking 7 points on the post-disaster ortho-image, which remained unchanged after the Mediane, for using them as pseudo-GCPs (Peppia *et al.*, 2018) during the photogrammetric procedure of the pre-disaster project (Figure 5).

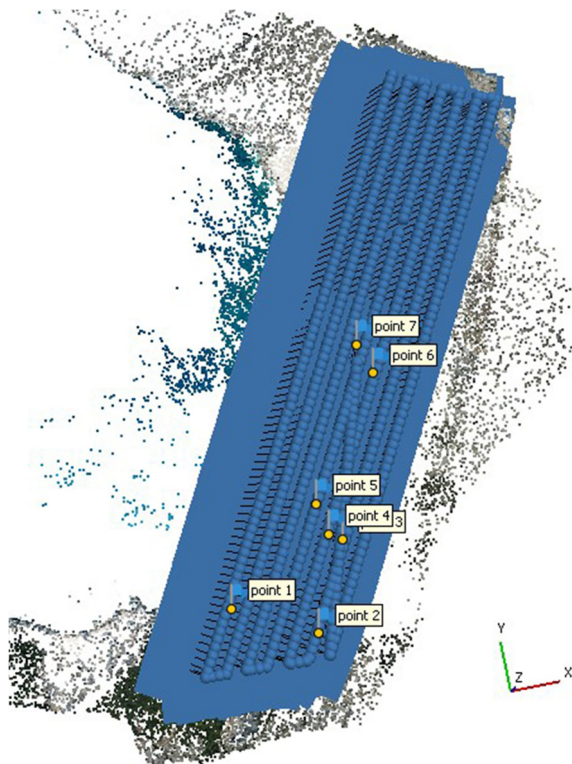


Figure 5. The locations of the UAS camera during an aerial photography survey along with the selected pseudo-GCPs, during the photogrammetric processing.

The camera calibration stored within the acquired image metadata, at both surveys, was found to be very sufficient for correlation within the photogrammetry processing, since the average error did not exceed 0.38 pixels. The pseudo-GCPs are used in the reference-dataset to easily bring the target-dataset at the exact same position with an error of 0.007 m which is rather satisfactory. The post-Medicane ortho-image was used for recording the X and Y coordinates, whilst the interpolated DSM was used for the extraction of every GCP elevation. The photogrammetric processing for both surveys led to the production of high-quality dense point clouds, consisting of about 75,000,000 points each (Table 1). Each point of the cloud includes information about the reflectance at the visible (RGB) spectra along with X, Y, Z coordinates (Westoby *et al.*, 2012).

By making spatial raster calculations between multi-temporal DSMs of the same study area, especially when acquired after a specific event that has significantly altered the surface morphology (*e.g.* flood, earthquake, mass movement), a new dataset called “DSM of Difference” can be created. The latter might be used for the quantification of any spatial alterations because of the natural event on the study area’s morphology (Williams, 2012). Volumes of moved material can be calculated, providing useful information for the researchers on the damage control and the protection measures that should be obtained for further fortification of the affected area, in order to prevent similar disaster in the future.

#### IV. RESULTS

The calculation/quantification of the detectable changes between the July and October surface was accomplished with the use of multiscale model-to-model cloud comparison-precision maps algorithm (M3C2-PM). The M3C2 algorithm computes directly the distance from a reference point cloud (PC1) to a target point cloud (PC2) and by including the ‘precision maps’ is not necessary to contain roughness estimates (Niethammer *et al.*, 2011). This technique is ideal considering point clouds generated by photogrammetric processing (James *et al.*, 2017). Performing this point analysis directly on the point clouds, removes the factors that can affect the result by converting data into a DSM, which could have a major impact on the study result considering the magnitude of the changes that are measured.

According to the data from the Ithaki meteorological station, no other significant weather phenomena occurred during this period, so we can assume that all the deformation observed is due to the studied Mediane. Most of the prone area, which hosts the road leading to the beach, was covered in debris from upstream (Figure 2), revealing large mudflows and debris cones caused by heavy rainfall during the Ianos event. The mass movement is more than clear by observing the post-event ortho-photo and in terms of quantification it can be demarcated quite effortlessly leading to an accurate measurement of the area covered by mudflow (Figure 6).

The described approach could be applied for detecting changes of the order of a few decimeters, and it is rather accurate since a total area of 59,419 square meters has been altered after the storm and 40,678 square meters have been covered with mud, mainly in the central part of the area.

A total area of 6,618 square meters located in the parking lot was covered with soil material, representing an estuary of a relatively small river trending SE-NW.

In addition, Mediane Ianos weather event caused highly dynamic changes on slope surface related to massive changes in soil loss and deposition rates. The M3C2 comparison resulted a total volume of difference

of 45,575.05 ( $\pm 8,247.79$ ) cubic meters, mainly at the central part of the studied area (Figure 7).

More specifically, it was calculated that a volume of 15,318.73 ( $\pm 3,158.05$ ) cubic meters were deposited at new locations within Myrtos beach and

30,256.33 ( $\pm 5,089.74$ ) cubic meters were removed from their original location, in which they were found before lanos. The latter indicates the filling volume needed in the reconstruction process.

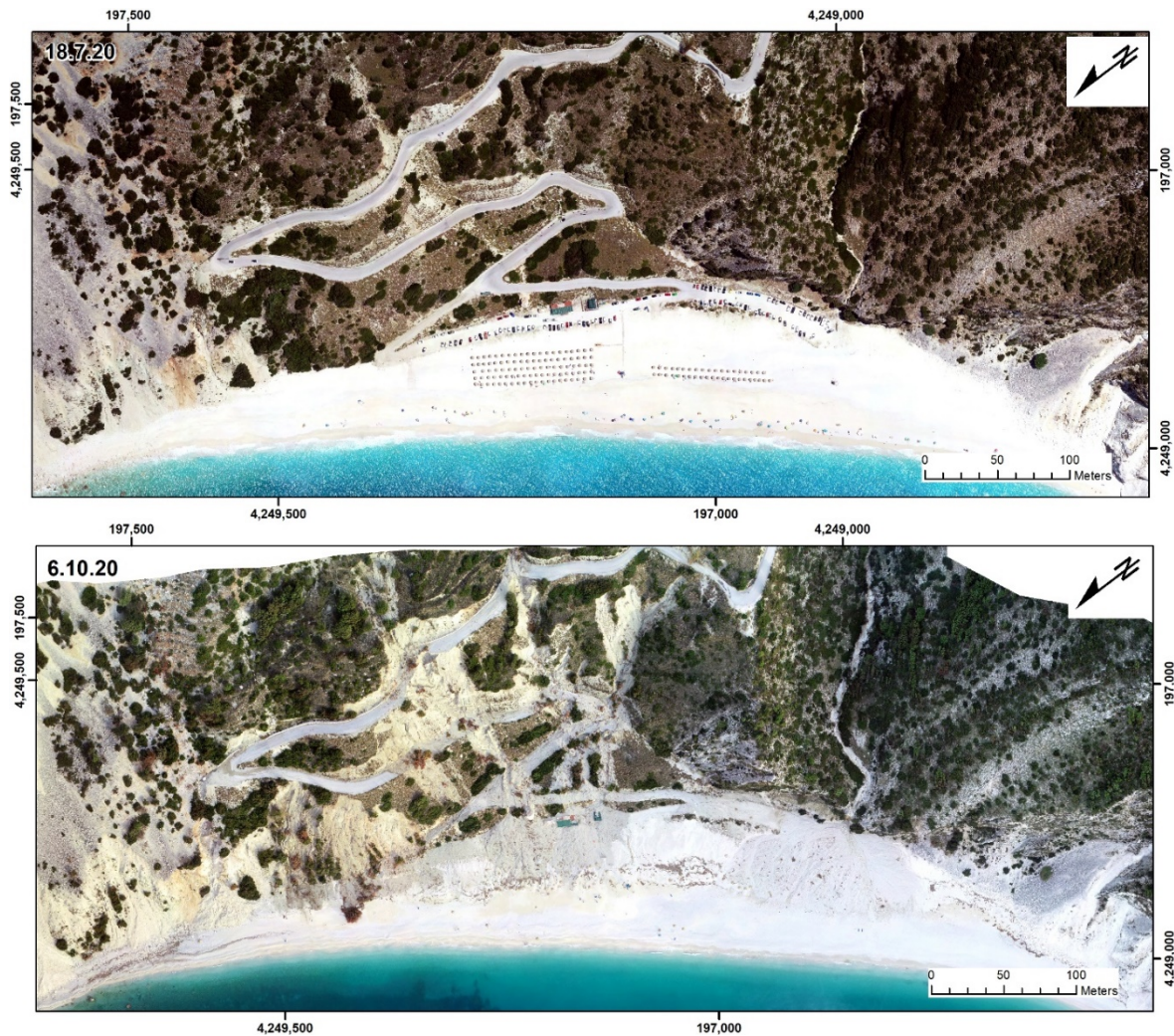


Figure 6. Ortho-photo-mosaics of Myrtos beach before (upper) and after (below) lanos. The traces of mudflows are clear at the latest image. The road to the beach and the parking lot are almost destroyed and the surface changes are more than detectable and measurable in two dimensions.

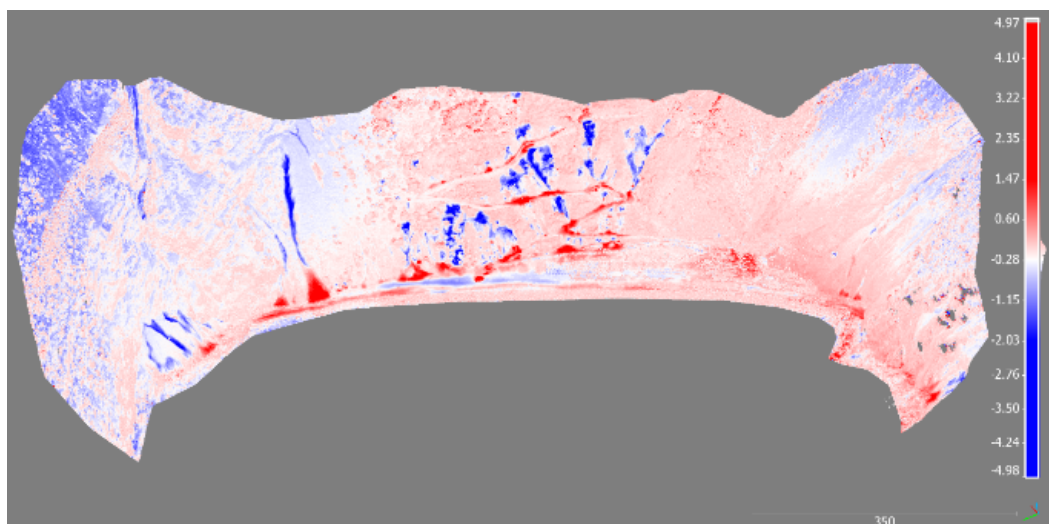


Figure 7. The point cloud comparison results across the Myrtos surrounding slopes showing areas of high incision (bluish) and deposition (reddish) of transported soil material due to lanos.

## V. CONCLUSIONS

The purpose of this research is the comparison of point clouds of the Natura protected Myrtos beach attributed to different periods after pounded by the severe Ianos Mediane. The described UAS-based methodology presents a quite simple and convenient way of comparing datasets of different time periods and achieving a co-registration of very high accuracy by using pseudo-GCPs.

The accuracy in the final photogrammetric product - including the co-registration between multi-temporal datasets- proved to be very crucial in terms of accurate results in measuring distances between the original point clouds and eventually the volume of mass movement through mudflows which leads consequently, to the quantification of the surface alteration.

Even though the UAS data collection proved to be quite challenging, in terms of both weather conditions and coverage of a quite large area, high quality results were obtained. Additional difficulty comes from handling of large datasets and the requirements in terms of computational resources to reduce processing time.

## VI. ACKNOWLEDGEMENTS

This research was partially funded by the Special Account for Research Grants of the National and Kapodistrian University of Athens, grant number 70/4/16599.

## References

- Fiorucci, F., Giordan, D., Santangelo, M., Dutto, F., Rossi, M., and Guzzetti, F., (2018). Criteria for the optimal selection of remote sensing optical images to map event landslides. *Nat. Hazards Earth Syst. Sci.*, 18(1), pp. 405-417.
- Granshaw, S.I., (2018). Structure from motion: origins and originality. *The Photogrammetric Record*, 33(161), pp. 6-10.
- Grayson, B., Penna, N.T., Mills, J.P., and Grant, D.S., (2018). GPS precise point positioning for UAV photogrammetry. *The Photogrammetric Record*, 33(164), pp. 427-447.
- James, M. R., Robson, S., and Smith, M. W., (2017). 3-D uncertainty-based topographic change detection with structure-from-motion photogrammetry: precision maps for ground control and directly georeferenced surveys. *Earth Surface Processes and Landforms*, v. 42, no. 12, pp. 1769-1788.
- Karantanellis, E., Marinos, V., and Vassilakis, E., (2019). 3D hazard analysis and object-based characterization of landslide motion mechanism using UAV imagery. *Int. Arch. Photogramm. Remote Sens. Spatial Inf. Sci.*, XLII-2/W13, pp. 425-430.
- Karantanellis, E., Marinos, V., Vassilakis, E., and Christaras, B., (2020). Object-Based Analysis Using Unmanned Aerial Vehicles (UAVs) for Site-Specific Landslide Assessment. *Remote Sensing*, 12(11), 1711.
- Klingbeil, L., Eling, C., Heinz, E., Wieland, M., and Kuhlmann, H., (2017). Direct Georeferencing for Portable Mapping Systems: In the Air and on the Ground. *Journal of Surveying Engineering*, 143(4), 04017010.
- Liu, C.-C., Chen, P.-L., Matsuo, T., and Chen, C.-Y., (2015). Rapidly responding to landslides and debris flow events using a low-cost unmanned aerial vehicle. *APPRES*, 9(1), pp. 1-18.
- Mancini, F., Dubbini, M., Gattelli, M., Stecchi, F., Fabbri, S., and Gabbianelli, G., (2013). Using Unmanned Aerial Vehicles (UAV) for High-Resolution Reconstruction of Topography: The Structure from Motion Approach on Coastal Environments. *Remote Sensing*, 5(12), 6880.
- Mauri, L., Straffelini, E., Cucchiario, S., and Tarolli, P., (2021). UAV-SfM 4D mapping of landslides activated in a steep terraced agricultural area. *Journal of Agricultural Engineering*, 52(1).
- Mavroulis, S., Diakakis, M., Kranis, H., Vassilakis, E., Kapetanidis, V., Spingos, I., Kaviris, G., Skourtsos, E., Voulgaris, N., and Lekkas, E., (2022). Inventory of Historical and Recent Earthquake-Triggered Landslides and Assessment of Related Susceptibility by GIS-Based Analytic Hierarchy Process: The Case of Cephalonia (Ionian Islands, Western Greece). *Applied Sciences*, 12(6), 2895.
- Niethammer, U., Rothmund, S., Schwaderer, U., Zeman, J., and Joswig, M., (2011). Open source image-processing tools for low-cost UAV-based landslide investigations. *Int. Arch. Photogramm. Remote Sens. Spat. Inf. Sci.*, 38(1/C22), 1-6.
- Niethammer, U., James, M.R., Rothmund, S., Travelletti, J., and Joswig, M., (2012). UAV-based remote sensing of the Super-Sauze landslide: Evaluation and results. *Engineering Geology*, 128, pp. 2-11.
- Panagiotopoulou, S., Erkeki, A., Antonakakis, A., Grigorakakis, P., Protopapa, V., Tsiostas, G., Vlachou, K., and Vassilakis, E., (2020). Evaluation of Network Real Time Kinematics contribution to the accuracy/productivity ratio for UAS-SfM Photogrammetry. In: *Proc. of The European Navigation Conference*, ENC 2020, Dresden, Germany.
- Peppas, M.V., Mills, J.P., Moore, P., Miller, P.E., and Chambers, J.E., (2019). Automated co-registration and calibration in SfM photogrammetry for landslide change detection. *Earth Surface Processes and Landforms*, 44(1), pp. 287-303.
- Rossi, G., Tanteri, L., Tofani, V., Vannocci, P., Moretti, S., and Casagli, N., (2018). Multitemporal UAV surveys for landslide mapping and characterization. *Landslides*, 15(5), pp. 1045-1052.
- Seier, G., Sulzer, W., Lindbichler, P., Gspurning, J., Hermann, S., Konrad, H.M., Irlinger, G., and Adelwöhrer, R., (2018). Contribution of UAS to the monitoring at the Lärchberg-Galgenwald landslide (Austria). *International Journal of Remote Sensing*, 39(15-16), pp. 5522-5549.
- Turner, D., Lucieer, A., and De Jong, S.M., (2015). Time Series Analysis of Landslide Dynamics Using an Unmanned Aerial Vehicle (UAV). *Remote Sensing*, 7(2), pp. 1736-1757.
- Vassilakis, E., Fomelis, M., Erkeki, A., Kotsi, E., and Lekkas, E., (2020). Post-event surface deformation of Amyntaio slide (Greece) by complementary analysis of Remotely Piloted Airborne System imagery and SAR interferometry. *Applied Geomatics*, 13(1), pp. 65-75.
- Westoby, M.J., Brasington, J., Glasser, N.F., Hambrey, M.J., and Reynolds, J.M., (2012). 'Structure-from-Motion' photogrammetry: A low-cost, effective tool for geoscientific applications. *Geomorphology*, 179, pp. 300-314.

- Williams, R.D. (2012). Section 2.3.2: DEMs of Difference. In: *Geomorphological Techniques (Online Edition)*, British Society for Geomorphology; London, UK. ISSN: 2047-0371.
- Zhang, H., Aldana-Jague, E., Clapuyt, F., Wilken, F., Vanacker, V., and Van Oost, K., (2019). Evaluating the potential of post-processing kinematic (PPK) georeferencing for UAV-based structure- from-motion (SfM) photogrammetry and surface change detection: *Earth Surf. Dynam.*, v. 7, no. 3, pp. 807-827.

## GLOMON-Monitoringportal for storage, management, advanced processing and intelligent visualization of GNSS- and other sensors data

Michael Schulz, Florian Schäfer, Jürgen Ruffer

ALLSAT GmbH, Sokelantstraße 5, 30165 Hannover, German, ([michael.schulz@allsat.de](mailto:michael.schulz@allsat.de); [florian.schaefer@allsat.de](mailto:florian.schaefer@allsat.de); [juergen.rueffer@allsat.de](mailto:juergen.rueffer@allsat.de))

**Key words:** *global monitoring; ground movements; dynamic network adjustment; GNSS time series*

### ABSTRACT

The earth is constantly exposed to endogenous and exogenous forces that cause temporally variable movements and deformations of varying degrees. The Global Monitoring (GLOMON) solution supports the monitoring of infrastructure or large areas such as mining regions using GNSS and other sensors, in order to detect deformations or surface movements. The GNSS reference stations enable the integration of other geodetic and geotechnical sensors in a global coordinate reference frame. Three dimensional coordinates are generated for each GNSS monitoring station with a precise time stamp, allowing for the web-based visualization of time series. One of the new developments presented here is the integration of the program system suite PANDA from GEOTEC GmbH into GLOMON, which supports a dynamic network adjustment. This procedure revolutionizes the approach of stable reference points for geodetic monitoring tasks, which has been valid and used for decades. The classic approach to such measurements is the assumption of a stable reference frame over a long period of time (zero measurement). Local measurements are connected to higher-level, supposedly stable reference points, such as first order GNSS reference stations. But these external reference points can also be subject to movements which, assuming stability, are projected onto the local measurements. To solve this problem, all GNSS stations are handed over to a deformation analysis after post-processing and network adjustment in order to detect displaced points. Furthermore, the concept of time-invariant reference station coordinates should be reconsidered. This means that those reference stations detected as displaced are not fundamentally excluded from the network evaluation, but their movement behavior is described by time-variant coordinates. With the introduction of movement models for reference stations, their movements are no longer projected onto local measurements of monitoring stations. This information can be used in the areas of interest, e.g. for the optimization of existing movement and deformation models. In this way, predictions about expected deformations can be made reliably.

### I. INTRODUCTION

The ground movement monitoring in areas affected by underground hardcoal mining in Germany is an obligation of RAG Aktiengesellschaft (RAG). Due to the extensive hardcoal mining in large areas in North Rhine-Westphalia and Saarland over centuries, the ground is still moving even after the end of active hardcoal mining. For the monitoring of ground movements, various sensors and methods such as levelling, GNSS, aero photogrammetry and InSAR are used. These measurement methods require a stable reference frame in order to be able to compare measurements and generate time series. The fundamental problem here is that the surface geometry changes continuously and supposedly stable reference points are exposed to ground movements as well.

Especially for GNSS monitoring it is common practice to assume that the reference stations are stable over a long time period. Due to the need of short baselines between reference and monitoring stations the area considered stable is often located near the monitoring area. Changes of the reference station coordinates can

remain undetected, with the result that their movements are projected onto the monitoring stations.

From this point of view, RAG started a R&D project in 2019 (Spreckels, 2022). The aim of the project was the realization and maintenance of a consistent and long-term stable reference frame for the GNSS station network and later other sensors.

RAG has been operating local GNSS reference and monitoring stations together with ALLSAT GmbH (ALLSAT) since 2014. These networks have grown steadily in recent years and now include over 30 GNSS stations within three networks in Ruhr area and Saarland (Spreckels *et al.*, 2020). The networks are extended by SAPOS GNSS reference stations (German satellite positioning service). In the monitoring portal GLOMON developed by ALLSAT, the data of all GNSS stations are fully automated edited, processed and the results are visualized. The enhancements made in the above-mentioned R&D project were integrated in this fully automated and proved process.

GLOMON and the fully automated process of GNSS data processing are shown in Section II. The new approaches of dynamic network adjustments are



shown in Section III. A conclusion and future prospects are shown in Section IV.

## II. GLOMON (GLOBAL MONITORING)

The idea for the GLOMON-Portal is to combine three megatrends for monitoring tasks: The Digitization of sensors allows to continuously measure and automatically record data. The Internet is used to transfer the measurements to our central processing and storage servers. This Big Data recorded is then analyzed, processed and reduced to the important information and stored in our database. The GLOMON-Portal ([www.GLOMON.de](http://www.GLOMON.de)) supports the monitoring of man-made structures or large areas such as steep slopes and mining regions for the detection of deformations or surface movements using GNSS and other sensors.

### A. GLOMON Architecture

The core software technology developed for the GLOMON monitoring portal is the service kernel, that parses the incoming data streams of GNSS stations and other sensors (Figure 1). These data streams are decoded and written in a dedicated file and directory structure to a network array storage (NAS). The multiple thread technology allows to define post processing jobs that can be scheduled in parallel for the automatic processing of GNSS data for results with highest precision and accuracy in the range of a few mm. The post processing results are automatically synchronized with the SQL database. For the simple interaction of the user with the GLOMON monitoring portal, a webserver allows for a secure password protected access and control of multiple projects, supporting all kinds of up-to-date web browsers. All user specific settings are stored in the SQL database. The chart analysis tools allow for the detection of smallest deformations in the time series, which is compared to predefined limits and handled by the alarming management module, so that preventive measures for humans and infrastructure can be initiated as fast as possible.

### B. GLOMON Functions

The GNSS stations are often the highest order reference points, which are locally densified by other geodetic or geotechnical sensors. The GLOMON-portal integrates all these different sensors into a single platform and supports a graphical overview of all relevant data in the monitoring region. In many cases, reliable interpretation of the data can only be made if different data sources are overlaid (e.g. GNSS time series with seasonal meteorological data).

The overview page (see Figure 2) shows all GNSS stations and other sensors included in a project. Each sensor is represented by a colored marker. The color indicates the connection state of the station and so the user gets a quick overview about the connection activity within the network. Furthermore, there are a variety of

functions clicking on a station marker, like links to the coordinate time series of this station or charts with information of connected sensors, like temperature or rainfall sensors.

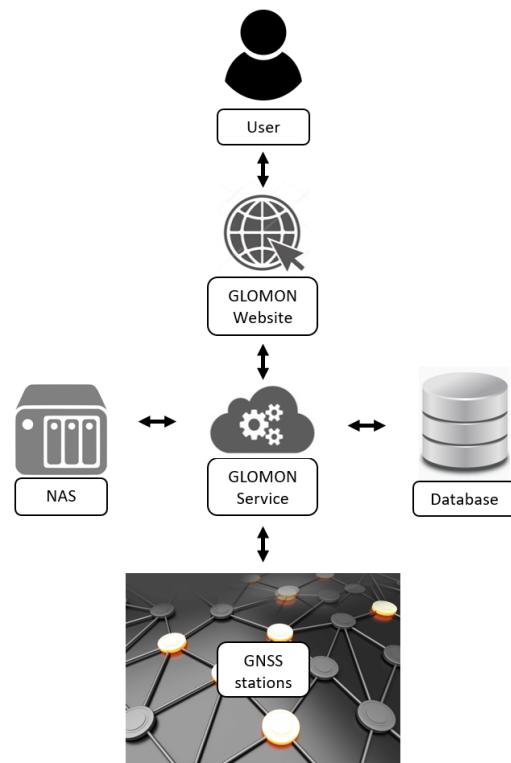


Figure 1. GLOMON Architecture.



Figure 2. GLOMON Overview.

The GNSS post processing software packages of WaSoft ([wasoft.de](http://wasoft.de)) and Geo++ ([geopp.de](http://geopp.de)) are integrated in GLOMON. The user is able to start manual or plan automatic jobs that are repeated in specific time intervals. A job includes for example the converting of the GNSS raw data on the NAS, the post processing of the GNSS data and the storage of the results into the database. Using the example of post processing a GNSS station network with WaPNet (WaSoft), usually 24 h of multi-frequency GNSS observations are collected. After the observation and orbit data as well as the antenna

correction files are checked, WaPNet processes baselines between the network stations including cycle-slip detection and repair as well as ambiguity fixing. When all stations are connected, all zero-differenced observations are on the same ambiguity level. The final network solution consists of an iterative process with outlier detection and estimation of variance components. In the end, a set of unknowns is determined which includes: station coordinates, tropospheric parameters and GLONASS inter-frequency biases. The three-dimensional coordinate time series can be shown and analyzed in GLOMON (see Figure 3).

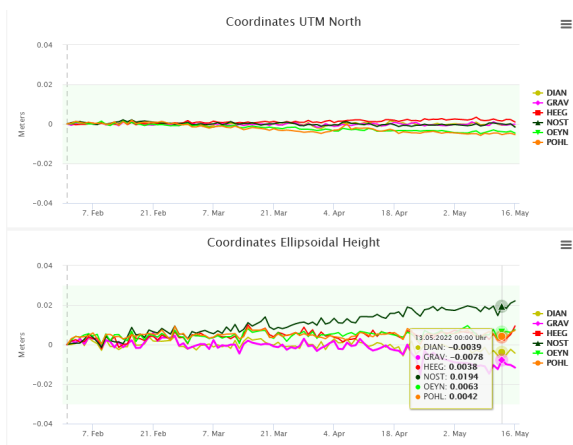


Figure 3. UTM-North and ell. Height time series of several GNSS monitoring stations in NRW Germany.

GLOMON uses a modern and intuitive charts library and offers some tools for data filtering and analysis. Furthermore, csv- and pdf-exports can be realized.

In addition to the fully automatic processing of GNSS data and a modern visualization of the results, GLOMON offers data quality analysis for reference station networks. For that, Leica SpiderQC GNSS data analysis software is integrated in GLOMON and can be used for a range of tests and analysis regarding data completeness, multipath, cycle slip and much more.

Furthermore, GLOMON supports the integration of geotechnical sensors, like triaxial tilt sensor, weather sensors including wind and rainfall as well as energy sensors. The information of the meteorologic sensors can help to interpret GNSS time series. Often there are correlations between the movement of a reference station and the temperature or soil water. In rural areas a permanent power line to the monitoring stations is not available in many cases, so that renewable energies must be used. Our solutions include energy sensors that are used on self-sufficient solar- and wind-powered monitoring stations. The voltage values of solar and wind energy supply can be monitored via these energy sensors. In GLOMON the voltage values can be shown as time series and are now also displayed on the overview page.

Moreover, GLOMON offers a multi-level alarming system, a download function for the RINEX observation data of the GNSS station and an online post processing

service by which users can upload their GNSS observation data and receive a precise position.

### III. DYNAMIC NETWORK ADJUSTMENT (DNA)

#### A. New Approach

The conventional approach for geodetic deformation monitoring is to create a reference frame from a certain number of reference points classified as stable (zero-epoch). As outlined in Figure 4 local measurements (orange) are repeated quite frequently in order to record the expected movements as completely as possible. These local measurement points are connected to near local reference points (green) which are usually connected in longer time intervals to high-level reference points like SAPOS GNSS reference stations at a larger distance.

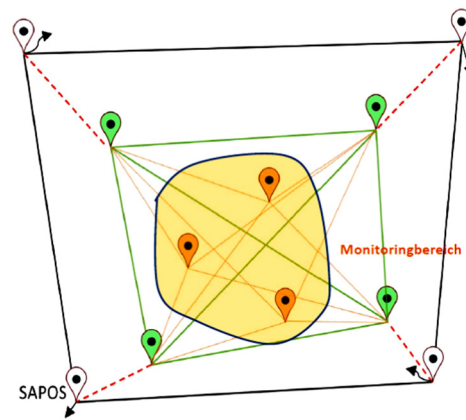


Figure 4. Cascading groups of monitoring and reference points in a conventional monitoring project.

This cascading approach is also assumed for the point stabilities: outer reference points are considered to be stable over a very long period of time. The (middle) reference points for the local measurements should be outside the actual monitoring area and should be stable over a certain period of time. The local measurements are in an unstable area, that means continuous movements are assumed for these points.

However, higher-level reference points can also be subject to movements. If these movements remain undetected, this may result in a misinterpretation of these movements as deformations of a certain object.

Especially in GNSS monitoring, the assumption of stability of reference stations over a long period of time is common in day-to-day business, but should be regarded critically. Due to the need for shortest possible baselines between reference stations and monitoring stations, the area considered to be stable is often chosen much too close to the monitoring area.

The challenge in longer monitoring projects is that smaller point movements as well as larger changes for individual points can often be registered (Niemeier *et al.*, 2020). In the classic approach, these movements often lead to a critical reduction in the number of stable reference points. For this reason, the points detected as

shifted should not be excluded from the group of reference points. Instead, a methodical approach has been developed that derives movement patterns for unstable reference stations to maintain their usability for the reference frame. The concept used to recognize movement patterns for repeatedly determined reference points was first described in (Tengen *et al.*, 2019).

### B. Implementation in GLOMON

In the last three years (2019-2021), the concept of time-invariant reference station coordinates has been fundamentally reconsidered, as part of a research and development project by RAG (Spreckels, 2022). The focus was set on a further development of the program system suite PANDA (Niemeier and Tengen, 2022) and its integration into GLOMON.

For more than 6 years, the data collected and stored from RAG's GNSS monitoring stations have been processed automatically within the GLOMON portal of ALLSAT. Over the years, numerous reference and monitoring stations have been added and until now three core GNSS networks have been established. In the former mining regions of the Ruhr Area and Ibbenbueren in the German federal state North-Rhine Westphalia (NRW), and in the federal state Saarland (Spreckels and Engel, 2022), the ground movements will be and have to be monitored alongside the rising of underground mine water levels (Hager and Wollnik, 2016).

The GNSS monitoring network in NRW currently includes various RAG-owned GNSS reference stations together with 10 SAPOS GNSS stations of NRW's surveying authority Geobasis NRW. The data is automatically processed on a daily basis with the post-processing software suite WaPNet from WaSoft. The post-processing results, specifically the 3-dimensional coordinates of all stations together with the respective covariance matrix, are used in weekly terms by PANDA for a deformation analysis, in order to detect relevant movements within the reference station network.

At the start of this PANDA algorithm, all daily solutions are merged into solution results for each week. Based on that, a strict deformation analysis is executed for each epoch. The individual points are either detected as stable, as outliers or as shifted. Then the deformation analysis is continued with all the stable points for the next epoch. This iterative process is cancelled, if the number of remaining points decreases below a defined minimum. All epochs processed are then transformed onto those stations detected to be stable and the changes in coordinates are calculated. For each station, the time series of coordinate changes is then analyzed and then subsequently a model of movement is estimated. If this model of movement fits within the accuracy limits defined, the respective station is set as a shifted point described by a movement model. The iteration is then started again

from the first remeasurement. In this second run the original zero-measurement coordinates, that were used in the first run, are replaced by the calculated coordinates from the model for all stations with movement model. A more detailed description of the whole process of PANDA-algorithm is given in (Niemeier and Tengen, 2022).

Those movement models are calculated once a week, using a sliding window of about two years of preceding observation data. The application in GLOMON requires coordinate updates on a daily basis. Therefore, the calculated movements of each station are extrapolated for the following week at the end of the PANDA-algorithm. Due to the sliding data window, the movement model parameters slightly change from week to week. But that would cause inadmissible jumps within the time series. Furthermore, previously calculated reference station coordinates for a particular point in time would change, when new epochs are added to the time period analyzed before. To avoid such jumps and changes of coordinates due to future data, the movement model is not applied for the coordinate calculation directly, but with a third order polynomial approach. This polynomial is extrapolated for the respective next week, following the deformation analysis and the model calculation. At the start and end point of each polynomial, the function value and the slope are similar to the previous respectively the next polynomial. These polynomials combine the weekly movement models without any jumps and are used for the calculation of station coordinates for a particular point in time.

Figure 5 shows the time series of the UTM-East coordinates of one SAPOS reference station in NRW (red). The total range of the coordinate axes (vertical) is 4 mm. The time period (horizontal) is 30 days. The green graph shows weekly data, calculated by the PANDA algorithm. The slight differences between the red time series from post processing and the weekly data are caused by the different geodetic datum. The weekly data is transformed onto the stations detected as stable, while the post processing results are transformed onto the SAPOS reference stations. The blue time series shows the movement model, that includes linear and seasonal terms for this specific station. The purple time series shows the polynomials.

This approach required extensive changes within the SQL coordinate database. The classical zero-epoch coordinates to which the time series differences have been referenced, was replaced by a dynamic time dependent model that accounts for slow seasonal movements and for certain jumps in station coordinates.

The movement models and the polynomials can be visualized within the existing three-dimensional coordinate time series of the reference stations (see Figure 6).

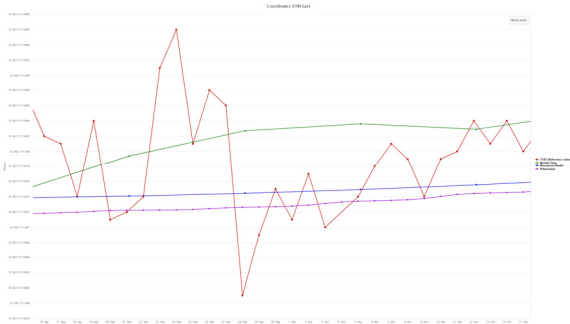


Figure 5. Coordinate times series (red), movement model (blue) and polynomials (purple) of a reference station in GLOMON.

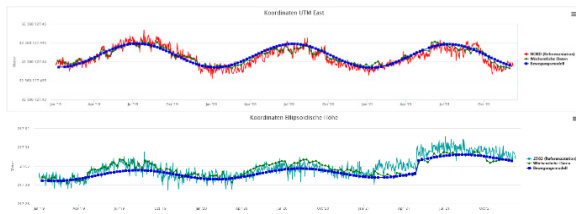


Figure 6. Above: time series of the UTM East coordinates (red) and below: time series of the ell. Height of SAPOS station 2582 (cyan), each with weekly data from the dynamic network adjustment (green) and motion model (blue).

Figure 6 shows the time series and the corresponding movement model of two different reference stations over a period of nearly three years. Figure 6 (above) shows an UTM-East coordinate times series with a significant movement with annual period. Figure 6 (bottom) shows the ellipsoidal Height of a SAPOS station with a detected jump at one point. Exactly at that time of this jump the GNSS antenna has been changed on this reference station. Although, individually calibrated antenna files were used for post processing of the GNSS observation data, the antenna change became obvious within the time series after processing with PANDA.

Furthermore, the time variant coordinates are used, for example, for post processing and adjustment of reference stations within the monitoring network and for downloading observation data (RINEX) from the GLOMON portal for post processing applications (Figure 7).

#### IV. CONCLUSION AND FUTURE WORK

The concept of time-variant coordinates for reference stations has the potential to revolutionize the approach of long-term stable reference points in mine surveying and geodesy, which has been valid for decades. This accounts for the fact, that the Earth's surface is constantly exposed to endogenous and exogenous forces, that cause temporally variable movements and deformations of varying degrees. These movements and deformations can now be modelled by PANDA, and can be applied into the GLOMON post processing and adjustment routines in order to give better and more reliable results (Figure 8).

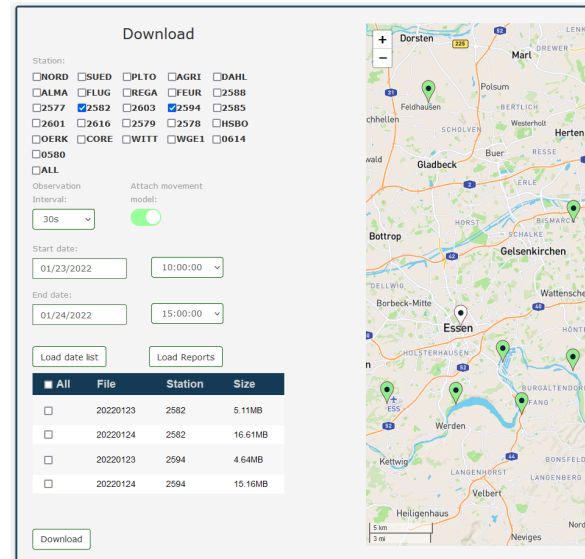


Figure 7. GLOMON RINEX download with possibility to attach movement model to specific coordinates.

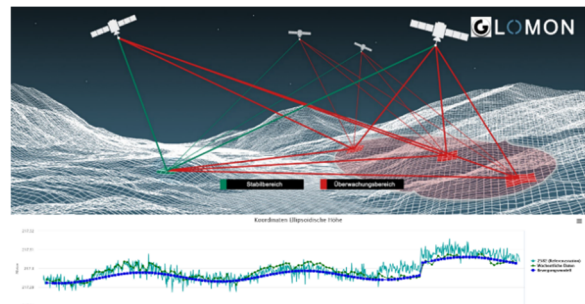


Figure 8. GLOMON Dynamic Network Adjustment.

Nevertheless, there are some points that have received little or no attention so far. The movement models currently generated as part of the dynamic network adjustment describe a linear trend, a seasonal component and, if necessary, offsets. However, the typical ground movements caused by former mining activities cannot only be described with these movements. Radial basis functions (RBF) are ideal for approximating such non-linear movement behavior. The approaches of using several RBFs have already been successfully tested in the area of the former Prosper-Haniel (NRW Germany) mine. An integration into the active dynamic network adjustment is still pending.

Another important aspect is the merging of the results from different sensors and measuring methods that are used for monitoring of ground movements. This will include also external sensors from free available sources, supporting the Open Data concept. Such an integration must take place time synchronized and spatially, since all sensors and the measurement methods used in monitoring have their characteristic strengths and weaknesses. A concept for combining different sensors for an easy 3D overview is the attribution of height changes to tiles (see Figure 9). In a first step, the integration of InSAR data should be tested in order to integrate area-related information for ground movements.

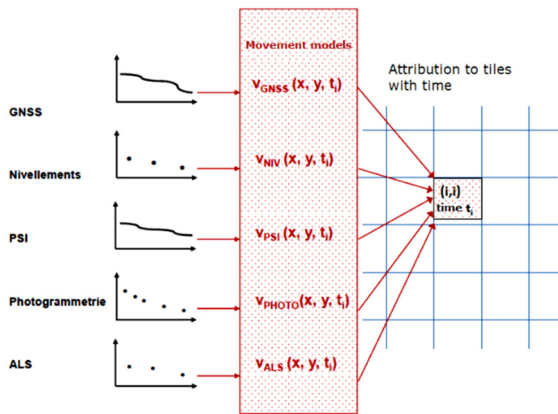


Figure 9. Concept for the integration of different sensors with non-linear movement behavior.

## References

- Hager, S., and F. Wollnik (2016). Mine Surveying and Post-Mining Activities of RAG Aktiengesellschaft / Markscheidewesen und Altbergbau der RAG Aktiengesellschaft. In: *Mining Report Glückauf - Fachzeitschrift für Bergbau, Rohstoffe und Energie*, No. 3, 152. Jahrgang, June 2016. Verlag Bergbau-Verwaltungsgesellschaft mbH, Herne. ISSN 2195-6529, pp 224-232.
- Niemeier, W., Riedel, A., Tengen, D., Riedel, B., and Gerke, M. (2020). Bestimmung flächenhafter vertikaler Landbewegungen entlang der deutschen Nord- und Ostseeküste. In: *Die Küste*, 91 (Online First). DOI: 10.18171/1.091102.
- Niemeier, W., and Tengen, D. (2022). Dynamic concepts to handle geodetic networks with continuous monitoring data in areas with ground movements. In: *Proceedings of the 5<sup>th</sup> Joint International Symposium on Deformation Monitoring JISDM 2022*, Valencia, Spain, June 20-22.
- Spreckels, V., Bechert, S., Schlienkamp, A., Drobniowski, M., Schulz, M., Schäfer, F., Kemkes, E., Ruffer, J., Niemeier, W., Tengen, D., Engel, T., Müller, M., and Schmitt, P. (2020). GNSS, Nivellement und Radar – einheitliche Multisensor-Referenzpunkte zur Überwachung von Bodenbewegungen in ehemaligen Bergbaubereichen. In: *GeoMonitoring 2020*, Technische Universität Braunschweig, S. pp. 207-231. DOI: 10.15488/9351.
- Spreckels, V., and T. Engel (2022). Set-up and application of multisensor-reference stations (MSST) for levelling, GNSS and InSAR in the former mining regions Saarland and Ruhrgebiet within Germany. In: *Proceedings of the 5<sup>th</sup> Joint International Symposium on Deformation Monitoring JISDM 2022*, Valencia, Spain, June 20-22, 2022.
- Spreckels, V. (2022): Multisensor monitoring of ground movements over large areas to conduct the change from the active underground hardcoal mining ages to the post-mining era. In: *Proceedings of the 5<sup>th</sup> Joint International Symposium on Deformation Monitoring JISDM 2022*, Valencia, Spain, June 20-22, 2022.
- Tengen, D., Riedel, A., Riedel, B., Gerke, M., and Niemeier, W. (2019). Ableitung vertikaler Landbewegungen an der deutschen Nord- und Ostseeküste aus GNSS- und PS-Auswertungen, In: *Tagungsband GeoMonitoring 2019*, Leibniz Universität Hannover, S. pp. 121-133. DOI: 10.15488/4517.

## Image segmentation of breakwater blocks by edge-base Hough transformation

Fernando Soares, Vinicius Barbon

Faculty of Sciences of the University of Lisbon, 1749-016 Lisboa, Portugal, ([fjsoares@fc.ul.pt](mailto:fjsoares@fc.ul.pt); [vbarbon99@gmail.com](mailto:vbarbon99@gmail.com))

**Key words:** *image segmentation; breakwaters; point clouds; Hough transformation*

### ABSTRACT

A rubble mound breakwater (BW) is a coastal engineering structure built for purposes of harbor protection in areas with severe wave regimes. Block displacements can lead to a weakening of the protection, making the harbor more vulnerable to waving hazard. During the phase of BW design/rehabilitation the effectiveness evaluation of both the shape and the protective elements is made throughout 3D scale models, built inside wave basins or wave flumes. The experiment consists of simulating the impact of the swell on the physical model of the BW. During the process, 3D point cloud (PC) data is recorded with time-of-flight sensors, or later generated by photogrammetry from recorded RGB images. Surface changes can be obtained by comparing the PCs, identifying common points and estimating differences in their positions. However, inaccurate identification of points on the PC may lead to inconclusive results on the location and movement of the blocks. In this study, the authors propose to use both synchronized and registered RGB and PC data to estimate the displacement/motion of breakwater blocks. An edge-based image segmentation method, based on the Hough transformation algorithm is proposed, in order to obtain the straight edges of block's faces that are mostly seen from above. For each extracted polygonal region, the 3D points on the PC are selected and used to determine a plane surface model by least squares. After, the 3D spatial coordinates of the block's center point can be obtained from the ones of the given polygonal face model. For this study RGB and PC data regions were selected from a scanned BW model, built with small cubic concrete blocks. The results obtained reinforce the positive contribution that the proposed image segmentation methodology can provide, regarding the improvement of displacement accuracy and spending time analysis, in BW monitoring work.

*This contribution was selected by the Scientific Committee for publication as an extended paper in the Journal of Applied Geodesy <https://www.degruyter.com/journal/key/jag/html>*

## Crustal velocity field in Baza and Galera faults: A new estimation from GPS position time series in 2009 - 2018 time span

Antonio J. Gil<sup>1,2,3</sup>, M. Jesús Borque<sup>1,2,3</sup>, Manuel Avilés<sup>1,2,3</sup>, M. Clara de Lacy<sup>1,2,3</sup>,  
Jesús Galindo-Zaldívar<sup>4</sup>, Pedro Alfaro<sup>5</sup>, F. J. García-Tortosa<sup>2,6</sup>, Alberto Sánchez-Alzola<sup>7</sup>,  
Iván Martín-Rojas<sup>5</sup>, Iván Medina-Cascales<sup>5</sup>, Patricia Ruano<sup>4</sup>, Víctor Tintero<sup>4</sup>,  
Asier Madarieta-Txurruka<sup>4</sup>, Sergio Blanca<sup>3</sup>, Moisés Madrigal<sup>3</sup>, Fernando Chacón<sup>3</sup>, Lucía Miras<sup>2</sup>

<sup>1</sup> Departamento de Ingeniería Cartográfica, Geodesia y Fotogrametría, Universidad de Jaén, Campus de las Lagunillas, 23071 Jaén, Spain, ([aigil@ujaen.es](mailto:aigil@ujaen.es); [mjborque@ujaen.es](mailto:mjborque@ujaen.es); [maviles@ujaen.es](mailto:maviles@ujaen.es); [mclacy@ujaen.es](mailto:mclacy@ujaen.es))

<sup>2</sup> Centro de Estudios Avanzados en Ciencias de la Tierra, Energía y Medio Ambiente (CEACTEMA), Universidad de Jaén, Campus de las Lagunillas, 23071 Jaén, Spain, ([Imp00043@red.ujaen.es](mailto:Imp00043@red.ujaen.es))

<sup>3</sup> Grupo de Investigación RNM282-Microgeodesia Jaén, Universidad de Jaén, Spain, ([sbmena@ujaen.es](mailto:sbmena@ujaen.es); [mmr00033@red.ujaen.es](mailto:mmr00033@red.ujaen.es); [fchacon@ujaen.es](mailto:fchacon@ujaen.es))

<sup>4</sup> Departamento de Geodinámica, Universidad de Granada, Spain, ([jgalindo@ugr.es](mailto:jgalindo@ugr.es); [pruano@ujaen.es](mailto:pruano@ujaen.es); [vtintero@ugr.es](mailto:vtintero@ugr.es); [amadatxu@ugr.es](mailto:amadatxu@ugr.es))

<sup>5</sup> Departamento de Ciencias de la Tierra y del Medio Ambiente, Universidad de Alicante, Spain, ([pedro.alfaro@ua.es](mailto:pedro.alfaro@ua.es); [ivan.martin@ua.es](mailto:ivan.martin@ua.es); [ivan.medina@ua.es](mailto:ivan.medina@ua.es))

<sup>6</sup> Departamento de Geología, Universidad de Jaén, Spain, ([gtortosa@ujaen.es](mailto:gtortosa@ujaen.es))

<sup>7</sup> Departamento de Estadística e Investigación Operativa, Universidad Cádiz, Spain, ([alberto.sanchez@uca.es](mailto:alberto.sanchez@uca.es))

**Key words:** *Baza and Galera Faults; Survey-mode campaigns; Position time series; velocity field*

### ABSTRACT

The Baza and Galera faults are two active geologic structures located in the central area of the Betic Cordillera (Southern Spain). The goal of our research is to constrain the activity of this faults from high quality GPS measurements to obtain precise deformation rates. In 2008 a GPS survey – mode network was installed to monitor this area. In previous works, we presented a velocity field based on the analysis of some GPS campaigns. Here we show the new results computed from nine GPS campaigns in the timespan 2009-2018. The measurements were done in September 2009, 2010, 2011, 2012, 2013, 2014, 2015, 2017 and 2018. The data process and analysis were performed in Precise Point Positioning by using GIPSYX 1.6 software. GIPSY is a GNSS-inferred positioning software developed by the Jet Propulsion Laboratory. Then, the new estimation of the crustal velocity field is computed from the IGB14 time series by SARI software. The model applied to the original time series, using weighted least squares, consists of an intercept, a site rate and an offset to account for an antenna change. The error term is composed of white noise and temporally correlated random error. The colored noise is described by a random-walk process. We have assumed a typical magnitude for this process of 1.0 mm/Vyr. Finally, we discuss the implications of the new results for the tectonic setting and seismic hazard assessment of this key tectonic area of the Betic Cordillera.

### I. STUDY AREA AND GPS NETWORK

The Betic Cordillera (Southern Spain) is located in the western part of the Peri-Mediterranean Alpine Orogen. At present it is undergoing to a NNW-SSE main shortening and, in its central sector, to an approximately perpendicular extension along the ENE-WSW to NE-SW direction. The extension is mainly accommodated by NNW-SSE normal faults. This extension deforms the materials belonging to the Internal and External zones of the mountain range, as well as the sedimentary infill of intramountain basins, including the Guadix-Baza Basin (GBB) (Alfaro *et al.*, 2008). Figure 1 is a simplified geological map of the Guadix-Baza Basin, showing the main active structures in the basin: Baza Fault, Galera Fault, Graena Fault, Zamborino Fault, Alfahuara-Botardo Fault, Guadix

Fault, Negratín Fault, Benamaurel Fault, and Cúllar Fault. In this area two main active structures stand out from the rest: the Galera and the Baza Faults. The Baza Fault is a normal fault of 40 km long, with a direction that varies from NW-SE to NS and a dip that ranges between 45° and 65° towards the ENE. The Galera Fault is a 25 km-long strike-slip fault striking N065E.

In 2008 a GPS survey – mode network that consisted of seven sites was built to analyse the kinematics of these faults (Gil *et al.*, 2012). These sites were located in well-defined areas in the two geological blocks of the faults (Figure 1). They were fixed to exposed rocks using self-centering mountings. The measurements cover a total of 9 GPS field campaigns, with a 5-day time span, in September 2009, 2010, 2011, 2012, 2013, 2014, 2015, 2017 and 2018. The main reason of

measuring in the same month of every year is to avoid seasonal effects that could impact the position time series and their further analysis. Figure 2 shows the GPS antenna AR10 with integrated radome installed on the site 5600 during a survey.

In 2008 a GPS survey – mode network that consisted of seven sites was built to analyse the kinematics of these faults (Gil *et al.*, 2012). These sites were located in well-defined areas in the two geological blocks of the faults (Figure 1). They were fixed to exposed rocks using self-centering mountings. The measurements cover a total of 9 GPS field campaigns, with a 5-day time span, in September 2009, 2010, 2011, 2012, 2013, 2014, 2015, 2017 and 2018. The main reason of measuring in the same month of every year is to avoid seasonal effects that could impact the position time series and their further analysis. Figure 2 shows the GPS antenna AR10 with integrated radome installed on the site 5600 during a survey.

Regarding the measurements, in the 2009 and 2010 campaigns the GPS receivers used were Leica

Geosystem GX1230 and LEIAX1202 antennas whereas in the subsequent campaigns 2011, 2012, 2013, 2014, 2015, 2017 and 2018 the sites were observed with LEICA Geosystem AR10 receivers and LEIAR10 antennas with integrated radome. The GPS data processing was performed by Precise Point Positioning using GipsyX software (Bertiger *et al.*, 2020). GipsyX is a GNSS-inferred positioning software developed by the Jet Propulsion Laboratory (JPL) and maintained by the Near Earth Tracking Applications and Systems groups. A similar standard procedure for all campaigns was used. All the JPL products are referred to the IGB14 reference frame (IGS Mail, 2018), ensuring an unchanged geodetic frame for all the observation campaigns. This methodology has been a good approach for an accurate crustal deformation analysis that has already been applied in many other geodetic studies (Sánchez-Alzola *et al.*, 2014; Gárate *et al.*, 2015; Gil *et al.*, 2017; Borque *et al.*, 2019).

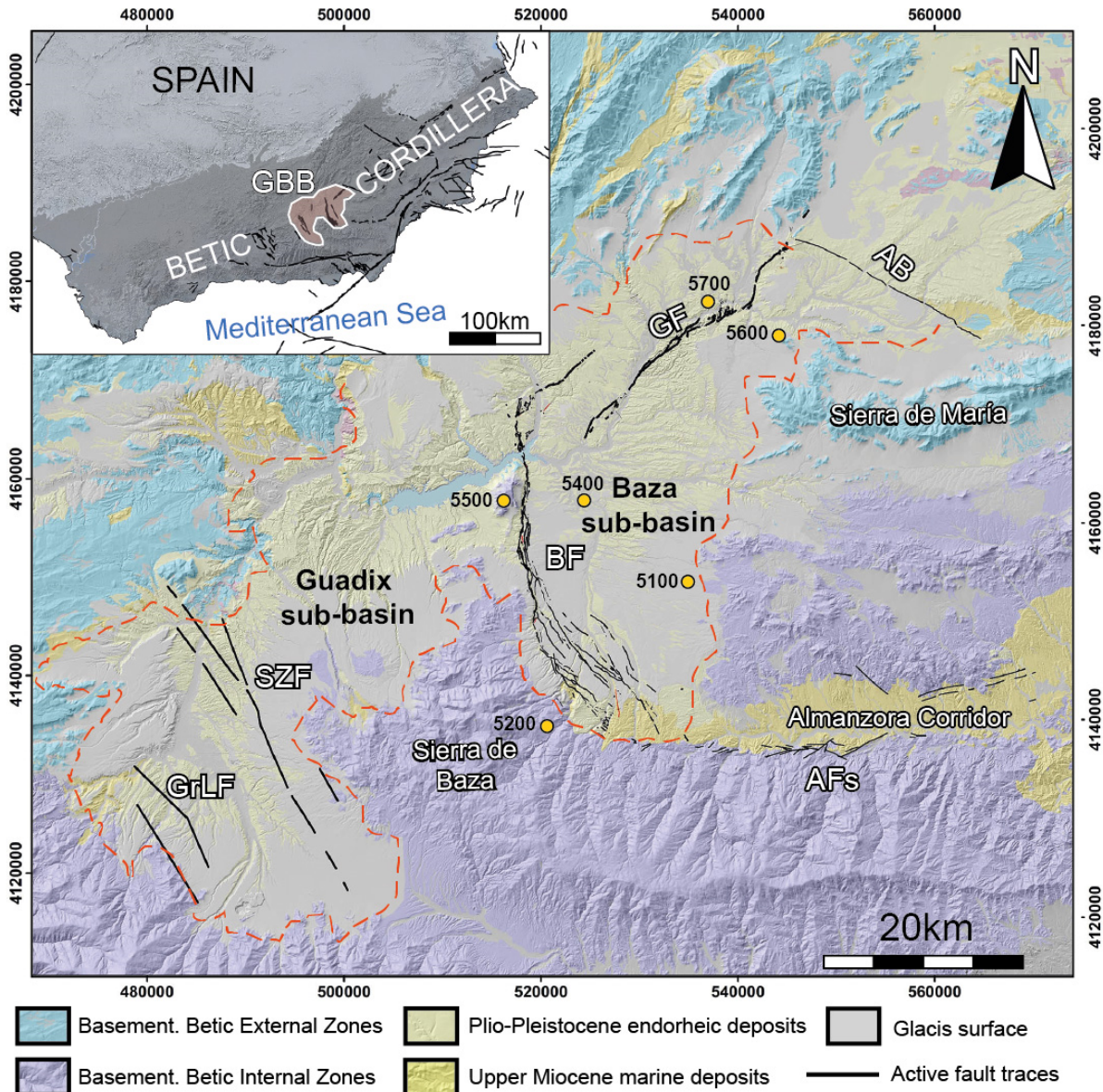


Figure 1. FGBB simplified geological map. UTM coordinates in m.





Figure 2. Site 5600 with the GPS antenna AR10 (integrated radome) during a survey.

## II. GPS TIME SERIES AND VELOCITY ESTIMATION

After processing all the daily data files with GipsyX in the IGB14 reference frame, the time series are displayed. It is highly important to consider the change of the GPS antennas and receivers between the 2011 and the 2012 campaigns which produces a slip in the time series. Then, the new estimation of the crustal velocity field is computed from the IGB14 time series by using the Time Series Analysis Software SARI (Santamaría-Gómez, 2019). The SARI software is able to estimate various complex theoretical adjustment models. In our case, the model applied to the original time series, using weighted least squares, consists of an intercept, a site rate and an offset to account for antenna changes. The uncertainties are computed using colored noise model. The error term is composed of white noise and temporally correlated random error. The colored noise is described by a random-walk process. We have assumed a typical magnitude for this process of 1.0 mm/vyr. Table 1 shows the East and North absolute velocities and uncertainties estimated in the Baza and Galera network sites. Figure 3 shows the de-trended position time series of the Baza and Galera GPS sites in horizontal components North and East.

Table 1. East and North absolute velocities and uncertainties estimated in the Baza and Galera network sites. Residual velocities are with respect to Eurasia

Site ID	Velocity [mm yr <sup>-1</sup> ]		Uncertainty [mm yr <sup>-1</sup> ]		Res. Velocity [mm yr <sup>-1</sup> ]	
	East	North	East	North	East	North
5100	19.3	16.5	±0.4	±0.5	-0.7	0.0
5200	18.5	16.7	±0.4	±0.6	-1.6	0.2
5400	17.9	16.7	±0.5	±0.6	-2.1	0.2
5500	18.7	16.4	±0.5	±0.5	-1.3	-0.1
5600	19.3	16.4	±0.5	±0.5	-0.7	-0.1
5700	18.8	16.6	±0.4	±0.4	-1.2	0.0

## III. RESULTS AND ANALYSIS

The absolute velocities (average of 18.75 mm/yr East and 16.55 mm/yr North) agree with the general movement of the area due to the tectonic (Figure 4). Table 1 shows the residual velocities calculated with

respect to a fixed Eurasia as defined by the ITRF2014 plate motion model (Altamimi *et al.*, 2017).

These residual velocities with respect to fixed Eurasia show the strain pattern of the area ranging from 0.7 mm/yr (5600) up to 2.1 mm/yr (5400) (Figure 5).

The results indicate a movement between the two blocks; on the one hand, the Galera Fault (sites 5600 and 5700 sites) shows a sinistral strike slip motion. On the other hand, the sites near the Baza Fault present remarkable differences. If we consider the North area (sites 5500 and 5400) the displacements are probably related with the kinematic of the North segment of the Fault, whereas in the South region (sites 5100 and 5200) the influence of minor faults should be considered. This outcome gives us a very valuable information of the involved geodynamics, standing out the differences between these geologic structures.

## IV. CONCLUSIONS

In this work we have performed an update of the velocity field in a key tectonic zone of the Betic Cordillera that is earthquake-prone. In spite of the low signal-to-noise ratios of the residual velocities which are related to the comparatively small deformation rate in this region, the results agree well with geological knowledge and regional geodetic outcomes (Alfaro *et al.*, 2021). Moreover, the residual velocities seem to show that the Baza and the Galera Faults are kinematically consistent and that the Baza sub-basin is structured in two main tectonic blocks with no significant internal deformation. This suggests a possible physical connection between the Baza and the Galera faults.

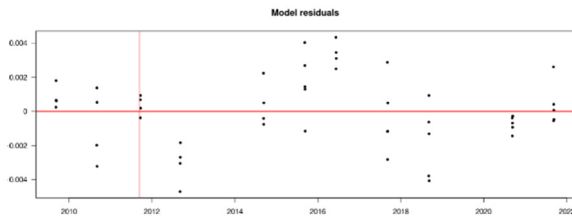
This research contributes to the prevention and mitigation of geological risks. Geodetic monitoring from episodic measurements in those geological fault control networks, has allowed the creation of strain maps that are very useful in the assessment of seismic and geological hazard with obvious benefits on the safety of Andalusian Society.

Finally, the consideration of longer time series with new GNSS campaigns in the upcoming years will help to improve the estimation of the velocity field in this area and will allow us to confirm these results.

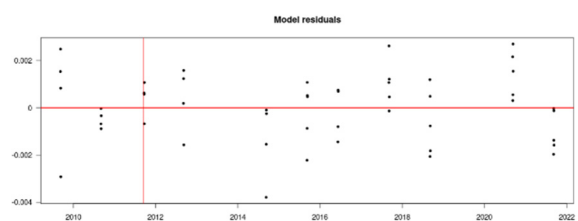
## V. ACKNOWLEDGEMENTS

This work has been funded by Programa Operativo FEDER Andalucía 2014-2020 - call made by University of Jaen in 2018, Ref. 1263446, POAIUJA 2021/2022, CEACTEMA, and RNM148 and RNM282 research groups of Junta de Andalucía.

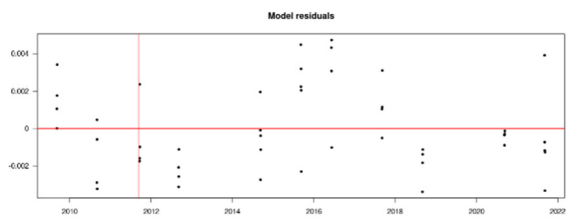
5100 North



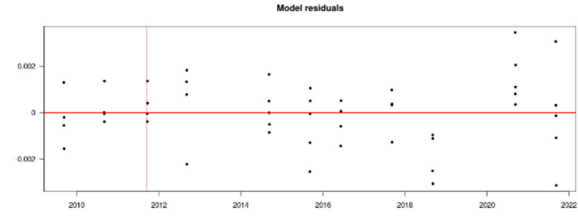
5100 East



5200 North



5200 East



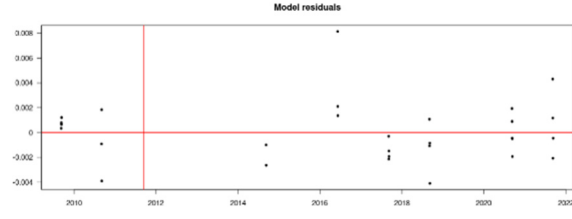
5400 North



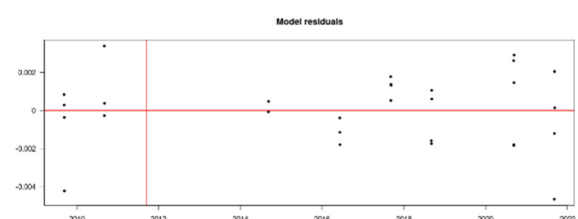
5400 East



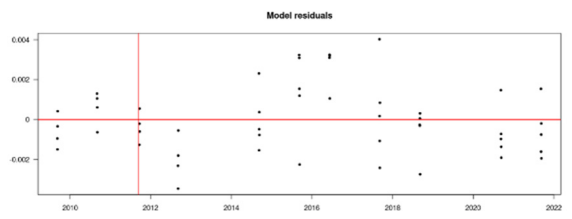
5500 North



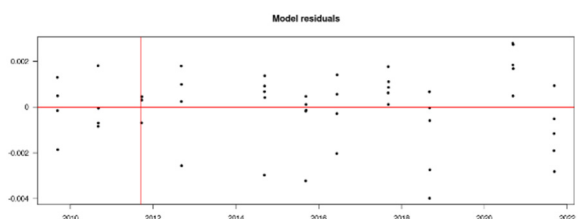
5500 East



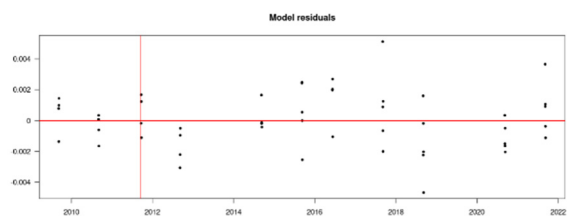
5600 North



5600 East



5700 North



5700 East



Figure 3. De-trended position time series of the Baza and Galera GPS sites. Vertical lines represent GPS antenna changes. Units are m.

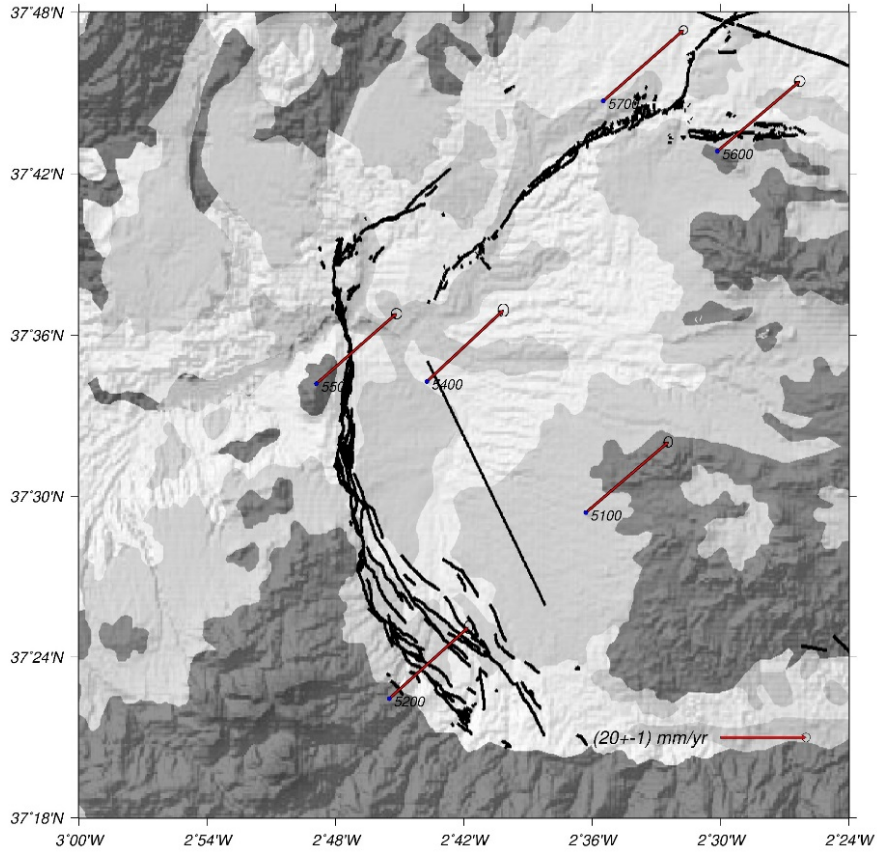


Figure 4. Absolute velocity field in IGB14 reference frame.

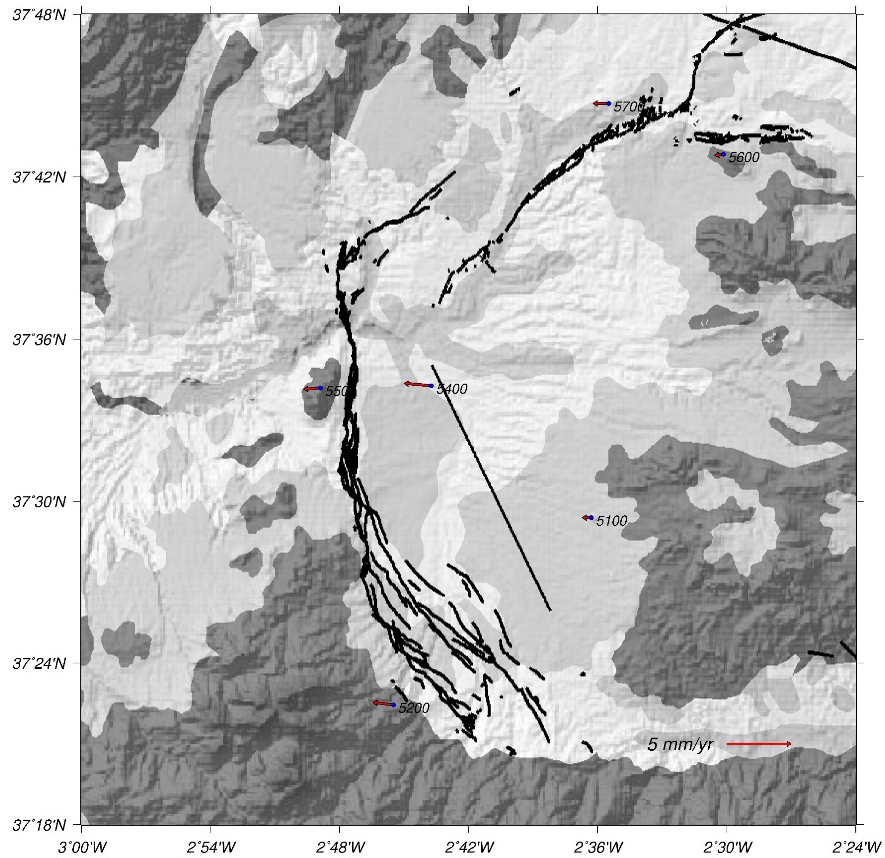


Figure 5. Residual velocity field with respect to Eurasia fixed.

## References

- Alfaro, P., Delgado, J., Sanz de Galdeano, C., Galindo-Zaldívar, J., García-Tortosa, F.J., López-Garrido, A.C., López-Casado, C., Marín, C., Gil, A., and Borque, M.J., (2008). The Baza Fault: a major active extensional fault in the Central Betic Cordillera (South Spain). *International Journal of Earth Sciences*, 97, pp. 1353–1365.
- Alfaro, P., A. Sánchez-Alzola, I. Martín-Rojas, F.J. García-Tortosa, J. Galindo-Zaldívar, M. Avilés, A.C. López Garrido, C. Sanz de Galdeano, P. Ruano, F.J. Martínez-Moreno, A. Pedrera, M.C. Lacy, M.J. Borque, I. Medina-Cascales, and Gil, A.J. (2021). Geodetic fault slip rates on active faults in the Baza sub-Basin (SE Spain): Insights for seismic hazard assessment. *Journal of Geodynamics*, 144, 101815.
- Altamimi, Z., Métivier, L., Rebischung, P. Rouby, H., and Collillieux, X. (2017). ITRF2014 plate motion model. *Geophysical Journal International*, 209.
- Bertiger, W., Bar-Sever, Y., Dorsey, A., Haines, B., Harvey, N., Hemberger, D., and Willis, P. (2020). GipsyX/RTGx, a new tool set for space geodetic operations and research. *Advances in space research*, 66(3), pp. 469-489. DOI: 10.1016/j.asr.2020.04.015.
- Borque, M. J., Sánchez-Alzola, A., Martín-Rojas, I., Alfaro, P., Molina, S., Rosa-Cintas, S., and Gil, A. J. (2019). How much Nubia-Eurasia convergence is accommodated by the NE end of the Eastern Betic Shear Zone (SE Spain)? Constraints from GPS velocities. *Tectonics*, 38(5), pp. 1824-1839.
- Gárate, J., Martín-Davila, J., Khazaradze, G., Echeverria, A., Asensio, E., Gil, A. J., and Harnafi, M. (2015). Topo-Iberia project: CGPS crustal velocity field in the Iberian Peninsula and Morocco. *GPS Solutions*, 19(2), pp. 287-295.
- Gil, A.J., García Tortosa, F.J., Alfaro, P., Galindo, J., López-Garrido, A.C., de Lacy, M.C, Ruano, P., Pedrera, A., Sanz, C., Borque, M.J., Armenteros, J.A., and Avilés M. (2012). Geodetic Deformation Monitoring of the Baza Fault from GPS. In *proceedings of 7<sup>a</sup> Asamblea Hispano-Portuguesa de Geodesia y Geofísica*. San Sebastián.
- Gil, A.J., Galindo-Zaldívar, J., Sanz de Galdeano, C., Borque, M.J., Sánchez-Alzola, A., Martínez-Campos, M., and Alfaro, P. (2017). The Padul normal fault activity constrained by GPS data: Brittle extension orthogonal to folding in the central Betic Cordillera. *Tectonophysics*, 712–713, pp. 64-71.
- IGS Mail, (2018). IGS Mail 7921, IGS Mail Archive. Available at: <https://lists.igs.org/mail-man/listinfo/igsmail>.
- Sánchez-Alzola, A., Sánchez, C., Giménez, J., Alfaro, P., Gelabert, B., Borque, M.J., and Gil, A.J. (2014). Crustal velocity and strain rate fields in the Balearic Islands based on continuous GPS time series from the XGAIB network (2010–2013). *Journal of geodynamics*, 82, pp. 78-86. DOI: 10.1016/j.jog.2014.05.005
- Santamaría-Gómez, A., (2019). SARI: interactive GNSS position time series analysis software. *GPS Solution*, 23, 52. DOI: 10.1007/s10291-019-0846-y

## Optical distance measurements at two wavelengths with air refractive index compensation

Joffray Guillory, Daniel Truong, Jean-Pierre Wallerand

Conservatoire national des arts et métiers (Cnam), Laboratoire Commun de Métrologie LNE-Cnam (LCM), LNE, 1 rue Gaston Boissier, 75015 Paris, France, ([joffray.guillory@cnam.fr](mailto:joffray.guillory@cnam.fr); [daniel.truong@cnam.fr](mailto:daniel.truong@cnam.fr); [jean-pierre.wallerand@cnam.fr](mailto:jean-pierre.wallerand@cnam.fr))

**Key words:** absolute distance meter; two-wavelength telemeter; length metrology; air index compensation

### ABSTRACT

We present our first results in the realization of an absolute distance meter that will bring well-defined and metrologically traceable measurements for distances of several kilometers. The purpose is to achieve an accuracy of 1 mm up to 5 km and beyond. To this end, the developed prototype operates at two different wavelengths, 780 nm and 1560 nm. For each of these wavelengths, the measured distance is determined from the phase accumulated by a radio-frequency carrier propagated in air by a laser beam modulated in intensity. Thus, using the dispersion relation between these two measurements, a compensation of the refractive index of air can be applied, *i.e.* no measurement of temperature, pressure and CO<sub>2</sub> content of the air is required. In this paper, the principle of the two-wavelength absolute distance meter is explained, and preliminary results are presented, for each wavelength and with air refractive index compensation.

### I. INTRODUCTION

The construction of large-scale facilities such as particle accelerators (Gervaise, 1983), the monitoring of civil engineering structures such as dams and tunnels (Curtis, 1992), or the survey of geological formations such as glaciers (Fruckacz *et al.*, 2016), volcanoes and faults (USGS, 2021) require absolute measurements of long distances with high accuracy. Therefore, we are developing an Absolute Distance Meter (ADM) that will bring metrologically traceable measurements for distances of several kilometers. The objective is to achieve an accuracy of 1 mm up to 5 km and beyond.

This instrument, an Electro-optical Distance Meter (EDM), is based on a well-known technique: a light beam is intensity modulated by a RF carrier, propagated in air up to a distant target, retroreflected, and finally detected by a photodetector. The distance to be measured is thus proportional to the phase delay  $\phi$  measured between the RF carrier detected after propagation in air and the emitted one (Eq. 1):

$$D = \frac{1}{2} \left( \frac{\phi}{2\pi} + k \right) \times \frac{c}{n \times f_{RF}} \quad (1)$$

with  $c$  the speed of light in vacuum,  $n$  the group refractive index of air,  $f_{RF}$  the frequency modulation of the light, and  $k$  an integer number corresponding to the number of times that the phase has rotated by  $2\pi$  during its propagation.

The major challenge for such EDMs when used for the surveying of long-distances lies in the determination of the air refractive index. Usually, it is calculated using the semi-empirical Edlén's equation (Edlén, 1966, or similar

updated formulas like Bönsch and Potulski, 1998) that depends on the vacuum optical wavelength, but also on the air temperature  $T$ , the pressure  $p$ , the partial pressure of water  $p_w$ , and the CO<sub>2</sub> content  $x$ . The air refractive index is the parameter that contributes the most to the uncertainty on long-distance measurements: for instance, an accuracy of 1 mm over 5 km would require a knowledge of the temperature at 0.2 °C, which is nearly impossible to achieve in practice using classical sensors.

### II. TWO-COLOUR ADM

#### A. Principle

To overcome this limitation, a two-colour system can be adopted (Earnshaw *et al.*, 1967). This consists in measuring two optical distances simultaneously at two different wavelengths. Thus, by using the dispersion relation between these two measurements, a compensation of the air refractive index can be applied (first velocity correction). This approach has led to a field instrument in the 1980's called Terrameter, which was able to measure a distance of 10 km with an uncertainty of 1 mm. It worked at wavelengths of 441.6 nm and 632.8 nm (Huggett, 1981; Gervaise, 1983). In the same period, a two-color Geodimeter was also developed: the performances were similar with an uncertainty of approximately 1.2 mm for a 10 km baseline (Langbein, 1987). However, these EDMs, produced in very limited series, are no more in operation because of their quite difficult use and of their complicated design.

The distance  $L$  measured by a two-colour ADM, *i.e.* the length of the wave paths also called air index

compensated distance (first velocity correction), is calculated as follows (Eq. 2):

$$L = D_{\lambda_1, n=1} - \frac{n(\lambda_1, T, p, x, p_\omega) - 1}{n(\lambda_2, \dots) - n(\lambda_1, \dots)} (D_{\lambda_2, n=1} - D_{\lambda_1, n=1}) \quad (2)$$

with  $D_{\lambda_1, n=1}$  and  $D_{\lambda_2, n=1}$  the two optical distances measured by the ADM at the wavelengths  $\lambda_1$  and  $\lambda_2$ . The optical distances  $D_{\lambda_1, n=1}$  and  $D_{\lambda_2, n=1}$  are measured in open air, taking in Equation 1 an air index equal to 1. They are defined as (Eq. 3):

$$L = \frac{D_{\lambda_1, n=1}}{n(\lambda_1, T, p, x, p_\omega)} = \frac{D_{\lambda_2, n=1}}{n(\lambda_2, T, p, x, p_\omega)} \quad (3)$$

According to Meiners-Hagen (Meiners-Hagen and Abou-Zeid, 2008), and using the Bönsch and Potulski (1998) notations, the compensated distance can be simplified as follows (Eq. 4):

$$L = \frac{K(\lambda_1)D_{\lambda_2, n=1} - K(\lambda_2)D_{\lambda_1, n=1}}{K(\lambda_1) - K(\lambda_2) + p_\omega \times (g(\lambda_1) \cdot K(\lambda_2) - g(\lambda_2) \cdot K(\lambda_1))} \quad (4)$$

where  $K$  and  $g$  are wavelength-dependent factors. It appears that the formula giving the compensated distance no longer depends on the temperature, pressure or CO<sub>2</sub> content, but only on the measurement of the partial pressure of water  $p_\omega$ . To reach an accuracy of 1 mm over 5 km,  $p_\omega$  has to be measured with an accuracy of 200 Pa, *i.e.* a relative humidity of 15.0 % at 10 °C or of 7.5 % at 20 °C.

In dry air, Equation 2 can be simplified as follows (Eq. 5):

$$L = D_{\lambda_1, n=1} - A(\lambda_1, \lambda_2) \times (D_{\lambda_2, n=1} - D_{\lambda_1, n=1}) \quad (5)$$

with (Eq. 6):

$$A(\lambda_1, \lambda_2) = \frac{K(\lambda_1)}{K(\lambda_1) - K(\lambda_2)} \quad (6)$$

Thus, for a given uncertainty on  $D_{\lambda_i, n=1}$ , the final uncertainty on the compensated distance  $L$  is degraded due to the factor  $A$ . Since this factor is considerably higher than unity, the uncertainty component due to the uncertainties on  $D_{\lambda_1, n=1}$  and  $D_{\lambda_2, n=1}$  is (Eq. 7):

$$\sigma(L) \simeq A \times \sqrt{\sigma(D_{\lambda_1, n=1})^2 + \sigma(D_{\lambda_2, n=1})^2} \quad (7)$$

when assuming the distance measurements performed at  $\lambda_1$  and  $\lambda_2$  are uncorrelated. It should be noted that even for wet air the scaling of the uncertainty by the factor  $A$  remains a good approximation.

### B. Design of the prototype

This approach has been implemented at 779.8 nm and 1559.6 nm. The low dispersion between these

wavelengths leads to a rather large factor  $A$  equal to 48. Thus, at each single-wavelength, an uncertainty around 20  $\mu\text{m}$  on the distance measurement is required to reach an uncertainty of 1 mm on the air index compensated distance. Dealing with such a large factor  $A$  is for sure challenging. It could be reduced by choosing shorter wavelengths or by increasing the spacing between them. Thus, from a theoretical point of view, the two-colour Terrameter and Geodimeter EDMs, with blue and red lights, lead to potential better uncertainty thanks to a factor  $A$  around 22. Nevertheless, the wavelengths of our prototype are interesting due to the wide availability of affordable fiber-optic components in this range, especially at 1560 nm, which is used in the telecommunication industry.

The developed prototype is presented in Figure 1. It is compact, easily transportable, and thus ready for measurements in the field.

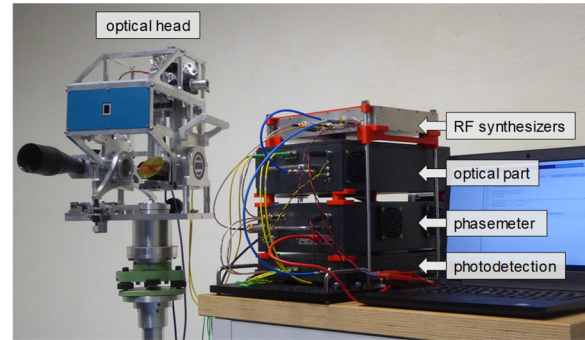


Figure 1. Photograph of the developed two-colour Absolute Distance Meter.

The setup of the two-colour telemeter is depicted in Figure 2. The optical carrier at 1560 nm is emitted by a laser diode, intensity-modulated by a RF carrier at 5060.75 MHz using an Electro-Absorption Modulator (EAM), then amplified by an optical amplifier. From this first signal, a second one at 780 nm is obtained by frequency doubling in a non-linear Periodically Poled Lithium Niobate (PPLN) waveguide. This second-harmonic generation results in a signal of half the wavelength of the pump at 1560 nm, but of modulation frequency unchanged.

Each of these optical signals passes through an optical splitter which acts as a high-isolation circulator. The two optical beams are then combined: after emission in free space and collimation by off-axis parabolic mirrors, the beam at 1560 nm passes through a dichroic mirror, while the one at 780 nm is reflected on it. Once the beams are superimposed, the spot sizes are magnified by a factor 10.2 thanks to a couple of parabolic mirrors to obtain, respectively, diameters of 28.0 mm and 29.0 mm (defined as twice the distance from the spot center where the intensity drops to  $1/e^2$  of the max value) at 780 nm and 1560 nm.

After propagation over a long distance up to a hollow corner cube, the two beams come back to the telemeter to be reinjected into the same fibers as previously. After a second pass through the optical

splitters, the two laser beams are directed towards their respective photodiode (PD). At this point, the RF signals are down-converted by a Local Oscillator (LO) into an Intermediate Frequency (IF) of 10.75 MHz, amplified by 70 dB, and finally converted by 14 bit and 250 MSa/s Analog to Digital Converters (ADC). The distances are then calculated from the phase difference between these measurement signals and an electrical reference built from the direct mixing of the RF and LO carriers. The signals are processed digitally by a Field-Programmable Gate Array (FPGA) and displayed on Matlab.

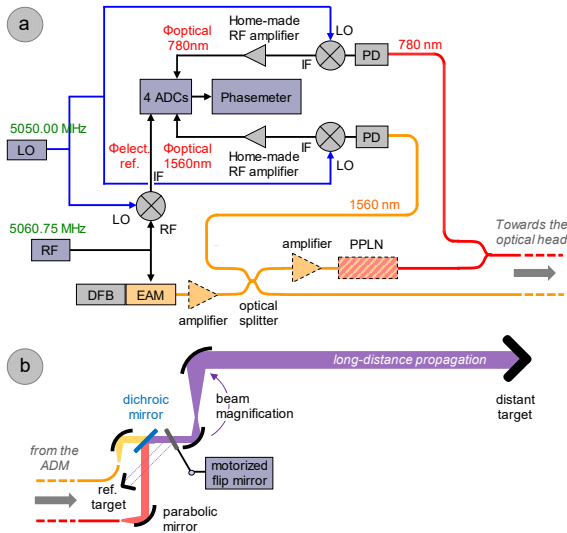


Figure 2. The two-colour fiber-optic Absolute Distance Meter (a), and its optical head for combination and collimation of the two optical beams, 780 nm and 1560 nm (b).

As shown in Figure 2, a motorized flip mirror has been implemented to deviate the free-space optical beams towards a small reference corner cube and thus compensate the phase variations induced by temperature changes in the optoelectronic, fibre-optic and microwave components. In practice, this mechanical zero measurement is performed every second.

It has to be noted that the distance resolution of our instrument is a function of the frequency modulation of the light: the higher the modulation frequency, the better the resolution. With a RF carrier around 5 GHz, a good compromise between cost and performances is obtained. For comparison, the two-colour Terrameter et Geodimeter EDMs had a RF carrier around 3 GHz (Gervaise, 1983; Langbein *et al.*, 1987).

At the end, the traceability of the measurement to the SI (Système International d'unités) is ensured by the knowledge of the modulation frequency and of the phase measurement. All the frequency synthesizers and the phasemeter are locked on a same reference, a Rubidium atomic clock accurate at  $4.8 \cdot 10^{-10}$  over a year (aging rate  $df_{RF}/f_{RF}$  of a Microsemi clock SA.22c).

As an example, a short distance of 0.5 m has been measured in a controlled environment ( $T = 23.6 \text{ }^\circ\text{C}$ ).

Figure 3 shows the results for both wavelengths, 780 nm and 1560 nm, and for an air refractive index equal to 1. This depicts the distances calculated from Equation 1, in relative for a better reading of the curves. However, the absolute distances are known.

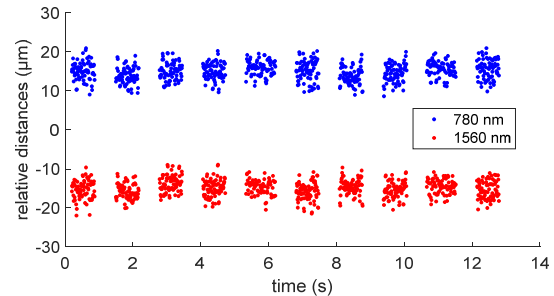


Figure 3. Distance measurement at 780 nm and 1560 nm over 0.5 m for  $n=1$ .

In Equation 1, the measured RF phase delay is wrapped into the interval  $[-\pi, +\pi]$ , therefore the integer number  $k$  of synthetic wavelengths  $c/f_{RF}$  has to be determined. In practice, the latter was deduced from several distance measurements performed at different RF carriers. In the example of the Figure 3,  $k$  equals to 17 and the measured distance to about 0.515 m.

For each measurement, 10 packets of 75 points (20 ms of integration time per point) have been recorded. Between these packets, a distance measurement of the reference target was performed to compensate for possible distance variations. At the end, the standard deviation of these curves is around  $2.3 \text{ } \mu\text{m}$ . However, the two distance measurements are in part correlated as the standard deviation of their difference is only  $1.5 \text{ } \mu\text{m}$ .

Figure 4 depicts the result after applying Equation 4, *i.e.* with air refractive index compensation. Due to the factor  $A$ , and as described by the Equation 7, the uncertainty is 48 times higher than the difference obtained between the two wavelengths: the observed standard deviation is equal to  $69.6 \text{ } \mu\text{m}$ . Nevertheless, in such a case, the knowledge of the air temperature and atmospheric pressure is not required to determine the compensated distance.

### III. EXPERIMENTAL MEASUREMENTS

#### A. 1560 nm: comparison with an interferometric bench

In the developed system, the optical carrier at 780 nm and its frequency modulation are generated from the modulated signal at 1560 nm. Therefore, as a prerequisite, it is necessary to ensure the correct functioning of the distance measurement at this wavelength. To this end, the ADM at 1560 nm has been compared to a 50 m-long interferometric bench, indoors, in a controlled environment. In this comparison, realized before the full completion of the prototype design, the optical beam at 1560 nm was directly collimated without passing through the dichroic mirror.

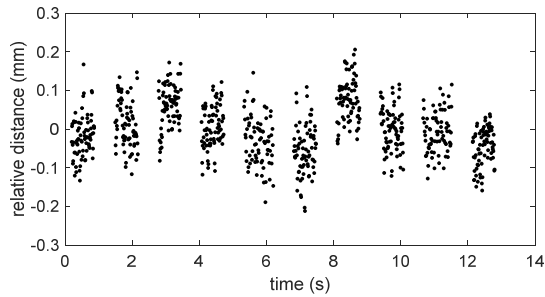


Figure 4. Distance measurement with air refractive index compensation over 0.5 m.

The results are depicted in Figure 5. The error (y-axis) represents the difference between the interferometric distance and an average distance over 10 packets measured by our ADM (like in Figure 3). Both distances have been corrected by the air refractive index, which has been estimated for the ADM wavelength (group index at 1560 nm) and the interferometric wavelength (phase index at 633 nm, Renishaw XL-80) thanks to weather stations. The displacement (x-axis) vary up to 100 m thanks to a double round trip.

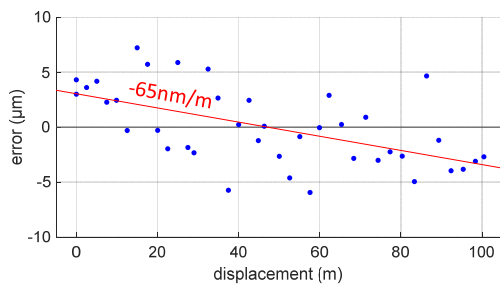


Figure 5. Comparison with an interferometric bench: errors for displacements up to 100 m.

Finally, we observe a standard deviation on the errors of  $3.5 \mu\text{m}$ . However, after a linear regression, we obtain a slope of  $-65 \text{ nm/m}$ . The uncertainties on the measured distances are mainly due to the uncertainties on the phase refractive index at 633 nm for the interferometer and the group refractive index at 1560 nm for the ADM, which are about  $2 \cdot 10^{-8}$ . The combined uncertainty is so around  $3 \cdot 10^{-8}$ , which could partly explain the observed slope. Further studies have shown that this slope is in fact dependent on time, not on the measured distance. Indeed, small temporal drifts can occur during the measurement time and induce the slope observed in Figure 5. This point is detailed in the next Section III B.

Once this slope is removed, the standard deviation on the errors is reduced to  $2.9 \mu\text{m}$ . As shown in Figure 6, the error has also been measured for small displacements within the 3-cm synthetic wavelength of the system for distances around 0 m and 1.9 m. No cyclic error is present. This demonstrates an uncertainty around  $3 \mu\text{m}$  for the two-colour system when it is used at 1560 nm.

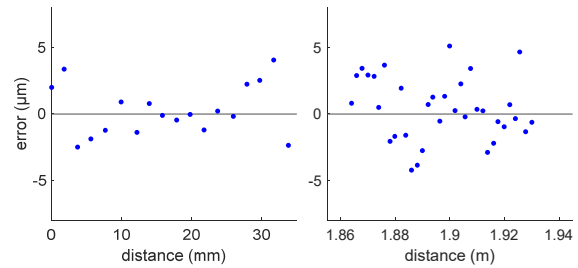


Figure 6. Comparison with an interferometric bench: small displacement steps to demonstrate absence of cyclic error.

At this moment, the second distance measurement at 780 nm has not been compared yet to an interferometric bench.

### B. 2-colour: long-term stability over 1 m

As explained previously, with a factor A of 48, the uncertainty on the distance difference between the two wavelengths must be lower than  $20 \mu\text{m}$  to reach an uncertainty better than 1 mm after the air refractive index compensation. Thus, as a first step, the stability of this distance difference has been evaluated over several days, for a fixed distance of 0.5 m and temperatures that vary between  $5.5 \text{ }^\circ\text{C}$  and  $23.6 \text{ }^\circ\text{C}$ . Results are depicted in Figure 7.

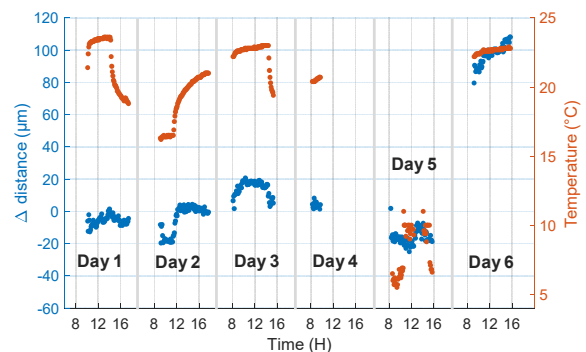


Figure 7. Evolution of the distance difference between the two wavelengths for a fixed distance, but different temperatures.

The variations of the distance difference between the two wavelengths are negligible at a fixed temperature, but when the temperature changes, variations of about  $40 \mu\text{m}$  are observed over the first five days. On day 5, the instrument was installed outdoors with temperatures below  $10 \text{ }^\circ\text{C}$ . When it returned inside the building on day 6, the thermal shock produces a huge change in the distance difference up to  $130 \mu\text{m}$ .

It could appear obvious to attribute these variations to the thermal expansion of the components of the optical head made of aluminium (linear thermal expansion around  $21 \mu\text{m/m}/^\circ\text{C}$ ), but the reference corner cube that compensates for the distance variations induced by temperature changes has been set up after the beam combination. Thus, by design, we should not observe drifts at this level of magnitude.

The origin of these drifts has been identified. Multiple reflections of the optical beam at 1560 nm inside the



dichroic mirror (designed with parallel faces) induce some crosstalks, *i.e.* the addition of a spurious signals to the ideal measurement signal, which change the measured phase delay  $\phi$  in Equation 1. Thus, it is planned in the short term to change the dichroic mirror for a new one designed with a slight wedge form to eliminate the effects of these reflections.

These instabilities currently limit the uncertainty of our ADM to several millimeters (error of 6.2 mm for the 130  $\mu\text{m}$  drift in Figure 7). However, as the distance difference between the two wavelengths remains quite stable in the absence of thermal shock, it is already possible to test the air refractive index compensation for the temperature variations that can occur outdoors.

### C. Instrument resolution over 5.2 km

The developed instrument was tested over 5.2 km, above a dense urban area. The two-colour ADM was located in Paris, on the rooftop of the Laboratoire National de métrologie et d'Essais (LNE) building, at 22 m above the ground, while the target was located in Meudon, in a public park at ground level. The target was a hollow corner cube with enhanced aluminum coating and 127 mm clear aperture.

As a first step, the resolution of the developed system has been estimated. To this end, the distant target has been mounted on a translation stage, then it has been displaced by a small step of 3.5 mm once every 30 seconds. This measurement took place on 7<sup>th</sup> April 2021, a day with an overcast sky, a wind of about 14 km/h. In Paris, the temperature was around 12.0 °C, the relative humidity was equal to 33 %, and the atmospheric pressure to 1025.2 hPa. The results are depicted in Figure 8 at each wavelength.

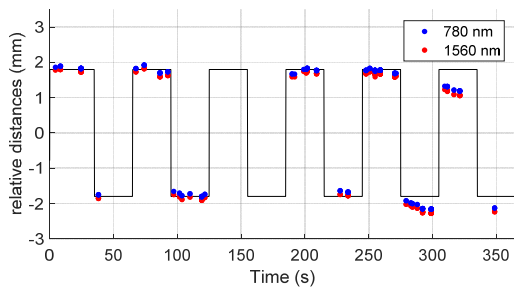


Figure 8. The measured distance displacements at each wavelength, 780 nm and 1560 nm, with no air refractive index compensation.

For a proper operation of the phasemeter, we have selected data with RF amplitudes between -25 dBm and +0 dBm for the wavelength at 780 nm, and between -15 dBm and +0 dBm for the wavelength at 1560 nm. Since there is no correction of the air refractive index in Figure 8, a distance drift up to 0.6 mm can be observed for each wavelength, especially after 275 seconds. However, the distance difference between the two measured distances is stable over this period with a standard deviation of only 13.4  $\mu\text{m}$  (or 11.3  $\mu\text{m}$  if the

points measured after 275 s are ignored). As shown in Figure 9, the distribution of this difference presents a gaussian shape.

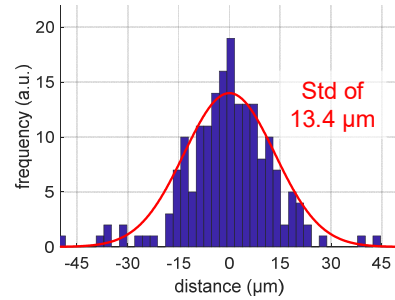


Figure 9. Distribution of the distance difference between the two wavelengths.

Lastly, Figure 10 depicts the results after air refractive index compensation, *i.e.* after the application of the Equation 4. This demonstrates that the two-colour system is able to distinguish the movements of a distant corner cube with has a resolution around 500  $\mu\text{m}$ , without the need to know the air temperature and the pressure, but only the partial pressure of water.

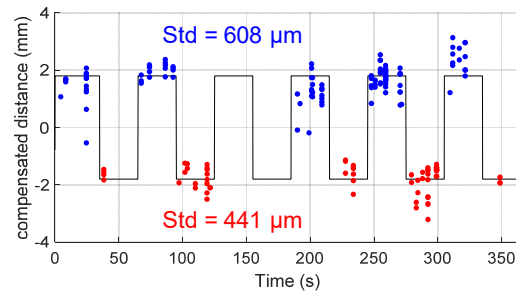


Figure 10. The measured distance displacements with air refractive index compensation.

The distribution of the results of Figure 10 has also been plotted as a histogram and fitted with two gaussian curves in Figure 11. The distance between the peaks of each gaussian curve is, as expected, equal to 3.5 mm.

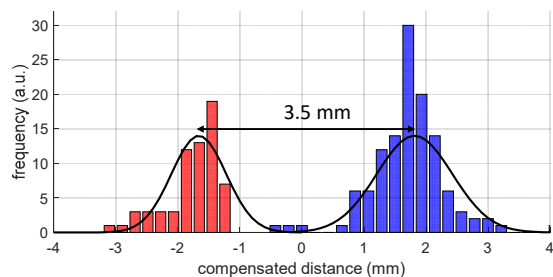


Figure 11. Distribution of the compensated distance measurements for a displacement of the target of 3 mm.

### D. Air index compensation over 5.2 km

As a second step, the ability of the two-colour ADM to compensate for temperature and pressure variations over 5.2 km has been estimated. The measurement took place on 8<sup>th</sup> December 2021, a day with a sky

partially overcast, a moderate wind of about 15 km/h, and a rising atmospheric pressure between 989 hPa and 991 hPa. As shown in Figure 12, the temperatures measured at Paris and at Meudon are in relative agreement with a maximum difference of 2°C between the two sites. However, the relative humidities can differ up to 18%.

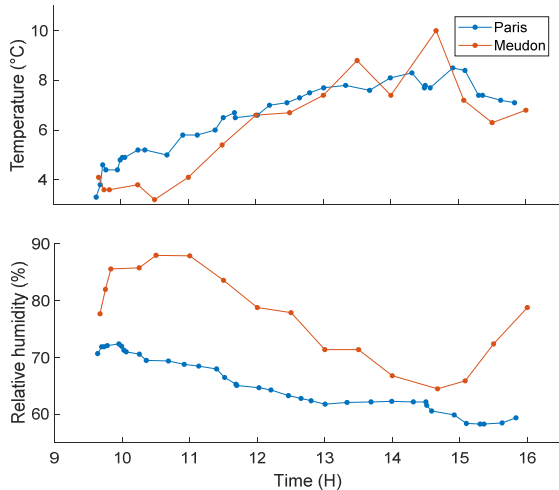


Figure 12. Evolution of the temperatures and relative humidities.

The value of the distance was unknown, so only the ability of the instrument to compensate from variations of the atmospheric parameters has been verified, not its accuracy. To this end, 30 continuous distance records were made between 9 a.m. and 4 p.m., each lasting between 1 min and 10 min. The signals detected after a 2×5.2 km round trip was not subject to large variations thanks to a day of low sunlight, and therefore of limited scintillations. For a proper operation of the phasemeter, we have selected data with RF amplitudes between -18 dBm and +0 dBm for both wavelengths. This represents 5% of the captured distances.

The results are presented in Figure 13 for each wavelength taken separately and for an air refractive index equal to 1. A drift of -14.5 mm can be observed during the day, which could be explained by an increase of the temperature of 2.9°C or a fall of the pressure of 10.3 hPa. In practice, it can be assumed that the variations of the measured pressures were relatively correct, which means that the real variations of the air temperature integrated over 5.2 km were probably less than the ones measured at each end of the baseline.

The shorter is the wavelength, the larger is the index  $n$ , and the greater will be the distance measured for  $n=1$ . Thus, the optical distance at 780 nm is about 3 cm longer than the one at 1560 nm. Moreover, as depicted in Figure 14, this difference between the two wavelengths evolves during the day, up to 300  $\mu\text{m}$ , due to changes in temperature and pressure.

In order to deduce the compensated distance, the Equation 4 has been applied. To this end, the partial pressure of water,  $p_w$ , was calculated from the values provided by the weather station located in Paris, more

stable during the day than the ones located at the opposite side of the baseline. The result of the application of Equation 4, *i.e.* the air index compensated distance, is depicted in Figure 15.

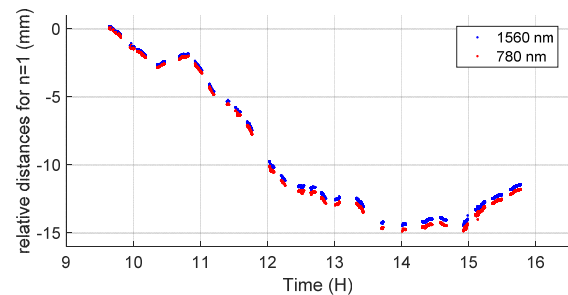


Figure 13. Distance measurement at 780 nm and 1560 nm for  $n=1$  over 5.2 km.

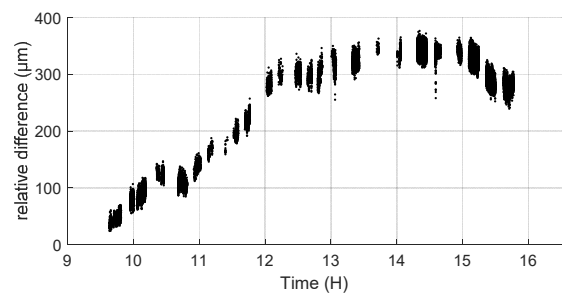


Figure 14. Distance difference between the two wavelengths.

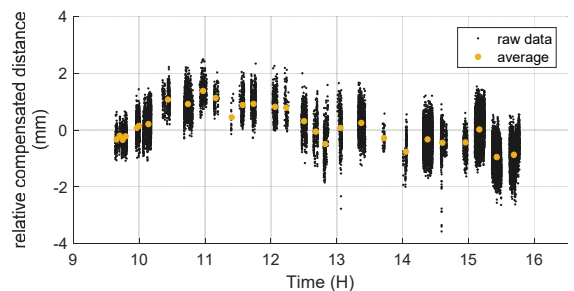


Figure 15. Distance measurement with air refractive index compensation.

To reach an uncertainty of 500  $\mu\text{m}$  over 5 km,  $p_w$  has to be measured with an uncertainty of 100 Pa, *i.e.* an uncertainty on the relative humidity of 7.5 % at 10 °C. Measuring the humidity at a single point is therefore critical since we have observed for similar temperatures up to 18 % difference between Paris and Meudon.

For a given distance record, the standard deviation on the raw data is typically around 420  $\mu\text{m}$ . However, the average value of these records varies of 2.3 mm peak-to-peak (yellow points in Figure 15). These variations probably come from a drift of 40  $\mu\text{m}$  between the two wavelengths as highlighted in Figure 7, or a bad estimate of the variations of the relative humidity of air.

Lastly, it has to be underlined that the stability of the building from where the distance measurements were performed in Paris has been measured. This was done using a digital level located at the ground level, a Leica DNA03, aiming at vertically, 22 m above thanks to a

deflector prism at its output, an invar levelling staff mounted on the roof of the building, horizontally in the direction of the baseline. According to the monitoring method, the possible instability of the building in the baseline direction was found to be less than 0.3 mm.

#### IV. CONCLUSION

We have developed a prototype of two-colour ADM. The latter, still under development, already shows promising preliminary results.

Indoors, in a controlled environment and for the wavelength at 1560 nm, an accuracy of 3.5  $\mu\text{m}$  has been demonstrated for distances up to 100 m. The second wavelength has yet to be characterized, but if similar results are obtained, this will lead to an uncertainty around 240  $\mu\text{m}$  after air refractive index compensation.

Outdoors, over 5.2 km, the resolution of the instrument is around 500  $\mu\text{m}$  with air refractive index compensation. This compensation was tested over 6 hours, with temperature and pressure variations of 7 °C and 2 hPa, respectively. This has demonstrated that a distance of 5.2 km can be measured without the knowledge of either the temperature or the atmospheric pressure: the peak-to-peak variation was only 2.3 mm. However, it is important to notice that these measurements were carried out under favourable weather conditions, *i.e.* days with low sunlight and so low atmospheric perturbations.

The crucial point to improve is the stability of the measured distances to reduce the residual drift between the two wavelengths. This limits the reproducibility of the current design to about 6 mm when large temperature variations occur. Nevertheless, the origin of this instability has been identified and should be greatly reduced by a new optical design. Once this is achieved, the accuracy will be estimated by a comparison with an interferometric bench for short distances up to 100 m and with the Nummela reference baseline for long distances up to 864 m (Jokela and Häkli, 2006). Lastly, a comparison with global navigation satellite systems (GNSS) will be carried out for longer distances, up to several kilometers.

#### V. ACKNOWLEDGEMENTS

This work was partially funded by Joint Research Project (JRP) 18SIB01 GeoMetre, project that has received funding from the European Metrology Programme for Innovation and Research (EMPIR) co-financed by the Participating States and from the European Union's Horizon 2020 research and innovation programme.

The authors are very grateful to J. Cali and S. Durand from École Supérieure des Géomètres et Topographes (ESGT, FR) for the availability of their interferometric bench, and to D. Pesce and A. Ruaud from Institut national de l'information géographique et forestière (IGN, FR) for the measurement of the movement of the LNE building in Paris.

#### References

- Bönsch, G., and E. Potulski (1998). Measurement of the refractive index of air and comparison with modified Edlén's formulae. In: *IOP Metrologia*, Vol. 35, No. 2, pp. 133-139.
- Curtis, C. J. (1992). Calibration and use of the Mekometer ME5000 in the survey of the Channel Tunnel. In: *Proc. of the Workshop 'the use and calibration of the Kern ME5000 Mekometer'*. Stanford Linear Accelerator Center, Stanford University, Stanford, California, USA, pp. 67-82.
- Earnshaw, K. B., and J. C. Owens (1967). Dual wavelength optical distance measuring instrument which corrects for air density. In: *IEEE Journal of Quantum Electronics*, Vol. 3, No. 11, pp. 544-550.
- Edlén, B. (1966). The Refractive Index of Air. In: *IOP Metrologia*. Vol. 2, No. 2, pp. 71-80.
- Frukacz, M., R. Presl, A. Wieser, and D. Favot (2016). Pushing the Sensitivity Limits of TPS-based Continuous Deformation Monitoring of an Alpine Valley. In: *Proc. Of the 3rd Joint International Symposium on Deformation Monitoring (JISDM)*. Vienna, Austria.
- Gervaise, J. (1983). First results of the geodetic measurements carried out with the Terrameter, two wavelength electronic distance measurement instrument. In: *Proc. of 'Geodätischen Seminar über Electrooptische Präzisionsstreckenmessung'*. Munich, Germany, pp. 213-229.
- Huggett, G. R. (1981). Two-Color Terrameter. In: *Developments in Geotectonics*, Vol. 16, pp. 29-39.
- Jokela, J., and P. Häkli (2006). Current Research and Development at the Nummela Standard Baseline. In: *Shaping the Change, XXIII FIG Congress*, Munich, Germany.
- Langbein, J. O., M. F. Linker, A. F. McGarr, and L. E. Slater (1987). Precision of two-color geodimeter measurements: Results from 15 months of observations. In: *Journal of Geophysical Research*, Vol. 92, No. B11, pp. 11644-11656.
- Meiners-Hagen, K., and A. Abou-Zeid (2008). Refractive index determination in length measurement by two-colour interferometry. In: *Measurement Science and Technology*, Vol. 19, No. 8, 084004.
- USGS (2021). Earthquake Hazards Program, consulted in 2021. Two-color Electronic Distance Meter (EDM). In: <https://earthquake.usgs.gov/monitoring/deformation/edm/>

## Preserving the heritage of world's monuments through Structural Health Monitoring – A case study: the Garisenda Tower

François-Baptiste Cartiaux<sup>1</sup>, Gian Carlo Olivetti<sup>2</sup>, Valeria Fort<sup>3</sup>, Patrice M. Pelletier<sup>1</sup>

<sup>1</sup> OSMOS Group SA, 37 rue la Pérouse, Paris, France, ([cartiaux@osmos-group.com](mailto:cartiaux@osmos-group.com); [pelletier@osmos-group.com](mailto:pelletier@osmos-group.com))

<sup>2</sup> Smart Monitoraggio Italia, Via Pitteri 10, Milan, Italy, ([g.olivetti@smartmonitoraggio.it](mailto:g.olivetti@smartmonitoraggio.it))

<sup>3</sup> OSMOS Italia Srl. Via Quintiliano 10, Rome, Italy, ([v.fort@osmos-group.com](mailto:v.fort@osmos-group.com))

**Key words:** *structural health monitoring; fibre optics sensing; deformation; heritage; Garisenda tower*

### ABSTRACT

The Italian peninsula has numerous heritage structures, including fifty-five sites registered under the UNESCO World Heritage Convention, living testimonies of the passage of man through times. Heritage structures are subject to aging and impact from the climate, resulting in deterioration of the structural behaviour. These phenomena can significantly reduce their usability, or even undermine the stability, and eventually induce safety, and rehabilitation issues. For those primary reasons, increasing attention is given by local authorities to understand the behaviour of structures and take the right action at the right time. To preserve the cultural heritage, Structural Health Monitoring (SHM) is becoming more important, as it allows to follow the evolution of structural behaviour. The study of meaningful variables allows to identify the activated structural mechanisms and, consequently, implement timely actions against ongoing degradation phenomena. A notable example is represented by the activities undertaken by the Municipality of Bologna on the Torre della Garisenda. The structure is monitored since 2019 to study the behaviour of its basement through measurements collected by deformation and temperature sensors. The installed monitoring system allows to carry out numerous analyses: evaluation of the structural response under dynamic actions, study of the evolution of the static behaviour of the tower and analysis of the effects induced by seasonal thermal variations. Advanced algorithms for data analysis allow to develop critical analysis and interpretation on the obtained results, providing information to support decision making process. Indications on the functionality of the system and typical examples of the collected results are provided.

### I. INTRODUCTION

An historic or heritage site is an official location where elements of political, military, artistic, cultural, or architectural, social history have been preserved due to their cultural heritage value. Historic sites are usually protected by law, and many have been recognized with the official national historic site status.

The status of historical monument marks, for an object or a building, the recognition of its heritage value in terms of history and art. As such, the owner of a historic monument is invested with an important responsibility for the preservation of this legacy of history and its transmission to future generations (Ministère de la Culture website, République Française).

UNESCO World Heritage Convention in an international treaty called the Convention concerning the Protection of the World Cultural and Natural Heritage, adopted by UNESCO in 1972. The world heritage list is impressive and includes 897 cultural sites. As of 2021, Italy has a total of 58 inscribed properties, including 53 cultural sites, making it the state party with the most World Heritage Sites just above China (56) (Unesco website, World Heritage List).

To take the case of a particular country, France has hundreds of thousands of heritage buildings, of which 45,600 are registered as Historic Monuments.

Heritage sites present a wide variety of structural cases. One common point though is the usual lack of knowledge regarding the construction and maintenance methods, which are by definition very different from the current ones, and by consequence the difficulty to conduct studies to check their structural safety.

Structural Health Monitoring (SHM) has been used as an effective solution for preserving the integrity of the Heritage sites, ensuring the safety to users, and assisting owners in developing real-time diagnostic for maintenance, repair or rehabilitation works.

OSMOS has a vast reference of sites it has monitored or is monitoring over the last 20 years including: the Tour Eiffel and Notre-Dame cathedral in Paris, France; the Sagrada Familia in Barcelona, Spain; the Propylaea of the Acropolis of Athens, Greece; and the 11<sup>th</sup> century Torre della Garisenda, in Bologna, Italy.

### II. ISSUES AND MONITORING SOLUTIONS FOR HERITAGE

Heritage buildings and assets appear as very challenging objects in the field of Structural Health Monitoring (SHM). Indeed, they are built with complex materials in terms of mechanical behaviour, including, for example, strong non-linearities in the case of

masonry, and both anisotropy and high sensitivity to the environmental conditions in the case of timber.

Several methods for the SHM of heritage structures have been documented in the literature. The most common approach is vibration-based monitoring, especially in regions with both numerous historical constructions and high seismic activity, like the Mediterranean area. Features resulting from an Operational Modal Analysis (OMA) can be used to detect damages by the mean of various data science tools: a recent example is the assessment of the Torre Gabbia in Mantua by Marrongelli *et al.* (2021). Another iconic building monitored with high sensitivity seismometers for vibration analysis is the main spire of the Duomo di Milano, with more than one full year of feedback as documented by Gentile and Ruccolo (2021). Apart of the vibration-based monitoring, other SHM techniques are used, which do not require the high sampling rate and massive data quantity required for OMA. Among them, an interesting combination of satellite and in-situ monitoring of cracks on the Palazzo dei Consoli of Gubbio has been presented by Cavalagli *et al.* (2021).

The approach proposed by OSMOS for the SHM of heritage buildings is an in-situ monitoring system which usually combines the measurement of strain variations, crack openings and tilts at a low sampling rate ("static" monitoring) with threshold-triggered records at a high sampling rate up to 100 Hz for alerts in case of rapid evolutions ("dynamic" monitoring), and eventually for dynamic assessment through OMA, using additional accelerometers. As an example, the evolution of vertical strain and the tilt of the main pillars of the Cathédrale Saint-Pierre in Beauvais, France (highest stone nave in the world), have been monitored since 2014.

Ancient masonry bridges are also of great interest, especially when they are both of historical value and important traffic infrastructures. For example, a permanent SHM system has been set up since 2017 on the Pont de Pierre in Libourne, France, combining strain measurements under one of the arches and on the spandrel walls, with settlement and water level measurements (OSMOS Group SA, 2018). This system allows to assess the correlations between surface strain of the masonry and both settlements and water level, including a strong effect of the tides on the compression of the arches. Moreover, the threshold-triggered dynamic strain records are sensitive enough to assess the effect of heavy traffic on the keystone of the arch, and the continuous monitoring of strain on the spandrel walls gave anticipated signs of a potential crack opening, which eventually appeared visually on the wall. In this case, it is worth to notice that the Optical Strand strain sensors were integrated inside the cladding during rehabilitation works and are totally invisible, preserving the visual appearance of the construction (Figure 1).



Figure 1. Optical Strand Strain sensor and temperature gauge integrated inside the cladding of the Pont de Pierre in Libourne, France. The picture is taken before completion of the cladding. ©OSMOS Group SA.

More recently, the continuous SHM of heritage buildings answered to a stringent necessity in the case of the fire which ravaged the Notre-Dame de Paris Cathedral on April 15, 2019 (Figure 2). Immediately after the disaster, the most critical parts of the damaged vaults have been instrumented with high-precision lasers to detect and anticipate any further movement. Then, up to more than 140 sensors have been in operation through the whole duration of the securing works, and furthermore for the assessment in view of the reconstruction. This complex system involves several different types of sensors, measurements and data analysis tools, including an immediate alert feature based on tilt and strain measurements on the damaged scaffolding of the spire during its dismantling until November 2020, a static monitoring of the deflection of the vaults with rows of tiltmeters, and OMA performed from numerous accelerometers on both the timber structures inside the two belfries and on the vaults and pillars of the nave (OSMOS Group SA, 2020).

These many examples show that the SHM of heritage buildings involves a wide discrepancy of different tools, from sensor types to data analysis methods. This is due to the extended complexity of this kind of structures, with uncertainties concerning the mechanical behaviour of the materials, difficulties to build relevant modelling near to reality, and variety of the structure types from massive walls to light vaults. Thus, gathering relevant information through SHM on these structures requires to combine different approaches.

In this paper, we will focus on one part of the SHM system of the Torre della Garisenda located in Bologna, Italy, dedicated to the assessment of the strain at the

basement of the tower. Other types of measurements have been taken on the tower in parallel for various purposes as described by Di Tommaso *et al.* (2021). Among them, studies have been carried out from GNSS measurements (Poluzzi *et al.*, 2019) and terrestrial laser scanning (Capra, 2015). The Torre Asinelli located nearby is also an interesting subject for scientific investigation (Invernizzi *et al.*, 2019).



Figure 2. Set-up of the monitoring system of Notre-Dame Cathedral in Paris. ©OSMOS Group SA.

The strain monitoring at the base of the tower is performed both in static mode for long-term and seasonal evolutions, and in triggered dynamic mode in the case of vibrations induced by the wind or by an earthquake. Such combined static and dynamic monitoring with a single system performing strain measurements has proven its efficiency in numerous contexts, including a study on one pier of the Viaduc de Millau in France as reported by Cartiaux *et al.* (2021).

### III. A CASE STUDY: THE TORRE DELLA GARISENDA

Bologna's towers, structures with both military and noble functions of medieval origin, are one of the city's characteristic features. Their number was very high, about 90 constructions, including real towers and tower-houses.

In general construction terms, the towers were square, with foundations a few metres deep in soils that were not always adequately performing. The base of the tower was built with large blocks of selenite and the rest of the construction was built with thinner and lighter walls as it rose, made of "sack" masonry, *i.e.* with a thicker inner wall and a thinner outer wall: the cavity was then filled with stones and mortar.

Today there are about twenty of them left, the best known of which are the so-called "two towers", known as Asinelli and Garisenda respectively, located in the historic centre of the ancient university city. The two towers are commonly recognised as a symbol of Bologna and stand in the heart of the city at the entry point of the ancient Via Emilia.

Probably built around 1109, they had a military function (signalling and defence) and represented the social prestige of the family responsible for their construction.

The Torre della Garisenda (Figure 3), with a square base structure of 7 m on each side and built in the same way as abovementioned, stands out for its lower height of only 47 m. It is known for its steep slope, with an angle of 4° (3.22 m overhang). Originally about 60 m high, it was lowered by about 12 m due to the dangerous inclination caused by the poor mechanical and load-bearing capacity of the foundation soil in the mid-14<sup>th</sup> century.



Figure 3. The two Towers: Garisenda (left) and Asinelli (right). The external side of the selenite basement of the Torre della Garisenda is clearly visible, as well as the entrance door.

The Municipality of Bologna, the current owner of the Torre della Garisenda, has long launched investigations, observations and even interventions with a view to its conservation, a priority for the entire community. To this end, through the Public Works Department-Maintenance Sector, the structural monitoring in place has been intensified, implementing from 2019 a system able to continuously follow the behaviour of the selenite base of the tower by detecting the vertical deformations of the same as well as the temperature values.

This monitoring system consists of 6 sensors based on optical fibres (called Optical Strand, hereinafter OS), installed inside the basement, 4 of which are 2 m long at the corners and 2 are 1 m long at a concavity of the basement straddling the SE corner. Table 1 summarises the installed sensors. The monitored parameter concerns the vertical strain on the inner face of the walls, as the sensors were installed inside the tower only, with an expected accuracy of 30  $\mu\epsilon$ . In addition to the deformation measurement sensors, a temperature sensor and an expert unit were installed which allows data acquisition at a frequency of 100 Hz. In addition, an earthquake early warning system has been recently installed at the base of the tower.

Table 1. Summary of installed OS sensors. \*Sensor removed on 2020/02/11

Sensor ID	Position
O1_NW	North-West corner
O2_NE	North-East corner
O3_SE	South-East corner
O4_SW*	South-West corner
O5_E	East wall
O6_S	South wall

The installed monitoring system allows to carry out a significant number of analyses: evaluation of the structural response under dynamic actions (wind, seismic), study of the evolution of the static behaviour of the tower and analysis of the effects induced by seasonal thermal variations on deformations. Advanced algorithms for data analysis allow to develop critical analysis and interpretation on the obtained results, providing useful information to support decision making process.

A possible extension of the presented monitoring system can be represented by the installation of additional 4 Optical Strands at the outer corners of the basement of the tower. In this way, it would be possible to quantify the difference in the movements of the sack masonry and the selenite external cover.

Figure 4 shows the positioning of the sensors inside the base.

The trend in static measurements from March 2019 to December 2021, for each sensor, is given below (Figure 5).

To perform the correction of the effects of the temperature from static measurements, a methodology consisting of two steps has been carried out:

- Quantify a linear law which links the temperature with the strain per each sensor, based on the 15-days long learning period showing the best correlation between the two considered parameters.
- After this first correction, large yearly cycles that seem to be also correlated with the temperature still appear. Thus, we propose a second

correction, with a smoothing time window of 10 days (instead of 24 hours) and a learning period of 180 days (6 months instead of 2 weeks).

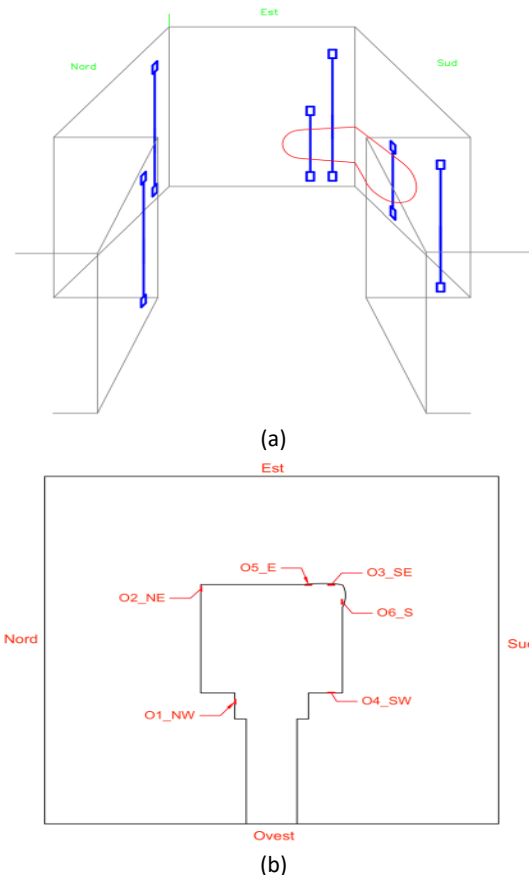


Figure 4. Torre della Garisenda – Configuration of Optical Strands inside the base: a) axonometric view; b) plan view.

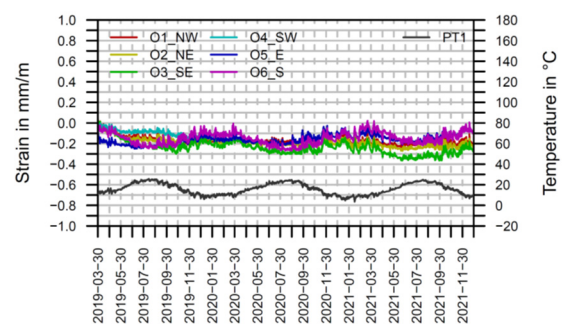


Figure 5. Recorded static measurements from March 2019 to December 2021.

The very good correlation between temperature and strain is confirmed, so the effect of the temperature follows different laws depending on the time scale: at a middle-term (1<sup>st</sup> correction) the masonry appears to be slightly blocked and is compressed by the heat, which is a typical behaviour for locally hyperstatic structures like a massive masonry wall is. At long-term scale (2<sup>nd</sup> correction) we have a normal dilatation factor with expansion in the case of heat.

Another conclusion is that we have no uniform trend in compression: on the results of the 2<sup>nd</sup> correction for the SE sensor given as an example, we first see a quick

compression to -0.1 mm/m during the first 3 months, which is due to the adaptation of the sensors to the masonry (we have Optical Strands in tension fixed on a material which is not perfectly rigid). So, the first 3 months may be omitted if we want to check actual trends over the long-term.

The results of this second correction on a “long-term” scale of 6 months are shown in Figure 6.

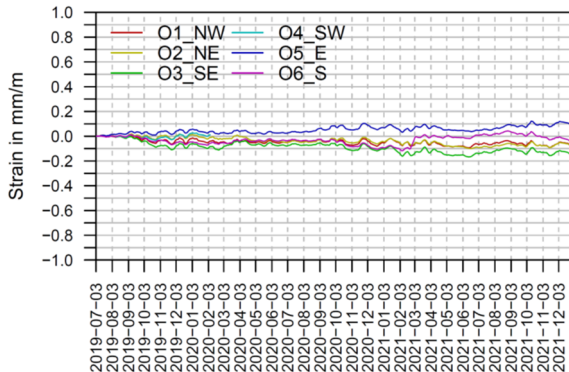


Figure 6. Corrected static measurements from temperature effects.

After two years and a half, the long-term evolution without effects of the temperature is as follows (Table 2).

Table 2. Final deformation values. \*Final value for the O4 SW sensor is on 2020/02/11, when this sensor was removed

Sensor ID	Final value [mm/m]
O1_NW	-0.082
O2_NE	-0.086
O3_SE	-0.157
O4_SW*	+0.012
O5_E	+0.086
O6_S	-0.047

The mean value of the trend is -0.045 mm/m, with more compression on the South-East corner and on the North side. We have less compression and even decompression on the South-West corner and on the East side.

These values have a significant order of magnitude compared to the dynamic effects also recorded: wind with 0.005 mm/m strain amplitude and earthquake with 0.010 mm/m strain amplitude.

However, considering that the static values are strongly influenced by the temperature, which we tried to correct through a purely empirical method, but also by other environmental conditions like humidity and whatever may have an incidence on the masonry blocks and mortar, it is too early to conclude about a real long-term trend.

For what concerns dynamic measurements, in what follows two noticeable events captured by the considered monitoring system are presented. For both events, the time series of the deformations and the Fourier transform of the recorded signals are shown, in

order to allow the identification of the frequencies peculiar to the structure during each of the events considered.

August 2<sup>nd</sup>, 2019, at 15:13 UTC: Strong wind inducing vibrations with a frequency of 0.68 Hz. No remaining strain is noticed after these vibrations, from which we conclude they did not have any harmful consequence on the monitored parts of the structure. The amplitude of the strain at the base of the tower reaches 0.005 mm/m (Figure 7).

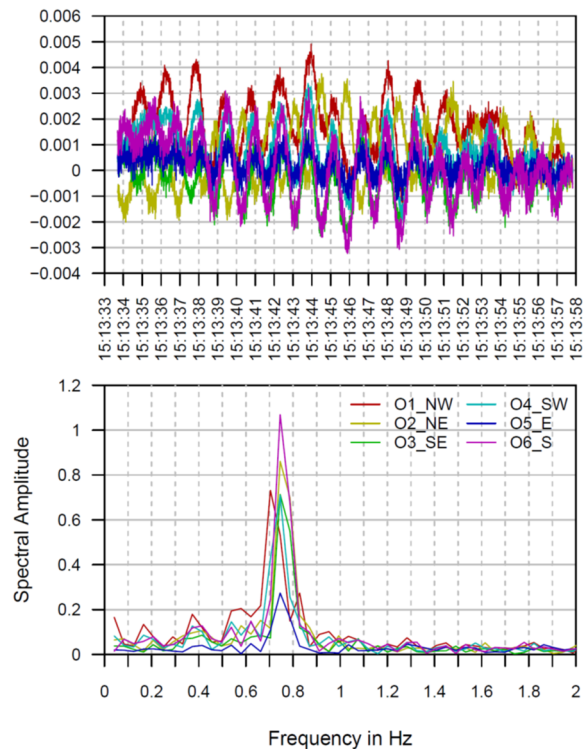


Figure 7. Deformation recording during 8/2/2019 wind event and corresponding frequency analysis.

December 9<sup>th</sup>, 2019, at 03:37 UTC: earthquake with a magnitude of 4.8, which epicenter was 75 km south to Bologna. This is by far the most important event on terms of bending vibrations of the tower with a maximal amplitude of 0.010 mm/m in the masonry. This however remains a low order of magnitude for a masonry wall. Vibrations are recorded with a main frequency of 0.68 Hz, mainly in the East–West direction. Additional vibrations in the North–South direction are also recorded with a frequency of 0.72 Hz. At the end of the event the tower recovers its initial state in terms of strain which means there have not been significant plastic effects due to the earthquake (Figure 8).

#### IV. CONCLUSIONS

The two years of vertical strain monitoring at the base of the Torre della Garisenda show a light global trend in compression, with an average of -0.045 mm/m and a maximal value for the South-East corner at -0.157 mm/m. At the opposite, the South and East sides appear to have a light trend in decompression, with a maximum value of +0.086 mm/m for the East side.



However, these values remain inside the uncertainty margins due to the difficulty of assessing the exact effect of the environmental condition, including the temperature.

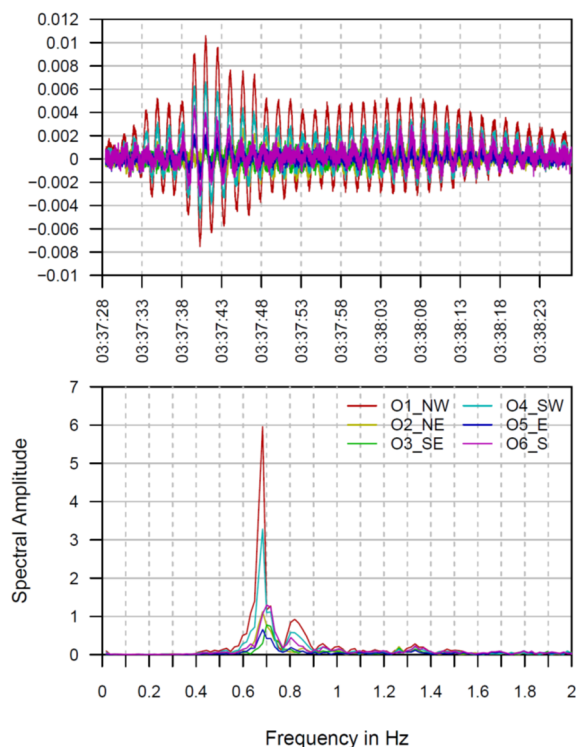


Figure 8. Deformation recording during 12/9/2019 earthquake event and corresponding frequency analysis.

The monitoring system has also proven its ability to release relevant insights both at long-term and dynamic time scales with the same Optical Strand strain sensors: threshold triggered records at a high sampling rate allow the assessment of the effects of wind and earthquakes, as well as the identification of the first vibration modes of the tower through a spectral analysis of the strain signal, which reflects the curvature of the tower at its basement.

The strain monitoring system of the Torre della Garisenda is still operational without maintenance operation since more than two years, which shows that the type of sensors chosen is both rugged and well adapted to the case of historical monuments built with old and heterogeneous masonry.

Structural Health Monitoring (SHM) has been demonstrated as an effective solution for heritage site preservation in terms of their legacy of history and their transmission to future generations by ensuring the safety to users, and assisting owners in developing real-time diagnostic for maintenance, repair or rehabilitation works.

Possible future developments of the presented activities may involve a deeper investigation of algorithms for temperature compensation, thanks to a longer observation period of the tower thermal response. Moreover, it would be very interesting to monitor strains on the external selenite coating to

quantify the sliding between the two components of the basement.

## V. ACKNOWLEDGEMENTS

We would like to thank Arch. Manuela Faustini Fustini, Director of the Maintenance sector and Ing. Vincenzo Daprile, Head of U.O. School buildings and digitalisation of contracts – Department of Public Works, Mobility, Heritage of the Municipality of Bologna, for their collaboration.

## References

- Capra, A., Bertacchini, E., Castagnetti, C., Rivola, R., and Dubbini, M. (2015). Recent approaches in geodesy and geomatics for structures monitoring. *Rendiconti Lincei*, 26(1), pp. 53-61.
- Cartiaux F.B., Le Corvec V., Cachot E., Vayssade T., and Servant C. (2021). Continuous Static and Dynamic Strain Measurements on Civil Infrastructures: Case Study on One Pier of the Millau Viaduct. In: Rizzo P., Milazzo A. (eds) *European Workshop on Structural Health Monitoring. EWSHM 2020*. Lecture Notes in Civil Engineering, vol 127. Springer
- Cavalaghi N., Kita A., Farneti E., Falco S., Trillo F., Costantini M., Fornaro G., Reale D., Verde S., and Ubertini F. (2021). Remote Sensing and In-Situ Measurements for the Structural Monitoring of Historical Monuments: The Consoli Palace of Gubbio, Italy. In: Rizzo P., Milazzo A. (eds) *European Workshop on Structural Health Monitoring. EWSHM 2020*. Lecture Notes in Civil Engineering, vol 128. Springer
- Di Tommaso A., Olivetti G.C., Niccolini G., Lacidogna G., Borla O., and Carpinteri A. (2021). Garisenda Tower in Bologna (Italy): Health monitoring by different nondestructive testing techniques. In: *MuRiCo 7 Congress, Nov. 24-26, 2021*
- Gentile C., and Ruccolo A. (2021). One-Year Dynamic Monitoring of the Main Spire of the Milan Cathedral. In: Rizzo P., Milazzo A. (eds) *European Workshop on Structural Health Monitoring. EWSHM 2020*. Lecture Notes in Civil Engineering, vol 127. Springer
- Invernizzi, S., Lacidogna, G., Lozano-Ramírez, N. E., and Carpinteri, A. (2019). Structural monitoring and assessment of an ancient masonry tower. *Engineering Fracture Mechanics*, 210, 429-443.
- Marrongelli G., Gentile C., and Saisi A. (2021). Vibration-Based Novelty Detection of Masonry Towers Using Pattern Recognition. In: Rizzo P., Milazzo A. (eds) *European Workshop on Structural Health Monitoring. EWSHM 2020*. Lecture Notes in Civil Engineering, vol 127. Springer
- Ministère de la Culture website (2021). République Française. Available in : <https://www.culture.gouv.fr/en/Regions/Drac-Centre-Val-de-Loire/Nos-secteurs-d-activite/Monuments-historiques>, consulted 2021/01/24.
- OSMOS Group SA (2018). Available in : <https://www.osmos-group.com/en/news/preservation-regional-heritage-stone-bridge-libourne>, consulted 2021/01/24.

OSMOS Group SA (2020). Available in :  
<https://www.osmos-group.com/en/news/osmos-group-heart-notre-dame-de-paris>, consulted 2021/01/24.

Poluzzi, L., Barbarella, M., Tavasci, L., Gandolfi, S., and Cenni, N. (2019). Monitoring of the Garisenda Tower through GNSS using advanced approaches toward the frame of reference stations. *Journal of Cultural Heritage*, 38, 231-241.

Unesco World Heritage List (2021). Available in :  
<https://whc.unesco.org/en/list/>, consulted 2021/01/24.

## Keypoint-based deformation monitoring using a terrestrial laser scanner from a single station: Case study of a bridge pier

Tomislav Medic<sup>1</sup>, Pia Ruttner<sup>1</sup>, Christoph Holst<sup>2</sup>, Andreas Wieser<sup>1</sup>

<sup>1</sup> Institute of Geodesy and Photogrammetry, ETH Zürich, Stefano-Francini-Platz 5, 8093 Zurich, Switzerland, ([tomislav.medic@geod.baug.ethz.ch](mailto:tomislav.medic@geod.baug.ethz.ch); [pia.ruttner@geod.baug.ethz.ch](mailto:pia.ruttner@geod.baug.ethz.ch); [andreas.wieser@geod.baug.ethz.ch](mailto:andreas.wieser@geod.baug.ethz.ch))

<sup>2</sup> TU Munich, TUM School of Engineering and Design, Chair of Engineering Geodesy, 80333 Munich, Germany, ([christoph.holst@tum.de](mailto:christoph.holst@tum.de))

**Key words:** *deformation monitoring; LiDAR; point clouds; change detection; time series; intensity image features*

### ABSTRACT

Terrestrial laser scanners (TLSs) offer a possibility for more automated and efficient deformation monitoring of civil engineering structures with higher spatial resolution than standard methods, as well as without the necessity of permanently installing the monitoring equipment. In such applications, scanners are usually placed so that the lines of sight are roughly aligned with the main directions of the expected deformations, and the deformations are estimated from point cloud differences between multiple epochs. This allows high sensitivity in the direction of the surface normal, but deformations along the surface are often undetected or hard to precisely quantify. In this work, we propose an algorithm based on the detection and matching of keypoints identified within TLS intensity images. This enables precise quantification of deformations along the scanned surfaces. We also present the application of the algorithm for monitoring a bridge pier of the Hochmoselbrücke in Germany, as a case study. Deformations up to about 4 cm due to thermal expansion and bending of the pier were successfully detected from scans taken throughout the day from a single location, up to 180 m from the monitored surfaces. The results agreed within a few millimeters to independent monitoring using state-of-the-art processing of TLS point clouds obtained from a different location and using a different type/brand of instrument. The newly proposed algorithm can either be used to complement existing TLS-based deformation analysis methods by adding sensitivity in certain directions, or it can be valuable as a standalone solution.

### I. INTRODUCTION

Terrestrial laser scanners (TLSs) are increasingly used for deformation monitoring of structures and landmasses (Mukupa *et al.*, 2017). The deformations are characterized as differences between point clouds represented in a common coordinate system. These differences are often defined as Euclidean distances between nearest neighbors in certain directions, *e.g.*, along the local surface normals. Commonly used algorithms are the cloud-to-cloud (C2C), cloud-to-mesh (C2M), and Multiscale Model-to-Model Cloud Comparison (M3C2) algorithm (Lague *et al.*, 2013), see *e.g.* (Holst *et al.*, 2017). Comparable alternatives are using patch-wise ICP (Iterative Closest Point) to estimate 3d displacement vectors (Friedli and Wieser 2016; Wujanz *et al.*, 2016) and parametric modeling of point cloud surfaces, where deformations are represented by parameter changes (Neuner *et al.*, 2016). Most of these methods are relatively insensitive (*i.e.* “blind”) to deformations occurring along the surface of the observed object.

A few algorithms were proposed to overcome these limitations (Gojicic *et al.*, 2020; 2021; Holst *et al.*, 2021). They substitute comparing nearest neighbors in Euclidian space by searching the corresponding points in a high-dimensional feature space. Feature

description algorithms are used to encode the geometry or structure of the neighborhood of the individual points in the point clouds. This allows finding the correct point correspondences, even if the deformations occurred along the surface of the observed object. The latter algorithms were successfully used in geomonitoring, where the irregular structure of landmasses provided a sufficient amount of details for unambiguous point description and matching. However, these algorithms cannot resolve the problem of detecting deformations along surfaces that lack (sufficiently pronounced and unique) geometric features which would characterize the neighborhood of the individual points unambiguously. This limits their use for structural monitoring where the surfaces are often smooth or composed of repetitive structure.

This problem can be solved by placing artificial laser-scanning targets at the surfaces. However, this will often be labor intensive –if not impossible (*e.g.*, with surfaces out of reach)–, and additionally questions the application of a scanner in the first place. Nevertheless, scanning targets often feature specific radiometric patterns and are used by processing the intensity data provided by the scanner rather than just the geometry.

Picking up this idea, we propose herein to substitute feature descriptors based on the geometric surface structure with a descriptor based on the intensity values of the returned laser beams. Although this could be combined with geometric features for monitoring, we will investigate the intensity-based approach on its own, herein. Instead of trying to find correspondences for all points in the point cloud (as in, *e.g.* Gojcic *et al.*, 2021), we adopt the approach of considering only keypoints, *i.e.* points that can be well located in the scan and whose neighborhood can be unambiguously described. The corresponding points are found automatically in the scene using the existing feature description and matching algorithms for 2D local image keypoints (Jing *et al.*, 2021). To achieve this, we exploit the regular and nearly continuous TLS scanning pattern to map the 3D TLS measurements onto 2D intensity images. To find multiple keypoint correspondences with sufficient localization accuracy for deformation monitoring, it is necessary to avoid strong changes in the measurement configuration, as they cause image distortions and changes in the intensity values. Hence, we limited our approach to deformation monitoring from a single scanner station herein and leave generalization for future work.

Similar approaches were used for the registration of TLS point clouds (Urban and Weinmann, 2015) and TLS calibration (Medić *et al.*, 2019). Moreover, a comparable approach was already described for deformation monitoring with scanning total stations, where feature description is based on RGB images taken by the internal camera (Wagner *et al.*, 2017). The approach proposed in this work deviates from the latter one, as it relies only on active sensing with an electronic distance measurement (EDM) unit. This offers some advantages such as insensitivity to ambient illumination allowing operations in changing visibility conditions, during the night and observing the objects that are partially in bright sunlight and partially in shadows.

We tested the algorithm on a particular case study of monitoring a bridge pier deformation from a single scanner station over several hours. In this paper, we compare the results to deformations estimated using the established M3C2 algorithm using point clouds acquired with another TLS from a different location. The presented results are an outcome of the initial analysis and the process is still a work in progress.

## II. IMPLEMENTED ALGORITHM

The inputs of the implemented algorithm<sup>1</sup> are registered point clouds, acquired at several epochs from a single scanner station. They refer to a common Cartesian Coordinate system and contain intensity information for each point. To use image processing algorithms for keypoint detection, description and

matching, the 3D TLS point cloud data needs to be mapped onto an intensity and range image.

We use the approach described in Medić *et al.* (2019), which relies on spherical image representation. Therein, the point cloud Cartesian coordinates are transformed into spherical ones (range, horizontal and vertical angle). Then, the spherical intensity and range images are generated by linearly interpolating the scanner measurements with a regular spacing, so that the pixel coordinates correspond to the scanner's horizontal and vertical angles and the pixel values correspond to the intensity and range measurements. The image resolution is made equal to the scanning resolutions (angular step sizes) to avoid information loss. It should be noted that such spherical representation has a disadvantage of strong image distortions at high elevation angles. However, such high elevation angles are rarely observed in deformation monitoring, making the approach largely applicable.

Within the spherical intensity images, the keypoints are automatically detected using the Speeded Up Robust Features (SURF) algorithm (Bay *et al.*, 2008) and described using the Binary Robust Invariant Scalable Keypoints (BRISK) algorithm (Leutenegger *et al.*, 2011). The choice is made based on our simplified analysis of different feature detectors and descriptors (Jing *et al.*, 2021), where the selected algorithms outperformed the rest (the differences were in some cases marginal).

The correspondences are searched in 64-dimensional feature space between the first point cloud in the series (epoch 0) and all following  $n$  point clouds (epochs  $i$ , where  $i = 1, 2, \dots, n$ ). The points with the minimum Euclidean distance (highest similarity) in the feature space are matched together. We use the prior knowledge that the expected deformations are small (several centimeters), and, therefore, that the corresponding keypoints should be close in space. Hence, only keypoints within a pre-defined neighborhood are considered. The extent of the neighborhood is defined with a spherical distance, corresponding to the pixel-wise distance in the spherical intensity image. We chose this over Euclidean distance in 3D space to avoid using interpolated range values, which could be erroneous when the keypoints are defined on corners and edges. The neighborhood extent is defined by a task-specific user-defined threshold (in this case study  $0.05^\circ$  based on an educated guess).

The keypoint detection returns the keypoint positions as pixel-wise 2D image coordinates. These coordinates are transformed into 3D spherical coordinates by linear interpolation based on the known direct correspondences between row vs. vertical and column vs. horizontal angle, and by directly interpolating ranges from spherical range images (see Medić *et al.*, 2019). Finally, we transform the spherical to Cartesian

<sup>1</sup> Source-code available at <https://github.com/ruttnerp/ikptlsdm>

coordinates and estimate deformation vectors  $\mathbf{v}_i^j$  for each pair of matched keypoints as (Eq. 1):

$$\mathbf{v}_i^j = [\Delta X, \Delta Y, \Delta Z]_i^j = \mathbf{k}_i^j(X, Y, Z) - \mathbf{k}_0^j(X, Y, Z) \quad (1)$$

where  $\mathbf{k}_i^j(X, Y, Z)$  are the coordinates of a keypoint  $j$  ( $j = 1, 2, \dots, w; w - \text{nr. of matched keypoints}$ ) in epoch  $i$ , and  $[\Delta X, \Delta Y, \Delta Z]_i^j$  are the corresponding coordinate differences relative to the position of the keypoint  $j$  at epoch 0 ( $\mathbf{k}_0^j$ ).

As the implemented keypoint matching strategy can still cause incorrect matches (Szeliski, 2022), we implemented an outlier removal strategy based on the local rigidity presumption. We presume that all keypoint coordinate differences within a predefined neighborhood should be similar. For this particular case study, the point cloud of the bridge pier is separated vertically into 5° segments over the spherical intensity images, resulting in overall 10 segments. The segment extent is based on the educated guess with the goal of assuring a sufficient number of matches for the outlier removal. The outliers are determined using the 2 times median absolute deviation from the median (MAD) threshold, multiplied by the scaling factor of 1.4826. The outliers are searched for the following quantities: 2D image coordinate differences, 3D coordinate differences (for each Cartesian and spherical coordinate), 3D vector magnitude and direction (cosine between individual vector to median vector). An example of the output within our case study is presented in Figure 1 (right).

Following the outlier removal step, we refine deformation estimates by averaging all deformation vectors  $\mathbf{v}_i^j$  for each segment and for each epoch separately (Eq. 2):

$$\begin{aligned} \bar{\mathbf{v}}_i^s &= [\overline{\Delta X}, \overline{\Delta Y}, \overline{\Delta Z}]_i^s \\ &= \left[ \frac{\sum (\Delta X_i^j)^s}{w_i^s}, \frac{\sum (\Delta Y_i^j)^s}{w_i^s}, \frac{\sum (\Delta Z_i^j)^s}{w_i^s} \right] \end{aligned} \quad (2)$$

where  $\bar{\mathbf{v}}_i^s$  is mean deformation vector of segment  $s$  in epoch  $i$ ;  $()^s$  denotes a subset of keypoint coordinate differences of epoch  $i$  falling within segment  $s$  ( $s = 1, 2, \dots, m; m - \text{nr. of segments}$ );  $w_i^s$  is a number of matched keypoints in segment  $s$  at epoch  $i$ . We set a user-defined threshold for a minimum number of keypoint matches per segment for computing  $\bar{\mathbf{v}}_i^s$  (default value 10 based on initial testing). If the threshold is not reached, we assume that the number of keypoint matches is inadequate for estimating  $\bar{\mathbf{v}}_i^s$  with sufficient precision. Hence, for such segments  $\bar{\mathbf{v}}_i^s$  is not defined.

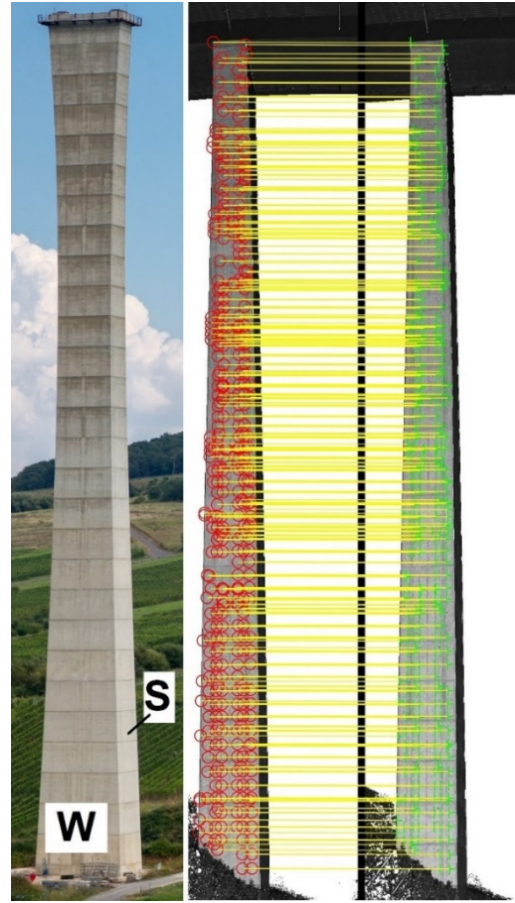


Figure 1. Left - Monitored bridge pier ( $\approx 140 \times 15 \times 7$  m), Image source: wikipedia.org; Right – Intensity images with keypoints distribution along the "S" side of the bridge pier after matching and outlier removal (red points - epoch 0, green points epoch  $i$ , yellow lines – correct matches).

To further improve the quality of deformation estimates, we introduced an additional step of functionally approximating deformations based on case-specific prior knowledge. For our task, the deformation magnitudes smoothly change along the surface of the measured object (highest at the top, zero at base), and with time (zero at epoch 0, maximal at epoch  $n$ ). The implemented functional approximation of the deformations rests upon the assumption that each pier segment is translated and not deformed over time, while the pier as a whole is deformed due to different translation magnitudes for different segments. The approximation is realized as a robustified best-fit algorithm (least absolute residual - LAR), with a 3<sup>rd</sup> degree polynomial for a function model (Eq. 3):

$$\begin{aligned} d_i^s(t_i, z_s) &= c_{00} + c_{10} t_i + c_{01} z_s + c_{11} t_i z_s \\ &\quad + c_{20} t_i^2 + c_{02} z_s^2 \\ &\quad + c_{21} t_i t_i^2 z_s + c_{12} t_i z_s^2 \\ &\quad + c_{30} t_i^3 + c_{03} z_s^3 \end{aligned} \quad (3)$$

where  $d_i^s(t_i, z_s)$  are the deformation magnitudes (observations) per pier segment  $s$  and per epoch  $i$ ,  $t_i$  – time of the epoch  $i$  (given values),  $z_s$  – mean height of the pier segment  $s$  (given values),  $c_{xx}$  – polynomial

coefficients (estimated parameters). The weight matrix is realized as a unit matrix. The deformation magnitudes  $d_i^s$  are calculated as norms of mean deformation vectors per segment (Eq. 4):

$$d_i^s = \|\bar{\mathbf{v}}_i^s\| = \|\overline{[\Delta X, \Delta Y, \Delta Z]}_i^s\| \quad (4)$$

The final output of the algorithm are estimated deformation magnitudes as a function of time and height along the pier. Such deformation representation reduces the amount of information to only the most relevant dimension (deformation magnitude). However, the keypoint-based deformation monitoring allows for generating 3D vector fields, which can also reveal the direction of deformations, de-compose the magnitude along different directions (*e.g.*, horizontally and vertically along the scanned surface or perpendicular to the surface) and uncover eventual inhomogeneities in the object's behavior. However, such interpretation is out of the scope of this work.

### III. EXPERIMENT

The implemented algorithm was tested in a case study of monitoring pier deformations of the Hochmosel-bridge in western Germany. The bridge was opened in 2019, is 1700 m long and is supported by ten reinforced concrete piers (heights ranging from 20 to 140 m). The experiment aimed to investigate daily deformation patterns of the highest bridge pier (Figure 1, left) with approximate dimensions: 140 m (height) x 15 m (width at west/east side) x 7 m (width at south/north side). For this purpose, the pier was measured from two perpendicular sides using two high-end TLSs (Figure 2): Leica ScanStation P50 and a Zoller+Fröhlich Imager 5016 (ZF5016). The main deformations are expected in the west-east direction (along the bridge).

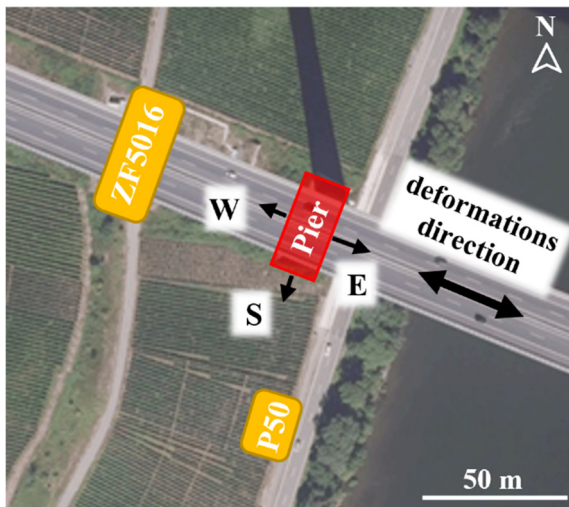


Figure 2. Sketch of the measurement setup (red rectangle - monitored pier, yellow rectangles - scanner positions).

Image source: geoportal.de.

For both scanners, the highest scanning resolution (0.8mm@10m) was used with the lowest measurement

quality (= no internal point averaging). Furthermore, the in-built dynamic dual axis compensators were used to assure the verticality of the instruments.

The measurements were conducted on 26 August 2020. The temperature changes of 13.4°C to 21.4°C during the day were expected to induce deformations due to thermal expansion in for us detectable range - up to 15 mm of the pier length extension (Brooks, 2014) accompanied with additional unknown shape deformations. However, due to a cloudy sky, which hinders direct and uneven material heating, the deformations were expected to be far from the extreme values. Namely, the bridge bearings are designed for the maximum pier movement of  $\pm 550$  mm at the highest elevation (Kuschnerus *et al.*, 2021).

The P50 was placed south of the pillar, perpendicular to the expected deformations, reaching measurement distances of 100-180 m. The measurements were taken between 11:37 and 18:02, where 26 epochs were measured with 15 min intervals. The ZF5016 was positioned west of the pillar, in line with the expected movement, being approximately 80 m away. The measurements were taken from 09:53 until 16:24, also with approximately 15 minutes intervals, resulting in 27 epochs.

The changes of atmospheric conditions through the measurement campaign had a systematic impact of up to 1 mm on the measured distances (1 ppm per 1°C), which is within the expected noise level. Hence, no atmospheric corrections were applied. To account for eventual instrument instability over time, which was reported in previous studies (Janßen *et al.*, 2020; Kuschnerus *et al.*, 2021), four dedicated BOTAS scanning targets (Janßen *et al.*, 2019) were placed on tripods around the scanner stations at distances of approximately 30 m. In the case of ZF5016, the targets were visible within each scan of the object of interest. Hence, all consecutive scans were registered to the local scanner coordinate system of the first scan (epoch 0).

For the point clouds acquired with P50 the same was not possible because: A) the scanner software does not allow simultaneous scanning in the front and the back without selecting a full panoramic scan, which would drastically increase scanning time and; B) it was not possible to place the targets in a way to circumvent the latter problem in the given surrounding. Hence, for efficiency, the targets were measured only at the very beginning and the end of the scanning campaign, to check for the eventual instrument instability. This solution was suboptimal, with an impact on the following analysis (see Section IV). However, it was a necessary compromise between the temporal resolution of consecutive scans and the assurance of instrument stability.

The target centers were estimated using the template matching algorithm described in (Janßen *et al.*, 2019), while the target-based point cloud registration was done in Leica Cyclone, using the in-built functionalities.

### A. Compared deformation magnitudes

As the ZF5016 was placed with the line of sight parallel to the direction of the expected pier deformations (Figure 2), its measurements were processed with the established M3C2 algorithm, which provides signed magnitudes as deformation estimates, with the sign depending on the deformation direction relative to the surface normal. These values served as an independent reference for validating the keypoint-based algorithm.

The P50 scans covered two perpendicular pier walls (Figure 2), the south wall with a 2.5° angle of incidence at instrument height and the east wall with an 85° incidence angle. As the line of sight was nearly perpendicular to the expected deformations (west-east direction, along the south wall), its scans were primarily used for testing the keypoint-based algorithm.

To get an additional (but not independent!) validation of the keypoint-based algorithm, the east wall surface was separated from P50 scans and additionally processed with the M3C2 algorithm. Hence, the three estimates of the pier deformation magnitudes were compared and analyzed: M3C2 differences of ZF5016 point clouds (west wall), M3C2 differences of P50 point clouds (east wall) and keypoint-based deformation estimates (Section II) from P50 point clouds (south wall).

The M3C2 deformation magnitude estimates are defined along the normal of the observed pier wall surfaces. As the east wall observed with P50 and the west wall observed with ZF5016 are parallel, both M3C2 deformation estimates can be directly compared. The deformation vectors retrieved with the keypoint-based approach have, however, arbitrary direction in space (Eq. 2). To compare their magnitudes to the M3C2 estimates, we first estimated the mean normal vector of the pier's east wall  $\mathbf{n}_E$  (from P50 scans), along which M3C2 differences are estimated. Then we projected the vectors estimated with keypoint-based approach ( $\bar{\mathbf{v}}_i^s$  in Eq. 2) onto this normal vector by (Eq. 5):

$$\bar{\mathbf{p}}_i^s = (\bar{\mathbf{v}}_i^s \cdot \mathbf{n}_E) \times \mathbf{n}_E \quad (5)$$

where  $\bar{\mathbf{p}}_i^s$  is the projected vector of deformations. To finally get signed deformation magnitudes comparable to M3C2 values,  $d_i^s$  are estimated as  $d_i^s = \|\bar{\mathbf{p}}_i^s\|$  instead of  $d_i^s = \|\bar{\mathbf{v}}_i^s\|$  (Eq. 4). And each  $d_i^s$  was given a positive sign for deformation in the west direction and a negative for the east. This strategy disregards the fact that the normals of the pier's east wall vary by maximally 2° over the whole surface. However, these changes influence the estimated deformation magnitudes by maximally 0.06 % of their value, which is negligible. Moreover, the angle between the Z-axis and normal vector  $\mathbf{n}_E$  is 89.3°. Hence, all compared deformation magnitudes can be considered as horizontal.

## IV. RESULTS AND DISCUSSION

The following section covers the results of the first analysis and the whole process is still a work in progress. Figure 3. presents the estimated signed deformation magnitudes relative to the pier height and time passed from epoch 0 ( $dt$  in hours). The data points are presented for every 10 m of the height and every 0.5 h for the passed time  $dt$  (lines of different colors). The values of the signed keypoint magnitudes are generated by evaluating the approximation function (Eq. 3), while the M3C2 values are estimated at specified heights and linearly interpolated considering scanning time.

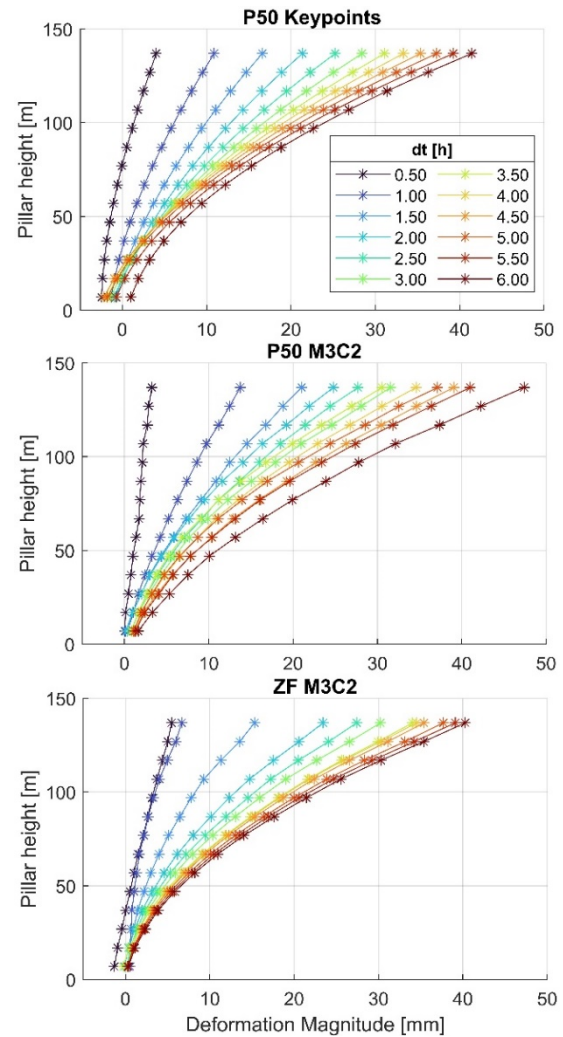


Figure 3. Pier deformation estimates (signed magnitudes) relative to the height and time passed from epoch 0: proposed approach (top) vs. reference values (middle and bottom).

The figure refers to the full scanning time series of both scanners (approx. 6 hours), with only partially overlapping scanning time (3 h overlap), where  $dt$  for each scanner refers to the different epoch 0 (ZF5016 09:53, P50 11:37). It serves only for a rough comparison of the algorithms and illustration of the range and form of the pier deformations over an extended period.

It can be observed that the pier exhibited non-linear deformations and bending over time due to temperature-related material expansion (an increase of tilt and curvature with time  $dt$ ), reaching the magnitudes of approximately 40 mm at the pier top after 6 h. The form and range of deformations are directly comparable for the proposed algorithm and M3C2 estimates. The latter holds true, although the scanning times of P50 and ZF5106 are not directly comparable. This is explainable by nearly linear temperature increase during the whole measurement campaign, reaching the highest point of 21.4°C somewhat before 18:00 (see Section II.).

To assure adequate quantitative evaluation of the approaches the following analysis focuses only on the overlapping time window of both scanners (from 13:00 until 16:15, presented in Figure 4). The reference epoch 0 used to define the initial state of the bridge pier is similar, but not perfectly matching between the scanners (12:57 for P50, 12:59 for ZF5016). To achieve a direct comparison, the deformation estimates refer to the same pillar heights and times of the day (evaluating an approximation function for the keypoints and linearly interpolating for M3C2).

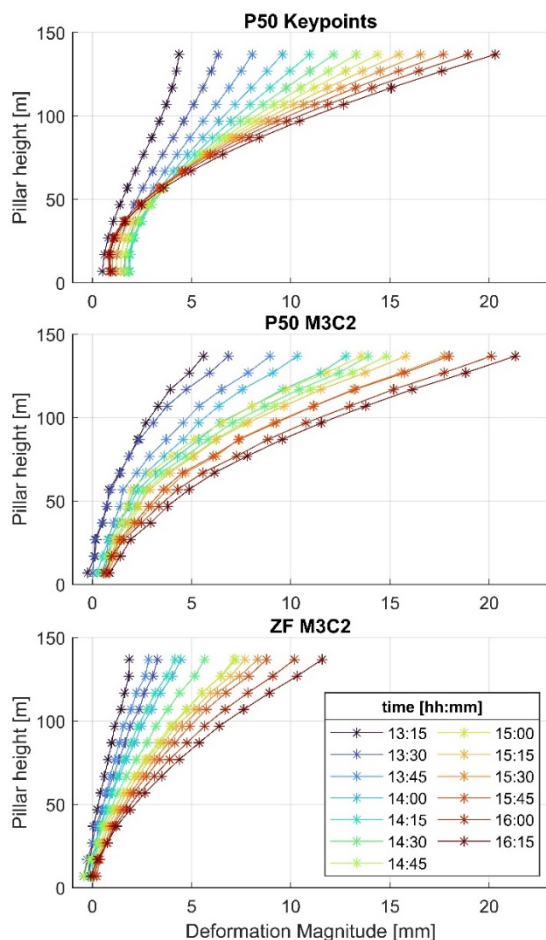


Figure 4. Pier deformation estimates (signed magnitudes) relative to the height and scanning time – focusing on the overlapping scanning times of ZF5016 and P50: proposed approach (top) vs. reference values (middle and bottom)

The mismatches between the estimated deformations of all 3 solutions (*P50 keypoints* vs. *ZF5016 M3C2* and *P50 M3C2*) were calculated as the differences of the corresponding data points in Figure 4. The mean differences between the corresponding data points were 2.4 mm for *ZF5016 M3C2* and 0.4 mm for *P50 M3C2* respectively, while the maximal differences reached almost 10 mm between *P50* and *ZF5016*. These large differences between the keypoint-based solution to the independent reference (*ZF5016 M3C2*) indicates a systematic bias. As the differences between *P50 keypoint-based* and *P50 M3C2-based* estimates are much smaller, it seems that the observed bias is due to the scanner, and not the estimation method. We assume that the source of the error is instrument instability, and we attribute it to the scans of P50 rather than ZF5016 due to the lack of an adequate registration regime for all scans (see Section III).

The standard deviation (std) between the P50 keypoint-based solution and ZF5016 M3C2 was 1.4 mm, and compared to P50 M3C2 was 0.9 mm. These values are within the expected range. Namely, the keypoint based deformation magnitudes  $d_i^j$  are estimated from the mean of approx. 40 keypoint matches (average of all segments and epochs), while the std of the coordinate differences  $[\Delta X, \Delta Y, \Delta Z]_i^j$  was on average 2.4 mm for  $\Delta X$  and  $\Delta Y$ , and 3.5 mm for  $\Delta Z$ . This results in a single vector ( $v_i^j$ ) magnitude uncertainty of approx. 5 mm. By using simple variance propagation by the square root of  $n$  matches, the expected std of the averaged deformation magnitude is 0.8 mm, falling close to the previously presented values.

Hence, this simple analysis suggests that the uncertainty is primarily influenced by the observed bias, while the precision of the proposed approach is within the expected range of a few millimeters. We argue that the instrument instability is the main limiting factor of the overall accuracy of the proposed approach. Our initial results (based on this case study) suggest that the keypoints detected in the intensity images can be used as natural targets to detect centimeter-level deformations with millimeter-level uncertainty if we take care of the instrument instability. However, further experiments are necessary to support these claims.

In the following sections, two aspects will be addressed, which we perceived as impactful and relevant for future applications of keypoint-based deformation monitoring: A - dealing with the abovementioned instrument instability, and B - specific adaptations and possible improvements of the implemented algorithm.

#### A. Instrument instability

To reach comparable deformations between ZF5016 and P50 data (Figure 3 and 4) it was necessary to account for instrument instabilities that can occur during long-term TLS observations (Janßen *et al.*, 2020; Kuschnerus *et al.*, 2021). In the case of the reference



dataset acquired by the ZF5016 scanner, this was done by accurate target-based registration (Section III).

In the case of P50 scans, such an approach was not possible (Section III). Instead, we used the presumption that the temperature-related material expansion during our measurements could not have caused the larger displacements of the pier just several meters above its 47 m deep and 20 m wide fundament (Schmidt-Hurtienne and Krumbein, 2019). The presumption is supported by the observation that the maximal M3C2 differences with ZF5016 were less than 2mm at the pier bottom (Figure 3). However, definite proof of validity is missing. We numerically implemented this presumption by subtracting the deformation magnitudes estimated with M3C2 for the lowest pier segment from all segments within each point cloud acquired by P50.

The M3C2 deformation estimates from P50 data initially indicated a slow movement (drift) of the bridge pier base reaching maximally 7.6 mm for the 8<sup>th</sup> scan in series (Figure 5, corresponds approximately to  $dt$  of 1.0 h in Figure 3). Such behavior is unexpected, and it was not observed in the independent ZF5016 dataset. Additional investigation, using two BOTAS laser-scanning targets that were included in each of 26 P50 scans, showed that this drift can be attributed to the scanner instability. Tracing the target center coordinate changes of two targets showed nearly identical drifting patterns over time (Figure 5), which can be explained by the scanner turning around its standing axis.

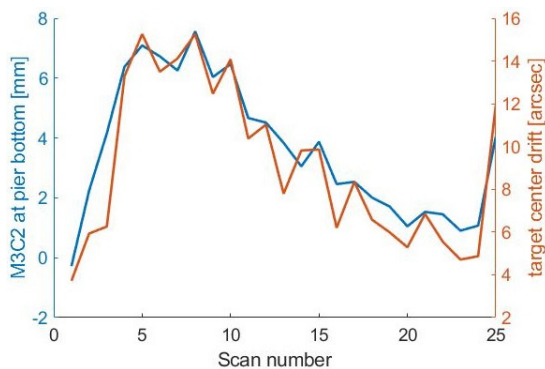


Figure 5. Drift of P50 M3C2 deformation magnitudes at lowest segment of the bridge pier vs. drift of the BOTAS target coordinates (polar coordinate – horizontal angle, average of 2 targets).

Within this work, we successfully mitigated some of the systematic bias due to scanner instability by leveraging prior presumption about the measurement object. Such a solution cannot be generalized and depending on the error source and its impact on the measurements it could be even impossible to separate it from the observed deformations. The non-zero mean differences between keypoint-based and M3C2 solutions (particularly with ZF5016 data) point out that some systematic errors (*e.g.*, scanner tilting perpendicular to the line of sight or instability of collimation and trunnion axis errors) are remaining in

our data and that they are limiting the achievable sensitivity and accuracy of the TLS based deformation monitoring.

The strategy we applied here can remove the impact of translational errors and the rotation around the instrument's standing axis. However, other systematic influences could have impacted our measurements in such a way that this bias would be nearly perfectly correlated with the observed deformation pattern. Such systematic influences are for example: tilting of the instrument, changes in dynamic compensator zero value, and changes of the instrument's internal systematic errors (*e.g.* trunnion or collimation axis error). All three effects can be induced by changes in the ambient and internal instrument temperature (Medić *et al.*, 2020; Janßen *et al.*, 2020).

The abovementioned influences can have an impact both on M3C2 differences and the keypoint-based deformation estimates. However, the majority of the known systematic effects impact the coordinates in the direction perpendicular to the line of sight and minor parts along the line of sight. Hence, the keypoint-based deformation estimates are generally more sensitive, as M3C2 differences are commonly estimated approximately along lines of sight. In this particular study, the latter applies for M3C2 differences of ZF5016, but not of P50, as the observed pier surface with P50 has nearly perpendicular normal to the line of sight (observed with a high incidence angle of 85°). Hence, both keypoint-based and M3C2 deformation estimates with P50 are similarly systematically influenced, causing their good correspondence (better than with ZF5016 data).

The conducted deformation monitoring experiment again highlights that great care should be placed in adequate registration and calibration of TLS point clouds to reach sufficient measurement accuracy for demanding deformation monitoring tasks.

## B. Aspects of the implemented algorithm

The implemented algorithm can be simply adapted for a more general case of deformation monitoring. First, the current implementation models deformations as a function of time, which can be adapted to any quantity of interest (*e.g.*, force or temperature). Second, introducing the local rigidity presumption and splitting the field of view into segments for outlier removal and averaging needs to be adapted according to the dimensions and expected behavior of the monitored object. Third, the functional approximation of the deformation behavior needs to be adapted to specific use cases.

The implemented algorithm can be further improved in several ways: parameter tuning; testing different feature detectors, descriptors, and their combinations; considering different solutions for the functional approximation of keypoint-based deformation estimates; as well as including automated point cloud

registration and in-situ calibration routines within the workflow. Furthermore, the algorithm is currently limited to scanning with a single instrument from a single scanner station. This could be extended to multiple stations at different locations and with different instruments, if the scanner intensity values could be radiometrically calibrated to achieve good correspondence between the scans. Also, any change in relative geometry between scanner station and scanned object introduces distortions of the intensity and range images which should be correctly modeled and removed. Lastly, the current algorithm implementation searches for keypoint correspondences only between epoch 0 and epoch  $i$ . This could be extended to searching corresponding keypoints between all combinations of scans increasing the number of observations and, hence the precision of deformation estimates.

The factors influencing the sensitivity of the implemented approach should be further investigated. Primarily this refers to the properties of the particular scanner and scanning settings. For example, the role of the footprint size and scanning resolution on the quantity and quality of the detected keypoints is unclear.

Finally, the proposed algorithm can be used as a stand-alone alternative to existing monitoring approaches, targeting certain monitoring tasks. However, there is an unexploited potential in combining it with other complementary existing TLS-based deformation analysis methods to increase sensitivity in certain directions. For example, combining it with M3C2 would assure sensitivity both in the directions parallel and perpendicular to the surface normal. Alternatively, the point clouds could be screened for regions with different geometric and radiometric properties and the choice of the deformation analysis method could be automatically adapted accordingly.

## V. CONCLUSION

In this work, we demonstrated a new 2D keypoint-based deformation monitoring algorithm for deformation monitoring with terrestrial laser scanners from a single scanner station. The algorithm relies on representing the series of TLS point clouds as spherical intensity and range images and using established 2D image feature detection and description algorithms. The approach was tested in a case study of monitoring daily deformations of a bridge pier due to temperature-related material expansion.

The achieved results show that the proposed method can be used to detect cm-level deformations with an uncertainty of several millimeters, even along the surface of the object of interest. This complements the established approaches for deformation monitoring with TLS point clouds, as they are mostly insensitive to deformations occurring laterally over the measured

surface. This is especially true in the case of structural health monitoring, where measured objects often lack sufficiently indented surface structures.

The analysis of the results indicated that the presence of systematic biases due to TLS instability is one of the main factors limiting the achievable accuracy. Hence, integrating adequate point cloud registration and TLS calibration routines is necessary to increase the achievable sensitivity of TLS-based deformation monitoring. Finally, we discussed in detail how the implemented algorithm can be further improved. Our future efforts will primarily focus on adapting the algorithm for a general case of TLS-based deformation monitoring.

## VI. ACKNOWLEDGEMENTS

Dido Monzel and Martin Blome have acquired the dataset.

## References

- Bay, H., A. Ess, T. Tuytelaars, and L. V. Gool (2008). Speeded-up Robust Features (SURF). *Computer Vision and Image Understanding* 110 (3): 346–59.
- Brooks, J. (2014). Concrete and masonry movements. Butterworth-Heinemann, pp. 459-460.
- Friedli, E., and A. Wieser (2016). Identification of Stable Surfaces within Point Clouds for Areal Deformation Monitoring. In *Proceedings of the 3rd Joint International Symposium on Deformation Monitoring (JISDM)*. Vienna, Austria. 30th March-1st April.
- Gojcic, Z., L., Schmid, and A. Wieser (2021). Dense 3D displacement vector fields for point cloud-based landslide monitoring. *Landslides* 18: 3821–3832.
- Gojcic, Z., C. Zhou, and A. Wieser (2020). F2S3: Robustified determination of 3D displacement vector fields using deep learning. *Journal of Applied Geodesy* 14(2): 177–189
- Holst, C., J. Janßen, B. Schmitz, M. Blome, M. Dercks, A. Schoch-Baumann, J. Blöthe, L. Schrott, H. Kuhlmann, and T. Medic (2021). Increasing Spatio-Temporal Resolution for Monitoring Alpine Solifluction Using Terrestrial Laser Scanners and 3d Vector Fields. *Remote Sensing* 13 (6).
- Holst, C., L. Klingbeil, F. Esser, and H. Kuhlmann (2017). Using Point Cloud Comparisons for Revealing Deformations of Natural and Artificial Objects. In *Proceedings of the 7th International Conference on Engineering Surveying (INGEO 2017)*, Lisbon, Portugal, pp. 18-20.
- Janßen, J., H. Kuhlmann, and C. Holst. (2020). Assessing the Temporal Stability of Terrestrial Laser Scanners during Long-Term Measurements. In *Contributions to International Conferences on Engineering Surveying, INGEO & SIG 2020*. Dubrovnik, Croatia.
- Janßen, J., T. Medić, H. Kuhlmann, and C. Holst (2019). Decreasing the Uncertainty of the Target Centre Estimation at Terrestrial Laser Scanning by Choosing the Best Algorithm and by Improving the Target Design. *Remote Sensing* 11 (7) (7).
- Jing, J., T., Gao, W., Zhang, Y., Gao, and C., Sun (2021). Image Feature Information Extraction for Interest Point Detection: A Comprehensive Review. *ArXiv Preprint ArXiv:2106.07929*.

- Lague, D., N. Brodu, and J. Leroux (2013). Accurate 3D Comparison of Complex Topography with Terrestrial Laser Scanner: Application to the Rangitikei Canyon (NZ). *ISPRS Journal of Photogrammetry and Remote Sensing* 82, pp. 10–26.
- Leutenegger, S., C. Margarita, and Y. S. Roland (2011). BRISK: Binary Robust Invariant Scalable Keypoints. In *2011 International conference on computer vision*, pp. 2548-255.
- Kuschnerus, M., D. Schröder and R. Lindenbergh (2021). Environmental influences on the stability of a permanently installed laser scanner. In: *Int. Arch. Photogramm. Remote Sens. Spat. Inf. Sci. - ISPRS Arch.*, 43, pp. 745–752.
- Medić, T., H. Kuhlmann, and C. Holst (2019). Automatic In-Situ Self-Calibration of a Panoramic TLS from a Single Station Using 2D Keypoints. In *ISPRS Ann. Photogramm. Remote Sens. Spat. Inf. Sci.*
- Medić, T., H. Kuhlmann, and C. Holst (2020). A Priori versus In-Situ Terrestrial Laser Scanner Calibration in the Context of the Instability of Calibration Parameters. In *Contributions to International Conferences on Engineering Surveying, INGEO & SIG 2020*, Dubrovnik, Croatia.
- Mukupu, W., G. W. Roberts, C. M. Hancock, and K. Al-Manasir (2017). A Review of the Use of Terrestrial Laser Scanning Application for Change Detection and Deformation Monitoring of Structures. *Survey Review* 49 (353), pp. 99–116.
- Neuner, H., C. Holst, and H. Kuhlmann (2016). Overview on Current Modelling Strategies of Point Clouds for Deformation Analysis. *Allgemeine Vermessungs-Nachrichten (AVN)* 123 (11–12), pp. 328–39.
- Schmidt-Hurtienne, B. and O. Krumbein (2019). Gründung und Unterbauten der Hochmoselbrücke – Planung und Ausführung. *Bautechnik*, 96, pp. 21–30.
- Szeliski, R. (2022). Feature detection and matching. In *Computer Vision*. Springer, pp. 333–399.
- Urban, S., and M. Weinmann (2015). Finding a Good Feature Detector-Descriptor Combination for the 2D Keypoint-Based Registration of TLS Point Clouds. In *ISPRS Ann. Photogramm. Remote Sens. Spat. Inf. Sci., ISPRS Geospatial Week 2015*, II-3/W5, pp. 121–28.
- Wagner, A., W. Wiedemann, and T. Wunderlich (2017). Fusion of Laser Scan and Image Data for Deformation Monitoring – Concept and Perspective. In *Proceedings of the 7th International Conference on Engineering Surveying (INGEO 2017)*, pp. 157-164.
- Wujanz, D., D. Krueger, and F. Neitzel (2016). Identification of Stable Areas in Unreferenced Laser Scans for Deformation Measurement. *Photogrammetric Record* 31 (155):, pp. 261–80.

## Vibration monitoring of a bridge using 2D profile laser scanning: Lessons learned from the comparison of two spatio-temporal processing strategies

Nicholas Meyer, Lorenz Schmid, Andreas Wieser, Tomislav Medic

Institute of Geodesy and Photogrammetry, ETH Zürich, Stefano-Franscini-Platz 5, 8093 Zürich, Switzerland,  
([nicholas.meyer@geod.baug.ethz.ch](mailto:nicholas.meyer@geod.baug.ethz.ch); [lorenz.schmid@geod.baug.ethz.ch](mailto:lorenz.schmid@geod.baug.ethz.ch); [andreas.wieser@geod.baug.ethz.ch](mailto:andreas.wieser@geod.baug.ethz.ch);  
[tomislav.medic@geod.baug.ethz.ch](mailto:tomislav.medic@geod.baug.ethz.ch))

**Key words:** *structural health monitoring; deformation monitoring; oscillations; LiDAR; point clouds*

### ABSTRACT

Profile laser scanning allows sub-millimeter precise contact-free measurements with high spatial and temporal resolution. That makes it an appealing solution for structural health monitoring focusing on vibrations of engineering structures, such as the analysis of eigenmodes and eigenfrequencies of bridges. In this work, we use the profile scanning mode of a Zoller+Fröhlich Imager 5016 terrestrial laser scanner (TLS) to observe bridge dynamics, focusing on the free decay processes following trains passing the bridge and exciting the structure. We compare two vibration monitoring strategies and implement an open-source semi-automatic software that integrates both approaches. We successfully estimate a spatio-temporal vibration model (including dampening coefficient) despite the maximum vibration amplitude reaching only 0.3 mm during the free decay process. Both strategies allow the estimation of the first eigenfrequency with a precision better than 0.1 Hz. Within the paper, we highlight the advantages and tackle the identified challenges of these vibration monitoring strategies. We also report on a preliminary investigation of appropriate instrument positioning for estimating the parameters of a spatio-temporal vibration model.

### I. INTRODUCTION

Scanners are progressively more used for structural health monitoring (SHM) of civil engineering structures (Mukupu *et al.*, 2017). Changes in geometry of 3D point clouds are used to monitor dams, bridges and tunnels under load or over time (Neuner *et al.*, 2016). Often, the analysis aims at low-frequency phenomena, *e.g.*, causing deformations on time scales from hours to years.

A special case of SHM with scanners introduced recently in Schill (2018) focuses on monitoring high-frequency phenomena, *e.g.*, geometry changes occurring with a frequency of 1 Hz or higher. In such applications, repeated 2D vertical profiles are typically collected instead of full 3D geometry to achieve coverage with sufficiently high frequency. The strategy was successfully used to characterize bridge deformations due to passing traffic, as well as for the vibration monitoring focusing on the free decay process after the bridge excitation (Schill and Eichhorn, 2019). It allowed for quantification of eigenfrequencies and related amplitudes nearly continuously over the whole bridge. The approach relies on a careful point cloud preprocessing, locally applying classical signal processing techniques (fast Fourier transform - FFT) and stacking this locally extracted information to get an overview of the behavior of the entire bridge.

Holst and Neuner (2021) proposed an additional processing step, estimating the optimal spatiotemporal

vibration model within a least-squares (LS) adjustment. This offers several advantages, *e.g.*, it increases sensitivity by improving the Nyquist frequency as compared to (half) the profile scan repetition rate. The authors validated this approach on a simulated dataset only, and its transfer to real-world applications requires tackling some challenges (see Section II B).

Within this work, we implemented both approaches and combined them in a single open-source software<sup>1</sup>. We tackled the mentioned challenges of the approach proposed in Holst and Neuner (2021), and successfully applied it to a real dataset: profile scans of a railway bridge in a free decay process following a train passing over. We conducted an eigenmode analysis and compared the results of both approaches against results obtained from multiple input multiple output synthetic aperture radar (MIMO-SAR), *i.e.*, an independent technology, confirming the plausibility of the estimated quantities. As a recommendation for the practitioners, we preliminarily analyzed the impact of the choice of the scanner position on the vibration monitoring results. Finally, we discuss relevant further development steps of the implemented software.

The article is organized as follows: Section II provides an overview of the mentioned vibration monitoring approaches (A – Schill and Eichhorn, 2019; B – Holst and Neuner, 2021) and presents our implemented workflow (C). Section III introduces the conducted experiment. The results and discussion are given in Section IV.

<sup>1</sup> Source-code available at <https://github.com/NixtonM/VM2dPLS>

## II. METHODS

### A. Schill and Eichhorn (2019)

The monitoring strategy proposed by Schill and Eichhorn (2019) primarily focuses on a careful point cloud pre-processing and provides a simplified vibration analysis in comparison to the approach by Holst and Neuner (2021) shown later in this section. The main goals of pre-processing are removing all scanned points not corresponding to the main structure of the bridge, removing outliers, and reducing the noise level, as the typical vibration amplitudes fall below the noise level of a single TLS measurement. The point cloud segmentation is realized using connected component clustering (Samet and Tamminen, 1988). De-noising is carried out using one of the three following strategies: spatial clustering and averaging per cluster within each 2D profile, approximating each scanned profile with a B-Spline function, or de-noising each profile using a discrete wavelet transform (Shensa, 1992).

The eigenmode analysis is then realized by applying the FFT on time series of de-noised displacements for individual positions along the bridge. The resulting amplitude spectra are displayed together to generate a spatio-temporal representation (see *e.g.*, Figure 1), where the eigenfrequencies and corresponding amplitudes can be quantified visually.

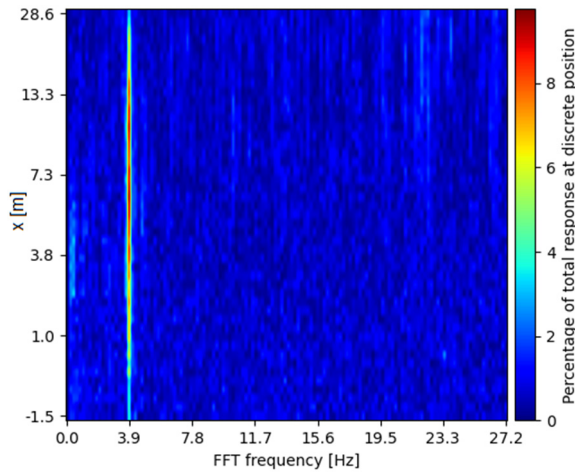


Figure 1. FFT amplitude spectra for discrete positions along the bridge (similar to results of Schill and Eichhorn, 2019).

### B. Holst and Neuner (2021)

The strategy proposed by Holst and Neuner (2021) relies on processing profile scans (2D Cartesian coordinates  $x$  and  $y$  with per point time stamps  $t$ ) within a LS adjustment with four different models differing by the prior knowledge or assumptions that are introduced within the functional and/or stochastic model. Here, we briefly present the two extreme cases which we implemented in the above software for the case of a single eigenfrequency. The first model is (Eq. 1):

$$y_{x_i}(t_i) = \bar{y}_{x_i} + A_{x_i} \cdot \sin(2\pi f_{x_i} t_i + \varphi_{x_i}) \quad (1)$$

where  $t_i$  is the measurement time stamp,  $y_{x_i}(t_i)$  is the observed vertical coordinate of point  $i$ , and this point is defined by its horizontal coordinate  $x_i$  along the bridge (given value). The searched eigenmode parameters are:  $\bar{y}_{x_i}$  - vertical position of the bridge at steady state (*i.e.*, mean position),  $A_{x_i}$  - vibration amplitude,  $f_{x_i}$  - frequency and  $\varphi_{x_i}$  - phase-shift. Using all observations and a Gauss-Markov model (GMM) the authors estimate an independent set of 4 parameters for each  $x_i$ , describing the vibration as a function of time for the respective location. Here, the encoded prior knowledge is only: A) each part of the bridge oscillates according to a single sine function around its steady-state position; and B) the deformation occurs in the vertical direction. Although this may not be realistic, this model imposes no spatial correlation of the vibration patterns and allows for (arbitrarily) different amplitudes along the bridge.

The second realization introduces additional prior assumptions: C) all positions along the bridge  $x_i$  have a common oscillation frequency and phase shift; D) there is a common amplitude, which is a sine function of space ( $x_i$ ) according to a single beam vibration model; E) the steady-state of the bridge (bridge shape and position in space) can be approximated by a function. This realization is represented by (Eq. 2):

$$y(x, t) = d \cdot x + b + A \cdot \sin(2\pi f_x x + \varphi_x) \cdot \sin(2\pi f_t t + \varphi_t) \quad (2)$$

where  $d$  and  $b$  are parameters used for linear approximation of the bridge shape and position at steady state;  $A$  is a vibration amplitude,  $f_x$  and  $\varphi_x$  are frequency and phase-shift in space ( $x_i$ ), while  $f_t$  and  $\varphi_t$  are frequency and phase-shift in time ( $t_i$ );  $y$  are observations, and  $x$  and  $t$  are given.

This second realization provides a spatio-temporal vibration model. However, it comes with the disadvantage of introducing additional nonlinearities in the functional model (additional spatial sine function). As all parameters are correlated, the solution becomes increasingly sensitive to the quality of initial parameter values. Even a small deviation (several percent off from the true value) can cause incorrect adjustment convergence.

A detailed analysis of this sensitivity is out of the scope of our work. However, it poses a significant challenge for transferring the approach to real measurement data, which was tackled within the implemented workflow (see C). Additionally, we observed that the correct convergence of the second realization depends on the instrument position with respect to the measurement subject, which will be further elaborated in Section IV.

C. Implemented workflow

The implemented workflow is summarized in Figure 2 and consists of a *Data Pre-Processing* step and three consecutive LS parameter estimation steps (*temporal*, *spatial*, and *combined*).

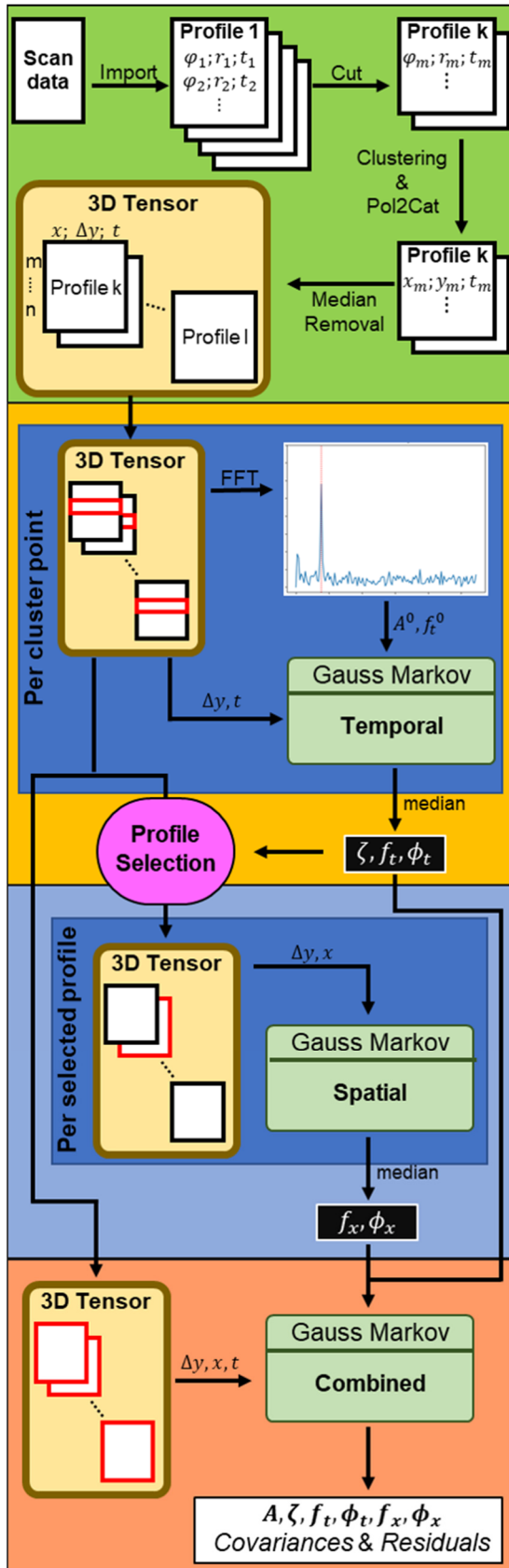


Figure 2. Flowchart of the implemented workflow.

The output of each adjustment step either narrows down the number of observation equations or determines the initial parameter values for the subsequent adjustment. The final adjustment provides the parameters for a combined spatio-temporal vibration model adapted from Holst and Neuner (2021). Due to practical considerations, we expand Equation 2 herein by a term describing the damping (with dampening coefficient  $\zeta$ ), and the linear approximation of the bridge shape at rest is replaced by median value reduction per location in the *data pre-processing* step. The resulting functional model for the displacements in the vertical is represented by (Eq. 3):

$$\Delta y(x, t) = A e^{-\zeta t} \cdot \sin(2\pi f_x x + \phi_x) \cdot \sin(2\pi f_t t + \phi_t) \quad (3)$$

Within the *Data Pre-Processing* step, we first retain only the measurements inside of the time window and field-of-view of interest (through the user interface). This is followed by spatial clustering wherein each profile is segmented by a common set of evenly spaced elevation angle boundaries, resulting in point clusters containing roughly the same number of points. Depending on point density due to the measurement range and angle of incidence, this approach results in varying spatial extents of the clusters (Figure 3). If the scanner output is in terms of polar coordinates ( $\varphi, r$ ), we convert them to Cartesian ( $x, y$ ). Furthermore, we calculate the median point per cluster, as one of the possible realizations of spatial low-pass filtering proposed by Schill and Eichhorn (2019). These median points are used in all further processing steps as: A) they provide a better signal-to-noise ratio (SNR) than raw observations; B) they remove the need to handle the varying number of points per profile (e.g., due to momentary occlusions); C) they assure more realistic parameter uncertainty estimates than when using raw observations, as the correlations between the observations are unknown and, hence, disregarded.

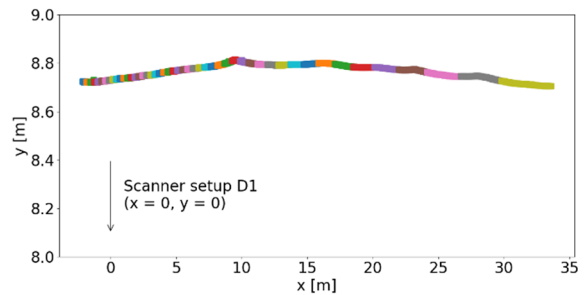


Figure 3. Implemented profile-wise spatial clustering (the example from the experiment in Section III).

In contrast to the simulations from Holst and Neuner (2021), we cannot model the shape of the bridge at the steady-state to the accuracy necessary with a simple function (Eq. 2). We therefore discretely approximate the shape of the bridge by calculating the median  $y$  values of each point over time. These values are subtracted from the  $y$  values of the points, thereby

transforming the height value of each point into a measure of displacement  $\Delta y$  from the steady-state in the vertical direction (Eq. 3).

In the *temporal* adjustment step, we simplify our functional model by removing the terms of Equation 3 that are dependent on the horizontal position  $x$ . To compensate for this simplification the adjustment is carried out for each point in space individually (Eq. 4):

$$\Delta y_x(t) = A_x \cdot e^{-\zeta \cdot t} \cdot \sin(2\pi f_t t + \phi_t) \quad (4)$$

While the resulting sets of parameters differ in amplitude, the values for  $\zeta$ ,  $f_t$  and  $\phi_t$  are ideally the same for all points in space. The starting values for  $f_t$  and  $A$  are acquired through the FFT on the time series of each cluster mean point, while  $\zeta$  and  $\phi_t$  are set to 0. The results of this step are gathered by calculating the parameters' medians after correcting the values for their cyclic nature. The amplitude spectra resulting from the abovementioned FFT are used to generate a spatio-temporal representation of observed vibrations (e.g., Figure 1), which corresponds to the results of Schill and Eichhorn (2019).

In the *spatial* adjustment step, we again simplify Equation 3 by removing the terms dependent on time and calculating the adjustment on individual profiles (Eq. 5):

$$\Delta y_t(x) = A_t \cdot \sin(2\pi f_x x + \phi_x) \quad (5)$$

Since most profiles have a very poor SNR when describing their displacement in the context of an idealized sinusoidal, we first reduce the number of profiles to those with maximal displacement from the steady-state. This is done by determining the median time for each profile and using these values in conjunction with the previously acquired temporal parameters to calculate a maximum amplitude factor. We then select only those profiles for which the maximum amplitude factor falls within the top 10%. In contrast to the previous adjustment step, the determination of the starting values cannot be achieved with FFT as our observations only capture the section of the bridge between two of its piers, which based on our assumed model has the extent of half of the spatial wavelength of the first eigenfrequency. We, therefore, use the horizontal distance between the two piers to compute the starting value of  $f_x$ , where  $f_x^0$  is the inverse of two times the length of the observed structure. The amplitude  $A$  is set to the maximum value within each profile and the phase shift  $\phi_x$  is set to 0. Again, the results for  $f_x$  and  $\phi_x$  are gathered by determining the median values.

In the *combined* adjustment step we finally estimate the parameters of Equation 3, their uncertainty estimates and observation residuals using all observations (covariance matrix = identity matrix). The starting values are set according to the results of the previous steps.

### III. EXPERIMENT

The implemented software was tested on a case study of vibration monitoring of a segment of the Hardbrücke railway bridge in Zürich, Switzerland. The bridge is realized as a simple reinforced concrete beam bridge supported by regularly spaced pillars (Figure 4). The bridge serves as a dedicated cargo train bridge.

We measured on two days (D1: October 18, 2021, and D2: January 5, 2022) using the profile scanning mode of a Zoller+Fröhlich Imager 5016. The scanner was placed at different positions under the investigated bridge segment on the two days: at the end of the segment on D1, and in the middle of the span on D2, see Figure 4. We acquired 2D profiles along the main bridge direction by manually aligning the scanning direction. The scanner was placed centrally considering the bridge width.



Figure 4. Investigated bridge segment and scanner positions at both measurement days (D1 and D2).

On the second day, a MIMO-SAR instrument was used in addition to the scanner to serve as an independent validation. The readers are referred to Baumann-Ouyang *et al.* (2022) for more information about that sensor and the measurement process.

The outcome of measurements at each day are time series lasting several minutes containing the following events: 1 – bridge at steady state, 2 – train passing over the bridge causing deformations, 3 – free decay process after unloading of the bridge, 4 – bridge at steady state again (Figure 5). The data analysis focused on analyzing the free decay process (3 in Figure 5), during which the structure is left vibrating in an excited state with its natural frequency for several seconds. As the trains passing the bridge were different on each day (e.g., different length, weight, and speed), the time series of the free decay process were expected to be slightly different. This primarily refers to the maximum observed vibration amplitude, while the eigenfrequency and other structure-related parameters are expected to be the same.

During these several minutes, the measurement conditions (measurement configuration, atmospheric conditions, etc.) remained stable. Hence, no systematic influences are expected to impact the results of the analysis. To assure high measurement stability and avoid eventual vibrations of the instrument itself (e.g., due to wind gusts), the instrument was placed on a heavy-duty scanning tripod at its lowest possible setup height. The measurements were conducted with the

following scanner settings: maximal mirror rotation speed of 52 Hz, lowest quality (minimal spatial point averaging), and maximal spatial resolution within each profile (0.8mm@10m). The expected range measurement noise of a single point was approximately 0.4 mm according to the manufacturer's specifications.

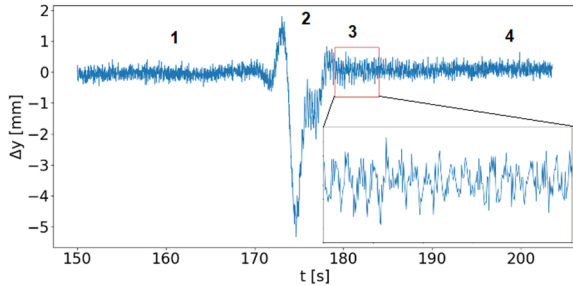


Figure 5. Time series of vertical displacements for D1 (numbers denoting different events).

#### IV. RESULTS AND DISCUSSION

This section contains: A) the results of the implemented workflow and discussion of the results in the context of two presented vibration monitoring strategies (Section II A and B); B) analysis of the impact of measurement configuration; and C) discussion about the further development of the implemented workflow.

##### A. Results of the implemented workflow

The intermediate results of the implemented workflow are amplitude spectra resolved along the bridge. Figure 1 visualizes the results for D1, while the results for D2 are negligibly different (see Table 1). The amplitudes are expressed as relative values over the whole spectrum (a percentage of the total response). Nearly over the whole bridge length, there is a clear single dominant vibration frequency at 3.834 Hz. The maximum amplitudes are detected approximately at the middle of the examined bridge segment, and they diminish towards the supporting pillars carrying it, which is expected for the first eigenfrequency of a simple beam model (a reasonable approximation for this bridge).

Table 1. Estimated vibration model parameters (D1 - the result of combined LS adjustment together with the uncertainty estimates, D2 – median results of temporal LS adjustments, and eigenfrequency estimated using MIMO SAR)

	D1		D2	MIMO SAR
	estim.	Std	estim.	estim.
$A$ [mm]	0.280	0.006	0.139	3.850
$\zeta$ [1/s]	0.142	0.008	0.142	
$f_t$ [1/s]	3.789	0.001	3.803	
$\phi_t$ [rad]	2.789	0.019	0.284	
$f_x$ [1/m]	0.0130	0.0002		
$\phi_x$ [rad]	0.227	0.013		

These results equal the results of the approach presented in Schill and Eichhorn (2019), with one clear

distinction. In the latter study, the authors succeeded to distinguish the first two eigenfrequencies using a similar instrument (dedicated 2D profiling scanner, Z+F Profiler 9012) and a similar experimental setup. If this is due to the differences in the experimental design, the used instrument (standard TLS vs. profiling scanner) or the object under investigation, should be further examined. However, this is out of the scope of this work. Here, we only confirm that preprocessed profile scans of a standard "3D" terrestrial laser scanner can be used to quantify eigenfrequency and vibration magnitude already by calculating spatially resolved amplitude spectra. The plausibility of these scanning-based results was confirmed with a MIMO SAR, where we analyzed a single amplitude spectrum for a narrow region in the middle of the investigated bridge segment (see Table 1).

The final output of the implemented workflow is an estimated vibration model describing the bridge vibration in space and time. The parameters and their uncertainty values are presented in Table 1. These results correspond to the results of the approach presented in Holst and Neuner (2021), which is herein successfully applied to a real dataset for the first time to the best of our knowledge. The final *combined* LS adjustment (Section III C) converged to unrealistic parameter values for D2. We attribute this to the unfavorable measurement configuration (see Section IV B). We thus report the median of the temporal LS adjustment results for D2 in Table 1.

There are several advantages of this extended analysis beyond the amplitude spectra presented in Figure 1. First, there is the possibility of estimating the dampening coefficient, which is relevant for SHM (Cao *et al.*, 2017). Our results indicate that the dampening coefficient can be well estimated using profile scanning, which is confirmed by: 1 – good agreement between D1 and D2, and 2 – by analyzing the adjustment residuals (Figure 6). The residuals show no apparent systematic behavior which would indicate an inadequate functional model that would be present in the data if the dampening coefficient was lacking or was incorrectly estimated. The only visible systematic behavior is due to the expected increase of the measurement noise with the increased distance and angle-of-incidence from the scanner (more in Section IV B).

The second advantage of the extended analysis are the parameter uncertainty estimates. Having them is indispensable for rigorous statistical testing of the hypothesis "*the structure retained the expected material properties since the last measurements*", which signals good structural health. In the case of the simplified data analysis from Schill and Eichhorn (2019), similar estimates are lacking.

Moreover, having a full spatio-temporal vibration model is indispensable for simulations and comparison with the designed structure behavior. However, the main potential of the SHM with the high spatial



resolution offered by profile scanning is a possibility to analyze if the structure is locally behaving differently than expected.

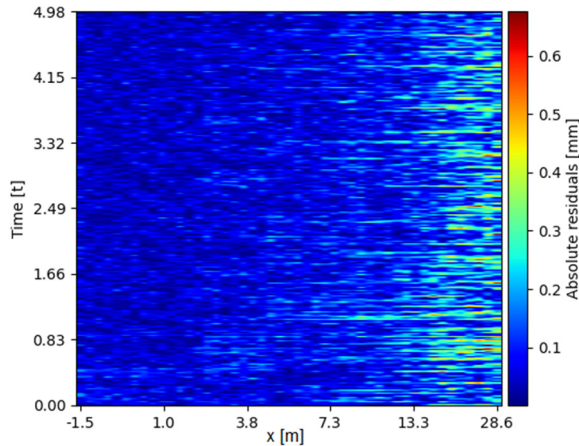


Figure 6. 2D Plot of the "combined" adjustment residuals.

Namely, obtaining the spatio-temporal model allows for systematically analyzing the adjustment residuals in the search for systematic patterns that would highlight unexpected building behavior. Additionally, by functionally modeling the detectable eigenmodes, they can be optimally removed from the measurement time series. Hence, analyzing the adjustment residuals which are free of their influence can increase the sensitivity of these local inspections. With the classical signal processing techniques, it is possible to filter out certain frequency bands corresponding to the frequencies with high oscillation amplitudes (approx. eigenfrequencies). However, due to possible spectral leakage (Harris, 1978), this could cause a loss of potentially relevant data.

To conclude, there are multiple benefits of the extended effort of obtaining the spatio-temporal deformation model proposed in Holst and Neuner (2021) from the data processing perspective. It remains to be analyzed in collaboration with structural engineers how this model needs to be adapted to properly reflect the physically determined deformations of the structure. In case of insufficient data quality for convergence of the full algorithm or if the model by Holst and Neuner (2021) is not justified from a structural point of view, using the simplified analysis from Schill and Eichhorn (2019) is preferable for estimating spatially resolved eigenfrequencies and vibration amplitudes.

### B. Influence of measurement configuration

Our experiments revealed that the selection of the scanner position has a notable impact on the success of estimating the spatio-temporal vibration model. Namely, we were able to obtain the "combined" spatio-temporal model only for D1 (Table 1), while for D2 the workflow failed after the *temporal* LS adjustment step (Section II C). The reason can be found in the SNR which is influenced by the spatial vibration pattern and

measurement configuration. The noise increases with distance and incidence angle (Soudarissanane *et al.*, 2011), while for the frequency of the first eigenmode, the amplitude diminishes from the bridge middle towards the supporting pillars (Figure 1).

Figure 7 presents the time series of a free decay process (Figure 5, event 3) for two locations along the bridge, the end (top) and the middle (bottom) of the investigated segment. The data are presented for D1 (blue) and D2 (orange) with different measurement configurations (Figure 4). Positioning the instrument directly in the middle of the investigated segment (D2) achieves the overall highest SNR directly above the scanner (Figure 7, bottom orange). However, at the same time, it achieves the overall worst SNR at the end of the segment, making the periodic signal due to natural frequency unobservable (Figure 7, top orange). This has a negative impact on estimating the complete spatio-temporal model, because it does not contain sufficient information for resolving the spatially related vibration parameters ( $f_x, \varphi_x$  in Eq. 3).

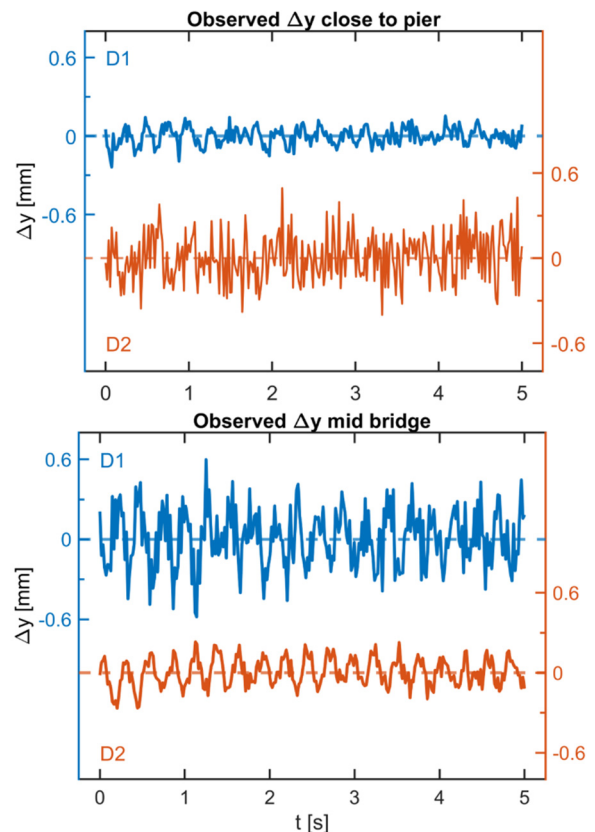


Figure 7. Time series of vertical displacements during a free decay process for D1 (blue) and D2 (orange) at the end (top) and the middle (bottom) of the bridge segment (y-axis presenting  $\Delta y$  in mm).

On the contrary, positioning the scanner at one end of the observed bridge segment (D1) assures overall lower, but more constant SNR along half of the segment. This leads to successfully estimating spatio-temporal vibration model (Table 1). Hence, this simplistic analysis indicates that for obtaining the

spatio-temporal vibration model, it is better to assure adequate SNR at the locations where the vibration amplitudes are expected to be small (close to the supporting bridge pillars). In our case, this is achieved by placing an instrument at one end of the observed bridge segment, which relies on the presumption of symmetrical bridge behavior (given by the functional model in Equation 3). Ideally, two instruments should be synchronized and used simultaneously at both ends of the investigated segment, which would lead to adequate SNR over the whole span.

### C. Further development of implemented workflow

The workflow described in Section II C, is a prototypical implementation with some practical simplifications. Hence, there are multiple possibilities for its further development.

One direction is further automation of the approach, to reduce the need for human intervention. For example, eigenmode analysis could be further automated by detecting the free decay process within the measurement time series using a continuous wavelet transform. Moreover, the current implementation requires manually selecting the functional model. The former could be resolved by automatically testing a range of plausible functional models and identifying the most suitable one, *e.g.*, by using one of the established approaches to model selection. Also, the current implementation hard-coded the knowledge about the deformation direction (Eq. 3, deformations solely occur along the  $y$ -axis). A more general approach (*e.g.*, extending to vertical structures) should incorporate a functional model, which is defined in a more general sense.

The second direction of development is refining the point cloud pre-processing steps, *e.g.*, by further optimizing de-noising, implementing outlier removal, and optimizing spatial cluster sizes (as a trade-off of improved SNR and reduced sampling frequency). Moreover, some additional processing steps such as inducing stochastic resonance (Gammaitoni *et al.*, 1998) could further improve the sensitivity of the approach.

The third direction is refining the parameter estimation, *e.g.*, by incorporating a stochastic model of the scanner's genuine polar coordinates. Here, it would be advisable to refine a stochastic model by accounting for measurement degradation with a higher incidence angle (*e.g.*, observable in Figure 6), and by introducing variance component estimation (VCE). Also, the functional model could be expanded to model the shape of the object's surface (*e.g.*, using B-Splines or polynomials). Finally, the discussed high sensitivity of the LS adjustment towards the quality of the initial parameter values could be mitigated by implementing global heuristic optimizers with a bounded domain of possible parameter values, either as a substitute or as

an addition to the currently implemented LS adjustment.

The last direction for development would be expanding the SHM analysis. One option is expanding it beyond analyzing the free-decay process, *e.g.*, by automatically detecting and functionally modeling the lower-frequency deformations (*e.g.*, caused by train crossing over the bridge), which would resemble classical load tests. Another option is developing already mentioned automatic analysis of the adjustment residuals to detect eventual local discrepancies relative to the expected global structure's behavior.

## V. CONCLUSION

In this paper, we report about the implementation of a workflow for vibration monitoring using 2D profile laser scanning, which combines the strategies proposed in Schill and Eichhorn (2019), and Holst and Neuner (2021) and about preliminary results obtained by applying the workflow to data from. We used the prototypical implementation of the open-source software for the eigenmode analysis of a railway bridge based on 2D profiles acquired with a standard terrestrial laser scanner (TLS). We estimated a spatiotemporal vibration model including dampening coefficient from observations obtained shortly after a cargo train had passed over the bridge and had induced oscillations at the bridge's natural frequency of about 3.8 Hz with an amplitude as low as 0.3 mm.

The interpretation of the results obtained using two different measurement configurations indicated that it is better to place the instrument close to the bridge piers, and not in the middle of the inspected bridge segment (the most intuitive position) for estimating the parameters of a spatio-temporal vibration model. Starting from the results obtained herein, we discussed several recommended options to further develop the implemented workflow, ideally in collaboration with structural engineers to support the selection of spatio-temporal models representing the respective structure appropriately.

## VI. ACKNOWLEDGEMENTS

Andreas Baumann provided and processed the MIMO-SAR data.

## References

- Baumann-Ouyang, A., Butt, J. and Wieser, A. (2022) Bridge deformations during train passage: monitoring multiple profiles using concurrently operating MIMO-SAR sensors. In: 5th Joint international *Symposium on Deformation Monitoring (JISDM)*. Valencia, Spain.
- Cao, M.S., Sha, G.G., Gao, Y.F. and Ostachowicz, W. (2017) Structural damage identification using damping: a compendium of uses and features. *Smart Materials and structures*, 26(4), p. 43001.

- Gammaitoni, L., Hänggi, P., Jung, P. and Marchesoni, F. (1998) Stochastic resonance. *Reviews of modern physics*, 70(1), p. 223.
- Harris, F. J. (1978) On the use of windows for harmonic analysis with the discrete Fourier transform. *Proceedings of the IEEE*, 66(1), pp. 51–83.
- Holst, C. and Neuner, H. (2021) Spatio-Temporal Models for Vibration Monitoring of Elongated Structures Using Profile Laser Scans. *Remote Sensing*, 13(7), p. 1369.
- Mukupa, W., Roberts, G.W., Hancock, C.M. and Al-Manasir, K. (2017) A review of the use of terrestrial laser scanning application for change detection and deformation monitoring of structures. *Survey Review*, 49(353), pp. 99–116.
- Neuner, H., Holst, C. and Kuhlmann, H. (2016) Overview on Current Modelling Strategies of Point Clouds for Deformation Analysis. *Allgemeine Vermessungs-Nachrichten (AVN)*, 123(11–12), pp. 328–339.
- Samet, H. and Tamminen, M. (1988) Efficient component labeling of images of arbitrary dimension represented by linear bintrees. *IEEE transactions on pattern analysis and machine intelligence*, 10(4), pp. 579–586.
- Schill, F. (2018) *Überwachung von Tragwerken mit Profilsclannern*. TU Darmstadt.
- Schill, F. and Eichhorn, A. (2019) Deformation Monitoring of Railway Bridges with a Profile Laser Scanner. *ZfV-Zeitschrift für Geodäsie, Geoinformation und Landmanagement*, 2, pp. 109–118. doi: 10.12902/zfv-0248-2018.
- Shensa, M. J. (1992) The discrete wavelet transform: wedding the a trous and Mallat algorithms. *IEEE Transactions on signal processing*, 40(10), pp. 2464–2482.
- Soudarissanane, S., Lindenbergh, R., Menenti, M. and Teunissen, P. (2011) Scanning geometry: Influencing factor on the quality of terrestrial laser scanning points. *ISPRS Journal of Photogrammetry and Remote Sensing*, 66(4), pp. 389–399.

## Extraction of key geometric parameters from segmented masonry arch bridge point clouds

Yixiong Jing, Brian Sheil, Sinan Acikgoz

Department of Engineering Science, University of Oxford, Parks Road, Oxford, OX1 3PJ,  
([yixiong.jing@wolfson.ox.ac.uk](mailto:yixiong.jing@wolfson.ox.ac.uk); [brian.sheil@eng.ox.ac.uk](mailto:brian.sheil@eng.ox.ac.uk); [sinan.acikgoz@eng.ox.ac.uk](mailto:sinan.acikgoz@eng.ox.ac.uk))

**Key words:** *point cloud; segmentation; deep learning (DL); BridgeNet; synthetic dataset; feature extraction*

### ABSTRACT

Masonry arch bridges constitute the majority of the European bridge stock. Most of these bridges were constructed in the 19<sup>th</sup> century and feature a wide range of geometric characteristics. Since construction drawings rarely exist, the first step in the assessment of these bridges is the characterisation of their in-situ geometry, which may involve significant geometric distortions. In recent years, LIDAR devices have been widely used by bridge owners due to their ability to remotely and rapidly collect point cloud data. To enable the engineering assessment practice to benefit from this data, this research uses the recently developed deep learning (DL) neural network BridgeNet to autonomously segment masonry bridge point clouds into different components. Due to the limited availability of 3D point clouds, BridgeNet is trained using a synthetic multi-span masonry arch bridge dataset; the network is then tested on real arch bridge point clouds. By fitting appropriate primitive shapes to bridge component point clouds using Random Consensus Sampling (RANSAC) techniques the bridge geometry is effectively characterised by a few parameters.

### I. INTRODUCTION

In the UK, there are approximately 18,000 operational masonry railway bridges which occupy 47% of the total bridge stock (Orbán, 2004). Increasing traffic loading has been hastening the rate of deterioration of these bridges. Therefore, regular inspections are required to ensure their safety (Acikgoz *et al.*, 2018). The evaluation of loading capacity requires detailed knowledge of the geometry of the structure, such as the radius of curvature of the arch. However, construction drawings are often unavailable for masonry arch bridges and measurements of geometric characteristics are sometimes limited by access issues.

Laser scanning provides an efficient and non-contact method of obtaining the in-situ 3D geometry of large-scale civil engineering infrastructure and representing them by using point clouds. Key geometric parameters describing the bridges can then be estimated by post-processing the point clouds (Riveiro *et al.*, 2011; Schnabel *et al.*, 2007). However, these estimations often require the manual segmentation of the point clouds which is time-consuming for large datasets. Therefore, an automatic algorithm is necessary for conducting both semantic and instance segmentation. For instance, to determine the radius of curvature of an arch, points belonging to the arches need to be first semantically classified and then clustered into different arch instances. Traditional feature-based segmentation algorithms usually make assumptions based on the shape and topological relationships of each component (Lu *et al.*, 2019; Riveiro *et al.*, 2016). Although these algorithms can achieve good segmentation accuracy, they cannot be generalized to other datasets since they are designed for specific geometric characteristics.

Compared with traditional segmentation algorithms, deep learning (DL) algorithms are known for their ability to offer generalized solutions that are robust to noise. One of the most popular 3D neural networks, PointNet++ (Qi *et al.*, 2017), achieves good performance on semantic segmentation with the multi-scale feature extraction design. However, the structure of PointNet++ only allows it to process less than ten thousand points at the same time while a common masonry arch bridge point cloud may contain millions of points. Recently, RandLA-Net (Hu *et al.*, 2020) was proposed to conduct semantic segmentation on large-scale point clouds efficiently by using random point sampling and a lightweight feature extractor. Similarly, FG-Net (Liu *et al.*, 2020) uses sophisticated yet efficient feature extractors to group local and global features which achieve the best results to date on the public partial segmentation dataset called PartNet (Mo *et al.*, 2019). Based on their work, BridgeNet (Jing *et al.*, 2022) was developed to perform segmentation on large-scale masonry arch bridge point clouds. To tackle data scarcity, a synthetic point cloud simulator was developed in the same study and it was used to generate a large synthetic training dataset. The trained algorithm was tested on real point clouds of seven masonry arch bridges from the UK. Semantic segmentation results were post-processed with a simple and memory-efficient clustering method called DBSCAN (Ester *et al.*, 1996) to perform instance segmentation.

To demonstrate how point cloud segmentation results can be used in the assessment of masonry arch bridges, the automated extraction of key geometric parameters from segmented point clouds is

investigated in this study. More specifically, key geometric parameters are extracted from BridgeNet segmented point clouds (Jing *et al.*, 2022). For the arch point clouds, the radius and direction of the generatrix are estimated by idealizing arch intrados geometry with partial cylinders. Some shape fitting algorithms rely on principal component analysis to identify the direction of the generatrix (Nurunnabi *et al.*, 2017; Proença *et al.*, 2018). However, these algorithms rely on the assumption that the length of the cylinder is larger than the radius of curvature, which is unsuitable for many masonry arch bridges. Instead, a RANSAC-based algorithm is used in this study by iteratively fitting a small group of points with a cylinder function and excluding outliers to obtain the best-fit geometry. Piers are combinations of multiple planes that sometimes feature complex geometric characteristics such as skewed flank surfaces. Another RANSAC-based algorithm is used to identify planes from pier instances and the skew angles of flank surfaces are then extracted from the planes.

The paper is organized as follows. Section II introduces the BridgeNet used for performing segmentation on masonry point clouds and the real and synthetic datasets. In Section III, training results from BridgeNet are presented. Section IV presents the extraction of key geometric parameters of arches and piers. Section V provides the conclusion of this paper.

## II. BRIDGENET AND DATASET

### A. BridgeNet

BridgeNet adapted the architecture from RandLA-Net (Hu *et al.*, 2020). RandLA-Net (Hu *et al.*, 2020) was proposed to perform semantic segmentation on large-scale point clouds efficiently. Instead of applying time-consuming sampling methods such as the farthest point sampling, it uses random point sampling to downsample the point clouds. To compensate for the lost information, a lightweight feature extractor was introduced to explicitly concatenate geometric information with encoded features. However, it is observed in our experiments that the feature extractor in RandLA-Net (Hu *et al.*, 2020), whilst achieving good accuracy in semantic segmentation such as city scene, could not satisfactorily capture the level of local feature details required in our segmentation tasks. Therefore, a more sophisticated feature extractor module was required. To obtain an optimal balance between computational efficiency and performance, we adopted the feature downsampling method from FG-Net (Liu *et al.*, 2020). As shown in Figure 1, the input has the size of  $N_i \times C_{in}$  in which  $N_i$  represents the number of points and  $C_{in}$  is the input feature dimension. To achieve memory efficiency, the feature dimension is first downsampled by a ratio of  $m$  (8 in our case) using a convolutional layer. Ball query is then used to group  $K$  neighbours of each point to capture the local relationship. The grouped feature tensor is finally

passed to convolutional layers to encode the local features and the output has the size of  $N_i \times K \times C_{out}$ , in which  $C_{out}$  is the output feature dimension. It is notable that step 3 in Figure 1 consumes the most GPU memory. Therefore, the downsampling of feature dimension alleviates the memory consumption by condensing the feature tensor into 1/8 of its original size. More details can be found in FG-Net (Liu *et al.*, 2020).

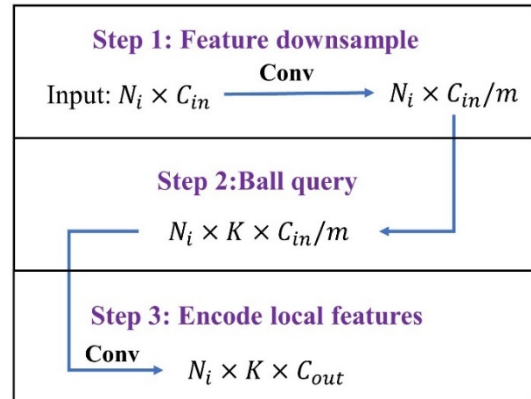


Figure 1. Illustrations of the feature extractor to encode local features of large-scale point clouds; the input is first downsampled in feature dimension by the ratio of  $m$ ,  $K$  neighbour points are then grouped for each point; the clustered features are finally passed through a convolutional layer for the output.

The input size of our neural network is  $N \times 3$ , in which  $N$  is the number of points and 3 are the raw  $x$ ,  $y$  and  $z$  point coordinates. The input is first passed through an encoder which is composed of four feature extractor layers to learn local features in different resolutions. The random point sampling adopted from RandLA-Net (Hu *et al.*, 2020) is applied after every single layer to downsample point clouds with a ratio of 4, which achieves time efficiency for large-scale point clouds. The features are then sent to a decoder to scale the number of points back to the original input by using the nearest interpolation method (Qi *et al.*, 2017). A  $1 \times 1$  convolution layer is subsequently applied to reshape the feature dimension corresponding to the semantic label with the size of  $N \times C_{sem}$ , in which  $C_{sem}$  represents the number of semantic classes. Details of BridgeNet can be found in (Jing *et al.*, 2022).

### B. Dataset

The dataset is composed of synthetic and real components, which are used for training and testing respectively.

The synthetic dataset is designed to represent the geometry of real masonry arch bridges. The geometry of each component for the masonry arch bridge is parameterized to automatically generate thousands of point clouds with different shapes. The noiseless synthetic point cloud produced in this way is then corrupted to simulate construction errors and geometric irregularities. For example, the height of the

pier is randomized to represent variations caused by irregular topography as shown in Figure 2.

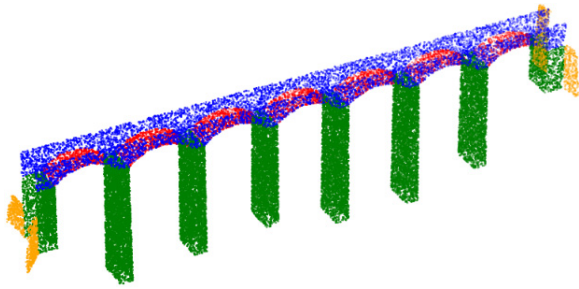


Figure 2. Example of synthetic masonry arch bridge point cloud with randomized geometry featuring different pier heights, span lengths and wingwall geometries.

The real dataset contains point clouds of seven multi-span masonry arch railway bridges from the UK. Marsh Lane Viaduct is shown in Figure 3 as an example in which the vegetations, parapet and poorly scanned areas are removed since they are not considered in the synthetic data simulator. The processed point clouds are then classified into five components which are the spandrel wall, pier/abutment, arch, hole and wingwall. The manually segmented Marsh Lane Viaduct point cloud data in Figure 4 features the first four components, as the viaduct did not have wingwalls. Other bridges in the real dataset include this feature.



Figure 3. Example of the real point cloud of Marsh Lane Viaduct used in the test dataset.

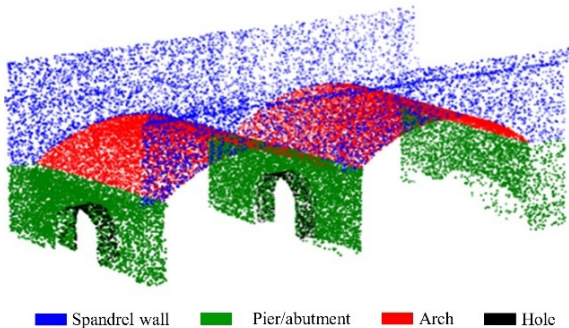


Figure 4. Manual semantic segmentation of the point cloud of Marsh Lane Viaduct into four primary components.

### III. TRAINING EXPERIMENTS

#### A. Implementation details and metrics

The training dataset contains only synthetic data sampled from the synthetic data generator introduced

in Section II. BridgeNet is trained with an increasing number of synthetic bridge point clouds from 500 to 3000. The trained BridgeNet is then tested on all seven real bridges each of which contains millions of points. The network can efficiently segment each point cloud in seconds. The experiments are conducted on an RTX 3080 GPU with 10 GB of memory.

Mean Intersection-over-Union ( $mIoU$ ) is adopted in the experiments to assess the performance of the network as shown in Equation 1, in which  $TP_i$  is the true positive for class  $i$ ,  $FP_i$  is the number of points being misclassified as class  $i$ ,  $FN_i$  is the number of misclassified points belonging to class  $i$  and  $n_{cls}$  is the number of components for the corresponding point cloud.

$$mIoU = \frac{\sum_{i=1}^{n_{cls}} \frac{TP_i}{TP_i + FP_i + FN_i}}{n_{cls}} \quad (1)$$

$mIoU$  can identify poorly segmented classes even when they occupy only a very small portion of the total point cloud such as the hole or wingwall classes.

#### B. Semantic segmentation results

The influence of an increasing number of point clouds on the segmentation accuracy of BridgeNet is shown using the  $mIoU$  results in Table 1. The best accuracy of 0.779 is achieved using 2000 point clouds during training. As the size of the training dataset is increased, the  $mIoU$  is first improved which indicates that the geometric information provided by the synthetic data provides useful training information. However, the  $mIoU$  for the case with 3000 training point clouds demonstrates poorer performance and experience overfitting related problems. Hence, the network trained with 2000 training point clouds will be used in the rest of the paper.

Table 1.  $mIoU$  of BridgeNet on test dataset with increasing training samples in the synthetic dataset

	$mIoU$
500	0.654
1000	0.682
1500	0.751
2000	0.779
3000	0.737

By way of example, the segmentation results for Marsh Lane Viaduct are visualized in Figure 5. The true labels are presented first, then the BridgeNet segmentation results. The hole in the Marsh Lane viaduct is mostly misclassified as a pier element. This could be attributed to the unbalanced proportions of classes in the dataset. The network tends to classify points belonging to holes into piers since the points of holes only occupy a small portion of the whole point cloud. However, the general shape of each component

is well captured for all data in the test set. The next section evaluates the accuracy of geometric parameters extraction in the presence of segmentation inaccuracy.

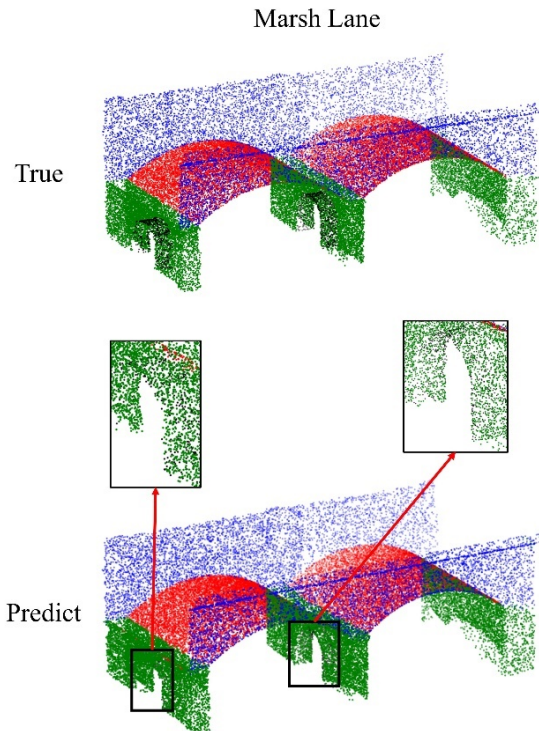


Figure 5. Visualizations of the true segmentation label of the Marsh Lane Viaduct compared with the semantic segmentation results from BridgeNet. Misclassifications are highlighted and shown inset with a zoomed-in view within black bounding boxes.

#### IV. GEOMETRIC EXTRACTION

##### A. Instance segmentation

Since the network only gives the semantic segmentation results, the unsupervised learning package DBSCAN (Pedregosa *et al.*, 2011) is used to perform instance segmentation to cluster points into separate objects as shown in Figure 6. The outliers were automatically removed by filtering out clusters that contain points lower than the defined threshold. The hyper-parameters used in the algorithm had to be adjusted following a trial and error approach to achieve the best instance segmentation performance.

##### B. Geometric feature extraction of arches

Geometric parameters are extracted from the ‘ground truth’ point cloud of arches, which were manually segmented. These are compared with the geometric parameters obtained from the arch point clouds segmented by BridgeNet and DBSCAN to demonstrate the feasibility of the proposed framework. Since the arch is assumed to approximate a partial cylinder, the radius and direction of the generatrix are extracted from the point clouds for comparison.

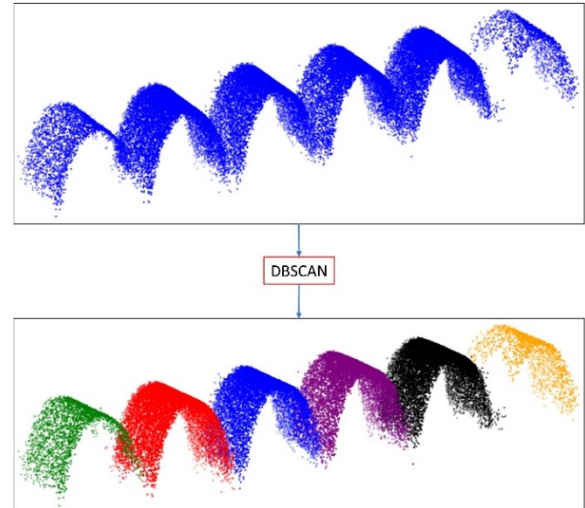


Figure 6. Instance segmentation performed after semantic segmentation for arches of the Chelmsford Viaduct by using DBSCAN.

Algorithm 1. Robust extraction of radius and generatrix of arches based on RANSAC and a cylinder fitting function

**Input:** point cloud for a single arch instance

$P_{arch} = \{p_i\}, i = 1, 2, \dots, N, p_i = (x_i, y_i, z_i)$ , where  $N$  is the number of points; maximum iteration  $n$ ; maximum radius error tolerance  $e_{radius\_tol}$ ; minimum number of points  $N_{cy\_tol}$  satisfying the radius difference tolerance  $r_{tol}$  compared with the radius from the fitted cylinder function; several points chosen from  $P_{arch}$  to fit the cylinder function  $N_{cy\_tol}$

**Output:** radius  $r_{out}$  and generatrix direction  $d_{out}$ , in which  $d_{out} = (x_{out}, y_{out}, z_{out})$

$m = 0$

**while**  $m < n$  **do**

Randomly sampling  $N_{cy}$  points from  $P_{arch}$  which produces a new point set of  $P_{cy}$ ;

$r_i, d_i, c_i = \text{cylinder\_fitting}(P_{cy})$ , which  $c_i$  is the centre of the middle cross-section of the cylinder in iteration  $i$ ;

Calculate the mean absolute deviation of the radius  $e_{radius}$  between the rest of the points in  $P_{arch}$  by using the fitted  $r_i, d_i, c_i$ ;

Calculate the number of points  $N_{cy}$  fitted to the cylinder which satisfies the radius tolerance  $r_{tol}$ ;

**if**  $N_{cy} > N_{cy\_tol}$  **and**  $e_{radius} < e_{radius\_tol}$  **then**

$r_{out} = r_i, d_{out} = d_i$ ;

**return**  $r_{out}, d_{out}$ ;

**else then**

$m = m + 1$ ;

**Continue**

The two parameters can be calculated by using a RANSAC-based iterative geometric extraction algorithm as shown in Algorithm 1. By randomly selecting a small set of points (15 points in our case) from the arch point cloud, the algorithm first fits the 3D parametric cylinder function for the radius  $r_i$ , generatrix direction  $d_i$  and the centre coordinates  $c_i$  in the middle cross-section. For the rest of the points, the shortest distance between them and the fitted cylinder generatrix (uniquely determined by  $c_i$  and  $d_i$ ) is then calculated.

By subtracting  $r_i$  from this value, the residual error of the radius is obtained for each point. The absolute value of errors is summed and averaged to obtain the mean absolute deviation  $e_{radius}$ . The number of points on the cylinder,  $N_{cy}$ , can then be determined by filtering points with residual errors larger than a pre-defined threshold  $r_{tol}$ . If  $N_{cy}$  is larger than  $N_{cy,tol}$  and  $e_{radius}$  is smaller than  $e_{radius,tol}$ , the fitted  $r_i$  and  $d_i$  are accepted and the loop ends. Otherwise, the loop continues until the maximum number  $n$  is reached.

The extracted geometric parameters in the final step of the algorithm for the segmented arches are compared to the parameters extracted from ground truth arches as shown in Table 2. Root mean squared errors (RMSE) are specified since the geometric extraction was conducted for multiple arches. The RMSE for the radius is typically smaller than 3 cm, indicating remarkable accuracy. The direction of the generatrix is captured with an RMSE of  $< 0.2^\circ$  which highlights the robustness of the segmentation results.

Table 2. RMSE values associated with the radius and the generatrix angle obtained by fitting cylinders to arch point clouds segmented using BridgeNet are presented. The errors are relative to the radius and generatrix estimations from cylinders fitted to manually segmented ground truth point clouds

	Radius [m]	Generatrix [°]
Chelmsford	$8.43 \cdot 10^{-3}$	$1.70 \cdot 10^{-1}$
Hertford	$6.08 \cdot 10^{-3}$	$1.57 \cdot 10^{-1}$
Peter 0	$1.87 \cdot 10^{-2}$	$8.57 \cdot 10^{-2}$
Peter 1	$1.30 \cdot 10^{-2}$	$1.70 \cdot 10^{-1}$
Digswell	$2.79 \cdot 10^{-2}$	$1.87 \cdot 10^{-1}$
Stapleton	$1.91 \cdot 10^{-2}$	$9.29 \cdot 10^{-2}$
Marsh Lane	$2.62 \cdot 10^{-2}$	$4.61 \cdot 10^{-2}$

### C. Geometric feature extraction of piers

Skewed pier flank surfaces are a feature of the Digswell Viaduct in the real dataset as shown in Figure 7. Therefore, this section considers Digswell Viaduct as an example to demonstrate the robustness of the proposed extraction process to capture complex geometric features. The skew angle is defined as the angle between the vector normal to the pier flank surface and the horizontal plane. Skew angles are first extracted from manually segmented planes as the ground truth values for subsequent comparison with predicted values.

Another RANSAC-based algorithm is used to separate planes of segmented pier point clouds. Three points are randomly chosen from point clouds to fit a 3D surface and the rest of the points would be checked whether they are on the plane or not based on a distance threshold. After reaching the maximum number of iterations or sufficient points being fitted to the 3D surface, it is accepted as the current best plane and all points belonging to this plane are removed from the pier point cloud. By repeating this procedure until

either the maximum number of planes is reached (four, for typical piers) or not enough points are left in the point cloud, the algorithm then stops and returns all extracted planes. An example of the plane extraction is visualized in Figure 8 where four planes are represented by red, grey, orange and black points.

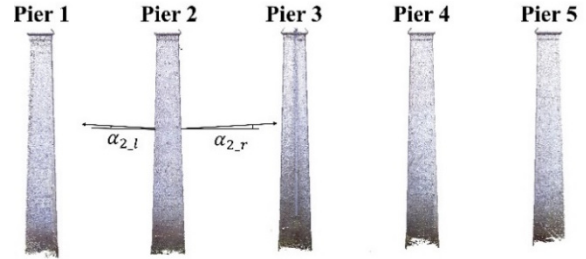


Figure 7. Piers of Digswell Viaduct, in which the flank surfaces are skewed. There are a total of five scanned piers and the right and left skew angles of pier 2 are denoted by  $\alpha_{2,r}$  and  $\alpha_{2,l}$  respectively.



Figure 8. Extractions of planes by using RANSAC-based algorithm for pier 2, four planes are represented by red, grey, orange and black points.

The flank surfaces along the bridge transverse direction are selected for calculating the angle of skew since they contained more points. As shown in Figure 7, the left and right skew angle for pier  $i$  is represented by  $\alpha_{i,l}$  and  $\alpha_{i,r}$ . Table 3 demonstrates that the skew angles of flanks are usually smaller than  $2^\circ$  and the total error is represented by the mean average deviation (MAD) of  $0.06^\circ$  which demonstrates the excellent accuracy of the proposed framework.

### V. CONCLUSION

In this paper, we proposed an automated and generalisable framework for extracting geometric features from masonry arch bridge point clouds to facilitate the assessment and inspection. Since there is no available or published neural network to tackle with partial segmentation of large-scale point clouds, BridgeNet (Jing *et al.*, 2022) was used to provide a general solution for infrastructure segmentations. Due to the scarcity of real data for training, that work developed a masonry arch bridge point cloud generator to create synthetic point clouds with different geometries. The synthetic point clouds were used to train the network, which was later tested on seven real railway bridge point clouds. The resulting segmentation



had good accuracy but featured some errors, which could influence geometric parameter extraction.

Table 3. The extracted skew angles by fitting the plane function with the manually segmented ground true pier point clouds, predicted ones and the absolute errors between them

		True [°]	Predict [°]	Abs errors [°]
Pier 1	$\alpha_{1,l}$	--	--	--
	$\alpha_{1,r}$	0.83	0.87	0.04
Pier 2	$\alpha_{2,l}$	1.98	2.03	0.05
	$\alpha_{2,r}$	1.05	0.99	0.06
Pier 3	$\alpha_{3,l}$	1.89	1.93	0.04
	$\alpha_{3,r}$	0.93	0.93	0.00
Pier 4	$\alpha_{4,l}$	1.87	1.82	0.05
	$\alpha_{4,r}$	1.04	0.93	0.11
Pier 5	$\alpha_{5,l}$	1.85	1.95	0.10
	$\alpha_{5,r}$	--	--	--
MAD	0.06			

To investigate the feasibility of using the BridgeNet segmentation results for extracting key geometric parameters of bridges, both true and predicted arches are fitted with partial cylinders using a RANSAC-based approach. Another RANSAC-based algorithm is used to separate and select flank surfaces of predicted piers to obtain the skew angle. The geometric parameters extracted from the segmentation results of BridgeNet were compared to true values, demonstrating high accuracy. The results emphasize the robustness of segmentation and highlighted the useful geometric information that can be gained from segmented point clouds.

## VI. ACKNOWLEDGEMENTS

The authors acknowledge Dan Brackenbury and Robert Gayer (University of Cambridge) and Matthew DeJong (University of Berkeley) who collected and shared the masonry arch bridge point cloud data used in this study.

## References

- Acikgoz, S., DeJong, M. J., and Soga, K (2018). Sensing dynamic displacements in masonry rail bridges using 2D digital image correlation. *Structural Control and Health Monitoring*, Vol. 25, No 8, pp. e2187.
- Ester, M., Kriegel, H. P., Sander, J., and Xu, X (1996). A density-based algorithm for discovering clusters in large spatial databases with noise. In: *Proc. 2nd Int. Conf. Knowledge Discovery and Data Mining (KDD'96)*, AAAI Press, Vol. 96, No. 34, pp. 226-231.
- Hu, Q., Yang, B., Xie, L., Rosa, S., Guo, Y., Wang, Z., Trigoni N and Markham, A (2020). Randla-net: Efficient semantic segmentation of large-scale point clouds. In: *Proc. Of the IEEE/CVF Conference on Computer Vision and Pattern Recognition*, pp. 11108-11117.
- Jing, Y., Sheil, B.B., and Acikgoz, S (2022). Segmentation of large-scale masonry arch bridge point clouds with a synthetic bridge simulator and the BridgeNet neural network. Under review.
- Liu, K., Gao, Z., Lin, F., and Chen, B. M (2020). FG-Net: Fast Large-Scale LiDAR Point Clouds Understanding Network Leveraging Correlated Feature Mining and Geometric-Aware Modelling. arXiv preprint.
- Lu, R., Brilakis, I., and Middleton, C. R (2019). Detection of Structural Components in Point Clouds of Existing RC Bridges. *Computer-Aided Civil and Infrastructure Engineering*, Vol. 34, No. 3, pp. 191-212.
- Mo, K., Zhu, S., Chang, A. X., Yi, L., Tripathi, S., Guibas, L. J., and Su, H (2019). PartNet: A Large-scale Benchmark for Fine-grained and Hierarchical Part-level 3D Object Understanding. In: *Proc. Of the IEEE/CVF conference on computer vision and pattern recognition*, pp. 909-918.
- Nurunnabi, A., Sadahiro, Y., and Lindenbergh, R (2017). Robust cylinder fitting in three-dimensional point cloud data. *International Archives of the Photogrammetry, Remote Sensing and Spatial Information Sciences*, Vol. XLII-1/W1, pp. 63-70.
- Orbán, Z (2004). Assessment, reliability and maintenance of masonry arch railway bridges in Europe. *Arch Bridges IV—Advances in Assessment, Structural Design and Construction*. Eds: P. Roca and C. Molins, Barcelona, pp. 152-161.
- Pedregosa, F., Varoquaux, G., Gramfort, A., Michel, V., Thirion, B., Grisel, O., and Duchesnay, E (2011). Scikit-learn: Machine learning in Python. *the Journal of machine Learning research*, Vol. 12, pp. 2825-2830.
- Proença, P. F., and Gao, Y (2018). Fast cylinder and plane extraction from depth cameras for visual odometry. In: *Proc. IEEE/RSJ Int. Conf. Intell. Robots Syst.*, pp. 6813-6820.
- Qi, C. R., Yi, L., Su, H., and Guibas, L. J (2017). Pointnet++: Deep hierarchical feature learning on point sets in a metric space. In: *Proc. Adv. Neural Inf. Process. Syst.*, pp. 5099-5108.
- Riveiro, B., DeJong, M. J., and Conde, B (2016). Automated processing of large point clouds for structural health monitoring of masonry arch bridges. *Automation in Construction*, Vol. 72, pp. 258-268.
- Riveiro, B., Morer, P., Arias, P., and De Arteaga, I (2011). Terrestrial laser scanning and limit analysis of masonry arch bridges. *Construction and Building Materials*, Vol. 25, No. 4, pp. 1726-1735.
- Schnabel, R., Wahl, R., and Klein, R (2007). Efficient RANSAC for Point-Cloud Shape Detection. *Computer Graphics Forum*, Vol. 26, No. 2, pp. 214-226.

## Drill bit grading using LiDAR and imagery on the apple smart devices

Fengman Jia<sup>1</sup>, Derek D. Lichti<sup>1</sup>, Roman Shor<sup>2</sup>, Arsh Khawaja<sup>2</sup>, Min Kang<sup>1</sup>, Max Kepler<sup>3</sup>

<sup>1</sup> Department of Geomatics Engineering, University of Calgary, 2500 University Dr NW, Calgary, AB, T2N 1N4, Canada, ([fengman.jia@ucalgary.ca](mailto:fengman.jia@ucalgary.ca); [ddlichti@ucalgary.ca](mailto:ddlichti@ucalgary.ca); [gyoungmin.kang@ucalgary.ca](mailto:gyoungmin.kang@ucalgary.ca))

<sup>2</sup> Department of Chemical and Petroleum Engineering, University of Calgary, 2500 University Dr NW, Calgary, AB, T2N 1N4, Canada, ([roman.shor@ucalgary.ca](mailto:roman.shor@ucalgary.ca); [arsh.khawaja@ucalgary.ca](mailto:arsh.khawaja@ucalgary.ca))

<sup>3</sup> Department of Mechanical Engineering, University of Calgary, 2500 University Dr NW, Calgary, AB, T2N 1N4, Canada, ([maxwell.kepler@ucalgary.ca](mailto:maxwell.kepler@ucalgary.ca))

**Key words:** *sensor; LiDAR; laser scanning; drill bit grading*

### ABSTRACT

Reservoir development in the petroleum industry starts with the drill bit. A drill bit's dull condition must be closely monitored since it significantly influences the efficiency and the cost of drilling operations. The dull condition check procedure is called drill bit grading and is essentially a change detection problem to determine the state of the drill bit, in particular the wear of the cutting teeth inserts. Currently, the grading is conducted manually on-site, which is error-prone and highly subjective. Laser scanning technology offers a potential solution to overcome the shortcomings of existing practice. The integration of LiDAR (Light Detection and Ranging) on the newly-launched iDevices, the iPhone 12 Pro and the iPad Pro 2020 offers new opportunities for close-range measurement given their huge customer base and low cost. The goal of this research is to investigate the performance of these devices, and to develop a tool for the drill bit grading. Since bit grading is significantly impacted by the performance of the sensor, several basic tests were first conducted under controlled experimental conditions, *e.g.*, the room temperature and ambient lighting and measurement surface. The temporal stability of the iDevices was examined by capturing a series of datasets of a flat wall over forty-five (45) minutes, then the effect of range, reflectivity and incidence angle on data quality was tested by measuring the Spectralon targets at different situations. The performance tests found that using only the LiDAR data was not sufficient for drill bit grading. Thus, a preliminary grading system based on the fusion of LiDAR and color camera is proposed by modelling the post-drilling bit and detecting the changes.

### I. INTRODUCTION

Being used in the first step in reservoir development, drill bits play a critical role in petroleum industry. The drill bit is connected to the head of a rotary drill pipe and then transmitted downward to the well. According to the cutting mechanism, drill bits are broadly classified into two main types, rolling cutter bits and fixed cutter bits. The focus of this paper is a particular type of the fixed cutter bits, the Polycrystalline Diamond Compact (PDC) bit. This type of bit is usually made with a matrix or steel body. On the bit body, several blades are constructed with multiple cylindrical cutter inserts. The bit also contains nozzles that transmit drilling fluid during the work and includes other supporting structures.

Apart from the maximum drilling performance, another design goal that a drill bit must satisfy is a long service life. Thus, the dullness of a post-drilling bit needs to be assessed to identify the damage, to guide future bit selection, and thus to optimize the efficiency and cost of the drilling work. The industry standard for drill bit grading is published by the IADC (International Association of Drilling Contractors; Brandon *et al.*, 1992). According to the IADC grading document, the dullness of a drill bit needs to be investigated in terms

of several aspects including the primary cutting structure wear, overall gauge undersize, etc. A score or code is used to either measure or describe the damage condition in each aspect. A detailed introduction to the drill bit grading will be covered in Section III.

Up until now, most dull grading is conducted by a manual and highly subjective screening approach, which is error prone and inconsistent. Some research has been conducted to replace of this subjective procedure. Ashok *et al.* (2020) developed an image-based drill bit grading method by using the trained Convolutional Neural Networks (CNN) to identify the drill bit and image processing techniques in damage assessment. Ekergebe *et al.* (2021) also proposed an approach using the deep learning, but the data analytics were based on a video that captures the drill bit in 360°.

As a technique that can remotely gather large volumes of 3D point information of an object, LiDAR has been used in widespread applications including surveying, autonomous vehicles, robotics, videogames, among others. The last two decades have witnessed a skyrocketing development of LiDAR, and laser scanning sensors have also experienced tremendous improvements in price, size, portability, and compatibility. The variety of the sensors ranges from

terrestrial laser scanners to the mobile LiDAR backpacks, from the handheld systems to smart devices.

In 2020, Apple launched their first two devices with an embedded LiDAR scanner, the iPhone Pro 12 and the iPad Pro 2020 (hereafter denoted as the iPhone and the iPad). However, not much information has been unveiled on this custom-designed LiDAR sensor except that it improves the camera's properties and allows taking 3D measurements and point clouds of an environment up to 5 m away, at ns speeds (Apple, 2021). Limited research has been found on investigating the performance of Apple's LiDAR sensor. Among them, Luetzenburg *et al.* (2021) tested the technical capabilities of the iPhone and iPad by repeatedly taking scans for fourteen (14) rectangular boxes varied from 14 cm × 6 cm × 2 cm up to 50 cm × 30 cm × 52 cm. Comparing with the photogrammetric point cloud, both the accuracy and the precision of the iPhone's LiDAR were found to increase with the object size in all dimensions. They also reported an 11 cm cloud-to-cloud distance between the iPhone and photogrammetric solutions in modelling a coastal cliff of 130 m × 15 m × 10 m. Vogt *et al.* (2021) conducted an accuracy test of the LiDAR and TrueDepth cameras on iPad by imaging Lego bricks from 300 mm with a 65° scanning angle. However, it was found that the iPad's LiDAR camera was impractical for the capture of small objects due to the selection of the data collection application. A comparison between the iPad's LiDAR and a professional mobile laser scanner on measuring tree parameters was made by Gollob *et al.* (2021). The precision for the tree diameter estimation from iPad was found to be up to 4.5 cm, while it was 1.6 cm for the professional scanner. Research regarding the iPad's performance on the tree diameter measurement can also be found in Wang *et al.* (2021), which indicated a bias of up to 4 cm in scanning one hundred one (101) trees with diameters of 39.72 cm ±19.42 cm. Spreafico *et al.* (2021) compared iPad with the Faro Focus<sup>3D</sup> X330 in the rapid architectural mapping. Their research implied that the iPad seemed promising as a portable cost-efficient solution, while 60% of the points achieved a less than 2 cm cloud-to-cloud distance.

The aim of our work is to first evaluate the iPhone and iPad's LiDAR sensors through a comparison with the industrial HDS6100 scanner manufactured by Leica, and then to determine the potential of these devices for drill bit modelling and dull grading.

This paper is structured as follows: the background of drill bit grading problems and the literature review for the LiDAR on Apple devices are provided in this section. In Section II, the performance of LiDAR on iPhone and iPad are investigated under controlled experiment environment. This includes the sensors' temporal stability during repeated tests over time and the range precision from various distances and incidence angles for objects having different reflectivity. A drill bit scanning strategy guided by the performance test

outcome is described in Section III, followed by the post-processing of the captured model that includes the drill bit isolation and point cloud denoising. In Section IV, a preliminary drill bit grading method involving both LiDAR and 2D camera is proposed. Finally, conclusions are drawn, and some future topics are suggested in Section V.

## II. LiDAR PERFORMANCE ANALYSIS

Several tests were conducted to examine the performance of the LiDAR integrated in the 2020 iDevices. The purpose of these tests is to quantify the quality of the lidar data and to further guide the data collection, so that the drill bit can be modelled precisely.

To mitigate the errors caused by environmental or personal factors, the following data capture method was used for all the tests in this section:

1. The devices were mounted on a tripod (Figure 1a and Figure 1b), and a plastic clamp mount was used to connect both devices to the tripod.
2. All the devices were operated by one person, under a controlled room temperature of 20.1°C and a stable artificial lighting conditions.

Among the available data collection applications, SiteScape (SiteScape, 2021) was used because unlike other applications, it does not perform any extra processing such as meshing or interpolation on the raw data. For each test, another set of data was also collected with a high-accuracy, commercially-available scanner, the Leica HDS6100. With a modelled surface precision of 1 mm at 25 m, data from HDS6100 were used as a benchmark to assess the quality of data from the iDevices.

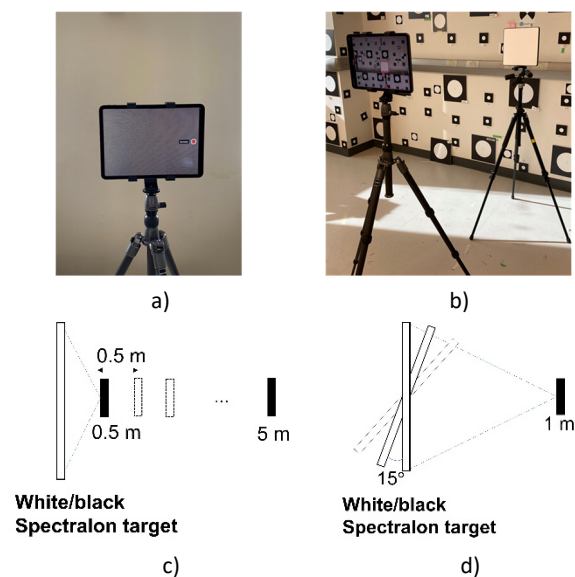


Figure 1. Experimental setup: a) Temporal stability tests; b) Range tests; c) Schematic diagram for the range, reflectivity, and incidence angle tests.

### A. Temporal stability analysis

1) *Experimental Description:* All three devices (the iPhone, the iPad, and the HDS6100) were set up to image a flat wall at 1.5 m range (Figure 1a). The wall is constructed of drywall and painted matte beige. Scans of the wall were captured every one (1) minute for iPhone/iPad, and every five (5) minutes for HDS6100 for a period of 45 minutes.

2) *Experimental results:* Each dataset was checked by performing a least-squares plane fit. The results are presented in Figure 2. The RMSE (root mean square error) is a measure of the quality of the plane fit and can indicate the level of random noise in the system. The HDS6100 RMSE, which is consistently below 1.0 mm (Figure 2a), sets the benchmark for data quality and confirms the degree of flatness of the wall. The results for the iDevices have larger RMSE values, which indicate a higher degree of noise. However, with this setup, the iDevices can also provide millimetre-level precision, which is only slightly worse than the HDS6100. No obvious evidence indicates the necessity of a warm-up period to ensure the stabilization of the LiDAR data.

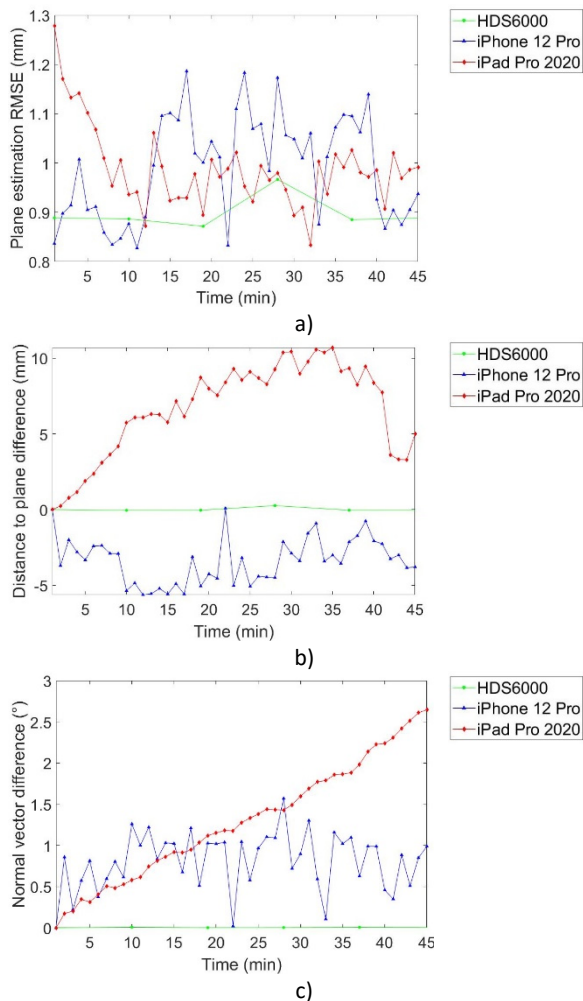


Figure 2. Temporal stability analysis: a) Plane fit precision; b) Distance to plane differences; c) Normal vector differences.

The device-to-plane orthogonal distance, and the normal vector of the plane were also estimated. When compared to the Leica HDS6100 reference, they can give an indication about the accuracy of reconstructing a planar surface in 3D. The results can identify instrument instability. The values reported in Figures 2b and 2c are the changes in orthogonal distance and normal vector orientation relative to the first data collection epoch. Values that are close to zero indicate a more stable reconstruction. The HDS6100 reference parameter values are clearly very stable, with little discernable change over time. One can see that the iDevices' results are less stable, especially the iPad. Figure 2c shows a clear trend of growing normal vector instability in the iPad. This could be from the wobble of the clamp that was caused by touching the screen for data collection. Physically touching the screen is necessary to commence the LiDAR data collection. That said, it is also possible that sensor instability contributes to the visible trend. Further investigation is required to test this hypothesis.

### B. Range, reflectivity, and incidence angle analysis

1) *Experimental Description:* Two 27 cm × 27 cm Spectralon targets were used to test the impact of range, reflectivity, and incidence angle on the LiDAR performance. The white target (Figure 1b) has 99% reflectivity and the black target has 25% reflectivity. Spectralon targets are used due to their nearly constant spectral reflectivity in the visible and NIR (near infrared) part of the spectrum and their near-Lambertian behaviour. Each the targets were imaged at normal incidence every 0.5 m from 0 m to 5 m as shown in Figure 1c. Then, the tests were repeated at 1 m but with various incidence angles to the target surface: every 15° from 0° to approximately 82° as shown in Figure 1d. Point clouds captured with each sensor were manually cropped so that only points lying within the extents of the Spectralon target were used in the plane fitting. Although the Spectralon target materials are quite different from that of drill bits, as accepted reference standards they give an indication of best-case data quality that can be expected.

2) *Experimental results:* Like the temporal stability tests, the plane fit precision was estimated to evaluate the LiDAR's range precision under different scenarios. As can be seen from Figure 3a, the target can only be measured up to a 4 m range with the iDevices. The working range for the iPhone/iPad's LiDAR is reported as up to 5 m. The Leica HDS6100 reference provides better than millimetre precision at distances above 1.5 m, which is consistent with its reported modelled surface precision of 1 mm at up to 25 m.

Poorer precision can be found at the closer distances for HDS6100, which is caused by placing the object within the reported minimum working range of the scanner, which is 1 m in this case. The range precision

for iPhone and iPad decreases with distance, and a 5 mm precision can be achieved if the object is captured within a 1.5 m range. Interestingly, the results for the black and the white targets are very similar. However, the RMSE values for the white Spectralon are larger than those from the wall test. This may be due to the higher reflectivity of the reflectance standard. The plots of plane fit residuals in Figure 3b indicate the “flatness” of the captured target. Green dots represent points that lie on the plane, while red and blue points represent points that deviate significantly from the estimated plane. These results show that the range measurements above 1.5 m do not accurately represent the shape of the flat Spectralon target.

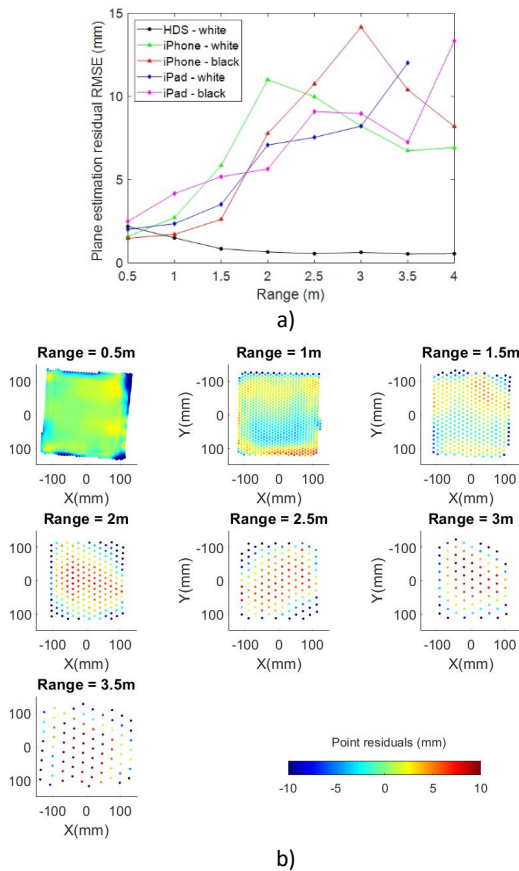


Figure 3. Impact of range on data quality: a) Plane fit precision; b) Plane fit residuals.

Plane fit precision from the incidence angle tests is shown in Figure 4. The reference data results from the HDS6100 are again of very high quality. The number and geometry of iDevice data points decreases dramatically at high incidence angles (above 45°). However, deeper investigation is required to uncover the cause of the spikes at 45°. Thus, the planes cannot be reliably estimated from the captured data. Results above this incidence angle should not be considered. Analysis of the remaining data reveals that the data captured at incidence angles below 30° exhibit compatible precision. Regarding the reflectivity, no significant differences has been observed in the data captured from the two targets.

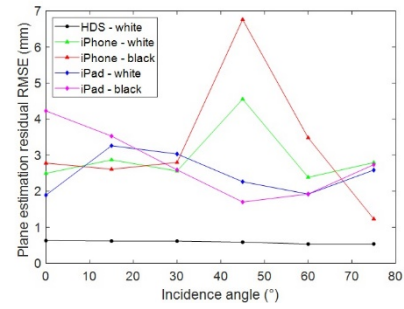


Figure 4. Plane fit precision from the incidence angle tests.

### III. THE MODELLING OF DRILL BIT

#### A. Introduction to the drill bit

As mentioned before, the fixed cutter PDC bit is the object of this research. Different PDC bits may vary in size and shape, but they have the similar primary cutting structure, which consists of several blades with PDC cutters inserted on each of them. On the PDC bit shown in Figure 5a, six (6) blades can be found, while four (4) to six (6) cutters are fixed on each blade. The dimensions of the bit and cutters are approximately 20 cm (L) × 20 cm (W) × 15 cm (H) and 1 cm (L) × 1 cm (W) × 1 cm (H), respectively.

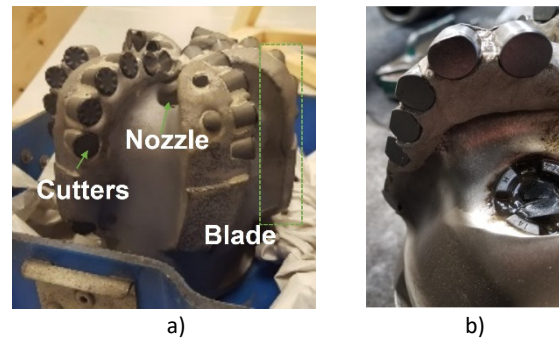


Figure 5. A PDC drill bit: a) Unused drill bit; b) Used drill bit with cutter wear.

According to the IADC regulation, the grading of a fixed cutter drill bit needs to be conducted in terms of the following four aspects:

1. Cutter wear. Figure 5b shows a PDC bit after removal from the drilling hole. Different levels of cutter wear can be observed. According to IADC, the cutter wear should be graded following the scale illustrated in Figure 6. By considering the cutter surface as a circle, it scores the cutter wear by estimating the worn amount of the circle. According to the grading scale between 0-8 listed in Table 1, the more the wear is, the higher the grade would be.
2. Primary dull characteristic and location. This is the description of the primary damage on the bit, e.g., lost cutters or worn cutters. The corresponding location is also recorded.
3. Gauge undersize. This test is conducted by placing a gauge ring over the largest diameter of

a post-drill bit and measuring the gap in between.

- Remarks. This includes the second most notable condition and the possible reasons for all the damages.



Figure 6. Schematic diagram for the cutter wear grading scale (BESTEBIT, 2021).

Table 1. Cutter wear grading scale

Grade	0	1	2	3	4	5	6	7	8
Wear	$\frac{0}{8}$	$\frac{1}{8}$	$\frac{2}{8}$	$\frac{3}{8}$	$\frac{4}{8}$	$\frac{5}{8}$	$\frac{6}{8}$	$\frac{7}{8}$	$\frac{8}{8}$

Following this IADC standards, this paper focuses on the grading of the primary cutting structure, which is the wear of the cutters. The overall goal is to replace the current subjective grading procedure with a more accurate and consistent method using an imaging sensor such as one of the iDevices.

### B. Suggested drill bit modelling procedure

According to the performance tests, the LiDAR from the iPhone/iPad has been found to perform best when the object is scanned within 1.5 m and with an incidence angle that is smaller than 30°. The SiteScape app integrates the IMU (Inertial Measurement Unit) data for real time registration while moving the device, thus provides a registered 3D model of the object.

Based on the above conditions and several test scans, the authors found that instead of scanning the entire drill bit (Figure 7a), which leads to many mixed-pixel errors, higher data quality can be achieved if the drill bit is scanned blade by blade (Figure 7b). As the cutters are distributed on the top half of the drill bit (Figure 5), it is recommended to start scanning from the top of each blade and gently move the devices to the bottom. By doing so, the registraion errors can be mitigated for the the best results.

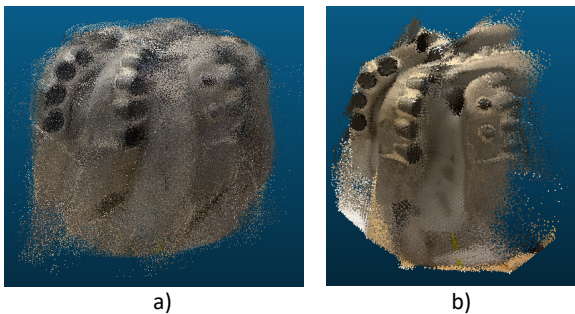


Figure 7. Drill bit and the test scans: a) Full drill bit scan; b) Single blade scan.

### C. Drill bit model post processing

The scanned model needs to be processed before being analyzed. This post-processing mainly includes the following two steps.

1) *Drill bit model segmentation*: Figure 8a shows a raw point cloud from a larger standoff distance and includes unwanted measurements in the background. Thus, the drill bit needs to be identified in the point cloud. Assuming that the drill bit was within a 1.5 m range of the devices, the drill bit isolation was realized by firstly removing points at longer ranges. Then, the remaining point cloud was segmented based on the colour information to separate the drill bit from other objects. Lastly, the segmented point cloud was extracted by connected components analysis. The largest cluster was saved as the identified drill bit model (Figure 8b). Note that the bit shown in Figure 8 has no PDC cutter bits. All bits were removed and replaced by with artificial bits made from wooden dowels to allow simulation different wear conditions.

2) *Point cloud denoising*: The point cloud denoising is required due the existence of outliers, many of which are mixed pixels. This was realized by the statistical outlier removal method. The idea of this method is that it will first calculate the average distance from each point to its fifty (50) nearest neighbours, which are found by the k-d tree method. Then, a distance threshold will be defined as the mean plus deviation of all these average distances. Points whose average neighbour distance are above this threshold will be considered as outliers and will be removed from the point cloud. The denoised drill bit model is shown in Figure 8c.

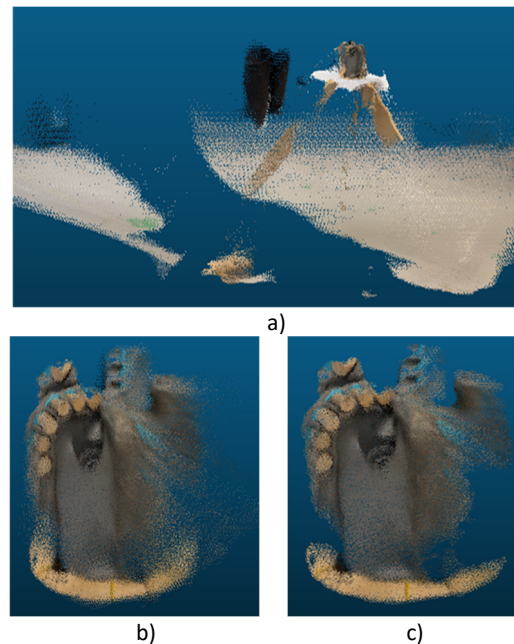


Figure 8. Point cloud post processing: a) A sample scan from iPhone; b) Isolated drill bit scan; c) Denoised drill bit model.

#### IV. DRILL BIT GRADING STRATEGY

The initial plan of this research was to test the performance of the LiDAR sensor on the new iDevices, and to determine the potential of using only one sensor to fulfill the goal of drill bit grading. However, based on our experimental findings, the LiDAR on these smart devices only captured the general geometry of the drill bit and was not capable allowing identification of the finer details like the wear of the cutters. This was largely due to mixed pixel data artefacts and registration errors from the IMU data. Thus, a drill bit grading technique presented in this paper also utilizes the iPhone/iPad colour camera images. The LiDAR data are used to provide 3D information that can improve the 2D-only solutions. One picture needs to be taken for each blade from a proper perspective, after which the following steps are performed to grade the cutter wears.

##### A. Image ortho-rectification

Ortho-rectification is the process of synthetically generating an orthophoto, which is an image of the object space in orthogonal parallel projection. By doing so, the distortions due to image tilt and relief displacement can be corrected.

Image ortho-rectification is essentially the process of transforming a central-perspective digital image by the analytical functions  $f_x$  and  $f_y$  in Equation 1, and assigning the color in the corresponding pixels (Novak, 1992). This can be done by either direct or indirect method as described by Equation 1.

$$x = f_x(x', y'); y = f_y(x', y') \quad (1)$$

where direct transformation means if:

$$\begin{aligned} x, y &= \text{pixels of the orthophoto} \\ x', y' &= \text{pixels of the original image} \end{aligned}$$

and indirect transformation means if:

$$\begin{aligned} x, y &= \text{pixels of the original image} \\ x', y' &= \text{pixels of the orthophoto} \end{aligned}$$

Since the direct method transforms the pixels on the original image to the orthophoto, it may happen that some pixels on the orthophoto have no correspondences on the original image and no color value can be assigned. Thus, the indirect method is more commonly used.

Among all the ways to determine the analytical function, a method is called projective transformation. This method is used if the object scene can be modelled as a plane, then the problem is reduced to mapping the pixels of the orthophoto plane into the original image (Figure 9).

The projective transformation models the geometric relationship between two planes. It is defined by eight (8) parameters from  $a_1$  to  $c_2$  in Equation 2. It can be solved by using four (4) control points lying in a plane in

the object space and their corresponding pixels in the original image.

$$\begin{aligned} x &= \frac{a_1x' + a_2y' + a_3}{c_1x' + c_2y' + 1} = f_x(x', y') \\ y &= \frac{b_1x' + b_2y' + b_3}{c_1x' + c_2y' + 1} = f_y(x', y') \end{aligned} \quad (2)$$

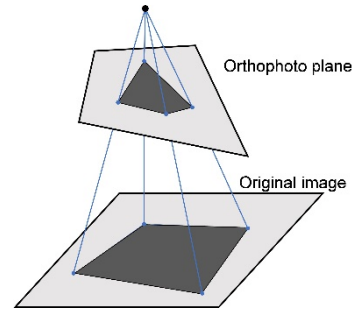


Figure 9. The projective transformation between the orthophoto plane and the original image. Four (4) points are required to solve the transformation function.

An image for the drill bit in Figure 10a was taken at a perspective that best captured the cutters on an individual blade. One can see that the circular shaped cutter surfaces were elongated to ellipses to different extents. As the cutter surfaces lie roughly on a plane in object space, the ortho-rectification can be done by using the projective transformation method. The 3D coordinates of the cutter centers were extracted from the previously generated LiDAR model, and then were transformed into the 2D pixel coordinates in the orthophoto. When combined with the coordinates in the distorted image, the transformation function parameters were estimated. By applying the transformation parameters to every pixel, the ortho-rectified image was generated. As shown in Figure 10b, the cutters have been mostly corrected to their true shapes, which are circles in this case. Some residual deformation to the circles still exists due to the deviation of the cutter surfaces from the hypothesized planar shape.

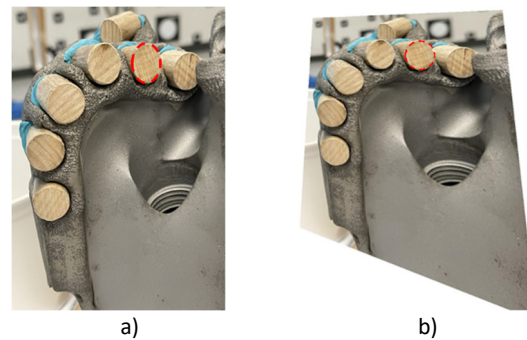


Figure 10. Image ortho-rectification: a) The original image; b) Rectified orthophoto.

**B. Circle detection and isolation**

The cutters were replaced by the worn ones for the following grading procedure. They were identified in the rectified image by considering them as individual circles. Each circle was detected by the circular Hough transform. Six (6) cutters were detected on the blade in Figure 11a. Even though cutter 5 is partially occluded, its circumference can still be partially extracted and the wear measurement made. With the estimated centers and radii, each cutter can be cropped out from the image for the following grading procedures. The isolated cutter images are shown in Figure 11b.

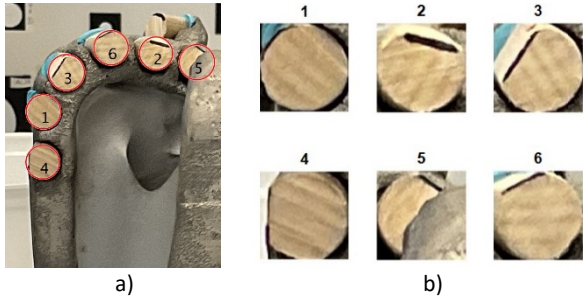


Figure 11. Circle detection. a) Detected circles; b) Isolated cutter images.

**C. Cutter wear grading**

The key point of the cutter wear grading is to recognize the edge that represents the location of wear. When using the artificial wooden cutter bits, accurate detection of the edge requires the aid of the edge marks as shown in Figure 11b. The edges were marked with black indelible marker to highlight the wear edges on the cutters so that they can be more easily detected in the image. The process for cutter wear grading can be summarized as the following three steps.

1) *Detection of the edge*: Pixels with a certain colour, i.e., black in this case, were detected as the potential edge points. Shadows were excluded by removing the points that are overlain with the detected circles. Next, the largest connected component was labelled as the edge of the cutter wear, as can be seen in Figure 12.

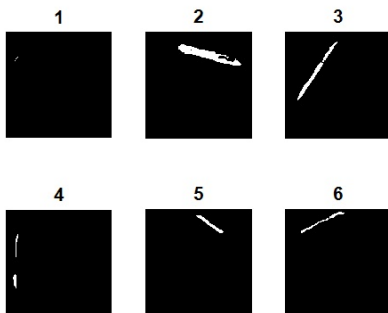


Figure 12. The detected edge of the cutter wear.

2) *Edge “recovery”*: By using the points found in the last step, lines that represented each edge were estimated. Two intersection points between the line and the circle, marked as the blue and red triangles in Figure 13, were found for each edge to indicate the location of the cutter wear.

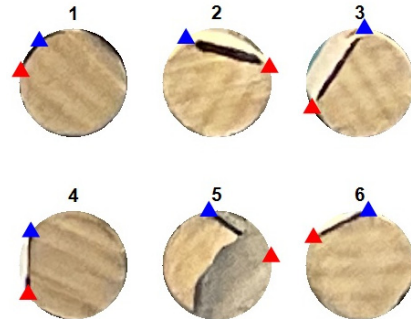


Figure 13. Edge “recovery” results.

3) *Wear estimation*: Following the grading strategy in Figure 6, the amount missing from each circle, which indicates the amount of cutter wear, is estimated. Table 2 lists the estimated wear of each cutter in Figure 13, and their grades determined based on Table 1. The value between two grades was rounded to the closer one.

Table 2. The estimated wear and grades.

ID	1	2	3	4	5	6
Wear	$\frac{0}{8}$	$\frac{2}{8}$	$\frac{2}{8}$	$\frac{1}{8}$	$\frac{1}{8}$	$\frac{1}{8}$
Grade	0	2	2	1	1	1

**V. CONCLUSION**

The current widely-used approach for grading a drilling bit is by visual inspection, which can be highly-subjective and inaccurate. Thus, a consistent and ideally automated solution is expected. The aim of this work was to develop a new remote sensing approach using the new Apple iDevice LiDAR sensors, which have made 3D point clouds accessible with consumer-level devices.

In this paper, several performance tests were first conducted on the new sensor. Results from the temporal stability test reveal that the iDevices provide millimetre-level precision in plane modelling at a range of 1 m, which is only slightly worse than the reference data results from the Leica HDS6100 scanner. It has also been found that the performance of the iDevice LiDAR is more greatly impacted by the range than by the incidence angle and the object’s reflectivity, which suggests an ideal scanning configuration of within a 1.5 m range and a 30° scanning angle.

According to the performance tests, it was found that more research needed to be done to realize the drill bit grading by only using the LiDAR. Thus, colour camera imagery was introduced in the proposed method. 3D information from LiDAR was used to help reduce the



image distortion and to improve the results from image processing. Experiment results on laboratory data show that drill bit grading is possible using the proposed new image based method.

Future work will be to pursue the LiDAR-only solution. As Apple doesn't publish the sensor's specifications, more comprehensive research needs to be implemented. It may include an application development so we can have direct access to the sensor and data. After that, more tests could be done regarding, for example, the scanning resolution, the measurement accuracy, the impact of placement angle of the device, the LiDAR sensor calibration. If the LiDAR data is sufficient for drill bit grading, new methodologies need to be proposed including the data registration, cutter segmentation and modelling. If not, the generated bit model can still be used to improve the current ortho-rectification results. Last but not the least, machine learning can be applied on the improved orthophoto to achieve more accurate image-based solution.

## VI. ACKNOWLEDGEMENTS

This project was funded by the Natural Sciences and Engineering Research Council (NSERC) of Canada (ALLRP 561422 – 20 and RGPIN-2018-03775).

## References

- Apple Inc. (2021). Apple Unveils New iPad Pro with Breakthrough LiDAR Scanner and Brings Trackpad Support to iPadOS. <https://www.apple.com/ca/newsroom/2020/03/apple-unveils-new-ipad-pro-with-lidar-scanner-and-trackpad-support-in-ipados/>. Retrieve date 22-Nov-2021.
- Ashok, P., P. Vashisht, H. Kong, Y. Witt-Doerring, J. Chu, Z. Yan, E. van Oort, and M. Behounek (2020). Drill Bit Damage Assessment Using Image Analysis and Deep Learning as an Alternative to Traditional IADC Dull Grading. In: *SPE Annual Technical Conference and Exhibition*. OnePetro.
- BESTEBIT (2021). IADC Dull Grading for PDC Drill Bits. <https://www.bestebit.com/wp-content/uploads/2016/12/PDC-Dull-Grading.pdf>. Retrieve date 22-Nov-2021.
- Brandon, B.D., J. Cerkovnik, E. Koskie, B. B. Bayoud, F. Colston, R. I. Clayton, M. E. Anderson, K. T. Hollister, J. Senger, and R. Niemi (1992). First Revision to the IADC Fixed Cutter Dull Grading System. In: *IADC/SPE Drilling Conference*.
- Ekeregbe, M. P., M. S. Khalaf, and R. Samuel (2021). Dull Bit Grading Using Video Intelligence. In: *SPE Annual Technical Conference and Exhibition*. OnePetro.
- Gollob, C., T. Ritter, R. Kraßnitzer, A. Tockner, and A. Nothdurft (2021). Measurement of Forest Inventory Parameters with Apple iPad Pro and Integrated LiDAR Technology. *Remote Sensing*, Vol. 13, No.16, pp. 3129.
- Luetzenburg, G., A. Kroon, and AA. Bjørk (2021). Evaluation of the Apple iPhone 12 Pro LiDAR for an Application in Geosciences. *Scientific reports*, Vol. 11, No. 1, pp. 1-9.
- Novak, K. (1992). Rectification of Digital Imagery. *Photogrammetric Engineering and Remote Sensing*, Vol. 58, pp. 339-339.
- SiteScape (2021). SiteScape Homepage. <https://sitescape-test.webflow.io/>. Retrieve date 15-Nov-2021.
- Spreafico, A., F. Chiabrando, L. T. Losè, and F. G. Tonolo (2021). The Ipad Pro Built-In LiDAR Sensor: 3d Rapid Mapping Tests and Quality Assessment. In: *The International Archives of Photogrammetry, Remote Sensing and Spatial Information Sciences*, Vol. 43, pp. 63-69.
- Vogt, M., A. Rips, and C. Emmelmann (2021). Comparison of iPad Pro's LiDAR and TrueDepth Capabilities with an Industrial 3D Scanning Solution. *Technologies*, Vol. 9, No. 2, pp. 25.
- Wang, X., A. Singh, Y. Pervysheva, K. E. Lamatungga, V. Murtinová, M. Mukarram, Q. Zhu, K. Song, P. Surový, and M. Mokroš. (2021). Evaluation of Ipad Pro 2020 LiDAR for Estimating Tree Diameters in Urban Forest. In: *ISPRS Annals of the Photogrammetry, Remote Sensing and Spatial Information Sciences*, Vol. 8, pp. 105-110.

## Two-epoch TLS deformation analysis of a double curved wooden structure using approximating B-spline surfaces and fully-populated synthetic covariance matrices

Gabriel Kerekes<sup>1</sup>, Jakob Raschhofer<sup>2</sup>, Corinna Harmening<sup>2</sup>, Hans Neuner<sup>2</sup>, Volker Schwieger<sup>1</sup>

<sup>1</sup> Institute of Engineering Geodesy, University of Stuttgart, Geschwister-Scholl-Str. 24D, 70174 Stuttgart, Germany, ([gabriel.kerekes@iigs.uni-stuttgart.de](mailto:gabriel.kerekes@iigs.uni-stuttgart.de); [volker.schwieger@iigs.uni-stuttgart.de](mailto:volker.schwieger@iigs.uni-stuttgart.de))

<sup>2</sup> Department of Geodesy and Geoinformation, TU Wien, Wiedner Hauptstr. 8/E120, 1040 Vienna, Austria, ([jakob.raschhofer@geo.tuwien.ac.at](mailto:jakob.raschhofer@geo.tuwien.ac.at); [corinna.harmening@geo.tuwien.ac.at](mailto:corinna.harmening@geo.tuwien.ac.at); [hans.neuner@geo.tuwien.ac.at](mailto:hans.neuner@geo.tuwien.ac.at))

**Key words:** *B-spline surfaces; deformation analysis; hypothesis tests; laser scanning; point clouds; synthetic variance-covariance matrix*

### ABSTRACT

This contribution presents a B-spline-based approach of area-wise deformation analysis applied on elements of a double curved wooden tower. The monitored object is the Urbach Tower with a height of 14 m. Terrestrial laser scans from two epochs acquired under real-world conditions are used for approximating two jointly parametrized B-spline surfaces of the tower's outer shell. The stochastic model of the observations used within the surface approximation is based on elementary error theory and is defined by a synthetic variance-covariance matrix (SVCM). In addition to previous work on this topic, the object's dimension is extended from a few dm to a few m and the measurement distance ranges from 20 to 60 m. Moreover, environment specific error sources are addressed in the SVCM, revealing the effect of the object's dimension as well as of additional elementary errors on the estimated B-spline surfaces and the subsequent deformation analysis. Based on constructed points pairs using a grid of surface parameters, rigid body movements of the object under investigation are estimated while at the same time distorted regions of the wooden tower are detected. All results of the deformation analysis are statistically verified using hypothesis tests based on the elementary error model propagated through the processing algorithms of surface estimation and deformation analysis. The results demonstrate that during the modelling and deformation analysis, the measurement noise is reduced and therefore distorted regions are detectable in a statistically correct way.

### I. INTRODUCTION

Area-wise deformation analysis has become a trend in the past 20 years, yet there is no general accepted workflow or method for conducting it (*cf.* Neuner *et al.*, 2016; Wunderlich *et al.*, 2016). Point clouds of natural or artificial object acquired by Terrestrial Laser Scanning (TLS) are in most cases simply compared to one another (Holst *et al.*, 2017). Popular open-source software like Cloud Compare (Girardeau-Montaut, 2019) offer tools for quick geometrical comparisons. However, typically in geodetic deformation analysis (Heunecke and Welsch, 2000) the estimated geometric changes, have to be assessed by statistical tests.

The current contribution presents an approach to area-wise deformation analysis for two epochs based on estimated B-Spline surfaces. The stochastic model of the TLS observations is defined by a synthetic variance-covariance matrix (SVCM) which contains the instrument related errors and environment related errors. The workflow is applied to a part of a double curved 14 m high wooden structure, called the Urbach Tower. This approach continues the work of Raschhofer *et al.* (2021) by extending the analysis to object dimension of several meters as well as to measurement

distances of tenth of meters. This implies including the atmospheric conditions in the SVCM, applying a different instrumental error model and using a different source of reference data. Additionally, this paper also focuses on deformation analysis. In contrast to other publications on similar topics (*cf.* Paffenholz and Wujanz, 2019; Kermarrec *et al.*, 2019), point pairs of the estimated B-splines in two epochs are constructed and rigid body movements are estimated while simultaneously distorted regions are detected.

In Section II, the new methods are presented and the theoretical background is briefly given. The experimental setup and deformation analysis are shown in Section III, while Section IV concludes this contribution.

### II. METHODS - DEFORMATION ANALYSIS

#### A. Estimation of rigid body movements and simultaneous localisation of non-distorted regions using sampled approximating B-spline surfaces

In this contribution the approach of Harmening *et al.*, (2021) is followed, which is based on B-spline models of epoch-wise acquired point clouds. Corresponding points in different epochs are constructed using

identical surface parameters on the different, epoch-related B-spline surface. These corresponding points, resulting from the discretizations of the B-spline surfaces, are used to robustly estimate rigid body movements and to initially define non-distorted regions of the object. Finally, the non-distorted regions are extended and their stability as well as their extents are statistically confirmed. The individual steps of this algorithm are explained in the following sections.

1) *Estimation of B-spline surfaces for deformation analysis*: A B-spline surface is usually defined by (Piegl and Tiller, 1997; Bureick *et al.*, 2016) (Eq. 1):

$$\hat{\mathbf{S}}(u, v) = \sum_{i=0}^n \sum_{j=0}^m N_{i,p}(u) N_{j,q}(v) \mathbf{P}_{i,j} \quad (1)$$

A three-dimensional surface point  $\hat{\mathbf{S}}(u, v)$  in Cartesian coordinates is expressed as the weighted average of the  $(n + 1) \times (m + 1)$  control points  $\mathbf{P}_{i,j}$ . The corresponding weights are the functional values of the B-spline basis functions of degree  $p$  and  $q$   $N_{i,p}(u)$  and  $N_{j,q}(v)$  which can be recursively computed (*cf.* Cox, 1972; De Boor, 1972). The B-spline's domain is split into knot spans by two knot vectors  $\mathbf{U} = [u_0, \dots, u_r]$  and  $\mathbf{V} = [v_0, \dots, v_s]$ , which are defined in direction of the surface parameters.

Before estimating the control points of the best-fitting B-spline surface, the measurements have to be located on the surface to be estimated. This is achieved by allocating them convenient surface parameters  $u$  and  $v$  (*cf.* Harmening and Neuner, 2015). Using these surface parameters, the knot vectors can also be estimated (Piegl and Tiller, 1997; Schmitt and Neuner, 2015; Bureick, 2020).

The choice of the appropriate number of control points (Harmening and Neuner, 2017) is usually specified a priori and cubic B-splines ( $p = q = 3$ ) are generally accepted.

When B-spline surfaces are used as a basis for deformation analysis, a joint parametrization is essential (*cf.* Harmening and Neuner, 2017). The projection of the measured point clouds onto a joint base surface and the use of its knot vectors make this approximately possible.

2) *Constructing point pairs on approximating B-spline surfaces*: By means of a regular grid of surface parameters, points  $\hat{\mathbf{S}}(u, v)$  (*cf.* Equation 1) are calculated on the B-spline surfaces estimated in each epoch.

These calculated points are treated as corresponding three-dimensional surface points. The VCM of the estimated control points is propagated for the constructed surface points.

In order to achieve a detailed statement regarding the position and extent of the distortions, the number

of sampled surface points  $\mu$  should considerably exceed the number of control points (Hobmaier, 2020). This, on the other hand, leads to singularities in the corresponding variance covariance matrix. The occurring singularities are handled using the pseudoinverse.

3) *Identification of stable regions for the determination of approximate values of the elements of rigid body movements*: Based on point pairs between epochs, the elements of the rigid body movements are determined, at first approximately. The required parameters of the rigid body movement are estimated by means of a three-dimensional similarity transformation (Heunecke *et al.*, 2013).

Unfortunately, it cannot be assumed that the object under investigation is subjected only to rigid body movements. Additional object distortions bias the estimated transformation parameters (Harmening *et al.*, 2021). Thus, the estimation of rigid body movements needs to be relay only on corresponding point pairs on the B-spline surfaces that are not subjected to distortions.

The iterative random sample consensus (RANSAC)-algorithm (Fischler and Bolles, 1981) is a suitable methodological tool enabling the identification of similarity transformation.

The basic principle of RANSAC is to firstly select randomly the minimal possible subset from a set of the maximum available corresponding points, which uniquely determines the model's parameters.

All corresponding surface points from the epoch 0 are transformed using the estimated parameters of the preliminary model. The Euclidean distance  $d_k$  ( $k = 0, \dots, \mu - 1$ ) between each transformed point belonging to epoch 0 and its corresponding point in epoch 1 provides the measure for including the corresponding points into the consensus set of model-conforming points. The distance is compared to the error tolerance. The latter is assessed individually using the  $\tau$ -fold standard deviations of the calculated distances  $\sigma_{k,d}$ . When (Eq. 2)

$$d_k \leq \tau \sigma_{d,k} \quad (2)$$

is fulfilled, the corresponding point pair is assigned to the consensus set. If the number of points satisfying Equation 2 is below a certain minimum number, another RANSAC-iteration is performed. Caspary, (2013) and Harmening *et al.* (2021) provide approaches to select freely definable parameters (factor  $\tau$ , maximum number of iterations, minimum number of model-compliant points  $n_{min}$ ) of this algorithm.

Provided that the amount of model-compliant points is larger than  $n_{min}$ , the model-compliant points are used to estimate the parameters of the similarity transformation in an over-determined extended model.

4) *Statistically Based Localization of Distortions:* Usually, the consensus set does not cover the entire non-distorted region of the B-spline surface. Therefore, the consensus set is extended using hypotheses tests of individual point pairs (starting with the point pair that has the smallest distance), which are not assigned to the consensus set (Harmening *et al.*, 2021). Based on this extension, the parameters of the rigid body movement are re-estimated. A final global test is used to check the consistency of non-distorted point pairs (Harmening *et al.*, 2021).

### III. CASE STUDY URBACH TOWER

#### A. Experimental set-up

The monitored object is a unique curved wooden 14 m tall structure, called the Urbach Tower (Figure 1). It was built in 2018 using new self-shaping processes for the curved wooden components and constitutes the first structure worldwide made from self-shaped building-scale components (ICD, 2019). Due to this, it is considered a challenging object for area-wise deformation analysis.

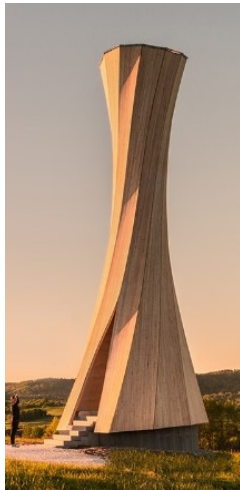


Figure 1. The Urbach Tower (ICD, 2019).

The tower was scanned in two epochs with a Riegl VZ2000 scanner from three different station points. The scanning positions were chosen to capture the front part of the tower from a single station point and were located at distances of 20 m, 40 m and 60 m from the tower. Additionally, the weather parameters air temperature and air pressure were recorded for both campaigns in the area of interest. This was done with a handheld precision Thermo-Barometer, Greisinger GTD1100 approximately at the instrument height (*e.g.* 1.8 m above ground). Figure 2 gives an overview of the on-site situation. In order to create a common geodetic datum for both epochs, fixed points were marked in the spring of 2020 before the actual measurement campaigns.

The tower is in the middle of a field and there are not many choices for stable areas with favourable geometric distribution of the network points.

Nevertheless, five network points were initially marked around the tower and the planned TLS station points. Three points were marked with concrete dowels in the tower base and the nearby bench foundation, one with wooden dowel in a wooden electricity pole and the other with an 80 cm aluminium peg near the access road. All points assure the same mechanical centre between different TLS target types and reflectors.

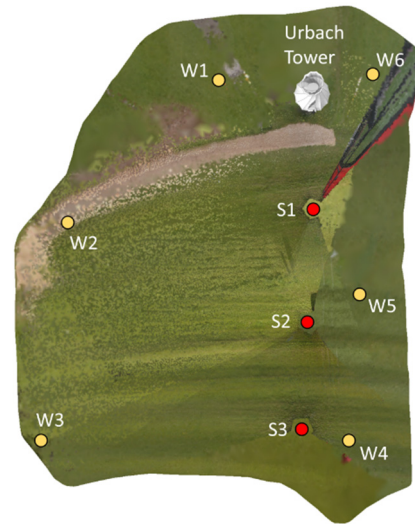


Figure 2. Overview of TLS station points ( $S_x$ ) and weather points ( $W_x$ ) relative to the Urbach tower.

In both epochs all network points were measured with a 0.5" Leica TS30 Total Station (TS) to verify whether the reference points are stable. After a deformation analysis (congruence test), no significant differences ( $\alpha=5\%$ ) were identified. Therefore, the coordinates of the reference network can be used for the TLS point cloud transformation without inducing errors due to different datums.

In each epoch, additional to the mentioned TLS scans, reference scans with a high precision close range scanner were made for several wooden plates. The Surphaser 100 HSX-SR was used due to its very low range noise <1 mm up to 4 m (Basis Software Inc., 2021). With a recommended working range of 1-7 m, the common points used for georeferencing are the points placed near the tower. The working range was also the restriction for the analysed part of the tower, as later explained (*cf.* Section III).

#### B. Stochastic model

The stochastic model used to describe the TLS observations' uncertainty is established based on the elementary error theory. Specifically, the model is represented by a synthetic variance-covariance matrix (SVCV) constructed as explained in Kauker and Schwieger (2017), Kerekes and Schwieger (2020) and Raschhofer *et al.* (2021). Without resuming the theory of defining fully populated VCM  $\Sigma_{ll}^{(\lambda\theta R)}$  in observation space or the equivalent  $\Sigma_{ll}^{(xyz)}$  in coordinate space, only

the relevant different aspects to the aforementioned publications are highlighted.

As before, errors are grouped in three classes according to their correlation nature: non-correlating, functional correlating and stochastic correlating errors. All three classes are represented as follows:

1. Non-correlating errors: angle noise ( $\lambda$  –horizontal and  $\theta$  - vertical) and range noise;
2. Functional correlating errors: calibration parameters of the hybrid TLS (a to c in Table 1);
3. Stochastic correlating errors: air temperature; air pressure and temperature gradient.

Starting values for the first two groups of non-correlating and functional correlating errors (Table 1) have been taken from the TLS technical specifications (cf. Riegl Laser Measurement Systems GmbH, 2021) and from available literature.

Table 1. Parameters of non-correlating and functional correlating errors (Riegl)

Type of error	Parameter	Standard deviation
Non-correlating errors	Range noise [mm]	5
	Angle noise [mgon]	$\lambda = 0.55$ $\theta = 1.66$
Functional correlating errors	a0 [mm]	0.34
	a1 [ppm]	40
	b4 [mgon]	3.18
	b6 [mgon]	1.91
	c0 [mgon]	1.08
	c1 [mgon]	1.85
	c4 [mgon]	0.64

An explanation of the parameters and their role in the functional mode is given in Kerekes and Schwieger (2020).

As for the stochastic correlating errors, a slightly improved approach is used (cf. Kerekes and Schwieger 2020). The covariances of the environmental elementary errors are not determined based on general correlation coefficients. In Kerekes and Schwieger (2020) section 3, this was done between the lowest and highest observation line of the spatial Vertical Gradient Temperature (VGT) model. Now it is possible to have specific values for covariances of air temperature, air pressure and vertical temperature gradient among observations between scanner and the scanned object. A prerequisite is a digital terrain model (DTM) and measurement for some of the meteorological parameters in the area (cf. Figure 2). An example for one epoch is given in Figure 3. The different values of air temperature obtained for the interpolated points and DTM are presented in different colours according to the temperature scale. As observed, within this small areal temperature differences are within less than 3°C. It is also mentioned that these values are not used to correct the observations, since this is not of interest in this contribution.

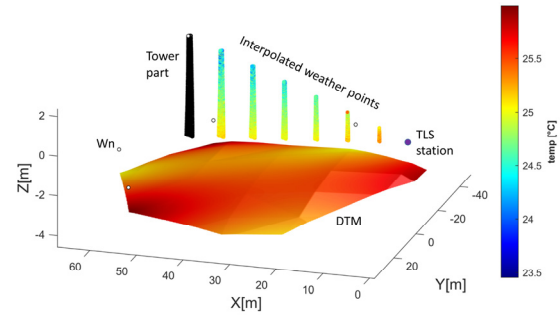


Figure 3. Example of how variance and covariance are determined for each observation based on environmental errors and interpolated points.

This resembles measurement set-ups used in permanent laser scanning for monitoring (Kuschnerus *et al.*, 2021) that are recently receiving increased importance.

Another important elementary error group constitutes the object surface properties, but this is not treated in this contribution.

### C. Constructing Corresponding Surface Points

The lower part of the tower façade with a height of 5m was used for the analysis, due to the good spatial precision ( $0.35 \text{ mm} \leq \sigma_{xyz} \leq 0.70 \text{ mm}$ ; Helmert's point error) assumed in this region using the reference Surphaser laser scanner. The resulting point cloud of the first epoch and subsequently the estimated B-spline surface using the identity matrix as stochastic model serve as reference surface. Since this surface is only used as reference surface and no functional correlating errors are known for the Surphaser scanner, the identity matrix is used here. As seen in Raschhofer *et al.* (2021), the differences of estimated control points position for an estimated surface at close range (section 4.1. in aforementioned publication) using identity, diagonal or fully populated matrix as a stochastic model are negligible. Since no stochastic information is needed for the projection, the identity matrix is chosen for simplicity.

To ensure a joint B-spline parameterization, the Riegl point clouds of both epochs are projected onto this reference surface to obtain surface parameters. Furthermore, the number of control points and the knot vectors are likewise used for the estimation.

As for the stochastic model, a SVCM is introduced into the estimation. For each point cloud, the SVCM is adjusted by varying the standard deviations of the non-correlating errors, as performed in Raschhofer *et al.*, (2021), so that the null hypothesis of the global test of the individual B-spline surface estimation cannot be rejected. Table 2 shows the values obtained for the standard deviations of the non-correlating errors.

The applied noise standard deviations differ between epochs due to the missing consideration of object surface properties in the SVCM and of the inter-epochal correlations. The tower outer appearance visibility changed between the epochs, varying from birch

natural light yellow colour to light grey. The other elementary errors types in the SVCM (instrumental and environmental group) have not been modified.

Table 2. Explicit standard deviations for non-correlating errors (Riegl scans E0: epoch 0; E1: epoch 1; S: station points)

Parameter	S1 E0	S1 E1	S2 E0	S2 E1	S3 E0	S3 E1
Range noise [mm]	5	5	5	5	5	5
Angle noise ( $\lambda$ ) [mgon]	5	6.1	2.5	2.8	2.2	2.7
Angle noise ( $\theta$ ) [mgon]	15	18.3	7.5	8.7	6.5	8.3

The epoch-wise estimated approximating B-spline surfaces are discretised as described in Section II A 2. Table 3 shows the different levels of discretisation chosen, where  $n_{u,v}$  indicates the number of points in the respective parameter direction.

Table 3. Overview of the discretization

Discretisation	$n_u * n_v$
V1	20 * 15
V2	30 * 20

The boundary regions of the estimated surfaces are estimated less accurately than the inner regions (Hobmaier, 2020). To avoid distortions in the deformation analysis caused by boundary points, the surfaces are discretised with surface parameters ( $u, v$ ) in the interval  $[0.05, 0.95]$ . In the inner regions of the surfaces, the discretised points obtain a homogeneous level of accuracy.

#### D. Detecting Non-Distorted and Distorted Regions

The result of the RANSAC method described in Section II A strongly depends on the freely chosen parameters, especially the parameters  $\tau$  and the minimum number of model-compliant points  $n_{min}$  (Harmening and Neuner, 2016). The influence of these parameters on the number of iterations  $\#i$  and the number of point pairs in the consensus set  $n_{cs}$  is shown in Table 4 for the respective station point and discretization. The aim of trying different combinations of  $\tau$  and  $n_{min}$  is to obtain a relatively high amount of points in  $n_{cs}$ . If  $n_{min}$  is chosen to high, the maximum amount of iterations exceeds. It is mentioned that only the parameters of the respective best results are given.

Table 4. Influence of selected RANSAC parameters

Discretization	$\tau$	$n_{min}$	$\#i$	$n_{cs}$
S1 - V1	2	22	2	184
S2 - V1	1	22	12	154
S3 - V1	2	22	647	77
S1 - V2	2	22	4	224
S2 - V2	2	22	41	167
S3 - V2	3	32	836	144

Values of  $\tau > 3$  were not considered with regard to the  $3\sigma$ -rule (Heuneke *et al.*, 2013).

Using data set S3-V1, a large number of iterations  $\#i$  is needed to find a comparatively small amount of point pairs in the consensus set  $n_{cs}$ . Although the choice of  $\tau = 3$  increases the error threshold (*cf.* Equation 2), similar behaviour is also observed for the data set S3-V2.

The focus in this contribution is on detecting distorted regions, since no large rigid-body movement of the tower is expected. The parameters of the similarity transformation are mainly intended to eliminate the residual misclosures from the georeferencing and, thus, are not discussed further.

An interpretation of the correctness of the following results presented is discussed in Section IV based on the reference result obtained with the Surphaser.

Using data set S1-V1, the results of the deformation analysis are shown in Figure 4. For the circled points, the null hypothesis (Eq. 3)

$$H_0: E(\hat{\mathbf{v}}) = 0 \quad (3)$$

stating that a certain point belongs to the consensus set, has to be rejected. It is therefore examined whether the estimated gross errors  $\hat{\mathbf{v}}$  differ significantly from the nominal value  $\hat{\mathbf{v}} = 0$ . Thus, these points are assumed to lie in the distorted region.

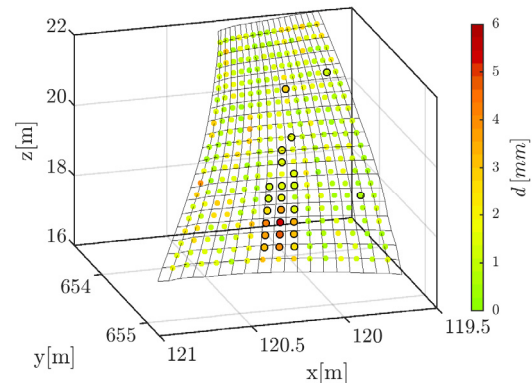


Figure 4. Distorted regions using data set S1-V1.

The result (see Figure 5) of the deformation analysis of data set S2-V1 supports the result of S1-V1.

The regions with deformations of 6 mm (see bottom centre) are detected from the different data sets. The occurrence of type I errors cannot be completely avoided, although a high confidence probability of  $1 - \alpha$  ( $\alpha = 3\%$ ) is chosen. Since type I errors usually do not occur in groups, most of them can be identified by investigating their direct neighbourhood. If their entire neighbourhood is located in the non-distorted region, it can be assumed that a type I error exists (Harmening *et al.*, 2021).

Figure 6 shows results of the deformation analysis with discretization V2 of the station points S2. A comparable result is also achieved using the S1-V2 data set.

The regions with large deformation agree with the results using data sets V1. However, there is a

noticeable increase of distorted regions using a denser discretization. In Figure 6, points with larger distances than others, which are classified to the distorted regions, are obviously included in the stable point set, especially in the upper area.

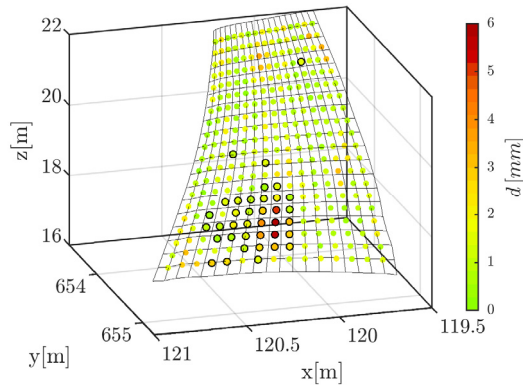


Figure 5. Distorted regions using data set S2-V1.

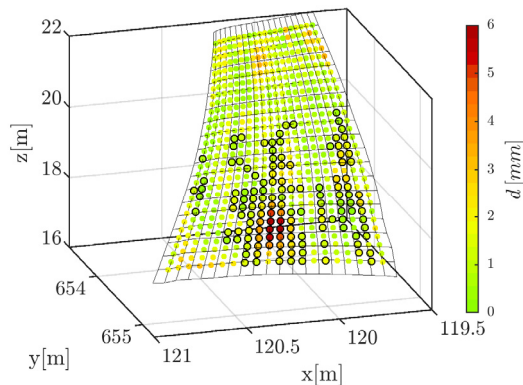


Figure 6. Distorted regions using data set S2-V2.

In order to investigate this behaviour, Figure 7 shows the initial stable point set (the upper region) of the data set S2-V2 obtained after applying RANSAC. Hobmaier, (2020) states that a dependency of the initial stable point set according to the RANSAC or the order of the individual tests occurs in the case of a test decision of a point. Thus, points that are initially part of the consensus set are more likely to be accepted as non-distorted than points that are not initially included. A comparison of Figure 6. and Figure 7. reinforces this thesis. The initial consensus set, hence, plays an essential role in the outcome of a deformation analysis.

The deformation analysis using the data sets of S3 also detects the largest deformations. However, there is a comparatively high number of deformed points observed over the entire surface. This can be explained due to the georeferencing of this station point with an accuracy up to 14 mm, which causes falsification of the joint B-spline parameterization. This leads to possible falsified distances, which play a major role in deformation analysis. (Harmening and Neuner, 2017) point out that reasonable comparison is only possible if the B-spline surfaces are based on the same parameterization.

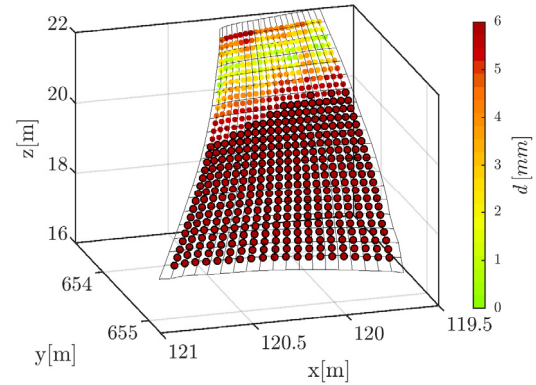


Figure 7. Initial solution (points without black circle) after RANSAC using data set S2-V2.

#### IV. VALIDATION AND EVALUATION

The aforementioned results are verified by a comparison with the Surphaser point clouds. For this purpose, a deformation analysis with a sampling-resolution V1 (cf. Table 3) of the Surphaser B-spline surfaces of both epochs is performed. It should be noted that the stochastic model  $\Sigma_{ll}^{(\lambda\theta R)}$  of the observations in the estimation process is only filled with values of range noise  $\sigma_R = 0.3 \text{ mm}$  and angle noise  $\sigma_{\lambda,\theta} = 4.6 \text{ mgon}$  (Basis Software Inc., 2021). Due to the lack of knowledge concerning functional correlating errors, no correlations are taken into account here. The values of the noise are slightly adjusted in such a way that the global test of the approximation model is passed. The selected RANSAC parameters are  $\tau = 2$  and  $n_{min} = 32$ . This results in  $\#i = 17$  and  $n_{cs} = 187$ . Figure 8 shows the distorted regions detected using the Surphaser point clouds.

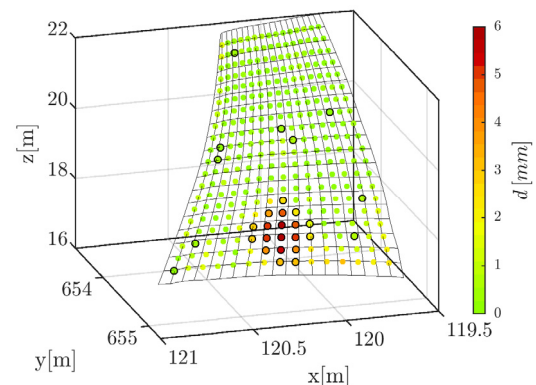


Figure 8. Distorted regions - Surphaser V1.

Comparing Figure 8 with the results in Section III.D it can be seen that the regions of deformation (max. 6 mm) are successfully detected from all data sets used. Keeping in mind that the range noise of the Riegl scanner alone is around 5 mm, a large extent of the measurement noise is reduced during the deformation analysis using B-spline surfaces.

Even with the deformation analysis using the data of the Surphaser, errors of type I cannot be completely avoided.

The comparison illustrates that even with the worse precisions values of the Riegl scanner in comparison to the Surphaser scanner (especially in range noise cf. Table 2), realistic results are achieved using the deformation analysis.

The advantage of including a fully populated SVCM in a deformations analysis is reinforced by a comparison with the outcomes of a deformation analysis, which uses a diagonal matrix as a stochastic model for the observations of the Riegl scans. In the latter, the observations are weighted in such a way that the global test of the approximation model is passed. Figure 9 shows the result of the data set S2-V1 using a diagonal matrix instead of the SVCM. It can be seen that many points are identified as significantly deformed (black circles), outside the deformed area indicated by the Surphaser data. Obviously, the inclusion of appropriate variances and covariances from the fully populated SVCM (cf. Figure 5) improves the result, especially with regard to the distribution of points detected as distorted with respect to lowering type I errors.

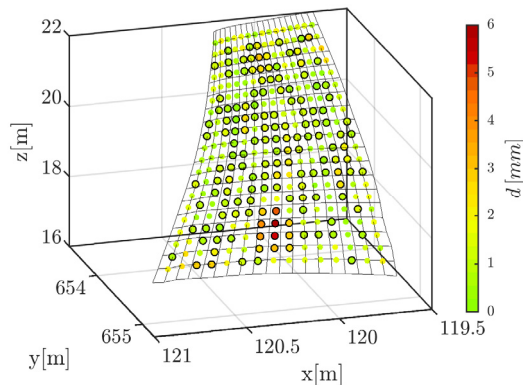


Figure 9. Distorted regions using data set S2-V2; stochastic model diagonal matrix as VCM.

From these findings, it can be assumed that a fully populated SVCM leads to an improvement also for the Surphaser data. Hence, realistic covariances play an essential role in the context of the deformation analysis presented using real TLS measurements.

## V. CONCLUSION

This paper introduces a strategy that allows for estimating rigid body movements and detection of distorted regions at the same time, using best-fit B-spline surfaces. The stochastic properties of the point clouds are described by fully populated SVCMs in the estimation of the B-spline surface.

The results demonstrate that during the modelling and deformation analysis, the measurement noise is reduced and therefore distorted regions are detectable in a statistically sound way.

As noticed for the station S3, a common surface parameterization in both epochs is important for the realistic deformations analysis.

Furthermore, a comparison of the results of the deformation analysis using different stochastic models

for the observations illustrates the advantages of including appropriate stochastic models in form of a SVCM in the B-spline estimation.

## VI. ACKNOWLEDGEMENTS

This research was partly funded by the DFG (German Research Foundation), SCHW 838/7-3 within the project IMKAD II “Integrated space-time modelling based on correlated measurements for the determination of survey configurations and the description of deformation processes”. The other funding party of IMKAD II (I3869) was the Austrian Science Fund (FWF). The authors express their gratitude to the DFG and the FWF for funding this project. The project was also an associated project (AP 07) with the Cluster of Excellence Integrative Computational Design and Construction for Architecture (IntCDC) partially supported by the DFG under Germany’s Excellence Strategy—EXC 2120/1—390831618.

## References

- Basic Software Inc. (2021). *Data sheet Surphaser 3D Laser Scanners*. Available at: <https://www.surphaser.com/pdf/Surphaser%20100HSX.pdf>, last accessed 10.11.2021.
- Bureick, J., Neuner, H., Harmening, C. and Neumann, I. (2016). Curve and surface approximation of 3D point clouds. *Allgemeine Vermessungsnachrichten*, Vol. 123, No. 11-12.
- Bureick, J. (2020). *Robuste Approximation von Laserscan-Profilen mit B-Spline-Kurven*. PhD Thesis, University of Hannover. Verlag der Bayerischen Akademie der Wissenschaften (eds.), DGK-C 852, Munich.
- Caspary, W. (2013). *Fehlertolerante Auswertung von Messdaten: Daten- und Modellanalyse, robuste Schätzung*. De Gruyter, New York.
- Cox, M.G. (1972). The Numerical Evaluation of B-Splines. *IMA Journal of Applied Mathematics*, Vol. 10, No. 2.
- De Boor, C. (1972). On calculating with B-splines. *Journal of Approximation Theory*, Vol. 6, No. 1.
- Fischler, M.A. and Bolles, R.C. (1981). Random sample consensus: A paradigm for model fitting with applications to image analysis and automated cartography. *Communications of the ACM*, Vol. 24, No. 6.
- Girardeau-Montaut, D. (2019) Point processing with Cloud Compare, In: *Proc. of Point Cloud Processing Workshop 2019 Stuttgart*. Available at: [pcp2019.ifp.uni-stuttgart.de/presentations/04-CloudCompare\\_PCP\\_2019\\_public.pdf](http://pcp2019.ifp.uni-stuttgart.de/presentations/04-CloudCompare_PCP_2019_public.pdf), last accessed 24.01.2020.
- Harmening, C., Hobmaier, C. and Neuner, H. (2021). Laser Scanner–Based Deformation Analysis Using Approximating B-Spline Surfaces. *Remote Sensing*, Vol. 13, No. 18.
- Harmening, C. and Neuner, H. (2015). A constraint-based parameterization technique for B-spline surfaces. *Journal of Applied Geodesy*, Vol. 9, No. 3.
- Harmening, C. and Neuner, H. (2016). Detecting rigid body movements from TLS-based areal deformation measurements. In: *Proc. of the FIG Working Week 2016*, FIG Christchurch, New Zealand.



- Harmening, C. and Neuner, H. (2017). Choosing the Optimal Number of B-spline Control Points (Part 2: Approximation of Surfaces and Applications). *Journal of Applied Geodesy*, Vol. 11, No. 1.
- Heunecke, O., Kuhlmann, H., Welsch, W., Eichhorn, A. and Neuner, H. (2013) (eds). *Auswertung Geodätischer Überwachungsmessungen - Handbuch Ingenieurgeodäsie* 2nd ed., Wichmann, Berlin.
- Heunecke, O., and Welsch, W.M. (2000). Models and Terminology for the Analysis of Geodetic Monitoring Observations. *Official Report of the Ad-Hoc Committee of FIG Working Group 6.1*.
- Hobmaier, C. (2020). *Flächenhafte Deformationsanalyse unter Verwendung von approximierenden B-Spline-Flächen*. Master's Thesis. Technical University of Vienna - Department für Geodäsie und Geoinformation/Ingenieurgeodäsie.
- Holst, C., Klingbeil, L., Esser, F. and Kuhlmann, H. (2017). Using point cloud comparisons for revealing deformations of natural and artificial objects. In: *Proc. of INGENEO 2017, 7<sup>th</sup> International Conference on Engineering Surveying*. Kopáčik, A., Kyrinovič, P., Henriques, M.J. (eds), Lisbon.
- ICD (2019). *Urbach Tower, Institute for Computational Design and Construction, University of Stuttgart*. Available at: <https://www.icd.uni-stuttgart.de/projects/remstal-gartenschau-2019-urbach-turm/>, last accessed 29.10.2021.
- Kauker, S. and Schwieger, V. (2017). A synthetic covariance matrix for monitoring by terrestrial laser scanning. *Journal of Applied Geodesy*, Vol. 11, No. 2.
- Kerekes, G. and Schwieger, V. (2020). Elementary Error Model Applied to Terrestrial Laser Scanning Measurements: Study Case Arch Dam Kops. *Mathematics*, Vol. 8, No. 4.
- Kermarrec, G., Alkhatib, H. and Paffenholz, J.-A. (2019). Original 3D-Punktwolken oder Approximation mit B-Splines: Verformungsanalyse mit CloudCompare. In: *Proc. of GeoMonitoring 2019*, online available at: <https://www.repo.uni-hannover.de/handle/123456789/4549>.
- Kuschnerus, M., Schröder, D. and Lindenbergh, R. (2021). Environmental Influences on the Stability of a Permanently Installed Laser Scanner. *The International Archives of the Photogrammetry, Remote Sensing and Spatial Information Sciences*, Vol. XLIII-B2-2021.
- Neuner, H., Holst, C. and Kuhlmann, H. (2016). Overview on Current Modelling Strategies of Point Clouds for Deformation Analysis. *Allgemeine Vermessungsnachrichten*, Vol. 123, No. 11-12.
- Paffenholz, J.-A. and Wujanz, D. (2019). Spatio-temporal monitoring of a bridge based on 3D point clouds - A comparison among several deformation measurement approaches. In: *Proc. of 4<sup>th</sup> Joint International Symposium on Deformation Monitoring (JISDM)*.
- Piegl, L. and Tiller, W. (1997). *The NURBS Book*. 2nd ed. Springer Berlin/Heidelberg.
- Raschhofer, J., Kerekes, G., Harmening, C., Neuner, H. and Schwieger, V. (2021). Estimating Control Points for B-Spline Surfaces Using Fully Populated Synthetic Variance-Covariance Matrices for TLS Point Clouds. *Remote Sensing*, Vol. 13, No. 16.

## Landslide monitoring using geotechnical, UAV, GNSS and MTInSAR instrumentation

Nikolaos Depountis<sup>1</sup>, Katerina Kavoura<sup>1</sup>, Konstantinos Nikolakopoulos<sup>1</sup>, George Drakatos<sup>2</sup>, Panagiotis Argyrakis<sup>3</sup>, Panagiotis Elias<sup>4</sup>, Nikolaos Sabatakakis<sup>1</sup>

<sup>1</sup> University of Patras, Department of Geology, Greece, ([ndepountis@upatras.gr](mailto:ndepountis@upatras.gr); [kavoura@upatras.gr](mailto:kavoura@upatras.gr); [knikolakop@upatras.gr](mailto:knikolakop@upatras.gr); [sabatak@upatras.gr](mailto:sabatak@upatras.gr))

<sup>2</sup> National Observatory of Athens, Institute of Geodynamics, Greece, ([g.drakat@noa.gr](mailto:g.drakat@noa.gr))

<sup>3</sup> University of West Attica, School of Engineering, Department of Surveying and Geoinformatics Engineering, Greece, ([pargyrak@uniwa.gr](mailto:pargyrak@uniwa.gr))

<sup>4</sup> National Observatory of Athens, Institute for Astronomy, Astrophysics, Space Applications and Remote Sensing, Greece, ([pelias@noa.gr](mailto:pelias@noa.gr))

**Key words:** *landslides; real-time monitoring; kinematics; inclinometers; interferometry; GNSS; UAV*

### ABSTRACT

Many mountainous villages have been struck by landslides in Western Greece due to growing urbanization and uncontrolled land use in landslide prone areas, without considering the engineering geological environment. The presence of the tectonically highly sheared and weathered geological formations of the alpine basement (such as flysch) and the intense geomorphological relief, strongly contribute to the periodically induced instability phenomena mainly triggered by heavy rainfalls and extreme meteorological events. The current research combines long-term monitoring of the parameters connected to the landslide activity with the real-time kinematics observation in a dense-populated mountainous village located in the Region of Epirus in Greece. The landslide movements evolve very low velocity values at different depths; thus, the landslide cases can be characterized as complex and "extremely slow". The long-term monitoring is carried out by several in-place and portable inclinometer probes that permit the detailed observation of subsurface displacements for an extended period. In addition, GNSS measurements, very high-resolution multitemporal interferometry (accompanied with the installation of corner reflectors) and Unmanned Aerial Vehicle (UAV) photogrammetric surveys are used for the monitoring of surface deformation. All instrumentation is installed in the wider area of the landslide zone and one of the main goals of this approach is to combine long-term monitoring of the parameters connected to the landslide activity with the observation of the landslide kinematics in real-time.

### I. INTRODUCTION

Nowadays, an active landslide can be monitored using different methods and approaches. These include geotechnical instrumentation like slope inclinometers, high resolution images acquired by Unmanned Aerial Vehicles (UAVs), Geodetic Global Navigation Satellite Systems (GNSS) receivers and multitemporal interferometry (MTInSAR).

Vertical inclinometers (in-place and portable) are widely used to determine the magnitude, rate, direction, and type of landslide movement in several depths. Along with the appropriate kinematic analysis and movement evolution modeling (Kavoura *et al.*, 2020), this information is important for understanding a landslide's cause, behavior, and remediation.

In addition, when extreme meteorological events trigger landslides, the data obtained from meteorological stations are also important. The quantification of the rainfall patterns that act as trigger mechanisms on landslides in a specific area is of great importance when analysis of selected landslide cases is

required and this may be used as a landslide forecasting tool in an applied form (Lainas *et al.*, 2021).

Following the above, the rapid development of the Geodetic global navigation satellite system (GNSS) receivers allows landslide monitoring, especially on the landslide's surface with increasing accuracy. The deformation monitoring with global navigation satellite system (GNSS) measurements is a well-known method which can be employed both for continental scale and local phenomena such as landslides. A geodetic GNSS receiver is used when a high level of accuracy (greater than centimeter) is needed (Leick, 2004).

Lately, UAVs are widely used on landslide precision mapping as it seems to be more efficient than the classical topographic survey, resulting in the creation of orthophotos and Digital Surface Models (DSMs) with extremely fine resolution (Nikolakopoulos *et al.*, 2017a). In this context, high-resolution and low-cost images acquired by UAVs are used to create and update maps by providing orthophotos with sub-decimeter accuracy (Koeva *et al.*, 2018). In addition, UAV-based point clouds and DSMs prove comparable to corresponding products derived from terrestrial laser

scanning (TLS) survey (Mancini *et al.*, 2013). As a result, repeated UAVs photogrammetric campaigns are proved to be an excellent tool for precise landslide mapping and monitoring aiming at the evaluation of the landslide activity (Nikolakopoulos *et al.*, 2017b; Kyriou *et al.*, 2021a; 2021b).

Finally, the exploitation of Persistent Scatterers interferometry (PSI) and Small BAselines Subset (SBAS) as well as the corner reflector (CR) methodologies allows an increased signal-to-noise ratio for monitoring crustal deformation and surface landslide movements.

In this work, results of the combined use of slope inclinometers, along with high-resolution images acquired by UAVs, GNSS measurements and multitemporal interferometry for a detailed landslide monitoring are presented. For this purpose, all the relevant instrumentation has been installed inside the landslide zones of two residential areas, in Metsovo and Zotiko, which are two well-known villages located in the Region of Epirus in Western Greece. The main goal of this approach is to combine short and long-term monitoring of the landslide's activity and kinematics, which with some minor modifications can be operated as a Landslide Early Warning System (LEWS).

## II. SITE DESCRIPTION AND INSTRUMENTATION

Landslide monitoring in the residential area of Metsovo is performed by installing inclinometer casing in several boreholes to permit the detailed observation of subsurface displacements, with the use of two in-place inclinometers (otherwise BH profile digital gauges) and a digital vertical inclinometer probe.

BH profile digital gauges are designed for automatic monitoring of critical depth locations where displacement monitoring request a continuous borehole profiling. The BH profile gauges used in the current research consist of a stainless steel and thermoplastic resin assembly with one fixed wheel (close to the joint) and one spring loaded wheel. Each BH profile has been installed into an inclinometer casing at least 20 m long and is composed by a string of 4 gauges 1 or 2 m long with carbon fiber extension rods and an upper terminal wheel's assembly to close the chain and. Each string is connected to its own datalogger with a single digital bus cable (S430HD digital model) for collecting and transmitting the relevant displacement data.

The digital vertical inclinometer probe used in the current research consists of a) a stainless-steel body with digitalized inclinometer MEMS to measure inclinations in two orthogonal directions, b) two-wheel assembly at a distance of 50 cm to slide along the grooves of the inclinometer casing, c) an inclinometer cable 50 m long connected to the probe and d) an android mobile readout unit for collecting the data.

Additionally, to the above, GNSS receivers, scatterers, and a meteorological station have been installed for the landslide's surface displacement observation and the

collection of hydrometeorological data (Figure 1). The GNSS receivers and the meteorological station have been adjusted to continuously collect real-time data, whereas the scatterers are used for periodically scheduled SAR acquisitions.

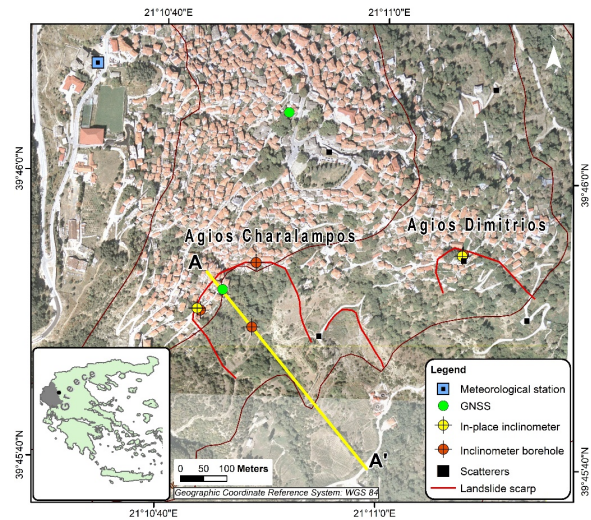


Figure 1. The study area of Metsovo in Greece and the installed instrumentation (cross-section AA' presented in Figure 3 is depicted with a yellow line).

On the other hand, landslide monitoring in the residential area of Zotiko is performed by installing inclinometer casing of 25 m in each of the two boreholes drilled for this purpose and by using a digital vertical inclinometer probe for the relevant subsurface displacement. A GNSS receiver and a meteorological station have also been installed in the surrounding area (Figure 2).

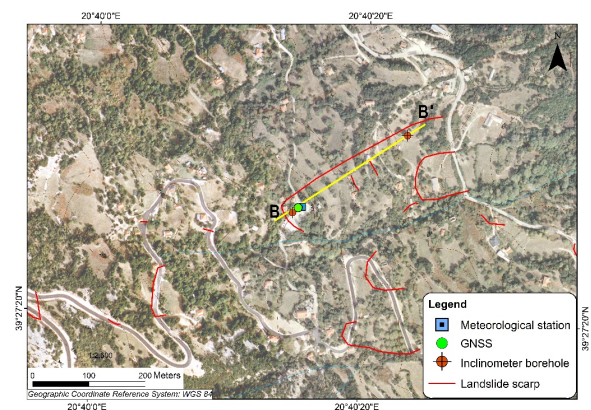


Figure 2. The study area of Zotiko in Greece and the installed instrumentation (cross-section BB' presented in Figure 5 is depicted with a yellow line).

## III. GEOTECHNICAL INSTRUMENTATION FOR LANDSLIDE MONITORING

In both areas, Metsovo and Zotiko, the tectonically highly sheared and weathered geological formation of flysch and the intense geomorphological relief, strongly contribute to periodically induced landslide phenomena, mainly triggered by heavy rainfalls and extreme meteorological events. The landslides in both

areas are still active and evolve extremely low-velocity values at different depths (2-16 mm/year); thus, the studied landslide cases can be characterized as complex and according to the WP/WLI (1995) guidelines as "extremely slow".

In the area of Metsovo three different areas of landslide events have been identified since 2010 with the largest one in the south-western part of the village. The landslide has a crown length of approximately 90 m and extends downwards with a length of approximately 200 m (Figure 1). From the geological and geotechnical investigation performed in the surrounding area, it seems that a main translational displacement slide has been occurred in the weathered flysch, which can be divided into two overlapping (successive) and a rotational slide with the maximum depth of the sliding surface approaching and may be exceeding the 30 m (Figure 3).

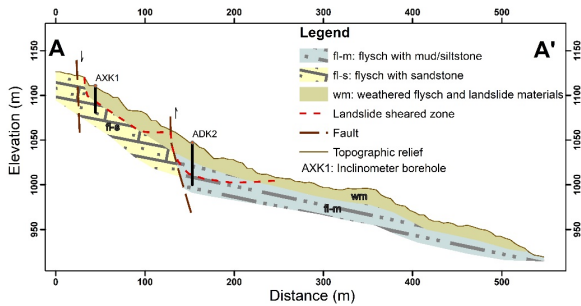


Figure 3. Geological cross-section AA' in Metsovo.

The general kinematics of the sliding zone suggests that this is a complex landslide where different types of movements take place in different areas of the sliding mass, usually simultaneously. According to the inclinometer observations the depth of the landslide sheared zone varies from 5-10 m near the residential area up to 25-30 m to south-east (Figure 4).



Figure 4. Orthophoto map of Metsovo (the red arrows represent the direction and rate of subsurface movement in mm/year at several depths below the ground surface).

The almost constant speeds 4 to 16 mm/year of the subsurface ground movement recorded with the use of portable inclinometer porbes during the last 10 years in the whole landslide area, identifies this landslide as "extremely slow", very close to the "slow" limit.

Regarding the measurements derived by the in-place inclinometers, from October 2020 until October 2021, a small movement of 0.25 mm/year has been recorded in the landslide's western part at a depth of 5 to 10 m.

In the village of Zotiko several areas of landslide events have been identified since 1979 with the largest one located in the north-eastern part of the village. The total length of the sliding mass is approximately 300 m and its width 130 m. (Figure 2). From the geological and geotechnical investigation performed, it seems that a slow translational displacement slide has been occurred inside the scree material and the weathered flysch, at depths varying from 10 to 15 m (Figure 5).

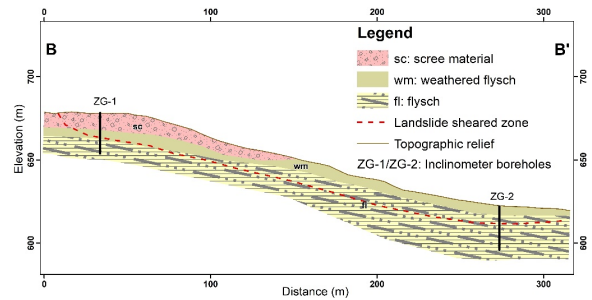


Figure 5. Geological cross-section BB' in Zotiko.

The general kinematics of the sliding zone certifies that this is a complex landslide with translational geometry. According to the inclinometer readings the depth of the landslide sheared zone varies from 14 m next to the landslide scarp up to 11 m further to north-east. The speeds of 2 to 10 mm/year of the subsurface ground movement recorded with the use of portable inclinometer probes within the period 2018-2020 in the whole landslide area, identifies this landslide as "extremely slow" (Figure 6).



Figure 6. Orthophoto map of Zotiko (the red arrows represent the direction and rate of subsurface ground movement in mm/year at several depths below the ground surface).

#### IV. UNMANNED AERIAL VEHICLE SURVEY

In both areas of Metsovo and Zotiko photogrammetric annual UAVs campaigns were planned and performed at 100 m above the ground level. UAV imagery was obtained using a DJI Phantom 4,

which is equipped with a built-in GNSS system and a CMOS camera (12.4 MP) with 4000 × 3000 resolution. The same grid with 80% overlap along and across the track was used every year resulting at 3 cm pixel size of the orthophotos and the DSMs. Furthermore, the same ground control points were used in every campaign. The ground control points were measured with a Leica GS08 RTK GNSS receiver. The UAV data processing was performed in Agisoft Photoscan Professional software. In more details, UAV data were processed according to the Structure from Motion (SfM) photogrammetric technique. SfM constitutes a low-cost and user-friendly technique which combines photogrammetry and computer vision for 3D reconstruction of an object or a surface model (Westoby *et al.*, 2021; Micheletti *et al.*, 2015; Eltner and Sofia, 2020).

Three annual sets (2018, 2019, 2020) of high resolution orthophotos and DSMs covering the study areas were finally generated and used for exploring the landslide surface deformation and as base maps for the design of landslide. The generated orthophoto maps of Metsovo and Zotiko, from the 2019 campaign, along with the direction and rate of the landslides movements are respectively presented in Figures 4 and 6.

#### V. GNSS INSTRUMENTATION AND MONITORING

Two GNSS stations were installed in Metsovo (Figure 1) and one station in Zotiko (Figure 2), with code names MTSV, MTS2, and ZOTI, respectively. The stations are equipped with dual-frequency GNSS receivers and continued network connections. The receivers are set to 30-second acquisition and 0 degrees elevation mask. The rinex files are transmitted via wired (MTSV) and wireless/3G (MTS2, ZOTI) internet connection to the central NAS at the University of Patras and checked every day for integrity.

After the integrity checks, the rinex files are processed for quality control with TEQC software to identify excess multipath or signal to noise errors and the data are processed with GIPSY-OASIS, which uses a Precise Point Positioning algorithm to solve the daily position. The tropospheric delays were eliminated in Precise Point Positioning by using appropriate modeling like GPT2 or VMF1 in the processing phase. The elevation mask was used only to remove bad satellite reception especially below 5°.

The solution is saved into a database, and the time series is extracted after the user query. The deformation time series as resolved for the areas of Metsovo and Zotiko are presented in Figures 7a, 7b and Figure 8, respectively.

#### VI. MULTITEMPORAL INTERFEROMETRY

The exploitation of a large volume of SAR acquisitions of the same ground track, forming a set of differential interferograms, between a single image and all the others, along with the proper application of the so-called method PSI (Ferretti *et al.*, 2011), allows an

increased signal-to-noise ratio for monitoring crustal deformation as well as landslide movements.

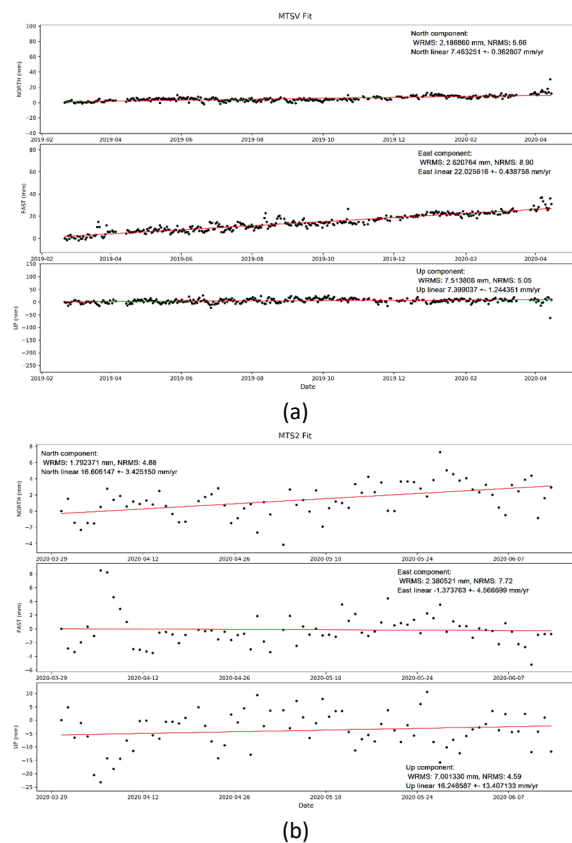


Figure 7. Time series and rate of the surface movement in Metsovo: (a) GNSS station MTSV; (b) GNSS station MTS2.

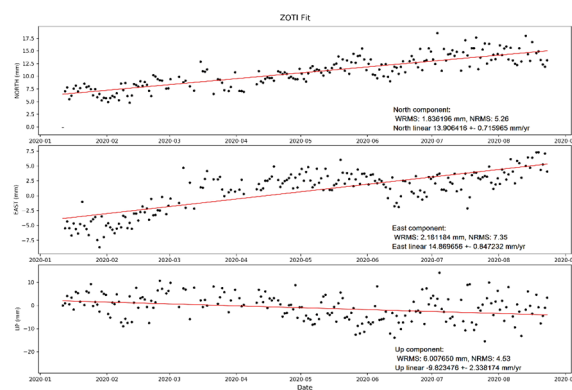


Figure 8. Time series and rate of the surface movement in Zotiko (GNSS station ZOTI).

It is based on the identification of target-scatterers with a stable radiometric behavior in time. This technique ensures the minimization of noise and the measurement of linear or nonlinear deformation phenomena along the Line Of Sight (LoS). PS (Persistent Scatterers) pixels (scatterers) are identified as those pixels whose phase histories match an assumed model of how displacement varies with time. This functional model of temporal displacement (*e.g.*, linear model) to identify PS, approximate knowledge of how the deformation varies with time is required a priori.

Commonly, deformation is assumed to be steady-state or periodic in nature.

In addition to the PSI approach, the SBAS method (Bernardino *et al.*, 2002), based on different combinations of the available SAR interferograms relative to a study area, is used. SBAS is an extension of the conventional SAR Interferometry (InSAR) techniques and addresses decorrelation and atmospheric delay problems. The SBAS technique relies on an appropriate combination of differential interferograms characterized by a small orbital separation and increases the sampling rate by using all the acquisitions included in the small baseline subsets and preserves the system's capabilities to provide spatially dense deformation maps (Casu *et al.*, 2006). As each of these two techniques is optimized for different models of ground scattering, they are complementary.

The passive CR, which has been implemented in this study, is a metal construction that backscatters the received microwave radiation back to its source. Its shape is triangular trihedral, consisting of three orthogonal and isosceles triangles, with orthogonal sides of 0.4 m. This design is not the one with the maximum backscatter peak gain, but its radiation pattern is wide, having a half-power response width of 40° (Rahmat-Samii, 2007).

In the area of Metsovo ten CRs were installed in five positions prior to the scheduled acquisitions. A pair of them placed back-to-back in each location, each one oriented for the ascending and descending track. The elevation and the azimuth of the focal point of the CRs was set to have maximum backscatter for the incidence angles of 44° for the ascending and 47° for the descending track.

A total number of forty acquisitions of the TERRASAR-X satellite in High-Resolution Spotlight mode were used. Twenty of them were acquired from the ascending track 70 during the period from 7/12/2019 to 5/8/2020 and another twenty from the descending track 47 during the period from 6/12/2019 to 15/8/2020.

To produce the original products of MTInSAR (MultiTemporal InSAR), the ENVI SARscape® software (L3Harris Geospatial, Boulder, CO, USA) software was used. Using both differential interferometry techniques over time, *i.e.*, PSI and SBAS for the ascending and descending orbits, we ended up with four sets of deformation rates for the ground and the overlying structures with different measuring properties. Herein only the SBAS products are presented. These were processed further to (1) remove remaining linear gradients in directions N-S and E-W, (2) calibrate them so that they have a reference (zero) to the GNSS Location and (3) remove unreliable measurements.

In the whole area of Metsovo for the ascending track no extensive deformation is observed apart from certain areas of limited extension within the residential fabric. In the deformation maps of the Distributed Scatterers (DS) for the descending track certain areas with deformations within the residential fabric are

observed, which are marked 'a' to 'h' (Figure 9). For example, in the ('h') area no deformation is observed, except at the east.

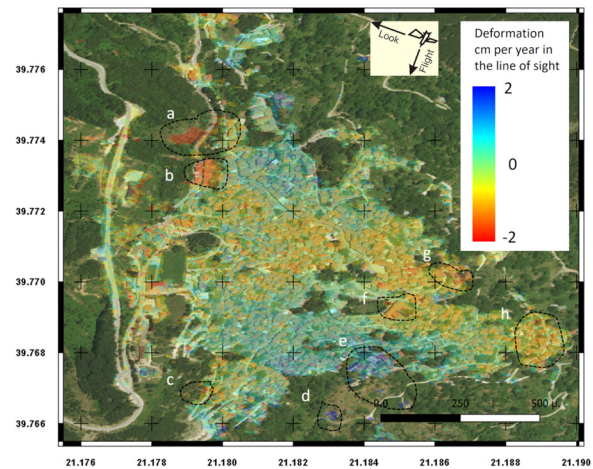


Figure 9. Deformation map of the DS descending track of the Metsovo area.

Concerning the ('d' and 'e') areas extensive failures occur in the residential fabric and the area around the corner reflector is deformed with a value of more than 2 cm/year (Figure 10).

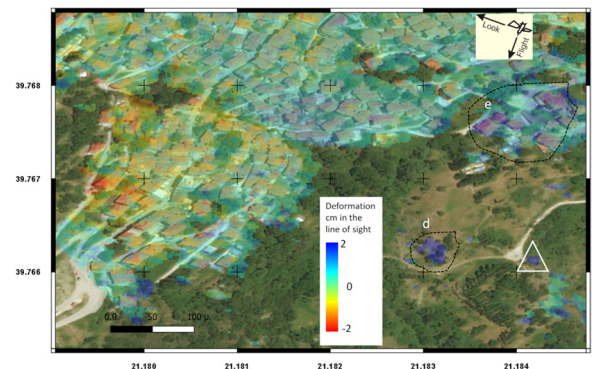


Figure 10. Deformation map of DS of the descending track focused in areas ('d' and 'e'). The white triangle shows the location of the corner reflector.

For the more complete mapping and utilization of satellite data, based on the products of DS for both tracks, vector records (polygons) were created, categorizing the deformation rates in four ranges as can be seen in Figure 11.

Moreover, for each of the polygons, the scatterers' multi-temporal ground deformation rate was created, as shown in a characteristic case in Figure 12.

## VII. DISCUSSION

The surface ground movements in Metsovo were recorded with a contribution of very high-resolution data TERRASAR-X acquired for the German Space Agency (DLR) science project. Practical issues and other factors as the low priority of the commercial schedules over those within the DLR science project limited the study period to nine months instead of two years (ideally) or at least one whole year, to cover once or

twice the seasonal cycle. Multitemporal interferometry was produced with two techniques and nominal spatial analysis of 2 x 2 m for the ascending and descending orbital geometries. They were corrected geometrically and quantitatively and plotted on maps. The corner reflectors placed before the acquisitions were used as stable measuring points.

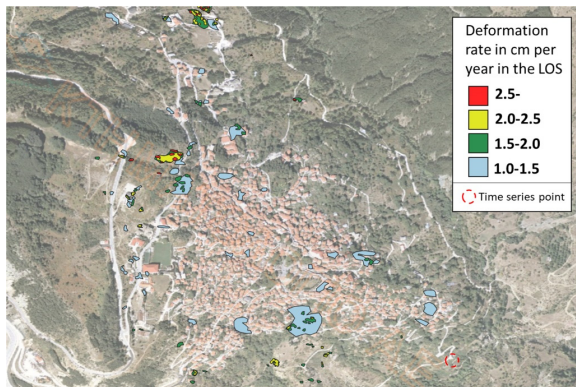


Figure 11. Polygons with all the deformation rate ranges of the DS of the descending track. With red dashed circle is marked the point that its time series is presented in Figure 12.

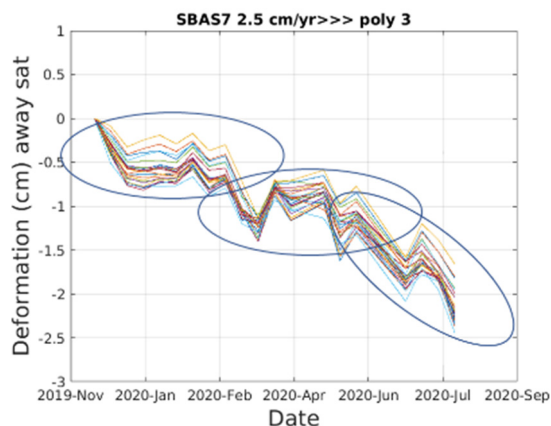


Figure 12. Characteristic time-series of deformation of a DS. Two sudden outbursts can be discriminated, in February and May 2020 with a constant deformation rate after June 2020. The location of the point is shown in Figure 11.

No failure of large importance and extension was observed for the studying time, apart from some focused or minor failures. In addition, small-width deformations were found in a set in moderate extended area ENE and SW within Metsovo with an order of magnitude approximately 5 mm/year. Eleven locations were detected with a very small spatial extension with deformation of about 1-2 cm/year and with a small spatial extension and values of about 1-1.5 cm/year. Five of these sites focus on the area where the inclinometers and a GNSS receiver were installed. In this area, apart from the focused deformations, there are indications of failure of the slope in SW of the corner reflector and inside and around it in the location of the corner reflector and positions 'd' and 'e'.

More detailed mapping (in larger scale) of the deformation rates (from InSAR product) were

performed, resulting in the creation of vector files (polygons), by grouping the deformation rates into four groups, providing, also, the deformation time series. According to this, the deformation rates in the largest spatially landslide is 1-2 cm/year. Compared with the detected rate of 4-16 mm/year of the subsurface ground movement as it has been recorded with the use of inclinometer probes leads to the conclusion that multitemporal interferometry and inclinometer results are in a good correlation, since the effect of the subsurface ground movement is visible on the surface with the use of MTInSAR.

However, detectable deformations are of slow deformation, which are limited in time during the period of satellite receptions. No information can be provided before or after the acquisition period but only possible sources of future failures, some of them characterized as precursors. Their persisting deformation in future monitoring studies, strengthen their characterization as such. The continuation of the monitoring, even at a lower spatial resolution, on an operational basis to monitor the evolution or detection of new slow displacements will be an investment to avoid large-scale failures with multiple costs, comparing to the monitoring ones.

Concerning the UAV campaigns proved to be an efficient tool for surface landslide small movement mapping. It is characteristic that small surface changes and altitude changes directly related to the landslide were recorded in the schoolyard of Zotiko. It was turned out that the cracks in the schoolyard are expanding. The comparative study of the DSMs confirmed a vertical surface deformation of 2 cm in some places within the period 2018-2020. This deformation is the effect of the recorded with inclinometer probes subsurface horizontal movement rate of 10 mm/year. This leads to the conclusion that the subsurface horizontal movement of 10mm/year in the depth of 14 m affects the whole area of the schoolyard, and the result in the surface is a vertical deformation of 2mm.

## VIII. CONCLUSIONS

The landslide study areas of Metsovo and Zotiko are typical examples of complex landslides, which are usually exist in Western Greece. In both areas landslides have been involved mainly in the weathered flysch and are still active with extremely slow movements.

The short and long-term monitoring is carried out with the use of a complete system consisting of geotechnical, meteorological and GNSS instrumentation as well as UAV and MTInSAR.

The obtained results of the system measurements are positively correlated, especially the combination among multitemporal interferometry, UAV and inclinometer readings. Concerning the GNSS receivers it seems that they need more time to get more realistic measurements. According to Carlà *et al.* (2019) realistic

results about landslides need at least four years of processed GNSS data.

Depountis *et al.* (2021), proposed that results from such a system may appear in real-time through a specially designed internet platform (WebGIS) and this could constitute a powerful tool for the local authorities in case of emergency. The combination of short- and long-term monitoring of the parameters connected to the landslide activity and kinematics, with the results presented efficiently in a WebGIS is the next step of this research, for the operation of the presented system as a Landslide Early Warning System (LEWS).

#### IX. ACKNOWLEDGEMENTS

This research was funded by the Regional Operation Programme Epirus 2014-2020. We would also like to acknowledge Deutsches Zentrum für Luft und Raumfahrt (DLR) to provide the TERRASAR-X satellite acquisitions within the science project GEO3659 as well as the TREE company for providing the data of the GNSS station GARD of the URANUS network.

#### References

- Berardino, P., Fornaro, G., Lanari, R., and Sansosti, E. (2002). A new algorithm for surface deformation monitoring based on small baseline differential SAR interferograms. *IEEE Transactions on Geoscience and Remote Sensing*, 40(11), pp. 2375–2383.
- Carlà, T., Tofani, V., Lombardi, L., Raspini, F., Bianchini, S., Bertolo, D., Thuegaz, P., and Casagli, N. (2019). Combination of GNSS, satellite InSAR, and GBInSAR remote sensing monitoring to improve the understanding of a large landslide in high alpine environment. *Geomorphology*, Vol.35, pp. 62-75. DOI: 10.1016/j.geomorph.2019.03.014.
- Casu, F., Manzo, M., and Lanari R. (2006). A quantitative assessment of the SBAS algorithm performance for surface deformation retrieval from DInSAR data. *Remote Sens. Environ.*, 102(3/4), pp. 195 -210.
- Depountis, N., Sabatakakis, N., Kavoura, K., Nikolakopoulos, K., Elias, P., and Drakaos, G. (2021). Establishment of an integrated landslide early warning and monitoring system in populated areas. In: *Understanding and Reducing Landslide Disaster Risk*. Casagli N. et al. (eds), Vol.3, pp. 189-194. ISBN 978-3-030-60311-3.
- Eltner, A., and Sofia, G. (2020). Structure from motion photogrammetric technique. In: *Developments in Earth Surface Processes*. Tarolli P. et al. (eds), Vol.23, pp. 1-24.
- Ferretti, A., Fumagalli, A., Novali, F., Prati, C., Rocca, F., and Rucci, A. (2011). A New Algorithm for Processing Interferometric Data-Stacks: SqueeSAR. *IEEE Transactions on Geoscience and Remote Sensing*, 49(9), pp. 3460-3470.
- Kavoura K, Konstantopoulou M, Depountis N, and Sabatakakis N (2020). Slow-moving landslides: kinematic analysis and movement evolution modelling *Environmental Earth Sciences*, 79:130, 11. DOI: 10.1007/s12665-020-8879-7.
- Koeva, M., Muneza, M., Gevaert, C., Gerke, M., and Nex, F. (2018). Using UAVs for map creation and updating. A case study in Rwanda. *Surv. Rev.*, 50, pp. 312–325. DOI: 10.1080/00396265.2016.1268756.
- Kyriou, A., Nikolakopoulos, K., Koukouvelas, I., and Lampropoulou, P. (2021a). Repeated UAV Campaigns, GNSS Measurements, GIS, and Petrographic Analyses for Landslide Mapping and Monitoring. *Minerals*, 11, 300. DOI: 10.3390/min11030300.
- Kyriou, A., Nikolakopoulos, K., and Koukouvelas, I. (2021b). How Image Acquisition Geometry of UAV Campaigns Affects the Derived Products and Their Accuracy in Areas with Complex Geomorphology. *ISPRS International Journal of Geo-Information*, 10(6):408. DOI: 10.3390/ijgi10060408.
- Lainas, S., Depountis, N., and Sabatakakis, N. (2021). Preliminary Forecasting of Rainfall-Induced Shallow Landslides in the Wildfire Burned Areas of Western Greece. *Land*, 10, 877. DOI: 10.3390/land10080877.
- Leick, A. (2004). GPS satellite surveying. Hoboken (NJ), John Wiley & Sons.
- Mancini, F., Dubbini, M., Gattelli, M., Stecchi, F., Fabbri, S., and Gabbianelli, G. (2013). Using Unmanned Aerial Vehicles (UAV) for High-Resolution Reconstruction of Topography: The Structure from Motion Approach on Coastal Environments. *Remote Sens.*, 5, 6880–6898. DOI: 10.3390/rs5126880.
- Micheletti, N., Chandler, J., and Lane, S.N. (2015). Structure from motion (SfM) photogrammetry. *Geomorphological Techniques*, Chap. 2, British Society for Geomorphology.
- Nikolakopoulos, K.G., Soura, K., Koukouvelas, I.K., and Argyropoulos, N.G. (2017a). UAV vs. classical aerial photogrammetry for archaeological studies. *J. Arch. Sci. Rep.*, 14, pp. 758–773. DOI: 10.1016/j.jasrep.2016.09.004.
- Nikolakopoulos, K.G., Kavoura, K., Depountis, N., Kyriou, A., Argyropoulos, N., Koukouvelas, I., and Sabatakakis, N. (2017b). Preliminary results from active landslide monitoring using multidisciplinary surveys. *European Journal of Remote Sensing*, 50:1, pp. 280-299. DOI: 10.1080/22797254.2017.1324741.
- Rahmat-Samii, Y. (2007). Antenna Engineering Handbook, Chap. 15–43 (Reflector Antennas). New York, NY: McGraw-Hill.
- RINEX (2014). The Receiver Independent Exchange Format Version 3.02, page 38, web.archive.org. International GNSS Service (IGS). 18 October 2014. Retrieved 30 May 2019.
- Westoby, M.J., Brasington, J., Glasser, N.F., Hambrey, M.J., and Reynolds, J.M. (2012). ‘Structure-from-Motion’ photogrammetry: A low-cost, effective tool for geoscience applications. *Geomorphology*, 179, pp. 300-314.
- WP/WLI (1995). A suggested Method For Describing the Rate of Movement of a Landslide. International Geotechnical Societies. In: *UNESCO Working Party on World Landslides Inventory, Working group on Rate of Movement*. Bonnard C. (ch), Bull. IAEG, 52, pp. 72-78.



## Monitoring the spatiotemporal variability of beach mesoforms by analyzing Sentinel-2 images

Josep E. Pardo-Pascual<sup>1</sup>, Carlos Cabezas-Rabadán<sup>1,2</sup>, Jesús Palomar-Vázquez<sup>1</sup>,  
Alfonso Fernández-Sarriá<sup>1</sup>

<sup>1</sup> Geo-Environmental Cartography and Remote Sensing Group, Department of Cartographic Engineering, Geodesy and Photogrammetry, Universitat Politècnica de València, Camí de Vera, s/n, 46022 València, Spain, ([jepardo@cgf.upv.es](mailto:jepardo@cgf.upv.es); [carcara4@upv.es](mailto:carcara4@upv.es); [jpalomav@upvnet.upv.es](mailto:jpalomav@upvnet.upv.es); [afernan@cgf.upv.es](mailto:afernan@cgf.upv.es))

<sup>2</sup> UMR 5805 EPOC, Université de Bordeaux-CNRS, Allée Geoffroy Saint-Hilaire, CS 50023-33615 Pessac, France, ([carlos.cabezas-rabadan@u-bordeaux.fr](mailto:carlos.cabezas-rabadan@u-bordeaux.fr))

**Key words:** *shoreline dynamics; beach morphology; monitoring beach variability; sentinel-2; SHOREX; western Mediterranean*

### ABSTRACT

Beaches are extremely dynamic natural environments that experience significant variations at different spatial and temporal scales. The processes of appearance and maintenance of morphological features as the beach mesoforms, as well as their characterization, may provide useful information on the morphodynamic evolution of a beach and the spatial variability of nearshore processes. The high availability of Sentinel-2 satellite images together with the development of tools such as the system SHOREX allows the automatic extraction of the position of the shore. The high accuracy of the resulting satellite-derived shorelines (SDS) offers high potential for the definition of relatively detailed morphological features. This work assesses the ability to apply the SDS for characterizing beach mesoforms appearing at Cala de Mijas, in Málaga (S Spain) as well as characterising their changes over time. The extraction of the SDS enables the characterisation of rhythmic coastal forms through the undulations described by the shoreline position along the beach face by using a sinuosity index and to start to address the study of their relationship with the registered wave conditions. This proves that the information derived from mid-resolution satellite images can become a key source of information to characterize the morphological dynamics of beach environments.

### I. INTRODUCTION

Beaches represent a vital resource for the coastal regions (Kuriyama *et al.*, 2012). They sustain unique ecosystems while sheltering the inland human settlements from the action of the waves and offering the physical space needed for the activities sustained on the 'sun, sea and sand' principles (Pranzini *et al.*, 2018).

Beaches are natural spaces that experience great dynamism along different spatial and time scales (Hansen *et al.*, 2010). Their morphology can experience strong variations from hourly and sub-weekly scales such as in the case of storm episodes (Senechal *et al.*, 2015), while cyclical oscillations or marked trends may appear over the years as a response to local and regional impacts or even to planetary drivers (Cooper, 2022).

As a response to diverse phenomena, beaches experience changes that may homogeneously affect their profile, while others may provoke different alongshore responses. Related with that latter one, the most obvious effect is the alteration of the subaerial beach width (Pranzini *et al.*, 2018) which may negatively affect and even jeopardize the recreational use of these spaces (Cabezas-Rabadán *et al.*, 2019a; 2019b).

Sometimes the alongshore differences are not progressive but oscillatory, with the shoreline position following a recurrent alongshore pattern of undulations. Thus, a nearly periodic spacing leads to cusped shapes with dimensions ranging from several to tens of meters (Schwartz, 2006). The rhythmic shoreline features may present different behaviours along the coast, sometimes being static along time and sometimes disappearing. Among the different theories describing their formation (Coco *et al.*, 1999; Holland *et al.*, 1998) the combination of swash mechanics, edge waves and self-organization seems to play a significant role in their appearance. Nevertheless, for the moment the current literature has not found a clear response to explain their evolution mechanisms (Vousdoukas, 2012).

The information describing mesoforms as the beach cusps is extremely valuable to increase the knowledge in this field, as well as to properly characterise the beach system. The mesoscale features may act as descriptors of the predominant nearshore processes taking place and controlling the dynamism of the coast (Montes *et al.*, 2018). Thus, a strong relationship appears between the oceanographic conditions, the presence of mesoscale forms as cusp systems and bars, and the formation of rip currents, which is of

importance for the recreational use of the beaches (Silva-Cavalcanti *et al.*, 2018).

Having updated information on the morphology of the beaches and their dynamism has strategic importance for coastal managers to make appropriate decisions. Nowadays satellite multispectral images are broadly used as a source of environmental information. Among those available free of charge, the Sentinel 2 images (acquired and managed by the European Space Agency) stand out due to their high frequency of acquisition (5 days) of the whole planet. These images may be systematically applied for monitoring purposes, constituting a great opportunity to obtain information on the physical reality of the coast.

The shoreline position appears as a feature able to represent the morphology of the beach (Boak and Turner, 2005) and, therefore, to describe its state and variability along time and space. In order to obtain large packages of shoreline position data, its definition has to be efficient and accurate. Recently, different algorithms and tools have been developed for this purpose, leading to the obtention of the so-called satellite-derived shorelines (SDS). This is the case of CoastSat (Vos *et al.*, 2019), CASSIE (Almeida *et al.*, 2021), SAET (Palomar-Vázquez *et al.*, 2021) and SHOREX (Cabezas-Rabadán *et al.*, 2021), being the accuracy of the latter one robustly checked in Mediterranean coasts (Pardo-Pascual *et al.*, 2021; Sánchez-García *et al.*, 2020)

Many studies have already started to apply the SDS to analyse the sub-weekly and decadal changes of the shoreline position (Cabezas-Rabadán *et al.*, 2019a; 2019c; Konlechner *et al.*, 2020; Liu *et al.*, 2017) as well as the consequences it may have over the beach use (Cabezas-Rabadán *et al.*, 2019b). Nevertheless, the

recently increased accuracy of these extraction techniques may help to study relatively detailed features such as the emerged beach mesoforms.

The present study aims to assess the potential of the satellite-derived shorelines for characterising the changes registered by the beach face mesoforms along time and space. For that purpose, the shoreline positions were extracted from Sentinel-2 imagery using the SHOREX system enabling to define a Sinuosity Index and to establish relations with the incident wave conditions.

## II. STUDY AREA

The study focuses on Cala de Mijas beach. It is a sandy beach located in the Málaga province, within the Costa del Sol (Andalusia, S Spain) (Figure 1). This coast is predominantly a low-lying beach and shore platform system composed of narrow and relatively steep beaches. They are usually sandy, with a grain size of about 1.5 mm or more (Málvarez and Navas, 2019).

It is a region defined by high anthropic pressure, with dense urbanization of the land close to the coast. This occurs linked to its activity as a renowned global tourist destination (Guisado-Pintado *et al.*, 2016). Partly as a consequence of this human occupation the vulnerability and the risk are high and require the attention of territorial managers. Concerning this, since the middle of the last century the Mediterranean Coast of Andalusia has experienced a negative sedimentary balance. The sector of Cala de Mijas appears relatively stable, although registering a moderate erosion in a 20% of the coast, and a high erosion at 15% of it (Molina *et al.*, 2019).

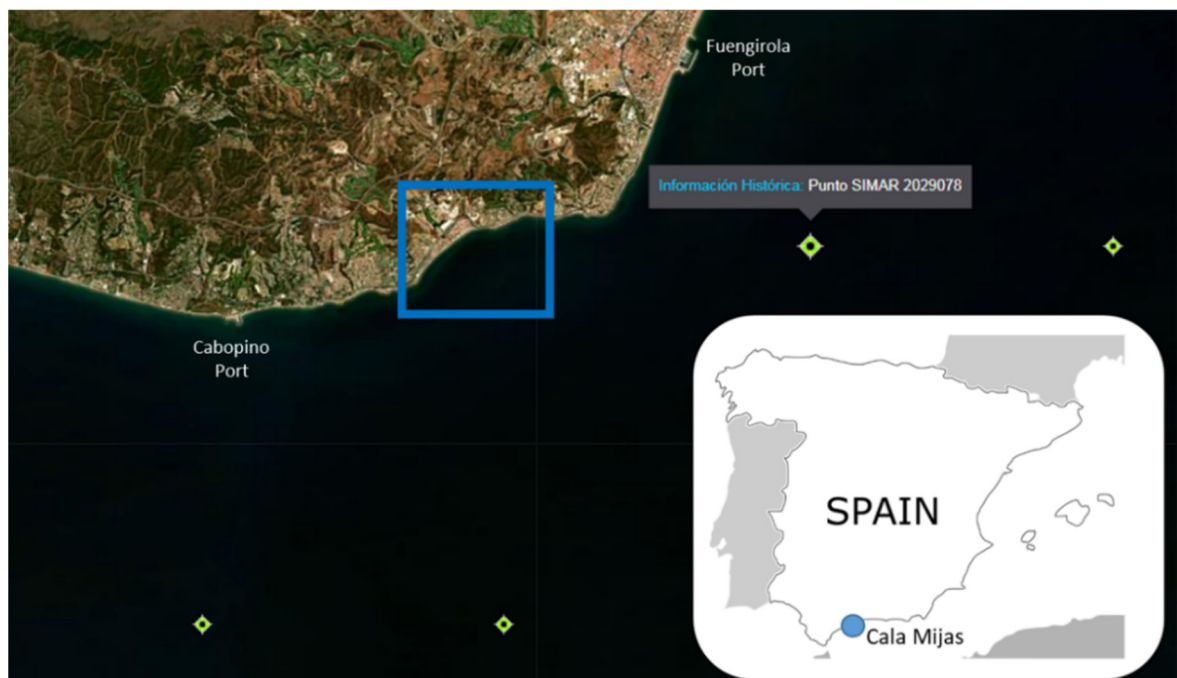


Figure 1. Location of the study area in Cala de Mijas in the province of Málaga (Costa del Sol, S Spain). The distribution of the points of the SIMAR model for the wave hindcast is also presented (green points). The closest point to the study area was selected for retrieving the oceanographic data.

Regarding the sediment, Cala de Mijas constitutes an independent cell related to the inputs offered by the Arroyo Cala del Moral and a large deposit accumulated on the platform which probably results from the combination of the transport of sediment from the Ensenada de Marbella and the bay of Fuengirola (Málvarez and Navas, 2019). In the past, the beach showed a semi-dissipative behaviour thanks to the accumulation of sand on the nearshore. Nevertheless, the insufficient beach width has led coastal managers to carry out nourishments which could result in a shift towards an intermediate/reflective behaviour more prone to erosion.

Hydrodynamically, this coast is controlled by a microtidal range (average 50 cm) and low-energy wave ( $H_s = 1.0$  m) conditions (Málvarez and Navas, 2019), influenced by two prevailing winds parallel to the main direction of the coast. Thus, the wave direction follows a bimodal pattern dominated by westerlies and easterlies, while the effective fetch is limited to an average of 500 km. This results in a predominant swash-aligned sector for Cala de Mijas (Molina *et al.*, 2019). These characteristics and the steep nearshore regions lead to beach types highly dependent on short-term sediment supply, which mainly takes place around seasonal heavy rainfall by reworking fluvial sands.

### III. MATERIALS AND METHODS

This study is based on the information provided by the images of the Sentinel, and the shoreline positions extracted using the SHOREX extraction system. The oceanographic data provided by the SIMAR model is considered as complementary information in order to understand the influence of the hydrodynamic forcing on the shoreline morphology.

#### A. Satellite imagery

This analysis employed 84 images acquired during 2018-2019 by the optical satellite Sentinel 2, sensor MSI (Figure 2). These mid-resolution images may be obtained free of charge from the Copernicus Open Access Hub (<https://scihub.copernicus.eu/>). They include the bands RGB, NIR, SWIR1, and SWIR2 with a spatial resolution between 10 and 30 m subsequently employed within the extraction process.

#### B. Oceanographic data

The SIMAR model for the wave hindcast (Spanish Port Authority) was employed for obtaining the wave conditions during the study period. In order to do so, the closest point of the grid to the studied beaches was selected (SIMAR 2029078) for acquiring the wave data. Thus, significant wave height, direction, and mean and peak period were retrieved, and their monthly averages were calculated (Table 1).

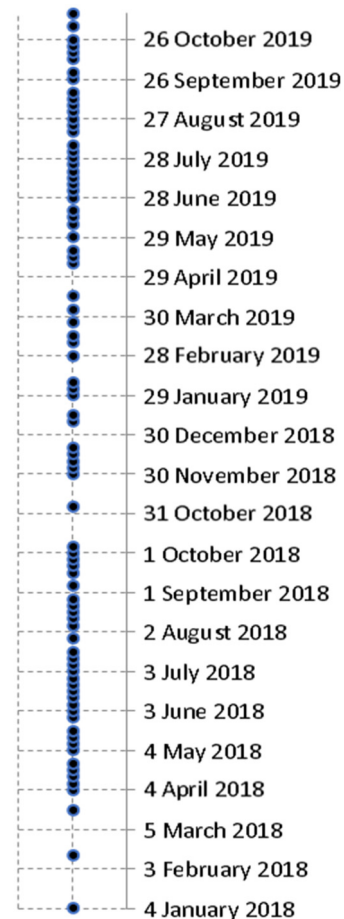


Figure 2. Sentinel 2 satellite imagery employed in this work.

Table 1. Monthly averages of the significant wave height ( $H_s$ ), direction (Dir), mean (Tm) and peak period (Tp) according to the data retrieved from the SIMAR point 2029078. The information is publicly available at <https://www.puertoes.es/>

Month	$H_s$ [m]	Dir [°]	Tm [s]	Tp [s]
Jan 2018	0.73	202.75	3.19	4.63
Feb 2018	0.46	183.64	2.95	4.16
Mar 2018	0.83	229.80	3.33	4.94
Apr 2018	0.94	169.89	4.07	5.85
May 2018	0.54	165.07	3.41	4.94
Jun 2018	0.58	174.50	3.78	5.21
Jul 2018	0.54	188.83	3.60	5.12
Aug 2018	0.53	113.00	3.93	5.48
Sep 2018	0.65	117.70	4.15	5.79
Oct 2018	0.68	149.75	3.53	4.98
Nov 2018	0.63	193.43	3.23	4.63
Dec 2018	0.53	156.26	3.02	4.33
Jan 2019	0.65	182.67	3.29	4.62
Feb 2019	0.87	141.08	3.77	5.58
Mar 2019	1.18	144.53	4.18	5.76
Apr 2019	0.76	183.73	3.62	5.45
May 2019	0.81	155.95	4.01	5.64
Jun 2019	0.73	153.60	3.99	5.74
Jul 2019	0.75	168.61	4.01	5.62
Aug 2019	0.61	149.58	3.95	5.70
Sep 2019	0.59	127.77	3.78	5.47
Oct 2019	0.53	182.53	3.36	4.61
Nov 2019	0.69	228.72	3.35	4.69

### C. Shoreline extraction and smoothing process

The definition of the shoreline position was carried out using the extraction system SHOREX as described by Cabezas-Rabadán *et al.* (2021). It is a tool developed by CGAT – UPV intended to allow the automatic download and pre-processing of the satellite images. A manual checking enabled discarding those images affected by significant cloud coverage over the coast prior to the georeferencing of the useful images using a orthorectified aerial photography. From the resulting images, the shoreline positions (Satellite-Derived Shorelines, SDS) were automatically defined as the water/land intersection in a polyline format. This definition was carried out at the subpixel level by applying the algorithm proposed in Pardo-Pascual *et al.* (2012). This solution was applied over the Short-Wave Infrared bands (SWIR1) using a third-degree polynomial, and 3x3 analysis kernel. According to previous assessments at micro-tidal beaches, the resulting SDS is expected to offer an accuracy of 3-4 m RMSE (Sánchez-García *et al.*, 2020).

A smoothing process was applied over each of the resulting shorelines (Figure 3). In order to do so, the Polynomial Approximation with Exponential Kernel (PAEK) is applied in Python allowing to obtain a smoothed shoreline that may have more vertices than the original one.



Figure 3. Satellite-derived shoreline from Sentinel-2 (red colour, 2075.39 m length) and the shoreline resulting from applying the smoothing process (yellow, 2019.09 m).

### D. Definition of the Sinuosity Index

For each of the resulting polylines, the Sinuosity Index (SI) was obtained as the length of the smoothed SDS divided by the length of the simplified definition of the coastal shape (Figure 4). Thus, values close to 1 indicated a straight shoreline, while values far from 1 were associated with a more sinuous and undulating shoreline.



Figure 4. Definition of the sinuosity index for a certain SDS (pink, 1081.85 m length). The black line is a simplified definition of the coastal shape (1054.44 m). The SI (0.97) is obtained as the division of both lengths.

## IV. RESULTS

The shoreline positions were extracted at 83 different instants and, after applying the smoothing process, the resulting lines were used to define the shoreline sinuosity index as a representative value of the occurrence of mesoforms on Cala de Mijas. This smoothing process is a necessary step so that the results can be processed metrically. Furthermore, it allows to remove the inflections associated with sub-pixel extraction, that on several occasions offered unrealistic results for describing the morphology of the shore (Figure 5).



Figure 5. Example of the different level of undulations recorded by the shoreline position. This is the case on the days 10/12/2018 (in green colour, SI=0.993) and 28/07/2018 (red colour, SI=0.955).

When analysing the temporal evolution of the SI, a series of variations appear over time, between values

close to 0.955 and 0.994 (Figure 6). It is also noteworthy that large variations sometimes are registered between very close dates. Regarding the mid-term oscillations, there is no clearly defined seasonality in them. However, it is striking that the minimum annual SI values are recorded during the summer months. Thus, in 2018 a minimum SI value of 0.955 is reached on the 28<sup>th</sup> of July (the minimum of the series), while in 2019 the minimum SI value (0.962) appears on the 18<sup>th</sup> of July. Thus, during certain dates of the summer months, the shoreline would be registering a more marked undulating pattern. On the other hand, the higher values of SI, related to a more rectilinear shoreline morphology, follow a less homogeneous distribution. Thus, in 2018 the maximum SI value (0.993) was recorded on 10 December, followed by other dates during winter and autumn. Similarly, in 2019 the maximum SI value (0.991) was recorded in autumn, followed by other dates during winter.

Since the morphology of the beach is to some extent determined by the wave conditions it can be assumed that there will be a relationship between the SI value of a given date and the wave values recorded nearby. As we do not know which period should be taken into consideration for this analysis in this first approach to the problem we have only tried to detect which wave parameters may be playing a more significant role. Thus, an analysis was carried out in an attempt to establish relationships between wave height, direction, and period on a monthly scale. For this analysis, the

monthly average SI was also defined, and the months with less than two SDS (and therefore SI values) were discarded (Figure 7). A statistically rather low relationship appeared between the SI values and the wave characteristics averaged over each of the months and treated individually. Still, it is noticeable how the monthly wave mean peak period does describe a pattern of changes that is to some extent the inverse of the SI, reaching a correlation of  $r = -0.38$ .

## V. DISCUSSION

The present work is a preliminary study of the application of satellite-derived shorelines with sub-pixel precision for the recognition of mesoscale features on the emerged beach. The results show that the SDSs enable characterising the rhythmic undulations on the beach at the land-water interface, demonstrating its usefulness in providing information on the beach cusps.

The SI values show how during certain dates of the summer months the shoreline would be registering a more marked undulatory pattern that would be associated with the presence of mesoforms on the emerged beach such as beach cusps. The joint analysis with the wave conditions registered in the area prior to the definition of the shoreline position shows how these more pronounced wave patterns are associated with periods of higher  $T_p$ .

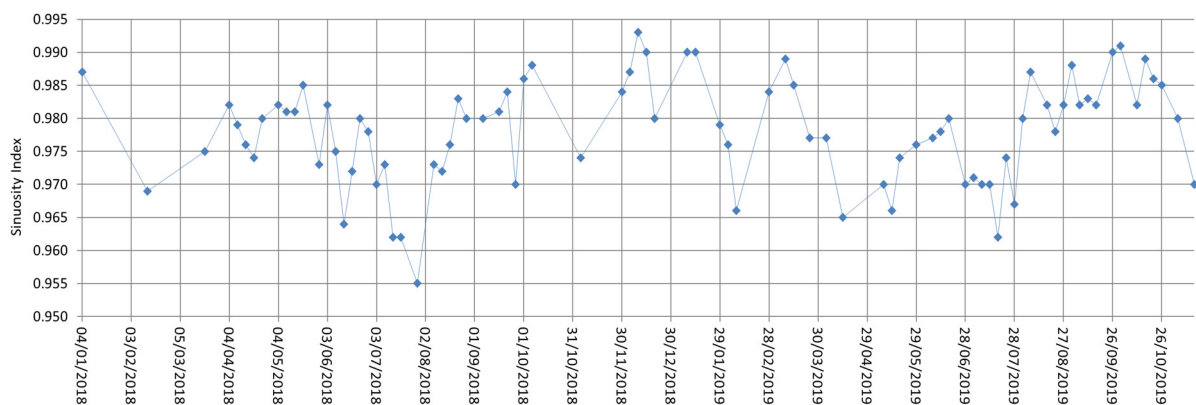


Figure 6. Evolution of the sinuosity index along time in Cala de Mijas.

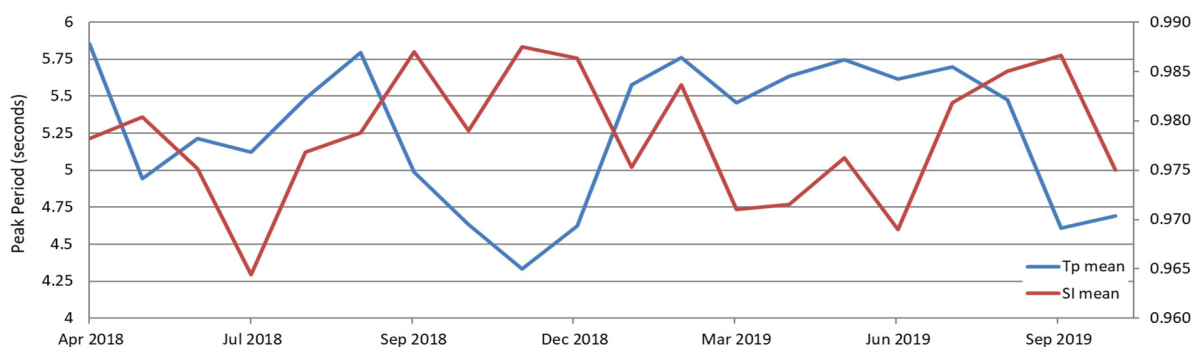


Figure 7. Relationship between the average monthly Sinuosity Index (red colour) and the monthly wave mean peak period (blue). Only those months with more than one SDS measurement have been considered.

These differences could be caused by to the presence of westerlies winds and the associated change in wave direction contrary to the eastern winds and the associated wave regime. Together with the simplicity of the preliminary analysis performed, the low correlation between the wave characteristics and the SI is largely caused by the multitude of oceanographic and geomorphological factors that may affect the formation of the coastal mesoforms. This is for example one of the reasons why is still unclear the role of the different parameters controlling the formation of beach cusps (Vousdoukas, 2012). While its origin may be linked to different wave characteristics, certain breaker types appear correlated with them (Coco *et al.*, 1999), which would enhance the importance of the beach morphological conditions prior to the SDS definition.

At this point, it is necessary to investigate further what morphological reality these SDS inflections are representing, as well as the utilization of other parameters more representative of the mesoforms than the SI. The alongshore oscillations may in part be a reflection of the three-dimensional morphology of the beach in the beachface zone. This morphology would define successive shoreline incurvations along the shore as a result of the position maintained by the total water level (TWL) over time. However, previous works have highlighted the impact that swash and foaming phenomena can have on the definition of the shoreline, both SHOREX (Cabezas-Rabadán *et al.*, 2020; Pardo-Pascual *et al.*, 2018) and other extraction tools. (Castelle *et al.*, 2021; Hagenaaers *et al.*, 2018). Thus, the inflections defined by the SDS could respond exclusively to spatial oscillations of the TWL, but also the maximum position reached by the swash. Thus, in addition to the morphological conditions of the emerged beach, the defined position of the shoreline would also be greatly affected by the specific wave conditions and the morphology of the submerged beach, which determine the wave breaking and the space covered during the swash processes.

Future analyses should be aimed at establishing relationships between shoreline morphology and hydrodynamic conditions using different representative parameters, as well as focusing the analysis on different spatial and temporal scales. With respect to beach morphology, the advance and retreat of the mean position of the shore, as well as its change of orientation, can play an essential role in the formation or maintenance of undulating forms. This analysis could be supported not only by the Sentinel-2 satellite presented in this work but also by the Landsat-8 and Landsat-9 satellites (the latter recently available), which would greatly increase the amount of data available over time, observing fields on more detailed time scales. Similarly, the characteristics of sediment and bottom morphology (bars) varying along the coastline are essential in the occurrence of this type of oscillating mesoforms on the shore. A correct characterisation of these elements along the coastline and an analysis

divided into different segments according to their nature can help to better understand the interrelationships with oceanographic features. This analysis, by narrowing down the studied coastal segment, is especially relevant on this coast where the prevailing drift currents, which can greatly condition the morphology of the beach phase, may change very abruptly between sectors (Molina *et al.*, 2019).

## VI. CONCLUSIONS

The present work is a first step towards the application of satellite-derived shorelines with sub-pixel precision for the study and monitoring of mesoscale features. The results of this work allow us to observe that the SDS clearly localise the existence of rhythmic waves on the beach and therefore demonstrate that they can be very useful for monitoring them.

The relationship observed with the wave regime, although statistically low, seems to indicate the existence of this logical relationship, with waves being the main modulator of the morphology of this coastal segment. The role of the different factors in the formation of beach cusps is not yet clear, so providing more information on their spatial and temporal evolution may be of great interest in this field.

Analysing the influence of these factors recorded over different periods may provide clues as to their influence on the behaviour of Mediterranean beaches such as the one presented in this paper.

## VII. ACKNOWLEDGEMENTS

This research is supported by the MONOBESAT project (PID2019-111435RB-I00) funded by the Spanish Ministry of Science, Innovation, and Universities, and the Margarita Salas contract within the Re-qualification programme by the Ministry of Universities financed by the European Union – NextGenerationEU to the corresponding author.

The authors acknowledge the European Space Agency for the access to the Sentinel-2 images and Puertos del Estado for the oceanographic data.

Authors want to thank the role of the CEDEX technicians, specially to José Francisco Sánchez González.

## References

- Almeida, L. P., de Oliveira, I. E., Lyra, R., Dazzi, R. L. S., Martins, V. G., and da Fontoura Klein, A. H. (2021). Coastal analyst system from space imagery engine (CASSIE): shoreline management module. *Environmental Modelling & Software*, 140, 1050
- Boak, E. H., and Turner, I. L. (2005). Shoreline definition and detection: a review. *Journal of coastal research*, 21(4), 688-703.33.
- Cabezas-Rabadán, C., Pardo-Pascual, J. E., and Palomar-Vázquez, J. (2021). Characterizing the Relationship between the Sediment Grain Size and the Shoreline

- Variability Defined from Sentinel-2 Derived Shorelines. *Remote Sensing*, 13(14), 2829
- Cabezas-Rabadán, C., Pardo-Pascual, J. E., Palomar-Vázquez, J., Ferreira, Ó., and Costas, S. (2020). Satellite derived shorelines at an exposed meso-tidal beach. *Journal of Coastal Research*, 95(SI), pp. 1027-1031.
- Cabezas-Rabadán, C., Pardo-Pascual, J. E., Palomar-Vázquez, J., and Fernández-Sarría, A. (2019a). Characterizing beach changes using high-frequency Sentinel-2 derived shorelines on the Valencian coast (Spanish Mediterranean). *Science of the Total Environment*, 691, pp. 216-231.
- Cabezas-Rabadán, C., Pardo-Pascual, J. E., Almonacid-Caballer, J., and Rodilla, M. (2019b). Detecting problematic beach widths for the recreational function along the Gulf of Valencia (Spain) from Landsat 8 subpixel shorelines. *Applied Geography*, 110, 102047.
- Cabezas-Rabadán, C., Pardo-Pascual, J. E., Almonacid-Caballer, J., Palomar-Vázquez, J., and Fernández-Sarría, A. (2019c). Monitorizando la respuesta de playas mediterráneas a temporales y actuaciones antrópicas mediante imágenes Landsat. *Geofocus: Revista Internacional de Ciencia y Tecnología de la Información Geográfica*, (23), pp. 119-139.
- Castelle, B., Masselink, G., Scott, T., Stokes, C., Konstantinou, A., Marieu, V., and Bujan, S. (2021). Satellite-derived shoreline detection at a high-energy meso-macrotidal beach. *Geomorphology*, 383, 107707.
- Coco, G.; O'hare, T.J.; Huntley, D.A. (1999) Beach Cusps: A Comparison of Data and Theories for Their Formation. *Source J. Coast. Res. J. Coast. Res.*, 15, pp. 741–749.
- Cooper, A. (2022). Response of natural, modified and artificial sandy beaches to sea-level rise. *Cuadernos de Investigación Geográfica*, 15. DOI: 10.18172/cig.5184
- Guisado-Pintado, E., Navas, F., Malvárez, G. (2016). Ecosystem Services and Their Benefits as Coastal Protection in Highly Urbanised Environments. *Journal of Coastal Research*, 75(sp1), pp. 1097–1101.
- Hagenaars, G., de Vries, S., Luijendijk, A. P., de Boer, W. P., and Reniers, A. J. (2018). On the accuracy of automated shoreline detection derived from satellite imagery: A case study of the sand motor mega-scale nourishment. *Coastal Engineering*, 133, pp. 113-125
- Hansen, J. E., and Barnard, P. L. (2010). Sub-weekly to interannual variability of a high-energy shoreline. *Coastal Engineering*, 57(11–12), pp. 959–972. Elsevier B.V. Retrieved from DOI: 10.1016/j.coastaleng.2010.05.011
- Holland, K. T. (1998). Beach cusp formation and spacings at Duck, USA. *Continental Shelf Research*, 18(10), pp. 1081-1098
- Konlechner, T. M., Kennedy, D. M., O'Grady, J. J., Leach, C., Ranasinghe, R., Carvalho, R. C., and Ierodiaconou, D. (2020). Mapping spatial variability in shoreline change hotspots from satellite data; a case study in southeast Australia. *Estuarine, coastal and shelf science*, 246, 107018.
- Kuriyama, Y., Banno, M., and Suzuki, T. (2012). Linkages among interannual variations of shoreline, wave and climate at Hasaki, Japan. *Geophysical Research Letters*, 39(6).
- Liu, Q., Trinder, J. C., and Turner, I. L. (2017). Automatic super-resolution shoreline change monitoring using Landsat archival data: A case study at Narrabeen–Collaroy Beach, Australia. *Journal of Applied Remote Sensing*, 11(1), 016036.
- Malvarez, G., and Navas, F. (2019). *Lineal Sandy Coasts and Beaches of Málaga: Andalusian Mediterranean Coast*. In *The Spanish Coastal Systems* (pp. 289-310). Springer, Cham.
- Molina, R., Anfuso, G., Manno, G., and Gracia Prieto, F. J. (2019). The Mediterranean coast of Andalusia (Spain): Medium-term evolution and impacts of coastal structures. *Sustainability*, 11(13), 3539.
- Montes, J., Simarro, G., Benavente, J., Plomaritis, T. A., and Del Río, L. (2018). Morphodynamics assessment by means of mesoforms and video-monitoring in a dissipative beach. *Geosciences*, 8(12), 448.
- Palomar-Vázquez, J., Almonacid-Caballer, J., Pardo-Pascual, J.E., and Cabezas-Rabadán, C. (2021). Shoreline Analysis and Extraction Tool, SAET V 1.0. Open source code. Universitat Politècnica de València, <http://www.upv.es/es>. Deliverable 3.2 - Algorithms for satellite derived shoreline mapping and shorelines dataset, ECFAS project (GA 101004211), [www.ecfas.eu](http://www.ecfas.eu). Zenodo. DOI: 10.5281/zenodo.5807711
- Pardo-Pascual, J.E., Almonacid-Caballer, J., Ruiz, L.A., Palomar-Vázquez, J. (2012). Automatic extraction of shorelines from Landsat TM and ETM+ multi-temporal images with subpixel precision. *Remote Sens. Environ.* 123, pp. 1–11. DOI: 10.1016/j.rse.2012.02.024
- Pardo-Pascual, J.E., Palomar-Vázquez, J.M., Cabezas-Rabadán, C., Almonacid-Caballer, J., Fernández-Sarría, A., Ruiz, L.A., Souto-Ceccon, P.E., and Montes-Perez, J. (2021). Shorelines dataset. Deliverable 3.2 - Algorithms for satellite derived shoreline mapping and shorelines dataset, ECFAS project (GA 101004211), [www.ecfas.eu](http://www.ecfas.eu). [Data set]. Zenodo. DOI: 10.5281/zenodo.5807713
- Pardo-Pascual, J. E., Sánchez-García, E., Almonacid-Caballer, J., Palomar-Vázquez, J. M., Priego De Los Santos, E., Fernández-Sarría, A., and Balaguer-Beser, Á. (2018). Assessing the accuracy of automatically extracted shorelines on microtidal beaches from Landsat 7, Landsat 8 and Sentinel-2 imagery. *Remote Sensing*, 10(2), 326.
- Pranzini, E., Pezzini, G., Anfuso, G., and Botero, C. M. (2018). Beach safety management. In *Beach Management Tools- Concepts, Methodologies and Case Studies* (pp. 397-420). Springer, Cham.
- Pranzini, E., Rossi, L., Lami, G., Jackson, N. L., and Nordstrom, K. F. (2018). Reshaping beach morphology by modifying offshore breakwaters. *Ocean & Coastal Management*, 154, pp. 168-177. Sallenger Jr, A. H. (1979). Beach-cusp formation. *Marine Geology*, 29(1-4), pp. 23-37.
- Sánchez-García, E.; Palomar-Vázquez, J.; Pardo-Pascual, J.; Almonacid-Caballer, J.; Cabezas-Rabadán, C.; Gómez-Pujol, L. (2020). An efficient protocol for accurate and massive shoreline definition from mid-resolution satellite imagery. *Coast. Eng.*, 160, 103732
- Schwartz, M. (Ed.). (2006). *Encyclopedia of coastal science*. Springer Science & Business Media.
- Senechal, N., Coco, G., Castelle, B., and Marieu, V. (2015). Storm impact on the seasonal shoreline dynamics of a meso- to macrotidal open sandy beach (Biscarrosse, France). *Geomorphology*, 228, pp. 448–461. Elsevier.
- Silva-Cavalcanti, J. S., Costa, M. F., and Pereira, P. S. (2018). Rip currents signaling and users behaviour at an

overcrowded urban beach. *Ocean & Coastal Management*, 155, 90-97.

Vos, K., Splinter, K. D., Harley, M. D., Simmons, J. A., and Turner, I. L. (2019). CoastSat: A Google Earth Engine-enabled Python toolkit to extract shorelines from publicly available satellite imagery. *Environmental Modelling & Software*, 122, 104528.

Vousdoukas, M. I. (2012). Erosion/accretion patterns and multiple beach cusp systems on a meso-tidal, steeply-sloping beach. *Geomorphology*, 141, 34-46.



## Design, establishment, analysis and quality control of a high-precision reference frame in Cortes de Pallás (Spain)

Luis García-Asenjo<sup>1</sup>, Laura Martínez<sup>2</sup>, Sergio Baselga<sup>1</sup>, Pascual Garrigues<sup>1</sup>, Raquel Luján<sup>1</sup>

<sup>1</sup> Department of Cartographic Engineering, Geodesy and Photogrammetry, Universitat Politècnica de València, Camino de Vera s/n, 46022 Valencia, Spain ([lugarcia@cgf.upv.es](mailto:lugarcia@cgf.upv.es); [serbamo@cgf.upv.es](mailto:serbamo@cgf.upv.es); [pasgarta@cgf.upv.es](mailto:pasgarta@cgf.upv.es); [ralugar@cgf.upv.es](mailto:ralugar@cgf.upv.es))

<sup>2</sup> Department of Roads and Infrastructures, Diputació de València, c/ Hugo de Moncada, 9, 46010 Valencia, Spain, ([laura.martinez@dival.es](mailto:laura.martinez@dival.es))

**Key words:** *geodetic network; reference frames; deformation monitoring; sub-millimetric EDM; ME5000; length metrology*

### ABSTRACT

A high-precision geodetic reference frame was required in Cortes de Pallás (Spain) to undertake a long-term deformation monitoring project. Involving distances up to 2000 m, the aimed accuracy was 1 mm and 3 mm for horizontal and vertical components, respectively. Such a high precision is necessary to detect possible displacements of selected points on a critical rocky area in a short period of time, *i.e.* two or three years, and also to provide ground control for the integration of precise 3D models periodically obtained by remote sensing techniques. Considering the historical geotechnical problems of the area, the possible influence of the hydroelectric power plant, and the peculiar orography of the zone, a proper analysis of the stability is crucial if the reference frame is to be used for rigorous over-time deformation monitoring. This paper describes the deformation monitoring of a 10-pillar geodetic network which was measured from 2018 to 2020 by using a sub-millimetric Mekometer ME5000 (0.2 mm + 0.2 ppm) along with a demanding observing methodology which includes a network of data loggers for temperature, humidity and air pressure as well as proper calibration of sensors and instruments to prevent potential inconsistencies between the scale of the network and the unit of length of the International System (SI-metre). The results demonstrated that the chosen methodology yielded the aimed accuracy. However, using such a high precision methodology entails the problem that small displacements of only one or two millimeters are significantly detected as deformations by conventional deformation analysis and then it arises the problem of finding a subset of stable points for a rigorous datum realization when all the points seem to displace. This general problem is analyzed in the particular case of Cortes de Pallás, where a balanced mix of deformation analysis and technical decisions was eventually adopted to define a precise and stable reference frame for rigorous over-time deformation monitoring.

*This contribution was selected by the Scientific Committee for publication as an extended paper in Applied Geomatics <https://www.springer.com/journal/12518>*

## BIM approach applied to urban tunneling interferences

Marco Trani<sup>1</sup>, [Silvia Longo](mailto:silvia1.longo@mail.polimi.it)<sup>1</sup>, Monica Conti<sup>2</sup>

<sup>1</sup> Department of Architecture, Built Environment and Construction Engineering, Politecnico di Milano, Milan, Italy, ([marco.trani@polimi.it](mailto:marco.trani@polimi.it); [silvia1.longo@mail.polimi.it](mailto:silvia1.longo@mail.polimi.it))

<sup>2</sup> Direzione Construction Management, MM S.p.A., Milan, Italy, ([m.conti@mmspa.eu](mailto:m.conti@mmspa.eu))

**Key words:** *BIM; urban tunneling; interference management; TBM machine; monitoring*

### ABSTRACT

Interferences management induced on buildings during underground works -including the excavation of a metro tunnel- is a topic that must be carefully studied and analysed. The paper provides a proposal for the creation of a BIM model by which it is possible to control, over time, the influencing parameters, to visualize subsidence values and foreseen harmful events for building falling in the subsidence basin of an excavation machine. The method is based on the creation of a model which allows to graphically monitor the subsidence to which the buildings may be subjected through the attribution of predefined thresholds. In the same way, in the model, the parameters linked to the excavation machine itself are also checked. This control is useful to predict the formation of chimneys that could damage buildings structures and façades. To import all the data in the 3D model, specific scripts have been written using the software Dynamo, to semi-automatically connect an Excel file with a Revit model. This method will be then applied to a specific case study, a portion of the central section of the new M4 metro line in Milan, built with EPB type TBM machines. To provide indications of the measures to be adopted if the different thresholds are reached, guidelines for interference management are subsequently proposed. The conclusion of the paper shows how the model, together with the guidelines, with the necessary implementations and modifications, is to be considered valid for the management of the same topic in other works.

*This contribution was selected by the Scientific Committee for publication as an extended paper in Applied Geomatics <https://www.springer.com/journal/12518>*

## Imaging land subsidence in the Guadalentín River Basin (SE Spain) using Advanced Differential SAR Interferometry

Guadalupe Bru<sup>1</sup>, Juan J. Portela<sup>2</sup>, Pablo Ezquerro<sup>1</sup>, M. Inés Navarro<sup>3</sup>, Alejandra Staller<sup>2</sup>,  
Marta Béjar-Pizarro<sup>1</sup>, Carolina Guardiola-Albert<sup>1</sup>, José A. Fernández-Merodo<sup>1</sup>,  
Juan López-Vinielles<sup>1</sup>, Roberto Tomás<sup>3</sup>, Juan M. López-Sánchez<sup>4</sup>

<sup>1</sup> Instituto Geológico y Minero de España (IGME, CSIC). Calle de Ríos Rosas 23, 28003 Madrid, Spain, ([g.bru@igme.es](mailto:g.bru@igme.es); [p.ezquerro@igme.es](mailto:p.ezquerro@igme.es); [c.guardiola@igme.es](mailto:c.guardiola@igme.es); [m.bejar@igme.es](mailto:m.bejar@igme.es); [jose.fernandez@igme.es](mailto:jose.fernandez@igme.es); [j.lopez@igme.es](mailto:j.lopez@igme.es))

<sup>2</sup> Universidad Politécnica de Madrid, RG Terra: Geomatics, Natural Hazards and Risks, C/ Mercator 2, 28031 Madrid, Spain, ([jj.portela@upm.es](mailto:jj.portela@upm.es); [a.staller@upm.es](mailto:a.staller@upm.es))

<sup>3</sup> Departamento de Ingeniería Civil, Universidad de Alicante, Carr. de San Vicente del Raspeig s/n, 03690 San Vicente del Raspeig, Spain, ([mainnahe@ua.es](mailto:mainnahe@ua.es); [roberto.tomas@ua.es](mailto:roberto.tomas@ua.es))

<sup>4</sup> Instituto Universitario de Investigación Informática, Universidad de Alicante, Carr. de San Vicente del Raspeig s/n, 03690 San Vicente del Raspeig, Spain, ([juanma.lopez@ua.es](mailto:juanma.lopez@ua.es))

**Key words:** *aquifer overexploitation; subsidence; P-SBAS; GNSS; Guadalentín River Basin*

### ABSTRACT

Aquifer overexploitation can lead to the irreversible loss of groundwater storage caused by the compaction or consolidation of unconsolidated fine-grained sediments resulting in land subsidence. Advanced Differential SAR Interferometry (A-DInSAR) is particularly efficient to monitor progressive ground movements, making it an appropriate method to study depleting aquifers undergoing overexploitation and land subsidence. The Guadalentín River Basin (Murcia, Spain) is a widely recognized subsiding area that exhibits the highest rates of groundwater-related land subsidence recorded in Europe (>10 cm/yr). The basin covers an extension of more than 500 km<sup>2</sup> and is underlain by an overexploited aquifer-system formed by two contiguous hydraulically connected units (Alto Guadalentín and Bajo Guadalentín). Although during the last years the piezometric levels have partially stabilized, the ongoing aquifer-system deformation is evident and significant, as revealed by the A-DInSAR analysis presented. In this work, we submit the first vertical and horizontal (E-W) decomposition results of the LOS velocity and displacement time series of the whole Guadalentín Basin obtained from two datasets of Sentinel-1 SAR acquisitions in ascending and descending modes. The images cover the period from 2015 to 2021 and they were processed using the Parallel Small Baseline Subset (P-SBAS) implemented by CNR-IREA in the Geohazards Exploitation Platform (GEP) on-demand web tool, which is funded by the European Space Agency. The output ascending and descending measurement points of P-SBAS lie on the same regular grid, which is particularly suited for the geometrical decomposition. Time series displacements are compared to a permanent GNSS station located in the Bajo Guadalentín basin.

### 1. INTRODUCTION

Aquifer overexploitation can lead to the irreversible loss of groundwater storage caused by the compaction or consolidation of unconsolidated fine-grained sediments, resulting in land subsidence. The displacement is mainly downward, though associated horizontal deformation often has significant damaging effects (Galloway and Burbey, 2011). Advanced Differential SAR Interferometry (A-DInSAR) is particularly efficient to monitor progressive ground movements, making it an appropriate method to study depleting aquifers undergoing overexploitation and land subsidence. Traditionally, in land subsidence studies it was assumed that the ground surface deformation obtained from A-DInSAR corresponds only to vertical deformation, but the availability of ascending and descending SAR satellites orbits allows

decomposing the LOS mean velocity and displacements into vertical and east-west components. The north-south remains unknown due to the quasi polar orbit of the satellites (Cigna and Tapete, 2021a; Fernandez *et al.*, 2018).

The Guadalentín River Basin (Murcia, Spain) is a widely recognized subsiding area that exhibits the highest rates of groundwater-related land subsidence recorded in Europe, reaching values over 10 cm/yr (González and Fernández, 2011). There are several studies that have used multi-sensor SAR images from ERS, ENVISAT, ALOS, Cosmo-SkyMed (CSK) and Sentinel-1 (S-1) satellites combined with GNSS measurements to study land subsidence in this area, however most of them have focused in the Alto Guadalentín aquifer (Béjar-Pizarro *et al.*, 2016; Boni *et al.*, 2015; Ezquerro *et al.*, 2020; Fernandez *et al.*, 2018). In this work, we have measured land subsidence of the

whole Guadalentín Basin for the 2015-2021 period using S-1 data, and we have produced, for the first time, a vertical and horizontal (E-W) deformation map of the entire basin, calculated from ascending and descending orbit geometry decomposition. The A-DInSAR processing has been run in a cloud computing server, the Geohazards Exploitation Platform (GEP).

The deformation results have been validated with GNSS data, by projecting the three components into the ascending and descending geometry, and have been compared to previous studies.

## II. STUDY AREA

The Guadalentín River Basin is located in the province of Murcia (SE Spain) within a NE-SW elongated alpine orogenic tectonic depression of the Betic Cordillera. It has an extension of more than 500 km<sup>2</sup> and underneath there is an overexploited aquifer-system formed by two contiguous hydraulically connected units: Alto Guadalentín and Bajo Guadalentín aquifers (Figure 1). The basement of the basin is formed by Paleozoic metamorphic rocks with a horst and graben pattern, overlined by Miocene detrital deposits of conglomerates and calcarenites. The top of the sequence is constituted by Plio-Quaternary detrital and alluvial materials (*i.e.* conglomerates, sand, silt, and clay) deposited by the Guadalentín ephemeral river (Cerón and Pulido-Bosch, 1996). In some areas of the basin the Plio-Quaternary layer can be split into two sublayers: compressible soft soils in the upper most part and coarse fraction materials at the bottom (Béjar-Pizarro *et al.*, 2016; Boni *et al.*, 2015). The coarse fraction of the Plio-Quaternary and the upper part of the Miocene are permeable. Therefore, the aquifer system can be considered as unconfined, consisting of two zones, an upper free layer and a lower layer semi-confined by the upper one and with the possibility of changing its state depending on the position of the piezometric surface (CHS, 2005). Nowadays, the Plio-Quaternary unconfined aquifer zone is almost drained, being the semi-confined Miocene the most productive zone.

The absence of permanent watercourses or positive transferences from other aquifer-systems makes the Guadalentín aquifer recharge almost limited to rainfall and watering returns (Ezquerro *et al.*, 2017). Considering the semi-arid climate of the region, with average annual precipitation of less than 250 mm for the last 20 years, it can be stated that the lowering of the groundwater level is strongly dependent on the extractions. The aquifer system has been extensively exploited for agricultural irrigation since the 1960's, causing an spatially heterogeneous decline in the aquifer-system levels of about 200 m in 50 years (Boni *et al.*, 2015). The aquifer was declared officially overexploited in 1987 (IGME, 1997) and currently is in a state of quantitative disrepair due to overexploitation (CHS, 2021). Previous studies have established that

there is relationship between groundwater changes and land subsidence on the entire Guadalentín aquifer-system (González and Fernández, 2011; Rigo *et al.*, 2013) and on the Alto Guadalentín basin (Boni *et al.*, 2015; Ezquerro *et al.*, 2017; Ezquerro *et al.*, 2020; Fernández-Merodo *et al.*, 2021; Fernandez *et al.*, 2018).

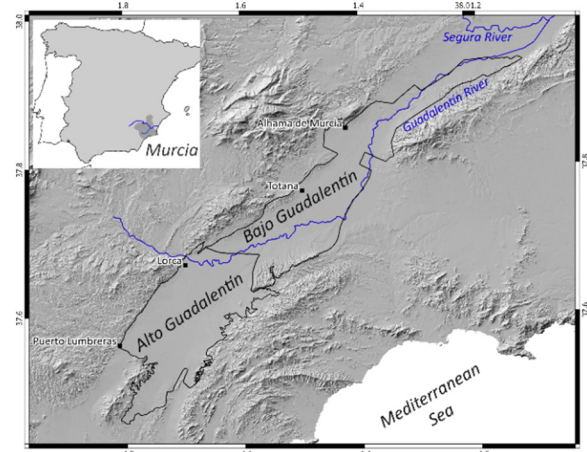


Figure 1. Location of the study area. Aquifers borders, rivers and main municipalities are shown.

## III. MATERIALS AND DATA

### A. SAR data and A-DInSAR processing

The S-1 mission from the European Space Agency (ESA) comprises a constellation of two polar-orbiting SAR satellites operating at C-band. In this study, two S-1 datasets acquired between March 2015 and June 2021 in ascending and descending orbit modes were used (Table 1). The minimum revisit period of the constellation over the site is 6 days. We selected 182 S-1 SAR images in ascending mode and 176 in descending, with an average frequency of 12 days.

Table 1. A-DInSAR data parameters

Data	Parameters	
	Ascending	Descending
Orbit mode	Ascending	Descending
Track	103	8
Number of images	182	176
Initial date	2015-03-05	2015-02-27
End date	2021-06-07	2021-06-07
DS per km <sup>2</sup>	150	150
LOS velocity range [cm/yr]	-7.3 to 1.6	-6.9 to 1.9
LOS velocity standard deviation	0.58	0.52

The multitemporal A-DInSAR analysis was performed using the Parallel computing solution of the Small Baseline Subset (P-SBAS) approach (Berardino *et al.*, 2002; Casu *et al.*, 2014; Manunta *et al.*, 2019) which was run in GEP (Foumelis *et al.*, 2019). The GEP is an on-demand web service funded by ESA, where A-DInSAR algorithms and computational resources are located together with the SAR data archives (De Luca *et al.*, 2015). Most of the parameters of the processing are settled automatically and have proven suitable in other land subsidence studies (Cigna and Tapete, 2021b). The

P-SBAS utilizes a small baseline interferogram arrangement, where a dense network is created linking multiple SAR images (Multi-master). It is a coherence-based method suited to Distributed Scatters (DS), *i.e.*, terrain patches whose scatter properties are not altered with time. The coherence estimation requires a spatial average within a two-dimension window, usually named as multilook (ML), which allows to reduce noise at the expenses of a spatial resolution loss (Mestre-Quereda *et al.*, 2018). P-SBAS applies a ML of  $5 \times 20$  (azimuth  $\times$  range) which generates DS of approximately  $90 \times 90$  m size. The coherence threshold limits the selection of pixels above the specified coherence value, which was set to 0.70. The reference point was placed in the stable mountainous areas that surround the basin, although the algorithm automatically refines it and selects the one with best coherence conditions close to the one selected by the user. Moreover, at the end of the processing, the algorithm implements an average reference on the whole scene to avoid the dependence to one single point. The P-SBAS outputs for the individual S-1 ascending and descending processing were two data points or DS maps (Figure 2). Each data point contains geographical location, mean LOS velocity, LOS displacement time series, and the components of LOS unit vector along the north, east and vertical directions. These unit vectors depend on the ground track of the satellite flight direction and on the radar antenna incidence angle, which varies from the near to the far range of the SAR scene. Both datasets were cropped to an area of interest of 3,000 km<sup>2</sup> that covers completely the Guadalentín River Basin and contains a point density of 150 DS per km<sup>2</sup> in the two of them. The mean LOS velocities range from -7.3 to 1.6 cm/yr for the ascending orbit dataset and from -6.9 to 1.9 cm/yr for the descending orbit dataset. Negative and positive values indicate movement away and towards the satellite, respectively. The time series LOS displacement trends in Alto Guadalentín maximum deformation areas, both in ascending and descending orbit, are linear. The piezometric levels in this area have remained stable since 2009, with slight seasonal variations as a consequence of the rainfall regime and the irrigation seasons (CHS, 2021). In Bajo Guadalentín the displacement time series also have a linear trend with slight fluctuations in the maximum deformation area near Alhama de Murcia, where the piezometric levels have a deepening tendency since 2008 until the last measures taken in 2019 (CHS, 2021).

#### B. GNSS Data

A permanent GNSS station named ALHA is located within the Bajo Guadalentín Basin (Figure 2). It is installed in the municipality of Alhama de Murcia and belongs to the REGAM regional network (<https://sitmurcia.carm.es/estaciones>). It has been active since 2010. The daily RINEX observation files (GPS+GLONASS) of the ALHA station have been

processed using Bernese 5.2 software (Dach *et al.*, 2015). We performed a static and relative processing (alongside other permanent GNSS stations in the region) to obtain a daily positioning solution referred to the ITRF2014 reference frame. Then, the horizontal tectonic plate movement was subtracted from the GNSS east and north components, after computing the predicted motion in ALHA with the Euler Pole defined for the region (Echeverria *et al.*, 2013). The displacement time series in the three components (*i.e.* east, north and up) for the same time period as the P-SBAS processing are represented in Figure 3. The resulting horizontal velocity is rather small, particularly in the north direction ( $\sim -0.7$  mm/yr) when compared to the east direction ( $\sim 2.3$  mm/yr). The subsiding vertical movement is moderate at this site ( $\sim -3.6$  mm/yr).

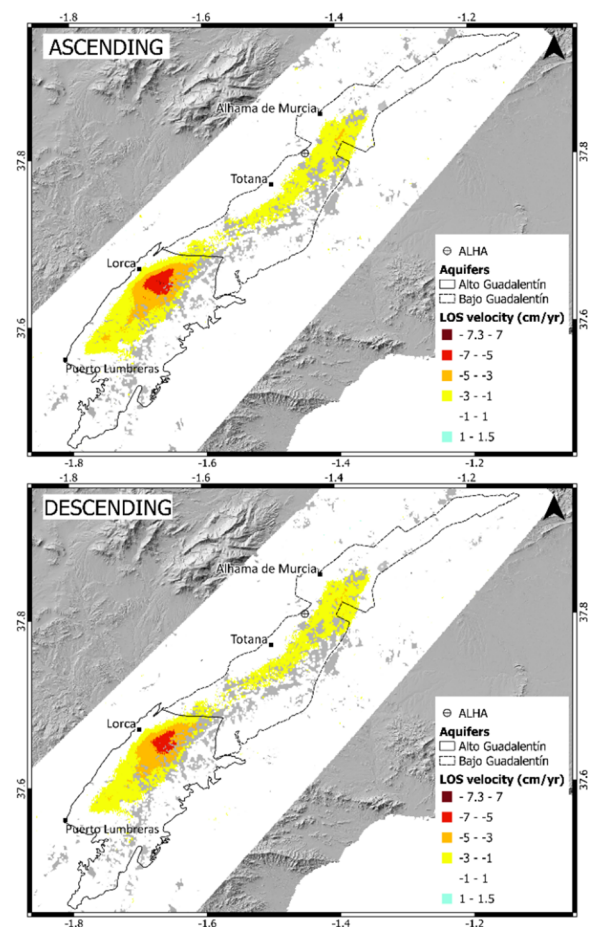


Figure 2. LOS mean velocity maps for the ascending (upper) and descending (bottom) S-1 datasets. Note magnitude is cm/yr.

## IV. METHODS

### A. Vertical and horizontal projection of SAR data

We calculated the 2-D deformation field (eastward and vertical motion) from A-DInSAR results combining the two different viewing geometries of the ascending and descending satellite orbit passes, and assuming that the north component is negligible. This assumption is based on previous GNSS studies (Ezquerro *et al.*, 2020; Fernandez *et al.*, 2018) and on the ALHA station

measurements stated in previous section. The P-SBAS measurement points output lie on the same regular grid, both in ascending and descending datasets, which is particularly suited for the geometrical decomposition. We geographically intersected the DS points and calculated for each of them the vertical and east-west velocity, using Equations 1 and 2 (Béjar-Pizarro *et al.*, 2017). The DS that did not intersect the other orbit were discarded. The calculations were performed with the vector calculator tool of the open source software Q-GIS.

$$V_{east-west} = \frac{\left(\frac{vLOS_d}{H_d} - \frac{vLOS_a}{H_a}\right)}{\frac{E_d}{H_d} - \frac{E_a}{H_a}} \quad (1)$$

$$V_{vertical} = \frac{\left(\frac{vLOS_d}{E_d} - \frac{vLOS_a}{E_a}\right)}{\frac{H_d}{E_d} - \frac{H_a}{E_a}} \quad (2)$$

where  $H_d, H_a$  = vertical directional cosine of descending and ascending LOS unit vector  
 $E_d, E_a$  = East-West directional cosine of descending and ascending LOS unit vector  
 $vLOS_d, vLOS_a$  = mean velocity in the Line Of Sight (LOS) of the descending and ascending satellite orbit modes

### B. Projection of GNSS data in LOS

The GNSS displacement time series were smoothed using a moving average window of 12 days. Then, to compare the displacement time series from both monitoring techniques, we projected the three displacement components of the GNSS data into the ascending and descending LOS vectors using Equation 3.

$$d_{LOS} = d_{E-W} \cdot E + d_{N-S} \cdot N + d_v \cdot H \quad (3)$$

where  $d_{E-W}, d_{N-S}, d_v$  = east-west, north-south and vertical GNSS displacements  
 $E, N, H$  = east-west, north-south and vertical LOS unit vectors at the location of the GNSS station

### C. Validation and comparison methodology

The displacement time series obtained with P-SBAS and GNSS overlap for the whole period. We quantitatively compare the GNSS data projected in both ascending and descending LOS with the corresponding P-SBAS results, by means of the root mean squared error (RMSE) and the relative error, which is the percentage of RMSE with respect to the accumulated deformation, as in Ezquerro *et al.* (2020). The P-SBAS time series are computed as the average of the monitoring points (DS) contained in a 200 m radius buffer around the ALHA GNSS station.

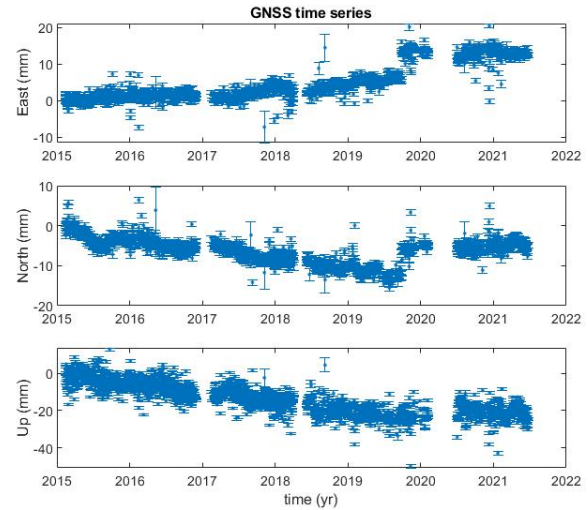


Figure 3. GNSS displacement time series at ALHA permanent station for the east, north and up components during the period 2015-2021. The error bars represent the uncertainties in the position. Note magnitude is mm.

## V. RESULTS

We have retrieved a complete picture of the Guadalentín River Basin spatial deformation for the period 2015-2021 in the vertical and horizontal (E-W) components, by the combination of ascending and descending SAR data (Figure 4). The sign criteria for the vertical component are negative values indicating downlift movement and positive uplift. In the case of the horizontal component, positive values indicate movement towards east and negative towards west. The vertical deformation concentrates along the central part of the Guadalentín valley, reaching up to -8.7 cm/yr in the north-western section of the Alto Guadalentín, near the city of Lorca. The vertical projection highlights an elongated down lift area towards Puerto Lumbreras that was not evident in the LOS mean velocity maps. The Bajo Guadalentín has lower vertical rates, reaching up to -5 cm/yr in the northern part of the Basin, where the industrial park of Alhama de Murcia is located. Horizontal E-W deformation magnitude in the Guadalentín River Basin is much lower than the vertical, ranging between -1.5 and 1.5 cm/yr, which is near the stable magnitude of 0.7 cm/yr considered, based on standard LOS deviation values. It is mainly detected in the left side of the Alto Guadalentín, with direction towards the east. At the right side of the basin, the pixel density is lower due to less temporal coherence and there are scarce DS indicating movement towards west.

Figure 5 plots the averaged ascending and descending P-SBAS time series within a 200 meters buffer from the ALHA station, along with the GNSS time series projected in the ascending and descending LOS geometry (that were previously smoothed and with the horizontal tectonic plate motion removed as explained above). The RMSE and its relative weight regarding the measured deformation (*i.e.* the relative error) were computed for the common epochs between the GNSS and PSBAS time series (see Table 2). The P-SBAS and

GNSS time series trends are relatively consistent in all the dataset, even though the magnitude of the displacement at ALHA station is low and below the stability threshold. Thus, the RMSE of the validation is small (~4 mm for both geometries), but the relative error with respect to the measured movements is high, particularly for the descending geometry (Table 2).

Table 2. RMSE and relative error of the PSBAS-LOS deformation with respect to GNSS LOS-projected deformation in ALHA

Orbit mode	RMSE [mm]	Rel. error [%]
Ascending	4.3	23.4
Descending	3.7	54.0

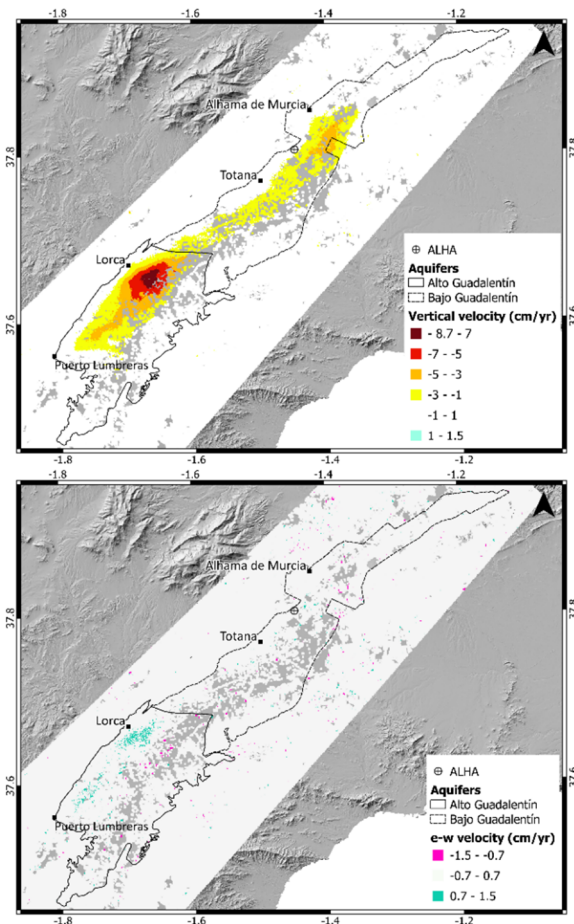


Figure 4. Mean velocity maps for the vertical (upper) and horizontal (bottom) components, projected from the S-1 ascending and descending datasets. Note velocity magnitude is in cm/yr.

## VI. DISCUSSION

The spatial deformation pattern obtained with the P-SBAS algorithm implemented in the GEP is in concordance with previous studies (Bonì *et al.*, 2015; Ezquerro *et al.*, 2020; Fernandez *et al.*, 2018), with maximum deformation areas located in the upper west side of Alto Guadalentín (south of the city of Lorca) and at the east of Alhama de Murcia in the Bajo Guadalentín. In previous works, the linear land subsidence displacements observed in the Alto

Guadalentín until 2016 have been related to the residual compaction of the soft soil (Fernández-Merodo *et al.*, 2021), even though the piezometric levels remained stable. We observe the linear trend pattern in LOS is preserved for the presented studied period. Further investigations are needed to establish the relationship between Bajo Guadalentín land subsidence and piezometric fluctuations. The assumption of negligible north-south displacements is validated by GNSS data from previous studies in Alto Guadalentín for the period 2011-2018 (Ezquerro *et al.*, 2020). The GNSS stations used in that study were located in the maximum deformation area of Alto Guadalentín, whereas in the present study we use a GNSS station located in an area where the magnitude of displacements is very low. Despite this, the north horizontal velocity is rather small (~0.7 mm/yr) when compared to the east direction (~2.3mm/yr), so we considered the premise valid.

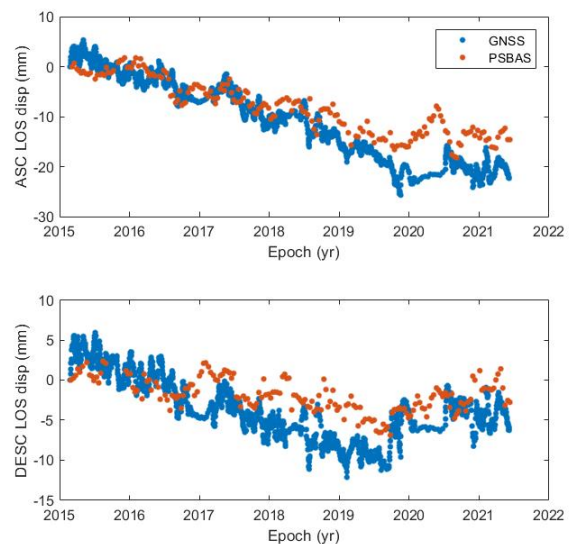


Figure 5. Comparison of the P-SBAS and GNSS time series in the LOS direction, at ALHA station, for ascending and descending orbits. Note displacement magnitude is in mm.

The projected P-SBAS velocities highlight the land subsidence spatial distribution and underscore the significance of horizontal displacements, especially in the Alto Guadalentín where rates are higher. The lower coherence at the right side of the valley can partially mask horizontal movements towards the west. On the contrary, horizontal motion towards east is evident in the right side of Alto Guadalentín where DS density is much higher. The magnitude of the horizontal rates in Alto Guadalentín are in concordance with the observations made by Fernandez *et al.* (2018) by means of GNSS campaigns (0.5–0.9 cm/yr) and S-1 data (1.0–1.5 cm/yr), and by Ezquerro *et al.* (2020) using S-1 and CSK data (0.7–1.5 cm/year), for the periods 2015-2017 and 2011-2016 respectively. Projected vertical velocities of those studies, up to -8 cm/yr and -7 cm/yr correspondingly, are also in the same order of magnitude that the present study.

It has to be considered that the rate of displacement at the ALHA location is below the order of P-SBAS stability threshold, that has been established as twice the standard LOS velocity deviation (1cm/yr). The temporal coherence values of the DS around ALHA station are higher than 0.88, which holds their reliability. The comparison between time series displacement of P-SBAS and GNSS in LOS shows in general a good agreement.

## VII. CONCLUSIONS

This work presents for the first time vertical and horizontal (E-W) decomposition of the LOS velocity and displacement time series over the whole Guadalentín River Basin obtained from two datasets of S-1 SAR acquisitions in ascending and descending modes. The period studied spans for almost six years, from March 2015 to June 2021. The P-SBAS processing has been run in the GEP web service, where all the technical resources are external, which simplifies the processing of big datasets. Although the tool is unsupervised, which means that the processing chains run automatically in the server without user interaction, the P-SBAS results have proven to be robust in the Guadalentín River Basin, where magnitude and spatial distribution of the land subsidence is well known. Future works will include further validation with more GNSS stations located in the valley and other monitoring techniques, such as leveling.

## VIII. ACKNOWLEDGEMENTS

This study has received funding in framework of the RESERVOIR project (Sustainable groundwater RESources management by integrating earth observation derived monitoring and flow modelling Results), funded by the Partnership for Research and Innovation in the Mediterranean Area (PRIMA) programme supported by the European Union (Grant Agreement 1924; <https://reservoir-prima.org/>).

The study has also been supported by the Grant FPU19/03929 (funded by MCIN/AEI/10.13039/501100011033 and by “FSE invests in your future”); the Project CGL2017-83931-C3-3-P (funded by MCIN/ AEI/10.13039/501100011033 and by “ERDF A way of making Europe”); the ESA-MOST China DRAGON-5 Project (ref. 59339) and the SARAI Project PID2020-116540RB-C22 (funded by MCIN/ AEI /10.13039/501100011033).

Copernicus Sentinel-1 IW SAR data were provided and processed in ESA’s Geohazards Exploitation Platform (GEP), in the framework of the GEP Early Adopters Programme.

## References

- Béjar-Pizarro, M., Guardiola-Albert, C., García-Cárdenas, R. P., Herrera, G., Barra, A., López Molina, A., Tessitore, S., Staller, A., Ortega-Becerril, J. A., and García-García, R. P., (2016). Interpolation of GPS and geological data using InSAR deformation maps: Method and application to land subsidence in the alto guadalentín aquifer (SE Spain): *Remote Sensing*, v. 8, no. 11, p. 965.
- Béjar-Pizarro, M., Notti, D., Mateos, R. M., Ezquerro, P., Centolanza, G., Herrera, G., Bru, G., Sanabria, M., Solari, L., and Duro, J., (2017). Mapping vulnerable urban areas affected by slow-moving landslides using Sentinel-1 InSAR data: *Remote Sensing*, v. 9, no. 9, p. 876.
- Berardino, P., Fornaro, G., Lanari, R., and Sansosti, E., (2002). A new algorithm for surface deformation monitoring based on small baseline differential SAR interferograms: *Geoscience and Remote Sensing*, IEEE Transactions on, v. 40, no. 11, pp. 2375-2383.
- Boni, R., Herrera, G., Meisina, C., Notti, D., Béjar-Pizarro, M., Zucca, F., González, P. J., Palano, M., Tomás, R., and Fernández, J., (2015). Twenty-year advanced DInSAR analysis of severe land subsidence: The Alto Guadalentín Basin (Spain) case study: *Engineering Geology*, v. 198, pp. 40-52.
- Casu, F., Elefante, S., Imperatore, P., Zinno, I., Manunta, M., De Luca, C., and Lanari, R., (2014). SBAS-DInSAR parallel processing for deformation time-series computation: IEEE Journal of Selected Topics in *Applied Earth Observations and Remote Sensing*, v. 7, no. 8, pp. 3285-3296.
- Cerón, J., and Pulido-Bosch, A., (1996). Groundwater problems resulting from CO 2 pollution and overexploitation in Alto Guadalentín aquifer (Murcia, Spain). *Environmental Geology*, v. 28, no. 4, pp. 223-228.
- Cigna, F., and Tapete, D., (2021a). Satellite InSAR survey of structurally-controlled land subsidence due to groundwater exploitation in the Aguascalientes Valley, Mexico. *Remote Sensing of Environment*, v. 254, p. 112254.
- Cigna, F., and Tapete, D., (2021b). Sentinel-1 BigData Processing with P-SBAS InSAR in the Geohazards Exploitation Platform: An Experiment on Coastal Land Subsidence and Landslides in Italy. *Remote Sensing*, v. 13, no. 5, p. 885.
- CHS, (2005). Asistencia técnica para el estudio de cuantificación del volumen anual de sobreexplotación de los acuíferos de la Unidad Hidrogeológica 07.28 Alto Guadalentín 07.33 Águilas.
- CHS, (2021). Memoria Plan Hidrológico de la Demarcación del Segura 2022/2027. Ministerio para la Transición Ecológica y el Reto Demográfico.
- Dach, R., Lutz, S., Walser, P., and Fridez, P., (2015). Bernese GNSS software version 5.2.
- De Luca, C., Cuccu, R., Elefante, S., Zinno, I., Manunta, M., Casola, V., Rivolta, G., Lanari, R., and Casu, F., (2015). An on-demand web tool for the unsupervised retrieval of earth’s surface deformation from SAR data: The P-SBAS service within the ESA G-POD environment. *Remote Sensing*, v. 7, no. 11, pp. 15630-15650.
- Echeverria, A., Khazaradze, G., Asensio, E., Gárate, J., Dávila, J. M., and Suriñach, E., (2013). Crustal deformation in eastern Betics from CuaTeNeo GPS network. *Tectonophysics*, v. 608, pp. 600-612.
- Ezquerro, P., Guardiola-Albert, C., Herrera, G., Fernández-Merodo, J. A., Béjar-Pizarro, M., and Boni, R., (2017). Groundwater and subsidence modeling combining geological and multi-satellite SAR data over the alto guadalentín aquifer (SE Spain). *Geofluids*, v. 2017.



- Ezquerro, P., Tomás, R., Béjar-Pizarro, M., Fernández-Merodo, J., Guardiola-Albert, C., Staller, A., Sánchez-Sobrino, J., and Herrera, G., (2020). Improving multi-technique monitoring using Sentinel-1 and Cosmo-SkyMed data and upgrading groundwater model capabilities. *Science of The Total Environment*, v. 703, p. 134757.
- Fernández-Merodo, J., Ezquerro, P., Manzanal, D., Béjar-Pizarro, M., Mateos, R., Guardiola-Albert, C., García-Davalillo, J., López-Vinielles, J., Sarro, R., and Bru, G., (2021). Modeling historical subsidence due to groundwater withdrawal in the Alto Guadalentín aquifer-system (Spain). *Engineering Geology*, v. 283, p. 105998.
- Fernandez, J., Prieto, J. F., Escayo, J., Camacho, A. G., Luzón, F., Tiampo, K. F., Palano, M., Abajo, T., Pérez, E., and Velasco, J., (2018). Modeling the two-and three-dimensional displacement field in Lorca, Spain, subsidence and the global implications. *Scientific reports*, v. 8, no. 1, p. 1-14.
- Foumelis, M., Papadopoulou, T., Bally, P., Pacini, F., Provost, F., and Patruno, J., (2019). Monitoring Geohazards using on-demand and systematic services on Esa's Geohazards exploitation platform, in *Proceedings IGARSS 2019 IEEE International Geoscience and Remote Sensing Symposium2019*, IEEE, pp. 5457-5460.
- Galloway, D. L., and Burbey, T. J., (2011). Regional land subsidence accompanying groundwater extraction. *Hydrogeology Journal*, v. 19, no. 8, pp. 1459-1486.
- González, P. J., and Fernández, J., 2011, Drought-driven transient aquifer compaction imaged using multitemporal satellite radar interferometry. *Geology*, v. 39, no. 6, pp. 551-554.
- IGME, (1997). Catálogo de acuíferos con problemas de sobreexplotación o salinización. Predefinición del programa de actuación: Segura, Ministerio de Medio Ambiente.
- Manunta, M., De Luca, C., Zinno, I., Casu, F., Manzo, M., Bonano, M., Fusco, A., Pepe, A., Onorato, G., and Berardino, P., (2019). The parallel SBAS approach for Sentinel-1 interferometric wide swath deformation time-series generation: algorithm description and products quality assessment. *IEEE Transactions on Geoscience and Remote Sensing*, v. 57, no. 9, pp. 6259-6281.
- Mestre-Quereda, A., Lopez-Sanchez, J. M., Ballester-Berman, J. D., Gonzalez, P. J., Hooper, A., and Wright, T. J., (2018). Evaluation of the Multilook Size in Polarimetric Optimization of Differential SAR Interferograms. *IEEE Geoscience and Remote Sensing Letters*, v. 15, no. 9, pp. 1407-1411.
- Rigo, A., Béjar-Pizarro, M., and Martínez-Díaz, J., (2013). Monitoring of Guadalentín valley (southern Spain) through a fast SAR Interferometry method. *Journal of Applied Geophysics*, v. 91, pp. 39-48.

## On the quality checking of persistent scatterer interferometry by spatial-temporal modelling

Mohammad Omidalizarandi<sup>1</sup>, Bahareh Mohammadivojdan<sup>1</sup>, Hamza Alkhatib<sup>1</sup>,  
Jens-André Paffenholtz<sup>2</sup>, Ingo Neumann<sup>1</sup>

<sup>1</sup> Geodetic Institute Hannover, Leibniz University Hannover, 30167 Hannover, Germany,  
([zarandi@gih.uni-hannover.de](mailto:zarandi@gih.uni-hannover.de); [mohammadivojdan@gih.uni-hannover.de](mailto:mohammadivojdan@gih.uni-hannover.de); [alkhatib@gih.uni-hannover.de](mailto:alkhatib@gih.uni-hannover.de);  
[neumann@gih.uni-hannover.de](mailto:neumann@gih.uni-hannover.de))

<sup>2</sup> Institute of Geo-Engineering, Clausthal University of Technology, 38678 Clausthal-Zellerfeld, Germany,  
([jens-andre.paffenholtz@tu-clausthal.de](mailto:jens-andre.paffenholtz@tu-clausthal.de))

**Key words:** *Persistent Scatterer Interferometry (PSI); spatio-temporal; quality model; classification; robust parameter estimation; deformation analysis*

### ABSTRACT

Today, rapid growth in infrastructure development and urbanization process increases the attention for accurate deformation monitoring on a relatively large-scale. Furthermore, such deformation monitoring is of great importance in the assessment and management of natural hazard processes like landslides, earthquakes, and floods. In this study, the Persistent Scatterer Interferometry (PSI) technique is applied using open-source synthetic aperture radar (SAR) data from the satellite Sentinel-1. It allows point-wise deformation monitoring based on time series analysis of specific points. It also enables performing spatio-temporal area-based deformation monitoring. Currently, these data do not have a sophisticated quality assurance process to judge the significance of deformations. To obtain different quality classes of the Persistent Scatterer (PS) data points, the first step is to classify them into buildings and ground types using LoD2 building models. Next, time series analysis of the PS points is performed to model systematic and random errors. It allows estimation of the offset and the deformation rate for each point. Finally, spatio-temporal modelling of neighbourhood relations of the PS points is carried out using local geometric patches which are approximated with a mathematical model, such as, *e.g.*, hierarchical B-Splines. Subsequently, the quality of SAR data from temporal and spatial neighbourhood relations is checked. Having an appropriate spatio-temporal quality model of the PS data, a deformation analysis is performed for areas of interest in the city of Hamburg. In the end, the results of the deformation analysis are compared with the *BodenBewegungsdienst* Deutschland (Ground Motion Service Germany) provided by the Federal Institute for Geosciences and Natural Resources (BGR), Germany.

*This contribution was selected by the Scientific Committee for publication as an extended paper in the Journal of Applied Geodesy <https://www.degruyter.com/journal/key/jag/html>*

## Towards an automated machine learning and image processing supported procedure for crack monitoring

Luigi Parente, Cristina Castagnetti, Eugenia Falvo, Francesca Grassi, Francesco Mancini,  
Paolo Rossi, Alessandro Capra

Department of Engineering “Enzo Ferrari”, University of Modena and Reggio Emilia, Via Pietro Vivarelli 10,  
41125 Modena, Italy, ([luigi.parente@unimore.it](mailto:luigi.parente@unimore.it); [cristina.castagnetti@unimore.it](mailto:cristina.castagnetti@unimore.it); [eugenia.falvo@unimore.it](mailto:eugenia.falvo@unimore.it);  
[francesca.grassi94@unimore.it](mailto:francesca.grassi94@unimore.it); [francesco.mancini@unimore.it](mailto:francesco.mancini@unimore.it); [paolo.rossi@unimore.it](mailto:paolo.rossi@unimore.it); [alessandro.capra@unimore.it](mailto:alessandro.capra@unimore.it))

**Key words:** *detection; crack; image processing; machine learning; automation; monitoring; open-source*

### ABSTRACT

Development of automated and remotely controlled procedures for accurate crack detection and analysis is an advantageous solution when compared to time-consuming and subjective crack examination conducted by operators. Recent studies have demonstrated that Machine Learning (ML) algorithms have sufficient potential for crack measurements. However, training of large amount of data is essential. When working on single sites with permanently installed fixed cameras adoption of ML solutions may be redundant. The purpose of this work is to assess the performance of a procedure for crack detection based on an easy to implement workflow supported by the use of ML and image processing algorithms. The datasets used in this work are composed of temporal sequence of single digital images. The workflow proposed includes three main modules covering acquisition, optimization and crack detection. Each module is automated and basic manual input by an operator is only required to train the classifier. The processing modules are implemented in modular open-source programs (*e.g.*, ImageJ and Ilastik). Results obtained in controlled conditions led to a satisfactory level of detection (about 99% of the crack pattern detected). Experiments conducted on real-sites highlighted variable detection capabilities of the proposed approach (from 12 to 96%). The main limitation of the approach is the production of false-positive detection due to significant variation in illumination conditions. Further work is being conducted to define scalability of the approach and to verify deformation detection capabilities.

### I. INTRODUCTION

Aging of the built environment worldwide demands for the adoption of cost-effective structural health monitoring approaches to ensure long-term integrity and adequate levels of safety. Crack patterns initiation and propagation are indicators of the structural integrity and health of a built element. Traditional crack visual inspections are conducted on the site by operators using conventional tools (such as measuring magnifiers, strain gauges, crack rulers, etc.). This task can produce subjective judgment on the state of the crack and introduces gross errors in the measurement.

Recent technological advances in software and sensors offer the unprecedented opportunity to acquire considerable amount of high-quality optical data and process them in real-time with less subjective methods (Nex *et al.*, 2019). For example, adoption of image processing (IP) techniques has been employed in the past for a range of monitoring applications (*e.g.*, Deshmukh and Mane, 2020; Garrido *et al.*, 2019; Guidi *et al.*, 2014). Many researchers have proposed valid IP-based solutions for accurate segmentation of the crack from digital images (Mohan and Poobal, 2018). However, the main limitation of detecting a set of cracks through IP algorithms lies in the little scalability of the approach that is usually only tailored for a certain application or for a limited dataset. When exporting the

approach to real-world sites a range of challenges (*e.g.*, light variations, shadows, stains, scratching, camera position, etc.) can severely reduce the efficiency of the detection approach.

Machine learning (ML) algorithms have been extensively applied to buildings research for the past decades. ML-based solutions allow to minimize human involvement and overcome some limitations encountered by solutions based solely on IP methods. Recent studies have demonstrated that sub-branch of ML (such as Convolutional Neural Networks, CNN) algorithms have sufficient potential for crack measurements (Teng *et al.*, 2021). When consistent amount of data is available, ML algorithms can automatically digest intrinsic knowledge of the data (such as hidden structures or relationships) and automatically perform difficult tasks such as localization and classification of different damages (*e.g.*, cracks, spalling, corrosion, etc.). Detailed reviews of research papers focusing on crack detection through ML algorithms are presented by Azimi *et al.* (2020) and Hsieh and Tsai (2020).

Working with ML algorithms certainly represent a suitable solution to the binary classification problems that include distinguishing ‘crack’ and ‘non-crack’ regions or pixels. A prerequisite to obtain an accurate and robust crack detection solution based on ML

algorithms is the availability of large datasets for training. Training can require a considerably long time. Also, skills and experience in computer vision and machine learning is required to set up proper crack detection solution. Furthermore, when working on single sites with permanently installed fixed cameras the need for training of large datasets may be unnecessary.

Another interesting point is that most of the past research works in the field of crack monitoring implemented solutions in controlled laboratory environments (Mohan and Poobal, 2018). Only recently research efforts are being addressed to develop solutions for real-world applications.

In this context, this paper presents the methodology and initial results of our recent research that is addressed at implementing an automated, cost-effective and user-friendly procedure to monitor cracks over time. The purpose is to implement and test the efficiency of a crack detection solution based on modern open-source image processing and ML software. A cost-effective commercial solution for data collection and transmission with a single digital camera is presented also. The overall system, based on the combination of the data collection solution with the crack detection solution, is intended for a diffuse exploitation among technicians in the AEC (Architecture Engineering Construction) market.

## II. METHODOLOGY

The proposed algorithm for automatic crack detection (summarized in Figure 1) consists of three main modules including photo acquisition (PAM), photo optimization (POM) and crack detection (CDM).

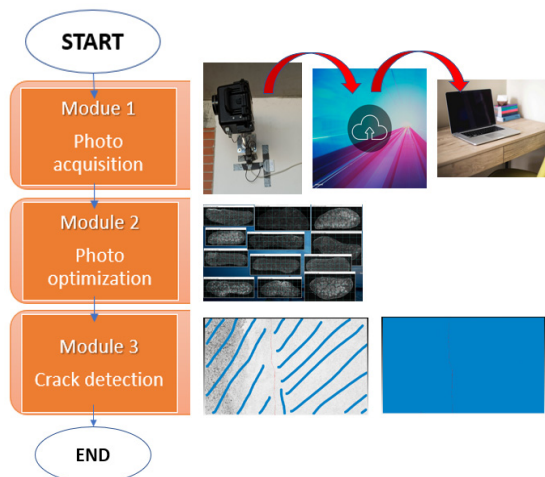


Figure 1. A summarization of the three modules proposed in this study that include image acquisition and transferring, image pre-processing and crack detection.

The PAM kit includes a single digital single-lens reflex (DSLR) camera, an intervalometer and a protective case (Figure 2). Specifically, a Canon 2000D (~24 megapixels, sensor APS-C CMOS and equipped with 18–55 mm lenses) was mounted in a protective case and installed

in a fixed location with the camera axis perpendicular to the photographed crack. Acquired images can be transferred using an FTP server or saved on a cloud storage service in just a few seconds for a near real-time data processing. The whole PAM kit used in this study was provided by the company Bixion ([www.bixion.com](http://www.bixion.com)).

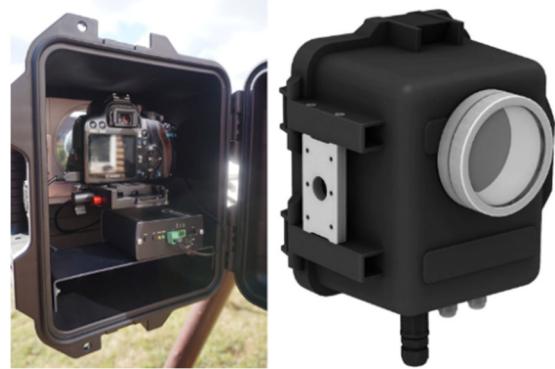


Figure 2. The acquisition kit provided by the company Bixion.

After acquisition, the POM conducts a radiometric optimization that is implemented using an open-source image-processing software, namely ImageJ (2021). Initial tests showed the presence of illumination-dependent deformation. Adoption of pre-processing steps (such as radiometric optimization) improves the repeatability of the implemented crack analysis workflow avoiding the estimation of false deformations. The output generated after the POM steps is a corrective image with a smoother distribution of pixel intensity that presents a decreased level of noise while maintaining information related to the crack patterns. The optimized image is passed to the CDM, which classifies the image pixels in classes. This module runs a semantic segmentation via an active learning system (Kan, 2017) and is completely implemented in Ilastik (2021), an open-source software that allows even unexperienced operators to adopt ML-based algorithms to classify image regions in different classes. More detailed information about the software is provided in Berg *et al.* (2019). For this work an innovative single-acquisition machine learning-based training method is proposed. With this method, user work is only required to train the model based on the first acquisition. The operator uses a mouse interface to label two classes on the image (namely “crack” and “background”). The software, based on the user-based selected classes, assigns labels to each pixel interactively based on a Random Forest non-linear classifier. The work by Geurts *et al.* (2009) is suggested for more technical information about this classifier. With such an approach, training is only required once on the first image. Images acquired subsequently are classified in batch mode by the trained classifier allowing for automatic crack detection.

The proposed modules were tested on three different sites to investigate the crack detection capabilities in a

range of conditions including controlled (namely 'Test1') and real-world sites (namely 'Test2' and 'Test3') conditions.

Test1 was carried indoor with stable light condition and the camera fixed at 4 m from the object during acquisition. Camera focal length was fixed at 27 mm. A simulated cracked wall was used to reduce challenges in the detection phase. A drawing representing a total of seven multi-scale and multi-orientation cracks was generated in AutoCAD, printed and attached on the photographed wall (Figure 3). Cracks width varies from a maximum of 1.75 to 0.05 cm. A total of three images (three epochs) are considered.

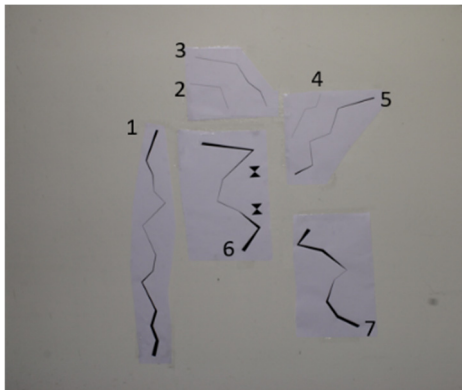


Figure 3. The seven artificial cracks used in Test1.

For Test2 a small portion of an indoor wall of a residential building was selected. The wall is characterized by the presence of multiple cracks with width  $<0.5$  mm and two areas of plaster removed (Figure 4). During acquisition the camera with focal length fixed at 37 mm was installed perpendicular to the cracked wall at about 4 m. For Test2 the proposed approach was tested on a total of six epochs.



Figure 4. Test2: the acquisition kit and the area of interest (red box).

Test3 was conducted outdoor acquiring drone-based images (Figure 5). The considered site was a residential wall presenting a minor crack with width  $<0.5$ mm. The drone used for Test3 is a DJI mini 2 that incorporates a camera with a  $1/2.3''$  12 Megapixel CMOS image sensor.

The camera has an  $83^\circ$  FOV, 24 mm equivalent, fixed aperture F2.8 lens. A total of 4 images were acquired (Figure 5). Specifically, the first flight (epoch0) conducted on a sunny day at 11am, allowed to capture two images (epoch 0\_A and 0\_B) from slightly different positions but with the same illumination conditions (images were acquired within only a few seconds difference). The second flight (epoch1) was conducted on the same day at 3 pm. A further image (epoch2) was acquired the next morning at 9 am on a cloudy day. All images were acquired with the drone flying manually at about 1.5 m from the crack pattern.

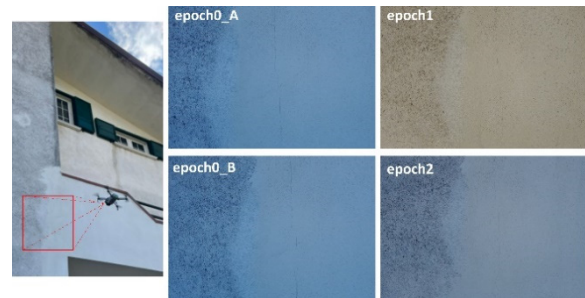


Figure 5. The four images acquired for Test3 with the drone-based approach. The red box is the area of interest.

A summarization of the three tests carried out in this work is presented in Table 1. For all tests the CDM and POM were carried out on a laptop Windows 10 Pro with an Intel Core i7-10750H Processor, operating a 2.60 GHz CPU and using 16 GB of RAM.

To validate the efficiency of the proposed crack detection both qualitative and quantitative assessment were carried out. Specifically, the assessment was conducted through a visual assessment of the multi-epoch segmentation and by comparing the automatic segmentation to a ground-truth. The ground-truth was obtained by manually determining all pixels appertaining to the cracked surface. Thus, the quantitative analysis was carried out by counting the total number of automatically detected crack-pixels and estimating their percentage against the crack-pixels identified from the ground-truth.

### III. RESULTS AND DISCUSSION

For each test described in this paper the training of the classifier was carried out in less than one hour while the subsequent processing in batch mode led to classification and segmentation of the defined classes (namely 'crack' and 'background') in only a few seconds.

Pixel-level crack segmentation outputs returned by the CDM for the Test1 are shown in Figure 6. Results demonstrate that the proposed approach correctly detected all cracks. Noise effects, false detection or poorly segmented cracks were not observed. Test1 results show that detection is not influenced by the crack orientation or size when using the proposed approach in controlled conditions.

Table 1. Summarization of the 3 tests main features

Conditions	Test1	Test2	Test3
Location	Indoor	Indoor	Outdoor
Illumination	Stable	Variable	Variable
Object	Only cracks	Cracks and noise	Cracks and noise
Camera	Canon 2000D	Canon 2000D	Built-in DJI Mini 2
Acquisition set-up	Ground-based fixed station; Distance: 4m	Ground-based fixed station; Distance: 4m	Aerial variable station; Average distance 1.5m

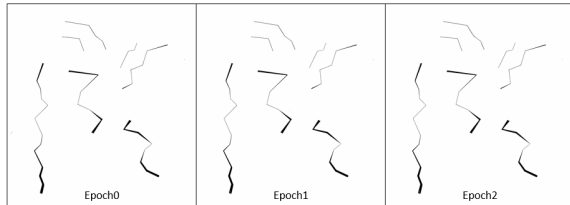


Figure 6. Detection outputs obtained in Test1.

Regarding Test2, the proposed crack detection method produced again acceptable results. Outputs of the CDM, plotted in Figure 7, are satisfactory considering that most of the cracks were correctly identified. Noise or other extraneous features were correctly classified as background while most of the crack patterns are detected. As illustrated in Table 2, for most epochs, a good level of completeness of automatically detected cracks is achieved (above 90%). On the other hand, with respect to the last two epochs the performance of the automatic detection was lower. In fact, only approximately between 65 and 69% of the crack pixels were correctly detected when compared to the ground-truth.

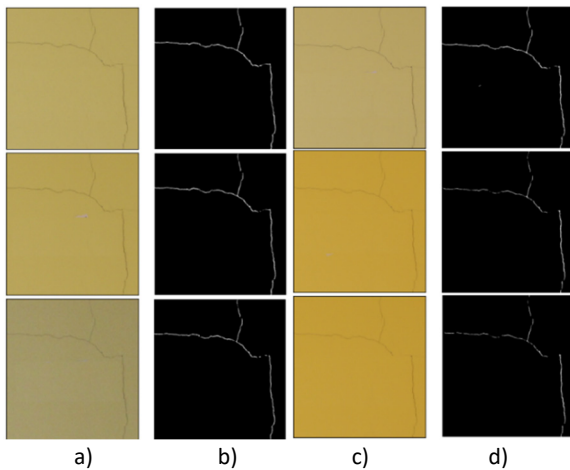


Figure 7. Test2: a) and c) RGB acquisition; b) and d) Detection results generated with the proposed approach.

According to results shown in Table 2 the proposed approach produced poor detection with images acquired for Test3. In fact, for this test, in epoch1 and epoch2 only <16% of the total crack-pixels were correctly identified. Figure 8 shows evidence of a moderate detection result when images are acquired with the same illumination condition (epoch0\_A and epoch0\_B). However, zooming in on the crack pattern

Figure 8b indicates that epoch1 and epoch2 are not suited to the proposed detection approach.

Table 2. Detection quality results for Test2 and Test3

Test	Epoch	Total crack-pixels	%
2	Ground-truth	6972	100
	1	6693	96
	2	6321	90.7
	3	6365	91.3
	4	4796	68.8
	5	4528	64.9
3	Ground-truth	4501	100
	0_B	3152	70
	1	712	15.8
	2	547	12.1

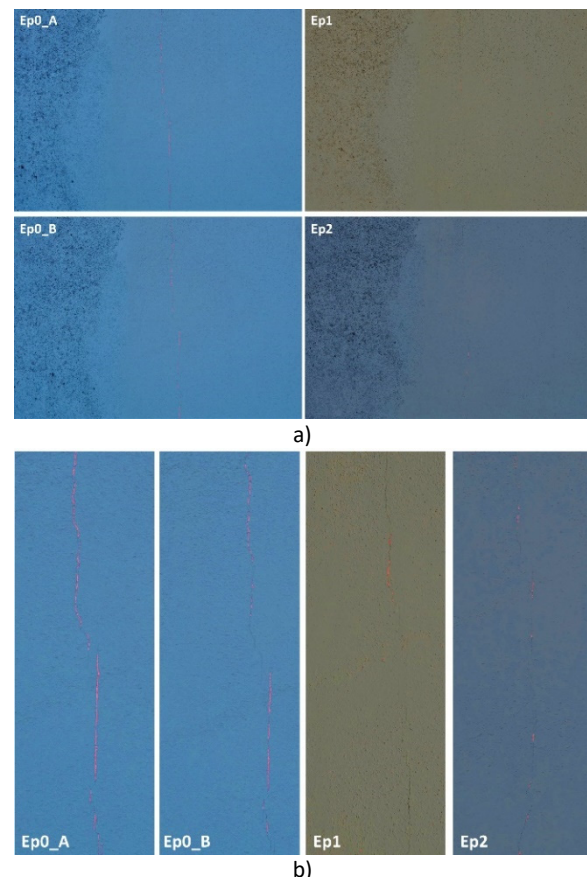


Figure 8. Test3: a) Detection results overlaying the original RGB image; b) Zoom-in on the crack. In red the detected crack.

Overall, the proposed method proved its efficiency in generating noise-free segmentation, avoiding the need for manual operations and further post-processing that

can affect the quality of the crack detection (Fujita and Hamamoto, 2011). This was possible thanks to the operator-based identification of not relevant features that is carried out on the first image of the dataset.

It is suggested that when a uniform illumination on the site is guaranteed during the whole acquisition period, it can certainly favor the results in terms of segmentation (see for example Test1). When dealing with a set of images acquired with minor variation in illumination conditions, adopting radiometric corrections shows its potential to diminish the probability to generate inaccurate crack-pixel identification. However, for some epochs of Test2, erroneous classification of pixels leading mainly to false negative outputs was still observed. In fact, for the last two epochs (see Figure 7) the proposed approach tends to fail crack detection. Specifically, small regions of the cracks are classified as non-crack, resulting in loss of the connectivity of the crack pattern. This is a common issue with image processing and machine learning-based detection algorithms (Weidner *et al.*, 2019) that is usually faced with the adoption of morphological operators (Galantucci and Fatiguso, 2019). Such solutions were not initially considered for the current study but must be carefully implemented to achieve a reliable crack monitoring system.

A different behavior was observed for results generated from Test3. For outdoor sites, images acquired on different days and times can present significant variation in illumination conditions (Figure 5). Furthermore, acquiring from similar positions flying the drone manually is a difficult task. As a consequence, drone-based acquisitions of this study were carried out with slightly different distances from the object affecting size of the field of view. Adoption of more stable and RTK-GNSS drones (Stott *et al.*, 2020) and the use of distance sensors (Park *et al.*, 2020) can support the operator in this task. Also, the proposed detection approach can potentially benefit from acquisition with a higher resolution camera. Previous suggested improvements can potentially lead to achieve a better level of detection even when dealing with highly variable light conditions.

Processing of the last two epochs of the drone-based test (Test3) highlighted a very poor ability of the proposed approach to detect crack. It is suggested that variation in illumination is the main limitation of the approach. The limited size of the studied crack in Test3 has potentially influenced the inadequate detection results also.

In summary, the presented single-acquisition machine learning-based training is better suited for applications where the set of crack site is well defined and not affected by significant illumination variation (typical of outdoor sites). Thus, the presented procedure may be successfully applied in those cases requiring a multi-temporal crack detection in indoor scenarios allowing for a fixed installation of the equipment typical of several monitoring applications of

the built environment. For different scenarios (*e.g.*, multiple set of cracks with undefined locations, outdoor sites, etc.) other solutions based for example on CNN techniques may be more adequate.

#### IV. CONCLUSION

Current technological advancement offers the tools for the development of a simple near-real time long-term monitoring approach based on a monoscopic system able to detect and analyse cracks with little operator intervention. This paper described an approach based on the combination of two open-source software (ImageJ and Ilastik) and a smart data acquisition and transferring kit (Bixion). The proposed method can greatly reduce the crack inspection time and has the potential to achieve higher measurement accuracy for long-term monitoring when compared to traditional and subjective approaches. The study highlighted that in presence of significant variation in illumination conditions alternative crack detection approaches must be considered. For more information about Test1 and Test2, including an assessment of the accuracy and precision of the proposed method, the reader can refer to Parente *et al.* (2022).

#### References

- Azimi, M., Eslamlou, A. D., and Pekcan, G. (2020). Data-driven structural health monitoring and damage detection through deep learning: State-of-the-art review. *Sensors*, 20(10), 2778.
- Berg, S., Kutra, D., Kroeger, T., Straehle, C. N., Kausler, B. X., Haubold, C., and Kreshuk, A. (2019). Ilastik: interactive machine learning for (bio) image analysis. *Nature methods*, 16(12), pp. 1226-1232.
- Deshmukh, S.S., and Mane, P.B. (2020). Bridge crack detection and monitoring using image processing. *Processing. International Research Journal of Engineering and Technology (IRJET)* 7(10): 1864–67.
- Fujita, Y., and Hamamoto, Y. (2011). A robust automatic crack detection method from noisy concrete surfaces. *Machine Vision and Applications*, 22(2), pp. 245-254.
- Galantucci, R. A., and Fatiguso, F. (2019). Advanced damage detection techniques in historical buildings using digital photogrammetry and 3D surface analysis. *Journal of Cultural Heritage*, 36, pp. 51-62.
- Garrido, I., Lagüela, S., Sfarra, S., Madruga, F. J. and Arias, P. (2019). Automatic Detection of Moistures in Different Construction Materials from Thermographic Images. *Journal of Thermal Analysis and Calorimetry*, 138(2), pp. 1649–68.
- Geurts, P., Irtthum, A., and Wehenkel, L. (2009). Supervised learning with decision tree-based methods in computational and systems biology. *Molecular Biosystems*, 5(12), pp. 1593-1605.
- Guidi, G., Gonizzi, S., and Micoli, L. (2014). Image pre-processing for optimizing automated photogrammetry performances. In *ISPRS Technical Commission V Symposium* (Vol. 2, pp. 145-152).

- Hsieh, Y. A., and Tsai, Y. J. (2020). Machine learning for crack detection: Review and model performance comparison. *Journal of Computing in Civil Engineering*, 34(5), 04020038.
- Ilastik (2021). Interactive machine learning for (bio)image analysis. Available in: <https://www.ilastik.org>, accessed on 18 December 2021.
- ImageJ (2021). Available in: <https://imagej.net/plugins/ridge-detection>, accessed on 18 December 2021.
- Kan, A. (2017). Machine learning applications in cell image analysis. *Immunology and cell biology*, 95(6), pp. 525-530.
- Mohan, A., and Poobal, S. (2018). Crack detection using image processing: A critical review and analysis. *Alexandria Engineering Journal*, 57(2), pp. 787-798.
- Nex, F., Duarte, D., Steenbeek, A., and Kerle, N. (2019). Towards real-time building damage mapping with low-cost UAV solutions. *Remote sensing*, 11(3), 287.
- Parente, L., Falvo, E., Castagnetti, C., Grassi, F., Mancini, F., Rossi, P., and Capra, A. (2022). Image-Based Monitoring of Cracks: Effectiveness Analysis of an Open-Source Machine Learning-Assisted Procedure. *Journal of Imaging*, 8(2), 22.
- Park, S. E., Eem, S. H., and Jeon, H. (2020). Concrete crack detection and quantification using deep learning and structured light. *Construction and Building Materials*, 252, 119096.
- Stott, E., Williams, R. D., and Hoey, T. B. (2020). Ground control point distribution for accurate kilometre-scale topographic mapping using an RTK-GNSS unmanned aerial vehicle and SfM photogrammetry. *Drones*, 4(3), 55.
- Teng, S., Liu, Z., Chen, G., and Cheng, L. (2021). Concrete crack detection based on well-known feature extractor model and the YOLO\_v2 network. *Applied Sciences*, 11(2), 813.
- Weidner, L., Walton, G., and Kromer, R. (2019). Classification methods for point clouds in rock slope monitoring: A novel machine learning approach and comparative analysis. *Engineering Geology*, 263, 105326.



## Pathological diagnostic tool based on the combination of different disciplines. Management of the preservation of cultural heritage. Application in the structural consolidation of rock structures

Jorge Juan Romo-Berlana<sup>1</sup>, Manuel Sánchez-Fernández<sup>2</sup>, José Juan de Sanjosé-Blasco<sup>2</sup>, Fernando Berenguer-Sempere<sup>3</sup>

<sup>1</sup> Path Ingeniería S.L., Avenida Virgen de la Montaña, 8, 10002 Cáceres, Spain, ([jromo@pathingenieria.es](mailto:jromo@pathingenieria.es))

<sup>2</sup> Departamento de Expresión Gráfica, INTERRA: Instituto en Desarrollo Territorial Sostenible, NEXUS: Grupo de investigación en Ingeniería, Territorio y Patrimonio, Universidad de Extremadura, Avenida de la Universidad s/n, 10003 Cáceres, Spain, ([msf@unex.es](mailto:msf@unex.es); [jjblasco@unex.es](mailto:jjblasco@unex.es))

<sup>3</sup> UCAM Universidad Católica San Antonio de Murcia Avenida de los Jerónimos, 135, 30107 Guadalupe de Maciascoque, Murcia, Spain, ([fjberenguer@ucam.edu](mailto:fjberenguer@ucam.edu))

**Key words:** *cultural heritage; survey techniques; inspection; pathology; terrestrial sensors*

### ABSTRACT

The preservation of cultural heritage must encompass different disciplines for its management to be optimal. The behaviour of a historic building depends on many factors, which include its real geometry, the characteristics of the materials with which it was built, pathologies arising throughout its existence and the conditions of its surroundings. Different techniques are therefore required and these must be complemented in order to manage our cultural heritage comprehensively. Coria Cathedral (Cáceres) is an example of a singular building with secular pathologies. This study of the cathedral combined modern techniques of analysis and description. Geomatic techniques were used (differential levelling, terrestrial laser scanner, GNSS), geophysical prospecting methods (electrical tomography), geotechnical descriptive methods, three-dimensional modelling and verification of structural systems. The results obtained served as the basis to determine and locate the origin building's pathologies and to develop a project for the structural consolidation.

### I. INTRODUCTION

The article presents the methodology used for the structural diagnosis of a secular building with star shaped groin vaults on pillars attached to load bearing walls. The geometry of the structure, properties of materials and surrounding conditions (foundations and orography) are analysed. The study centres on the cathedral of the city of Coria (Cáceres), a building that has suffered structural problems for centuries.

Coria Cathedral (Cathedral of Santa María de la Asunción) was built on the site occupied by the primitive visigoth cathedral, which was substituted by the Arabic mosque up until the old cathedral was built following the Christian reconquest and later military stabilization of the area. In the last years of the XV<sup>th</sup> century the cathedral's incumbents declared that "this, our church, is very dilapidated and old, and falling down, and also because it is so low and small that not even half the townspeople can fit into it", and decided to proceed with the construction of what is known today as the 'New Cathedral'.

The site of the building is on the edge of a slope with a descent of around 40 m, the geology of which is made up of a deep stratum of clay overlain with a layer of loose clay based stones of thicknesses varying between 3 m and 6 m. At the foot of the slope lies the old bed of the nearby river Alagón, which altered its natural course

towards the south by around 400 m following a flood, dated by some authors as occurring in the middle of the XVII<sup>th</sup> century (Mogollón, 1999; Núñez and Molina, 2011; Travesí, 2013; Rodríguez, 2015).

The first 150 years of the history of this cathedral, the approximate time it took to build it, are ridden with hazards, incidents, structural failures, demolitions and reconstructions that gave many problems to the canonry and required the intervention of many master masons and architects (e.g. Martín de Solórzano, Bartolomé de Pelayos, Sebastián de Lasarte, Esteban de Lazcano, Pedro de Ybarra, Rodrigo Gil de Hontañón, Juan Bravo, Manuel de Larra y Churriguera, etc.) as well as considerable funding (Mogollón, 1999). A full description of the causes and solutions that these masters adduced and proposed cannot be undertaken here, though it can be said that during this period many and varied explanations were put forward, such as the weakness of the foundations or the excessive weight of the vaults (Travesí, 2013; Martínez, 1999). In addition to this trouble ridden history, the cathedral suffered serious damage on the morning of the 1st of November 1755 when the Lisbon earthquake (Rodríguez-Pascua *et al.*, 2011) struck, destroying part of the tower and caving in the main sanctuary and part of the vault of the main hall of the church (Mogollón, 1999).

To make a structural diagnosis of a building, its geometry, deformations and the loads it bears must be known. New metric surveying techniques can be applied to this task to construct complex 3D models using geometric information (Bitelli *et al.*, 2017). Terrestrial Laser Scanner (TLS) and photogrammetry based on structure for motion (SfM) are two techniques that have been used by several authors in the work of reconstructing and preserving heritage sites (Bitelli *et al.*, 2017). HBIM methods (Historical Building Information Modelling), used to analyse the damage suffered by a building as a result of an earthquake, are supported by 3D models of dense 3D point cloud obtained using TLS technology (Oreni *et al.*, 2017).

To gain the fullest knowledge of the development of possible deformations and movements of the building, periodic geometric monitoring of its structural elements and outer points was carried out. Thus, a reference system was created to distinguish between relative movements within the building itself and general movements of the surroundings. This work saw the application of Global Navigation Satellite System (GNSS) and high precision differential levelling, which gave millimetric or undercentimetric precision (Lovse *et al.*, 1995).

This work presents a pathological diagnostic tool based on the combination of different disciplines. From the data obtained by these techniques together with the geotechnical analysis and the analysis of the stability of the slope, a modelling was made of the ground and building as a whole in order to reveal the origin of its structural problems. This study establishes the basis for the necessary knowledge to be able to carry out the work needed to improve the structure and preserve the building (Jurado, 2014).

## II. RESEARCH AIM

This work is part of the study of the dynamics of a structure, transferred to a real case of analysis and prediction of deformations of a singular building of high historical heritage value in a precarious state of conservation. The aim of the research is to study the methodology to be followed for the diagnosis of the visible structural problems of a factory building. To this end, the study focuses on a building with serious structural pathologies and is analyzed based on multidisciplinary techniques that define the origin of structural problems. The behavior of the foundation and the terrain on which it is located and loads that the structure is supporting is analyzed. The repair work described in the study forms the basis for the definition and execution of the rehabilitation works in order to ensure the integrity of the building in a safe condition.

## III. MATERIALS AND METHODS

Following the work of repairing the damage caused to the cathedral by the earthquake of Lisbon (1755), the existing documented data regarding the structural

problems of the building disappeared. Even so, the cathedral has long been known for its glaring pathologies, particularly the cracks in the eastern façade (Figure 1a) and the vaults of the central nave (Figure 1b) (Mogollón, 1999; Martínez, 1999).

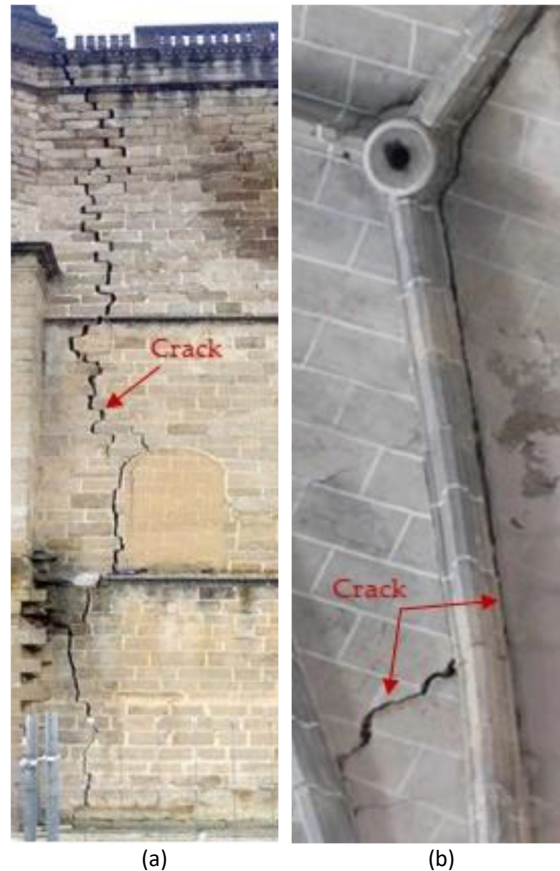


Figure 1. The cathedral: a) Cracks in the wall of the eastern façade; b) Cracks in the vault of the central nave.

Using the most advanced technology and teams of multidisciplinary experts, uncovered the underlying problems causing the structural defects of the cathedral. These techniques included comprehensive geotechnical studies of the stability of the slope and foundations of the cathedral, implementation of modern monitoring systems and comprehensive modelling of the building using laser scanning technology, which, in addition to providing a three-dimensional model with sufficient geometric precision, formed the basis for a realistic analysis of the behaviour of the structure of the building. All of these studies culminated in the preparation of a constructive project aimed at the structural consolidation and restoration of the building.

Prior to the structural calculation, any movements in the foundations or structural elements (analysis of movements), the geometric configuration of the building (geometric analysis) and the carrying capacity and stability of the foundation grounds (geotechnical analysis) must be known. Also XIX<sup>th</sup> century terrestrial photogrammetry techniques were used for 3D architectural surveys of historic monuments. Other

cases of preservation studies of buildings with high heritage value have used geomatics techniques of geometric assessment or to catalogue damage using 3D techniques (SfM and TLS), integrating the results into a HBIM system (Bitelli *et al.*, 2017).

TLS became available at the end of the XX<sup>th</sup> century and is used in a multitude of tasks. It is a tool for the collection of geometric information from a constructed element from which a 3D point cloud is created, or which serves as the basis for obtaining 3D models of the element scanned. Photogrammetry close range techniques from SfM technology offer a similar result, though this methodology requires greater effort in the data collection.

#### A. Movement monitoring: Differential levelling and GNSS

Visible structural damage to the walls and vaults of the cathedral (Figure 1) is a reflection of the differential movements the building has undergone. It must be determined whether these anomalous structural movements are the result of past problems or whether the structural movements still follow similar patterns today. Studies by Dierendonck *et al.* (1992); Lovse *et al.*, (1995); Caputo *et al.*, (2015) use geomatics techniques to monitor infrastructure movements, and the methodology manages to determine movements of sub-centimetric order. Differential relative movements of the elements of the building and general movements of its surroundings were needed, and for this purpose two different techniques were implemented: a high precision differential levelling, for the study of movements at the base of walls, and GNSS for the analysis of roofs and surroundings.

Four sets of measurements were carried out between 2012 and 2015 to monitor movements so that any trend there may be in the structure could be analysed.

High precision differential levelling is a technique used as a basis or check in altimetry surveys (Caputo *et al.*, 2015; Calina *et al.*, 2015). A closed ring of levelling was followed containing readings of the GNSS bases of the proximity network and 17 points located in stone blocks, bases of walls of the cathedral structure and interior floor. An arbitrary high was established at one of the points in the first survey with the aim of obtaining a result that could be compared among surveys. The monitoring of this fixed point was maintained throughout the process.

For the analysis of movements using GNSS an external reference network was set up using stable points and this was connected to another network close to the cathedral building. Both networks were set up through the placement of permanent signalisations. The external network was located in cleared and stable areas for work using GNSS; the internal network was set up next to the cathedral, a building of significant height and surrounded by the buildings of the town centre. This latter network presented a challenge during

processing, which was conditioned by the covered areas and possible reflections of the signal from satellites. The external network was adjusted by post-process using the data provided by the GNSS system of Extremadura (permanent antenna located in Coria).

All baselines are <1.3 km in length and have been observed for at least 3h post-processing (Heinrich-Wild-Strasse, 2008). These long observation periods ensure greater redundancy in ambiguity resolution and network adjustment. Likewise, these long post-process observations allow an exhaustive analysis to detect possible systematic and gross errors such as those caused by cycle slips or multipath. An initial adjustment of the network made in 2012 was established as a starting point on which to carry out the following checks. To minimize systematic errors, a GNSS observation protocol was established in which: the same sensor was always used at each point, the same anchor bolt and the same method of placement. The network close to the cathedral building was calculated from the data taken by the external network using a direct intersection in post-process with 5 base lines.

#### B. Geometric analysis: TLS

For the study of deformations in the cathedral structure requires the three-dimensional representation of the building, which in this case was performed using the terrestrial laser scanner technique (TLS), by which topographical and architectural surveys of structures can be carried out quickly and efficiently with great precision (less than a centimetre). The purpose of this method is to generate a 3D model that can identify cracks, twists, collapses, displacements, etc... Other non-invasive instruments (fissurometers, clinometers, micrometers...) provide data which, though they measure this kind of pathologies, offer specific values, whereas laser scanner facilitates knowledge of overall and all inclusive movement of the entire structure. Other highly useful information obtained using this methodology, thanks to the information stored in orthoprojected images, is any kind of section or view of the building, and this enables the generation of 2D views of the real geometry of the cathedral.

In this case a Leica C10 scanner was used, which provides precision  $\leq 6$  mm at under 100 m, a speed of measurement of up to 400,000 points per second and a field of vision capacity of 360° horizontally and 270° vertically. The resolution at which the work is carried out is 7 cm, which is the distance between the points on a mesh projected onto a wall face perpendicular to the scanner at a distance of 100 m. The configuration chosen is that of greater resolution in productive work times depending on the equipment available (18 minutes).

For the complete survey of Coria Cathedral ninety two measurements (11 on the exterior, 8 on the roof and 73 in the interior) were taken containing

information on the point cloud, and six more of transition which, while not providing specific information, were necessary for putting the model together. To link together all the scans, 206 targets were used. Information processing was performed using the software Leica Cyclone.

The 3D model was placed in an overall system of coordinates, in this case the projected system of coordinates ETRS89 UTM H29, as this is the official system of coordinates in the region. In this way, taking the concept BIM, it is feasible and easy to integrate the cartography and the 3D model. Figure 2 shows the resulting 3D point cloud of the cathedral taken from the southwest.



Figure 2. Full point cloud from the southwest view of Coria Cathedral.

Metric quality and photographic detail were obtained in the point cloud orthoimages, making them highly useful in the preparation of a qualitative assessment that distinguishes colours, materials, imperfections, etc. Twenty eight orthoimages were generated. The GSD (Ground Sample Distance) used was of one centimetre, though in most of the orthophotographs it was below this limit.

### C. Geotechnical studies

The history and antecedents of Coria Cathedral and the stated aims of searching for the ultimate causes of its pathologies necessarily lead to a deep study of the geotechnical characteristics of the ground on which the cathedral stands. Previous studies have been limited to providing results of tests on samples obtained either from pitches or from surveys. It was necessary to go deeper in the sense that a geotechnical study is not an end in itself, but rather one step in a broader process of calculating the behaviour of the building-foundations-slope as a whole. It is strange that in the most recent studies (the end of the XX<sup>th</sup> century and beginning of the XXI<sup>st</sup>) the possible harmful effects of the cathedral's location next to a 40 m high slope were overlooked, more so we consider that old cathedral experts had warned of the problem and even designed solutions for the contention of the slope, such as Juan del Ribero Rada in his proposal in 1597 (Mogollón, 1999; Núñez and Molina, 2011).

Geometric definition is inconsistent if the model is not given robust mechanical content, so a model of calculation is required that takes geometry and geotechnics into consideration. Previous studies are complemented by tests to determine the geotechnical properties of the foundation grounds and slope. On one hand, the heritage value of the working area does not allow the use of destructive techniques (sampling), and on the other the size of the cathedral and slope require high yielding methods. Geotechnical characterization is used as a prospection technique that applies several electrical tomography profiles (Figure 3), determining the real electrical resistance which, together with augers in which the diameter of rotation is 86 mm with a perpetually recovered drill hole samples, permits geological levels to be established depending on their depth.

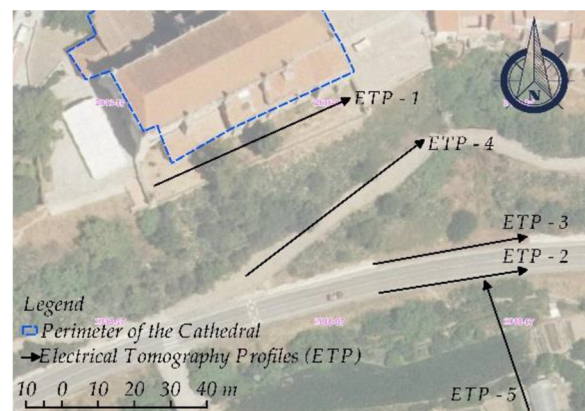


Figure 3. Floor plan of electrical tomography profiles.  
Source: Canonry Cathedral Coria-Cáceres (geotechnical study by LACOEX and GA-MA GEOFÍSICA).

Using the 3D geometric models and geotechnical description the stability of the slope building as a whole was estimated for different hypotheses. Elaborations were made using the program Geo-Studio, which estimates safety factors according to the Morgenstern & Price method (Cuenca, 2001; Kamanbedast and Delvari, 2012), a method that has been more widely used and which is more precise than the methods of Bishop and Jambu (Cuenca, 2001), following Mohr-Coulomb constitutive tension models (Bishop and Morgenstern, 1960; Bishop, 2008), in which the different geological materials of the undersoil are considered, as well as the fabric of the cathedral building and the loads borne (Figure 4).

### D. Structural analysis

One of the aims was to elaborate a three-dimensional model that permits the structural analysis of its behaviour based on its real geometry, the product of its constructive evolution and the accumulation of movements, and not on the original projected dimensions that may have undergone considerable variations. Using the 3D model and the description of the materials of the structural elements of the

cathedral by means of the extraction of drill hole samples in wall faces and resistance tests, the structural system of the building was modelled using bars and thick sheet finite elements. The analysis of movements and tensor deformational states of the different structural elements was performed with the software Sap2000 v.14.

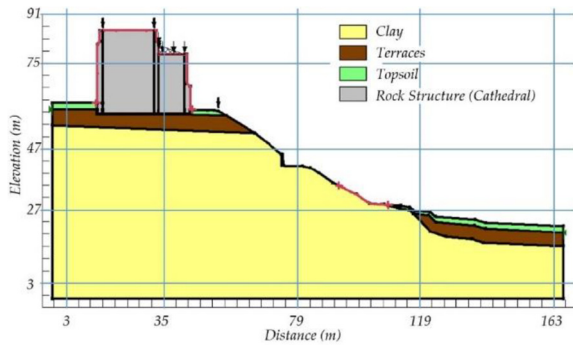


Figure 4. Geotechnical modelling of a topographic profile of the slope cathedral complex.

Using the estimation model, which considers the real dimensions of walls, arches and vaults as well as the resistant characteristics of materials, tensional behaviour under different hypothetical loads is studied. The model reproduced the pathologies present in the cathedral locating the main cracks and deformations.

#### IV. RESULTS

From the analysis of the cathedral it was deduced that, during development of the works, it does not suffer movements tending towards any imbalance in its structure.

##### A. Obtaining the orthoimages

The orthoimages of the floors elevations and sections were obtained from the projection of a plane to infinity, that is, with an orthographic view, such that its content and parallel to the plane their real measurements were retained. The floors were generated from the section of the point cloud by a plane of a certain level, Z, and the planimetry obtained is expressed in an overall system of coordinates.

From these orthoimages the wall faces and elements of interest (Figure 5) were digitalized using CAD software.

##### B. Topographic calculations and geometry

The comparison of results according to the precision achieved reflects the absence of movement of the structure and of the foundation ground. High precision levelling throughout the surveys and of the points read presented maximum drops of 2 mm. The work carried out by high precision levelling reflects measurement tolerances of 0.1 mm. Of the 24 points studied, 20 remained materialized from 2012 until 2015.

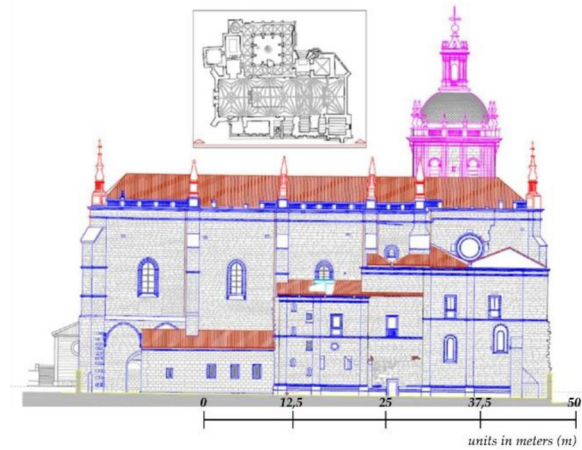


Figure 5. Delineated plane in CAD, seen from the eastern façade of the Coria Cathedral.

Regarding the measurements with GNSS in the different surveys, the fit of the external network presented maximum differences of 3 mm in planimetry and 5 mm in altimetry. The proximity network, processed from the data of the external network and for the coordinates obtained in the first processing, presented maximum variations of 7 mm in planimetry and altimetry. The differences found were of less than 10 mm, which is the precision of the measuring system, reflecting the absence of greater movements of this range in the foundation platform of the cathedral. The proximity network posed some difficulty in data collection and processing: problems in the location of the bases (accessibility, stability and robustness of the signals over time); errors due to occlusion or obstruction of satellites; errors due to the poor rebound of the multichannel signal; errors due to jumps in the cycle in the resolution of ambiguities.

The problem that arises in data collection resides in the location where the GNSS reading points are located. As they are situated in the interior of the streets of the town, shadows and reflections in satellite readings are inevitable. Moreover, during the measuring process the sensors used are exposed to passersby and vehicles, which increase the effects of shadows and reflections. The methodology was difficult to implement, above all that of the proximity network, to a great extent owing to the characteristics of the area of measurement within the urban centre surrounded by so many buildings of significant height.

With TLS, an exhaustive knowledge of the structural configuration of the cathedral was obtained with 2,987 million of points. This information facilitated a reliable structural calculation of the building in its real state, eliminating assumptions or simplifications of parameters and provided the real thicknesses of walls, the deviation of vault ribs and their thicknesses, the height of the backfill of the vault, all leading to the correct estimation of the loads that the structure is bearing.

An equally exhaustive study was made of existing pathologies. Figure 6 and Table 1 reflect the study of

cracks in the eastern façade. In order to obtain the geometry of the cracks (Table 1) two procedures were used. Firstly, direct measurement on the point cloud at 60 different locations. Table 1 shows the highest value obtained. In order to check it is measured once more in CAD from the orthophotographs of elevations generated with a resolution of 0.5 centimetres. The difference in the results of the two methods is below the resolution limit.

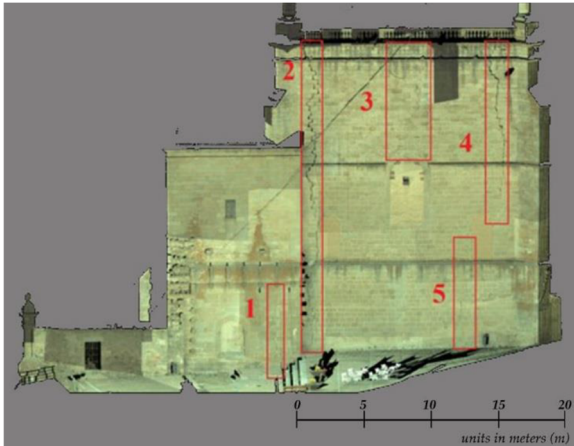


Figure 6. Analysis of the cracks in the eastern façade.

Table 1. Results of the geometric analysis of cracks in the eastern façade

Crack number	Length [m]	Maximum width [cm]
1	6.467	8.2
2	24.322	10.1
3	8.066	4.8
4	14.235	8.8
5	9.219	6.2

Vaults 2 and 5 (in the central nave) are those that have the best preserved symmetry (Figure 7a) (Figure 7b). Vaults 1 and 4, particularly the latter, are those with the greatest deformations with respect to their theoretical model. Vault 4 presents a marked deformation in the upper left part, both in the intrados (Figure 7a) and in the extrados (Figure 7b).

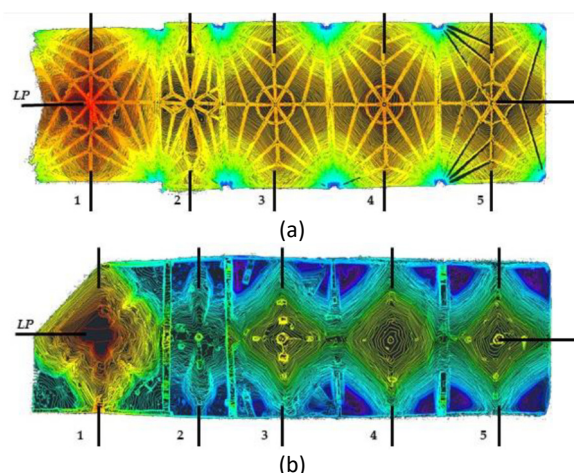


Figure 7. Topography of the vaults obtained from the 3D point cloud: a) Bottom of vaults; b) Top of vaults

### C. Structural stability

The cathedral rests on a granular upper layer, a few meters thick, of siliceous gravel with a clay silt matrix from the Quaternary, draining, with medium compactness and sufficient capacity to bear the load. Under the granular substrate there is another of clay silt, of great depth, cohesive, non-expansive and with low plasticity.

The foundations of the cathedral are direct, in which the load bearing walls, hardly increasing its section, are supported by both the described substrates. The estimated tensions transmitted to the foundation grounds reach maximum values of around 7 kp/cm<sup>2</sup> which is higher than that required for this kind of material in a new construction.

From the studies carried out on the stability of the slope we can conclude that the slope on which the cathedral sits, specifically the east-south area, presents tension and deformation states close to a limit situation, and local phenomena of instability may arise in conditions of ground saturation within the foundations or of moderately intense seismic waves.

The laws of effort the structural elements withstand have been calculated and the main pathologies exhibited by the cathedral are reproduced. The results of vertical descent movements, horizontal deformation, movements according to different directions, maximum and minimum tensions, Von Mises tensions, for both vaults and walls, are obtained for different hypotheses of calculation. The model finds the existing cracks. From the geometric information of the building, the laws regarding efforts and deformations of the model bar elements, as complete arches of vault, have also been calculated, locating which areas of the arches are working a traction effort.

## V. DISCUSSION

Coria Cathedral is a special case of a large building which has suffered a long history of damage. The incorporation of modern geomatic techniques in which structural and geotechnical analyses have been used to support the work have helped to deepen the research into the secular causes of the building's ills. These have been narrowed down and identified.

The three-dimensional model of the whole building and its most immediate surroundings were essential for the development of the remaining activities, such as the geometric analysis of the elements making up the building, the study of the pathologies according to the cathedral's distribution and real dimensions, the elaboration of a structural model that fits the reality and the geometric basis for the drawing up of a constructive project.

The preparation of valid graphic documentation for the preparation of the project and the construction of models requires a manual process using CAD for the transformation of the point cloud and orthoimages to vectorial geometric entities that define floors,

elevations and sections. This manual work requires the development by qualified personnel with knowledge not only of geometry, but also of architecture and engineering.

The TLS data collection work was efficiently, the problem really arose in the upper parts outside the building (roofs), because of inaccessible areas or those difficult to access and the possible dangers the work may involve on steeply sloping surfaces at height. Nevertheless, despite these difficulties, practically the entire building was surveyed with the exception of individual points that are not of the utmost importance to the studies carried out, such as, for example, the upper part of the lantern that crowns the tower vault, which is inaccessible.

No movements were detected in the cathedral surroundings during the surveys. The three-dimensional geometric model is a suitable basis for the elaboration of the corresponding analysis model and structural calculation used. Its validity would only be in doubt as a result of possible differential movements or displacements of sufficient size as to invalidate the model, which would certainly be reflected in the increase in the size of the existing cracks in the building, the appearance of new ones or variations in the verticality of the walls, among other phenomena. None of these were detected during the work. The results of the structural and geotechnical calculations have shown the behavior of the building and its surroundings.

## VI. CONCLUSIONS

The studies and works carried out on the cathedral of Coria are an example of how an interdisciplinary approach must be applied in the comprehensive conservation of buildings of historic heritage.

The validity of the application of geomatic techniques with terrestrial sensors in the management of the preservation of cultural heritage is clear. Through the technique of TLS exhaustive knowledge of the geometry of an individual building is achieved permitting the later development of exact studies of geometric, structural and even geotechnical analyses. They are, therefore, techniques that can be used within a much broader spectrum of uses than simply data collection itself.

The combination of these Terrestrial Laser Scanner (TLS) and Global Navigation Satellite System (GNSS) establishes reliable bases of graphic and exact information which clears the way to creating models of structural and geotechnique analysis, that can lead to the design of projects whose aim is the preservation and stabilization of buildings of heritage value. The case of the work performed on Coria Cathedral is the paradigm of the use and interrelationship of different techniques leading to the definition and execution of restoration works and structural consolidation in which geomatic techniques are placed, if not as the starting

point, at least as the fundamental basis that opens the way to other disciplines.

The techniques and methodologies used offer results of real and exact geometry associated with the date the data are collected. The monitoring of movements in this kind of buildings with secular pathological problems must involve the analysis of the evolution of movements of structural elements or those that constitute the building itself.

Traditionally, analysis has been made using fixed apparatus auscultation of relative movements in local elements. These are high precision sensors with relatively short runs, which can measure the opening of cracks and fissures (fissurometers), twists in wall faces (clinometer), relative movements between wall faces (convergence cells) etc. These sensors have the advantage that they offer readings with cadence to be defined by the user by means of suitable software, though they have the drawback of their location at one point and the need to keep the auscultation system itself in place for a long time. It would be interesting to explore the possibility of a system that coordinates both techniques, one of high precision auscultation sensors and of periodic data collection by complete geomatic techniques of singular or sensitive elements on an initial model of the entire building.

The works and studies described in this article have been of great importance to the development of technical projects of consolidation and restoration of Coria Cathedral.

## VII. ACKNOWLEDGEMENTS

The works described in this article have been made possible thanks to financing by the Diocese and Cathedral Council of Coria-Cáceres, cultural funding of 1.5% from the Ministry of Development of the Government of Spain and subsidy from the Junta of Extremadura. In the preparation of the article, the collaboration of the Cathedral Council of Coria-Cáceres, the Diocesan. Also, this publication has been made possible thanks to funding granted by the Consejería de Economía, Ciencia y Agenda Digital de la Junta de Extremadura and by the European Regional Development Fund of the European Union through the reference grant GR21156.

## References

- Bishop, A., and Morgenstern, N. (1960). Stability Coefficients for Earth Slopes. *Géotechnique*, 10(4), pp. 129-153.
- Bishop, A. W. (2008). The use of the slip circle in the stability analysis of slopes *The Essence of Geotechnical Engineering: 60 years of Géotechnique* (pp. 223-233): *Thomas Telford Publishing*.
- Bitelli, G., Dellapasqua, M., Girelli, V., Sanchini, E., and Tini, M. (2017). 3D geomatics techniques for an integrated approach to cultural heritage knowledge: the case of San Michele in Acerboli's church in Santarcangelo di Romagna. *International Archives of the Photogrammetry, Remote Sensing & Spatial Information Sciences*, 42.

- Calina, A., Calina, J., and Milut, M. (2015). Study on Levelling Works Made for Drawing Tridimensional Models of Surface and Calculus of the Volume of Earthwork. *Agriculture and Agricultural Science Procedia*, 6(Supplement C), 413-420. doi: <https://doi.org/10.1016/j.aaspro.2015.08.109>
- Caputo, R., Pellegrinelli, A., Bignami, C., Bondesan, A., Mantovani, A., Stramondo, S., and Russo, P. (2015). High-precision levelling, DInSAR and geomorphological effects in the Emilia 2012 epicentral area. *Geomorphology*, 235(Supplement C), 106-117. doi: <https://doi.org/10.1016/j.geomorph.2015.02.002>
- Cuenca Payá, A. (2001). Comentarios para el cálculo de taludes.
- Dierendonck, A. J. V., Fenton, P., and Ford, T. (1992). Theory and performance of narrow correlator spacing in a GPS receiver. *Navigation*, 39, 265.
- Heinrich-Wild-Strasse. (2008). Leica GPS1200 User Manual. Switzerland: Leica Geosystems AG.
- Jurado, F. (2014). Consolidación Estructural y Restauración de la Catedral de Coria, Cáceres, cuya primera fase se aborda en la actualidad: *Oficina de Arquitectura de Francisco Jurado*.
- Kamanbedast, A., and Delvari, A. (2012). Analysis of Earth Dam: Seepage and Stability Using Ansys and Geo-Studio Software. *World Applied Sciences Journal*, 17(9), pp. 1087-1094.
- Lovse, J. W., Teskey, W. F., Lachapelle, G., and Cannon, M. E. (1995). Dynamic Deformation Monitoring of Tall Structure Using GPS Technology. *Journal of Surveying Engineering*, 121(1), pp. 35-40. doi: [doi:10.1061/\(ASCE\)0733-9453\(1995\)121:1\(35\)](https://doi.org/10.1061/(ASCE)0733-9453(1995)121:1(35))
- Martínez Vázquez, F. (1999). El terremoto de Lisboa y la catedral de Coria.(Vicisitudes del Cabildo), pp. 1755-1759. *Colección Temas Cauriacienses*, 5.
- Mogollón, F.J. G. (1999). La catedral de Coria: arcón de historia y fe: Edileisa.
- Núñez Martín, M. L., and Molina Delgado, P. A. (2011). Las murallas medievales de Coria y la construcción de la Catedral. *II Jornadas de Arqueología Medieval de la Marca Inferior de Al-Andalus*, Mérida (España).
- Oreni, D., Brumana, R., Torre, S. D., and Banfi, F. (2017). Survey, HBIM and conservation plan of a monumental building damaged by earthquake. *International Archives of the Photogrammetry, Remote Sensing & Spatial Information Sciences*, 42.
- Rodríguez Martín, M. (2015). El Puente de Hierro de Coria: *Ayuntamiento de Coria*.
- Rodríguez-Pascua, M., Silva, P., Atienza, P., Giner-Robles, J., and Pérez-López, R. (2011). Earthquake archaeological effects generated by the Lisbon earthquake (first of november 1755) in the Coria's cathedral (Cáceres, western Spain). Paper presented at the Proceedings of the 2nd INQUA-IGCP 567 *International Workshop on Active Tectonics, Earthquake Geology, Archaeology and Engineering*, 19-24 September.
- Travesí, E. A. (2013). Fuentes impresas e historiografía del obispado y diócesis de Coria en la Edad Media. Printed sources and historiography in the Coria's bishopric and diocese in Middle Ages. *De Medio Aevo*, 2(1), pp. 43-90.



## Monitoring the production process of lightweight fibrous structures using terrestrial laser scanning

Laura Balangé<sup>1,2</sup>, Corinna Harmening<sup>3</sup>, Rebeca Duque Estrada<sup>4,2</sup>, Achim Menges<sup>4,2</sup>, Hans Neuner<sup>5</sup>,  
Volker Schwieger<sup>1,2</sup>

<sup>1</sup> Institute of Engineering Geodesy, University of Stuttgart, Geschwister-Scholl-Str. 24D, 70174 Stuttgart, Germany, ([laura.balange@iigs.uni-stuttgart.de](mailto:laura.balange@iigs.uni-stuttgart.de); [volker.schwieger@iigs.uni-stuttgart.de](mailto:volker.schwieger@iigs.uni-stuttgart.de))

<sup>2</sup> Cluster of Excellence “Integrative Computational Design and Construction for Architecture”, University of Stuttgart Keplerstraße 11, 70174 Stuttgart, Germany

<sup>3</sup> Geodetic Institute, Karlsruhe Institute of Technology, Englerstr. 7, 76131 Karlsruhe, Germany, ([corinna.harmening@kit.edu](mailto:corinna.harmening@kit.edu))

<sup>4</sup> Institute for Computational Design and Construction, University of Stuttgart, Keplerstraße 11, 70174 Stuttgart, Germany, ([rebeca.duque@icd.uni-stuttgart.de](mailto:rebeca.duque@icd.uni-stuttgart.de); [achim.menges@icd.uni-stuttgart.de](mailto:achim.menges@icd.uni-stuttgart.de))

<sup>5</sup> Department of Geodesy and Geoinformation, Research Division Engineering Geodesy, TU Wien, Wiedner Hauptstraße 8, 1040 Vienna, Austria, ([hans.neuner@geo.tuwien.ac.at](mailto:hans.neuner@geo.tuwien.ac.at))

**Key words:** *B-spline approximation; cross-sectional areas; laser scanning; lightweight fiber structures; monitoring; convex hull; quality assurance*

### ABSTRACT

The Cluster of Excellence *Integrative Computational Design and Construction for Architecture* at the University of Stuttgart brings together various disciplines to jointly develop amongst other things a better understanding of processes in the manufacturing and construction domain. One of the cluster’s aims is to create new solutions for the construction of lightweight fibrous structures using coreless winding of lightweight fiber composite systems. For this purpose, a precise geometry and an understanding of the fibers’ behavior during the production process are of major importance. The fibers’ production process is monitored by repeatedly scanning the fibers during different stages of the process using a terrestrial laser scanner. In order to determine the geometry of the fibers’ axes as well as their cross-sections, two different strategies are used. The first strategy focuses on the segmentation of several straight lines between two intersection points. For the comparison of the individual fabrication steps, the positions of the intersection points are contrasted. For the cross-sectional areas of the fibers, orthogonal planes of intersection are then defined and all points within a predefined area are projected onto this plane. Then the area is calculated using a convex hull. In the second strategy, the fibers’ main axes are represented by best-fitting B-spline curves. The borders of the cross-sections of interest are also approximated by best-fitting B-spline curves, forming the basis for the final determination of the cross-sectional areas. In this case study two epochs are analyzed with a deformation of the size of around 1cm. For both epochs the cross-sections are calculated in cm steps.

### I. INTRODUCTION

Fiber-reinforced polymers (FRP) have been used for structural applications for many years in industries like automotive, aeronautics, and ship-building. Their wide application in these fields is due to a number of impressive properties, which in the case of carbon-fiber composites, include their low thermal expansion, high corrosion resistance, and their high strength to weight ratio (Fitzer, 1985).

Advances in robotic fabrication processes, such as coreless filament winding (CFW), enabled the manufacturing of highly differentiated FRP components, by relying the creation of a component on a designed sequence of fiber-fiber interaction instead of prefabricated winding mandrels or expensive formwork as commonly used in the industry (Prado *et al.*, 2014). This fabrication technique has been

developed and improved over the last decade at the University of Stuttgart through a series of projects and built demonstrators (Menges and Knippers, 2015; Prado *et al.*, 2017; Dambrosio *et al.*, 2019; Bodea *et al.*, 2021).

Such a fabrication system requires a high level of control over the fiber orientation since geometries are formed by the systematic sequence of fiber placement within a defined boundary condition. Geometrical differentiation is achieved through the combination of customized parameters, such as boundary geometry, winding pin locations, and sequence, also known as syntax. Their structural performance is directly dependent on good fiber-fiber interaction, that is when fibers are pressed against each other, ensuring that the system forms a lattice structure with reduced buckling length of each fiber segment (Prado *et al.*, 2014).

Predicting the interaction between fibers resulting from CFW is considered one of the biggest challenges during the design phase of such structures. As non-cured impregnated fibers do not possess any bending resistance during fabrication, every new fiber segment will deform the previously wound ones (Waimer *et al.*, 2013). The resulting deformation that induces the tension on the existing fibers will also be directly related to the final resulting form. This highly dynamic and incrementally changing system presents a challenge when being translated into a digital domain. A way to better inform and improve the simulation of CFW structures is by knowing more about what happens during the winding process. Understanding how different parameters can affect the consecutive deformations and final geometry can be helpful for fine-tuning the simulation method as well as for informing future design decisions.

The challenge from geodetic perspective is, that in contrast to conventional deformation analysis, the deformations are large compared to the object size (Dupuis *et al.*, 2016). For the cross-sections the challenge is, that they are very small compared to conventional applications like the cross-section of a tunnel or tree stem (Wang *et al.*, 2015; Eto *et al.*, 2020).

The aim of this contribution is to investigate the fiber geometry in each epoch. Therefore, the production process is monitored by repeatedly scanning different stages of the resulting fibers using terrestrial laser scanning. The parameters of interest, the position and orientation, describing the fibers' final geometry as well as the deformation between different production steps, the intersection between fibers and the area of fiber cross-sections are afterwards derived using two different strategies.

The paper is structured as follows: In Section II the mathematical basics that are required to derive the parameters of interest are provided. Section III presents details regarding the monitoring set-up. The two strategies used in this contribution to determine deformations and the final geometry are developed in Section IV. Section V presents, compares and discusses the results delivered by the two different strategies. Finally, Section VI concludes the paper.

## II. MATHEMATICAL BASICS

In this section, the mathematical basics of both algorithms are explained, which are needed to determine the position and orientation of the fibers as well as the area of the cross sections.

### A. Line Estimation

The definition of a line is given by a direction vector as well as a base point. A main direction of a point cloud is in general given by the principal component analyses according to Pearson (1901). For the estimation of this direction the mean value of all points need to be

calculated firstly. Afterwards the residuals of the point cloud are calculated by (Eq. 1):

$$\delta X = X - i \cdot X_{mean} \quad (1)$$

where  $\delta X$  = Residuals of the point cloud  
 $X$  = Points of the point cloud  
 $i$  = Matrix with ones with the dimension  $n \times 3$   
 $X_{mean}$  = Mean value of all points.

Using the residuals ordered as a line vector and the number of points the variance-covariance matrix is calculated by (Eq. 2):

$$C = \frac{\delta X' \cdot \delta X}{n - 1} \quad (2)$$

where  $C$  = variance-covariance matrix  
 $\delta X$  = Residuals of the point cloud  
 $n$  = Number of points.

A singular value decomposition of the variance-covariance matrix delivers the main direction of the point observations.

### B. Convex hull and area of polygon

The convex hull of a planar data set is the minimum area convex polygon including all data points. For the estimation of the vertices of the convex hull several algorithms are established (Graham, 1972; Jarvis, 1973). In this investigation, the QuickHull algorithm was used (Green and Silvermann, 1979). Here, first the two points of the point set are determined with the minimum and maximum x coordinates, since these are certainly part of the convex hull. Then a line is drawn through both points and the set of points is divided into two halves by this line. Now the points with the maximum distance to the line in each point cloud half are searched for and a triangle is formed with it. All points within the triangle are not vertices of the convex hull. This is repeated with the two new triangle sides until all points are either a vertex of the convex hull or are within the convex hull.

With the vertices of the convex hull the area can be calculated by the equation calculated for convex polygons according to Bronstein *et al.* (2001) as (Eq. 3):

$$A = \frac{1}{2} \sum_{j=1}^k (x_j y_{j+1} - x_{j+1} y_j) \quad (3)$$

where  $A$  = Area of the convex hull  
 $x, y$  = Coordinates of the points  
 $k$  = Number of points  
 $j$  = point index, for  $j = k: j + 1 = 1$

### C. Estimating best-fitting B-spline curves

A B-spline curve  $\mathbf{C}(u)$  is defined by Piegl and Tiller (1997) (Eq. 4):

$$\mathbf{C}(u) = \sum_{i=0}^{n_p} N_{i,p}(u) \cdot \mathbf{P}_i. \quad (4)$$

According to formula (Eq. 4), a three-dimensional curve point  $\mathbf{C}(u) = [C_x(u) \ C_y(u) \ C_z(u)]^T$  is computed as the weighted average of the control points  $\mathbf{P}_i$ , with the weights being defined by the B-spline basis functions  $N_{i,p}(u)$  of degree  $p$ . The basis functions can be computed recursively (Cox, 1972; de Boor, 1972) and are functions of the curve parameter  $u$ , locating a curve point on the curve. The corresponding parameter space  $0 \leq u \leq 1$  is subdivided by means of a knot vector  $\mathbf{U} = [u_0 \ \dots \ u_r]^T$ , providing the B-spline's property of locality: The shifting of a single control point changes the curve only locally.

When using B-spline curves to approximate point clouds, the data points  $\mathbf{C}(u)$  are the observations within a Gauss-Markov-Model (Bureick *et al.*, 2016) (Eq. 5):

$$\hat{\mathbf{C}}(u) = \mathbf{C}(u) + \boldsymbol{\varepsilon} = f(\mathbf{P}_i), \quad (5)$$

where  $\boldsymbol{\varepsilon}$  = residuals

Allowing for the estimation of the B-spline control points' positions. In order to obtain a linear estimation model, the remaining parameter groups (degree of the basis functions, knots, number of control points, curve parameters) are usually excluded from the estimation procedure and are determined in a different way. Choosing the optimal number of control points can be interpreted to be a model selection problem (Harmening and Neuner, 2016) and can be for example solved by classical model selection strategies e. g. BIC (Bayesian Information Criterion) or by means of structural risk minimization. If the latter strategy is used, the choice of the optimal degree of the basis functions can be included in the model selection task (Harmening, 2020). Sophisticated strategies for estimating the knot positions can be e. g. found in Bureick *et al.* (2019), whereas Piegl and Tiller (1997) propose a more simple, but also less computational complex method. For ordered data points standard strategies exist to allocate appropriate curve parameters to the observations (*cf. e. g.* Piegl and Tiller, 1997).

### III. MONITORING SET-UP

For the test, a robotic fabrication setup was designed and implemented (*cf.* Figure 1). It was comprised of a 6-axis robotic arm coupled with a custom end-effector as well as a two-axis positioner and a reconfigurable frame. The material used was in the form of towpregs,

which are pre-impregnated carbon fiber bundles pre-wound on spools. The spools were placed on the end-effector and the fiber was guided through rollers, eyelets, and a tube in order to be hooked around the anchors.

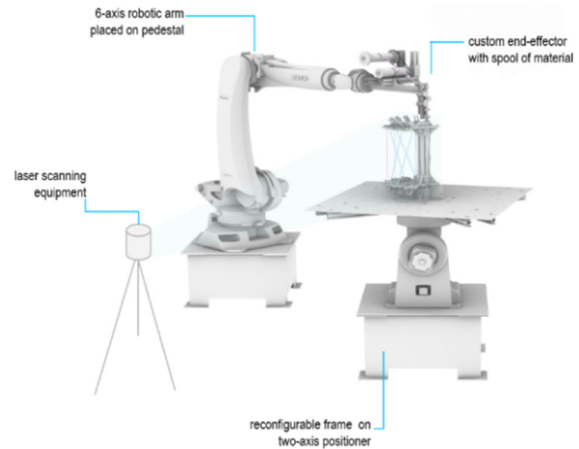


Figure 1. Robotic setup for coreless filament winding comprised of a 6-axis robotic arm coupled with an end-effector containing the spool of pre-impregnated carbon fibers, a two-axis positioner supporting the reconfigurable frame, and the laser scanning equipment.

All samples were fabricated with carbon fiber rovings pre-impregnated with epoxy resin. The fiber bundle was formed by two untwisted rovings with filament counts of 48 k and a 50-50 fiber/resin ratio. After being impregnated, the spools were stored in a cooling compartment in order to avoid the curing process to start. Before the beginning of fabrication, spools needed around 40 minutes to defrost. After reaching room temperature, the curing process starts, directly affecting the resin's viscosity. Even though fabrication time was kept to a minimum, it was still possible to observe different material behaviors related to the time the material was exposed to room temperature.

Considering the goal to understand how every new wound fiber could affect the whole system, the test required the scanning of the full fiber geometry after every new intersection was created.

In this study, measurements were taken with a Trimble X7 laser scanner. The measurements were carried out with a resolution of 5 mm at a distance of 10 m and a 3D point accuracy of 2.4 mm at 10 m (Trimble Inc., 2020). The elements have a height of approximately 40 cm and a width of 20 cm (*cf.* Figure 2) and a diameter of the fibers of 1 cm. The required accuracy for the measurements is in the range of several millimeters.

As part of the data pre-processing, a target based registration, as well as some filtering using the Statistical Outlier Removal (SOR) filter in CloudCompare was performed to detect and remove isolated points. For further data processing, the frame was also cut out and only the individual fibers were investigated. For the following investigations two measurement epochs

were considered. The measured epochs are visualized in Figure 3.

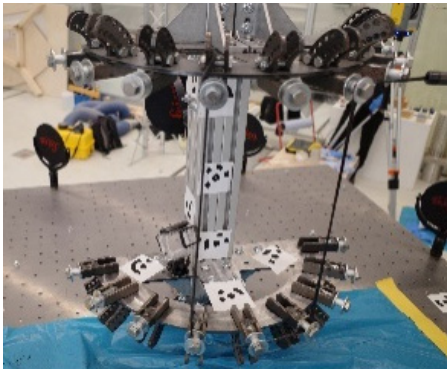


Figure 2. Monitoring set-up with the element in Epoch 1.

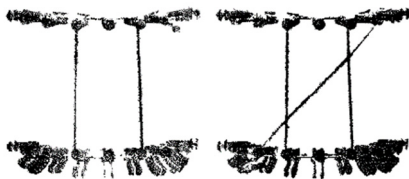


Figure 3. Measured Epochs. Left: first epoch with two separated fibers. Right: second epoch with one additionally crossed fiber.

The aim of this investigation is to determine the fiber geometry in each epoch. Here, the position and orientation of the fibers as well as the shape, namely the cross-sections, are taken into account.

#### IV. DETERMINING THE SHAPE OF LIGHTWEIGHT FIBROUS STRUCTURES

For the determination of the shape of the fiber two approaches were used. They are similar in their general procedure but differ in the specific calculation methods that are used. Figure 4 shows the workflow of both algorithms. The exact procedure is afterwards explained in the sections A and B.

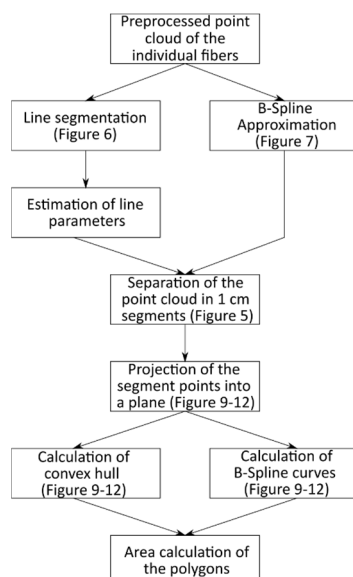


Figure 4. Workflow of the two approaches for shape detection of lightweight fibrous structures.

#### A. Fiber approximation and area calculation using line segmentation and a convex hull

In this approach, represented by the left side of Figure 4, the individual line segments are firstly segmented manually. A line estimation is then performed for the individual line segments. For this purpose, the direction of the straight line is determined by using a principal component analysis. In addition, the beginning and end of the segments are determined.

If the line parameter and the start and end point of all segments are available, the intersection points can be calculated. Therefore, all possible combinations between two segments are formed and the point of the minimal distance between the segments is calculated. To check whether the calculated point is an intersection point or not, firstly it is checked whether the point is within the volume of the point cloud. The second criteria for the decision is the distance to the segments. Here a limit of 5 mm has proven to be suitable in empirical tests. If all intersection points are found a clustering of these points needs to be done to find identical intersection points.

For this purpose, one of the selected intersection points is chosen randomly and the distances to all other points are calculated. All points with a distance less than 5 mm are combined into one intersection point. This value was chosen due to the fact, that in this case a distance between 5 mm between two intersections can be guaranteed. Among all assigned lines a common intersection point is determined. Since not all lines usually intersect at a single point, the sum of the distances of all lines to a common intersection point is minimized. This process is carried out iteratively until all intersection points are assigned.

In order to determine the deformation of the individual fibers between two epochs, the corresponding intersection point in the previous epoch must be determined. However, in the data set considered in this study, the intersection points in the first epoch do not yet exist. Therefore, to calculate the deformation, the minimum distance from the intersection point to all lines in the previous epoch is determined. The line with the minimum distance to the new intersection point is specified as the corresponding line. In addition, the perpendicular base point on this line is determined and the deformation can be calculated as the Euclidean distance between base point and intersection point.

In addition to the line parameters and intersections points, the cross-sectional areas of the individual line segments are also of importance. For this purpose, the line is firstly divided into 1 cm segments as shown in Figure 5.

The calculation of the cross-sectional areas takes place at these predefined positions. To calculate the area of a segment, a plane with the direction vector of the associated line is defined by the starting point of the segment on the line. Then a cylinder is created with the

direction vector of the estimated straight line as the axis of rotation with a radius of 15 mm around the segment. This limit was chosen, because it is larger than the actual radius of the fiber, but still small enough that no other fiber will be in the cylinder. Afterwards, all points that lie within the cylinder are determined and projected onto the previously created plane. For the calculation of the cross-sectional area, the convex hull is now formed around all projected points and then their surface area is calculated according to Equation (4).

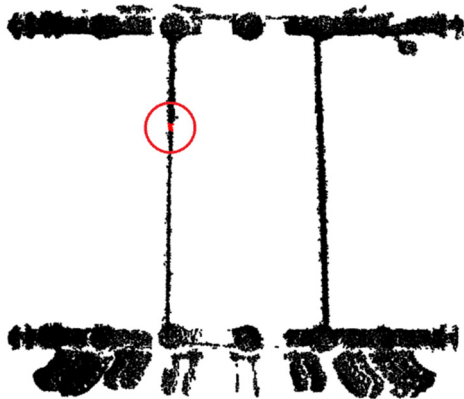


Figure 5. Point cloud of Epoch 1 (black) with one exemplary 1 cm segment (red).

#### B. Fiber approximation and area calculation using B-spline curves

The second strategy, represented by the right side of Figure 4, uses best-fitting B-spline curves to determine the shape of the fibers. For this purpose, point clouds representing a fiber are approximated by means of best fitting B-spline curves as described in Section II C. For all fibers cubic curves are chosen, with the optimal number of control points being determined by means of the Bayesian information criterion (Schwarz, 1978). The knot vectors are determined as proposed by Piegler and Tiller (1997) and the centripetal parameterization (cf. Piegler and Tiller, 1997) is chosen to allocate curve parameters to the observations. This strategy results in two B-spline curves for epoch 1 and three curves for epoch 2.

In analogy to approach A, the deformation of the fibers is represented by means of the behavior of two characteristic points. For this purpose, the intersection points of the fibers of the second epoch are determined: Therefore, the best-fitting B-spline curves are sampled with a very high resolution. Afterwards, for the curve representing the crossing fiber (cf. Figure 3), the nearest neighbors of the curve points representing the other two curves are determined. The results are two point pairs with minimal distance (for each pair, one point lies on the crossing fiber, the other point lies on one of the other two fibers). The final intersection points are then determined as the average of these point pairs. The correspondences of these points in the first measurement epoch are then defined by the

nearest neighbors of these intersection points on the B-spline curves representing the fibers of the first measurement epoch.

The two characteristic points are complemented by means of the cross-sectional areas, completing the shape description of the fibers. To keep the determined cross-sectional areas comparable with the corresponding results delivered by strategy A, the same 1 cm-segments of the point clouds are used for the computations (see Figure 5).

In order to determine the cross-sectional areas, all points of the respective segment are initially projected in a plane by means of a principal component analysis. Afterwards, the boundary points of the projected segment are determined by means of the variant of the Douglas-Peucker-algorithm proposed in Harmening (2013). The detected boundary points provide the basis for the estimation of a closed B-spline curve, representing the segment's boundary. In principle, there exist three possibilities to obtain closed B-spline curves: The use of rational B-spline curves also allows for the representation of conic boundaries. However, in this application the number of observations is usually too small to jointly estimate control points and the corresponding weights. The second possibility is to stay with the non-rational B-splines and to close them by wrapping either the knots or the control points by means of constraints. This strategy also does not lead to satisfactory results due to the very few observations available. For this reason, the third and simplest approach is chosen: By selecting one of the boundary points as both the start and end points of the curve, a closed curve results.

Finally, the area surrounded by the B-spline curve is determined by interpreting the curve points of the sampled curve as a very fine polygon and by computing the area enclosed by this polygon.

## V. RESULTS

#### A. Determination of the fibers' geometry and their deformation

In the first part of the investigations, the fiber segments' geometry is determined by a segment-based line estimation as well as by means of a B-spline approximation. Both approximations of the point clouds are then used to determine characteristic points and to compute the deformation of these points.

Figure 6 graphically presents the results of the fibers' approximation by means of approach A (line approximation) in terms of the best fitting lines and the computed intersection points.

The results of approach B (B-spline fitting) are presented in Figure 7. Unlike approach A, in this approach the fibers are modeled as a whole and do not need to be further subdivided.

Finally, Table 1 contrasts the coordinates of the determined characteristic intersection points as well as the subsequently derived displacements of both

approaches. As can be seen, both the coordinates of the characteristic points as well as the deformation in terms of the absolute distance between these characteristic points are identical.

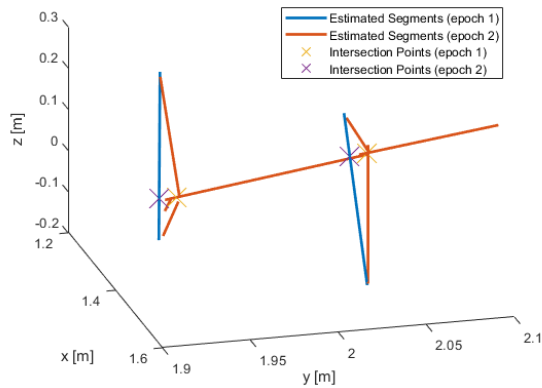


Figure 6. Results of line estimation and calculation of line intersection points.

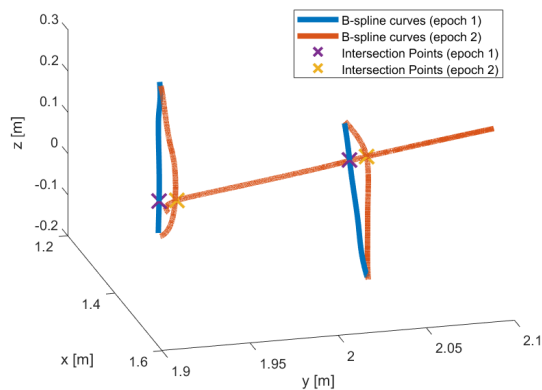


Figure 7. Results of the B-spline estimation and calculation of the respective intersection points.

Table 1. Intersection points and determined deformations

Intersection Point	Coordinates [m]			Deformation [m]
	X	Y	Z	
Point 1 (Line)	1.315	1.946	-0.051	0.010
Point 1 (B-Spline)	1.316	1.947	-0.051	0.010
Point 2 (Line)	1.498	2.030	0.152	0.012
Point 2 (B-Spline)	1.498	2.030	0.151	0.012

### B. Determination of the cross-sectional areas

The results of the determination of the cross-sectional areas are summarized by means of Figure 8 as well as Table 2.

In Figure 8 the cross-sectional areas determined with the two described approaches are graphically opposed for the first measurement epoch as an example. Obviously, for most of the segments the B-spline-based approach determines the cross-sectional areas smaller than the approach based on the convex hull.

This result is supported by Table 2, summarizing the differences (Eq. 6)

$$d = ||A_B - A_C||, \quad (6)$$

where  $A_B$  = Cross-sectional areas delivered by the B-spline based approach

$A_C$  = Cross-sectional areas delivered by the convex hull based approach

Of the determined cross-sectional areas by means of three parameters (mean value as well as minimum and maximum value).

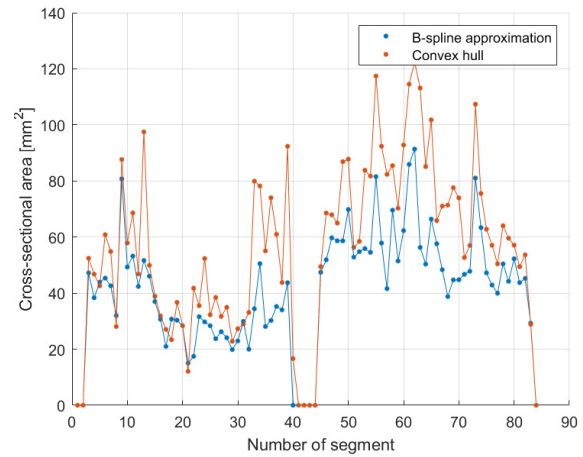


Figure 8. Cross-sectional areas of the first measurement epoch.

Table 2. Differences of the determined cross-sectional areas

	Epoch 1	Epoch 2
Mean(d) [mm <sup>2</sup> ]	-16.21	-3.79
Min(d) [mm <sup>2</sup> ]	-56.82	-70.80
Max(d) [mm <sup>2</sup> ]	7.36	39.66

As can be seen, the mean values of the differences are negative in both epochs, underlining the fact that - on average - the B-spline-based approach delivers smaller cross-sectional areas than the approach based on the convex hull. However, this does not apply to all segments, as indicated by the maximum values of the differences, which are positive for both epochs. Hence, there do exist segments, for which approach A delivers smaller areas than approach B.

As furthermore indicated by the range of the differences, the magnitude of the differences varies strongly over the segments.

In order to investigate the causes of these deviations in more detail, the results of selected and representative individual segments are regarded. Figures 9 - 12 presents the results of four segments, which demonstrate the advantages and disadvantages of both approaches and, hence, allow for the explanation of the results in Figure 8 and Table 2. In all four figures the blue points represent the projected point cloud of the segment. The purple triangles are those points of the point cloud which define the convex hull (plotted in green), whereas the red crosses are the points detected to be boundary points that provide the

basis for the estimation of the surrounding B-spline curve (plotted in yellow).

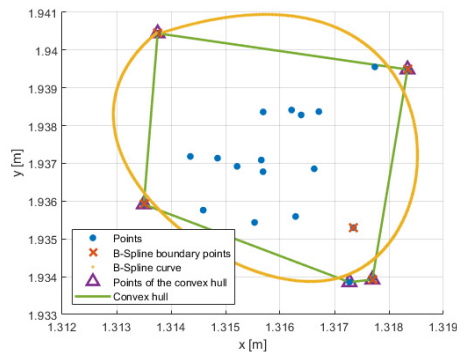


Figure 9. In detail investigation of the segments: Swinging out of the B-spline curve.

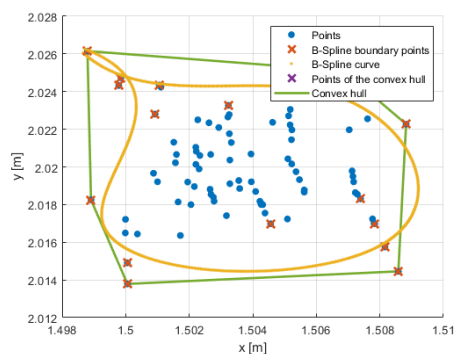


Figure 10. In detail investigation of the segments: Crossing over of the B-spline curve.

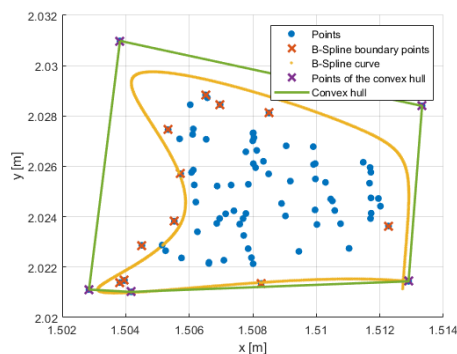


Figure 11. In detail investigation of the segments: Sensivity of the convex hull with respect to outliers.

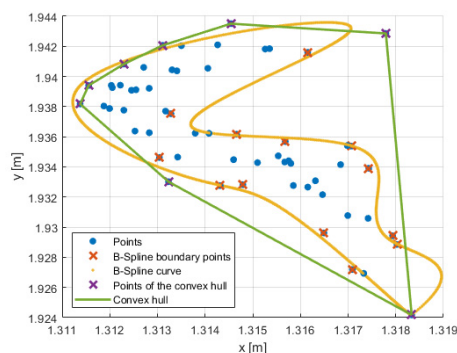


Figure 12. In detail investigation of the segments: Overestimation of the areas using the convex hull in case of complex and concave shaped boundaries.

In Figure 9 one of the rare situations, in which the B-spline-based approach results in a larger cross-sectional area than the convex hull-based approach, is presented. As can be seen, it is a segment with only few data points and, consequently, only few (six in this case) boundary points can be detected. With these six observations it is only possible to estimate a very simple B-spline curve, the shape of which is determined by less than six control points in order to maintain redundancy within the estimation problem (in the case presented four control points have been chosen). This simple B-spline curves swings off and does not any longer follow the actual boundary of the segment.

Figure 10 presents another weakness of the B-spline-based approach when only few boundary points can be detected. Due to the large gaps between the boundary points, the entire course of the curve is inadequately defined, allowing for the curve to cross over, a situation which is not desirable.

However, Figure 11 and Figure 12 present two situations in which the B-spline-based approach outperforms the convex-hull-based approach, pointing out the disadvantages of the latter as well the strengths of the former.

In both figures situations can be seen in which the cross-sectional areas determined by means of approach B are clearly smaller than those delivered by approach A. The reason for this becomes obvious when observing the point clouds: Apparently, some of the segments have concave boundaries, which cannot be approximated sufficiently well by means of a convex hull, resulting in overestimated cross-sectional areas.

Another reason for the convex-hull-based approach to overestimate the cross-sectional areas is its sensitivity with respect to outliers: The two upper purple triangles in Figure 11 do not seem to be part of the actual cross-section, rather it looks like they are outliers. However, being the boundary points of the segment, they define the convex-hull and, thus, the cross-section. These two points are also detected as boundary points within the B-spline-based approach. However, due to the redundancy within the estimation of the best-fitting B-spline curves, their influence on the curve's shape and, thus, on the cross-sectional area, is considerably smaller. As a consequence, the cross-sectional area delivered by approach B seems to be more realistic than the area resulting from approach A.

Finally, Figure 12 highlights another strength of the B-spline-based approach compared to the convex-hull-based approach: As indicated by the data points' distribution, some of the segments have very complex shapes. The flexibility of B-spline curves allows for the accurate modelling of these complex boundaries, whereas the use of the convex-hull does not.

Thus, the in detail investigation of the individual segments allows for the conclusion that approach A is the more appropriate method when the segments consist of only few data points and when the boundary is indeed convex. By contrast, the B-spline-based

approach delivers more satisfactory results when the boundaries are complex and/or concave shaped as well as when outliers exist.

## VI. CONCLUSION

Within the framework of this project, the possibilities of two approaches were investigated in order to be able to realize a monitoring of the production process in the field of CFW and thus to be able to provide information about the interactions of the individual fibers during the production process. In addition, the shape of the fibers themselves, especially their cross-sectional area, was analyzed. In this study, point clouds from two measurement epochs were used to compare the two evaluation approaches. In the first approach a line estimation with subsequent calculation of the intersection points was carried out. In the second, the individual fibers were approximated by means of B-splines. In addition, the point cloud was separated in smaller segments with the size of 1 cm and the cross-section area was calculated with both approaches. Here approach one uses a convex hull and in approach two the area was calculated by the B-spline approach.

The comparison of the two approaches shows that both methods have their advantages as well as weaknesses and finally both methods achieve good results. For the calculation of the intersection points and thus also the path of the segments, both methods provide identical results and can therefore be considered equivalent. The calculation of the cross-sectional areas shows that the results of both methods strongly depend on the number and distribution of the measured points. The two methods were tested in this work on the basis of the same data, so that the uncertainties from the measurement process could be neglected for the comparison. An idea for the future is also to include some kind of outlier detection for the convex hull approach to improve the quality of the estimated area. A future improvement of the B-spline-based approach can be achieved by introducing constraints that prevent possible crossings of the curve. Furthermore, future research will include stochastic quantities to compare the results achieved by means of the two approaches. A necessary step for this are investigations regarding the stochastic properties of convex hulls.

However, in order to be able to make reliable statements about the geometry and shape of the fibers in the future, the quality of the used data set must be improved. Therefore, the material properties must also be taken into account. In addition to the specific properties of the resin, the fibers are moist during production and continue to dry over time. The investigation of these influences is therefore the focus of future work. This investigation is necessary as surface related uncertainties are of crucial importance for the final result (Chaudry, 2021). An idea for this is also the use of a multi-color laser.

Another point that should be considered in future work is the possibility of automated segmentation of line segments, especially for larger and more complex elements. Also, the measurement configuration becomes more important, since the problem of covering individual fibers increases with the complexity.

## VII. ACKNOWLEDGEMENTS

The research published in this article is supported by the Deutsche Forschungsgemeinschaft (DFG, German Research Foundation) under Germany's Excellence Strategy – EXC 2120/1 – 390831618. The authors cordially thank the DFG.

A part of the research was realized within a one-month research stay of the second author at the University of Stuttgart within the IntCDC incoming programme.

## References

- Bodea, S., C. Zechmeister, N. Dambrosio, M. Dörstelmann, and A. Menges (2021). *Robotic coreless filament winding for hyperboloid tubular composite components in construction*. *Automation in Construction*, Elsevier. DOI: 10.1016/j.autcon.2021.103649.
- Bronstein, I. N., K. A. Semendjajew, G. Musiol, and H. Mühligh (2001). *Taschenbuch der Mathematik*. Edited by überarbeitete und erweiterte Auflage 5. Frankfurt am Main: Verlag Harri Deutsch.
- Bureick, J., H. Alkhatib, and I. Neumann (2019). Fast converging elitist genetic algorithm for knot adjustment in B-spline curve approximation. *Journal of Applied Geodesy*. Vol. 13, Issue 4, pp. 317-328.
- Bureick, J., H. Neuner, C. Harmening, and I. Neumann (2016). Curve and Surface Approximation of 3D Point Clouds. *Allgemeine Vermessungsnachrichten*, Vol. 123, Issue 11-12, pp. 315-327.
- Chaudry, S. (2021). *Surface related uncertainties of laser scanning: a simulation-based and experimental study*. Dissertation. ETH Zürich, Zürich, Switzerland.
- Cox, M.G. (1972). The Numerical Evaluation of B-Splines. *IMA Journal of Applied Mathematics*, Vol. 10, Issue 2, pp. 134-149.
- de Boor, C. (1972). On calculating with B-splines. *Journal of Approximation Theory*, Vol. 6, Issue 1, pp. 50-62.
- Dambrosio, N., C. Zechmeister, S. Bodea, V. Koslowski, M. Gil-Pérez, B. Rongen, J. Knippers, and A. Menges (2019). Towards an architectural application of novel fiber composite building systems – The BUGA Fibre Pavilion. In *ACADIA – Ubiquity and Autonomy [Proceedings of the ACADIA Conference 2019]*. The University of Texas, Austin. (ISBN 978-0-578-59179-7).
- Dupuis, J., C. Holst, and H. Kuhlmann (2016). Laser scanning based growth analysis of plants as a new challenge for deformation monitoring. *Journal of Applied Geodesy*, Vol. 10, No. 1, 2016, pp. 37-44.
- Eto, S., H. Masuda, Y. Hiraoka, M. Matsushita, Michinari, M., and Takahashi, M. (2020). Precise Calculation Of Cross Sections And Volume For Tree Stem Using Point Clouds. *ISPRS - International Archives of the Photogrammetry, Remote Sensing and Spatial Information Sciences*. XLIII-B2-



2020. 205-210. DOI: 10.5194/isprs-archives-XLIII-B2-2020-205-2020.
- Fitzer, E. (1985). Technical Status and Future Prospects of Carbon Fibres and their Application in Composites with Polymer Matrix (CFRPs). *Carbon Fibres and Their Composites*, 3–45. DOI:10.1007/978-3-642-70725-4\_
- Graham, R.L. (1972). An efficient algorithm for determining the convex hull of a finite planar set. *Information Processing Letters*, Vol 1, Issue 4, pp. 132-133.
- Green, P.J., and B.W. Silvermann (1979). Constructing the convex hull of a set of points in the plane. *The Computer Journal*, Vol 22, Issue 3, pp. 262-266.
- Harmening, C. (2013). Raum-zeitliche Segmentierung von natürlichen Objekten in stark verdeckten Szenen. Master thesis (unpublished). Leibniz University Hanover, Hanover, Germany.
- Harmening, C. (2020). Spatio-temporal deformation analysis using enhanced B-spline models of laser scanning point clouds. Dissertation. TU Vienna, Vienna, Austria.
- Harmening, C., and H. Neuner (2016). Choosing the Optimal Number of B-spline Control Points (Part 1: Methodology and Approximation of Curves). *Journal of Applied Geodesy*, Vol. 10, Issue 3, pp. 139-157.
- Jarvis, R.A. (1973). On the identification of the convex hull of a finite set of points in the plane. *Information Processing Letters*, Vol 2, Issue 1, pp. 18-21.
- Menges, A., and J. Knippers (2015). *Fibrous Tectonics, Architectural Design*, Vol. 85 No. 5, Wiley, London, pp. 40-47. ISBN 978-11118878378; DOI: 10.1002/ad.1952.
- Pearson, K. F.R.S. (1901). LIII. On lines and planes of closest fit to systems of points in space. *The London, Edinburgh, and Dublin Philosophical Magazine and Journal of Science*, Vol. 2, Issue 11, pp. 559-572. DOI: 10.1080/14786440109462720.
- Piegl, L., and W. Tiller (1997). *The NURBS Book*. Monographs in Visual Communication. Springer, Berlin and Heidelberg, 2<sup>nd</sup> edition.
- Prado, M., M. Doerstelmann, J. Solly, A. Menges, and J. Knippers (2017). Elytra Filament Pavilion: Robotic Filament Winding for Structural Composite Building Systems. *In Fabricate – Rethinking Design and Construction [Proceedings of the Fabricate Conference 2017]*, Stuttgart, pp. 224–233. (ISBN: 978 1 78735 001 4; JSTORE: j.ctt1n7qkg7.35).
- Prado, M., M. Dörstelmann, T. Schwinn, A. Menges, and J. Knippers, (2014). Core-Less Filament Winding. DOI: 10.1007/978-3-319-04663-1\_19.
- Schwarz, G. (1978). Estimating the Dimension of a Model. *The Annals of Statistics*, Vol. 6, Issue 2, pp. 461-464.
- Trimble Inc. (2020). Datasheet - Trimble X7. Available in: <https://geospatial.trimble.com> (accessed: 2021-12-10).
- Waimer, F., R. La Magna, and J. Knippers (2013). Integrative Numerical Techniques for Fibre Reinforced Polymers - Forming Process and Analysis of Differentiated Anisotropy. *Journal of the International Association for Shell and Spatial Structures*. 54.
- Wang, Z., Q. Lan, and E. Wang (2015). Automatically extracting contours of cross-sections from 3D point clouds of tunnel. *Proceedings of the International Conference on Advances in Mechanical Engineering and Industrial Informatics*. pp.8-15. DOI:10.2991/ameii-15.2015.2.

## The potential of UAV-based Laser Scanning for Deformation Monitoring – Case Study on a Water Dam

Ansgar Dreier, Heiner Kuhlmann, Lasse Klingbeil

Institute of Geodesy and Geoinformation, University of Bonn, Nussallee 17, 53115 Bonn, Germany,  
([dreier@igg.uni-bonn.de](mailto:dreier@igg.uni-bonn.de); [heiner.kuhlmann@uni-bonn.de](mailto:heiner.kuhlmann@uni-bonn.de); [klingbeil@igg.uni-bonn.de](mailto:klingbeil@igg.uni-bonn.de))

**Key words:** *deformation analysis; UAV LiDAR; accuracy evaluation; Terrestrial Laser scanning*

### ABSTRACT

The use of unmanned aerial vehicles (UAV) in monitoring applications is constantly increasing due to the improvement in sensor technology and the associated higher accuracy that can be achieved. As a result, UAV-based laser scanning is already being used in various deformation monitoring applications such as the monitoring of landslides or land deformations. The main challenges, which also limit the accuracy of the resulting georeferenced point cloud are given by the trajectory estimation, the measurement environment and the flight planning. Difficult conditions and high accuracy demands are especially given for the monitoring of a water dam. While the use of area-based measurements such as terrestrial laser scanning (TLS) is an already established approach for such monitoring tasks, the use of a similar technology on a platform such as a UAV is promising and investigated in this study by acquiring a single measurement epoch at a water dam. In addition to the proposal of a flight pattern for the measurements, the trajectory estimation results are evaluated in detail. Due to critical GNSS conditions, positioning errors lead to systematic shifts between single flight strips. Subsequent optimization with known control points allows the point cloud to be compared to a TLS reference. The difference between the two is shown to have a mean difference of 5 mm with a 9.2 mm standard deviation. This can be considered a highly promising result, especially as the potential for further improvement by using additional targets and sensors (*e.g.* camera) has been identified.

### I. INTRODUCTION

Many structures are subject to periodic or even abrupt deformations due to natural and human influences. These include water dams, which are strongly influenced by effects like the annual temperature variations and the water level change. To ensure the safety and stability of such structures, monitoring is carried out using various sensors. The choice of sensor used for monitoring depends strongly on the required temporal and spatial resolution and thus on the expected deformation during the year.

Due to the complexity of dams and their deformation, multiple sensors are usually used to monitor specific parts such as the main barrage, the water reservoir or the stability of the surrounding area. Besides the main task to warn in case of risk, monitoring should also provide conclusions for restoration or possible improvements in future constructions (Scaioni *et al.*, 2018). The typical approach to dam monitoring is divided into sensors capable of continuously measuring local deformation (*e.g.*, tiltmeter, extensometer, inclinometer) and measurements of absolute and relative displacement of the structure and surrounding areas. The second task is usually accomplished by using a geodetic network with various sensors (*e.g.*, total station, GNSS) and individual planned measurement campaigns, as the effort involved is quite significant.

With technological developments in recent years, area-based measurements such as terrestrial laser

scanning (TLS) or ground-based SAR (Synthetic Aperture Radar) have increased and led to various advantages, such as the high spatial resolution (Scaioni *et al.*, 2018). The potential of monitoring with TLS has been demonstrated in several studies and, in particular, the area-based approach leads to a more detailed analysis of the structural movement of the dam (Alba *et al.*, 2006; Xu *et al.*, 2018).

In addition to static measurement with TLS, the use and availability of kinematic laser scanning technology have increased in the last decades. Thus, the use of laser scanning on a moving platform with additional sensors for localization on the ground (*e.g.*, cars) or with unmanned aerial vehicles (UAVs) is being developed further. The limiting factor for the use of UAV-based laser scanning for applications such as deformation monitoring has been due to the additional uncertainties resulting from the estimation of the trajectory, describing the position and orientation of the platform over time. This study investigates the potential use of such a UAV system for the task of deformation monitoring of a dam based on a single measurement epoch and is designed to address specific challenges:

- What would be a suitable flight planning and how does it affect the accuracy of the initial trajectory estimate?
- What is needed to handle different flight strips to obtain a consistent and optimized point cloud?

- How can the registration to the same datum with a higher order reference provided by TLS be realized?
- How large is the difference between the captured point clouds from TLS and UAV?
- What are the conclusions and recommendations for further improvements in such an application?

To analyze the use of UAV-based laser scanning for deformation monitoring of a dam, a measurement campaign with TLS reference is presented below. The paper is organized as follows. In Section II, the state of the art of UAV-based laser scanning for deformation monitoring is presented. Then, the measurement campaign is described in Section III. The main part of this study is presented in Section IV with the detailed analysis and summarized in Section V with the conclusion and outlook.

## II. UAV-BASED LASER SCANNING FOR APPLICATIONS OF DEFORMATION MONITORING

The use of UAV-based laser scanning has been integrated into various applications, with the focus on monitoring larger areas such as landslides, glaciers, land deformation or applications in forestry. In addition to the use of laser scanning systems, the use of camera sensors on UAVs has also been increasingly addressed in multiple studies. One of the major advantages of aerial-based methods is the ability to deploy a UAV system in hard-to-reach areas, making the surveys both more efficient and safer. One example is the monitoring of power lines and transmission towers, where the stability of the structures is monitored (Lu *et al.*, 2022). Other studies are investigating the use of UAVs with a camera to monitor landslides compared to methods such as TLS (Ćwiąkała *et al.*, 2020; Eker *et al.*, 2018; Jiang *et al.*, 2021).

However, there are also initial studies from recent years on the use of laser scanning systems on UAVs for monitoring tasks. These are also used for landslide monitoring by utilizing estimated roof areas for comparison between different epochs (Zieher *et al.*, 2019). In addition, several studies are evaluating the use to monitor land deformations that may result from mining activities, for example. In combination with TLS and UAV photogrammetry, deformations in the range of several dm can be detected (Józków *et al.*, 2021). For land deformation detection, the digital elevation model (DEM) is usually derived to detect deformations from different epochs. This is demonstrated in several examples and typically compared to methods such as TLS or total stations (Moudrý *et al.*, 2019; Wang *et al.*, 2020, Zheng *et al.*, 2022).

Overall, the use of UAV-based laser scanning is mostly integrated for deformations with a magnitude of cm-dm and not for higher requirements as might be necessary for a dam analysis. Since the use of TLS is already a common method for dam monitoring, in which the analysis is based on the resulting point cloud

(Alba *et al.*, 2006; Scaioni *et al.*, 2018; Xu *et al.*, 2018), a similar approach on a UAV is well feasible but neglected so far due to the lack of accuracy. For these reasons, and because of the advantages of UAVs, their use for dam monitoring is investigated below.

## III. MEASUREMENT CAMPAIGN

The measurement campaign consists of two parts, divided into the generation of a reference point cloud based on the terrestrial laser scanning (TLS) measurements and the acquisition of two similar flights with the UAV-based laser scanning system. Special UAV targets are used below to register the UAV system derived point cloud to the TLS reference. Therefore, the datum definition for comparisons is defined by the TLS registration with a local coordinate system. Since the evaluation in this paper analysis especially the precision of the UAV point cloud, the capability of direct georeferencing is only used for the trajectory processing. In the following, Section III A will first describe the water dam (Figure 1). Section III B discusses the TLS measurement performed, including the estimation of the target centers, which provide the local datum for all comparisons within the analysis. Furthermore, Section III C presents the UAV system used, including the integrated sensors, the flight parameters, and the flight pattern performed during the measurement.



Figure 1. Water dam as monitoring object.

### A. Study area water dam

Deformation monitoring of dams is a necessary and proven procedure to ensure the stability of these structures in the long term. There are different techniques and sensors suitable for continuous monitoring or specific control measurements. For the analysis of the use and thus monitoring with a UAV-based laser scanning system, the study area with the dam shown in Figure 1 was selected. This dam, like most dams, is subject to annual deformations that need to be monitored regularly. The deformations are caused by the changes of the water level, but mainly by the temperature variations during the year. Therefore, this object is well suited for the evaluation of the survey

using the UAV-based laser scanning system. The dam is approximately 27.7 m high and has a crest length of 152 m. During the measurement campaign in June 2021, the surrounding area was also heavily covered with vegetation, which is why flight planning, in particular, proved to be challenging under very difficult conditions.

### B. Reference point cloud and datum definition

The assessment of the UAV-based laser scanning is mainly done in comparison to a reference point cloud acquired with TLS. The TLS measurements and thus the different stations in the study area are shown in Figure 2 with the corresponding TLS targets required to register the different stations to each other. The laser

scanner used is the Leica ScanStation P50 and the targets are BOTA8 (Bonner target with 8-fold pattern) developed for high accuracy demands using target-based registration (Janßen *et al.*, 2019). The different scans for stations 1-7 were measured with a scan resolution of either 1.6mm@10m or 3.1mm@10m. Based on the estimate of the target center of each TLS target, registration in Leica Cyclone was performed with an RMS of less than 1 mm for the included targets. In addition to the TLS targets, the target centers of the larger BOTA8 targets (0.8 m x 0.8 m), also labeled as UAV targets in Figure 2, are estimated for the registration of the UAV point cloud. Since the point cloud of one station is sufficient for the following point cloud comparison, only station 7 is used since it provides the best view of the middle part of the dam.

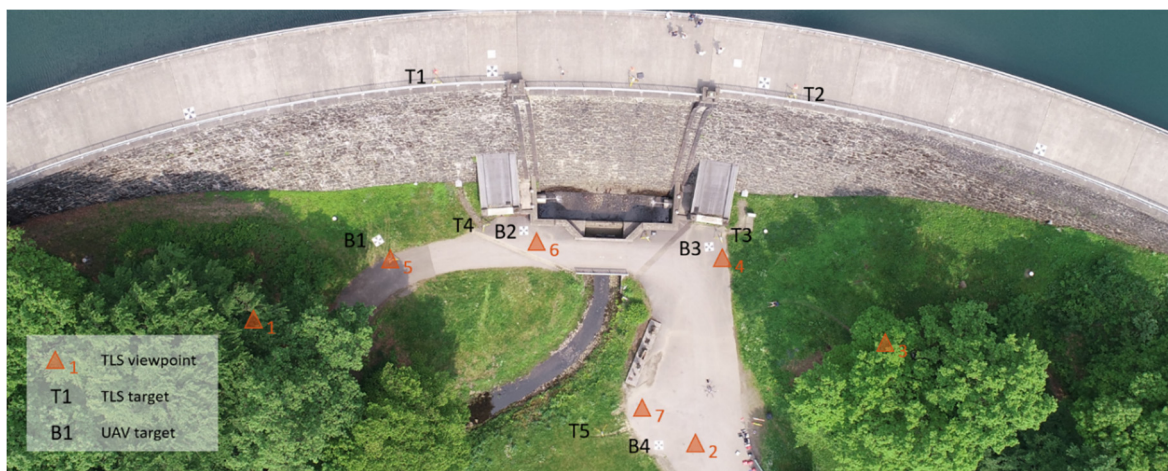


Figure 2. Overview of the study area with locations of TLS stations, TLS targets and UAV targets.

### C. UAV-based acquisition of the water dam

The UAV-based laser scanning system used to survey the dam consists of a DJI Matrice 600 platform with a RIEGL miniVUX-SYS, as shown in Figure 3. Integrated into this is a high-quality Trimble APX-20 UAV IMU/GNSS combination for estimating position and orientation over time defined as the UAV's trajectory. The additional full waveform 2D laser scanner RIEGL miniVUX-2UAV is used for object detection. By combining it with the trajectory a georeferenced 3D point cloud can be derived. The first part of the trajectory estimation is performed by using an additional GNSS master station for differential GNSS processing and subsequent sensor fusion with the IMU data using a Kalman filter. The master station is a virtual reference station (VRS) provided by SAPOS, which gives GPS, GLONASS, BeiDou, and Galileo observations. All processing is done in Applanix POSPac UAV software, which calculates a smoothed trajectory with additional accuracy metrics for analysis. The laser scanner has a maximum laser pulse repetition rate of 200 kHz and a field of view of 360°. When used at the dam, the field of view results in good scanning geometry as it is flying parallel to the dam. The only limitation is the obstruction by the rotor arm, so the field of view to be

processed is limited to 80° - 280°. The subsequent combination of the estimated trajectory with the laser scans is done in RIEGL RiPROCESS, which also includes the additional sensor calibration. The error budget, and thus the accuracy of the UAV system, can be also divided into the trajectory and laser scanning parts and are shown in Table 1.

Table 1. Error budget of the UAV-based laser scanning system according to the manufacturer (Riegl, 2020)

Accuracy	Values
Trajectory estimation – position vertical [m]	< 0.10
Trajectory estimation – position horizontal [m]	< 0.05
Trajectory estimation – roll & pitch [deg]	0.015
Trajectory estimation – heading [deg]	0.035
Laser scanner [m]	0.015

Regarding the accuracy of the product with a georeferenced 3D point cloud, the crucial part is given with the estimation of the trajectory (Dreier *et al.*, 2021). According to the manufacturer, the accuracy for the position is < 0.05 m for the horizontal direction and < 0.10 m for the vertical direction. Furthermore, the orientation is about 0.015 degrees for roll & pitch and about 0.035 degrees for heading. Compared with the

accuracy of the trajectory, the accuracy of the laser scanner is relatively high at 0.015 m. The given quantification depends especially on the measurement conditions like GNSS constellation and flight parameters. Investigations by Dreier *et al.* (2021) have shown even better results for the use of this UAV system, especially regarding the precision. This is also advantageous because the inner geometry of the UAV point cloud is more important for the application than the georeferencing, since it is registered to the local control points. Therefore, the potential of a direct georeferenced point cloud is not exploited in this study, although it might be useful for future projects.



Figure 3. UAV system with the RIEGL miniVUX-SYS.

Flight planning and execution were performed using UgCS software according to the flight pattern shown in Figure 4. Since a detailed representation of the entire dam is required, the flight is conducted with parallel flight strips at ascending heights, starting at the lowest point. This flight pattern is similar to a facade scan typically performed for image-based acquisition with a UAV. Since the laser scanner measures in a plane orthogonal to the flight direction, the scan geometry is advantageous. However, the flight pattern chosen is very unusual for UAV-based laser scanning with no cross flights or flight curves instead of sharp turns at the end of a flight strip. Unfortunately, with this object and the surrounding conditions with many trees, it is not possible to do otherwise. The flight parameters used are the flight speed of 0.5 m/s, a lateral distance of about 10 m from the water dam, and successive strips

with flight heights of 5 m, 10 m, 15 m, 20 m, 25 m, 30 m, 40 m and 50 m. Using the laser scanner's line speed of 53.8 lines per second, the average point density is approximately 3650 points/m<sup>2</sup>, although this is not entirely uniform because the distance to the dam is not identical for each flight strip. As described in this part, the final point cloud is calculated in RIEGL's RiPROCESS software and the different flight strips are calculated individually. In the subsequent analysis of the data, the RiPRECISION tool is also used to perform various optimization strategies for an improved point cloud. The possibilities and procedures will be discussed in the next part.

#### IV. ANALYSIS

The objective of this study is to compare and verify the suitability of UAV-based laser scanning for applications such as deformation monitoring. In the following analysis, the point cloud obtained with the UAV is checked for consistency in Section V A. This is done by relating the different flight strips to each other and attempting to clarify the difficult conditions for trajectory estimation. The optimization of the UAV point cloud using RIEGL's software follows in Section V B, the comparison with the TLS reference is performed in Section V C. using the UAV targets for registration. Several aspects are investigated in comparison to the TLS point cloud. First, the spatial resolution of the UAV point cloud and thus the level of detail is highlighted. Next, the inner geometry of the UAV point cloud is analyzed to determine how it compares to the reference.

##### A. Analysis of the point cloud acquired with the UAV

The complete point cloud from the UAV-based laser scanning system is initially split into separate point clouds from the individual flight strips starting at a flight height of 5 m. Since the trajectory estimate will likely contain larger uncertainties after the 180° turn and upward movement, the separation into strips is reasonable. Before evaluating the computed point cloud, the prevailing measurement conditions should be highlighted, focusing on the GNSS conditions.

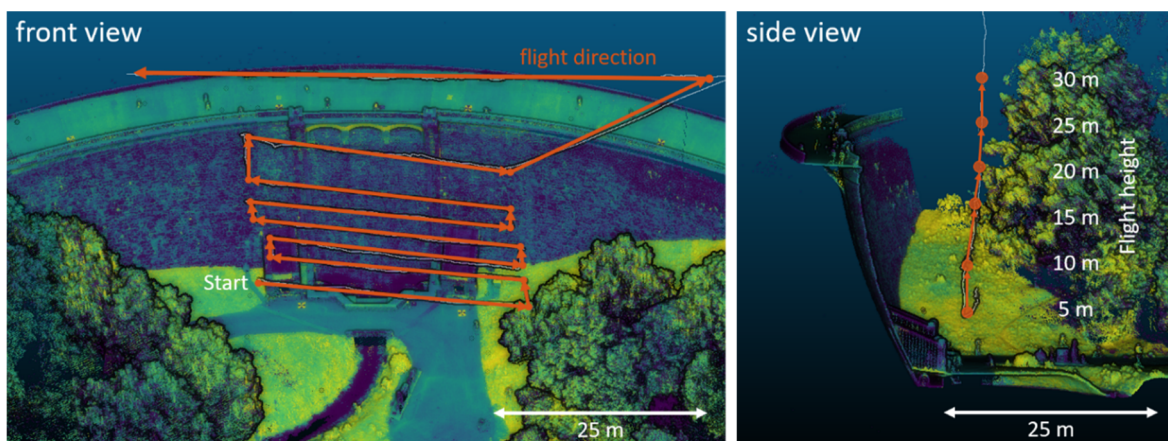


Figure 4. Flight pattern performed for the UAV measurements with a front view (left) and side view (right).

Figure 5 shows the satellite visibility and PDOP values in relation to each flight strip. With the additional heading of the UAV in the top plot, the individual flight strips can be identified with the 180° turn included. The time series showed starts with the first flight strip at 5 m height to the fourth flight strip at 20 m flight height. It can be seen that the number of satellites for the first strip is very low with 10-13 satellites and a corresponding PDOP above 2. In addition, there are several signal interruptions of individual satellites, which leads to smaller jumps in the number of satellites and also the PDOP. For this reason, it is assumed that the signals are partially obscured by objects or vegetation and thus there is a high probability of outliers. In addition, the measurement environment has a very high probability of the occurrence of errors such as far-field multipath and diffraction, which cannot be safely handled in the positioning algorithm (Zimmermann, 2020). These aspects with a small number of satellites, the very error-prone environment, and poor satellite geometry lead to a very difficult task for trajectory estimation, which may involve higher uncertainties compared to better conditions. The challenging environment described above improves with increasing UAV height, although the situation at 20 m seems to be sufficiently good considering the number of satellites and the corresponding PDOP. However, since a continuous high-resolution point cloud is desired, low flight heights are also taken into account. Since the evaluation of the accuracy of the trajectory estimation itself is not possible, the point clouds of individual flight strips are used for investigation in the following part.

The point clouds from 5 flight strips taken at a flight height of 5-25 m are shown in Figure 6, with the combined point cloud on the left and two selected areas on the right. The point cloud on the left, colored with intensity values from the laser scanner, provides an initial overview of the level of detail that can be captured by the UAV system. Inspecting the detail view in the right part of the figure, the uncertainty of the

trajectory estimation can be seen. Each flight strip is individually colored and systematic errors between them become visible. These can be explained by the unusual flight pattern and the critical GNSS conditions. However, initial conclusions can also be drawn from the offsets shown between the flight strips. The top view of a part in the center of the water dam shows a shift of several cm-dm in the horizontal position of the individual strips with respect to each other without additional tilting. The same applies to the part in the lower right area shown from the side view. This angle of view primarily shows a shift between the flight strips in the vertical direction without any additional tilting of the flight strips with respect to each other. Finally, this leads to the conclusion that due to the critical environment and conditions for GNSS positioning, systematic errors in the position in the global coordinate system cause offsets between different flight strips.

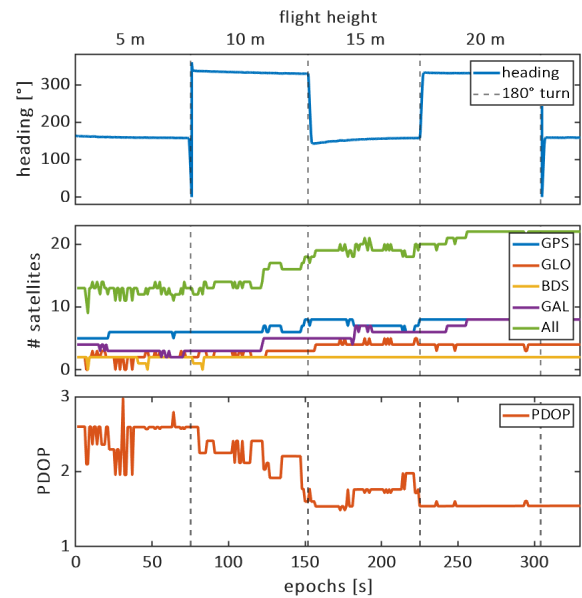


Figure 5. GNSS condition for the first four flight strips of one flight with corresponding heading and 180° turns.

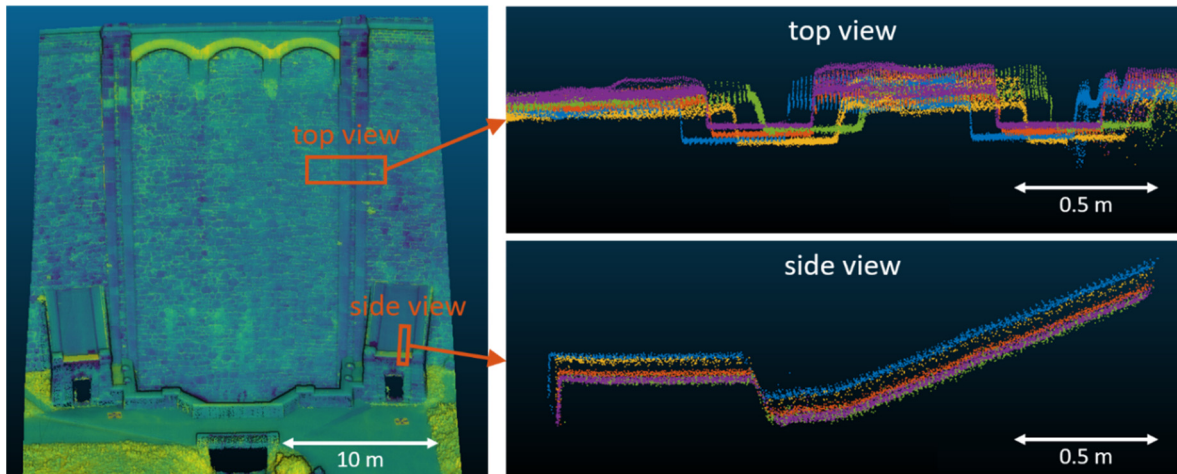


Figure 6. UAV point cloud from 5 different flight strips (different colours) with side and top view for specific areas.

To verify the inner geometry of multiple flight strips, UAV targets B2 and B3 are used to compare the 3D distance between the two target centers (see Figure 7). Since there are no other UAV targets measured with good scan geometry, only one distance is calculated for each flight strip and compared to the reference distance derived from the TLS point cloud. The difference in calculated distance from the reference is shown for flight strips 1-6, and in this case also for the two separate flights with similar flight patterns, to demonstrate the repeatability of an independent measurement. The differences are all less than 3 cm and, in most cases, even less than 2 cm. In particular, the second flight shows good results for flight strips 3-6 with differences below 1 cm. This investigation shows the high precision and thus the consistency of the inner geometry of the individual flight strips. From the previous detailed evaluation of the derived point cloud, several conclusions can be drawn. First, the critical conditions for GNSS positioning can already be suspected by examining the number of satellites and the resulting PDOP values. Furthermore, the atypical flight pattern could lead to additional uncertainties in the trajectory estimation. These assumptions are supported by looking at the point cloud and the systematic offsets between the flight strips. Nevertheless, the inner geometry seems to be almost unaffected by this, and therefore the most important information for the monitoring task is preserved.

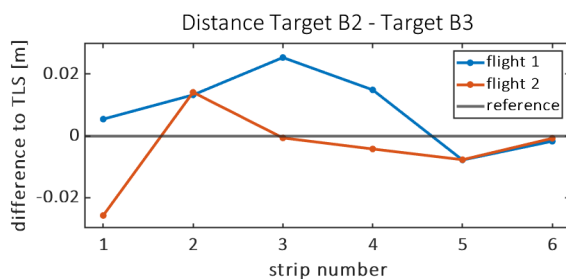


Figure 7. Comparison of distances between Target B2 – B3 from two UAV flights compared to TLS.

### B. Optimisation of the point cloud

There are various options to improve the quality of the derived point cloud and in particular the consistency between different flight strips. For this task, the RIEGL software RiPRECISION is used, which is able to perform different optimization strategies to correct the trajectory based on measurements from multiple strips. Besides the automatic identification of areas and features to improve the point cloud, it is also possible to introduce control planes or points to adjust the trajectory. The performance of the optimization procedure has been demonstrated in several studies and can be classified as a reliable tool if the object and also a beneficial flight pattern are chosen (Dreier *et al.* 2021). For the evaluation of the optimization and also the following comparison with the TLS reference, only the second flight is used, since the results are very

similar. Besides the features, which are automatically detected by RiPRECISION, the control points for the UAV targets B2, B3 and B4 are also included in the optimization. The result is shown in Figure 8 for the example of two different flight strips in orange (10 m flight height) and blue (20 m flight height). In this case, the visual inspection shows a consistent point cloud that fits in both horizontal and vertical directions. There are only local variations between the flight strips, which are of the order of less than 1 cm. For clarification, the improvement is shown only for two strips, because the optimization does not work for all contained strips of the dataset. There are still deviations especially in the horizontal direction, as can be seen in the upper right part of Figure 6. The height offset on the other side is completely eliminated since the ground can be used for adjustment.

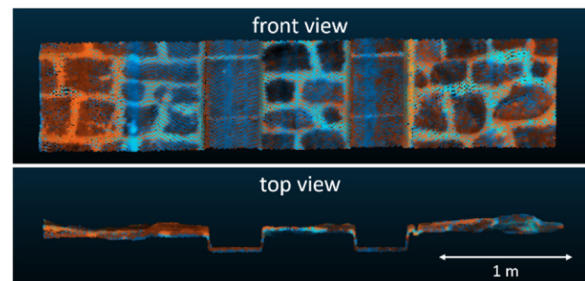


Figure 8. Two flight strips with 10 m (orange) and 20 m (blue) flight height.

The reason for the remaining offsets is the difficulty in capturing the object and the lack of structures such as concrete walls or roofs to enhance the point cloud. Moreover, this is usually achieved by additional flight strips in the cross direction, which can fix or correct the point cloud in the direction of the water dam. These facts influencing the optimization process are one of the main challenges when we consider an object like the dam, where the structure and scan geometry is pretty much the same for the whole data set.

Therefore, several aspects can already be summarized based on the point cloud acquired by the UAV. Trajectory estimation is the most critical part of the processing and also the most error-prone. This can be corrected by different optimization strategies in post-processing, for example by including control objects. Since this approach cannot correct the entire data set with multiple flight strips, in this case, additional aid for trajectory estimation is recommended. This could be done by integrating additional information from simultaneously acquired images or by introducing additional artificial objects to adjust the trajectory. For the following comparison with the TLS, only single flight strips are used to show the potential of the derived UAV point clouds without considering errors that might have been preserved due to uncorrected offsets.

### C. Comparison with TLS

The optimized point cloud derived from the UAV system is compared with the reference point cloud measured with TLS described in Section III B. In order to apply a method of point cloud comparison, the UAV point cloud must be transformed into the local coordinate system and thus into the datum definition given by the TLS. The Helmert transformation between the two systems is based on the UAV target centers estimated from both data sets. Since the scale of both point clouds is well defined, only the parameters for three translations and three rotations are applied. A critical aspect of this transformation is the small number of UAV targets, which leads to a lack of redundancy as usually recommended. Nevertheless, the transformed point cloud derived with the UAV system and analyzed in the following fits the TLS point cloud in an order of magnitude that the transformation parameters can be evaluated as sufficiently accurate.

A first comparison of the two results is shown in Figure 9 with a detail of the middle part of the dam. The left part shows the UAV point cloud and the right part is the TLS point cloud, both colored by intensity value. This visual inspection should highlight several aspects if UAV-based laser scanning is to be considered a viable alternative. First, the geometry of the dam with stones and joints in between can be seen in similar detail at the scale shown. In addition, the direct transition between the two demonstrates the potential of the UAV system in being able to accurately reproduce the geometry, at least from this perspective. Overall, these inspections show the potential and precision of the UAV point cloud, even though they are only done on a visual basis. To quantify the differences between the two point clouds, the method Multiscale Model to Model Cloud Comparison (M3C2, Lague *et al.*, 2013) is applied and the result is shown in Figure 10. For this comparison, the flight strip with a flight height of 20 m is again used, covering only the central part of the dam. Besides the colored parts with a M3C2 distance, the gray part represents only the TLS point cloud used. The distribution of differences shown on the right results in a mean difference of +5 mm and a corresponding standard deviation of 9.2 mm. Based on the error

budget shown in Table 1, the differences can be considered better than expected. The combination of the uncertainties from the trajectory estimation with the additional uncertainty due to the laser scanner supplied by the manufacturer is significantly higher than in the comparisons shown.

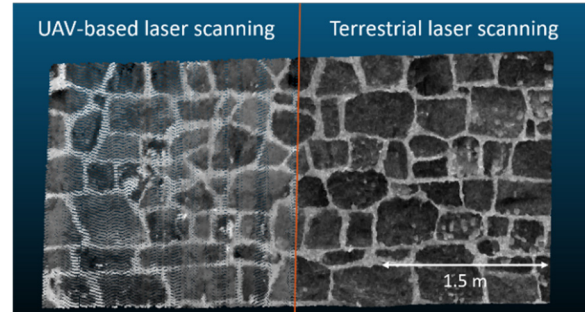


Figure 9. Detailed part of the point clouds coming from UAV-based laser scanning and TLS.

Nevertheless, the comparison shows systematic effects in different areas of the dam that can be attributed to the precision of the trajectory, which cannot be detected by the evaluation steps done before. Another possible uncertainty contributing to this comparison is given with the Helmert transformation of the UAV point cloud to the local datum where only three control points were used. Since an incorrect set of transformation parameters would lead to even larger systematic differences between the two point clouds, this can be neglected. Overall, the M3C2 comparison produced good results for the challenging measurement conditions and highlighted several aspects with potential for improvement.

### V. CONCLUSION AND OUTLOOK

In this study, we presented the use of UAV-based laser scanning for the task of deformation monitoring using a single measurement epoch of a water dam as an example. With the presented approach for the measurement, the analysis of the trajectory with corresponding flight strips and the final comparisons between the UAV point cloud and the TLS reference, several conclusions and challenges can be drawn.

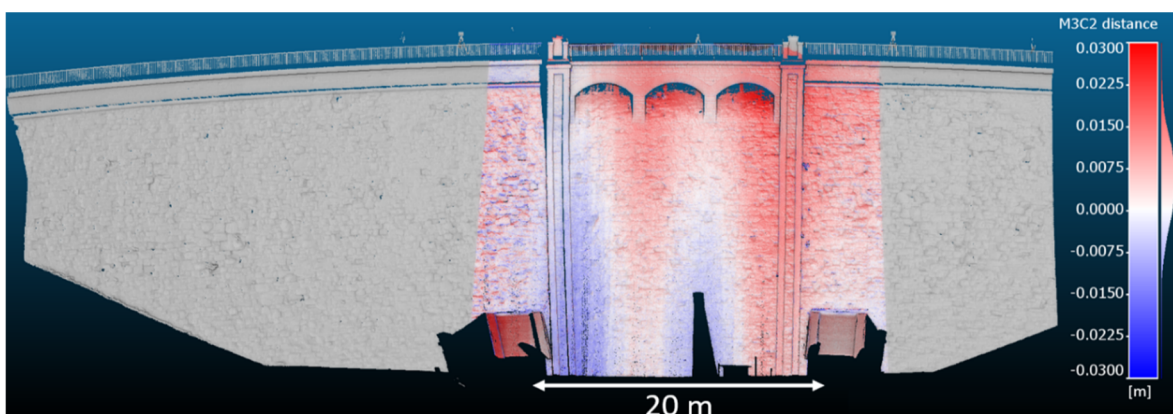


Figure 10. M3C2 distances between UAV point cloud from the 20m flight strip and TLS.



First of all, the environment and flight planning for such a dam were very challenging and highly error-prone, especially considering the GNSS conditions and their impact on the trajectory estimation. Therefore, optimization algorithms for the UAV point cloud are highly recommended to improve the consistency of the different flight strips. However, the object of the dam and the corresponding flight pattern is very challenging for the available optimization methods, so it was not always possible to correct every flight strip as desired. In this study, the subsequent transformation to an identical datum for comparison with TLS could contain additional errors that can be easily avoided. The final results from the comparison are very promising considering the poor measurement conditions and the uncertainties included in the processing chain. These conclusions can be formulated in the following aspects:

- The environment imposes high demands on the flight planning, but also on the resulting measurement conditions, especially on the GNSS reception.
- An improvement of the trajectory estimation is necessary by using the strip optimization between several flight strips.
- The optimization should be supported by additional artificial objects such as targets, which can also be used for accuracy assessment or comparison to other measurements like TLS.
- The integration of additional sensors that support trajectory estimation, such as cameras, is conceivable.
- For comparisons with TLS or other sensors, registration should be solved separately or known in advance.

The conclusions presented are mainly related to the trajectory estimation part or the subsequent optimization part to achieve higher precision of the resulting point cloud. Since the shown comparison of the point clouds from the dam already gives a mean difference of 5 mm with a standard deviation of 9.2 mm, even better results can be expected for further new measurements with improved planning. In particular, the use of additional UAV targets that can be included in the optimization process will be tested in the future.

## VI. FUNDING

This work was funded by the Deutsche Forschungsgemeinschaft (DFG, German Research Foundation) under Germany's Excellence Strategy–EXC 2070–390732324.

## References

Alba, M., Fregonese, L., Prandi, F., Scaioni, M., and Valgoi, P. (2006). Structural monitoring of a large dam by terrestrial laser scanning. *International Archives of Photogrammetry, Remote Sensing and Spatial Information Sciences*, 36(5), 6.

Ćwiąkała, P., Gruszczyński, W., Stoch, T., Puniach, E., rocheń, D., Matwij, W., and Wójcik, A. (2020). UAV applications for determination of land deformations caused by underground mining. *Remote Sensing*, 12(11), 1733.

Dreier, A., Janßen, J., Kuhlmann, H., and Klingbeil, L. (2021). Quality Analysis of Direct Georeferencing in Aspects of Absolute Accuracy and Precision for a UAV-Based Laser Scanning System. *Remote Sens.* 2021, 13, 3564. DOI: 10.3390/rs13183564

Eker, R., Aydın, A., and Hübl, J. (2018). Unmanned aerial vehicle (UAV)-based monitoring of a landslide: Gallenzerkogel landslide (Ybbs-Lower Austria) case study. *Environmental monitoring and assessment*, 190(1), 1-14.

Janßen, J., Medic, T., Kuhlmann, H., and Holst, C. (2019). Decreasing the uncertainty of the target center estimation at terrestrial laser scanning by choosing the best algorithm and by improving the target design. *Remote Sens.* 2019, 11, 845.

Jiang, N., Li, H., Hu, Y., Zhang, J., Dai, W., Li, C., and Zhou, J. W. (2021). A Monitoring Method Integrating Terrestrial Laser Scanning and Unmanned Aerial Vehicles for Different Landslide Deformation Patterns. *IEEE Journal of Selected Topics in Applied Earth Observations and Remote Sensing*, 14, 10242-10255.

Józków, G., Walicka, A., and Borkowski, A. (2021). Monitoring Terrain Deformations Caused by Underground Mining Using Uav Data. *The International Archives of Photogrammetry, Remote Sensing and Spatial Information Sciences*, 43, pp. 737-744.

Lague, D., Brodu, N., and Leroux, J. (2013). Accurate 3D comparison of complex topography with terrestrial laser scanner: Application to the Rangitikei canyon (NZ). *ISPRS journal of photogrammetry and remote sensing*, 82, pp. 10-26.

Lu, Z., Gong, H., Jin, Q., Hu, Q., and Wang, S.A. (2022). Transmission Tower Tilt State Assessment Approach Based on Dense Point Cloud from UAV-Based LiDAR. *Remote Sens.*, 14, 408. DOI: 10.3390/rs14020408

Moudrý, V., Gdulová, K., Fogl, M., Klápště, P., Urban, R., Komárek, J., and Solský, M. (2019). Comparison of leaf-off and leaf-on combined UAV imagery and airborne LiDAR for assessment of a post-mining site terrain and vegetation structure: Prospects for monitoring hazards and restoration success. *Applied geography*, 104, pp. 32-41.

Riegl GmbH (2020). RIEGL miniVUX-SYS. Available online: [http://www.riegl.com/uploads/tx\\_pxprigldownloads/RIEGL\\_miniVUX-SYS\\_Datasheet\\_2020-10-05\\_01.pdf](http://www.riegl.com/uploads/tx_pxprigldownloads/RIEGL_miniVUX-SYS_Datasheet_2020-10-05_01.pdf) (accessed on 21 April 2021).

Scaioni, M., Marsella, M., Crosetto, M., Tornatore, V., and Wang, J. (2018). Geodetic and remote-sensing sensors for dam deformation monitoring. *Sensors*, 18(11), 3682.

Wang, G., Li, P., Li, Z., Ding, D., Qiao, L., Xu, J., Li, G. and Wang, H. (2020). Coastal Dam Inundation Assessment for the Yellow River Delta: Measurements, Analysis and Scenario. *Remote Sensing*, 12(21), 3658.

Xu, H., Li, H., Yang, X., Qi, S., and Zhou, J. (2018). Integration of terrestrial laser scanning and nurbs modeling for the deformation monitoring of an earth-rock dam. *Sensors*, 19(1), 22.

Zheng, J., Yao, W., Lin, X., Ma, B., and Bai, L. (2022). An Accurate Digital Subsidence Model for Deformation

Detection of Coal Mining Areas Using a UAV-Based LiDAR.  
*Remote Sens.*, 14, 421. DOI: 10.3390/rs14020421

Zieher, T., Bremer, M., Rutzinger, M., Pfeiffer, J., Fritzmann, P., and Wichmann, V. (2019). Assessment of landslide-induced displacement and deformation of above-ground objects using UAV-borne and airborne laser scanning data. *ISPRS Annals of Photogrammetry, Remote Sensing & Spatial Information Sciences*, 4.

Zimmermann, F. (2020). *Analysis and mitigation of site-dependent effects in static and kinematic GNSS applications*. Dissertation, University of Bonn.

## **S-Wave detection using continuously operated GNSS stations: A case study of two Mw 7.1 earthquake events**

Vassiliki Krey, Iordanis Galanis, Vangelis Zacharis, Maria Tsakiri

School of Rural, Surveying and Geoinformatics Engineering, National Technical University of Athens, Greece, ([vasiliki\\_krey@mail.ntua.gr](mailto:vasiliki_krey@mail.ntua.gr); [jorgalan@mail.ntua.gr](mailto:jorgalan@mail.ntua.gr); [vanzach@mail.ntua.gr](mailto:vanzach@mail.ntua.gr); [mtsakiri@mail.ntua.gr](mailto:mtsakiri@mail.ntua.gr))

**Key words:** *geohazard; earthquakes; S-waves; GNSS data; timeseries analysis*

### **ABSTRACT**

This study presents a method developed to analyze the position timeseries of continuously operated GNSS stations located in the area around the epicenter of an earthquake, aiming at the detection of secondary seismic waves. Specifically, 5 Hz positioning data from 14 GNSS stations operated by UNAVCO were used, located in the areas of Southern California and Alaska, for two distinct earthquake events of a 7.1 moment magnitude each. The method described follows three steps: rotation of the position components, noise filtering of timeseries using Kalman's filter and the use of a moving average to statistically indicate the point of time in which the maximum displacement induced by the S-wave takes place. This method statistically proves the existence of a motion generated from a geohazard in a position timeseries of continuously operated station(s) of interest and, in addition, it indicates the exact time of the incident. The method can be employed in testing for displacement of continuous GNSS stations in areas affected by an earthquake, as well as for generating conclusions on the velocity and direction of seismic waves' propagation.

*This contribution was selected by the Scientific Committee for publication as an extended paper in the Journal of Applied Geodesy <https://www.degruyter.com/journal/key/jag/html>*

## Planning UAV surveys: can we rely on wind forecasts?

Maria Henriques, Dora Roque

LNec-National Laboratory for Civil Engineering, Lisbon, Portugal, ([mjoao@lnec.pt](mailto:mjoao@lnec.pt); [droque@lnec.pt](mailto:droque@lnec.pt))

**Key words:** UAV; flight; wind; forecast; website

### ABSTRACT

Like in other surveying works, UAV flights require prior work that involves flight planning and equipment preparation and, often, many complementary tasks. These may involve bringing together technicians from different domains, booking a car and possibly accommodation, and some time-consuming complementary bureaucratic work. Teams operating UAVs know how much the flights are affected by weather conditions. The wind is the weather variable that, in proportion (number of occurrences per year), causes the major number of changes to a scheduled work. Obtaining reliable information about the intensity of the wind, a few days in advance, is an asset for those who have to carry out the various tasks mentioned previously. There are several websites from which one can access weather forecasts. Is any website better because it presents more reliable data? The data and the analysis presented in the paper will give some clues. The data includes wind speed, registered daily, at 12:00 (pm) for a year, by a meteorological station with online data, which belongs to a meteorological institute. Also on a daily basis, several websites with meteorological data were consulted, and wind speed forecasts for the same hour for up to four days in advance were collected. An analysis of the data can provide information about whether there is a website that stands out for the quality of the forecasts, and if there is a need to consult several websites to have better information.

### I. INTRODUCTION

Given the effect of atmospheric elements on aerial UAV surveys (light way of referring to a photographic survey using an unmanned aerial vehicle as a carrier of a digital camera), it is imperative that the organization of the travel to carry out photographic surveys includes the collection of meteorological information to assess whether there are adequate atmospheric conditions at the location of the survey. And, if the survey team belongs to an entity that has heavy bureaucratic procedures, that needs several authorizations to provide allowance, a vehicle, sometimes accommodation, to activate insurance for the team members, not to refer the authorizations from official entities, the evaluation of the local conditions is even more important. And, as if this was not enough, it is also important to have in consideration the existence of adequate light conditions during the survey, or, when this happens in coastal areas, the level of the tide. For all the reasons is very important to have access to reliable weather forecasts.

Wind (see Figure 1) and rain are the weather elements that most influence a UAV flight. Of these two, we focused solely on the wind factor (in the form of the speed of wind). The reason why we didn't have interest in analyzing precipitation forecasts is because is very easy to obtain information about the real situation (based in satellite infra-red images and ground-based radar images), being simple to predict the occurrence of rain.

Being the focus the wind forecast, we had to choose a station with reliable data. We chose the online station

Peniche (see Section II). Data from this station and from several free weather websites (see Section III) was gathered. We registered the measurement made at noon and, also, the predictions for that hour up to four days in advance. The analysis is presented in the Section IV and the conclusions in the last Section.

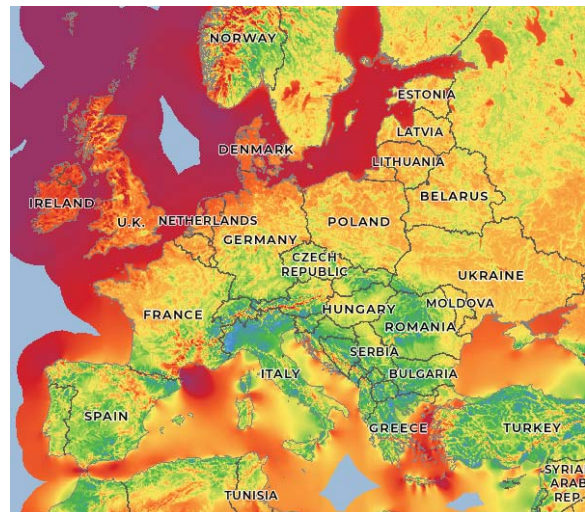


Figure 1. Wind speed at 50 m height (<https://globalwindatlas.info/>)

### II. THE WEATHER STATION

We chose the online weather station Peniche from the Portuguese Institute for Sea and Atmosphere (IPMA). On its website, one can access atmospheric data measured hourly in several online stations (as for beginning of 2022): 136 in Portugal mainland; 21 in Madeira islands; 23 in Azores islands. The data available is air

temperature, precipitation, wind speed, air humidity and atmospheric pressure (this one only available in some stations).

The Peniche station (Figure 2) is located on the rocky peninsula where the city with the same name was built. The peninsula is a relatively flat plain, at 30 m of altitude, with low vegetation. The station is only 60 m away from the sea (Figure 3).



Figure 2. Peniche weather station.



Figure 3. Peniche peninsula near the weather station (red dot in the photo).

Next to the city is a major fishing port, the westernmost port in continental Europe. This port is protected by two breakwaters being the western frequently hit by huge waves. This breakwater is often chosen as case study for projects, such as BSafe4Sea, a funded project that aims to develop, test and prove the concept of forecasting the structural behaviour of rubble mound breakwaters, which will form the basis of an innovative decision support system (LNEC, 2020).

### III. THE WEATHER WEBSITES

There are many websites with wind forecasts. We chose seven websites with free access. One of this (windy.com) can present, at the same time, data from several services of weather. Concerning the models of forecast used, some websites provide complete information, while others not that much. We also included, between square brackets, the name of the

model used by the services, the resolution, and the update frequency (the number of times the model runs per day). If data of the wind gust is available, we join the letters WG.

As an example of the models used: i) ECMWF (developed by the European Centre for Medium-Range Weather Forecasts); ii) Arome (Application of Research to Operations at Mesoscale, used operationally by Meteo France, is the result of the cooperation between organizations from France and other countries); iii) WRF (Weather Research and Forecasting Model, developed by U.S. entities); iv) GFS (Global Forecast System, run by the U.S. National Weather Service, a service from NOAA); v) ICON-EU (ICOsahedral Nonhydrostatic, a model worldwide created by the German Weather Service, with a higher-resolution model for regional forecasts for Europe, ICON-EU).

The websites were:

- a) ipma.pt developed by the Portuguese state laboratory IPMA whose mission is to promote and coordinate scientific research, technological development, innovation and service on the seas and atmosphere. It provides forecasts for mainland Portugal and islands. In situations of significant differences between forecast and reality, forecasts made available for district capitals and islands can be corrected by meteorologists [Arome, 2.5 km, and ECMWF, 9 km; 2];
- b) meteo.tecnico.ulisboa.pt developed by a research group of the university of Lisbon (IST) that works in high-resolution meteorological modeling and forecasting. It provides forecasts for Portugal mainland, only [WRF, 9 km; 4];
- c) wunderground.com developed by The Weather Underground, that has its roots at the University of Michigan, and was acquired by The Weather Channel in 2012 [IBM GRAF, 3 km; 24];
- d) windy.com owned by Windy, a Czech company. The website can present data from several weather services (namely, through the “compare” link available at the bottom of the webpage) being that the values of the wind gust are not presented in the “compare” mode. In the case of Peniche, windy presents forecasts of five models:
  - d1) The US National Oceanic and Atmospheric Administration, NOAA [GFS, 22 km; 4; WG];
  - d2) The European Centre for Medium-Range Weather Forecasts [ECMWF, 9 km; 4; WG];
  - d3) MeteoBlue, developed by Swiss company Meteoblue [combines over 25 different weather models; 2; WG];
  - d4) Deutscher Wetterdienst, DWD, the German Weather Service [ICON-EU, 7 km; 4; WG];
  - d5) Meteo France: in France and nearby countries is used a model [Arome, 2.5 km; 8] while in the rest of the world another model

is used [Arpège, from 7.5 km in France to 35 km in the antipodes; 4];

- e) otempo.pt owned by the Canadian enterprise Pelmorex Corporation. It has weather websites dedicated to several countries in the world [OnPoint, 5 km];
- f) ventusky.com developed by the Czech meteorological company InMeteo, focused on weather prediction and meteorological data visualization. The main providers of meteorological data are DWD and NOAA [WG];
- g) windfinder.com developed by a German company to provide information on weather and waves in relevant spots for water sports and outdoor activities. The provider of meteorological data is NOAA [WG].

Except for the services a), b) and d5), all the others provide worldwide forecasts. All the models use data, official and/or personals, from weather stations, radars, satellites (Figure 4). Several websites refer in their FAQ and other help information, the need for correct inconsistencies because data is not homogeneous neither in space nor in time (Meteo France, 2015). Some also refer the use of orographic databases.

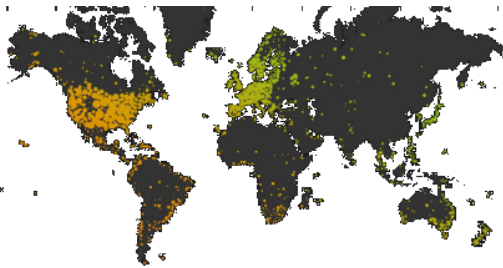


Figure 4. Wunderground: location of the personal weather stations.

Concerning the forecasts, it was recorded the speed at 12 h of the first four days available. Some websites can have up to two weeks of forecast. Some websites have the possibility of choosing hourly forecast or a presentation more condensed (three to four sets of data/day). In these websites we collect the data only from the hourly forecasts. On the third day and beyond, some websites reduce the frequency of the data provided (to, usually, every three hours).

#### IV. THE DATA

##### A. From the weather station

During a period of 369 days, almost every day, data at the 12 h was registered. There are very few periods with no data, a few due to forgetfulness (a total of 4 days) others because no data from the Peniche station was available when the website was consulted (4 days).

The values of the wind speed registered in Peniche are presented in Figure 5. The frequency of days in the five classes of wind speed by month, are presented in the graph of Figure 6. For instance, April was the month with

a larger number of days with light wind. The classes were chosen according to a classification made by IPMA, presented in Table 1. The most common drones used for surveys, monitoring, etc., can fly with light or moderate wind speed, a smaller number also with strong wind.

Table 1. Classification of the wind speed (km/h)

Speed	Classification
[0,15[	Light wind
[15,35[	Moderate wind
[35,55[	Strong wind
[55,75[	Very strong wind
[75, ∞[	Exceptionally strong wind

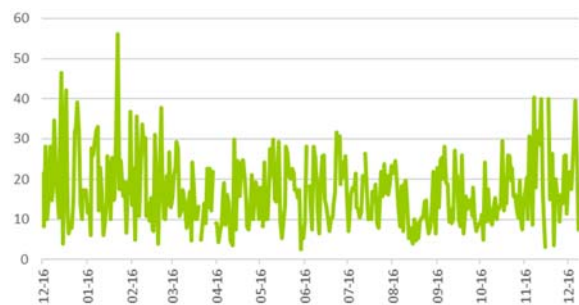


Figure 5. Wind speed (km/h) measured in Peniche.

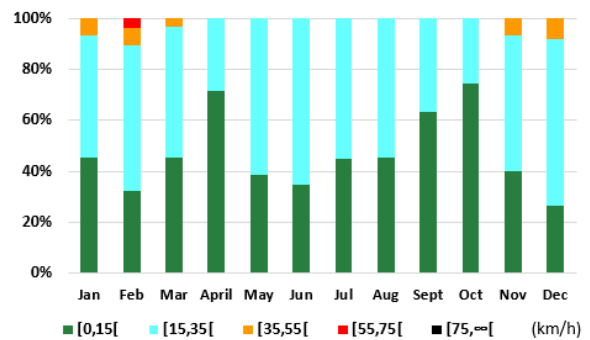


Figure 6. Frequency of the five groups of speed (km/h) in each month.

There are days when, in a short period of time, very significant variations may occur. See an example in Figure 7, a graph presented by IPMA with values measured at Peniche station for a day in January 2021, where one can notice a decrease of almost 20 km/h in one hour.

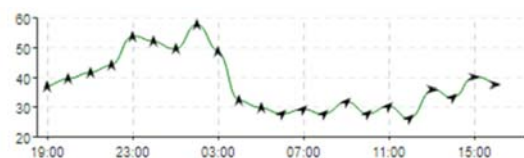


Figure 7. Wind speed (km/h) and direction registered during 22 hours in Peniche (winter of 2021).

##### B. From the websites

Each day all the seven websites were consulted and the data of the forecasts of the next four days were registered. Taking as example IPMA, IPMA.1 refers to the forecast for the following day, IPMA.4 the forecast

for the 4<sup>th</sup> day. Concerning the lack of data on the websites, model b-IST was the less reliable, with no data in 25 days (some of these due to an update of the website). For a period of six days in February of 2021, there was no data in d5-MeteoFrance.4. All the websites provide forecast data in an hourly format, except for d-windy that, in compare mode, provides values with three hours intervals.

Comparing the forecasts, it is noted that, sometimes, on the same day, there are large differences between the values presented on the websites. Sometimes this is because a model predicts that an event (either a large increase of the speed, or a large decrease) will occur sooner than another model does. The data presented in Figure 8 was designed with information from d-windy and illustrates well the differences between forecasts. It presents the values of the wind speed predicted by the five models every three hours for 3, 5 days. In the first two days the predictions were very similar; the third day the differences between models attained 16 km/h; the last period was again more homogeneous. During the third day, four models presented a large decrease in three hours, with a large increase the following day.

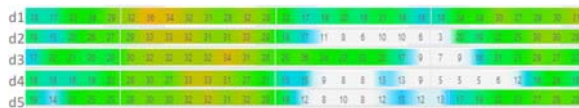


Figure 8. Wind speed (km/h) presented by the five models included in Windy.com (data starts the 30 July 2021, at 9 h).

The data included in the graph of Figure 8 was transferred to a graph (presented in Figure 9) which was supplemented with the speed measured at Peniche station. This graph also highlights a general fact (it happened in 77% of the days) that the dispersion of the values of the data (forecasts) is lower with the proximity of the dispersion day.

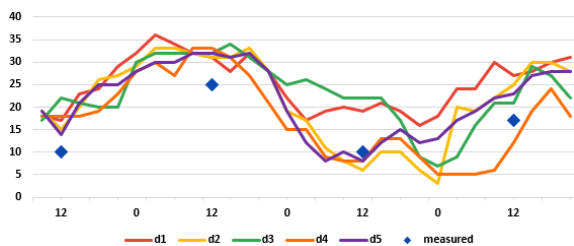


Figure 9. Wind speed (km/h) forecast every 3 h (graph with data presented in Figure 8), supplemented with the values measured at 12 h.

The largest difference between predicted values occurred for the 3<sup>rd</sup> day forecast of 30 November 2021. The predicted values vary between 9 km/h (d2-ECMWF) and 50 km/h (b-IST). In Figure 10 we present the forecast (4d until 1d) of all websites and the value measured (which was 14 km/h). The best forecast was presented by a-IPMA.

Each model presents also, sometimes, big changes from a day to the next. The biggest one was a variation of -33 km/h on model g-windfinder: a day it was

predicted a value of 54 km/h, the following day a value of 21 km/h. In Figure 10 we can also notice this kind of occurrence: a variation of 30 km/h presented by d5-MeteoFrance from 3d to 2d.

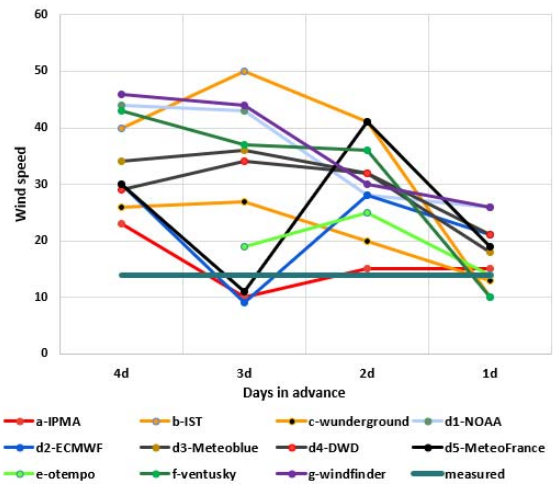


Figure 10. Wind speed (km/h) forecast for 30 November 2021 supplemented with the value measured.

We also calculated the correlation between models. For each pair of models, we calculated the correlation coefficients between the predicted values along the year, for each of the four days of forecast. Some results of the analysis are presented in Table 2. This is divided in two areas: i) upper triangle (reddish colors): the average of the four values of correlation; ii) lower triangle (greenish colors) the amplitude of the four values.

Table 2. Correlation between values presented by the websites (upper triangle). Amplitude of the four values of correlation (lower triangle). a-IPMA; b-IST; c-wunderground; d1-NOAA; d2-ECMWF; d3-Meteoblu; d4-DWD; d5-MeteoFrance; e-otempo; f-ventusky; g-windfinder

	a	b	c	d1	d2	d3	d4	d5	e	f	g
a		0,74	0,89	0,78	0,90	0,73	0,80	0,90	0,91	0,79	0,75
b	0,22		0,82	0,78	0,76	0,75	0,75	0,75	0,85	0,76	0,76
c	0,18	0,09		0,89	0,91	0,83	0,88	0,90	0,95	0,88	0,85
d1	0,16	0,19	0,07		0,82	0,81	0,83	0,82	0,90	0,87	0,94
d2	0,24	0,03	0,07	0,18		0,76	0,84	0,98	0,95	0,82	0,79
d3	0,18	0,19	0,08	0,08	0,18		0,77	0,77	0,83	0,77	0,77
d4	0,24	0,17	0,09	0,15	0,15	0,15		0,84	0,89	0,90	0,80
d5	0,23	0,01	0,07	0,18	0,02	0,18	0,16		0,94	0,82	0,79
e	0,11	0,03	0,01	0,05	0,01	0,10	0,05	0,01		0,89	0,88
f	0,21	0,22	0,11	0,14	0,21	0,15	0,21	0,21	0,07		0,84
g	0,17	0,21	0,08	0,03	0,20	0,16	0,16	0,19	0,06	0,10	

From the information available on the websites, we know that some only explore new formats of presenting the forecasts, more friendly for the users. It is the case of d-windy, f-ventusky and g-windfinder. The data they present are calculated by other services. For instance, the results of model ICON-EU, calculated by DWD, are presented by d4-windy and f-ventusky. The results of model ECMWF are presented by d1-windy and g-windfinder. Consulting Table 2 we can see that, in both cases, the values of correlation are high, in the

interval [0.9,1]. But the highest correlation is between models ECMWF and Arome (presented by windy, models d2 and d5).

## V. THE ANALYSIS

Data of the websites was compared with the data measured. The frequency of occurrences is presented in Figure 11. Negative values mean that the value predicted was lower than the measured; positive higher than the measured. All the models tend to be “pessimistic”, as they predict higher wind speed than the value measured.

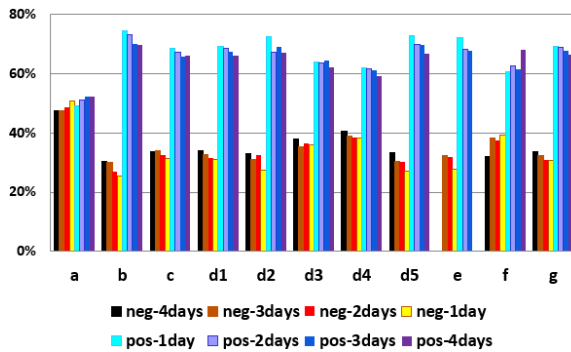


Figure 11. Frequencies of over and underestimation of wind speed for each model up to four days in advance.

The following analysis were performed using the R software package (R Core Team, 2018).

The comparison between the time series of observed and predicted wind speed values provides information on the forecasts quality along the year. The comparison is performed through the determination of dissimilarity measures between a pair of time series, such as the distance between them (Esling and Agon, 2012; Fu, 2011). In this case, Euclidean distance between the time series of observed and predicted wind speeds was used. The Euclidean distance between two time series corresponds to the sum of the Euclidean distances between each observed value and a prediction for the corresponding day, for all days in the considered time interval.

It was verified that, for each model, the dissimilarities decrease with the proximity to the chosen day (Figure 8), showing the forecasts improve as the that day gets closer.

For each day in advance, the dissimilarities between the time series of observed and predicted values were compared for the several models. It was observed (see Figure 12) that for the forecasts up to three days in advance, a-IPMA leads to the smallest dissimilarities, which suggests that its predictions are the most similar to the observed values along the year in analysis. Four days in advance, both a-IPMA and c-wunderground present the lowest values.

These results are in accordance to Figure 11, which shows that a-IPMA tends to equally over- and underestimate the wind speed values. The balance between over- and underestimations leads to a large similarity between observed and predicted time series. On

the other hand, the other models tend to overestimate the wind speeds (Figure 11), which results in a larger distance between the forecasts and the observations.

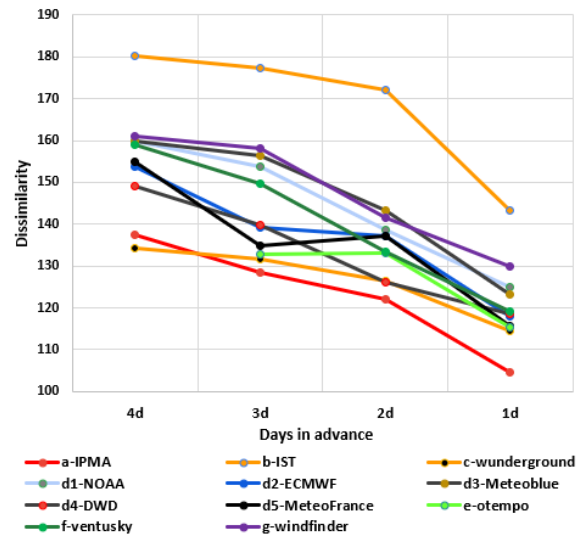


Figure 12. Dissimilarities between the time series of observed wind speeds and the time series of forecasts, for each day in advance.

The dissimilarities between the time series of observed and predicted wind speeds provide an assessment of each model’s performance along the year. To evaluate the quality of individual forecasts, scatter plots between observed and predicted values were computed. They show that the dispersion of the forecasted values decreases with the proximity to the prediction day (Figure 13), *i.e.*, forecasts become closer to the observed values. For almost all models, the forecasted values are larger than the observed ones (more dots are above the red lines), suggesting the models tend to overestimate the wind speeds, as already seen in Figure 11.

The regression lines (blue lines in Figure 13) also provide information about the quality of the forecasts. The closer the slope of the regression line is to 1, the larger is the similarity between the forecasts and the observed wind speed values. It is verified that the slope gets closer to 1 as the number of days before the chosen date decreases. The values of the coefficient of determination provide insight into the dispersion of the forecasts. The larger the coefficient of determination, the lower is the dispersion of the predicted values and forecasts have larger precision. Dispersion tends to decrease with the proximity to the chosen day.

The best situation would be a regression line matching the diagonal line (blue line equal to the red line) *i.e.*, regression line with a slope of 1, in conjunction with a low dispersion. This can be parameterized by coefficient of determination,  $R^2$ , where 1 is the best value. The values obtained for two models, b-IST and d5-MeteoFrance, are presented in Table 3. This data (slope and  $R^2$ ), for all models, is presented in the Figure 14. To identify the data of each model more easily the points were connected by lines. In all models



the highest values for “slope” are obtained for the forecasts of the previous day (day .1).

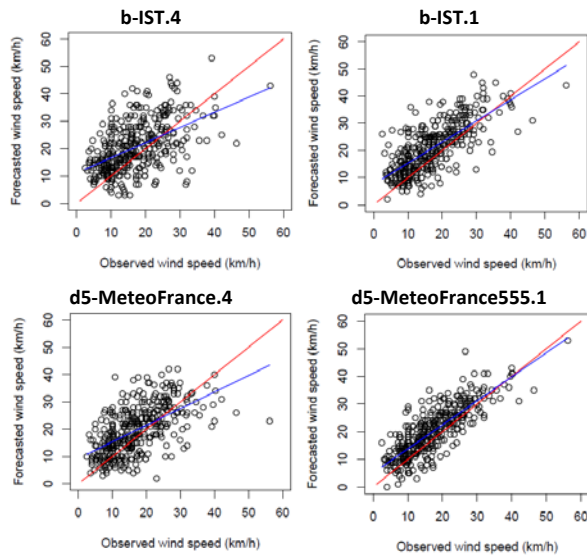


Figure 13. Scatter plots of observed and forecasted wind speeds for b-IST and d5-MeteoFrance models; the numbers in the chart titles are the number of days in advance of the forecast; the red lines correspond to the situation where forecasted values are equal to the observations and the blue lines are the regression lines.

Table 3. Slope and coefficient of determination ( $R^2$ ) for the regression lines, for two models

Model	.4	.3	.2	.1
b-IST				
Slope	0.55	0.65	0.74	0.78
$R^2$	0.26	0.34	0.41	0.53
d5-MeteoFrance				
Slope	0.61	0.72	0.77	0.87
$R^2$	0.34	0.49	0.52	0.67

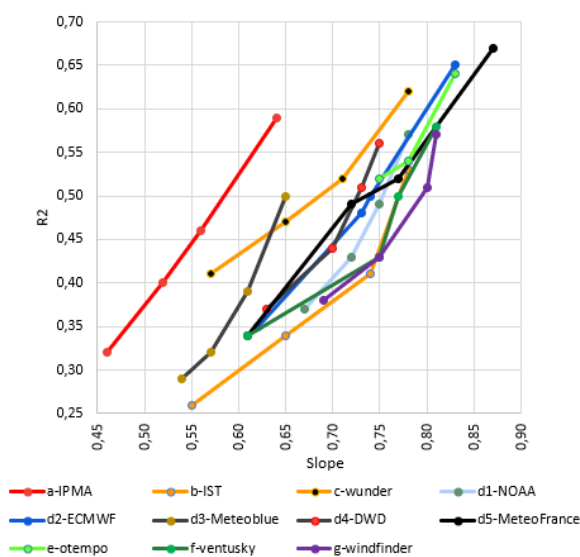


Figure 14. Relationship between slope and coefficient of determination for the regression lines associated to each model.

## VI. CONCLUSIONS

In this paper we present the analysis of values of wind speed presented in several websites. The data is the wind speed at 12 h, from the forecasts one day until four days of Peniche, in Portugal. Peniche has a meteorological weather station with data available online every hour.

From the analysis of the values of the wind speed measured and predicted we concluded that we could reduce the number of websites visited, due to correlation between data presented in different websites and, also, because some don't present very high values of similarity with the values measured.

It was also noted a tendency of the models to over-estimate the speed of the wind. The authors think this over-estimation is better than the under-estimation: it is less harmful not to travel, even it turns out that, on the day, the conditions were adequate to carry out flights. Worse is to travel to find that there are not good conditions to flight.

On the days that proceed the chosen day, it is advisable to consult, daily, several websites. Those websites that also provide wind gust (data that is available on few websites) should be included.

We finish answering to “Planning UAV surveys: can we rely on wind forecasts?": Yes, we can.

## VII. ACKNOWLEDGEMENTS

The work has received funding from the Portuguese Foundation for Science and Technology (FCT), Portugal, through project BSAFE4SEA - Breakwaters SAFETY control through a FORecast and decision support SystEm Analysis, Ref. PTDC/ECI-EGC/31090/2017.

## References

- Esling, P., and C. Agon (2012). Time series data mining. *ACM Computing Surveys*, Vol. 45, No. 1, pp. 1-34. DOI: 10.1145/2379776.2379788.
- Fu, T.C. (2011). A review on time series data mining. *Engineering Applications of Artificial Intelligence*, Vol. 24, No. 1, pp. 164-181. DOI: 10.1016/j.engappai.2010.09.007.
- Meteo France (2015). Les systèmes de prévision numérique du temps Arpège et Arome de Météo-France. [https://donneespubliques.meteofrance.fr/client/document/presentation\\_modeles\\_arome-arpege-v2\\_187.pdf](https://donneespubliques.meteofrance.fr/client/document/presentation_modeles_arome-arpege-v2_187.pdf).
- R Core Team (2018). R: A language and environment for statistical computing. R Foundation for Statistical Computing, Vienna, Austria. <http://www.r-project.org>.

## Deformation analysis in landslides NE Bulgaria using GNSS data complemented by InSAR for better interpretation results

Mila Atanasova<sup>1</sup>, Hristo Nikolov<sup>2</sup>, Ivan Georgiev<sup>1</sup>, Anton Ivanov<sup>1</sup>

<sup>1</sup> National Institute of Geophysics, Geodesy and Geography, Bulgarian Academy of Sciences, Acad. G. Bonchev bl. 3, Sofia 1113, Bulgaria, ([mila\\_at\\_zl@abv.bg](mailto:mila_at_zl@abv.bg); [ivan@bas.bg](mailto:ivan@bas.bg); [anton\\_iv66@abv.bg](mailto:anton_iv66@abv.bg))

<sup>2</sup> Space Research and Technology Institute (SRTI) - Bulgarian Academy of Sciences, Acad. G. Bonchev bl. 1, Sofia 1113, Bulgaria, ([hristo@stil.bas.bg](mailto:hristo@stil.bas.bg))

**Key words:** *monitoring landslide, geodynamic GNSS network, deformation analysis, DinSAR*

### ABSTRACT

The Bulgarian northern Black Sea coast is affected by many landslides. Landslide research is important as these phenomena cause loss of human lives and infrastructural damages. For this study a landslide area called "Dalgiya yar" was selected. The objective of this study is to provide solid grounds for monitoring the landslide processes using GNSS and SAR data. To achieve the set goals a geodynamic network was established. Those networks consist generally of two types of points – reference (located on geologically stable terrain) and survey points located within the landslide. The overall deformation analysis of the geodynamic networks is done after the third measurement cycle. The main approach to obtain the final results is based on determination of deformation components of spatially oriented triangles. For the studied period and for the mentioned area three main types of deformations have been determined by Finite Elements Method – station displacements, relative side deformations and relative principal deformations. It needs to be mentioned that due to peculiarities of the researched zone the condition that the final elements must to be configured approximately as equilateral triangles with approximately equal areas and not overlapping was not possible to be met. This is the reason to complement the GNSS results with such produced by DinSAR processing of Sentinel-1 data for the mentioned periods.

### I. INTRODUCTION

The development of contemporary geodetic techniques and its combination remote sensing is a sufficient prerequisite for getting more detailed, comprehensive and accurate information on the dynamic behavior of the earth's crust. In this case it is essential to underline the need to guarantee the most complete and accurate information that reflects the peculiarities of the Earth dynamics. This information will be achieved using GNSS data from local and continuously operating reference stations (CORS) networks complemented by freely available SAR data from the Copernicus program. In this study the authors propose that the data from the stable points to be provided by continuously operating reference stations National GNSS network. On the other hand local survey points in the studied landslide which consist of a total of 30 points were measured in static mode in three consecutive cycles in the period June 2019-2021. The main axes of deformation are determined by Methods for determining the deformation components of spatially oriented triangles. Graphic analysis was made and comparison of the results obtained and justified is the need for regular monitoring of landslides processes registering the ongoing surface movements and changes in the landslides body.

### II. RESEARCH AREAS

The study area "Dalgiya yar" is a landslide circus located in the Varna landslide region, which includes the coastline that begins at north of Varna town and reaches the valley of the river Batova, near the village of Kranevo. The formation of deep landslides in this area is mainly due to sea abrasion. These are large landslide complexes of circus type found on the eastern slope of the Frangen plateau - from its edge to the beach. Besides these old stabilized landslides being result of the complex impact of natural factors and man-made activity, modern active local landslides are emerge as well (Bruchev *et al.*, 2007; Evlogiev and Evstatiev, 2011). In the mentioned study area of "Dalgiya yar" included are several active landslides which boundaries overlap and therefore are difficult to distinguish from one another. Even for some of the studied landslides located in this area, a smaller landslide can be located inside them. The "Fara" landslide filed under the identification number VAR 02.54145-01-17 in the register of landslides of the Republic of Bulgaria, that is located between the village of Kranevo and the tourist resort "Panorama" and covers only the lower steps of the circus "Dalgiya yar" has activated on 13 October 2012 destroying the lighthouse and the villas around it.

### III. GNSS NETWORK

#### A. GNSS permanent network

In this research specific method for monitoring the deformations of the landslide processes using GNSS technology has been proposed. It is based on data from two types of GNSS networks - reference CORS stations located on geologically stable terrain and points located in the landslide body that forms a local geodetic network. Data for the stable points located in non-deformable zones in the investigated region are provided by the stations from the permanent National GNSS network (Georgiev *et al.*, 2020) maintained and pre-processed by NIGGG-BAS (see Figure 1).



Figure 1. Stations from national permanent geodetic network (red triangles).

All measurements from the local geodetic network are processed and analyzed using data from the CORS points located the research area. In this study long-term processing of data from continuously operating reference stations is performed to obtain the coordinates and velocities of the stations, because this also affects the local geodetic network built established for studying the landslide area.

It needs to be pointed out that the velocities of the points from the National GNSS network in the northern Black Sea region are relatively small, less than 1 mm/year (Georgiev *et al.*, 2020) while for other regions of territory of Bulgaria they can reach 3-4 mm/year. To obtain the movements of the points from the local geodynamic networks, it is possible to process their GNSS measurements together with the GNSS measurements from the points of National GNSS network but the velocities of the CORS station must be taken in to account as well (Atanasova *et al.*, 2021).

#### B. Local geodetic network

For this specific study a local GNSS network covering the landslide area "Dalgiya yar" (see Figure 2) was established. It consists of a total 30 stabilized points with some being metal pipes 35 cm long while other are metal bolts nailed in the stable rocks. In the mentioned geodynamic network "Dalgiya yar" previously points used for GNSS measurements in the network used to

monitor deformations along the road above the landslide are included were found on the ground and used too (see Figure 2).

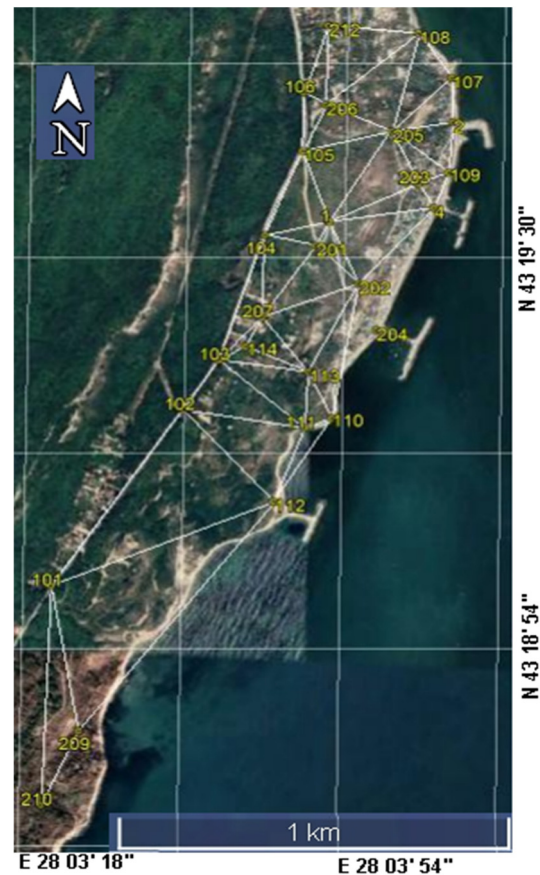


Figure 2. Local GNSS geodetic network at Dalgiya yar.

The GNSS measurements were carried with 2 receivers of type CHC i80 with horizontal precision 2.5 mm + 0.1 ppm RMS and vertical 3.5 mm + 0.4 ppm RMS and 1 receiver - P3E GNSS sensor used as reference station. Static mode with an interval 1 sec. and duration of one hour was applied for the GNSS measurements. The results of the GNSS measurements were processed using "CHC Geomatics Office 2" software in the coordinate system WGS84. This newly established geodynamic network located inside the landslide area was measured once a year. The first measurement cycle of the geodynamic network was carried out in June 19-23 2019, second in June 22-27 2020 and the third cycle was measured in June 21-28 2021. The deformation analysis of the geodynamic networks was done after the third measurement cycle. Points 0204, 0208, 0211 were destroyed after the first cycle and no measurements were made thereafter.

To approximate the velocities linear regression model was used. During processing it can be selected whether all measurements from all epochs should be included in further calculations or those exhibiting strong deviation should be removed. The spatial coordinates X, Y, Z, are transformed into local coordinates with components north N, east E and up U while the epoch 2019.4658 is considered zero. In this case the increase along the

northern (eastern) component is determined and the coordinates of the point for each subsequent epoch are reduced by the values of the coordinates from the zero epoch. The abscissa graphically shows the increase along the northern (eastern) component and along the ordinate the time intervals. Approximate the value of the velocity as a linear function (linear regression) Figure 3 show the approximation of the velocity values along the northern and eastern components for point 102, the approach is analogous for the other 30 points of the network.

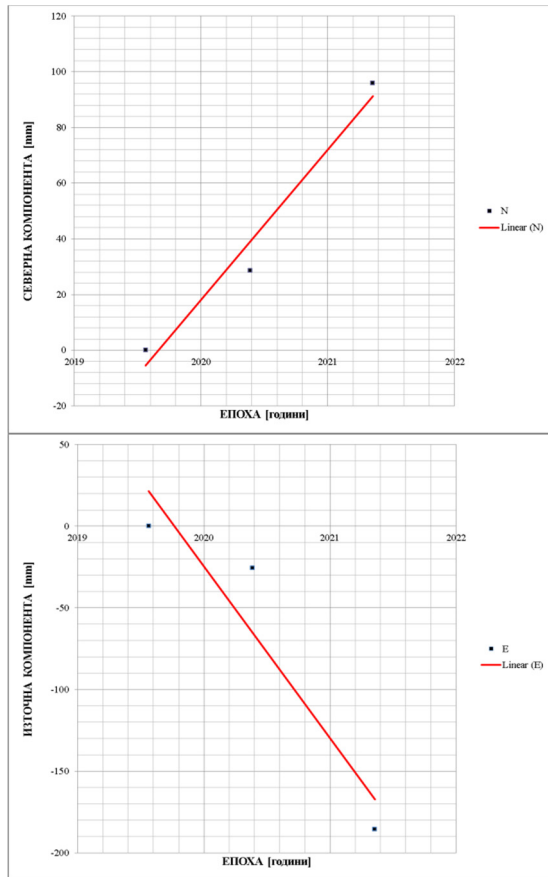


Figure 3. Determination of velocity by a linear regression along the north and eastern component for each point of the local geodetic network.

Displacements of local GNSS points (located in the body of the landslide circus) calculated by between epochs 2019-2021 (between the first and second, second and third and first and third cycles) are based on the coordinates adjustment for each cycle and are presented in Figure 4 for the northern, east and up components. The 2D magnitude of the displacement vector for each point of the local network was calculated too.

For the majority of geodetic studies the finite element model (FEM) is mainly used in the analysis of movements of stations based on results from GNSS data processing in order to obtain the strain tensors and strain accumulation (Bogusz *et al.*, 2013; Vassileva and Valev, 2015; Vassileva and Atanasova, 2017). More

details on theory of the developed method has been presented in (Vassileva *et al.*, 2017).

ID	2020-2019 [mm]				2021-2019 [mm]				2021-2020 [mm]			
	n	e	h	2D	n	e	u	2D	n	e	u	2D
1	12.6	4.2	32.1	13.3	4	2.4	21.5	4.66	-8.6	-1.8	-10.6	8.79
2	1.8	16.1	2.8	16.2	1.3	16.7	8.4	16.8	-0.5	0.6	5.6	0.78
4	-15.9	12.6	-24.6	20.3	-13.5	20.4	63.9	24.5	2.4	7.8	88.5	8.16
101	-13.5	15.6	0.5	20.6	-19.4	34	3.2	39.1	-5.9	18.4	2.7	19.3
102	-28.5	25.1	24.2	38	-95.9	18.6	93.7	209	-67	160.5	69.5	174
103	-20.2	20.2	34.5	28.6	-28.2	53.1	21	60.1	-8	32.9	-13.5	33.9
104	-14.1	5.5	27	15.1	-21.3	-9.3	25.3	23.2	-7.2	-14.8	-1.7	16.5
105	-8.3	7.4	-4.3	11.1	-6.1	-9	14.9	10.9	2.2	-16.4	19.2	16.5
106	-2.7	0.1	-0.7	2.7	5.6	-24.8	24	25.4	8.3	-24.9	24.7	26.2
107	10.6	10.7	-3.4	15.1	10.8	6.3	24	12.5	0.2	-4.4	27.4	4.4
108	5.2	8.9	0.1	10.3	16.4	2	10.8	16.5	11	-6.9	10.7	13.2
109	8.1	-3.8	-60	8.95	13	-1	-5.1	13	4.9	2.8	54.9	5.64
110	-14.4	69.9	80.6	15.9	-15.4	10.7	87.4	18.7	-9.9	37.4	6.8	38.7
111	-21.2	5.7	-22	22	-11.3	24.3	32.6	26.8	9.9	18.6	54.6	21.1
112	-7.6	2	17.7	7.86	21	15.6	59.2	26.2	29	13.6	41.5	31.7
113	-23.3	16.4	31.6	28.5	-24.4	39.9	41.3	46.8	-1.1	23.5	9.7	23.5
114	8.3	12.8	-24	15.3	1.9	6.2	5.3	6.48	-6.4	-6.6	29.3	9.19
201	1	1.5	15.1	1.8	-9.4	3	32	9.87	-10	1.5	16.9	10.5
202	-5	2.9	12.7	5.78	-14.3	-1.1	26.4	14.3	-9.3	-4	13.7	10.1
203	3.4	3.5	17.1	4.88	8.3	-0.7	33.7	8.33	4.9	-4.2	16.6	6.45
205	-15.9	-14.8	24.2	21.7	-41	55.1	90.9	68.7	-25	69.9	66.7	74.3
206	2	-6.1	4.7	6.42	-5.9	3.9	32.2	7.07	-7.9	10	27.5	12.7
207	-18.1	4.7	40.1	18.7	-4.2	5.2	42.9	6.68	14	0.5	28.1	13.9
209	11	24.9	-50.3	27.2	54.8	34.2	-50	64.6	44	9.3	0.2	44.8
210	-21	-17.26	-21.4	17.4	-21.1	-17.4	-22	17.6	-0.6	-17.1	-24.3	17.1
212	-11.3	-1.5	37.1	11.4	-11.9	15.3	51.5	19.4	-0.6	16.8	14.4	16.8

Figure 4. Displacements for the points from the local GNSS network calculated for epochs 2019-2021.

Common practice is the use of reduced (to the surface of a reference ellipsoid or in a map projection) geodetic measurements. Such an approach, which is imperatively applicable in regular geodesy leads to significant manipulation (inaccuracies) of the deformation model. The main reasons for such a statement are the following: the reduced geodetically determined elements (most often distance) on the reference ellipsoid are directly dependent on the ellipsoidal heights of the defining points. It is not considered that it is quite possible that sections with different heights are actually subject to the deformation processes having same intensity. As it is known the length of the reduced baseline depends on the parameters of the selected reference ellipsoid. The length of the distance in projection is definitely influenced by the distance of the main meridian (parallel). Thus, too often elements that have undergone deformations with purely geometric nature are used without these deformations being of geodynamic origin. Thereby, consciously or not, created is a manipulated deformation model with altered sensitivity and reliability. It needs mentioning that there are various geodetic methods that are used to determine the displacements of points on the earth's

surface covering fixed period of time caused by activation of various geodynamic phenomena. Those displacements are related to the selection of a fixed origin used coordinate system. It should be underlined that absolutely fixed points on the earth's surface do not exist - so the movements themselves are to some extent quite relative. Therefore, it is more appropriate to base the analysis of the studied geodynamic phenomena on elements independent of the coordinate origin – baselines. Baselines whose deformations in time will be the basis for determining the main deformation components of the studied object in two main ways are determined; by the coordinates of their endpoints and by direct measurement of the baselines. The direct determination of the lengths of the chords in space is in-line with the most accurate and modern geodetic methods (GNSS, Laser scanners, LIDAR). This is an additional advantage in the implementation of this method. In this study the adopted strategy is to study the deformation processes through the use spatial chords based on geodetic measurements, based on the theory of deformation and the FEM. Extract of baselines are presented in Table 2.

Table 2. Extract of baselines (Ellipsoid Distance) on geodetic measurements, between epochs 2019-2021

Baseline ID	2019	2020	2021
0001->0203	255.3331	255.3306	255.3326
0001->0202	196.0049	196.0235	196.0192
0001->0201	75.4893	75.5011	75.5091
0001->0205	304.7517	304.7176	304.7179
0001->0206	337.2371	337.2221	337.2279
0001->0105	217.2407	217.2401	217.2343
0001->0106	378.8347	378.8397	378.8419
0002->0107	128.0989	128.1059	128.1179
0002->0108	270.0403	270.052	270.0633
0002->0109	144.131	144.1192	144.1143
0002->0207	741.9788	742.0012	742.0229
0111->0004	699.9488	699.9462	699.9451
112->0004	929.0988	929.0588	929.0694
0113->0004	567.9632	567.96	567.9611

Below shown are the results from using results periodic measurements on which calculated are the components of deformation in the region of the landslide. This is considered as possibility to study the deformation processes through the use of measured parameters – spatial chords based on geodetic measurements carried out based on the theory of deformations and FEM. Calculated were the spatial chords between the points that cover the main structures in the area of the specific landslides (geodynamic) areas using the results from GNSS measurements for the epochs 2019, 2020 and 2021.

As basis for calculation used is the well-known formula (Toshev, 1967) that gives the relationships between the components of deformation tensor and the linear deformation of a section of a deformation

environment. For each of the triangles composed and determined is a system of three equations as a result of which the received tensor components of a "pure" deformation. Calculated are the major axes of relative deformation to the median's center of the triangle too. All these elements characterize the deformation processes reduced to the plane of the respective triangle. Graphical representations of the major axes of deformation are given in Figure 3. The results of GNSS measurements for the period 2019 - 2021 were used, on the basis of which the baselines were calculated between the points (Figure 3).

### C. Relative principle deformations

The relative principal deformations of each finite element are obtained and they are shown in Figure 5 (compression in blue and extension in red). Relative principal deformations of finite elements in the areas in the circus reveals that during the studied time period the movements are dominantly of extension ranging from 0.5 mm up to 30 mm and the directions are mainly west-east. In the maps shown are the extensions in the north part and in the south part of the landslide circus which are approximately of the same magnitude.

The relationship between directions of the principal deformations of each finite element and the directions of its side deformations are very close. Directions of the principal deformations of extension or compression of every finite element dominantly are defined by the type of deformations of the sides of the respective finite element (Vassileva *et al.*, 2017). The obtained results for the principal deformations in this study confirm this relation (Figure 5).

## IV. DINSAR PROCESSING OF SENTINEL-1

As noted above it needs to be mentioned that due to peculiarities of the researched zone the condition that the finite elements must configured approximately as equilateral triangles with approximately equal areas and thus the requirement for not overlapping was not possible to be met. This is the reason why it was necessary to complement the GNSS results with such produced by DInSAR processing of Sentinel-1 (S-1) data for the mentioned periods.

The color-coded earth displacements in LOS calculated from the phase signal for several periods by processing S-1 data are shown on Figure 6. The time period covers 4 months for the winter months starting in November 2015 up to March 2020. As it can be seen the calculated displacements are in the range between 30 mm (uplift) and -50 mm (subsidence). The obtained IFIs reveal that the registered deformations are concentrated in some local areas with uneven structure. A map of the concentration of deformations of the earth's crust was created from them. The pixels having coherence values below 0.3 in each IFI have been removed because they are considered unreliable.

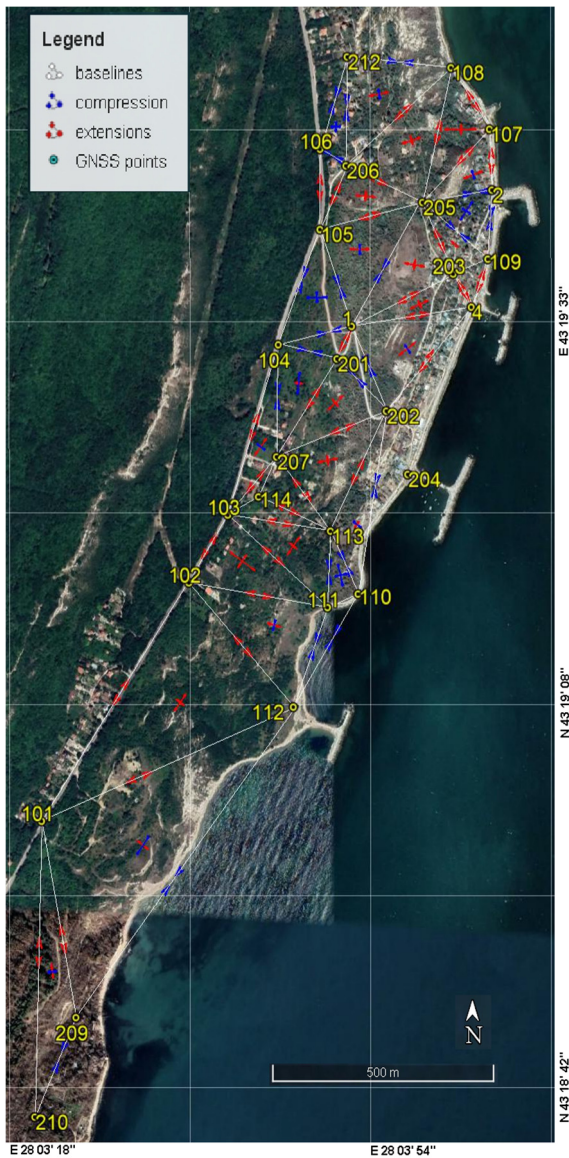


Figure 5. Relative side and principal deformations for the time span 2019-2021 (red vectors- extensions; blue vectors compression). Main axes of relative deformation to the median's center of the triangles.

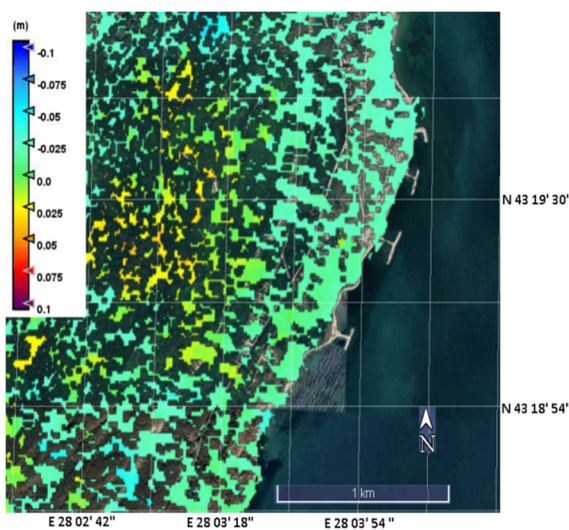


Figure 6. Case of application of the DInSAR research method for the "Dalgiya Yar" landslide: surface displacement maps 29Nov2019\_28Mar2020.

The color of the pixels represents the movement of the surface in the meter units for the studied period, ranging from dark blue to purple (Atanasova *et al.*, 2021). The most vulnerable areas are shown in purple and less vulnerable ones are in yellow and green, but our the case is prevailing from yellow to light blue. The area enclosed by the polygon of geodetic points 208, 209, 101, 102, 111 and 112 (see Figures 5 and 6) is inaccessible because it is on steep slope with high inclination. These points were not monitored by GNSS measurements during the campaigns (Atanasova *et al.*, 2019; Dimitrov *et al.*, 2020). It is worth noting that the earth surface movements in this area are monitored only by SAR data and have some of the most significant subsidence values for the studied period. The maps portraying the mean surface displacements in the LOS direction are shown on Figure 6. The research approach applied demonstrates the potential and ability of DInSAR to study and monitor landslides and measure their trend in LOS with centimetre accuracy over time using freely available data and software for such inaccessible areas. For monitoring the ground deformation, due to the relativity of the DInSAR technique, other types of measurements such as GNSS, precise levelling, and UAS or LiDAR are needed to supplement the data from the satellite remote sensing.

## V. CONCLUSION

The results of study showed that registered motions on the Earth's crust in the area are reliable. They also confirmed that the GNSS and InSAR methods used are appropriate for determining the induced surface movements. Provided are major conclusions about the nature of the deformation processes and the possible status of their development. The results from the geodetic monitoring of the deformation in the landslide region allow conclusions to be drawn with regard to the local deformations that are taking place of the ground surface. These deformation processes could be explained with concentration of the landslide developments the region. The question stays open whether local movements or the induced anthropogenic ones prevail. For clarifying this issue needed is new deep and complex approach including modern interpretation of the results using geological information as well.

## VI. ACKNOWLEDGEMENTS

This study was conducted with financial support of the Bulgarian NSF under the Project № KP-06-OPR 06/1 14.12.2018, "Monitoring of landslide processes on the Northern Black Sea coast of Bulgaria through cooperate use of data from global navigation satellite systems and interferometric images from synthetic aperture radar".

## References

Atanasova M., H. Nikolov, I. Georgiev, A. Ivanov, and N. Dimitrov, (2019). Monitoring of landslide processes at the

- NE Bulgaria by joint use of GNSS and InSAR, In: *Proceeding 10th Congress of Balkan Geophysical Society*, 18-22 September 2019, Albena Resort, Bulgaria, EAGE.
- Atanasova M., Nikolov H., Georgiev I, Vassilev K, Dimitrov N, and Ivanov A., (2021) Creating a thematic geodatabase for monitoring the landslide processes of the landslide circus "DALGIA YAR". *7<sup>th</sup> World Multidisciplinary Earth Sciences Symposium 7-11 September 2020 – Prague (Czech Republic)*, IOP Conf. Series: Earth and Environmental Science 906 (2021) 012035, 2021, DOI: 10.1088/1755-1315/906/1/012035
- Bogusz, J., A. Klos, M. Figurski, M. Jarosinski, and B. Kontny, (2013). Investigation of the reliability of local strain analysis by means of the triangle modelling. *Acta Geodyn. Geomater.*, Vol. 10, No. 3 (171), pp. 293–305.
- Bruchev, I., Dobrev, N., Frangov, G., Ivanov, Pl., Varbanov, R., Berov, B., Nankin, R., and Krastanov, M., (2007). The landslides in Bulgaria — factors and distribution, *Geologica Balcanica*, 36, 3-4, pp. 3-12.
- Dimitrov N., Georgiev I., Atanasova M., and Ivanov A., (2020). Monitoring of the landslide processes at the "Dalgiya Yar" landslide. Conference *Proceedings of Selected papers, Section Geodesy and Mine Surveying, Volume 20, Book 2.2, 20<sup>th</sup> International Multidisciplinary Scientific GeoConference (SGEM 2020)* 18-24 August, Albena, Bulgaria, ISBN: 978-619-7603-07-1, ISSN: 1314-2704, DOI: 10.5593/sgem2020/2.2/s09.011, 87-94.
- Georgiev, I., Mihailov, G., Danchev, P., Dimitrov, N., Minchev, M., and Gabenski, P., (2020). State GPS network: processing and analysis of measurements of points from the basic class 2004 - 2018. *Thematic Series " Geodesy", 1, 23*, Military Geographical Service, Center for Geoinformation Services, 2020, ISBN: 978-954-9649-13-0, 125(in Bulgarian)
- Evlogiev, Y., and D. Evstatiev, (2011). New geological model for the landslides between the Kranevo village and the Panorama camping-site (North Black Sea coast). – *Eng. Geol. and Hydrogeol.*, 26, pp. 3–26
- Toshev, B.N., (1967) *Theory of stresses and deformations*, Publ. house Technique (in Bulgarian)
- Vassileva, K., and G. Valev, (2015). Application of Finite Elements Method in space for deformation analysis of the territory of Bulgaria, *Proceedings of the 8-th Congress of the Balkan Geophysical Society*, 4-8 October, Crete, Chania, Greece, 5p. art. N. 26716.
- Vassileva, K., and M. Atanasova, (2016). Earth movements on the territory of Bulgaria and northern Greece from GPS observations. *Comptes rendus de l'Académie bulgare des Sciences*, Volume 69, Issue 11, 1473-1478
- Vassileva, K., G. Valev, and M. Atanasova, (2017). Deformation analysis of the Balkan Peninsula from GPS data 2011-2016 *Coordinates*, Volume XIII, Issue 12, p31-34

## InSAR displacement time series post-processing to back-analyze a slope failure

Dora Roque<sup>1</sup>, Martino Correia<sup>2</sup>, Ricardo Cabral<sup>2</sup>, Steffan Davies<sup>2</sup>, Tiago Cordeiro<sup>2</sup>, Ana Fonseca<sup>1</sup>, Paulo Barreto<sup>3</sup>

<sup>1</sup>Laboratório Nacional de Engenharia Civil, Lisboa, Portugal, ([droque@lnec.pt](mailto:droque@lnec.pt); [anafonseca@lnec.pt](mailto:anafonseca@lnec.pt))

<sup>2</sup>THEIA, Coimbra, Portugal, ([hello@theia.pt](mailto:hello@theia.pt))

<sup>3</sup>EGIS Road Operation Portugal, Lamego, Portugal, ([paulo.barreto@egisportugal.pt](mailto:paulo.barreto@egisportugal.pt))

**Key words:** *InSAR; time series post-processing; back-analysis; slope failure*

### ABSTRACT

In this study, the failure of a slope adjacent to a motorway was back-analyzed based on InSAR data. The location of the slided area and the exact date of the event were not known in advance. A post-processing strategy was applied on the displacement time series in order to aid the detection of instability signs and to enable the identification of the location and the narrowing down of the time interval of the slide. InSAR displacement time series were obtained following the small baseline subset approach implemented on an automatic processing platform. Distributed scatterers were clustered based on the similarity of their displacement time series, in order to form clusters of scatterers with similar behavior. This procedure allowed the computation of displacement time series representative of each cluster, aiding the detection of instability signs on the slope. One of the clusters showed a sudden movement away from the SAR sensor. It was later confirmed that the slide had occurred at the location of the scatterers belonging to that cluster and during the time interval between the two observation epochs corresponding to the break in the time series. In conclusion, the proposed method was effective in the back-analysis of the slope failure, hopefully contributing to the uptake of InSAR technology by structural safety experts.

### I. INTRODUCTION

Interferometric Synthetic Aperture Radar (InSAR) has proved to be an effective technology for the monitoring of deformation caused by earthquakes, volcanic eruptions, glacier movement, urban subsidence, landslides, among others (Crosetto *et al.*, 2016). Some authors have also used InSAR to monitor civil infrastructures (*e.g.* Di Martire *et al.*, 2014; Emadali *et al.*, 2017; Giardina *et al.*, 2019; Lazecky *et al.*, 2017; Milillo *et al.*, 2019), profiting from its spatial coverage and temporal resolution. However, its application in this field remains a challenging task, due to several factors:

1. Typical structure monitoring methods achieve higher accuracies;
2. Lack of redundant observations;
3. Displacements are measured along the SAR line-of-sight (LOS);
4. Observation frequency does not enable the monitoring of structure dynamic behavior;
5. Large volume of data may be difficult to interpret by InSAR non-experts.

The aforementioned reasons prevent the uptake of InSAR technology in the field of structural safety.

Typically, large volumes of data are achieved using InSAR, in which hundreds or even thousands of measurement points are obtained per square kilometer, each of them having displacement time

series possibly with hundreds of observation epochs associated. The exploration of these results is a big data problem and turn the displacement interpretation difficult to perform by InSAR non-experts. In the particular case of structural behavior, which varies over time, variables typically analyzed in InSAR products, such as average velocity or cumulative displacement during a certain time interval, do not provide all the potential knowledge InSAR data contain for structure monitoring. Therefore, the development of automatic methods to extract information from the displacement time series is of the utmost importance in this field.

This study aims at contributing to increase the trust of structural safety experts in InSAR data by evaluating the capabilities of this technology to back-analyze movement on a slope affected by a landslide. A blind test was performed, in which the goal was to use InSAR data to identify the slope area affected by the landslide and to narrow down the time interval of its occurrence. InSAR displacements were computed through an automatic InSAR processing platform for a motorway and its surroundings, including the slope that is the study object of this paper. The InSAR displacement time series of the points located on the slope were evaluated through a semi-automatic procedure to form clusters of points with similar behavior. This aggregation of information allowed the detection of slope behavior patterns in space and time and enabled the attainment of the answers sought in the blind test. The applied



method is an improvement of that presented in Roque *et al.* (2018), by including a post-processing method to correct unwrapping errors and to analyze partial time series.

The paper is organized as follows. Section II presents the methods used in the study, with Subsection A describing the InSAR processing and Subsection B presenting the time series clustering. Section III contains a description of the area of interest (AOI) and of the SAR image dataset. Section IV shows the achieved results and is followed by their discussion in Section V. The paper is finished by the main conclusions of the study in Section VI.

## II. METHODS

### A. InSAR processing

Displacements were computed from a stack of SAR images through an automatic InSAR processing platform. In order to prepare the dataset for multi-temporal analysis, GMTSAR was employed to coregister the products from the stack and generate interferograms using the SBAS model. A maximum temporal baseline was limited to 48 days, maximum spatial baseline was defined as 100 metres, and the threshold for acceptable amplitude dispersion was set to 0.6. The scene was divided into 4 patches, which was sufficient considering the relatively small area of interest.

GMTSAR results were properly structured in order to be recognised by the StaMPS/MTI software, where point processing was performed in order to extract subsidence values for the area of interest. No point weeding was undertaken. After processing, the data was inverted in order to convert from multi-master to single-master displacement estimation.

The points from StaMPS/MTI processing were exported in a tabular data format for post-processing compatible with the StaMPS-Visualizer application. Average velocity and displacement time series were achieved for each point.

### B. Time series clustering

The goal of the post-processing of the InSAR data was the identification of spatiotemporal patterns in the behavior of the distributed scatterers, by clustering them according to the similarity between their displacement time series. The clustering algorithm was composed by several steps and was implemented in R software (R Core Team, 2021).

1) *Input data*: InSAR displacement time series were the only data required for the algorithm application, with a displacement observation for each SAR image acquisition date. Gaps in the acquisition were filled with interpolated values.

The displacement time series were complemented by auxiliary (and optional) information achieved in the InSAR processing, but also by external data provided as

raster files. In this study, InSAR derived velocities and slope data were considered.

2) *Removal of reference point effect*: In case the point used as reference presented some movement, its displacements influenced the time series of all the other points. In this study, an adaptation of the method presented in Notti *et al.* (2015) was applied in order to remove this effect. The points presenting absolute value of average velocity lower or equal than 0.5 mm/year were considered to be stable and the average of their displacement time series, which corresponded to the effect of the reference point on the other points, was removed from the displacement time series of all points in the AOI.

3) *Correction of unwrapping errors*: Unwrapping errors were detected in the displacement time series and were corrected following Notti *et al.* (2015). Time series were searched for consecutive displacement values with absolute difference larger than  $\frac{1}{4}$  of the SAR signal wavelength. In such cases, the second displacement value in the pair might be affected by an unwrapping error and became a candidate to a potential correction. However, the displacement value was corrected only if an external factor capable of causing a large displacement occurred at that date. Rainfall is an external factor that frequently works as a trigger to landslides. Therefore, daily rainfall data were collected from a meteorological station near the AOI for the same time interval of the displacement analysis. Dates were eligible for unwrapping error correction in case the amount of rainfall in that day was greater or equal than the 90% percentile of the daily rainfall in the whole time interval. The correction was applied on the displacement values if the displacement and rainfall conditions were both met for the same date. If the displacement value to be corrected was greater than that from the previous epoch,  $\frac{1}{2}$  of the SAR signal wavelength was subtracted to that displacement value. On the other hand, if the displacement value to correct was lower than the previous one,  $\frac{1}{2}$  of the SAR signal wavelength was added to it (Figure 1).

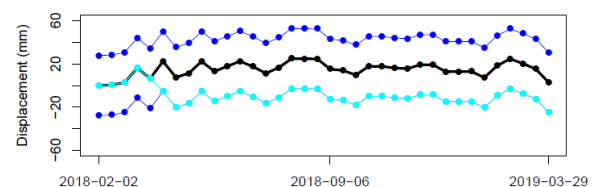


Figure 1. Displacement time series obtained during InSAR processing (black), displacement time series  $\pm\frac{1}{2}$  of the SAR signal wavelength (dark blue) and corrected displacement time series (cyan).

4) *Time series cut*: Previous studies have shown that the time series post-processing method was little sensitive to small magnitude changes in long time series (Roque, 2020).

In order to increase its sensitivity to signs of instability on the AOI around the time of the landslide, temporal subsets of the time series were considered. The removal of the reference point effect and the unwrapping error correction were performed on the complete displacement time series; however, they were later cut into a smaller time interval, narrowing down the analysis to the approximate date of the landslide occurrence (Section III).

5) *Compute dissimilarity matrix*: The clustering procedure was applied on the cut displacement time series. A hierarchical agglomerative clustering was used. In the first step, each point was considered as an individual cluster. The similarities between each pair of groups were computed and the most similar ones were merged. This procedure was performed iteratively until all clusters were aggregated into a single one. The similarities were the distances between the displacement time series, which were determined through the Dynamic Time Warping (DTW) method (Berndt and Clifford, 1994). DTW distance between two time series corresponds to the minimum cumulative path among several possibilities of connecting the data points (displacement observations in this case) from both series (Figure 2). Connections are not required to be between data points from the same epochs.

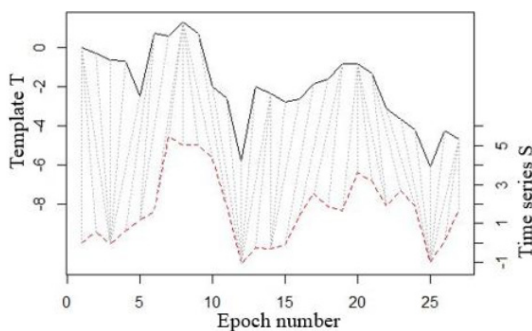


Figure 2. Connections between the data points from the template time series T and a generic time series S.

The aggregation method used in the clustering was the complete linkage, which considers the farthest elements in a pair of clusters to determine the distance between the two groups, *i.e.*, in this study, the distance between a pair of clusters was calculated as the DTW distance between the most dissimilar displacement time series from both groups. This method formed homogeneous clusters and was sensitive to the presence of outliers. The distances between each pair of clusters, in each iteration, were organized in a dissimilarity matrix, which provided the information for the cluster formation.

6) *Selection of the number of clusters*: For each iteration, the pair of clusters presenting the smallest value in the dissimilarity matrix was merged. The distance between two merged clusters is called linkage distance.

The analysis of linkage distances from all iterations assisted the selection of the number of clusters to be considered for analysis. The largest values were observed at the last iterations (top of the chart in Figure 3), when the merged clusters were already distinct. The number of clusters to analyze was selected in order to assure that the linkage distances connecting the elements inside each group were low. This procedure led to the construction of clusters formed by points with similar displacement time series. It also assured the clusters had different behavior among each other.

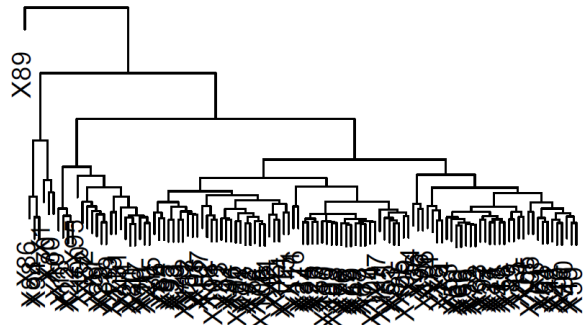


Figure 3. Chart of linkage distances (vertical black lines); the alphanumeric codes at the bottom of the chart correspond to the individual clusters in the first step.

After the cluster formation, data for their interpretation were computed. The displacement time series representative of the behavior of each cluster were achieved by averaging the displacement time series of all points in each group. Furthermore, the values of the auxiliary variables were used to compute cluster centroids. Velocities were already associated to the points during the InSAR processing, while slope values from the raster file were attributed to each point according to their location. The values from both variables were averaged for each cluster.

### III. STUDY AREA AND DATASET

The AOI for this study was a slope adjacent to a motorway, in Portugal. It was located at a granite area and it was built in the 2000 s. The slope occupies an area of approximately 10000 m<sup>2</sup>, it faces east and its average slope is 15° (Figure 4).

For the blind test performed in this study, it was known in advance that a landslide occurred on part of the slope during March 2019. In order to identify the affected area and to narrow down the time interval of the event, InSAR displacements were computed through the InSAR processing platform from Section II A and then evaluated through the time series post-processing method from Section II B.

The SAR dataset was composed of 33 Sentinel-1 A SLC (Single Look Complex) products in IW (Interferometric Wide) swath mode, using a descending orbit, starting on 2<sup>nd</sup> of February 2018 and ending on the 29<sup>th</sup> of March 2019, with a minimum interval of 12 days. The orbit path and frame of these products was 52 and 458,

respectively. ESA's SNAP (Sentinel Application Platform) software was used to determine the ideal master product from the stack, based on satellite baselines and dates, which was the product corresponding to the 18<sup>th</sup> of September 2018.



Figure 4. Slope adjacent to motorway.

At the post-processing analysis, the time series were cut to the time interval between January and March 2019 to increase the algorithm sensitivity to the displacements occurred in March 2019 (Section II B 4).

#### IV. RESULTS

##### A. InSAR processing

The InSAR processing led to 116 points on the slope, with average velocities between 22.3 mm/year away from the sensor and 11.3 mm/year towards it, from February 2018 to March 2019 (Figure 5).

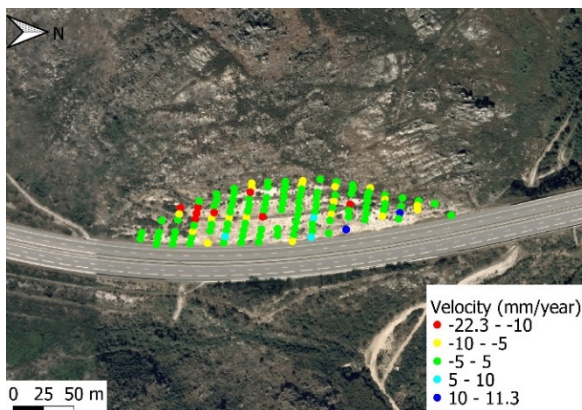


Figure 5. Velocity map for the points on the slope.

The velocity map presented several points with average velocities away from the sensor above 10 mm/year at the southernmost area of the slope. However, there were other areas with similar velocity values. Furthermore, there were also points presenting velocities towards the sensor with magnitudes of centimeters per year, which might correspond to horizontal displacement from west to east, *i.e.*, towards the motorway.

##### B. Time series clustering

The analysis of the linkage distance chart from Figure 3 led to the organization of the points into seven clusters, with a varying number of elements (Table 1).

Table 1. Point distribution throughout the clusters

Cluster	Points	
	Number	Percentage (%)
1	3	2.6
2	54	46.6
3	35	30.2
4	16	13.8
5	4	3.4
6	3	2.6
7	1	0.9

Figure 6 presents the spatial distribution of the points throughout the clusters. Some of the groups were spatially cohesive (cluster 5 and most of clusters 4 and 6), while the others were spread throughout the slope. Cluster 7 was formed by a single point, meaning it was the point identified in Figure 3 with the alphanumeric code X89. The chart shows this point had a displacement time series distinct from those of the remaining ones, as this was the last point being aggregated to the main cluster.

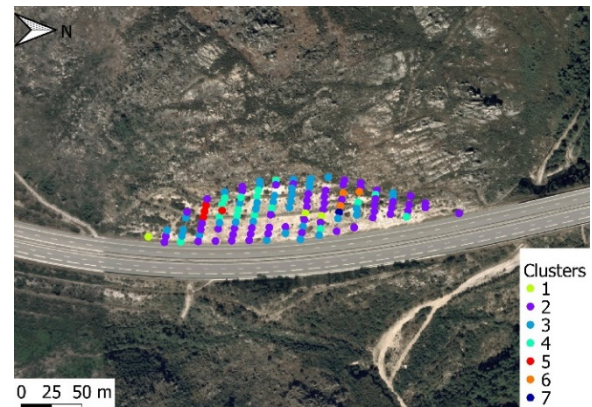


Figure 6. Cluster spatial distribution.

Displacement time series representative of each cluster behavior were determined for each group and they are presented in Figure 7. During the first three months of 2019, average displacements varied between 20 mm away from the sensor and 15 mm towards it.

The centroids for velocity and slope were computed for each cluster and are presented in Figures 8 and 9, respectively. Although the clusters were built based on the displacement time series between January and March 2019, in order to increase the chances of isolating the area affected by the landslide in a single cluster, the velocity values in the chart correspond to the complete time interval of the analysis (February 2018 – March 2019) to capture possible early signs of instability.

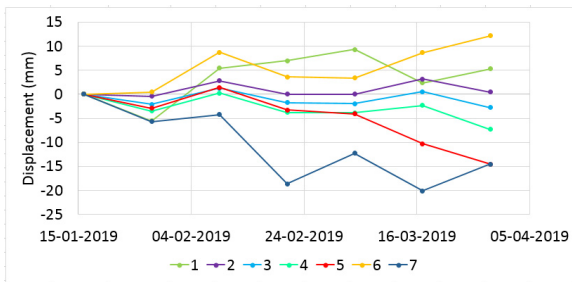


Figure 7. Displacement time series representative of cluster behavior.

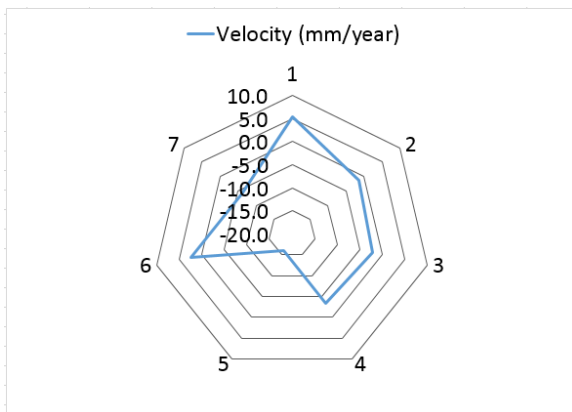


Figure 8. Centroids for velocity between February 2018 and March 2019.

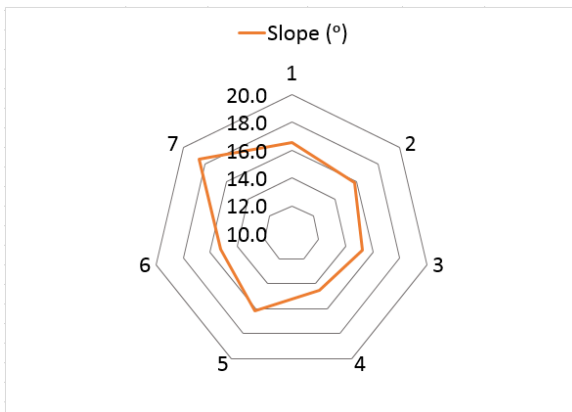


Figure 9. Centroids for slope.

From Figure 8, it was verified that cluster 5 presented the largest average velocity away from the sensor (more than 15 mm/year) and was followed by cluster 7, with average velocity around 5 mm/year. On the other hand, clusters 1 and 6 moved towards the sensor during the 14 months of the analysis. Clusters 2, 3 and 4 had average velocities close to 0 mm/year. Slope centroids in Figure 9 show that cluster 7 was the one located on the steepest slope region, followed by clusters 1 and 5. The three clusters all had average slope above 16°. Clusters 2, 3, 4 and 6 had slightly lower slopes, but still large enough for these areas to be susceptible to landslide occurrence.

## V. DISCUSSION

The results presented in the previous section were analyzed in order to achieve the answers required for

the blind test. The velocity map showed several points with velocities above 10 mm/year between February 2018 and March 2019, either away from the sensor or towards it. On one hand, movement away from the sensor might correspond to settlement and could be a sign of slope instability. There were a few points with movement away from the sensor at the southernmost part of the slope forming a spatially cohesive group, which suggested the landslide might have occurred on that area. However, there were points on other areas of the slope with similar behavior. On the other hand, some points presented movement towards the sensor, which might also correspond to slope instability, as they were compatible to horizontal movement towards the motorway. Therefore, the analysis of the displacement time series was required to identify univocally the affected area.

Seven distinct behavior patterns were identified on the slope through the clustering of the displacement time series. Clusters 2, 3 and 4 presented similar behavior, with the displacement time series showing identical trends. Together, the three clusters contained 90.6% of the points on the slope. The representative displacement time series presented oscillations around 0 mm, suggesting the three clusters mostly had a stable behavior from January to March 2019 and their movement could be considered as the expected behavior of the slope. The remaining clusters (1, 5, 6 and 7) presented behavior distinct from the expected one, which might correspond to signs of instability (Figure 10). The analysis of velocity centroids from Figure 8 for clusters 1, 5, 6 and 7 revealed that cluster 5 was the one with the largest velocity between February 2018 and March 2019 (above 15 mm/year away from the sensor), *i.e.*, the points in this cluster were already moving for several months before the landslide in March 2019. The slope centroids from Figure 9 showed all clusters were subjected to similar slope conditions; however, cluster 5 was located on one of the steepest areas of the slope, which might have contributed to increase the landslide susceptibility in the area. The aforementioned analysis suggested that the points forming cluster 5 were the most likely to be located on the area affected by the landslide.

Analyzing the displacement time series representative of the behavior of cluster 5 (Figure 7), it was observed that it was very similar to that of cluster 4, following the expected behavior of the slope, until the 5<sup>th</sup> observation epoch (5<sup>th</sup> of March 2019). After this date, the points in cluster 5 began to move away from the sensor with a displacement rate of 159 mm/year. This behavior was in accordance with the hypothesis that cluster 5 might be the one corresponding to the affected area. Furthermore, the representative displacement time series suggested that the landslide might have occurred between the 5<sup>th</sup> and the 6<sup>th</sup> observation epochs (5<sup>th</sup> of March and 17<sup>th</sup> of March, respectively), when the change in the cluster behavior was verified. Indeed, after the performed

analysis, the structural safety experts revealed the landslide occurred at the southernmost area of the slope (the location of cluster 5) on the 5<sup>th</sup> of March.

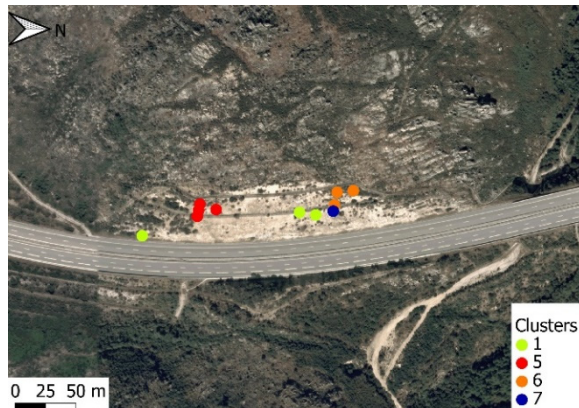


Figure 10. Spatial distribution of clusters potentially corresponding to slope instability areas.

Besides the correct identification of the landslide area, the performed analysis identified other areas of the slope presenting displacements deviating from the expected behavior (clusters 1, 6 and 7). These areas should keep being monitored through InSAR or in situ techniques, to detect eventual signs of instability in the future.

## VI. CONCLUSIONS

This study intended to contribute to the uptake of InSAR technology by structural safety experts. The blind test was performed with the goal of verifying the capability of InSAR displacements to provide information about the slope behavior in the months before the landslide and the identifications of the affected area and of the approximate date of the event.

InSAR technology allowed a large spatial coverage of the slope, with a small number of gaps without observations. The usage of archived images enabled the analysis of the slope behavior in the year before the landslide occurrence. InSAR data alone enabled the identification of a few areas on the slope showing signs of potential instability. However, only the post-processing analysis of the displacement time series enabled the correct identification of the wanted answers. This strategy allowed the reduction of the data dimensionality into a small number of clusters, facilitating the detection of patterns in the points in both space and time. This led to the identification of deviations from the structure expected behavior, which can be used as early warning signs and trigger other monitoring activities, for example through in situ techniques.

In conclusion, InSAR data is capable of providing valuable knowledge on structural safety, especially when complemented with post-processing strategies.

## VII. ACKNOWLEDGEMENTS

The authors would like to thank the Astropreneurs – Space Start-up Accelerator Programme for funding this study. Sentinel-1 data were provided by the European Space Agency. The orthophotographs were provided by the Portuguese Directorate-General for the Territory through the National Geographic Information System.

## References

- Berndt, D., and J. Clifford, (1994). Using dynamic time warping to find patterns in time series. In: *Workshop on Knowledge Discovery in Databases*, Seattle, Washington, July, pp. 359-370.
- Crosetto, M., O. Monserrat, M. Cuevas-González, N. Devanthery, and B. Crippa, (2016). Persistent Scatterer Interferometry: A review. *ISPRS Journal of Photogrammetry and Remote Sensing*, Vol 115, pp. 78-89.
- Di Martire, D., R. Iglesias, D. Monells, G. Centolanza, S.Sica, M. Ramondini, L. Pagano, J.J. Mallorquí, and D. Calcaterra, (2014). Comparison between differential SAR interferometry and ground measurements data in the displacement monitoring of the earth-dam of Conza della Campania (Italy). *Remote Sensing of Environment*, Vol 148, pp. 58-69.
- Emadali, L., M. Motagh, and M.H. Haghighi, (2017). Characterizing post-construction settlement of the Masjed-Soleyman embankment dam, Southwest Iran, using terraSAR-X SpotLight radar imagery. *Engineering Structures*, Vol 143, pp. 261-273.
- Giardina, G., P. Milillo, M.J. DeJong, D. Perissin, and G. Milillo, (2019). Evaluation of InSAR monitoring data for post-tunneling settlement damage assessment. *Structural Control and Health Monitoring*, Vol 26, No. 2, p. e2285.
- Lazecky, M., I. Hlavacova, M. Bakon, J.J. Sousa, D. Perissin, and G. Patrício, (2017). Bridge displacements monitoring using space-borne X-band SAR interferometry. *IEEE Journal of Selected Topics in Applied Earth Observations and Remote Sensing*, Vol 10, No. 1, pp. 205-210.
- Milillo, P., G. Giardina, D. Perissin, G. Milillo, A. Coletta, and C. Terranova, (2019). Pre-collapse space geodetic observations of critical infrastructure: The Morandi Bridge, Genoa, Italy. *Remote Sensing*, Vol 11, No. 12, p. 1403.
- Notti, D., F. Calò, F. Cigna, M. Manunta, G. Herrera, M. Berti, C. Meisina, D. Tapete, and F. Zucca, (2015). A user-oriented methodology for DInSAR time series analysis and interpretation: Landslides and subsidence case studies. *Pure and Applied Geophysics*, Vol 172, No. 11, pp. 3081-3105.
- R Core Team, (2021). R: A language and environment for statistical computing. R Foundation for Statistical Computing, Vienna, Austria. URL: <https://www.R-project.org/>
- Roque, D., (2020). Displacement measurement through InSAR geodesy for structural health monitoring. PhD thesis, Instituto Superior Técnico da Universidade de Lisboa, Lisboa, Portugal.
- Roque, D., D. Perissin, A.P. Falcão, C. Amado, J.V. Lemos, and A.M. Fonseca, (2018). Analysis of InSAR displacements for the slopes around Odelouca reservoir. *Procedia Computer Science*, Vol 138, pp. 338-345.

## Including virtual target points from laser scanning into the point-wise rigorous deformation analysis at geo-monitoring applications

Lukas Raffl, Christoph Holst

Chair of Engineering Geodesy, TUM School of Engineering and Design, Technical University of Munich, 80333 München, Germany, ([lukas.raffl@tum.de](mailto:lukas.raffl@tum.de); [christoph.holst@tum.de](mailto:christoph.holst@tum.de))

**Key words:** *point clouds; deformation vectors; virtual targets; congruence model; scanning total station*

### ABSTRACT

We present a method to include virtual target points from laser scanning into the point-based rigorous deformation analysis to derive precise 3D deformation vectors. This method overcomes the challenge of missing point identities in laser scans and is developed especially for geo-monitoring applications that demand an early identification of deformations at previously unknown positions. Our approach is based on virtual targets represented by local scan patches. Each patch is matched between overlapping stations and across different measurement epochs using the Iterative Closest Point Algorithm (ICP). Thus, similar to feature points, a number of homologous points is created and polar pseudo-observations are derived. This allows to integrate the observations into a free network adjustment and into a rigorous deformation analysis. We apply this method to the geo-monitoring of rock surfaces on Mt. Hochvogel where we use a scanning total station combining point-wise measurements to signalized targets and pseudo-observations derived from area-wise laser scans. In our application, numerous virtual target points could be created throughout the deformation object. The results show that the new method improves the accuracy and reliability of the subsequent rigorous deformation analysis and it, thus, allows for an early identification of deformations at geo-monitoring applications. Still there is some improvement in the selection of suitable patches needed, as the matching accuracy of the ICP strongly depends on the point distribution within the patches.

### I. INTRODUCTION

Geo-monitoring is one aspect of risk prevention in the alpine regions. Nowadays, terrestrial laser scanners are frequently used not only to monitor deformations of infrastructural buildings (Mukupu *et al.*, 2016), but also deformations in the context of those geo-applications, such as landslides (Kromer *et al.*, 2017; Pfeiffer *et al.*, 2018), rockfalls (Kenner *et al.*, 2022; Abellán *et al.*, 2011), solifluctional processes (Holst *et al.*, 2021) or other mass movements (*e.g.*, Anders *et al.*, 2021). The broad use of laser scanner point clouds for those applications can be reasoned by the fact that point clouds provide a nearly continuous digitalization of the reality that allows for detecting geometric changes with high spatial resolution.

However, for a reliable quantification of potentially existing deformations, a rigorous deformation analysis is needed that also relies on a straightforward and comprehensive error propagation. The implementation of such a rigorous strategy is currently focused in many publications using different methods (*e.g.*, Winiwarter *et al.*, 2021; Wunderlich *et al.*, 2020). Within this topic, our study will show first results of a new method that combines point-wise measurements of a total station with laser scans in a rigorous deformation analysis. Precisely, we will:

- Extend point-wise measurements by small-scale laser scans;

- Extract virtual target points from those point clouds and integrate them into the network adjustment and subsequent deformation analysis;
- Apply the method to a rockfall at Mt. Hochvogel and;
- Identify the limits of our method and propose possible solutions for those limits.

In this context, Section II recapitulates the state of the art related to our strategy, Section III introduces our strategy that is applied to a landslide at Mt. Hochvogel in Section IV. Section V discusses the results and Section VI provides a conclusion and outlook.

### II. BASICS OF RELATED STRATEGIES FOR DEFORMATION ANALYSIS

The aim of geodetic monitoring is to determine geometrical deformations in shape or position of an object between two measurement epochs (Heunecke *et al.*, 2013). Besides the quantification of geometric changes also the identification of its statistical significance based on the measurement uncertainties is a major part of the deformation analysis in engineering geodesy (Kuhlmann *et al.*, 2014). Depending on the desired aim of the deformation analysis, different deformation models might be chosen that differ in the fact whether they integrate the acting force and whether they explicitly model the time as variable or

not (Welsch and Heunecke, 2001). If neither acting forces are measured nor does exist a long history of epochs, the congruence model is chosen. This also holds for many geo-monitoring applications.

Since Pelzer (1971), the standard process of geodetic deformation analyses within the congruence model is based upon measuring signalized points, estimating their coordinates using a network adjustment and identifying their stability or their movement using a significance test. While this strategy is timelessly suited to provide reliable results for those individual signalized points, it currently fails when trying to integrate laser scans due to two reasons (Holst and Kuhlmann, 2016):

- a) Firstly, individual points within laser scans cannot be estimated based upon a network adjustment straightforward due to missing point identities.
- b) Secondly, the stochastic model of laser scans is more complex than the one of point-wise measurements as, *e.g.*, of total stations. Thus, a comprehensive assessment of all relevant errors is a broad research topic for itself (Medić *et al.*, 2020; Wujanz *et al.*, 2017).

Consequently, for point-cloud-based monitoring, different strategies evolved (Lindenbergh and Pietrzyk, 2015; Neuner *et al.*, 2016). Herein, point clouds are compared, *e.g.*, based on the M3C2 algorithm (Lague *et al.*, 2013; Winiwarter *et al.*, 2021), best-fitting surfaces from triangulation (Akca, 2007; Ge, 2016) or free-form parametrizations (Harmening and Neuner, 2016), or geometrical primitives (Holst *et al.*, 2012; Scaioni *et al.*, 2014). Alternatively, the point clouds are reduced to individual points that can be found again in each epoch. This makes it possible to integrate them into the standard procedure according to Pelzer (1971). One strategy to create corresponding points is to interpolate the irregular point clouds of all epochs to the same regular grid (Schäfer *et al.*, 2004). However, because of the grid interpolation displacements are only detectable in one dimension and no actual 3D deformation vectors can be derived. Individual points can also be modelled by estimating and intersecting planes (Raffl *et al.*, 2019), but this approach is limited on a specific surface geometry. More suitable for irregular rock faces is the extraction of corresponding feature points, either based on machine learning (Gojčić *et al.*, 2019) or on additional RGB images (Wagner, 2016). Furthermore, features can be extracted from the 2D representation of a digital elevation model (DEM) created from the laser scans for each epoch (Holst *et al.*, 2021).

A special case of point-cloud-based monitoring is subdividing the point cloud into patches using the iterative closest point algorithm (ICP, Besl and McKay, 1992) as is done in the ICPprox (Wujanz, 2016). This is very suitable for irregular structures and therefore for the monitoring of landslides and rockfalls (Pfeiffer *et al.*, 2018). The patches can even be seen as virtual target points (Frangez *et al.*, 2020; Raffl *et al.*, 2019).

For the present study, we implemented a combination of those approaches that reduces the point cloud to individual patches that are integrated into the point-wise deformation analysis according to Pelzer (1971). This reduction to patches either allows to compare point identities (aspect a) and it as well simplifies the determination of the measurements' stochastic model within the deformation analysis (aspect b).

### III. METHODOLOGY

We introduce an extended network-based monitoring strategy. On top of traditional network observations like tacheometric or GNSS baseline observations, scan patches are included as non-signalized target points. By raising the number of potential object points, this novel method makes it possible to (i) increase the spatial coverage also in inaccessible areas and to (ii) improve the network geometry. In this section, we describe the workflow for the integration of virtual target points from laser scanning into the rigorous deformation analysis based on ICP matching. This workflow was specially developed for scanning total stations where the resulting point clouds are already georeferenced via the stationing of the instrument, but it is also transferable to laser scanner data.

#### A. ICP Matching

Non-signalized targets are represented by small-scale laser scanning patches. Each patch defines one virtual target point and has a typical diameter of 0.3 to 0.5 m. In the zero epoch, for each patch a master point cloud is captured and the coordinates of the virtual target point  $\mathbf{P}_0$  are assigned (*e.g.*, the centroid of the patch) (Figure 1a). The same patches are then scanned in all following measurement epochs.

Under the assumption that the inner geometry of each patch is not changing over time, its rigid-body movement between two epochs can be determined by a classical cloud-to-cloud matching based on the ICP algorithm. Neglecting an eventual registration error, the ICP already gives the rigid-body movement of the patch between the epochs. However, no reliable stochastic model for the deformation vector is available. Therefore, in a first step, we use the result of the ICP matching to create point identities between the two epochs. By applying the resulting transformation  $\mathbf{T}$  on the virtual point  $\mathbf{P}_0$  of the zero epoch, it is transferred into the current epoch creating the point  $\mathbf{P}_1$  and thus a pair of corresponding points (Figure 1a).

With this strategy, point identities can not only be created across different epochs, but also between two stations, creating redundancy within one epoch (Figure 1b). The procedure is the same, however, when scanning from two different instrument stations, it must be ensured that the ICP matching gives reliable results despite different viewing angles.

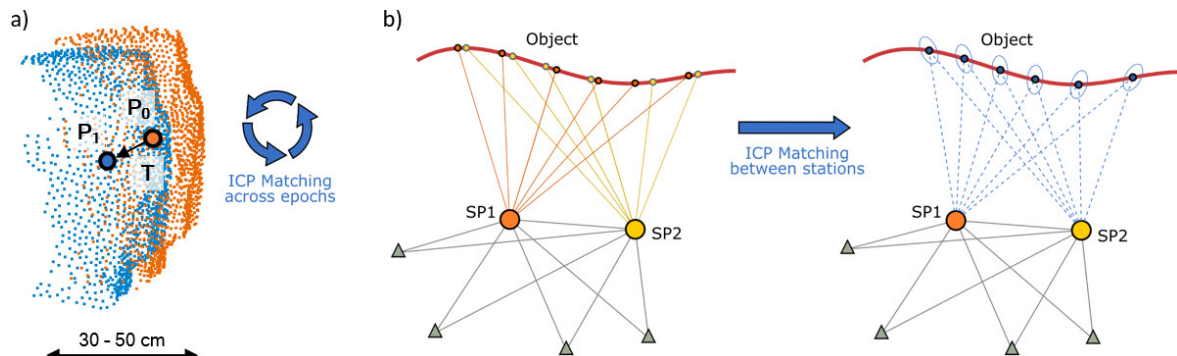


Figure 1. a) ICP matching across two epochs and updating the virtual point; b) ICP matching between two stations and integration into the geodetic network consisting of control points (triangles) and object points (circles).

### B. Network adjustment and deformation analysis

Creating point identities between different stations and across different epochs enables the integration of the virtual target points into the network adjustment and the network-based deformation analysis. For this purpose, polar single-point observations are derived. Considering the related station coordinates for each virtual point, a pseudo-observation is determined composed of horizontal angle, vertical angle and slope distance, identical to a tacheometric observation. These are now treated as conventional polar observations and combined with other network observations like actual total station measurements to signalized points or GNSS baseline observations. In general, the datum is realised by a set of stable control points observed with GNSS.

All network measurements of one epoch are then evaluated in a hybrid free network adjustment, whereby individual variance components are estimated for each of the different observation types (Heunecke *et al.*, 2013; Niemeier, 2008). If the virtual points are observed from more than one station, their variance level is automatically adapted to the actual observation quality based on the resulting redundancy within the network adjustment. Thus a comprehensive a priori error propagation can be omitted. In the following rigorous deformation analysis, the accuracy information is then used to perform a statistic significance test for all calculated deformation vectors.

In general, the additional non-signalized points help to improve the network geometry and may improve the overall variance level. Consequently, also the sensitivity towards the detection of significant deformations may become higher, and thus eventual displacements of the monitoring object might be revealed earlier.

As mentioned, the here introduced simple approach of converting the updated point coordinates into tacheometric pseudo-observations is especially useful for scanning total stations. In this case, the point clouds are levelled, which is necessary to distinguish correctly between horizontal and vertical angle within the calculation of the pseudo-observations. Furthermore, the registration of the laser scans is already solved through the stationing of the total station.

Consequently, when using a laser scanner, the point clouds need to be levelled as well in order to derive correct pseudo-observations. This can be realized either by precise levelling of the laser scanner or solving the rotation via registration points. If hybrid network measurements are carried out, pseudo-observations to registration points are also needed to connect the virtual laser scanner network to the total station and GNSS network. In all cases a rough registration of the laser scans is sufficient, as within the network adjustment the station coordinates may be corrected and thus implicitly also the registration of the point clouds is improved.

## IV. APPLICATION AT THE GEO-MONITORING ON MT. HOCHVOGEL

In this section, we present the application of our combined method at the geo-monitoring of Mt. Hochvogel. After introducing the study area, we explain the data acquisition and evaluation process and finally show the results of the combined deformation analysis and improvements we gained by the inclusion of laser scan data.

### A. Study area

Mt. Hochvogel is located in the south of Germany directly on the border to Austria. With an altitude of 2,592 m a.s.l., it is the highest summit of the surrounding mountains and therefore exposed to strong erosion. Over the last decades, an enormous cleft has formed right on the summit, splitting the entire mountain top into two parts (Figure 2).

Consequently, on the southern part, an estimated volume of up to 260,000 m<sup>3</sup> threatens to break off and fall on the Austrian side. The main fissure opens up by several millimetres per month and to date already extend over a length of about 35 m in the SW-NE direction and is gaping more than 5 m at its widest points. Besides, there are several smaller fissures showing high opening rates as well and making the modelling of the failure process more complicated (Leinauer *et al.*, 2020).

In order to better understand the present failure process and to implement an early warning system,



several measurement systems were set up on the mountain including a geodetic monitoring network (Raffl and Wunderlich, 2020).



Figure 2. The summit of Mt. Hochvogel (2,592 m a.s.l.), located on the German-Austrian border, with its enormous cleft. The southern part (left part in the image) is moving several mm per month and threatens to break off completely.

### B. Geodetic network and observations

The deformation monitoring carried out on the summit of Mt. Hochvogel is based on conventional geodetic network observations. The network-based monitoring combining tacheometric measurements and GNSS baseline observations allows determining precise 3D vectors within a deformation analysis based on the congruence model.

Problems occur as traditionally all network points have to be marked. Especially the moving part of the summit is only reachable by abseiling, which makes the point installation difficult and dangerous. Nonetheless, a number of object points could have been installed in the hazardous area, mainly signalized by permanently remaining reflective tapes. An overview of the marked network points in the area of the main fissure is given in Figure 3. Most points on the northern side of the cleft can be considered stable whereas all points on the southern part are moving. More control points are located at a larger distance.

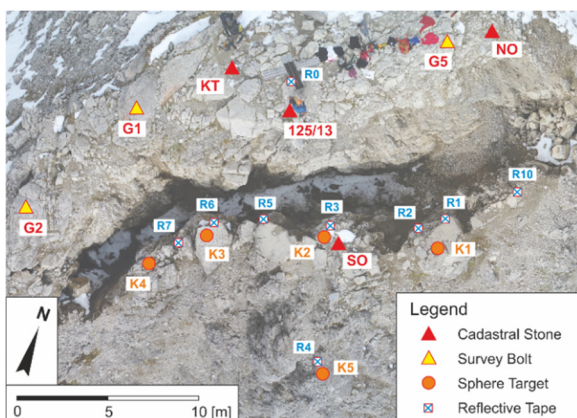


Figure 3. Overview of the marked geodetic network points in the vicinity of the main fissure.

In all measurement epochs, GNSS baseline observations and total station measurements are carried out. With this setup, the network points can be determined with an accuracy of 2-3 mm.

### C. Extension by small-scale laser scans

In order to increase the spatial resolution on the moving side, the point network is extended by non-signalized object points. For the network measurements, a Leica Nova Multistation MS60 is used, which is an Image Assisted Scanning Total Station (IASTS). Therefore, it can be also used to capture laser scans of the moving southern part of the main fissure. There are two thinkable strategies of capturing a number of patches on the object:

- Scanning the whole object and clipping suitable patches in the post-processing, or;
- Already preselecting possible structures in the field and only scanning those selected patches (especially suitable for scanning total stations).

We decided to follow option a) and scanned the entire rock face from two stations: station 1 on G1 and station 2 on NO. The average scan resolution in both scans is about 1 cm on the object, whereby the two point clouds are not overlapping completely. In the scans of the zero epoch a total of 23 patches were manually selected (Figure 4). Hereby, structures like single blocks were chosen where no inner deformation is expected. The patches have a diameter of 0.3 to 0.5 m. However, the measurement configuration is not optimal as the viewing angle from the two stations on the object varies about 90°. This is desirable for the network geometry, but depending on the structures geometry the ICP matching between the stations is more likely to fail because of lower overlapping. Consequently, some of the virtual targets are observed only from one station (blue patches: station 1, yellow patches: station 2) and some from both stations (green patches).

After matching the patches between the two stations and across all epochs, the pseudo-observations are added to the belonging networks. Thus, the number of object points in the hardly accessible area could be raised significantly and the spatial resolution has increased.

### D. Results

The first complete measurement epoch was carried out in September 2018 and the second followed in July 2019. Besides the marked points, the 23 patches depicted in Figure 4 were observed. The deformation analysis between those two epochs reveals almost no vertical movements but a significant opening of the cleft in horizontal direction. Figure 5 shows the deformation vectors in the horizontal plane. The blue lines represent the measurement network that underlies the deformation analysis. The black arrows

visualize the deformations of marked points, whereas the green arrows depict the movements of the non-signalized virtual target points. In the time between the two epochs, the horizontal movement of the object points on the southern part of the summit was about 21 mm.

The accuracy of the horizontal deformation vectors is represented by the red error ellipses and lays between 1-3 mm. Consequently, all shown deformation vectors are significant based on a significance level of 95 %. Regarding the orientation of the error ellipses it can be seen that the in-line-of-sight accuracy of the virtual targets is higher than that of the signalized points. This can be explained by a good ICP matching accuracy in line of sight and the fact that distance measurement noise is reduced due to the large number of points that is used within the matching. However, the angular accuracy of both observation types is quite similar, because of the lower in-plane matching accuracy of the ICP. In overall, the accuracy of the non-signalized points is slightly better than the accuracy of the signalized points. Furthermore, the non-signalized points give the same deformation results in direction and magnitude as the marked points. That can be seen as a first proof for the validity and precision of the approach for geo-monitoring applications.

#### V. DISCUSSION

The results at Mt. Hochvogel are a first proof of our concept. However, the movement on Mt. Hochvogel mostly occurs in direction of the surface normal. In this case, also the M3C2 algorithm would give good results (Holst *et al.*, 2017). Nonetheless, we showed that the extension by small-scale laser scans works for the monitoring on Mt. Hochvogel. The number of object points in the inaccessible part of the summit could have been raised, which allows getting a more detailed picture of the deformation process. For almost every single rock, a precise 3D deformation vector can be determined.

The strength of the method is that point identities are created, also between two or more stations of the same epoch. In comparison to feature-based approaches (Gojic *et al.*, 2021), the ICP matching does not search

for corresponding object points in the existing sets of points, but creates new ones. Thus, the matching resolution is not restricted by the scanning resolution.

Moreover, based on the redundant observation of the virtual points within one epoch a realistic accuracy is estimated within the free network adjustment. Thus, also the significance tests within the subsequent deformation analysis give trustful results.

In comparison to the M3C2 algorithm, our approach also allows the detection of in-plane displacements. One requirement for that, however, is the use of suitable patches. The geometry of the structures has a major impact on the matching quality. It has to be unambiguous in the context of ICP matching. The geometry of a plane structure for example contains not enough information for a cloud-to-cloud match as the solution is ambiguous in the in-plane directions. This inevitably leads to incorrect point identities. It is therefore crucial to check the geometry of each selected structure beforehand. Besides others, two possible solutions could be:

- Analysing the histogram of the normal vectors. If all normal vectors of a patch tend to point in the same direction or lay on a plane, the structure is not suitable for a reproducible matching. The more the normal directions vary the better the matching accuracy.
- Estimating the matching accuracy of the ICP by simulating various displacements. This could be done within a Monte Carlo Simulation where the point cloud of the second epoch is shifted to different 3D starting positions and the accuracy of the matching outcome is analysed.

Apart from the structure's geometry, also other parameters like the scanning resolution affect the appearance of the point cloud and thus the matching accuracy (Wujan, 2019). This includes, for example, also the measurement configuration between the structure and the two stations from which it is observed. If the viewing angle from the stations on the object is similar, the matching accuracy is potentially higher than when observing the structure from very different angles.

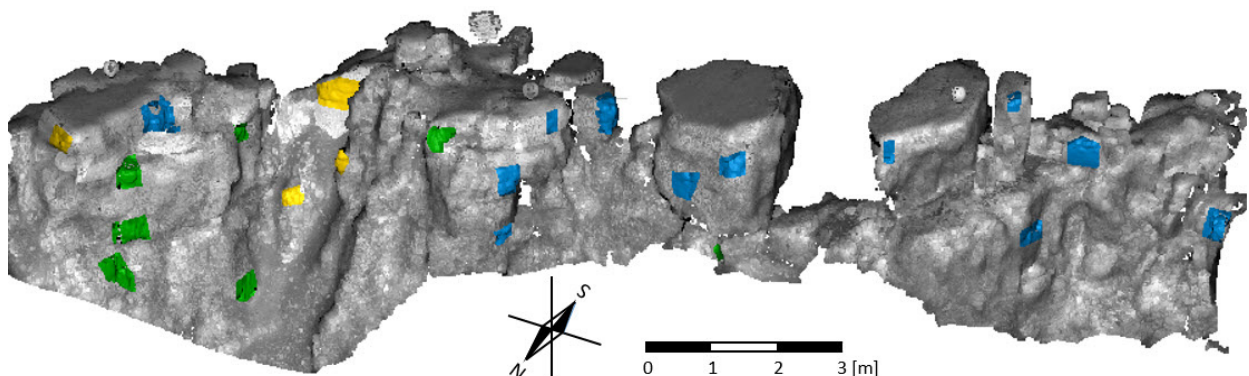


Figure 4. Point cloud of the southern, moving part of the cleft and manually selected patches (blue: station 1, yellow: station 2, green: both stations).

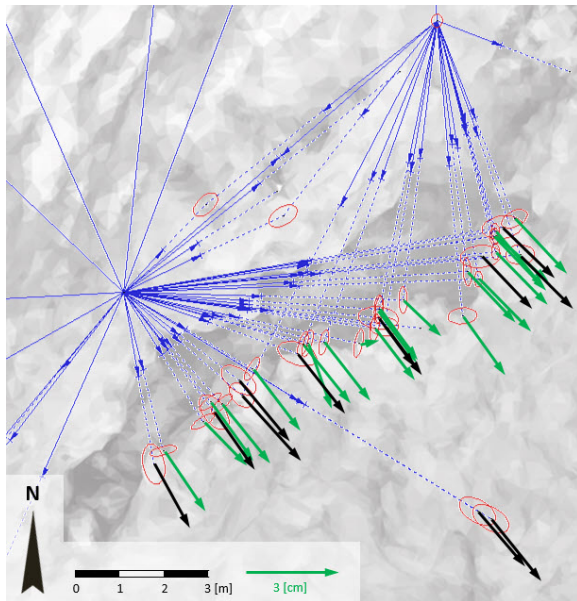


Figure 5. Resulting 2D deformation vectors of marked (black arrows) and virtual target points (green arrows) and their related error ellipses (red).

Those additional effects cannot be considered by analysing the normal histogram (solution a) of one point cloud. On the other hand, the Monte Carlo Simulation (option b) already takes the point cloud pair into account and directly analyses the outcome of the ICP matching. However, this will be investigated in future research.

Either way, the requirements on the structures limit the number of suitable patches. Nonetheless, on Mt. Hochvogel, a sufficient number of scan patches could be identified by a careful manual selection.

## VI. CONCLUSION AND OUTLOOK

In this paper, we introduced and applied a new monitoring strategy extending the conventional network measurements by small-scale laser scans. This allows to increase the number of object points and thus the spatial resolution of the monitoring. By creating virtual target points based on ICP matching, we (i) solved the problem of missing point identities and (ii) estimated a suitable stochastic model by integrating them into the free network adjustment. As a result, we are able to perform a rigorous deformation analysis including a statistical significance test.

We applied our proposed method at the geomonitoring of Mt. Hochvogel and were able to significantly increase the number of object points, especially in the inaccessible hazardous area. Moreover, the network geometry was improved and thus the accuracy of the network adjustment. Consequently, also the accuracy of the deformation vectors is higher and small deformations can be detected earlier. The deformation vectors resulting from virtual targets show the same movement as the vectors from marked network points.

However, there are some limitations. The number of useful structures and thus the spatial distribution of monitoring points, of course strongly depends on the object's surface. On very flat rock faces the identification of suitable patches might not be possible. Especially in these cases, an evaluation process that analyses the selected patches beforehand would help to ensure sufficient accuracy in the ICP matching. This will be investigated in future research also towards a fully automatic selection of patches in the point cloud.

## VII. ACKNOWLEDGEMENTS

This research is done within the research project "AlpSenseRely" financed by the Bavarian State Ministry of the Environment and Consumer Protection.

## References

- Abellán, A., J.M. Vilaplana, J. Calvet, D. García-Sellés, and E. Asensio (2011). Rockfall monitoring by Terrestrial Laser Scanning – case study of the basaltic rock face at Castellfollit de la Roca (Catalonia, Spain). *Natural Hazards and Earth System Sciences*, Vol. 11, No. 3, pp. 829-841.
- Akca, D. (2007). 3D Modelling, Texturing and Applications in Cultural Heritage. In: *Lecture notes for ISPRS WG VI/5 & summer school «Theory and Application of Laser Scanning»*, Ljubljana, Slovenia.
- Anders, K., L. Winiwarter, H. Mara, R. Lindenbergh, S.E. Vos, and B. Höfle (2021). Fully automatic spatiotemporal segmentation of 3D LiDAR time series for the extraction of natural surface changes. *ISPRS Journal of Photogrammetry and Remote Sensing*, Vol. 173, No. 3, pp. 297-308.
- Besl, P.J., and N.D. McKay (1992). Method for registration of 3-D shapes. *Sensor Fusion IV: Control Paradigms and Data Structures. International Society for Optics and Photonics*, Vol. 1611, pp. 586-607.
- Frangé, V., E. Serantoni, and A. Wieser (2020). Geodetic Monitoring of Digitally Fabricated Structures Early After Construction. In: *Proc. of the FIG Working Week 2020*, Amsterdam, May 10-14, 10556.
- Ge, X. (2016). *Terrestrial Laser Scanning Technology from Calibration to Registration with Respect to Deformation Monitoring*. Dissertation. Technical University of Munich.
- Gojčić, Z., L. Schmid, and A. Wieser (2021). Dense 3D displacement vector fields for point cloud-based landslide monitoring. *Landslides*, Vol. 18, No. 12, pp. 3821-3832.
- Gojčić, Z., C. Zhou, and A. Wieser (2019). Robust Pointwise Correspondences for Point Cloud based Deformation Monitoring of Natural Scenes. In: *Proc. of the 4th Joint International Symposium*, Athens, Greece, 15-17 May 2019.
- Harmening, C., and H. Neuner (2016). Detecting Rigid Body Movements from TLS-based Areal Deformation Measurements. *Proc. of the 78th FIG Working Week 2016*.
- Heunecke, O., H. Kuhlmann, W. Welsch, A. Eichhorn, and H. Neuner (2013). *Auswertung geodätischer Überwachungsmessungen*, 2<sup>nd</sup> ed. Berlin, Offenbach: Wichmann.
- Holst, C., J. Janßen, B. Schmitz, M. Blome, M. Dercks, A. Schoch-Baumann, J. Blöthe, L. Schrott, H. Kuhlmann, and T. Medic (2021). Increasing Spatio-Temporal Resolution for Monitoring Alpine Solifluction Using Terrestrial Laser

- Scanners and 3D Vector Fields. *Remote Sensing*, Vol. 13, No. 6, 1192.
- Holst, C., and H. Kuhlmann (2016). Challenges and Present Fields of Action at Laser Scanner Based Deformation Analyses. *Journal of Applied Geodesy*, Vol. 10, No. 1, pp. 17-25.
- Holst, C., B. Schmitz, and H. Kuhlmann (2017). Investigating the applicability of standard software packages for laser scanner based deformation analyses. In: *Proc. of the FIG Working Week*, Helsinki, Finland, 29 May–2 June.
- Holst, C., P. Zeimet, A. Nothnagel, W. Schauerte, and H. Kuhlmann (2012). Estimation of Focal Length Variations of a 100-m Radio Telescope's Main Reflector by Laser Scanner Measurements. *Journal of Surveying Engineering*, Vol. 138, No. 3, pp. 126-135.
- Kenner, R., V. Gischig, Z. Gojic, Y. Quéau, C. Kienholz, D. Figi, R. Thöny, and Y. Bonanomi (2022). The potential of point clouds for the analysis of rock kinematics in large slope instabilities: examples from the Swiss Alps: Brinzauls, Pizzo Cengalo and Spitze Stei. *Landslides*, Vol. 39, No. 4, p. 80.
- Kromer, R.A., A. Abellán, D.J. Hutchinson, M. Lato, M.-A. Chanut, L. Dubois, and M. Jaboyedoff (2017). Automated terrestrial laser scanning with near-real-time change detection – monitoring of the Séchilienne landslide. *Earth Surface Dynamics*, Vol. 5, No. 2, pp. 293-310.
- Kuhlmann, H., V. Schwieger, A. Wieser, and W. Niemeier (2014). Engineering Geodesy - Definition and Core Competencies. *Journal of Applied Geodesy*, Vol. 8, No. 4, pp. 327-334.
- Lague, D., N. Brodu, and J. Leroux (2013). Accurate 3D comparison of complex topography with terrestrial laser scanner: Application to the Rangitikei canyon (N-Z). *ISPRS Journal of Photogrammetry and Remote Sensing*, Vol. 82, No. 2, pp. 10-26.
- Leinauer, J., B. Jacobs, and M. Krautblatter (2020). Anticipating an imminent large rock slope failure at the Hochvogel (Allgäu Alps). *Geomechanics and Tunneling*, Vol. 13, No. 6, pp. 597-603.
- Lindenbergh, R., and P. Pietrzyk (2015). Change detection and deformation analysis using static and mobile laser scanning. *Applied Geomatics*, Vol. 7, No. 2, pp. 65-74.
- Medić, T., H. Kuhlmann, and C. Holst (2020). Designing and Evaluating a User-Oriented Calibration Field for the Target-Based Self-Calibration of Panoramic Terrestrial Laser Scanners. *Remote Sensing*, Vol. 12, No. 1, 15.
- Mukupia, W., G.W. Roberts, C.M. Hancock, and K. Al-Manasir (2016). A review of the use of terrestrial laser scanning application for change detection and deformation monitoring of structures. *Survey Review*, Vol. 36, No. 5, pp. 1-18.
- Neuner, H., C. Holst, and H. Kuhlmann (2016). Overview on Current Modelling Strategies of Point Clouds for Deformation Analysis. *allgemeine vermessungs-nachrichten (avn)*, Vol. 123, 11-12, pp. 328-339.
- Niemeier, W. (2008). *Ausgleichsrechnung: Statistische Auswertemethoden*, 2<sup>nd</sup> ed. Berlin: de Gruyter.
- Pelzer, H. (1971). Zur Analyse geodätischer Deformationsmessungen. *Deutsche Geodätische Kommission bei der Bayerischen Akademie der Wissenschaften Reihe C: Dissertationen*, No. 164.
- Pfeiffer, J., T. Zieher, M. Bremer, V. Wichmann, and M. Rutzinger (2018). Derivation of Three-Dimensional Displacement Vectors from Multi-Temporal Long-Range Terrestrial Laser Scanning at the Reissenschuh Landslide (Tyrol, Austria). *Remote Sensing*, Vol. 10, No. 11, p. 1688.
- Raffl, L., W. Wiedemann, and T. Wunderlich (2019). Non-signalized Structural Monitoring using Scanning Total Stations. In: *Proc. of the 4th Joint International Symposium*, Athens, Greece, 15-17 May.
- Raffl, L., and T. Wunderlich (2020). Challenges and Hybrid Approaches in Alpine Rockslide Prevention - An alarming Case Study. In: *Proc. of the 8th INGEO International Conference on Engineering Surveying & 4th SIG Symposium on Engineering Geodesy*, Dubrovnik, Croatia.
- Scaioni, M., L. Longoni, V. Melillo, and M. Papini (2014). Remote Sensing for Landslide Investigations: An Overview of Recent Achievements and Perspectives. *Remote Sensing*, Vol. 6, No. 10, pp. 9600-9652.
- Schäfer, T., T. Weber, P. Kyrinovic, and M. Zamecnikova (2004). Deformation Measurement Using Terrestrial Laser Scanning at the Hydropower Station of Gabčíkovo. In: *Proc. of INGEO 2004 and FIG Regional Central and Eastern European Conference on Engineering Surveying*, Bratislava, Slovakia.
- Wagner, A. (2016). A new Approach for Geo-Monitoring using Modern Total Stations and RGB+D Images. *Measurement*, Vol. 82, pp. 64-74.
- Welsch, W.M., and O. Heunecke (2001). Models and Terminology for the Analysis of Geodetic Monitoring Observations: Official Report of the Ad Hoc Committee WG 6.1. In: *Proc. of the 10th FIG International Symposium on Deformation Monitoring*, Orange, pp. 390-412.
- Winiwarter, L., K. Anders, and B. Höfle (2021). M3C2-EP: Pushing the limits of 3D topographic point cloud change detection by error propagation. *ISPRS Journal of Photogrammetry and Remote Sensing*, Vol. 178, pp. 240-258.
- Wujanz, D. (2016). *Terrestrial Laser Scanning for Geodetic Deformation Monitoring*. Dissertation. Technische Universität Berlin, Fakultät VI – Institut für Geodäsie und Geoinformationstechnik.
- Wujanz, D. (2019). Araneo: Bestimmung eines erweiterten Unsicherheitsbudgets für die Deformationsmessung basierend auf terrestrischen Laserscans. *allgemeine vermessungs-nachrichten (avn)*, Vol. 126, No. 3, pp. 53-63.
- Wujanz, D., M. Burger, M. Mettenleiter, and F. Neitzel (2017). An Intensity-based Stochastic Model for Terrestrial Laser Scanners. *ISPRS Journal of Photogrammetry and Remote Sensing*, Vol. 125, pp. 146-155.
- Wunderlich, T., L. Raffl, and W. Wiedemann (2020). Creating Identities – Two Solutions for Rigorous Deformation Analysis of Areal Observations in Engineering Geodesy. *allgemeine vermessungs-nachrichten (avn)*, Vol. 127, No. 2, pp. 61-68.

## MOMPA: InSAR monitoring in the Eastern Pyrenees

Anna Barra<sup>1</sup>, Ivan Fabregat<sup>2</sup>, Anna Echeverria<sup>3</sup>, Jordi Marturià<sup>2</sup>, Qi Gao<sup>1</sup>, Guido Luzi<sup>1</sup>,  
María Cuevas<sup>1</sup>, Pere Buxó<sup>2</sup>, Laura Traperó<sup>3</sup>, Muriel Gasc<sup>4</sup>, Pedro Espin<sup>1</sup>, Michele Crosetto<sup>1</sup>

<sup>1</sup> Centre Tecnològic de Telecomunicacions de Catalunya (CTTC/CERCA), Geomatics Division, 08860 Castelldefels, Spain, ([anna.barra@cttc.cat](mailto:anna.barra@cttc.cat), [qi.gao@cttc.cat](mailto:qi.gao@cttc.cat); [guido.luzi@cttc.cat](mailto:guido.luzi@cttc.cat); [maria.cuevas@cttc.cat](mailto:maria.cuevas@cttc.cat); [pedro.espin@cttc.cat](mailto:pedro.espin@cttc.cat); [michele.crosetto@cttc.cat](mailto:michele.crosetto@cttc.cat))

<sup>2</sup> Institut Cartogràfic i Geològic de Catalunya (ICGC), Parc de Montjuïc., 08038 Barcelona, Spain, ([Ivan.Fabregat@icgc.cat](mailto:Ivan.Fabregat@icgc.cat); [Jordi.Marturia@icgc.cat](mailto:Jordi.Marturia@icgc.cat); [Pere.Buxo@icgc.cat](mailto:Pere.Buxo@icgc.cat))

<sup>3</sup> Andorra Recerca + Innovació (AR+I), Av. Rocafort 21-23, AD600 Sant Julià de Lòria, Andorra, ([aecheverria@ari.ad](mailto:aecheverria@ari.ad); [ltrapero@ari.ad](mailto:ltrapero@ari.ad))

<sup>4</sup> Centre d'études et d'expertise sur les risques, l'environnement, la mobilité et l'aménagement (CEREMA), 31400 Toulouse, France, ([muriel.gasc@cerema.fr](mailto:muriel.gasc@cerema.fr))

**Key words:** *Interferometric SAR; landslide; monitoring*

### ABSTRACT

This paper describes the main outcomes of the European research project MOMPA (Monitoring of Ground Movements and Action Protocol). Its objective is to provide useful tools for the prevention and management of risks due to slope movements, based on the satellite monitoring InSAR (Interferometric SAR) technique. The project includes two parts: risk evaluation and the integration of InSAR in an action protocol for Civil Protections. The study area encompasses 4000 km<sup>2</sup> including a part of the eastern Pyrenees. The project exploited medium-resolution (Sentinel-1) and high-resolution (COSMO-SkyMed) satellite images to generate ground displacement maps at interregional scale and detect the Active Deformation Areas (ADA). The ADA map was used to select movements with potential risk which were further examined by a local analysis using photo interpretation and fieldwork.

### I. INTRODUCTION

The MOMPA project (Monitoring of Ground Movements and Action Protocol) is co-financed by the European Regional Development Fund (ERDF) through the Interreg V-A Spain-France-Andorra Program (POCTEFA 2014-2020). MOMPA is part of Strategic Axis 2 of POCTEFA, "Promote adaptation to climate change and risk prevention and management", with the specific objective of "Improving the capacity of anticipation and response of the actors of the territory to the specific risks management of natural catastrophes". The project consortium is composed of four partners specialized in remote sensing, risk analysis and management techniques: the Centre Tecnològic de Telecomunicacions de Catalunya (CTTC), Andorra Research + Innovation (AR+I), the Cartographic and Geological Institute of Catalonia (ICGC), and the Centre d'études et d'expertise sur les risques, l'environnement, la mobilité et l'aménagement (CEREMA). It counts as associate partners the civil protections of each territory and the company Euroconsult Andorra S.A. The main expected results of the project are the following: (i) monitoring maps of ground movements in an area included in the territories of l'Alt Urgell, Cerdanya, Capcir, Conflent and Andorra; (ii) associated risk assessment; and (iii) action protocols to support Civil Protections. The idea of the project is to have a pyramidal approach to risk management. From satellite

interferometry (InSAR) based deformation maps (regional scale), the Active Deformation Areas (ADA) are detected and classified according to the associated potential risk level. Then, the classified ADAs allows focusing over the most critical ones, where a local and detailed study is carried out. The main technical work packages (actions) are:

- Action 3 - Monitoring of ground movements: generation of annual deformation velocity maps and deformation time series using medium (Sentinel-1) and high-resolution (COSMO-SkyMed) satellite imagery. Extraction of the detected ADAs.
- Action 4 - Risk analysis associated with ground movements: risk assessment of the exposed elements based on a delimitation of the geological phenomena associated with the ADAs detected in Action 3. Two analyzes are planned: the first will be based on deformation maps and deformation time series at medium resolution, the second will be based on the data at high resolution.
- Action 5 - Action protocol involves carrying out two main activities: the analysis of the pre-alert or alert thresholds of the analyzed movements, and the methodological development of the action protocols for Civil Protection.

The aim of this work is to present some results achieved in the Action 3.

## II. DEFORMATION MONITORING

Action 3 focuses on the use of InSAR for ground movements monitoring. Its results are the main input data of Actions 4 and 5. The deformation monitoring is based on the InSAR technique, which uses a series of SAR images acquired over the same area. The technique works well on urban areas, infrastructures, rocky areas, etc., while usually obtaining few measurements (or none at all) over vegetated areas (Hanssen, 2005; Bernardino *et al.*, 2002; Barra *et al.*, 2016; Crosetto *et al.*, 2016). In Action 3 the deformation estimation has been made using the PSIG software of CTTC, using a processing tailored to the study area. For more details see Devanthéry *et al.* (2014). It is worth underlining that all the estimated deformations are in the Line of Sight (LOS) of the satellite.

The first processing has been based on medium-resolution (4 by 14 m) Sentinel-1 images in descending geometry. The entire MOMPA area of interest fits within the frame of a single image (see Figure 1). The interferograms have been generated from six bursts (sub-images) and two swaths. A total of 203 images have been processed that cover the period from July 4, 2015, to December 28, 2020. The images typically have a time gap of 6 or 12 days. However, several images of the winter periods (from December-May) have been

removed to avoid problems due to snow cover (Solari *et al.*, 2020a; 2020b; Mirmazloumi *et al.*, 2021). Using this data, a velocity map over the entire study area has been generated (Figure 2).

From the velocity map, the ADAs have been extracted using the ADAFinder tool (Barra *et al.*, 2017; Tomas *et al.*, 2019; Navarro *et al.*, 2020). An ADA is extracted as a polygon if there are at least 5 adjacent measurement points that have a velocity greater than two times the standard deviation of the velocity map ( $2\sigma = 3.5$  mm/year). The ADA map facilitate the interpretation and use of the InSAR products, helping to focus the analysis on the areas of deformation. Thanks to the ADA detection, areas of greatest interest have been selected due to their potential risk. Over these areas, locally, the deformation time series have been generated with the method of Devanthéry *et al.* (2014). Other methods are described in Ferretti *et al.* (2000; 2001).

A second processing has been based on high-resolution data (3 by 3 m) acquired by the COSMO-SkyMED satellites in Stripmap acquisition mode, with descending geometry. The frame of these images is marked in yellow in Figure 1. It covers Andorra and the northern part of Alt Urgell. For the first high-resolution results, 36 available images covering the period between July 2013 and July 2020 have been processed. A map of annual deformation velocity covering the main urban centers has been generated, see Figure 3.

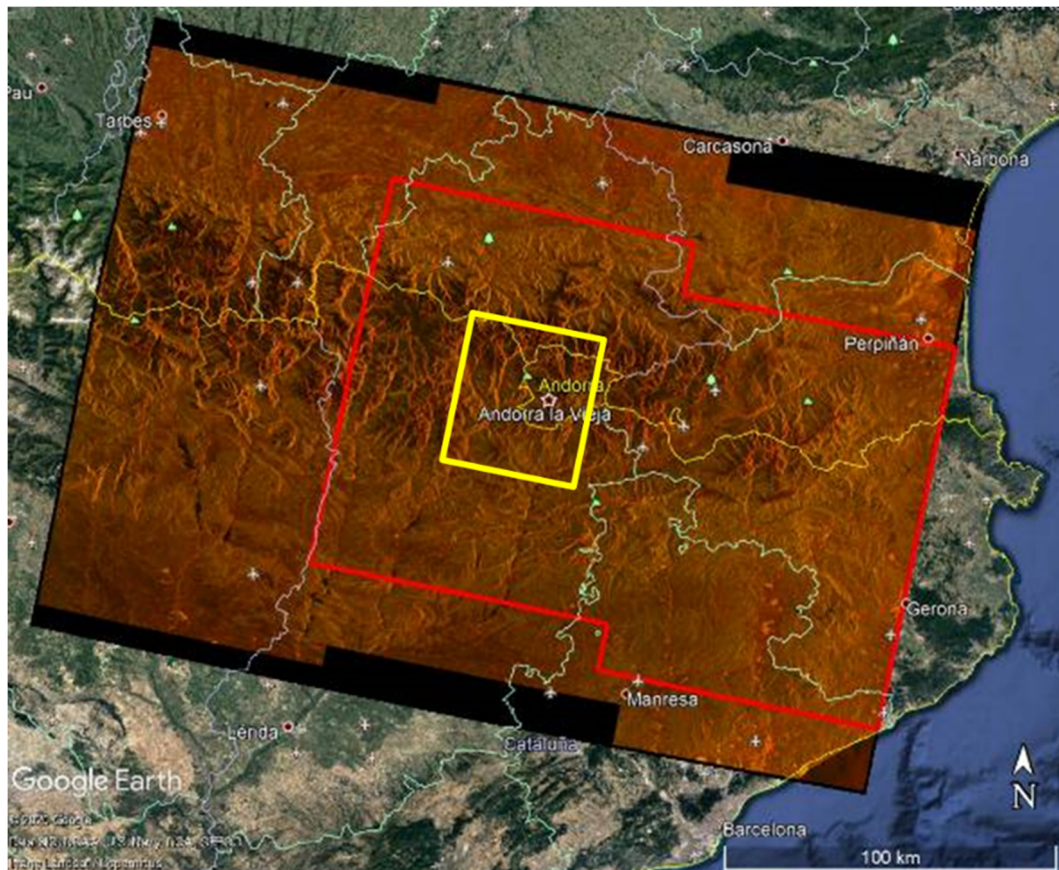


Figure 1. Extent of the Sentinel-1 images is shown in brown. The red polygon indicates the part of the processed image. The yellow polygon indicates the extent of the COSMO-SkyMed images. Google Earth is the background image.

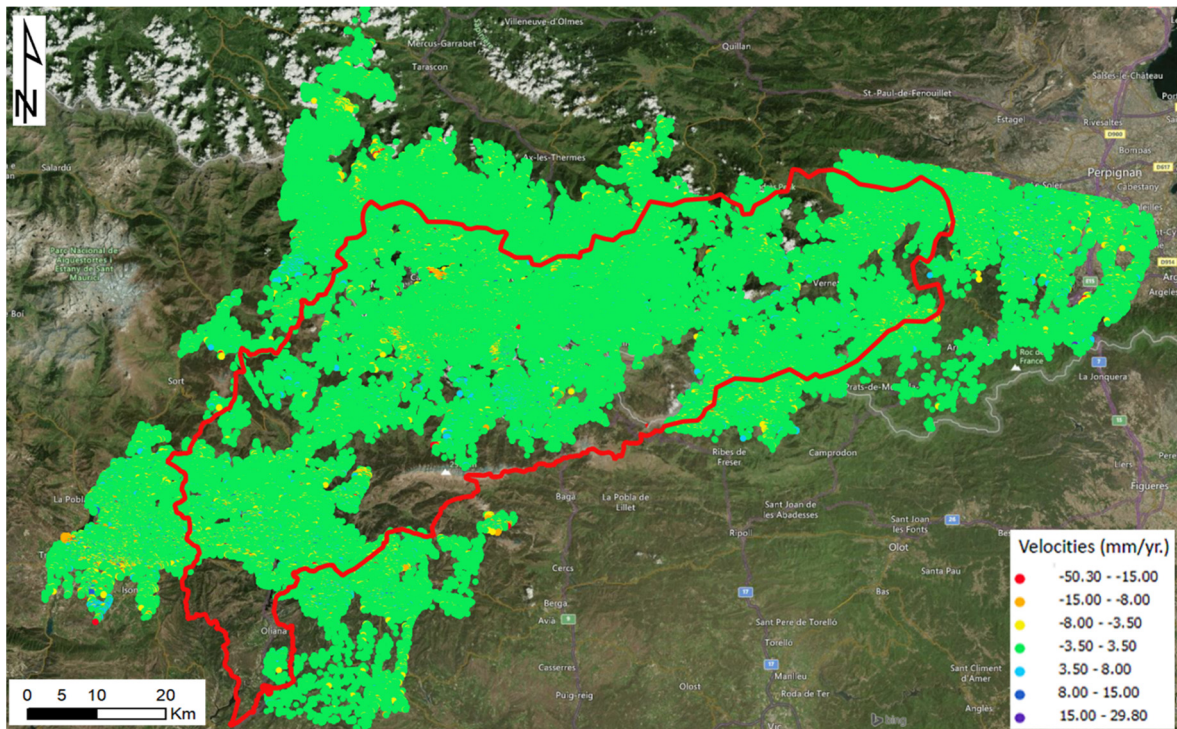


Figure 2. Map of deformation velocity (in mm/year) estimated using Sentinel-1 medium-resolution data. The map includes 2.904.322 measurement points. In red is delimited the area of study of MOMPA.

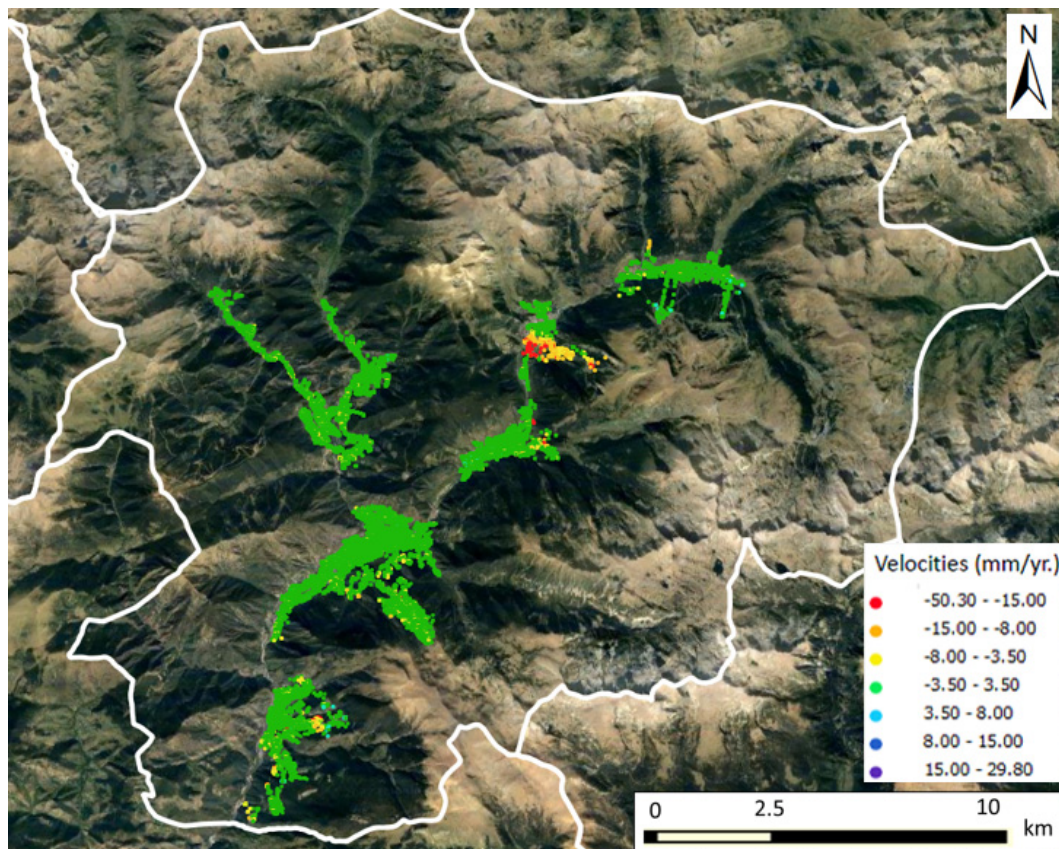


Figure 3. Map of deformation velocity (in mm/year) estimated using COSMO-SkyMed high-resolution data. The map covers the main urban areas of Andorra. White lines represent administrative limits (here the limit of Andorra).

### III. DISCUSSION OF THE RESULTS

In this project we have experienced the power of a wide-area monitoring. In fact, this monitoring based on Sentinel-1 data has detected many interesting

deformation phenomena. An example of landslide detected in a mountain area that includes a dam and a reservoir is shown in Figure 4. The upper left image of Figure 4 shows the deformation velocity map where several deformation areas were detected. The

corresponding ADAs are illustrated in the upper right image of the same Figure. Finally, the lower image of Figure 4 shows a 3D view of the area using the color-coded deformation velocity values.

As mentioned above, the project involves deformation monitoring using X-band SAR data. Compared to the medium-resolution data, the high-resolution COSMO-SkyMed data offer very detailed deformation measurement results (Wegmüller *et al.*,

2010). With them, it is possible to follow the displacements of single localized features, see the examples in Figure 5.

It is interesting to compare the deformation results from Sentinel-1 and COSMO-SkyMed. Figure 6 shows an example of a localized landslide in Andorra, measured with both medium and high-resolution data. Both datasets describe very well the extent of the slide at hand.

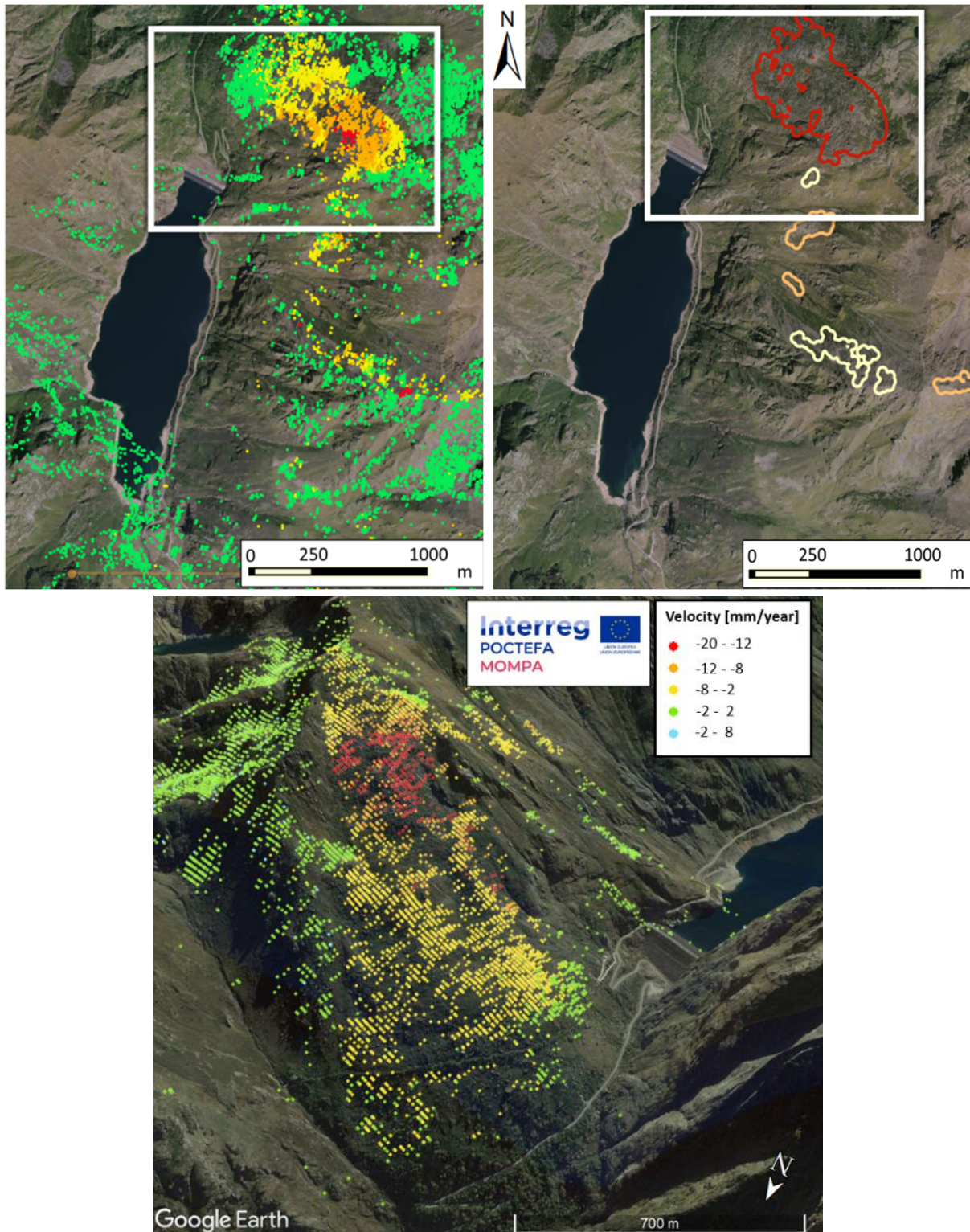


Figure 4. Example of monitoring result using the Sentinel-1 data. Deformation velocity map of an area that includes a dam (upper left). ADAs of the same area (upper right). 3D view of the area using the estimated velocities (lower image).



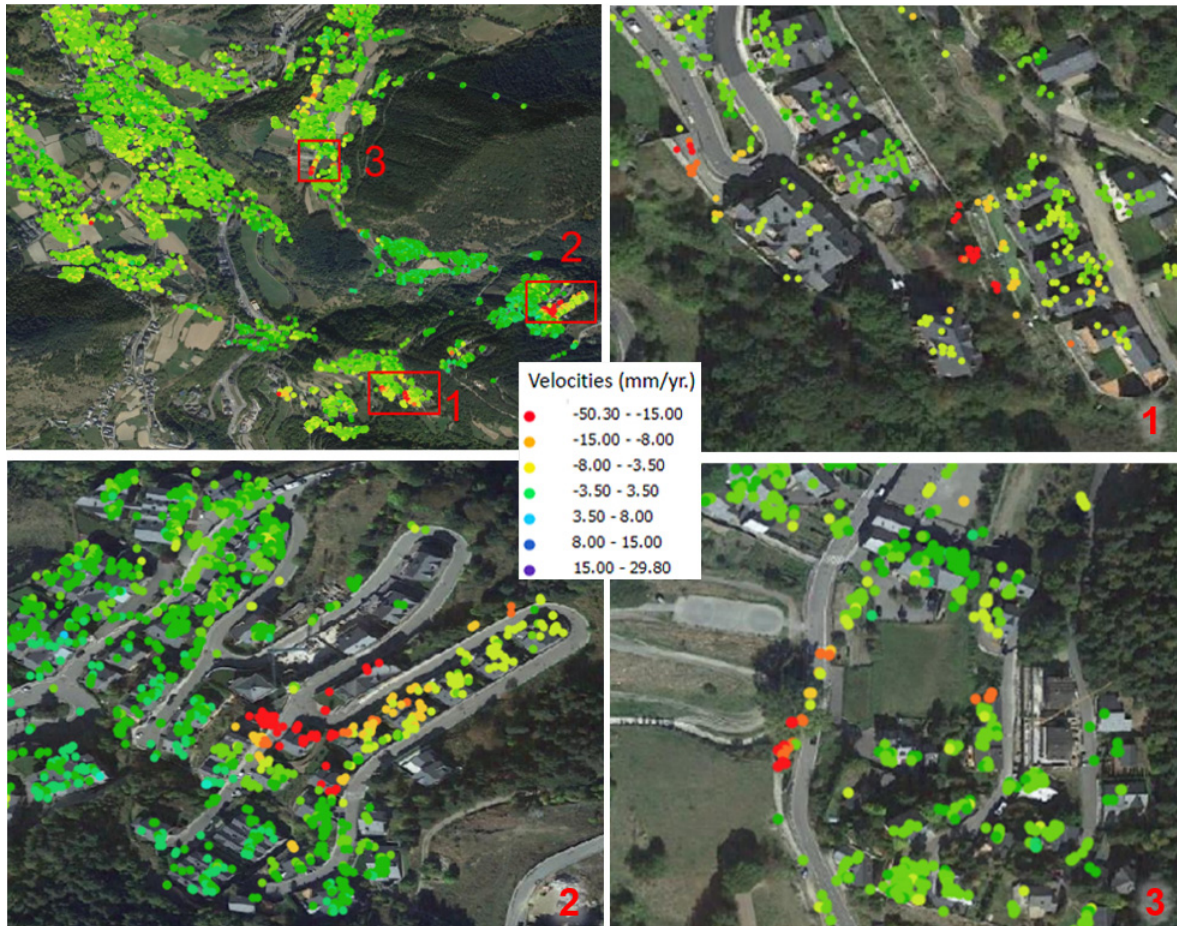


Figure 5. Example of deformation monitoring result using high-resolution COSMO-SkyMed data. Deformation velocity map of an urban area (above, left) and three zooms (area 1, upper right; area 2, lower left; area 3, lower right).

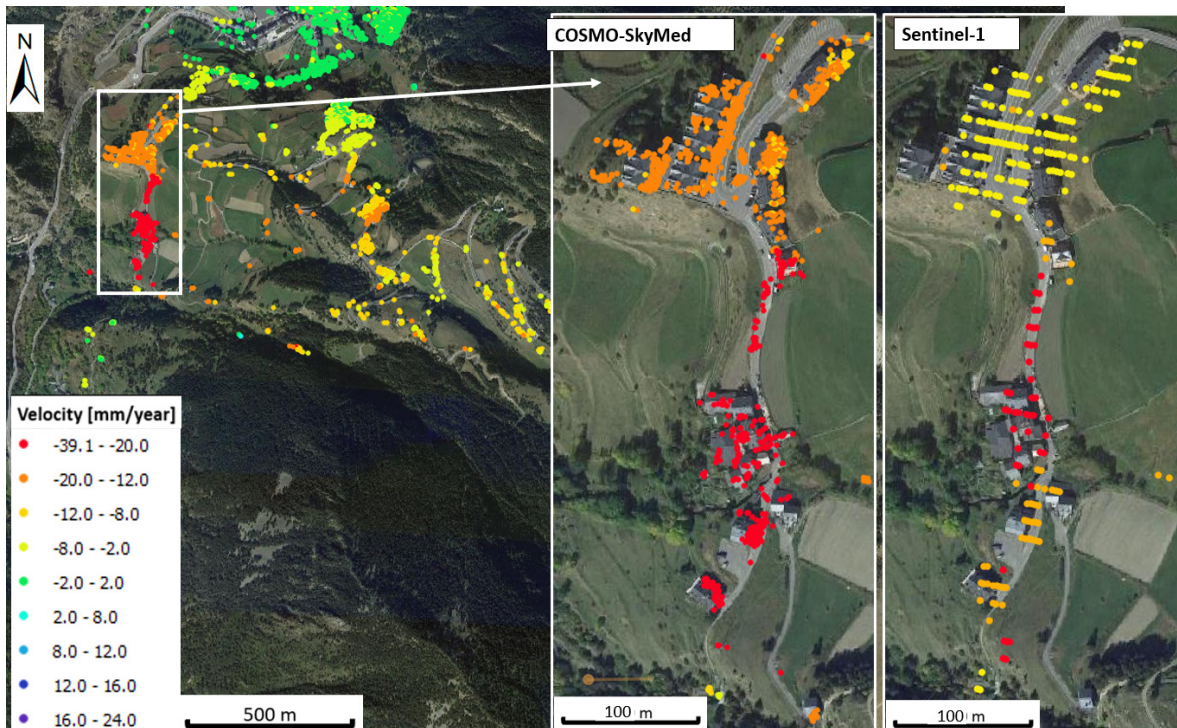


Figure 6. Comparison between Sentinel-1 and COSMO-SkyMed data over the same area, which includes a landslide. Deformation velocity map (left) and two zooms that show the measurement density of COSMO-SkyMed (centre) and Sentinel-1 (right).

Globally, Sentinel-1 offers a more complete and extensive coverage due to its greater coherence on vegetated areas. This is a clear advantage with respect to COSMO-SkyMed. On the other hand, observing the two zooms, it is evident how COSMO-SkyMed offers a very detailed sampling (approximately one point every 3 by 3 m), in correspondence with buildings, structures and infrastructures.

#### IV. ACKNOWLEDGEMENTS

This work has been co-funded by the European Regional Development Fund through the Interreg V-A Spain, France, and Andorra (POCTEFA 2014-2020), project EFA295/19.

#### References

- Barra, A., Monserrat, O., Mazzanti, P., Esposito, C., Crosetto, M., and Scarascia Mugnozza, G. (2016). First insights on the potential of Sentinel-1 for landslides detection. *Geomat Nat Haz Risk*, 7, pp. 1–10
- Barra, A., Solari, L., Béjar-Pizarro, M., Monserrat, O., Bianchini, S., Herrera, G., Crosetto, M., Sarro, R., González-Alonso, E., and Mateos, R.M. (2017). A Methodology to Detect and Update Active Deformation Areas Based on Sentinel-1 SAR Images, *Remote Sensing*, 9(10), 1002.
- Berardino, P., Fornaro, G., Lanari, R., and Sansosti, E. (2002). A new algorithm for surface deformation monitoring based on small baseline differential SAR interferograms. *IEEE TGARS*, 40(11), pp. 2375-2383.
- Crosetto, M., Monserrat, O., Cuevas-González, M., Devanthéry, N., and Crippa, B. (2016). Persistent Scatterer Interferometry: A review. *ISPRS J. Photogramm. Remote Sensing* 115, pp.: 78–89.
- Devanthéry, N., Crosetto, M., Monserrat, O., Cuevas-González, M., and Crippa, B. (2014). An approach to persistent scatterer interferometry. *Remote Sensing* 6(7), pp. 6662–6679.
- Ferretti, A., Prati, C., and Rocca, F. (2000). Nonlinear subsidence rate estimation using permanent scatterers in differential SAR interferometry. *IEEE TGARS*, 38(5), pp. 2202-2212.
- Ferretti, A., Prati, C., and Rocca, F. (2001). Permanent scatterers in SAR interferometry. *IEEE TGARS*, 39(1), pp. 8-20.
- Hanssen, R.F. (2005). Satellite radar interferometry for deformation monitoring: a priori assessment of feasibility and accuracy. *International Journal of Applied Earth Observation and Geoinformation*, 6(3-4), pp. 253-260.
- Mirmazloumi, S.M., Barra, A., Crosetto, M., Monserrat, O., and Crippa, B. (2021). Pyrenees deformation monitoring using sentinel-1 data and the persistent scatterer interferometry technique. *Procedia computer science*, 181, pp.671-677.
- Navarro, J. A., Tomás, R., Barra, A., Pagán, J. I., Reyes-Carmona, C., Solari, L., Vinielles, J. L., Falco, S., and Crosetto, M. (2020). ADAtools: Automatic Detection and Classification of Active Deformation Areas from PSI Displacement Maps. *ISPRS International Journal of Geo-Information*, 9(10), p. 584.
- Solari, L., Bianchini, S., Franceschini, R., Barra, A., Monserrat, O., Thuegaz, P., Bertolo, D., Crosetto, M., and Catani, F. (2020a). Satellite interferometric data for landslide intensity evaluation in mountainous regions. *International Journal of Applied Earth Observation and Geoinformation*, 87, 102028.
- Solari, L., Del Soldato, M., Raspini, F., Barra, A., Bianchini, S., Confuorto, P., Casagli, N., and Crosetto, M. (2020b). Review of satellite interferometry for landslide detection in Italy. *Remote Sensing*, 12, 1351.
- Tomás, R., J. Pagán, J. I., Navarro, J.A., Cano, M., Pastor, J. L., Riquelme, A., Cuevas-González, M., Crosetto, M., Barra, A., and Monserrat, O. (2019). Semi-Automatic Identification and Pre-Screening of Geological-Geotechnical Deformational Processes Using Persistent Scatterer Interferometry Datasets, *Remote Sensing*, 11(14), p. 1675.
- Wegmüller, U., Walter, D., Spreckels, V., and Werner, C.L. (2010). Nonuniform ground motion monitoring with TerraSAR-X persistent scatterer interferometry. *IEEE TGARS*, 48, pp. 895–904.

## Registering the ground deformations at the area of the archaeological site “Solnitsata”

Hristo Nikolov<sup>1</sup>, Mila Atanasova<sup>2</sup>

<sup>1</sup> Space Research and Technology Institute (SRTI) - Bulgarian Academy of Sciences, Acad. G. Bonchev bl.3, Sofia 1113, Bulgaria, ([hristo@stil.bas.bg](mailto:hristo@stil.bas.bg))

<sup>2</sup> National Institute of Geophysics, Geodesy and Geography, Bulgarian Academy of Sciences, Acad. G. Bonchev bl.3, Sofia 1113, Bulgaria, ([mila\\_at\\_zl@abv.bg](mailto:mila_at_zl@abv.bg))

**Key words:** *archaeological site; deformations; DInSAR processing; cultural heritage protection*

### ABSTRACT

In this paper we used synthetic aperture radar (SAR) data to investigate the surface displacements in the area of archaeological site Solnitsata dated VI-V millennium BC. The researched zone is situated in the neighborhood of the Provadia town, NE Bulgaria found and is considered to be one of the most ancient in Europe. Close to it the industrial Mirovo salt deposit is located. From decadal observations it was established that in the area of both sites there are ground motions due to local tectonic movements (several faults are closely located) and active exploitation of the orebody. To study the geodynamic processes in this zone for the period 2015 – 2020 the Differential Interferometry Synthetic Aperture Radar (DInSAR) method was used for their registration. The results presented are from processing SAR data from ESA’s Sentinel-1 mission and coincide with the results obtained by geodetic measurements. Definite advantage of the used technique is the possibility to deliver information for much larger areas than the one provided by geodetic measurements. Other plus of the method is the availability of results regardless of the weather conditions.

### I. INTRODUCTION

#### A. Archaeological site

The studied site, prehistorical archaeological complex Provadia-Solnitsata, is dated back to 5500 millennium BC being located about 5 km south of the modern town of Provadia NE Bulgaria covering an area about 13 ha (see Figure 1). In the ancient times it was the only center for salt production for the area of the Balkan Peninsula which makes it an important source of this mineral. According to the work of Nikolov (2016) in area of this site found are salt production area, a fortified settlement and several ritual zones that makes it unique for Europe and for this reason its preservation is essential.

#### B. Geological features of the region

From geological point of view the zone around the studied site is defined as complex, because several confirmed crustal faults are manifested. As stated by Cavazza in (Cavazza *et al.*, 2004) this zone was formed by an uplift of the eastern part of the Moesian platform during Mesozoic and Cenozoic epochs, and is being characterized by block faulting, grabens of different rank and horsts. For this research specific focus is set on the Provadia syncline which has developed as negative structure from the Paleozoic to modern era being product of the activity of several local faults. This activity made by slow movements on Lower Jurassic sediments is the reason for ongoing surface

displacements around them (Yankova and Dimovski 2015).

#### C. Mirovo salt deposit

Based on geophysical investigations the form of the underground deposit has roughly the shape of a truncated cone which upper part is 20 m below the surface reaching depths of 3.6 km. According to the monograph of Ivanov (Ivanov, 2017) the salt body is surrounded by Cretaceous limestones and dolomites and Paleogene marlstones.

The industrial exploitation of this salt deposit started in 1920, 35 years later industrial exploitation started with building dedicated processing plant. The technology used to extract the mineral is based on leaching brine by injecting high-pressured water in boreholes that form wells in a regular grid 200 x 200 m.

#### D. Seismic and geodetic investigations

After starting active brine extraction from the deposit in order to guarantee the stability of the boreholes and the other infrastructural objects in the area two local networks for monitoring the ground motions were purposely established. The geodetic network was set up in 1990 and the seismological was deployed in 1993. In the late 90-ties of last century both networks were redesigned and upgraded and since then they provide reliable information concerning earthquakes and surface deformations.

The seismological network is comprised of six permanent measurement stations. The data from them reveals that for the last 20 years no events with magnitude larger than 4.4 Mw were registered, but on the other hand the number of events having magnitude less than 3.5 Mw has increased (Dimitrova *et al.*, 2020).

In 1986 the geodetic measurements in the area started by creating a network consisting of 26 pillars and additional 200 leveling benchmarks in order to allow precise angular and distance measurements as well as leveling ones. Since then this network was maintained and upgraded constantly in order to meet the growing requirements posed by new technological developments. Up to date over this network 35 measuring cycles were carried out (see Figure 2a). After processing the acquired data each geodetic survey it was established and repeatedly confirmed that the registered surface motions are towards the projected center of the salt body with the magnitude of the registered velocities being larger than those showed by the continuously operating reference GNSS stations set up in this part of the country (Kenyeres *et al.*, 2019). Following the findings of Valev (Valev and Kastreva, 2014) for one of the leveling points it was established for the period from 1983 to 2011 that the cumulative subsidence is 0.7 m and if we presuppose a linear model for the subsidence process this value currently should be about 0.9 m.

Since the InSAR approach is relatively new for routine investigations in studying the surface motions at national level. It must be underlined that there are no many papers presenting results on the surface

deformations that are taking place in the area (*e.g.* Atanasova and Nikolov, 2016; 2017; Ponçoş *et al.*, 2022) This is the reason comparison with other papers is not possible to implement.

## II. DATA USED, PROCESSING METHOD AND RESULTS

### A. Data

The data used for this research are the SAR data from Sentinel-1 (S-1) mission launched in 2014 and operated by ESA that are made accessible at no cost under a license. Due to large swath (250 km in IW mode) of the radar instrument its data are suitable for regional investigations with moderate resolution of the ground element (in SLC format of IW mode the cell is 20 m).

It needs to be pointed out that those data are the main source for the new Copernicus Pan-European product – European Ground Motion Service (EGMS, 2021) – which is under its pilot phase to provide information concerning the ground motions at continental level. In order to increase the reliability of the produced results SAR data from both types of orbits of the satellite – ascending and descending – were considered in order to eliminate the effects of the topography in the researched region. Other factor that is increasing the accuracy of the final results about the surface motions is the well maintained orbital position. It needs to be mentioned that the processed SAR data sets were delivered by two identical satellites thus shortening the time resolution and increasing the number of images that could be selected to form single interferometric pair.



Figure 1. Location of the studied archaeological site (photo credit Anthony Georgieff, 2020).

For this study we created a local repository with SAR data downloaded from two main repositories – ESA and NASA. The purpose of those archives is to provide quick access to all registered SAR products for the studied region for years 2015 – 2021 and to make possible the selection of the most suitable ones for further processing.

During the data selection step the specific features of the studied site should be taken into account. Namely, since during the late spring – early autumn excavation works are taking place at the studied archaeological site and this is the reason to process only data acquired for the rest months in order not to produce incorrect information regarding the surface motions that happened at the site.

### B. Method

The processing of SAR data was done by implementing the widely accepted DInSAR technique (Ferretti *et al.*, 2007) to obtain large set of interferometric images that are to be used to study the temporal changes of the surface. Those images represent the changes occurred at specific place on the Earth's surface based on difference between the number cycles of the backscattered phase component of the radar signal emitted by the SAR instrument at two passes of the satellite (for S-1 the minimum interval is six days). During the SAR data processing there are some peculiarities that were accounted – use for processing only the imagery with high modelled coherence (above 0.75); select only initial data sets that overlap geometrically as much as possible in order to

have better co-registration between both initial images (possibly use data from same orbit/track); utilize the most accurate external digital elevation model that has spatial resolution comparable to those of the SAR data (30 m or less). When elaborating the interferometric product besides the phase band one more image band, named coherence, is obtained whose values are between 0 and 1 and further this band is used as quality measure for ground elements in the interferometric band. In case in the produced interferometric image there are zones with gradually changing colors it could be inferred that in those areas some displacements have occurred between the two acquisition dates. After that step in order to increase the quality of the interferometric image spatial filtering was done.

Next a procedure to transform the phase signal, which is wrapped in the interval  $[-\pi ; \pi]$  to integers of  $\pi$  a specialized procedure known as phase unwrapping (Goldstein *et al.*, 1988), should be executed.

Since this procedure could produce ambiguous results it has to be implemented with proper selection of processing parameters with regard to extent of the area that is processed and presence of image elements that have high values in the coherence image band. Next follows recalculation of those values into metric units. Final step in the processing chain used to elaborate the results reported below is to convert the produced images from radar geometry to geodetic coordinate system. The experience of the authors for producing results from DInSAR processing for this region was outlined in (Atanasova and Nikolov, 2016; 2017).

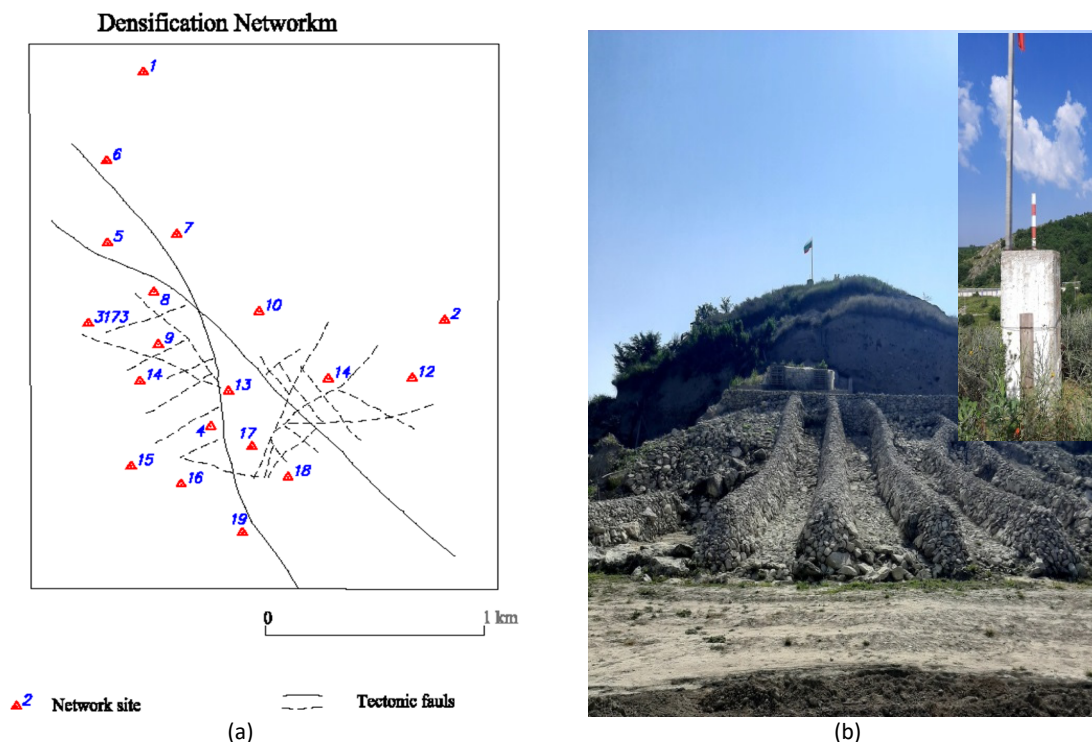


Figure 2. The geodynamic network for the area of the Mirovo salt deposit - general scheme (a) (Valev *et al.*, 2015) and single measurement point at the Solnitsata site (b).

It needs to be underlined that obtaining results by the procedure described above all produced results are in line-of-sight of the instrument and can't be directly attributed to single ground motion vector (E-W, N-S or vertical) that could have arbitrary direction so additional processing is needed (Vassileva *et al.*, 2017).

Also it should kept in mind that the registered magnitude of the results reflects only the surface changes in the period between both SAR data acquisitions *i.e.* they are relative in time.

### C. Results

All processing steps set out in the above paragraphs were executed in SNAP software, which is freely distributed by ESA. In order to produce unified results and to speed up the SAR data processing the authors prepared several graphs. After selecting the candidate primary/secondary pairs further processed were only those sets that had perpendicular baseline  $B_{\text{perp}}$  for both acquisitions below 100 m (see Table 1).

Table 1. Parameters of the SAR data sets selected for processing

Primary	Secondary	B <sub>perp</sub> [m]	Modelled coherence
29 Oct 2018	10 Mar 2019	-40.77	0.85
05 Nov 2019	28 Mar 2020	-29.47	0.84
11 Nov 2020	23 Mar 2021	-88.94	0.81
05 Nov 2018	10 Apr 2019	-88.04	0.79
12 Nov 2019	29 Mar 2020	-76.46	0.82
06 Nov 2020	11 Apr 2021	-1.80	0.85

This was needed since the expected displacements are not large and the low values of  $B_{\text{perp}}$  increase the sensitivity to ground displacements (Ferretti *et al.*, 2007). The values of the perpendicular baselines for each processed pair are provided in Table 1 (the values in italic are for descending orbit).

As shown on Figure 3 the presented upwrapped interferometric image are the final results for the calculated ground displacements overlaying a raster image in Google Earth. From those images, geocoded in WGS84 projection, we removed the pixels that had values for the coherence band of the same product below 0.3. In this case the presence of large areas that lack coherence was expected since large patches in the zone around the studied site are agricultural and forest plots where the low coherence is due to changes in the vegetation during their different phenophases.

Other reason why the results portrayed on the same figure don't exhibit uniform behavior is the fact that they are from ascending and descending orbits which results in different position of the antenna at the time of data registration. As mentioned above this was essential in order to be able to make comparison

between results from different orbits and thus to produce information regarding the direction of the surface motions occurred. As pointed out in work of Vassileva *et al.* (2017) if the sign of the values for single pixel from both orbits coincide the detected surface movement is predominantly vertical while if the signs are opposite the motion is mostly in west-east direction. In our case as seen from Figure 3 for most of the valid pixels we infer that the deformation is predominantly vertical that follows the surface motion detected from the geodetic surveys.

### D. Discussion

Despite the middle spatial resolution of 14 x 14 m of the interferometric images the presented results clearly confirm the trend for subsidence in the researched area which is also established by the results produced by the measurements made in the local geodetic network. Compared to the geodetic approach the one used for this study provides more flexibility since the repeatability of the results is limited only by the revisiting time of the satellite, which in case of Sentinel-1 is six or twelve days. On the other hand at least yearly data from geodetic measurements are needed to check the consistency of the SAR-produced results. This is the reason why both approaches are often seen as complementary not as competitive ones.

With regard to the seismicity in the region the information produced by SAR data processing can't contribute to the registration of earthquakes. This statement is based on the fact that earthquakes larger than 4.4 occur rarely and are not easy to detect due to dominant agricultural and forest landscape (Dimitrov *et al.*, 2013). Nevertheless if earthquake event with magnitude larger than 5 Mw occurs in the area SAR data could deliver information regarding the surface motions that took place. This assertion is based on the model of Solakov *et al.* (2003), into which for the researched region the expected seismic event would have Mw = 5.6 – 6.0 maximum.

## III. CONCLUSIONS

In this study we proposed an approach for regular monitoring for one of the most ancient sites in Europe – Solnitsata near the town Provadia predominantly based on SAR data. This method will decrease the human effort to establish the overall trend for the surface motions in the area and to take the necessary actions to prevent possible damages on it. This research had also two more goals – to demonstrate the possibilities to produce reliable information by DInSAR method as well as to facilitate the user uptake and to raise awareness about EGMS (EGMS, 2022).

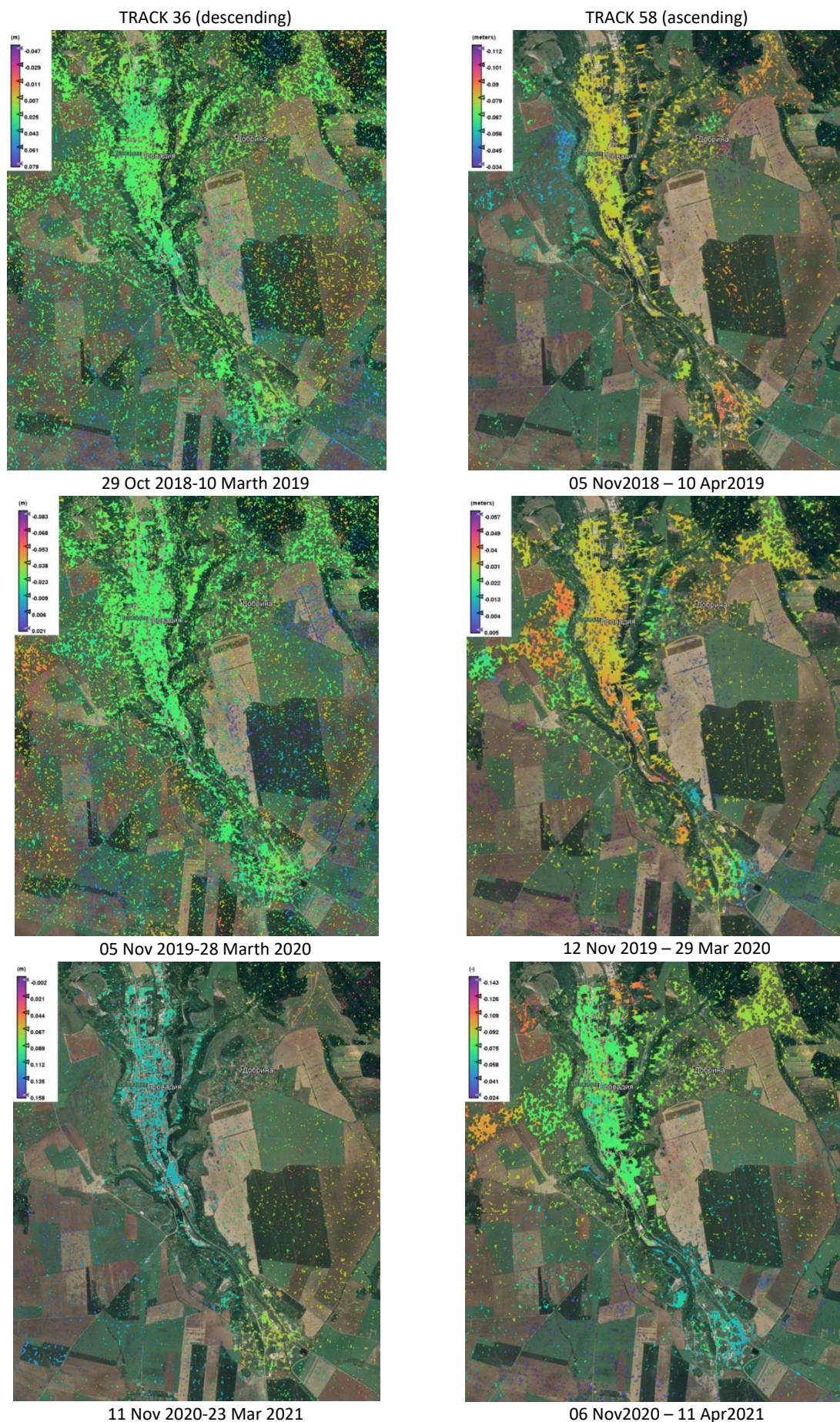


Figure 3. Comparison of the results obtained from ascending and descending orbits for the researched area (located lower right). This figure shows the modified Copernicus data.

#### IV. ACKNOWLEDGEMENTS

This study was supported by the Contract No D01-404/18.12.2020 (project “National Geoinformation Center (NGIC)” financed by the National Roadmap for Scientific Infrastructure 2020-2027.

The authors would like to express their gratitude to European Space Agency for providing Sentinel-1 SAR data and geospatial processing software SNAP at no cost.

#### References

- Atanasova, M., and Nikolov, H., (2016). Detection of the Earth's crust deformation in Provadia area using InSAR technique. *Proceedings of XXVI International symposium on “Modern technologies, education and professional practice in geodesy and related fields”*, pp. 1-12.
- Atanasova-Zlatareva, M., and Nikolov, H., (2017). Detection of vertical displacements in the area of Mirovo salt deposit by means of D-InSAR and geodetic measurements. *Proceedings of the XXVII International symposium on “Modern technologies, education and professional practice in geodesy and related fields”*.
- Cavazza, W., Roure, F.M., Spakman, W., Stampfli, G.M., and Ziegler, P.A., (2004). *The TRANSMED Atlas. The Mediterranean region from Crust to Mantle*. Elsevier, Amsterdam.
- Dimitrov, D., Georgiev, I., Dimitrova, L., and Botev, E., (2013). Deformations and Seismicity in the Region of Mirovo Salt Deposit, Bulgaria, *Conference Proceedings, 7th Congress of the Balkan Geophysical Society*.
- Dimitrova, L., Georgieva, G., and Trifonova, P. (2020). Seismic sources and Earth structure in the transition zone between Fore-Balkan unit and Moesian platform, NE Bulgaria. *Acta Geod Geophys* 55, pp. 183–202.
- EGMS, (2022). European Ground Motion Service. Available in: <https://land.copernicus.eu/pan-european/european-ground-motionservice>, (accessed Jan 2022).
- Ferretti, A., Monti-Guarnieri, A., Prati, C., Rocca, F., and Massonnet, D., (2007). *InSAR Principles: Guidelines for SAR Interferometry Processing and Interpretation [TM-19]*, ESA Publications, Noordwijk, The Netherlands.
- Goldstein, R.M., Zebker, H.A., and Werner, C.L., (1988). Satellite radar interferometry: Two-dimensional phase unwrapping. *Radio Sci.*, 23, pp. 713–720.
- Ivanov Z, (2017). *Tectonics of Bulgaria*. University Press of SU “Sv. Kliment Ohridski”, Sofia.
- Kenyeres, A., Bellet, J.G., and Bruyninx, C., (2019). Regional integration of long-term national dense GNSS network solutions. *GPS Solut*, 23, 122.
- Nikolov V., (2016). The prehistoric salt-production and urban center of Provadia-Solnitsata, Northeastern Bulgaria, *Méditerranée*, vol. 126, pp. 71-78.
- Poncoş, V., Stanciu, I., Teleagă, D., Maţenco, L., Bozsó, I., Szakács, A., and Rădulescu, V., (2022). An Integrated Platform for Ground-Motion Mapping, Local to Regional Scale; Examples from SE Europe. *Remote Sensing*, 14(4), 1046.
- Solakov, D., Simeonova, S., Hristoskov, L., and Dimitrova, L., (2003). *Magazine Sci.*, 29, Nos 1–4, 43–47.
- Valev, G., and Kastreva, P., (2014). Application of the statistical methods in study of the deformation of the ground surface. *Scientific Journal: Micro Macro & Mezzo Geo Information (MMM-G) Nr/No 2*; pp 6 - 19.
- Valev, G., Rainov, G., and Vassileva, K., (2015). Geodetic measurements and study of the Mirovo salt deposit, *7th BgGS National conference with international participation “GEOPHYSICS 2015”*, May 2015.
- Vassileva, M., F.G., Tonolo, P. Riccardi, D. Lecci, P. Boccardo and G. Chiesa, (2017). Satellite SAR interferometric techniques in support to emergency mapping, *European Journal of Remote Sensing*, 50:1, 464-477.
- Yankova, M., and Dimovski, S., (2015). Application of borehole log analysis for evaluating the reservoir properties of thick terrigenous rocks,. In: *Proceedings of 7th BGS conference on “Geophysics 2015”*, Sofia (in Bulgarian).



## First experiment of long-range panoramic images on a high-precision geodetic reference frame

Peyman Javadi, José Luis Lerma, Luis García-Asenjo

Department of Cartographic Engineering, Geodesy and Photogrammetry, Universitat Politècnica de València, Camino de Vera s/n, 46022 Valencia, Spain, ([pjavadi@doctor.upv.es](mailto:pjavadi@doctor.upv.es); [jllerma@cgf.upv.es](mailto:jllerma@cgf.upv.es); [lugarcia@cgf.upv.es](mailto:lugarcia@cgf.upv.es))

**Key words:** *panorama photogrammetry; panoramic images; geodetic reference frame; deformation monitoring; long distances*

### ABSTRACT

Geomonitoring of rockfalls and landslides is increasingly carried out by solutions that integrate different geomatics techniques to provide quickly 3D point clouds or models that are required to be rigorously in the same reference system. Methods based on remote sensing such as terrestrial laser scanning or photogrammetry need precise ground control, which is usually provided by means of geodetic surveys. However, when the study area is large with strong limitations due to particular orography, those geodetic techniques cannot always grant accurate target points optimally distributed within the monitored object, and only an external reference frame is available to provide absolute orientation to those 3D point clouds or models. In that case, terrestrial photogrammetry shows clear advantages compared to terrestrial laser scanning. Still, it may require a large number of high-quality images taken from well-distributed stations, thus hampering the desired fast data collection. A possible alternative to cope with this problem is the use of the panoramic photogrammetry method by using robotic devices like Gigapan along with a systematic collection procedure from stable stations of a reference frame whose coordinates are accurate and well-controlled. This contribution describes an experiment conducted in Cortes de Pallás (Spain), where an existing infrastructure consisting of 10 pillars and 15 check points is annually monitored at millimetric level, to investigate the potential of long-range panoramic photogrammetry as applied to deformation monitoring. The panoramic images were taken from 7 selected pillars using the Gigapan robotic device. The accuracy of oriented panoramic images, the performance of the method in long-ranges (500-1000 m), and the consistency with the geodetic techniques in the 15 check points were analyzed. Finally, some conclusions about the suitability of panoramic photogrammetry as applied to long-range deformation monitoring are drawn.

### I. INTRODUCTION

Accuracy and consistency of the measured data are critical aspects for reliable rock slope modelling based on periodical point clouds or models obtained by integrating different remote sensing techniques such as terrestrial laser scanning (TLS), digital photogrammetry (DP), or mobile mapping systems (MMS). Since efficiency is also a general requirement for a quick deformation diagnosis, the collection of accurate and consistent data should be carried out by using optimal field processes that minimize the acquisition time and the need for external ground control as much as possible (Francioni *et al.*, 2018).

Nevertheless, external ground control cannot be eliminated completely because rigorous statistical assessment of possible displacements requires all point clouds or models to be strictly referred to a unique reference system. Furthermore, to prevent sub-optimal use of the remote sensing techniques, the reference system should have accuracy at least one order of magnitude better than the intrinsic precision provided by those techniques, which constitutes a real challenge. For instance, if the precision of a remote sensing technique in a broad area is expected to be around 1 cm

to 3 cm, the reference system should be realized with an accuracy of 1 mm to 3 mm, which is beyond the capacity of standard surveying techniques based on GNSS or total stations. Therefore, irrespective of the technique used to collect the data, the proper integration into a consistent and reliable reference frame becomes critical and does not always receive all the attention it deserves. Cortes de Pallás (Spain), a complex area equipped with a ten-pillar network whose stability is periodically monitored at millimeter level by using high-precision geodetic techniques, is an ideal site for testing different remote sensing solutions as applied to deformation monitoring (García-Asenjo *et al.*, 2019; García-Asenjo *et al.*, 2022). Some of the techniques that were previously tested with dissimilar results are long-range TLS, terrestrial DP, or handheld MMS.

TLS is a recurrent and efficient solution for distances shorter than 200 m, but for distances longer than 800 m and complex orography, the technique becomes expensive and additional problems such as systematic instrumental errors, inaccurate registration or atmospheric refraction may arise (Fan *et al.*, 2015; Friedli *et al.*, 2019; Harmening and Neuner, 2019). In the case at hand, TLS provided unsatisfactory results

because the point clouds were not detailed enough for the registration process, even though the CPs on the pillars were equipped with large white spheres ( $\varnothing$  500 mm).

On the other hand, terrestrial DP proved to yield an accuracy of 1 – 3 cm as long as precise ground control is provided on-site. However, in broad and complex areas where a large number of long and close images from multiple stations are necessary, it is complicated to know the coordinates of each camera location with the required precision, and thus, the unique option for integrating the photogrammetric models into the reference system is the traditional approach, which relies on using CPs optimally distributed within the monitoring area. Nonetheless, this usual approach entails two disadvantages for rigorous deformation monitoring: first, it is paradoxical that points assumed not to be stable act as CPs for model orientation; second, the possible instability of CPs makes necessary the inclusion of a high-precision geodetic survey concurrent to each photogrammetric campaign, which is time-consuming and clearly diminishes the efficiency of the method.

Some alternatives to optimize terrestrial DP are the use of Unmanned Aerial Vehicles (UAVs) or MMS, but these solutions are not always feasible in areas like Cortes de Pallás. In this case, the use of UAVs was disregarded because the complexity of the site, which includes a hydraulic power plant with many electricity power lines, car traffic, and tourism activities, does not favour the method. Concerning MMS, a test carried out in 2019 showed that the maximum attainable accuracy is in the range of 3 to 8 cm (Di Stefano *et al.*, 2020).

The panoramic images collected using a Gigapan robotic device may be a possible alternative to the aforementioned methods. Previous experiments conducted in smaller and well-controlled areas have demonstrated that both single-strip and spherical panoramas can be produced with an accuracy of several millimetres and centimetres, respectively. It proves to be accurate and efficient enough for deformation monitoring (Javadi *et al.*, 2021; Lee *et al.*, 2019).

One advantage of panoramic photogrammetry is that the number of images required can be largely reduced with respect to traditional terrestrial photogrammetry. Moreover, the entire area can be efficiently surveyed by systematically setting the Gigapan on well-distributed permanent pillars. In this way, if permanent and well-controlled reference frames can be optimally integrated into the resulting 3D models, there would be no need for additional ground control.

Additional advantages of using panoramic images are the possibility of 3D model reconstruction with photorealistic and high-resolution texture, and the use of dedicated algorithms for panorama orientation and restitution (D'Annibale *et al.*, 2013).

This paper describes a first experiment conducted in Cortes de Pallás (Spain) to evaluate the potentiality of the long-range panoramic photogrammetry method for

deformation monitoring as an alternative to other remote sensing solutions which were previously tested under similar conditions. The following sections describe all the steps leading to the results obtained.

## II. PANORAMIC PHOTOGRAMMETRY

### A. Panoramic images

Panoramic photography, also known as wide format photography, is a special technique that stitches multiple images acquired from the same camera position together to form a single image with a field of view similar or greater than that of the human eye. Panoramic photography can be classified into three types: cylindrical, spherical, and planar. The cylindrical panorama includes inner-cylinder and outer-cylinder panoramas. The shooting technique of the cylindrical panoramic image involves three methods: horizontal, vertical, and oblique (Luhmann, 2004).

The aforementioned types of panoramic images can either be photographed in a single row (meaning one row of vertical or horizontal images) or multiple rows (higher focal length is often used to yield much higher resolutions. Multi-row panoramas often require special panoramic equipment). The mathematical model of panorama images is usually based on cylindrical coordinates. Since collinearity equations can be derived easily, all standard photogrammetric algorithms from space intersection to bundle adjustment can be applied (Luhmann, 2010).

### B. Image stitching

The biggest challenge with panoramic photography is the proper stitching due to low quality of images, poor image correspondence, or possible parallax errors. Therefore, achieving a high-quality panoramic image requires adequate planning and selection of correct instruments and methods, such as stable mountings (tripods or pillars), automatic rotation devices, proper selection of image format, image overlapping, shooting mode, and white balance, among others. Moreover, determining the nodal point according to the lens used becomes crucial to eliminating the parallax error. Once the images have been taken, they have to be stitched automatically by using specialized software in order to produce panoramic images.

There is a variety of software for stitching images and creating panoramas. For this project, we opted for Microsoft Image Composite Editor. Among other advantages, this software has the ability to introduce the structure of the captured images, stitch images based on automatic matching, high speed processing, as well as good quality of the output panoramic images. Figure 1 shows an example of one of the panoramic images created for this project.



Figure 1. Panoramic image created from one reference station.

### C. Absolute orientation of panoramic images

Panoramic images can be related to each other without the need for external information. However, the resulting 3D model has to be scaled and orientated to be consistent with the terrestrial coordinate system chosen as the reference system. The relationship between the model coordinates ( $x, y, z$ ) and the terrestrial coordinates ( $X, Y, Z$ ) are given by the well-known expression (Laganière and Kangni, 2010) (Eq. 1):

$$\begin{bmatrix} X_i \\ Y_i \\ Z_i \end{bmatrix} = \lambda R \begin{bmatrix} x_i \\ y_i \\ z_i \end{bmatrix} + \begin{bmatrix} B_X \\ B_Y \\ B_Z \end{bmatrix} \quad (1)$$

where  $(X_i . Y_i . Z_i)^T$  = terrestrial coordinates for point  $i$   
 $\lambda$  = scale factor  
 $R$  = rotation matrix  
 $(B_X . B_Y . B_Z)^T$  = translation vector

The seven transformation parameters are obtained by using at least three no-aligned CPs whose terrestrial coordinates have to be known with better accuracy than the expected one provided by the photogrammetry method. This step of the process was carried out by using the Agisoft Metashape software.

## III. MEASUREMENT SETUP

### A. Description of the test field

The test field used in this project is located in Cortes de Pallás (Spain). This site, which has recurrent geotechnical problems, was affected in April 2015 by a cliff collapse which seriously damaged some facilities of the near electricity power plant and the main access road to the village (Figure 2). In 2017, a geodetic network was commissioned by the *Diputació de València* as a primary component of a deformation monitoring plan to detect possible displacements of huge boulders and potential malfunctioning of the anchoring systems installed after the consolidation works. However, the detection of possible displacements of some centimetres with the required level of significance in a short period, *e.g.* two or three years, is a challenging task due to the peculiar topography of the site, which involves distances from 500 to 2000 m with height differences reaching 500 m. Furthermore, since the cliff of interest is facing a water reservoir, the measurements have to be undertaken from the opposite shoreline, which is about 600 m away. As a balanced solution, the *Diputació de València* eventually opted for both geodetic and image-based techniques (Di Stefano *et al.*, 2020).



Figure 2. Study site of Cortes de Pallás highlighted in red: top) oblique aerial view; bottom) front view.

### B. Permanent points

The study area includes two types of points which are permanently installed on-site. The first type consists in a set of 10 pillars fixed on the ground (Figure 3a), which will be considered as reference CPs, while the second type consists of a set of 15 check points (ChPs) rigidly fixed to the object rock wall with small white spheres ( $\varnothing$  145 mm) on top of 360-degree prisms (Figure 3b).

During the measurements, pillars were equipped with Testo 176P1 meteorological sensors (Figure 3a) for subsequent refraction correction of the EDM-based distances.

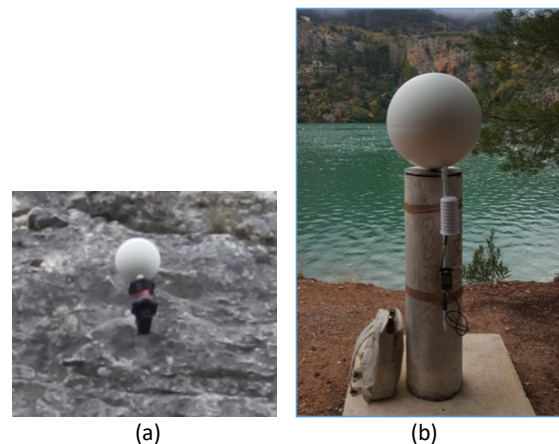


Figure 3. (a) Check point; (b) Reference CP.

### C. Geodetic survey

The geodetic instruments and their ancillary devices that were used for the geodetic observations: a sub-millimetric EDM Kern Mekometer ME5000 (Figure 4a) and a robotic total station Leica TM30 (Figure 4b). They

were respectively used to detect the possible displacement of CPs on the pillars and ChPs from the years 2018 to 2020, and to monitor the CPs automatically and simultaneously with the Gigapan image acquisition.

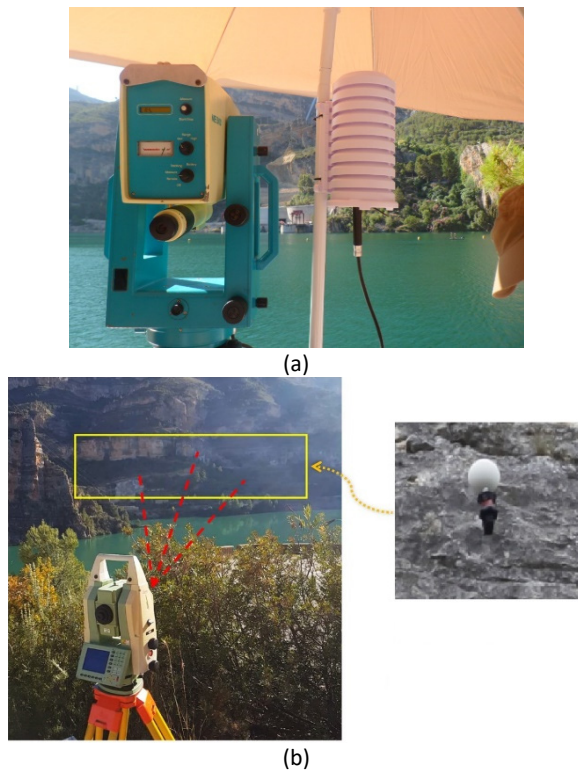


Figure 4. (a) Sub-millimetric EDM Mekometer ME5000; (b) Robotic Total Station for automatic CPs observation.

The ten-pillar geodetic reference frame and the 15 ChPs fixed to the rock wall were annually measured from the years 2018 to 2020 by using sub-millimetric EDM techniques. For each annual campaign, coordinates for CPs and ChPs were obtained in a two-step process. In the first step, only distances between pillars were adjusted to provide a solution for the reference frame. In the second step, distances to CPs were included in order to obtain their 3D coordinates. The applied method provided coordinates with an overall accuracy of 0.5–1 mm for CPs and 1–3 mm for ChPs, respectively (García-Asenjo *et al.*, 2019).

Therefore, the geodetic reference frame along with the 15 ChPs can be safely and reliably used to evaluate the accuracy and performance of panoramic photogrammetry over long distances.

#### D. Photogrammetric survey

A Gigapan robotic rotating device was equipped with a Canon 5DSR full-frame camera. The set was installed on seven selected pillars to acquire automatically 360° images of the area (Figure 5). Since the pictures were taken using a fixed 50 mm lens, each panorama included around 23 images.

Factors concerning the camera settings, the overlap and the software used for subsequent processing can

strongly affect the overall quality of the produced panoramic images and, therefore, the geometric accuracy of the 3D models derived from them (Guerroui *et al.*, 2015; Javadi *et al.*, 2021). As mentioned earlier, Microsoft Image Composite Editor software was firstly used to create panoramic images. Afterwards, Agisoft Metashape software was used to orient the images in the geodetic reference frame.



Figure 5. Camera mounted on the Gigapan for acquiring the panoramic images.

We opted for a Canon 5DSR full-frame camera equipped with a fixed focal length of 50 mm to achieve a ground sampling distance (GSD) of 5 cm.

Concerning the geometry of the site, it was deemed optimal to form 360° panoramic images by taking only one horizontal strip with a 60% overlap (Figure 6), reaching 23 images per station and around 20 minutes, including the time required to set up the Gigapan device. In total, seven panoramas were collected from seven selected pillars of the reference frame.

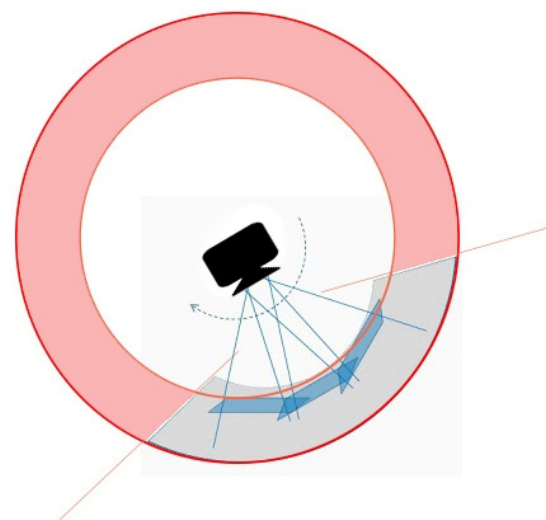


Figure 6. Overlapping frame pictures to build up eventually a panoramic image.

Please note that the difference in size between the spheres that are mounted temporarily on the pillars (Figure 3b), and the spheres mounted permanently on the wall (Figure 3a) is significant. Therefore, only panoramic images close to the targets will be considered as ChPs.

Agisoft Metashape software was used to process, align and orient the images, which were tested in two different types: (a) cylindrical panoramas (Figure 7); (b) partial frame panoramas (Figure 8).



Figure 7. The cylindrical (360°) panorama images from seven fixed stations.



Figure 8. The partial frame panorama images from the seven fixed stations.

In (a), the entire captured area was involved in processing, also the average distance between the CPs was about 1000 m and the average distance of the stations to the ChPs was about 600 m (Figure 7).

On the contrary, for (b), a smaller target area was separated, processed and modelled (Figure 8). In this method, it was decided to remove areas with the bad and critical vision from the processing, which as a result made it possible to align the image, select manual markers and process at a higher speed.

The blue part in (Figure 6) is an example of the selected pictures in (b). This cut was made because, in some stations, the distance from the camera to the study area was about 600 m. In the opposite direction, the distance of features such as the road or the walls of the facility to the camera was about 50 m, and this caused aligning troubles.

#### IV. RESULTS

The results of the cylindrical panoramas (a) are summarized in Tables 1 and 2.

Table 1. Orientation of the seven cylindrical panoramic images

	Number
Stations	7
Photos	7
Markers	21
Reference Points	21
Control Points	3
Check Points	18
Tie Points	6,767

Table 2. RMSE obtained in the orientation of the seven cylindrical panoramic images

	RMSE [m]	Error [pix]
Control Points	0.392	54.735
Check Points	4.907	39.448

The information resulting from the partial frame panoramas (b) is displayed in Table 3. According to Table 4, the orientation of the photographs is done with greater accuracy by calculating the CPs, ChPs, and tie points. In this processing type, was found to be 2 cm accurate at the points selected as the CP and 17 cm accurate at the ChPs.

Table 3. Orientation of the seven partial panoramic images

	Number
Stations	7
Photos	37
Markers	37
Reference Points	19
Control Points	3
Check Points	16
Tie Points	1,948,279

Table 4. RMSE obtained in the orientation of partial panoramic images

	RMSE [m]	Error [pix]
Control Points	0.028	1.170
Check Points	0.170	1.284

To improve the accuracy and quality of the output results, the final processing was continued by removing additional ranges as shown in (Figure 9).



Figure 9. Position of markers and cameras in orientation.

Tables 5 and 6 show the root mean square error (RMSE) for each point.

Table 5. Control points RMSE

Label	X error [cm]	Y error [cm]	Z error [cm]	Total [cm]	Image [pix]
8003	1.87	0.11	-0.37	1.91	0.8 (7)
8004	1.74	-1.52	-0.39	2.34	0.8 (11)
8006	-3.61	1.41	0.76	3.95	1.4 (17)
Total	2.55	1.20	0.54	2.87	1.170

Table 6. Example Check points RMSE

Label	X error [cm]	Y error [cm]	Z error [cm]	Total [cm]	Image [pix]
8005	-34.09	-43.50	12.50	56.66	2.1 (10)
1001	-3.69	0.59	-0.89	3.85	0.6 (15)
1002	-3.24	0.24	-1.14	3.45	0.4 (13)
1003	-2.10	3.68	-1.21	4.41	0.7 (14)
1004	-1.85	-3.12	-2.23	4.26	0.3 (13)
1005	-1.71	-5.27	-2.29	6.00	0.4 (13)
1006	-0.33	-5.61	-2.55	6.17	0.3 (13)
1007	0.76	-6.80	-7.95	10.49	0.6 (14)
1008	3.58	-0.22	-3.04	4.71	1.7 (20)
1009	-0.23	2.07	-3.88	4.41	2.7 (19)
1010	-1.73	6.81	-8.24	10.84	0.3 (17)
1011	-11.81	10.53	-5.22	16.66	0.8 (14)
1012	-12.55	9.30	-1.49	15.69	1.2 (10)
1013	-5.14	8.60	-2.91	10.43	1.2 (10)
1014	-12.44	10.16	-2.97	16.34	1.6 (14)
1015	-1.20	-7.53	-7.40	10.63	0.7 (15)
Total	10.28	12.51	5.20	17.01	1.284

Given that there are 37 markers, 19 have coordinates, and 18 are just chosen on the images and manually to orient the images more accurately, so they are not shown in the table above.

These results are promising for such a large-scale project. Despite the small number of images, about 2 million points were obtained for surface determination, points cloud production and initial 3D modelling. Due to the good quality of the processed data, a dense cloud of points was built (Figure 10) in this small range, based on only 37 photos taken from different angles. However, by including the texture of the image, the 3D model of the area is produced to an acceptable level, which is shown in (Figure 11).



Figure 10. Dense point cloud of the main area.

Next, the tile model is made with a resolution of 5 cm/pix, which ultimately achieves the initial DEM

production of the area. The result of its production can be seen in (Figure 12), with a GSD of 10 cm.



Figure 11. 3D model of the main area.

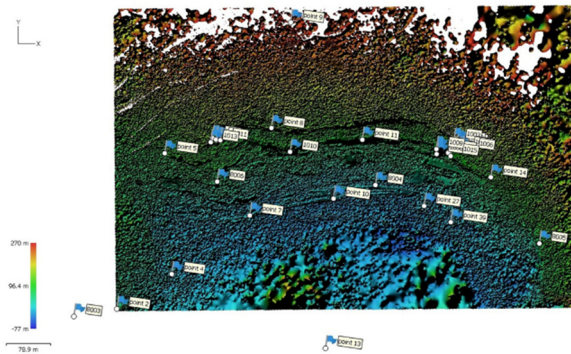


Figure 12. DEM of the main area.

## V. DISCUSSION

In the light of the experiment conducted in Cortes de Pallás for testing the use of panoramic images as applied to long-range deformation monitoring, some critical aspects have been revealed.

First, the comparison of the proposed method with other remote sensing techniques, which has been only possible by the fact that there were both a well-controlled geodetic reference frame and ChPs available on the site, cannot be considered conclusive because the orientation of the 3D models obtained by other methods was done by using the traditional approach which is only based on ChPs on the wall and considered sub-optimal. Furthermore, the geometry of the seven pillars used as stations for collecting images was originally designed for geodetic surveying without considering their potential future usage as stations for collecting images.

Second, the right selection of camera, including sensor dimensions and lens used, is crucial when deformation monitoring is aimed. Those features strongly affect the quality of images, and thus the accuracy of the 3D models obtained. In the case at hand, the different size of the targeting spheres,  $\varnothing$  500 mm and  $\varnothing$  145 mm for CPs and ChPs respectively, did not help to make a balanced selection of the camera features.

Third, when it comes to efficiency, panoramic photogrammetry proved clearly superior to terrestrial photogrammetry. Concerning time for collecting the images, the proposed method took only 20 minutes for

each station, while the terrestrial one required one complete day. The number of images taken is reduced and they can be easily processed. Alternatively, creating a 3D model is much faster. In addition, the angle of view of these panoramic images is not reduced because the whole area has been completely photographed (Fangi and Nardinocchi, 2013). Nevertheless, the current geometry of pillars, which was originally designed for geodetic purposes, does not prevent the photogrammetric survey from having hidden angles. For this reason, several stations have been included to cover the study area. Thus, the current network should be improved by including additional stations with precise coordinates in the same reference frame.

Fourth, as mentioned in the previous sections, the aim is to evaluate the performance of panoramic photogrammetry over long distances. However, the results showed that the accuracy obtained in the use of cylindrical panoramic images is not satisfactory, which can also be due to factors such as changing the dimensions of the final panoramic images after stitching, and different distances between some land features with the camera. However, the strategy of utilizing partial panoramic images, which concentrates primarily on the study region, has shown favourable and promising results. Therefore, it can be said that taking panoramic images, not in cylindrical (360°), but in the form of taking partial panoramic images only from the desired area can boost the rapidity of field operations, processing RMSE, and end result quality.

## VI. CONCLUSION

Experience using panoramic images to monitor deformation can be an optimal solution for detecting instability over long distances. In this regard, orienting the overlap images taken from several different stations requires a network with the correct geometry. In addition, in close-range photogrammetry, it is important to select reference CPs to orient the images. But what sets this research apart is the use of panoramic images for possible adaptation to deformation monitoring from the reference CPs. In this research, instead of using traditional photogrammetry and taking several hundred photos to model an object (especially in open and natural environments), these images were used in two ways: cylindrical panorama (a), and partial frame panorama (b). However, taking panoramic images is much simpler and easier and reduces the time and cost of operations. Therefore, in the case of this project, where the reference stations are located at an average distance of about 1 km from each other, they should be oriented relative to each other in a cylindrical panorama (360°). But if we reduce this 360° panorama to just the part that is the main area and suspected of slipping, then there is no need to align and orient the extra areas. Also, the distance of the stations to the target area will be about 600 meters. As a result, the images will be oriented more accurately

and the output will be improved. With this method an accuracy of 2 cm was obtained for CPs and about 17 cm for ChPs. This is a promising and acceptable result for image-based panoramic photogrammetry that opens the door to deformation monitoring at long distances.

## References

- D'Annibale, E., Tasseti, A. N., and Malinverni, E. S. (2013). From panoramic photos to a low-cost photogrammetric workflow for cultural heritage 3D documentation. In: *The International Archives of the Photogrammetry, Remote Sensing and Spatial Information Sciences*. XL-5/W2, pp. 213–218. DOI: 10.5194/isprsarchives-xl-5-w2-213-2013
- Di Stefano, F., Cabrelles, M., García-Asenjo, L., Lerma, J. L., Malinverni, E. S., Baselga, S., Garrigues, P., and Pierdicca, R. (2020). Evaluation of Long-Range Mobile Mapping System (MMS) and Close-Range Photogrammetry for Deformation Monitoring. A Case Study of Cortes de Pallás in Valencia (Spain). In: *Applied Sciences*, 10(19), pp. 6831. DOI: 10.3390/app10196831
- Fan, L., Smethurst, J. A., Atkinson, P. M., and Powrie, W. (2015). Error in target-based georeferencing and registration in terrestrial laser scanning. *Comp. and Geosc.*, 83, pp. 54–64. DOI: 10.1016/j.cageo.2015.06.021
- Fangi, G., and Nardinocchi, C. (2013). Photogrammetric processing of spherical panoramas. *Photogrammetric Record*, 28(143), pp. 293–311. DOI: 10.1111/phor.12031
- Francioni, M., Salvini, R., Stead, D., and Coggan, J. (2018). Improvements in the integration of remote sensing and rock slope modelling. *Natural Hazards*, 90, pp. 975–1004. DOI: 10.1007/s11069-017-3116-8
- Friedli, E., Presl, R., and Wieser, A. (2019). Influence of atmospheric refraction on terrestrial laser scanning at long range. 4<sup>th</sup> Joint International Symposium on Deformation Monitoring (JISDM).
- García-Asenjo, L., Baselga, S., Atkins, C., and Garrigues, P. (2021). Development of a submillimetric gnss-based distance meter for length metrology. *Sensors* (Switzerland). 21(4), pp. 1145. DOI: 10.3390/s21041145
- Guerroui, N., Kouahla, M. N., and Séridi, H. (2015). Automatic Unbounded Panoramas. In: *International Journal of Computer Science, Communication & Information Technology (CSCIT)*, 2(2), 16–20.
- Harmening, C., and Neuner, H. (2019). Evaluating the performance of a space-and time-continuous deformation model. 4<sup>th</sup> Joint International Symposium on Deformation Monitoring (JISDM).
- Javadi, P., Lerma, J. L., García-Asenjo, L., and Garrigues, P. (2021). Quality assessment of spherical panoramic images. DOI: 10.4995/cigeo2021.2021.12728
- Laganière, R., and Kangni, F. (2010). Orientation and pose estimation for panoramic imagery. *Machine Graphics and Vision*, 19(3), pp. 339–363.
- Lee, R.J., Maxwell, Brandon, V., David W., and Valentino, J. D. (2019). Applications of High-Resolution Gigapan Imagery in Mapping Fracture Systems: An Example from the Adirondack Basement Massif, New York. In: *Adirondack Journal of Environmental Studies*, 23(1), pp. 9–35. <https://digitalworks.union.edu/ajes/vol23/iss1/4>
- Luhmann, T. (2004). A historical review on panorama photogrammetry. *Proceedings of Panoramic*

*Photogrammetry Workshop*. Available in:  
<http://citeseerx.ist.psu.edu/viewdoc/download?doi=10.1.1.101.2588&rep=rep1&type=pdf>

Luhmann, T. (2010). Panorama Photogrammetry for Architectural Applications. *Mapping*, 139, pp. 40–45.



## Transferability of an estimation procedure for distance deviations of terrestrial laser scanners from laboratory to on-site conditions

Finn Linzer, Hans-Berndt Neuner

Department of Geodesy and Geoinformation, TU Wien, Wiedner Hauptstraße 8-10, 1040 Vienna, Austria,  
([finn.linzer@tuwien.ac.at](mailto:finn.linzer@tuwien.ac.at); [hans.neuner@geo.tuwien.ac.at](mailto:hans.neuner@geo.tuwien.ac.at))

**Key words:** monitoring; laser scanning; systematic deviation; absolute distance; incidence angle (IA); automation; robot operating system (ROS)

### ABSTRACT

Employing terrestrial laser scanners (TLS) for geodetic deformation measurements requires attaining the highest possible accuracy. In this paper, we estimate the influence of varying incidence angles (IA) and materials on measurements regarding the distance component. Considering not only stochastic characteristics, the use of a scanning total station enables additionally the study of systematic distance deviations. By using the total station ocular, the device is brought into the local coordinate system of a laser tracker via position resection and intersection. The point cloud recording, with a Close-Range scanner, represents the reference. Due to transformation into a common coordinate system, defined by a laser tracker, a distance driven point comparison is possible. To test a large number of conditions an automated setup was developed. For each device, a suitable interface was implemented in the Robot Operating System. After the specimen has been set up, an automatic measurement can be performed for data acquisition. We can demonstrate that different building materials and varying IAs cause systematic distance deviations up to 3 mm magnitude. For measurement objects, this kind of correction must be considered, especially when the measurement configuration varies between measurement epochs. It can be demonstrated that the values and characteristics observed in the laboratory agree to those obtained on-site. However, the chosen approach thereby reveals previously unrecognized challenges that need to be considered for the use of TLS in high-accuracy deformation analysis.

### I. INTRODUCTION

To detect deformations by using terrestrial laser scanners (TLS), it is necessary to further increase the accuracy with focus on the distance component. Sources of error can be divided into four groups: instrumental imperfection, atmospheric influences, scan geometry and object properties (Soudarissanane, 2016). To obtain a sophisticated model, systematic influences must be exposed, as they should no longer be confused with structural deformation.

The characteristics of the systematic distance deviations are not yet well understood. As it was stated by Zámečníková *et al.* (2014), varying the incidence angle (IA) alters the result. Following up on that methodology, the data acquisition was fully automated, so that research questions, such as the behavior with different materials, can be answered in even faster succession (Linzer *et al.*, 2021).

The methodology itself is driven by a straightforward distance comparison. Corresponding TLS- and reference measurements are examined in relation to a specific tilted specimen. The transformation  $\mathcal{T}_{[6]}$  between the instruments in use is determined by a highly accurate network measurement. Figure 1 shows an overlay where the targeted points (51, 53, 61, 63) can be brought to a final correspondence by means of a spatial backward resection computation.

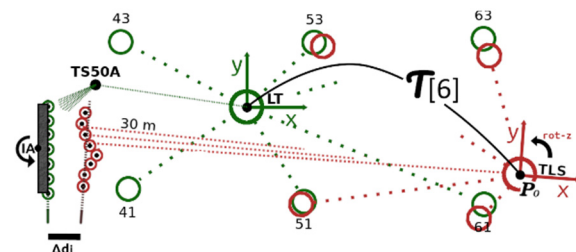


Figure 1. The transformation between TLS and LT system enable a direct comparison of the analyzed point clouds. The IA can set by a twistable specimen.

Ideally, after applying  $\mathcal{T}_{[6]}$ , point clouds of the TLS (in red) will be coincident with the points acquired by the reference (green). As laser radiation is affected by material properties and IA, deviations arise ( $\Delta di$ ).

As a superficial basis of laser radiation hitting various materials, "structure leads to properties" applies here (Shakelford, 2015). Following quantities can also be assumed to interfere: wavelength, distance, transmission, inhomogeneity, roughness, chem. composition, density, thickness, refraction, permeability, laser spot diameter and beam power. Thus, a penetration effect can be assumed for some materials, but can be ruled out for others. These findings must not be neglected when it comes to further developing of a potentially strong model for deformation analysis.

Furthermore, a stochastic description as a valid variance-covariance matrix (VCM) methodically has to meet the requirements of the elementary error model. In an on-site consideration a method was investigated in which especially the influences of atmosphere and geometry play a role (Kerekes and Schwieger, 2020). Wujanz *et al.* (2017) presented an intensity-based model that considered the reflectance properties of several laboratory setups. Based on the intensity value, a standard deviation of the distance component could be assigned to each point. To fill in the missing VCM entries Schmitz *et al.* (2021) made an effort, where a reference wall for TLS quality studies was established. The modeling of, for instance, the temporal influences on the geometry (*e.g.* daily influences) should ensure that deformations are not mistaken as device-specific phenomena. Through a large number of measurements and with a variety of instruments, the aim is to determine stochastic properties empirically.

In this paper, the transferability of results is examined on the basis of systematic deviations. If laboratory and on-sight results fit, we presume that subsequently laboratory findings have significance in outdoor applications as well. Due to a more complex setting, harsh conditions can obscure assumptions of results in a way not expected. If effects are similar, the sensitivity of deformation measurements can be increased by adapting and applying the given method to monitoring projects and its materials. The transfer to an outdoor structure, the historic aqueduct in Vienna, was achieved by using identical material that was available in the laboratory as well as on-site.

## II. SENSORS AUTOMATION AND DATA TRANSFORMATION

In connection to a Leica LTD800 laser tracker, point clouds are acquired by a Close-Range scanner (T-Scan TS50A). Due to its high level of accuracy, these scans can be used as a reference (Table 1). The TLS results are acquired with three different Leica MS60 instruments, which, in addition to the usual tachymetric application, have a scanning function as a built-in feature. With an acquisition rate of up to 30.000 points per second, the MS60 is already capable for handling many geodetic applications. The three instruments are referred to as:

- 1) Loan1-MS60: A device loaned in March 2021.
- 2) Institute-MS60: This TLS belongs to the institute since May 2021.
- 3) Loan2-MS60: A device loaned in September 2021.

The methodology for measuring distance differences can be divided into four steps:

- First, a network measurement is carried out to define a common coordinate system for both devices. Identical points are targeted to, using a Corner Cube Reflector (CCR) for both systems. In the laboratory, the CCR is placed onto permanently installed consoles. For a network

outside the laboratory, nests are spatially distributed and temporarily glued to the building facades.

- Thereafter specimens are examined in the laboratory for various IA. The materials chosen change in terms of roughness, reflection or permeability. On-Site, the IAs are realized by the geometric relationship towards the structure. However, the scan procedure always includes both the TLS and reference point clouds.
- Concluding control measurements must comply with the previous network measurement. It completes the acquisition and allows the detection of irregularities such as instability.
- At last, results can be evaluated using a scripted program.

Table 1. Properties of used devices

Parameter	Leica MS60	Leica LTD800 with T-Scan TS50A
Angular	0.3 mgon	0.6 mgon (LTD)
Distance	1 mm + 1.5 ppm	10 $\mu$ m + 10 $\mu$ m/m (IFM) and 3 $\mu$ m (CCR)
Scanning	0.5 mm @ 25 m	80 $\mu$ m + 3 $\mu$ m/m (TS)
Laserspot	ca. 7 x 10 mm @30 m	4.5 mm (LTD, collimated)

After the transformation, the point clouds of both instruments are present in an overlapping arrangement – both with the origin at  $P_0$ . However, if differences in the distance component persist, those systematic influences can be revealed for any given setup by multiple straightforward distance comparisons. For any TLS point (red), a corresponding reference measurement is to be found (green). The assumed distance deviations  $\Delta d_i$  arise and align closely on the line of sight. Therefore, matching point pairs are determined as nearest neighbors in polar space (Figure 2).

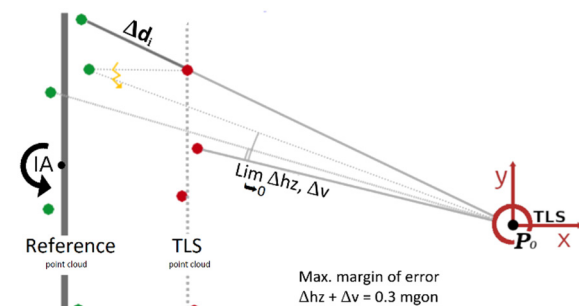


Figure 2. In the laboratory, the specimen is set to a certain IA. The corresponding point is assessed according to the deviation in Hz, V.

For measured distances of about 7 meters, the maximum angular difference allowed was set to 0.3 mgon. As the overall distance increases, the width may be reduced to remain a negligible impact on  $\Delta d_i$ .

To the extent that the transformation parameters  $\mathcal{T}_{[6]}$  diverge, the distance deviation  $\Delta d_i$  is also biased. A

Monte-Carlo-Simulation was carried out to estimate a priori accuracies with the values depicted in Table 1. The laboratory setup led to accuracy magnitudes of less than 0.1 mm in translation and about 0.5 mgon in orientation. In positioning, error proportions, which align to the line of site, fully affect the result of the distance component. An error on the z-axis orientation of 1 mgon would add about 0.15 mm to the error propagation of  $\Delta d_i$  (Figure 2). Its actual influence depends on the IA and increases when the total distance becomes larger than the 7 meters assumed for this calculation.

#### A. Robotized Method

The effort required to determine the absolute distance deviations for a whole range of materials and incidence angles soon becomes overwhelming. Therefore, the automation of the data collection process was achieved. It facilitates an orderly structure and even makes it possible to answer emerging research questions in faster succession.

To adopt to the appropriate traverse path, a robotic arm is programmed with the Close-Range scanner. A setup was chosen in which a step angle motor controls the rotation of the plate around the vertical axis so that the rotation can be flexibly adjusted.

The estimation procedure is based on the Robot Operating System (ROS); an open source framework, which allows the modular design of complex geodetic systems (Linzer *et al.*, 2019; Rejchrt *et al.*, 2019). Individual function libraries are combined in packages for specific tasks. Preferred programming languages are C++ and Python. These packages enable the control and evaluation of certain devices. For the robot arm and the stepper motor, packages from the manufacturers were available, which simplified their integration considerably. For the TLS, the laser tracker and the Close-Range scanner, the packages first had to be developed by the RD EG at TU Wien. Other packages may contain task-related algorithms, which, for example, can be used to transform point clouds. Within the ROS environment, these packages can be easily exchanged, published and tested by anyone with respect to its own research. If another TLS is to be integrated, only the exchange of this single module is necessary. For future work, this principle allows us to focus on the essence of the task at hand. The sensor-processing packages are addressed via the appropriate interface:

- The total station acquires data via GeoCom (Leica, 2013).
- The laser tracker is addressed via the EmScon interface (Hexagon, 2019).
- The move-it package is used for a Universal Robot 5 robot arm (Universal Robotics, 2022).
- The rotation of the plate is adjusted by a dynamixel-stepper motor (ROBOTIS, 2022).

#### B. Measurement campaigns and epochs

A measurement campaign can extend over several measurement epochs, while the instrument's setup will remain. One epoch comprises the analysis of a certain material, which is examined in respect to different IAs.

1) *Laboratory*: The specimens are nearly planar plates, thus, when a certain position on the rotating table is approached, an approximately uniform IA is assumed. As the robotic arm reaches an area of about 40 cm x 40 cm, the plates are shaped alike. The measurement series of an epoch is set in a range from -60 to +60 gon. Turning the specimen, scanning with the TLS and the recording of the Close-Range scanner takes about 8 minutes for each new IA. With angular increments of two gon, 61 IA are examined in total. With such configuration, one epoch takes about 8 hours.

In the laboratory, the distance to the specimen was modified from 7 m to 30 m at times. Respectively the instrument lies inside or outside the convex hull of consoles used for transformation. Still feasible in the laboratory, 30 m was chosen as a typical distance in TLS. The 7-meter arrangement refers to the distances to the aqueduct measured on-site.

2) *On-Site*: Due to the complexity of the setup, the automated point cloud acquisition can only be used in the laboratory. In the outdoor area, however, the environment must be captured manually. For this purpose, a structure was selected as an example for which the very same material is accessible, both, in the laboratory and in the outdoor area. For the historic aqueduct in Mauer, which still ensures Vienna's water supply today; Wien Wasser, the public utility authorities were able to provide the same type of bricks that are being used in ongoing renovation work. The surveyed wall is assembled from two kinds of bricks, which seem to differ only in color. The situation on-site allows a setup that permits observations of geometrically different IAs corresponding to the TLS standpoint.

### III. INVESTIGATIONS UNDER LABORATORY CONDITIONS

In relation to the number of epochs and materials examined, conducting a campaign may take several days to complete. Therefore, climatically stable conditions in the laboratory must prevail. The devices are ideally in uninterrupted operation to avoid heating effects. After each epoch, the specimen is changed and the setup stability is repeatedly verified.

Two major campaigns were carried out in March and August 2021. Up to seven epochs and therefore transformations  $\overline{T}_{[6]}$  were measured. This allows an empirical consideration of the transformation parameter's precision (Table 2).

The translation's standard deviation of the campaign in March is rather high. This might be caused by the poor geometrical choice, as the instrument is located

outside all given console points. This arrangement is a compromise concerning the measuring distance. The results obtained in this way are yet satisfactory in terms of the absolute accuracy of the distance component. In contrast, the standard deviation of the rotation parameter obtained in the August campaign is raised. The network measurements reveal a slight increase of the rotation value between each epoch. An industrial tripod was used to achieve a comparable distance to the on-site measurements. It is less stable compared to the survey pillar used in March and maybe moved marginally. Adding the reported empirical transformation accuracy from Table 2 and the chosen margin of error for pairing, the total impact on  $\Delta d_i$  will be in the range of 0.1 to 0.2 millimeters. In future projects, however, it must be taken care of even more intensively.

Table 2. Standard deviation of transformation parameters

$\mathcal{T}_{[6]}$ - campaign	March 2021	August 2021
Translation $\sigma_x$	71.18 $\mu\text{m}$	16.40 $\mu\text{m}$
Rotation $\sigma_z$	0.15 mgon	1.03 mgon
numb. of. tr.	7	6
convex hull	outside	inside
Distance	30 meter	7 meter
Device	Loan1-MS60	Institute-MS60

#### A. Distance deviations and axis misalignment

Once the acquisition and transformation is completed, the matching of the TLS- and reference-points can be carried out. Furthermore, the IA of the surface can be determined for each pair. At its origin, a flat surface is fitted into the reference point cloud, which corresponds approximately to the size of the laser spot. The orientation of this surface indicates the IA. In the following figures, each individual point represents a single computed distance deviation (as in Figure 3). In close proximity, more than 1000-point pairs are given for any observed IA. The distance comparison is determined in terms of the mean value and its standard deviation.

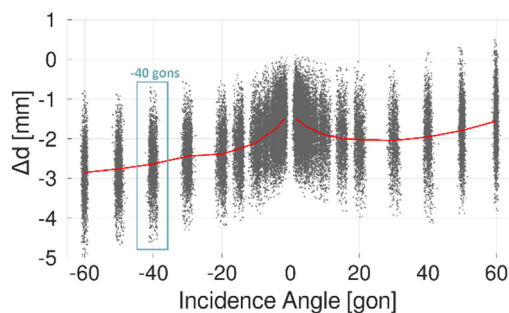


Figure 3. Distance Deviations of smooth granite for several IA (Institute-MS60).

The curve of a smooth granite plate was already examined in previous work and could be reproduced (compare Figure 3 to Linzer *et al.*, 2021). The range of

recorded IA per lineup also represents the limitation of the resolving capability. It depends on the width and curvature of the specimen. For this case, a width of 2 - 3 gon can be accepted. Assuming planarity of the specimen, minor fluctuations will be omitted for the moment. One notes, that with respect to the orthogonal TLS axis, a slight horizontal inclination causes that the 0-gon situation cannot be observed (as in Figure 3). To validate the errors remained as random, the deviations obtained were tested against normal distribution. With the quantity and distribution shown exemplarily in Figure 4, for the IA at -40 gon a mean value of about 2.6 mm can be accepted.

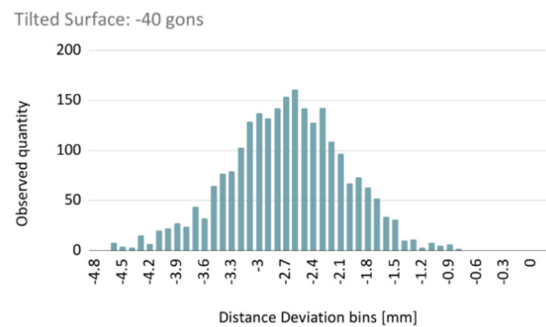


Figure 4. Distance Deviations of smooth granite for several IA (Institute-MS60).

The resulting standard deviation is about 0.6 mm for brick stones and the granite plate alike. This fits approximately the manufacturer's specifications for measurement noise in scanning mode (as in Table 1). The standard deviation of  $\Delta d_i$  when scanning on different materials and IAs can be used to append the gained information to the VCM.

The present trend in the observed space of slightly more than 1 mm can be explained by an existing axis skew of the collimation and distance measurement axis (Zámečníková and Neuner, 2018). Ideally, there should be no such divergence, especially since its influence is growing with increasing distance. Such an axial skew was found for each of the three devices tested so far. The effect occurred both left- and right-skewed and was of varying magnitude. During the investigations of the past two years, it did not occur that this trend changed without external input. Only after a device was sent to the manufacturer for recalibration, it turned out that the collimation had been readjusted, but not fully eliminated. For the Loan2-MS60 device, which was investigated for outdoor use in the upcoming chapter, an influence could be determined which seems to be negligible due to a trend in the sub-millimeter range (Figure 11). To which extent a device shows such a trend can hardly be determined without the implemented methodology. Because the devices measure in only one position of the telescope, such effects are largely obscured in point clouds.

In addition to the smooth granite plate, Figure 5 shows the behavior of a shiny metal plate (blue). The curves have opposite characteristics, yet the reason for

this presence is not comprehensively researched yet. If the laser beam is incident on the smooth granite, the distance is measured about 2 millimeters too long. The ability of laser radiation to penetrate granite can be used as evidence. Specific characteristics can be found around 0 gon IA which must be related to the material properties. However, in the case of a metal plate, it is physically impossible for laser emissions to pass through (Shakelford, 2015). Thus, it appears that the diode might be overloaded by the reflective behavior of the metal plate below an IA with an absolute value of 15 gon. The time interval of the pulsed response could be disturbed. A possible argument for this could be that no measurement data can be obtained in the case of heavy directional reflection. The finding would be somewhat similar to the studies on some round-prisms, where it is also not advisable to target them at their direct angle of reflection (Lackner and Lienhart, 2016).

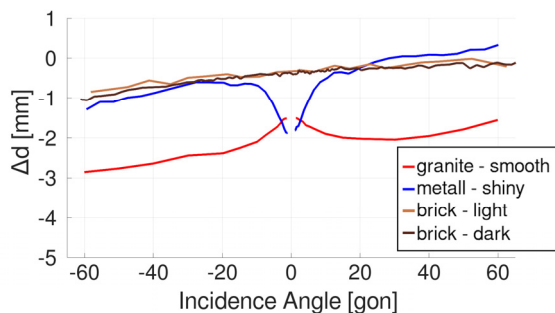


Figure 5. Distance Deviations of four different materials (Institute-MS60).

As the robotized setup is working appropriately, it is a straightforward process to evaluate further materials. To support the relevance of the findings presented, their transferability is examined in Section IV. For comparison, the same dark and light brownish bricks of which the aqueduct is built were brought to the laboratory as specimens. Opposed to granite or metal, both curves of the brick stones show no particular influence (Figure 5).

With such properties, they are particularly well qualified, thus any phenomena that may occur outdoors is not to be confused, in terms of distance deviation. The slightly different trend value might be plausible considering the transformation standard deviation discussed above. However, for some materials, there appears to be no obvious impact with varying IA. Besides, only a constant distance bias has to be reduced.

### B. Absolute Distance Deviation

The trend results from the mechanical misalignment of the collimation and rangefinding axis. To highlight the material-dependent impact, its influence is eliminated by averaging two opposing IAs.

This also allows checking for the repeatability quality of results. The curves from two different devices and campaigns were stacked (Figure 6). These can be

directly compared in the range of one to two tenths of a millimeter. To achieve similarity, the curves of the Loan1-MS60 instrument had to be reduced by an offset of 0.6 mm. Thus, it reveals the possible displacement among devices.

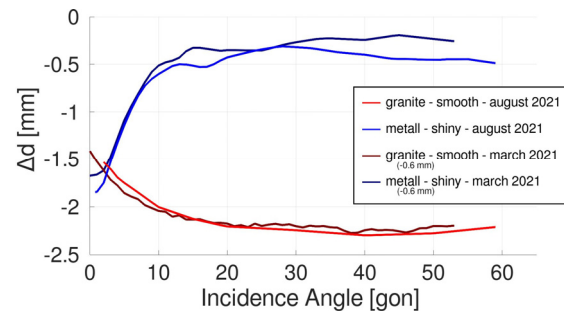


Figure 6. Distance Deviation: Instrument comparison (Institute and Loan1-MS60).

It is evident that an interaction of the laser radiation and the material generates deviations of several millimeters. Of all the materials that have been tested so far, the metal plate and granite stone show the clearest difference in direct comparison and mark the extreme cases according to the current findings. However, the extent to which this result depends on material properties or on the detection-capacity of the device can only be determined once results from any different TLS support these findings.

Figure 7 shows the curve progression of selected materials to illustrate the effects that can be assumed. If a diffuse reflection can be adopted for example due to roughness, occasionally no variation regarding the IA can be detected. This is also true for the observed wooden plate and roughened granite stone, although a possible penetration of the laser radiation could be detected as well. In many cases, applications regard deformations of concrete structures. Conforming our results (yellow-line) for such materials, an IA-specific correction seems negligible.

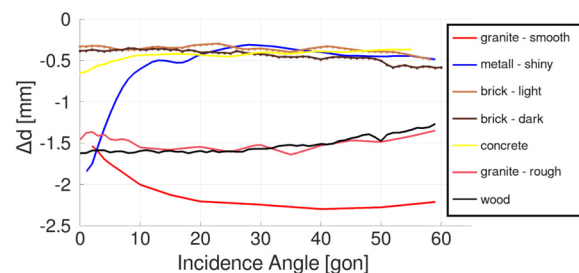


Figure 7. Absolute Distance Deviations of various materials (Institute-MS60).

### C. Intensities

Intensities provide a potential insight into the underlying processes. Differences, such as surface characteristics can be revealed in relation to the IAs observed. Different levels of intensity can also be used to segment the given set of points or to apply a specific accuracy-model as proposed by Wujanz *et al.* (2017).

The distribution of the intensity (Figure 8) reveals a large gradient for the metal plate. However, the smooth granite plate and the measured concrete surface also show such an increase, albeit to a lesser extent. These materials can be assumed “smooth” in an immediate qualitative comparison. When running the fingertips over these materials, no pronounced irregularities can be perceived. Although concrete is similarly recognized as a smooth surface, the variations of the distance deviation is only weakly pronounced. The other materials reveal a pattern that can be attributed to diffuse back radiation. This loosely can be compared to a Lambertian radiator at different levels. Wood shows an increased level, but the overall interpretation remains difficult due to the lack of reference specifications so far.

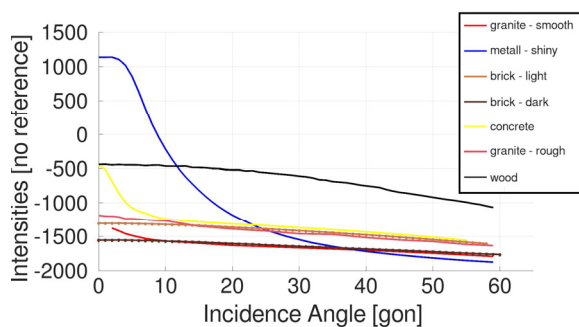


Figure 8. Absolute Intensities of various materials (Institute-MS60).

In the following chapter, the light and dark colored clinker bricks are examined in the field. These can be described as diffuse and not particularly pronounced. Nevertheless, as shown in Figure 8, both brick types can be distinguished based on IA and intensity (dotted lines), which may be relevant for segmentation efforts.

#### IV. PRACTICAL USE UNDER GENUINE CONDITIONS

As in the laboratory, the stability of the instruments used was ensured by multiple  $\mathcal{T}_{[6]}$  network determinations. In addition, a concrete foundation was laid out to stabilize the laser tracker and the values of the circular bubbles of the TLS were monitored. As anticipated accuracy of the transformation, the values of the Monte-Carlo-Simulation from chapter II are to be assumed.

Unlike the empirical assessment, this statement is to be trusted as it is rather difficult to verify. In order to gain reliability, two measuring campaigns were evaluated. Campaign 1 and 2 were measured on 28<sup>th</sup> September and 09<sup>th</sup> November 2021. Figure 9 provides an impression of the conditions on-site. When examining both walls of the aqueduct, the IA is again determined by the orientation of the point cloud itself. Additionally the separation between brick fronts and gaps can be revealed by identifying points that are not part of a planar structure. Once the transformation is applied, the whole TLS point cloud had to be searched to find matching point pairs in the reference (as in

Figure 2). Since both types of bricks adopt very similar values under laboratory conditions, no differentiation was initially made during the on-site evaluation. The determined curves should thus ideally lie within the range of the laboratory examination.



Figure 9. Instrument setup and left wall of aqueduct.

#### A. Campaign 1: Eccentric location, two Devices

Campaign 1 included the investigation of two scanning total stations, Institute- and Loan2-MS60 (Figure 9). Therefore, it allows the results to be reviewed against each other. In order to achieve a high IA, measurements were made eccentrically (Figure 10).

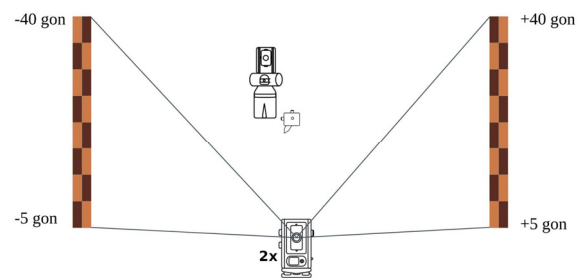


Figure 10. Schematic sketch of the eccentric setup (bird-eye).

1) *Loan2-MS60*: The blue curve from Figure 11 approximates the distance deviations measured on-site. Compared to the laboratory data (brown), the overall data and axis offset could be reproduced. The on-sight and laboratory results of the Loan2-MS60 agree within a range of about one tenth of a millimeter. Furthermore, a similar order of magnitude could be determined for the offset, according to which all distance measurements are overshoot by about 0.8 mm.

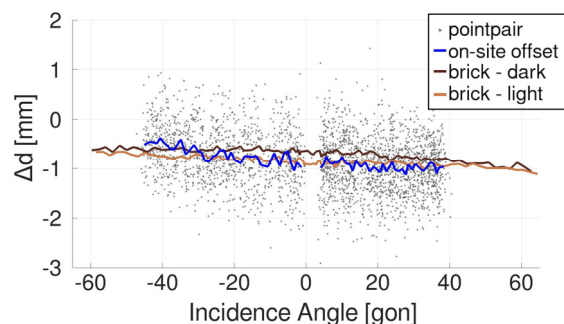


Figure 11. On-site offset compared to laboratory values (Loan2-MS60).

2) *Institute-MS60*: However, a general statement on the transferability is not yet permissible. Figure 12 reveals that it was not possible to obtain consistent data for the Institute-MS60. Therefore, a case distinction from device to device seems necessary. The data with negative IA (respectively the left wall) seems to match the overall deviation, but over the course of IAs, the laboratory examination fits poorly with a residue of about half a millimeter. Possibly, an unexpected and previously unobserved effect is revealed which does not follow any established pattern. In this evaluation, the left and right side of the wall can be clearly distinguished. This may occur as the walls are measured on very distinct parts of the TLS angular encoder.

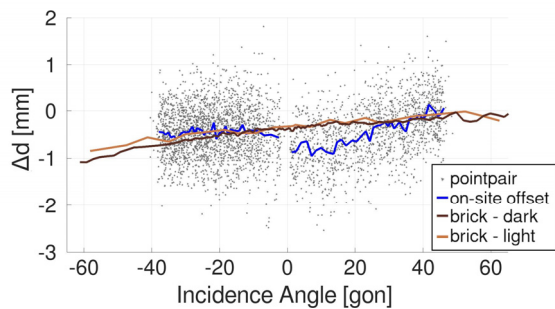


Figure 12. On-site offset compared to laboratory values (Institute-MS60).

### B. Campaign 2: Rerun eccentric measurement

In Campaign 2 the Institute-MS60 was used only, in this case with the walls measured both eccentrically (Figure 10) and centric later on. An identical measurement setup was carried out in order to exclude external influences for the detected phenomenon. As Figure 13 shows, the phenomenon still occurred with similar characteristics. This justifies our finding, which clearly involves an external phenomenon that was out of our scope until yet. Since it is currently too early to identify a clear relationship, the results stand for themselves.

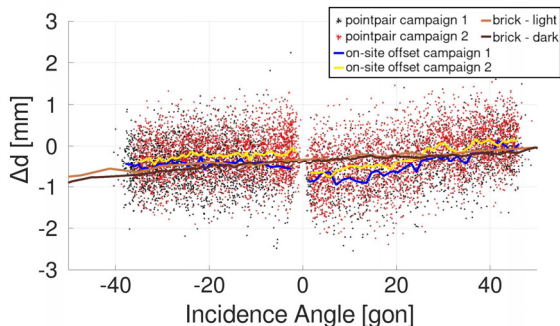


Figure 13. Two On-site offsets compared (Institute-MS60).

### C. Campaign 2: Centric measurement

To gain further knowledge, the measurement setup was altered by placing the TLS right between the walls. This reduces the explorable range of IAs, but with positive and negative IAs respectively occurring on both

walls for another result comparison (Figure 14). Using again the Institute-MS60, much more consistent results were obtained. In Figure 15, both sides of the wall show a progression that can be compared with the laboratory results. This might be because the angle encoder uses a section that covers an area that is not as affected. Thus, before a judgment can be made about its origin, we are seeking further investigations to determine its cause. For this purpose, a measurement setup is beneficial where the procedure can be realized over the full span of the angle encoder.

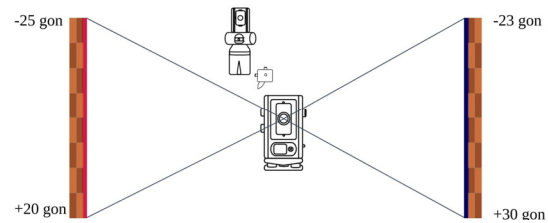


Figure 14. Schematic sketch of the centric setup, (bird-eye) (Institute-MS60 only).

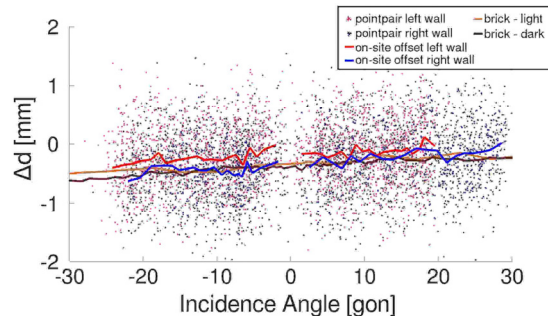


Figure 15. Centric setup: two walls offset comparison (Institute-MS60).

### D. Campaign 2: Centric measurement intensities

A view on the intensities reveals another interesting aspect (Figure 16). Dark and light brown bricks can be distinguished based on intensity and IA. The range of light brown bricks is measured with an intensity roughly above -1400. Segmentation would be promising, since the areas overlap only marginally. However, the distance to both sides of the wall (blue and reddish) is approximately the same, yet there is a difference in the reflectance of about 200 units. These findings correspond to the laboratory examination, which matches regarding the characteristic, but not in terms of given magnitude. It must be noted that these intensity variations are as large as would be expected if the range to the object were shifted. Further investigations are necessary to clarify why these anomalies occur.

## V. CONCLUSION

In a larger context, the present findings reveal that the inclusion of systematic distance deviation is crucial for TLS-driven deformation analysis. With regard to the material, millimeter accuracies can only be achieved if IA-dependent influences are taken into account.

Furthermore, the method makes it possible to detect the potential axis skew of the collimation and rangefinding axis.

The migration from the laboratory to the exterior is in agreement according to the values and characteristics observed. Moreover, a previously unrecognized phenomenon has been revealed and it is yet to be investigated how it relates to the deviation. As a first indication, the field-of-view and accordingly the angular encoder-usage differ between the inside and outside setup. Due to the narrow observation angle, with respect to the specimen in the laboratory, the mismatch had not been visible so far. It is of particular relevance that only for the Institute-MS60 such influences were uncovered.

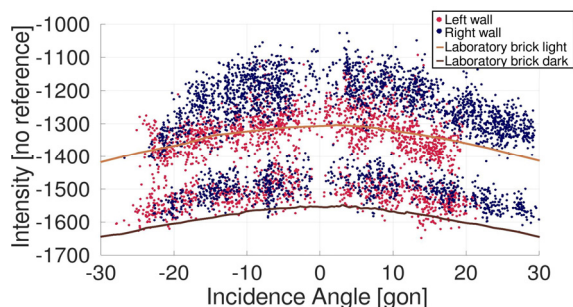


Figure 16. Centric setup: brick intensity comparison, campaign 2 (Institute-MS60).

Following up, the implementation of different types of TLS is planned. This poses a challenge in terms of the achievable transformation accuracy. Conventional 3D laser scanners cannot be positioned in the lower submillimeter range using current methods. It is beneficial that a recent paper by Janßen *et al.* (2021) indicates that the complete potential is not yet exploited. Taking not only the center of the targets but also their orientation into the registration adjustment is a step into the right direction.

In addition, a TLS that also includes the impulse answer would be of further interest. This could be used to uncover current questions about material dependences. The aim is to define more claims in a context that has general validity for laser radiation and its backscattering characteristics. In the next step, many more measurements are to be performed in a structured manner in order to make a statement about the roughness or the penetration effects. The robotized setup will support these efforts.

## VI. ACKNOWLEDGEMENTS

We would like to thank Wien Wasser MA31 for their kind support and Leica Austria for the loaning of two MS60 TLS.

## References

Hexagon (2019). emScon Reference Manual. Hexagon AB <https://support.hexagonmi.com/s/article/What-is-emScon> (retrieved 31.01.2022).

Janßen, J., Kuhlmann, H., and Holst, C. (2021). Target-based terrestrial laser scan registration extended by target orientation. *J. Appl. Geodesy*. (ahead of print). DOI: 10.1515/jag-2020-0030

Kerekes, G., and Schwieger, V. (2020). Elementary Error Model Applied to Terrestrial Laser Scanning Measurements: Study Case Arch Dam Kops. *Mathematics*. 2020; 8(4):593. DOI: 10.3390/math8040593

Lackner, S., and Lienhart, W. (2016). Impact of Prism Type and Prism Orientation on the Accuracy of Automated Total Station Measurements. Proceedings of the *Joint International Symposium on Deformation Monitoring (JISDM)*, Vienna, Austria, 30 March–1 April 2016.

Leica (2013). GeoCOM Reference Manual. Leica Geosystems Heerbrugg (Switzerland).

Linzer, F., Barnefske, E., and Sternberg, H. (2019). Robot Operating System zur Steuerung eines Modulare Mobile-Mapping-Systems – Aufbau, Validierung und Anwendung. (peer-reviewed) avn Ausgabe 126 1-2, Wichmann Verlag im VDE VERLAG GMBH, Berlin.

Linzer F., Papčová M., and Neuner H. (2021). Quantification of Systematic Distance Deviations for Scanning Total Stations Using Robotic Applications. In: Kopáček A., Kyrinovič P., Erdélyi J., Paar R., Marendić A. (eds) *Contributions to International Conferences on Engineering Surveying. Springer Proceedings in Earth and Environmental Sciences*. Springer. DOI: 10.1007/978-3-030-51953-7\_8

Rejchrt, D., Thalmann, T., Ettliger, A., and Neuner, H. (2019). Robot Operating System – A Modular and Flexible Framework for Geodetic Multi-Sensor Systems. avn Ausgabe 6-7, Wichmann Verlag-VDE VERLAG GMBH, Berlin.

ROBOTIS (2022). ROBOTIS Dynamixel SDK (Protocol1.0/2.0) [http://wiki.ros.org/dynamixel\\_sdk](http://wiki.ros.org/dynamixel_sdk) (retrieved 31.01.2022)

Schmitz, B., Kuhlmann, H., and Holst, C., (2021). Deformation analysis of a reference wall towards the uncertainty investigation of terrestrial laser scanners. *J. Appl. Geodesy* 15 (3), pp. 189–206.

Shackelford, J.F. (2015). *Introduction to Materials Science for Engineers*. Pearson Education Limited. University of California, Davis.

Soudarissanane, S.S. (2016). *The Geometry of Terrestrial Laser Scanning-identification of Errors, Modeling and Mitigation of Scanning Geometry*. Ph.D. Thesis, Technical University of Delft, The Netherlands.

Universal Robots (2022). Universal\_Robots\_ROS\_Driver. [http://wiki.ros.org/ur\\_robot\\_driver](http://wiki.ros.org/ur_robot_driver) (retrieved 31.01.2022)

Wujanz, D., Burger, M., Mettenleiter, M., and Neitzel, F. (2017). An intensity-based stochastic model for terrestrial laser scanners. *ISPRS Journal of Photogrammetry and Remote Sensing*, 125, pp. 146-155.

Zámečníková, M., Wieser, A., Woschitz, H., and Ressler, C. (2014). Influence of surface reflectivity on reflectorless electronic distance measurement and terrestrial laser scanning. *Journal of Applied Geodesy*, 8(4), pp. 311-326.

Zámečníková, M., and Neuner, H. (2018). Methods for quantification of systematic distance deviations under incidence angle with scanning total stations. *ISPRS Journal of Photogrammetry and Remote Sensing*, 144, pp. 268 - 284.



## Identifying individual rocks within laser scans for a rigorous deformation analysis of water dams

Wolfgang Wiedemann, Christoph Holst

Chair of Engineering Geodesy, School of Engineering and Design, Technical University of Munich, 80333 München, Germany, ([w.wiedemann@tum.de](mailto:w.wiedemann@tum.de); [christoph.holst@tum.de](mailto:christoph.holst@tum.de))

**Key words:** *terrestrial laser scanning; point cloud segmentation; deformation monitoring; water dam*

### ABSTRACT

Water dams are an important infrastructure component for energy generation, water supply and flood control. Regular inspections of the structures for damage and deformation are necessary for safe operation and to ensure stability. In addition to the traditional concepts of geodetic network measurement, laser scan data can be used to deliver areal information on deformation. Within this topic, we aim at developing a method that identifies individual rocks of dam walls within the laser scans to introduce them as identical feature points for a rigorous deformation analysis. For this purpose, it is necessary to identify the solid stone surfaces on the water dams from scan data, and separated them from vegetation and joints. In this paper, we investigate method for identification of individual stones on gravity dams made of rubble stones. For the segmentation, the intensity values, RGB color information and local geometric structure from textured point clouds acquired with Terrestrial Laser Scanners are investigated. The classification should be robust against outer measurement conditions and provide sharp object boundaries. Our results show that – although many different methods are available – a reliable classification of single rubble stones is still a challenge task.

### I. INTRODUCTION

In today's society, dams and barrages have become indispensable infrastructure components with a wide range of benefits. Among other things, they make an important contribution to the generation of electrical energy, ensure the water supply for the population (both as drinking water and as water for agriculture) and enable waterways to be made navigable. They are also an important component of flood protection and flood management. Finally yet importantly, they also play an important role in the field of leisure and tourism (BMU / UBA, 2017).

According to the international dam register of International Commission On Large Dams (ICOLD), there are 371 large dams in Germany alone (Deutsches Talsperren Komitee e. V., 2013). The category of "large dams" includes dams if either the height of the dam structure from the lowest point of the foundation to the top of the structure is 15 m or more, or in the case of smaller dam structures (height between 5 m and 15 m), the dam capacity is more than 3 million cubic meters of water. In addition to those large dams, there are a very large number of smaller structures such as dams and reservoirs, retention basin basins.

In order to guarantee the safe operation and stability of these structures, these dams and reservoirs must undergo regular inspections and monitoring measurements. In addition to permanent sensors such as plumb bobs, inclinometers, extensometers, joint gap measurements, strain gauges, pressure gauges, seepage water measuring points, etc., which are permanently installed in the dam, these also include

geodetic measuring methods. Here, traditionally, levelling, tacheometric measurements and GNSS networks are used to build up a geodetic measurement network (Möser *et al.*, 2013). Even if those networks are highly accurate and allow a rigorous deformation analysis with statistical determined statements on significance of changes between the epochs, they have one big disadvantage: the low number of control point. Thus, a deformation of the structure is only be detectable if on measurement point is representative for the deformation (generalization problem). Deformations that occur between the individual points of the monitoring network cannot be detected and might be overlooked or can only be detected proportionally (Pelzer, 1985).

To overcome those gaps in the monitoring networks, different measuring procedures and methods for an aerial deformation monitoring are investigated and under development for several years. In addition to remote sensing methods (*e.g.*, Milillo *et al.*, 2016; or Di Martire *et al.*, 2014), ground-based SAR (*e.g.* Scaioni *et al.*, 2018; or Huang *et al.*, 2017), and purely photogrammetric approaches (*e.g.* Buffi *et al.*, 2017), 3D terrestrial laser scanning (TLS) have become established in engineering geodesy for areal detection of deformations on dams (see Section IA). The advanced technology of 3D scanners hardware allows nowadays – even objects in the size of a dam wall - to be captured very accurately and in a short time. Beside a dense point cloud, image information (RGB) and the intensity of the reflected laser point can be acquired.

The obtained 3D point clouds can then be examined for deformations.

The following Section I A provides a brief overview of common deformation analysis methods, and in Section I B, the targeted approach for a feature-based method for shallow deformation analysis of dams with rubble stone surface.

#### A. Deformation monitoring with TLS point clouds

For the derivation of areal deformations from TLS point clouds, different methods have been developed in recent years and have been verified on dam structures. The methods can be divided in five classes (Ohlmann-Lauber and Schäfer, 2011): “point based strategies” (e.g. Schäfer *et al.*, 2004), “point cloud based methods”, “surface based methods” (e.g. Alba *et al.*, 2006), “geometry based methods” (e.g. Grimm-Pitzinger and Rudig, 2005) or González-Aguilera *et al.* (2008), and “parameter based procedures” (e.g. Eling, 2009).

For natural objects whose exact target geometry is unknown, mostly point cloud-based methods or surface based methods are used, *i.e.* cloud-to-cloud, cloud-to-mesh or model-to-model computation methods are used to derive the distances between two point clouds. Some of these methods have already been performed on dams (compare Holst *et al.*, 2017a & Holst *et al.*, 2017b).

The results of that deformation analysis are usually color-coded point clouds or vector fields, which are supposed to illustrate the deformation. However, these methods of calculating and illustrating deformations are challenging to interpret and have the disadvantage, that no statistical analysis of the results for significance can be performed precisely because a lack of identical points and unknown stochastic accuracy models of the laser scanners (Wunderlich *et al.*, 2016). Due to the system, slightly different object points are appropriate at each epoch in TLS, so that no direct point-to-point assignment between individual scans is possible, as in classical network measurements. Additionally, due to the lack of identical points, those methods are not sensitive to in-plane movements and are most sensitive to movements in line of site of the laser scanner.

Likewise, iterative closest point (ICP) based approaches can be used for deformation monitoring (Chmelina *et al.*, 2012; Wujanz *et al.*, 2014). Here, small patches of the point clouds are matched between the individual temporal epochs. The determined transformation parameters can then be used to infer any deformations. Due to the low sensitivity for in-plane movements and the danger of snapping into local minimums, the ICP method is not suitable for all objects, depending on their shape and the expected class of deformations (rigid body movement or shape change).

Another point cloud based method for deformation monitoring is identifying identical (artificially) points, described with a feature vector derived from the point

clouds (for example 3D-SIFT, Scovanner *et al.*, 2007; PPFH, Rusu *et al.*, 2009; or learned features, Deng *et al.*, 2018; Gojic *et al.*, 2019). That feature descriptors can be matched between different monitoring epochs and a deformation vector can be directly calculated by the differences of the feature key points.

#### B. Aim of this work

Because dams have to undergo regular monitoring measurements to ensure their stability, it is worthwhile to look for automatable solutions for an areal deformation analysis. In order not to miss movements perpendicular to the surface of the structure, a feature-based deformation analysis method should be developed. As revealed in our previous research on feature-based deformation monitoring (Wiedemann *et al.*, 2017), the extraction and matching of feature descriptors proves to be difficult on a global level. Thus, we aim to reduce the search space for identical points on the object.

In our case study with two water dams clad with rubble stones (see Section II), we plan to generate a stone cadaster as proposed in Holst (2019), clustering a bounded subset of points for every single stone, as a first step towards a feature-based deformation monitoring. The regions of the different stones should be segmented automatically from the RGB-colored TLS point clouds. This pre-segmentation of solid stone faces, as regions where a pure rigid body motion and no shape change is expected, helps to reduce the search space and lead to more stable feature descriptors. It is also intended to avoid incorrect assignments during the feature matching and time-consuming filtering of those outliers. Depending on which feature type is selected for the subsequent deformation analysis - here, for example, the center of gravity of the object, the point of the strongest curvature, etc. could be used - the segmentation must be carried out reliably and with clear object boundaries. In order to achieve this, the first step is to label the individual points of the point cloud according to their object type. Subsequently, in a second step, the classified points need to be merged into groups of points of individual stones.

In the following, different possibilities and approaches for the classification and point labeling process for 3D point clouds are discussed and evaluated for their suitability based on the collected measurement data.

## II. OBJECT OF INVESTIGATION & MEASUREMENT DATA

For our analysis, the point clouds of two water dams - the Brucher dam and the Jubach dam, both in the state of North Rhine-Westphalia, Germany - were scanned. The investigated structures are gravity dams, which are clad with rubble stones (greywacke stones) on the air side (see. Figure 1). The crown length is about 200 m for the Brucher dam and 140 m for the Jubach dam, with a maximum height of approximately 25 m both.



Figure 1. Impression of the Jubach dam, showing the challenging weather conditions.

The two investigated objects are a widely spread construction form of gravity dams in Germany. Many of these walls go back to the civil engineer Prof. Otto Intze, who built more than 40 dams of the same or similar design at the turn of the 20th century, of which most are still in operation today.

The walls have a  $\sim 2$  m high vertical part under the dams crown, and then spread to its base in a slight curve, leading to an inclination of  $\sim 55^\circ - 65^\circ$  at the food of the wall. These quite flat lower parts, are strongly exposed to rain and favors the growth of vegetation in the form of moss, grass and even small bushes.

The rubble stones, which are mostly only roughly hewn, show almost natural structures on their surface and are connected with grout joints. The stones vary in size, shape and color over the scenes. The masonry wall also does not have a clear topology. The bricks can both protrude from the mortar joints, and come to lie behind them (see Figure 2). The joint width also varies in size structure and color.

The point cloud of the dams are taken under ordinary realistic conditions (foggy weather and drizzling rain) using a Leica ScanStation P50 with high spatial resolution ( $1.6 \text{ mm}@10 \text{ m}$ ) from one station approximately in the center of each the wall. Thus, the resolution of the point cloud on the dam surface is

approximately 3.5 mm in the center of the wall (closest range to the scanner) and approximately 14 mm in the outer areas. During data acquisition, panoramic images are captured with the scanner's integrated camera system to texture the point clouds with RGB color (see Figure 3).



Figure 2. Challenging structure for geometric features as stone and joins have very similar surface characteristics and no clear topology.

### III. INVESTIGATION OF DIFFERENT CLASSIFICATION METHODS

As mentioned above, the aim of this work is to separate as much solid rock areas on the wall as possible from the disturbing background, such as joints, vegetation or other attachments. For the segmentation procedure, there are essentially two different types of information available in the point clouds:

- A. Radiometric information.
- B. Geometric information.

These two types of information will now be examined in more detail and analyzed how they can contribute to robust segmentation of single stone surfaces in the 3D point clouds.

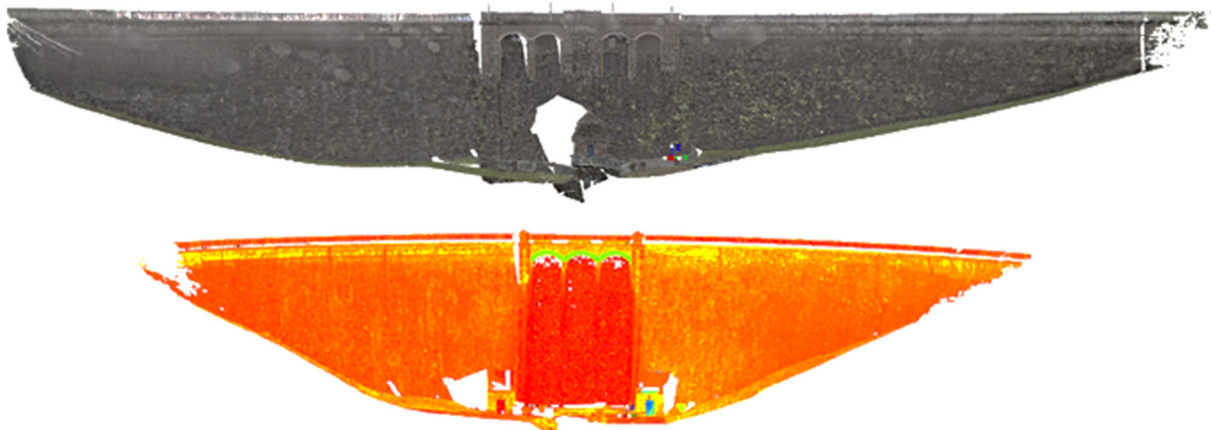


Figure 3. RGB-colored point cloud of Burcher dam (top), point cloud colored by raw intensities of Jubach dam (bottom).

### A. Radiometric information

Laser scanners provide not only the 3D coordinates of the point cloud, but also radiometric information to the user. In general, the intensity of each reflected laser spot is recorded during the measurement. As the used scanner is equipped with an internal camera, also color information from panoramic images can be projected to the point cloud without shadowing or parallax effects. Therefore, every point has additional RGB color information.

1) *Intensity-Information*: As stated above, modern laser scanners store an intensity value in addition to the measured coordinates for every point. The intensity indicates how much of the emitted laser light is reflected from the object back to the laser scanner and detected. The raw intensities depend on the material properties, the color and the surface structure of the object, as well as the angle of incidence of the laser beam, the measuring distance and the laser wavelength used (Wujanz *et al.*, 2018).

A previous work as shown, that in certain parts of the wall, with a distinct joint pattern, regular structure and a dry wall condition, stones can be segmented using intensity values. For that in Steffens (2020), the k-mean algorithm (Lloyd, 1982) is used to divide the point cloud into two classes based on their intensity. In a further step, the DBSCAN algorithm (Ester *et al.*, 1996) is used to cluster the points labeled as stone to groups of individual stones segments.

With this method, precision values of ~80-95 % can be achieved (percentage of points classified as stone, which are also stones in reality). However, only recall values (number of real stones which are identified by the algorithm) of ~49-70 % are achieved (compare Steffens, 2020).

Similar approaches performed by us show that the accuracy of the segmentation based on the intensity values decreases rapidly if the wall is not scanned under optimal conditions. In particular, moisture on the wall will worsen the result. This is mainly attributed due to the wavelength of the laser scanner used. The Leica ScanStation P50 – like most other TLS systems – uses a laser source in the near infrared spectrum (often 1550 nm) as they are usually eye-safe. However, laser light in the near infrared spectrum is highly absorbed by water, so that the intensity is strongly reduced by humidity or accumulating wetness on the wall (Wojtanowski *et al.*, 2014). As a result, objects that show differences in intensity in dry state, have an almost identical, very low intensity value when they are wet (see Figure 4).

As a result, in this case study dataset, a segmentation by intensity is only possible in a small dry part of the dam. On the wet parts, an assignment of the categories "stone" or "joint" by the k-mean algorithm is no longer possible, even if the class boundaries are adjusted to the local environment. The variation in intensity

between is too small to distinguish the two object classes precisely (see Figure 5). Small-scale changes in intensity are more likely to be linked to differences in the incident angle of the laser beam or the humidity, and cannot be attributed to the structural characteristics of the wall.

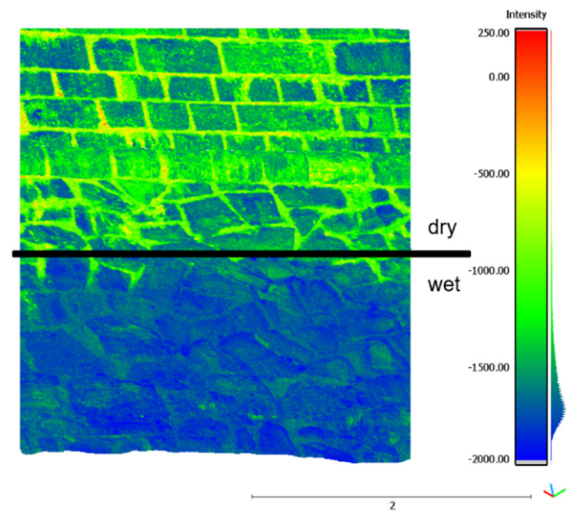


Figure 4. Distribution of intensity values: dry upper part and lower wet part of the wall.

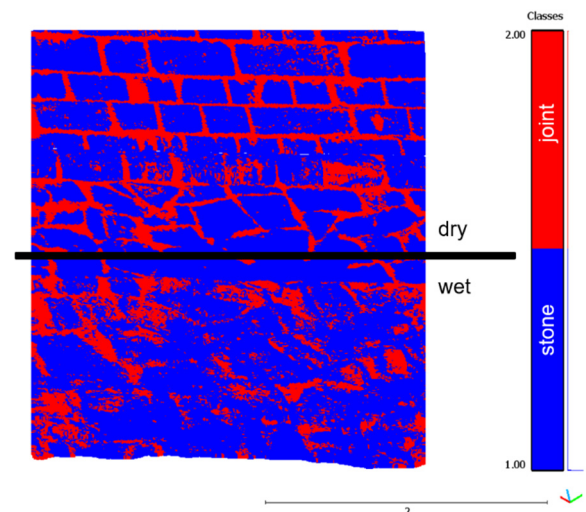


Figure 5. Results of the k-mean classification based on the intensity: acceptable results in dry areas (upper part) and insufficient results wet parts (lower part) of the dam.

2) *RGB-Information*: For a classification with respect to the RGB colors, or gray scale images derived from them, a wide range of functions from the image processing domain can be used (Gauch and Hsia, 1992; Valero *et al.*, 2018; Wang *et al.*, 2014) for 2D images. These images can be obtained from the raw camera data of the scanner, or by projecting the RGB values of point cloud onto an artificial image plane. After a classification, the derived classes must then be projected back into the point clouds to generate labels for the individual points. For a segmentation directly in the 3D point cloud, color-based region-growing algorithms can be applied (Zhana *et al.*, 2009).

In general, RGB segmentation is a promising method for scenes wherein the object's color differs

significantly from the background. For our outdoor scenes, this does not apply. A closer look to the color information reveals the following: Firstly, the colors of the stone surface and the joints are very similar, so that no general color value can be assigned to the different object classes. Secondly, local color changes are often not lined up with the structural characteristic, but are more related to the current illumination conditions, shadowing effects and the state (dry/wet) of the local surface. Also, mineral efflorescence disturbs the color pattern. In summary, it cannot be assumed that the color information can contribute to a reliable segmentation (see Figure 6).



Figure 6. Typical section of the RGB textured point cloud. Only slight differences between joint and stones are visible, mineral efflorescence disturbs the joint pattern.

In addition, several general disadvantages must be taken into account for this kind of information. As a passive sensor captures the RGB information, the color impression and brightness is highly depending on current external illumination condition.

### B. Geometric information

Geometric statements about the local structure of the point cloud can be calculated by observing the neighborhoods of a core point. Such derived geometric features can be for example the linearity, planarity, curvature, point density, roughness, normal direction, omnivariance, spherically, eigenentropy, etc. and are well described in the literature (e.g. Weinmann *et al.*, 2014; or Hackel *et al.*, 2016). Such features can serve as input for a subsequent classification if the object classes can be separated in the feature space.

Methods proposed in the literature (specifically Brodu and Lague, 2012, CANUPO-algorithm and Weinmann *et al.*, 2017) for a proper selection of neighborhood size, for feature calculation and the assessment of relevant features, haven't provided meaningful results in this case study. Other supervised classification methods like SVM, nearest neighbor, and design trees – which can be trained with the Matlab classification toolbox by manual labeled data – do not provide clear class assignment to the precisely

calculated geometrical features. A closer look to distribution of the calculated geometrical features show, that they are very similar for both object classes 'stone' and 'joint' (see Figure 7).

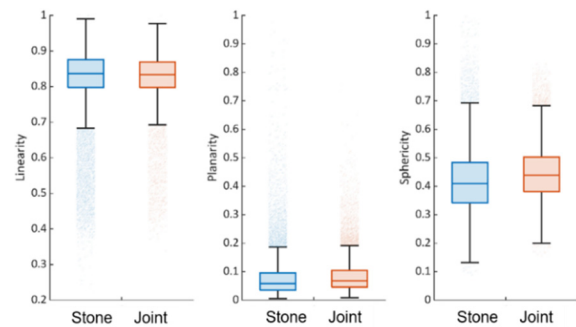


Figure 7. Three exemplary geometrical features (linearity, planarity, spherically (left to right)) showing very similar distributions for both object classes (stone/joint).

The unfavorable combination of the low resolution of the point cloud relative to a very little surface change, the unclear topology between joints and stones (see Figure 3) cause that the determined geometric descriptors cannot be reliably assigned to the object classes.

A different approach based on the use of local geometry can be applied, if the objects to be segmented are distinct clearly from the background. Then, the computed distance of the point cloud to a previously estimated control geometry can be used for segmentation (see Figure 8). In this case study, this procedure is suitable in the upper part of the dam, which is very evenly masoned and has clearly separated of individual stones by joints (see Figure 8).

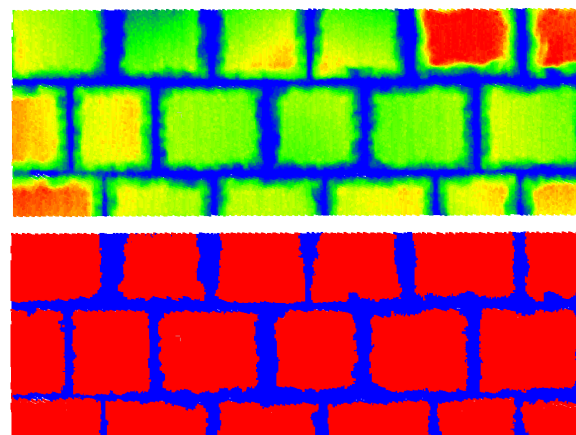


Figure 8. Depth map for segmentation- top: depth map, bottom: segmentation result with threshold method.

Using a best-fit plane as a reference geometry, a depth map can be obtained by calculating the perpendicular distance between the point cloud and the plane. For the segmentation of the stones in this area, a simple threshold method for the reliable segmentation is sufficient. Since the dam is curved

along its longitudinal axis, only the estimation of the plane must be continuously adjusted.

However, in regions where the stones do not stick out above the joints, this method fails completely. Likewise, vegetation, which protrudes above the wall, is added to the class stone.

For fixed geometries, *e.g.* planes, also region growing methods can be used (Ötsch, 2021). In this case, the adjacent points are added to a seed point until a threshold value for a local geometric descriptor is exceeded. Due to the irregular stone shapes and the uneven surfaces, this method cannot be used successfully at the investigated dams.

#### IV. CONCLUSION

As a pre-segmentation of a follow-up feature-based deformation analysis, the surfaces of individual stones should be identified in the point clouds of rubble stone water dams. This should simplify the calculation of the final features and stabilize the matching. In this case study, different segmentation methods were investigated on the TLS point clouds of two water dams built of rubble stones, which were scanned under challenging weather conditions. In this point clouds, all included information types – RGB colors, intensity and the intrinsic geometry of the point cloud – were examined for their suitability for a segmentation approach.

We found, that under challenging, but ordinary weather conditions with wet object surfaces, radiometric information can only contribute to the segmentation to a limited extent. On the mostly wet surface, differences in RGB color and intensity are too low to distinguish between solid stone faces from other objects reliable. In dry areas, a classification based on intensity values seems a promising strategy but is often interfered by efflorescence of the joint material leading misclassification in these areas.

The two investigated classification methods based on the point clouds geometries show different results at our test sides. The feature-based approach fails because the complicated, unstructured wall offers too few distinguishable geometrical characteristics between stones and joints. This is mainly due to the distance-related poor resolution of the point clouds in comparison with the little surface undulations. Thus, the distribution of the feature values are practically identical in the hole point cloud. However, segmentation results from locally computed depth maps with respect to best fitting geometries are suitable for well-structured parts of the scanned wall, even if in large part the complicated structural shape of the walls surface also prevents this classification approach.

In summary, the data we have collected show that the investigated segmentation procedures described in the literature are not sufficient to perform a reliable

segmentation in all areas of the investigated rubble stone dams.

#### References

- Alba, M., L. Fregonese, F. Prandi, M. Scaioni, and P. Valgoi, (2006). Structural monitoring of a large dam by terrestrial laser scanning. *International Archives of Photogrammetry, Remote Sensing and Spatial Information Sciences*, Vol. 35, No. 5.
- BMU / UBA (ed.) (2017). *Wasserwirtschaft in Deutschland. Grundlagen, Belastungen, Maßnahmen*. Dessau-Roßlau: Umweltbundesamt.
- Brodu, N., and D. Lague (2012). 3D terrestrial lidar data classification of complex natural scenes using a multi-scale dimensionality criterion: Applications in geomorphology. *ISPRS Journal of Photogrammetry and Remote Sensing*, Vol. 68, pp. 121-134.
- Buffi, G., P. Manciola, S. Grassi, M. Barberini, and A. Gambi (2017). Survey of the Ridracoli Dam: UAV-based photogrammetry and traditional topographic techniques in the inspection of vertical structures. *Geomatics, Natural Hazards and Risk*, Vol. 8, No. 2, pp. 1562-1579.
- Chmelina, K., J. Jansa, G. Hesina, and C. Traxler (2012). A 3-d laser scanning system and scan data processing method for the monitoring of tunnel deformations. *Journal of Applied Geodesy*, Vol. 6, 3-4, pp. 177-185.
- Deng, H., T. Birdal, and S. Ilic, (2018). PPF-FoldNet: Unsupervised Learning of Rotation Invariant 3D Local Descriptors. In: *Computer Vision – ECCV 2018*. Cham, pp. 620-638.
- Deutsches Talsperren Komitee e. V. (2013). *Talsperren in Deutschland*. Wiesbaden: Springer Fachmedien Wiesbaden.
- Di Martire, D., R. Iglesias, D. Monells, G. Centolanza, S. Sica, M. Ramondini, L. Pagano, J. J. Mallorquí, and D. Calcaterra (2014). Comparison between Differential SAR interferometry and ground measurements data in the displacement monitoring of the earth-dam of Conza della Campania (Italy). *Remote Sensing of Environment*, Vol. 148, pp. 58-69.
- Eling, D. (2009). *Terrestrisches Laserscanning für die Bauwerksüberwachung*. In: *Veröffentlichungen der DGK (Deutsch Geodätische Kommission), Reihe C - Dissertationen, Nr. 641*.
- Ester, M., H.-P. Kriegel, J. Sander, and X. Xu (1996). A density-based algorithm for discovering clusters in large spatial databases with noise. In: *Proceedings of the Second International Conference on Knowledge Discovery and Data Mining (KDD-96)*, pp. 226-231.
- Gauch, J. M., and C. W. Hsia (1992). Comparison of three-color image segmentation algorithms in four color spaces. In: *Visual Communications and Image Processing '92*, Boston, MA, Sunday 15 November 1992, pp. 1168-1181.
- Gojcic, Z., C. Zhou, J. D. Wegner, and A. Wieser (2019). The Perfect Match: 3D Point Cloud Matching With Smoothed Densities. In: *2019 IEEE/CVF Conference on Computer Vision and Pattern Recognition (CVPR)*, Long Beach, CA, USA, Jun. 15-20, 2019, pp. 5540-5549.
- González-Aguilera, D., J. Gómez-Lahoz, and J. Sánchez (2008). *A New Approach for Structural Monitoring of Large Dams*

- with a Three-Dimensional Laser Scanner. *Sensors* (Basel, Switzerland), Vol. 8, No. 9, pp. 5866-5883.
- Grimm-Pitzinger, A., and S. Rudig (2005). Freiformflächen zur Modellierung von Deformationsmessungen. *ZfV-Zeitschrift für Geodäsie, Geoinformation und Landmanagement*, Vol. 130, No. 3, pp. 180-183.
- Hackel, T., J. D. Wegner, and K. Schindler (2016). Contour Detection in Unstructured 3D Point Clouds. In: *2016 IEEE Conference on Computer Vision and Pattern Recognition (CVPR)*, Las Vegas, NV, USA, Jun. 27-30, 2016, pp. 1610-1618.
- Holst, C., B. Schmitz, A. Schraven, and H. Kuhlmann (2017a). Eignen sich in Standardsoftware implementierte Punktwolkenvergleiche zur flächenhaften Deformationsanalyse von Bauwerken? Eine Fallstudie anhand von Laserscans einer Holzplatte und einer Staumauer. *ZfV-Zeitschrift für Geodäsie, Geoinformation und Landmanagement*, Vol. 142, No. 2, pp. 98-110.
- Holst, C., L. Klingbeil, F. Esser, and H. Kuhlmann (2017b). Using point cloud comparisons for revealing deformations of natural and artificial objects. In: *7<sup>th</sup> International Conference on Engineering Surveying (INGEO)*, Lisbon, Portugal, 8-20 October 2017.
- Holst, C. (2019). Terrestrisches Laserscanning 2019: Von großen Chancen, großen Herausforderungen und großen Radioteleskopen. *ZfV-Zeitschrift für Geodäsie, Geoinformation und Landmanagement*, Vol. 144, No. 2, pp. 94-108.
- Huang, Q., G. Luzi, O. Monserrat, and M. Crosetto (2017). Ground-based synthetic aperture radar interferometry for deformation monitoring: a case study at Geheyan Dam, China. *Journal of Applied Remote Sensing*, Vol. 11, No. 03, 036030.
- Lloyd, S. (1982). Least squares quantization in PCM. *IEEE Transactions on Information Theory*, Vol. 28, No. 2, pp. 129-137.
- Milillo, P., D. Perissin, J. T. Salzer, P. Lundgren, G. Lacava, G. Milillo, and C. Serio (2016). Monitoring dam structural health from space: Insights from novel InSAR techniques and multi-parametric modeling applied to the Pertusillo dam Basilicata, Italy. *International Journal of Applied Earth Observation and Geoinformation*, Vol. 52, November (4), pp. 221-229.
- Möser, M., Müller, G. and Schlemmer, H. (eds) (2013). Auswertung geodätischer Überwachungsmessungen. Berlin: Wichmann.
- Ohlmann-Lauber, J., and T. Schäfer (2011). Ansätze zur Ableitung von Deformationen aus TLS-Daten. In: *Terrestrisches Laserscanning - TLS 2011 mit TLS-Challenge*, pp. 147-157.
- Ötsch, E. (2021). *Modellierung der Deformationen von Mauerwerkstrukturen aus terrestrischen Laserscans*. Diploma Thesis. Technische Universität Wien.
- Pelzer, H. (ed.) (1985). *Geodätische Netze in Landes- und Ingenieurvermessung, Band 2, Vorträge des Kontaktstudiums 1985*. Stuttgart: Wittwer.
- Rusu, R. B., N. Blodow, and M. Beetz (2009). Fast Point Feature Histograms (FPFH) for 3D registration. In: *2009 IEEE International Conference on Robotics and Automation*, Kobe, May 12-17, 2009, pp. 3212-3217.
- Scaioni, M., M. Marsella, M. Crosetto, V. Tornatore, and J. Wang (2018). Geodetic and Remote-Sensing Sensors for Dam Deformation Monitoring. *Sensors* (Basel, Switzerland), Vol. 18, No. 11, 3682.
- Schäfer, T., T. Weber, P. Kyrinovič, and M. Zámečniková (2004). Deformation Measurement Using Terrestrial Laser Scanning at the Hydropower Station of Gabčíkovo. In: *INGEO 2004 and FIG Regional Central and Eastern European Conference on Engineering Surveying*.
- Scovanner, P., S. Ali, and M. Shah (2007). A 3-dimensional sift descriptor and its application to action recognition. In: *Proceedings of the 15<sup>th</sup> international conference on Multimedia - MULTIMEDIA '07*, Augsburg, Germany, Sep. 24-29, 2007, pp. 357-360.
- Steffens, R. (2020). *Laserscanbasierte Deformationsanalyse einer Staumauer auf Basis eines Kongruenztests identischer Mauersteine*. Master's Thesis. Rheinischen Friedrich-Wilhelms-Universität Bonn.
- Valero, E., F. Bosché, and A. Forster (2018). Automatic segmentation of 3D point clouds of rubble masonry walls, and its application to building surveying, repair and maintenance. *Automation in Construction*, Vol. 96, pp. 29-39.
- Wang, X., R. Hänsch, M. Lizhuang, and O. Hellwich (2014). Comparison of Different Color Spaces for Image Segmentation using Graph-cut. In: *Proceedings of the 9<sup>th</sup> International Conference on Computer Vision Theory and Applications*, Lisbon, Portugal, Jan. 05-08, 2014, pp. 301-308.
- Weinmann, M., B. Jutzi, and C. Mallet (2014). Semantic 3D scene interpretation: A framework combining optimal neighborhood size selection with relevant features. *ISPRS Annals of the Photogrammetry, Remote Sensing and Spatial Information Sciences*, II-3, pp. 181-188.
- Weinmann, M., B. Jutzi, and C. Mallet (2017). Geometric Features and their Relevance for 3D Point Classification. *ISPRS Annals of the Photogrammetry, Remote Sensing and Spatial Information Sciences*, IV-1/W1, pp. 157-164.
- Wiedemann, W., A. Wagner, and T. Wunderlich (2017). Ableitung von 3D-Verschiebungsvektoren aus fusionierten Laserscan- und Bilddaten. *avn. - allgemeine vermessungs-nachrichten*, Vol. 124, 11-12, pp. 362-369.
- Wojtanowski, J., M. Zygmunt, M. Kaszczuk, Z. Mierczyk, and M. Muzal (2014). Comparison of 905 nm and 1550 nm semiconductor laser rangefinders' performance deterioration due to adverse environmental conditions. *Opto-Electronics Review*, Vol. 22, No. 3, pp. 183-190.
- Wujanz, D., D. Krueger, F. Neitzel, and C. Manthe (2014). DefoScan++: Oberflächenbasierte Registrierung terrestrischer Laserscans für die Deformationsanalyse. *avn. - allgemeine vermessungs-nachrichten*, Vol. 121, No. 1, pp. 26-37.
- Wujanz, D., M. Burger, F. Tschirschwitz, T. Nietzsche, F. Neitzel, and T. P. Kersten (2018). Determination of Intensity-Based Stochastic Models for Terrestrial Laser Scanners Utilising 3D-Point Clouds. *Sensors* (Basel, Switzerland), Vol. 18, No. 7, pp. 2187.
- Wunderlich, T., W. Niemeier, D. Wujanz, C. Holst, F. Neitzel, and H. Kuhlmann (2016). Areal Deformation Analysis from TLS Point Clouds – The Challenge. *avn. - allgemeine vermessungs-nachrichten*, Vol. 123, 11-12, pp. 340-351.

Zhana, Q., Y. Liangb, and Y. Xiaoa (2009). Color-based segmentation of point clouds. In: *IAPRS Vol XXXVIII*, Part 3/W8. Laserscanning 09.



## Evaluation of synthetic aperture radar interferometric techniques for monitoring of fast deformation caused by underground mining exploitation

Kamila Pawłuszek-Filipiak, Maya Ilieva, Natalia Wielgocka, Krzysztof Stasch

Institute of Geodesy and Geoinformatics, Wrocław University of Environmental and Life Sciences, 50-375 Wrocław, Poland, ([kamila.pawluszek-filipiak@upwr.edu.pl](mailto:kamila.pawluszek-filipiak@upwr.edu.pl); [maya.ilieva@upwr.edu.pl](mailto:maya.ilieva@upwr.edu.pl); [natalia.wielgocka@upwr.edu.pl](mailto:natalia.wielgocka@upwr.edu.pl); [krzysztof.stasch@upwr.edu.pl](mailto:krzysztof.stasch@upwr.edu.pl))

**Key words:** *differential synthetic aperture radar interferometry; small baseline subset; persistent scatterers interferometry; mining*

### ABSTRACT

EPOS-PL+ is the Polish national realization of the European Plate Observing System (EPOS) project that aims to build a multidisciplinary infrastructure. It allows integration of a variety of geoscience expertise and techniques to better understand the geohazard related to the underground mining of coal in the Upper Silesian Coal Basin (USCB) in Poland. The study case in this project is the Marcel Mine, located within USCB, where the detected subsidence for the analyzed period of four months reaches 91 cm. Various interferometric processing techniques demonstrated some advantages and also some limitations in the context of mining deformation measurement, including accuracy, spatial resolution, detectable deformation rate, atmospheric delay, and ability to detect the maximal deformation gradients. This is especially important from a mining perspective. Therefore, we investigated three different interferometric processing techniques to monitor fast mining deformation in the Marcel hard coal mine area. More specifically, we used conventional DInSAR, Small Baseline Subsets (SBAS), and Persistent Scattered Interferometry (PSInSAR). The result confirmed that none of these methods can be considered as the best. The DInSAR approach allows capturing the maximal deformation gradient, which was not possible with the PSInSAR and SBAS approaches. On the contrary, PSInSAR and SBAS allow us to provide less noisy and reliable results in the area of safety pillars.

### 1. INTRODUCTION

Having considered the great potential offered by Synthetic Aperture Radar (SAR) data, within the framework of the European Plate Observing System (EPOS) EPOS-PL+ project, the Satellite Data Infrastructure Center (CIBDS) is established, which aims to build a system to monitor land surface deformation using satellite radar interferometry (Aimaiti *et al.*, 2017) from various SAR missions. CIBDS mainly focuses on creating automated algorithms for collecting and processing satellite data, as well as modeling and prediction of land surface deformation. These products will be generated from various SAR sensors (Zhao *et al.*, 2019), as well as various interferometric SAR (InSAR) processing techniques (Chang *et al.*, 2010) integrated with other geodetic techniques such as leveling, Global Navigation Satellite Systems (GNSS), Light Detection and Ranging (LiDAR) (Froese and Mei, 2008), and photogrammetric techniques (Martins *et al.*, 2020). The products generated within CIBDS will be used to assess the risk of severe damage caused by mining activities (Morgan *et al.*, 2019) and will be the main source of information necessary to plan future mining works. The main area of monitoring is the safety pillars within the Marcel hard coal mine, located in USCB.

Mining-induced deformation is characterized by high magnitude and nonlinearity and usually leads to serious construction damage (Orwat and Gromysz, 2021).

Various interferometric processing techniques demonstrated some advantages and also some limitations in the context of mining deformation measurement, including accuracy, spatial resolution, detectable deformation rate, and atmospheric delay. (Pawłuszek-Filipiak and Borkowski 2020; 2021; Zhang *et al.*, 2020). Especially from a mining perspective, one of the most important aspects is the estimation of the maximal deformation gradient within the subsiding area. As presented by Ilieva *et al.* (2019); Pawłuszek and Borkowski (2021), Differential Synthetic Aperture Radar Interferometry (DInSAR) is shown to be capable of capturing maximal deformation rate. Persistent Scattered Interferometric (PSInSAR) techniques, in addition to their high accuracy, were unable to estimate such a high deformation gradient (Fan *et al.*, 2014).

Therefore, the objective of this study was to verify these findings in the Marcel mine area. We investigated three different interferometric processing techniques to monitor rapid mining deformation in the area of the Marcel hard coal mine. More specifically, we used conventional DInSAR, Small Baseline Subsets (SBAS) proposed by Berardino *et al.* (2002), and Persistent Scattered Interferometry (PSInSAR) proposed by Ferretti *et al.* (2000). Evaluation of these techniques has been carried out on Sentinel-1 data.

## II. STUDY AREA

The study area of the Marcel mine is located in USCB, one of the largest hard coal mining areas in Europe. The largest part of USCB is located in Poland, and the remainder lies in the Czech Republic. Within USCB many active hard coal mines are located. The ‘Marcel’ mine (until 1949, the mine was called ‘Emma’) dates back to the mid-19th century. The mine was fully launched on November 13, 1883. Construction of the mine took 10 years. Currently, the mine employs 3,168 people and its daily net hard coal production is 11,000 tons (Dreger, 2019).

Figure 1 presents the location of the safety pillars within the ‘Marcel’ mine, which are the main objective of the deformation monitoring in this area. The investigated study covers 25 km<sup>2</sup> and ranges from 18°29’0”E to 18°33’0”E in longitude and from 50°1’0”N up to 50°3’0”N in latitude. As can be seen in Figure 1, the study area is mainly covered by agricultural areas with sparse buildings, which means that the number of persistent natural scatters will be limited. Therefore, the application of distributed scatters (DS) seems to provide a better information of the spatial coverage of (Sun *et al.*, 2018).

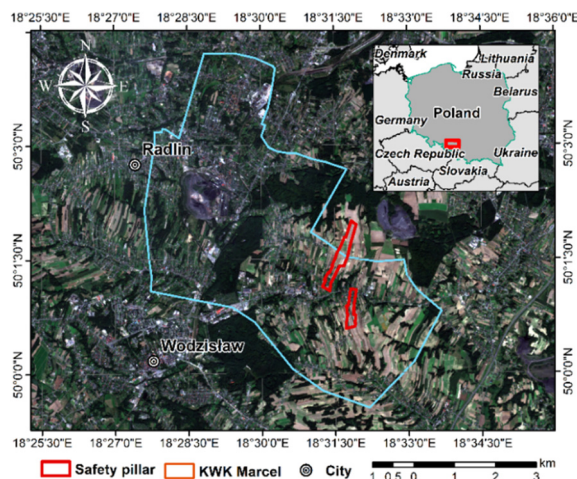


Figure 1. Location of the safety pillars within the study area of Marcel mine.

## III. METHODOLOGY

The overall methodology applied in this study is presented in Figure 2. The ascending and descending SAR dataset captured from the Sentinel Open Access Hub, as well as from Alaska Satellite Facility were used. The location of the safety pillars with the Marcel mine was also provided by the Polish Mining Group within the EPOS-PL+ project. For InSAR processing European Space Agency (ESA) SNAP and SARscape<sup>®</sup> software were used. Cumulated deformation maps for the last four months of 2020 were used to create deformation profiles and make a comparison of these methods.

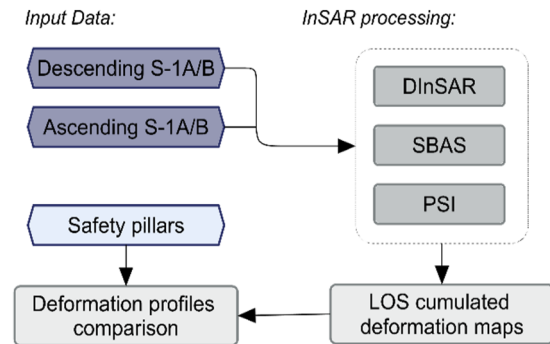


Figure 2. Methodology utilized in this study.

### A. Data used

In the presented study, we used only SAR data of the C-band (~5.55 cm wavelength) of the ESA Sentinel-1A/B satellites, which are freely available online on the ESA’s Copernicus Sentinel data hub.

The chosen data are acquired in Interferometric Wide Swath (IW) mode of ascending and descending geometry, in Single Look Complex (SLC) format, and cover the time period between last four months of the year 2020; more specifically, ascending data cover the period from 3<sup>th</sup> of September 2020 up to 26<sup>th</sup> of December 2020 while ascending data cover the period from 26<sup>th</sup> of August up to 5<sup>th</sup> of January. Having considered the dense vegetation cover in the study area, the investigated period was shortened into the time span of approximately 4 months. This allows to mitigate the effect of the decorrelation and to collect more information in the vegetated areas. Table 1 presents the specific characteristics of the data used in this study.

Table 1. Specification of the data used

	Ascending S-1A/B	Descending S-1A/B
Number of images	20	21
Period	2020/09/03 - 2020/12/26	2020/08/26 - 2021/01/05
Mean Incidence Angle [°]	38.3	43.7
Mean Azimuth [°]	81.7	-78.9
Relative Orbit	175	51
Mode	IW	IW

### B. Interferometric processing

As mentioned previously, the study area is mostly agricultural and thus the number of coherent areas with stable backscattering signal will be low. Since the CIBDS aim to effectively monitor safety pillars within the Marcel mine, the high density and accuracy of the measurement are beneficial. Therefore, various SAR sensors as well as various interferometric processing techniques should be evaluated in this context to provide higher density and precision. In the literature, there are many diverse interferometric processing methods, but we decided to apply and compare three techniques, namely conventional consecutive DInSAR, SBAS, and PSInSAR. The PSInSAR and SBAS processing

was performed with SARscape software (Sahraoui *et al.*, 2006), while the consecutive DInSAR approach was applied using the ESA Sentinel Application Platform (SNAP).

The data set described in Table 1 was processed as separate DInSAR interferograms, formed by 6-day pairs of consecutive Sentinel-1 images to minimize the temporal decorrelation considering the land cover of the area of interest. The Shuttle Radar Topography Mission (SRTM) 1 arc second (30 m resolution) Digital Elevation Model (DEM) was applied for topographic phase removal. Goldstein filters (Goldstein and Werner, 1998) are applied to the received wrapped interferograms, aiming to reduce the noise and to support the unwrapping of the radar phases. The minimum cost flow (MCF) function was used for phase unwrapping (Chen and Zebker, 2000). In all processing steps, a threshold of 0.3 for the pixel coherence was used, while the final results are interpolated and resampled to 20 m pixel spacing. A selection of forest features from the CORINE Land Cover (version 2018) (© European Union, 2018) inventory was applied to exclude densely vegetated areas with extremely low coherence. By combining consecutive interferograms, the total amount of the subsidence in the area of investigation is retrieved with some of the atmospheric artifacts also canceled out.

More advanced DInSAR processing involves the SBAS method, which presents a key advantage compared with other interferometric processing methods (Berardino *et al.*, 2002). SBAS generates interferograms from appropriately selected pairs of SAR images to minimize the spatial and temporal baseline between two images in the pairs. In the presented study, normal baseline constraints were set at 2% of the critical baseline. Additionally, the maximum temporal baseline constraint was set to 30 days for both SBAS processing steps (in ascending and descending orbits). This allows us to mitigate the decorrelation problem that occurs with longer baselines. Generally, SBAS estimates various interferometric components (deformation, atmosphere, and other components) and provides almost error-free results (Iglesias *et al.*, 2015). SBAS takes advantage of the interferogram redundancy and estimates deformation using singular value decomposition. The atmospheric phase screen (APS) is estimated by using high-pass and low-pass filtering of the phase. In addition, the quadratic deformation model was used to estimate various interferometric components. The MCF function with 0.4 coherence threshold was used for phase unwrapping.

The third technique in the current comparison is the PSInSAR method that allows one to identify most coherent points with high resolution and with high spatial density (Ferretti, 2000; 2001). However, to properly estimate all interferometric components, in this approach a linear deformation model in time is adopted within InSAR processing. Therefore, PS points that have strongly nonlinear deformation behavior in

time will not be selected as PS candidates since they did not meet the model fitting criteria (temporal coherence is low). Therefore, estimating the maximal deformation gradient using these techniques is very often a challenge. However, from another point of view, phase unwrapping is carried out in the sparse grid; therefore, the probability of phase jumps errors which are very probable to occur in noncoherent areas using spatial phase unwrapping is lower.

It is worth mentioning that in literature there are also other PSInSAR methods which did not apply linear deformation models in processing. For instance, StaMPS (Stanford Method for Persistent Scatterers) utilizes spatial correlation method which is dedicated to the vegetated areas (Hooper *et al.*, 2007; Delgado 2019).

#### IV. RESULTS

Figure 3 presents InSAR processing results using different techniques: PSInSAR in the upper row (a and b), SBAS in the middle row (c and d) and DInSAR in the lower row (e and f), with ascending results to the left (a, c, and e) and descending to the right (b, d, and f). As can be observed, in general the results are similar to each other but severe differences occur. However, the results of PSInSAR did not allow us to estimate deformation with a fast gradient. The maximum deformation estimated using PSInSAR for the ascending and descending orbits is not greater than 20 cm. Nevertheless, it can be observed that stable areas are represented as green and that values oscillate around zero. Furthermore, processing using the SBAS technique allows us to effectively estimate fast deformation in the center of the subsidence bowls, as well as accurate estimation of the deformation within the stable areas. It was possible to capture the maximum deformation gradient for ascending and descending images of -48 cm and -39 cm, respectively.

Moreover, observing results from DInSAR processing, it can be noted that the maximal deformation gradient for one of the detected subsidence basins is 91 cm and 87 cm for ascending and descending orbits. Therefore, it indicated that none of the multi-temporal interferometric processing techniques such as PSInSAR or SBAS allow us to capture the full deformation gradient. Nevertheless, observing results in stable areas, it can be seen that more noisy pixels exist, especially for the results of descending orbit. One of the reasons could be the presence of some atmospheric artifacts that were not fully modeled and subtracted from the DInSAR results. To better understand the advantages and limitations of each technique, deformation profiles were generated and presented in Figure 4. These deformation profiles were extracted from areas with the highest deformation gradient detected as well as from two safety pillars. As can be observed, the maximal deformation gradient was detected in various locations for ascending and

descending geometry. This probably indicates that significant horizontal deformation exists within the investigated area. Many previous works demonstrated that considerable horizontal movement (approximately

30-40% of the maximal vertical gradient) exists on the edges of the subsidence bowls caused by underground coal excavation (Li *et al.*, 2015; Pawluszek-Filipiak and Borkowski 2020).

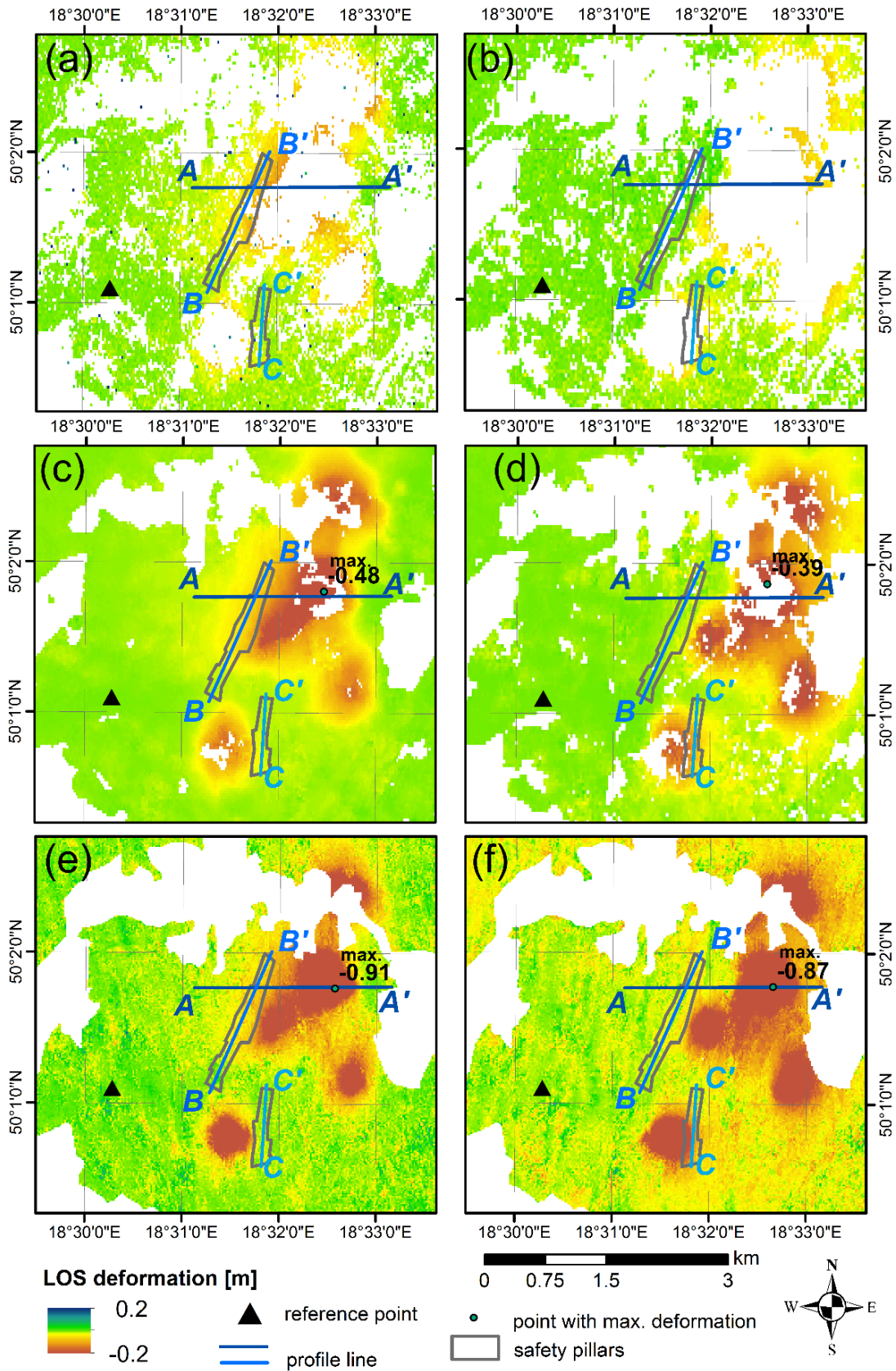


Figure 3. InSAR results using different processing techniques: PSInSAR (a, b), SBAS (c, d) and DInSAR (e, f) from ascending (a, c, and e) and descending (b, d, and f) geometries.

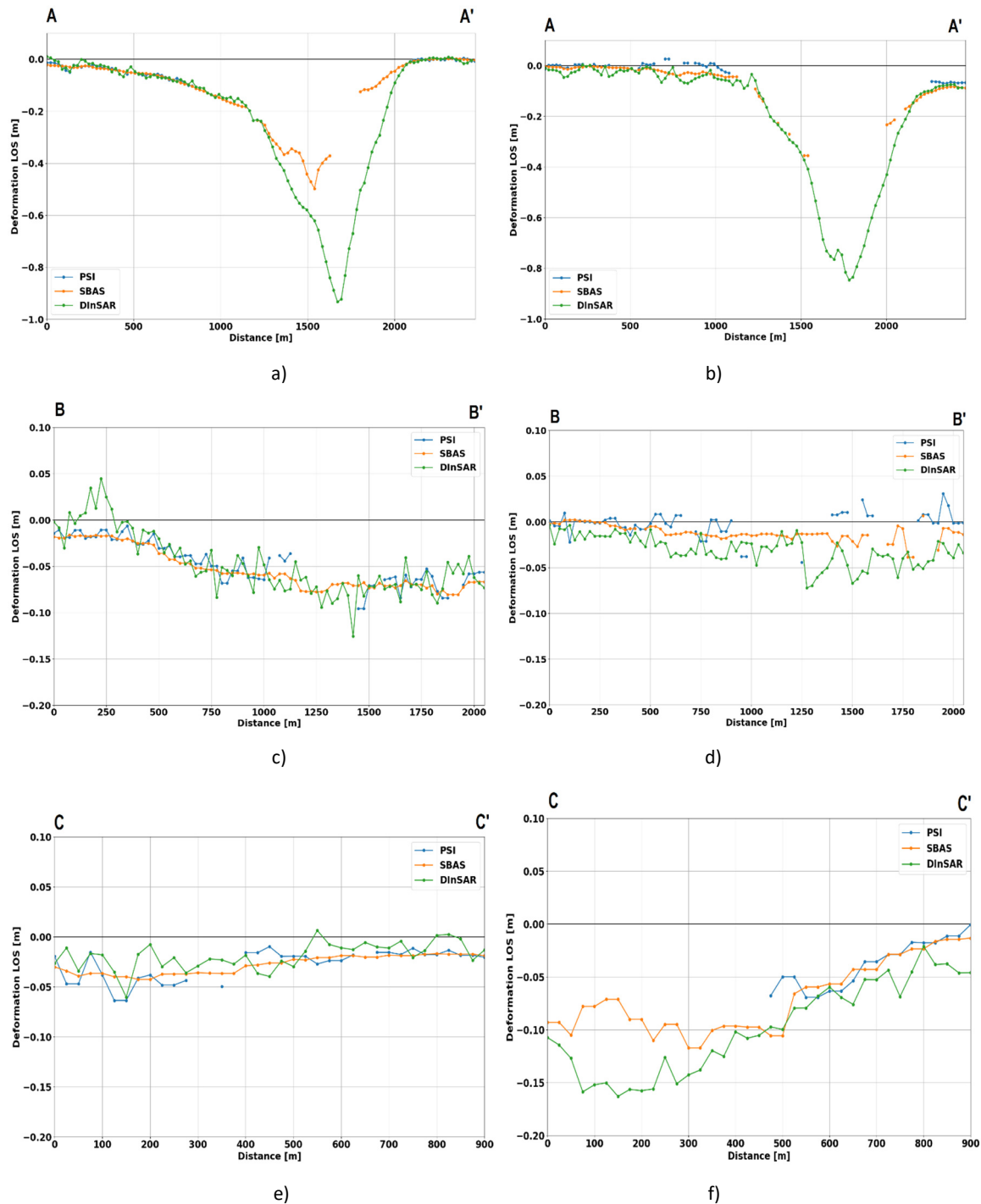


Figure 4. Deformation profiles across the area of maximum detected deformation for ascending (a) and descending (b), for first safety pillar from ascending (a) and descending (d) and second safety pillar for ascending (e) and descending orbit (f).

Additionally, for ascending geometry, it is visible that the SBAS method underestimated the deformation gradient. Since the atmospheric effect is assumed to be similar for the surrounding pixels, the incompatibility between DInSAR and SBAS rather corresponds to phase unwrapping errors in the SBAS results. Moreover, for the descending orbit (Figure 4a), some disagreement between DInSAR and SBAS results exists in the profile distance 1600-1620m. This can contribute to some interferometric processing errors in one of the applied methods (such as phase jumps or phase aliasing problems in SBAS results or atmospheric effect in

DInSAR results). Unfortunately, by the preparation of this report we did not have ground-truth geodetic measurements for comparison and evaluation of the accuracy of the delivered products.

Observing the results for the profiles extracted for the areas where safety pillars are located, it can be observed that in this case the PSInSAR and SBAS results are more smooth for both profiles (BB') and (CC'). However, it can be observed that the smoothest results are present for SBAS products. The PSInSAR processing results are interrupted due to the lower number of PS points.

## V. DISCUSSION

The comparison of the three InSAR processing techniques evaluated indicated that each of them provide different results in terms of maximum detected deformation, density of the points. Meeting all criteria for the effective monitoring of mining areas such as high accuracy, high measurement point density, and capability to capture maximal deformation gradient is very challenging. As observed, the DInSAR approach allows to capture maximal deformation gradients which was not possible with the PSInSAR and SBAS approaches. In contrast, PSInSAR and SBAS allow us to provide less noisy and reliable results in the area of safety pillars.

Additionally, PSInSAR due to the high constraints imposed on coherence (0.7) amplitude dispersion (0.25) and deformation model in time provide less measurement points which affect understanding of the partial behavior of the subsidence basin. Moreover, considering the constraints about the minimum number of SAR images, the PSInSAR method is the most critical since in this case at least 20 images are needed to correctly evaluate interferometric components.

## VI. CONCLUSIONS AND FUTURE WORK

Interferometric techniques are shown to be a powerful tool for monitoring mining deformation. Unfortunately, the high deformation gradient experience in that study (0.9 m / 4 month) indicated that more targeted solutions must be prepared to accurately measure the mining deformation from space and, at the same time, provide the highest possible accuracy.

The result in this study demonstrated that each of the interferometric techniques has its own advantages and limitations in the context of high accuracy, high measurement point density, and the capabilities to capture the maximal deformation gradient of the mining subsidence bowls.

Therefore, in the future we will try to tailor InSAR processing towards these critical aspects and the proposed integrated and complex approach of monitoring mining deformations. The products will be evaluated based on ground-truth data which we have already started to capture. More specifically, we located more than 250 stable points along more than 18 kilometers of roads in the Marcel mine area. We are planning ground-truth measurements in six-month intervals. The first one was already performed in the fourth quarter of 2021, which includes leveling, total station, and satellite measurements of the Global National Satellite System (GNSS). The control points located on the safety pillars are connected to GNSS permanent stations, located outside of the deformation zone.

Also, in the future work the application of L- band data from ALOS-2 mission will be evaluated in the context of accuracy and ability to capture such a high

deformation gradient in non-coherent vegetated areas to mitigate the mining needs.

## VII. ACKNOWLEDGEMENTS

The research infrastructure that has been used for computation purposes was created within the project EPOS-PL (POIR.04.02.00-14-A003/16) and EPOS-PL+ (POIR.04.02.00-00-C005/19-00) European Plate Observing System, funded by the Operational Programme Smart Growth 2014–2020, Priority IV: Increasing the research potential, Action 4.2: Development of modern research infrastructure of the science sector and co-financed by the European Regional Development Fund. Kamila Pawluszek-Filipiak is supported by the Ministry of Science and Education in the framework of Scholarship for the best young scientists (SMN/16/1429/2020)

## References

- © European Union, (2018). Copernicus Land Monitoring Service European Environment Agency (EEA), <https://land.copernicus.eu/pan-european/corine-land-cover/clc2018>
- Aimaiti, Y., Yamazaki, F., Liu, W., and Kasimu, A. (2017). Monitoring of land-surface deformation in the karamay oilfield, Xinjiang, China, using sar interferometry. *Applied Sciences*, 7(8), 772. DOI: 10.3390/app7080772
- Berardino, P., Fornaro, G., Lanari, R., and Sansosti, E. (2002). A new algorithm for surface deformation monitoring based on small baseline differential SAR interferograms. *IEEE Transactions on geoscience and remote sensing*, 40(11), 2375-2383, DOI: 10.1109/TGRS.2002.803792
- Chang, C. P., Yen, J. Y., Hooper, A., Chou, F. M., Chen, Y. A., Hou, C. S., and Lin, M. S. (2010). Monitoring of Surface Deformation in Northern Taiwan Using DInSAR and PSInSAR Techniques. *Terrestrial, Atmospheric & Oceanic Sciences*, 21(3). DOI: 10.3319/TAO.2009.11.20.01(TH)
- Chen, C.W. and Zebker, H.A. (2000). Network approaches to two-dimensional phase unwrapping: Intractability and two new algorithms. *Journal of the Optical Society of America A*, 17(3), 401-414, DOI: 10.1364/JOSAA.17.000401
- Delgado Blasco, J. M., Fomelis, M., Stewart, C., and Hooper, A. (2019). Measuring urban subsidence in the Rome metropolitan area (Italy) with Sentinel-1 SNAP-StaMPS persistent scatterer interferometry. *Remote Sensing*, 11(2), 129.
- Dreger, M. (2019). Methane emissions in selected hard-coal mines of the Upper Silesian Coal Basin in 1997–2016. *Geology, Geophysics and Environment*, 45(2). DOI: 10.7494/geol.2019.45.2.121
- Fan, H. D., Wei, G., Yong, Q., Xue, J. Q., and Chen, B. Q. (2014). A model for extracting large deformation mining subsidence using D-InSAR technique and probability integral method. *Transactions of Nonferrous Metals Society of China*, 24(4), 1242-1247. DOI: 10.3390/rs11070812
- Ferretti, A., Prati, C., and Rocca, F. (2000). Nonlinear subsidence rate estimation using permanent scatterers in differential SAR interferometry. *IEEE Transactions on geoscience and remote sensing*, 38(5), 2202-2212, DOI: 10.1109/36.868878

- Ferretti, A., Prati, C., and Rocca, F. (2001). Permanent scatterers in SAR interferometry. *IEEE Transactions on geoscience and remote sensing*, 39(1), 8-20, DOI: 10.1109/36.898661
- Froese, C. R., and Mei, S. (2008). Mapping and monitoring coal mine subsidence using LiDAR and InSAR. *GeoEdmonton*, 8, 1127-1133. DOI: 10.34218/IJCET.11.6.2020.003
- Goldstein, R. M. and Werner, C. L. (1998). Radar interferogram filtering for geophysical applications. *Geophysical Journal International*, 25(21), pp. 4035-4038, DOI: 10.1029/1998GL900033
- Hooper, A., Segall, P., and Zebker, H. (2007). Persistent scatterer interferometric synthetic aperture radar for crustal deformation analysis, with application to Volcán Alcedo, Galápagos. *Journal of Geophysical Research: Solid Earth*, 112(B7).
- Iglesias, R., Mallorqui, J. J., Monells, D., López-Martínez, C., Fabregas, X., Aguasca, A., and Corominas, J. (2015). PSI deformation map retrieval by means of temporal sublook coherence on reduced sets of SAR images. *Remote Sensing*, 7(1), 530-563. DOI: 10.3390/rs70100530
- Ilieva, M., Polanin, P., Borkowski, A., Gruchlik, P., Smolak, K., Kowalski, A., Rohm, W. (2019). Mining Deformation Life Cycle in the Light of InSAR and Deformation Models. *Remote Sensing*, 11, 745. DOI:10.3390/rs11070745
- Li, Z. W., Yang, Z. F., Zhu, J. J., Hu, J., Wang, Y. J., Li, P. X., and Chen, G. L. (2015). Retrieving three-dimensional displacement fields of mining areas from a single InSAR pair. *Journal of Geodesy*, 89(1), pp. 17-32. DOI: 10.1007/s00190-014-0757-1
- Martins, B. H., Suzuki, M., Yastika, P. E., and Shimizu, N. (2020). Ground Surface Deformation Detection in Complex Landslide Area—Bobonaro, Timor-Leste—Using SBAS DInSAR, UAV Photogrammetry, and Field Observations. *Geosciences*, 10(6), 245. DOI: 10.3390/geosciences10060245
- Morgan, J. L., Colombo, D., and Meloni, F. (2019, April). InSAR tools for risk assessment over mine assets. In Proceedings of the First International Conference on Mining Geomechanical Risk (pp. 159-170). Australian Centre for Geomechanics. DOI: 10.36487/ACG\_rep/1905\_06\_Morgan
- Orwat, J., and Gromysz, K. (2021, February). Occurrence consequences of mining terrain surface discontinuous linear deformations in a residential building. In *Journal of Physics: Conference Series* (Vol. 1781, No. 1, p. 012013). IOP Publishing, DOI: 10.1088/1742-6596/1781/1/012013
- Pawluszek-Filipiak, K., and Borkowski, A. (2020). Integration of DInSAR and SBAS Techniques to determine mining-related deformations using sentinel-1 data: The case study of Rydułtowy mine in Poland. *Remote Sensing*, 12(2), 242. DOI: 10.3390/rs12020242
- Pawluszek-Filipiak, K., and Borkowski, A. (2021). Monitoring mining-induced subsidence by integrating differential radar interferometry and persistent scatterer techniques. *European Journal of Remote Sensing*, 54(sup1), pp. 18-30, DOI: 10.1080/22797254.2020.1759455
- Sahraoui, O. H., Hassaine, B., Serief, C., and Hasni, K. (2006). Radar interferometry with Sarscape software. *Photogrammetry and Remote Sensing*.
- SNAP, ESA (2021). Sentinel Application Platform v8.0.0, <http://step.esa.int>
- Sun, Q., Jiang, L., Jiang, M., Lin, H., Ma, P., and Wang, H. (2018). Monitoring coastal reclamation subsidence in Hong Kong with distributed scatterer interferometry. *Remote Sensing*, 10(11), 1738. DOI: 10.3390/rs10111738
- Zhang, L., Cai, X., Wang, Y., Wei, W., Liu, B., Jia, S., ... and Wei, Z. (2020). Long-term ground multi-level deformation fusion and analysis based on a combination of deformation prior fusion model and OTD-InSAR for longwall mining activity. *Measurement*, 161, 107911, DOI: 10.1016/j.measurement.2020.107911
- Zhao, Q., Ma, G., Wang, Q., Yang, T., Liu, M., Gao, W., ... and Pepe, A. (2019). Generation of long-term InSAR ground displacement time-series through a novel multi-sensor data merging technique: The case study of the Shanghai coastal area. *ISPRS Journal of Photogrammetry and Remote Sensing*, 154, pp. 10-27. DOI: 10.1016/j.isprsjprs.2019.05.005

## ADATools: a set of tools for the analysis of terrain movement maps obtained with SAR Interferometry

Oriol Monserrat<sup>1</sup>, Anna Barra<sup>1</sup>, Cristina Reyes-Carmona<sup>2</sup>, María Cuevas<sup>1</sup>, Marta Bejar-Pizarro<sup>2</sup>, José Navarro<sup>1</sup>, Roberto Tomas<sup>3</sup>, Jorge Pedro Galve<sup>4</sup>, Lorenzo Solari<sup>1</sup>, Roberto Sarro<sup>2</sup>, Rosa María Mateos<sup>2</sup>, José Miguel Azañon<sup>4</sup>, Gerardo Herrera<sup>2</sup>, Bruno Crippa<sup>5</sup>

<sup>1</sup> Centre Tecnològic de Telecomunicacions de Catalunya (CTTC/CERCA), Geomatics Division, Avinguda Carl Friedrich Gauss 7, 08860 Castelldefels, Spain, ([omonserrat@cttc.cat](mailto:omonserrat@cttc.cat); [abarra@cttc.cat](mailto:abarra@cttc.cat); [mcuevas@cttc.cat](mailto:mcuevas@cttc.cat); [jnavarro@cttc.cat](mailto:jnavarro@cttc.cat); [lsolari@cttc.cat](mailto:lsolari@cttc.cat))

<sup>2</sup> Geohazards InSAR laboratory and Modelling group (InSARlab), Geoscience Research Department, Geological Survey of Spain (IGME), Alenza 1, 28003 Madrid, Spain, ([c.reyes@igme.es](mailto:c.reyes@igme.es); [m.bejar@igme.es](mailto:m.bejar@igme.es); [r.sarro@igme.es](mailto:r.sarro@igme.es); [rm.mateos@igme.es](mailto:rm.mateos@igme.es); [g.herrera@igme.es](mailto:g.herrera@igme.es))

<sup>3</sup> Departamento de Ingeniería Civil, Universidad de Alicante, Alicante, Spain, ([roberto.tomas@ua.es](mailto:roberto.tomas@ua.es))

<sup>4</sup> Departamento de Geodinámica, Universidad de Granada, Avda. del Hospicio s/n, 18010 Granada, Spain, ([jpgalve@gmail.com](mailto:jpgalve@gmail.com); [jazanon@ugr.es](mailto:jazanon@ugr.es))

<sup>5</sup> Department of Earth Sciences, Section of Geophysics, University of Milan, Via Cicognara 7, I-20129 Milan, Italy, ([bruno.crippa@unimi.it](mailto:bruno.crippa@unimi.it))

**Key words:** *ground displacements; InSAR; natural hazards; satellite imagery*

### ABSTRACT

The SAR Interferometry techniques, Persistent Scatterer Interferometry (PSI) among them, are nowadays known as important tools for monitoring Earth surface movements. Several regional and national Ground Motion Services based on PSI already exist. Moreover, since 2022 the European Ground Motion Service will be operational and will annually provide an updated displacement map over the whole Europe. This will suppose a big amount of ground displacement measurements along the European territory. For each measurement EGMS will provide the annual velocity and the time series of deformation covering the period 2014 to one year prior to each delivery. In this context, it will be more and more necessary having tools to ease the management, analysis, and interpretation, of those wide areas and huge amount of data. We present here a first step in this direction: the ADATools are a set of tools to automatically have secondary, and more operational, products derived from a PSI map. Starting from a fast extraction of the most significant Active Deformation Areas (ADA), with the ADAFinder tool, then we can have a preliminary classification of the most probable phenomena (landslides, subsidence, settlements, or sinkholes) that is behind the detected movement, with the ADAClassifier tool. Moreover, LOS2hv tool allows to derive the horizontal (east-west) and vertical components of the movement in case we have maps of ascending and descending geometries. Finally, it is presented a product that analyzes the local displacement gradients to generate potential damage maps in urban areas. The tools will be presented through some results obtained on an area of the Granada County with the use of Sentinel-1 data. All the results have been achieved within the framework of the Riskcoast Project (financed by the Interreg Sudoe Program through the European Regional Development Fund, ERDF).

### I. INTRODUCTION

Satellite SAR interferometry (InSAR) is nowadays a consolidated technique for ground movement detection and monitoring. InSAR based techniques allow processing areas from regional/national scale up to local scale such as single buildings, providing a high density of displacement measurements at low cost (Carlà *et al.*, 2019; Galve *et al.*, 2017; Crosetto *et al.*, 2016). However, the outputs provided by such techniques are usually not easy to manage, difficult to understand, and demand the need of an expert to interpret those results. This might turn out to be a time-consuming task for users who are not familiar with radar data (Barra *et al.*, 2017).

Since 2014, Sentinel-1 satellites are acquiring data worldwide with a revisit time of 6-12 day. The data have been made available to everyone at no cost. This has prompted the tendency of increasingly using this technique for operational tasks related to monitor ground displacements like for example risk management activities, urban planning or geohazards monitoring. Such tendency is even more consolidated thanks to the regional, national, and European programs to investigate and improve the processing performances and broaden the operational use and application of the InSAR results to monitor ground displacements (Crosetto *et al.*, 2020).



In this context, the development of methodologies and tools to automatize the retrieval of information and to ease the interpretation of the results is a need to improve its operational use. In this work a set of tools, developed in the framework of the projects MOMIT, SAFETY, U-Geohaz and RiskCoast, is presented and an example of use in the framework of the project RiskCoast is shown. The RISKCOAST project focuses its work on the development of tools, methodologies and innovative solutions focused on the prevention and management of geological risks on the coast in a more effective way.

The presented work is as an example of multi scale application of InSAR for geohazard applications. It exploits the Active Deformation Areas tools (Barra *et al.*, 2017) developed with the aim of facilitating the management, use and interpretation of InSAR-based results. The test site is the Coast of Granada County. The displacement velocity and the displacement time series have been estimated over the area by processing Sentinel-1 (A and B) SAR images. From these initial InSAR outputs the most significant Active Displacement Areas (ADAs) are semi-automatically extracted using the ADAfinder tool (Barra *et al.*, 2017 and Navarro *et al.*, 2019). Then we show the subsequent application of ADA classifier and potential damage map generation on different ADAs located in the test area. All the used tools go in the same direction of the European Ground Motion Service (EU-GMS) project, which will provide consistent, regular, and reliable information regarding natural and anthropogenic ground motion phenomena all over Europe (Crosetto *et al.*, 2020).

## II. METHODOLOGY

### A. Dataset

A stack of 230 co-registered SAR Sentinel-1 Wide Swath Single Look Complex (SLC) images acquired in Ascending geometry during the period November 2015 to May 2020 has been processed at full resolution. The resolution of Sentinel-1 data is approximately  $4 \times 14 \text{ m}^2$ . Specifically, one burst has been processed to cover the area of interest. Images from Sentinel-1A and Sentinel-1B satellites have been exploited with a minimum temporal sampling of 6 days. The SRTM Digital Elevation Model provided by NASA was used to process the interferometric products.

### B. Data processing

This section summarizes the methodology applied in this test site to generate the different products. The methodology applied is based in a multi-step processing procedure which includes four main stages: InSAR processing, ADAs extraction, ADAs classification and Potential Damage maps generation.

The goal of the InSAR processing stage of the procedure is to derive the deformation information of the area of interest from SAR data. The approach is independent of the used PS/SBAS method. In this work,

the Persistent Scatterer Interferometry chain of the Geomatics (PSIG) Division of the CTTC described in Devanthery *et al.* (2014) has been used. The main steps of PSIG are: (1) interferogram generation; (2) interferogram network selection taking into account the temporal behavior of the coherence. Such analysis allows to locate and remove those interferograms characterized by low coherence (*e.g.*, snow periods in mountain areas); (3) selection of points based on the dispersion of amplitude; (4) estimation of the residual topographic error and subsequent removal from original single-look interferograms; (5) 2+1D phase unwrapping of the redundant interferograms which generates a set of N unwrapped phase images, which are temporally ordered in correspondence with the dates of the SAR images processed, hereafter referred as time series of deformation (TSD); (6) atmospheric phase screening estimation using spatio-temporal filters and removal from the TSDs generated in the previous step; (7) estimation of the velocity of deformation from the TSDs and; (8) geocoding of the results.

The main outputs of the InSAR processing stage is a deformation map composed of a set of selected points, called Persistent Scatterers (PSs), with information on the estimated Line of Sight (LOS) velocity of deformation and the accumulated deformation at each Sentinel-1 image acquisition time, *i.e.* TSDs.

The second step is the ADAs extraction. The main goal is the identification and mapping of those areas where deformation has been measured by the PSIG processing. To this aim we have used the ADAfinder tool (Barra *et al.*, 2017; Navarro *et al.*, 2019). The input of this stage is the PS cloud of the area of interest generated in the previous step. ADAfinder allows to filter the input potential outlier PSs and ease the detection of ADAs. The ADAfinder employs the information contained in the PS cloud to define each ADA on the basis of their location and density of PSs. It requires some thresholds as the minimum number of PSs making an ADA or the area of influence of each PS need to be defined. In this study the minimum number of PS is set to 5 and the area of influence of each PS was set to 26 m. Each ADA is associated with a quality index which describes the noise level and the consistency of the displacement TSDs among the PSs forming each ADA. The QI ranges from Class 1, which represents the ADA characterized by very high quality TSDs to Class 4. The areas with Class 4 have been neglected in the next steps of this study. For detailed information regarding the procedure to identify the ADAs and assess their quality please refer to Barra *et al.* (2017) and Navarro *et al.* (2019). The outputs of the ADAs extraction stage are two shapefiles containing the filtered deformation map and the ADA map.

The third step is to apply the ADA classifier. The tool provides a preliminary assessment on the nature of the detected ADA. It semi-automatically categorizes each ADA into potential deformational processes using the

information provided by ADA finder, PS clouds and ancillary external information. The output of ADAclassifier is an extended version of the ADA shapefile. It adds extra fields to the attributes of the ADAs providing information about the certainty to belong to each one of the four considered processes: Landslides, sinkholes, subsidence's and settlements. A more in-depth description of the ADA classifier tool can be found at Tomas *et al.* (2018).

Finally, in the last step, the gradients of the displacement of each ADA are used to detect those buildings which are strongly affected by the measured displacements and thus which can be potentially damaged in the future. It works ADA wise. The output of this step is, for each ADA, a 5-class map describing the potential level of damage of the building within the ADA. It is worth noting that it only considers the intensity of the gradient of displacement to anticipate which areas would require a more in detail analysis.

### III. RESULTS

The results of the application of the proposed methodology are described in this section. Specifically, we are going to focus on different moving areas located along the coast of Granada. Figure 1 shows the obtained displacement velocity map and the subsequently derived ADA maps.

#### A. Displacement maps and ADAs identification

Figure 1 shows the deformation velocity map generated with the PSIG processing in a test site of the project, approximately 40 x 15 km<sup>2</sup> between Nerja and Castell de Ferro (both located in Granada County, Spain). The green points indicate stability, the red colors indicate movements away from the satellite and the blue colors movements towards the satellite. A total of 215000 PSs were measured in that area. The estimated precision is 1.5 mm/yr. Several sectors affected by deformation phenomena can be easily identified.

The ADAfinder tool extracted 148 ADAs with QI higher than 4. Figure 1 bottom shows its distribution along the area of study. It can be clearly observed that some of them are located along the coastal line.

Figure 2 shows an example of the area framed by the red square in the Figure 1. The figure shows two different examples of identified ADAs along the Highway A7. One with QI=1 and one with QI=4. The figure shows the ADA polygons together with the displacement velocity maps and some displacement time series.

In this case, the TSDs (Figure 2a) show a low level of noise and display a consistent deformation behavior with movements away from the satellite of up to -60 mm (QI=1). On the contrary, ADA (b), with a QI=4, represents the lowest quality of ADA that can be extracted. The TSDs of three of the PSs (Figure 2b) that make that ADA show a higher level of noise and different behavior. In this case, TSD3 exhibits a near

linear movement away from the satellite that seems to stabilize at the end of the observation period with a maximum displacement of up to -70 mm, TSD4 displays stability at the beginning of the observation period followed by a small window of time where there is movement away from the satellite and then stability with a maximum displacement of -40 mm, and finally TSD5 showing a smaller movement away from the satellite at the beginning of the observation period and the remains more or less stable compared with the other two TSDs.

#### B. ADA classifier

Figure 3 shows the ADA Classifier main output. It shows the obtained classification for three different processes. Given a process, the ADA classifier assign to each ADA a level of certainty to belong or not to this type of process. Figure 3 shows the level of certainty of the detected ADAs to belong to landslides, subsidence's or settlements class. The level of certainty is 4-class parameters: red means that the ADA is explained by the tested process, yellow is that the ADA is potentially explained by the tested process, green it is not the tested process and grey mean that there is not enough information to classify the ADA.

The results show some potential landslide. Some of them are already known slope instabilities affecting the coast of Granada. Among them can be find the urbanizations of Los Almendros and Alfamar which will be discussed later in this document.

5 areas have been classified as settlements. Some of them lay on the recently built A-7 railway and one on a building close to the port of Motril; both structures were built between 2014 and 2015.

It may be observed that it can be that an ADA can be classified as two or more phenomena. This can happen for different reasons like insufficient ancillary data or simply that the ADA fulfills the different requirements to lay in one or another phenomenon. However, a multiple classification of the same ADA lets the final user know that the detected movement is a complex case.

#### C. Potential damage maps

The last step of the procedure is to perform an analysis of the displacement's gradients at the ADA level. The aim of this analysis is to assess the potential damage to be suffered by a building or infrastructure along time. Such analysis is performed considering only the intensity of the differential displacements affecting each structure.

Figure 4 shows the examples of the obtained potential damage maps in two different areas: Monte de Los Almendros (a) and Alfa Mar (c).

The methodology is still under development. Here we show the preliminary results. The Figure 4a shows the potential damage map obtained over the Urbanization Monte de Los Almendros. The color assigned to each

building represent the different level of potential damages considering the intensity of the differential displacements affecting the building. Red color represents the highest level of probability to be damaged along time while green means very low probability. Figure 4c shows the same result but for the Alfa Mar urbanization. The right column of Figure 4

shows the damage inventories obtained from a field work during the year 2019. At a first glance one may see that there is a disagreement between the maps obtained with the proposed methodology and the infield observations. This point is developed in the discussion section.

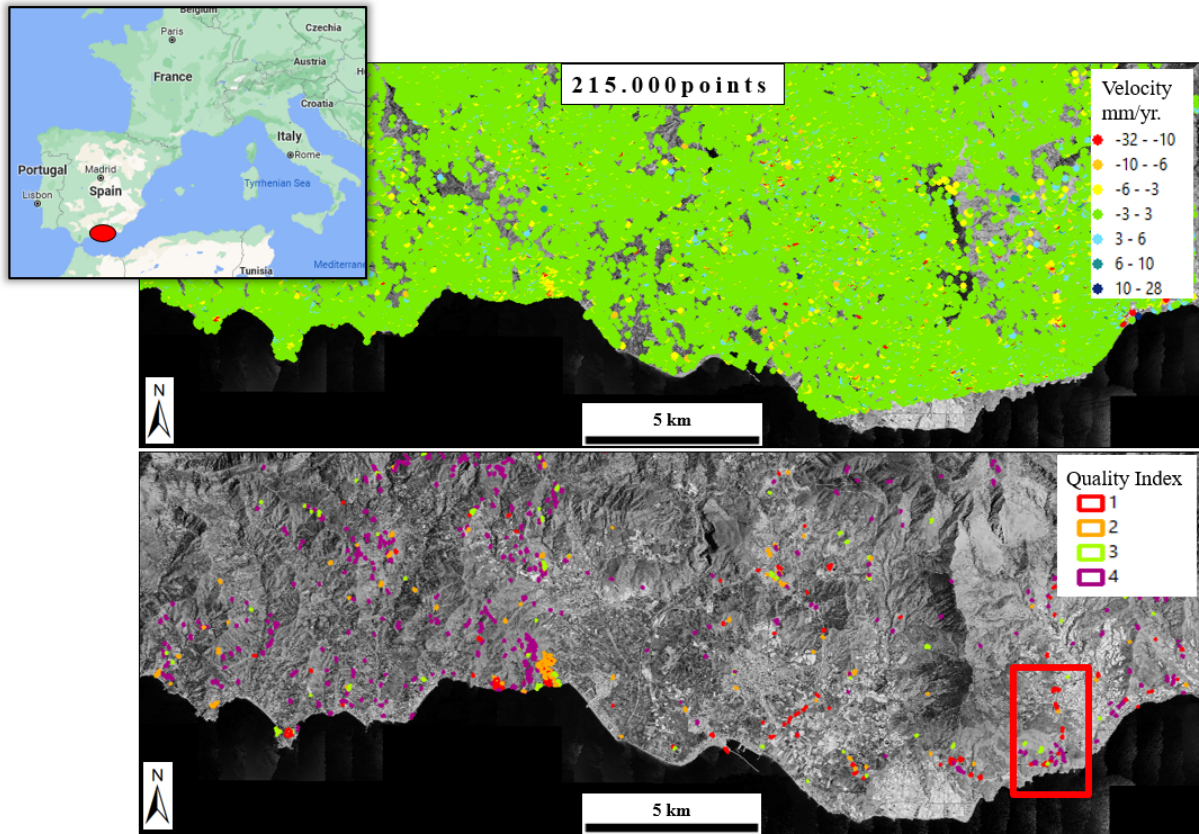


Figure 1. Global view of the results over the area of study. Deformation velocity map (up) and detected ADAs (bottom).

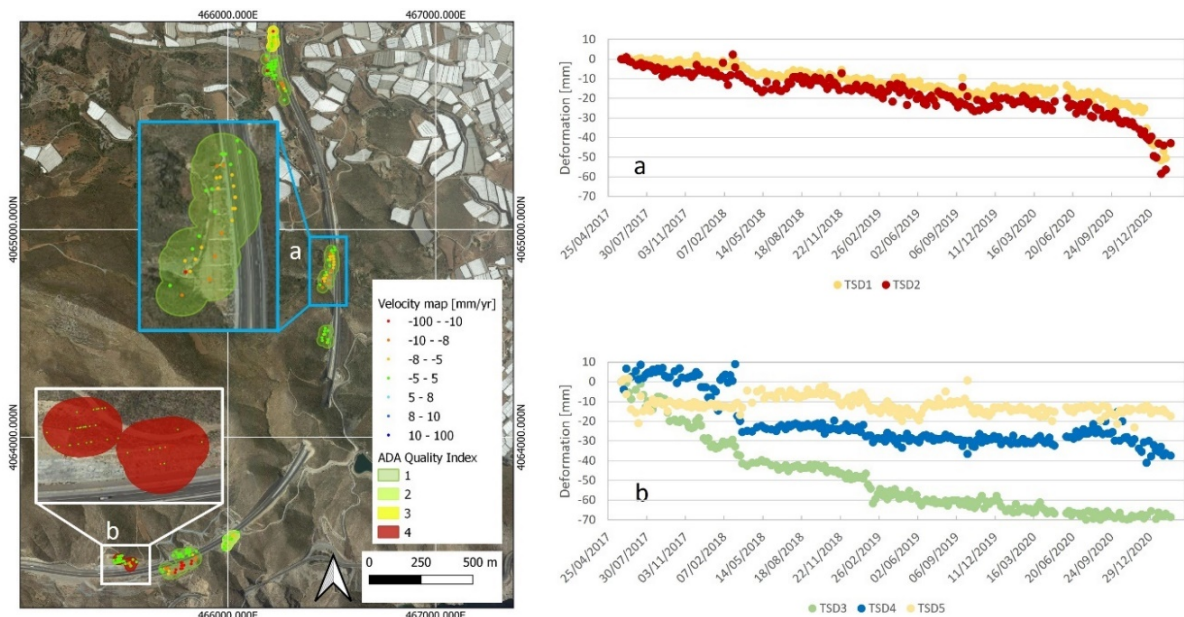


Figure 2. ADA map of the area highlighted by the red frame in Fig. 1, with two amplified ADAs (a and b) affecting two sectors of the A-7 highway. The velocity of deformation of the active PSs showing instability are displayed in this map. Stable PSs have been filtered out by the ADAfinder tool. Two time series of deformation (TSD) are displayed for each sector as example.

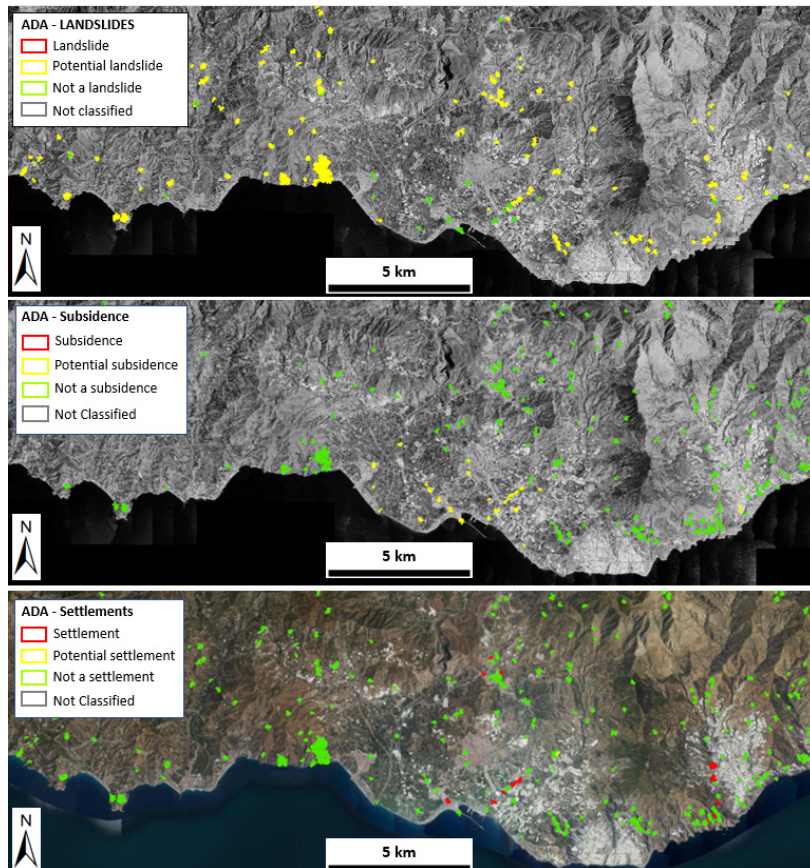


Figure 3. Results of the ADA classifier for three types of processes: (up) Landslide classified phenomena; (centre) Subsidence classified phenomena; and (bottom) settlements classified phenomena.

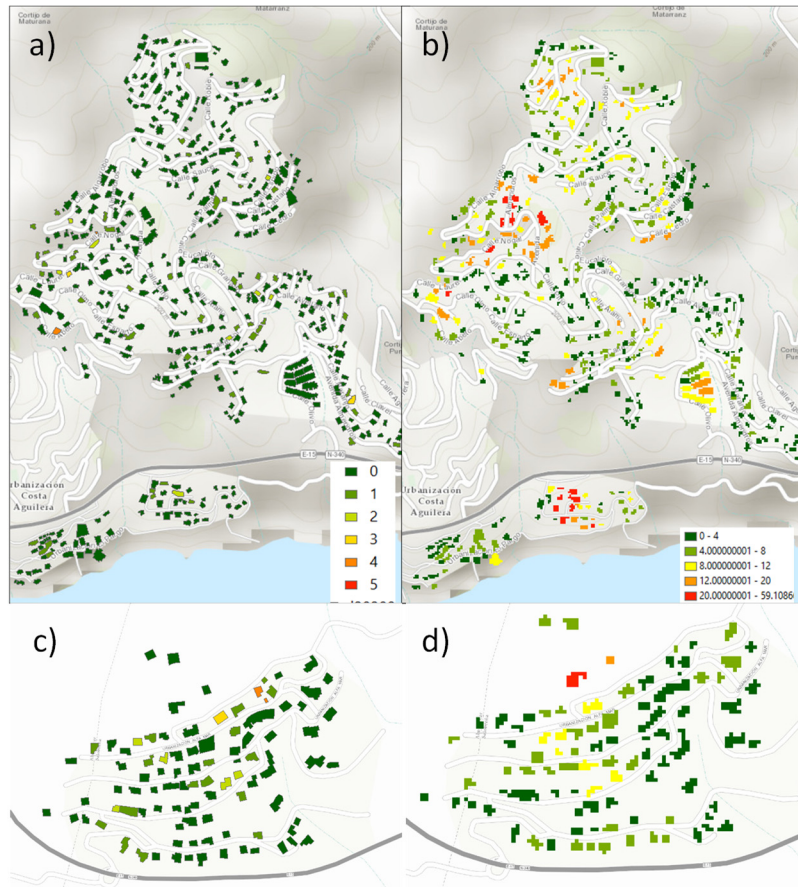


Figure 4. On the left part, the potential damage maps of Monte de Los Almendros (a) and Alfa mar (c). On the right part, the damage inventories obtained from a field work during the year 2019 in Monte de Los Almendros (b) and Alfa Mar (d).

#### IV. DISCUSSION

The work presented in this article represents an integration of the PSIG processing chain and the ADAtools developed at the Geomatics Division of the CTTC. The main goals are two: (i) to simply and ease the interpretation of the velocity map and TSDs resulting from Advanced DInSAR processing methods, and (ii) to provide more advanced products to support prevention against geohazards and urban-planning activities.

The first aspect to be underlined is that ADA detection does not overcome the intrinsic limitations of the InSAR techniques, *i.e.* the absence of ADAs does not necessarily imply stability since it could also mean non-detectable movement due to unfavorable geometry (Ferretti *et al.*, 2007) or lack of information due to low coherence.

The approach has been tested in the Coast of Granada (Spain). Several displacement phenomena have been detected. 148 Active Deformation Areas have been detected. Among them, 5 have been classified unambiguously as settlements and corresponds to recently constructed areas. Some other areas have been classified as potential landslides. The field work and the existing literatures have confirmed that most of them area actually active landslides. The results illustrate very well the high potential of the ADA finder and Classifier. The first one only depends on the DInSAR based results and thus its quality is strongly linked to them. However, the reliability of the ADA classifier relies on the available ancillary data. This can be a strong constrain at different places of the world.

Regarding the Potential Damage maps, we have shown the preliminary results obtained in two active areas: Monte de Los Almendros y Alfa Mar. The results show that there is a noticeable disagreement between the field survey and the maps obtained from DInSAR. However, this disagreement can be explained by different aspects:

- The satellite-based results only take into account the detected local differential displacements. Nor the structural characteristics of the building its foundations. This can strongly condition its vulnerability.
- The disagreement can be also explained because the in-situ damage maps are based on the visual inspection of the visible part of the buildings. Thus, it can happen that the damages are simply invisible.
- Finally, a third reason of disagreement could be explained by the time of inspection. We are looking to a long process on time. This means that the movement has still not damaged the building or that the damages have been repaired. We refer here to those points where damages have been observed in the field but not in our approach.

The results obtained prove that the method applied in this work might prove useful for a fast and semi-automatic detection of geohazards and assessment of its potential effects. The ADAfinder and Classifier tools provide an approach to rapidly assess the InSAR products to detect critical unstable areas that can be easily used by Civil Protections and Geological Surveys. Moreover, the potential damage maps together with the European Ground Motion Service can be a powerful tool for urban planning.

#### V. CONCLUSIONS

The implemented methodology detects and analyzes ground displacements based on satellite InSAR techniques and the ADAtools. A description and analysis of the results obtained for an area located in Granada County (Spain) have been presented in this paper. The complementarity of the PSIG InSAR technique and the ADA tools have been demonstrated. On one hand, InSAR techniques are able to provide displacement measurements over large areas at low cost, but the difficulty to interpret those results by non-expert users hamper their use by decisions makers. On the other hand, the ADA tools allows a semi-automatic identification of critical areas affected by instability, *i.e.* the ADAs, and provides a preliminary assessment on the nature of the moving process. The ADA tool might be exploited to obtain a fast selection of deformation areas. However, an advanced analysis and interpretation is possible with the combination of all outputs as presented in this work. An integrated analysis of the velocity of deformation map, the TSDs and the ADA map might prove very useful to interpret the geological and geotechnical processes affecting wide areas and to assess the potential effects on buildings and infrastructures. Furthermore, this set of techniques will support the exploitation of the European Ground Motion Service (EU-GMS), which will provide consistent, regular and reliable information on natural and anthropogenic ground motion phenomena all over Europe.

#### VI. ACKNOWLEDGEMENTS

This work was mainly supported by the European Regional Development Fund (ERDF) through the project "RISKCOAST" (SOE3/P4/E0868) of the Interreg SUDOE Programme.

#### References

- Barra, A., Solari, L., Béjar-Pizarro, M., Monserrat, O., Bianchini, S., Herrera, G., Crosetto, M., Sarro, R., González-Alonso, E., Mateos, R.M., Ligüerzana, S., López, C., and Moretti, S. (2017). A methodology to detect and update active deformation areas based on Sentinel-1 SAR images. *Remote Sens* 9: 1002. DOI: 10.3390/rs9101002
- Carlà, T., Intrieri, E., Raspini, F., Bardi, F., Farina, P., Ferretti, A., Colombo, D., Novali, F., and Casagli, N. (2019). Perspectives on the prediction of catastrophic slope failures

- from satellite InSAR. *Sci Rep* 9: 1-9. DOI: 10.1038/s41598-019-50792-y
- Crosetto, M., Monserrat, O., Cuevas-González, M., Devanthéry, N., and Crippa, B. (2016). Persistent scatterer interferometry: A review. *ISPRS Journal of Photogrammetry and Remote Sensing*, 115, pp. 78-89.
- Crosetto, M., Solari, L., Mróz, M., Balasis-Levinsen, J., Casagli, and N., Frei, (2020). The evolution of wide-area DInSAR: From regional and national services to the European Ground Motion Service. *Remote Sensing*, 12(12), 2043.
- Devanthéry, N., Crosetto, M., Monserrat, O., Cuevas-González, M., and Crippa, B. (2014). An approach to Persistent Scatterer Interferometry. *Remote Sens.*, 6, pp. 6662–6679
- Ferretti, A., Monti-Guarnieri, A., Prati, C., Rocca, F., and Massonet, D. (2007). *InSAR Principles-Guidelines for SAR Interferometry Processing and Interpretation, TM-19*; ESA Publications: Auckland, New Zealand.
- Galve, J. P., Pérez-Peña, J. V., Azañón, J. M., Closson, D., Caló, F., Reyes-Carmona, C., and Bally, P. (2017). Evaluation of the SBAS InSAR service of the European space Agency's Geohazard Exploitation Platform (GEP). *Remote Sensing*, 9(12), 1291.
- Navarro, J. A., Cuevas, M., Tomás, R., Barra, A., and Crosetto, M. (2019). Automating the Detection and Classification of Active Deformation Areas—A Sentinel-Based Toolset. In *Multidisciplinary Digital Publishing Institute Proceedings* (Vol. 19, No. 1, p. 15).
- Tomás, R., Pagán, J. I., Navarro, J. A., Cano, M., Pastor, and J. L., Riquelme, (2019). Semi-automatic identification and pre-screening of geological-geotechnical deformational processes using persistent scatterer interferometry datasets. *Remote Sensing*, 11(14), 1675.

## Static and Dynamic Monitoring of the Notre Dame de Paris Cathedral

Véronique Le Corvec, Patrick Lézin, François-Baptiste Cartiaux

OSMOS Group SA, 37 rue La Pérouse, Paris, France, ([lecorvec@osmos-group.com](mailto:lecorvec@osmos-group.com); [lezin@osmos-group.com](mailto:lezin@osmos-group.com); [cartiaux@osmos-group.com](mailto:cartiaux@osmos-group.com))

**Key words:** *cultural heritage; vibration monitoring; tiltmeter chain; continuous monitoring*

### ABSTRACT

During the fire which took place on 15<sup>th</sup> April 2019, the Cathedral of Notre Dame de Paris underwent extensive structural damages: most of the roof was destroyed, part of the stone vaulted ceiling collapsed, and the wooden framework of the north tower was partially burned. After the fire, a list of actions was carried on in order to secure the remaining structure, prevent any further damage and start the rehabilitation. Very early on, a monitoring system was used to assist the project manager in these tasks. With the progress of site works, the monitoring system was updated to provide more insightful information. The present paper focuses on the monitoring system deployed on the towers and the stone vaulted ceiling with the objective to produce a first assessment of the current state and follow the evolution during the reconstruction phase. The monitoring campaign was carried out from December 2020 to December 2021 with two distinct sets of sensors. The first objective was to characterize the current state and identify the dynamic behavior of the structure, for that purpose 48 directional accelerometers were installed on the two towers and the two vaults lane. Acceleration measurements and analytical methods lead to the identification of the fundamental modes of these structural elements. In a second time, to follow the evolution of the vaults, 56 inclinometers were positioned on the outer side of the vaults, constituting 15 inclinometer measuring chains. Set up to transmit data continuously with a 10 min frequency, measurements allow to notify settlements or uprisings and correlate these evolutions with external factors (weather conditions or rehabilitation works).

### I. INTRODUCTION

The Cathedral Notre-Dame in Paris is one of the most important heritage buildings in France, included in the UNESCO World Heritage Sites list since 1991 as part of Paris, Banks of the Seine (Unesco World Heritage List, 2021). Thus, the fire which destroyed the roof, the spire, and parts of the stone vaults on April 15, 2019, had a considerable emotional echo not only in France, but also in the world.

Immediately after the disaster, important works have been carried out, first to ensure the safety of the structure during the expertise and the dismantling of the damaged scaffolding, which was installed around the spire the day of the fire. As a part of the safety works, a comprehensive Structural Health Monitoring (SHM) system has been implemented on various parts of the building by OSMOS, including high-precision lasers to detect and anticipate movements of the damaged vaults first, and then up to more than 140 sensors.

This complex system involves several different types of sensors, measurements and data analysis tools, including an immediate alert feature based on tilt and strain measurements on the damaged scaffolding of the spire during its dismantling until November 2020, a static monitoring of the deflection of the vaults with rows of tiltmeters, and Operational Modal Analysis (OMA) performed from numerous accelerometers on both the timber structures inside the two belfries and

on the vaults and pillars of the nave (OSMOS Group SA, 2020).

Such OMA are often performed on historical buildings, in particular on belfries, in order to assess structural behaviors in relation with bell swings (Metz Cathedral; Patron-Solares, 2005) or when damaged by earthquake (St Silvestro belfry in L'Aquila 2021; Capanna, 2021).

This paper focuses on two tasks of this vast SHM enterprise: first the monitoring of the vibrations of the vaults and belfries, to identify the free vibration modes of the structure, and then the continuous assessment of the movements of the vaults of the nave.

### II. VIBRATION MONITORING

#### A. Aim of the Vibration Monitoring

The Vibration Monitoring of the Notre-Dame de Paris Cathedral was a short-term operation conceived to give inputs for structural models of the building, in view of the future reconstruction works. The monitoring system, which consists in 48 accelerometers, was in operation from December 14, 2020, to January 28, 2021. However, as the aim was only to get modal characteristics of the structure, the analysis was carried out from one single data sample of one hour, recorded on December 27, 2020.

The Monitoring System covered three separate parts of the cathedral, considered as structurally independent: the timber structure inside the North

belfry, the timber structure inside the South belfry, and a sample of two vaults of the nave (Figure 1). Thus, the OMA was performed on each one of these three objects separately.

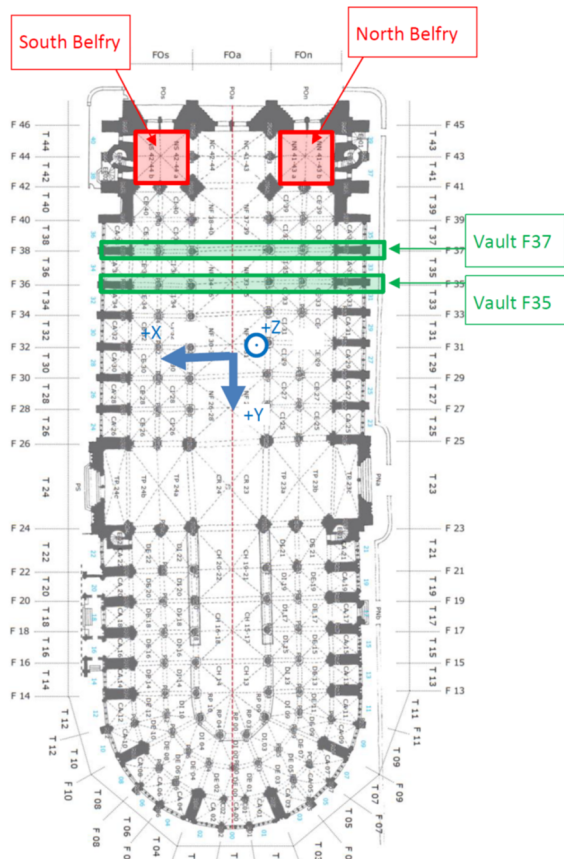


Figure 1. Plan view of the cathedral with the zones instrumented for the vibration analysis.

The results of the analysis consisted in lists of modal characteristics, including frequency, damping ratio and mode shape, directly deduced from the synchronized acceleration measurements taken under ambient noise conditions only. There was no dedicated dynamic excitation, considering the criticality of the situation of the structure, dating from the 12<sup>th</sup> century and just recovering from a catastrophic fire.

### B. Sensor layout

The 48 accelerometers were set to catch the most significant movements due to the free vibrations of the structures.

In the case of the timber structures inside the belfries, three different levels were instrumented, each of them with three accelerometers on two different locations, to assess horizontal movements in both transverse directions and in rotation for each level. In addition, a three-axis accelerometer was installed at the location of the support of the main bell, to check the risk of resonance for future bell ringing (Figures 2 - 3, Table1).

In the case of the two stone vaults of the nave, the set of accelerometers was conceived to assess the vertical

movement (Z axis) of the vault on three different locations, and the transverse horizontal movement (North-South, X axis) of the pillars at the junction with the arches of the vault and at the top (Figure 4, Table 2). In addition, the movement in both horizontal directions at the top of the buttresses was also measured, as well as the movement of the keystone in the longitudinal direction (East-West, Y Axis).

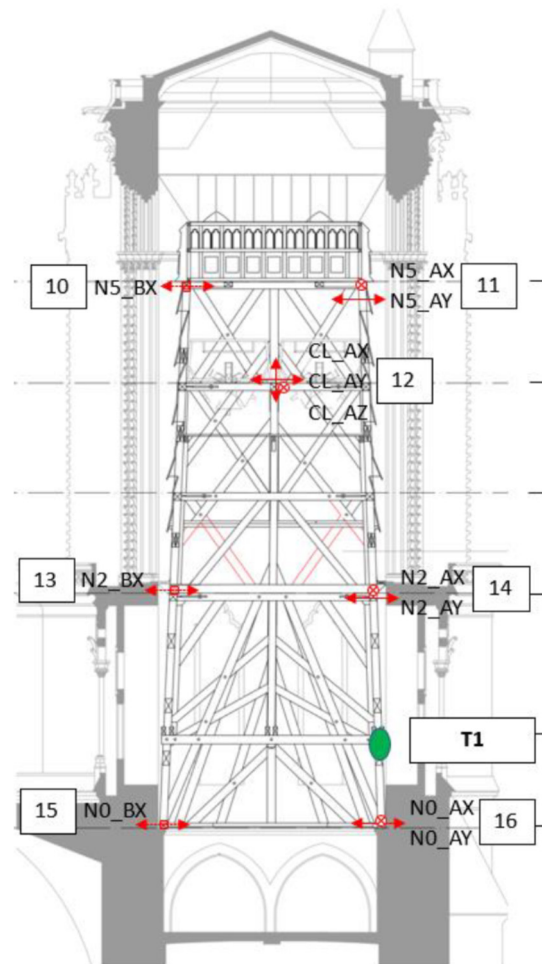


Figure 2. Accelerometer layout for the vibration analysis of the North belfry. The sensors are set on the timber structure supporting the bells inside the masonry tower.

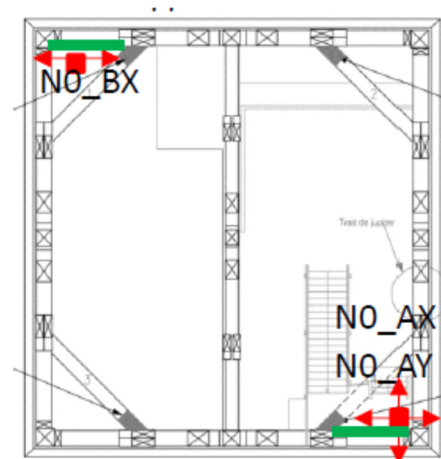


Figure 3. Accelerometer layout at a belfry level (similar arrangement for both belfry).



Table 1. Accelerometers position on the belfry (identical repartition for the north and south belfry)

Name	Height [m]	Direction	Position
N0_AX	69	+X	Bottom-Right Corner
N0_AY	69	-Y	
N0_BX	69	-X	Upper-Left Corner
N2_AX	79	+X	Bottom-Right Corner
N2_AY	79	-Y	
N2_BX	79	-X	Upper-Left Corner
CL_AX	88	+X	Bell support
CL_AY	88	+Y	
CL_AZ	88	+Z	
N5_AX	93	+X	Bottom-Right Corner
N5_AY	93	-Y	
N5_BX	93	-X	Upper-Left Corner

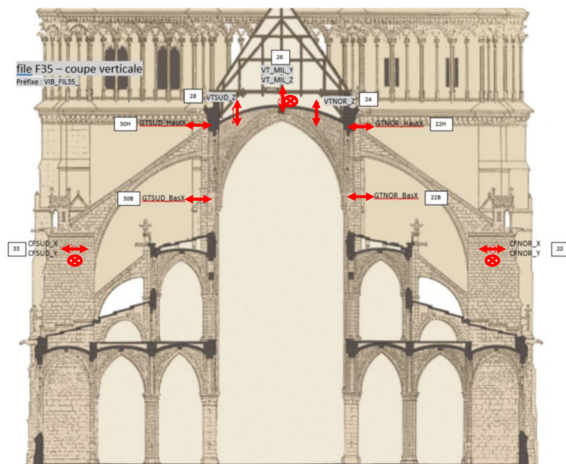


Figure 4. Accelerometer layout for the vibration analysis of one of the vault of the nave.

Table 2. Accelerometers position on the nave vault (identical repartition for the two vaults)

Name	Height [m]	Direction	Position
CFNOR_X	55	-X	North buttress
CFNOR_Y	55	+Y	
CFSUD_X	55	-X	South buttress
CFSUD_Y	55	+Y	
GTNOR_BasX	60	+X	Great transept
GTNOR_HautX	64	+X	North wall
GTSUD_BasX	60	-X	Great transept
GTSUD_HautX	64	-X	South wall
VTMIL_Y	68	-Y	Middle of the vault
VTMIL_Z	68	+Z	
VTNOR_Z	67	+Z	North Vault
VTSUD_Z	67	+Z	South Vault

The whole layout consisted in four groups of 12 accelerometers each: North belfry, South belfry, vault nb 35 and vault nb 37. The accelerometers were OSMOS AAA sensors with a measurement range of +/- 4g, a noise density of 20 µg/√Hz and 1% horizontal axis sensitivity (OSMOS Group AAA Tri-Axial Analogue Accelerometer Specifications, 2022). Each group of 12 sensors was connected to an OSMOS EDAS data acquisition system, which performed the interrogation of the sensors with a 100 Hz sampling rate and the

synchronization of the measurements, necessary for the OMA.

### C. Operational Modal Analysis Methodology

The OMA was performed on the synchronized acceleration measurements by the mean of an Eigensystem Realization Algorithm (ERA) after Juang and Pappa (1985), recently documented for applications in the identification of the vibration modes of buildings and civil structures (Bulut *et al.*, 2019). In the ERA methodology, the state-space model is obtained from a factorization of a Hankel matrix of Markov parameters using the singular value decomposition. For this application, an output-only way of using the ERA was implemented, in which the Markov parameters are obtained as correlation matrices between the output different channels, 12 for each one of the four zones.

This method was recently applied in the frame of an experimental study on one pier of the Millau viaduct in France, from strain measurements on two different levels on the pier, under the effects of strong winds (Cartiaux *et al.*, 2021). In the case of Notre-Dame, the data used for the OMA was acceleration data, in a more classical way, however this method has been proven to be robust to other types of measurements.

The ERA gives results in the form of a stabilization diagram, from which abstract modes can be deduced. An abstract mode has the frequency and the damping ratio of an actual free vibration mode, and its shape is described by a set of factors, with one (real number) value associated with each one of the accelerometer channels.

Once the abstract modes have been identified, the actual mode shapes are built by considering the locations and directions of the accelerometer channels. The shape between two sensor locations is then interpolated according to the geometry of the structure. In the case of the belfries, the accelerometer layout allows to quantify both horizontal displacements (bending modes) and rotation (torsion modes) for each one of the instrumented levels of the timber structure.

The data used for the OMA was recorded on December 27, 2020. It is one single sample of one full hour for all 48 accelerometers, including some episodes of significant wind with a wind speed up to 70 km/h. The results have then been confirmed by a similar analysis performed on four other samples of data at different dates in January 2021.

### D. Results on the belfries

The timber structures inside the belfries are classical objects for an OMA, similar in some way to high-rise buildings, for example. Thus, the locations and directions of the accelerometer channels were decided following usual guidelines, to assess bending and torsion modes through the movement of rigid floors, at three main levels.

However, the complexity of the timber bracings, also different between the North belfry and the South one, induced interesting dynamic characteristics with strong differences from North to South. Tables 3 and 4 summarize the results of the OMA for each belfry. X (North-South) and Y (East-West) directions refer to Figure 1.

Table 3. OMA for the North Belfry

Frequency [Hz]	Damping Ratio [%]	Shape
1.2	2.7	Y Bending
3.4	4.7	Y Bending
4.5	4.3	X Bending
4.6	3.3	XY Bending
5.6	5.4	Torsion
6.1	5.1	Torsion

Table 4. OMA for the South Belfry

Frequency [Hz]	Damping Ratio [%]	Shape
1.3	2.0	XY Bending
1.5	2.6	XY Bending
1.9	2.3	XY Bending
3.8	3.7	XY Bending
4.3	2.5	X Bending
4.7	2.2	Torsion
5.5	2.8	Torsion
5.8	4.1	Torsion

For both belfries, the first mode is a bending mode with similar frequencies around 1.2-1.3 Hz. Torsion modes appear starting around 5 Hz (5.6 Hz North and 4.7 Hz South). Differences appear mainly for the second and next bending modes, both in terms of frequencies and mode shapes: on the North belfry, bending modes mostly have a main direction X or Y, while on the South we have mixed modes combining both directions. The frequencies are also higher in the case of the North belfry, except for the first bending mode.

It is also noted that few modes, except the first one, induce movements of all the levels along the height of the belfries. Only the top half of the timber structure has a significant participation in higher bending modes and in the torsion modes, while the lower half appears to be retained by the surrounding masonry tower. The visualization of some of the mode shapes is released on Figures 5 and 6.

E. Results on the vaults

The stone vaults of the nave are more exotic objects for an OMA than the belfries. They are composed of very different types of masonry structures, from massive buttresses to thin pillars and light keystone. The 12 accelerometers layout is then a compromise between comprehensiveness of the measurements and economical possibility. It allows to assess the global movements of each one of the two instrumented vaults along the nave at the locations where it is expected to be the most significant, including the keystone, the top

of the buttresses and of the pillars. However, some assumptions had to be accepted to deduce whole mode shapes from the limited number of measurement locations, like fixed bearing conditions at the soil interface.

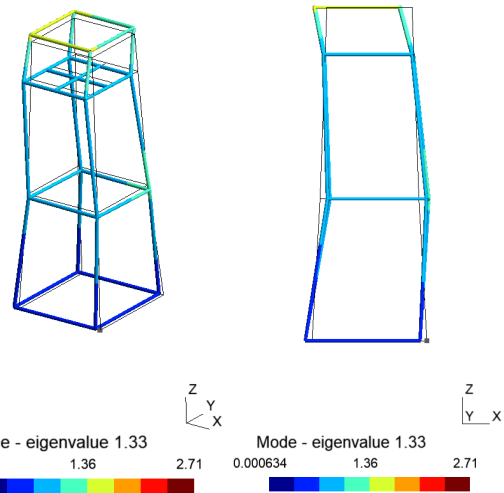


Figure 5. First bending mode of the timber structure inside the South belfry, at 1.33 Hz. The mode shape shows bending in both X and Y directions on all levels along the height of the tower.

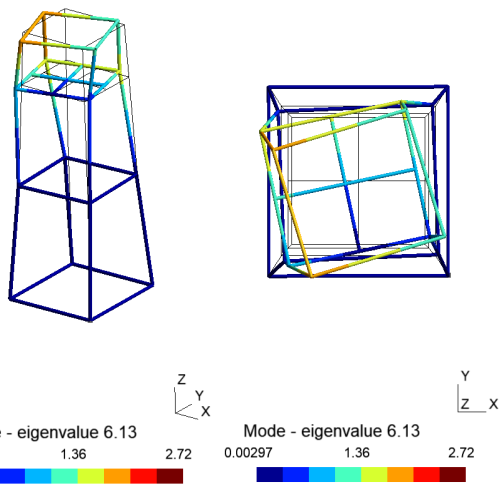


Figure 6. Torsion mode of the timber structure inside the North belfry, at 6.13 Hz. The torsion appears as a local mode of the top of the structure, while the lower part has very few movements.

Unlike the case of the two belfries, the two vaults show good similarities concerning the frequencies of the main vibration modes, but also slight differences. Tables 5 and 6 summarize the results of the OMA for each vault. X (North-South) and Y (East-West) directions refer to Figure 1.

In both cases, the first vibration modes are local vibrations of the South buttress in the East-West direction (2.1 Hz and 1.9 Hz, Figure 7), then a similar main bending mode of the whole vault in the North-South direction (2.4 Hz and 2.3 Hz, Figure 8), and then the local vibrations of the North buttress in the East-West direction (2.6 Hz for both). The fourth mode is also

similar with another global bending in the North-South direction (3.1 Hz and 3.4 Hz), as well as the local vertical bending modes of the keystone at higher frequencies around 11 Hz.

Table 5. OMA for the vault nb 35

Frequency [Hz]	Damping Ratio [%]	Shape
2.1	2.8	South buttress in dir. Y
2.4	8.9	Global bending in dir. X
2.6	2.7	North buttress in dir. Y
3.1	3.1	Global bending in dir. X
3.4	3.6	Bending of North side in dir. X
4.8	6.5	Keystone in dir. Z
11.2	6.5	Keystone in dir. Z

Table 6. OMA for the vault nb 37

Frequency [Hz]	Damping Ratio [%]	Shape
1.9	1.3	South buttress in dir. Y
2.3	2.3	Global bending in dir. X
2.6	2.6	North buttress in dir. Y
3.4	4.3	Global bending in dir. X
4.2	4.0	Bending of South side in dir. X
4.7	8.1	Global bending in dir. X
10.7	4.1	Keystone in dir. Z
11.2	8.9	Keystone in dir. Z

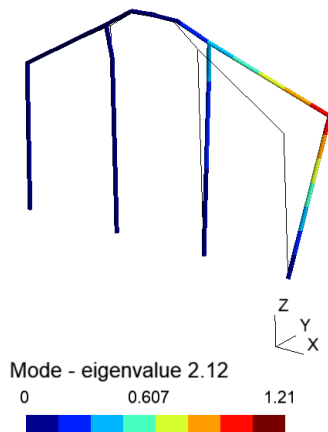


Figure 7. Local mode of the South buttress in direction Y (East-West) on the vault nb 35.

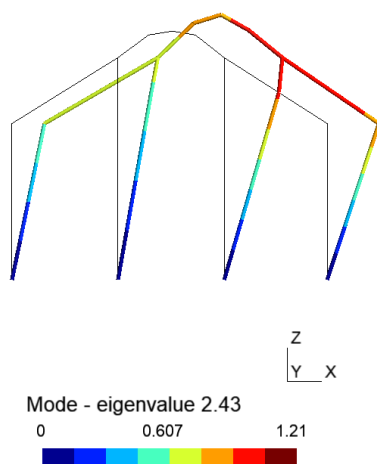


Figure 8. Global bending mode in the direction X (North-South) on the vault nb 35.

Intermediate modes present some discrepancies between the two vaults: bending of either the North side (Vault nb 35, 3.4 Hz) or the South side only (Vault nb 37, 4.2 Hz), and a specific mode shape at 4.7 Hz for the vault nb 37, combining a vertical displacement of the keystone and opposite bending on both North and South sides (Figure 9).

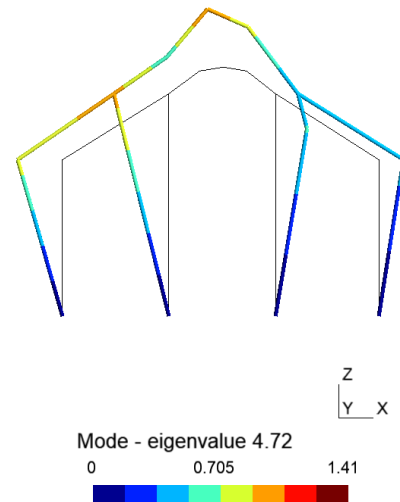


Figure 9. Specific combined mode on the vault nb 37, with vertical displacement and opposite bending of both North and South sides.

The OMA performed on the vaults from a one-hour sample of acceleration records at 100 Hz sampling rate gave consistent results in terms of frequencies and mode shapes. The damping ratio is less reliable, as it is not easy to deduce from ambient noise only. Indeed, the accurate estimation of the damping ratio by the mean of an ERA requires the assumption of pure white noise as an input, which for sure is not perfectly fulfilled under real conditions on site. However, the order of magnitude of the estimated damping ratios is still consistent with a masonry structure.

### III. SETTLEMENTS OF THE VAULTS

#### A. Aim of the settlement monitoring and sensor layout

The fire of April 15, 2019, induced strong evolutions concerning the descent of loads on the vault structure: the whole roof was destroyed, and some parts of the vaults themselves did not resist to the collapse of the spire. Within the first two weeks after the fire, a first monitoring system was set up to detect any further movement of the damaged vaults, by the mean of high precision lasers (La Fabrique de Notre-Dame, 2021). This was the only option, as the access to the vault was not possible to install sensors or targets.

However, this solution faced numerous issues during the safety works, since the space between the laser and its target point on the vault is supposed to remain clear. This condition imposed to displace some lasers regularly, which troubled the continuity of the data acquisition, and eventually the configuration of the

workplace imposed to seek another way to assess the settlements of the vaults.

Thus, a new monitoring system was set up in February 2021. Since it had become possible to access the cleaned vaults, the sensors could be set directly on the structure at that time. The solution consisted in tiltmeter chains along the transverse profile of the vault: each chain is composed of five high-resolution Senceive autonomous tiltmeters, fixed on the upper side of the vault with plaster.

The variations of the tilt for each one of the sensors reflects the average slope of the vault at its location, and the integration of the successive slopes allows an estimation of the settlement along the transverse profile. Four of the tiltmeters are used for the slope estimation, and the fifth one is set on a fixed point (relatively to the vault, i.e., on the next wall) and is used as a reference (Figure 10).

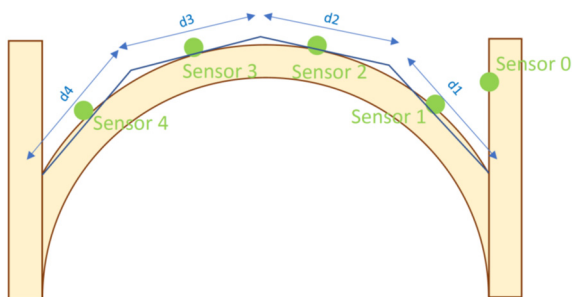


Figure 10. Schematic view of a tiltmeter chain on a vault with four slopes. Sensor 0 is the reference.

15 tiltmeter chains have been used on the vaults of Notre-Dame de Paris: six on the nave, six on the choir and three on the transept.

### B. Main results

On the period from February 2021 to June 2021, very few movements of the vaults have been measured. Indeed, at this stage of the safety works, the structure of the whole cathedral was already strongly stabilized with additional supports.

Millimetric fluctuations are cyclically observed every day, due to the effect of the temperature variations. Apart of these variations, global trends have been assessed only for the choir, with settlements on the south part of the vaults near to the transept, where the vaults collapsed during the fire (Figure 11). The same is observed on the north part of transept, also consistent with the vicinity of collapsed vaults.

## IV. CONCLUSION

The very complex and challenging operation to ensure the structural safety and then restore the Notre-Dame de Paris cathedral involves a comprehensive continuous SHM system for this iconic heritage, with various problematics, sensor types, and methods for data analysis.

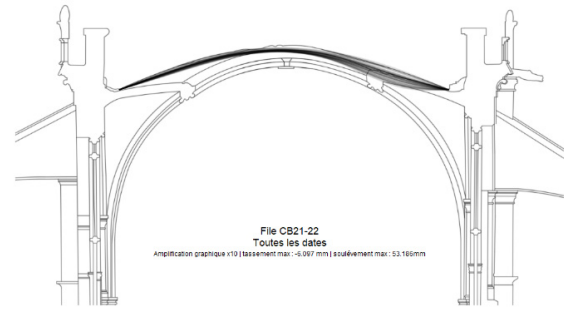


Figure 11. Envelop of the settlements of the vaults of the choir, near to the collapsed vaults of the transept, February 2021 to June 2021 (amplified 10 times).

Among the numerous missions for which the SHM enables to give an immediate and consistent knowledge about the evolution of the structure, including real time alerts, if necessary, the two examples described in this publication show relevant applications for two very different purposes at different time scales.

As part of the diagnosis, in view of getting reliable inputs for a structural model, the natural vibration modes of different important elements of the cathedral have been efficiently identified through the use of OMA on relatively short samples of records (one hour) at a high sampling rate, using a combination of numerous accelerometers.

At the other hand, the stability of the vaults has been assessed on a long period with static tilt measurements every hour, which enabled to estimate the shape of the vault settlements on several parts of the nave, transept, and choir.

All the data collected during this exceptional project and the resulting analysis may be further used by scientists to enhance the knowledge about the wonderful and living witness of the human heritage that is Notre-Dame de Paris. As a research perspective, the obtained modal analysis may be compared with theoretical models (as finite element model) of the cathedral to assess the actual structural properties, accounting of aging and damages. These results could be also compared with further modal analysis after the reinforcement of the cathedral, in particular for the vaults.

## V. ACKNOWLEDGEMENTS

The authors wish to thank the Public Establishment dedicated to the Conservation and Restoration of the Notre-Dame de Paris Cathedral for supporting this publication.

## References

- Bulut Y., Unal B., and Bernal D. (2019) Performance Evaluation of System Identification Algorithms for Structural Health Monitoring. In: *5th International Conference on Earthquake Engineering and Seismology, Ankara, 8-11 October 2019*.
- Capanna I., Cirella R., Aloisio A., Alaggio R., Di Faio F., and Fragiaco M. (2021). Operational Modal Analysis, Model Update and Fragility Curves Estimation, through Truncated

- Incremental Dynamic Analysis, of a Masonry Belfry. *Buildings*, 11, 120. DOI: 10.3390/buildings11030120.
- Cartiaux F.B., Le Corvec V., Cachot E., Vayssade T., and Servant C. (2021) Continuous Static and Dynamic Strain Measurements on Civil Infrastructures: Case Study on One Pier of the Millau Viaduct. In: Rizzo P., Milazzo A. (eds) *European Workshop on Structural Health Monitoring. EWSHM 2020*. Lecture Notes in Civil Engineering, vol 127. Springer.
- Juang J. N., and Pappa R. S. (1985). An eigensystem realization algorithm for modal parameter identification and model reduction. In: *Journal of guidance, control, and dynamics*, 8(5), pp. 620-627.
- La Fabrique de Notre-Dame, (2021). Available in: <https://fr.calameo.com/read/00557636894eb0332971f?authid=TW18VI9mAvBC>, consulted 2022/01/25.
- OSMOS Group SA, 2020, <https://www.osmos-group.com/en/news/osmos-group-heart-notre-dame-de-paris>, consulted 2022/01/25.
- Patron-Solares A., Cremona C., Bottineau C., Leconte R. and Goepper F. (2005) *Experimental Vibration Analysis for Civil Engineering Structures*, Bordeaux France, 26-28 October 2005.
- OSMOS Group AAA Tri-Axial Analogue Accelerometer Specifications <http://www.sanlien.com.tw/product/aaa-tri-axial-analogue-accelerometer/>, consulted 2022/05/10
- Unesco World Heritage List, (2021). Paris, Banks of the Seine: Available in: <https://whc.unesco.org/en/list/600>, consulted 2022/01/25.

## Comparison of TLS and sUAS point clouds for monitoring embankment dams

Dimitrios Bolkas<sup>1</sup>, Matthew O'Banion<sup>2</sup>, Jakeb Prickett<sup>2</sup>, Gregory Ellsworth<sup>1</sup>, Gerald Rusek<sup>1</sup>,  
Hannah Corson<sup>1</sup>

<sup>1</sup> Department of Surveying Engineering, The Pennsylvania State University, Wilkes-Barre Campus, 44 University Drive, Dallas, PA 18612, USA, ([dx80@psu.edu](mailto:dx80@psu.edu); [gje5059@psu.edu](mailto:gje5059@psu.edu); [gjr5221@psu.edu](mailto:gjr5221@psu.edu); [hrc5135@psu.edu](mailto:hrc5135@psu.edu))

<sup>2</sup> Department of Geography & Environmental Engineering, United States Military Academy, 745 Brewerton Rd., West Point, NY 10996, USA, ([matthew.obanion@westpoint.edu](mailto:matthew.obanion@westpoint.edu); [jakeb.prickett@westpoint.edu](mailto:jakeb.prickett@westpoint.edu))

**Key words:** dam monitoring; terrestrial laser scanning; sUAS; accuracy assessment; point clouds

### ABSTRACT

Monitoring of dams is an essential surveying task to guarantee the safety of operation and understand the physical processes concerning their movement. Point cloud generating technologies are increasingly being utilized for monitoring of engineered structures. This paper compares point clouds acquired from terrestrial laser scanning (TLS) and small unmanned aerial systems (sUAS)-based photogrammetry for monitoring of the Francis E. Walter dam in northeast Pennsylvania. Authorized for construction by the Flood Control Act of 1946, and with renewed interest due to extensive flooding in 1955 caused by the back-to-back hurricanes Connie and Diane, this earth-filled embankment dam was completed in June of 1961 by the U.S. Army Corps of Engineers. It is currently operated in conjunction with Beltzville Lake for stage reductions on the Lehigh River. The dam is being monitored through conventional surveying methods (total station) every five years. In spring of 2021 a TLS and sUAS data acquisition took place to assess the feasibility and utility of using modern point cloud technologies for monitoring. This paper presents a comprehensive comparison and accuracy assessment of the two point cloud collection methods, considering several parameters for the generation of the sUAS photogrammetric point cloud. Results show the advantages and disadvantages of the two methods. For instance, TLS offers high accuracy (cm-level), but suffers from data gaps due to line of sight blockage/occlusion. On the other hand, sUAS photogrammetry offers more complete point clouds, but presents more challenges in georeferencing and in the generation of accurate point clouds. Similar insights and lessons learned are useful for future surveying tasks and monitoring of similar embankment dam structures.

### I. INTRODUCTION

Periodic and frequent monitoring of engineering structures is important for ensuring their integrity and guarantee their safety of operation (Scaioni *et al.*, 2018). Surveying methods have long been used to monitor engineering structures such as dams to monitor and understand the physical processes concerning their movement. While traditional surveying methods, using total station instruments and/or global navigation satellite system (GNSS) observations, have been proven accurate and reliable (Jeon *et al.*, 2009; Xi *et al.*, 2018; Xiao *et al.*, 2019) they do pose limitations. For instance, they require lengthy data acquisition durations which limits the number of discrete points that can be monitored. To address the issue of long data acquisitions, permanent robotic total stations and GNSS receivers are being installed for monitoring dams in frequent intervals or near-real time. Ground based synthetic aperture radar (GBSAR) is a technology that can provide measurements at the  $\pm 1$  mm level and can be used to capture displacement patterns in high spatial resolution than just at a few discrete points. In its continuous mode of operation, the unit needs to be installed permanently (Alba *et al.*,

2008; Scaioni *et al.*, 2018), and its discontinuous mode necessitates revisiting the site periodically (Alba *et al.*, 2006; Mascolo *et al.*, 2014), which can introduce challenges in phase ambiguity estimations. Furthermore, displacements are given along the line of sight and not in 3D coordinates (Scaioni *et al.*, 2018).

On the other hand, point cloud technologies from terrestrial laser scanning (TLS) are gaining ground as they offer high spatial resolution with accuracies around  $\pm 1-2$  cm (Mukupu *et al.*, 2017); however, this also depends on the registration approach. When monitoring concrete dams, deformation levels are observed at the mm-level (Scaioni *et al.*, 2018), making TLS monitoring a challenging task. In this case rigorous estimation of TLS errors and error propagation is necessary to distinguish between noise and deformation (Mukupu *et al.*, 2017; Scaioni *et al.*, 2018; Li *et al.*, 2021). In addition, in concrete dams TLS can take advantage of their physical shape and fit a parametric surface on the point cloud such as polynomial surface (Alba *et al.*, 2006) or radial basis functions (González-Aguilera *et al.*, 2008). TLS is more appropriate for monitoring earth-rock embankment

dams, due to the higher magnitude tolerated, which can be at the few cm- to dm-level (Xu *et al.*, 2019).

Recently small unmanned aerial system (sUAS) photogrammetry has been used to monitor dams with accuracies on the order of a few cm-level (e.g., Buffi *et al.*, 2017; Ridolfi *et al.*, 2017; Khaloo *et al.*, 2018; Zhao *et al.*, 2021); therefore, making this technology more suitable for monitoring earth-rock dams. For concrete dams, use of sUAS is better suited for inspection of the dam structure and identification of cracks (Zhao *et al.*, 2021). Despite the lower accuracy of sUAS photogrammetry compared to TLS, the technology offers some advantages such as an improved vantage point and a less obscured line of sight when compared to many perspectives (e.g., O'Banion *et al.*, 2018; Bolkas *et al.*, 2021). In general, sUAS and TLS methods also provide a relatively fast data acquisition solution that results in the generation of a dense point cloud dataset. The major drawback is that sUAS and TLS methods often need an extensive network of control points for georeferencing.

Considering the differences in the TLS and sUAS technologies, this paper makes a comparison of TLS and sUAS derived point clouds for monitoring earth-filled embankment dams. The Francis E. Walter Dam that is being investigated in this paper, has been monitored with traditional total station methods. The paper provides a comprehensive analysis of TLS and sUAS methods and discusses their potential for continued monitoring of this site in the following years.

## II. STUDY AREA AND DATASETS

### A. Francis E. Walter dam

The Francis E. Walter dam is located in northeast Pennsylvania approximately 7 km northeast from the town of White Haven, PA. It is an earth-filled embankment dam that was completed in 1961 by the U.S. Army Corps of Engineers (U.S. Army Corps of Engineers 2021). The dam represents a flood control project and is currently operated in conjunction with Beltzville Lake for stage reductions on the Lehigh River. The dam is also a popular recreation destination for fishing, boating, and various paddle sports. The dam has prevented over \$296 million in cumulative damages between 1961 and 2021. The dam has a maximum length of about 910 m, a height of 71 m (foundation to crest), and a base width of 370 m. The capacity of the dam's reservoir is 0.1365 km<sup>3</sup>, and its drainage catchment area is around 750 km<sup>2</sup>.

The embankment is composed of essentially six different types of material. The central core is composed of an impervious fill that extends into the embankment foundation. In addition, a blanket of impervious fill has been placed along the foundation on the upstream side of this core. Above, and upstream of the central core, is a zone of pervious fill. Adjacent to the downstream side of the core, and along the downstream foundation, is a thin layer of pervious

material. Downstream, and above this thin layer is a zone of non-engineered fill. Around the entirely exposed periphery of the embankment, except for the 9 m wide top and downstream toe, there is a protective layer of riprap. The downstream toe of the embankment, in a vertical direction, is composed of rock, impervious fill and non-engineered fill. The top of the dam is 9 m wide at an elevation of 449 m. The last major Lehigh River Basin flood occurred in June of 2006 and resulted in a record pool elevation of 439 m.

### B. Control network

To support the TLS and sUAS data acquisitions a network of 27 points was created. Two control points about one kilometer away from the dam were used as stable references. Some of the 27 points are pre-existing monument disks, some are drill holes in bedrock, mag nails driven into asphalt, and sensor pins (Figure 1). A rapid static Global Navigation Satellite System (GNSS) network was created with at least of 15 minutes of common occupation between baselines. The post adjustment standard deviations were at the 2-3 mm-level, which reflects the internal consistency of the network. With consideration of centering errors, it is estimated that positional accuracy of the control network is at the  $\pm 1$  cm level, which is sufficient for supporting the TLS and sUAS surveys.

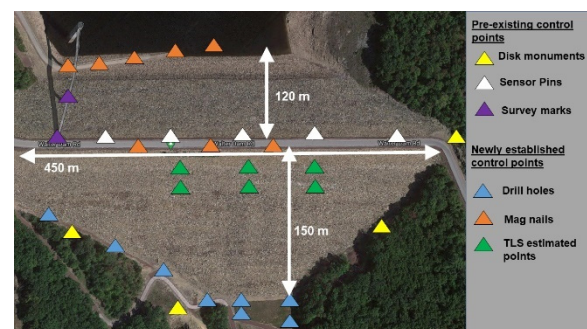


Figure 1. Overview of Francis E. Walter dam and control points for the TLS and sUAS surveys. Dimensions shown are length (450 m) and width (150 m and 120 m). Background image from Google Maps.

### C. TLS survey

A Leica Scan Station P50 was used for the TLS survey (instrument specifications are presented in Table 1). The P50 is a panoramic scanner that offers fast scan rates allowing for fast data acquisition. Its range and angular accuracies are high, ensuring point clouds that are high in accuracy and quality.

The scanning resolution was set to 2 cm at a range of 120 m. Maximum scanning range was set to 120 m, as points can be captured with as little as 8% reflectivity. At a range of 270 m, minimum target reflectivity is significantly higher at 34%. This decrease in sensor sensitivity in conjunction with any registration and measurement errors can lead to higher overall errors in the point cloud. Therefore, it was decided to decrease

the maximum range and increase the number of TLS station setups, which also helps to reduce data gaps due to line of sight obstructions.

Table 1. Leica Scan Station P50 technical specifications information were retrieved from: Leica Geosystems (2021)

Technical specifications	Value
Range accuracy	1.2 mm + 10 ppm
Angular accuracy	8" horizontal; 8" vertical
Dual-axis compensator	Resolution 1", dynamic range $\pm 5'$ , accuracy 1.5"
Beam diameter at front window and beam divergence	3.5 mm, 0.23 mrad Full width at half maximum
Scan rate	1,000,000 points per second

Data collection took place one week after the establishment of the GNSS network on March 21, 2021. Multiple scans were acquired from the base and crest of the dam. The previously discussed control network was used to register the numerous TLS scans. The method of resection was chosen to increase redundancy and derive standard deviations for the estimation of registration accuracy. In most cases at least three control points were used for the resection, except for cases where a third control point was not in view. A resection estimation of only four parameters (three translations and one rotation around the z-axis) was necessary given the use of the P50's accurate onboard dual-axis tilt compensator. Standard deviations for resection did not exceed  $\pm 1$  cm for each coordinate component (easting, northing, elevation).

D. sUAS survey

sUAS data were collected on April 13, 2021, about 20 days after the TLS data collection due to bad weather and higher winds throughout the region. At the time of the sUAS data collection, the reservoir water level was higher and for safety reasons only the protected side was surveyed.

The sUAS survey was completed using an Aibotix sUAS carrying a Sony  $\alpha 6000$  mirrorless digital camera. The digital camera has a 24-megapixel imaging sensor. Aerial images were taken with a 16 mm focal length and a 1/2,000 second shutter speed. The sUAS payload includes a GNSS- Real Time Kinematic (RTK) antenna, allowing for cm level positioning when a base station is used. A GNSS base station was setup at the base of the downstream side of the dam.

Two flights were conducted covering a smaller region than the TLS survey (see Table 2 and Figures 2 and 3). The two flights followed different patterns. The first flight was conducted at a fixed altitude of around 110 m above ground at the base of the dam on the downstream side, which reduced to about 50 m above ground level at the crest of the dam. The orientation of this flight was perpendicular to the road as shown in Figure 3d. A total of 10 flight lines were used, and 156

images were captured. Image endlap was 85%, with 85% sidelap reduced to 60% at the crest. For the second flight, flight line orientation was parallel to the road and the altitude changed for each flight line to maintain more constant heights above ground. A total of five flight lines were used and 190 images were captured. Flying heights remained constant around 60 m except for the last flight line at the dam crest that was closer 50 m above ground level. Image endlap was 85% and 75% sidelap, which reduced to about 60% for the last flight line at the crest of the dam. The resulting average ground sample density (GSD) of the point cloud for the across flight is 4 cm., and the average GSD of the point cloud for the parallel flight is 3 cm. The average GSD are a result of the trade-offs and limitations of the available sUAS and resources for this project.

Table 2. sUAS flight characteristics for April 2021

Parameter	Across flight	Parallel flight
Altitude [m]	50 to 110	60 (50 for last flight line at crest)
Flightlines	10	5
Images	156	190
Endlap	85%	85%
Sidelap	60% to 85%	75% (60% for last flight line at crest)
GSD [cm]	4	3

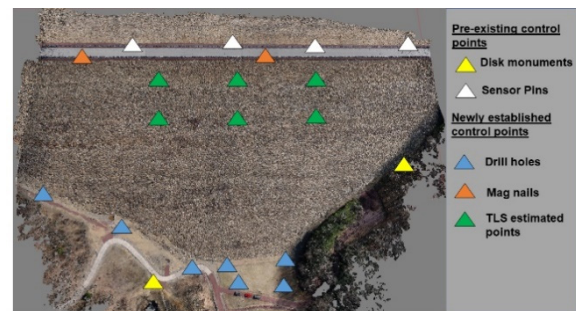


Figure 2. Control points used by the sUAS flights and sUAS point cloud using both the Across and Parallel flights.

Agisoft Metashape was used for photogrammetric processing of the sUAS images. Of the 27 control points, 14 control points were in view. To comply with the United States Federal Aviation Administration (FAA) regulations, the sUAS remained a minimum of 20 m from the roadway located on the crest of the dam. This offset resulted in two control points being hidden from view due to the location of the roadway guardrail relative to the sUAS perspective. Control point coverage was adequate at the base and crest of the dam; however, no control points were set on the downstream face of the dam due to safety concerns associated with traversing the riprap. To augment georeferencing and reduce control network gaps, we extracted six control points from the TLS point cloud. These control points represent corners on piezometer boxes that were well captured in the TLS survey. Three planes were fitted using random sample consensus



(RANSAC) and their intersection was used to estimate a corner point. Thus, a total of 20 control points were used. In addition, six points along the guardrail were also extracted to serve as checkpoints.

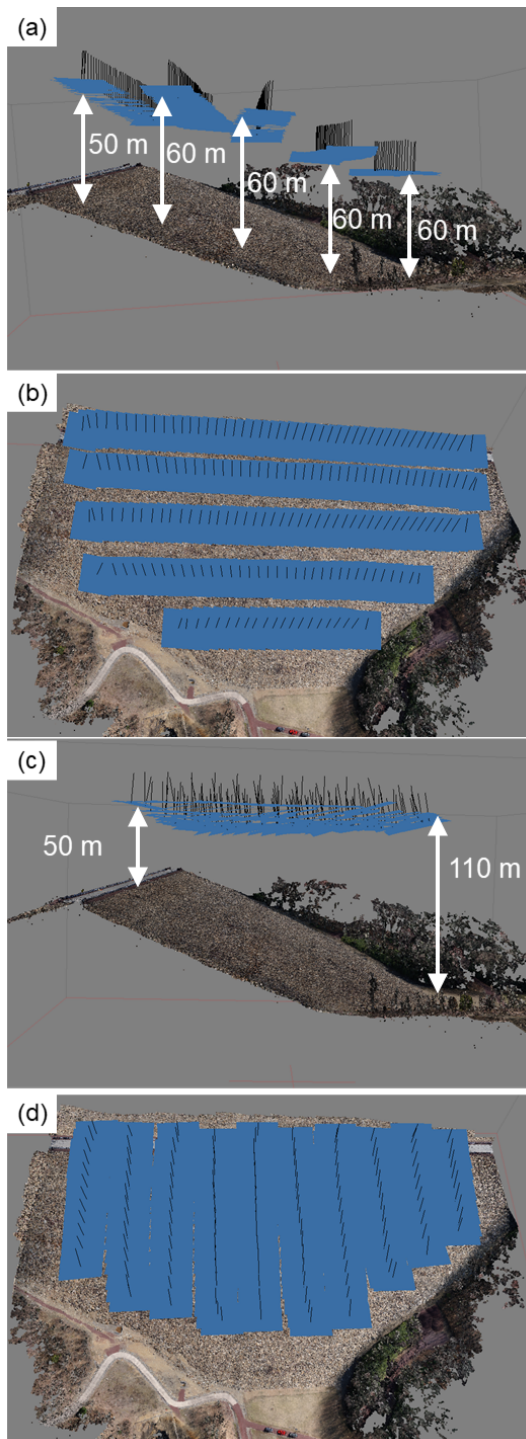


Figure 3. sUAS flights, (a) and (b) show the flight lines that run parallel to the Francis E. Walter dam road, and (c) and (d) show the flight lines that run perpendicular to the Francis E. Walter dam road.

Based on previous experience with the AiBotix sUAS, 4 to 6 control points are known to be sufficient for achieving cm-level georeferencing accuracy (Bolkas, 2019), but this conclusion was based on smaller sites of about 5.5 acres in size.

### III. RESULTS

#### A. Data acquisition discussion

Before going into the accuracy comparison of the two methodologies, we compare and discuss the data acquisition process, safety, and completeness of the data. With respect to time spent in the field, about two days (16 hours of work) were needed to capture the TLS point clouds on both sides of the dam. For the sUAS surveys, the biggest constraint was the common occurrence of high-speed winds in the region. Wind strength often increases throughout the dam site after 10 am, resulting in a narrow window that is suitable for sUAS operation. The manufacturer of the Aibotrix sUAS recommends that flights should not be conducted when winds exceed 8 m/s. In addition, the increased reservoir water level observed in April flooded the access roads on the upstream side of the dam, which forced the cancellation of the upstream flight due to absence of an adequate takeoff and landing site and access issues.

Despite the many TLS station setups, the resulting point cloud had several data gaps at the half meter level due to line-of-sight obstructions. Figure 4 shows data gaps in the TLS dataset, which for the most part are around 0.5 m, except for some areas where line of sight was significantly blocked leading to gaps of about 2.0 m. On the other hand, sUAS surveys generated a more consistent point cloud devoid of any large data gaps, as it offers a more unobstructed view of the dam. This shows how the two technologies have different advantages and disadvantages, which should be considered before deciding which technology is preferable. In the next paragraphs we discuss the accuracy comparison between the two surveying methods.

#### B. Comparison of sUAS Photogrammetry and TLS

A significant challenge in estimating deformations using point clouds is that the available technologies do not survey the exact same point over time (Mukupa *et al.*, 2017). The estimation of differences between multi-epoch point clouds is often implemented using the model-to-model cloud comparison (M3C2) algorithm (Lague *et al.*, 2013), which allows for robust cloud-to-cloud comparison. This approach was followed here to estimate the difference between the TLS and the sUAS point clouds.

We found that when using the TLS datasets as the reference, RMSE values were considerably higher than they should be (at the 20 cm level). We attribute this to the data gaps present in the TLS data and the TLS core points that are generated in the M3C2 distance calculation. In addition, we had to restrict the projection and normal diameter in the M3C2 distance calculations to 25 cm, otherwise distances had a bias of up to 8 cm. This can also be attributed to the TLS point cloud data gaps, as larger projections and diameters would increase the chance of including data gap regions in the distance calculation. Table 3 shows the first order

statistics, mean and standard deviation (SD), using the sUAS datasets as the reference. The table shows a high level of agreement between the sUAS and TLS point clouds with almost zero mean values and SD values at the 3.3 to 3.6 cm level. The across flight is slightly better than the parallel flight, as the latter had some higher errors in the top left side of the study site. The combined dataset shows a mean value of 0.1 cm and SD of 3.3 cm, indicating a strong agreement between the two datasets. The analysis in this section shows that despite the different flight pattern, similar sUAS point clouds were retrieved, especially for the across flight, where a fixed flying height was followed, and therefore distance from the ground was variable because of the dam slope.

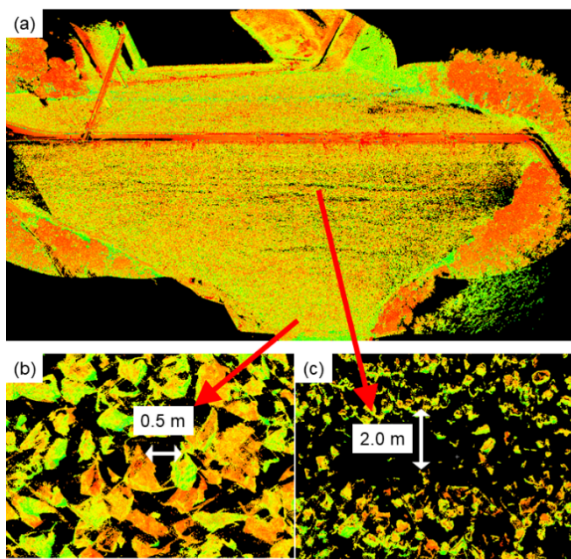


Figure 4. TLS point cloud and data gaps resulting from line-of-sight obstructions.

Table 3. Mean and SD values for various scenarios. All sUAS datasets are processed with Agisoft Metashape

Comparison	Mean [cm]	SD [cm]
sUAS Across vs TLS	0.1	3.3
sUAS Parallel vs TLS	0.4	3.6
sUAS Combined vs TLS	0.1	3.3
sUAS Across vs sUAS Parallel	0.0	3.0

Figure 5 shows the histogram based on the M3C2 distances between the sUAS point clouds and the TLS point cloud, while Figure 6 shows a spatial visualization of the M3C2 distances. Both the across and parallel sUAS point clouds have a similar histogram shape, with the across flight having a slightly higher peak. The spatial visualization of the M3C2 distances shows that the parallel flight has some higher error in the left side of the dam, which are due to misalignment of the photos. In the parallel flight two of the leftmost control points shown in Figure 2 were only visible from two images each, decreasing alignment accuracy.

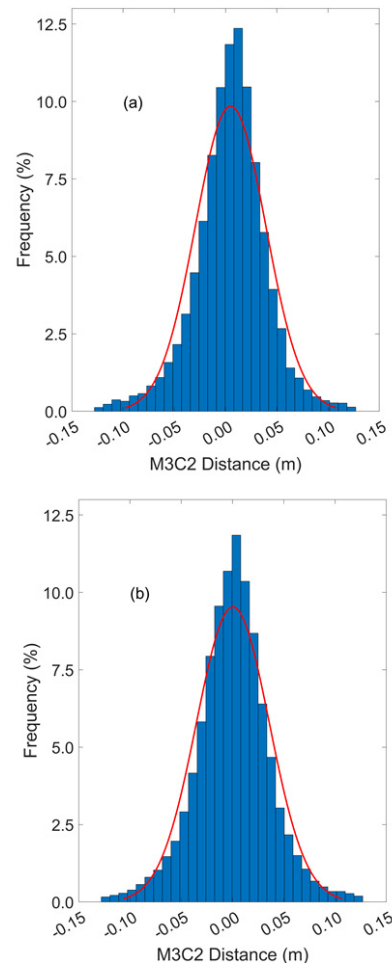


Figure 5. Histograms based on the M3C2 distance: (a) sUAS Across flight vs TLS, mean of 0.1 cm, and SD of 3.3 cm; (b) sUAS parallel flight vs TLS mean of 0.4 cm, and SD of 3.6 cm.

Assuming that the TLS dataset has an accuracy at the  $\pm 1.5$  cm level, then the estimated accuracy of the sUAS point cloud is about  $\pm 2.9$  cm to  $\pm 3.1$  cm. This is considered reasonable, considering the average GSD of 3.0 cm for the photogrammetric point cloud. The U.S. Army Corps of Engineers accuracy requirements for performing deformation surveys state that for each survey, final positioning accuracy (at the 95% confidence level), should be less or equal to one-fourth of the predicted (maximum) displacement (U.S. Army Corps of Engineers, 2009). This indicates that the present sUAS point clouds can be used to detect displacements of 23 cm – 24.6 cm or greater. Normal vertical settlement of earth-filled embankment dams is at the level of 40.0 cm over 5-10 years during the stabilizing phase (U.S. Army Corps of Engineers, 2009). Therefore, photogrammetric methods with resulting accuracy at the  $\pm 3$ -4 cm level, can be used for monitoring comparison over 5–10-year intervals; however, a greater accuracy at the level of  $\pm 1$ -2 cm is needed for year-to-year comparisons. Such accuracies are easier met by TLS methods. Another approach is to upgrade the sUAS system, e.g., upgrading the sUAS camera, from 24 megapixels to 40 megapixels in our case, which would result in a higher GSD. Indeed, this

will be our future approach to enhance our assessment of earth-filled embankment dams using sUAS methods and assess monitoring for shorter periods of time.

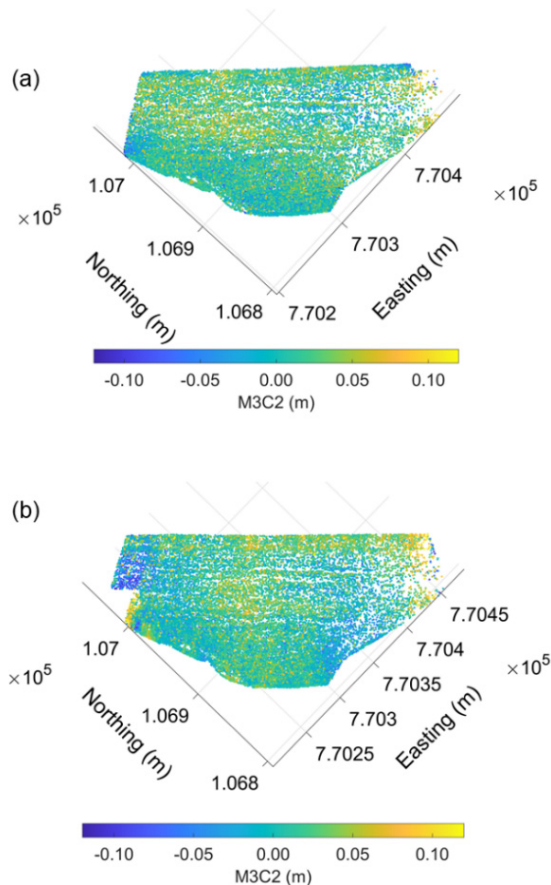


Figure 6. Spatial visualization of M3C2 distances: (a) sUAS Across flight vs TLS, mean of 0.1 cm, and SD of 3.3 cm; (b) sUAS parallel flight vs TLS mean of 0.4 cm, and SD of 3.6 cm.

### C. Comparison of photogrammetry software

We processed the sUAS images with both Agisoft Metashape and Leica Infinity software and found that the Metashape point cloud to be more accurate. The Leica Infinity dataset has a mean value of 1.3 cm, which indicates the presence of a small bias, and a higher SD of 4.3 cm (Table 4). The histogram comparison in Figure 7 shows a higher peak of the sUAS point cloud when processed with Agisoft Metashape than the Leica Infinity. In addition, Figure 7a shows that most differences between the TLS and the sUAS point cloud are within a range of  $\pm 10$  cm.

A spatial visualization of the M3C2 distances is shown in Figure 8. Figure 8a indicates that lower errors exist in the middle of the dam. Higher (positive) errors existing at the right of the dam, which can be attributed to the larger data gaps in the TLS dataset. Also, high (negative) errors exist in the left side of the dam in Figure 8a, indicating a small misalignment error. In the same left side of the dam, higher errors (positive) are found for the Leica Infinity point cloud in Figure 8b, suggesting a bigger misalignment issue. On this side of the dam not all control points were visible, as a couple of the control points on the left side of the main road where hidden

by the guard-rail in some images and only visible in 2-3 images. The field crew did not want to fly close to the road for safety and this issue was not noticed until the images were processed. Therefore, better flight planning in the future would be able to address this issue and provide an even more accurate sUAS point cloud.

Table 4. Mean and SD values for scenarios of Agisoft Metashape versus Leica Infinity

Comparison	Mean [cm]	SD [cm]
sUAS Combined (Agisoft) vs TL	0.1	3.3
sUAS Combined (Infinity) vs TLS	1.3	4.3
sUAS combined (Infinity) vs sUAS Combined (Agisoft)	0.0	4.4

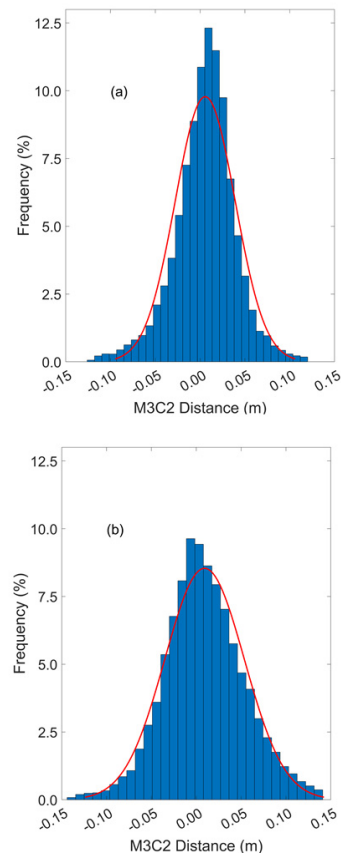


Figure 7. Histograms based on the M3C2 distance: (a) sUAS Combined (Agisoft) vs TLS, mean of 0.1 cm, and SD of 3.3 cm; (b) sUAS Combined (Infinity) vs TLS mean of 1.3 cm, and SD of 4.3 cm.

### IV. CONCLUSIONS

Monitoring of engineering structures such as bridges, dams, levees, etc., is important for ensuring their integrity and safety of operation. This paper presented an evaluation and comparison of sUAS photogrammetry and TLS technologies at the Francis E. Walter Dam in northeast Pennsylvania. The network of control points was expanded to accommodate the registration of TLS stations through resection and the georeferencing of sUAS photogrammetric data. Datasets presented here were from the same epoch.

The accuracy assessment indicates that the TLS data is consistent to within  $\pm 1$  cm, and the sUAS derived data aligns with TLS data at the  $\pm 3.3$  cm level. The TLS accuracy levels of accuracy are considered sufficient for year-to-year monitoring of earth-filled embankment dams where smaller displacements are expected (e.g., 5.0 - 14.0 cm per year), while the sUAS accuracy level is more suitable for 5–10-year intervals where larger displacements are expected (e.g., about 40.0 cm).

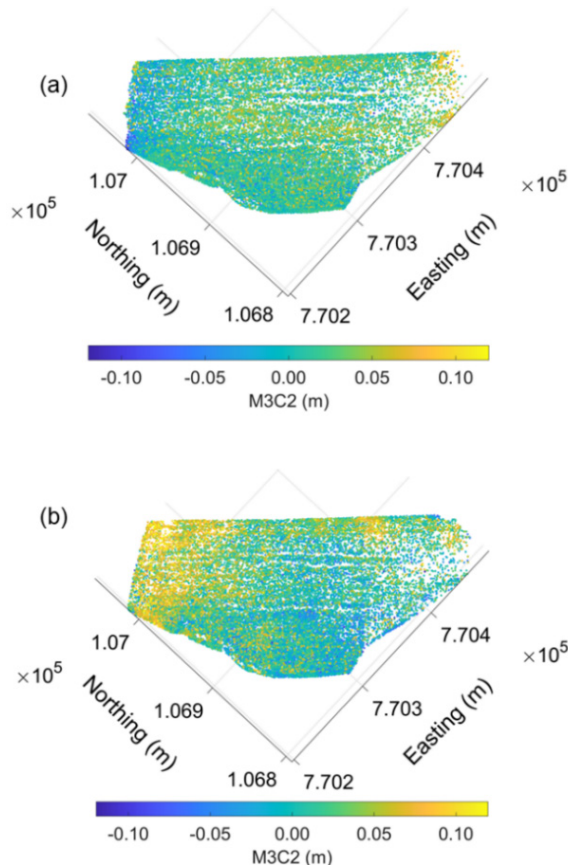


Figure 8. Spatial visualization of M3C2 distances: (a) sUAS Combined (Agisoft) vs TLS, mean of 0.1 cm, and SD of 3.3 cm; (b) sUAS Combined (Infinity) vs TLS mean of 1.3 cm, and SD of 4.3 cm.

Future work will entail the use of a sUAS that includes a higher resolution 42-megapixel digital camera, an onboard post-processed kinematic (PPK) GNSS receiver, and the ability to safely fly in higher speed winds. This will allow us to assess the capacity and extend of sUAS photogrammetry to monitor displacement in shorter periods of time. Hence, monitoring of the site will continue with the same sensors in the following years (with one dataset every year) to create a multi-epoch and multi-platform time lapse. The existence of data gaps in the TLS dataset can introduce challenges in estimating multi-epoch differences. Therefore, another future goal will be on developing an algorithm for robust estimation of multi-epoch differences for similar earth-rock dams.

## V. ACKNOWLEDGEMENTS

This project has received funding from Chancellor Endowment Funds, Penn State University, Wilkes-Barre Campus. The authors would like to acknowledge David Williams and Brett Anderton, U.S. Army Corps of Engineers, for their assistance in this project. In addition, undergraduate student Nick Lawler is thanked for his contribution in the data collection.

## References

- Alba, M., Fregonese, L., Prandi, F., Scaioni, M., and Valgoi, P. (2006). Structural monitoring of a large dam by terrestrial laser scanning. *International Archives of Photogrammetry, Remote Sensing and Spatial Information Sciences*, Vol. 36, No. 5, pp. 6.
- Alba, M., Bernardini, G., Giussani, A., Ricci, P. P., Roncoroni, F., Scaioni, M., Valgoi P., and Zhang, K. (2008). Measurement of dam deformations by terrestrial interferometric techniques. *International Archives of Photogrammetry, Remote Sensing and Spatial Information Sciences*, Vol. 37, No. B1, pp. 133-139.
- Bolkas, D. (2019). Assessment of GCP number and separation distance for small UAS surveys with and without GNSS-PPK positioning. *Journal of Surveying Engineering*, Vol. 145, No. 3, pp. 04019007.
- Bolkas, D., Walton, G., Kromer, R., and Sichler, T. (2021). Registration of multi-platform point clouds using edge detection for rockfall monitoring. *ISPRS Journal of Photogrammetry and Remote Sensing*, Vol. 175, pp. 366-385.
- Buffi, G., Manciola, P., Grassi, S., Barberini, M., and Gambi, A. (2017). Survey of the Ridracoli Dam: UAV-based photogrammetry and traditional topographic techniques in the inspection of vertical structures. *Geomatics, natural hazards and risk*, Vol. 8, No. 2, pp. 1562-1579.
- González-Aguilera, D., Gómez-Lahoz, J., and Sánchez, J. (2008). A new approach for structural monitoring of large dams with a three-dimensional laser scanner. *Sensors*, Vol. 8, No. 9, pp. 5866-5883.
- Jeon, J., Lee, J., Shin, D., and Park, H. (2009). Development of dam safety management system. *Advances in Engineering Software*, Vol. 40, No. 8, pp. 554-563.
- Khaloo, A., Lattanzi, D., Jachimowicz, A., and Devaney, C. (2018). Utilizing UAV and 3D computer vision for visual inspection of a large gravity dam. *Frontiers in Built Environment*, Vol. 4, No. 31.
- Lague, D., Brodu, N., and Leroux, J. (2013). Accurate 3D comparison of complex topography with terrestrial laser scanner: Application to the Rangitikei canyon (NZ). *ISPRS Journal of Photogrammetry and Remote Sensing*, Vol. 82, pp. 10-26.
- Leica Geosystems (2021). Leica ScanStation P50 – Long Range 3D Terrestrial Laser Scanner. Accessed online on November 30, 2021: <https://leica-geosystems.com/en-us/products/laser-scanners/scanners/leica-scanstation-p50>
- Li, Y., Liu, P., Li, H., and Huang, F. (2021). A Comparison Method for 3D Laser Point Clouds in Displacement Change Detection for Arch Dams. *ISPRS International Journal of Geo-Information*, Vol. 10, No. 3, pp. 184.

- Mascolo, L., Nico, G., Di Pasquale, A., and Pitullo, A. (2014). Use of advanced SAR monitoring techniques for the assessment of the behaviour of old embankment dams. In: *Proc of Earth Resources and Environmental Remote Sensing/GIS Applications V*, Vol. 9245, p. 92450N. International Society for Optics and Photonics.
- Mukupi, W., Roberts, G. W., Hancock, C. M., and Al-Manasir, K. (2017). A review of the use of terrestrial laser scanning application for change detection and deformation monitoring of structures. *Survey review*, Vol. 49, No. 353, pp. 99-116.
- O'Banion, M.S., Olsen, M.J., Rault, C., Wartman, J., Cunningham, K. (2018). *Suitability of Structure from Motion for Rock Slope Assessment*. The Photogrammetric Record, Vol. 33, No. 162, pp. 217-242.
- Ridolfi, E., Buffi, G., Venturi, S., and Manciola, P. (2017). Accuracy analysis of a dam model from drone surveys. *Sensors*, Vol. 17, No. 8, pp. 1777.
- Scaioni, M., Marsella, M., Crosetto, M., Tornatore, V., and Wang, J. (2018). Geodetic and remote-sensing sensors for dam deformation monitoring. *Sensors*, Vol. 18, No. 11, pp. 3682.
- U.S. Army Corps of Engineers (2009) *Engineering and Design: Structural Deformation Surveying*. Department of the Army, U.S. Army Corps of Engineers, Washington, DC, Manual No. 1110-2-1009.
- U.S. Army Corps of Engineers (2021). Francis E. Walter Dam. <https://www.nap.usace.army.mil/Missions/Civil-Works/Francis-E-Walter-Dam/> [Accessed November 11 2021]
- Xi, R., Zhou, X., Jiang, W., and Chen, Q. (2018). Simultaneous estimation of dam displacements and reservoir level variation from GPS measurements. *Measurement*, Vol. 122, pp. 247-256.
- Xiao, R., Shi, H., He, X., Li, Z., Jia, D., and Yang, Z. (2019). Deformation monitoring of reservoir dams using GNSS: an application to south-to-north water diversion project, China. *IEEE Access*, Vol. 7, pp. 54981-54992.
- Xu, H., Li, H., Yang, X., Qi, S., and Zhou, J. (2019). Integration of terrestrial laser scanning and nurbs modeling for the deformation monitoring of an earth-rock dam. *Sensors*, Vol. 19, No. 1, pp. 22.
- Zhao, S., Kang, F., Li, J., and Ma, C. (2021). Structural health monitoring and inspection of dams based on UAV photogrammetry with image 3D reconstruction. *Automation in Construction*, Vol. 130, pp. 103832.

## PS-InSAR and UAV technology used in the stability study of Ankang expansive soil airport

Jinzhao Si<sup>1</sup>, Shuangcheng Zhang<sup>1</sup>, Yufen Niu<sup>2</sup>

<sup>1</sup> College of Geology Engineering and Geomatics, Chang'an University, Xi'an 710054, China,

([SiJinzhao\\_chd@163.com](mailto:SiJinzhao_chd@163.com); [shuangcheng369@chd.edu.cn](mailto:shuangcheng369@chd.edu.cn))

<sup>2</sup> College of Mining and Geomatics Engineering, Hebei University of Engineering, Handan 056038, China,

([niuyufenpippa@163.com](mailto:niuyufenpippa@163.com))

**Key words:** PS-InSAR; corner reflectors; expansive soil; UAV measurement; stability analysis; Ankang airport

### ABSTRACT

Expansive soil is a natural geological body with obvious expansion and contraction, multiple fissures and other undesirable properties. The deformation monitoring of expansive soil in high-fill areas under the combined action of wet expansion and dry contraction has become a hotspot of related research. To large-scale soil disasters. Time-series Interferometric Synthetic Aperture Radar (InSAR) technology is widely used in the monitoring of various geological hazards due to its advantages of wide coverage, high monitoring accuracy, and all-weather operation. This study takes Ankang Airport (AKA) expansive soil airport as an example. First, the ground digital elevation model (DEM) of the airport filling area was obtained by using UAV; secondly, the deformation rate and deformation time series of the expansive soil airport were obtained by using the persistent scatterer InSAR (PS-InSAR) technology; third, for the coherence in poor areas, artificial corner reflectors (CR) are arranged to increase stable scattering points; Finally, the deformation time series of feature points are extracted, combined with regional precipitation data analysis, the relationship between the periodic deformation of the airport expansive soil slope and rainfall. There is a subsidence trend along the LOS direction in the dry season, which is consistent with the expansion and contraction characteristics of expansive soils. Finally, the deformation rate is proportional to the depth of the expansive soil fill. It is judged that the existing small surface deformation and its periodic deformation distribution are caused by the combined action of the settlement after construction of the expansive soil filling area and the expansion and contraction characteristics of the expansive soil.

### 1. INTRODUCTION

Ankang Airport (AKA) started construction in 2016, and the airport was completed in May 2020. This airport is located in the Ankang Yuehe Basin at the southern of the Qinling Mountains in China. The Expansive soil is widely distributed in this area. Expansive soil is a naturally formed multi-fractured geological body, which has unfavourable properties such as significant expansion and shrinkage, over-consolidation and multi-fracture. In addition, the topographic drop at the original site of AKA is large, therefore during the construction of the airport, the filling volume has reached 30,000,000 m<sup>3</sup>, and the vertical height difference has reached 94 m. To sum up, the consolidation and compression characteristics of large-scale fill soil and the special hydraulic characteristics of expansive soil have caused certain hidden dangers, threatening the safe navigation of AKA at all times. Therefore, it is very necessary to conduct real-time monitoring and stability analysis of AKA.

The widely applied methods for the airport surface deformation include global navigation satellite system (GNSS) measurement and levelling measurement. However, these methods have high cost of manual equipment and can only obtain relatively discrete point

deformation data, making it difficult to monitor the overall deformation of the study area. InSAR (synthetic aperture radar interferometry) technology, as a new type of earth observation method, can overcome the shortcomings of traditional observation methods. Through the two kinds of observation values of intensity and phase, InSAR technology can obtain high-resolution surface deformation information, and realize large-scale spatial detection and long-period precision monitoring (Berardino *et al.*, 2002). Recently, time-series InSAR technology has been widely used in various airports for long-term deformation monitoring and mechanism analysis, such as China Shanghai Pudong Airport (Jiang *et al.*, 2016), Xiamen Xiang'an Airport (Zhuo *et al.*, 2020; Liu *et al.*, 2019) and Hong Kong Chek Lap Kok Airport (Wu *et al.*, 2020; Jiang and Lin, 2010), and Kuala Lumpur International Airport in Malaysia (Jiang *et al.*, 2016) where the special properties of tropical peat cause subsidence. In addition, InSAR technology is also applied to some mountainous airports with similar geological conditions to Ankang Airport, such as Iqaluit Airport in Canada (Short *et al.*, 2014), and Yan'an New Airport in China (Wu *et al.*, 2019).

In recent years, the characteristics of time series InSAR technology have also been proved to be suitable for monitoring Periodic slow deformation caused by special hydraulic properties of expansive soil (Gabriel et al., 1989). In this paper, we attempt to identify and understand local subsidence activity in the AKA area by using MT-InSAR techniques. The dataset used in this paper consists of 26 Sentinel-1A scenes, with a time span from May 2020 to June 2021. First, considering the migration of a large amount of surface material in the AKA will cause the historical DEM products to be unable to remove the topographic phase effectively, we choose the UAV to obtain the high-precision DEM of the AKA. In addition, in order to avoid the inability to obtain sufficiently stable scattering points, we arrange artificial corner reflectors in the de-coherence region according to the spatiotemporal distribution of coherence; secondly, the PS-InSAR method is used to monitor the surface deformation of AKA; finally, the deformation time of the feature points is extracted sequence, combined with regional geological and hydrological data, to analyse deformation inducement and stability.

## II. STUDY AREA AND DATASETS

Ankang Airport is located in the Ankang, Shanxi, China, as shown in Figure 1, which is about 15 km to the city center of the Ankang. The terminal area of AKA is 5,500 m<sup>2</sup>; the runway is 2,600 m long and 45 m wide, which can meet the annual passenger needs. Demand for a throughput of 300,000 passengers and a cargo and mail throughput of 750 tons. AKA is located in the platform area on the northern margin of the Yue he Basin. There are a lot of expansive soils in this area, including clay, silty clay, gravel-like soil, sandstone, mudstone and conglomerate. The special hydraulic action of expansive soil is the fundamental cause of the instability of expansive soil, which mainly includes the effects of expansion and contraction deformation, crack development and strength reduction caused by changes in moisture and stress. These characteristics can easily cause potential geological hazards to the infrastructure on the soil.

Considering the large degree of excavation and filling in the airport and the drastic historical changes of the ground surface, external DEM products such as SRTM DEM and ASTER GDEM often cause serious DEM errors due to their poor timeliness. Therefore, a DEM with a regular grid spacing of 5 m and a vertical resolution of 2 m acquired by UAV was used to simulate and remove the terrain phase contribution during the generation of the interferogram, and from the range Doppler coordinates to those corresponding to the WGS84 coordinate system Geo-recoding, DEM products are shown in Figure 1b.

The monitoring experiment selects the SAR image data of 26 scenes in Interferometric Wide (IW) mode provided by Sentinel-1A satellite covering the study area from 2020-5 to 2021-7. The polarization mode is

VV and VH dual polarization, the incident angle is 39.5°, and the resolution in the azimuth × range direction is 2.33 m × 13.99 m. The image data is as follows: track number 100, track configuration ASCENDING, and acquisition dates are May 2020. June 24; June 5, 17, 29; July 11, 23; August 4, 16, 28; September 21; October 3, 15, 27; November 8, 20; December 2, 26; January 7, 19, 31, 2021; February 12, 24; March 8, 20; March 8, 20; April 1, 13, 25; June 12; July 6. Detailed spatial and temporal baselines of these Sentinel-1 datasets are shown in Figure 2.

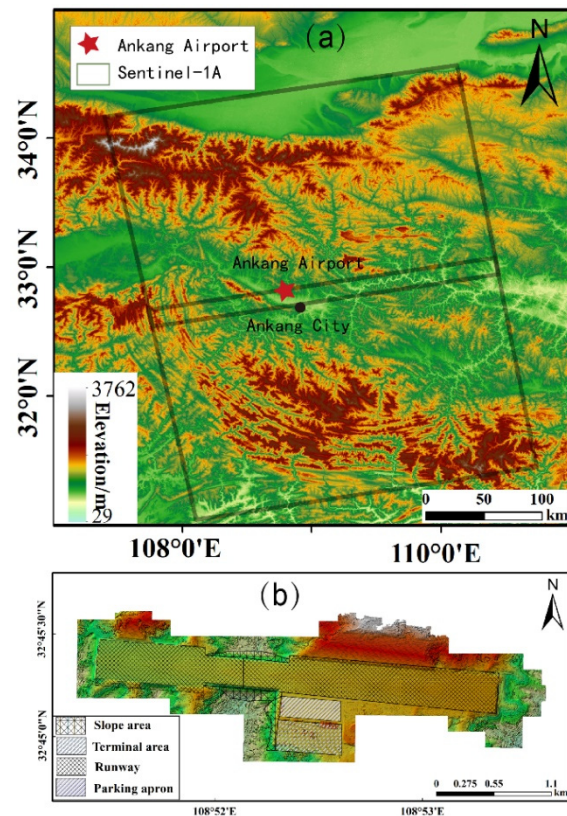


Figure 1. (a) Study area and data coverage; (b) DEM data and airport area division map.

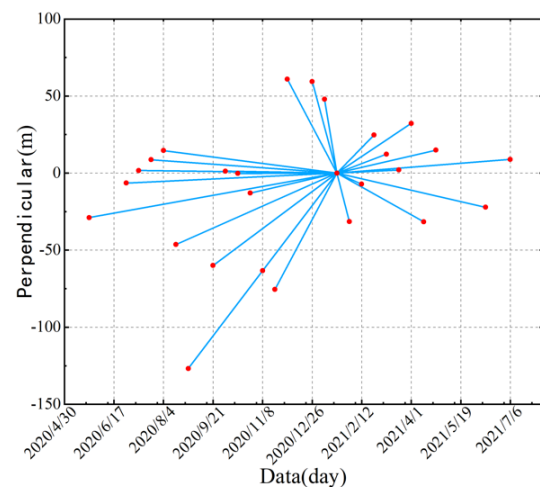


Figure 2. PS-InSAR Baseline Maps.

To restrain deformation, the airport operator planted low shrubs on the airport slopes and fill platforms. It is

well known that dense vegetation coverage tends to cause large changes in backscatter coefficients during repeated imaging, which can lead to regional de-coherence problems. (Touzi *et al.*, 1999).

As shown in Figure 3, We calculated the mean coherence of the selected interference pairs covering the study area. From the spatial distribution of the coherence coefficient, it can be clearly seen that there is an obvious de-coherence phenomenon in the filled slope, therefore we arrange artificial corner reflectors in this area to increase the stable scattering points in the de-coherent area.

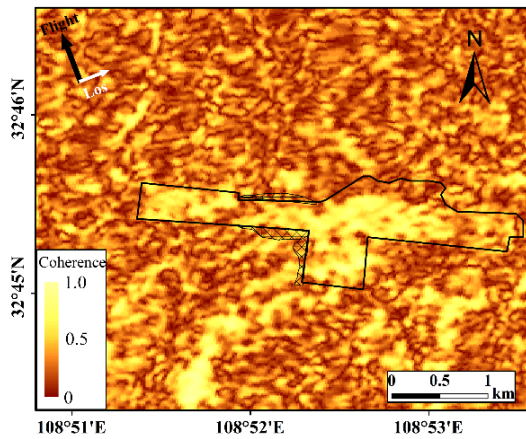


Figure 3. Coherence map.

The pictures of artificial corner are shown as Figure 4a and 4b. Figure 4c and 4d depicts the change of backscattering in the study area before and after the installation of the corner reflector. It can be seen from Figure 4 that after the corner reflector is installed, stable scattering points appear on the filled slope, which can increase the number of PS points and improve the InSAR monitoring accuracy.

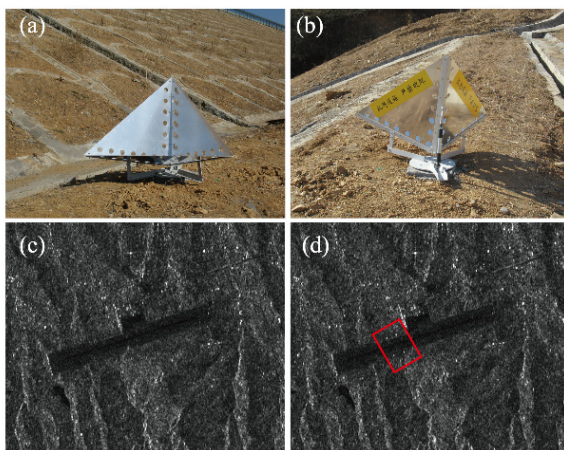


Figure 4. (a), (b) Site photo of artificial corner reflector; (c) backscattering map before the installation; (d) backscattering map after the installation.

### III. DATA PROCESSING

The traditional differential interferometry technique is severely restricted in its application range due to the

influence of time and space de-correlation and atmospheric delay. To solve these problems, the "Permanent Scatterers InSAR Technique" (PS-InSAR) has been proposed (Ferretti *et al.*, 2001). This technique utilizes the characteristic that the permanent scatterer (PS) can still maintain good coherence in a long period of time. Since PS-InSAR technology was proposed, related algorithms have also been developed one after another.

In this paper, the StaMPS approach proposed by Hooper (Hooper *et al.*, 2004.) is applied to process SAR data, and the corner reflectors are arranged in advance based on the interferometric pair coherence distribution to obtain enough PS points. The stamps approach selects the target with smaller amplitude dispersion and stable phase as the PS point, which can select a larger number of PS points than the conventional PS algorithm.

Assuming that there are  $N+1$  SAR images in the study area, according to the perpendicular baseline, time baseline and Doppler frequency, a scene image is selected as the single main image,  $N$  interference pairs can be generated by interfering other images with this main image.

STAMPS approach is to form interferograms and remove most of the topographic phase signature using a digital elevation model (DEM). The residual phase:  $\varphi$ , of the  $x$  pixel in the  $i$  topographically corrected interferogram can be written as the sum of 5 terms (Eq. 1):

$$\varphi_{x,i} = \varphi_{def,x,i} + \varphi_{\alpha,x,i} + \varphi_{orb,x,i} + \varphi_{\varepsilon,x,i} + n_{x,i} \quad (1)$$

where  $\varphi_{def}$  = the phase change due to movement of the pixel in the satellite line-of-sight (LOS) direction

$\varphi_{\alpha}$  = the phase equivalent of the difference in atmospheric retardation between passes

$\varphi_{orb}$  = the phase due to orbit inaccuracies

$\varphi_{\varepsilon}$  = the residual topographic phase due to error in the DEM

$n$  = the noise term due to variability in scattering from the pixel

We assume that that  $\varphi_{def}$ ,  $\varphi_{\alpha}$ ,  $\varphi_{orb}$  are spatially correlated over a specified length,  $L$ , on the contrary,  $\varphi_{\varepsilon}$  and  $\varphi_{\varepsilon}$  are spatially uncorrelated over the same distance, with mean 0. If the positions of the other PS are known, averaging over all phases within a circular block of radius  $L$  centered at pixel  $x$  means that (Eq. 2):

$$\overline{\varphi}_{x,i} = \overline{\varphi}_{def,x,i} + \overline{\varphi}_{\alpha,x,i} + \overline{\varphi}_{orb,x,i} + \overline{\varphi}_{\varepsilon,x,i} + \overline{n}_{x,i} \quad (2)$$

where  $\overline{\varphi}_{def}$  = the average of  $\varphi_{def}$

$\overline{\varphi}_{\alpha}$  = the average of  $\varphi_{\alpha}$

$\overline{\varphi}_{orb}$  = the average of  $\varphi_{orb}$



$\bar{\varphi}_\varepsilon$  = the average of  $\varphi_\varepsilon$   
 $\bar{n}$  = the average of  $n$

The small values of  $\varphi_\varepsilon$  and  $n$  can be ignored, subtracting Equation 2 from Equation 1 leaves (Eq. 3):

$$\varphi_{x,i} - \bar{\varphi}_{x,i} = \varphi_{\varepsilon,x,i} + n_{x,i} - \bar{n}'_{x,i} \quad (3)$$

where  $\bar{n}'_{x,i} = n_{x,i} + \bar{\varphi}_{def,x,i} - \varphi_{def} + \bar{\varphi}_\alpha - \varphi_\alpha + \bar{\varphi}_{orb} - \varphi_{orb}$

The phase error from uncertainty in the DEM is proportional to the perpendicular component of the baseline (Fattahi and Amelung, 2013.) (Eq. 4):

$$\varphi_{\varepsilon,x,i} = B_{\perp,x,i} \cdot K_{\varepsilon,x} \quad (4)$$

where  $B_{\perp,x,i}$  = the phase error from DEM  
 $K_{\varepsilon,x}$  = a proportionality constant

Equation 3 can be written as (Eq. 5):

$$\varphi_{x,i} - \bar{\varphi}_{x,i} = B_{\perp,x,i} \cdot K_{\varepsilon,x} + n_{x,i} - \bar{n}'_{x,i} \quad (5)$$

The phase stability evaluation method based on pixel time correlation is defined as (Eq. 6):

$$\gamma_x = \frac{1}{N} \left| \sum_{i=1}^n \exp \{ j(\varphi_{x,i} - \bar{\varphi}_{x,i} - \hat{\varphi}_{\varepsilon,x,i}) \} \right| \quad (6)$$

where  $\gamma_x$  = the phase stability of the pixel  
 $N$  = the number of available interferograms  
 $\hat{\varphi}_{\varepsilon,x,i}$  = the estimate of  $\varphi_{\varepsilon,x,i}$

After the step of selecting PS based on the calculated values of  $\gamma_x$  in Equation 5, we estimate the DEM error and subtract it to get the corrected interferometric phase (Eq. 7):

$$\varphi_{x,i} - \Delta \hat{\varphi}_{\varepsilon,x,i} = \varphi_{def,x,i} + \varphi_{\alpha,x,i} + \varphi_{orb,x,i} + \varphi_{\varepsilon,x,i} + n_{x,i} \quad (7)$$

After unwrapping, four error terms remain in Equation 6 which is assumed to be uncorrelated temporally, we use some filters to remove these terms. The overall data processing flow is shown in Figure 5.

#### IV. RESULT AND ANALYSE

We have applied the STAMPS technique to the Sentinel-1 SAR scene covering AKA (2020/5 – 2021/7), and obtained the deformation rate distribution in the AKA area, and its deformation rate along the LOS direction is shown in Figure. 6

The results in Figure 6 show that the maximum deformation rate of Ankang expansive soil airport during the 14 months after the completion of

construction is less than -45 mm/year, and the maximum deformation rate inside the airport is between -21 mm/year and -33 mm/year. Basically stable. Three large deformation areas I, II and III are identified in the monitoring area, and these three areas belong to the expansive soil fill slope area around the airport. The maximum deformation rate occurs at point P1 on expansive soil slope III on the east side of the airport, which is -44.1 mm/year. Areas I and II belong to the expansive soil slopes on both sides of the airport runway, and large deformations have also occurred in these two areas. The maximum deformation rate is between -33 mm/year and -45 mm/year.

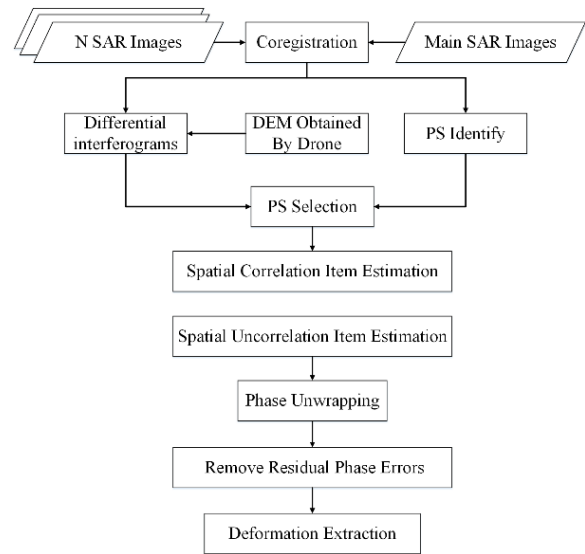


Figure 5. Flowchart of data processing.

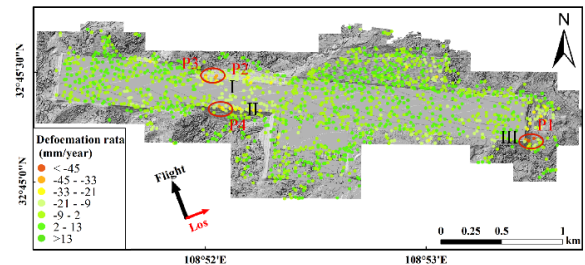


Figure 6. Spatial deformation velocity map of Ankang Airport.

In order to analyze the stability of different functional areas of Ankang Airport, we divided Ankang Airport into terminal area, runway and fill slope area, and extracted characteristic point deformation time series in the three areas for analysis.

##### A. Terminal area and runway stability analysis

As shown in Figure 5, InSAR technology successfully identified three obvious deformation areas in the fill slope area of Ankang Airport. The fill slope area is distributed around the airport flight area, all of which belong to the high fill area. The maximum fill depth reaches about 50 m. During the construction process, protective measures such as concrete pouring and

construction of anti-skid retaining walls were carried out. However, since the foundation and filling soil were mainly composed of expansive soil, the deformation in this area showed characteristics related to rainfall. Therefore, in order to analyze the relationship between the regional deformation law and rainfall of expansive soil filled slopes, the deformation time series of characteristic points (P1-P4 in Figure 5) were extracted in the I, II, and III deformation regions respectively, and the regional rainfall data such as shown in Figure 7.

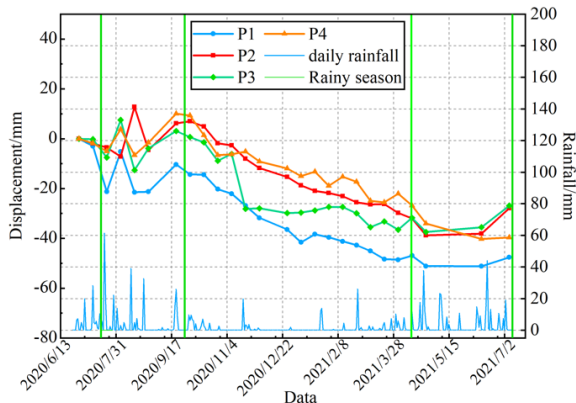


Figure 7. Time series deformation of point position in terminal area.

The Ankang area is in a subtropical monsoon climate. As can be seen from the regional rainfall information in Figure 7, the rainfall is concentrated from June to August. Therefore, we combined the local climate data to mark two more obvious rainy seasons during the monitoring period.

As shown in the P1-P4 deformation time series in Figure 7, the maximum deformation value along the LOS direction is -52.3 mm, the overall deformation interval is distributed between 15 mm and -55 mm, and the maximum accumulated deformation value at P1 is -46.7mm. The deformation trends of the characteristic points of the three filled deformation areas are similar and have certain regularity: the deformation rate gradually slows down in the rainy season, and even rebounds in the abundant rainfall environment, while the deformation trend in the non-rainy season shows the displacement along the LOS direction.

Combined with the time series deformation distribution and precipitation analysis of characteristic points in the expansive soil filling area, we believe that from June to August in Ankang, the rainfall increased, and the hydraulic properties of the expansive soil of Ankang Airport due to water absorption and expansion compensated for the post-construction deformation of the airport surface. Small deformation caused by factors such as soil consolidation and compression. This phenomenon is consistent with the expansion-shrinkage deformation characteristics of expansive soils in relation to soil moisture.

## B. Terminal area and runway stability analysis

It can be seen from Figure 6 that the terminal area and runway of Ankang Airport are basically stable, the deformation rate is small, and the deformation points are all below -33 mm/year. According to the distribution of excavation and filling in Figure 1b, the runway and terminal area of Ankang Airport were subjected to excavation and excavation, and feature points were extracted for time series deformation analysis, as shown in Figure 8.

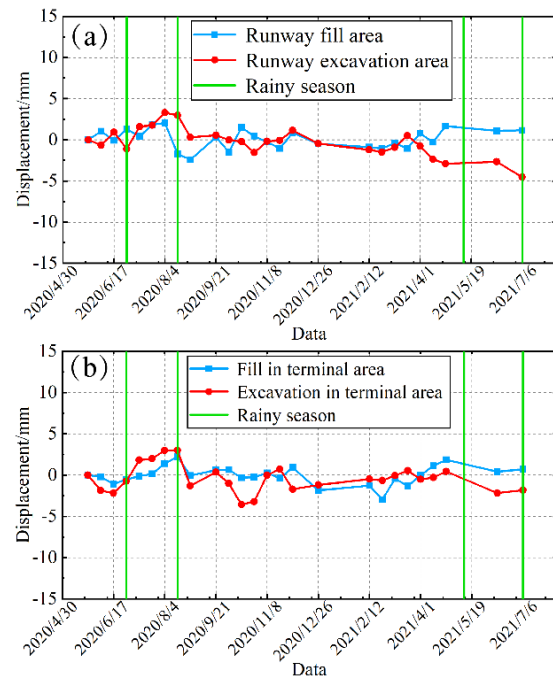


Figure 8. Deformation diagram of the point position of the runway and terminal area.

Figure 8a shows the deformation time series of the feature points in the area with the maximum depth of the excavation and filling layers of the airport runway. From the time series deformation information of the points, it can be clearly seen that the ground rebound in a small range occurs in the runway fill area during the wet season, and the maximum deformation value is 3.6 mm. Between  $\pm 5$  mm, this deformation interval belongs to the normal post-construction settlement range, the runway deformation trend is stable, and the overall stability is sufficient to meet the functional requirements such as navigation.

Figure 8b shows the deformation time series of the feature points in the area with the maximum depth of excavation and filling layers in the airport terminal area. From the point time series deformation information, it can be seen that the deformation trend of the airport plane (station) flat area and the runway filling area is similar. The elastic phenomenon, the maximum deformation amount reaches 3.6 mm, and the cumulative deformation amount is small, which is -2 mm, which is basically in a stable state; the time series deformation information of the points in the excavation area within the machine (station) flat can be

seen that the point has continuous deformation, and the cumulative deformation Variable less than -4 mm. The overall deformation of the machine (station) flat area is small, and the deformation is distributed between  $\pm 4$  mm and tends to be stable.

C. Filled area deformation analysis

In general, the consolidation settlement of the foundation under the fill, the post-construction settlement caused by the self-compression of the fill part, and the uneven settlement caused by the discontinuous construction are the main reasons for the deformation of high-fill buildings. The original terrain of Ankang Airport is a mountainous area with large undulating terrain, so Ankang Airport has carried out intense excavation and filling construction. According to the collected engineering data, the distribution of excavation and filling is shown in Figure 9.

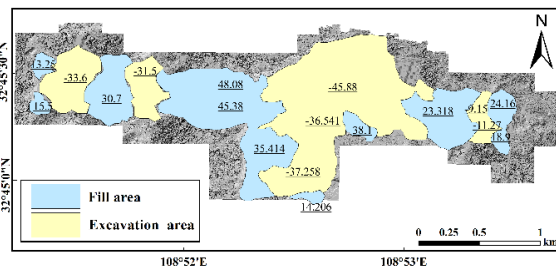


Figure 9. Ankang Airport excavation and filling distribution map.

As shown in Figure 9, the maximum fill thickness of Ankang Airport is over 48 m, the maximum excavation depth is over 45 m. The excavation and fill areas are staggered, and the fill is over 30,000,000 m<sup>3</sup>. In order to analyze the relationship between Ankang expansive soil airport fill and surface deformation, we combined the construction distribution of excavation and filling with the InSAR deformation monitoring results shown in Figure 5. The deformation rate of the monitoring points in the study area and the depth of the filling volume where they are located are extracted for analysis, as shown in Figure 10.

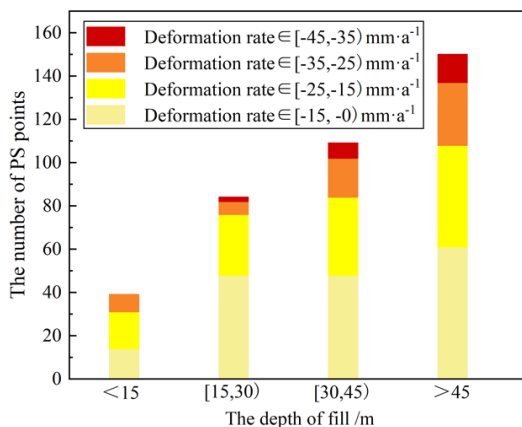


Figure 10. Relationship between deformation rate and filling depth.

It can be seen from Figure 10 that with the increase of the thickness of the fill body, the number of settlement observation points and the deformation rate increase significantly, and the distribution and thickness of the fill soil obviously affect the distribution and size of the surface deformation. The areas with the most obvious deformation are all distributed in the area where the depth of the fill layer is greater than 30 m, and the deformation monitoring points in this area account for 70% of all the monitoring points of deformation and settlement. The monitoring points with velocity  $> -35$  mm/year, and the larger deformation points with deformation rate  $> -25$  mm/year are concentrated in the area with layer depth  $> 45$  m. On the contrary, in the area of fill layer depth  $< 15$  m, the number of settlement points is less and the deformation rate value is smaller. This shows that the compressive deformation of the fill soil at different depths and the pressure on the undisturbed soil below increase with the depth of the fill layer. Therefore, the compressive deformation of the fill soil of Ankang Airport is an important cause of surface deformation.

From the analysis in this chapter, it can be seen that the main factors affecting the deformation law of Ankang Airport can be summarized as follows:

- 1) Combining the data of excavation and filling, it is found that the degree of deformation has a strong correlation with the depth of filling;
- 2) The deformation trend of the filling area is similar, and there are different degrees of rebound phenomenon in the rainy season;
- 3) The change of the deformation trend of Ankang Airport There is a strong correlation with regional precipitation.

V. CONCLUSIONS

To meet the local economic development and improve the regional aviation network, Ankang Airport was built in the expansive soil area after a huge filling project. However, due to the expansion and contraction characteristics of expansive soils and the weakness of fill soil foundations, Ankang Airport faces adverse environmental impacts. At present, the airport has been fully put into use, therefore, the stability of the airport area is a matter of public concern.

We have retrieved for the first time the deformation history and rate of the Ankang Airport platform using data from SAR sensors and drone sensor. The results from MT-InSAR have demonstrated that the Ankang Airport platform has experienced heterogeneous ground deformation Since the airport was put into use.

A total of 26 ascending Sentinel-1 images were used, which were acquired from May 2020 to July 2021. The pattern and spatiotemporal evolution characteristics of the surface deformation of Ankang Airport after main construction were fully Completed, providing important deformation information on Xiamen New Airport. The research results have important guiding

significance for airport stability rating, safe operation and unstable area governance. In addition, the special dilatation-contraction deformation characteristics that are closely related to expansive soil and rainfall have also been successfully verified. The main conclusions that can be drawn are as follows:

- 1) From May 2020 to July 2021, a total of three main deformation areas were identified in the Ankang Airport area, all of which belong to expansive soil fill slopes. The instability of expansive soil slope is the main geological disaster facing Ankang Airport at present.
- 2) The relationship between deformation rate and filling depth, as well as the relationship between deformation time series and rainfall, indicate that the surface deformation of the Ankang expansive soil airport is caused by the combined action of the consolidation and compression of the filling soil and the expansion and shrinkage characteristics of the expansive soil.
- 3) The Ankang Airport runway and the terminal area have small ground deformation variables, and the overall stability meets the design requirements and can meet the official operation needs of the airport.

In general, the monitoring results of the time-series InSAR monitoring technology based on elevation correction in the Ankang airport area show that the deformation law of the airport area is highly consistent with the expansion and contraction characteristics of expansive soil. Although the airport has not experienced significant surface deformation for the time being, its temporal deformation trend related to precipitation shows that long-term deformation monitoring of Ankang expansive soil airport is very necessary after the airport starts operation, and related research needs a shorter revisit period. The SAR data and soil moisture data can be used for longer-term deformation monitoring and mechanism analysis.

## VI. ACKNOWLEDGEMENTS

Project supported by the National Key Research and Development Program of China (2019YFC1509802).

Projects supported by the National Science Foundation of China (42074041;41731066).

Projects supported by the Open Fund of the State Key Laboratory of Geo-Information Engineering (SKLGIE2019-Z-2-1).

## References

Berardino, P., Fornaro, G., and Lanari, R. (2002). A New Algorithm for Surface Deformation Monitoring Based on Small Baseline Differential SAR Interferograms. *IEEE Transactions on Geoscience and Remote Sensing*, Vol 40, No.11, pp. 2375-2383.

Fattahi, H., and Amelung, F. (2013). DEM Error Correction in InSAR Time Series [J]. *IEEE Transactions on Geoscience and Remote Sensing*, Vol 51, No.7, pp. 4249-4259.

Ferretti, A., Prati, C., and Rocca, F. (2001). Permanent Scatterers in SAR Interferometry. *IEEE Transactions on Geoscience and Remote Sensing*, Vol 39, No.1.

Gabriel, A.K., Goldstein, R.M., and Zebker, H.A. (1989). Mapping Small Elevation Changes over Large Areas: Differential Radar Interferometry. *Journal of Geophysical Research Solid Earth*, Vol 94, pp. 9183-9191.

Hooper, A., Zebker, H., Segall, P. and Kampes, B. (2004). A new method for measuring deformation on volcanoes and other natural terrains using InSAR persistent scatterers. *Geophysical Research Letters*, 31, No 23, pp. 1-5.

Jiang, Y., Liao, M., and Wang, H. (2016). Deformation Monitoring and Analysis of the Geological Environment of Pudong International Airport with Persistent Scatterer SAR Interferometry. *Remote Sensing*, 8, No 12, pp. 1021.

Jiang, L., and Lin, H. (2010). Integrated Analysis of SAR Interferometric and Geological Data for Investigating Long-Term Reclamation Settlement of Chek Lap Kok Airport, Hong Kong. *Engineering Geology*, 110, pp. 77-92.

Liu, X., Zhao, C., and Zhang, Q. (2019). Characterizing and Monitoring Ground Settlement of Marine Reclamation Land of Xiamen New Airport, China with Sentinel-1 SAR Datasets. *Remote Sensing*, 11, No 5, pp. 585.

Short, N., Leblanc, A.M., Laden, W., Olden Berger, G., Mathon-Dufour, V., and Brisco, B. (2014). Radarsat-2 d-insar for ground displacement in permafrost terrain, validation from Iqaluit Airport, Baffin Island, Canada. *Remote Sensing of Environment*, 141, pp. 40-51.

Touzi, R., and Lopes, A. (1999). Bruniquel J, et al. Coherence estimation for SAR imagery. *IEEE Transactions on Geoscience and Remote Sensing*, 37, No 1, pp. 135-149.

Wu, Q., Jia, C., Chen, S., and Li, H. (2019). SBAS-InSAR Based Deformation Detection of Urban Land, created from Mega-Scale Mountain Excavating and Valley Filling in the Loess Plateau: The Case Study of Yan'an City. *Remote Sensing*, 11, No. 14, pp. 1673.

Wu, S., Yang, Z., and Ding, X. (2020). Two Decades of Settlement of Hong Kong International Airport Measured with Multi-temporal InSAR [J]. *Remote Sensing of Environment*, 24, No 8, pp. 111976.

Zhuo, G., Dai, K., and Huang, H. (2020). Evaluating Potential Ground Subsidence Geo-Hazard of Xiamen Xiang'an New Airport on Reclaimed Land by SAR Interferometry. *Sustainability*, 12, pp. 6991.

# Terrestrial Laser Scanning based deformation monitoring for masonry buildings subjected to ground movements induced by underground construction

Yiyan Liu, Sinan Acikgoz, Harvey Burd

Department of Engineering Science, University of Oxford, 15 Parks Road, OX1 3PJ Oxford, United Kingdom,  
([yiyan.liu@eng.ox.ac.uk](mailto:yiyan.liu@eng.ox.ac.uk); [sinan.acikgoz@eng.ox.ac.uk](mailto:sinan.acikgoz@eng.ox.ac.uk); [harvey.burd@eng.ox.ac.uk](mailto:harvey.burd@eng.ox.ac.uk))

**Key words:** *Terrestrial Laser Scanning; ground movement; masonry; monitoring; non-rigid iterative closest point (N-ICP)*

## ABSTRACT

Tunnelling and deep excavation activities cause ground movements. Monitoring the influence of these ground movements on nearby surface assets is a major component of urban underground construction projects. Such projects often require large-scale and comprehensive monitoring of nearby buildings to track displacements and identify structural damage. Masonry assets are particularly vulnerable to ground movements due to the low tensile strength of the material; these structures may experience unsightly cracking and structural stability issues. Current monitoring practice for these buildings is labour intensive and cannot fully characterise the response of the assets due to the limited number of measurement points. This paper presents a non-contact monitoring solution using terrestrial laser scan (TLS) data, which develops a modified non-rigid iterative closest point (N-ICP) algorithm. This algorithm optimises the displacement fields by establishing point to point correspondences that penalise non-smooth deformations and deviations from landmarks (*i.e.* feature points where displacements are known). The algorithm outputs rich 3D displacement fields that can be used in established assessment and decision-making procedures. To demonstrate this algorithm's ability to estimate 3D displacement fields from point clouds, several synthetic datasets are processed in this study. The results demonstrate the algorithm's potential for recovering underlying deformations with the help of landmarks and optimisation weightings.

## I. INTRODUCTION

Urban underground construction requires rigorous and comprehensive monitoring and survey schemes on nearby buildings. For example, Crossrail and High Speed Two require all buildings in risk category 3 (moderate) and above to be monitored from one year prior to construction until the ground movement has ceased (Crossrail Limited, 2008; High Speed Two Limited, 2017). During Crossrail alone, according to Lazarus and Jung (2018), there were approximately 4000 affected buildings along the route, including 300 listed buildings. Instrumenting and monitoring these buildings required expenditure in excess of £60 million (VINCI Construction, 2014).

In underground construction, the monitoring of surface properties forms part of the ground movement control and asset management strategy (British Tunnelling Society, 2011). The monitoring data are used to assess the impact of the ground movements, verify design parameters and models, and inform construction control procedures. The monitoring results are often used as performance indicators for the asset. It is common practice for the main contractor to operate a "traffic light" system so that appropriate actions can be undertaken when "trigger values" are exceeded (Crossrail Limited, 2008; High Speed Two

Limited, 2017). Such systems are often at the core of the contractor risk management strategy. Therefore, the reliability and timeliness of the monitoring data are of great importance.

As evidenced in the Jubilee Line Extension (see Burland *et al.*, 2001) and the more recent Crossrail projects, the monitoring of surface assets mainly comprises manual monitoring of studs and invar calibrated scales using precise levels and "automatic" monitoring of prisms using total stations. According to Burland *et al.* (2001) and the Tunnel Lining Design Guide published by the British Tunnelling Society (2004), the practical measurement errors of total stations and precise levels can be as high as 0.5 mm. However, the use of precise levels and total stations require the installation of "targets" on the façade. Hence only isolated points can be monitored for movements, and these points may not reflect the response of the building. According to Lazarus and Jung (2018), although extensive monitoring was carried out along tunnel alignments in Crossrail, data collected were often insufficient to understand the behaviour and response of individual buildings to ground movements. Moreover, surveying using precise levels is considered labour intensive.

Point cloud data is a collection of 3D points that represent the external and visible surfaces of 3D

objects, which can be obtained using laser scans or images. The efficient, remote, and contactless data acquisition process generates a dense point cloud that is rich in geometric information. An example of point cloud data of a building façade is shown in Figure 1. Depending on the setup and external factors, the point accuracy of the point cloud obtained from laser scanners or reconstructed from Structure from Motion (SfM) and MultiView Stereo (MVS) techniques is in the order of millimetres. The point accuracy can be as high as one to two millimetres for terrestrial laser scans (TLS) when in the appropriate range (Kersten *et al.*, 2021).

In the construction industry, it is common practice to use 3D point cloud data, particularly from laser scans, to create an as-built BIM model upon completion of construction (Wang and Kim, 2019). The data have also been widely used for geometric inspection and construction progress tracking. However, using point cloud data for displacement monitoring is still in its infancy (Mukupa *et al.*, 2017). To the best of the authors' knowledge, there is no current standard, specification or guidance on using point cloud data for displacement monitoring. To this end, this paper will first review existing methodologies for displacement analysis using point cloud data before presenting and evaluating their performance with synthetic data.

## II. REVIEW OF DISPLACEMENT ANALYSIS USING POINT CLOUD DATA

Due to the advantages of point cloud data mentioned above, various cloud comparison methods have been developed for displacement analysis, including Cloud-to-Cloud (C2C) comparison, Cloud-to-Mesh (C2M)

comparison and Multiscale Model to Model Cloud Comparison (M3C2), which have been comprehensively reviewed in Lague *et al.* (2013). The displacement models and characteristics of these methods are summarised below.

### A. Cloud-to-Cloud comparison (C2C)

C2C method establishes point correspondence between two-point clouds based on the Euclidean distance between points. The same idea was used in the popular iterative closest point algorithm proposed by Besl and McKay (1992). The point in the deformed point cloud, which has the closest distance to a point in the undeformed point cloud, is chosen as its corresponding point. The displacement is calculated as the difference in coordinates between these corresponding point pairs.

This method is the simplest and fastest method for cloud comparison as it does not require calculating surface normals or meshing. However, the method is sensitive to measurement noise (Lague *et al.*, 2013) and point density (Mukupa *et al.*, 2017). More importantly, when used for relatively complex geometries, *e.g.* a curved surface, the correspondence established by the closest point method is influenced significantly by point cloud and deformation geometry. In such cases, the closest distances between point clouds are not representative of deformations and can result in erroneous displacement interpretations (Acikgoz *et al.*, 2017). Examples of the use of the C2C method for displacement analysis include Jafari *et al.* (2017) and Gawronek *et al.* (2019).

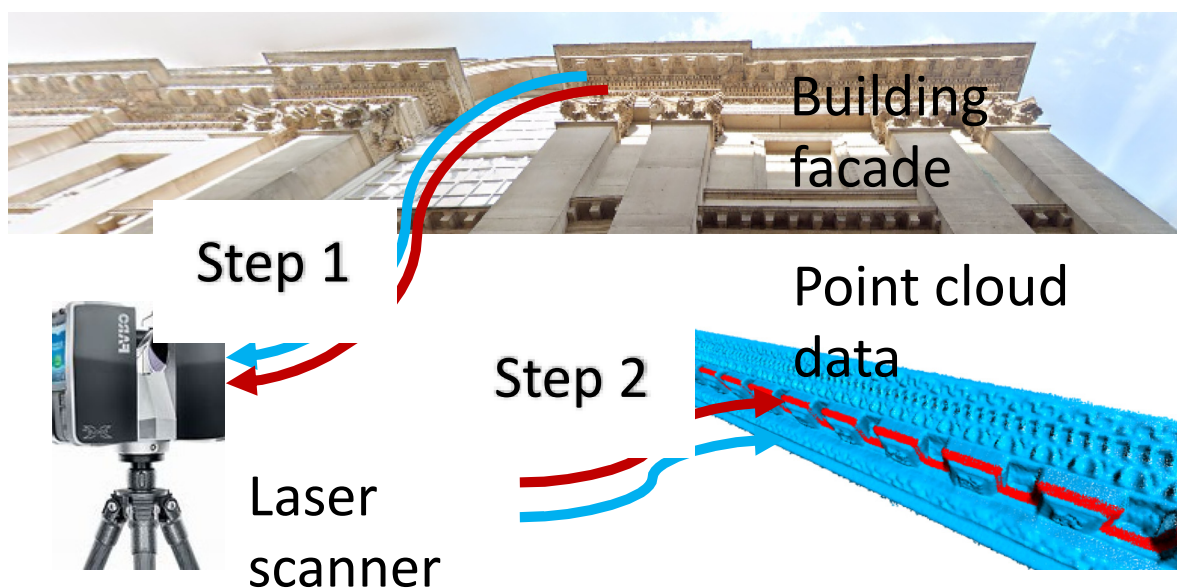


Figure 1. Acquisition of point cloud data of the building façade at Mansion House using a laser scanner. The details of façade ornaments are preserved in the point cloud. Two scans obtained at two different states shown as red and blue point clouds aligned together. For illustration purposes, only part of the red point cloud is shown. The image of Mansion House east façade was extracted from Google Street View. The image of the Faro X330 laser scanner was extracted from image.bing.com under a creative commons license.

### B. Cloud-to-Mesh comparison (C2M)

C2M method defines the point displacement as the distance between a point in the undeformed point cloud and the nearest element of the mesh of the deformed point cloud along its surface normal. This method requires meshing of the deformed cloud and searching for the nearest mesh element, which is computationally expensive. The method works well on out-of-plane displacements of flat surfaces (Lague *et al.*, 2013), but since the true correspondence between points and mesh vertices is not established, the in-plane displacements are challenging to identify. Examples of the use of the C2M method for displacement analysis include Caudal *et al.* (2017) and Mugnai *et al.* (2019).

### C. Multiscale Model to Model Cloud Comparison (M3C2)

M3C2 method involves selecting core points in the deformed cloud, constructing a cylinder through each core point in a specified direction and calculating the average distance between points in both point clouds in the cylinder along the predefined direction. The M3C2 method is useful for determining displacements of flat surfaces and minimising the influence of measurement noise on displacement estimations. However, like C2C and C2M methods, the arbitrary nature of determining correspondences in M3C2 may lead to inaccurate deformation estimates (Acikgoz *et al.*, 2017). While the method provides reasonable estimates for out of plane deformations of flat surfaces (Acikgoz *et al.*, 2021), it can struggle with complex geometries and in-plane displacements. Examples of the use of the M3C2 method for displacement analysis include Jafari *et al.* (2017) and Acikgoz *et al.* (2017).

## III. OPTIMAL STEP NON-RIGID ICP (N-ICP) ALGORITHM

The optimal step N-ICP algorithm was proposed by Amberg *et al.* (2007). It is a point cloud registration algorithm which aims to find the optimal affine transformation for each vertex of a point cloud that deforms it to corresponding points in another point cloud subject to stiffness and landmark constraints. The N-ICP algorithm, and its predecessor proposed by Allen *et al.* (2003), were originally intended to register templates to human face or body scans while allowing the template to deform.

The N-ICP algorithm is a popular point cloud registration algorithm in the computer vision community and is capable of registering point clouds of complex geometry with small reconstruction errors. To the best of our knowledge, the algorithm has not been used for displacement analysis in structural health monitoring. It has the potential to address issues with existing cloud comparison methods reviewed in Section II because: (i) the displacement of each vertex can be recovered by the non-rigid registration of two point clouds; (ii) the number of degree-of-freedom for each vertex and the use of stiffness constraints are

compatible with the physics of deformation; (iii) with the additional landmark constraints, the algorithm has a mechanism to control the optimisation path and capture true point correspondences. A schematic of the N-ICP algorithm is shown in Figure 2 below.

The N-ICP algorithm, in essence, solves the optimisation problem for the cost function (Eq. 1):

$$\bar{E}(X) = \bar{E}_d(X) + \alpha \bar{E}_s(X) + \beta \bar{E}_l(X) \quad (1)$$

where  $\bar{E}(X)$  is the cost function;  $\bar{E}_d(X)$  is the distance term;  $\bar{E}_s(X)$  is the stiffness term;  $\bar{E}_l(X)$  is the landmark term;  $\alpha$ ,  $\beta$  are stiffness and landmark weightings, respectively;  $X$  is the transformation matrix for the source cloud. Through minimising the cost function with the optimal transformation  $X$ , the best affine transformation for each vertex can be obtained under fixed stiffness and landmark weightings. At each step, a new correspondence is determined through the closest point search.

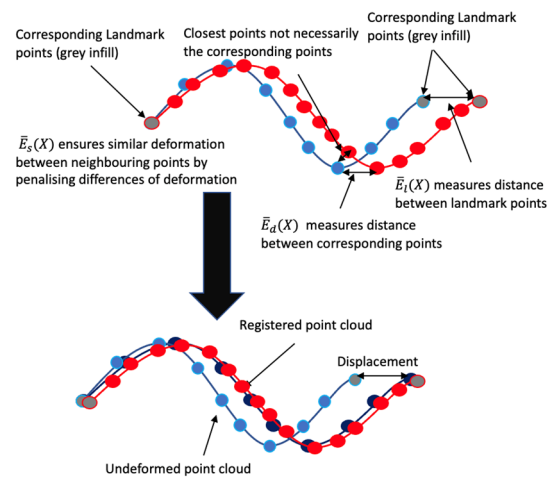


Figure 2. A schematic of the N-ICP algorithm.

Displacements are recovered by registering the undeformed point cloud (blue point cloud) to the deformed point cloud (red point cloud). Landmark points are marked with grey infill in both undeformed and deformed point clouds. The registered point cloud after N-ICP is shown in dark blue in the bottom. Registration errors (the difference between dark blue points and red points) are exaggerated for illustration purposes.

However, it is not possible to know the optimal stiffness  $\alpha$  beforehand. A high value of  $\alpha$  leads to a globally affine transformation, which may be suitable for early algorithm steps to capture gross rigid body movements. A small value of  $\alpha$  leads to non-rigid deformations, which may be suitable for consecutive steps to minimise the distance between point clouds. Following this logic, Amberg *et al.* (2007) introduced iterative steps to find a globally optimal solution.

With this setup, a list of stiffness values is used over a for-loop. The stiffness values start from high value to ensure global registration and gradually reduce to allow more localised deformation. For each stiffness value, the best affine transformation is determined by

minimising the cost function in Equation 1. The solution is then used to update the undeformed point cloud before undertaking the closest point search again. Based on the new correspondence, another minimisation is conducted. This iteration is repeated until the Frobenius norm of the difference between the two most recent transformation matrices is below a threshold, *i.e.*, the change in deformation is too small, and no new correspondences are found.

Similar to stiffness weights, Amberg *et al.* (2007) recommended the use of a series of decreasing landmark weights to account for inaccuracies associated with landmark correspondence. However, it is not clear from the paper how the initial landmark weight is determined. In the implementation and evaluation below, an additional dynamic mechanism to determine the landmark weighting  $\beta$  based on the ratio of landmark term and distance terms in Equation 1 is introduced. This is used to prioritise landmark registration at the beginning of the iteration as (Eq. 2):

$$\beta = 1.5 \times \frac{\bar{E}_d(X)}{\bar{E}_l(X)} \quad (2)$$

where  $\bar{E}_d(X)$  is determined by the original point coordinates of the undeformed cloud and corresponding points in the deformed point cloud;  $\bar{E}_l(X)$  is determined by the original coordinates of selected landmark points in the deformed and undeformed point clouds. Before registration, there is no deformation, the stiffness term is zero, therefore, not included in the above determination.

#### IV. EXPERIMENT SETUP

The façade under consideration here is 2 m long and 1 m wide, as shown in Figure 3a. Two point clouds of the main plane of the façade are simulated by two sets of 20,000 randomly generated points (through the generation of 20,000 uniformly distributed float numbers between 0 and 1, and scaled by the length and width, respectively), which are used to account for the correspondence uncertainty. The measurement errors associated with point positions due to laser scan single point accuracy is referred to as measurement noise and is simulated by a random number between 0 to 0.002 (uniformly distributed) in metre unit. This random number describes each point's  $z$  coordinate. Four "extrusions" that have a size of  $0.25 \times 0.2 \times 0.1$  m and are of the same point density as the main plane are added to simulate common features, *i.e.*, exterior elements, ornaments and finishes on the building facades.

This study considers "in-plane" deformation and "out-of-plane" deformation as two basic deformation patterns, which are commonly observed in field monitoring. "In-plane" and "out-of-plane" deformations are defined in relation to the main plane of the façade in the  $xy$  plane. The displacement field is

added to one of the point clouds while another point cloud is used as the undeformed cloud. By taking these two point clouds as inputs, the results from the N-ICP algorithm, C2C, C2M and M3C2, are compared to the known displacement field to assess their relative performance. Benchmark C2C, C2M and M3C2 cloud comparison methods are performed using the software CloudCompare. Bespoke software was written in Python to implement N-ICP. For N-ICP, unless otherwise stated, a list of 10 stiffness weighting ranging from 10000 to 1 is used. Landmarks are used for some examples. When in use, the landmark weighting is determined in accordance with Equation 2.

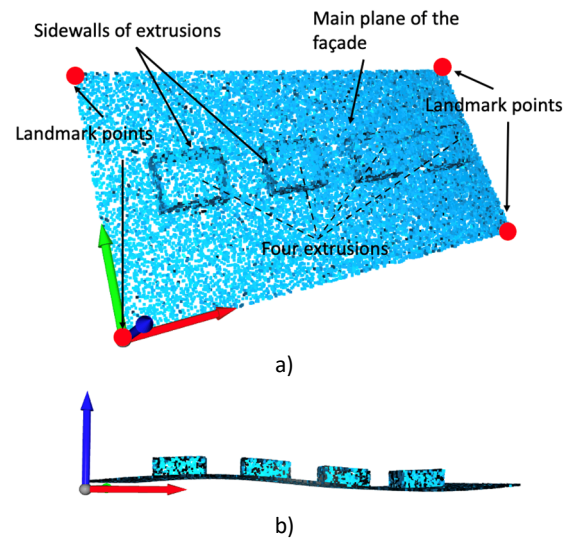


Figure 3. a) Synthetic façade considered in this study; b) Deformed point cloud subjected to "out-of-plane" deformation (Deformation exaggerated for illustration purpose) (Red, green, blue arrows indicate x, y, z directions respectively).

In the following discussion, the point normal refers to the surface normal of a local region represented by that point and its neighbouring points. The points that form the sidewall of the extrusions on the façade, as shown in Figure 3a, have their point normal significantly different to the point normal of the main plane of the façade. These points are referred to as feature points.

#### V. DISCUSSION OF RESULTS

##### A. Façade subjected to out-of-plane displacement

A sine displacement is added to the  $z$  direction (as indicated by the blue arrow shown in Figure 3a) of the point cloud as a function of the  $x$  coordinate (coordinate direction along the façade as indicated by the red arrow in Figure 3a). The out-of-plane displacement  $d_z$  has a maximum value of 5mm and is defined as (Eq. 3):

$$d_z = 0.005 \times \sin(\pi x) \quad (3)$$

For the simple out-of-plane displacement case, C2C, C2M, M3C2 and N-ICP all capture the small displacement reasonably well, as shown in Figure 4a.



The relative performance of C2C, C2M, M3C2 and N-ICP can be further assessed by computing their standard deviations from true values using (Eq. 4):

$$\sigma = \sqrt{\frac{1}{n} \sum_{i=1}^n (d_i - d_i^t)^2} \quad (4)$$

where  $\sigma$  is the standard deviation from true values and referred to as the error index in the text below, and its units (m) are omitted for brevity;  $d_i$  is the measured displacement;  $d_i^t$  is the true displacement from the displacement field in Equation 3;  $n$  is the number of measurements.

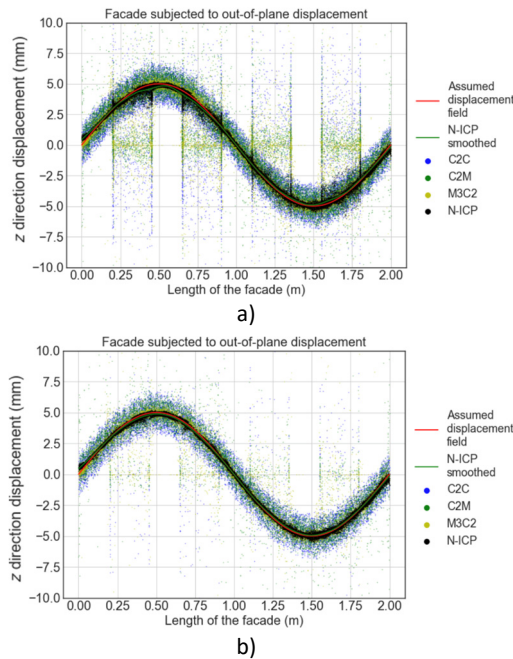


Figure 4. Comparison of out-of-plane displacement analysis of a façade using N-ICP with benchmark methods C2C, C2M and M3C2. (a: all points used in the analysis; b: feature points removed).

The error indices of C2C, C2M, M3C2 and N-ICP are  $\sigma_{c2c} = 2.23 \times 10^{-3}$ ,  $\sigma_{c2m} = 2.04 \times 10^{-3}$ ,  $\sigma_{m3c2} = 3.78 \times 10^{-3}$ ,  $\sigma_{N-ICP} = 0.52 \times 10^{-3}$  respectively, as illustrated in Figure 4a. N-ICP has a considerably smaller error index compared to other methods.

The majority of errors associated with C2C, C2M and M3C2 are due to the feature points, whose point normals are not along the  $z$  direction. The feature points are either in the  $xz$  or  $yz$  plane; therefore, the displacement along the  $z$  direction is, in fact, "in-plane" displacement. The C2C, C2M and M3C2 algorithms struggle with such displacements. If the feature points are filtered out by setting a normal threshold, the errors reduce considerably, as shown in Figure 4b. The error indices of C2C, C2M, M3C2 and N-ICP become  $\sigma_{c2c} = 1.42 \times 10^{-3}$ ,  $\sigma_{c2m} = 1.58 \times 10^{-3}$ ,  $\sigma_{m3c2} = 2.79 \times 10^{-3}$ ,  $\sigma_{N-ICP} = 0.26 \times 10^{-3}$  respectively.

The uniformly distributed measurement noise in  $z$  direction is bounded by 0 and 0.002. The standard deviation of the noise is  $0.58 \times 10^{-3}$ . For out-of-plane displacements, the N-ICP algorithm manages to reduce the error index below the standard deviation of the measurement noise. If a locally estimated scatterplot smoothing is applied to the N-ICP results, as shown in Figure 5a, the performance can be further improved to  $\sigma_{N-ICP\_Smoothed} = 6.70 \times 10^{-5}$ .

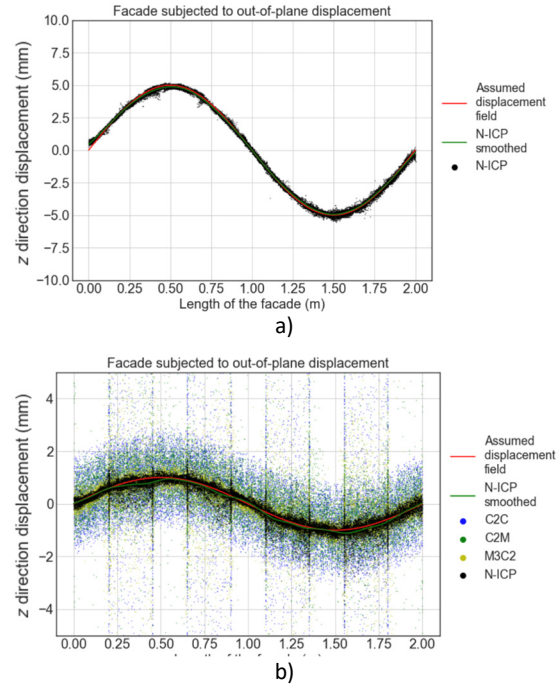


Figure 5. a) Assumed displacement  $d_z = 0.005 \times \sin(\pi x)$  – Performance of N-ICP further enhanced by using locally estimated scatterplot smoothing (out-of-plane displacement only); b) Assumed displacement  $d_z = 0.001 \times \sin(\pi x)$  - Comparison of out-of-plane displacement analysis of a façade using N-ICP with benchmark methods C2C, C2M and M3C2.

When the introduced out-of-plane displacement is within the range of measurement noise, *i.e.*,  $d_z = 0.001 \times \sin(\pi x)$  as shown in Figure 5b, N-ICP continues to perform well. The error indices of N-ICP and N-ICP smoothed are  $0.51 \times 10^{-3}$  and  $8.03 \times 10^{-5}$ , compared to  $1.73 \times 10^{-3}$  for C2C,  $1.67 \times 10^{-3}$  for C2M and  $2.41 \times 10^{-3}$  for M3C2. The error indices of M3C2, C2C and C2M are all substantially greater than the introduced maximum displacement, while the error index for N-ICP remains less than the standard deviation of the measurement noise.

This example demonstrates that for the analysis of a façade subjected to out-of-plane displacement: (i) N-ICP outperforms C2C, C2M and M3C2; (ii) for small displacements, the relatively large error indices of C2C, C2M and M3C2 may invalidate displacement estimations whereas N-ICP can recover accurate displacement fields after smoothing when the measurement noise is uniformly distributed.

The ability of N-ICP to recover small displacements within the range of measurement noise is an important property as it puts less stringent requirements on laser scan single point accuracy.

**B. Façade subjected to in-plane displacement**

For in-plane displacement analysis, a quadratic displacement is added to the y direction of the point cloud (as indicated by the green arrow shown in Figure 6a) as a function of the x coordinate (Eq. 5):

$$d_y = -0.01 x^2 \quad (5)$$

Without using any landmarks, N-ICP successfully captures the trend of the displacements (see Figure 6b). However, at both ends of the façade, the displacement diverges from the true values. For x values between 0 m to 0.2 m and 1.8 m to 2 m, there are no features, and N-ICP finds an "optimum" solution primarily based on closest point correspondence; this yields erroneous displacement estimates. On the other hand, C2C cannot detect meaningful in-plane displacement along the y direction except for some points at the extrusions. M3C2 also picks up some displacement at the features but, overall, fails to capture the displacement pattern.

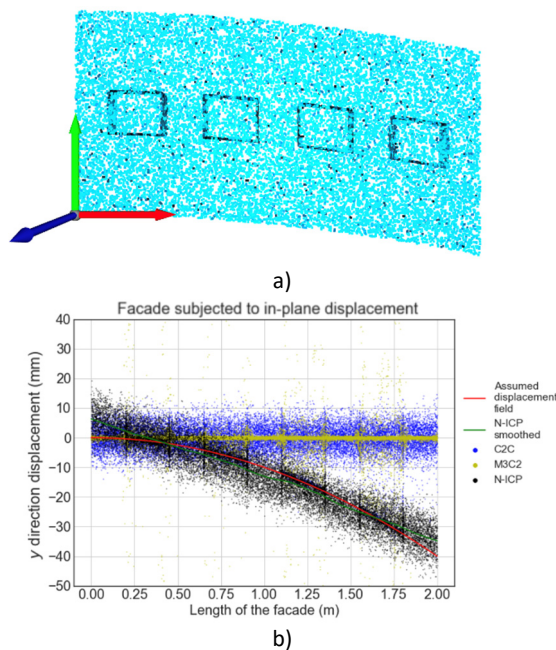


Figure 6. a) Point cloud subjected to "in-plane" deformation along the y direction (Deformation exaggerated for illustration purpose; Red, green, blue arrows indicate x, y, z directions respectively); b) Comparison of in-plane displacement analysis of the façade using N-ICP with C2C and M3C2.

The error index of N-ICP in Figure 6b is  $4.8 \times 10^{-3}$ , which is significantly greater than the out-of-plane case. However, the performance of N-ICP is still much better than C2C and M3C2, whose error indices are in excess of  $1.70 \times 10^{-2}$ .

To understand the increased error index of N-ICP, analyses of two point clouds of the 2m by 1m façade subjected to no displacement field are conducted. For the 2 m by 1 m façade, two sets of 20,000 (Case 1) or 200,000 (Case 2) uniformly distributed random points were generated, and the differences of the x coordinates of closest points between the two sets of points were determined as shown in Figure 7. The normalised count numbers in Figure 7 are the raw counts of points within a specific interval divided by the total point number and the width of the selected interval so that the total area under the histogram is unity. The analyses in Figure 7 were undertaken using the x coordinate, but the y coordinate could also have been used. This difference in x coordinates of the two closest points is seen as a potential source of error for displacement analysis, which is intrinsic to the point density of the point cloud. With 200,000 points over the same façade, the error index (standard deviation of the difference in x coordinates) has reduced from  $4 \times 10^{-3}$  in Figure 7a to  $1.3 \times 10^{-3}$  in Figure 7b.

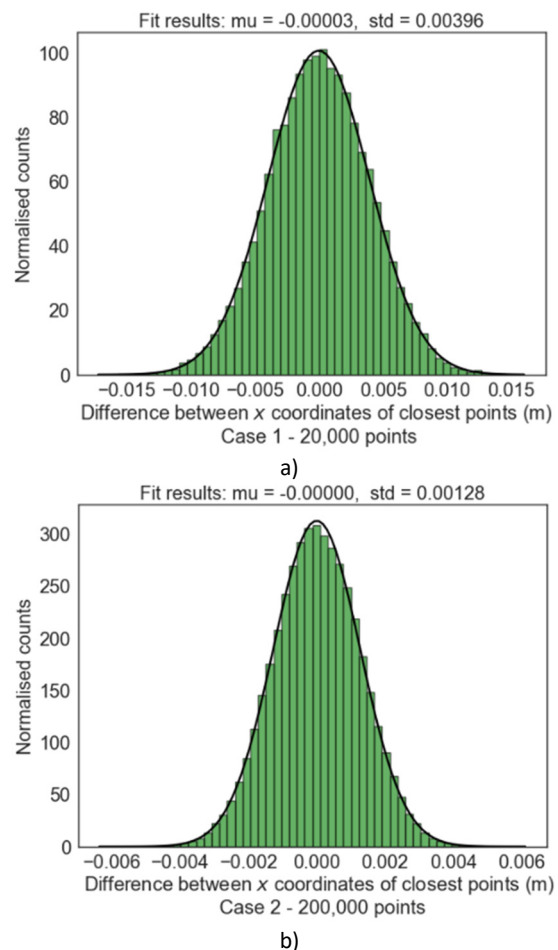


Figure 7. Distributions of x coordinate differences between closest points: a) Case 1 – 20,000 points; b) Case 2 – 200,000 points.

By comparing the error indices associated with N-ICP data in Figure 6b ( $4.8 \times 10^{-3}$ ) and Figure 7a ( $4 \times 10^{-3}$ ), it is noted that the error index of N-ICP for in-plane displacement is similar to the error index that

is obtained when the displacements of undeformed point clouds are evaluated. This indicates that the error index of N-ICP is significantly influenced by the point density, *e.g.* the  $x$  coordinate differences of closest point sets.

It is worth noting that the sensitivity of the error index due to point density can be mitigated by smoothing if the point cloud is of even density. For the case where the façade is subjected to  $d_y = -0.01x^2$ , the error index of smoothed N-ICP results become  $2.33 \times 10^{-3}$  (see Figure 6b).

How the measurement error indices vary with the amplitude of the displacement field can also be investigated. Suppose the façade is subjected to  $d_y = -0.001x^2$  and  $d_x = -0.005x^2$ . The corresponding error indices of N-ICP become  $3.70 \times 10^{-3}$  and  $4.24 \times 10^{-3}$ , respectively. In the above examples, the error indices remain in the same order of magnitude despite an increase in the maximum displacement from 4 mm to 20 mm. As such, for in-plane displacements smaller than the point spacing, it would be difficult to distinguish displacement from the background noise.

The performance of N-ICP can be further enhanced by using landmark terms. Four corner points of the rectangular façade are selected as landmarks (as indicated in Figure 3a), and passed in as inputs. As a consequence, the error index of N-ICP reduces from  $4.82 \times 10^{-3}$  in Figure 6b (where landmarks were not used) to  $4.44 \times 10^{-3}$  in Figure 8b. It can be seen that sections between features, *i.e.*, the section between 0.20 to 0.45 m and 0.65 m to 0.90 m in  $x$  direction, as shown in Figure 8, have the largest errors. Points where features are located and whose normal is along the displacement direction (Figure 8a) have the most reliable results.

In summary, we have shown that for the examined in-plane deformation: (i) C2C and M3C2 cannot capture displacements except at specific locations, (ii) without the landmark term, N-ICP can recover the displacement of the entire façade using available features; (iii) in the absence of features or landmarks, N-ICP primarily uses closest points to establish the correspondence and this may lead to erroneous results; (iii) N-ICP's performance can be enhanced by using the landmark term; (iv) the in-plane measurement accuracy of N-ICP depends on the point density and this can be mitigated using smoothing.

## VI. SUMMARY

This paper evaluated the performance of several point cloud comparison techniques previously used to estimate deformations. Synthetic point clouds of predominantly planar surfaces, inspired by façades, were generated and deformed in a non-rigid manner. The known deformation fields were compared to deformations estimated by four different algorithms, including a modified version of the non-rigid iterative point cloud algorithm, N-ICP. This algorithm

outperforms the other examined techniques (C2C, C2M and M3C2 algorithms). Sources of errors for the N-ICP algorithm are analysed for different deformation scenarios, and the accuracy of the algorithm is quantified using simple statistical measures. The results demonstrate that this algorithm can achieve deformation estimates with smaller errors than the single point measurement accuracy of the point cloud, particularly for displacements in the out-of-plane direction. Compared to out-of-plane displacements, the proposed method predicts in-plane displacements with a greater error margin. The errors are particularly influenced by the point density of the point cloud. However, the algorithm is able to accurately estimate in-plane displacements when landmarks are used, and feature points constrain the registration.

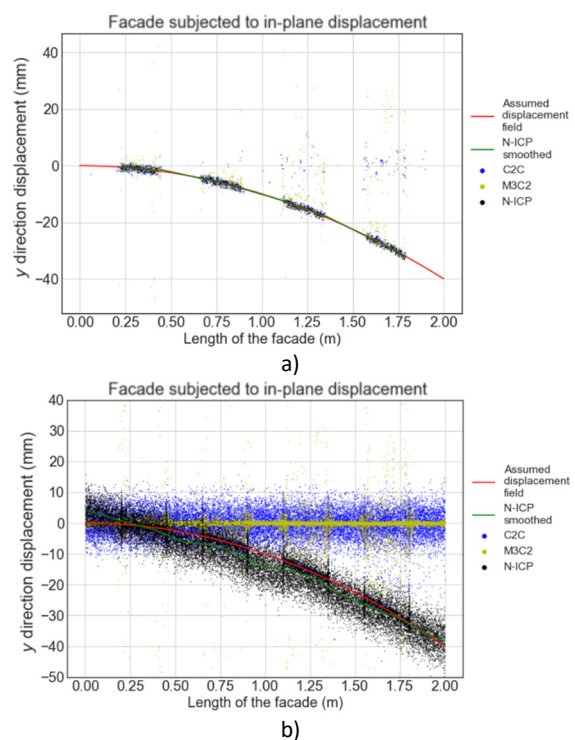


Figure 8. N-ICP performance for in-plane displacement analysis with the use of landmarks: (a) displacement of points in the  $xz$  plane; b) all points used in the analysis.

Deformations of buildings subjected to ground movements due to underground construction works include both in-plane and out-of-plane displacements. To obtain accurate displacement results using the proposed N-ICP algorithm in field applications would require establishing reliable landmark correspondence. Furthermore, stiffness weightings used in the current N-ICP algorithm are not based on material properties and are determined somewhat arbitrarily. Further research by the authors will aim to address these issues to support the use of point cloud monitoring in future applications.

## VII. ACKNOWLEDGEMENTS

This research was funded by the Engineering and Physical Sciences Research Council (EPSRC) of the United Kingdom and Arup Group Ltd through the iCASE project (Project Reference: 2280800).

## References

- Acikgoz, S., Luciano, A., Dewhurst, M., Dejong, M.J., and Mair, R., (2021). Innovative monitoring of the response of a heritage masonry building to nearby tunnelling in London Clay. *Géotechnique*, pp. 1–16.
- Acikgoz, S., Soga, K., and Woodhams, J., (2017). Evaluation of the response of a vaulted masonry structure to differential settlements using point cloud data and limit analyses. *Constr. Build. Mater.* 150, pp. 916–931.
- Allen, B., Curless, B., and Popović, Z., (2003). The space of human body shapes: Reconstruction and parameterization from range scans. *ACM Trans. Graph.* 22, pp. 587–594.
- Amberg, B., Romdhani, S., and Vetter, T., (2007). Optimal Step Nonrigid ICP Algorithms for Surface Registration. In: *2007 IEEE Conference on Computer Vision and Pattern Recognition*, pp. 1–8.
- Besl, P.J., and McKay, N.D., (1992). A method for registration of 3-D shapes. *IEEE Trans. Pattern Anal. Mach. Intell.* ,14, pp. 239–256.
- British Tunnelling Society (2004). *Tunnel lining design guide, Tunnel lining design guide*. Thomas Telford Ltd, London.
- British Tunnelling Society (2011). *Monitoring Underground Construction*, ICE Publishing. Thomas Telford Ltd, London.
- Caudal, P., Grenon, M., Turmel, D., Locat, J., (2017). Analysis of a Large Rock Slope Failure on the East Wall of the LAB Chrysotile Mine in Canada: LiDAR Monitoring and Displacement Analyses. *Rock Mech. Rock Eng.* 50, pp. 807–824.
- Crossrail Limited (2008). Crossrail Information Paper D12 – Ground Settlement [WWW Document]. URL <http://74f85f59f39b887b696f-ab656259048fb93837ecc0ecbcf0c557.r23.cf3.rackcdn.com/assets/library/document/d/original/d12groundsettlement.pdf> (accessed 7.28.20).
- Gawronek, P., Makuch, M., Mitka, B., and Gargula, T., (2019). Measurements of the Vertical Displacements of a Railway Bridge Using TLS Technology in the Context of the Upgrade of the Polish Railway Transport. *Sensors* ,19, 4275.
- High Speed Two Limited (2017). High Speed Two Phase One C3: Ground Settlement [WWW Document]. URL [https://assets.publishing.service.gov.uk/government/uploads/system/uploads/attachment\\_data/file/672194/C3\\_-\\_Ground\\_Settlement\\_\\_v1.pdf](https://assets.publishing.service.gov.uk/government/uploads/system/uploads/attachment_data/file/672194/C3_-_Ground_Settlement__v1.pdf) (accessed 7.28.20).
- Jafari, B., Khaloo, A., and Lattanzi, D., (2017). Deformation Tracking in 3D Point Clouds Via Statistical Sampling of Direct Cloud-to-Cloud Distances. *J. Nondestruct. Eval.* 36, pp. 1-10.
- Kersten, T.P., Lindstaedt, M., and Stange, M., (2021). Investigations into the geometric accuracy of latest terrestrial laser scanners in the laboratory and in the field. *AVN Allg. Vermessungs-Nachrichten*, 128, pp. 59–67.
- Lague, D., Brodu, N., and Leroux, J., (2013). Accurate 3D comparison of complex topography with terrestrial laser scanner: Application to the Rangitikei canyon (N-Z). *ISPRS J. Photogramm. Remote Sens.*, 82, pp. 10–26.
- Lazarus, D., and Jung, H. II, (2018). Damage assessment and monitoring for buildings on the Elizabeth line. *Struct. Eng.* 96, pp. 14–24.
- Mugnai, F., Lombardi, L., Tucci, G., Nocentini, M., Gigli, G., and Fanti, R., (2019). Geomatics in bridge structural health monitoring, integrating terrestrial laser scanning techniques and geotechnical inspections on a high value cultural heritage. *ISPRS Ann. Photogramm. Remote Sens. Spat. Inf. Sci.* 42, pp. 895–900.
- Mukupa, W., Roberts, G.W., Hancock, C.M., and Al-Manasir, K., (2017). A review of the use of terrestrial laser scanning application for change detection and deformation monitoring of structures. *Surv. Rev.* 49, pp. 99–116.
- Burland, J. B., Standing, J. R., and Jardine, F. M. (2001). *Building response to tunnelling. Case studies from construction of the jubilee line extension*. London, pp. 134-145.
- VINCI Construction (2014). Crossrail C510 - Overview Crossrail C510 [WWW Document]. URL <http://www.aftes.asso.fr/contenus/upload/File/Publications/Autres/2015-03-26/9-VGP - Crossrail-.pdf> (accessed 7.9.20).
- Wang, Q., and Kim, M.K., (2019). Applications of 3D point cloud data in the construction industry: A fifteen-year review from 2004 to 2018. *Adv. Eng. Informatics*, 39, pp. 306–319.

## Pan-European deformation monitoring: The European Ground Motion Service

Michele Crosetto<sup>1</sup>, Lorenzo Solari<sup>1,2</sup>, Marek Mróz<sup>3</sup>

<sup>1</sup> Centre Tecnològic de Telecomunicacions de Catalunya, Geomatics Research Unit, Av. Gauss, 7 E-08860 Castelldefels, Spain, ([mcrosetto@cttc.cat](mailto:mcrosetto@cttc.cat); [lsolari@cttc.cat](mailto:lsolari@cttc.cat))

<sup>2</sup> European Environment Agency, Kongens Nytorv 6, 1050 København, Denmark

<sup>3</sup> Institute of Geodesy and Civil Engineering, University of Warmia and Mazury in Olsztyn, 10-719 Olsztyn, Poland, ([marek.mroz@uwm.edu.pl](mailto:marek.mroz@uwm.edu.pl))

**Key words:** *deformation; monitoring; SAR; Copernicus; Europe*

### ABSTRACT

This paper describes the first results of the European Ground Motion Service (EGMS). The EGMS is part of the Copernicus Land Monitoring Service and represents a unique initiative for performing ground deformation monitoring at a European scale. This service makes use of Advanced Differential Interferometric SAR (A-DInSAR) techniques based on satellite Synthetic Aperture Radar (SAR) imagery. In particular, it exploits the Sentinel-1A/B SAR images of the Copernicus Programme, acquired over Europe. The paper briefly summarizes the main characteristics of the EGMS, describing different products of this Service. Then it presents some case studies extracted from the EGMS products. Examples of natural and human-induced geohazards are described.

### I. INTRODUCTION

The Differential Interferometric SAR (DInSAR) technique exploits at least two SAR images acquired over the same area in different times to derive the interferometric phase, *i.e.* the difference of the phases contained in the two SAR images. The interferometric phase contains two components: one is related to the topography of the observed scene and the other one to the ground deformation occurred between the two image acquisition times. In DInSAR, the first component is usually removed using a Digital Elevation Model of the scene. In the last three decades DInSAR has been successfully used in several fields, especially in geophysics (seismology, volcanology, and glaciology) landslide, ground subsidence and uplift, etc. Several examples of DInSAR applications are reviewed in Massonnet and Feigl (1998) and Hanssen (2001).

Compared to classical DInSAR techniques, the A-DInSAR techniques provide advanced monitoring capabilities. This is achieved by exploiting large stacks of SAR images acquired over the same area, and by using of advanced data processing, modelling and analysis tools (Crosetto *et al.*, 2016).

In the last decade, three different facts have remarkably increased the potential of the A-DInSAR techniques. The first fact is the improvement and reliability of the A-DInSAR data processing and analysis tools. The second fact is the availability of several SAR satellite missions. In the context of this paper, the most important SAR data sources are the twin satellites Sentinel-1A and Sentinel-1B. Finally, the third fact is the substantial boost in the data processing capabilities. Thanks to these facts, now the monitoring over wide

areas (*e.g.* country wise or beyond) is technically feasible.

This is exploited in the European Ground Motion Service, which is focused on deformation monitoring at European scale (Crosetto *et al.*, 2020). This is a new service, which is part of the Copernicus Land Monitoring Service managed by the European Environment Agency (EEA). The EGMS is based on A-DInSAR techniques.

This paper briefly describes the main characteristics of the European Ground Motion Service. A more in-depth description of the EGMS can be found in Crosetto *et al.* (2020). The second part of the paper presents some case studies based on the EGMS products. This includes examples of natural and human-induced geohazards.

### II. THE EUROPEAN GROUND MOTION SERVICE

In the last years, the interest to implement wide area A-DInSAR deformation monitoring services over wide areas has increased. As mentioned earlier, the wide area monitoring is technically feasible. This has been already demonstrated in several international initiatives. Costantini *et al.* (2017) describe a Ground Motion Service (GMS) covering Italy; the service was based on ERS 1/2, ENVISAT and COSMO-SkyMed SAR images. In 2018, this was followed by Norway, with a GMS based on Sentinel-1 data. Germany launched its GMS at the end of 2019 (Kalia *et al.*, 2020). In Italy, the GMS have been implemented at regional level, *e.g.* see Del Soldato *et al.* (2019). Other initiatives are already operational, *e.g.* in Denmark and The Netherlands. Other countries are discussing the need for such services.

Taking advantage of the different GMS initiatives, a much more ambitious Service is now under implementations: the EGMS. It is part of the Copernicus Land Monitoring Service, and it is implemented by the European Environment Agency. The main features of EGMS are stated in the EGMS White Paper (EGMS Task Force, 2017). A more detailed definition of the Service is described in Larsen *et al.* (2020).

According to the White Paper, the EGMS must provide consistent, updated, standardized, harmonized across national borders and reliable information regarding natural and anthropogenic ground motion phenomena over Europe.

The products will be disseminated using a dedicated web platform. It is important to underline that the EGMS products will be free and open for everybody, following the Copernicus data policy. There will be a dedicated viewer and download interface for experienced and inexperienced users.

The ground motion is estimated using full resolution Sentinel-1 SAR and exploiting both ascending and descending passes. The EGMS covers most of Europe, including all the Copernicus Participating States. The Service includes two types of monitoring. The first one covers the period from 2015 up to the end of 2020. This is the so-called baseline product. The baseline product will be published in Q1 of 2022. For this product, on average 260 SAR scenes will be available. However, for the regions affected by seasonal snow cover, the processing will be limited to the snow-free scenes. Especially in North Europe this represents an important reduction of the available scenes. The baseline product will be followed by a series of updates, which will be delivered yearly.

The production of the baseline product is ongoing. It is carried out by a consortium ORIGINAL, “OpeRational Ground motion INsar ALLiance”. This consortium includes four companies specialized in A-DInSAR (e-GEOS, TRE Altamira, NORCE, and GAF). Europe has been divided in four main areas. Each company processes one of these areas making use of its own A-DInSAR processing chain. There will be overlaps between the different areas that will be used to ensure seamless harmonization between the products.

The Service will deliver three types of products, which are briefly outlined below.

The first product type is called *Basic Product* or Level 2a. It is the classical A-DInSAR product, which includes deformation velocity and deformation time series. This will be delivered following the geometry of the frames of the Sentinel-1 scenes. All Europe is covered by approximately 750 Sentinel-1 scenes. The Basic Product will be generated using the Sentinel-1 imagery at full SAR resolution (approximately 4 by 14 m). The deformation estimates will be provided in the so-called Line-of-Sight direction (LoS), which is the line that connects the satellite and the given point on the ground. The deformations of the Basic Product will be

relative measurements that are referred to a reference point for each scene.

The second product is the so-called *Calibrated Product* or Level 2b. This is a more elaborated product, which requires as input the A-DInSAR data and data from a wide network of GNSS stations that cover the entire area of interest. In this case, the frames of the Basic Product are mosaicked to generate a seamless product, and then are adjusted to the GNSS data. In this way, the high spatial frequency deformation components come from A-DInSAR and the low spatial frequencies from GNSS. The deformation velocities and deformation time series of the Calibrated Product will be in the LoS direction. It is worth noting that the density of GNSS stations over Europe is not uniform. A 50 km grid velocity model, derived from GNSS information, is used to calibrate the LoS velocities.

The third product is the so-called *Ortho Product* or Level 3. This is the most elaborated product of the Service. The previous two products provide a mono-dimensional deformation, which refer to the LoS direction. This product provides a more complete information of the deformation: 2D deformation components. These are the horizontal East-West component, and the Up-Down vertical component. In order to derive the two components of the deformation, each location (*i.e.* grid cell) on the ground is required to have two deformation measurements, one coming from the so-called ascending dataset, and the other one coming from the descending dataset. The Ortho Product is generated at a coarser resolution: 100 by 100 m. It is worth noting that for all locations where only one observation is available, this product will not provide information.

Quality is an important aspect of the Service. This is key to guarantee an acceptability of the deformation products, especially to open new application fields, and to ensure a good product exploitation. Appropriate internal quality control procedures are implemented in the production process. In addition, an independent validation team will perform a comprehensive validation of the EGMS products.

The EGMS aims at expanding the current range of ground motion-based applications. A non-exhaustive list of possible users includes the academic centres; the geological, geophysical, and geodetic surveys; civil protection authorities; public authorities (at European, national, regional, and municipal levels); road and railway administrations; water management authorities; mining industry; oil and gas industry; engineering companies; cultural heritage institutions; insurance industry; and the citizens in general. This implies that the EGMS results must be easily accessed. In order to facilitate the exploitation of the products, the Service will provide tools for visualization and interactive data exploration. In addition, different types of guidelines and other supporting material will be published. The user uptake will be supported by

organizing workshops, webinars and user training sessions.

### III. EXAMPLES FROM EGMS

This section presents some case studies extracted from the EGMS products. Natural and human-induced geohazards are presented below.

Note that the interferometric data shown in this section are to be considered as demonstrational. At the moment of writing this paper, the production of the EGMS is still ongoing. For this reason, only the Basic products are shown below.

#### A. Subsidence (water exploitation)

Subsidence in urban areas where water is exploited for agricultural and industrial purposes is one of the most classical targets for satellite interferometry.

Figure 1 shows the EGMS Basic product in the Firenze-Prato-Pistoia Basin (Tuscany, Italy). This is an intermontane sedimentary basin with an extension of approx. 824 km<sup>2</sup>. The Basin hosts a complex and multi-layered aquifer system which is constantly stressed by the high demand of water for industrial and, mainly, agricultural activities (Ceccatelli *et al.*, 2021). In addition to water resource depletion, ground subsidence is a direct consequence.

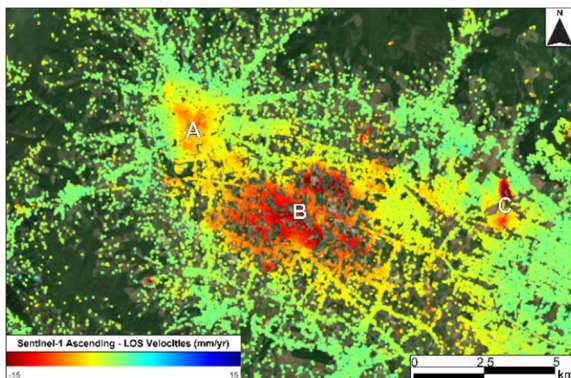


Figure 1. Subsidence in the Firenze-Prato-Pistoia Basin (Tuscany, Italy). A, Pistoia historic city centre; B, Bottegone area; C, Montemurlo. EGMS Basic product.

Because of the high population density, there is a high demand for ground motion measurements to estimate the effect of water exploitation. The Basin has already been the target of satellite interferometric analyses in the early days of the technique (Colombo *et al.*, 2003). Nowadays, using different SAR datasets and the Sentinel-1 data allow us to build up an almost 30 years long time series.

The results shown in Figure 1 offer a recent snapshot of ground subsidence in the Firenze-Prato-Pistoia Basin. Sentinel-1 data are acquired in ascending orbit and cover the period February 2015 – December 2020. Two-hundred and ninety-four images compose the interferometric stack. Velocities are calculated along the LoS of the sensor. A general lowering in the order of 2-3 mm/yr is registered through the Basin, but 3 areas

show an evident increase of LoS velocities (letters A, B and C in Figure 1).

The first area is Pistoia (letter A in Figure 1) and its historic city centre. This area did not record any relevant ground motion in the last 20 years, whereas, from 2015, LoS velocities increased up to -10 mm/yr. Time series show a linear displacement increase until June 2018 when the motion stabilized. On average, subsidence in the city centre is estimated in -6 mm/yr. The real cause of this unexpected phenomenon is yet to be found, although a link to ground water extraction in the outer parts of the city has been hypothesized (Ceccatelli *et al.*, 2021).

Letter B in Figure 1 refers to the Bottegone area. Here, the effect of water exploitation for plant nursery activities is well known and has been investigated since the ERS 1/2 era (Colombo *et al.*, 2003). Although some efforts have been made in the last years to reduce the amount of water exploited, Sentinel-1 data confirm the presence of a wide subsidence bowl in this area. Subsidence rates are on average equal to -10 mm/yr and reach a minimum of -22 mm/yr in the northern part of the bowl. Time series show a constant displacement rate with variations related to the seasonal demand of water.

The third area is smaller in size, but the subsidence rates are the highest in the entire basin (letter C in Figure 1). In fact, this small subsidence bowl reaches maximum subsidence rates of ~-40 mm/yr and an average value of ~-20 mm/yr. Time series show an abrupt trend change in July 2017 when the time series passes from the pure stability to an exponential acceleration. The phenomenon was promptly investigated following a regional procedure (Del Soldato *et al.*, 2019). It was possible to link the ground motion acceleration with an unauthorized over-pumping of water for textile production.

#### B. Subsidence (mining)

Ground motion induced by subsurface or surface mining is another usual application of multi-temporal satellite interferometry.

Figure 2 presents the EMGS Basic product in the surroundings of the Hambach open pit mine (North Rhine-Westphalia, Germany). The lignite extraction begun in 1978 and created a depression of ~50 km<sup>2</sup>, almost 500 m deep. The mine has an obvious environmental impact with deforestation and the destruction of biodiversity. Moreover, the groundwater circulation is altered by the presence of the mine. The water level must be maintained low enough to guarantee the excavation; thus, subsidence is triggered in the surroundings of the mine.

The EGMS data in Figure 2 allow delimitating the extension of the subsidence area (roughly 600 km<sup>2</sup>). The deformation map is derived from 286 Sentinel-1 images acquired in descending orbit. Velocities are referred to the LoS of the sensor. Two major cities (Düren and

Kerpen – few kilometres south of the mine) are located in the moving area. Subsidence rates can reach -60 to -70 mm/yr in the proximity of the mine. The first 10 km around the mine record an average subsidence rate of ~-20 mm/yr. Time series show a linear deformation without big seasonal variations.

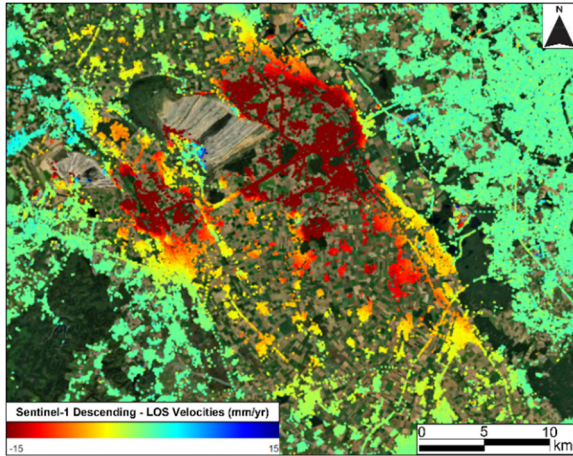


Figure 2. Subsidence in the surroundings of the Hambach mine (North Rhine-Westphalia, Germany). EGMS Basic product.

It is important to notice that the measurement point density falls off in the active mining area because of the decorrelation due to the frequent surface changes induced by the excavation of new coal levels (Crosetto *et al.*, 2020).

### C. Landslides

The use of satellite interferometric dataset for monitoring and mapping landslides is nowadays an everyday practice for a lot of research groups and end users. These data are a huge support for landslide risk management, especially where the terrain conditions do not allow on site surveys and ground measurements.

Figure 3 shows the EGMS Basic product in one of the headlines that characterizes the coast of Granada, between Motril and Malaga. From a geological point of view, the headline of Punta de la Mona is located along a cataclastic zone with graphite schists, quartzites and blocks of marbles. Karstic processes affect the area. Thus, this is an area intrinsically unstable and commonly affected by rockfalls (Notti *et al.*, 2015).

Punta de la Mona, as the whole coast of Granada, went through a widespread and sometimes uncontrolled urban development in the 90 s. The whole Marina del Este resort (letter B in Figure 3) was built on top of a complex landslide (Notti *et al.*, 2015). The motion of this landslide, seasonally accelerated by heavy rainfalls, severely damaged some of the buildings part of the resort (Notti *et al.*, 2015).

The EGMS Basic product confirms the motion of the Marina del Este landslide (letter B in Figure 3), but also allow the detection of another phenomenon on the western side of the headline (letter A in Figure 3). The motion of this landslide was not detected by previous

authors that analysed ENVISAT images (Notti *et al.*, 2015; Galve *et al.*, 2017).

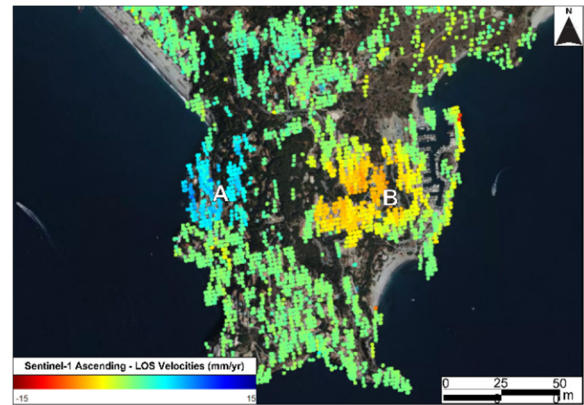


Figure 3. Landslides in the headland of Punta de la Mona in the municipality of Almuñécar (Granada, Spain). A, East landslide – Marina del Este; B, West landslide – Urbanización Punta de la Mona. EGMS Basic product.

The deformation map of Figure 3 is derived from 305 Sentinel-1 images acquired in ascending orbit. Velocities are calculated along the LoS of the sensor. Figure 3 is a self-explanatory representation of the role of LoS wrt slope orientation. The west landslide (letter A in Figure 2) records an average LoS velocity of 4 mm/yr, with a peak of 7 mm/yr in correspondence of the landslide foot. LoS velocities have a positive sign coherent with a motion towards the sensor, along the west-looking slope. The east landslide (letter B in Figure 3) records an average LoS velocity of -5 mm/yr, with a peak of -7.5 mm/yr in the central portion of the slope. LoS velocities have a negative sign coherent with a motion away from the sensor, along the east-looking slope. The dataset derived from descending orbit images will show the opposite situation, with negative velocities along the western flank and positive velocities registered along the eastern flank. Time series of deformation show a linear rate with only minor seasonal variations; the eastern landslides record a small deceleration after the second half of 2019.

Another example of EGMS Basic product used for landslide mapping is presented in Figure 4. The landslide is a deep-seated gravitational slope deformation (DSGSD), *i.e.* a flank scale landslide whose main sliding surface is hundred meters deep, located in the municipality of Emarese of the Valle d'Aosta Region (Italy). The landslide involves the entire mountain flank of the Tete de Comagne from an altitude of ~1800 m.a.s.l to the valley bottom. The boundary of the landslide, defined through photointerpretation aided by interferometric data, is known and it is part of the regional landslide catalogue (Solari *et al.*, 2020).

As many DSGSD, the Emarese DSGSD has a main large landslide body with several more superficial complex landslides. Thus, it is subdivided in sectors with different velocities and behaviours. This is confirmed by the distribution of LoS velocities in Figure 4. The deformation map is derived from Sentinel-1 images



acquired in descending orbit; 294 images compose the time series of deformation. The whole landslide body records an average LoS velocity of  $-6$  mm/yr. High velocity sectors reach LoS velocities from  $-10$  to  $-20$  mm/yr. The velocity sign is coherent with a movement away from the sensor and along the slope direction. It is worth noting that the point density on the landslide body is uneven due to the vegetation coverage of the mountain flank. This is an unsolvable issue, especially using X- and C-band imagery. Nonetheless, more than 3500 moving points are found within the landslide area, making it possible to quantify the general motion of the landslide.

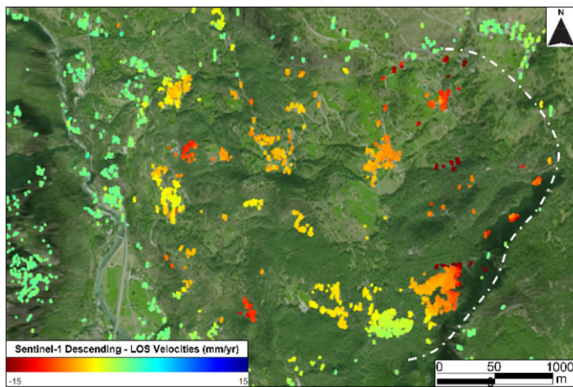


Figure 4. Deep seated gravitational slope deformation in the municipality of Emarese (Valle d'Aosta, Italy). EGMS Basic product.

#### D. Exploitation of geothermal reservoirs

The exploration and exploitation of geothermal reservoirs for power production has some environmental drawbacks such as air and water pollution, seismicity, and ground subsidence. The latter can be easily detected by satellite interferometry.

Figure 5 shows the EGMS Basic product in the Larderello geothermal field (Tuscany, Italy). Larderello is the oldest geothermal power plant in the world; the activity started in early 1900s. Nowadays, 34 power plants produce roughly 30% of the regional electricity demand. The geothermal reservoir reach temperatures of  $200^{\circ}\text{C}$  to  $350^{\circ}\text{C}$  at a depth between 400 and 3500 m and it is hosted by carbonate and metamorphic formations (Bertini *et al.*, 2005).

Previous investigations based on ERS 1/2 and Envisat data revealed the presence of a large subsidence bowl with maximum subsidence rates of  $\sim -30$  mm/yr (Solari *et al.*, 2018). This is confirmed by the EGMS data in Figure 5. Sentinel-1 data acquired in ascending orbit (295 images) allow us to draw the contour of a subsidence area which extends for roughly 12 km in the NE-SW direction (Larderello-Lagoni Rossi axis) and for 10 km in the SE-NW direction (Sasso Pisano-Serrazzano axis). Subsidence rates are on average equal to  $-8$  mm/yr with a maximum of  $-25$  mm/yr in the centre of the valley.

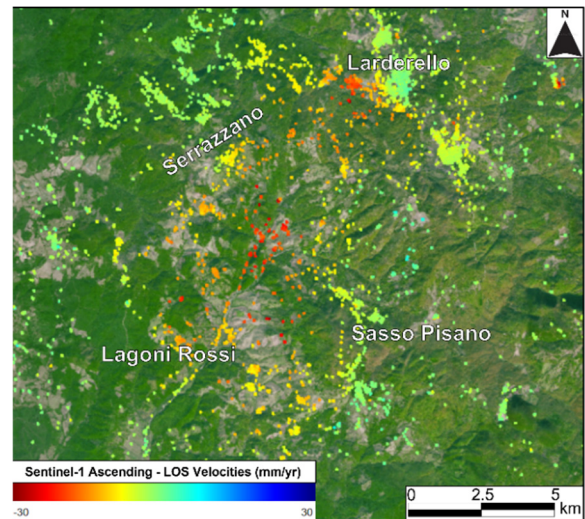


Figure 5. Ground motion in the Larderello geothermal field (Tuscany, Italy). EGMS Basic product.

#### E. Infrastructures

The EGMS is designed to target wide-area deformation; nonetheless, its data can also be used to detect localized motion affecting single infrastructures. Note that the EGMS is not intended for full structural analyses; rather, it provides a useful starting point for further studies, which can rely on *e.g.* X-band interferometric products or other types of in-situ data.

Figure 6 presents the EGMS Basic product in the fishing village of Thyborøn (Midtjylland, Denmark). The detection of ground motion in coastal areas of Denmark is particularly relevant due to the increasing impact of storm surges on the coastal communities. Thyborøn with a land elevation of 1 to 2.5 m is one of these highly vulnerable to flooding areas. By the geological point of view, the village is built on top of a sequence of marine sand and clay with landfill on top (Sørensen *et al.*, 2016).

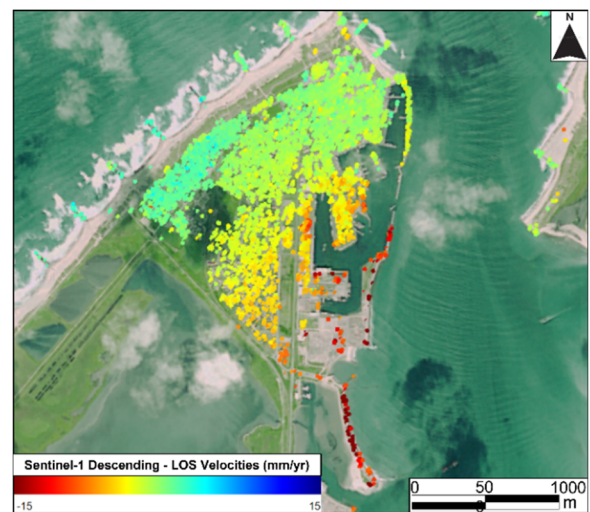


Figure 6. Ground motion in the Thyborøn harbour (Midtjylland, Denmark). EGMS Basic product.

Thanks to the EGMS data, it is possible to characterize the ongoing deformation in the Thyborøn harbour. The deformation map in Figure 6 is derived from 259 Sentinel-1 images in descending orbit. Velocities are referred to the LoS of the sensor. The deformation map depicts a clear pattern of velocity increase from west to the east. Maximum subsidence rates, up to -15 to -20 mm/yr, are recorded in correspondence of the harbour docks and of the internal breakwaters. EGMS data can capture the deformation of single buildings and of linear structures as the breakwaters.

The velocity pattern recorded in Thyborøn is connected to a geological factor, *i.e.* the increase of the landfill thickness in the harbour area, and to an anthropogenic factor, *i.e.* the age of the structures wrt consolidation processes (Sørensen *et al.*, 2016).

#### IV. CONCLUSIONS

In this paper, the main characteristics of the EGMS have been presented. The examples presented in the second part of the paper illustrate the potential of the EGMS. It is worth recalling that they only concern the first type of products, the Basic Product. Further examples will be published soon.

#### V. ACKNOWLEDGEMENTS

This work is part of the Spanish Grant SARAI, PID2020-116540RB-C21, funded by MCIN/AEI/ 10.13039/501100011033. This work has also been partially funded by the European Environment Agency through the project “Copernicus European Ground Motion Service – Supporting Services” (Project n° 3436/RO-COPERNICUS/EEA.57704).

#### References

- Bertini, G., Cappelletti, G., and Fiordelisi, A. (2005). Characteristics of geothermal fields in Italy. *G. Geologia Appl.*, 1, pp. 247-254.
- Ceccatelli, M., Del Soldato, M., Solari, L., Fanti, R., Mannori, G., and Castelli, F. (2021). Numerical modelling of land subsidence related to groundwater withdrawal in the Firenze-Prato-Pistoia basin (central Italy). *Hydrogeology Journal*, 29(2), pp. 629-649.
- Colombo, D., Farina, P., Moretti, S., Nico, G., and Prati, C. (2003). Land subsidence in the Firenze-Prato-Pistoia basin measured by means of spaceborne SAR interferometry. *Proc. IGARSS 2003*. Vol. 4, pp. 2927-2929.
- Costantini, M., Ferretti, A., Minati, F., Falco, S., Trillo, F., Colombo, D., and Costabile, S (2017). Analysis of surface deformations over the whole Italian territory by interferometric processing of ERS, Envisat and COSMO-SkyMed radar data. *Remote Sensing of Environment*, 202, pp. 250-275.
- Crosetto, M., Monserrat, O., Cuevas-González, M. Devanthery, N., and Crippa, B. (2016). Persistent Scatterer Interferometry: a review. *ISPRS Journal of Photogrammetry and Remote Sensing*, 115, pp. 78-89.
- Crosetto, M., Solari, L., Mróz, M., Balasis-Levinsen, J., Casagli, N., Frei, M., and Andersen, H. S. (2020). The evolution of wide-area DInSAR: From regional and national services to the European Ground Motion Service. *Remote Sensing*, 12(12), 2043.
- Del Soldato, M., Solari, L., Raspini, F., Bianchini, S., Ciampalini, A., Montalti, R., and Casagli, N. (2019). Monitoring ground instabilities using SAR satellite data: A practical approach. *ISPRS Int. J. of Geo-Information*, 8(7), 307.
- EGMS Task Force (2017). Available in: <https://land.copernicus.eu/user-corner/technical-library/egms-white-paper>.
- Galve, J. P., Pérez-Peña, J. V., Azañón, J. M., Closson, D., Caló, F., Reyes-Carmona, C. and Bally, P. (2017). Evaluation of the SBAS InSAR service of the European Space Agency's Geohazard Exploitation Platform (GEP). *Remote Sensing*, 9(12), 1291.
- Hanssen, R. (2001). Radar interferometry. *Kluwer Academic Publishers*, Dordrecht (The Netherlands).
- Kalia, A.C., Frei, M., and Lege, T. (2017). A Copernicus downstream-service for the nationwide monitoring of surface displacements in Germany. *Rem Sen Env*, 202, pp.234-249.
- Larsen, Y., Marinkovic, P., Dehls, J.F., Bredal, M., Bishop, C., Jøkulsson, G., and Vøge, M. (2020). European Ground Motion Service: Service Implementation. Copernicus Land Monitoring Service report. Available in: <https://land.copernicus.eu/user-corner/technical-library/egms-specification-and-implementation-plan>.
- Massonnet, D., and Feigl, K.L. (1998). Radar interferometry and its application to changes in the Earth's surface. *Reviews of Geophysics*. 36(4), 441-500.
- Notti, D., Galve, J. P., Mateos, R. M., Monserrat, O., Lamas-Fernández, F., Fernández-Chacón, F., and Azañón, J. M. (2015). Human-induced coastal landslide reactivation. Monitoring by PSInSAR techniques and urban damage survey (SE Spain). *Landslides*, 12(5), pp. 1007-1014.
- Solari, L., Del Soldato, M., Bianchini, S., Ciampalini, A., Ezquerro, P., Montalti, R., Raspini, F., and Moretti, S. (2018). From ERS 1/2 to Sentinel-1: subsidence monitoring in Italy in the last two decades. *Frontiers in Earth Science*, 6, 149.
- Solari, L., Bianchini, S., Franceschini, R., Barra, A., Monserrat, O., Thuegaz, P., and Catani, F. (2020). Satellite interferometric data for landslide intensity evaluation in mountainous regions. *Int J. of Applied Earth Observation and Geoinformation*, 87, 102028.
- Sørensen, C., Broge, N. H., Mølgaard, M. R., Levinsen, J. F., Okkels, N., and Knudsen, P. (2016). Advancing Coastal Climate Adaptation in Denmark by Land Subsidence Mapping using Sentinel-1 Satellite Imagery. *Geoforum Perspektiv*, 15(28), 46-59.

## Selected aspects of geometrical analyses of surfaces measured using terrestrial laser scanning (TLS)

Janina Zaczek-Peplinska, Maria Elżbieta Kowalska, Krystian Ryczko, Cezary Sekular

Faculty of Geodesy and Cartography, Warsaw University of Technology, Politechniki Square 1, 00-661 Warsaw, Poland, ([janina.peplinska@pw.edu.pl](mailto:janina.peplinska@pw.edu.pl); [maria.kowalska@pw.edu.pl](mailto:maria.kowalska@pw.edu.pl); [krystian.ryczko.stud@pw.edu.pl](mailto:krystian.ryczko.stud@pw.edu.pl); [cezary.sekular.stud@pw.edu.pl](mailto:cezary.sekular.stud@pw.edu.pl))

**Key words:** *terrestrial laser scanning; surface roughness parameters; deformations; surface monitoring; expansion of a cylindrical space to a plane; control surveys*

### ABSTRACT

Modern measurement technologies are widely used for the monitoring and determination of surface deformations. One more frequently used measurement technology is terrestrial laser scanning (TLS), which provides quasi-continuous information about the tested surface in the form of a point cloud at a given resolution. At the same time, TLS is based on measuring the distance in a given direction, thanks to which we can obtain a high precision of measurement, often compared to tacheometric measurements. This paper presents a study on the determination of surface flatness parameters extracted from a point cloud. It takes into account the roughness characteristics of the different structures on the measured surfaces and analyzes them using the most popular algorithms for determining the distance of points from the reference surface. Additionally, the review presents the issue of expanding selected surfaces onto a plane to analyze their geometric parameters, and thus to determine the deformation. The applied solution can be used to monitor the deformation of objects such as tunnels and interiors of collectors or large-diameter downpipes, the shape of which is similar to a cylinder surface. Thanks to the expansion of the cylinder surface into a plane, it is possible to perform a comprehensive analysis of surface deformation, and not only selected fragments in the form of sections. The conducted analyses show the great potential of data obtained using terrestrial laser scanning, when an appropriate procedure and data processing method are applied. This paper focuses on two types of studies; the study of surface flatness and analysis of the deformation of cylindrical surfaces. These types of studies are extremely useful in assessing the technical condition of structures, especially in studying the deformation of structures built underground (tunnels, passages, warehouses), where the loads from the surrounding earth are significant.

### I. INTRODUCTION

#### A. Terrestrial Laser Scanning

The main purpose of the research presented in the paper is to indicate the possible use of the terrestrial laser scanning in assessing the condition of structures, especially deformations in underground structures (tunnels, passages, warehouses) with significant loads from the surrounding ground. This article presents generally available tools thanks to which it will be possible to widely use the proposed solutions in commercial analyses of deformations in engineering objects. Terrestrial laser scanning (TLS) technology is widely used for the monitoring and determination of surface deformations (Harmening *et al.*, 2021; Yang *et al.*, 2021; Gawronek *et al.*, 2019; Kovanič *et al.*, 2019; Liu *et al.*, 2020). It provides quasi-continuous information about the surveyed surface in the form of a point cloud with  $X, Y, Z$  coordinates, complemented by the reflection intensity. Terrestrial laser scanning is based on the measurement of distance in a specified direction and gives high precision measurements comparable to tacheometric measurements. It makes it

possible to monitor a greater number of points on surfaces and from practically any place, provided that an appropriate point cloud resolution is maintained. For the assessment of deformations of the surface of a structure, the scanning resolution is selected based on the geometry of the surveyed structure, the measurement plan and the expected deviations from the norm.

#### B. TLS data quality

Terrestrial laser scanning, like any other measurement technology, is subject to a variety of measurement errors. Many publications have detailed the significance of appropriate calibration of terrestrial laser scanners (Medić *et al.*, 2020; Reshetyuk, 2006; Abbas *et al.*, 2013; Li *et al.*, 2018), while equipment manufacturers use increasingly advanced technical solutions and algorithms to improve the accuracy of the acquired data. While the problem of external errors still remains, they have an influence that is difficult to model and which greatly affect the accuracy of the geometric data and recorded spectral values. Knowledge of the factors that affect the quality of TLS

data, such as systematic and random errors, is crucial in performing reliable analyses. Wang *et al.* (2016) introduced some mathematical modeling of external errors and how it can be applied in real TLS measurements. Their results revealed an up to 50% increase in point cloud accuracy; however, the authors emphasize that this remains difficult and is still an unsolved issue. Errors affecting the quality of TLS data can be divided by their various factors. For example, Kashani *et al.* (2015) divided them into four main categories: (i) target surface characteristics (reflectivity and roughness), (ii) data acquisition geometry (range and incidence angle), (iii) instrumentation effects, and (iv) environmental influences.

The occurrence of the various types of errors in measurements has a direct impact on the quality of the analyses performed with the point clouds and requires an appropriate methodology. This paper focuses on two types of studies: the study of surface flatness and analysis of the deformation of cylindrical surfaces. These types of studies are extremely useful in assessing the technical condition of structures, especially in studying the deformation of structures built underground (tunnels, passages, warehouses), where the loads from the surrounding earth are significant.

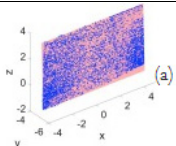
## II. MATERIALS AND METHODS

### A. Surface flatness test

The first issue addressed in this paper is the study of surface flatness. This task is performed in the context of many engineering structures, a classic example being large floor areas of facilities or high storage warehouses, which must meet increasingly demanding flatness criteria. The situation is analogous to the context of road surfaces, squares and other engineering structures which are subject to inspections checking their compliance with design requirements or standards (Wyczałek *et al.*, 2017). Therefore, it is safe to say that the quality control of flatness is essential in construction. There is a growing need to propose an automated and rapid approach for flatness quality assessment to replace the tedious traditional manual measurement methods (Li *et al.*, 2020), hence the increasing use of terrestrial laser scanning for this task, allowing the registration of millions of survey points in a very short time. The study of surface flatness based on a point cloud can be implemented in two ways. In the first variant, the plane is fitted to the measured points, *e.g.* by the method of least squares. This solution is connected with the problem of selection of measured points that actually represent the flat surface and are not measurement noise or were not measured in the places of surface deformation. The second variant is testing flatness of the surface by comparing it with a theoretical model, but in this case it is necessary to provide a common orientation for the measured surface and its model.

Reliably fitting a plane to a point cloud requires an assessment of the accuracy of the fit. Table 1 summarizes the equations used to fit the plane (Ye *et al.*, 2018).

Table 1. Parameters for fitting a plane to a point cloud (Ye *et al.*, 2018)

	Plane fit
Diagram	
Equation (vector form)	$(\mathbf{p}-\mathbf{p}_0) \cdot \mathbf{n}=0$ , where $\mathbf{n}=(n_x,n_y,n_z)$ is the normal vector of the plane, $\mathbf{p}_0=(x_0,y_0,z_0)$ is a point on the plane, and $\mathbf{p}=(x,y,z)$ is a point in the point cloud
Equation (Cartesian form)	$Ax+By+Cz+D=0$

Evaluation of the accuracy and quality of the fit can be made based on the global plane fitting error -  $e_a$  (Eq. 1) (Qian and Ye, 2014). For an extracted plane containing M data points, the plane-fitting error is given by:

$$e_a = \sqrt{\frac{\sum_{i=1}^M d_i^2}{M}} \quad (1)$$

where  $d_i$  = the distance from the  $i^{th}$  data point to the plane

One publication (Ye *et al.*, 2018) also proposes evaluating the accuracy of the plane fit based on the formula for the distance of a point from the plane (Eq. 2).

$$e = \frac{Ax_i + By_i + Cz_i + D}{\sqrt{A^2 + B^2 + C^2}} \quad (2)$$

where  $e$  = point position error  
 $A, B, C, D$  = parameters of the plane equation in Cartesian notation  
 $x_i, y_i, z_i$  = point in the point cloud

It should be noted that when fitting a plane to a point cloud using the least squares method, we minimize the distances of the points from the surface, and thus the question arises whether such a fitted plane is an appropriate basis for evaluating the surface flatness. A solution to this dilemma could be to select points (randomly or a certain percentage) to represent the surface and use these to fit a reference plane (Ye *et al.*, 2018). However, this raises another question of which criteria should be used to select these points. A solution may be in selection of the areas of the surface for which, with a high probability based on analysis of the design and the results of archival measurements (if

performed), there are no deformations, *e.g.* in the vicinity of contact with other surfaces, in places where the structure is stiffened by additional supports, etc.

A second very important aspect in the context of analysis of surface flatness is surface roughness, which will affect both the accuracy of fitting the plane to the cloud and the determination of local deformations.

The classification of surface roughness according to Eurocode 2 distinguishes three types of surface: very smooth, smooth and rough. This classification is distinctly inexact as it depends on the subjective estimation of the designer. Selection of the most relevant 3D roughness parameters is a key issue (Muszyński and Wyjadłowski, 2020). The most popular parameters that determine the surface roughness, written in a mathematical way, are summarized in Table 2.

Table 2. Selected surface roughness parameters (Eurocode 2)

Parameter	Equation
Root-mean-square height	$S_q = \sqrt{\frac{1}{A} \iint_A (Z(x, y))^2 dx dy}$
Maximum peak height	$S_p = \sup\{Z(x_i, y_i)\}$
Maximum pit height	$S_v =  \inf\{Z(x_i, y_i)\} $
Maximum height	$S_z = S_p + S_v$

It is worth noting that these parameters are determined with respect to a line or mean surface, which again leaves room for discussion in the context of fitting a plane to a point cloud and their use in the context of determining the parameters of that plane. In the next part of the article we will try to deal with these problems.

Surface flatness testing is also applied in quality inspection and acceptance of a tunnel project (Xiang *et al.*, 2021), hence the second issue considered in this paper is the development of selected cylindrical surfaces into a plane.

### B. Expansion of selected surfaces to a plane

The expansion of selected surfaces into a plane is an effective method of presenting measurement results of complex objects by terrestrial laser scanner. Currently, the process of identifying individual technical elements and defining the spatial structure of the object takes place in the three-dimensional space of the point cloud, and the final elaborations are made in the form of local cross-sections. This approach makes the data analysis more difficult and reduces the potential use. In the case of large and complex structures, analyses require selecting a particular fragment of the point cloud and performing local analyses. Otherwise, the displayed point cloud is unreadable due to overlapping points in the current perspective or in the orthogonal view. The solution to this problem is to use surface expansion to a plane. This approach is used both for objects with

known geometry such as a sphere or cylinder (Xu *et al.*, 2019; Pinpin *et al.*, 2021) and for more complex objects such as telecommunication antennas (Dabrowski *et al.*, 2019). Dabrowski and Specht (2019) present the advantages of using spatial expansions:

1. Improved legibility of the measured point cloud of the object.
2. Obtaining information about the distance of the point from the object construction axis in the form of the coordinate of the projected point cloud.
3. Obtaining information about angular spatial configuration of individual elements of a measured symmetrical object.
4. Ability to create two-dimensional datasheets containing detailed geometric and descriptive information on the point cloud.

In that paper, the authors focused on the development of a cylinder surface as a shape that is representative for tunnel objects. The spatial projection of a point cloud onto the side surface of a cylinder requires the determination of three parameters. Two of them are linear parameters and the third is an angular parameter. The first is the radius of the cylinder - *R*. Evaluation of the parameter depends on the spatial structure of the point cloud and has a direct influence on the distortion distribution in the expansion. Performing the projection is possible for any non-zero value of the parameter *R*. However, the optimal choice of the cylinder radius determines the distortion distribution and directly affects the readability of the final product (Dabrowski and Specht, 2019). The second, a linear parameter, is the horizontal distance from the vertical extension axis *h*. While the angular projection parameter is  $\phi$ , the direction of point *P* is relative to the initial direction of expansion in the horizontal XY plane (Dabrowski and Specht, 2019).

The functions of the spatial projection of a point cloud to the lateral of the cylinder in matrix notation (Eq. 3) are expressed in the following formulas:

$$\begin{bmatrix} x_P^R \\ y_P^R \\ z_P^R \end{bmatrix} = \begin{bmatrix} U(x_P, y_P) \\ V(z_P) \\ W(x_P, y_P) \end{bmatrix} = \begin{bmatrix} R * \Phi(x_P, y_P) \\ z_P \\ h(x_P, y_P) \end{bmatrix} \quad (3)$$

- where  $x_P^R, y_P^R, z_P^R$  = projected (spatially expanded) point coordinates  
*U(x<sub>P</sub>, y<sub>P</sub>), V(z<sub>P</sub>), W(x<sub>P</sub>, y<sub>P</sub>)* = spatial projection functions  
*x<sub>P</sub>, y<sub>P</sub>, z<sub>P</sub>* = coordinates of the point of the original surface (point cloud)  
*R* = cylinder radius  
 $\phi(x_P, y_P)$  = direction angle of point P (angular parameter of the expansion)  
*h(x<sub>P</sub>, y<sub>P</sub>)* = point distance from the expansion axis (linear parameter of the expansion)

Developing a point cloud representing a cylindrical surface into a plane allows for many analyses and a simplified representation of the surface deformation. In the case of a deformation, we can use methods analogous to surface flatness analysis.

### C. Research Facility - Subway Tunnel

In this paper, the flat ceiling of the entrance hall and a fragment of the connecting tunnel built to connect the 1<sup>st</sup> line with the 2<sup>nd</sup> line of the Warsaw Metro were used as the test object. The analyzed tunnel runs along a curve between the hall with side tracks on the east side of the C-10 Rondo ONZ station on Line II and the hall with side tracks on the north side of the A-13 Centrum station on Line I. It has a technical function, so it does not serve regular passenger traffic. A tunnel boring machine was used to create it, and as a result it is encased in distinctive rings made of concrete. There is a concrete platform in the tunnel along the track.

## III. RESULTS

### A. Development of terrestrial laser scanning data

For the study, measurements were taken with a Leica RTC360 laser scanner, which has a scanning speed of up to 2 million points/sec, a declared scanning resolution of 3 mm, 6 mm or 12 mm at 10 m, an angular accuracy of 18", a distance measurement accuracy of 1 mm + 10 ppm, and a 3D point position accuracy of 1.9 mm (at 10 m) and 2.9 mm (at 20 m). The measurements included two components: the ceiling of the entrance hall and the connecting tunnel itself. The point cloud orientation process was performed using Leica Cyclone Register360 software. The mutual orientation of the acquired point clouds was performed on the basis of automatic detection of the object's features, while the external orientation of the entire object to the PL-2000 state space reference system was performed on the basis of known target coordinates. The accuracy of the performed point cloud orientation process is determined by the parameters: Bundle Error, Overlap, Strength, Cloud-to-Cloud and Target Error (Table 3). Each scan orientation has its own accuracy characteristics, and bundle error is a parameter that determines the accuracy of the entire combination of scans. The overlap parameter defines the percentage of overlap between each configuration. The strength parameter defines the relative stiffness of all bindings in arbitrary directions. The last parameter is cloud-to-cloud, whose value indicates the mutual fit of the point cloud geometries, thus preserving the characteristics of the measured object. The obtained point cloud orientation parameters were found to be satisfactory.

### B. Surface flatness

As already mentioned, performing a scan of horizontal elements is one of the basic issues of engineering geodesy. The effects of such

measurements are most often compared with the design and then communicated to the responsible persons, *e.g.* construction management. However, we do not always have a three-dimensional base model of the object which can serve as a reference surface for the flatness analysis. This paper presents examples of surface flatness analysis based on comparing a point cloud to a surface fitted using the least squares method. Figure 1 presents the analyzed point cloud in intensity colors recorded for the entrance hall of the connecting tunnel.

Table 3. Accuracy parameters of the conducted orientation

Parameter	Connecting tunnel
Bundle error [mm]	0.001
Overlap	60%
Strength	54%
Cloud-to-Cloud [mm]	0.001

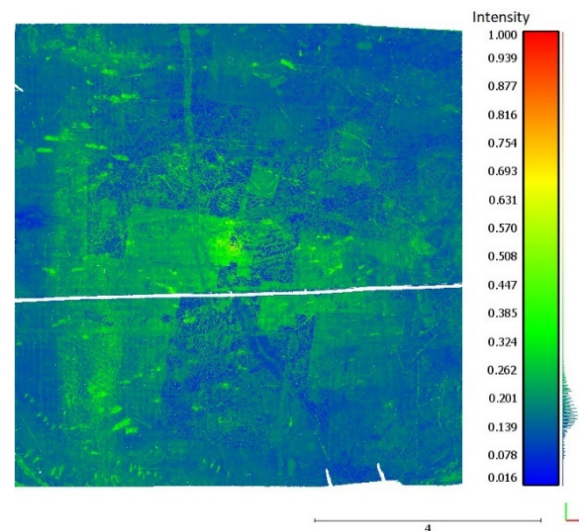


Figure 1. Point cloud representing the ceiling of the entrance hall of the connecting tunnel in intensity colors.

Based on the acquired data, the analysis was performed in two variants. The first variant involved fitting a plane to all the measured points and then determining the distance of the points from the plane using the Cloud To Mesh (C2M) algorithm (Figure 2).

For the analysis performed, the value of the global plane fitting error was determined to be  $e_{\sigma}=6.4$  mm. In the second variant, only some points were used to fit the plane. For this purpose, a frame was cut out of the basic point cloud (Figure 3) and then the plane was fitted into it. This approach was based on the assumption that the ceiling plane undergoes the least deformation at the point of contact with vertical walls (which resulted from the design).

Figure 4 presents a map of the distances of points from the plane defined in variant II, determined by the Cloud To Mesh (C2M) algorithm. The global plane fitting error value was  $e_{\sigma}=8.7$  mm.

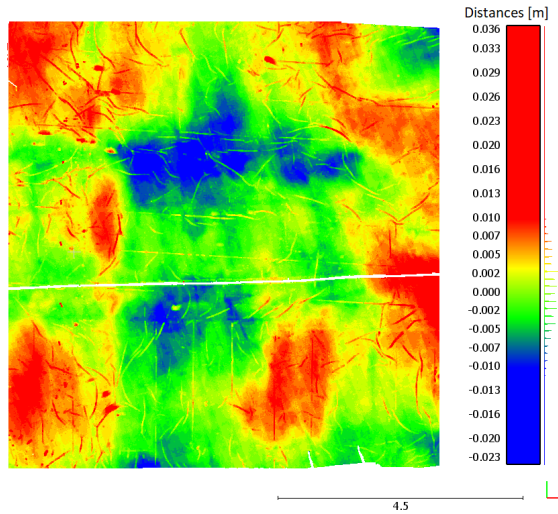


Figure 2. Cloud To Mesh (C2M) distance analysis for a section of the entrance hall ceiling using a reference plane fitted to all measured points.

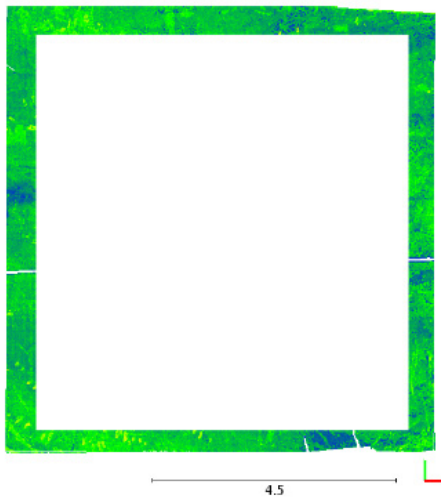


Figure 3. A set of points located at the floor-wall interface selected as the reference frame for the surface fit.

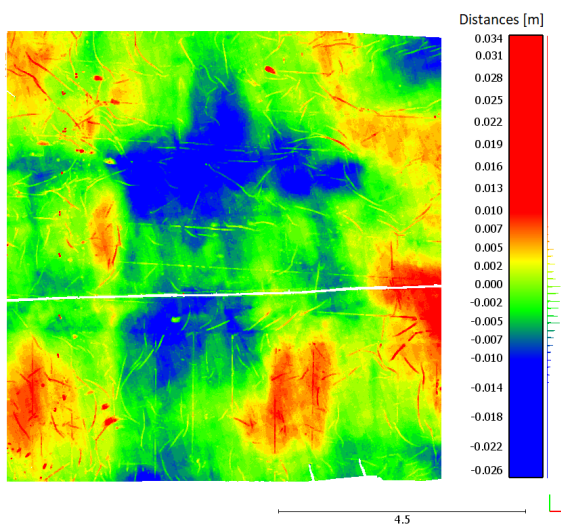


Figure 4. Cloud To Mesh (C2M) distance analysis for a section of the entrance hall ceiling using a reference plane fitted to a selected frame (Figure 3).

The comparison of distance maps determined by the C2M method for reference planes determined in two

different ways (Figure 2 and 4), as well as the analysis of histograms of C2M distances (Figure 5 and 6) for these two variants, indicate the great importance of the selection of points as the basis for determining the plane parameters. The choice of the plane directly affects the results of the comparisons, and thus the analyzed values of deviation from the flatness of the surface. In both analyzed cases, the trend of changes looks similar. Figures 2 and 4 both show two significant areas in blue where the ceiling is curved towards the floor, yet the values obtained in both cases differ. In the case of the area shown in Figure 2 most of the points are between -0.01 m and 0.01 m, while in the case of the area shown in Figure 4, the distances of the points from the reference plane are mostly between -0.02 m and 0.01 m. Figures 5 and 6 show histograms of the distribution of point distances from the plane for both variants of the plane definition.

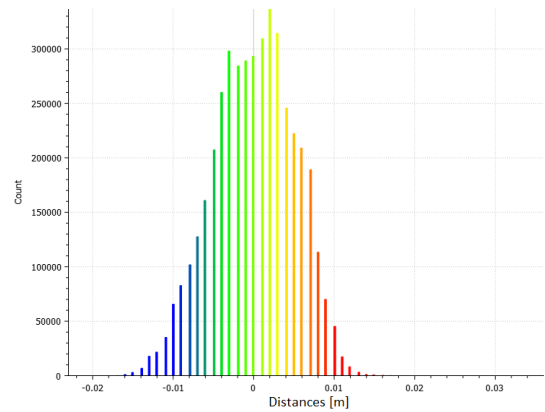


Figure 5. Cloud To Mesh (C2M) distance histogram for a section of the ceiling of the entrance hall of the connecting tunnel, using a reference plane fitted to all measured points.

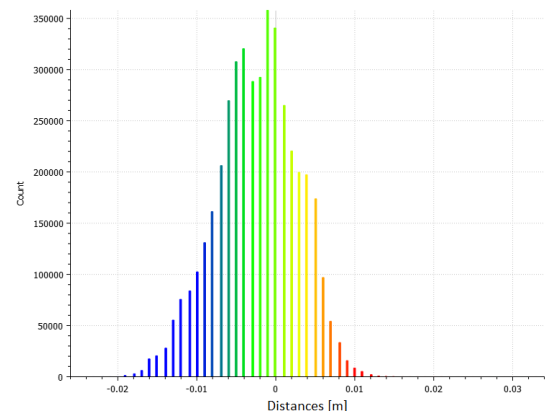


Figure 6. Cloud To Mesh (C2M) distance histogram for a section of the ceiling of the entrance hall of the connecting tunnel, using a reference plane fitted into a selected frame (Figure 3).

Table 4 lists the values of the normal vectors for the fitted planes in both variants. As can be seen, the differences are small (on the order of 1/10,000), and the values of the normal components in the Z direction indicating the horizontality of the plane are the same.

Table 4. Normal vectors of the designated planes

	Normal vector of the plane
Plane fitted to the entire point cloud	(0.00369531; 0.00127337; 0.999992)
Plane fitted to a sample frame	(0.00388479; 0.000977652; 0.999992)

Table 5 summarizes the roughness parameters determined based on the plane fitted to all points and the plane fitted to the points forming the frame in Figure 3. Based on the summarized quantities, it can be concluded that even a slight difference in the definition of the reference plane affects the determined roughness parameters.

Table 5. Roughness parameters determined based on the plane fitted to all points and the plane fitted to the points forming the frame in Figure 5

Parameter	Fitting a plane into the whole cloud [m]	Fitting a cloud into a frame [m]
Sq	0.006	0.009
Sp	0.035	0.033
Sv	0.023	0.026
Sz	0.058	0.059

In Figure 7, the authors have presented a histogram of the distribution of the Z coordinate for the investigated floor surface. The dominant value is  $Z = 78.000\text{m}$ , which indicates that it is possible to undertake a deformation analysis of the floor with respect to a horizontal plane located at a constant height of  $77.995\text{ m}$ .

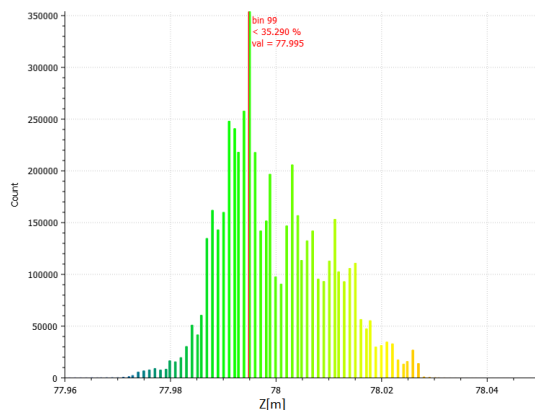


Figure 7. Histogram of the Z-coordinate distribution for the tested floor area.

The differences in the distances of the points from the horizontally defined plane at  $77.995\text{ m}$  are shown in Figure 8. The distance distribution obtained clearly indicates the slope of the floor on the left side.

The analyses of distances of points from variously defined planes show the importance of proper selection of the definition of the reference surface.

### C. Expansion of the tunnel surface into a plane

The next stage of analysis is the cylindrical fit based on the acquired point cloud. For this purpose, the function implemented in CloudCompare software was used, built on the basis of the Automatic RANSAC Shape Detection method with Schnabel's modifications (Schnabel *et al.*, 2007). The tool is composed of 5 basic parameters: the minimum number of points defining a given shape, the parameter  $e$  - the maximum distance of a point to the analyzed model, the parameter  $b$  - the resolution of the point cloud, the parameter  $a$  - the maximum deviation of the best fitted cylinder shape with respect to the normal vector (expressed in degrees), and the probability parameter (Marjasiewicz and Malej, 2014). For the above-mentioned parameters, there is no single correct value. In the case of the presented problem, the authors performed a number of tests to select the most optimal parameter values. The basic assumption of the performed tests was to obtain the best-fitting cylinder model. The criteria for the selection of the best solution was to obtain the nominal value of the radius of the tunnel casing -  $2.7\text{ m}$ , and to select the largest number of points for the fitting process. Empirically determined parameters take the following values: minimum number of points -  $500\ 000$ ,  $e = 2\text{ cm}$ ,  $b = 4\text{ cm}$ ,  $a = 25^\circ$ , overlook probability =  $3\text{ cm}$ .

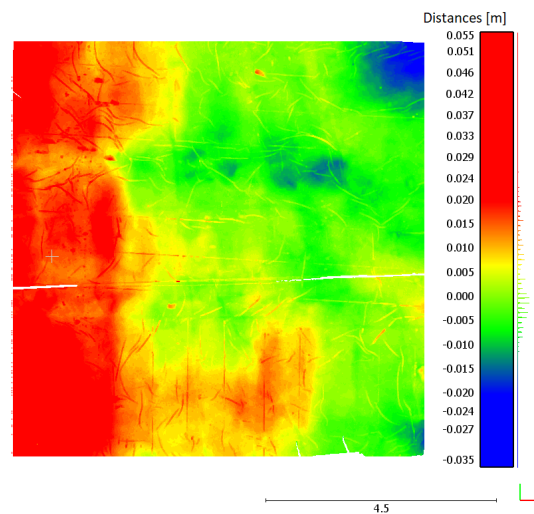


Figure 8. Analysis of the distance of points from the ordinate of  $77.995\text{ m}$  for the section of the ceiling of the entrance hall of the connecting tunnel.

Figure 9 presents the relation of the initial point cloud to the cylinder model expressed by the distance of points from the model surface (algorithm - C2M).

The values presented in the color scale in Figure 9 range from  $-5\text{ cm}$  (blue color) to  $+5\text{ cm}$  (red color). The dominant colors for the first part of the tunnel are shades of green and shades of yellow - in the range  $-2\text{ cm}$  to  $+3\text{ cm}$ . For the second fragment of the object, undulations and high color contrast resulting from the geometry of the object are visible. This results in larger differences contained in the whole span of the selected



range. Hence empty fields can be observed, which result from the fact that in these parts the distances are longer than 5 cm in absolute values. Additionally, 5 cm wide "stripes" are noticeable, representing all elements of the technical equipment of the subway tunnel, *i.e.* tracks, platforms.

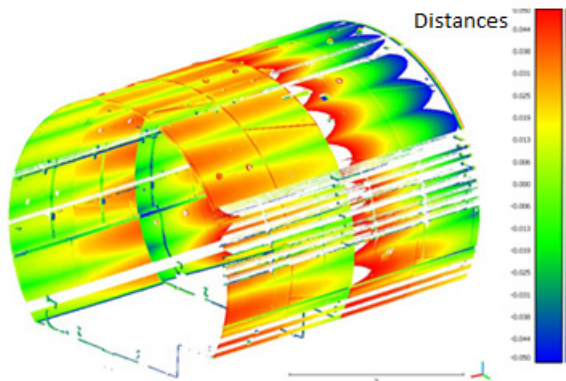


Figure 9. Relation of the initial point cloud to the cylinder model (C2M).

In the next step, the point cloud representing the tunnel fragment was expanded onto a plane. For this purpose, the unroll function in CloudCompare software was used. Its parameters included:

- Expansion type.
- The parameter that defines the figure - in the case of a cylinder, it is the radius.
- Axis - select the axis around which the expansion is performed.
- Base point - which determines the position of the selected axis in space.
- The angle of expansion - determining what part of the cylinder is subject to expansion.

The results of the expansion are presented in Figure 10, on the left is the expanded point cloud in intensity colors, while on the right is the analysis of the distance of the points (C2M algorithm) from the fitted plane using the least squares method.

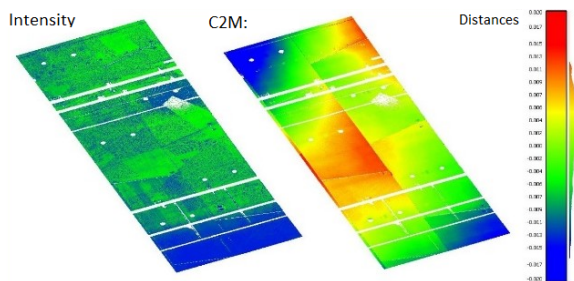


Figure 10. Expansion results, on the left the expanded point cloud in intensity colors, on the right the analysis of the distance of the points (C2M algorithm) from the fitted plane based on the least squares method.

The parameters adopted for the development include the nominal radius value, the angle of development of the whole - from 0 to 360 degrees, and the base point defined as the center of gravity of the cylinder. A color

scale was adopted for the roll-out, with distances ranging from -20 mm to +20 mm. The central part of the roll-out is dominated by green, yellow and orange colors, with values ranging from -4 mm to +10 mm. The upper left and lower right ends are dominated by blue, which corresponds to the largest differences - a value of about -15 mm. The situation is different between the opposite ends, with the upper right corner having a value of about +10mm and the lower left corner having an extreme of -7 mm. The mentioned values are influenced by taking into account a section consisting of 2 tubing units, which causes some curvature. However, this approach has highlighted the joints between the individual precast elements. It should be noted that some of the precast elements differ significantly in color, which leads to the conclusion that there are shifts - deformations between them. In the middle part of the expansion, at the border of two tubing units, there is a sudden peak of color, where it can be concluded that the difference between the position of these precast elements is about 7 mm. There are white circles on the expansion - being remnants after removing the prefabricate fixings in the process of manual filtering of the point cloud.

#### IV. DISCUSSION

This paper presents both a theoretical basis and the results of practical analyses related to fitting a plane to a point cloud. Analyses of the distances of the points from the variously defined planes show the importance of a proper choice of a reference surface definition. Fitting the plane to all the measured points, according to the definition of the method of least squares, will minimize the distances of the points from the plane, and thus show the trend of changes, but not their actual values. The second variant presented in this paper, in which the plane is fitted to points forming the contact frame with supports (in this case the walls), a fixed base for fitting, allows the plane to be defined by excluding the points representing the actual deformation of the surface. Hence the slight differences in the results obtained with respect to the first variant. Also in this case we do not have the certainty of whether the points forming the frame were not registered in the area where the surface change occurred. Therefore the authors undertook another analysis in which they assumed that the reference surface is ideally horizontal and the choice of its height was based on the histogram of the Z coordinate for the examined ceiling surface. In this case the analysis indicated a clear slope of the ceiling towards the right side.

The second aspect presented in this paper concerned analysis of the surface deformation mapped with cylindrical unfolding of a subway tunnel in Warsaw. In this case, the authors proposed to perform an expansion of the scanned surface into a plane so that it will be easier to represent the changes, and it will be

possible to apply the conclusions drawn from the analysis of the plane.

The methods of flatness analysis and deformation assessment proposed in this article are applicable to many tasks in the field of engineering geodesy performed at a construction site, with their results and interpretation having a real impact on the safety measures and construction works. In our opinion, increasing the reliability of analysis results is very important to ensure the structure's safety.

## References

- Abbas, M. A., H. Setan, Z. Majid, A.K. Chong, K.M. Idris, and A. Aspuri (2013). Calibration and accuracy assessment of leica scanstation c10 terrestrial laser scanner. In: *Developments in Multidimensional Spatial Data Models*. Springer, Berlin, Heidelberg, pp. 33-47.
- Dabrowski, P. S., and C. Specht (2019). Spatial expansion of the symmetrical objects point clouds to the lateral surface of the cylinder-Mathematical model. *Measurement*, Vol. 134, pp. 40-47.
- EN 1992-1-1:2004 Eurocode 2: Design of concrete structures - Part 1-1: General rules and rules for buildings, (2004).
- Gawronek, P., and M. Makuch (2019). Tls measurement during static load testing of a railway bridge. *ISPRS International Journal of Geo-Information*, Vol. 8(1), pp. 44.
- Harmening, C., Hobmaier, C., and Neuner, H (2021) Laser Scanner-Based Deformation Analysis Using Approximating B-Spline Surfaces. *Remote Sens.*, 13, 3551. DOI: 10.3390/rs13183551
- Kashani, A. G., M.J. Olsen, C.E. Parrish, and N. Wilson (2015). A review of LiDAR radiometric processing: From ad hoc intensity correction to rigorous radiometric calibration. *Sensors*, Vol. 15(11), pp. 28099-28128.
- Kovanič, L., P. Blištan, V. Zelizňakova, J. Palkova, J., and Baulovič (2019). Deformation investigation of the shell of rotary kiln using terrestrial laser scanning (TLS) measurement. *Metallurgija*, Vol. 58(3-4), pp. 311-314.
- Li, X., Y. Li, X. Xie, and L. Xu (2018). Terrestrial laser scanner autonomous self-calibration with no prior knowledge of point-clouds. *IEEE Sensors Journal*, Vol. 18(22), pp. 9277-9285.
- Li, D., J. Liu, L. Feng, Y. Zhou, P. Liu, and Y.F. Chen (2020). Terrestrial laser scanning assisted flatness quality assessment for two different types of concrete surfaces. *Measurement*, Vol. 154, pp. 107436.
- Liu, M., X. Sun, Y. Wang, Y. Shao, and Y. You (2020). Deformation Measurement of Highway Bridge Head Based on Mobile TLS Data. *IEEE Access*, Vol. 8, pp. 85605-85615.
- Marjasiewicz, M., and T. Malej (2014). Półautomatyczne modelowanie brył budynków na podstawie danych z lotniczego skaningu laserowego. *Archiwum Fotogrametrii, Kartografii i Teledetekcji*, Vol. 26.
- Medić, T., Kuhlmann, H., and C. Holst (2020) Designing and Evaluating a User-Oriented Calibration Field for the Target-Based Self-Calibration of Panoramic Terrestrial Laser Scanners. *Remote Sens.*, 12, 15. DOI: 10.3390/rs12010015
- Muszyński, Z., and M. Wyjadłowski (2020). Assessment of surface parameters of VDW foundation piles using geodetic measurement techniques. *Open Geosciences*, Vol. 12(1), pp. 547-567.
- Pinpin, L., Q. Wenge, C. Yunjian, and L. Feng (2021). Application of 3D laser scanning in underground station cavity clusters. *Advances in Civil Engineering*.
- Reshetyuk, Y. (2006). Investigation and calibration of pulsed time-of-flight terrestrial laser scanners (*Doctoral dissertation, KTH*).
- Schnabel R., R. Wahl, and R. Klein (2007) Efficient RANSAC for Point-Cloud Shape Detection, *Computer graphics forum*.
- Qian, X., and C. Ye (2014). NCC-RANSAC: a fast plane extraction method for 3-D range data segmentation. *IEEE transactions on cybernetics*, Vol. 44(12), pp. 2771-2783.
- Wang, J., H. Kutterer, and X. Fang (2016). External error modelling with combined model in terrestrial laser scanning. *Survey review*, Vol. 48(346), pp. 40-50.
- Wyczałek, I., A. Plichta, and M. Wyczałek (2017). Badania możliwości technicznych pomiaru płaskości powierzchni kinematyczną metodą trygonometryczną. *Zeszyty Naukowe. Inżynieria Środowiska/Uniwersytet Zielonogórski*.
- Xiang, L., Y. Ding, Z. Wei, H. Zhang, and Z. Li (2021). Research on the Detection Method of Tunnel Surface Flatness Based on Point Cloud Data. *Symmetry*, Vol. 13(12), pp. 2239.
- Xu, X., H. Yang, and B. Kargoll (2019). Robust and automatic modeling of tunnel structures based on terrestrial laser scanning measurement. *International Journal of Distributed Sensor Networks*, Vol. 15(11), pp. 1550147719884886.
- Yang, H., and X. Xu (2021). Structure monitoring and deformation analysis of tunnel structure. *Composite Structures*, Vol. 276, pp. 114565.
- Ye, C., S. Acikgoz, S. Pendrigh, E. Riley, and M.J. DeJong (2018). Mapping deformations and inferring movements of masonry arch bridges using point cloud data. *Engineering Structures*, Vol. 173, pp. 530-545.

## Monitoring embankment dams from space using satellite radar interferometry: Case studies from RemoDams project

Antonio M. Ruiz-Armenteros<sup>1,2,3</sup>, José Manuel Delgado-Blasco<sup>3</sup>, Matus Bakon<sup>4,5</sup>,  
Francisco Lamas-Fernández<sup>6</sup>, Miguel Marchamalo-Sacristán<sup>7</sup>, Antonio J. Gil-Cruz<sup>1,2,3</sup>, Juraj Papco<sup>8</sup>,  
Beatriz González-Rodrigo<sup>9</sup>, Milan Lazecky<sup>10,11</sup>, Daniele Perissin<sup>12,13</sup>, Joaquim J. Sousa<sup>14,15</sup>

<sup>1</sup> Department of Cartographic, Geodetic and Photogrammetry Engineering, University of Jaén, Campus Las Lagunillas s/n, 23071 Jaén, Spain, ([amruiz@ujaen.es](mailto:amruiz@ujaen.es); [ajgil@ujaen.es](mailto:ajgil@ujaen.es))

<sup>2</sup> Centre for Advanced Studies in Earth Sciences, Energy and Environment (CEACTEMA), University of Jaén, Campus Las Lagunillas s/n, 23071 Jaén, Spain

<sup>3</sup> Research Group RNM-282 Microgeodesia Jaén, University of Jaén, Campus Las Lagunillas s/n, 23071 Jaén, Spain, ([jdblasco@ujaen.es](mailto:jdblasco@ujaen.es))

<sup>4</sup> insar.sk s.r.o., Slovakia, ([matusbakon@insar.sk](mailto:matusbakon@insar.sk))

<sup>5</sup> Department of Environmental Management, University of Presov, Slovakia

<sup>6</sup> Department of Civil Engineering, University of Granada, Spain, ([flamas@ugr.es](mailto:flamas@ugr.es))

<sup>7</sup> Topography and Geomatics Lab. ETS ICCP, Universidad Politécnica de Madrid, Spain, ([miguel.marchamalo@upm.es](mailto:miguel.marchamalo@upm.es))

<sup>8</sup> Department of Theoretical Geodesy, Slovak University of Technology in Bratislava, Slovakia, ([juraj.papco@stuba.sk](mailto:juraj.papco@stuba.sk))

<sup>9</sup> Departamento de Ingeniería Civil: construcciones, infraestructura y transportes, ETS Ingeniería Civil, Universidad Politécnica de Madrid, Spain, ([beatriz.gonzalez.rodrigo@upm.es](mailto:beatriz.gonzalez.rodrigo@upm.es))

<sup>10</sup> School of Earth and Environment, University of Leeds, United Kingdom, ([M.Lazecky@leeds.ac.uk](mailto:M.Lazecky@leeds.ac.uk))

<sup>11</sup> IT4Innovations, VSB-TU Ostrava, Czechia

<sup>12</sup> Raser Limited, Hong Kong, China, ([daniele.perissin@sarproz.com](mailto:daniele.perissin@sarproz.com))

<sup>13</sup> CIRGEO, Università degli Studi di Padova, Italy

<sup>14</sup> Universidade de Trás-os-Montes e Alto Douro, Vila Real, Portugal, ([jj Sousa@utad.pt](mailto:jj Sousa@utad.pt))

<sup>15</sup> INESC-TEC - INESC Technology and Science, Porto, 4200-465, Portugal

**Key words:** *dam monitoring; deformation; MT-InSAR; embankment dams; satellite radar interferometry*

### ABSTRACT

The monitoring procedures with different geotechnical/structural sensors and classical geodetic techniques including GNSS are the usual practices in most of the dams where these controls are established. Other geomatic techniques such as TLS, GB-SAR and multi-temporal InSAR (MT-InSAR), allow the determination of 3D displacements with the advantage of covering a large number of control points. In particular, MT-InSAR techniques enable the detection of displacements at a very low cost compared to other techniques, and without the need for field work or the installation of special equipment. In addition, they can provide a single source of information on the stability of the dam when monitoring programs are not carried out due to lack of funding, resources or other reasons. These techniques provide measurement uncertainties of the order of 1 mm/year, interpreting time series of interferometric phases of coherent reflectors present in the area, called Persistent Scatterers. In this work, we present the adaptation and application of MT-InSAR techniques to monitor embankment dams, obtaining vertical displacements, characterizing their consolidation rates, and allowing the identification of potential problems surrounding the reservoir that require further field investigation. This study is part of the ReMoDams project, a Spanish research initiative developed for monitoring dam structural stability from space using satellite radar interferometry.

### I. INTRODUCTION

After experiencing huge infrastructure development activities in the 20<sup>th</sup> century, many engineering infrastructures in the world require security monitoring. Detailed inspection plans and monitoring

these infrastructures (such as reservoir dams) are critical to ensure the security of citizens and properties. These interventions are usually expensive and time-consuming. In many cases, resource constraints make practically impossible to monitor each infrastructure

individually, which may represent a potential safety risk.

Global changes are rapidly transforming the needs and requirements of water supply systems in the world, especially in areas where drought has increased in recent decades (Estrela *et al.*, 2012; Forero-Ortiz *et al.*, 2020). Dams are an important part of the water cycle infrastructure, which can provide our society with water, energy and food, and need to urgently adapt to the ever-changing environment. The construction and management of dams is one of the main strategies to adapt to climate change. Dams are critical infrastructures, and their failure has high economic and social consequences, although usually very low, there exist related risks that must be properly managed in a continuously updated process (ICOLD, 2003; Fluijá-Sanmartín *et al.*, 2018). The rapid changes in the factors leading to dam risks may make traditional monitoring programs no longer suitable for long-term safety management of dams (Bowles *et al.*, 2013; USBR, 2016; USACE, 2016).

A reliable and safe monitoring and management system suitable for the characteristics of the dam and the manager's needs is needed. The required system should integrate the best available technology to ensure social and economic reliability, efficiency and profitability.

Monitoring the deformation of large man-made structures is essential to avoid catastrophic infrastructure and loss of life. Many structures that need to be monitored may span hundreds of meters, such as dams, and tens of kilometers, such as dikes and embankments. The widespread deterioration of these man-made structures and some recent collapses (Dam failure, n. d.) highlight the importance of developing effective structural monitoring strategies that can help identify structural problems before they become serious and endanger public safety problem. In addition, the rapid pace of development has led to the establishment of a large number of linear structures, such as reservoir dams. The spatial stability and operational safety of these man-made facilities have become the focus of attention because the deformation implies potential hazards or risks in or around these structures.

Measuring and monitoring the deformation of these man-made objects and structures is the key task of applied geodesy and geomatics. However, although these deformation measurement technologies are undoubtedly very accurate and reliable, they are based on detecting changes in specific points and require prior investment of human resources or special equipment. Deformation monitoring schemes may target different deformation schemes and mechanisms, and therefore may be very different. For example, laser alignment, laser scanning, total station, leveling and inverse plummet are widely used in dam deformation monitoring. These specialized equipments are

sometimes integrated with Global Navigation Satellite System (GNSS) for specific surveillance purposes.

In the past few years, international researchers have made great efforts to find an effective method to monitor the deformation of man-made structures. However, dam monitoring is still a difficult task. As far as dams are concerned, due to the high risks they represent, the supervision work is supervised by the competent national bodies. The main goal of public supervision is to ensure that the safety level of dams and auxiliary structures is uniform, so as to ensure that they do not pose a threat to life, property or the environment. The rapid development of space technology in recent decades has enabled to detect the displacement of the earth's surface from space with high accuracy, which has brought unexpected results to earth observation and related research. This progress has been made due to the development of microwave images obtained through synthetic aperture radar (SAR) mounted on satellites and multi-temporal interferometry (MTI or MT-InSAR) technology. MTI has the potential to support the development of new and more effective methods for monitoring and analyzing the health of dams, and to increase redundant monitoring at low cost to support and assist early warning systems. With the help of SAR interferometry, specific dams can be monitored to identify and investigate suspiciously displaced targets on a monthly (ERS, Envisat and Radarsat data) or weekly (TerraSAR-X, COSMO-SkyMed, PAZ and Sentinel-1) time scales. As a result, timely detection of potential problems can help mitigate their impact on structural health and reduce infrastructure repair costs. In addition, there are two main characteristics that make interferometric technology attractive to the scientific community. The first is that it provides a high-resolution two-dimensional representation of the deformation from 10 s to more than 200 s kilometers. The second is the high accuracy of the deformation that can be measured (up to 1 mm/year) (Hooper *et al.*, 2012). In addition, in some cases, the data can be analyzed retrospectively to obtain past deformation information.

In this paper, we present some case studies of the monitoring of embankment dams. They belong to ReMoDams project, a research Spanish initiative devoted to the application of MT-InSAR techniques for monitoring dam structural stability from space using satellite data.

## II. STUDY AREA – TEST SITES

With the aim of remote monitoring of their structural health from space using satellite radar interferometry, four dams were selected. One of them (The Aswan High Dam) is located in Egypt and the others (Benínar, La Viñuela and El Arenoso dams) in southern Spain (Figure 1).

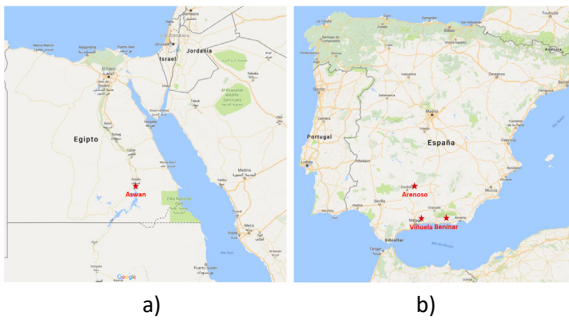


Figure 1. Location maps of the study areas: a) Egypt; b) Spain. (Source: Google Maps).

The Aswan High Dam (Egypt) (Figure 2a) is one of the major artificial structures ever built. This dam, which construction finished in 1979, has 3600 m in length and is 1000 m wide at the base. It is a rockfill dam that forms an artificial lake (Lake Nasser) covering, at maximum capacity, an area of 5250 Km<sup>2</sup>, storing a water volume of 135 Km<sup>3</sup>. Nasser Lake was created as a result of the construction of the Aswan High Dam across the waters of the Nile between 1958 and 1970. It is located in a very active tectonic area mainly because of the complexity of its fault system. The safety of dams during earthquakes is extremely important because the failure of such structures may have disastrous consequences on life and property. Therefore, different factors must be considered as part of a site assessment.

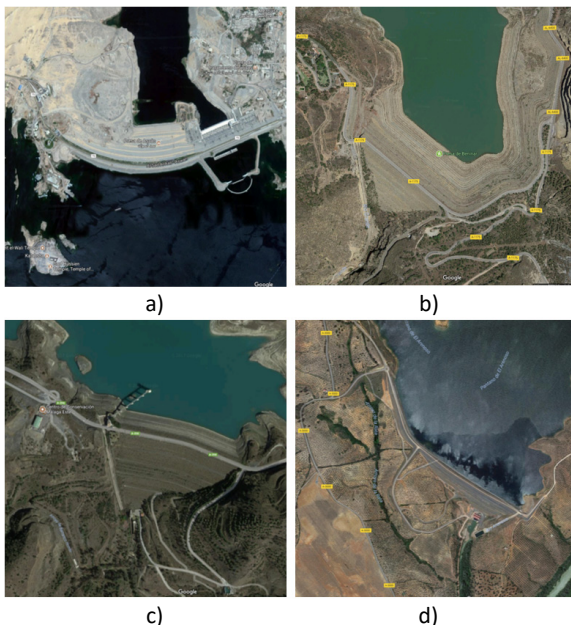


Figure 2. a) The Aswan High dam; b) The Benínar dam; c) La Viñuela dam; d) El Arenoso dam. (Source: Google Maps).

Benínar dam (Almería, Spain) (Figure 2b) is located on the Grande de Adra River, in the Andalusian municipality of Benínar, in the Almería province. Today, the village of Benínar is submerged under the waters of the reservoir and administratively depends on Berja Town Hall. The dam whose construction finished in 1983 was built with loose materials, with distinct profile inclined impervious core, and rockfill shoulders. It has a

height of 87 m and a length of 400 m; the reservoir has a volume of 68,2 hm<sup>3</sup>. Its catchment area (521 km<sup>2</sup>) affects the provinces of Granada and Almería on its eastern and western boundaries. Population water supply and irrigation are the main use of this dam. According to water flow records and geotechnical studies, this dam has always had water leakage issues since it was constructed.

La Viñuela dam (Málaga, Spain) (Figure 2c) is located on the Guaro River in the municipality of La Viñuela and stores inflows from the hydrographic network of the region of La Axarquía. It was built to supply water to the region and to improve irrigation. The basin of La Viñuela reservoir has a surface of 119 km<sup>2</sup>, an average yearly rainfall of 893 mm, and an average yearly contribution of 25 hm<sup>3</sup>. It is an embankment dam of mixed plant, having a crest length of 460 m and heights of 90 and 96 m over riverbed and foundations, respectively. The reservoir has a capacity of 170 hm<sup>3</sup>. Its construction finished in 1989. The main purposes of this dam are to supply drinkable water to the urban centers of the eastern Costa del Sol, between Málaga and Nerja, the irrigation of 8000 ha of subtropical and extra-early horticultural crops, and potentially, to supply the city of Málaga.

El Arenoso dam (Cordova, Spain) (Figure 2d) is located in the Arenoso riverbed, a tributary of the Guadalquivir on the right bank, in the Andalusian municipality of Montoro, province of Cordova. Its reservoir has a capacity of 166,97 hm<sup>3</sup> and an area of 764,12 ha. It is an embankment dam, with a central clay core, slates, and greywacke shoulders. The core is covered downstream by a filter material, and upstream by a transition material. It also has a cofferdam with a similar section and materials, which remains leaning against the dam's body. The dam has a maximum height of 80 m, a crest length of 1481 m, and a coronation width of 11,30 m. The construction of the dam increased the water available in the Guadalquivir which improved the economic and social development of the Guadalquivir basin. Its construction finished in May 2008.

### III. DATA AND METHODS

#### A. *Insar data*

For this study, we used different satellite SAR data. In this paper, we present the results of medium resolution C-band SAR data (~5,7 cm wavelength) that come from the European satellites ERS-1/2, Envisat, and Sentinel-1A/B. ERS-1/2 SAR and Envisat ASAR that have been used to reconstruct historical time series of deformation in the different dams where they were available. ERS-1/2 SAR data allow us to monitor the deformation in the period 1992-2000 and Envisat in 2002-2010. In the case of Sentinel-1A/B satellites, the -1A started the mission in 2014 and -1B in 2016. When both satellites -1A and -1B are combined, they offer a 6-days revisit time. All the SAR data are in SLC format, and in the case of Sentinel-1A/B we used the

Interferometric Wide (IW) swath mode. Table 1 summarizes the different data sets used for each test site.

## B. Methods

InSAR relies on the processing of two SAR images of the same part of the earth's surface. These images are obtained from two slightly shifted passes of the SAR antenna at different times (repeated-pass interferometry), or from two antennas being placed on the same platform and separated perpendicularly to the flight path (single-pass SAR interferometry). However, despite the many successes of InSAR, the applicability of this technology is limited by the problems caused by the time-varying scattering characteristics of the earth's surface and the incidence angle in the direction of the radar's line of sight. This especially makes the detection of slow deformation processes challenging to detect with the standard InSAR techniques.

In the late 1990s, it was noticed that certain radar targets maintained stable backscatter characteristics for months or years, as well as the phase information from these stable targets (hereinafter referred to as "Persistent scatterer" or PS) can be used, even for a long period of time, profiting from a SAR scene archive in existence since 1991 (ERS-1) which allows the establishment of long time series of SAR images. This led to the development of time-series SAR interferometry methodology, or also known as multi-interferogram technology (MTI or MT-InSAR). Because of their ability to overcome the limitations of conventional InSAR, they are becoming more and more popular being considered currently as standard deformation measurement tools.

MT-InSAR is an extension of conventional DInSAR, which aims to solve the problems caused by decorrelation and atmospheric delay. These techniques involve processing multiple SAR acquisitions simultaneously on the same area to correct for uncorrelated phase noise terms, thereby reducing errors related to distortion estimation. MT-InSAR is a collective term used in the InSAR community to distinguish between a single interferogram DInSAR and the second-generation InSAR technology. The first of these methods appeared in 1999 as the Permanent Scatterer algorithm (PSInSAR™) (Ferretti, 2001). The interferogram is the core of all MT-InSAR technology, and the main driving force for its development is the need to overcome the error in the signal phase value introduced by atmospheric artifacts. These limitations can be resolved by using the phase behavior in time to select the pixels with minimal decorrelation noise. Then, the undistorted signal is estimated through a combination of time series modeling and filtering. MT-InSAR algorithms are divided into two categories, the first is Persistent Scatterers InSAR (PSI or PS-InSAR), and the second is the more general Small BASeline

(SBAS) method. Each of these methods is designed for a specific type of scattering mechanism.

The main spaceborne medium resolution C-band SAR sensors used for deformation monitoring include ERS-1/2, Envisat, and Sentinel-1 from ESA (Europe), and Radarsat-1/Radarsat-2 from CSA (Canada). Among all these sensors, Sentinel-1 is the first (civilian) sensor specially designed for large-area surface deformation monitoring, being their data completely open for any user/application. Modern spaceborne SAR sensors can provide a spatial resolution of about 1 meter or lower. In high-resolution X-band SAR data (TerraSAR-X, TanDEM-X, COSMO-SkyMed, PAZ, ICEYE, and Capella), even small dams are covered by a large number of pixels. These data are being tested for structural health monitoring (SHM) applications, and the results are very satisfactory. The new generation of high-resolution radar images acquired by SAR sensors and the development of advanced MTI algorithms can retrieve the deformation time series and velocity maps from a stack of SAR images acquired at different times in the area. In recent years, our ability to use MTI technology for high-precision deformation monitoring has been enhanced and is related to engineering infrastructure. With the advent of even more advanced MT-InSAR processing technology that combines both PS and SBAS methods, these sensors have been used to monitor the deformation of a series of natural and man-made structures, including large structures such as dams and dikes. Several tests carried out with different types of structures have helped to establish a standard procedure for structural monitoring using interferometric techniques, and it can be concluded that although the temporal and spatial resolution of the C-band is relatively coarse (Sentinel-1 greatly improves this state), it can be used to monitor major structures, including dams. Obviously, it was quickly discovered that the geometric resolution of satellite images (X-band with 0.5-1 m) did not match the size of typical defects, such as in concrete dams (0.01-0.5 m). Therefore, it is not possible to use SAR satellite images to identify problems such as cracking and raveling; however, the only spaceborne sensor that can help structural inspections by measuring deformation is the synthetic aperture radar. Several tests conducted by research and working teams have shown the potential of C-band SAR interferometry technology in dam monitoring (Sousa *et al.*, 2016; Lazecky *et al.*, 2017; Delgado-Blasco *et al.*, 2017). The application of radar interferometry technology may potentially reduce in millions of euros the operating costs of monitoring structure tasks, while providing more detailed and frequent monitoring, which will inevitably lead to better security conditions.

Regardless of the method used, all measurements are made in the satellite LOS and are relative to a reference point or area. Once the data are analyzed, it is possible to develop the movement history (deformation time series) of the entire region of interest. This is achieved

by sequentially calculating the relative displacement between a single radar target and the reference point throughout the analysis period. Therefore, deformation is relative in time and space. A lot of research has been conducted to study the accuracy, potential, and limitations of this technology in a variety of applications. Xue *et al.* (2020) and Ho Tong Minh *et al.* (2020) offer a review of these multi-interferogram algorithms. Table 2 summarizes the different MT-InSAR methods and software used in this study with the different data sets.

IV. RESULT AND DISCUSSION

In the case of The Aswan High Dam, we performed both PS-InSAR and SBAS processing as well as the combination of them using StaMPS-MTI software with Envisat descending images. Figure 3 shows a subsidence zone in the central part of the dam with a mean LOS velocity around -3 mm/year at the crest. In addition, it has also been detected a slope subsiding in the east

bank 1 km north of the dam. The analyzed period is from 19/12/2003 to 03/09/2010.

Sentinel-1A/B ascending images were processed using a classical PS-InSAR approach using SARPROZ. The stability of the dam is confirmed in the period 01/05/2015 - 26/10/2021 showing LOS velocities lower than -3 mm/year (Figure 4). To investigate the expected theoretical subsiding behavior due to the material consolidation through time a preliminary calculation of stress-strain modeling of the dam has been performed using Limit Equilibrium Method (LEM) and Finite Element Method (FEM). It has been done along the wider section on the river axis since it is the most unfavorable due to the hydraulic load. According to this model, a possible vertical deformation of 22.8 cm is obtained. This estimated settlement is caused by the secondary consolidation or fluency from 1970 to present without considering the settlement during the construction of the dam or other external influences from other sources such as the power plant attached to the dam.

Table 1. C-band SAR data sets used in this study. The number of images for each stack, the orbit direction (ascending or descending) as well as the time span are indicated

Dam	ERS-1/2	Envisat	Sentinel-1A/B
Aswan	---	31 descending 19/12/2003 - 03/09/2010	319 ascending 01/05/2015 - 26/10/2021
Benínar	22 descending 06/06/1992 - 31/10/2000	32 ascending 02/12/2002 - 29/06/2010	192 ascending 10/11/2014 - 07/03/2019
La Viñuela	24 descending 05/02/1992 - 28/01/2000	27 ascending 21/03/2003 - 01/08/2008	188 descending 16/11/2014 - 01/03/2019
El Arenoso	---	---	309 ascending 03/10/2015 - 24/02/2021
			194 ascending. 03/03/2015 - 28/02/2019
			303 descending 16/03/2015 - 24/02/2021
			188 descending 16/11/2014 - 01/03/2019

Table 2. C-band SAR data sets used in this study. The number of images for each stack, the orbit direction (ascending or descending) as well as the time span are indicated

Dam	ERS-1/2	Envisat	Sentinel-1A/B
Aswan	---	PSI+SBAS; StaMPS-MTI	PSI SARPROZ
Benínar	PSI+SBAS; StaMPS-MTI	PSI+SBAS; StaMPS-MTI	PSI; SARPROZ   PSI; SNAP-StaMPS
La Viñuela	PSI+SBAS; StaMPS-MTI	PSI+SBAS; StaMPS-MTI	PSI; SARPROZ   PSI; SARPROZ
El Arenoso	---	---	PSI; SARPROZ   PSI; SARPROZ



Figure 3. a) Mean LOS velocity derived from Envisat ASAR data over The Aswan High dam (2003-2010); b) Location of a possible landslide 1 km north of the dam (red pixels in the center of the image).



Figure 4. Mean LOS velocity derived from Sentinel-1A/B ascending data over The Aswan High dam (2015-2021).

For the case of Benínar dam, we processed C-band images from ERS-1/2, Envisat, and Sentinel-1A/B ESA satellites, covering a period of more than 25 years, that is, from 1992 to 2019. The ERS-1/2 (06/06/1992-31/10/2000) and Envisat (03/12/2000-29/06/2010) data sets were processed using a combination of these two MT-InSAR methods PSI and SBAS using StaMPS-MTI software. The ascending Sentinel-1A/B data set (10/11/2014-07/03/2019) was processed using a PSI analysis with SARPROZ software (Perissin, 2022) while the descending one (16/11/2014-01/03/2019) was processed with SNAP-StaMPS using a PSI analysis.

Construction works of the dam were initiated in 1974 and concluded in 1983, although it was not finally put into service until 1988, following various projects to waterproof the base. Nowadays, after 32 years since its construction, it is clear that this dam has not satisfied expectations due to severe leakage that has occurred through the reservoir bottom. The complex and unfavorable geological characteristics, together with an initial concept that made little effort to integrate the possibilities of surface and groundwater resources, gave rise to this failure. In early 1991, the authorities revised the initial focus of the regulatory project and took action to tap the water that was escaping into the underlying carbonate aquifer into which the reservoir water is draining (García-López *et al.*, 2009). Figure 5 shows the mean LOS velocity maps for ERS-1/2 and Envisat data sets. The results indicate a subsiding zone in the central part of the dam with a mean LOS velocity in the order of -3/-5 mm/year in all periods (ERS-1/2: 1992-2000, Envisat: 2002-2010 and Sentinel-1A/B: 2014-2019) (Figure 5). This behavior is partially coherent with the dam typology (earth fill) but the expected attenuation in time is not observed. Currently, mathematical modeling of the dam is being performed to investigate the expected theoretical subsiding behavior due to the material consolidation through time. The obtained results must be validated/compared to this stress-strain analysis to know if the measured satellite deformation matches the expected one for this kind of dam. In the same way, some investigations are

being carried out to get information from field measurements over the dam as well as other geotechnical monitoring systems which may help to prove the effectivity of this remote sensing technique.

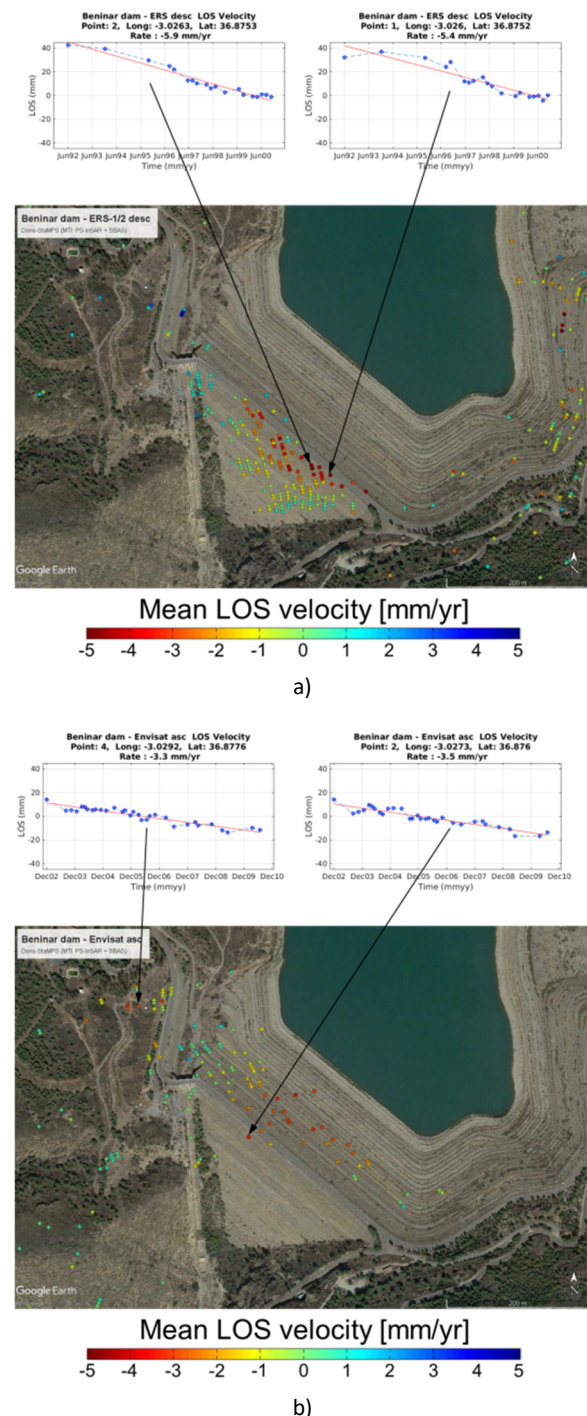


Figure 5. Mean LOS velocity maps over the Benínar dam: a) ERS-1/2 desc (1992-2000); b) Envisat asc (2000-2010).

In the case of La Viñuela dam, we used C-band radar data from the European satellites ERS-1/2, Envisat, and Sentinel-1A/B. The ERS-1/2 (02/05/1992-28/02/2000) and Envisat (21/03/2003-01/08/2008) data sets were processed using StaMPS-MTI (PSI + SBAS). The ascending and descending Sentinel-1A/B images (2015-2021) were processed using the standard PSI analysis using SARPROZ. Mean LOS velocity maps for ERS-1/2



and Envisat were derived from StaMPS-MTI processing. Both results correspond to the combined (PSI+SBAS) processing. In the case of ERS-1/2, a subsidence pattern can be clearly detected with maximum subsidence around -7 mm/year on the crest of the dam. In the Envisat period, the subsidence pattern is lower, with maximum subsidence in the order of -4 mm/year. The standard deviations of the LOS velocity are quite low, in the order of  $\pm 1$  mm/year. The standard PSI approach from SARPROZ with the linear model assumption for the deformation estimates confirmed that the investigated area of the dam's body is prone to subsidence of up to -5 mm/year (LOS velocity) in the whole monitoring period of Sentinel-1 (2015-2021) (Figure 6).

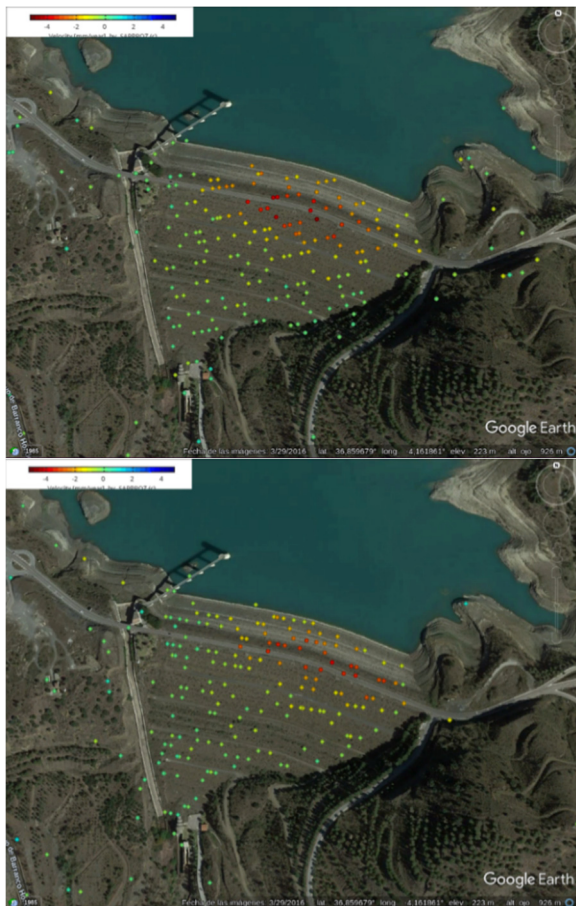


Figure 6. Mean LOS velocity maps over La Viñuela dam in the period 2015-2021. Top: ascending. Bottom: descending.

Finally, in the case of El Arenoso dam, we selected and processed two independent sets of Sentinel-1A/B SAR images acquired along ascending and descending orbits. The ascending set is composed by 194 (03/03/2015-28/02/2019) and the descending one by 188 (16/11/2014 – 01/03/2019) SAR images. The processing was done using the standard PSI technique using SARPROZ. Figure 7 shows the mean LOS velocity maps for both ascending and descending data sets. The general picture is quite similar. According to the depicted patterns, both tracks indicate the presence of a subsiding sector in the crest of the dam reaching

linear values of the order of -8/-10 mm/year which represents cumulative displacement in the LOS direction up to about -40 mm in 4 years.

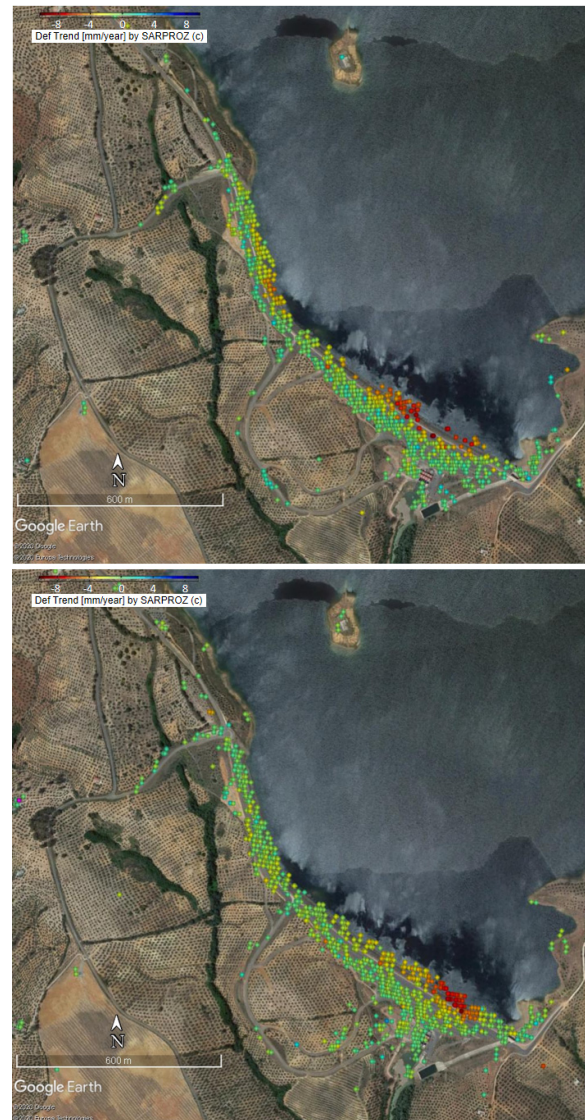


Figure 7. Mean LOS velocity maps over El Arenoso dam in the period 2015-2019. Top: ascending. Bottom: descending.

## V. CONCLUSIONS

In this work, we present the applicability of satellite radar interferometry for deformation studies in civil engineering, in particular, for monitoring embankment dams. Different case studies are presented in the framework of ReMoDams project, a Spanish research initiative to monitor dam infrastructures from space using satellite radar interferometry, such as The Aswan High dam in Egypt, and Benínar, La Viñuela and El Arenoso dams in southern Spain. Today, MT-InSAR can be considered a consolidated technique whose effectivity for deformation studies has been proved in many cases. For infrastructure monitoring, if there is SAR data available of the study area, the technique is demonstrated to be of high value at a very low cost as compared with classical geodetic monitoring techniques. In case of other geotechnical or geodetic

data are available, they can be successfully complemented.

We also show the potential of SAR long time series scenes and the MT-InSAR technique for deformation monitoring in some important infrastructures such as dams. To our best knowledge, this study represents the first attempt to monitor the presented dams using this technology. The MT-InSAR results indicate different deformation periods in all the analyzed dams with rates of subsidence in the LOS direction of -10 mm/year maximum.

This is an ongoing project that will be extended in the future analyzing more SAR data provided from these medium resolution C-band SAR images and incorporating high-resolution X-band data to increase the potential of the technique. Continuous processing of InSAR information could be successfully integrated in regular structural monitoring programs as a component of the implementation of early warning systems.

## VI. ACKNOWLEDGEMENTS

ERS-1/2 and Envisat data sets were provided by the European Space Agency (ESA). Sentinel-1A/B data were freely provided by ESA through Copernicus Programme. Data have been processed by DORIS (TUDelft), StaMPS (Andy Hooper), SARPROZ (Copyright (c) 2009-2020 Daniele Perissin), and SNAP (ESA). The satellite orbits are from TUDelft and ESA, as well as from the ESA Quality control Group of Sentinel-1. Research was supported by: (a) ESA Research and Service Support for providing hardware resources employed in this work, (b) ReMoDams project ESP2017-89344-R (AEI/FEDER, UE) from Spanish Ministry of Economy, Industry and Competitiveness, POAIUJA-2021/2022 and CEACTEMA from University of Jaén (Spain), and RNM-282 research group from the Junta de Andalucía (Spain), (c) ERDF through the Operational Programme for Competitiveness and Internationalisation - COMPETE 2020 Programme within project «POCI-01-0145-FEDER-006961», and by National Funds through the FCT – Fundação para a Ciência e a Tecnologia (Portuguese Foundation for Science and Technology) as part of project UID/EEA/50014/2013, (d) The Ministry of Education, Youth and Sports from the National Programme of Sustainability (NPU II) project «IT4Innovations excellence in science - LQ1602» (Czech Republic), and (e) Slovak Grant Agency VEGA under projects No. 2/0100/20.

## References

- Bowles, D., Brown, A., Hughes, A., Morris, M., Sayers, P., Topple, A., Wallis, M., and Gardiner, K. (2013). Guide to risk assessment for reservoir safety management, Volume 1: Guide, Environment Agency, Horison House, Deanery Road, Bristol, BS1 9AH.
- Delgado-Blasco, J.M., Ruiz-Armenteros, A.M., Caro-Cuenca, M., Lazecky, M., Bakon, M., Sousa, J.J., Lamas-Fernández, F.J., Verstraeten, G., and Hanssen, R.F. (2017). Aswan High Dam structural stability analysed by Persistent Scatterer Interferometry from 2004 until 2010. *10<sup>th</sup> International Workshop on “Advances in the Science and applications of SAR interferometry and Sentinel-1 InSAR”*, Fringe 2017, pp. 5-7 junio, Helsinki (Finlandia).
- Estrela, T., Pérez-Martin, M.A., and Vargas, E. (2012). Impacts of climate change on water resources in Spain. *Hydrological Sciences Journal*, 57 (6), pp. 1154–1167.
- Ferretti, A., C. Prati, and F. Rocca (2001). Permanent Scatterers in SAR Interferometry. *IEEE Transactions on Geoscience and Remote Sensing*, Vol 39, No. 1, pp 8-20.
- Fluixá-Sanmartín, J., Altarejos García, L., Morales Torres, A., and Escuder Bueno, I. (2018). Climate change impacts on dam safety. *Natural Hazards and Earth System Sciences* 18 (9), pp. 2471-2488.
- Forero-Ortiz, E., Martínez-Gomariz, E., and Monjo, R. (2020). Climate Change Implications for Water Availability: A Case Study of Barcelona City. *Sustainability*, 12, 1779.
- García-López, S., Benavente, S., Cruz-Sanjulián, J.J., and Olías, M. (2009). Conjunctive use of water resources as an alternative to a leaky reservoir in a mountainous, semiarid area (Adra River basin, SE Spain). *Hydrogeology Journal* 17, pp. 1779–1790.
- Ho Tong Minh, D., Hanssen, R., and Rocca, F. (2020). Radar interferometry: 20 years of development in time series techniques and future perspectives. *Remote Sensing*, 12(9), 1364.
- Hooper, A., Bekaert, D., Spaans, K., and Arikani, M. (2012). Recent advances in SAR interferometry time series analysis for measuring crustal deformation. *Tectonophysics*, 514-517, 1-13, DOI: 10.1016/j.tecto.2011.10.013.
- ICOLD (2003). *Bulletin on risk assessment in dam safety management*, International Commission on Large Dams., 2003.
- Lazecky, M., Bakon, M., Perissin, D., Papco, J., and Gamse, S. (2017). Analysis of dam displacements by space borne SAR Interferometry. *85<sup>th</sup> Annual Meeting of International Commission on Large Dams*. July 3-7, 2017. Prague, Czech Republic.
- Perissin, D. (2022). “SARPROZ software”. Official Product Web page: <http://www.sarproz.com>
- Sousa, J.J., Ruiz, A.M., Bakon, M., Lazecky, M., Hlavacova, I., Patricio, G., Delgado, J.M., and Perissin, D. (2016). Potential of C-Band SAR Interferometry for dam monitoring. *Procedia Computer Sciend* 100, pp. 1103-1114.
- USACE (2016). *Guidance for Incorporating Climate Change Impacts to Inland Hydrology in Civil Works Studies, Designs, and Projects*, EBC.
- USBR. (2016). *Climate Change Adaptation Strategy: 2016 Progress Report*, U.S. Department of the Interior. Bureau of Reclamation.
- Xue, F., Lv, X., Dou, F., and Yun, Y. (2020). A review of time-series interferometric SAR techniques: A tutorial for surface deformation analysis. *IEEE Geoscience and Remote Sensing Magazine*, 8(1), pp. 22-42.

## Deep machine learning in bridge structures durability analysis

Karolina Tomasziewicz, Tomasz Owerko

Department of Engineering Surveying and Civil Engineering, Faculty of Geo-Data Science, Geodesy and Environmental Engineering, AGH University of Science and Technology, Mickiewicza 30 Av., 30-059 Krakow, Poland, ([tomaszki@agh.edu.pl](mailto:tomaszki@agh.edu.pl); [owerko@agh.edu.pl](mailto:owerko@agh.edu.pl))

**Key words:** *deep machine learning; transfer learning; concrete cracks; bridge structure; durability*

### ABSTRACT

According to Eurocode 0 structural durability is next to ultimate and serviceability one of the basic criteria in the structural design process. This article discusses the subject of concrete cracks observation in bridge structures, as one of the factors determining their durability. The durability of bridge structures is important due to both social, economic aspects and also the defense aspects of countries. Cracking of the reinforced concrete structures is a natural effect in concrete. The aim in the design and construction of structures is not to prevent the formation of cracks, but to limit their width to acceptable values. At the same time, there is a need for structure tests that allow for non-contact, fast measurements and algorithms that allow for efficient analysis of large amounts of measurement data. Deep machine learning algorithms can be used here. They can be used to analyse data which are acquired by means of photogrammetric methods (especially helpful during construction to inventory concealed works). Moreover, they can also be applied to standard data acquisition methods, consisting in photographing objects damage during works acceptance or periodic inspections. This paper discusses the application of deep machine learning to assess the condition of bridge structures based on photographs of object damage. The use of this method makes it possible to observe the rate and extent of damage development. Consequently, this method makes it possible to predict the development of damage in time and space in order to prevent failures and take structures out of service.

### I. INTRODUCTION

According to Eurocode 0, structural durability is one of the basic criteria in the process of designing buildings, in addition to ultimate and serviceability. It has a significant influence on the adopted structural and material solutions. This paper concentrates on the subject of bridge structures damage observation, the reliability of which is crucial due to social and economic aspects as an element of transport and transit infrastructure. These objects also play an important role due to the aspects of national defense.

The cracks are occurring when the force in a given point in the structure exceeds concrete maximum tensile strength. The phenomenon of cracking in reinforced concrete structures is a natural phenomenon of concrete. The aim in the design and construction of structures is not to prevent the formation of cracks, but to limit their expansion to the values specified in national standards.

Identifying the location of the crack line in a concrete member is an equally important aspect that can give knowledge about the nature of the factor causing the crack in the structure. The progression of the crack over time must also be considered. Some cracks occurring on the surface of a structure do not increase in dilation over time and remain present on the surface of the structure throughout its life cycle. The conclusion is that not every crack may be a potential threat to the

durability of the structure. However, expert knowledge is needed to clearly and responsibly identify potentially dangerous locations.

The phenomenon of concrete cracking can be caused by many factors, which makes the problem complicated (Zhang, 2018). The problem of cracking concerns in particular the massive elements of the bridge such as foundations, abutments, pillars and pylons. Cracking occurs due to the increase of thermal-shrinkage stresses in the concrete of these elements. Under the influence of loads it may lead to the propagation of cracks through the entire thickness of the element, and as a consequence to the loss of monolithicity of the element and changes in the static scheme, or to the development of corrosion processes under the influence of water penetrating through cracks into the element.

At each stage of the life cycle of the structure, a number of factors can be listed that affect its durability (Germaniuk *et al.*, 2016; Zhang, 2018). It requires close cooperation between the designer, contractor, concrete technologist, inspector, and the investor or user of the facility to ensure durability. Examples of factors at different stages of the structural life cycle that influence the possibility of cracking are presented in Figure 1. All this makes the aspect of crack identification seem to be crucial for the durability of the structure.

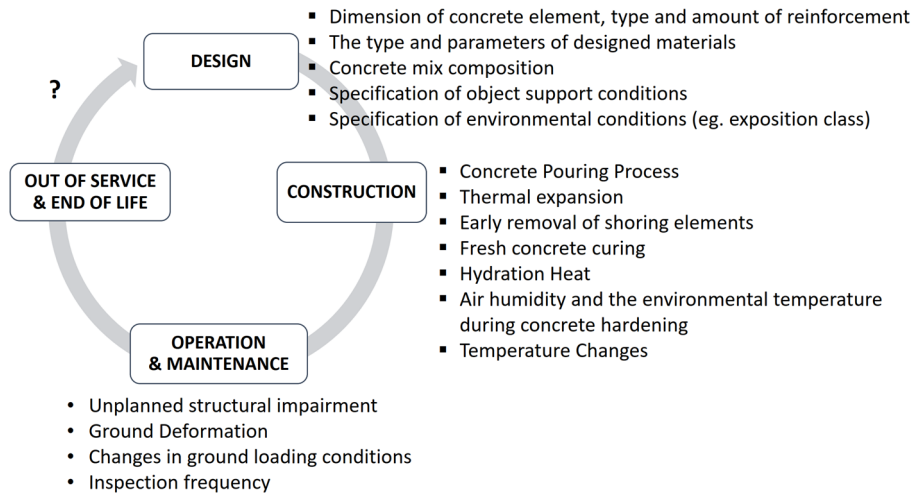


Figure 1. Examples of factors at different stages of the structural life cycle that influence the possibility of cracking.

The inspection, condition assessment and maintenance procedures for bridges are different in each country. Helmerich *et al.* (2008) describe bridge infrastructure maintenance requirements, inspection and condition assessment procedures, and ongoing testing programs. A review of bridge management system (BMS) and bridge inspection practices in China, Japan, Korea, and the US are presented in (Jeong *et al.*, 2018).

Currently, the still popular method for collecting data on concrete surface cracks is to obtain them from the results of an inspector's inspection. However, this process has many limitations (Kim *et al.*, 2015). Among other things, we can point out the costliness of this process, the time-consuming nature of the inspections performed, and the labor-intensive nature of the report preparation. Moreover, this process requires the use of specialized equipment to inspect surfaces located at height or in difficult terrain, thus posing a danger to the person performing the inspection. In addition, the process is dependent on the experience and subjective judgment of the inspector (Xu *et al.*, 2021).

It should be noted that current methods require the person performing the inspection to manually create an inspection map and mark damage locations. This further increases the labor intensity and cost of performing the inspection. Currently, in connection with the digitalization of construction, solutions have already been created to support the construction engineer and supervisor in their daily work. Kim *et al.* (2018) present an approach in which they use deep learning to simultaneously classify and locate cracks acquired with UAVs. In addition, they create a model of the bridge structure based on the point cloud and create a map of the structure on which the cracks identified by the network are marked. This makes it possible to link the results to the bridge management system (BMS) and process them automatically over time. Visualization of the detected damage on a 3D model based on photographs is also used by (Wu *et al.*, 2019).

Nowadays there is a need to use such construction surveys that allow for non-contact, quick measurements and algorithms that allow for efficient analysis of large amounts of measurement data. The algorithms of deep machine learning used to analyze data acquired by means of photogrammetric methods (especially helpful in the course of construction for inventory of disappearing works) as well as standard methods consisting in taking pictures of object damages with the use of cameras during works acceptance or periodic inspections are applicable here.

The aim of this work is to verify the possibility of using deep machine learning algorithms to assess the condition of structures on the basis of images of object damage taken with the camera, without prior preparation. The aim of the research is to show the possibilities of using this method to detect and locate cracks and to observe the rate and extent of processes causing damage. The goal is to be able to predict the development of cracks in time and space on the basis of damage images in order to prevent failures.

The use of machine learning algorithms can be a tool that will support the engineer in his daily work. Moreover, it can be particularly helpful for hard-to-reach sites, especially when combined with photogrammetric data acquisition methods. Well-crafted machine learning algorithms can help detect cracks at an early stage of their formation, where the human eye does not always perceive the danger anymore.

## II. PROBLEM DESCRIPTION

The use of deep machine learning including transfer learning for structural condition assessment from images of object damage is a rising trend. The possibilities arising from using transfer learning and comparing the performance of several proposed deep convolutional neural networks in the problem of image-based automatic detection of concrete surface cracks on a small dataset are discussed in (Słowski, 2019). A comparison of the performance of pre-trained

networks on datasets of different sizes is presented in (Ali *et al.*, 2021). Network architecture selection in the context of limited computational resources is mentioned by Su *et al.* (2020). The impact of model parameter selection and network learning rate is presented in (Li and Zhao, 2019).

Classifying damage images as cracked and non-cracked is a binary problem. Solving the problem based on convolutional neural networks requires selecting the neural network architecture and model parameters such that the measures used to evaluate model accuracy are satisfactory. Convolutional networks are typically trained using a back propagation algorithm to compute the gradient of the loss function to iteratively update the model weights.

Based on the proposed network architecture and model parameters using a training dataset, which is part of the whole dataset, the network model is trained. Based on another validation subset extracted from the whole dataset, the solution is verified. The purpose of this activity is to validate the performance of the network against data that the model has not seen before. The testing and validation process is an iterative process until such an architecture and model parameters are selected that produce stable and satisfactory classification results. The network thus trained is tested on test sets that are either a subset of the dataset on which we have been working, or is a completely independent dataset.

The problem that occurs in deep machine learning is the need for very large datasets on which the neural network is trained. Moreover, the stage of architecture selection, model parameter tuning, as well as the network learning process itself are complicated, labor-intensive and costly issues. A frequently used practice in this case is transfer learning. It consists in using the neural network model, which was previously learned on a large dataset, to solve a new problem. This makes it possible to solve problems for which we have a relatively small amount of data.

In this paper, transfer learning was used. It is based on learning a convolutional base and retraining the classifier. The convolutional base was frozen, *i.e.*, for the layers included in the convolutional base, the weights adopted in the model were not updated in subsequent training steps. The images of concrete surface cracks were passed through the selected network, and by retraining the proposed classifier, it was possible to adapt the network to the dedicated crack detection problem. The model thus trained was validated on the test set and showed satisfactory prediction results.

### III. METHODOLOGY AND COMPUTATIONAL IMPLEMENTATION

#### A. Training, validation and test datasets

The dataset used to train, validate and test the convolutional neural network model is the publicly

available dataset "Concrete Crack Images for Classification" (Özgenel, 2019). The dataset contains 40,000 images with 227 x 227 pixels with RGB channels. The dataset was based on 458 high-resolution images. These images have variance in terms of illumination conditions and surface finish. The images were divided into 2 classes: "Positive", containing images of cracked concrete surfaces, and "Negative", which is a dataset of images of non-cracked surfaces. Each class contains 20,000 images. Examples of images from this collection are shown in Figure 2 and Figure 3. This images were randomly divided into 3 subsets: train, validation, test. The images were divided in a percentage ratio of 60:20:20 (*i.e.* 24000, 8000, 8000 images). Each subset was equally divided into "Positive" and "Negative".



Figure 2. Examples of cracked surfaces ("Positive") (Özgenel, 2019).

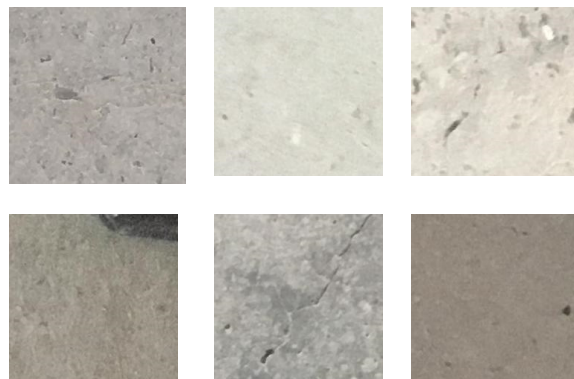


Figure 3. Examples of non-cracked surfaces ("Negative") (Özgenel, 2019).

The second dataset is the authors' own collection. The photographs of the damaged concrete surfaces were taken using a camera and a mobile phone camera and were taken without prior conditioning. The purpose of this form of data acquisition was to verify the possibility of using images taken without paying attention to the parameters and settings of the equipment used to acquire the image. This is particularly important because under construction conditions it is not always possible to have full access to the study area and to focus carefully on cropping and sharpening the image. Hence, one aspect of this work is to verify the feasibility of using deep machine learning for crack detection regardless of the quality of the

concrete surface image taken, the lighting conditions, and the type and parameter of the equipment used to capture the image.

The authors' own dataset was built from images of 16 bridge structure elements (abutments, pillars) that were segmented into 4665 sub-images with 227 x 227 pixels. The images were manually classified and labeled as "Positive" if there was a crack in the image or "Negative" if there was no crack - to maintain analogy with the dataset described above (Özgenel, 2019). Finally, 309 images of the cracked concrete surface (*i.e.*, "Positive") and 4356 images of the non-cracked surface (*i.e.*, "Negative") were obtained. The authors' own dataset consists of cracks of various dilation. It contains images with various obstructions including shadows, varying illumination, surface roughness, holes, and background contamination. Examples of images from the authors' dataset are shown in Figures 4 and 5.



Figure 4. Examples of cracked surfaces ("Positive") - authors' own dataset.

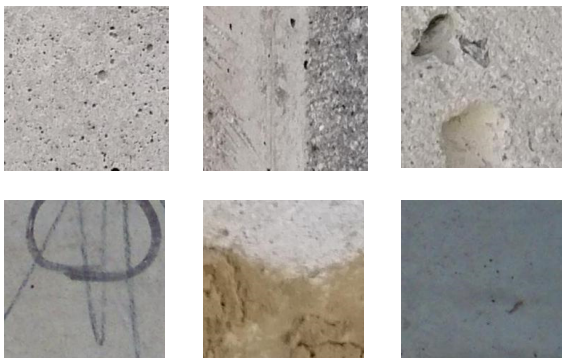


Figure 5. Examples of non-cracked surfaces ("Negative") - authors' own dataset.

### B. Architecture of convolutional neural network

The computer implementation was programmed in Python using the open-source Keras library. This library runs on the open-source TensorFlow machine learning library developed by Google.

This paper uses transfer learning using the VGG-16 network proposed by (Simonyan and Zisserman, 2015), trained on the ImageNet dataset. The VGG-16 model consists of 16 layers, including 13 convolutional layers for feature extraction and a classifier composed of three fully connected layers with a filter size of 3 × 3.

In the approach used in this study, the frozen convolutional basis of the VGG-16 model was used for feature extraction and a custom classifier was proposed. This procedure was intended to adapt the network to the dedicated problem of concrete surface crack detection. The overall architecture of the proposed CNN is shown in Figure 6.

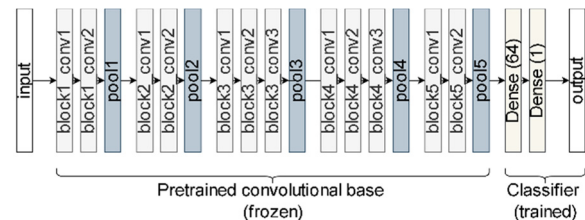


Figure 6. Proposed architecture of a convolutional neural network.

The image size at the output of the VGG16 network was (512, 7, 7), and the total number of network parameters at this stage was 14 714 688.

The proposed classifier consisted of a deep layer with ReLu activation function. Before entering the data into this layer, the vector was flattened to a one-dimensional form, because this is the form of data required by the Dense layer. Additionally, Dropout layer with probability 0,4 was used for regularization. This technique, which involves random freezing of individual neurons in the network during the learning process, allows for more accurate matching of the model to the data. In particular, this is useful for small data sets that tend to over-fit, and using dropout allows the network to be taught in a more generalized way. The second deep layer uses the Sigmoid activation function to determine the probability that the analyzed image is outlined.

As described earlier, the network learning process used a frozen convolutional base, *i.e.*, the parameters included in it were not subject to the learning process. The weights obtained for the network learned on the ImageNet dataset were adopted. Only the parameters included in the proposed classifier were trained. As part of the classifier selection, the performance of the network was tested as a function of the number of filters used in the first Dense layer, and thus the number of parameters learned in training the network. The use of 16, 32 and 64 filters in this dense layer was verified.

The total number of parameters depending on the number of dense layer filters is shown in Table 1. In addition, the table shows the number of trainable and non- trainable parameters.

Table 1. The number of model parameters

Number	Filters		
	16	32	64
Total	15 116 129	15 517 569	16 320 449
Trainable	401 441	802 881	1 605 761
Non-trainable	14 714 688		

Results showed that using a Dense layer with 64 filters produces satisfactory results. In the following section we present results for a classifier consisting of this Dense layer with 64 filters.

### C. Network training, validation and testing

Calculations were performed on a laptop with a GPU. The computations were performed on a platform with the parameters: CPU - Intel(R) Core(TM) i7-8750H, GPU - NVIDIA Quadro P1000, 16GB RAM. The use of such hardware has shown that it is not necessary to use specialized hardware to perform such analysis. Therefore, such analyses are within the range of equipment available to all the engineers.

Due to the binary nature of the problem, a binary cross-entropy loss function was used. The use of different optimizers in the training process was considered. Results show that the highest accuracy was obtained using the Adam type optimizer. Finally the Adam optimizer was used for parameter updates. A validation set was used to monitor during learning the accuracy of the model on data that the network had never seen before. This consisted of images previously extracted from the output set (Özgenel, 2019), as described in paragraph III.A The performance of the network was tested by prediction on two datasets. The first consisted of samples separated from the output set (Özgenel, 2019). The second consisted only of samples from the authors' own dataset.

Various metrics were used to evaluate the network, such as accuracy, precision, sensitivity and specificity (König *et al.*, 2022). This metrics are explained in more detail below. The symbols in the formulas denote elements of the confusion matrix, where: TP - True Positive - number of true cracked images correctly predicted as cracked, FP - False Positive - number of true non-cracked images predicted as cracked, TN - True Negative - number of true non-cracked images predicted as non-cracked, FN - False Negative - number of true cracked images predicted as non-cracked.

Accuracy can be defined as the ratio of correct model predictions to the total number of tested images, as shown in Equation 1:

$$\text{accuracy} = \frac{TP+TN}{TP+FP+TN+FN} \quad (1)$$

Precision (Eq. 2) defines how many of the images predicted as positive were predicted by the model correctly:

$$\text{precision} = \frac{TP}{TP+FP} \quad (2)$$

Sensitivity, shown in Equation 3, defines how many of all true positive images were correctly predicted by the model:

$$\text{sensitivity} = \frac{TP}{TP+FN} \quad (3)$$

Specificity (Eq. 4) defines how many of all true negative images were correctly predicted by the model:

$$\text{specificity} = \frac{TN}{TN+FP} \quad (4)$$

F1 score can be defined as the harmonic mean of precision and recall, as shown in Equation 5:

$$\text{F1 score} = \frac{2 \times \text{precision} \times \text{recall}}{\text{precision} + \text{recall}} \quad (5)$$

Because the authors' test dataset is imbalanced, a balanced accuracy metric (Eq. 6) was used to evaluate the model for this dataset. This metric is defined as the arithmetic mean of sensitivity and specificity:

$$\text{balanced accuracy} = \frac{\text{sensitivity} + \text{specificity}}{2} \quad (6)$$

The values of each metric for both test datasets are presented in the following section.

### D. Results

Verification of damage classification shown in images of cracked and non-cracked concrete surfaces for a test dataset extracted from (Özgenel, 2019) showed a 99% accuracy. The confusion matrix for this set is shown in Table 2. Using the network to classify cracks on the authors' own dataset showed a accuracy of over 91%, but because the authors' own dataset is an imbalanced dataset the balanced accuracy metric was used as more adequate. The value of balanced accuracy for the authors' own dataset is over 55%. The confusion matrix for this set is shown in Table 3. The metrics for both test datasets are shown in Table 4.

Table 2. Confusion matrix for publicly available dataset (Özgenel, 2019)

	Predicted non-cracked	Predicted cracked
True non-cracked	3996	4
True cracked	6	3994

Table 3. Confusion matrix for authors' own dataset

	Predicted non-cracked	Predicted cracked
True non-cracked	4315	41
True cracked	295	14

The analysis showed that the presented network architecture allows for high accuracy, but the architecture is not very universal. For the test dataset of images with crack character corresponding to the cracks on which the model was trained, high precision is obtained (over 99%). This is shown by the analysis

performed using the test set extracted from the public data (Özgenel, 2019). However, as the analysis performed on the authors' own data set shows, the network is able to detect mainly such cracks whose nature is similar to that of the images that were used to train the model. This is confirmed by an analysis of classification results examples for cracked images from the authors' own dataset which is shown in Figure 7.

Table 4. Metrics for test datasets [%]

	Publicly available dataset (Özgenel, 2019)	Authors' own dataset
Accuracy	99,88	91,55
Balanced accuracy	-	57,44
Precision	99,90	28,43
Sensitivity	99,85	18,12
Specificity	99,90	96,76
F1 score	99,88	22,13

The analyzed network correctly classifies images with similar crack types, but is limited in its ability to detect damage of a different nature. To obtain higher levels of accuracy, the type of damage shown in the analyzed image must belong to the hypothesis space of the model.

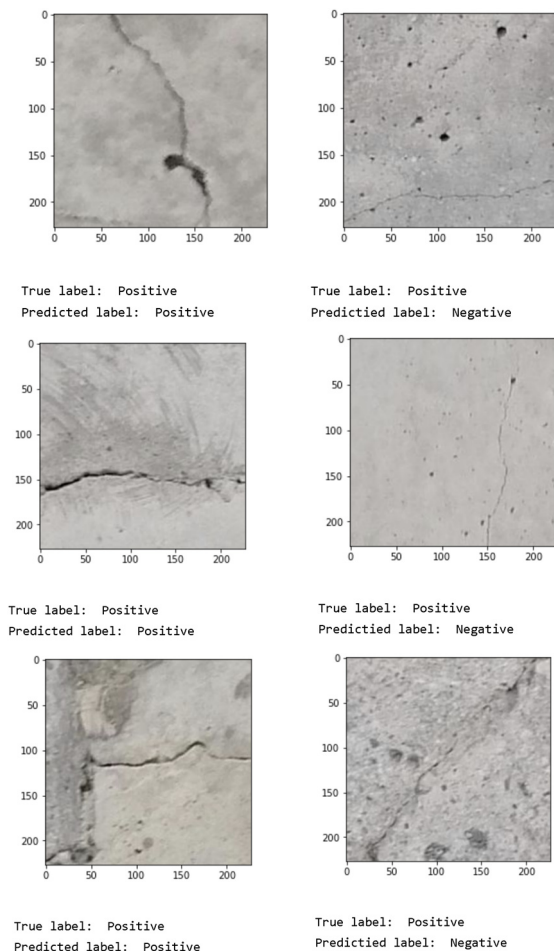


Figure 7. Examples of classification results for cracked images from the authors' own dataset.

#### IV. CONCLUSION

The crack detection is critical in the diagnosis of bridge structures. Early detection of defects allows for faster response to damage and planning of necessary repair work. This is expected to lead to a situation where the bridge structure does not need to be taken out of service. There is a need for research that allows for non-contact, high-speed measurements of objects and algorithms that allow for efficient analysis of large amounts of measurement data. It is also important to be able to store this data in a single facility management system so that you have a complete database and can observe the development of damage over time.

The application of deep machine learning to assess the condition of bridge structures based on images of structure damage is a response to these needs and one of the better developing trends today. This paper presents an example of using transfer learning to train a network based on publicly available data. The model trained on these data was used to predict damage on the authors' own dataset. The result of the research is one of the stages of work aimed at presenting a solution that would make it possible not only to detect the presence of cracks, but also to distinguish those cracks that constitute an excess of permissible norms based on their dilation value.

The results of the authors' research confirm the feasibility of using deep machine learning for cracks detection from photos. Importantly, as the results show, it is also possible to use photos that were taken with a camera or phone camera without configuring its settings or preparing the shot. This is extremely important in construction conditions or during the inspection of the object, where it is not always possible to have full access to photograph the element of interest and the possibility to take an accurate shot.

As the analysis for the applied network architecture shows it can be concluded that despite obtaining high accuracy this architecture is not very universal and the obtained results depend on whether the analyzed crack belongs to the model hypothesis space. In future steps, the authors plan to use the proposed model architecture to identify pavement cracks as having a crack character similar in size to that presented in the used publicly available dataset. In addition, other architectures will be tested to verify the possibility of finding a more universal architecture. It should allow the use of transfer learning to classify cracks regardless of their nature.

The aim of all works is to create such a tool which will be helpful for civil engineer in everyday work and will not require him/her to train network, special preparation of data. This solution will allow real-time assessment of the tested concrete surfaces with indication of the location of those damages which, in accordance with the regulations in force in a given country, are beyond the serviceability limit state and are a danger to the structure.



References

- Ali, L., Alnajjar, F., Jassmi, H.A., Gocho, M., Khan, W., and Serhani, M.A., (2021). Performance Evaluation of Deep CNN-Based Crack Detection and Localization Techniques for Concrete Structures. *Sensors* 21, 1688. DOI: 0.3390/s21051688
- Germaniuk, K., Gajda, T., Sakowski, A., Wierzbicki, T., and Kamiński, P., (2016). Bridge Structures Cracks – What Made that Phenomena so Common? *Transportation Research Procedia* 14, pp. 4030–4039. DOI: 10.1016/j.trpro.2016.05.500
- Helmerich, R., Niederleithinger, E., Algernon, D., Streicher, D., and Wiggenhauser, H., (2008). Bridge Inspection and Condition Assessment in Europe. *Transportation Research Record* 2044, pp. 31–38. DOI: 10.3141/2044-04
- Jeong, Y., Kim, W., Lee, I., and Lee, J., (2018). Bridge inspection practices and bridge management programs in China, Japan, Korea, and U.S. *Journal of Structural Integrity and Maintenance* 3, pp. 126–135. DOI: 10.1080/24705314.2018.1461548
- Kim, H., Sim, S.H., and Cho, S., (2015). Unmanned Aerial Vehicle (UAV)-powered Concrete Crack Detection based on Digital Image Processing. Presented at the 6<sup>th</sup> International Conference on Advances in Experimental Structural Engineering 11<sup>th</sup> International Workshop on Advanced Smart Materials and Smart Structures Technology, Urbana-Champaign, United States.
- Kim, I.-H., Jeon, H., Baek, S.-C., Hong, W.-H., and Jung, H.-J., (2018). Application of Crack Identification Techniques for an Aging Concrete Bridge Inspection Using an Unmanned Aerial Vehicle. *Sensors* 18, 1881. DOI: /10.3390/s18061881
- König, J., Jenkins, M., Mannion, M., Barrie, P., and Morison, G., (2022). What's Cracking? A Review and Analysis of Deep Learning Methods for Structural Crack Segmentation, Detection and Quantification. DOI: 10.48550/ARXIV.2202.03714
- Li, S., and Zhao, X., (2019). Image-Based Concrete Crack Detection Using Convolutional Neural Network and Exhaustive Search Technique. *Advances in Civil Engineering* 2019, 1–12. DOI: 10.1155/2019/6520620
- Özgenel, Ç.F., (2019). Concrete Crack Images for Classification. DOI: 10.17632/5Y9WDSG2ZT.2
- Simonyan, K., and Zisserman, A., (2015). Very Deep Convolutional Networks for Large-Scale Image Recognition. CoRR.
- Słoński, M., (2019). A comparison of deep convolutional neural networks for image-based detection of concrete surface cracks. *Computer Assisted Methods in Engineering and Science* 26, pp. 105–112. DOI: 10.24423/CAMES.267
- Su, C., and Wang, W., (2020). Concrete Cracks Detection Using Convolutional NeuralNetwork Based on Transfer Learning. *Mathematical Problems in Engineering* 2020, 1–10. DOI: 10.1155/2020/7240129
- Wu, Z.Y., Kalfarisi, R., and Systems, B., (2019). Deep Learning-based Defect Detection and Assessment for Engineering Structures. Presented at the 5<sup>th</sup> International Conference on Smart Monitoring, Assessment and Rehabilitation of Civil Structures (SMAR 2019), Potsdam, Germany.
- Xu, Z., Qian, S., Ran, X., and Zhou, J., (2021). Application of Deep Convolution Neural Network in Crack Identification. *Applied Artificial Intelligence* 1–22. DOI: 10.1080/08839514.2021.2014188
- Zhang, T., (2018). Analysis on the Causes of Cracks in Bridges. *Journal of Construction Research* 1. DOI: 10.30564/jcr.v1i1.83

## Monitoring instabilities by MT-InSAR in a mesa placed town (Arjona, Guadalquivir valley, South Spain)

Antonio Miguel Ruiz-Armenteros<sup>1, 2, 3</sup>, Mario Sánchez-Gómez<sup>2, 4</sup>, José Manuel Delgado-Blasco<sup>3</sup>, Matus Bakon<sup>5, 6</sup>, Ana Ruiz-Constán<sup>7</sup>, Jesús Galindo-Zaldívar<sup>8, 9</sup>, Milan Lazecky<sup>10, 11</sup>, Miguel Marchamalo-Sacristán<sup>12</sup>, Joaquim J. Sousa<sup>13, 14</sup>

<sup>1</sup> Department of Cartographic, Geodetic and Photogrammetry Engineering, University of Jaén, Campus Las Lagunillas s/n, 23071 Jaén, Spain, ([amruiz@ujaen.es](mailto:amruiz@ujaen.es))

<sup>2</sup> Centre for Advanced Studies in Earth Sciences, Energy and Environment (CEACTEMA), University of Jaén, Campus Las Lagunillas s/n, 23071 Jaén, Spain

<sup>3</sup> Research Group RNM-282 Microgeodesia Jaén, University of Jaén, Campus Las Lagunillas s/n, 23071 Jaén, Spain, ([jdblasco@ujaen.es](mailto:jdblasco@ujaen.es))

<sup>4</sup> Department of Geology, University of Jaén, Campus Las Lagunillas s/n, 23071 Jaén, Spain, ([msgomez@ugr.es](mailto:msgomez@ugr.es))

<sup>5</sup> insar.sk s.r.o., Slovakia, ([matusbakon@insar.sk](mailto:matusbakon@insar.sk))

<sup>6</sup> Department of Finance, Accounting and Mathematical Methods, University of Presov, Slovakia

<sup>7</sup> Instituto Geológico y Minero de España, 18006 Granada, Spain, ([a.ruiz@igme.es](mailto:a.ruiz@igme.es))

<sup>8</sup> Department of Geodynamics, University of Granada, 18071 Granada, Spain, ([jgalindo@ugr.es](mailto:jgalindo@ugr.es))

<sup>9</sup> Instituto Andaluz de Ciencias de la Tierra (CSIC-UGR), Granada, Spain

<sup>10</sup> School of Earth and Environment, University of Leeds, United Kingdom, ([M.Lazecky@leeds.ac.uk](mailto:M.Lazecky@leeds.ac.uk))

<sup>11</sup> IT4Innovations, VSB-TU Ostrava, Czechia

<sup>12</sup> Topography and Geomatics Lab. ETS ICCP, Universidad Politécnica de Madrid, 28040 Madrid, Spain, ([miguel.marchamalo@upm.es](mailto:miguel.marchamalo@upm.es))

<sup>13</sup> Universidade de Trás-os-Montes e Alto Douro, Vila Real, Portugal, ([jj Sousa@utad.pt](mailto:jj Sousa@utad.pt))

<sup>14</sup> INESC-TEC - INESC Technology and Science, Porto, 4200-465, Portugal

**Key words:** *InSAR; landslide; deformation; monitoring; mesa; satellite radar interferometry*

### ABSTRACT

Cities in Spain used to be overgrown around old towns (pre-roman, roman and medieval) constructed on topographic defensive heights of singular geological features. In the upper Guadalquivir valley, a tabular body of Miocene sediments has been eroded forming mesas where most of its population has been living since the Middle Age. As the towns grew, new neighborhoods settled towards the edges and cliffs of these mesas, in areas prone to instability. The town of Arjona is a good example of this geological-urbanistic setup, located on the tabular hill formed by clay marls topped by bioclastic limestones that protect it from erosion. Modern buildings from a few sectors of the town show important cracks, even the 16<sup>th</sup>-century bell tower has a 4° inclination indicating problems in the foundations. Multi-temporal SAR interferometry (MT-InSAR) is a powerful technique to derive displacement time series over coherent targets on the Earth associated with geological or structural instabilities phenomena. In this work, we use MT-InSAR with Sentinel-1 data to reveal that, at the present day, the periphery of Arjona is active, being recognized a large landslide in the south side of this mesa town which affects buildings and civil infrastructures. In addition, fieldwork is being carried out to investigate the sources of these instabilities.

### I. INTRODUCTION

Small cities and towns in Spain used to be integrated into a rural environment, where slope instabilities are common due to relief evolution and land management. Southern Spain is a geologically active area with an important tectonic uplift since the Pliocene (Sanz de Galdeano and Alfaro, 2004). Thus, high gradients together with soft lithologies produce slope instabilities even in areas of arid and semi-arid climate.

Cities in Spain used to be overgrown around old towns (pre-roman, roman and medieval) constructed on topographic defensive heights (Ruiz and Molinos, 1993; Castillo-Armenteros, 1998). As the towns grew, new neighborhoods settled towards the edges and cliffs, in areas with high probabilities of instability. The town of Arjona, in the Upper Guadalquivir valley, is a good example of this topographic-urbanistic setup and is subject to slope movements due to its singular topographic and geological features.

Most of the slope movements in the region are related to highly rainy events that show a return period greater than 10-20 years (Carpena *et al.*, 2021). In these events, landslides can be exhaustively followed by photogrammetry and LiDAR techniques (Fernández *et al.*, 2021), or by UAV surveys (Fernández *et al.*, 2016). Nevertheless, slow and continuous displacements must be previously identified by a technique that covers a much larger area such as the Interferometric Synthetic Aperture Radar (InSAR) technique. In this sense, the study of the highly settled towns in the Upper Guadalquivir by InSAR could provide valuable information about natural slope processes that modern urbanization has masked out and that suppose an important hazard.

Interferometric Synthetic Aperture Radar (InSAR) technique can provide more detailed land deformation mapping over larger areas than any other technique. InSAR is successfully applied for monitoring natural hazards such as volcanoes, landslides, and earthquakes/tremors. The advantages of this technique are its cost-effectiveness and very precise measurement of land deformation, and in the areas with good radar scattering characteristics, it is theoretically possible to detect even millimeter-sized surface deformation. Measurements can be done entirely retroactively by acquiring historic repeat satellite Synthetic Aperture Radar (SAR) datasets for the area of interest, and then processing the SAR data using interferometric techniques to determine changes in the distance satellite-terrain over large areas with high precision. The technique allows us to have a global outlook of the deformation phenomena occurring in a wider area, keeping at the same time the capability to measure deformation at millimeter accuracy on individual features, like dams, bridges, or buildings using multi-temporal interferometric techniques (MT-InSAR) (Crosetto *et al.*, 2016; Xue *et al.*, 2020; Ho Tong Minh *et al.*, 2020).

This paper presents the preliminary results from the application of MT-InSAR techniques to land deformation monitoring in the study of mesa towns. In particular, some deformation spots are identified in Arjona town and its temporal evolution is studied using Sentinel-1 SAR data, which is related to the geological/geomorphological processes that configure the relief. A field survey will corroborate the nature of the displacements.

## II. GEOGRAPHICAL AND GEOLOGICAL SETTINGS

The Arjona town is located in the Upper Guadalquivir valley (Figure 1) that coincides approximately with the administrative province of Jaén (south Spain). The Upper Guadalquivir includes the headwater areas from Cazorla and Segura Ranges belonging to the Betic Cordillera. Discarding these Betic mountains, the valley varies in altitude from about 200 to 1000 m, with slopes generally below 10°.



Figure 1. Location of Arjona town in the province of Jaén (South Spain). Lat: 37.93652°, Lon: -4.0601° (Source: Google Maps).

The Guadalquivir valley is developed over the Betic foreland basin, which was an NE-SW elongated marine basin from the Lower Miocene until the Pliocene (García-Castellanos *et al.*, 2002). The Guadalquivir basin shows two contrasting margins. Towards the south, tectonic units from the Betic Thrust Front formed an accretionary prism imbricating sediments of the basin (Pérez-Valera *et al.*, 2017). Towards the north, Mesozoic and Miocene sediments of the basin above the Variscan basement form a near-horizontal cover, the so-called Tabular Cover, slightly folded and faulted (Pedrera *et al.*, 2013). Most of the deformation occurred during the Miocene (Pérez-Valera *et al.*, 2017), after which vertical isostatic readjustment caused regional uplift (Sanz de Galdeano and Alfaro, 2004). Nevertheless, there are evidences of Pleistocene and Holocene horizontal and vertical tectonic displacements (Sánchez-Gómez and Pérez-Valera, 2018), including an intense seismic activity (Pedrera *et al.*, 2013; Sánchez-Gómez *et al.*, 2014; Morales *et al.*, 2015).

The Miocene sedimentation consists in a sequence of alternances of sandstones and marls with large volumes of active clays, and relatively resistant layers of calcarenites (Martínez del Olmo and Martín-Sánchez, 2019). When the uplift of the basin after Pliocene exposed the sediments to erosion, the calcarenite, or thick sandstone, strata formed mesas along the Guadalquivir valley. These mesas are up to 400 m higher than the present Guadalquivir talweg, although abrupt slopes are only a few tens of meters high (Figure 2 top). The town of Arjona occupies one of these mesas of approximately 75 ha, with cliffs or steep slopes on the north and southeast sides, and a less defined border towards the west (Figure 2 bottom).

The Miocene marls below the resistant layers include a more than 140 m thick sequence of the so-called Blue Marls, a clay-rich formation with associated geotechnical problems on all the upper Guadalquivir valley. The Blue Marls in the region have an average of clay between 28% and 59%, and activity between 0.55

and 0.88 (Mellado *et al.*, 2021). Geotechnically, these can be classified as inorganic clays of high plasticity (CH). This geotechnical context produced historical ground instabilities, as can be deduced from the 16<sup>th</sup> century bell tower with a 4° deviation from the vertical.

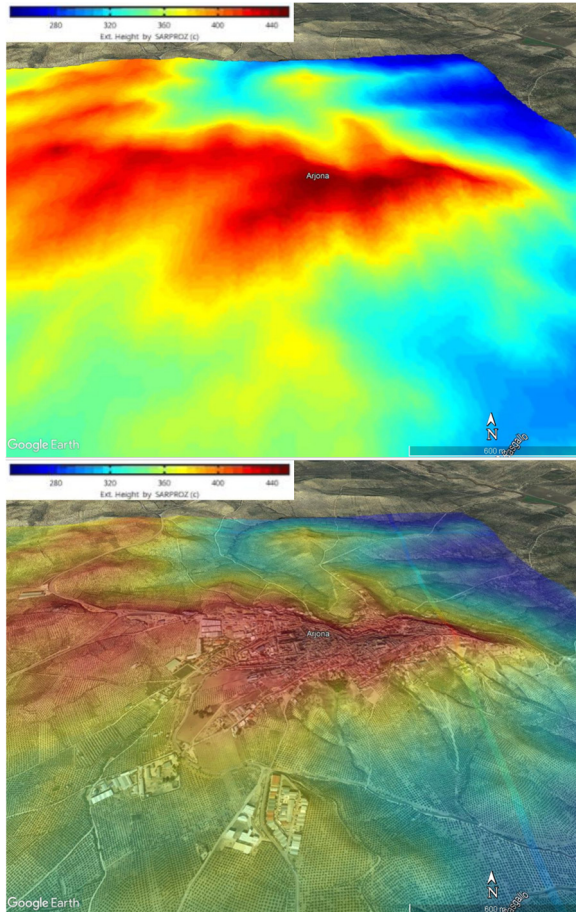


Figure 2. Top. 3D view of the 1-arcsec SRTM DEM over the study area. Heights range between 250 and 450 m. Bottom. 3D view of Arjona and the SRTM DEM. Arjona is located on the mesa formed in the highest altitudes of this area. (Source: Google Maps).

### III. DATA AND METHODS

#### A. InSAR data

We used Sentinel-1A/B SLC data in our study. The ascending stack is composed of 314 IW images from Track 74 in the period March 3, 2015 – February 23, 2021, with an average incidence angle of 43.8443°. The descending dataset is composed of 340 IW images from Track 81 in the period March 16, 2015, to October 4, 2021, with an average incidence angle of 39.3819°. In both cases, the ground sampling is in the order of 3.5 x 13.8 m. Figure 3 shows the information of the ascending and descending datasets.

#### B. Multi-temporal InSAR

For processing the Sentinel-1 ascending and descending datasets we used a Multi-temporal time series analysis (MT-InSAR) using SARPROZ software,

following the classical PS-InSAR approach (Ferretti *et al.*, 2001; Kampes, 2006).

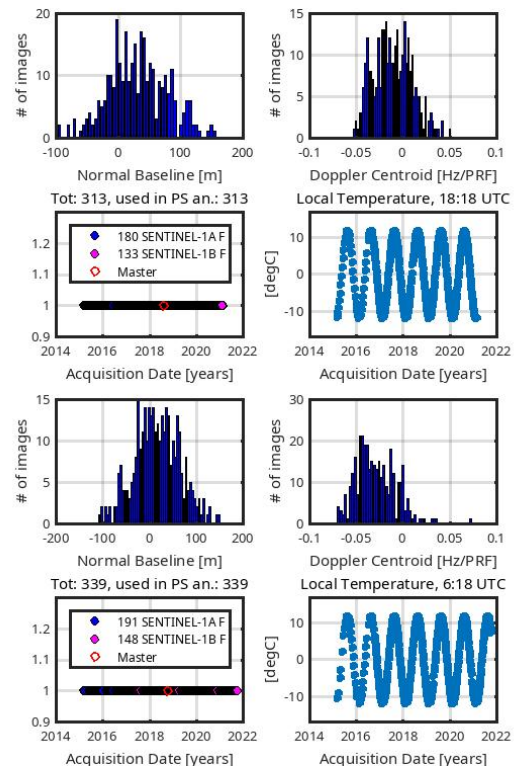


Figure 3. Information about the ascending (top) and descending (bottom) datasets. For both, the normal baseline and Doppler centroid plots are shown, together with the acquisition date and the synthetic temperature sinusoid for each acquisition time.

The objective of the PS-InSAR technique is to identify stable scatterers in a series of images and to separate the different phase components to isolate the phase displacement from the others, such as the atmospheric disturbance, topography, and flat-Earth terms. These stable scatterers, named Persistent Scatterers (PS), must remain physically stable along the period of study covered by the image stack, so they have high phase stability, and has to be smaller in size than the resolution cell, as they have a strong backscatter reflection of the incident wave to the satellite, avoiding the geometric decorrelation. The technique is particularly useful in urban environments because the man-made elements, such as buildings, road, railways, or exposed rocks, are not affected by geometrical and temporal decorrelation (Mazzanti *et al.*, 2015).

For each dataset, the first step is co-registering all the images with respect to a master image, selected by minimizing the temporal and perpendicular baselines in order to maximize the temporal coherence. The image acquired on August 2, 2018, was selected for the ascending dataset and on October 14, 2018, for the descending one (Figure 4).

After co-registering each dataset, the reflectivity map, that is, the temporal average of all the images in the stack, and the amplitude stability index (ASI) are computed. ASI is computed as 1-DA, where DA is the

amplitude dispersion index. DA is a measure of phase stability and is computed as the ratio between the standard deviation of a pixel and the mean amplitude value. If a pixel has a high amplitude, that is, small DA, similar in all the images, is expected to have minor phase dispersion than if it has low amplitude. Figure 5 shows the reflectivity maps for each dataset. It can be noted the low reflectivity of the terrain surrounding the town due to the fact that it is completely covered with olive tree plantings (Figure 1).

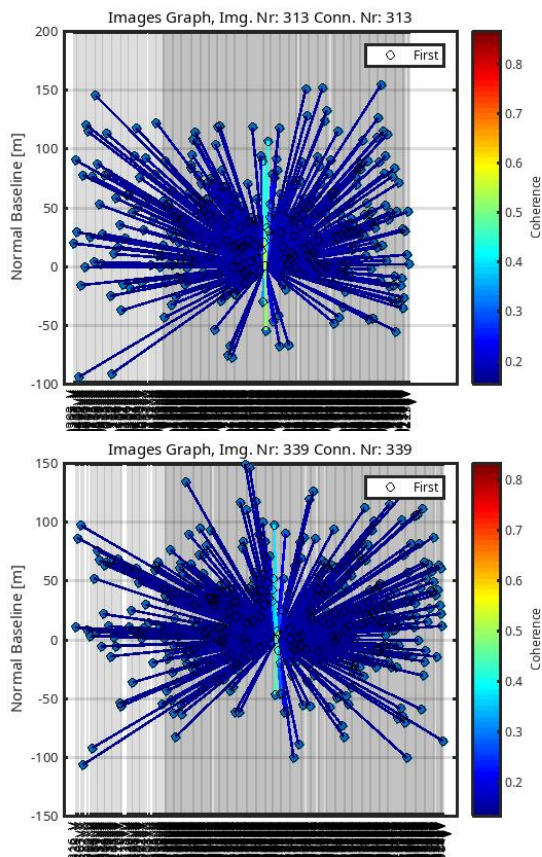


Figure 4. Normal vs. temporal baseline plots for the ascending (top) and descending (bottom) datasets. The ascending dataset is composed of 314 acquisitions from Track 74 in the period March 3, 2015 – February 23, 2021. The descending dataset is composed of 340 acquisitions from March 16, 2015, to October 4, 2021.

To remove the topographic phase component and geocode the results, we used the SRTM 1-arcsec DEM with 30 m resolution. After these initial steps, the Atmospheric Phase Screen (APS) is estimated based on the fact that the atmosphere is spatially but not temporally correlated, one of the main advantages of the MT-InSAR techniques. For this estimation, an initial spatial network is formed by an initial selection of PS candidates (PSC). The selection is done using the ASI index as phase stability with a threshold of 0.75. This network is used to estimate the DEM error (residual topographic phase term) and the deformation rate as the unknown parameters for each connection between two PSCs, maximizing a periodogram (Perissin *et al.*,

2012). To derive the deformation rates we assumed a linear model.

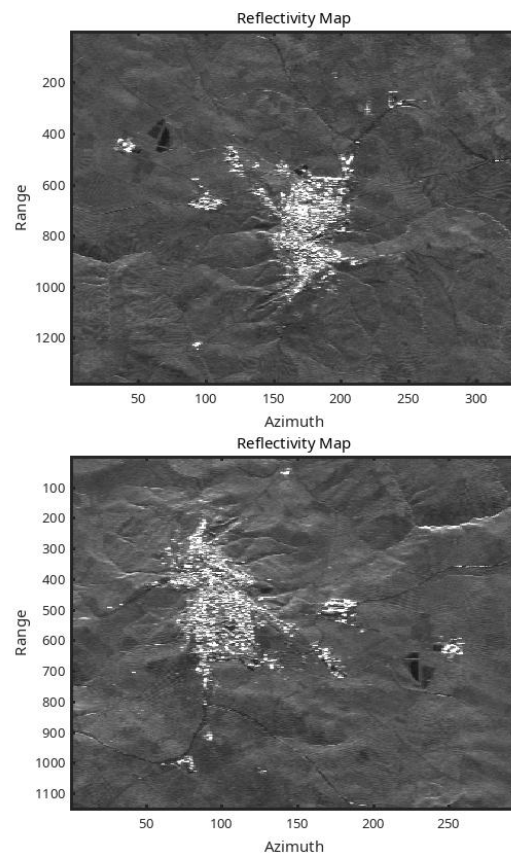


Figure 5. Reflectivity map for the ascending (top) and descending (bottom) datasets. They are shown in radar coordinates.

Phase differences are relative both in time and space, so, these deformation rates are computed with respect to a reference point supposedly stable and selected in this case in the center of the town. In the APS estimation, for the estimation of the atmospheric signal in the master image, the average residual phase is computed for each PSC after the correction for the modeled parameters. Using high-pass filtering, the atmospheric signal of each slave image and the phase noise are separated from the un-modeled deformation signal. To increase the density of PS, after the APS estimation, a second selection of PS is done based on a threshold, in this case, a lower value of ASI. Again, to re-estimate the unknown parameters, that is, the residual heights and velocity rates, another maximization of the periodogram is carried out. The final result is the height and the mean Line-of-Sight (LOS) velocity for each PS. The final selection of PS is filtered out based on the temporal coherence, which is a function of the residual phase noise.

#### IV. RESULT AND DISCUSSION

After the MT-InSAR analysis, the mean line-of-sight (LOS) velocity maps are derived for each dataset (Figure 6).

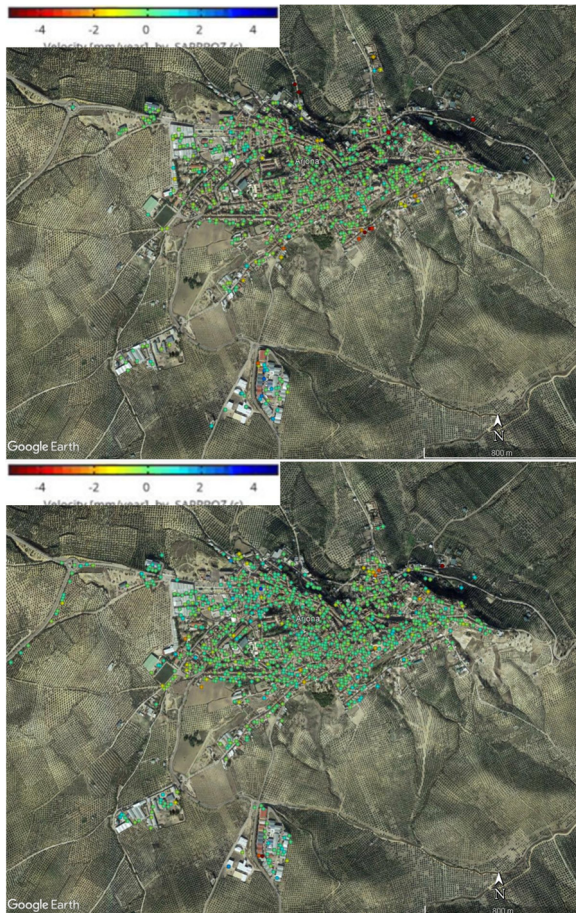


Figure 6. Mean LOS velocity map for the ascending (top) and descending (bottom) datasets.

Three sectors with a near-continuous movement have been identified: the southeast shoulder, the north foot-slope, and the northeast slope. Three time series plots are shown for these three areas respectively in Figure 7.

The movements of the southeast shoulder (Figure 7 top) can be interpreted as those of the crown of a large single mass movement. Almost all the houses of the street show cracks consistent with an incipient south-faced landslide (Figure 8), although the owners are not aware of this fact, and blame poor foundations.

The second sector, the north foot-slope (Figure 7 bottom), is situated in an area with limited inclination, and in the preliminary field survey, movements could be attributed to some kind of subsidence related to the operation of an irrigation well, located near to the observed targets. The causes of the northeast slope displacements (Figure 7 middle) are less clear, and it cannot be established a specific type of slope movement (*v.g.* creeping, local landslide). Nevertheless, the effects observed in the field are evident (Figure 9) and congruent with most of them.

All the described displacements have a velocity of very few mm/year. They occurred after 2015, a period particularly dry in the region. Recent studies (Carpena *et al.*, 2021) show that landslides and erosion in the Upper Guadalquivir are associated with recurrent wet periods that include rainfall events with a return period

between 5 to 20 years. Thus, in the next foreseeable rainy event, it can be expected that the velocity of movement in the observed sectors will increase dramatically, producing even catastrophic episodes.

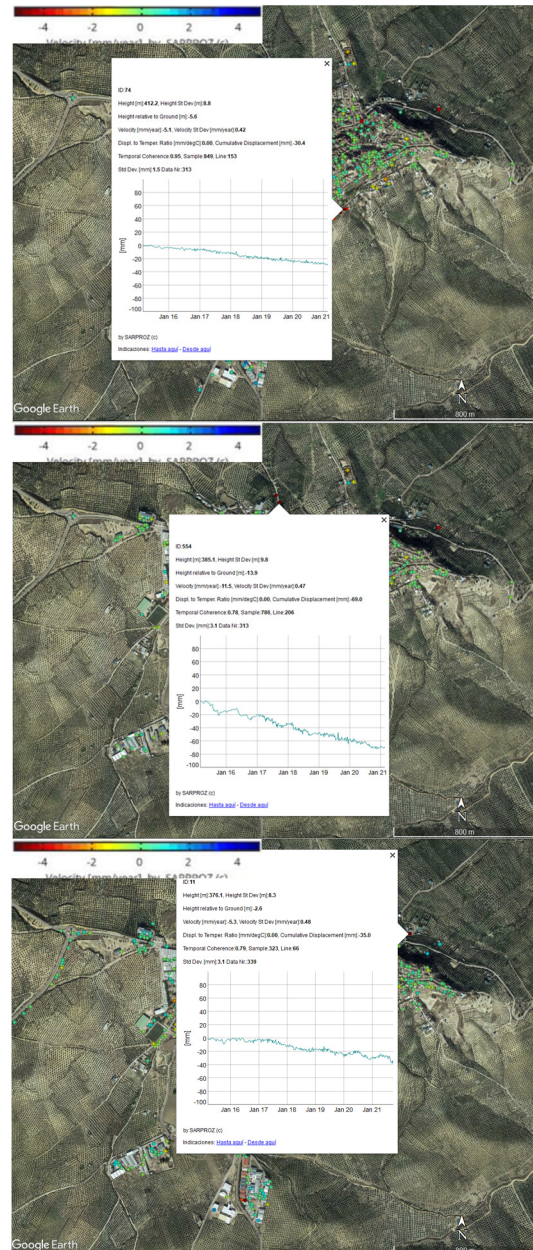


Figure 7. Time series plots of the LOS displacement for the three identified areas, the southeast shoulder (top), the northeast slope displacements (middle), and the north foot-slope (bottom).

## V. CONCLUSIONS

MT-InSAR technique demonstrates the utility to detect silent slope processes. The good and stable reflectors found in the rural towns allow us to distinguish slow but continuous displacements and identify the geomorphological processes that originate them, particularly in historical villages grown above mesa hills. Vertical and horizontal movements are interpreted by the inhabitants as their own foundation problems, but they are unaware of the scope of the

processes in which they are involved. Then MT-InSAR should be considered a helpful tool for the risk assessment, and prevent catastrophic and recurrent episodes during rainfall events.



Figure 8. Cracks in a build from the southeast shoulder sector. The wall shown is oriented N160°E (north to the left), the observed displacement being strictly parallel to this orientation.



Figure 9. Cracks in a build from the northeast slope sector. The shown wall is oriented N145°E (northwest to the right). Other cracks can be seen in different walls of the same construction, not visible in the picture.

## VI. ACKNOWLEDGEMENTS

Sentinel-1A/B data were freely provided by ESA through the Copernicus Programme. Data have been processed SARPROZ (Copyright (c) 2009-2022 Daniele Perissin). The satellite orbits are from ESA Quality control Group of Sentinel-1. Research was supported by: (a) Project “Identificación de riesgos geológicos en

la provincia de Jaén mediante satélites de observación de la Tierra” from Instituto de Estudios Giennenses, Diputación Provincial de Jaén (2021-2022); (b) POAIUJA-2021/2022 and CEACTEMA from University of Jaén (Spain); (c) the convene “Risks associated to the Road Network of the Jaén Province” of the Jaén Provincial Council; and RNM-282 and RNM-325 research groups from the Junta de Andalucía (Spain). We thank M.M. Jiménez-Cañaveras for her assistance in the field work.

## References

- Carpena, R., Tovar-Pescador, J., Sánchez-Gómez, M., Calero, J., Mellado, I., Moya, F., and Fernández, T., (2021). Rainfall-induced landslides and erosion processes in the road network of the Jaén Province (Southern Spain). *Hydrology* 8, 100. DOI: 10.3390/hydrology8030100
- Castillo-Armenteros, J.C., (1998). *La Campiña de Jaén en época emiral, siglo VIII-X*. Universidad de Jaén, 326 pp.
- Crosetto, M., Monserrat, O., Cuevas-González, M., Devanthéry, N., and Crippa, B., (2016). Persistent scatterer interferometry: A review. *ISPRS Journal of Photogrammetry and Remote Sensing*, 115, pp. 78–89. DOI: 10.1016/j.isprsjprs.2015.10.011.
- Fernández, T., Pérez, J.L., Cardenal, F.J., Gómez, J.M., Colomo, C., and Delgado, J., (2016). Analysis of Landslide Evolution Affecting Olive Groves Using UAV and Photogrammetric Techniques. *Remote Sensing* 8, 10: 837. DOI: 10.3390/rs8100837
- Fernández, T., Pérez-García, J.L., Gómez-López, J.M., Cardenal, F.J., Moya, F., and Delgado, J., (2021). Multitemporal Landslide Inventory and Activity Analysis by Means of Aerial Photogrammetry and LiDAR Techniques in an Area of Southern Spain. *Remote Sensing* 13, 11: 2110. DOI: 10.3390/rs13112110
- Ferretti, A., Prati, C., and Rocca, F., (2001). Permanent Scatterers in SAR interferometry. *IEEE Trans. Geosci. Remote Sens.*, 39, 8–20.
- García-Castellanos, D., Fernández, M., and Torné, M., (2002). Modeling the evolution of the Guadalquivir foreland basin (southern Spain). *Tectonics*, 21, 1018.
- Ho Tong Minh, D., Hanssen, R., and Rocca, F., (2020). Radar Interferometry: 20 Years of Development in Time Series Techniques and Future Perspectives. *Remote Sensing*, 12; 1364.
- Kampes, B.M., (2006). *Radar Interferometry*; Springer: Dordrecht, *The Netherlands*.
- Martínez del Olmo, W., and Martín Sánchez, D., (2019). Surcos erosivos, sistemas de turbiditas y episodios climáticos en el Tortonense y Messiniense de la Cuenca del Guadalquivir (SO de España). *Rev. la Soc. Geológica España* 32, pp. 97–112.
- Mazzanti, P., Perissin, D., and Rocca, A., (2015). Structural health monitoring of dams by advanced satellite SAR interferometry: investigation of past processes and future monitoring perspectives. In 7th International Conference on Structural Health Monitoring of Intelligent Infrastructure, Torino, Italy.
- Mellado, J.I., Calero, J.A., Sánchez-Gómez, M., Fernández, T., Carpena, R., and Pérez de la Torre, A., (2021).

- Caracterización litogeotécnica de las margas del Mioceno Superior del Alto Guadalquivir. In: Errandonea-Martín *et al.* (Eds.), *X Congreso Geológico de España*. Sociedad Geológica de España, Vitoria, p. 518.
- Morales, J., Azañón, J.M., Stich, D., Roldán, F.J., Pérez-Peña, J.V., Martín, R., Cantavella, J.V., Martín, J.B., Mancilla, F., and González-Ramón, A., (2015). The 2012–2013 earthquake swarm in the eastern Guadalquivir basin (South Spain): A case of heterogeneous faulting due to oroclinal bending. *Gondwana Res.* 28, pp. 1566–1578. DOI: 10.1016/j.gr.2014.10.017
- Pedraza, A., Ruiz-Constán, A., Marín-Lechado, C., Galindo-Zaldívar, J., González, A., and Peláez, J.A., (2013). Seismic transpressive basement faults and monocline development in a foreland basin (Eastern Guadalquivir, SE Spain). *Tectonics* 32, 2013TC003397. DOI: 10.1002/2013TC003397
- Pérez-Valera, F., Sánchez-Gómez, M., Pérez-López, A., and Pérez-Valera, L.A., (2017). An evaporite-bearing accretionary complex in the northern front of the Betic-Rif Orogen. *Tectonics* 36, pp. 1006–1036. DOI: 10.1002/2016TC004414
- Perissin, D., Wang, Z., and Lin, H., (2012). Shanghai subway tunnels and highways monitoring through Cosmo-SkyMed Persistent Scatterers. *ISPRS J. Photogramm. Remote Sens.* 2012, 73, pp. 58–67.
- Ruiz, A., and Molinos, M., (1993). *Los Iberos. Análisis arqueológico de un proceso histórico*. Crítica, Barcelona. 325 pp.
- Sánchez-Gómez, M., and Pérez-Valera, F., (2018). Evidence of recent tectonics (Late Pleistocene) at the Betic Cordillera-Guadalquivir Basin boundary (province of Jaén). In: Canora, C., Martín, F., Masana, E., Pérez, R., Ortuño, M. (Eds.), *III Reunión Ibérica Sobre Fallas Activas y Paleosismología*. Alicante (Spain), pp. 107–110.
- Sánchez-Gómez, M., Peláez, J.A., García-Tortosa, F.J., Pérez-Valera, F., and Sanz de Galdeano, C., (2014). La serie sísmica de Torreperogil (Jaén, Cuenca del Guadalquivir oriental): evidencias de deformación tectónica en el área epicentral. *Rev. la Soc. Geol. España* 27, pp. 301–318.
- Sanz de Galdeano, C., and Alfaro, P., (2004). Tectonic significance of the present relief of the Betic Cordillera. *Geomorphology* 63, pp. 175–190. DOI: 10.1016/j.geomorph.2004.04.002
- Xue, F., LV, X., Dou, F., and Yun, Y., (2020). A Review of Time-Series Interferometric SAR Techniques. A tutorial for surface deformation analysis. *IEEE Geoscience and Remote Sensing Magazine*. March 2020.



## Forecasting post-earthquake rockfall activity

Michael J. Olsen<sup>1</sup>, Chris Massey<sup>2</sup>, Ben Leshchinsky<sup>1</sup>, Joseph Wartman<sup>1</sup>, Andrew Senogles<sup>1</sup>

<sup>1</sup> Oregon State University, 101 Kearney Hall, Corvallis, OR 97333, USA, ([michael.olsen@oregonstate.edu](mailto:michael.olsen@oregonstate.edu); [ben.leshchinsky@oregonstate.edu](mailto:ben.leshchinsky@oregonstate.edu); [wartman@uw.edu](mailto:wartman@uw.edu); [senoglea@oregonstate.edu](mailto:senoglea@oregonstate.edu))

<sup>2</sup> GNS Science, 101 Kearney Hall, Corvallis, OR 97333, USA, ([C.Massey@gns.cri.nz](mailto:C.Massey@gns.cri.nz))

**Key words:** *lidar; rockslope; monitoring; erosion; earthquakes*

### ABSTRACT

Important infrastructure such as highways or railways traverse unstable terrain in many mountainous and scenic parts of the world. Rockfalls and landslides result in frequent maintenance needs, system unreliability due to frequent closures and restrictions, and safety hazards. Seismic activity significantly amplifies these negative economic and community impacts by generating large rockfalls and landslides as well as weakening the terrain. This paper interrogates a rich database of repeat terrestrial lidar scans collected during the Canterbury New Zealand Earthquake Sequence to document geomorphic processes as well as quantify rockfall activity rates through time. Changes in the activity rate (spatial distribution) and failure depths (size) were observed based on the Rockfall Activity Index (RAI) morphological classification. Forecasting models can be developed from these relationships that can be utilized by transportation agencies to estimate increased maintenance needs for debris removal to minimize road closures from rockfalls after seismic events.

*This contribution was selected by the Scientific Committee for publication as an extended paper in the Journal of Applied Geodesy <https://www.degruyter.com/journal/key/jag/html>*

## Monitoring of underwater animal forests: geometry and biometry

Paolo Rossi<sup>1</sup>, Cristina Castagnetti<sup>1</sup>, Stefano Cattini<sup>1</sup>, Giorgio Di Loro<sup>1</sup>, Francesca Grassi<sup>1</sup>,  
Luigi Parente<sup>1</sup>, Sara Righi<sup>1,2</sup>, Luigi Rovati<sup>1</sup>, Roberto Simonini<sup>2</sup>, Alessandro Capra<sup>1</sup>

<sup>1</sup> Engineering Department “Enzo Ferrari”, University of Modena and Reggio Emilia, 41121 Modena MO, Italy, ([paolo.rossi@unimore.it](mailto:paolo.rossi@unimore.it); [cristina.castagnetti@unimore.it](mailto:cristina.castagnetti@unimore.it); [stefano.cattini@unimore.it](mailto:stefano.cattini@unimore.it); [giorgio.diloro@unimore.it](mailto:giorgio.diloro@unimore.it); [francesca.grassi94@unimore.it](mailto:francesca.grassi94@unimore.it); [luigi.parente@unimore.it](mailto:luigi.parente@unimore.it); [sara.righi@unimore.it](mailto:sara.righi@unimore.it); [luigi.rovati@unimore.it](mailto:luigi.rovati@unimore.it); [alessandro.capra@unimore.it](mailto:alessandro.capra@unimore.it))

<sup>2</sup> Life Sciences Department, University of Modena and Reggio Emilia, 41121 Modena MO, Italy, ([roberto.simonini@unimore.it](mailto:roberto.simonini@unimore.it))

**Key words:** *high resolution; UW animal forest; deformation monitoring; photogrammetry; fluorescence; ROV*

### ABSTRACT

The development and testing of innovative technologies and automated data analysis methodologies offer tools for investigations in numerous scenarios including the monitoring of complex marine ecosystems and the direct and indirect effects of climate change on natural heritage. In the underwater environment, the creation of products with accurate metric and colorimetric content is a scientific and technological challenge, that can offer tools for new investigations including the monitoring of ecosystems and the study of biodiversity. The research group developed a technological solution consisting of a remotely operating platform and a measuring system that includes RGB and fluorescence optical sensors for the 3D reconstruction of the underwater environment and the study of the health-state of investigated species. The proposed solution aspires to high-accuracy multiscale reconstruction of underwater animal forests with a special focus on metric content. Methodologies and technical solutions for the management and calibration of the system have been developed: the design of proper calibration frames and the fluorescence sensor, the choice of a proper illumination system, the implementation of the system on a customizable Remotely Operating Vehicle, the integration of the different sensors, the combination of metric and colorimetric results for monitoring the occurred deformations and the health status. The results of laboratory activities and preliminary tests on field tests are discussed.

### I. INTRODUCTION

The creation of 3D products with accurate metric and colorimetric content for the reconstruction of the underwater environment represents a scientific and technological challenge that may offer new tools for investigations in numerous contexts, including the study of biodiversity and the monitoring of ecosystems such as the marine animal forests (Rossi *et al.*, 2020).

Animal forests are seabed communities dominated by sessile filter feeders, including sponges, bivalves, gorgonians, and corals. They have a high naturalistic and tourist-cultural value hosting a wide range of species and creating complex and spectacular underwater landscapes (Rossi *et al.*, 2017). These ecosystems are threatened by climatic and anthropogenic pressures acting on local and global scales (Guarnieri *et al.*, 2016). Among the species at risk, the scleractinian *Cladocora caespitosa* (the only endemic bioconstructor coral in the Mediterranean Sea) and the gorgonian *Eunicella singularis* are habitat formers threatened by seawater warming. Thermal anomalies can cause stress and increase mass mortality events, altering the structure of animal forests with effects on the entire associated communities (Heron *et al.*, 2016; Kersting *et al.*, 2013). The study and analysis of habitat formers need the implementation of new

observation systems to be mounted on underwater drones or used by divers, and the definition of high-resolution mapping procedures based on new survey methodologies. *C. caespitosa* and *E. singularis* are zooxanthellate species that emit green fluorescence. Thus, their health state could be assessed by analyzing both intensity of fluorescence and natural color and investigating the 3D complexity of their skeleton. This contribution will deal with photogrammetry, which allows a non-invasive investigation capable of returning metric and colorimetric information of the detected object (Drap *et al.*, 2015; Storlazzi *et al.*, 2016); and fluorescence and reflectance, which are widely used to assess the health of plants and other organisms, but have still not been commonly employed in underwater investigations (Eyal *et al.*, 2015).

The traditional photogrammetric technique is based on stereoscopy, although its application for underwater surveys is tricky due to several issues related to the acquisition of images and their processing. Recently, Structure from Motion (SfM) techniques have enhanced photogrammetric 3D reconstruction also in the underwater environment (Figueira *et al.*, 2015; Shortis *et al.*, 2015). The use of computer vision algorithms allowed a simplification of images acquisition, moving the camera around the object (Lavy

*et al.*, 2015). However, if the purpose of the 3D reconstruction is the measurement of geometric parameters of benthic organisms or the monitoring of deformations over time, it is also necessary to guarantee metric and georeferenced products, that require the installation of targets and ground control points with known coordinates. Some experiments (Burns *et al.*, 2017; Raoult *et al.*, 2017; Nocerino *et al.*, 2020; Rossi *et al.*, 2020) have been carried out in submerged environments for the monitoring of the seabed and the health of corals, but the methodology is still little applied and has not been scientifically validated yet.

Within this contribution, the authors show the first stages of the design and development of a measuring system integrating optical sensors capable of acquiring natural color (RGB) and fluorescence images. These instrumentations are useful for the 3D reconstruction of the submerged environment and the state of health of corals and gorgonians. The aim of the research project is the implementation and testing of new methodologies and sensors for monitoring marine ecosystems with high-resolution data over time. Besides, also the evaluation of cost-effectiveness, safety, and repeatability of these environmental observations will be investigated, as the work of divers is often limited and endangered by depth and difficulty of exploration. The general setup and usability of the prototype of sensors were initially assessed at sea by divers and integrated on a submarine Remotely Operating Vehicle (ROV) (after referred to as “on-field test”). Then, its performances were further tested and validated in controlled conditions in an aquarium (after referred to as “laboratory test”).

## II. CASE STUDY

On-field tests were run on small colonies of the corals *Astroides calycularis* and *C. caespitosa*, and the gorgonian *E. singularis* (Figure 1). Organisms were collected by SCUBA diving at San Vito Lo Capo (Trapani, Southern Tyrrhenian Sea, Italy) among those accidentally detached from the seabed during fishing operations or storms. The on-field measuring site was created attaching the base of corals and gorgonians on metal nets with an epoxy resin (TUNZE Coral Gum Instant). Then, the nets were fixed on bricks, which allowed to raise the target organisms from the bottom and constituted a 3D well-defined measuring site. At the end of the on-field tests, the organisms were transferred to the aquarium for laboratory tests. There, each colony was fixed on stable supports and detected individually.

## III. METHODS AND MATERIALS

### A. Camera and housing

Both the on-field (seawater) and laboratory acquisitions of RGB images for 3D reconstruction were

performed with a CANON 2000D Reflex camera and 18-55 mm EFS lens. The resolution of 24.1 MPixels and the short distances allowed the detection of numerous details of the investigated organisms and the generation of a high-resolution photogrammetric reconstruction. On-field, the turbidity of water suspended materials and the light attenuation given by the water medium confined the acquisition distances to 2 m.

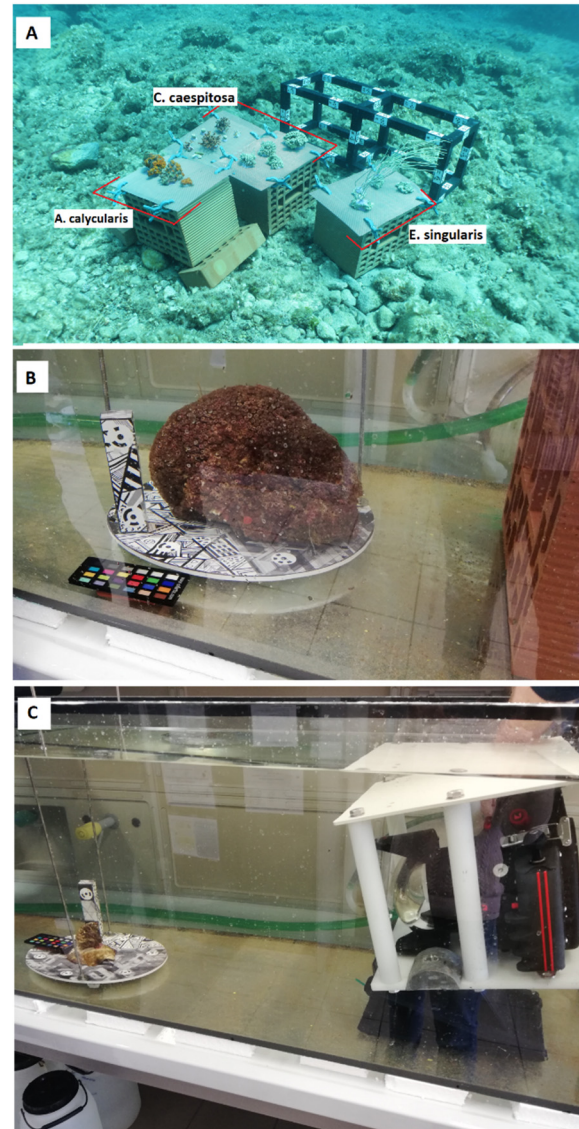


Figure 1. Survey and investigated organisms. A: on-field test site, with corals and gorgonians fixed on nets placed on bricks next to the calibration frame (parallelepipedon). B: laboratory test with the calibration plate, a color checker, and a colony of *C. caespitosa*. C: overall equipment employed for the photogrammetric survey during laboratory tests: the calibration plate with a coral and the color checker on the left, and the underwater housing with the camera on a support on the right.

The camera was placed in an underwater housing equipped with a dome port (Easy Dive LEO3). This housing was chosen because of its durability and versatility, the electronic transmission of the commands, and the compatibility with several models

and series of cameras. The use of a dome port allowed a reduction of image distortions and the achievement of accurate results in the photogrammetric reconstruction. Indeed, several studies demonstrated that flat ports perform worse than the dome, providing higher image residuals, and lower precision and accuracy in object space (Menna *et al.*, 2016; 2017).

### B. Calibration frame

Photogrammetric processing requires external references to obtain a scaled and accurate 3D reconstruction and the reduction of distortion effects due to errors in images' relative orientation. External references are also defined as Ground Control Points (GCPs) and often consist of targets. In air/terrestrial applications, coordinates of GCPs are generally detected with traditional survey methodologies (*e.g.*, GNSS system). In the underwater environment, it is not possible to implement traditional solutions, so the use of fixed points, objects of known dimensions or known distances, is largely adopted (Capra *et al.*, 2017; Rossi *et al.*, 2020). In this study, two different reference frames were used to constraint photogrammetric reconstruction: in the on-field test, a parallelepipedon (80 cm large, 30 cm height and long made of HDPE material) with 100 targets of known position (see Figure 1A); in laboratory tests, a 30 cm diameter plate with 12 targets printed in known positions (see Figure 1B and 1C). In both cases, a homogeneous and 3D distribution of the targets was employed.

### C. 3D reconstruction and deformation monitoring

Image acquisition was designed to optimize the photogrammetric processing and obtain high-resolution results: high redundancy, different viewing angles, natural light conditions, and automatic focus were set. The acquired images were then processed, together with metric constraints, in the SfM photogrammetry software Agisoft Metashape (v. 1.6.1, [www.agisoft.com](http://www.agisoft.com)) that is largely used for activities in the underwater environment (Menna *et al.*, 2019; Bayley and Mogg, 2020; Rossi *et al.*, 2020; Ventura *et al.*, 2022). The processing took the following steps: image alignment (highest settings); targets collimation, integration with reference coordinates, optimization of alignments; dense cloud creation (highest settings, aggressive noise filter); automatic filtering of low accurate points; generation of textured meshes.

The image acquisition geometries were differently designed for on-field and laboratory tests. In particular, the key points consisted of:

- On-field, a time-lapse of 5 s was set up for the automatic acquisition of images. The ROV or the divers followed circular trajectories around the object, maintaining a constant distance of about 1–2 m and changing the angle of view in order to avoid occlusions (Figure 2A).

- In the laboratory, during the acquisition, the camera was mounted over a specific support, while the object was slightly rotated after each shoot (10° to 15°), and the pitching angle of the camera was manually adjusted in order to reduce occlusions and provide a complete reconstruction (Figure 1C, Figures 2B and 2C). Considering the results of on-field tests, a color checker was positioned inside the aquarium as a reference for color variability, allowing to correct the effects of water medium (Bianco *et al.*, 2015) and the detection of changes in colony health status (Figures 1B and 1C).

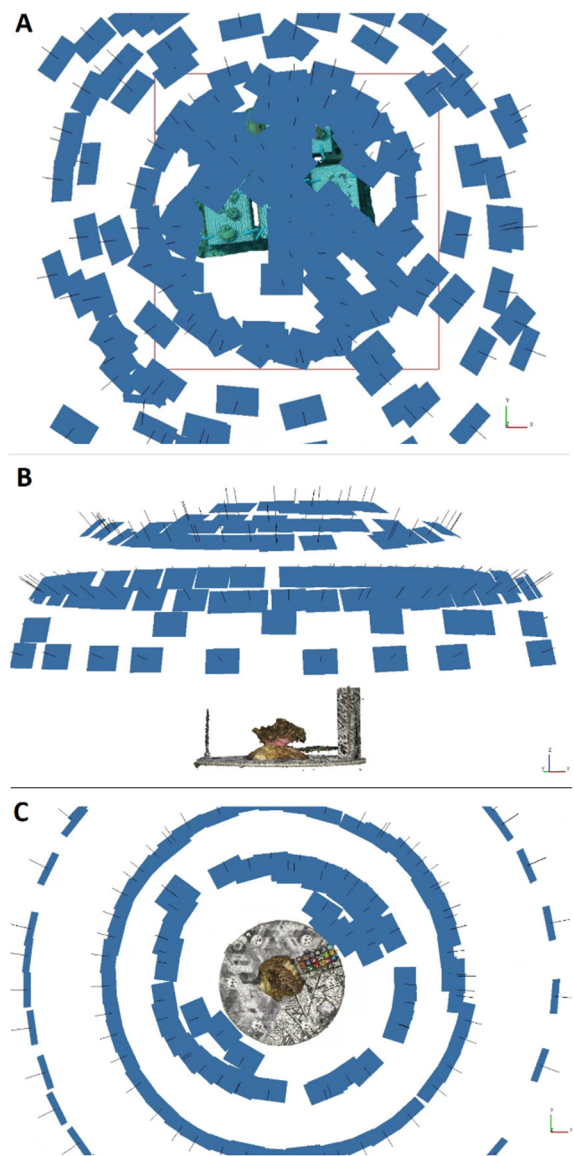


Figure 2. Acquisition of the photogrammetric datasets. A: on-field test, view from the top. B, C: laboratory test, front view, and from the top, respectively.

Generally, the monitoring of geometric deformations (*i.e.*, growth of organisms, loss of 3D complexity, portion removal) is carried out through direct comparison of 3D models generated at subsequent epochs. This approach is widespread in numerous

disciplines (cultural heritage, geosciences, infrastructure management, ...), and requires the definition of a reference system unique and stable over time (Valença *et al.*, 2012; Abate, 2019; Laporte-Fauret *et al.*, 2019). In underwater applications, it is complex to guarantee a unique reference system, and there are few applications to this end (see Nocerino *et al.*, 2020; Rossi *et al.*, 2020). In this study, on-field activities had the goal of testing the instrumentations and the ROV implementation in real conditions, thus no monitoring activity was planned in this preliminary phase. In the laboratory tests, the 3D reconstruction of the target organisms and the analysis of their geometry aimed at monitoring their health state. The comparison of the resulting point clouds was performed after a co-registration of models based on unchanged portions (the bases on which the organisms were fixed), and then deformations were evaluated.

#### D. On-field fluorescence imagery

In order to observe the fluorescence emitted by healthy specimens of *C. caespitosa* and *E. singularis* in on-field tests, the instrumentation used was the following: a FLIR Blackfly S BFS-PGE-51S5P camera with a TAMRON M23FM16 lens filtered with an emission filter, model FST001 – Alexa 488 (FMF001). The FLIR camera was housed in an acrylic cylinder equipped with a dome port. A white LED-based light source (with CREE XP-E2 LEDs) filtered with an excitation filter, model FST001 – Alexa 488 (FXF001), was applied. The excitation filter applied on the light source allowed to illuminate the organisms with the blue component of the light, that triggers fluorescence. The emission filter applied to the lens of the camera allowed removing the blue light of excitation, letting the green light pass instead (green light both due to the fluorescence and environmental lighting). To separate the signal of interest, that is, the fluorescence generated by the organisms, from the green light component due to ambient lighting, the images were acquired as two frames: a former image, the blank image, in which the excitation light source was switched off (only the ambient light contribution was captured), and, immediately after, a latter image, the fluorescence image, in which the light source was on and both the natural light and fluorescence contributions were captured. To isolate the fluorescence contribution alone, a pixel-by-pixel subtraction was performed between the last frame acquired (light source on, fluorescence image) and the previous one (light source off, blank image), after some pre-processing aimed at re-aligning the two images.

#### E. ROV

The needs outlined in this study led to the search for a ROV easy to handle, highly customizable, and low-cost. The BluROV2 with 8-thrusters configuration (<https://bluerobotics.com/>), was chosen for the

underwater monitoring of corals and gorgonians geometry and health state. The 8-thrusters configuration allows to operate with strong currents; the vertical, lateral, and rotational movements are very effective and fast, and no large maneuvering spaces are required. The software architecture of the system is open and therefore easily customizable. The hardware structure of the ROV is modular and allows the addition of sensors and elements, including expansion kits. At the time of writing, RGB and fluorescence sensors were mounted on the ROV, and both the handling in navigation and the ability to acquire data were tested.

The ROV's full configuration was based on (from top to bottom): a first layer consisting of rotors, electronics, integrated camera, and battery pack; an expansion kit containing the fluorescence sensor and the associated electronics; a polypropylene structure that supports and protect the reflex camera. Several issues have been pointed out in the proposed architecture, and several improvements are planned. These aspects will be deepened in the discussion.

## IV. RESULTS

The on-field tests highlighted some weaknesses of the developed systems and their integration on the ROV. Issues in varying the pitching of the ROV without compromising its stability prevented the acquisition of an RGB dataset suitable for photogrammetric processing. The acquired images lacked sufficient redundancy and a complete investigation of the object. Instead, images acquired by the diver gave promising results: an average resolution of the 3D model of about 1 mm, and an overall accuracy on targets of about 1 mm (see Figure 3B). The resolution was sufficient to monitor the individual polyps constituting the colony. Despite the short acquisition distance (1.5 m), the chromatic distortion introduced by the water medium was evident (Figure 1A) since the use of a color checker for color correction had not been considered yet. Moreover, the implemented approach failed in the reconstruction of the thin branches of *E. singularis* (Figure 3B, red polygons).

Tests with the fluorescence camera revealed some critical issues that did not allow the estimation of the fluorescence content. Due to limits in the minimum time distance between the acquisition of blank and fluorescence images that prevented the acquisition of images sufficiently close together in time, the pixel-to-pixel subtraction with the blank image, introduced in the methodologies section, was not effective, since in addition to the pitch angle of the ROV (as described above), also the stability of the vehicle prevented to achieve the result. Figure 3A shows an example of a fluorescence image acquired on-field. The measured values are not representative of the fluorescence emitted by the organism as they are not purged of environmental and reflection contributions.

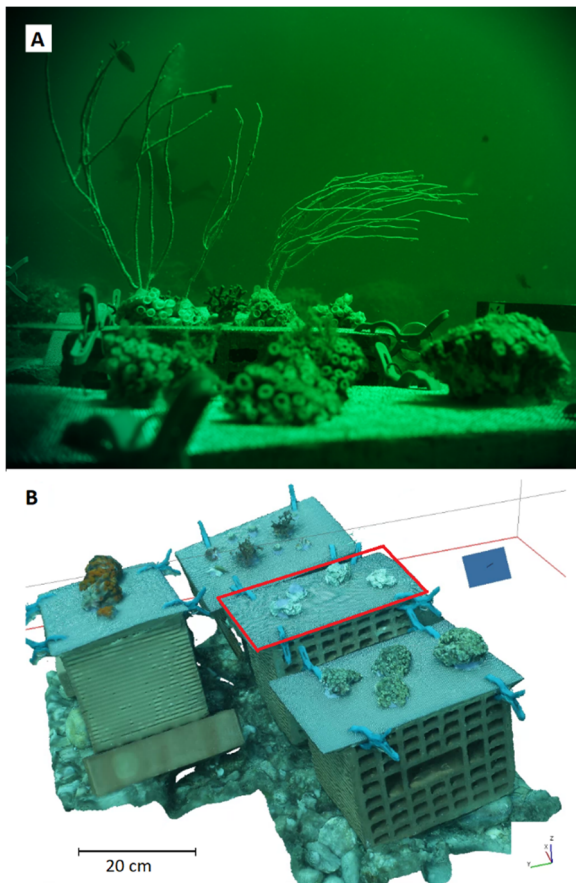


Figure 3. A: example of a fluorescence image acquired during on-field tests. B: view of the 3D model obtained with the images acquired by the diver.

In the laboratory, the acquisitions of the photogrammetric datasets led to the creation of 3D models with a sub-millimeter resolution (0.1 mm) and accuracy on GCPs of the same order (see Figure 4A). The obtained results were suitable to identify single polyps and potentially monitor their changes after exposure to stressful conditions. The color distortion effect generated by the water medium was not appreciable in this case, but the presence of a color checker allowed color calibration and the repeatability of colorimetric analyses.

As regards the monitoring of geometric deformations, the time elapsed did not allow to identify significant changes in the organisms and no artificial stresses were applied. Thus, the repeatability and accuracy of the proposed approach for deformation monitoring were tested by comparing the 3D models obtained for the same organism in immediate succession (from 40 min to 60 min). Figures 4A and 4B shows the areas used for registering the models: the calibration frame, the bases on which the colonies were fixed, and unchanged lower portions. Coregistration provided a mean distance between the unchanged portions of 0.17 mm and a standard deviation (std.dev.) of 0.2 mm (Figure 4C). The “potential geometric deformation” was defined through a comparison of the two 3D models: the mean distance was almost 0 mm with a std.dev of 0.3 mm (Figure 4D).

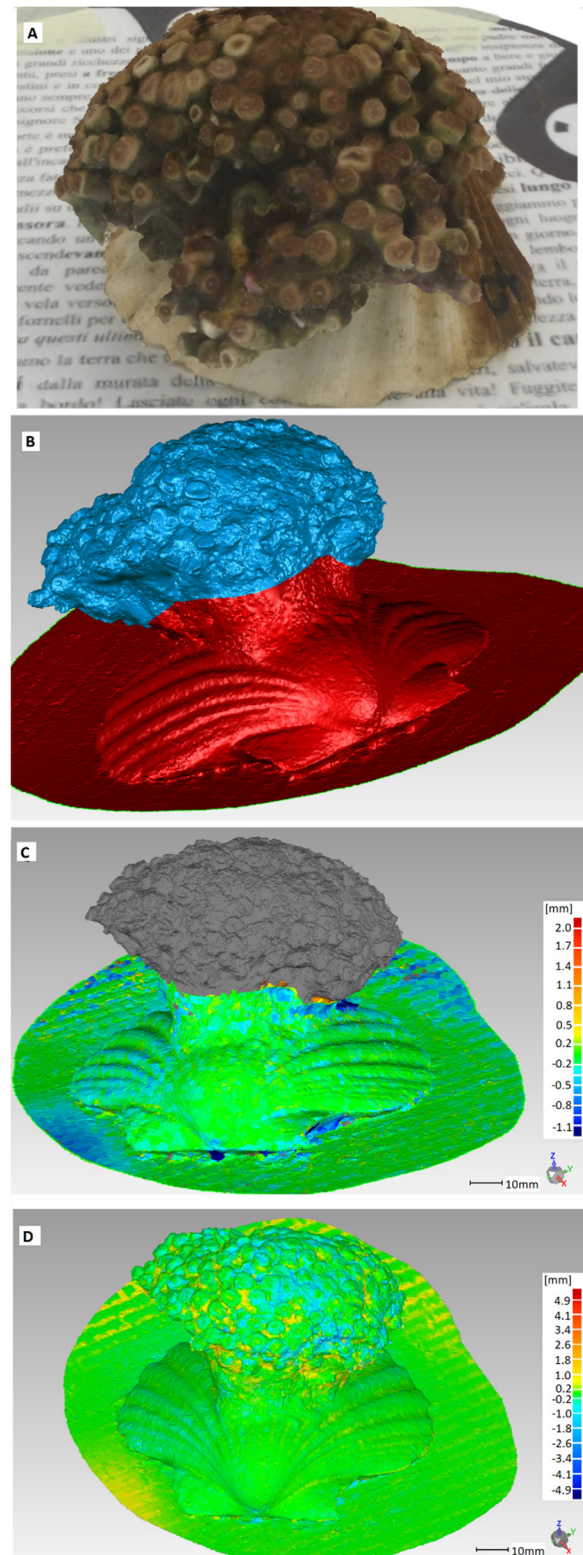


Figure 4. A: 3D model generated during laboratory tests. B: view of the portion used to coregister the subsequent 3D models (red area). C: coregistration results. D: comparison of the subsequent 3D models, detection, and mapping of “potential deformations”.

## V. DISCUSSIONS AND CONCLUSIONS

Laboratory tests led to high-resolution 3D products with sub-millimeter accuracy. Besides, the methodology proposed for the multitemporal comparison of 3D models was promising for

deformation monitoring. No relevant coregistration errors were added, and the detection of a few millimeters deformations was guaranteed. These results were hopeful also in the perspective of future estimations of corals and gorgonians health changes.

The use of a color checker will allow quantitative evaluations of the color variation in the organisms, as a crucial factor to detect the onset of stressful conditions. Authors are considering whether to: apply the same color correction to the entire photogrammetric dataset, correct each image individually, or apply the correction to the texture of the final 3D model. The stability of the camera during the acquisition of fluorescence images had been increased refining the support and acquiring higher-frequency images (2-3 images *per second*) to make the alignment of the fluorescence and blank images more effective, thus allowing an effective compensation of the ambient light. The implementation of the measuring system on a commercial ROV still requires further tests and research. Authors are figuring out: a camera support capable of changing the orientation of the optical axis (from horizontal to nadiral) that could be mounted under the ROV; a raspberry-pie-based system to remotely control the RGB and fluorescence cameras and set the start of the acquisitions and the frame rate, triggering the cameras and illuminators in a sequence suitable for the measurements.

The main goal of the overall project is the implementation and testing of new methodologies and sensors for the monitoring of marine communities providing high-resolution data over time. The preliminary activities described in this paper gave useful information about the potentialities and critical issues of the technologies tested. Methodologies for a high-resolution 3D reconstruction and deformation monitoring are fully operating. Laboratory activities on *C. caespitosa* provided promising results, and similar investigations are ongoing on *E. singularis*. Besides, further data are expected in the short term also for the monitoring of changes in coral health status, since various issues have been resolved. The implementation of the developed measuring system on the ROV still requires numerous tests, hardware and software customization, that are ongoing to face the main emerging issues.

## VI. ACKNOWLEDGEMENTS

Research funded by University of Modena and Reggio Emilia, FAR (Fondi di Ateneo per la Ricerca) 2020.

## References

- Abate, D. (2019). Built-heritage multi-temporal monitoring through photogrammetry and 2D/3D change detection algorithms. *Studies in Conservation*, 64(7), pp. 423-434.
- Bayley, D. T., and Mogg, A. O. (2020). A protocol for the large-scale analysis of reefs using Structure from Motion photogrammetry. *Methods in Ecology and Evolution*, 11(11), pp. 1410-1420.
- Bianco, G., Muzzupappa, M., Bruno, F., Garcia, R., and Neumann, L. (2015). A new color correction method for underwater imaging. *The International Archives of Photogrammetry, Remote Sensing and Spatial Information Sciences*, 40(5), 25.
- Burns J.H.R., Delparte D., Gates R.D. and Takabayashi, M. (2015). Integrating structure-from-motion photogrammetry with geospatial software as a novel technique for quantifying 3D ecological characteristics of coral reefs. *PeerJ*, 3, p.e1077.
- Capra, A., Castagnetti, C., Dubbini, M., Gruen, A., Guo, T., Mancini, F. T., and Troyer, M. (2017, October). High Accuracy Underwater Photogrammetric Surveying. In *3<sup>rd</sup> IMEKO International Conference on Metrology for Archeology and Cultural Heritage*.
- Drap P., Seinturier J., Hijazi B., Merad D., Boi J.M., Chemisky B., Seguin E., and Long L. (2015). The ROV 3D Project: Deep-sea underwater survey using photogrammetry: Applications for underwater archaeology. *Journal on Computing and Cultural Heritage (JOCCH)*, 8(4):1-24.
- Eyal G., Wiedenmann J., Grinblat M., D'Angelo C., Kramarsky-Winter E., Treibitz T., Ben-Zvi O., Shaked Y., Smith T.B., Harii S., and Denis V. (2015). Spectral diversity and regulation of coral fluorescence in a mesophotic reef habitat in the Red Sea. *PLoS one*, 10(6), p.e0128697.
- Figueira W., Ferrari R., Weatherby E., Porter A., Hawes S., and Byrne M. (2015). Accuracy and precision of habitat structural complexity metrics derived from underwater photogrammetry. *Remote Sensing*, 7(12), 16883-16900.
- Guarnieri, G., Bevilacqua S., De Leo F., Farella G., Maffia A., Terlizzi A., and Frascchetti, S. (2016). The challenge of planning conservation strategies in threatened seascapes: understanding the role of fine scale assessments of community response to cumulative human pressures. *PLoS one*, 11(2), p.e0149253.
- Heron S.F., Maynard J.A., Van Hooijdonk R., and Eakin, C.M. (2016). Warming trends and bleaching stress of the world's coral reefs 1985–2012. *Scientific reports*, 6, p.38402.
- Kersting D.K., Bensoussan N., and Linares, C. (2013). Long-term responses of the endemic reef-builder *Cladocora caespitosa* to Mediterranean warming. *PLoS One*, 8(8), p.e70820.
- Laporte-Fauret, Q., Marieu, V., Castelle, B., Michalet, R., Bujan, S., and Rosebery, D. (2019). Low-cost UAV for high-resolution and large-scale coastal dune change monitoring using photogrammetry. *Journal of Marine Science and Engineering*, 7(3), 63.
- Lavy, A., Eyal, G., Neal, B., Keren, R., Loya, Y. and Ilan, M. (2015). A quick, easy and non-intrusive method for underwater volume and surface area evaluation of benthic organisms by 3D computer modelling. *Methods in Ecology and Evolution*, 6(5), pp.521-531.
- Menna, F., Nocerino, E., and Remondino, F. (2017). Flat versus hemispherical dome ports in underwater photogrammetry. *The International Archives of Photogrammetry, Remote Sensing and Spatial Information Sciences*, 42, 481.
- Menna, F., Nocerino, E., Fassi, F., and Remondino, F. (2016). Geometric and optic characterization of a hemispherical dome port for underwater photogrammetry. *Sensors*, 16(1), 48.

- Menna, F., Nocerino, E., Nawaf, M. M., Seinturier, J., Torresani, A., Drap, P., and Chemisky, B. (2019, June). Towards real-time underwater photogrammetry for subsea metrology applications. In *OCEANS 2019-Marseille* (pp. 1-10). IEEE.
- Nocerino, E., Menna, F., Gruen, A., Troyer, M., Capra, A., Castagnetti, C., and Holbrook, S. J. (2020). Coral Reef Monitoring by Scuba Divers Using Underwater Photogrammetry and Geodetic Surveying. *Remote Sensing*, 12(18), 3036.
- Raoult V., Reid-Anderson S., Ferri A., and Williamson J.E. (2017). How Reliable Is Structure from Motion (SfM) over Time and between Observers? A Case Study Using Coral Reef Bommies. *Remote Sensing*, 9(7), 740.
- Rossi S., Bramanti L., Gori A., and Orejas C. (2017). *Marine animal forests. The ecology of benthic biodiversity hotspots*. Cham, Switzerland: Springer International Publishing.
- Rossi, P., Castagnetti, C., Capra, A., Brooks, A. J., and Mancini, F. (2020). Detecting change in coral reef 3D structure using underwater photogrammetry: critical issues and performance metrics. *Applied Geomatics*, 12(1), 3-17.
- Shortis M. (2015). Calibration techniques for accurate measurements by underwater camera systems. *Sensors*, 15(12), pp.30810-30826.
- Storlazzi C.D., Dartnell P., Hatcher G.A., and Gibbs A.E. (2016). End of the chain? Rugosity and fine-scale bathymetry from existing underwater digital imagery using structure-from-motion (SfM) technology. *Coral Reefs*, 35(3):889-94.
- Valença, J., Júlio, E. N. B. S., and Araújo, H. J. (2012). Applications of photogrammetry to structural assessment. *Experimental Techniques*, 36(5), 71-81.
- Ventura, D., Mancini, G., Casoli, E., Pace, D. S., Lasinio, G. J., Belluscio, A., and Ardizzone, G. (2022). Seagrass restoration monitoring and shallow-water benthic habitat mapping through a photogrammetry-based protocol. *Journal of Environmental Management*, 304, 114262.



## Structural analysis of monitoring results of long-span roof structures

Roman Shults

Kyiv National University of Construction and Architecture, Povitroflotskij Ave 31, 03037 Kyiv, Ukraine,  
([shults.rv@knuba.edu.ua](mailto:shults.rv@knuba.edu.ua))

**Key words:** *displacement; method of joints; truss; load; geospatial monitoring*

### ABSTRACT

The concept of analysis of geodetic monitoring results solely from a geometric point of view is recognized as an obsolete approach. A complex analysis of geodetic measurements (geometric approach) and the structure stress-strain analysis (mechanical approach) allows obtaining the whole picture of any engineering structure displacements. The detailed scheme of the structural analysis of geospatial monitoring results of the long-span roof structures has been given in the presented paper. The results of the geospatial monitoring of the large warehouse have been chosen as a study subject. The structure's roof consists of planar trusses, the main objects of external loads combined with dead loads. According to the complex analysis procedure, the trusses were analyzed using the method of joints with the determination of partial member forces. At the next step, these forces were leveraged in the following order member force–member deformation–node displacement. To obtain the actual displacements of the truss nodes, one has to account for the vertical displacements of the leaning points where the truss touched the column. That step is also being accomplished using the method of joints. Having the actual node displacements, one may compare them with geodetic monitoring results. The comparison results generally allow us to reveal the places with unacceptable displacements and estimate whether they are determined with the necessary accuracy. In this particular case, the final node's displacements were yielded as an output of combined analysis, both geometric and mechanical. That, in turn, lets to acquire the deformation process's genuine parameters. The study results have shown the high efficiency of the presented research methodology.

### I. INTRODUCTION

The analysis of geospatial monitoring results is always a complex and multistage issue (Welsch and Heunecke, 2001; Eichhorn, 2017). Today, no one will object that only geometrical analysis is not enough to comprehend the reasons and aftermaths of the deformation of a structure. The times when it was sufficient to calculate the values of displacements and simulate the displacements using polynomial models or other ones have gone. Thanks to the powerful computational possibilities of modern equipment and software, it has become possible to apply highly complex mathematical models to simulate and analyze the deformation process. The mathematical models that were hard to use or time-consuming (Szostak-Chrzanowski and Chrzanowski, 2004; Szostak-Chrzanowski *et al.*, 2008) have come up accessible to anyone who is familiar with PC. Recent studies being explored the use of new models and methods in geospatial monitoring analysis, *e.g.*, neural networks, machine learning, etc. Among those methods, structural mechanics takes a particular place. The design, construction, and exploitation of any engineering structure obey the principles of structural mechanics. Civil engineers perform sophisticated calculations to provide the structure stability, durability, and safety requirements in general. These calculations are of importance for construction management and building deployment. At the same

time, the results of these calculations serve as a base for building control and monitoring. However, the calculation results are given in a form that works well for builders but do not account needs of surveyors. To date, no study has explicitly looked at the role of structural mechanics in geospatial monitoring and their relationship. During building exploitation, especially when geospatial monitoring tasks come up, the surveyor cannot bind structural mechanics calculations' results with monitoring requirements. Moreover, the criteria for monitoring (accuracy, target emplacement, etc.) are frequently up to the surveyor. Under such circumstances, the surveyor's requirements are based on his experience or literature. It is evident that such an approach cannot be considered correct and reliable. The best way is to determine the requirements using a civil engineer's calculations. However, those calculations either do not fit the surveyor's requirements or even are not being done. But even having the requirements, the analysis of monitoring results all the more so needs the structure simulation using structural mechanics. The reason is that different loads and conditions may lead to unpredictable displacements and distort the analysis results. In such a case, the surveyor must have the necessary skills to analyze construction using modern software. It would not have been possible if the BIM had not come in handy. BIM contains all the required information concerning the structure and the calculation model of

particularly. The primary calculation approach embedded into BIM is the finite element method (FEM) (Logan, 2012; Lee, 2015). The pros and cons of this method are given in (Shults, 2020). The calculation procedure is simple and may be repeated for different conditions. The surveyors actively use FEM in their studies (Taşçi, 2015; Alizadeh-Khameneh *et al.*, 2018). Therefore, today the surveyor may carry out structure simulation and facilitate the monitoring results analysis. Before implementing FEM, the primary method for structure calculation was the method of joints. It is worth mentioning that the method of joints gives the same results as FEM for simple structures. The long-span roof leaning on plane trusses is a sample of such simple structures. This study examines the relationship between structural mechanics and geospatial monitoring of long-span roof structures. The method of joints has been chosen as the main method of structural mechanics. The paper comprises five parts. Part one deals with the introduction, and part two presents the study object. The third part outlines some of the critical principles of the method of joints and its liaison with geospatial monitoring results. Part four details the findings of monitoring results analysis. The fifth part is dedicated to conclusions.

II. STUDY OBJECT AND MONITORING DESIGN

The study object is the large warehouse in Kyiv, Ukraine (Figure 1). Geospatial monitoring was organized due to periodic damages that the warehouse owner observed during a year. The spatial geodetic network inside the warehouse with external referencing has been created to embark on the monitoring (Figure 2). The accuracy of the created network is presented in Table 1.



Figure 1. General view of the warehouse.

After the preliminary analysis of the structure's geometry and design scheme, it was decided that the major concern and possible reason for the periodic damages is the deformation of the roof construction and vertical displacements of columns. The roof structure is made up of planar steel trusses that are leaned onto the cantilevers of the concrete columns. Therefore, the primary goal of geospatial monitoring was to determine the vertical displacements of the

system "truss-columns" and the probable inclination of the columns. According to these demands, at the belt of each truss, three targets for reflectorless measurements were installed (Figure 3).

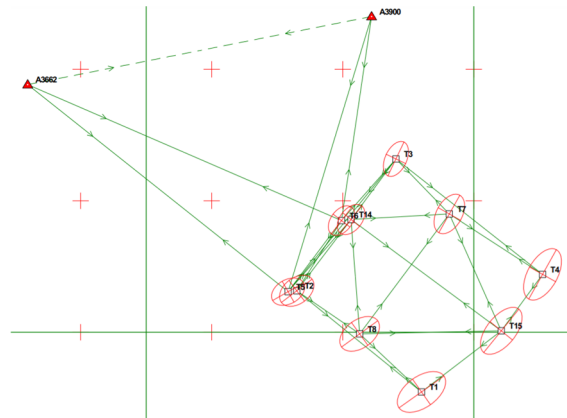


Figure 2. Horizontal view of the spatial geodetic network for monitoring with error ellipses.

Table 1. Network accuracy

Point	$m_{xy}$ [m]	$m_z$ [m]
T1	0.0024	0.0014
T2	0.0018	0.0009
T3	0.0016	0.0008
T4	0.0024	0.0013
T5	0.0016	0.0010
T6	0.0015	0.0010
T7	0.0019	0.0010
T8	0.0020	0.0010
T14	0.0016	0.0009
T15	0.0024	0.0012

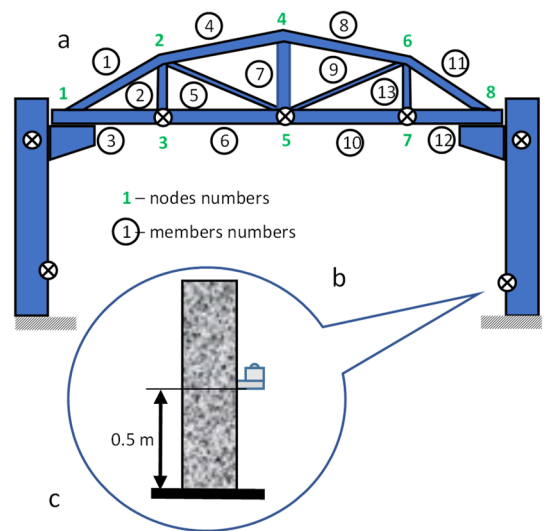


Figure 3. System "truss-columns" and the emplacement of targets: a - system "truss-columns" with the marks emplacement and numbers of joints and members; b - deformation benchmark emplacement at the bottom of a column; c - the warehouse cross-section that shows the order of columns and trusses.

In addition, each column was marked by one reflectorless target at the top and one benchmark near the floor to afford prism installation (Figure 3). Two hundred and forty targets and seventy benchmarks were installed in total. The observations for each epoch were accomplished by a precise total station using the free-station method. The first observation epoch was conducted in June 2016. Twelve observation cycles were carried out in total. The geometrical analysis of the obtained results has revealed unpredictable relationships. As a result, the necessity of structural analysis has become evident. It has been decided to apply the structural mechanics approach, namely the method of joints, for the complex analysis of monitoring results.

### III. METHOD OF JOINTS

Before analyzing monitoring results, let's briefly consider the idea of the method of joints and how it can be related to geospatial monitoring tasks. It is generally known that the spatial displacement  $\Delta S$  of any structure is considered in three dimensions with the corresponding constituents  $\Delta S_x$ ,  $\Delta S_y$ , and  $\Delta S_z$ . These values are the sum of particular displacements due to the displacement of the structure under its weight (dead load)  $\Delta l_x$ ,  $\Delta l_y$ ,  $\Delta l_z$ ; temperature loads, and other external influences (wind, snow, etc.) or loads (live load, equipment load, etc.)  $\Delta t_x$ ,  $\Delta t_y$ ,  $\Delta t_z$ ; the displacement due to the structure elements manufacturing errors  $\Delta m_x$ ,  $\Delta m_y$ ,  $\Delta m_z$ ; the ground displacements of the structure as a function of the structure weight pressure on the base  $\Delta g_x$ ,  $\Delta g_y$ ,  $\Delta g_z$ . So we may write down the following expressions (Shults *et al.*, 2020) (Eq. 1):

$$\begin{aligned} \Delta S_x &= \Delta l_x + \Delta t_x + \Delta m_x + \Delta g_x \\ \Delta S_y &= \Delta l_y + \Delta t_y + \Delta m_y + \Delta g_y \\ \Delta S_z &= \Delta l_z + \Delta t_z + \Delta m_z + \Delta g_z \end{aligned} \quad (1)$$

$$\Delta S = \sqrt{\Delta S_x^2 + \Delta S_y^2 + \Delta S_z^2}$$

The values in Equation 1 are typically calculated during structural analysis performed by a designer or civil engineer. As mentioned, there are different approaches to carrying out such an analysis. In structural mechanics for simple structures (frames, trusses, etc.) and their combinations, there is a well-known relationship (Connor and Faraji, 2016) (Eq. 2):

$$e = e_{load} + e_{temperature} + e_{manufacturing} \quad (2)$$

where  $e_{load}$  = structure element deformation due to various loads, including its own weight  
 $e_{temperature}$  = structure element deformation due to temperature variation  
 $e_{manufacturing}$  = structure element deformation due to manufacturing error

If one considers the planar truss, then the Equation 2 describes the extension of each member as a sum of partial extensions due to loads (dead load), temperature, and member's manufacturing error. The relationship between extensions and displacements is being presented in the form of deformation–displacement relations for the structure (Connor and Faraji, 2016) (Eq.3):

$$\mathbf{e} = \mathbf{B}^T \mathbf{U} \quad (3)$$

where  $\mathbf{e}$  = vector of members' deformation  
 $\mathbf{B}$  = extended matrix of members' cosines of direction  
 $\mathbf{U}$  = extended vector of nodes displacements

The Equation 3 describes a well-known relationship between applied forces, extension or contraction of each member, and node displacements. In Equation 3, the ground displacements or support movements are also included. The given study treats the columns' vertical displacements as support movements. If the structure is statically determinate, one may estimate the reactions from equilibrium equations and then find the effect of supports' movements. The equations of the method of joints in matrix form (Eq. 4):

$$\begin{aligned} \mathbf{F} &= \mathbf{B}^{-1} \mathbf{P} \\ \mathbf{e} &= \left( \frac{L_i}{A_i E_i} \right) \mathbf{F} + (\alpha_i \Delta T_i L_i) \delta \mathbf{F} + e_{manufacturing} \delta \mathbf{F} \quad (4) \\ \mathbf{U} &= (\mathbf{B}^{-1})^T \mathbf{e} \end{aligned}$$

where  $\mathbf{P}$  = vector of applied forces  
 $\mathbf{F}$  = vector of member forces  
 $\mathbf{B}$  = matrix of members' cosines of direction  
 $A$  = area of  $i^{\text{th}}$  member cross-section (different values for different members)  
 $L$  = the  $i^{\text{th}}$  member length  
 $E$  = modulus of elasticity for the  $i^{\text{th}}$  member  
 $\Delta T$  = temperature change  
 $\alpha$  = coefficient of thermal expansion for the  $i^{\text{th}}$  member (for this case, the coefficient of armed concrete)  
 $\delta \mathbf{F}$  = vector of virtual unit force (force equals one and applied to each node consequently)

In Equations 3 and 4, the designator  $\mathbf{U}$  for the displacements vector has been taken from structural mechanics.

Therefore, if one knows the above-listed parameters, it is possible to calculate the structure displacements  $\mathbf{U}$  under specific loads  $\mathbf{P}$  in the model (Eq. 4). During the structure design, these parameters are defined in such a way that does not lead to the failure of the structure. In turn, it means that the allowable errors in geospatial monitoring should not lead to additional forces  $\mathbf{F}$  in structure members that exceed 20%. This requirement is typical for structural mechanics.

So, having the displacements  $\mathbf{U}$  from the simulation, we may treat any measured displacement  $\Delta S$  that exceeds the value (Eq. 5):

$$\Delta S \geq 0.2U \quad (5)$$

as significant.

In what follows, we will analyze just the vertical displacements as those which take the foremost concern; then, we may write down (Eq. 6):

$$\Delta S_z \geq 0.2U_z. \quad (6)$$

To find the vector  $\mathbf{U}$ , the simulation of the roof truss has been accomplished. The truss was considered statically determinate, subjected to the loads from the roof cover and dead weight. The simulation results are presented in Figure 4.

It is clear that the truss deformed almost uniformly for the given loads. A random simulation has been carried out to calculate the effect of manufacturing error. The root mean square error of truss members manufacturing was accepted 4 mm. The output of the joined impact of loads and manufacturing error for one particular simulation is given in Figure 5. The largest displacements were observed in the middle. The calculation results have shown that maximum displacements have reached the value  $U_z = -8.6$  mm for the vertical component. According to Equation 6, any measured vertical displacement  $\Delta S_z$ , which will be more than 1.7 mm considered significant. This value will be used for further analysis. However, the given computation does not account for the displacements due to temperature, environment (snow), and support movements. These displacements are unique for each span and observation epoch. That is why these displacements were calculated separately during the further structural analysis of monitoring results.

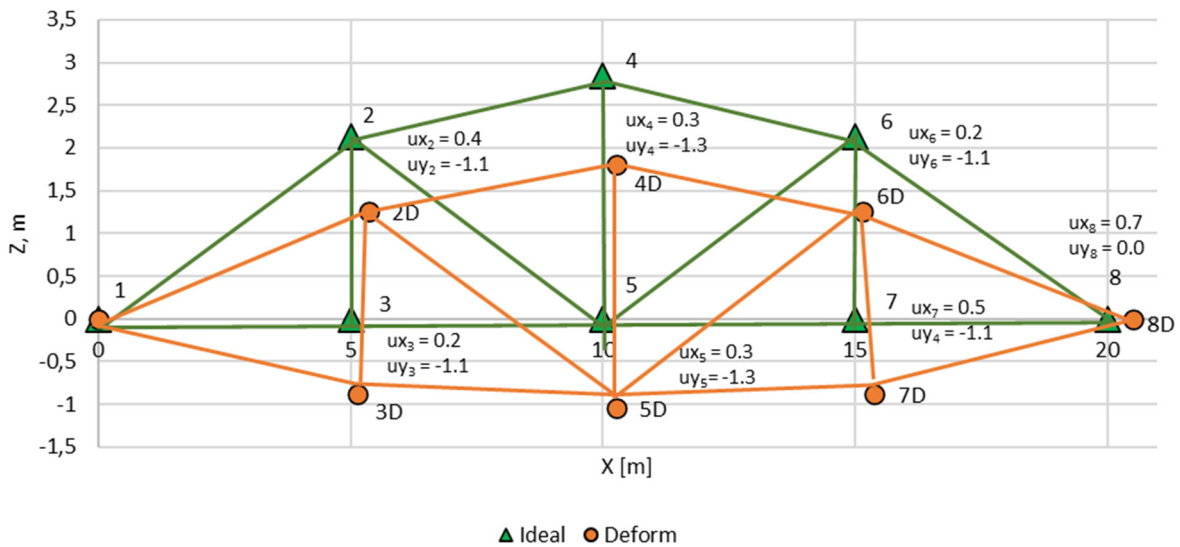


Figure 4. The picture of geometrically ideal truss and deformed truss (displacements are given in mm and have been scaled for visibility).

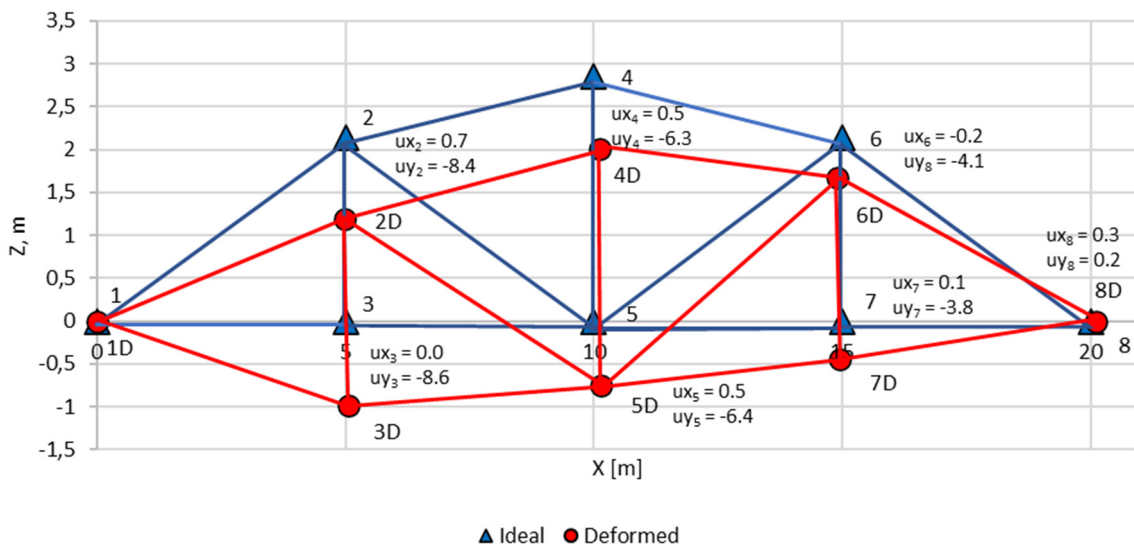


Figure 5. The picture of the combined impact of the loads and manufacturing errors (displacements are given in mm and have been scaled for visibility).

IV. STRUCTURAL ANALYSIS OF MONITORING RESULTS

The observation period lasted from June 2016 to August 2017. Thus the observation time included the snowy months with a significant temperature change. Therefore, some loads are time-dependent and act periodically. But, first of all, it is necessary to demonstrate the results of actual measurements that have been gathered during the monitoring period. Due to the vast set of measurements, it is impossible to present all the results. Below are the charts (Figure 6 – Figure 11) of vertical displacements for two trusses from different roof parts.

It is evident that the displacements have, unlike nature, even for Figure 6 – Figure 11. The given cases provide preliminary evidence that the deformation process is non-uniform and cannot be comprehended just from displacement analysis. A possible reason for these discrepancies might be various loads and their combination. Therefore, the only way to figure out whether the displacements are really exceeding allowable values or not is to carry out structural analysis. For the sake of the study, the following geometrical and physical parameters have been used (Table 2).

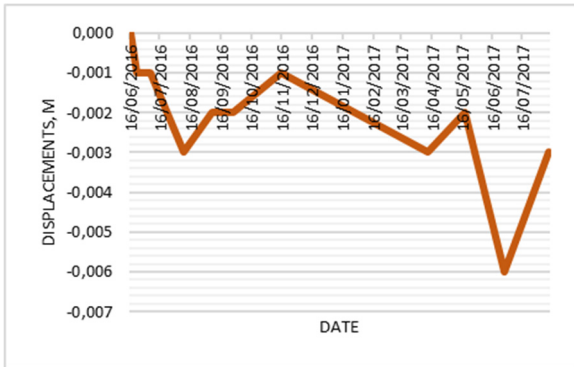


Figure 6. The vertical displacements chart for truss A3/B1 (point 3).

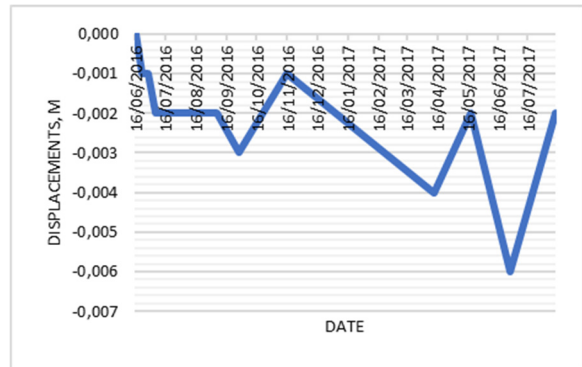


Figure 9. The vertical displacements chart for truss A5L/B4 (point 3).

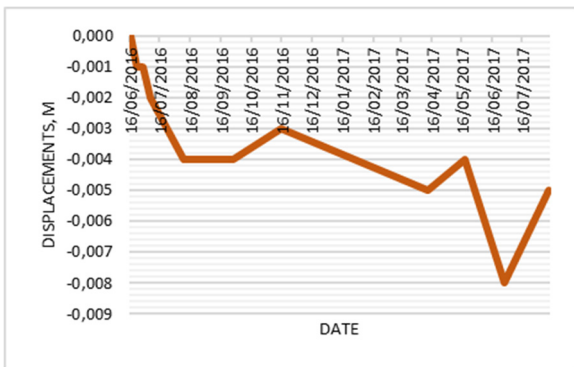


Figure 7. The vertical displacements chart for truss A3/B1 (point 5).

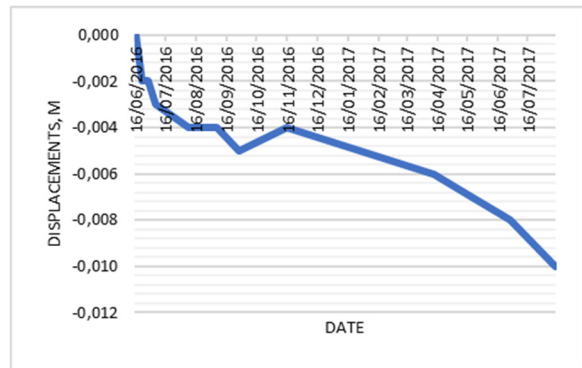


Figure 10. The vertical displacements chart for truss A5L/B4 (point 5).

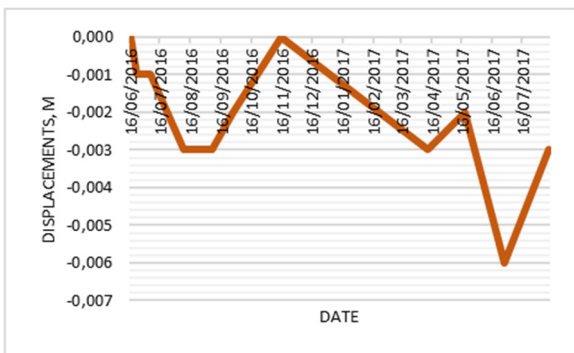


Figure 8. The vertical displacements chart for truss A3/B1 (point 7).

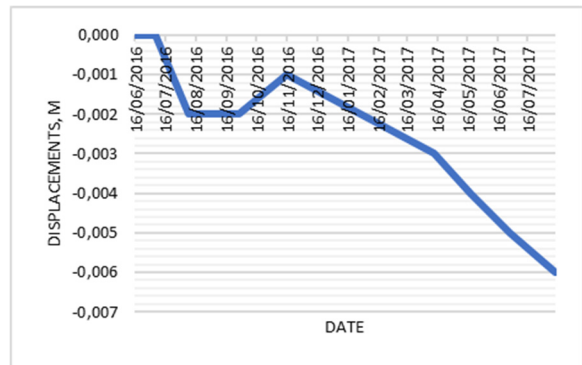


Figure 11. The vertical displacements chart for truss A5L/B4 (point 7).

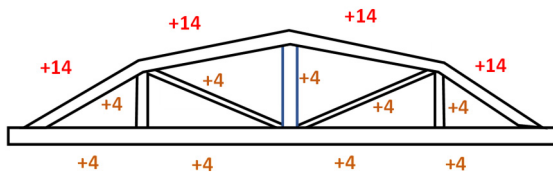
The charts visualize the vertical displacements of each truss at points 3, 5, and 7 (see Figure 4). These charts show the final values bigger than 1.7 mm, so the displacements are significant and need further analysis.

In Table 2, the temperature deformation had been accepted according to the results of actual observations. It was determined that for the truss

members, the temperature variation has the following view (Figure 12).

Table 2. The initial geometrical and physical parameters of truss members for simulation

Member	$L_i$ [m]	$\Delta T_i$ [°]	$L_i/A_iE_i$	$\alpha_i\Delta TL_i$
1	5.439	12	6.53691E-06	0.000979
2	2.140	4	1.11458E-05	0.000128
3	5.000	4	6.51042E-06	0.000300
4	5.050	12	6.0699E-06	0.000909
5	5.439	4	9.44221E-06	0.000326
6	5.000	4	6.51042E-06	0.000300
7	2.850	4	1.48438E-05	0.000171
8	5.050	12	6.0699E-06	0.000909
9	5.439	4	9.44221E-06	0.000326
10	5.000	4	6.51042E-06	0.000300
11	5.439	12	6.53691E-06	0.000979
12	5.000	4	6.51042E-06	0.000300
13	2.140	4	1.11458E-05	0.000128



+4 – member temperature C°, regarding the design temperature +20 C°

Figure 12. Truss temperature variation regarding the design temperature.

Figure 12 shows the summertime temperature variation from +4 C° up to +14 C° for members adjoining the roof.

The combinations of different displacements invoked by different loads are presented in Figure 13.

There are different causes of roof displacement. For the case in Figure 13a, the roof's truss is deforming under the additional loads (snow in our case) and temperature difference for the upper and bottom parts of the truss. The case in Figure 13b demonstrates the opposite process when a non-deformed truss is just inclined due to supports' movements or columns' vertical displacements, in other words. The case in Figure 13c combines both previous ones. It is obvious that only pure vertical displacements of truss points make sense for analysis. To find the pure vertical displacements, one needs to eliminate the displacements due to mentioned reasons. The study involved the calculation of the displacements from temperature change, columns' displacements, and additional loads for each monitoring epoch. These displacements have been ruled out from actually measured displacements at the next step. So the pure vertical displacements of the roof's trusses for the whole structure were determined. As a case study, below are the simulation results for the same truss for wintertime (Table 3) and summertime (Table 4) are

given when environmental parameters were significantly changed.

Table 3. The simulation results for the system "truss-columns" for the specific loads for wintertime

Nodes	Nodes displacements due to loads [mm]				
	$\Delta l_z$	$\Delta t_z$	$\Delta g_z$ [-6]	$\Delta g_z$ [-2]	$\Delta S_z$
$u_1$	0.0	0.0	0.0	0	0.0
$v_1$	0.0	0.0	-6.0	0	-6.0
$u_2$	0.4	0.2	0.0	0	0.2
$v_2$	-1.1	-2.2	-4.5	-0.5	-3.8
$u_3$	0.2	-0.3	0.0	0	0.2
$v_3$	-1.1	-2.0	-4.5	-0.5	-3.8
$u_4$	0.3	-0.6	0.0	0	0.3
$v_4$	-1.3	-3.0	-3.0	-1	-1.5
$u_5$	0.3	-0.6	0.0	0	0.3
$v_5$	-1.3	-2.8	-3.0	-1	-1.5
$u_6$	0.2	-1.4	0.0	0	0.5
$v_6$	-1.1	-2.2	-1.5	-1.5	0.2
$u_7$	0.5	-0.9	0.0	0	0.5
$v_7$	-1.1	-2.0	-1.5	-1.5	0.2
$u_8$	0.7	-1.2	0.0	0	0.7
$v_8$	0.0	0.0	0.0	0.0	-2.0

Table 4. The simulation results for the system "truss-columns" for the specific loads for summertime

Nodes	Nodes displacements due to loads [mm]				
	$\Delta l_z$	$\Delta t_z$	$\Delta g_z$ [-9]	$\Delta g_z$ [-3]	$\Delta S_z$
$u_1$	0.0	0.0	0.0	0	0.0
$v_1$	0.0	0.0	-9.0	0	-9.0
$u_2$	0.0	0.3	0.0	0	0.3
$v_2$	0.0	-2.8	-6.8	-0.75	-8.8
$u_3$	0.0	-0.3	0.0	0	-0.3
$v_3$	0.0	-2.7	-6.8	-0.75	-8.7
$u_4$	0.0	-0.1	0.0	0	-0.1
$v_4$	0.0	-2.3	-4.5	-1.5	-5.3
$u_5$	0.0	-0.6	0.0	0	-0.6
$v_5$	0.0	-2.2	-4.5	-1.5	-5.2
$u_6$	0.0	-1.1	0.0	0	-1.1
$v_6$	0.0	-2.0	-2.3	-2.25	-2.0
$u_7$	0.0	-0.9	0.0	0	-0.9
$v_7$	0.0	-1.9	-2.3	-2.25	-1.9
$u_8$	0.0	-1.2	0.0	0	-1.2
$v_8$	0.0	0.0	0.0	-3	-3.0

As one may notice, the vertical displacements are entirely due to the supports' movements or columns' vertical displacements for the chosen truss. In turn, it means that there are no actual displacements of the truss and roof consequently. The only reason for roof displacements is the columns' vertical displacements. The map with vertical displacements' distribution has been created (Figure 14) to figure out the actual deformation of the roof. This map has been constructed for the last observation epoch. The distribution in Figure 14 is not applicable for analysis since it seems that the whole roof is being deformed. However, after structural analysis, the picture has changed substantially. In Figure 15, the map of the roof's vertical displacements after structural analysis is presented.

The map provides convincing evidence that the columns' vertical displacements cause the roof deformation.

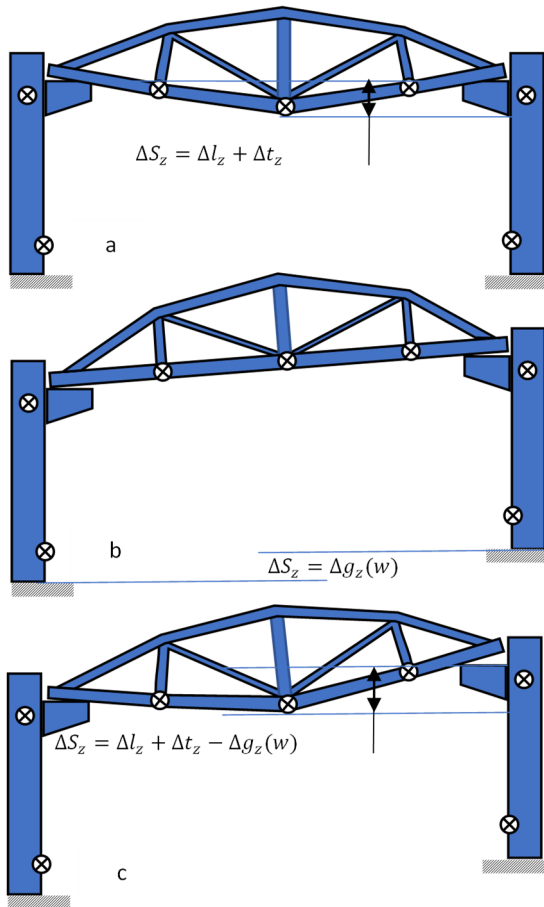


Figure 13. The various cases of the deformation of the system "truss-columns": a – pure truss displacement; b – columns' displacements; c – combined displacement.

The roof deformation occurs only in regions with considerable vertical displacements of columns. Therefore, the structural analysis has proved its high efficiency and allowed avoiding the wrong decisions by the results of geospatial monitoring.

### V. CONCLUSIONS

The presented study examines the results of geospatial monitoring of the long-span roof structures using the structural analysis approach. A combined analysis based on geometrical and mechanical methods has been suggested in the paper. In light of the study, few conclusions can be drawn from the achieved results. The general picture emerging from the study is that the application of the structural analysis allows avoiding the wrong decisions concerning the structure deformation. The deformation picture becomes clear and reveals the true reason for displacements and their values. In the presented study, the suggested approach has let to eliminate the displacements, which had periodic nature.

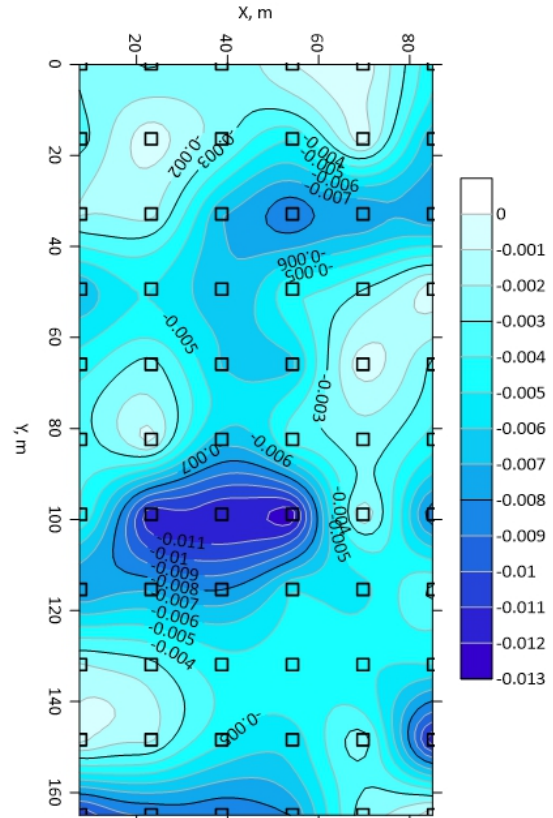


Figure 14. Map of the vertical displacements of the roof before structural analysis (columns depicted as rectangular).

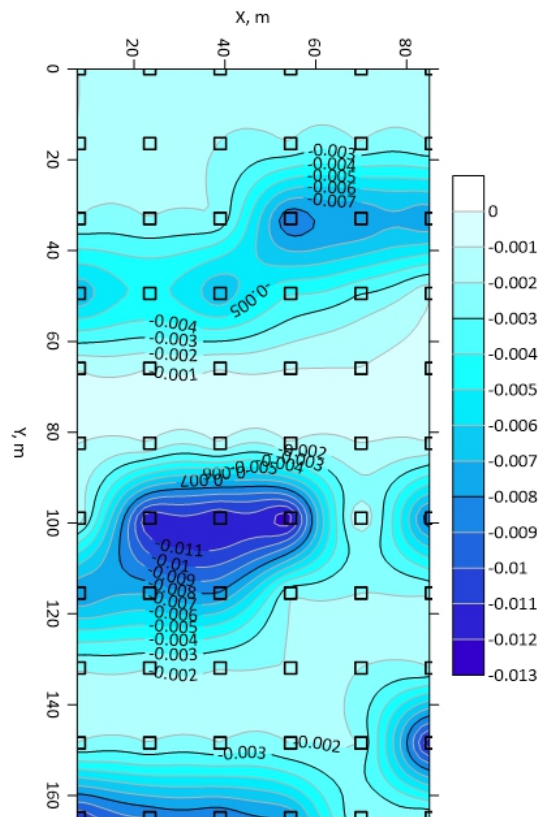


Figure 15. Map of the vertical displacements of the roof after structural analysis (columns depicted as rectangular).

Although the allowable displacements for the roof's trusses should have been in a range + 1.7 mm, the

measurement results have shown values exceeding 12 mm. However, thanks to the structural analysis, it is become possible to rule out the additional displacements and find the source and reason for the roof deformation. Future research will have to address the offered approach in more detail. The study region has to be extended to more complicated structures. Of course, if the structures for analysis get complicated, a more robust method is needed. In what follows, for complex structures, FEM is preferable to use. Keeping in mind that current BIMs contain FEM since the design stage, the new branches of analysis become open for surveyors, particularly those dealing with geospatial monitoring analysis.

Welsch, W.M., and Heunecke, O. (2001). Models and terminology for the analysis of geodetic monitoring observations - Official Report of the Ad-Hoc Committee of FIG Working Group 6.1. In: *Proc of the 10<sup>th</sup> FIG International Symposium on Deformation Measurements*, 19–22 March 2001 Orange, California, USA, pp 390–412.

### References

- Alizadeh-Khameneh, A. M., Eshagh, M., and Jensen, A. B. O. (2018). Optimization of deformation monitoring networks using finite element strain analysis. *Journal of Applied Geodesy*, 12(2), pp. 187–197. DOI: 10.1515/jag-2017-0040
- Connor, J. J., and Faraji, S. (2016). *Fundamentals of structural engineering* (2<sup>nd</sup> ed). Springer. DOI: 10.1007/978-3-319-24331-3
- Eichhorn, A. (2007). Tasks and newest trends in geodetic deformation analysis: A tutorial. In: *Proc of the 15<sup>th</sup> European Signal Processing Conference (EUSIPCO)*, Poznan, Poland.
- Lee, H.-H. (2015) *Finite Element Simulations with ANSYS Workbench 16: Theory, Applications, Case Studies*. SDC Publications.
- Logan, D.L. (2012) *A First Course in the Finite Element Method*. 5<sup>th</sup> ed. CENGAGE Learning, University of Wisconsin-Platteville.
- Shults, R. (2020). The Models of Structural Mechanics for Geodetic Accuracy Assignment: A Case Study of the Finite Element Method. In *Contributions to International Conferences on Engineering Surveying*, SPEES, pp. 187–197. DOI: 10.1007/978-3-030-51953-7\_16
- Shults, R., Soltabayeva, S., Seitkazina, G., Nukarbekova, Z., and Kucherenko, O. (2020). Geospatial Monitoring and Structural Mechanics Models: a Case Study of Sports Structures. In: *Proc of the 11th International Conference "Environmental Engineering"*, Vilnius Lithuania, 21–22 May 2020. DOI: 10.3846/enviro.2020.685
- Szostak-Chrzanowski, A., and Chrzanowski, A. (2004). Physical interpretation of ground subsidence surveys – a case study. *Journal of Geospatial Engineering*, 6(1), pp. 21–28.
- Szostak-Chrzanowski, A., Chrzanowski, A., Massiera, M., Bazanowski, M., and Whitaker, C. (2008). Study of a long-term behavior of large earth dam combining monitoring and finite element analysis results. In: *Proc of the 13th FIG Symposium on Deformation Measurement and Analysis, 4th IAG Symposium on Geodesy for Geotechnical and Structural Engineering*, 12–18 May 2008 Lisbon, Portugal, pp 1–10.
- Taşçi, L. (2015). Deformation monitoring in steel arch bridges through close-range photogrammetry and the finite element method. *Experimental Techniques*, 39, pp. 3–10. DOI: 10.1111/ext.12022.



## Monitoring of land subsidence in the city of Recife/Brazil using Sentinel-1 SAR interferometry

Wendson de Oliveira Souza<sup>1</sup>, Antonio Miguel Ruiz-Armenteros<sup>2</sup>, Jaime J. da Silva Pereira Cabral<sup>3, 4</sup>

<sup>1</sup> Department of Transports, Federal University of Piauí (UFPI), 64049-550 Teresina, Brazil,

([wendsonsouza@ufpi.edu.br](mailto:wendsonsouza@ufpi.edu.br))

<sup>2</sup> Department of Cartographic, Geodetic and Photogrammetry Engineering, Microgeodesia Jaén Research Group (PAIDI RNM-282), Center for Advanced Studies on Earth Sciences, Energy and Environment CEAETEMA, University of Jaén, 23071 Jaén, Spain, ([amruiz@ujaen.es](mailto:amruiz@ujaen.es))

<sup>3</sup> Department of Civil and Environmental Engineering, Federal University of Pernambuco (UFPE), 50670-901 Recife, Brazil, ([jaime.cabral@ufpe.br](mailto:jaime.cabral@ufpe.br))

<sup>4</sup> Department of Civil Engineering, Polytechnic School University of Pernambuco (UPE), 50720-001 Recife, Brazil

**Key words:** *land subsidence; Sentinel-1; PSInSAR; Recife*

### ABSTRACT

One of the main causes of land subsidence in the world is the exploitation of groundwater above the regeneration capacity of the aquifer systems. However, the rapid urban growth in estuarine areas can also contribute to the development of this phenomenon. An example of this occurs in the city of Recife, northeastern Brazil. The municipality is built on an estuarine plain composed of several rivers (Capibaribe, Beberibe, Tejipió), which formation results from the occupation of humid areas and mangroves. In recent decades, the excessive removal of water resources from the subsoil has caused the reduction of more than 100 meters of the deep aquifer piezometric level in some places. The presence of these factors in Recife may contribute to land subsidence. To detect this phenomenon, the Persistent Scatterer Interferometric Synthetic Aperture Radar (PSInSAR) technique was used. The dataset consisted of 135 Sentinel-1A Interferometric Wide (IW) Single Look Complex (SLC) images from September 2016 to April 2021. The images were acquired in descending orbits and VV polarization. The results of the PSInSAR analysis reveal that in Recife there are several areas of land subsidence with a rate close to -15 mm/year. The main occurrence of soil settlement is observed in large recently built areas in the west zone, and small areas in the north zone. Minor cases occur in the southern zone due to the exploitation of groundwater. The identification of these land subsidence areas can help in the study of urban drainage to avoid flooding sites and in the adoption of mitigating measures for the suitable use of underground water resources.

### I. INTRODUCTION

Land subsidence is present in several locations around the world. Surface movement can occur in native and/or built-up areas. In general, the displacement is slow and gradual. However, over the years its effects can accumulate and reach significant values. This can cause irreversible damage to the population and the environment.

Land subsidence is related to natural and human factors (Prokopovich, 1979). The main cause of this phenomenon comes, above all, from the anthropic influence on natural resources. That is, in the capture of groundwater, ores, oil, and natural gas. Among these, the excessive exploitation of groundwater represents the main cause of land subsidence on the world stage. The surface changes motivated by the use of aquifer systems account for almost 80% of the occurrences on the planet (Wang, 2017).

In that regard, urban development is a complex challenge. It is present, mainly, in large cities and metropolises. It involves social, economic, and housing

issues. Urban sprawl can impact the environment and infrastructure. Sometimes, the damage is significant in emerging countries due to the disorderly occupation of urban spaces and the pressure that it exerts on the water supply system.

The description of this reality can be seen in several Brazilian cities. An example of this occurs in Recife, the capital of Pernambuco state, located in the northeast Brazil. The municipality is built on an estuarine plain made up of several rivers (Capibaribe, Beberibe, Tejipió), precisely in an area of the delta and lower valley of the Capibaribe River that establishes a kind of archipelago city in its layout (Melo, 1978).

In the last 40 years, the urbanization of Recife has presented high growth in the sectors of industry, commerce, transport, and real estate. The rapid urban expansion, however, reveals several environmental problems, such as suffocation of drainage with the emergence of flooding areas, insufficient recharge of aquifers due to surface impermeabilization, reduction of the aquifer level due to the accentuated exploitation

of groundwater, landfill of flooded areas with surface instability (Gusmão Filho, 1998).

The participation of these last three problems contributes to the development of land subsidence in several places of Recife (Luna *et al.*, 2017; Bedini, 2020). This geological phenomenon implies a lowering of the surface and causes greater concern in urban areas. Land deformation can cause significant impacts on infrastructure and the environment, cause economic and social damage, and jeopardize people's quality of life (Abidin *et al.*, 2015).

In Recife, over the last four decades, the population growth has caused extensive intervention in the physical environment with changes in the physiognomy and structure of the city. This may have resulted from the absence or fragility of measures adopted in territorial planning. This finding can be seen in the sharp use of groundwater resources and in urban expansion over unstable plains (estuarine zones, reclaimed areas).

The use of groundwater has occurred in large part in the plain, effectively, since the 1970s. The use intensified between 1993 and 1998 when the population of the Metropolitan Region of Recife (RMR) goes through a long period of water rationing due to drought in the region. However, the excessive withdrawal of aquifer systems during this period causes the lowering of the piezometric surface, which reaches 100 m in the south of the city (Cabral *et al.*, 2008; Montenegro *et al.*, 2009).

The city of Recife has one of the highest densities of wells in the country with almost 13,000 captures, most of which are illegal and of unknown existence by Organs public administration agencies (Alisson, 2013). The southern zone of Recife is responsible for the largest number of wells in the city. The region concentrates a large portion of the high-income population which leads to the concentration and verticalization of buildings.

In order to avoid the excessive exploitation of groundwater in Recife, at the end of the last century, a zoning scheme for exploitable areas was created. By means of this model, the drilling of new wells for pumping groundwater in the neighborhood of Boa Viagem (zone A) is prohibited due to the water decrease in the Cabo aquifer, located in the southern region (Costa *et al.*, 1998).

The risk of lowering the land in this region is a matter of attention on the part of the technical-scientific community, management bodies, and inhabitants. The excessive exploitation of groundwater decreases the potentiometric surface of the aquifer and reduces the pressure of the pores that support the overlying layers of the soil. In addition, as a result, it can lead to reduced water supply and compromised water security.

The study of land subsidence due to the reduction of groundwater using a geodetic technique originates from the application of terrestrial measurement methods, such as GNSS (Romão *et al.*, 2003; Santos *et al.*, 2010; Santos *et al.*, 2012; Luna *et al.*, 2021) and

precision geometric leveling (Luna *et al.*, 2017). Among these techniques, so far, the slow sinking of soils in the southern zone is capable of being detected by geometric leveling.

The investigation using this method reveals a drop of -3.86 cm in altitude value for one of the levels analyzed between 1958 and 2015. The vertical displacement speed is estimated at -0.68 mm/year for the area of restriction of the zone "A" of the zoning of exploitable sites, in the neighborhood of Boa Viagem (Luna *et al.*, 2017). The slow lowering of the terrain in this region may indicate that the phenomenon is at an early stage of development (Santos *et al.*, 2012).

According to Scott (1978), the time interval required to complete soil consolidation varies from a few years to tens of years (compaction, large-scale water exploitation, surface loading, hydrocompaction). In this sense, the process of land subsidence can be difficult to predict. It demands specific studies for each case.

In addition to the exploitation of groundwater, the subsidence of Recife's soils is also the result of rapid urban growth in estuarine areas. The municipality is built on the estuary of the Capibaribe River and other small rivers that share the same river mouth. Over the last five centuries, Recife has developed with the recovery of large areas of land in stretches of streams, swamps, and mangroves (Cabral *et al.*, 2008).

Historically, the urban expansion of Recife began in the 17<sup>th</sup> century with port activity in the city center. From that time until the 19<sup>th</sup> century, changes took place from the center of Recife towards the areas drained by the Capibaribe River due to the presence of existing rural activity in its vicinity. This involves using this river to transport sugarcane production to its mouth in the Atlantic Ocean, where the port of Recife is located.

From the 20<sup>th</sup> century to the present time, the urban evolution of Recife remains active with changes in the contour and stability of the city due to the incorporation of new spaces and geographic features. During this period, Recife grows at an accelerated rate through the creation of landfills in flooded areas. The urban growth over these sites represents 19 km<sup>2</sup>. This is equivalent to 17.5% of the plain geological unit and 9.1% of the total area of the city (Gusmão Filho, 1998).

The use of PSInSAR technology in the determination of areas of surface instability due to recent urbanization in Recife occurs in a pioneering way in the work of Bedini (2020). That study uses Sentinel-1 images (from April 2017 to September 2019) to detect drawdown values of up to -15 mm/year in several neighborhoods in the west zone. In some cases, the rate is up to -25 mm/year in small areas due to the construction of buildings in the last decade.

In this context, it is observed that the extensive human intervention in the physical environment of Recife contributes to surface instability. The city lives with the risk of land subsidence due to two factors: the exploitation of underground water resources and

recent urbanization. In view of this, the objective of the research is to detect surface displacement. For that, it uses the PSInSAR technique in this study.

The use of this technology employs a SAR dataset consisting of 135 Sentinel-1A images, Single Look Complex (SLC), and Interferometric Wide (IW) mode for the period from September 2016 to April 2021. The images are acquired in orbits descending and VV polarization. The PSInSAR results reveal that land subsidence in Recife remains active. There are several drawdown areas with a rate close to -15 mm/year.

The main occurrence of land subsidence is observed in large newly built areas in the west zone, and small areas in the north zone. There are indications of smaller cases in the southern zone resulting from the exploitation of groundwater. The identification of cases of land subsidence can help in the urban planning of the city, such as: improving urban drainage and promoting the sustainable use of groundwater resources.

## II. STUDY AREA

Recife has an area close to 218 km<sup>2</sup> and it is delimited by latitudes (8°9'S and 7°55'S) and longitudes (35°1'W and 34°50'W). It is the capital of the State of Pernambuco, located in northeastern Brazil (Figure 1). It is a commercial and tourist city, formed by a coastal plain. The formation of the plain results from fluvio-marine sediments, produced by marine transgressions and regressions.

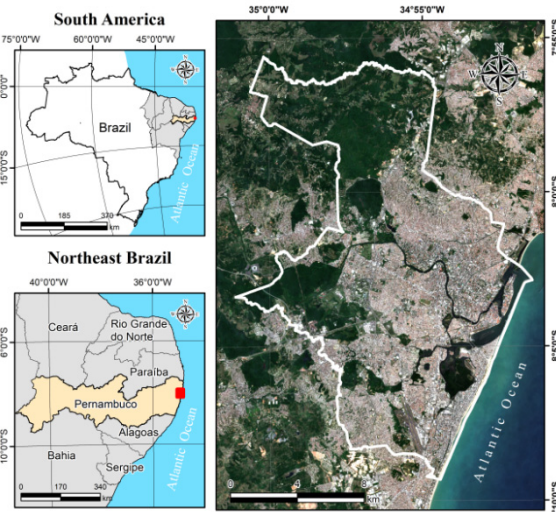


Figure 1. Location of Recife in Sentinel-2 image.

Recife is surrounded by hills, the Atlantic Ocean and several rivers (Capibaribe, Beberibe, Tejiú) that cross its domains. The composition of its area is distributed in: 67.43% of hills, 23.26% of plains, and 9.31% of aquatic. Much of the urbanization of the city is inserted in a relief surface of the plain. It has an altitude a little above sea level (Figure 2).

The urban expansion of Recife occurs in the areas of plains towards the hills. It has a high rate of urbanization due to the presence of buildings and

paved road systems. It has large vertical buildings in the most coastal locations of the city, that is, in real estate areas with great monetary value. Currently, the human occupation of Recife represents more than three-quarters of natural spaces in the municipality.

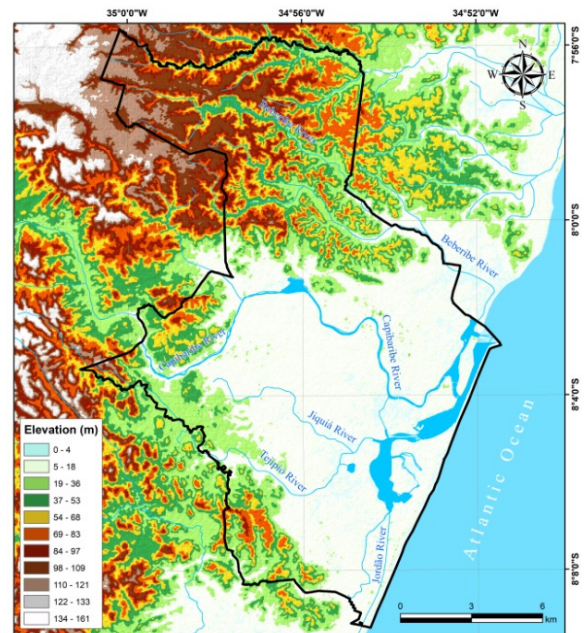


Figure 2. Elevation of Recife in SRTM image.

## III. INSAR DATA AND METHODS

From the Copernicus Open Access Hub platform (<https://scihub.copernicus.eu/dhus>) of the European Space Agency (ESA) and the European Commission (EC), 135 Sentinel-1A VV-polarization images were obtained for the period from 25 September 2016 to 8 April 2021 from the descending Track 9. The selected sub-swath was IW1 with a mean incidence angle of 32.9° and a spatial resolution of 3.4 x 22.5 m (range x azimuth).

The deformation determination resulted from the exploration of the interferometric phase calculated from the phase difference between two SAR images acquired at different times (Figure 3), in almost the same satellite position (Hanssen, 2001).

The displacement information derives from the interferometric phase which is influenced by several factors, according to Equation 1 (Crosetto *et al.*, 2016):

$$\varphi_{Int} = \varphi_{Displ} + \varphi_{Topo} + \varphi_{Atm} + \varphi_{Orb} + \varphi_{Noise} + 2k\pi \quad (1)$$

where  $\varphi_{Int}$  = interferometric phase  
 $\varphi_{Displ}$  = displacement phase  
 $\varphi_{Topo}$  = topographic phase  
 $\varphi_{Atm}$  = atmospheric phase  
 $\varphi_{Orb}$  = orbital phase  
 $\varphi_{Noise}$  = noise phase  
 $k$  = noise phase

The PSInSAR technique (Ferretti *et al.*, 2001) was used to monitor the deformation of the urban area of Recife.

The method selects a number of points (or targets) known as Persistent Scatterers (PS).

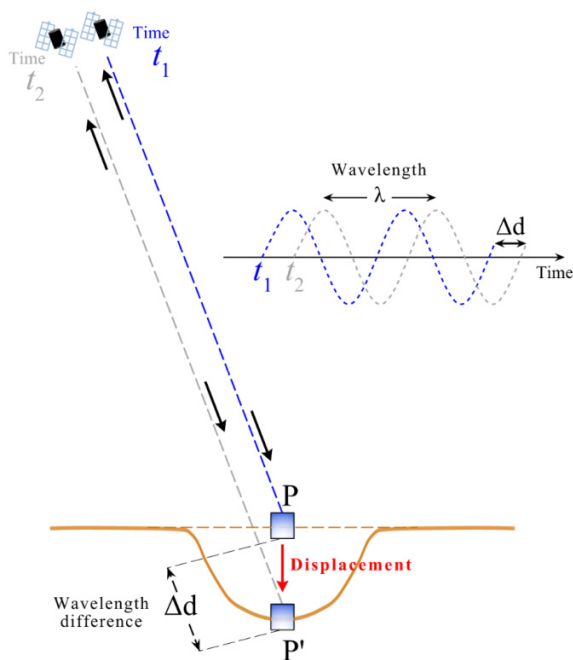


Figure 3. Deformation measurement scheme.

According to Crosetto *et al.* (2016), the PSs represent a specific class of DInSAR techniques, which exploits multiple SAR images acquired over the same area, and appropriate data processing and analysis procedures to separate  $\varphi_{Displ}$  from the other phase components represented in Equation 1.

The conduction of PSInSAR analysis in this work took place using SARPROZ (Perissin, 2020). The technique was used in the classical multitemporal InSAR (MT-InSAR) processing, in which the linear deformation estimate was adopted in time to generate deformation time series.

The set formed by  $N-1$  differential interferograms was made from the choice of a single  $N$  master SAR image, chosen on October 21, 2018 (Figure 4). The software selected the master image automatically to minimize spatial and temporal decorrelations.

The co-registration of the SAR images was related to the master image using Precise Orbit Ephemerides (POE), then the initial differential phase was extracted. Topographic phase removal was performed with a Digital Elevation Model (DEM) SRTM 30 m. The selection of PSs candidates (PSC) was based on different parameters, such as Amplitude Stability Index (ASI), spatial coherence, and reflectivity.

The Atmospheric Phase Screen (APS) estimate resulted from PSC over stable locations in the area of interest (Figure 5). The removal of APS occurred using PS points with a value equal to 0.8 for the ASI. For the final processing step, PS pixels with temporal coherence greater than 0.7 were selected. The main products of the PS procedure resulted in the Line-Of-Sight (LOS) velocity and deformation time series.

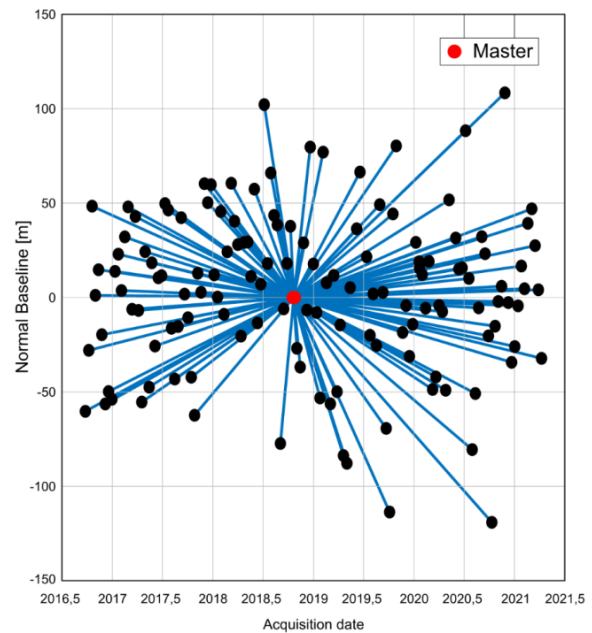


Figure 4. Each point represents an image in the normal baseline/temporal baseline space and each link is an interferogram.

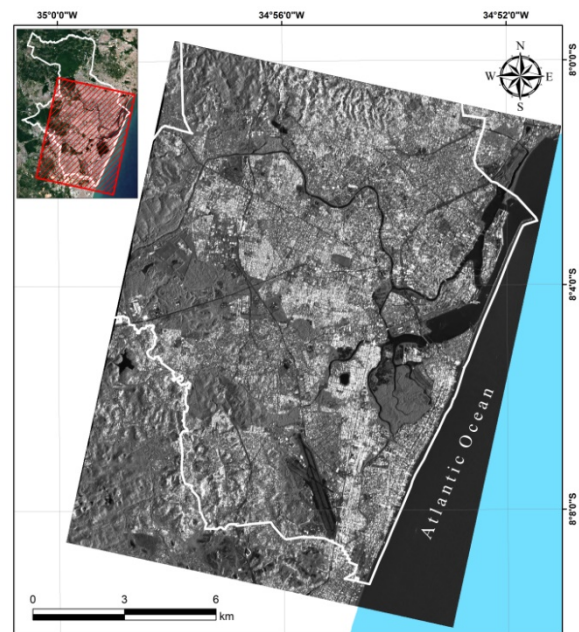


Figure 5. Sentinel-1 image of the Recife study area.

#### IV. RESULT AND DISCUSSION

The investigation of land subsidence in the city of Recife covered a time interval of 4.5 years of InSAR interferometric monitoring, from September 25, 2016 to April 8, 2021. Over this period, the average revisit time of Sentinel-1 images was of 12.2 days, with a maximum variation of 24 days and a minimum of 12 days.

The PSInSAR monitoring study involved 44,588 measurement points, most with a temporal coherence value equal to 0.75. The points covered an area of 153,037 km<sup>2</sup> of Recife. Analysis of these data revealed several sites of land subsidence in the city (Figures 6 and 7). The main occurrences were in the west zone.

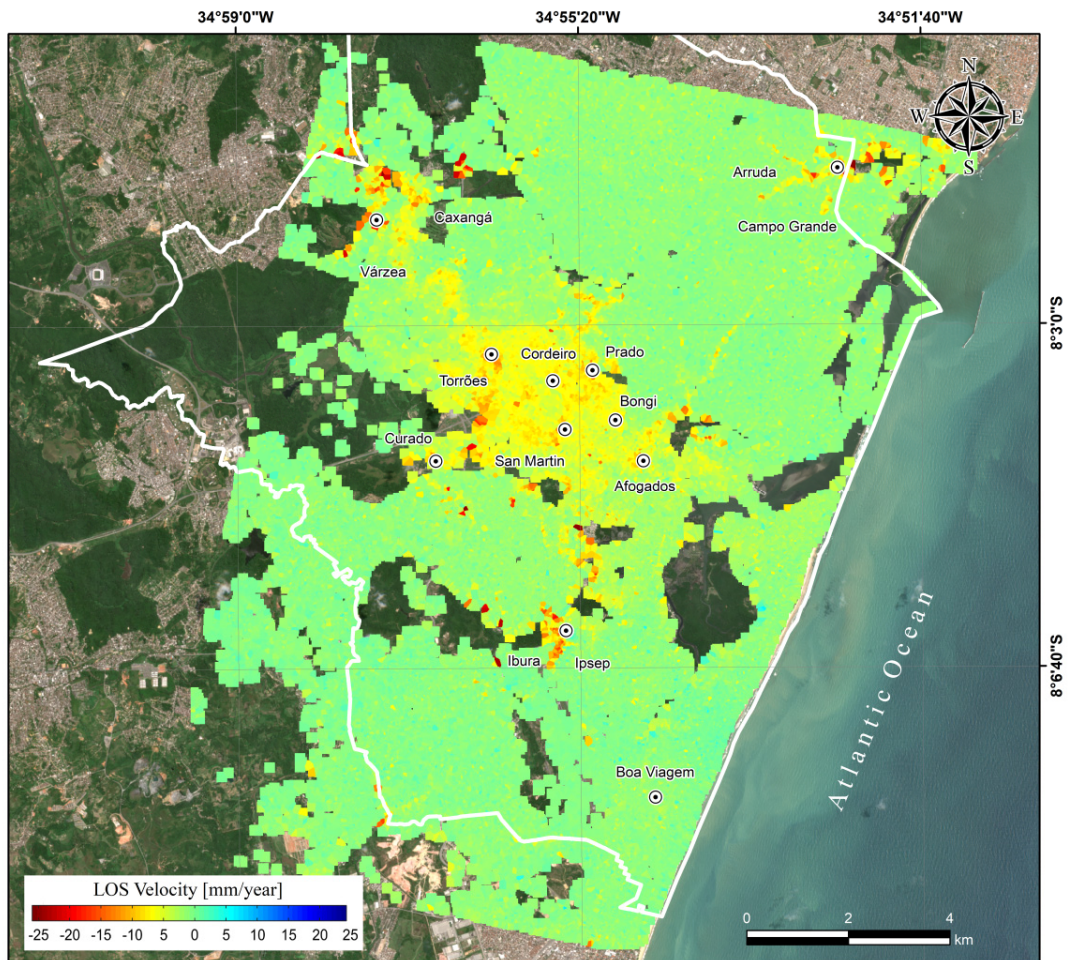


Figure 6. Deformation LOS velocity map.

In this region, large areas of drawdown with a rate of up to  $-15$  mm/year were observed in the neighborhoods of Curado, Cordeiro, Torrões, San Martin, Afogados, Bongí, Prado, Várzea and Caxangá. Similar cases, but with a smaller area, occurred between the neighborhoods of Ibura and Ipsep, responsible for the largest sinking rate in the city, with a rate close to  $-18$  mm/year. The situation in the west may be due to the compaction of soils in newly built areas.

In this regard, similar case, but with a smaller area, also occurs in the northern zone of city between the neighborhoods of Arruda and Campo Grande with a velocity equal to  $-16.8$  mm/year.

In addition to these locations, there were signs of lowering in the south due to the exploitation of groundwater. The velocity was  $-2.5$  mm/year in areas affected by the piezometric reduction in Boa Viagem neighborhood.

## V. CONCLUSIONS

The use of the PSInSAR technique reveals several cases of land subsidence of Recife. The widespread human intervention is responsible for surface instability. This is due to the recent urbanization process with the recovery of flooded areas and the

exploitation of groundwater with piezometric level reduction.

The main occurrences occur in the west of Recife. The region has large areas of drawdown with a LOS rate of up to  $-15$  mm/year in the neighborhoods of Curado, Cordeiro, Torrões, San Martin, Afogados, Bongí, Prado, Várzea and Caxangá. There are cases of smaller area with a value close to  $-18$  mm/year in the neighborhoods of Ibura and Ipsep, responsible for the biggest sinking in the city. The causes may be due to soil compaction in newly built areas. The process can take several years for settlement.

The recent urbanization also caused smaller areas of land subsidence in the northern zone, with a velocity close to  $-17$  mm/year between the neighborhoods of Arruda and Campo Grande.

In addition to these regions, there are signs of lowering in the south related to the exploitation of groundwater. The LOS velocity is around  $-2.5$  mm/year in areas affected by the piezometric reduction in the neighborhood of Boa Viagem.

Thus, the development of Recife requires care in several aspects. The identification of land subsidence areas can help in the study of urban drainage to avoid flooding sites and in the adoption of mitigating measures for the suitable use of groundwater resources.

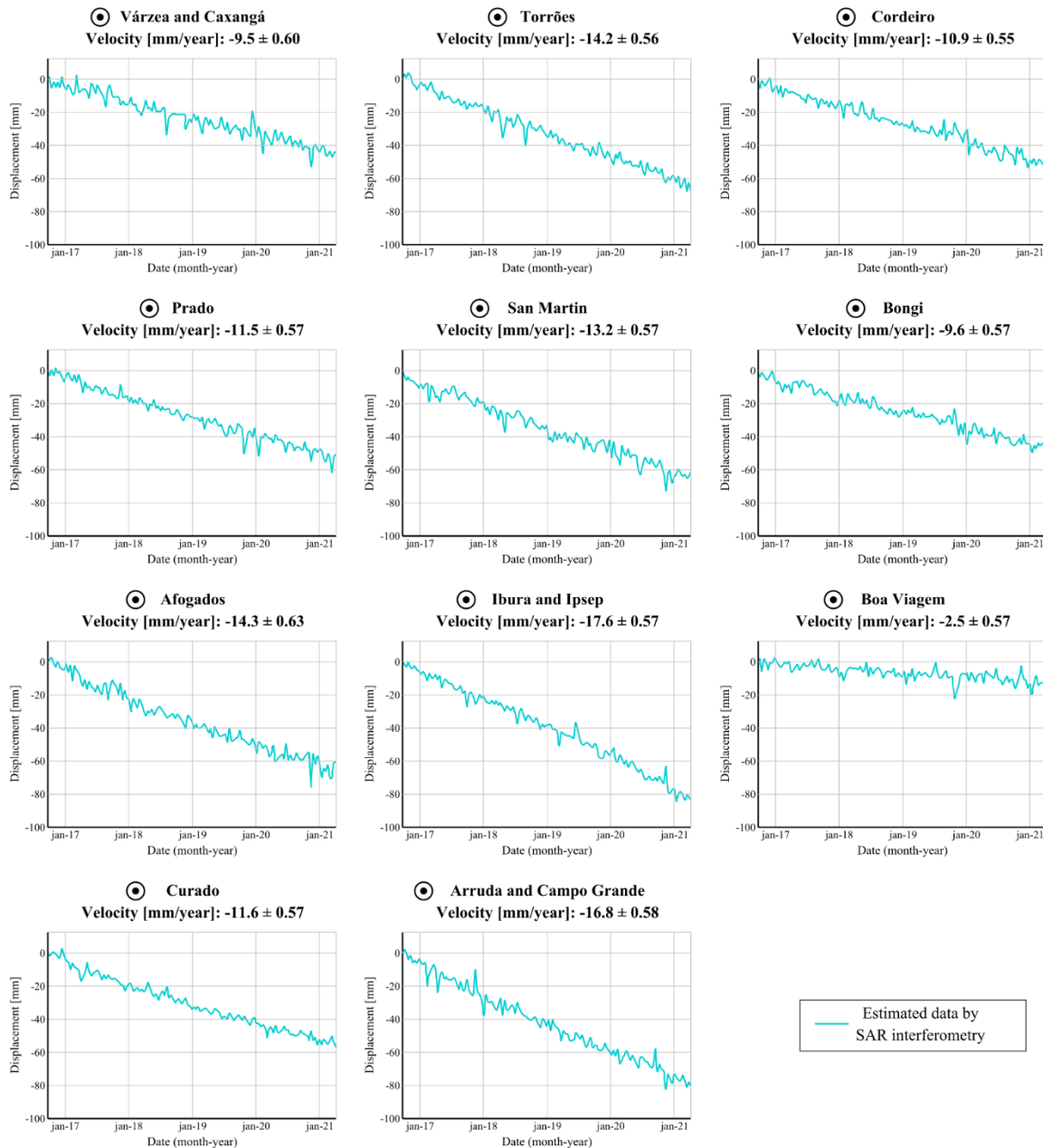


Figure 7. Estimated deformation time series.

## VI. ACKNOWLEDGEMENTS

Sentinel-1 data were freely provided by ESA through Copernicus Programme. Data have been processed by SARPROZ (Copyright (c) 2009-2022 Daniele Perissin). Research was supported by POIUJA-2021/2022 and CEACTEMA from University of Jaén (Spain), and RNM-282 research group from the Junta de Andalucía (Spain).

## References

- Abidin, H.Z., H. Andreas, I. Gumilar, T.P. Sidiq, and M. Gamal, (2015). Environmental Impacts of Land Subsidence in Urban Areas of Indonesia. In: *FIG Working Week 2015*, Sofia, Bulgaria, pp. 1-12.
- Alisson, E. (2013). Aquíferos do Recife correm risco de salinização. Available in: <https://agencia.fapesp.br/aquiferos-do-recife-correm-risco-de-salinizacao/183778>.
- Bedini, E. (2020). Persistent Scatterer Interferometry of Sentinel-1 Time Series to Detect Ground Subsidence in the City of Recife, Brazil. *Journal of Hyperspectral Remote Sensing*, Vol 10, No. 1, pp. 1-9.
- Cabral, J.J.S.P., V.P. Farias, M.D.C. Sobral, A.L.R. De Paiva, and R.B. Santos, (2008). Groundwater management in Recife. *Water International*, Vol 33, No. 1, pp. 86-99.
- Costa, W.D., J. Manoel Filho, A. Santos, W.D. Costa Filho, A.B. Monteiro, F.J.A. Souza, A.V.G. Lopes, A.J.C. Santos, M.C. Silva Filho, and M.J. Silva, (1998). *Estudo Hidrogeológico da Região Metropolitana do Recife*. Convênio IDRC-UFPE-FADE. Recife, p. 128.
- Crosetto, M., O. Monserrat, M. Cuevas-González, N. Devanthery, and B. Crippa, (2016). Persistent Scatterer Interferometry: A Review. *ISPRS Journal of Photogrammetry and Remote Sensing*, Vol 115, pp. 78-89.
- Ferretti, A., C. Prati, and F. Rocca, (2001). Permanent Scatterers in SAR Interferometry. *IEEE Transactions on Geoscience and Remote Sensing*, Vol 39, No. 1, pp. 8-20.

- Gusmão Filho, J.A., (1998). *Fundações do Conhecimento Geológico à Prática da Engenharia*. Recife: Editora Universitária UFPE, p. 345.
- Hanssen, R.F., (2001). *Radar Interferometry: Data Interpretation and Error Analysis*. Kluwer Academic Publishers, p. 308.
- Luna, R.M.R., S.J.D.A. Garnés, J.J.S.P. Cabral, and S.M. Santos, (2017). Groundwater Overexploitation and Soil Subsidence Monitoring on Recife Plain (Brazil). *Natural Hazards*, Vol 86, No. 3, pp. 1363-1376.
- Luna, R.M.R., S.J.D.A. Garnés, J.J.S.P. Cabral, and S.M. Santos, (2021). Suitability of GNSS for Analysis of Soil Subsidence in Recife in a Highly Urbanized Coastal Area. *Natural Hazards*, Vol 106, No. 3, pp. 1821-1837.
- Melo, M.L., (1978). *Metropolitan Expansion and Underdevelopment: The Case of Recife*. Recife: UFPE, p. 257.
- Montenegro, S.M.G.L., J.J.S.P. Cabral, A.L.R. Paiva, A.A.A. Montenegro, J.G.A. Demetrio, and G.L. Cavalcanti, (2009). Águas Subterrâneas na Zona Costeira da Planície do Recife (PE): Evolução da Salinização e Perspectivas de Gerenciamento. *Revista Brasileira de Recursos Hídricos*, Vol 14, No. 3, pp. 81-93.
- Perissin, D., (2022). SARPROZ software. Official product web page: <http://www.sarproz.com>.
- Prokopovich, N.P., (1979). Genetic Classification of Land Subsidence. In: *Evaluation and Prediction of Subsidence*, ASCE, pp. 389-399.
- Romão, V.M.C., A.S. Silva, and S.M. Santos, (2003). Metodologia para Determinação de Subsidência de Solo na Região Metropolitana do Recife. In: *III Colóquio Brasileiro de Ciências Geodésicas*, Curitiba, pp. 1-12.
- Santos, S.M., V.M.C. Romão, G.G. Seeber, and J.J.S.P. Cabral, (2010). Detecção de Deslocamentos Verticais Usando GPS em Áreas Costeiras. *Revista Brasileira de Cartografia*, Vol 62, No. 2, pp. 137-144.
- Santos, S.M., J.J.S.P. Cabral, and I.D.D.S., Pontes Filho, (2012). Monitoring of Soil Subsidence in Urban and Coastal Areas Due to Groundwater Overexploitation Using GPS. *Natural Hazards*, Vol 64, No. 1, pp. 421-439.
- Scott, R.F., (1978). Subsidence – A Review. In: *Evaluation and prediction of subsidence*, ASCE, pp. 1-25.
- Wang, N., (2017). Estudio de Subsistencia por Extracción de Fluido. *Dissertation (Master)*, Escuela Técnica Superior, Universidad Politécnica de Madrid, pp. 33.

## Monitoring Gravitational Deformations of the Wettzell 20 m Radio Telescope's Main Reflector Using a Leica RTC360

Agnes Weinhuber<sup>1</sup>, Alexander Neidhardt<sup>2</sup>, Christoph Holst<sup>1</sup>

<sup>1</sup> Technical University of Munich, School of Engineering and Design, Chair of Engineering Geodesy, Arcisstr. 21, 80333 Munich, Germany, ([a.weinhuber@tum.de](mailto:a.weinhuber@tum.de); [christoph.holst@tum.de](mailto:christoph.holst@tum.de))

<sup>2</sup> Research Facility Satellite Geodesy, Technical University of Munich, Geodetic Observatory Wettzell, Sackenrieder Strasse 25, 93444 Bad Kötzing, Germany, ([alexander.neidhardt@tum.de](mailto:alexander.neidhardt@tum.de))

**Key words:** *laser scanning; deformation analysis; in situ calibration; VLBI; radio telescope; alignment*

### ABSTRACT

Quasars are nowadays the basis to determine the world's absolute orientation in space by radio interferometry (VLBI). The global network of baselines measured by the used radio telescopes, which vary greatly in size, is subject to various influences that have an impact on the International Terrestrial Reference Frame. Among others, those influences are imperfections of individual panels of the dishes, a possible elevation dependent deformation of the whole dish and a shift of the reference point due to gravitational influences. In this study, we monitor the elevation dependent deformation of the main reflector of the 20 m radio telescope of the Geodetic Observatory Wettzell by a Leica RTC360 laser scanner. For this task, we mount the terrestrial laser scanner overhead near the subreflector to capture the surface of the moving dish at each elevation angle. This study focusses on 1) introducing further redundancy in the measurement and processing strategy to gain a reliable and accurate result even the used scanner is a no high-end one. This furthermore leads to 2) investigations whether there are differences in the results between in related work used high-end scanners and the RTC360 and thus 3) whether the RTC360 proves to be capable to detect deformations at a radio telescope's main reflector. Using these three foci, we show that deformations in the main reflector between elevations can be reliably determined areal and in focal length by redundant measurements with the RTC360. It is also shown that the results are less sensitive to axis errors compared to those obtained with high-end scanners. However, the compensations also show that the application scanner has certain systematics, which must be investigated in further steps.

### I. INTRODUCTION

Globally distributed radio telescopes are used for the determination of the earth's absolute orientation in space, the linkage of different reference frames and also the establishment of the International Terrestrial Reference Frame (ITRF) (Nothnagel *et al.*, 2017). For the realization, radio telescopes – distribute all around the globe – record the radio signals emitted from quasars. By correlating the received signals of different radio telescopes, runtime differences in the signal and therefore differences in the distance between these telescopes and the quasars can be determined. Using multiple of dose measurements, a global network of baselines with uncertainties of 5 mm to 15 mm depending on the distance between the ground stations can be formed (Nothnagel *et al.*, 2004). This procedure is called very long baseline interferometry (VLBI). The positions of the radio telescopes, which are integrated into the local reference networks, can thus be determined with high precision of 1 - 4 mm (Nothnagel *et al.*, 2004).

In order to enable a highly accurate determination of the individual positions and guarantee a precise realization and maintenance of the global reference system, high accuracy requirements are

correspondingly placed on the so-called local-ties. Therefore, all external circumstances, which may affect the reflectors of the radio telescopes, have to be taken into account. VLBI data already show different correction models. Nevertheless, but also not yet completely investigated and thus still unconsidered influences can, if they are uncovered and their magnitude made nameable, possibly lead to an improvement and support of the VLBI measurements (Nothnagel *et al.*, 2019). For example, Lösler *et al.* (2010) considered the effects of the ambient temperature on a possible change of position (2D) of the reference point of the radio telescope.

Laser scanning, which has come to the fore in recent years, allows radio telescope's geometries to be determined precisely and areal over their antenna surface. This now makes it possible, among other things, to detect possible imperfections of the entire reflector or of the individual panels (Holst *et al.*, 2015). Also, a determination of deformations of the telescope due to its own weight by approaching different elevation angles is and a possible influence on the reference point can be possible (Holst *et al.*, 2019). Due to the fact that laser scanning is becoming more and more popular and is used in many different application



fields, manufacturers are also producing laser scanners for mainstream consumers without any geodetic background and with lower requirements regarding accuracy and individual measurement procedures (e.g., scanning in two faces, scanning only individual sections). As an example, the Leica RTC360 was built regarding this background.

This paper investigates how far measurements of the RTC360 for monitoring the radio telescope differ from comparable measurements with a high-end scanner. The recognizable differences and conspicuities in the course of the deformation analysis of the main reflector are highlighted. Furthermore, it is investigated whether this scanner is also suitable to detect the deformations at the telescope. Additionally, because a none high-end instrument is used, the measurements in this study are performed with higher redundancy to obtain reliable and accurate results.

After a short introduction of the monitoring procedures of radio telescopes in related work, technical data of the radio telescope in Wettzell and the used scanner are given and the chosen measuring procedure is described. In the main part the realization of the monitoring including the processing of the data and the deformation analysis is explained. Subsequently, the obtained results are evaluated regarding the deformation analysis and the used scanner.

## II. RELATED WORK

Laser scanning measurements enable a high quantity of points to be measured, which reflect the scanned object areal and with high precision. Thus, it is also possible to investigate deformations of objects in their entire surface. However, it is known from several investigations that a strict deformation analysis between individual points is not possible, since the recorded points are random points and not discrete points (Wunderlich *et al.*, 2019).

Several approaches have been developed to determine deformations between point clouds with high accuracy. One of them is the M3C2 algorithm, with which point clouds of different epochs, here the different elevations, can be compared to each other. The algorithm estimates planes and plane normals for so-called core points in suitably selected diameters in order to compare distances between these and the second point cloud (Lague *et al.*, 2013). However, this algorithm does not work optimally for detecting deformations of radio telescopes, even if the curvature of the main reflector is not steep. The required accuracies with which a deformation can be determined, however, cannot be achieved.

Since the design of a radio telescope is always a mathematically defined geometry, approaches are being developed which take the main reflector's shape into account and thus contribute to a successful deformation analysis. Using a CAD model describing the

shape and comparing all elevations with this model turns out not to be useful. In a Cloud to Mesh comparison (C2M) the shortest distance of each point of the point cloud to the triangular surfaces is calculated. The algorithm is therefore suitable for objects that are as flat as possible (Lague *et al.*, 2013; Holst *et al.*, 2017). If a deformation is present, this will be detected, but due to the calculation of the point distance in a given direction, false assignments can occur, especially in the edge region of the reflector.

The mathematical description of a main reflector is thereby a mathematical rotational paraboloid defined by its focal length (Schlüter *et al.*, 2007). To gain a new approach for areal and meaningful deformation analysis for radio telescopes, Holst *et al.* (2012) develops a method where for each point cloud an estimation of a paraboloid is performed. By estimating the parameters of the reflector at each individual scanned state, the different elevation angles, the parameters for the focal length of the telescope are also estimated. The variation of the estimated focal lengths can therefore provide information about a deformation to the different elevation angles (Holst *et al.*, 2012). Previous work and analyses with 3D TLS data related to the observed radio telescope, deformations of the telescope can be detected by this method (Holst *et al.*, 2017; Holst *et al.* 2015).

## III. REALIZATION OF THE MONITORING

### A. Measurement Object

The 20 m radio telescope at the Wettzell geodetic observatory, operated for almost 40 years now by the Federal Agency for Cartography and Geodesy (BKG) and the Satellite Geodesy Research Facility (FESG) of the Technical University of Munich, makes a decisive contribution to the realization and maintenance of the global reference system (Schlüter *et al.*, 2007). This radio telescope is a Cassegrain arrangement with main reflector and subreflector (BKG, 2022). The main reflector to be investigated can be described by a mathematical rotational paraboloid with a focal length of 9 m (Schlüter *et al.*, 2007). Here, possible influences of gravity due to the different elevation angles on the reflector are to be detected and determined.

### B. Measuring Procedure

To cover the entire main reflector at the selected elevations in fine gradation of 5°, 10°, 20°, 30°, 40°, 50°, 60°, 70°, 80°, 90°, the scanner is mounted in the radio telescope (Figure 1). Thus, it can move with the dish at increasing elevations and there will be nearly no uncovered scan area. For the realization, the scanner was attached to one of the struts in the telescope with a mounting specially made for this radio telescope. Measuring in an inclined position is possible with the RTC360, but Leica Geosystems only recommends angles of up to 15° here (Leica, 2018). Accordingly, the mount allows the scanner to swing along to return to a vertical

upside-down orientation as the radio telescope moves to the next elevation step (Figure 2). The mount consists of an element with a magnetic brake in order to fix the laser scanner, which is oriented according to gravity, for the respective scan. This shall prevent the scanner from oscillating due to its own motion caused by the rotation of the scanner. To ensure the best possible view of the main reflector at each elevation angle, the scanner was therefore attached to one of the upper struts. It is also necessary to mount it as close as possible to the subreflector in order to minimize shadowing effects by the feed horn in the main reflector.



Figure 1. Mounting of the RTC360 in the 20 m Radio Telescope Wettzell.

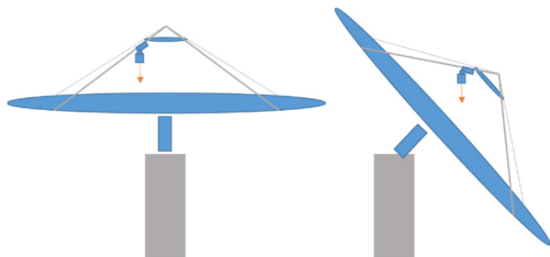


Figure 2. Mounting of the Laser Scanner and Measurement Principle in Different Elevation Angles (without scale)

In order to obtain redundant data for each selected elevation angle, the main reflector was scanned with a resolution of 3 mm at 10 m for each elevation angle when the radio telescope was raised to the upper elevations and it was also scanned when it lowered again. In the further writing, the differentiation between the increasing elevations (5° to 90°) and the decreasing (90° back to 5°) will be made by first and second measurement series. This results in two redundant scans for each of the elevation angle.

### C. Data Pre-Processing

Calculating with high resolution point clouds requires an efficient data pre-processing. This pre-processing can be divided into several individual steps. When examining the radio telescope for deformations, the focus is on the main reflector. Therefore, this part must be extracted from the point cloud. For this purpose, all points outside the telescope are removed in a first step. Then, the components inside the telescope that do not belong to the parabolic main reflector, namely the sub-reflector, the feed and the struts, have to be removed (Figure 3). In a further step, outliers which often occur at edges or object boundaries during laser scanning are detected and removed manually (Figure 3). The outliers

can be easily segmented by their intensity value, which is clearly different from the intensity values of the valid points on the telescope surface. The selected threshold value is thereby clearly defined that it can be applied to all point clouds and does not need to be adjusted.

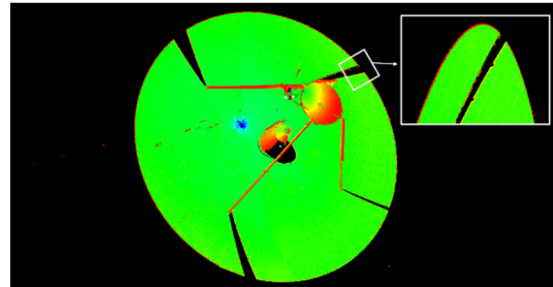


Figure 3. Point Clouds with Outliers. Detailed Cut-Out Shows the Higher Intensities in the Edge Area, Which Can Be Eliminated Via an Intensity Filter.

After removing the clearly detectable outlier points, there are still glancing points occurring between the single panels of the reflector, which are difficult to remove manually due to the curved shape (Figure 4). To remove them semi-automatically, the filter algorithm “Hidden Point Removal” in CloudCompare can be used. This filter is filtering all the points that lie in the background of the object from the current point of view (Katz *et al.*, 2007). By slightly tilting the point cloud and change the viewpoints, the glancing points between the panels and all close outlier points to the back of the reflector can be removed.

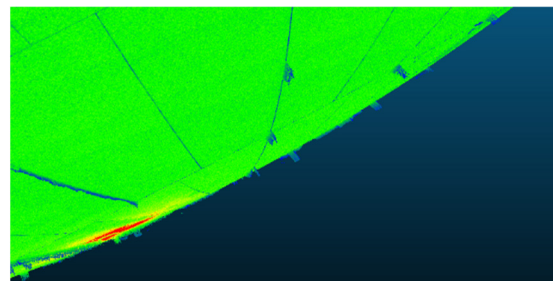


Figure 4. Back Side of a Scan Before Filtering with Hidden Point Removal, Outlier Between Panels.

To reduce the calculation time and the memory usage, the point clouds are also to be subsampled. Considering the further calculation steps to fit a concrete shape into the point clouds, a homogeneous point density in the point clouds of the main reflector are required. Only with an equal distribution an accurate parameter estimation is ensured (Holst *et al.*, 2017). The point clouds in this paper are subsampled to 1 cm point to point spacing. Therefore, the spatial subsampling tool of CloudCompare is used (CloudCompare, 2015).

### D. Data Processing – Shape Estimation

In order to detect a possible deformation of the main reflector within the measured data, it must be taken into account for the further steps, that the reflectors

position changes in relation to the scanner due to the different elevation angles and the self-adjustment of the scanner in vertical direction.

The main reflector of the radio telescope in Wettzell consists of 3 rows of concentrically arranged panels, which together form the shape of a rotational paraboloid (Schlüter *et al.*, 2007). This allows the recorded measurement data to be parameterized with a functional model of a rotational paraboloid. In related work on deformation analysis of radio telescopes (Holst *et al.* 2018), it is outlined that the rotational paraboloid can be described in terms of focal length, for example as follows, if the axis of rotation equals the Z-axis of the [X, Y, Z] coordinate system (Eq. 1):

$$\frac{X_i^2 + Y_i^2}{4 \cdot f} - Z_i = 0 \quad (1)$$

where  $i$  = point cloud of  $i = 1, \dots, n$  sampling points  
 $f$  = focal length

However, since the coordinates [x, y, z] of the point clouds are located in the scanner intrinsic coordinate system the paraboloid must be transformed by a three-dimensional Helmert transformation using two rotations and three translations (Niemeier, 2008) (Eq. 2):

$$\begin{bmatrix} X_i \\ Y_i \\ Z_i \end{bmatrix} = R_y(\phi_y) \cdot R_x(\phi_x) \cdot \begin{bmatrix} x_i \\ y_i \\ z_i \end{bmatrix} + \begin{bmatrix} X_t \\ Y_t \\ Z_t \end{bmatrix} \quad (2)$$

Accordingly, a rotational paraboloid can be described by 6 parameters in any position and orientation, here in the local scanner coordinate system, by: three translations in X, Y and Z direction, two rotations around x and y and the focal length f (Holst, 2017) (Eq. 3):

$$p = [X_t, Y_t, Z_t, \phi_x, \phi_y, f]^T \quad (3)$$

For the estimation of the parameters of the rotational paraboloid in the local scanner system, the measured coordinates in their original polar coordinates [d,  $\varphi$ ,  $\theta$ ] must be integrated into the paraboloid model (Eq. 4):

$$\begin{bmatrix} x_i \\ y_i \\ z_i \end{bmatrix} = \begin{bmatrix} d_i \cdot \sin \varphi_i \cdot \cos \theta_i \\ d_i \cdot \sin \varphi_i \cdot \sin \theta_i \\ d_i \cdot \cos \varphi_i \end{bmatrix} \quad (4)$$

For this purpose, the coordinates have to be recalculated from the received Cartesian coordinates to their origin measured polar coordinates and for the further steps recalculated to the Cartesian coordinates again to then transform them into the coordinates of the paraboloid.

For the respective accuracies of the distances and angle measurements for the stochastic model  $\Sigma_{il}$ , the manufacturer's specifications are used for the angel

measurements  $\varphi$  and  $\theta$ :  $\sigma_{\varphi, \theta} = 5.6$  mgon (Leica, 2018) and for the range accuracy,  $\sigma_d$  is set to 1.5 mm for the stochastic model.

The parameters are calculated using the general case of adjustment (Gauß-Helmert-Model): the residuals  $\hat{v}$  which represent the errors between the observations  $l$  and the adjusted observations  $\hat{l}$  are reduced to a minimum (Mikhail and Ackermann, 1976):  $v^T \Sigma_{ll}^{-1} v$ .

To indicate possible deformations in the main reflector, the estimated paraboloid parameters  $\hat{p}$  and the estimated residuals  $\hat{v}$  are used. By using the residuals, information about the deformation of the reflector can be obtained as well as, for further research, systematic errors of the scanner can be detected (Holst *et al.*, 2018). This statement is based on the fact that the surface accuracy of the main reflector of the radio telescope is given as 0.35 mm rms (BKG, 2022) which is better than the scans.

#### E. Deformation Analysis – Focal Length

To get information about the deformation of the radio telescope, the estimated parameters can be examined. In Table 1, the estimated values for each elevation step of the first measurement series are considered. As described before, the shape of a rotational paraboloid is solely related to the size of the focal length f. It is prominent that the standard deviation of the focal length is estimated with  $\sigma_f [mm] = 0.017$  for all elevation angles. This is too optimistic, which may be due to the fact that spatial correlation between neighboring points is neglected yet (Holst *et al.*, 2012). To get a better impression of the different focal lengths to the different elevation steps, differences of the increasing elevation steps to elevation step 5° are also shown as  $\Delta f$  in the table. The maximum difference reaches -5.0 mm between elevation 5° and elevation 80°, which validates the assumption that gravity effects the radio telescope's geometry in its different elevation angles.

Over the increasing elevation steps, the focal length becomes noticeably larger. To show this change graphically, the focal lengths of both measurement series are plotted for each elevation step in Figure 5. In the first measurement series (blue), there are rather none-smooth steps in the course of the connecting line between the values of the individual focal lengths. The maximum difference in the focal lengths between the first and the second measurement series is 0.4 mm (Table 2). If those finding are due to systematic measurement errors, will be evaluated in a prospective study.

#### F. Deformation Analysis – Residuals

In addition to considering the focal length, the areal measurement of the main reflector provides yet another way to visualize the deformations and check the success of the adjustments. Related work shows that by estimating the residuals and plotting the errors

in the points between the individual scans and the respective estimated paraboloid, deformations can be detected (Holst *et al.*, 2017). For this purpose, the errors are represented as intensities in the XY position of the rotational paraboloid.

The shown residuals in the range of - 5 to + 5 mm in the single plots show hardly any optical visible differences between the continuous elevation steps (Figure 6), but if the two extrema – elevation step 5° and 90° – are compared (additionally with another suitable color bar), visible differences appear in the maxima of the residuals (Figure 7). There are less maxima in the single points in elevation step 90°, which can be due to the fact that in elevation 90° the main reflector lies like an upward opened bowl and thus the force of the gravitation affects all areas approximately equally.

If the residuals are not considered in their total effect, but in their local maxima in the main reflector, then, on the one hand, the individual panels are clearly discernible. In the middle of the three concentric

circles, the higher residuals occur more in the center of the panels, at the edges they tend to go into the negative range. In the outer and inner circles, the behavior seems to be reversed. The residuals can therefore also provide information about local deformations (Holst *et al.*, 2017).

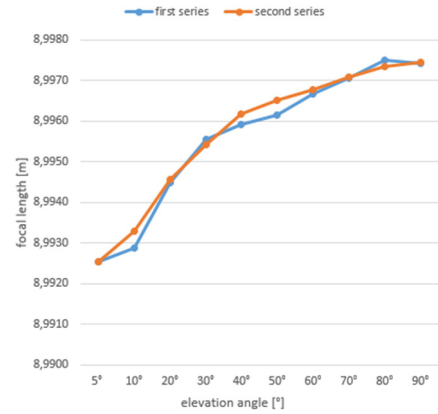


Figure 5. Focal Lengths  $f$  for all Elevation Levels in Both Measurement Series

Table 1. Estimated Parameters, First Series

p	Elevation angles [°]										
	5	10	20	30	40	50	60	70	80	90	
$X_t$ [m]	1.3589	0.9868	0.7603	0.1486	0.0179	0.1068	-0.3439	-0.5441	-0.8321	-1.2484	
$Y_t$ [m]	-1.1803	-1.5069	-1.6403	-1.8130	-1.8388	-1.8613	-1.8582	-1.8420	-1.7686	-1.5512	
$Z_t$ [m]	6.8021	6.7855	6.7352	6.6929	6.6498	6.6106	6.5815	6.5580	6.5432	6.5373	
$\phi_x$ [gon]	-92.8248	-75.3197	-62.2525	-39.5589	-32.0068	-28.7366	-16.0541	-9.2608	-3.3473	-0.0241	
$\phi_y$ [gon]	45.6064	70.0086	58.3387	58.0302	47.6971	35.26131	29.6200	20.3403	10.6671	0.0219	
$f$ [m]	8.9926	8.9929	8.9945	8.9956	8.9959	8.9962	8.9967	8.9971	8.9975	8.9974	
$\sigma_f$ [mm]	0.017	0.017	0.017	0.017	0.017	0.017	0.017	0.017	0.017	0.017	
$\Delta f$ [mm]	-	-0.3	-1.9	-3.0	-3.4	-3.6	-4.1	-4.5	-5.0	-4.9	

Table 2. Differences in  $f$  between First and Second Measurement Series

p	Elevation angles [°]										
	5	10	20	30	40	50	60	70	80	90	
$f_1$ [m]	8.9926	8.9929	8.9945	8.9956	8.9959	8.9962	8.9967	8.9971	8.9975	8.9974	
$f_2$ [m]	8.9926	8.9933	8.9946	8.9954	8.9962	8.9965	8.9968	8.9971	8.9973	8.9974	
$\Delta f_{2-1}$ [mm]	0	0.43	0.06	0.14	0.26	0.36	0.11	0.03	0.17	0.02	

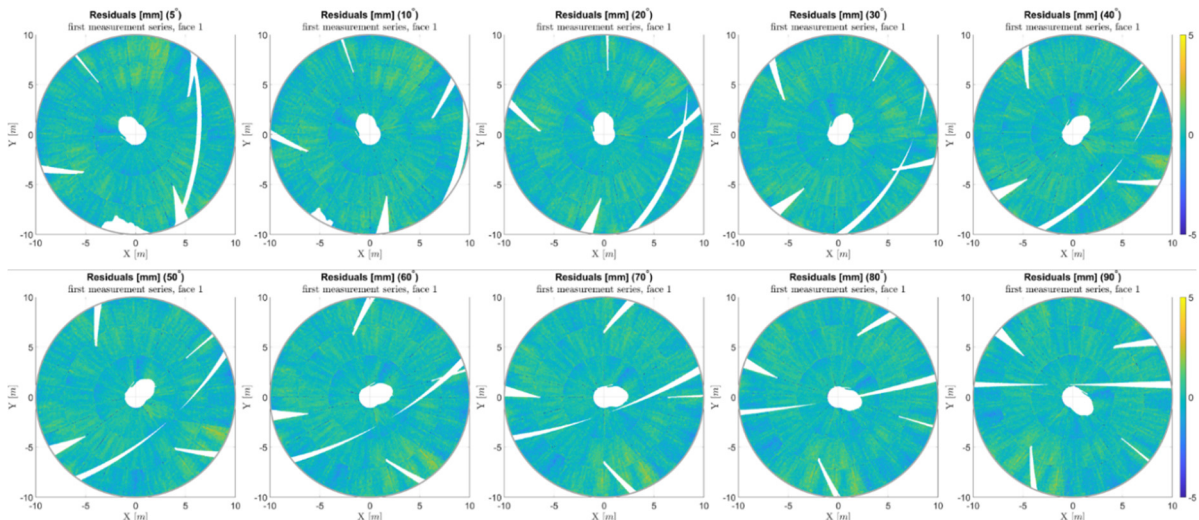


Figure 6. Residuals from 5° Elevation up to 90° Elevation in First Measurement Series.

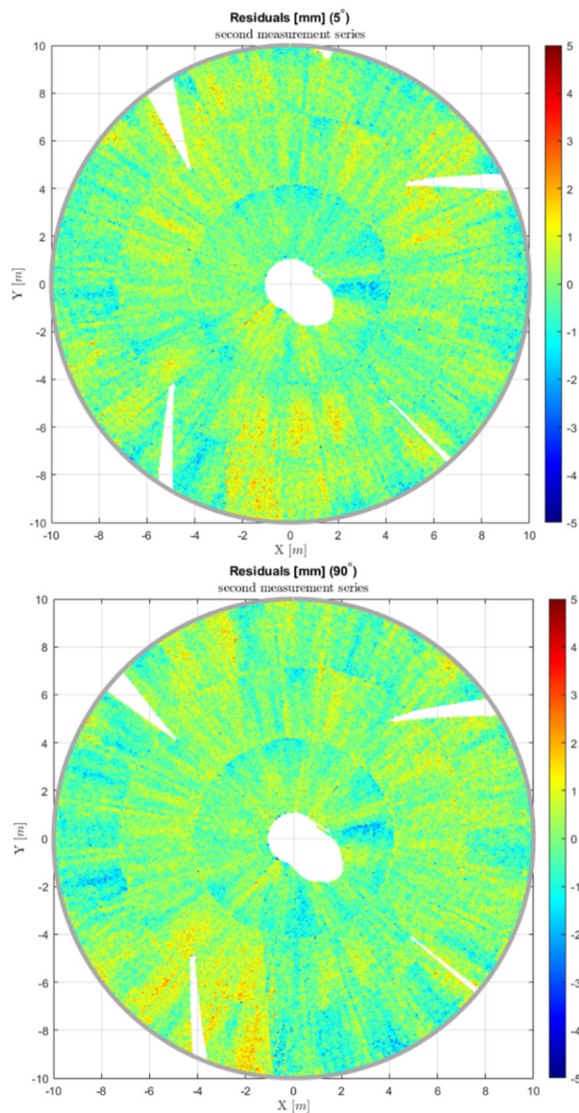


Figure 7. Residuals for the Elevations 5° and 90° in the Second Measurement Series.

Furthermore, a leap in the representation between positive and negative residuals is clearly visible, which indicates systematic deviations of the scanner due to its axis error (Figure 8). This systematic is to be expected, but it is interesting to note that the differences are much smaller than in the previous works (Holst *et al.*, 2018), which is to be investigated in further steps. As well, a purely optical comparison of the plots of the first and second measurement series does not show any recognizable differences between the two plots of the 90° elevation (not shown here). In elevation 5°, however, the positive maxima in the plot is more clearly recognizable.

When zooming in close to one of the plots, stripe-like patterns that converge from the upper edge of the main reflector to the center appear (Figure 8). This effect indicates that the holder was possibly not quite stable during the scan and the scanner could oscillate. Furthermore, the change of sign in the residuals (around  $X=-1\text{m}$ ) clearly indicates systematic calibration errors of the scanner (compare to Holst *et al.*, 2017).

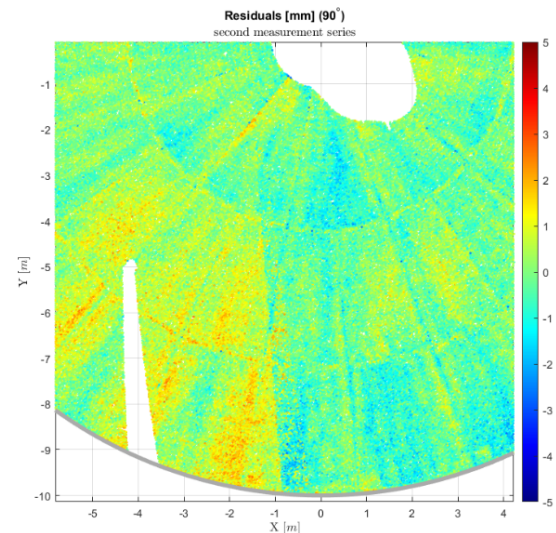


Figure 8. Leap Due to Systematic Deviations of the Scanner Axis Errors.

#### IV. EVALUATION OF THE RESULTS

##### A. Deformation Analysis

In this study, it was demonstrated that by means of the areal measurements and the high resolution of terrestrial laser scanning, conclusions can be made about the deformations of the main reflector of a radio telescope. By the calculated residuals between the single scans and the equivalent estimated rotational paraboloid, local deformations at the panels can be detected (Holst *et al.*, 2017) and highlighted by meaningful values in further investigations as well as in related work. Deformations of the entire reflector can also be highlighted via a holistic view of the plotted residuals. With further scans of the main reflector in a first and second cycle, scanner-internal effects can be eliminated by co-estimating calibration parameters in an in-situ calibration (Holst *et al.*, 2015). Related work also shows that by estimating calibration parameters, there is the possibility of a clear separation between influences of the scanner and the actual deformations due to the effect of gravity on the reflector at different elevation angles (Holst and Kuhlmann, 2016).

Furthermore, this paper shows that by estimating the parameters for the individual scans, unambiguous statements can be made about the deformations depending on the elevation when the parameters for the focal lengths are compared. A rotational paraboloid flattens with increasing focal length. If this is transferred to the data obtained, the effect can be seen. If the reflector is in the elevation step 90°, the gravitation has the same effect on the whole dish due to the position, the focal length is larger and the paraboloid is therefore flatter. If the dish is lowered towards the ground, the focal lengths become steadily smaller, which indicates that the upper edge of the dish presses down more strongly and a deformation due to gravity is confirmed.

Although the differences in the focal lengths between the two series of measurements shown in Figure 5 only

reach values in the sub-millimeter range, these must be considered in further investigations. An estimation of the parameters in the adjustment in ascending as well as in descending direction for the first and second measurement series, which would result four values for the focal length, could lead to more insights. In this study, both series were calculated with initial values for the elevation of 5° in ascending elevation direction.

### B. RTC360 Investigations

It has been shown that the RTC360 is suitable for upside-down measurements and detecting deformations in the radio telescope's shape. The systematic axis errors that are clearly visible in previous work occurring with scanners not explicitly designed for upside-down measurement are also present in the measurements with the RTC360 but are far less noticeable. The range of deviations that can occur in a single panel are almost as large as the leap due to the axis error. No reason has been found yet why the RTC360 results seem less prone to error.

To smooth the small visible transition due to the axis errors and get more insights about the scanner itself, the RTC360 can be brought in a second manually rotated position to measure cycle 2. By that, an estimation of the calibration parameters can be made (Holst *et al.*, 2017).

Another systematic is also revealed: It seemed like the local coordinate system of the RTC360 changes between the individual scans. This effect can be clearly seen in the rotation of the main reflector in the plots of the residuals (Figure 6). To check the effect, all scans of the first measurement series and second measurement series were displayed together (Figure 9). Without this effect, series 1 and 2 should be congruent. However, a fanning out and a rotation like a twisting to each other can be seen. How the coordinate system is moving and if this systematic degrades the deformation analysis, need to be investigated and proven in further steps.

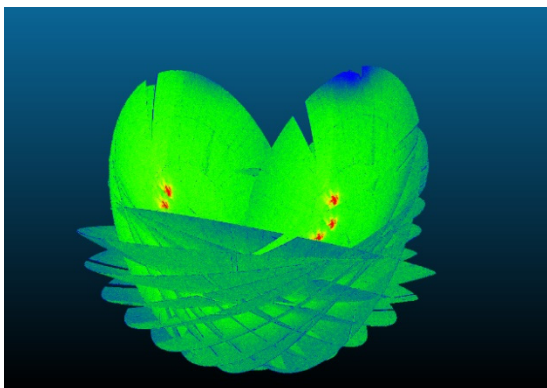


Figure 9. Systematic of RTC360 in Ongoing Scans (left: First Measurement Series; right: Second Measurement Series).

Here, a difficulty is that the exact internal pre-processing steps of a laser scanner remain hidden from the user and are not communicated by the manufacturer or only to a limited extent, what leads to

the designation of a black box system (Woschitz and Heister, 2017). Because the RTC360, in order to facilitate operation for the general and non-professional use, has a strongly predefined and limited selection of operating settings, which manipulate the data on the run (*e.g.*, the Doule Scan function), the internal processing steps behind it make it even more of a black box system. Thus, it is not only difficult to obtain further information about raw data but especially about the integrated sensors data like the IMU. To get an idea about the behavior of the scanner, further studies have to be done to investigate the rotations in Figure 9.

### V. CONCLUSION

By the approved method to estimate a rotation paraboloid for each elevation by means of an adjustment into each scan, statements about elevation dependent deformation of the main reflector of the 20 m radio telescope of the Geodetic Observatory Wettzell can be made. The results of the adjustment show that the application scanner has some peculiarities and systematics compared to the high-end scanners used in previous works, which have to be investigated in further steps. Nevertheless, the results of the RTC360 can be assumed to be valid. This is supported by comparisons of the estimated parameters of the rotational paraboloid at each elevation angle between the redundant measurements in ascending order and again in descending order.

### References

- BKG, (2022). Bundesamt für Kartographie und Geodäsie. Available in: <http://www.bkg.bund.de/DE/Observatorium-Wettzell/>, last accessed January 28.
- Cloudcompare, (2015). Girardeau-Montaut, D.. Available in: <http://www.danielgm.net/cc/>, last accessed January 27, 2022.
- Holst, C., P. Zeimetz, A. Nothnagel, W. Schauerte, and H. Kuhlmann, (2012). Estimation of focal length variations of a 100-m radio telescope's main reflector by laser scanner measurements. In: *Journal of Surveying Engineering*, 138(3), pp 126-135.
- Holst, C., A. Nothnagel, M. Blome, P. Becker, M. Eichborn, and H. Kuhlmann, (2015). Improved area-based deformation analysis of a radio telescope's main reflector based on terrestrial laser scanning. In: *Journal of Applied Geodesy*, 9(1), pp 1-14.
- Holst, C., and H. Kuhlmann, (2016). Challenges and present fields of action at laser scanner based deformation analyses. In: *Journal of Applied Geodesy*, 10(1), pp 17-25.
- Holst, C., B. Schmitz, A. Schraven, and H. Kuhlmann, (2017). Eignen sich in Standardsoftware implementierte Punktwolkenvergleiche zur flächenhaften Deformationsanalyse von Bauwerken? Eine Fallstudie anhand von Laserscans einer Holzplatte und einer Stauwand. In: *Zeitschrift für Vermessungswesen (zfv)*, 2.
- Holst, C., D. Schunck, A. Nothnagel, R. Haas, L. Wennerbäck, H. Olofsson, R. Hammargren, and H. Kuhlmann, (2017).

- Terrestrial laser scanner two-face measurements for analyzing the elevation-dependent deformation of the Onsala space observatory 20-m radio telescope's main reflector in a bundle adjustment. In: *Sensors*, 17(8), 1833.
- Holst, C., T. Medić, and H. Kuhlmann, (2018). Dealing with systematic laser scanner errors due to misalignment at area-based deformation analyses. In: *Journal of Applied Geodesy*, 12(2), pp 169-185.
- Holst, C., A. Nothnagel, R. Haas, and H. Kuhlmann, (2019). Investigating the gravitational stability of a radio telescope's reference point using a terrestrial laser scanner: Case study at the Onsala Space Observatory 20-m radio telescope. In: *ISPRS Journal of Photogrammetry and Remote Sensing*, 149, pp 67-76.
- Katz, S., A. Tal, and R. Basri, (2007). Direct visibility of point sets. In: *ACM SIGGRAPH 2007 papers*, pp. 24-es.
- Lague, D., N. Brodu, and J. Leroux, (2013). Accurate 3D comparison of complex topography with terrestrial laser scanner: Application to the Rangitikei canyon (NZ). In: *ISPRS Journal of Photogrammetry and Remote Sensing*, 82, pp 10-26.
- Leica Geosystems AG, (2018). RTC360. Available in: <https://leica-geosystems.com/>, last accessed January 28.
- Lösler, M., C. Eschelbach, A. Schenk, and A. Neidhardt, (2010). Permanentüberwachung des 20 m VLBI-Radioteleskops an der Fundamentalstation in Wettzell. In: *Zeitschrift für Vermessungswesen (zfv)*, 135(1), pp 40-48.
- Mikhail, E., and F. Ackermann, (1976). *Observations and Least Squares* (1976). In: Dun-Donnelly, New York, NY, pp 497.
- Niemeier, W., (2008). *Ausgleichsrechnung. Statistische Auswertemethoden*. Berlin: de Gruyter, 2. Auflage.
- Nothnagel, A., W. Schlüter, and H. Seeger, (2004). Die geodätische VLBI in Deutschland. In: *Zeitschrift für Vermessungswesen (zfv)*, 129, pp 219-226.
- Nothnagel, A., T. Artz, D. Behrend, and Z. Malkin, (2017). International VLBI service for geodesy and astrometry. In: *Journal of Geodesy*, 91(7), pp 711-721.
- Nothnagel, A., C. Holst, and R. Haas, (2019). A VLBI delay model for gravitational deformations of the Onsala 20 m radio telescope and the impact on its global coordinates. *Journal of Geodesy*, 93(10), pp 2019-2036.
- Schlüter, W., N. Brandl, R. Dassing, H. Hase, T. Klügel, R. Kilger, P. Lauber, A. Neidhardt, C. Plötz, S. Riepl, and U. Schreiber, (2007). Fundamentalstation Wettzell-ein geodätisches Observatorium. In: *Zeitschrift für Vermessungswesen (zfv)*, 132(3), pp 158-167.
- Woschitz, H., and H. Heister, (2017). *Überprüfung und Kalibrierung der Messmittel in der Geodäsie*. In: *Ingenieurgeodäsie*, Springer Spektrum, Berlin, Heidelberg, pp 403-461.
- Wunderlich, T., L. Raffl, and W. Wiedemann, (2019). *Wiedererkennung-zwei Lösungen für die strenge Deformationsanalyse flächenhafter Beobachtungen der Ingenieurgeodäsie*. In: Hanke K, Weinold T (eds), 20, pp 264-273.

## High-rate real-time PPP for dynamic motion detection in vertical direction

Baris Karadeniz<sup>1</sup>, Mert Bezcioglu<sup>1</sup>, Cemal Ozer Yigit<sup>1</sup>, Ahmet Anil Dindar<sup>2</sup>, Burak Akpınar<sup>3</sup>

<sup>1</sup> Department of Geomatics Engineering, Gebze Technical University, Turkey, ([mbezcioglu@gtu.edu.tr](mailto:mbezcioglu@gtu.edu.tr); [b.karadeniz@gtu.edu.tr](mailto:b.karadeniz@gtu.edu.tr); [cyigit@gtu.edu.tr](mailto:cyigit@gtu.edu.tr))

<sup>2</sup> Department of Civil Engineering, Gebze Technical University, Turkey, ([adindar@gtu.edu.tr](mailto:adindar@gtu.edu.tr))

<sup>3</sup> Department of Geomatics Engineering, Yildiz Technical University, Turkey, ([bakpinar@yildiz.edu.tr](mailto:bakpinar@yildiz.edu.tr))

**Key words:** *RT-PPP; IGS-RTS; GNSS; SHM; spline interpolation method; dynamic motion*

### ABSTRACT

Nowadays, with the developments in GNSS (Global Navigation Satellite System) technology, the data storage and data processing capacity of GPS (Global Positioning System) receivers has been gradually increased. This situation is widely used in the detection and monitoring of horizontal and vertical vibrations that occur in the structure when high temporal resolution geodetic GPS receivers are under the influence of dynamic loads such as earth crust motions, wind load, traffic load, which affect man-made engineering structures. In the study, RT DF-PPP (Real Time Dual Frequency-Precise Point Positioning) method was applied together with a GPS sensor with a sampling interval of 20 Hz, using a steel bar mounted on a steel tree model designed as a structure model, and a steel bar on which different sensors can be integrated and can provide simulation of vertical motions in detecting vertical motions occurring in structures. To evaluate the performance of the method used and to test the performance of capturing vertical displacements, the DF-RP (Dual Frequency-Relative Positioning) method was taken as reference and the results were compared with the PP-PPP (Post Process-PPP) method using the IGS-Final (International GNSS Service-Final) product. When the results are compared with the RP and PP-PPP solutions in the frequency domain of vertical motions as a result of harmonic oscillations of the high-rate RT-PPP method, it has been seen that the amplitudes and frequencies are compatible with each other. Therefore, dynamic motions that occur as a result of natural events such as earthquakes, tsunamis, landslides and volcanic eruptions can be instantly and reliably monitored and detected by the high-rate RT-PPP method. When the results were evaluated in the time domain, an improvement was observed in the RMSE (Root Mean Square Error) and maximum values of RT-PPP and PP-PPP methods according to RP after filtering. When the statistical results are examined, vertical harmonic motions of the solutions made by using both RT-PPP and PP-PPP methods can be detected with accuracy below centimeters. These results clearly show that it can detect vertical dynamic motions in engineering structures such as bridges, skyscrapers and viaducts with RT-PPP method to evaluate. Thus, by detecting the effects of dynamic motions occurring in the structure on the health of the structure, a safe environment will be provided by making a rapid hazard assessment for life safety.

### I. INTRODUCTION

High temporal resolution GPS receivers have been widely used in the monitoring and detection of instantaneous displacements as a result of natural events, the monitoring of dynamic motions in the structure and the detection of deformations that occur in the structure (Larson *et al.*, 2003; Larson, 2009; Kouba, 2003; Yi *et al.*, 2013; Moschas and Stiros, 2015; Wang *et al.*, 2016; Yu *et al.*, 2016; Yigit and Gurlek, 2017). Nowadays, the ability of high-rate GPS receivers used in many areas to capture dynamic motions occurring horizontally and vertically with Precise Point Positioning (PPP) technique (Zumberge *et al.*, 1997; Kouba and Heroux, 2001) using precise satellite orbit and clock corrections produced by analysis centers without being connected to a fixed point has been evaluated in many studies. In addition, the Relative Positioning (RP) technique was taken as a reference for comparison in the studies.

In many studies conducted with the PPP method, IGS-Final, IGS-Rapid and IGS-Ultra-rapid products produced by the International GNSS Service (IGS) analysis center were used. Although these products differ in terms of broadcasting time and accuracy, they have been evaluated with the post-process PPP method in areas such as GPS seismology and structural health monitoring (SHM) (Kouba 2003; Avallone *et al.*, 2011; Xu *et al.*, 2013; Nie *et al.*, 2016; Paziewski *et al.*, 2018; Xu *et al.*, 2019; Moschas *et al.*, 2014; Yigit, 2016; Yigit and Gurlek, 2017; Tang *et al.*, 2017; Kaloop *et al.*, 2018). The use of the products produced by the IGS analysis center in the monitoring of instantaneous dynamic motions due to the delay time limits these products. For this reason, real-time satellite orbit and clock correction information are provided free of charge to the user through the Real Time Service (RTS), which was established by IGS in 2013, in order to ensure the instantaneous data stream continuously. In this case, the idea of real-time monitoring of dynamic motions



has emerged and these studies have begun to be carried out in many areas today. In the studies, the performance of the Real Time (RT)-PPP method and the correction products used were tested by monitoring the displacements that occur in natural events such as earthquakes and tsunamis. (Hadas and Bosy, 2015; Krzan and Przechodzinski, 2016; Elsobeiey and Al Harbi, 2016; El-Mowafy *et al.*, 2016; Alcay and Turgut, 2017; Alcay, 2019; Takahashi *et al.*, 2014, Tu *et al.*, 2017, El-Mowafy and Deo, 2017; Li *et al.*, 2019; Li *et al.*, 2014; Zheng *et al.*, 2019; Zhang *et al.*, 2021). This method, which is also used in deformation monitoring of engineering structures, has been emphasized as an alternative method to the RP method (Martin *et al.*, 2015; Tang *et al.*, 2017). In addition to the real-time data stream offered by IGS, it offers satellite orbit and clock products with a sampling interval of 30 seconds, which are derived from the IGC01 data stream presented under real-time conditions and can be used for post-evaluation PPP solutions. However, the use of these products has been tested for near real-time rapid hazard assessment in order to detect the oscillations caused by the motions of the earth's crust in the structures and the damage to the structure. It has been tested that under real-time conditions, correction products produced from IGC01 can be detected at the centimeter or even millimeter level in the detection of earthquake-induced surface wave motions (Li *et al.*, 2019; Li *et al.*, 2014; Zheng *et al.*, 2019; Zhang *et al.*, 2021).

In this study, real-time evaluation of vertically damped harmonic motions with the RT-PPP method and the performance of the method are tested. The raw observation data collected from the geodetic quality GNSS receiver with 20 Hz sampling interval integrated into the steel bar capable of producing vertical damped harmonic motion has been solved with the RT-PPP method based on the IGC01 product offered by IGS-RTS. Moreover, the results were compared with the PP-PPP method, with reference to the RP method, which is widely used in many studies on the evaluation of dynamic motions occurring in engineering structures.

## II. TRADITIONAL PPP METHOD AND DESCRIPTION OF EXPERIMENTS

### A. Methodology

Dual frequency GNSS raw code and undifferenced carrier phase observation equations:

$$P_{r,j}^s = \rho_r^s + c \cdot \delta t_r - c \cdot \delta t^s + T_r^s + I_r^s + m_{r,j}^s + \varepsilon_{r,p}^s \quad (1)$$

$$\Phi_{r,j}^s = \rho_r^s + c \cdot \delta t_r - c \cdot \delta t^s + \lambda_j N_{r,j}^s + T_r^s - I_r^s + m_{r,j}^s + \varepsilon_{r,\phi}^s \quad (2)$$

Defined by the Equations 1 and 2. The symbols used in the equations are respectively:

$P_{r,j}^s$  = Pseudorange observation of the carrier frequency ( $j$ ) with respect to the satellite ( $s$ ) of the GPS receiver ( $r$ ) (m)

$\Phi_{r,j}^s$  = Carrier-phase observation of the carrier frequency ( $j$ ) with respect to the satellite ( $s$ ) of the GPS receiver ( $r$ ) (m)

$\rho$  = Geometric distance between satellite and receiver (m)

$c$  = Speed of light (m/s)

$\delta t_r$  = Receiver clock correction (s)

$\delta t^s$  = Satellite clock correction (s)

$T_r^s$  = Tropospheric delay between satellite and receiver (m)

$I_r^s$  = Ionospheric delay between satellite and receiver (m)

$\lambda_j$  = Carrier-phase wavelength (m)

$N_{r,j}^s$  = Integer ambiguity (cycle)

$m_{r,j}^s$  = multipath effect of code and phase observations (m)

$\varepsilon_r^s$  = noise effect of code and phase observations (m)

In the equation, using both code and carrier phase observations increases the point positioning accuracy of the Traditional-PPP method, and dual-frequency observation models are proposed to reduce the effect of ionospheric errors.

### B. Experiment Design for RT-PPP method

In order to detect vertical displacements of engineering structures under the influence of dynamic loads, a vertical steel flat simulation bar, which can produce vertically damped harmonic motion and on which measurements can be made by integrating different sensors, has been used throughout the experiment. In addition, the steel flat simulation bar is mounted on the steel tree model, as seen in Figure 1 to produce harmonic oscillations by fixing one edge and applying force to the other free edge. The main purpose of using this model is to simulate the multipath effect caused by bridge elements (tower, main cable, suspension cables) while measuring in engineering structures such as bridges. Moreover, the building seen in Figure 1 causes the most multipath effect in the experiments.

Damped harmonic motions with different initial amplitude are produced by the steel flat simulation bar. Among these motions, example one case was selected. It was chosen to test the performance of RT-PPP in applications such as structural health monitoring of vertical displacements due to the effect of dynamic loads in engineering structures, earthquake early warning system and rapid hazard assessment.

### C. Processing Strategy

Trimble MB-2 OEM receiver with dual frequency, GPS observation data collection and 20 Hz sampling interval was used for the RT-PPP method in the experiments. In

addition, in order to evaluate the performance of this method, data was collected throughout the experiment with a CHC I80 GNSS receiver with 2 dual-frequency 20 Hz sampling intervals and a solution was made with the RP method. Another GNSS receiver was fixedly installed at approximately 75 meters from the experiment location, and the other GNSS receiver was mounted on a vertical steel flat simulation bar as a rover, as shown in Figure 1 and data was collected. GPS observation data were collected by setting the cut-off angle of these two receivers to 10° and the data sampling interval to 20 Hz. The experiments were carried out in front of the Civil Engineering Department of the Gebze Technical University campus on July 13, 2021 for approximately 1 hour.

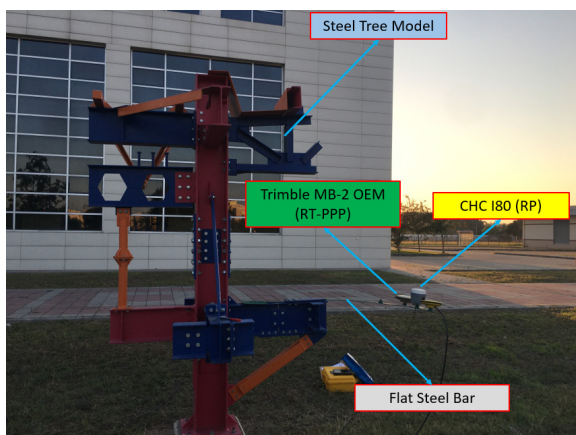


Figure 1. Experiment setup in which damped vertical harmonic motions are performed.

For the RT-PPP solution, a RT-PPP solution was made with the satellite orbit and clock corrections obtained by broadcasting the IGC01 product, which is the RTS product, and the raw observation data recorded from the Trimble MB-2 OEM GNSS receiver. The rtknavi application of RTKLIB demo5\_34a software, which is an open source software package, was used to evaluate the RT-PPP method in real time. In addition, to evaluate the performance of RT-PPP after the experiments, PP-PPP solutions were made in the rtkpost application of the RTKLIB software based on the IGS-Final products produced by IGS, with reference to the RP method.

### III. RESULTS AND DISCUSSION

In this section, the results obtained from 5 cases of damped harmonic motion experiments with different initial amplitudes are examined in the time and frequency domain. In the experiments, the vertical oscillations obtained from the solution of the RT-PPP method and the vertical oscillations obtained from the PP-PPP method based on the satellite orbit and clock correction of the IGS-Final product were compared with reference to the RP method. In order to produce damped harmonic motions, a downward thrust of approximately 3-10 cm was applied to the free end of the steel bar during the experiment.

During the experiment, the oscillation motions were instantly monitored by the RT-PPP method. Figure 2 shows the displacements of 5 free-decayed vertical harmonic motions in the instantaneous time domain. Figure 2 contains the dataset of vertical harmonic motions performed on 13 July 2021. In all methods, solutions were made with only-GPS observations. Experiment time lasted approximately 2.5 minutes. The characteristics of all experimental cases shown in Figure 2 are summarized in Table 1.

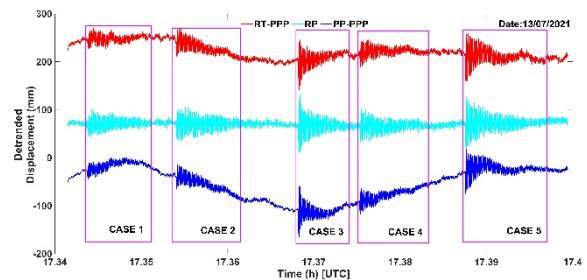


Figure 2. Vertical displacements obtained from the RT-PPP method, RP method and the PP-PPP method.

Table 1. Properties of five Cases discussed in the study

Case	Time [s]	Init. Amp. [mm]	Freq. [Hz]
1	25.5	20	1.64
2	38	30	1.64
3	20	60	1.65
4	32	30	1.64
5	28	55	1.62

During the experiments, data loss was experienced in some epochs while solving with the RT-PPP method. This is due to the fact that the receiving antenna cannot collect data at intervals of 0.05 seconds in some cases. These data losses were eliminated with the spline interpolation method. The same situation was applied to the PP-PPP method since the raw observation data used in the RT-PPP method were also used in the PP-PPP method. As seen in the figure, fluctuations are seen in the displacement time series of all cases in both RT-PPP and PP-PPP methods. The reason for this behavior is due to the convergence time of the PPP, the limitations of the models used, and the accuracy of the products (Cai, 2009). The offsets and fluctuations in displacements is not a major problem, as the aim of this study is focused on detecting short-term (15 - 35 s) dynamic motions with the RT-PPP approach. In addition, it was observed that the displacements obtained by the RP method were straight along the center of the motions during the oscillation case.

Different filters can be used to eliminate the short-term and long-term fluctuations in the RT-PPP and PP-PPP seen in Figure 2. For this, in the time domain of the experiments with five different harmonic oscillations and all the methods used in the study, a Butterworth high-pass filter with a stop frequency of 0.5 Hz and a pass frequency of 1 Hz was applied. The filtered time series of all methods is shown in Figure 3. Case 2 was

chosen as a representative example to examine the performance of real-time PPP in capturing vertical damped harmonic oscillations and compare it with post-process PPP with reference to RP. In Figure 4, the detrended displacement time series obtained from the RT-PPP, RP and PP-PPP methods is shown in the upper part of the figure. The initial amplitude of the harmonic motion is about 30 mm and the total time is 38 seconds. In cases where the time series of the three methods whose displacements were obtained were consistent with each other, but the oscillation decreased, fluctuations occurred. These fluctuations seen in short-term motions are corrected by applying a high-pass filter as seen in the middle of Figure 4.

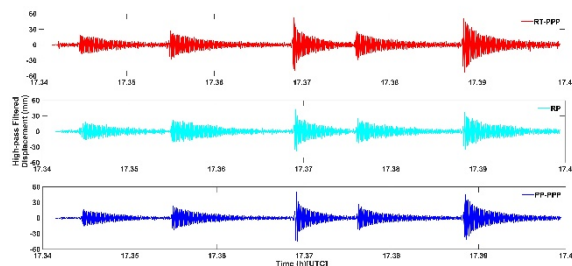


Figure 3. Displacement time series filtered by applying a Butterworth high-pass filter.

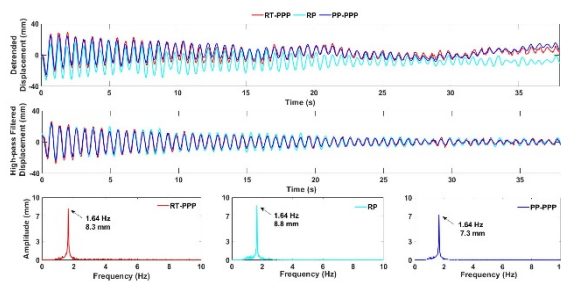


Figure 4. Displacement time series and FFT spectrum of the RT-PPP, RP and PP-PPP methods for Case 2.

The main purpose of this study is to evaluate the performance of the methods used in capturing vertical dynamic motions. Therefore, the frequency and amplitude values corresponding to the Fast Fourier Transform (FFT) spectrum in the frequency domain of the three methods were compared with each other. As can be seen in the figure, the harmonic oscillation frequencies obtained by the three methods are equal and 1.64 Hz. There are small differences at the level of millimeter in the amplitude values corresponding to the dominant frequency. The results show that the amplitude value obtained by the RT-PPP method is close to the RP. The reason for this difference is the noise level of methods due to the accuracy of products used and different GNSS antenna/receiver, among others.

When the FFT results of all the cases selected in Table 2 are examined, it is observed that the displacements can be captured under centimeters with the RT-PPP method and give similar results when compared to other methods. In addition, in cases where

the dominant amplitude values are at the centimeter level, it was seen that the dominant frequency values were the same in all 3 methods, and the amplitude values were compatible with each other. Considering these results, the RT-PPP method gave reliable results compared to the RP method, which is the ability to capture vertical motions occurring in engineering structures. In order to analyze the time domain accuracy of the RT-PPP and PP-PPP methods, the RMSE was calculated with reference to the RP method and shown in Table 3.

Table 2. Dominant frequency and amplitude values of 3 methods

Case	RT-PPP		RP		PP-PPP	
	Amp. [mm]	Freq. [Hz]	Amp. [mm]	Freq. [Hz]	Amp. [mm]	Freq. [Hz]
1	8.0	1.64	8.0	1.64	6.8	1.64
2	8.3	1.64	8.8	1.64	7.3	1.64
3	14.4	1.65	12.9	1.65	12.8	1.65
4	8.3	1.64	7.9	1.64	7.0	1.64
5	15.4	1.62	12.3	1.62	12.8	1.62

Table 3. RMSE and Maximum values of difference between RP and PPP methods

Case	RT-PPP		PP-PPP	
	RMSE [mm]	Max [mm]	RMSE [mm]	Max [mm]
1	6.1 [2.6]	17.3 [9.0]	6.7 [2.2]	17.3 [6.7]
2	6.5 [2.6]	19.7 [9.2]	7.3 [2.2]	19.5 [7.1]
3	7.0 [4.4]	22.4 [14.8]	8.7 [2.6]	22.9 [12.3]
4	6.0 [2.8]	23.7 [12.4]	6.0 [2.1]	17.9 [6.2]
5	7.4 [5.3]	22.2 [20.9]	6.8 [2.7]	22.7 [10.8]

The RMSE and maximum values of the PP-PPP and RT-PPP methods calculated with reference to RP for all cases are given in Table 3. Values in square brackets in this table are filtered results, while others show unfiltered results. After applying filtering, RMSE and maximum values decreased. In the RT-PPP approach, after filtering, there is an improvement between 9% and 57% in RMSE values, while there is an improvement between 8% and 48% in maximum values. When the same situation was examined for the PP-PPP approach, an improvement was observed between 16% and 70% in the RMSE values, while an improvement between 9% and 61% in the maximum values. It shows that after filtering, RT-PPP can give reliable results in monitoring vertical short-time dynamic behavior with an accuracy of millimeter-level. In addition, small displacements of about 1 cm were detected with high accuracy at the millimeter level with the RT-PPP approach. These results in the time domain clearly show that the performance of the RT-PPP method for capturing displacements of vertical motions that may occur in engineering structures with a high-rate GNSS receiver gives reliable results without the need for a reference receiver. Thus, it has been revealed that the RT-PPP approach is an alternative method to the RP method in capturing

short-term dynamic motions caused by natural events such as earthquake, tsunami, and wind in engineering structures.

#### IV. CONCLUSION

In this study, the ability to capture vertical displacements resulting from dynamic motions in engineering structures with real-time PPP technique was investigated. In order to produce these vertical motions occurring in the structures, 5 vertical damped harmonic motion simulation tests were carried out using flat steel bars. In order to test the performance of the RT-PPP method, the RP method, which is widely used in many studies to capture dynamic motions in structures, was taken as reference. In addition, the real-time solutions obtained from the RT-PPP method were compared with the solutions of the PP-PPP method in the time and frequency domain, using precise satellite orbit and clock correction information. When the FFT spectrum analysis of the 5 harmonic oscillation test results was performed, it was clearly seen that RT-PPP gave the same frequency values for each case compared to the other two methods. Although there are small differences at millimeter level in the amplitude values corresponding to the dominant frequencies, it is obvious that the RT-PPP method achieves successful results in vertical harmonic oscillations. These differences are caused by the signal-to-noise ratios caused by the hardware of GNSS receivers, the accuracy of the satellite orbit and clock correction information used in PPP solutions, and the delays caused by real-time broadcast products. Statistical analyzes in the time domain were performed to test the accuracy of monitoring the instantaneous displacements in the structures with the RT-PPP method. Considering the results, it has been seen that the RMSE values of the RT-PPP method varied between 0.4 and 2.5 millimeters compared to the PP-PPP method. In addition, the accuracy of the harmonic oscillations of the 5 cases according to the RT-PPP method was obtained below about 5.5 millimeters. These results in the time domain clearly show that the performance of the RT-PPP method for capturing displacements of vertical motions that may occur in engineering structures with a high-rate GNSS receiver gives reliable results without the need for a reference receiver. Thus, it has been revealed that the RT-PPP approach is an alternative method to the relative positioning method in capturing short-term dynamic motions caused by natural events such as earthquake, tsunami, and wind in engineering structures. After applying a high-pass filter to the RT-PPP approach, it has been observed that the dominant frequencies and amplitudes of vertical dynamic motions can be determined accurately and reliably. In addition, the RT-PPP approach provides reliable results in applications such as structural health monitoring, early warning system, rapid hazard assessment, and real-time

products in the detection of short-term vertical dynamic motions that gave similar results compared to IGS-Final products used in post-process.

#### References

- Alcay, S., and Turgut, M. (2017). Performance Evaluation of Real-Time Precise Point Positioning Method. *IOP Conf. Series: Earth and Environmental Science*, 95, 032023, 2017. DOI: 10.1088/1755-1315/95/3/032023.
- Alcay, S. (2019). Investigation of The Positioning Performance of Real Time Precise Point Positioning Method (RT-PPP) In *Terms Of Accuracy And Precision. OHU J. Eng. Sci.*, 8 (1), pp. 121-133. (In Turkish)
- Avallone, A., Marzario, M., Cirella, A., Piatanesi, A., Rovelli, A., Di Alessandro, C., D'Anastasio, E., D'Agostino, N., Giuliani, R., and Mattone, M. (2011). Very high rate (10 Hz) GPS seismology for moderate-magnitude earthquakes: the case of the Mw6.3 L'Aquila. (central Italy) even. *J. Geophys. Res.*, 116, B02305.
- Cai, C. (2009). *Precise point positioning using dual-frequency GPS and GLONASS measurement* [master thesis]. Calgary: University of Calgary.
- El-Mowafy, A., Deo, M., and Kubo, N. (2016). Maintaining real-time precise point positioning during outages of orbit and clock corrections. *GPS Solut.*, pp. 1–11.
- El-Mowafy, A., and Deo, M. (2017). Bridging Real-Time Precise Point Positioning in Natural Hazard Warning Systems during Outages of MADOCA Corrections. *Proceedings of the ION Pacific PNT 2017 Conference, ION PNT 2017, Honolulu, Hawaii, May 1-4, 2017.*
- Elsobeiey, M., and Al-Harbi, S. (2016). Performance of real-time Precise Point Positioning using IGS real-time service. *GPS Solut.*, 20(3), pp. 565–571.
- Hadas, T., and Bosy, J. (2015). IGS RTS precise orbits and clocks verification and quality degradation over time. *GPS Solutions*, 19(1), pp. 93–105.
- Kaloop, M. R., Yigit, C.O. and J. H., Hu. (2018). Analysis of the dynamic behavior of structures using the high-rate GNSS-PPP method combined with a wavelet-neural model: Numerical simulation and experimental tests. *Adv. Space Res.*, 61 (6), pp. 1512–1524.
- Kouba, J., and Heroux, P. (2001). Precise Point Positioning using IGS orbit and clock products. *GPS Solutions*, 5(2), pp. 12-28.
- Kouba, J. (2003). Measuring Seismic Waves Induced by Large Earthquakes with GPS. *Stud. Geophys. Geod.*, 47, pp. 741–755.
- Krzan, G. and Przestrzelski, P. (2016). GPS/GLONASS Precise Point Positioning with IGS Real-time service product. *Acta Geodynamica et Geomaterialia*, 13 (1), pp. 69–81.
- Larson, K. M., Bodin, P., and Gomberg, J. (2003). Using 1-Hz GPS data to measure deformations caused by the Denali fault earthquake. *Science*, 300(5624), pp. 1421-1424.
- Larson, K.M. (2009). GPS seismology. *J. Geod.*, 83, pp. 227–233.
- Li, X., Guo, B., Lu, C., Ge, M., Wickert, J., and Schuh, H. (2014). Real-time GNSS seismology using a single receiver. *Geophys J. Int.*, 198(1), pp.72–89.
- Li, X., Zheng, K., Li, X., Liu, G., Ge, M., Wickert, J., and Schuh, H., (2019). Real-time capturing of seismic waveforms using

- high-rate BDS, GPS and GLONASS observations: the 2017 Mw 6.5 Jiuzhaigou earthquake in China. *GPS Solut*, 23(1), pp. 1–12.
- Martín, A., Anquela, A.B., Dimas-Pagés, A., and Cos-Gayón, F. (2015). Validation of performance of real-time kinematic PPP. A possible tool for deformation monitoring. *Measurement*, 69, pp. 95–108.
- Moschas, F., A. Avallone, V. Saltogianni, and S. C. Stiros. (2014). Strong motion displacement waveforms using 10-Hz precise point positioning GPS: An assessment based on free oscillation experiments. *Earthquake Eng. Struct. Dyn.*, 43 (12), pp. 1853–1866.
- Moschas, F. and Stiros, S. (2015). Dynamic deflections of a stiff footbridge using 100-Hz GNSS and accelerometer data. *Journal of Surveying Engineering*, 141 (4), 4015003.
- Nie, Z., R. Zhang, G. Liu, Z. Jia, D. Wang, Y. Zhou, and M. Lin. (2016). GNSS seismometer: Seismic phase recognition of real-time high-rate GNSS deformation waves. *J. Appl. Geophys.* 135 (Dec), pp. 328–337.
- Paziewski, J., R. Sieradzki, and R. Baryla. (2018). Multi-GNSS high-rate RTK, PPP and novel direct phase observation processing method: Application to precise dynamic displacement detection. *Meas. Sci. Technol.* 29 (3): 035002.
- Takahashi, N., Ishihara, Y., Ochi, H., Fukuda, T., Tahara, J., Maeda, Y., Kido, M., Ohta, Y., Mutoh, K., Hashimoto, G., Kogure, S., and Kaneda, Y. (2014). New buoy observation system for tsunami and crustal deformation. *Mar Geophys Res.*, 35(3), pp. 243–253.
- Tang, X., Roberts, G. W., Li, X. and Hancock, C. (2017). Real-time kinematic PPP GPS for structure monitoring applied on the Severn suspension bridge, UK. *Adv. Space Res.*, 60 (5), pp. 925–937.
- Tu, R., Liu, J., Lu, C., Zhang, R., Zhang, P., and Lu, X. (2017). Cooperating the BDS, GPS, GLONASS and strong-motion observations for real-time deformation monitoring. *Geophys J. Int.*, 209(3), pp. 1408–1417.
- Wang, J., Meng, X., Qin, C., and Yi, J. (2016). Vibration frequencies extraction of the forth road bridge using high sampling GPS data. *Shock and Vibration*, 2016.
- Xu, P., Shi, C., Fang, R., Liu, J., Niu, X., Zhang, Q., and Yanagidani, T. (2013). High-rate precise point positioning (PPP) to measure seismic wave motions: an experimental comparison of GPS PPP with inertial measurement units. *J. Geod.*, 87 (4), pp. 361–372.
- Xu, P., Y. Shu, X. Niu, W. Yao, and Q. Chen. (2019). High-rate multi-GNSS attitude determination: Experiments, comparisons with inertial measurement units and applications of GNSS rotational seismology to the 2011 Tohoku Mw9.0 earthquake. *Meas. Sci. Technol.*, 30 (2): 024003.
- Yi, T., Li, H., and Gu, M. (2013). Recent research and applications of GPS-based monitoring technology for high-rise structures. *Structural Control and Health Monitoring*, 20 (5), pp. 649–670.
- Yigit, C. O. (2016). Experimental assessment of essed kinematic precise point positioning method for structural health monitoring. *Geomat. Nat. Hazards Risk*, 7 (1), pp. 363–380.
- Yigit, C.O., and Gurlek, E. (2017). Experimental testing of high-rate GNSS precise point positioning (PPP) method for detecting dynamic vertical displacement response of engineering structure. *Geomatics, Natural Hazards and Risk*, 8(2), pp. 893-904.
- Yu, J., Yan, B., and Meng, X. (2016). Measurement of bridge dynamic responses using network-based real-time kinematic GNSS techniqu. *J. Surv. Eng.*, 142 (3), 04015013.
- Zhang, Y., Nie, Z., Wang, Z., Wu, H., and Xu, X. (2021). Real-time coseismic displacement retrieval based on temporal point positioning with igs rts correction products. *Sensors (Switzerland)*, 21(2), pp. 1–17.
- Zheng, K., Zhang, X., Li, X., Li, P., Sang, J., Ma, T., and Schuh, H. (2019). Capturing coseismic displacement in real time with mixed single- and dual-frequency receivers: application to the 2018 Mw7.9 Alaska earthquake. *GPS Solut*, 23(1), pp. 1–14.
- Zumberge, J.F., Heflin, M.B., Jefferson, D.C., Watkins, M.M., and Webb, F.H. (1997). Precise point positioning for the efficient and robust analysis of GPS data from large networks. *J. Geophys Res. Solid Earth*, 102(B3), pp. 5005–5017.

## High-rate real-time single-frequency PPP for structural motion detection in horizontal directions

Mert Bezioglu<sup>1</sup>, Baris Karadeniz<sup>1</sup>, Cemal Ozer Yigit<sup>1</sup>, Ahmet Anil Dindar<sup>2</sup>, Burak Akpınar<sup>3</sup>

<sup>1</sup> Department of Geomatics Engineering, Gebze Technical University, Turkey, ([mbezioglu@gtu.edu.tr](mailto:mbezioglu@gtu.edu.tr); [b.karadeniz@gtu.edu.tr](mailto:b.karadeniz@gtu.edu.tr); [cyigit@gtu.edu.tr](mailto:cyigit@gtu.edu.tr))

<sup>2</sup> Department of Civil Engineering, Gebze Technical University, Turkey, ([adindar@gtu.edu.tr](mailto:adindar@gtu.edu.tr))

<sup>3</sup> Department of Geomatics Engineering, Yildiz Technical University, Turkey, ([bakpinar@yildiz.edu.tr](mailto:bakpinar@yildiz.edu.tr))

**Key words:** *single-frequency PPP; real-time monitoring; structural health monitoring; GPS*

### ABSTRACT

Thanks to advances in receiver and software technology, the high-rate GPS (Global Positioning System) technique has become very important in monitoring the dynamic behavior of man-made structures in both real-time and post-missions. Real-time monitoring of the changes in the behavior of structures due to effects such as natural disasters, wind effect, traffic loading is critical in order to take precautions in time. In this study, the performance of the Real-Time Single Frequency Precision Point Positioning (RT SF-PPP) method based on IGS (International GNSS Service) RTS (real-time stream) products to capture the behavior of dynamic motions was evaluated. The performance of the SF RT-PPP method to detect dynamic behaviors was evaluated based on 20 Hz single frequency GPS observations obtained from shake table experiments, including 10 mm amplitude and different oscillation frequencies including 0.1, 0.6, 1.0, 2.0 and 3.0 Hz. RT SF-PPP results were compared with reference LVDT (Linear Variable Differential Transformer) and relative (or double difference) GPS positioning both frequency and time domain. Results show that the high-rate RT SF-PPP method can capture the frequencies and amplitudes of harmonic motions and it is comparable to LVDT and Relative GPS positioning solutions. These results show that the high-rate RT SF-PPP method can monitor earthquake-induced real-time vibration frequencies and amplitudes, which is especially important for early warning systems.

### 1. INTRODUCTION

For high-precision structural displacement retrieval, high-rate GNSS has been widely employed. The advancements in GNSS receivers enable a wide variety of structural engineering applications. Therefore, high-rate GNSS PPP is an essential instrument for structural health monitoring applications. Because it does not require a reference GNSS station, the GNSS PPP technique has been developed and is widely used (Zumberge *et al.*, 1997; Kouba and Heroux, 2001). Using precise orbit and clock products, the PPP approach can provide position information with precision ranging from centimeters to decimeters (El-Mowafy *et al.*, 2017). Numerous studies on the high-frequency PPP technique have proven the method to be a cost-effective absolute positioning method for GPS seismology (Savage *et al.*, 2004; Calais *et al.*, 2006; Kouba, 2003; Avallone *et al.*, 2011; Xu *et al.*, 2013; Yigit *et al.*, 2016; Alcay *et al.*, 2019) and structural health monitoring (Moschas *et al.*, 2014; Yigit, 2016; Yigit and Gurlek, 2017; Kaloop *et al.*, 2018; Yigit *et al.*, 2020; Kaloop *et al.*, 2020; Yigit *et al.*, 2021).

The PPP approach commonly employs IGS Rapid or Final products, however they are provided to users at least 17 hours and two weeks after the previous observation, respectively (Wang *et al.*, 2018a). IGS also provides Ultra-Rapid products that are available two hours after the last observation, but these three

products are not useful for real-time applications due to their latency. The PPP approach can be also employed in real-time with real-time precise satellite orbit and clock corrections. Earthquake-induced ground motions can be monitored instantaneously, and damage assessments can be performed rapidly using the real-time PPP approach. The Real-time GPS-PPP approach has recently applied to real bridge monitoring, and PPP-derived outcomes were compared to relative positioning results (Tang *et al.*, 2017). They demonstrated that Real-time PPP can be deployed as an alternate way to the relative method for monitoring man-made engineering structures. IGS provides real-time satellite orbit and clock products to users who want to obtain RT-PPP solutions through IGS RT Service (RTS). (Chen *et al.*, 2018; Wang *et al.*, 2018b; Bahadur, 2021). IGS also offers users combined real-time analysis products that allow post-mission PPP under real-time conditions. These products are provided to users at 10 s for clock and 30 s for orbit sampling interval, and they are derived from the IGC01 stream. The combined IGC01 orbit and clock products currently include GPS corrections (Defraigne *et al.*, 2015).

The RT-PPP approach based on combined IGC01 products was assessed in this investigation for capturing high-rate dynamic motions. Based on 20 Hz single-frequency GPS observations from shake table tests with different amplitude and frequency of

oscillations, the RT-PPP approach for detecting dynamic motions was evaluated. The results of the RT-PPP were compared to those of the reference relative GPS positioning and LVDT sensors.

## II. BASICS OF PPP AND DESCRIPTION OF EXPERIMENTS

### A. Methodology

The basic pseudorange and carrier-phase observation equations of GPS for PPP are as follows (Eqs. 1 and 2):

$$P = \rho + cdt_r + cdt^s + T + I + c(d_r - d^s) + e \quad (1)$$

$$\phi = \rho + cdt_r + cdt^s + T - I + c(\delta_r - \delta^s) + \lambda N + \varepsilon \quad (2)$$

where  $P$  = GPS pseudorange measurement in meters  
 $\phi$  = GPS carrier-phase measurement in meters  
 $\rho$  = true geometric distance in meters  
 $c$  = speed of light in vacuum  
 $dt_r$  = clock errors for receiver  
 $dt^s$  = clock errors for satellite  
 $T$  = tropospheric component in meters  
 $I$  = ionospheric component in meters  
 $d_r$  = receiver's frequency-dependent code hardware delay in seconds  
 $d^s$  = satellite's frequency-dependent code hardware delay in seconds  
 $e$  = unmodelled residual errors and relevant system noise in meters for code observations  
 $\delta_r$  = receiver's frequency-dependent carrier-phase hardware delay in seconds  
 $\delta^s$  = satellite's frequency-dependent carrier-phase hardware delay in seconds  
 $\varepsilon$  = unmodelled residual errors and relevant system noise in meters for phase observations  
 $\lambda$  = the wavelengths of the carrier frequency in meters  
 $N$  = integer ambiguity parameters in cycles

### B. Experiment design

A shake table, which can generate the sinusoidal harmonic motion at various frequencies and amplitudes, was employed in this study to assess the detecting dynamic motions performance of high-rate real-time SF-PPP. The shake table is made up of three parts: a control unit that controls the frequency and amplitude of dynamic motions, a reference table from which movements are generated, and a motion table that travels in a single axis. Figure 1 shows the shake table employed in this study's tests. The GNSS receiver is placed on a black flat plate, which has a 190 mm total stroke and moves within 95 mm in the uniaxial direction. The table motion is provided by an electric system that produces negligible oscillations and has a maximum speed of 400 mm/s. The position of the table is validated using an LVDT integrated beneath the motion table. Moreover, the LVDT sensor in the table

can collect data at 100 Hz sampling rate, provide precision at mm level, and is controlled by computer software.



Figure 1. Employed shake table and GPS receiver in experiments.

Five harmonic motion cases with various amplitudes and frequencies generated by the shake table and detailed in Table 1 were chosen to examine the performance of SF-PPP in structural health monitoring applications. As shown in Table 1, 5 harmonic motions with frequencies ranging from 0.1 to 3.0 Hz and amplitudes of 5 mm were simulated.

Table 1. The frequency and amplitude of oscillations in each case chosen for this investigation

Frequency of Motions	Amplitude of Motions 10 mm
0.1 Hz	Case 1
0.6 Hz	Case 2
1.0 Hz	Case 3
2.0 Hz	Case 4
3.0 Hz	Case 5

### C. Processing strategy

Two dual-frequency CHC I80 GNSS receivers are used in this investigation and GPS observations were collected with 10° cut-off angle at 20 Hz sampling rate and. One GNSS receiver collected the data for the PPP solution on the shake table, while the other GNSS receiver was placed at a known point to perform a relative positioning solution approximately 60 m from the shake table. The tests lasted approximately one hour, and were conducted at the Gebze Technical University campus in Gebze. During the experiment, 7 to 9 GPS satellites were observed. RTKLIB 2.4.2, an open-source library, was used to process single-frequency only-GPS data for relative positioning (Takasu and Yasuda, 2009). gLAB v5.5.1 software was used to implement SF-PPP solutions based on IGS-RT products (Ibáñez *et al.*, 2018). Displacements in the North and East directions derived from both relative positioning and RT-PPP are projected onto the

movement direction of the shake table as defined by Yigit *et al.* (2021).

### III. RESULTS AND DISCUSSION

Evaluation of the results obtained from the SF-PP method from harmonic motion experiments in various frequency and amplitude ranges is discussed in this section. To validate the performance of the high-rate RT SF-PPP, LVDT data and only-GPS SF-RP data were used as a reference in all experiments. The displacement time series of the north and east components derived from the SF-RP (top) and SF RT-PP (second from top) for harmonic oscillations are shown in Figure 2. The displacements derived from the SF-PPP methods have some low frequency fluctuations and trends in the long and short term for both components, whereas the time series of SF-RP are very consistent. Since the structural health monitoring applications focus on short-term dynamic movements of one minute or less, low-frequency components are not a problem. Moreover, various filtering techniques can successfully eliminate these short- and long-term oscillations. To remove the long-term fluctuations, all GNSS-based techniques' time series were filtered using a fifth-order Butterworth high-pass filter. For the first example, different cut-off frequencies were used, and for the next four cases, different cut-off frequencies were used. The purpose for using two separate cut-off frequencies was that when the entire time series was evaluated by FFT, unexpected peak frequencies between 0.1 Hz and 0.3 Hz were detected. As a result, the cut-off frequency of the filter for Case 1 was 0.08 Hz, whereas the cut-off frequency for all other cases was 0.20 Hz. The time series obtained as a result of the filter applied to SF-RP (third from top) and SF RT-PPP (fourth from top) solutions used in this paper can be seen in Figure 2. The figure demonstrates that after applying the high pass filter, the long-term components in the displacement time series obtained from SF RT-PPP solutions are eliminated. It is obvious, in particular, that the SF-PPP method is strongly compatible with the SF-RP time series.

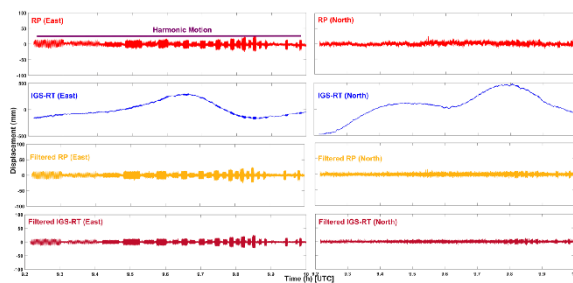


Figure 2. North and East time series for GPS-based solutions.

Case 3 was chosen as a representative example to examine the performance of the RT SF-PPP in capturing harmonic oscillations and compare it to the reference LVDT and RP. Figure 3 illustrates Case 3 for GPS-based

solutions and LVDT, which shows the LVDT, filtered and unfiltered SF-RP, and SF-PPP-derived displacement, as well as their corresponding FFT spectrums. It is obvious that the low frequency components in the time series of the SF RT-PPP' time series disappear once the filter is applied. The effectiveness of the applied filtering is obviously seen when comparing the unfiltered and filtered time series of SF RT-PPP. Figure 3 illustrates that the RT SF-PPP-derived displacements agree well with the LVDT and SF-RP-derived displacements. The peak frequency and amplitude corresponding to the peak frequency remained stable before and after the filtering process for all GPS-based solutions.

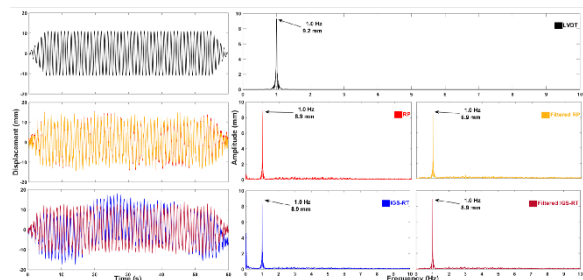


Figure 3. Time series (left) and corresponding FFT spectrums (right) for LVDT, RP and SF-PPP.

Table 2 summarizes the detected peak frequency and corresponding amplitude obtained from all sensors discussed in the study for all harmonic oscillation cases. Values indicate unfiltered outcomes, whereas values in square brackets ([]) represent filtered results. The oscillation frequencies obtained by the LVDT, SF-RP, and SF RT-PPP solutions for all cases are in good agreement, as shown in the table. The filtered and unfiltered GPS-based methods performed similarly in determining the amplitudes corresponding to the peak frequencies. However, there are slight differences with LVDT. The differences of detected amplitude between SF RT-PPP and LVDT vary between 0 mm and 0.6 mm, whereas the differences for SF-RP vary between 0.1 mm and 0.4 mm. This indicates that the SF RT-PPP is a powerful tool for structural health monitoring applications and the natural frequency of structures can be detected with low-cost GNSS receivers in real-time.

Table 2. The detected frequency and amplitude from all sensors

Case	LVDT		Relative Positioning		IGS Real Time PPP	
	Freq. [Hz]	Amp. [mm]	Freq. [Hz]	Amp. [mm]	Freq. [Hz]	Amp. [mm]
1	0.1	10.0	0.1	10.4 [10.1]	0.1	10.4 [10.1]
2	0.6	9.5	0.6	9.9 [9.9]	0.6	10.0 [10.1]
3	1.0	9.3	1.0	8.9 [8.9]	1.0	8.9 [8.9]
4	2.0	11.4	2.0	11.6 [11.6]	2.0	11.1 [11.1]
5	3.0	11.4	3.0	11.3 [11.3]	3.0	11.4 [11.3]

The maximum and RMSE (Root Mean Square Error) values of difference between LVDT and GPS-based techniques for all designed cases were computed to



investigate the performance of SF RT-PPP in detecting dynamic displacements and compare with the reference sensor LVDT, and results are given in Table 3. Values in square brackets are filtered results, whereas others refer to unfiltered. The maximum and RMSE values were significantly reduced after filtering, as seen in the table. Maximum values after filtering show an improvement of between 33% and 69% for IGS-RT based SF-PPP. According to the table, SF-RP has the smallest RMSE values for all events, varying between 1.7 and 5.2 mm, considering the unfiltered raw findings. Moreover, the RMSE values of differences from the LVDT of the raw solutions obtained from SF RT-PPP show slightly worse performance for all cases. However, it is obvious that after filtering, this performance improves significantly. While an average of 46% improvement was reached in all cases following the filtering process, it is obvious that improvements ranging from 46% to 84% were achieved. This finding demonstrates that the performance of RT SF PPP in determining dynamic displacements after applying a high-pass filter is comparable to that of the SF-RP, and SF-PPP provides a high potential for short-term dynamic behavior monitoring applications.

Table 3. Maximum and RMSE values of difference between LVDT and GPS-based methods

Case	Relative Positioning		IGS Real Time	
	Max [mm]	RMSE [mm]	Max [mm]	RMSE [mm]
1	8.7 [7.8]	1.7 [1.5]	22.9 [7.0]	8.5 [1.4]
2	13.3 [11.0]	2.9 [2.6]	13.2 [8.1]	4.4 [2.2]
3	8.3 [8.6]	2.1 [2.0]	10.5 [8.3]	3.7 [1.5]
4	12.5 [11.7]	3.9 [3.8]	13.1 [11.2]	4.3 [3.5]
5	16.6 [16.3]	5.2 [5.1]	17.7 [14.0]	5.6 [4.6]

#### IV. CONCLUSION

The performance of SF-PPP, which reduces measurement costs, and RT products are investigated in this study. A shake table was used to simulate 5 harmonic oscillation tests reflecting the natural behavior of engineering structures in the study. In the time and frequency domains, the SF RT-PPP approaches were compared to the LVDT sensor and the SF-RP. The findings of the frequency domain harmonic oscillation experiment reveal that the high-rate SF RT-PPP is comparable to SF-RP and has good agreement with LVDT. These frequency domain analyses indicate that oscillation frequencies of structures may be estimated effectively employing a single-frequency receiver and real-time products. Furthermore, given that the amplitude values corresponding to the peak frequency detected in SF RT-PPP solutions for all cases, there was no error higher than 0.5 mm. However, it was concluded that SF-PPP results require filtering in the time domain analysis. As a result, all GNSS-based approaches' time series were filtered using a fifth-order Butterworth high-pass filter to reduce long-term

components. The RMSE and maximum error values improved significantly after the apply high-pass filter. The results of this study reveal that in structural health monitoring applications, the SF-PPP approach is as effective as the relative positioning method. Furthermore, this research demonstrates the SF-PPP approach may provide accurate and reliable displacement information when high pass filtering is used. This means that when structural health monitoring and early warning systems are operated with single frequency receivers, the SF-PPP approach provides reliable results, and real-time products are as accurate as final products in capturing short-term dynamic motions.

#### V. ACKNOWLEDGEMENTS

This work was supported by the Research Fund of the Gebze Technical University, Project Number: 2020-A-102-20.

#### References

- Alcay, S., S. Ogutcu, I. Kalayci, and C.O. Yigit, (2019). Displacement monitoring performance of relative positioning and Precise Point Positioning (PPP) methods using simulation apparatus. *Advances in Space Research*, 63, pp. 1697-1707.
- Avallone, A.M. Marzario, A. Cirella, A. Piatanesi, A. Rovelli, C. Di Alessandro, E. D'Anastasio, N. D'Agostino, R. Giuliani, and M. Mattone, (2011). Very high rate (10 Hz) GPS seismology for moderate-magnitude earthquakes: the case of the Mw 6.3 L'Aquila (central Italy) event. *J Geophys Res*, 116, pp. 1–14.
- Bahadur, B. (2021). Real-time single-frequency precise positioning with Galileo satellites. *The Journal of Navigation*, 21(1), pp. 1-17.
- Calais, E., J.Y. Han, C. Demets, and J.M. Nocquet, (2006). Deformation of the North American plate interior from a decade of continuous GPS measurements. *J Geophys Res*, 111, pp. 1–23.
- Chen, L., Q. Zhao, Z. Hu, X. Jiang, C. Geng, M. Ge, and C. Shi (2018). GNSS global real-time augmentation positioning ,Real-time precise satellite clock estimation, prototype system construction and performance analysis. *Advances in Space Research*, 61 (1), pp. 367–384.
- Defraigne, P., W. Aerts, and E. Pottiaux, (2015). Monitoring of UTC(k)'s using PPP and IGS real-time products. *GPS Solutions*, 19 (1), pp. 165–172.
- El-Mowafy, A., M. Deo, and N. Kubo, (2017). Maintaining real-time precise point positioning during outages of orbit and clock corrections. *GPS Solution*, 21, pp. 937-947.
- Ibáñez D., A. Rovira-García, J. Sanz, J.M. Juan, G. Gonzalez-Casado, D. Jimenez-Baños, C. López-Echazarreta, and I. Lapin, (2018). The GNSS Laboratory Tool Suite (gLAB) updates: SBAS, DGNS and Global Monitoring System. *9th ESA Workshop on Satellite Navigation Technologies (NAVITEC 2018)*, Noordwijk, The Netherlands. December 5 - 7.
- Kalooop R.M., C.O. Yigit, A. El-Mowafy, A.A. Dindar, M. Bezzioğlu M., and J.H. Hu, (2020). Hybrid Wavelet and Principal Component Analyses Approach for Extracting

- Dynamic Motion Characteristics from Displacement Series Derived from Multipath-affected High-rate GNSS Observations. *Remote Sensing*, 12(1):79
- Kaloop, M.R., C.O. Yigit, and J.H. Hu, (2018). Analysis of the dynamic behavior of structures using the high-rate GNSS-PPP method combined with a wavelet-neural model: Numerical simulation and experimental tests. *Adv. Space Res*, 61, pp. 1512-1524.
- Kouba, J. (2003). Measuring seismic waves induced by large earthquakes with GPS. *Stud Geophys Geod*, 47, pp. 741–755.
- Kouba, J., and P. Héroux, (2001). Precise Point Positioning using IGS orbit and clock products. *GPS Solution*, 5, pp. 12–28.
- Moschas, F., A. Avallone, V. Saltogianni, and S.C. Stiros, (2014). Strong motion displacement waveforms using 10-Hz precise point positioning GPS: an assessment based on free oscillation experiments. *Earthquake Eng Struct Dyn*, 43, pp. 1853–1866.
- Savage, J.C., W. Gan, W.H. Prescott, and J.L. Svarc, (2004). Strain accumulation across the coast ranges at the latitude of San Francisco, 1994–2000. *J Geophys Res*, 109, pp. 1–11.
- Takasu, T., and A. Yasuda, (2009). Development of the low-cost RTK-GPS receiver with an open-source program package RTKLIB. In: *International Symposium on GPS/GNSS, Seogwipo-si Jungmundong*, Korea, November 4–6.
- Tang, X., G.W. Roberts, X. Li, and C. Hancock, (2017). Real-time kinematic PPP GPS for structure monitoring applied on the Severn suspension bridge, UK. *Adv. Space Res*, 60, pp. 925–937.
- Wang, Z., Z. Li, L. Wang, X. Wang, and H. Yuan, (2018a) Assessment of multiple GNSS real-time SSR products from different analysis centers. *ISPRS International Journal of Geo-Information*, 7 (3).
- Wang, L., Z. Li, M. Ge, F. Neitzel, Z. Wang, and H. Yuan, (2018b) Validation and assessment of multi-GNSS real-time precise point positioning in simulated kinematic mode using IGS real-time service. *Remote Sensing*, 10 (2).
- Xu, P., C. Shi, R. Fang, J. Liu, X. Niu, Q. Zhang, and T. Yanagidani, (2013). High-rate precise point positioning (PPP) to measure seismic wave motions: an experimental comparison of GPS PPP with inertial measurement units. *J Geod*, 87, pp. 361–372.
- Yigit, C.O. (2016). Experimental assessment of post processed kinematic precise point positioning method for structural health monitoring. *Geomat Nat Hazards Risk*, 7, pp. 363–380
- Yigit, C.O., A. El-Mowafy, A.A. Dindar, M. Bezcioglu, and I. Tiryakioglu, (2021). Investigating Performance of High-Rate GNSS-PPP and PPP-AR for Structural Health Monitoring: Dynamic Tests on Shake Table, *Journal of Surveying Engineering*, 147(1): 05020011:1-14.
- Yigit, C.O., A. El-Mowafy, M. Bezcioglu, and A.A. Dindar, (2020) Investigating the effects of ultra-rapid, rapid vs. final precise orbit and clock products on high-rate GNSS-PPP for capturing dynamic displacements. *Structural Engineering and Mechanics*, 73(4), pp. 427-436.
- Yigit, C.O., and E. Gurlek, (2017). Experimental testing of high-rate GNSS precise point positioning (PPP) method for detecting dynamic vertical displacement response of engineering structures. *Geomat Nat. Haz. Risk*, 8, pp. 893-904.
- Yigit, C.O., M.Z. Coskun, H. Yavasoglu, A. Arslan, and Y. Kalkan, (2016). The potential of GPS Precise Point Positioning Method for Point Displacement Monitoring: A Case Study, *Measurement*, 91, pp. 398-404.
- Yigit, C.O., A. El-Mowafy, A.A. Dindar, M. Bezcioglu, and I. Tiryakioglu, (2021). Investigating Performance of High-Rate GNSS-PPP and PPP-AR for Structural Health Monitoring: Dynamic Tests on Shake Table, *Journal of Surveying Engineering*, 147(1).
- Zumberge, J.F., M.B. Heflin, D.C. Jefferson, M.M. Watkins, and F.H. Webb, (1997). Precise Point Positioning for the efficient and robust analysis of GPS data from large networks. *J Geophys Res*, 102, pp. 5005–5017.

## Assessment of accuracy and performance of terrestrial laser scanner in monitoring of retaining walls

Ali Algadhi<sup>1,2</sup>, Panos Psimoulis<sup>1,3</sup>, Athina Grizi<sup>3</sup>, Luis Neves<sup>3</sup>

<sup>1</sup> Nottingham Geospatial Institute, University of Nottingham, Nottingham, UK, ([aalgadhi@ksu.edu.sa](mailto:aalgadhi@ksu.edu.sa))

<sup>2</sup> Department of Civil Engineering, King Saud University, Riyadh, KSA

<sup>3</sup> Department of Civil Engineering, University of Nottingham, Nottingham, UK,

([Panagiotis.Psimoulis@nottingham.ac.uk](mailto:Panagiotis.Psimoulis@nottingham.ac.uk); [A.Grizi@nottingham.ac.uk](mailto:A.Grizi@nottingham.ac.uk); [Luis.Neves@nottingham.ac.uk](mailto:Luis.Neves@nottingham.ac.uk))

**Key words:** *terrestrial laser scanner; deformation monitoring; retaining walls; accuracy; C2C; C2M; M3C2*

### ABSTRACT

Retaining walls are a critical infrastructure of transportation networks and the monitoring of their condition is crucial for the efficient and reliable maintenance of the network. The condition of retaining walls is frequently assessed using qualitative criteria and visual inspection, which are susceptible to human-bias and errors. To improve the management of these structures, reducing the probability of failure and the maintenance costs, it is critical to develop more efficient, reliable and quantitative monitoring approaches for these structures. The current study aims to evaluate the performance of Terrestrial Laser Scanner (TLS) in deformation monitoring of retaining walls, based on the analysis of single scans (without registering the point clouds to build 3D models). The evaluation was based on a controlled experiment, where a wooden frame (1.5m x 1m) was used to simulate deformation scenarios for retaining walls, with an amplitude between 2 to 16 mm. A Leica RTC360 scanner was used to scan the wooden frame from distances varying between 10 to 27 m and angles varying between 0° to 20°. Five methods were applied to analyse the laser-scanner data and estimate the displacement: a target-based approach and four cloud-based approaches including the Cloud-to-Cloud (C2C), the Cloud-to-Mesh (C2M), the Multiscale-Model-to-Model-Cloud-Comparison (M3C2), and an alternative cloud-based method where the mean average of the point-cloud was used to estimate the displacement in the axis of the deformation. A Robotic Total Station Leica TS30 was also used to measure the deformation of the wooden frame and provide the ground truth values of the introduced deformation for each scenario. The results showed that the RTC360 had an accuracy of 1.3 mm with a confidence level of 95%.

### I. INTRODUCTION

The potential of using the Terrestrial Laser Scanning technology (TLS) in the field of structural health monitoring has been the focus of many researchers (Kim *et al.*, 2019; Athanasopoulos-Zekkos *et al.*, 2020), due to the precise and practical solution that the TLS can provide compared to other instruments, such as inclinometers, strain gages and photogrammetry (Athanasopoulos-Zekkos *et al.*, 2020). In monitoring retaining structures, geometric deformations are the main defects that need to be monitored (Kim *et al.*, 2019; Athanasopoulos-Zekkos *et al.*, 2020). The TLS can also be used for monitoring non-geometric related defects in retaining walls, such as monitoring the change in temperature of concrete surface (Mukupu, 2017), cracks and long-term deterioration (Law *et al.*, 2018), moisture content (Suchocki and Katzer, 2018; Živec *et al.*, 2019) and dynamic deformation of structures (Jatmiko and Psimoulis, 2017).

The accuracy of monitoring the geometric deformations in retaining walls using the TLS has been investigated. Although some studies concluded that TLS could assess the performance of retaining walls in service (Oskouie *et al.*, 2016; Aldosari *et al.*, 2020; Al-Rawabdeh *et al.*, 2020; Jia *et al.*, 2021), in the study of

Seo *et al.* (2019) it is suggested that the TLS cannot provide the level of accuracy that is required to monitor retaining walls within the construction phase, reaching the maximum daily deformation of 4 mm in their case.

The sources of errors in monitoring structures using the TLS can be categorised in three main types: (i) instrumental-related; (ii) errors related to the monitored surface; and (iii) cloud registration errors (Lague *et al.*, 2013). Furthermore, the method that is used to analyse the point clouds does also affect the accuracy of the monitoring results (Lague *et al.*, 2013; Seo *et al.*, 2019). Although the accuracy of this methods was investigated, further work is necessary to better understand and quantify the accuracy of laser-scanning in monitoring retaining walls and how the accuracy is affected by monitoring parameters, such as the scanning distance. In the current study, we evaluate the impact of the scanning distance and the angle of incidence in the accuracy of the deformation estimation.

The main principle of this study is that the estimation of the deformation derives from the comparative analysis between two single scans of two different states of the retaining wall. Apart from the impact of the scanning distance and the angle of incidence, the

performance of different methods of point-cloud analysis are examined for the estimation of the retaining wall deformation. Although, three different types of deformation of retaining wall were examined (lateral displacement, vertical displacement and tilt), only the results of the lateral displacement experiment are presented in this paper.

## II. EXPERIMENTAL SETUP

A wooden frame (1.5 m x 1 m) was built to simulate the surface of a retaining wall which would be subjected to different types of deformation (see Figure 1). The horizontal displacement was introduced via a bolt on the back of the wooden frame and the movement was measured using a metallic measure tape attached to the frame arm (see Figure 1c). Five black/white paper targets were glued to five key locations on the wooden frame (the four corners and the centre) and used as reference points to monitor the change in the frame position (see Figure 1a).

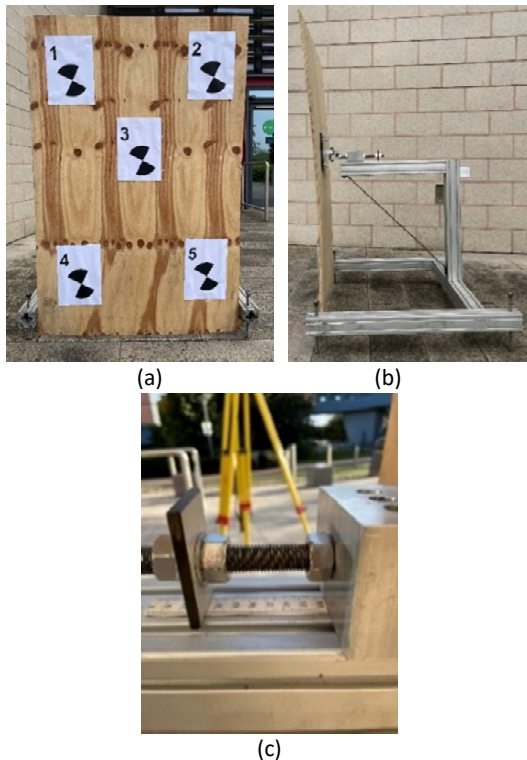


Figure 1. The designed wooden frame: (a) front view; (b) side view; and (c) bolt to adjust the frame position laterally.

A Leica RTC360 laser scanner was used to scan the wooden frame from six different scanning stations: three different scanning distances and two different incidence angles (see Figure 2). The scans were taken from 10 m, 20 m and 27 m scanning distances and with angles of incidence of 0° and 20° (see Table 1). A robotic total station (Leica TS30) was also used to provide the ground truth for the monitoring measurements. The application of RTS measurements in structural monitoring has been successfully assessed in experiments and real structural monitoring

applications, proving to be reliable even for mm-level deformation (Psimoulis and Stiros, 2007; 2008). The TS30 was used in a singular location unlike the RTC360 that was used in six scanning stations. Three Leica GZT21 scanning targets were established on three wooden tripods on different locations in the field as shown in Figure 2. The main purpose for these targets was to introduce a common coordinate system for the point clouds. The TS30 was used to survey these targets before and after the experiment to ensure that the entire network (*i.e.* TS30 and the static targets) remained stationary during the experiment. The TS30 was also used to survey the targets that were glued to the wooden frame (see Figure 1a) to perform the monitoring process. The experiment was conducted outdoor, and the measurements were taken under the same weather condition as the experiment was completed on the same day.

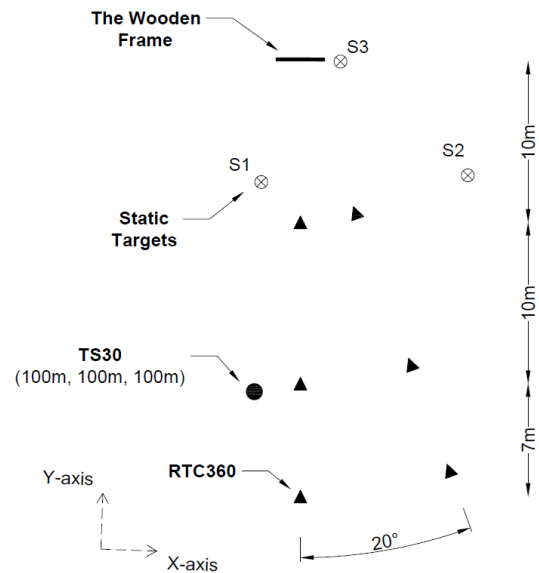


Figure 2. Figure Overview of the experimental site (top view), with the location of (i) RTC360, (ii) TS30, (iii) the wooden frame and (iv) the static targets. The Y-axis was parallel to the line between the TS30 and the static target "S1". This was the coordinate system that was introduced in the field using the TS30. This coordinate system was then rotated as explained in the data registration section. The drawing is not to scale.

Table 1. Experiment set-up and the scenarios of deformations that were simulated

	Experiment set-up		Deformation Scenario
	Distance [m]	Angle of incidence [degrees]	Lateral Disp. [mm]
RTC360	10	0	Initial
	20	20	2
	27		4
			8
TS30	20	0	16

The frame was firstly set up on one of the five states (*i.e.* deformation scenario) presented in Table 1. Then, the glued targets were surveyed using the TS30, by taking measurements in face left and face right. The

RTC360 was set to scan with the highest available resolution (*i.e.* 3 mm at 10 m) and by using the “double scan” function in order to remove any moveable objects captured during the scans. Each deformation scenario was examined for the three scanning distances and the two angles of incidence. After the completion of one of the deformation scenarios (taking measurements using the TS30 and scanning the frame using the RTC360 from six scanning stations), the wooden frame was set up on the next deformation scenario and the same procedure was applied.

### III. DATA REGISTRATION

In any monitoring project, the measurements need to be registered in the same coordinate system. This step is not only essential to perform the monitoring (compare different states of the wooden frame) but also to compare the results that were taken by the RTC360 with those taken by the TS30. This section explains the process of introducing a common coordinate system for all the measurements (TS30 and RTC360). For the RTC360 point-clouds, each single scan was registered individually to that common coordinate system in order to perform the monitoring but not for the sake of building a 3D model of the scanned surface.

A Cartesian coordinate system was established based on the TS30 measurements; by defining the position of TS30 ( $X_0 = 100$  m,  $Y_0 = 100$  m and  $Z_0 = 100$  m) and setting the Y-axis where the TS30 was pointing towards the target “S1” (see Figure 2). Then, a line was fitted in the horizontal plane defined by X- and Y-axes, based on the targets that were glued to the wooden frame, as shown in Figure 3a. The fitted line was used to rotate the X-Y plane to make the X-axis parallel to the frame surface and Y-axis aiming perpendicular towards the frame surface (see Figure 3b). The Z-axis remained vertical pointing upwards. The lateral displacement was then calculated in the Y-axis.

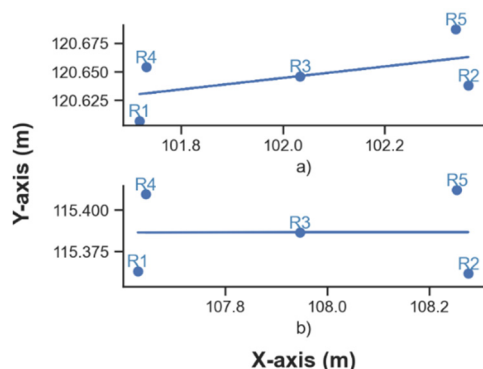


Figure 3. The five targets that were glued to the wooden frame along with the fitted line (top view): a) before, and b) after rotating the coordinate system in the X-Y plane.

The registration process for the RTC360 scans was executed using the seven-parameter-transformation (Helmert transformation) method (Zavoti and Kalmar, 2016). The seven parameters are: three translations

between the two coordinate systems ( $t_x, t_y, t_z$ ), three rotation parameters (around X, Y and Z axes –  $\omega, \varphi, \kappa$ ), and one scale factor  $\lambda$ . The three static targets (see Figure 2) were used to provide nine equations (three equations for the coordinates of each target). Two additional equations allowed the Least Square’s method to be adjusted to find the statistical solution.

### IV. PRINCIPLES OF THE MONITORING METHODS

Two approaches were adopted to estimate the deformation of the wooden frame using the RTC360 point-clouds: (i) target-based; (ii) cloud-based. In the target-based approach, the coordinates of the five targets were used to estimate the deformation of the wooden frame (see Figure 1a). The coordinates of the targets were extracted via an automated feature to identify the centre of the targets using the Leica Cyclone software (Leica Geosystems, 2021). The coordinates of the five targets were calculated for the initial-reference position of the wooden frame without any induced lateral displacement and for each of the scenarios of lateral displacement, as the average of the coordinates of the five points. The lateral displacement was then calculated based on the difference between each scenario and the reference position of the wooden frame. The same approach was adopted to calculate the lateral displacement based on the TS30 measurements, which was used as the true amplitude of lateral displacement.

In the Cloud-based approach, the change was calculated in two sets of clouds; the first is called the reference cloud and the other called the compared cloud. There are three well-known techniques to calculate the distance between the point-clouds: Cloud-to-Cloud (C2C), Cloud-to-Mesh (C2M), and Multiscale-Model-to-Model-Cloud-Comparison (M3C2). These methods were performed using an open-source software; CloudCompare (2021). The C2C method finds for each point in the compared cloud its closest point in the reference cloud. This method was improved by fitting a surface over a group of neighbouring points in the reference cloud with using the K-nearest neighbours’ algorithm (K=6 in this experiment). The surface was fitted using the Least Square’s method. The resulted distances were split in X, Y and Z components and only the component in the Y-axis was used to compute the lateral displacement. The C2M method was executed by creating a surface mesh for the point clouds in “initial” state scans (from six scanning positions). The fitted surface for the reference cloud was “2.5D quadric” and the closest distance for each point in the compared cloud was then calculated. The M3C2 method was performed using the entire reference cloud as core points, a normal scale (diameter) and a projection scale (diameter) of 0.018 m, and with a maximum depth (maximum distance to be calculated) of 0.090 m. The calculation mode was set to be in “Horizontal” and the preferred

orientation was set to be along the “-Y” axis. Additional information on these three methods (C2C, C2M & M3C2) can be found in Lague *et al.* (2013). Since these methods calculate the distance between the two point-clouds for large number of points in the point-clouds, the statistical mode of the calculated distances was used as the magnitude of lateral displacement. An additional Cloud-based method for estimating the lateral displacement in the wooden frame was proposed through monitoring the mean of each cloud in the Y-axis. These four cloud-based methods as well as the target-based method was analysed and compared to the ground truth measurements which were taken from the Leica TS30.

## V. MONITORING RESULTS

The first step of the analysis was to check whether the static targets, which were used to define the coordinate system remain stable during the measurements. Table 2 presents the difference in coordinates of the static targets that were surveyed before and after conducting the experiment using the TS30. The change in coordinates did not exceed 1 mm for any of the targets and they were distributed in different axes, meaning that the targets were stable during the experiments and susceptible only to random errors.

Table 2. The change in coordinates of the static targets before and after the experiment using the TS30

Target ID	Ex [mm]	Ey [mm]	Ez [mm]
S1	-1	0	1
S2	0	0	0
S3	-1	0	0

For the RTC360, the clouds were registered to the local coordinate system that was defined by the TS30 measurements. Initially, each point-cloud of the RTC360 was in an arbitrary coordinate system, which was transformed by using the three static targets, which were also surveyed by the TS30, as reference points. The standard deviations of the seven transformations parameters ( $t_x$ ,  $t_y$ ,  $t_z$ ,  $\omega$ ,  $\phi$ ,  $\kappa$ ,  $\lambda$ ), which derived as the diagonal elements of the variance-covariance matrix, are plotted in Figure 4. The accuracy of the coordinate transformation of the point clouds was evaluated by plotting the errors in defining the coordinates of the static targets (see Figure 5). The value of zero corresponds to the true-reference value, as it was derived from the TS30 measurements. These errors show the accuracy of the RTC360 point-clouds as well as the accuracy of the least square solution (since the Least Square’s method estimates the optimum but not the exact solution). In addition, the errors were influenced by the automatic feature tool to define the centre of the targets in the Leica Cyclone software (Leica Geosystems, 2021). It is noticeable that the error is distributed in the three static targets, as it is expected from the Least Squares adjustments solution. The

errors mostly fall in the zone of 0.5 mm. However, this was not the case for some scans, such as the scan of “initial” state that was taken from 20m and angle of incidence of 0°. Theoretically, the error of defining the static targets is not affected by the deformation scenario as the static targets remained stationary. This was observed in Figure 5 where the errors seem to be constant regardless of the deformation scenario.

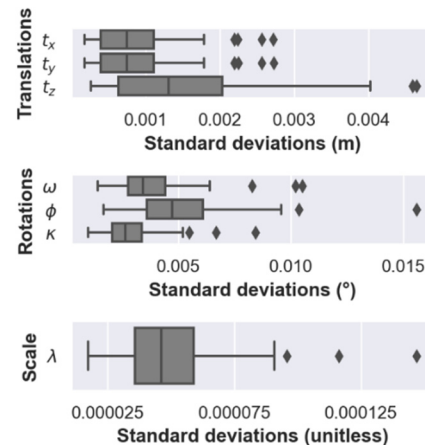


Figure 4. Box plots for the standard deviations for the transformation parameters to register the RTC360 clouds in the local coordinate system (introduced using the TS30 measurements). The middle line of the box corresponds to the statistical median whereas the box expresses the 25 and 75% thresholds of the distribution. The box is also referred to as the Interquartile range (IQR). The two bars express the minimum and maximum values which have a distance of  $1.5 \cdot \text{IQR}$  from the first and third quartiles. The external points show the outliers.

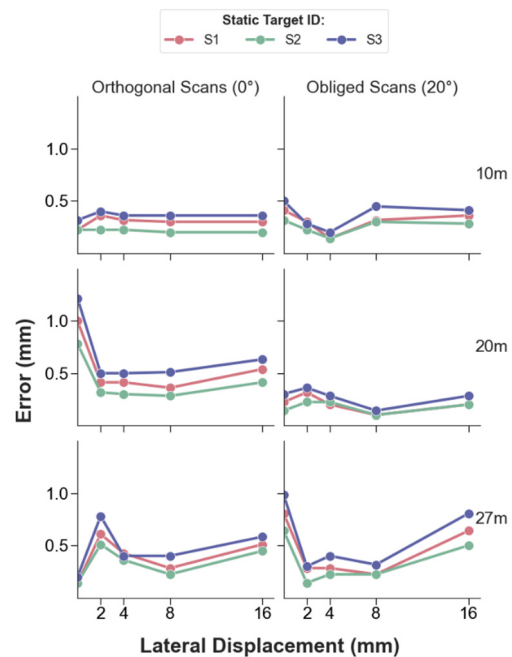


Figure 5. Error of the 3D-coordinate of the three static targets from the RTC360 scans, after the coordinate system transformation. The errors are grouped by the scanning distance and angle of incidence. The error is with respect the coordinates estimation using the TS30 measurements. The error of zero magnitude of lateral displacement refers to the “initial” state of deformation.

After registering all the point-clouds, the monitoring of the lateral displacement in the wooden frame was performed. The “initial” state of the wooden frame, as shown in Table 1, was used as the reference state, against which the four other scenarios were compared. The deformations were estimated using the five monitoring methods: (i) target method, (ii) cloud-mean method, (iii) C2C method, (iv) C2M method, and (v) M3C2 method. After obtaining the lateral displacements, the results were compared to the TS30. Figure 6 shows the absolute errors in the estimated lateral displacement for each monitoring method. The results are plotted according to the scanning distance and the angle of incidence. In general, it is observed that the target-method and the cloud-mean method obtained results of similar accuracy and very close to the measurements that were taken by the TS30. Obtaining very similar values and pattern means that these two methods are validated, and are expected to obtain consistence deformation estimation. Regarding the other three cloud comparison techniques (C2C, C2M and M3C2), they resulted in errors of less than 2.5mm and they seemed to be generally less accurate than the target and cloud-mean methods.

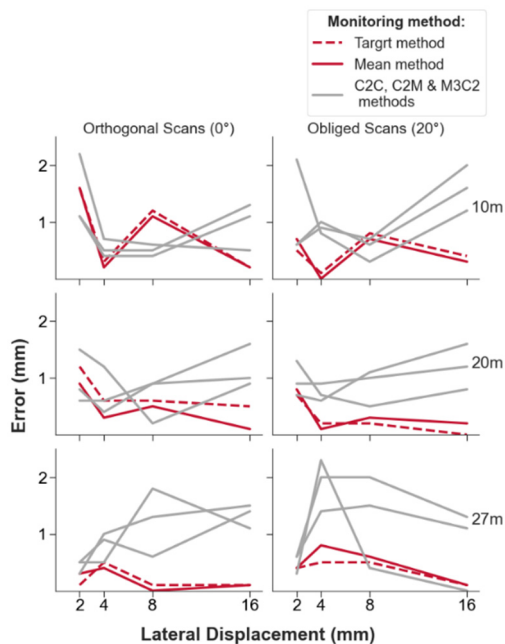


Figure 6. The absolute errors in estimating the lateral displacements for the wooden frame (the zero magnitude of error refers to the TS30 estimation).

The target and cloud-mean methods obtained similar results and pattern over different angles of incidence.

Characteristic example is the scenarios of scanning distance 10m, where for both incidence angles the error pattern was similar (see Figure 6). Furthermore, the similarity of the error pattern is mainly observed between the two angles of incidence, which means that the error seems to be affected by the scanning distance more than the angle of incidence (for angles of the examined range: from 0° to 20°).

Since all the comparisons were made between independent scans, the common pattern of the errors should be the result of a common error between the scans. One potential error could be caused by the coordinate transformation, which however was characterised by error about 0.5mm, as it was indicated in Figure 5. Furthermore, potential errors of TS30 should not have significant impact on the scans through the coordinate system definition, as the TS30 error was limited in less than 1 mm, reflected on static targets coordinates definition. Also, the TS30 measurements, which were made in face-left and face-right had an average misalignment of less than 1 mm, indicating that potential error of TS30 should not affect the displacement estimations in Figure 6. Another parameter which seems to affect the performance of the point-clouds accuracy is the network geometry of the static targets and their relative position with respect to the TLS position. The geometry of the static targets affects the accuracy of the point-clouds as was investigated by Fan *et al.* (2015). This is supported by the fact that as the scanning distance in Figure 6 decreases, the error patterns of the target and cloud-mean methods for the two incidence angles become closer. That is because the effect of the scanning angle in the geometry of the static targets increases as the distance increases.

To further investigate the accuracy of each monitoring method, the average error of each method was plotted in Figure 7. This average error was calculated based on all the errors from the six different scanning stations (with different scanning distances and incidence angles). The standard deviation of that average error was multiplied by two and was also plotted in Figure 7 to show the 95% confidence level of that error. Hence, the total length of the bar represents the expected error of each monitoring method with a confidence level of 95%. The deformations that were estimated using the cloud-mean method as well as the target method provided the highest accuracies among the other methods. Generally, the accuracy of all the methods were about 2 mm with 95% confidence level. The average of the errors for the mean and target methods were 0.45 mm and 0.48 mm with standard deviations of 0.39 mm and 0.40 mm, respectively. Although the M3C2 had an average error similar to the values estimated by the C2C and C2M, the standard deviation of the errors was the overall lowest (0.37 mm). Therefore, the M3C2 had an overall accuracy of 1.7 mm with 95% confidence level, which is better than those obtained by the C2C and C2M methods (see Figure 7). The C2M method provided the least accurate estimation, and that mainly because it calculates the Euclidean distance to the mesh (*i.e.* does not calculate the distance along the desired axis, Y-axis, whereas the C2C and M3C2 methods do).

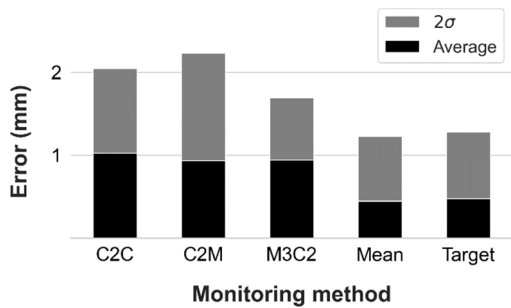


Figure 7. Bar plot for the average errors for each monitoring method. The black part of the bar represents the average error whereas the full length of the bar shows the error budget with a confidence level of 95%. The zero magnitude of error refers to the TS30 estimation.

The effect of the scanning distance and angle of incidence was also studied. Figure 8 shows the average errors of each monitoring method for the various examined scanning distance, whereas the errors were grouped by the angle of incidence in Figure 9. It is expected that the error increases as the scanning distance and angle of incidence increase; however, this was not always the case for the mean and target methods. For example, errors in the orthogonal scans in Figure 8 were decreasing as the scanning distance increases. Since this was not consistent among all the results, for example the error at a scanning distance of 27 m in Figure 9 was smaller in the orthogonal scans (for the cloud-mean and target methods) than the obliged scan. Consequently, these errors were mainly affected by the registration accuracy.

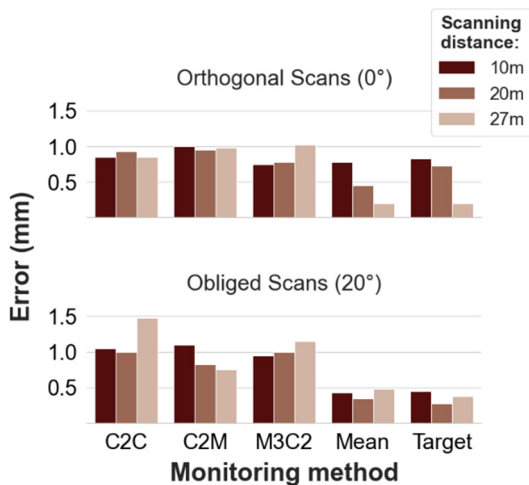


Figure 8. Bar plot for the average errors for each monitoring method filtered by the scanning distance (the zero magnitude of error refers to the TS30 estimation).

Similarly, the average errors were plotted for each monitoring method filtered by the deformation scenario in Figure 10. The C2C and M3C2 methods, which use the raw point clouds to estimate the displacement, seemed to have better accuracies when the introduced displacement was small. The mean and target methods did not have a clear pattern and the errors seemed to be just random errors. It is important

to mention that since the deformation results for the mean and targets were almost identical over all the presented figures, these methods are most efficient methods for estimating the lateral displacement in the wooden frame.

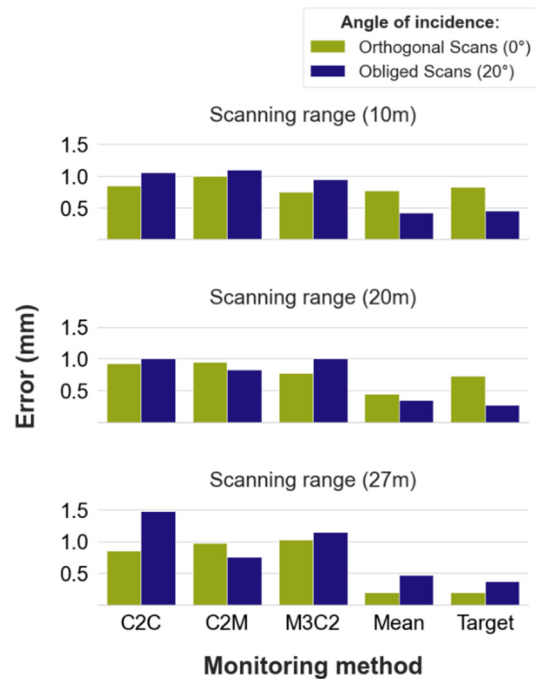


Figure 9. Bar plot for the average errors for each monitoring method filtered by the angle of incidence (the zero magnitude of error refers to the TS30 estimation).

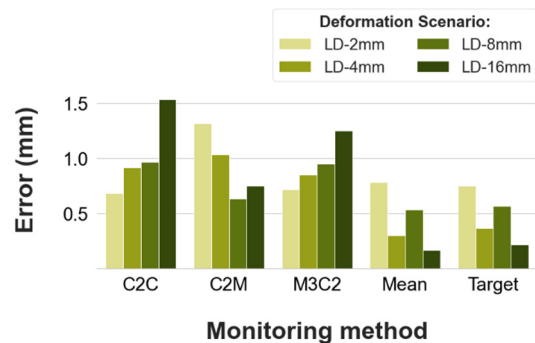


Figure 10. Bar plot for the average errors for each monitoring method filtered by the deformation scenario (the zero magnitude of error refers to the TS30 estimation).

## VI. CONCLUSION

This paper investigated the effect of the scanning distance and angle of incidence on the accuracy of monitoring lateral displacements in a wooden frame that was designed to simulate the deformations of retaining walls. Various methods were used for estimating the deformation of the wooden frame using single scans (without building a 3D model of the scanned surface). The results showed that the cloud-mean method obtained the best accuracies, and its performance was very similar to the target method. The results showed also that the cloud comparison techniques (C2C, C2M and M3C2) are capable of estimating the lateral displacement in the wooden frame using the statistical mode of the calculated



distances of the two point-clouds. The results showed also that the accuracy was more affected by the accuracy of the coordinate transformation and the geometry of the static targets. The research findings suggest that the scanning distance and the angle of incidence are not the main sources of error.

The findings of this study have to be seen in light of some limitations. In this study, the reference coordinate system was introduced by using the TS30 measurements whereas if the RTC360 was used in practice, the first scan would be used as the reference coordinate system. This, however, might introduce a large error in the registration process, which was eliminated in this study. In addition, the use of only three static targets leaves no independent checks for the accuracy of the scans. The use of single scans in this study eliminated the error caused by registering point-clouds that are taken for a surface from different scanning positions to build the 3D model. Furthermore, the results showed the performance of the TLS for monitoring only the lateral displacements. Therefore, future research should address the performance of the TLS in monitoring other deformations scenarios for retaining walls. The effect of distance and angle of incidence can be investigated further. Since in practice, it is expected to scan retaining walls from a different location at a time, it is important to investigate the accuracy of the deformation estimations with different scanning set-up. For example, the scan of “initial” state that was taken orthogonally with a scanning distance of 10 m can be used as the reference cloud and be compared to the scan of “lateral displacement (2 mm)” state that was taken with an angle of 20° and a scanning distance of 20 m.

## References

- Aldosari, M., Al-Rawabdeh, A., Bullock, D., and Habib, A. (2020). A Mobile LiDAR for Monitoring Mechanically Stabilized Earth Walls with Textured Precast Concrete Panels. *Remote Sensing*, Vol 12, No.2, pp. 306.
- Al-Rawabdeh, A., Aldosari, M., Bullock, D., and Habib, A. (2020). Mobile LiDAR for Scalable Monitoring of Mechanically Stabilized Earth Walls with Smooth Panels. *Applied Sciences*, Vol 10, No. 13, pp. 4480.
- Athanasopoulos-Zekkos, A. A., Lynch, J., Athanasopoulos-Zekkos, D., Grizi, A., Admassu, K., Benhamida, B., Spino R. J., and Mikolajczyk, M., (2020). Asset Management for Retaining Walls. Michigan: University of Michigan.
- CloudCompare (2021). CloudCompare v2.12 beta [Windows 64-bit]. Available from <<http://www.cloudcompare.org/>>
- Fan, L., Smethurst, J.A., Atkinson, P.M., and Powrie, W. (2015). Error in Target-Based Georeferencing and Registration in Terrestrial Laser Scanning. *Computers & Geosciences*, Vol 83, pp. 54-64.
- Jatmiko, J. and Psimoulis, P., (2017). Deformation Monitoring of a Steel Structure Using 3D Terrestrial Laser Scanner (TLS). In: *Proceedings of the 24th International Workshop on Intelligent Computing in Engineering*, Nottingham, UK. pp. 10-12.
- Jia, D., Zhang, W., and Liu, Y. (2021). Systematic Approach for Tunnel Deformation Monitoring with Terrestrial Laser Scanning. *Remote Sensing*, Vol 13, No. 17, pp. 3519.
- Kim, M.-K., Wang, Q., and Li, H. (2019). Non-Contact Sensing Based Geometric Quality Assessment of Buildings and Civil Structures: A Review. *Automation in Construction*, Vol 100, pp. 163-179.
- Lague, D., Brodu, N., and Leroux, J. (2013). Accurate 3D Comparison of Complex Topography with Terrestrial Laser Scanner: Application to the Rangitikei Canyon (N-Z). *ISPRS Journal of Photogrammetry and Remote Sensing*, Vol 82, pp. 10-26.
- Law, D.W., Silcock, D., and Holden, L. (2018). Terrestrial Laser Scanner Assessment of Deteriorating Concrete Structures. *Structural Control and Health Monitoring*, Vol 25, No. 5, e2156
- Leica Geosystems, AG. (2021). Leica Cyclone v2021.1.1 [Windows 64-bit]. Available from <<https://leica-geosystems.com/>>
- Mukupa, W. (2017). Change Detection and Deformation Monitoring of Concrete Structures Using Terrestrial Laser Scanning. Nottingham: University of Nottingham.
- Oskouie, P., Becerik-Gerber, B., and Soibelman, L. (2016). Automated Measurement of Highway Retaining Wall Displacements Using Terrestrial Laser Scanners. *Automation in Construction*, Vol 65, pp. 86-101.
- Psimoulis, P., and Stiros, S. (2007). Measurement of deflections and of oscillation frequencies of engineering structures using Robotic Theodolites (RTS). *Engineering Structures*, 29(12), pp. 3312-3324.
- Psimoulis, P., and Stiros, S. (2008). Experimental assessment of the accuracy of GPS and RTS for the determination of the parameters of oscillation of major structures. *Computer-Aided Civil and Infrastructure Engineering*, 23(5), pp. 389-403.
- Seo, H.J., Zhao, Y., and Wang, J. (2019). Monitoring of Retaining Structures on an Open Excavation Site with 3D Laser Scanning. In: International Conference on Smart Infrastructure and Construction 2019 (ICSIC) [online] Cambridge, UK. *ICE Publishing*, pp. 665-672.
- Suchocki, C., and Katzer, J. (2018). Terrestrial laser scanning harnessed for moisture detection in building materials - Problems and limitations. *Automation in Construction*, Vol 94, pp. 127-134.
- Závoti, J., and Kalmár, J. (2016). A Comparison of Different Solutions of the Bursa-Wolf Model and of the 3D, 7-Parameter Datum Transformation. *Acta Geodaetica et Geophysica*, Vol 51, No. 2, pp. 245-256
- Živec, T., Anžur, A., and Verbovšek, T. (2019). Determination of rock type and moisture content in flysch using TLS intensity in the Elerji quarry (south-west Slovenia). *Bulletin of Engineering Geology and the Environment*, Vol 78, No. 3, pp. 1631-1643.

## Assessment of the accuracy of low-cost multi-GNSS receivers in monitoring bridge response

Chenyu Xue<sup>1</sup>, Panos Psimoulis<sup>1</sup>, Qiuzhao Zhang<sup>2</sup>, Xiaolin Meng<sup>3</sup>

<sup>1</sup> Nottingham Geospatial Institute, University of Nottingham, Nottingham, UK, ([Chenyu.Xue@nottingham.ac.uk](mailto:Chenyu.Xue@nottingham.ac.uk); [Panagiotis.Psimoulis@nottingham.ac.uk](mailto:Panagiotis.Psimoulis@nottingham.ac.uk))

<sup>2</sup> Department of Civil Engineering, China University of Mining Technology, Xuzhou, China, ([Qiuzhao.Zhang@cumt.edu.cn](mailto:Qiuzhao.Zhang@cumt.edu.cn))

<sup>3</sup> Beijing University of Technology, Beijing, China, ([Xiaolin.Meng2013@gmail.com](mailto:Xiaolin.Meng2013@gmail.com))

**Key words:** *low-cost GNSS receiver; multi-GNSS; bridge monitoring; accuracy; modal frequency*

### ABSTRACT

The monitoring of bridges is a crucial operation for their maintenance and safe operation. Several methodologies have been developed the last decades, where different sensors are deployed to measure the bridge response (displacement, acceleration, tilt, strain, etc.). GNSS technology is one of the methods which are applied with the main advantage the direct measurement of the bridge displacement is carried out in an independent global coordinate system. However, the high cost of the GNSS stations, consisted of dual frequency receiver and geodetic GNSS antenna, is the main reason of the limited application of GNSS for bridge monitoring. In the current study, we assess the accuracy of low-cost multi-GNSS receivers in monitoring dynamic motion, similar to that of bridge response. The precision of low-cost GNSS receivers was assessed against high-performance dual frequency GNSS receivers, by executing controlled circular motion of predefined radius, of amplitude ranging between 5 to 50 cm, and frequency of 0.363 Hz. From the analysis of the GNSS measurements it was assessed the precision of GPS-only and the potential beneficial contribution of multi-GNSS constellation by enhancing the accuracy of GNSS solution. Then, a low-cost monitoring system formed by two closely-spaced low-cost GNSS receivers was applied in dynamic displacement monitoring of the Wilford pedestrian bridge. The analysis from low-cost GNSS data shows similar accuracy in monitoring the bridge dynamic response to that of the survey-grade GNSS receiver, with same main modal frequency of the bridge identified.

*This contribution was selected by the Scientific Committee for publication as an extended paper in Applied Geomatics <https://www.springer.com/journal/12518>*

## Sensitivity analysis of control networks in terms of minimal detectable displacements

Krzysztof Książek, Sławomir Łapiński

Warsaw University of Technology, Faculty of Geodesy and Cartography, Pl. Politechniki 1, 00-661 Warsaw, Poland, ([krzysztof.ksiazek@pw.edu.pl](mailto:krzysztof.ksiazek@pw.edu.pl); [slawomir.lapinski@pw.edu.pl](mailto:slawomir.lapinski@pw.edu.pl))

**Key words:** *sensitivity analysis; minimal detectable displacement; global test; power of the test; mean success rate*

### ABSTRACT

Sensitivity analysis is one aspect of the calculation process in displacement measurement. For this purpose, sensitivity measures are used in the form of minimal detectable displacements (MDD), derived from the definition of minimal detectable bias (MDB). Analyses were performed based on disturbing the parameter vector with the MDD value (calculated from principal component analysis). Analyses were considered for displacements of the levelling network based on the global vector ( $\mathbf{MDD}_{\text{network}}$ ). The calculations were conducted using the least squares adjustment with pseudo-random observations. The mean success rate (MSR) was used to perform the detection analyses. The effectiveness of the global test agrees with the assumed power of the test. Local tests for a single point showed 48.6 % displacements of more than one point. It should be considered using another local test for the case of displacements of multiple points. This study concludes that in addition to the accuracy of the designed network points, the network configuration is also important in sensitivity analyses. The research shows that sensitivity analyses should be considered at the design stage of control networks, *i.e.* to determine at what level a given network is able to detect displacement.

### I. INTRODUCTION

To (better) design the optimum control network, it is important to obtain a priori information about the magnitudes and rates of displacement (or deformation). In the literature on geodetic network design (*e.g.* Alizadeh-Khameneh, 2015), accuracy and reliability criteria for one observation epoch are used. In control networks (apart from accuracy and reliability analyses), the aim is to design a network that is sensitive to the displacements (or coordinate differences) between two or more measurement epochs (Niemeier, 1982; Niemeier *et al.*, 1982). Even-Tzur in works (2010; 2002) also indicates that monitoring networks should be analysed according to three criteria: accuracy, reliability and sensitivity.

The network's sensitivity is a criterion to be taken into account for the optimisation of control networks (Kuang, 1991) as it gives information on what level of displacement (or deformation) will be detected. Sensitivity measures, namely Minimal Detectable Displacement (MDD), are calculated to determine this level. The concept of MDD is based on the definition of Minimal Detectable Bias (MDB) pioneered in the work of (Baarda, 1968; 1967). It can be noted that as the concept of reliability, the measure of internal reliability is the internal reliability index  $\{\mathbf{R}\}_{ii}$  and the minimal detectable bias in observation (MDB). The transfer of considerations into displacement studies was initiated in the 1970s and 1980s, mainly by German authors, *e.g.*, Pelzer (1972) and Niemeier (1982; 1981). Thus, Prof.

Pelzer can be considered the precursor of displacement sensitivity analyses in control networks (Pelzer, 1972).

Although nearly fifty years have passed, the subject of network sensitivity to displacement detection is still commonly addressed in research. The main issues found in the literature on the subject include:

- Sensitivity of the control network to displacements (or deformations).
- Definition of the minimal detectable displacement.
- Selection of statistical test parameters for displacement assessment
- Examples of the use of sensitivity analyses for applied solutions.

Considering the subject of network sensitivity analysis, Heck in his work (1986), gives the quantities that are required to carry it out. These should therefore be listed:

- Network configuration (coefficient matrix  $\mathbf{A}$ ).
- Measurement accuracy (weighting matrix  $\mathbf{P}$ , a priori variance factor  $\sigma_a^2$ ).
- The distribution of test statistics to be used in the displacement (deformation) analysis for  $H_0$  and  $H_a$  (non-centrality parameters  $\lambda_0$  or probabilities  $\alpha_0$  and  $\beta_0$ ).

Knowing that all this information is available before the measurements are made, sensitivity analysis can be performed during the planning stage. If the sensitivity of the designed network is not suitable for the intended

use, the parameters used must be modified so that the final requirements are fulfilled. A new proposal is extending the application area of the MDD. The research focuses on the probabilistic aspect of the combination of significance and detectability (Prószyński and Łapiński, 2021).

## II. MATHEMATICAL BASICS

Modelling multidimensional data acquired as part of the measurements performed requires a specific mathematical model of the object, showing the relationships between real quantities in the adopted reference system. A common object known to the surveyor is a geodetic network, particularly a displacement control network, which consists of geometric elements defined on a set of points of a given network.

The well-known Gauss-Markov model is assumed to adjust the measured values (Eq. 1):

$$\mathbf{A} \mathbf{x} = \mathbf{l} + \mathbf{v} \quad , \quad \mathbf{C}_l \quad (1)$$

where  $\mathbf{A} (n \times u)$  = design matrix  
 $\mathbf{x} (u \times 1)$  = vector of parameters  
 $\mathbf{l} (n \times 1)$  = vector of observation  
 $\mathbf{v} (n \times 1)$  = vector of random errors in  $\mathbf{l}$  (with opposite sign  $\mathbf{v} = -\boldsymbol{\varepsilon}$ )  
 $\mathbf{C}_l (n \times n)$  = covariance matrix for  $\mathbf{l}$  (positive definite)  
 $n$  = number of observations  
 $u$  = number of parameters

After standardising (*i.e.* reducing to unit weight) the model from Equation 1, the final model in the stochastic approach will take the form (Eq. 2):

$$\mathbf{A}_s \mathbf{x} = \mathbf{L} + \mathbf{v}_s \quad , \quad \mathbf{C}_l \equiv \mathbf{I} \quad (2)$$

where  $\mathbf{A}_s = \mathbf{D} \mathbf{A}$ ,  $\mathbf{L} = \mathbf{D} \mathbf{l}$ ,  $\mathbf{v}_s = \mathbf{D} \mathbf{v}$   
 $\mathbf{D}$  = standardisation matrix such that  $\mathbf{D}^T \mathbf{D} = \mathbf{C}_l^{-1}$

The control networks for displacement analysis are local networks without connections to the known reference system, so there is the network defect, which is determined by the fact that the matrix of coefficients in the system of observation Equations 2 is of non-full rank (Eq. 3):

$$\text{rank}(\mathbf{A}_s) = u - d_s \quad (3)$$

where  $d_s$  = the number of network defects

The coefficient matrix  $\mathbf{A}_s$  in the system of normal equations is a singular matrix therefore  $\det(\mathbf{A}_s^T \mathbf{A}_s) = 0$ , and it is impossible to compute the inverse of such a matrix (the case with an infinite number of system solutions). To obtain a solution, the generalised inverse of the matrix  $\mathbf{A}_s^T \mathbf{A}_s$  can be used (Perelmuter, 1979),

where a special case is the use of Moore-Penrose pseudoinverse. Then the determined parameter vector is of the least Euclidean norm and the covariance matrix of the unknowns (parameters)  $\mathbf{C}_{\hat{\mathbf{x}}}$  has the smallest trace value (Equations 4 and 5) under the condition  $\hat{\mathbf{v}}_s^T \hat{\mathbf{v}}_s = \min$  as a postulate of the least squares method.

$$\hat{\mathbf{x}}^T \hat{\mathbf{x}} = \min \quad (4)$$

$$\text{Tr}(\mathbf{C}_{\hat{\mathbf{x}}}) = \min \quad (5)$$

The parameter vector is determined from the formula (Eq. 6):

$$\hat{\mathbf{x}} = \mathbf{Q}_{\hat{\mathbf{x}}} (\mathbf{A}_s^T \mathbf{L}) = (\mathbf{A}_s^T \mathbf{A}_s)^+ (\mathbf{A}_s^T \mathbf{L}) \quad (6)$$

where  $\mathbf{Q}_{\hat{\mathbf{x}}}$  = cofactor matrix of the parameter vector  
 $(\dots)^+$  = Moore-Penrose pseudoinverse

Based on Equation 6, the displacement vector  $\mathbf{d}$  is obtained (Eq. 7):

$$\mathbf{d} = \hat{\mathbf{x}}_2 - \hat{\mathbf{x}}_1 \quad (7)$$

where  $\hat{\mathbf{x}}_1$  = vector of parameters in the initial position  
 $\hat{\mathbf{x}}_2$  = vector of parameters in the present position

while the cofactor matrix of displacement vector  $\mathbf{d}$  (Eq. 8):

$$\mathbf{Q}_d = \mathbf{Q}_{\hat{\mathbf{x}}_1} + \mathbf{Q}_{\hat{\mathbf{x}}_2} \quad (8)$$

The global test procedure, as with many geodetic tasks, involves separating two hypotheses: the null ( $H_0$ ) and the alternative ( $H_a$ ) (Eqs. 9 and 10):

$$H_0: E(\mathbf{d}) = \mathbf{0} \quad (9)$$

$$H_a: E(\mathbf{d}) \neq \mathbf{0} = \mathbf{d}_A \quad (10)$$

where  $\mathbf{d}_A (u \times 1)$  = the displacement vector

If the null hypothesis  $H_0$  is rejected, the alternative hypothesis  $H_a$  is accepted.

The test statistic takes the form (Eq. 11):

$$T = \frac{\mathbf{d}^T \mathbf{Q}_d^+ \mathbf{d}}{\sigma_d^2} \sim \chi^2(h) \quad (11)$$

where  $\sigma_d^2$  = the a priori variance factor  $\sigma_d^2 = 1$   
 $h$  = rank of the cofactor matrix in the vector of parameters

Checking the global test condition consists in comparing the corresponding test statistic being the

value of  $T$  from Equation 11 and comparing it with the threshold value  $\kappa = \chi_{h,1-\alpha_0}^2$ .

Possible cases for checking the condition in Equation 11:

- When  $T < \kappa$ , then the null hypothesis  $H_0$  is satisfied with probability  $1 - \alpha_0$  ( $\alpha_0$  being the significance level). In this case, there are no displacements in the given network, and thus the resulting vector  $\mathbf{d}$  is due only to random errors between the two measurement periods.
- When  $T \geq \kappa$ , then the alternative hypothesis  $H_a$  is accepted. In this case, there are displacements in the given network, and we cannot identify a point (or points) that has moved. It is only possible to say that at least one point has moved.

The single point test statistic  $T_i$  will take the form (Eq. 12):

$$T_i = \frac{\mathbf{d}_i^T \mathbf{Q}_i^{-1} \mathbf{d}_i}{\sigma_d^2} \sim \chi^2(h_i) \quad (12)$$

where  $\mathbf{d}_i(h_i \times 1)$  = the displacement vector of the  $i$ -th point,  
 $\mathbf{Q}_i(h_i \times h_i)$  = the cofactor matrix of the  $i$ -th point,  
 $h_i$  = rank of the matrix of the point in the network.

The test statistic is compared with the threshold value  $\kappa_i = \chi_{h_i,1-\alpha_0}^2$ :

- $T_i < \kappa_i$  then the point under test is not displaced, with probability  $1 - \alpha_0$ .
- $T_i \geq \kappa_i$  then the point under test shall be regarded as displaced.

The terms global test and local test are used for this paper regarding the parameter vector. The former is when the detectability of a displacement is tested on the whole network. In turn, analyses of detectability in terms of performed statistical tests for individual points in this paper will be called a local test of a single point.

Based on equations 10 and 11, the value of the non-centrality parameter  $\lambda$  of the distribution calculated from the pre-set or well-defined displacement vector  $\mathbf{d}_A$  (Eq. 13):

$$\lambda = \frac{\mathbf{d}_A^T \mathbf{Q}_d^+ \mathbf{d}_A}{\sigma_d^2} \quad (13)$$

The value of the non-centrality parameter calculated from Equation 13 is compared with the lower limit of the value of the non-centrality parameter obtained from Baarda's nomograms (note that only for the  $\chi^2$  distribution) (Baarda, 1968) or using a computational algorithm (Aydin and Demirel, 2005). The threshold value of the non-centrality parameter  $\lambda_0$  is determined

by the significance level  $\alpha_0$  (type I error probabilities) and the power of the test  $1 - \beta_0$  ( $\beta_0$  - type II error probabilities).

Then, if the inequality (Eq. 14):

$$\lambda \geq \lambda_0 \quad (14)$$

where  $\mathbf{d}_A$  is detectable.

Then it can be concluded that the given network is sensitive to expected displacements. If the inequality is not true, the network must be redesigned to be capable of detecting expected displacement values.

Based on the inequality (Equation 14) and the knowledge about the magnitude of the displacement of the test object (vector  $\mathbf{g}$ ), it is possible to make an evaluation to determine the detectable displacement.

Then the alternative hypothesis takes the form (Eq. 15):

$$H_a: \mathbf{d}_A = c \mathbf{g} \quad (15)$$

where  $c$  = scalar factor.

The displacement vector  $\mathbf{d}_A$  is detectable when (Eq. 16):

$$\lambda = \frac{(c \mathbf{g})^T \mathbf{Q}_d^+ (c \mathbf{g})}{\sigma_d^2} > \lambda_0 \quad (16)$$

Based on Equation 16, the value of the scalar factor  $c$  can be calculated (Eq. 17):

$$c \geq \sigma_d \sqrt{\frac{\lambda_0}{\mathbf{g}^T \mathbf{Q}_d^+ \mathbf{g}}} \quad (17)$$

As a result, it is possible to determine the minimal detectable displacement vector **MDD** in the assumed model of the network (Eq. 18):

$$\mathbf{MDD} = c_{min} \cdot \mathbf{g} \quad (18)$$

The Minimal Detectable Displacement vector, a measure of network sensitivity, was obtained.

The papers (Aydin, 2011; Niemeier, 1982) take into account that in some cases, the directional vector  $\mathbf{g}$  is not known. Then, in order to calculate the minimal detectable displacement, the eigenvector  $\mathbf{g}_{min}$  belonging to the minimum eigenvalue  $\lambda_{min}$  calculated from the decomposition of the cofactor matrix  $\mathbf{Q}_d^+$  should be used. This is the direction with the maximum deformability of the network (Niemeier, 1982). The formula takes the form (Eq. 19):

$$c_{min} \geq \sigma_d \sqrt{\frac{\lambda_0}{\mathbf{g}_{min}^T \mathbf{Q}_d^+ \mathbf{g}_{min}}} \quad (19)$$

Finally, the minimal detectable displacement vector for the whole network  $\mathbf{MDD}_{network}$  in the eigenvector direction  $\mathbf{g}_{min}$  is obtained for a given power test  $1 - \beta_0$  and significance level  $\alpha_0$  (Eq. 20):

$$\mathbf{MDD}_{network} = c_{min} \cdot \mathbf{g}_{min} \quad (20)$$

Using the Moore-Penrose pseudoinverse (Eq. 6), in this solution, the cofactor matrix  $\mathbf{Q}_d$  (Eq. 8) and displacement vector  $\mathbf{d}$  (Eq. 7) are related to the centre of gravity of the net. This solution gives the lowest minimal detectable displacement value (Łapiński, 2019).

### III. EMPIRICAL TESTS

For a computational example of sensitivity analysis, let us assume a levelling network consisting of eight points numbered P1 from P8. These are eight unknowns in the adjustment process. The defect of the network ( $d_s$ ) is an equal one. The geometry of the vertical network is shown in Figure 1.

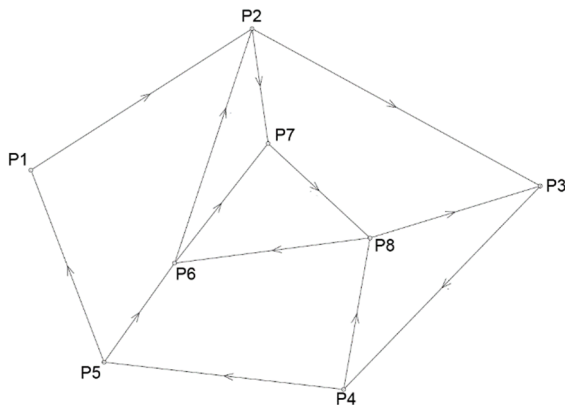


Figure 1. The geometry of the levelling network.

The observations consist of 13 differences in elevation between network points from the two measurement epochs - Table 1.

Table 1. Observations in levelling network

No.	Observation code		Number of stations in one measurement epoch
1	P1	P2	5
2	P2	P3	6
3	P3	P4	5
4	P4	P5	4
5	P5	P1	4
6	P5	P6	1
7	P6	P7	2
8	P7	P8	3
9	P8	P6	3
10	P4	P8	3
11	P8	P3	3
12	P6	P2	2
13	P2	P7	1

The numerical study considered the case of uncorrelated observations. The calculation of displacements with the method of observation

differences was applied, assuming the same number of stations in levelling lines for both measurement epochs. The standard deviations for the differences  $\sigma_i = \sigma_0 \sqrt{n}$ , where  $\sigma_0 = 1 \text{ mm}$ ,  $n$  – number of stations. It was assumed that the observations did not have gross errors or were correctly eliminated by diagnostic tests.

The study assumed a sample number of 50 000 using Monte-Carlo Simulations (Koch, 2018) (with such a sample is the compatibility of results between simulations). But at the same time, imposed a condition on the pseudo-random vector (corresponding to standardised random errors), *i.e.*, the typical true error is between 0.85 and 1.15. A self-developed algorithm in MATLAB was implemented to perform the sensitivity analyses and the presentation of the results.

In the first step, the value of minimal detectable displacement for the network was calculated based on Equation 20, assuming  $\chi^2(h)$  distribution,  $\alpha_0 = 0.05$ ,  $1 - \beta_0 = 0.80$ . The values of  $\mathbf{MDD}_{network}$  are presented in Table 2.

Table 2. Summary of  $\mathbf{MDD}_{network}$  values

$\mathbf{MDD}_{network}$ [mm]	6.61
	0.70
	-3.87
	-3.02
	1.21
	0.45
	0.13
	-2.21
$\ \mathbf{MDD}_{network}\ $ [mm]	8.65

A displacement sensitivity analysis was then performed by distorting the parameter vector with the value of the minimal detectable displacement. The known parameter vector is then converted into a vector of observations (with a fixed matrix  $\mathbf{A}_s$ ), then the pseudo-random part of the observations is added. An adjustment by the least squares method is performed based on the calculated new observation vector. The result of each adjustment is a displacement vector, and the value of the non-centrality parameter is calculated from Equation 13, which is then compared with its threshold value (Eq. 14).

The results from the analyses performed are presented using the mean success rate (*MSR*) proposed in the work (Hekimoglu and Koch, 1999). According to the case study, the experiments are appropriately tested in the simulation procedure. After applying the appropriate test procedure, those that exceeded the threshold value (so-called successful results) are counted for each experiment. The *MSR* is calculated as follows (Eq. 21):

$$MSR = \frac{\text{number of successful results}}{\text{number of experiments}} \quad (21)$$

The results for each analysis are related to the case of displacement detection, *i.e.* information based on a statistical test. Three different graphs were produced to present the results. The first one shows the effectiveness of individual statistical tests, *i.e.* global test, local test, both tests at the same time and in the case of lack of information about a possible displacement. The effectiveness of the static test means that a displacement of at least one point in the network was detected. The calculated efficiencies for each statistical test are shown in Figure 2.

Based on Figure 2, the highest efficiency, *i.e.* with a value of 80.8%, was obtained for the local test. It means that the displacement of at least one point in the network was detected. The effectiveness of the global test is 79.5%, where 75.9% refers to the displacement detection effectiveness for both tests simultaneously. It can be said that the tests have similar effectiveness, with the exception of 15.6% of all tests where displacement was not detected. It should be added that an 80% probability power of the tests was assumed.

The second graph shows more detailed results for the test performed for each point in the network. Efficiencies are presented with information on the number of points in the network considered to be displaced. These results are shown in Figure 3.

Based on Figure 3, the highest efficiency, *i.e.* with a value of 32.2%, is characterised by the single point detection case. Although, for two points of the network, the efficiency of detecting displaced points is slightly lower, reaching a value of 30.9%. It can be seen from Figure 3 that the effectiveness decreases as the number of detected points increases. In this analysis, a maximum of 5 network points were detected. Although for the case of five points detected, the effectiveness is very low, equal 0.5%. The sum of all values is 80.8%, which is the total effectiveness of the local test. It is worth reminding that there are 8 points in the network.

More detailed results, as they relate to the effectiveness of detecting individual point numbers in the network, are presented in the third type of graph, as illustrated in Figure 4.

Based on Figure 4, the highest efficiency of 70.5% was obtained for point P1. In the second order, the highest efficiency was obtained for point P3. The successive points are P4, P8, P5, P2, P6, and P7. Figure 4 (100% cumulative columnar) for each network point should be interpreted as follows, *e.g.* for point P1 in 70.5% of all trials, the local test detected displacement. In comparison, the displacements were not detected for 29.5% of all experiments.

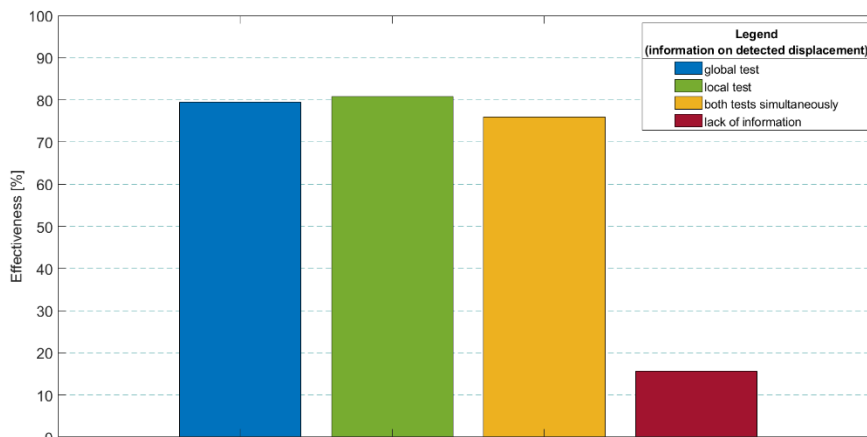


Figure 2. Effectiveness diagram for different statistical tests.

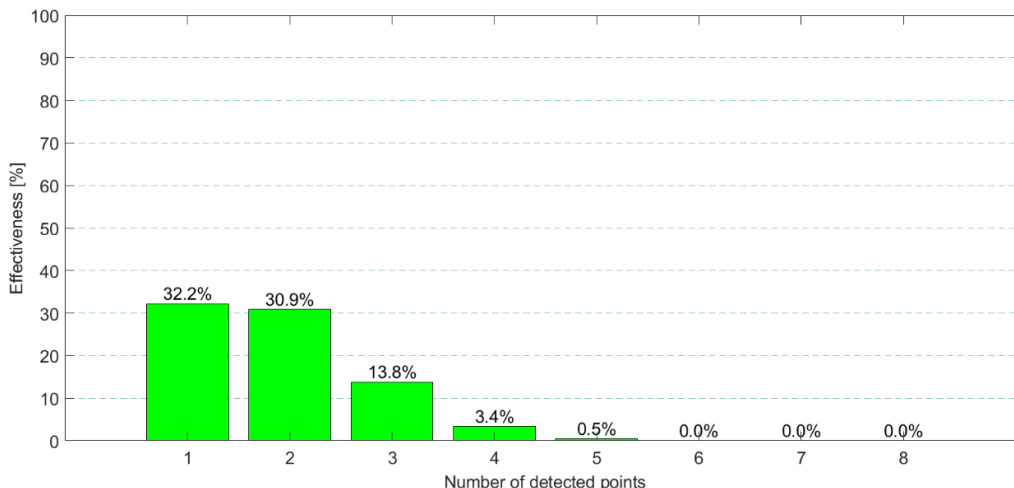


Figure 3. Determination of the effectiveness of local tests with information on the number of points considered to be displaced.

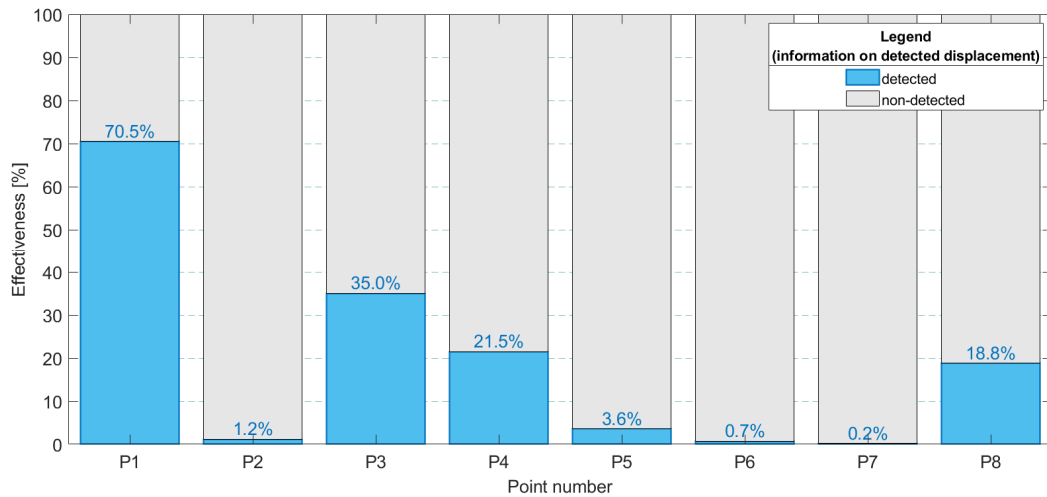


Figure 4. Summary of the detection effectiveness of each network points.

#### IV. CONCLUSIONS

This work on geodetic displacement measurements deals with sensitivity analyses. The disturbance analyses with the value of the minimal detectable displacement (constant vector) in the direction of the maximum deformability of the network were carried out. The work aimed to check the efficiency of displacement detection with a large simulated test sample.

The results are shown in Figures 2-4. Concerning Figure 4, to indicate why there is such an order of detection efficiency of individual points, reference should be made to the cofactor matrix  $Q_d$ . This matrix also calculates the accuracy characteristics, so the relationship between the value of the minimal detectable displacement for the whole network and the accuracy characteristics can be assumed. Table 3 shows the values of the mean errors of point position of all network. Thus, it confirms the obtained order of the resulting effectiveness. Only for point P7, a low efficiency was obtained, despite having a higher accuracy of 0.16 mm than point P6 and 0.03 mm than point P2. However, it should be noted that this relates to a (very low) efficiency of less than 1.2 %. Point P1 has the lowest point accuracy and, according to work (Kutterer, 1998), can be the weakest area of the network.

Table 3. Mean error of point position

Point number	Mean error of point position [mm]
P1	2.0
P2	1.1
P3	1.6
P4	1.5
P5	1.2
P6	0.9
P7	1.1
P8	1.2

By distorting the parameter vector (displacements) with the value of  $MDD_{network}$  the effectiveness of the

global test agrees with the assumed power of the test. Local tests for a single point showed that there are displacements of more than one point in 48.6 %. It should be considered using another local test for the case of displacement of multiple points.

When designing a network, the geometry of the network is important, as is the accuracy of the determination of the network points (mean error). Therefore, sensitivity analysis is used as one of the criteria for network optimisation to meet the assumed requirements for the control network. Depending on the purpose of the geodetic network, different criteria can be selected for implementation in the optimisation procedure. The definition of  $MDD_{network}$  can be used to compare the magnitude of minimal detectable displacements for different control networks design options.

#### References

- Alizadeh-Khameneh, M.A., (2015). *On optimisation and design of geodetic networks*. Printed by Universitetservice US AB, Stockholm, Sweden.
- Aydin, C., (2011). Power of Global Test in Deformation Analysis. *J. Surv. Eng.*, 138, pp. 51–56. DOI: 10.1061/(ASCE)SU.1943-5428.0000064
- Aydin, C., and Demirel, H., (2005). Computation of Baarda's lower bound of the non-centrality parameter. *J. Geod.*, 78, pp. 437–441. DOI: 10.1007/s00190-004-0406-1
- Baarda, W., (1968). *A testing procedure for use in geodetic network*. Publications on Geodesy, New Series, Netherlands Geodetic Commission, Delft.
- Baarda, W., (1967). *Statistical concepts in geodesy*. Publications on Geodesy, New Series, Netherlands Geodetic Commission, Delft.
- Even-Tzur, G., (2010). More on sensitivity of a geodetic monitoring network. *J. Appl. Geod.*, 4, pp. 55–59. DOI: 10.1515/jag.2010.006
- Even-Tzur, G., (2002). GPS vector configuration design for monitoring deformation networks. *J. Geod.*, 76, pp. 455–461. DOI: 10.1007/s00190-002-0274-5



- Heck, B. (1986). Sensitivitätsanalyse geodätischer Deformationsnetze. *Allgemeine Vermessungs-Nachrichten (AVN)*, 93(5), pp. 169-181.
- Hekimoglu, S., and Koch, K.R., (1999). How Can Reliability of the Robust Methods be Measured?, in: Gründing, A. and (Ed.), *Third Turkish German Joint Geodetic Days*. 1-4 June, Istanbul, Turkey, pp. 179–196.
- Koch, K.R., (2018). Monte Carlo methods. *GEM - Int. J. Geomathematics*, 9, pp. 117–143. DOI: 10.1007/s13137-017-0101-z
- Kuang, S., (1991). *Optimisation and Design of Deformation Monitoring Schemes*. Ph.D. dissertation. University of New Brunswick, Department of Surveying Engineering, New Brunswick, Canada.
- Kutterer, H., (1998). Quality aspects of a GPS reference network in Antarctica - A simulation study. *J. Geod.*, 72, pp. 51–63. DOI: 10.1007/s001900050148
- Łapiński, S., (2019). *A study of minimal detectable displacements in a control networks for different reference system definitions*. PhD Thesis (in Polish). Warsaw University of Technology.
- Niemeier, W., (1982). Principal Component Analysis and Geodetic Networks – Some Basic Considerations. *Proc. Surv. Control Networks Heft 7*, pp. 275–291.
- Niemeier, W., (1981). Statistical Tests for Detecting Movements in Repeatedly Measured Geodetic Networks. *Tectonophysics*, 71, pp. 335–351. DOI: 10.1016/B978-0-444-41953-8.50041-4
- Niemeier, W., Teskey, W.F., and Lyall, R.G., (1982). Precision, reliability and sensitivity aspects of an open pit monitoring network. *Aust. J. Geod. Photogramm. Surv.* 1–27.
- Pelzer, H., (1972). *Nachweis von Staumauerdeformationen unter Anwendung statistischer Verfahren*. Berichte Arbeitsgruppe B, Deutscher Geodätentag Braunschweig.
- Perelmuter, A., (1979). Adjustment of free networks. *Bull. Géodésique*, 53, pp. 291–295. DOI: 10.1007/BF02522272
- Prószyński, W., and Łapiński, S., (2021). Investigating support by minimal detectable displacement in confidence region determination and significance test of displacements. *J. Geod.* 95. DOI: 10.1007/s00190-021-01550-4

## Long and close-range terrestrial photogrammetry for rocky landscape deformation monitoring

Miriam Cabrelles<sup>1</sup>, [José Luis Lerma](mailto:jillerma@cgf.upv.es)<sup>1</sup>, Luis García-Asenjo<sup>1</sup>, Pascual Garrigues<sup>1</sup>, Laura Martínez<sup>2</sup>

<sup>1</sup> Department of Cartographic Engineering, Geodesy and Photogrammetry, Universitat Politècnica de València, Camino de Vera s/n, 46022 Valencia, Spain, ([micablo@doctor.upv.es](mailto:micablo@doctor.upv.es); [jillerma@cgf.upv.es](mailto:jillerma@cgf.upv.es); [lugarcia@cgf.upv.es](mailto:lugarcia@cgf.upv.es); [pasgarta@cgf.upv.es](mailto:pasgarta@cgf.upv.es))

<sup>2</sup> Department of Roads and Infrastructures, Diputació de València, c/ Hugo de Moncada 9, 46010 Valencia, Spain, ([laura.martinez@dival.es](mailto:laura.martinez@dival.es))

**Key words:** *SfM photogrammetry; EDM-based geodetic techniques; 3D modelling; deformation; monitoring; landslides*

### ABSTRACT

The paper describes the processing and validation of a series of terrestrial photogrammetric surveys carried out from 2017 to 2020 for monitoring the stability of a cliff in Cortes de Pallás (Spain). The complexity of the target area, which has a strong orography, a water reservoir, and many obstacles such as electrical power lines or vegetation, makes difficult the use of any measurement technique. After considering solutions such as long-range laser scanning or close-range mobile mapping, which were unsatisfactorily tested and therefore rejected for future campaigns, the use of combined short and long terrestrial photogrammetry proved an efficient method for quick and massive monitoring of the entire cliff with an overall accuracy of several centimetres. All the steps undertaken for the centimetre level accuracy deliverables, which include camera calibration, bundle-adjustment, dense point cloud generation, 3D modelling, and validation of the 3D models by using external geodetic information, will be presented. For the sake of conciseness, only results for the last two campaigns (5<sup>th</sup> and 6<sup>th</sup>), as well as the comparison between the last (6<sup>th</sup>) and the first (1<sup>st</sup>) campaigns, will be discussed. In addition, photogrammetric results will be validated by analyzing the metrics on four target-based micro-geodetic check points, located on key critical areas of the cliff selected by civil and geotechnical engineers from the Department of Roads and Infrastructures.

### I. INTRODUCTION

Rockfalls and landslides are common geohazards that can be found in many places all over the world. When they affect sensitive areas with settlements, natural resources, or civil infrastructures like the case at hand in Cortes de Pallás (Spain), government authorities usually demand experts to provide reliable information about the potential risk of those hazards.

Conventional surveying techniques based on global navigation satellite system (GNSS), geodetic instruments like electronic distance meters (EDM), or total stations (TS) can provide accurate coordinates, but they are restricted to only a discrete number of points (Arbanas *et al.*, 2012; Cina and Piras, 2015; Tsai *et al.*, 2012). In the present case, for instance, EDM-based geodetic techniques were applied to establish a ten-pillar high-precision reference frame which was in turn used to determine the coordinates of the check points (ChPs) permanently installed on the cliff with an overall accuracy of 1 mm – 3 mm (García-Asenjo *et al.*, 2019).

On the other hand, image-based sensors and techniques can provide massive information of large areas, although their suitability to rock slope modelling ultimately depends on the quality of ground control, the overall good geometry, and the distance between the sensor and the object (Francioni *et al.*, 2018).

Terrestrial laser scanning (TLS) is also a recurrent and efficient solution for distances shorter than 200 m, but for distances longer than 800 m, the technique becomes expensive and additional problems may arise, *e.g.* inaccurate registration and/or atmospheric refraction (Fan *et al.*, 2015; Harmening and Neuner, 2019; Friedli *et al.*, 2019).

Nowadays, LiDAR mobile mapping systems (MMS) can be an alternative to perform extensive measurement campaigns. Although the attainable accuracy for low-cost solutions when the area has strong limitations is in the range of 3-8 cm, (Di Stefano *et al.*, 2020; Jaboyedoff *et al.*, 2012; Oppikofer *et al.*, 2009) have investigated the usage of light detection and ranging (LiDAR) technology for landslide, rockfall and debris-flow, classifying its applications into four categories: (1) landslide detection and characterisation; (2) hazard assessment and susceptibility mapping; (3) modelling; and (4) monitoring. The authors alerted about the real challenge: to develop new methods to take benefit from high-resolution digital elevation models (HRDEM). Similarly, (Royán *et al.*, 2014) also broadened the concept of forwarding spatial predictions of future failures, understanding pre-failure behaviours of rockfalls, and their implications for implementing early warning systems.

In the present case, the authors tested the possibility of using both static and dynamic LiDAR for long-range mapping, but taking into account the strong site limitations described in Section II A, unsatisfactory results were obtained for two reasons. First, the long-range measurements over 500 m were not detailed enough. Second, the registration over those ranges failed to achieve the high accuracy required for rock cracking patterns characterization.

The usage of digital photogrammetry and unmanned aerial vehicle (UAVs)/drones for landslide mapping and displacement monitoring is also well-known in literature, even for large landslides (Lindner *et al.*, 2016; Rossi *et al.*, 2018). Nevertheless, the use of UAVs in Cortes de Pallás was disregarded because the complexity of the area, which includes a hydraulic power plant with many electricity power lines, car traffic, and tourism activities, does not favour the method. Eventually, the combination of close-range and long-range photogrammetry by using different cameras and lenses was deemed to be the optimal solution for mapping and monitoring the complex area of Cortes de Pallás.

This study analyses the attainable performance that can be achieved with the integration of terrestrial photogrammetry (close-range up to 50 m and long-range from 400 m to 800 m) by using well-defined CPs, 3D modelling, and mapping to monitor the area over three years. The results are additionally validated by using four well-defined ChPs whose coordinates were independently determined by making use of precise geodetic techniques. For the sake of conciseness, only 1<sup>st</sup>, 5<sup>th</sup> and 6<sup>th</sup> campaigns are compared and discussed.

The paper is structured as follows: Section II deals with the Materials and Methods; Section III presents the results of three photogrammetric campaigns between 2019 and 2021; Section IV discusses the results from different points of view; and finally Section V draws some conclusions.

## II. MATERIALS AND METHODS

### A. Study site

The target area is a broad cliff (650 m long, 200 m high and 300 m wide) facing the north side of a flat-topped hill in Cortes de Pallás, Spain (Figures 1 and 2). In 2015,

the power plant facilities and several roads skirting the cliff were seriously damaged due to a sudden rockfall. The refurbishment and consolidation work finished at the end of 2017. Then, the Department of Roads and Infrastructures of the *Diputació de València* commissioned the Department of Cartographic Engineering, Geodesy and Photogrammetry, Universitat Politècnica de València (UPV) a three-year project to monitor both the installed anchoring systems as well as the cliff as a whole. The monitoring project includes, among other components, a ten-pillar geodetic network whose stability is periodically monitored by using sub-millimetric EDM techniques (García-Asenjo *et al.*, 2019) along with deformation analysis based on repeatedly measured geodetic networks (Caspary, 1987; Niemeier, 1981). Additionally, the coordinates of the 15 reflectors installed permanently at critical points in the cliff are periodically determined from the pillars with an accuracy of several millimetres by using similar geodetic techniques. As it will be described in Section II B, a subset of those pillars and reflectors was additionally used for the registration and validation of the 3D photogrammetric models.



Figure 1. Overall view of the site area. The area to be monitored is displayed in yellow. Location of the 4 CPs used in the 5<sup>th</sup> and 6<sup>th</sup> photogrammetric campaigns.

However, the area presents serious limitations for any measurement technique. Aside from the usual problems with obstacles or vegetation, there is a water reservoir that strongly limits the selection of optimal stations for both photogrammetric and geodetic techniques. The stations have to be either very close, thus impeding optimal geometries, or they have to be placed on the opposite shoreline involving distances ranging from 400 m to 1000 m.

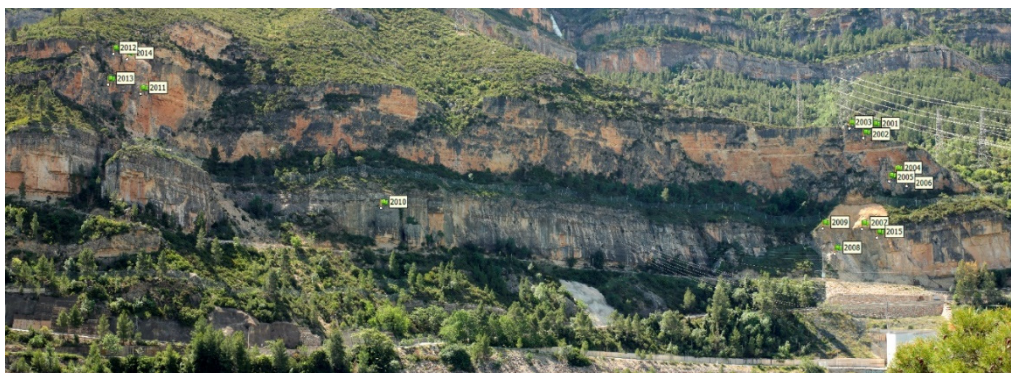


Figure 2. Northside of the hilly area. Location of the 15 ChPs on the slope.

## B. Materials

Normal and convergent long-range and close-range photogrammetry was used for data acquisition using two digital single-lens reflex (SLR) cameras during the three photogrammetric campaigns: 1) Canon EOS 5D SR (50 MP) with a Carl Zeiss 50 mm lens; and 2) Canon EOS Mark III (21 MP) with a Canon 200 mm lens.

The first camera was used for both close-range and long-range images taken along the roads from both shorelines and from the bridge crossing the reservoir and connecting the shorelines, while the second camera was only used for acquiring the long-range images targeting both the CPs and the ChPs (Figures 1 and 2).

CPs were materialised by big white spheres ( $\varnothing$  500 mm) temporarily set up on top of the concrete pillars, while ChPs were materialised by small white spheres ( $\varnothing$  145 mm) which are installed on top of 360° prisms permanently attached to the cliff (Figure 3). The software used for the photogrammetric processing was Agisoft Metashape.



Figure 3. ChPs on the slope.

As ground control for the registration process, there is a significant difference between the first campaign and the subsequent ones. Since the geodetic pillars were not settled yet, the ground control for the first campaign was provided by means of a static GNSS campaign with an overall precision of several centimetres. On the contrary, for subsequent campaigns the ground control was accurately provided by the CPs installed on the pillars of the geodetic reference frame, whose coordinates were determined with an accuracy of several tenths of a millimetre and one millimetre in the horizontal and vertical components, respectively.

## C. Methods

1) *Photogrammetry*: Structure-from-motion (SfM) photogrammetry was used to determine the orientation and sparse point cloud for the different campaigns. The cameras were calibrated following self-calibration bundle adjustment using an ideal subset of the images used during the data acquisition. Afterwards, the two calibration reports were used to undertake the bundle adjustment yielding a sparse point cloud. A summary of the photogrammetric data is presented in Table 1.

Table 1. Summary of the 1<sup>st</sup>, 5<sup>th</sup> and 6<sup>th</sup> photogrammetric campaigns

	1 <sup>st</sup>	5 <sup>th</sup>	6 <sup>th</sup>
Date	15/12/17	16/12/20	10/05/21
No. 50 mm images	164	150	166
No. 200 mm images	--	93	137
Avg. GSD [cm]	6.1	3.0	3.0
Avg. distance [m]	515	495	504
No. CPs	5	4	4
No. of ChPs	13	15	15
CPs Error X [cm]	1.5	0.9	0.8
CPs Error Y [cm]	0.9	0.5	0.7
CPs Error Z [cm]	0.7	0.2	0.3
CPs Error XYZ [cm]	1.9	1.0	1.1

For the absolute orientation, the CPs were used to reference the photogrammetric survey to the geodetic survey. Nevertheless, the 15 ChPs were also measured to determine the quality of the photogrammetric survey in each campaign.

The next step tackles the dense point cloud generation, plus cleaning and filtering (Figure 4a and 4c). As the area is extremely large for high resolution 3D modelling, the point cloud was segmented into a mesh of 50 m x 50 m.

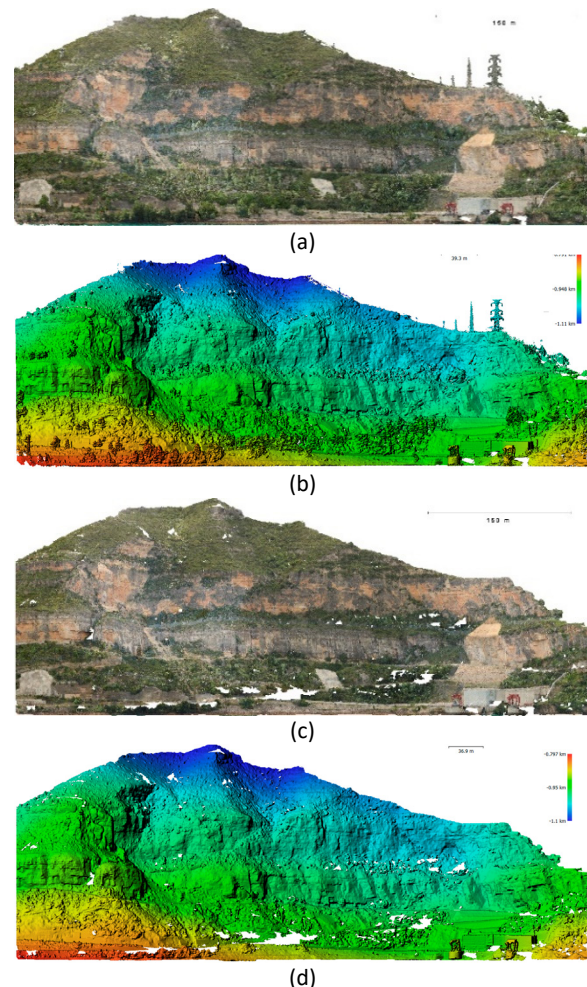


Figure 4. Generated point cloud and HRDEM for the front hill from the 6<sup>th</sup> campaign: a) point cloud without filtering; b) HRDSM; c) point cloud filtered; d) HRDEM.

Then, a high-resolution 3D mesh was computed for each meshing patch. It included the 3D meshing refinement, filling small holes and checking/correcting the topology.

Both the digital surface model (DSM) and the digital elevation model (DEM) of the site were also generated at high resolution (HR, Figure 4b and 4d, respectively). Both models can be used to confirm whether the vegetation was properly removed from the hill or not.

The final two image-based steps included texturing and orthoimage creation continued following the conventional SfM photogrammetric pipeline.

This photogrammetric pipeline was repeated for the three campaigns (some numeric values are reported in Table 1). In Section III, the results achieved will be presented.

2) *Geodetic measurements*: Three EDM-based field campaigns were carried out from 2018 to 2020. For each campaign, around 250 distances were measured using the Kern ME5000 Mekometer (SN 357050). Four original Kern RMO5035 reflectors were used to measure inter-pillar distances (CPs), while distances to reflectors installed permanently in the wall (ChPs) were measured by targeting fifteen Leica 360 reflectors. All the reflectors were calibrated at the UPV calibration baseline (García-Asenjo *et al.*, 2016) in accordance with the full procedure of ISO 17123-4.

The measurement of each distance takes approximately two minutes while the observer measures the meteorological parameters using a traditional Thies Clima Assmann-Type psychrometer ( $\pm 0.2$  K) and a Thommen 3B4.01.1 aneroid barometer ( $\pm 0.3$  hPa). Additionally, all the pillars were equipped with a data-logger Testo 176P1 and a parasol (Figure 5).



Figure 5. Kern ME5000 Mekometer on pillar equipped with a parasol and a data-logger for dry and wet temperatures as well as air pressure.

Prior to the adjustment of each campaign, the following corrections were applied: refraction correction, EDM frequency drift correction and geometric correction. Once these corrections were applied and their corresponding errors computed in order to contribute to the stochastic model, the resulting slope distances were 3D adjusted in two steps. In the first step, only distances between pillars were

adjusted to provide a solution for the frame. In the second step, only distances to target points in the wall were adjusted with the pillar coordinates kept fixed.

Finally, as requested by the Diputació de València, all the resulting coordinates and precisions were converted into ETRS89 geodetic coordinates with ellipsoidal height ( $\varphi, \lambda, h$ ), ETRS89-TM30 with orthometric height ( $E, N, H$ ), and the local system CP2017 ( $x, y, z$ ), which is the coordinate system used for the photogrammetric process.

After three years no significant displacement was found in the 15 ChPs installed on the cliff, although displacements of several millimetres were detected in some pillars by using congruency tests for deformation analysis (Caspary, 1987; Niemeier, 1981).

Further details about the geodetic measurements and subsequent computations are described in (García-Asenjo *et al.*, 2019; García-Asenjo *et al.*, 2022).

### III. RESULTS

The results are presented in two subsections: A) the overall north side of the cliff; B) on the 15 ChPs attached to the wall.

#### A. Overall area

The photogrammetric survey yielded comprehensive results in the form of point clouds (with and without filtering, Figure 4). As stated in Section II, low-resolution and high-resolution 3D models for the different campaigns were computed. Figure 6 displays a picture of a sector determined at high-resolution.

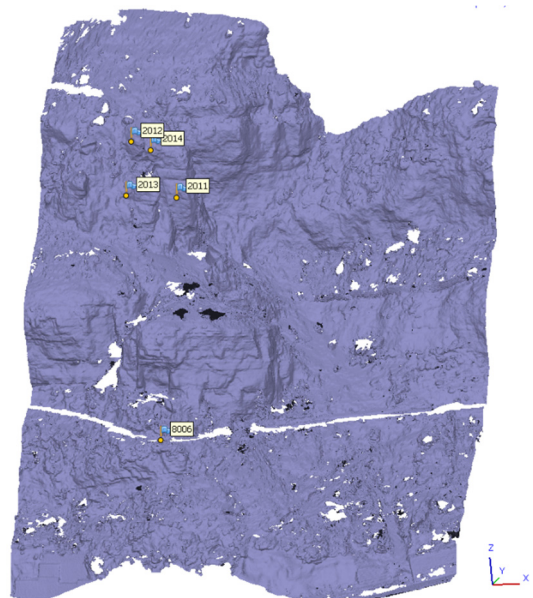


Figure 6. Detail of high-resolution 3D model for the front hill from the 6<sup>th</sup> photogrammetric campaign.

From them, different geometric comparisons were obtained among campaigns 1-6 (Figure 7a), and 5-6 (Figure 7b), using CloudCompare v. 2.10.2. The quantification of the differences, categorised by ranges, is displayed in Table 2.

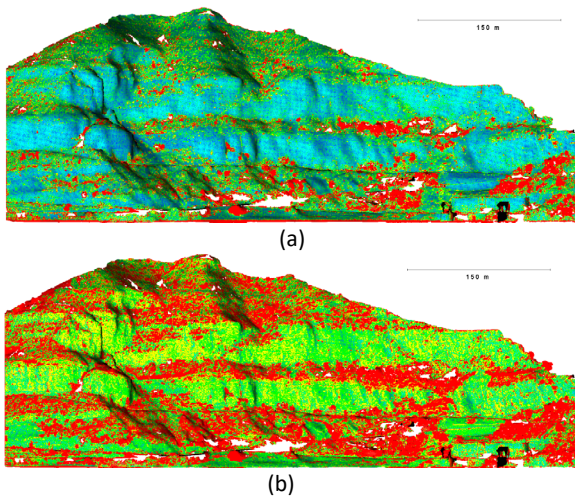


Figure 7. Height differences from the 3D models among campaigns: a) 5-6; b) 1-6.

Table 2. Quantitative differences categorised by ranges and photogrammetric campaigns. The first column displays the full colour shading used in Figure 7

Cat.	Distance [cm]	6 <sup>th</sup> -5 <sup>th</sup> (%)	6 <sup>th</sup> -1 <sup>st</sup> [%]
0-3	0-3	12,55	1,77
3-6	3-6	<b>40,49</b>	10,37
6-9	6-9	18,00	<b>16,27</b>
9-12	9-12	7,91	14,11
12-15	12-15	4,68	9,74
15-18	15-18	3,04	6,84
18-21	18-21	2,11	5,31
21-24	21-24	11,88	<b>35,59</b>

From the HRDEM, an orthoimage was created for the 1<sup>st</sup> photogrammetric campaign.

### B. Check points

A summary of the metric comparisons on the three campaigns on the left-hand side area targeting four ChPs (Figures 2 and 6) is presented in Tables 3 and 4 for the three campaigns.

Table 3. Coordinates comparison on ChPs between 1<sup>st</sup> and 6<sup>th</sup> campaigns

ID	Dx [cm]	Dy [cm]	Dz [cm]	Total [cm]
2011	-0.2	-10.7	-3.9	11.3
2012	2.3	-7.1	-3.4	8.2
2013	-1.0	-10.3	-3.2	10.9
2014	0.2	-9.8	-5.0	11.0

Table 4. Coordinates comparison on ChPs between 5<sup>th</sup> and 6<sup>th</sup> campaigns

ID	Dx [cm]	Dy [cm]	Dz [cm]	Total [cm]
2011	1.5	-1.1	-2.4	3.0
2012	1.0	-0.3	-2.1	2.3
2013	1.7	-0.7	-2.2	2.8
2014	1.3	-0.5	-1.7	2.2

Additionally, the differences between the close-range photogrammetry and the EDM coordinates are presented in Tables 5 and 6 for the 5<sup>th</sup> and 6<sup>th</sup> photogrammetric campaigns.

Table 5. Coordinates comparison on ChPs between the 5<sup>th</sup> photogrammetric survey and the geodesy

ID	Dx [cm]	Dy [cm]	Dz [cm]	Total [cm]
2011	-2.7	2.4	-1.8	4.0
2012	-0.4	3.1	-2.1	3.8
2013	2.7	1.8	-1.5	3.6
2014	-2.3	1.3	-1.7	3.1

Table 6. Coordinates comparison on ChPs between the 6<sup>th</sup> photogrammetric survey and the geodesy

ID	Dx [cm]	Dy [cm]	Dz [cm]	Total [cm]
2011	-0.8	1.4	-3.8	4.1
2012	0.9	2.7	-3.5	4.5
2013	4.6	1.2	-3.9	6.2
2014	-0.9	0.9	-4.2	4.3

## IV. DISCUSSION

The bundle adjustment results of the photogrammetric method improved from 1.9 cm (1<sup>st</sup> campaign) to 1.1 cm (5<sup>th</sup> and 6<sup>th</sup> campaigns) (CPs Error XYZ, Table 1). The two main reasons for this improvement can be: first, the inclusion of the 200 mm telelens in the photogrammetric data acquisition; second, the use of the geodetic reference frame as ground control. For campaigns 5<sup>th</sup> and 6<sup>th</sup>, the images were only targeting with convergent shots of the white spheres either of the CPs (50 cm in diameter) or the ChPs (14.5 cm in diameter, Figure 3). As it can be seen, substantial improvement was achieved in the Y-axis when comparing the last two photogrammetric campaigns versus the first one.

The centimetric level accuracy (1-2 cm) achieved in the photogrammetric surveys allowed us to determine the height differences among the campaigns, yielding relevant results (Table 2). Most of the differences are in the range of 3-6 cm between the last two campaigns (40,19%, Table 2); 21-24 cm between the 1<sup>st</sup> and the 6<sup>th</sup> campaigns (35,59%, Table 2). A plausible explanation for these systematic differences around 25 cm, which are shown in red and form systematic horizontal strips, is that there was substantial vegetation growing from the year 2017 to the year 2020. Therefore, an additional effort in removing vegetation should have been applied. Another significant feature is that there is substantial stability (bluish and greenish colours, Figure 7a) from the last campaigns 5<sup>th</sup> and 6<sup>th</sup>, ranging just five months between them.

Taking into account the metric quality of the photogrammetric survey ( $\pm 2.54 \sigma$ ), the resulting no significant movement was detected for ChPs 2012 and 2014, while ChPs number 2011 and 2013, show minor vertical displacements (Table 4). On the contrary,

systematic displacements can be seen when the 1<sup>st</sup> and the 6<sup>th</sup> campaigns are compared (Table 3). Furthermore, these displacements are only present in both height (Dz) and depth (Dy). Since this systematic shift cannot be reasonably explained by a possible terrain deformation, it should be attributed to deficiencies in the ground control used for the first campaign.

This study confirms that there is no doubt that image-based photogrammetric solutions are an ideal solution for rockfall and landslide monitoring, as suggested for UAVs by (Lindner *et al.*, 2016; Rossi *et al.*, 2018). The terrestrial photogrammetric solutions were always implemented simultaneously with other static long-range terrestrial laser scanners, and one dynamic short-range mobile mapping system (Di Stefano *et al.*, 2020); the latter was not still at the accuracy level of photogrammetry.

## V. CONCLUSIONS

The multi-image orthogonal and convergent terrestrial photogrammetry acquired with both close-range and long-range visible imagery over a large rocky landscape has demonstrated its capability to achieve centimetre level accuracy. The results from the photogrammetric survey were presented as both graphical and metric reports among the different campaigns.

The integration of 3D photogrammetric models with the external information provided by geodetic techniques is deemed crucial to improve the accuracy of the resulting models so that they can be used for reliable overtime deformation monitoring. Firstly, the ground control of the first campaign, which was based on a single GNSS campaign, has proved to be clearly less accurate than the precise geodetic reference frame periodically monitored. Secondly, the external validation of the photogrammetric 3D models has been only possible because the geodetic techniques provided coordinates for the ChPs with an accuracy one order of magnitude better than those provided by photogrammetry (1 cm – 3 cm).

Metric products such as high-resolution 3D point clouds, low-resolution DEM, HRDEM and orthoimages were deliverables used for deformation monitoring of the large complex and harsh area, not only on the fixed ChPs but also for the entire rough and complex rocky wall.

In the future, the authors would like to integrate SfM photogrammetric solutions with panoramic photogrammetric, taking advantage of the existing geodetic pillars. The idea of integrating mobile mapping solutions, either terrestrial or aerial, is also considered to increase the metric accuracy of the photogrammetric surveys below one centimetre.

## VI. ACKNOWLEDGEMENTS

The authors acknowledge the support of the Department of Roads and Infrastructures, *Diputació de València* to the research and innovation contract 'Control de deformaciones en la ladera norte de la muela de Cortes de Pallás anexa a la carretera CV-428 entre el pk. 14+800 y el pk. 15+950, objeto de las obras de emergencia de sostenimiento y protección (B-267) (T-726)'.

## References

- Arbanas, Ž., Sassa, K., Marui, H., and Mihalic, S. (2012). Comprehensive monitoring system on the Grohovo Landslide, Croatia. In *Landslides and Engineered Slopes: Protecting Society through Improved Understanding* (pp. 1441–1447). London: Taylor & Francis Group.
- Caspary, W. F. (1987). *Concepts of network and deformation analysis* (School of Surveying, The University of New South Wales, Australia), Monograph 11.
- Cina, A., and Piras, M. (2015). Performance of low-cost GNSS receiver for landslides monitoring: test and results. *Geomatics, Natural Hazards and Risk*, 6(5–7), pp. 497–514.
- Di Stefano, F., Cabrelles, M., García-Asenjo, L., Lerma, J.L., Malinverni, E.S., Baselga, S., and Pierdicca, R. (2020). Evaluation of long-range mobile mapping system (MMS) and close-range photogrammetry for deformation monitoring. A case study of Cortes de Pallás in Valencia (Spain). *Applied Sciences*, 10(6831), pp. 1–21.
- Fan, L., Smethurst, J., Atkinson, P., and Powrie, W. (2015). Error in target-based georeferencing and registration in terrestrial laser scanning. *Computers and Geosciences*, 83, pp. 54–64.
- Friedli, E., Presl, R., and Wieser, A. (2019). Influence of atmospheric refraction on terrestrial laser scanning at long range. *Proc. 4<sup>th</sup> Joint International Symposium on Deformation Monitoring (JISDM)*, 15-17 May 2019, Athens, Greece.
- Francioni, M., Salvini, R., Stead, D., and Coggan, J. (2018). Improvements in the integration of remote sensing and rock slope modelling. *Nat. Hazards*, 90, pp. 975–1004.
- García-Asenjo, L., Baselga, S., and Garrigues, P. (2016). Deformation Monitoring of the Submillimetric UPV Calibration Baseline. *Journal of Applied Geodesy*, 11(2), pp. 107–114.
- García-Asenjo, L., Martínez, L., Baselga, S., and Garrigues, P. (2019). Establishment of a multi-purpose 3D geodetic reference frame for deformation monitoring in Cortes de Pallás (Spain). *Proc. 4<sup>th</sup> Joint International Symposium on Deformation Monitoring (JISDM)*, 15-17 May 2019, Athens, Greece.
- García-Asenjo, L., Martínez, L., Baselga, S., Garrigues, P., and Luján, R. (2022). Geodetic monitoring of a high-precision reference frame in Cortes de Pallás (Spain). *5<sup>th</sup> Joint International Symposium on Deformation Monitoring (JISDM)*, 20-22 June 2022, Valencia, Spain.
- Harmening, C., and Neuner, H. (2019). Evaluating the performance of a space-and time-continuous deformation model. *Proc. 4<sup>th</sup> Joint International Symposium on Deformation Monitoring (JISDM)*, 15-17 May 2019, Athens, Greece.

- Jaboyedoff, M., Oppikofer, T., Abellán, A., Derron, M.H., Loya, A., Metzger, R., and Pedrazzini, A. (2012). Use of LIDAR in landslide investigations: A review. *Natural Hazards*, 61(1), pp. 5–28.
- Lindner, G., Schraml, K., Mansberger, R., and Hübl, J. (2016). UAV monitoring and documentation of a large landslide. *Applied Geomatics*, 8(1), pp. 1–11.
- Niemeier, W. (1981). Statistical tests for detecting movements in repeatedly measured geodetic networks. *Developments in Geotectonics*, 16, pp. 335-351.
- Oppikofer, T., Jaboyedoff, M., Blikra, L., Derron, M.H., and Metzger, R. (2009). Characterization and monitoring of the Åknes rockslide using terrestrial laser scanning. *Natural Hazards and Earth System Sciences*, 9(3), pp. 1003–1019.
- Rossi, G., Tanteri, L., Tofani, V., Vannocci, P., Moretti, S., and Casagli, N. (2018). Multitemporal UAV surveys for landslide mapping and characterization. *Landslides*, 15(5), pp. 1045–1052.
- Royán, M.J., Abellán, A., Jaboyedoff, M., Vilaplana, J.M., and Calvet, J. (2014). Spatio-temporal analysis of rockfall pre-failure deformation using Terrestrial LiDAR. *Landslides*, 11(4), pp. 697–709.
- Tsai, Z.X., You, G. J.Y., Lee, H.Y., and Chiu, Y.J. (2012). Use of a total station to monitor post-failure sediment yields in landslide sites of the Shihmen reservoir watershed, Taiwan. *Geomorphology*, 139–140, pp. 438–451.



## A self-acting mobile robot for monitoring floor flatness

Christoph Naab

Karlsruhe Institute of Technology (KIT), Geodetic Institute, Englerstraße 7, 76131 Karlsruhe, Germany,  
([naab@kit.edu](mailto:naab@kit.edu))

**Key words:** *deformation; flatness; tolerance control; civil engineering; mobile robot; tacheometer; total-station*

### ABSTRACT

As part of the structural inspection, compliance with the specified flatness tolerances according to DIN (in particular DIN 18202:2019-07) has to be checked. Today, the monitoring of the flatness is carried out mainly with levelling instruments and tacheometers. However, these measuring methods are time-consuming, as staking out the measuring grid and capturing the heights are performed manually. In addition, the data evaluation must be done in a separate work step. Therefore, we developed the mobile robot RITA for height measurement in combination with a stationary tacheometer. Now, the entire process of flatness control is carried out automatically, and heights are recorded reliably in real-time. For practicality, we developed a compact design of the mobile robot in combination with hardware modules. Our reflector tracking unit makes it possible to follow the reflector on the robotic platform in order to maintain the line of sight to the tacheometer. Furthermore, our mechanical pendulum unit ensures that the height measurement is always carried out vertically, even if the robot itself is tilted. Initial practical tests have shown that the high demands on the robotic platform are met and that the implementation of the flatness control can be automated. For that, investigations concerning the location accuracy of the robot were carried out, and the height measurement was validated. It turns out, that demands in the lowest millimeter range are fulfilled. Overall, these tests showed the enormous gain in performance due to the newly developed height measurement robot compared to the previous slow, complex, and tiring manual process.

*This contribution was selected by the Scientific Committee for publication as an extended paper in the Journal of Applied Geodesy <https://www.degruyter.com/journal/key/jag/html>*

## Multispectral imaging for the documentation of graffiti in an urban environment

Max Rahrig, José Luis Lerma

GIFLE – Photogrammetry and Laser Scanning Research Group, Universitat Politècnica de València, C/ de Vera s/n, 46022 Valencia, Spain, ([mrahrig@cgf.upv.es](mailto:mrahrig@cgf.upv.es); [jllerma@cgf.upv.es](mailto:jllerma@cgf.upv.es))

**Key words:** *cultural heritage; preventive conservation; NDT; multispectral/multiband imaging; wall paintings*

### ABSTRACT

Multispectral imaging (MSI) is increasingly used for the documentation and analysis of cultural heritage. It provides conservators a powerful non-destructive technique (NDT) and non-contact tool for detecting damage, hidden features and material-specific characteristics. Hereby multispectral documentation of wall paintings in an urban environment poses special challenges for the art expert. For example, these are often large works of art located outdoors on building façades. Excitation with artificial light in well-defined spectral ranges, as should ideally be the case in MSI, is therefore often not possible. In the following, low-cost variants of MSI (ultraviolet reflectography, visible light imaging and infrared reflectography) in combination with 3D photogrammetry and statistical methods for analysing image data are tested and discussed. Hereby, a metrically correct, large-scale documentation of wall paintings with accurate superimposed images of different spectral ranges will be generated by linking the MSI data in a photogrammetric image cluster to create individual texture maps for each spectral band. Furthermore, Principal Component Analysis (PCA) is used to extract additional information from the MSI data. The case studies are located on the campus of the Universitat Politècnica de València.

### I. INTRODUCTION

A large variety of imaging techniques are used to examine cultural heritage objects. Multispectral (MSI) and hyperspectral imaging (HIS) find increasingly vast fields of application. Spectral imaging is a broad field of optical metrology, where different wavelengths of electromagnetic radiation are used to capture image data of an object (Cucci and Casini, 2020). The spectrum of wavelengths that human eyes can observe as visible light represents only a small range of those wavelengths usable for multispectral imaging. It starts with very short and thus high-frequency and high-energy wavelengths, such as gamma and X-rays, and ends with long-wave, low-energy radiation, the micro and radio waves. In between are the ultraviolet (UV), visible (VIS) and infrared (IR) light spectra. The best-known imaging variants include, for example, UV fluorescence photography and infrared reflectography. For many years, both have been used to document polychrome surfaces, such as frescos, panel and canvas paintings, as common standard methods for detecting preliminary drawings, damage, and material differentiation. Most standard multispectral and hyperspectral imaging techniques are non-contact and non-destructive methods and will not cause any risk or harm to historical objects during the examination.

The difference between multispectral and hyperspectral imaging is related to the number of images taken. For multispectral images, each spectral band is captured separately by using different filters or detectors, while in hyperspectral imaging, an entire spectral range is captured simultaneously (Amigo,

2020; Amigo and Grassi, 2020). For the documentation of cultural heritage MSI is more often used. The most common examination methods cover the spectral ranges in the vicinity of visible light: visible light (VIS: 400-700 nm), ultraviolet (UV-A: 315-400 nm) and near-infrared (NIR: 700-1,400 nm). However, longer wavelengths are also used; here, special consideration should be given to the different areas of the infrared. In addition to the NIR, infrared is divided into short-wavelength infrared (SWIR: 1,400-3,000 nm), mid-wavelength infrared (MWIR: 3000-8000 nm) and long-wavelength infrared (LWIR: 8,000-15,000 nm). The last is well known used in Thermography. In addition, terahertz (THz), X-rays or radar, for example, are also used to examine cultural heritage (Dyer *et al.*, 2013; Badea *et al.*, 2008; Picollo *et al.*, 2019; Privitera *et al.*, 2021; Cosentino, 2015a; Alberghina *et al.*, 2019).

A consensus is that using a single spectral band usually produces only limited information about an object. Only a combined use of a range of methods can provide valuable results (Cavallo *et al.*, 2020; Keller *et al.*, 2019). Investigations in the UV-VIS-NIR can be made with a modified camera and different filters in front of the lens (Cosentino, 2014, Verhoeven, 2012; Dyer *et al.*, 2013; Webb *et al.*, 2018). In this case, referencing the individual images to each other is relatively simple, as the camera does not have to be moved between the single pictures. The photos overlap almost precisely. In other spectral ranges, however, very different devices are used. The resolution of the image sensors varies greatly, making correct superimposition and thus comparability of the data more difficult. Furthermore,

it is often impossible to image an entirely cultural heritage object with a single image section. Therefore, for a comprehensive examination, various image positions are needed. Alternatively, exemplary examination areas must be defined to represent the entire object. This creates particular challenges for the user, especially when investigating complex, three-dimensional objects.

Monitoring and damage assessment are other essential fields for using MSI in cultural heritage. However, evaluating a large number of different spectral bands and sensor data can be very challenging. Nevertheless, the superimposed image data of several monitoring campaigns can provide important information about the condition and the course of damage processes of an object. Principal Component Analysis (PCA) can make an important contribution to the interpretation of the data. This multivariate statistical approach makes it possible to analyse an almost unlimited number of image data and detect differences (Marengo *et al.*, 2011). A correct overlay of the image data and a complete protocol of all acquisition parameters is essential to ensure that the images are not affected by varying external conditions (Jones *et al.*, 2020).

In the following, different spectral imaging methods and their application in the documentation and examination of modern wall paintings will be presented. This includes a description of the methodology and an overview of the current state of research. Based on case studies, methods of combining and linking spectral images, including computer-assisted analysis, will be presented and discussed.

## II. METHODOLOGY

### A. UV-VIS-IR imaging

UV-VIS-IR photography uses the phenomenon that different materials react characteristically to varying wavelengths of light (Cosentino, 2014; Webb *et al.*, 2018). If an object is exposed to electromagnetic waves, such as irradiated with a light bulb, the surface can react differently. The material may appear translucent to the wavelength. In this case, electromagnetic waves can pass through the material. For example, this is known from X-rays and window panels. The electromagnetic radiation can also be absorbed completely or reflected by the material, like a mirror. The reflection occurs in the same wavelength as the excitation. Furthermore, some materials can react fluorescently to excitation with electromagnetic radiation. Part of the radiation is absorbed, and electromagnetic radiation is emitted in a longer wavelength. This happens especially with certain pigments and living organisms that glow colourfully in the visible spectral range during excitation with UV light (blacklight) (Dyer *et al.*, 2013; Cosentino, 2015a; Webb, 2019).

A CMOS image sensor of a commercially available digital camera can capture the spectral range from

about 350 to 1,050 nm. However, this requires removing the IR cut filter, which is usually placed in front of the image sensor and replacing it with protective glass, allowing the entire spectral range to pass through, *e.g.* Schott N-WG280. Such cameras are called modified cameras. Some manufacturers also offer cameras without IR cut filters ex-works. To reduce the incoming light to a specific wavelength requires special filters placed in front of the camera lens (Cosentino, 2014; Verhoeven, 2012; Dyer *et al.*, 2013; Webb *et al.*, 2018).

If the outgoing wavelengths of the light source are controlled, and its reflections or emission are recorded in a deliberately selected spectrum, characteristic features of individual materials can be identified. For example, this can be used as a non-contact and non-destructive examination method in cultural heritage research to determine the pigments used in a painting (Cosentino, 2014; Dyer *et al.*, 2013; Webb *et al.*, 2018). Table 1 gives an overview of combinations of induced (emitted) and detected spectral range commonly used for UV-VIS-IR imaging (Keller *et al.*, 2019; Bläuer and Keller, 2020; Sfarra *et al.*, 2014; Dyer *et al.*, 2013; Cosentino, 2014; Lang and Lenz, 2017; Keller and Lenz, 2021).

### B. Combination of the techniques

Linking the MSI variants is a significant challenge and is particularly important for a detailed examination of objects. In addition, the image file of a single spectral band provides only limited information; only the comparison with other bandwidths enables a well-founded analysis (Keller *et al.*, 2019). The image series of different bandwidths of a modified camera can be combined relatively easily. The viewpoint does not have to be changed between the single images; only the light source and the filters on the camera have to be changed. So the individual image data are already almost pixel-precise superimposed onto each other; otherwise, warping will be required to avoid parallax. There are also open-source solutions for processing and overlaying the images of MSI (Dyer *et al.*, 2013). However, to link additional MSI data, for example thermography images, a correct superimposition already poses specific challenges to the user since both the sections and the resolution of the images vary greatly. Usually, it is impossible to capture an entire object with a single image section. Depending on the size and geometry, many different image viewpoints are required. In the case of flat objects, such as paintings and murals, stitching is often used to link overlapping images (Keller and Lenz, 2021). Such photo mosaic generated by image stitching can provide high resolutions over a large area. However, these images are not metrically correct and can only be used to a limited extent for mapping purposes. Three-dimensional objects, such as sculptures or vaulted ceilings, cannot be captured in this way.

Table 1. Different methods of UV-VIS-IR imaging

Name	Imaging Method	Also known as	Radiation Source	Filter sensitivity
UVR	UV-induced UV-reflectography	UV-reflectance imaging	UV (~365 nm), UV-LED, Wood's Lamp	UV band-pass filter (320-390 nm)
UVF/UVL	UV-induced VIS-luminescence	UV-fluorescence imaging	UV (~365 nm), UV-LED, Wood's Lamp	UV/IR-cut filter (380-750 nm)
VIS	Visible-reflected imaging	VIS-reflected images, Colour photography	LED, Tungsten, Flash	UV/IR-cut filter (380-750 nm)
IRF/VIL	VIS-induced IR-luminescence	IR-fluorescence	VIS 380-750 nm	IR long-pass filter (starting at 830 nm or 1000 nm)
IRR	IR-induced IR-reflectography	IR-reflectography	IR (700-1050 nm), LED	IR long-pass filter (starting at 830 nm or 1000 nm)
IRR	VIS-IR-induced IR-Reflectography	Variant of IRR with undefined light-source	Tungsten, Flash, Halogen lamp (VIS-IR 400-1050 nm)	IR long-pass filter (starting at 830 nm or 1000 nm)

Photogrammetry can offer a solution. Some applications to generate 3D models from MSI image series were already made in recent years. Rahrig *et al.* (2018) rectified individual multispectral images from different documentation campaigns using 3D data and superimposed them as orthophotos in CAD, enabling close monitoring of surfaces across several campaigns Mathys *et al.* (2019), Zainuddin *et al.* (2019), Webb (2015; 2017; 2019) have compared the quality of point clouds from different spectral images. An overlay of different spectral bands as textures for the 3D model was also tested for VIS and UVL by Nocerino *et al.* (2018) and for 17 spectral bands between UV and NIR by Mathys *et al.* (2019). Mathys used a modified camera and only changed the filters in front of the lens and the light source for changing spectral bands. In post-processing, she then calculated the alignment of the imaging positions and the basic 3D model based on a series of VIS photos (RGB colour photos). She then exchanged the individual images according to the spectral band and recalculated only the texture map using the orientation of the VIS images also for the other spectral ranges. Nocerino, on the other hand aligned each spectral band separately and combined the results via one uniform coordinate system.

Both variants offer certain advantages. Exchanging the photos and only recalculating the texture map reduces the time required significantly, especially when processing multiple spectral ranges in the VIS. Away from the VIS, however, a slight shift of the focal point takes place so that a recalculation of the image orientation could be helpful to improve the quality of the results. If image data from different sensors are to be linked, the individual clusters must generally be aligned separately and connected via one uniform coordinate system for all spectral bands.

### III. CASE STUDIES

#### A. Case Study 1: Hand

Exemplary image series of modern murals were produced outdoors in UVR, VIS and IRR to test the

superimposition and analysis of variable spectral bands. The murals were created in the context of the 16<sup>th</sup> urban art festival "Poliniza Dos x Hyuro" 2021 and are easily accessible on the campus of the Universitat Politècnica de València. A section of a graffiti made by students of Painting and Environment (Figure 1) was captured from different camera positions to document the surface in high resolution in a larger area and in 3D.



Figure 1. Overview of the wall painting. Case study 1 is highlighted in red.

Three photographs (UVR, VIS and IRR) were taken at each of nine camera locations using a Fujifilm IS Pro camera. The camera is produced ex-works as a modified camera and has a Super CCD Pro image sensor (APS-C: 23 x 15.5 mm) with a resolution of 4256 x 2848 pixels. The lens used was a 60mm UV-VIS-IR Apo Macro by CostalOpt. The excitation of the surface was done by direct sunlight, so there was enough energy from UV to NIR. For the VIS images, a UV/IR blocking filter was used (BP550 Near-IR/UV Block Visible Bandpass Filter, by MIDOPT®. Range: 405-690 nm). IRR images were taken with a long-pass filter that filters all spectral regions shorter than 930 nm (LP920 Short-Wave Infrared Longpass Filter, by MIDOPT®, Range 930-2300 nm). The UVR images were made with a UV band-pass filter, and an IR cut filter (BP365 Near-UV Bandpass Filter, by MIDOPT®. Range: 335-400 nm + 830-1100 nm. Combined with SP730 Near-IR Shortpass Filter by MIDOPT®. Range: 320-730 nm). The UV band-pass filter has a peak in the NIR, so the additional IR cut filter is

necessary to avoid interference in the IR. The image sections of the nine camera positions have an overlap of about 80%, so sufficient data for a photogrammetric alignment was available.

The photographs were taken in manual mode with constant settings in RAW format. For this purpose, the ideal settings were tested at the first camera position. The pictures were taken at ISO 100 and f-number 8 to achieve good images. So only the exposure time had to be changed on-site: 1/500 sec for the VIS images, 1/10 sec for the UVR and 1/20 sec for the IRR 1/20 sec. The exposure time was controlled via the RGB histogram, whereby all channels (R, G, B) were checked, and uniform distribution of the colour values was ensured. The white balance of the photos was also done manually using a reflection target with a medium grey value. Two image sets were taken at the first camera position—the first with the target in the image centre, the second without the target. The settings were applied consistently to all camera positions. White balance was adjusted in the software RawTherapee, which allows batch processing of the image series. The tone curve was also set to "linear" to eliminate automated, camera-specific colour manipulations. Furthermore, the UVR and IRR images were converted into monochrome images. For this purpose, the UVR images were reduced to the blue channel and the IRR images to the red channel. Processing the photos follows the recommendations of Dyer *et al.*, 2013, which were developed within the framework of the EU project CHARISMA.

In addition to the monochrome UVR and IRR photos, false colour images were created. For UV false colour photos (UVR-FC), the monochrome UVR was combined with the green and blue channels of the VIS to create a new image. In this image file, the R/G/B channel corresponds to the G/B/UV band of the original data. For the IR false colour images (IRR-FC), the monochrome IRR images were combined with the red and green channel of the VIS to form a new image file. Here, the R/G/B channels of the new image data correspond to the IR/R/G bands of the initial data.

After processing the individual images was completed, the images were combined in 3D using photogrammetry. For this purpose, the image series were imported into Agisoft Metashape and divided into separate chunks according to their acquisition technique (VIS, UVR, UVR-FC, IRR and IRR-FC). The spectral bands were aligned separately, and dense point clouds were calculated. The point clouds served as an additional optical check to improve the alignment. Using natural control points, which could be clearly identified on the single photos, the alignment of the image chunks to each other was carried out. Scaling was also done using natural control points; the distance was measured on a flat surface of the object by using a ruler (Figure 2). For proper scaling the use of scale bars is recommended, to guarantee a higher accuracy of the scaling.

The 3D surface model was only processed for one image group (VIS) and then copied to the other groups. After that, a high-resolution texture map was generated for each image band (VIS, UVR, UVR-FC, IRR and IRR-FC). Superimposed high-resolution orthophotos can now be generated directly in the Metashape software for further evaluation and comparison between the spectral bands. This allows a fast visualisation and observation in 2D, with a correct metric representation (Figure 3).

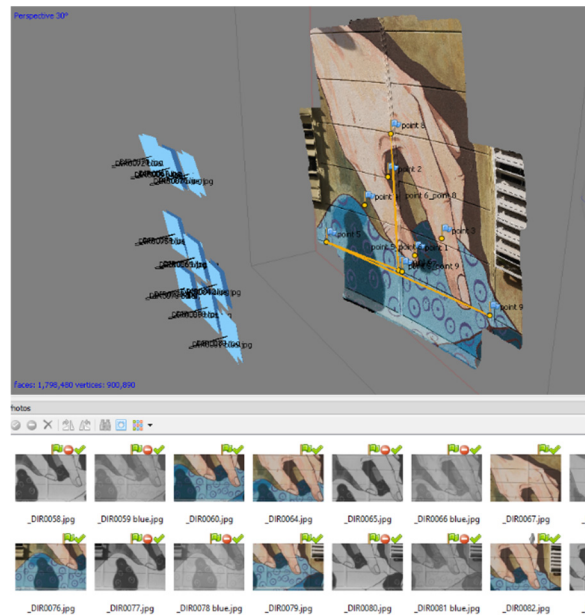


Figure 2. 3D point cloud of the MSI image set. The reference points for orientation and scaling are shown on the wall painting.

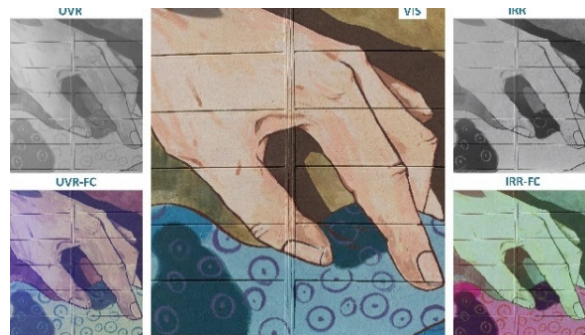


Figure 3. FMSI orthoimages of the different spectral bands.

In this way it is also possible to compare the spectral bands directly on the 3D model. Especially with complex surface geometries, this allows a dynamic inspection and offers particular advantages in observing areas that would be hidden in a 2D orthophoto. Linking spectral bands with a single 3D model were tested in the software Blender. First, the geometry, *i.e.* the surface model, is imported. Then the different texture maps of the spectral bands can be imported and linked to the 3D model as materials. When observing in Blender, it is now possible to switch dynamically between the materials, allowing the spectral bands and false colour

images to be compared with pinpoint accuracy (Figure 4).



Figure 4. Detail of the multi textured 3D Modell in Blender. Left: VIS texture, right IRR texture. The pigment used for the purple circles has the same characteristics as the blue background under IR.

### B. Case study 2: Vase

The second wall painting discussed here was created by the artist JAZ. The graffiti is located on the northwest façade of the Directorate building; it covers a width of approx. 7 m over a height of 3 floors (Figure 5). Due to its location in a corner situation, it is never entirely exposed to the sun. For image acquisition, a time was chosen when the graffiti was completely in shadow to ensure uniform illumination. It was documented exemplarily from one point of view using UVR, VIS, and IRR to test whether the passive illumination was sufficient for the MSI images. Furthermore, the application of statistical methods for the evaluation of MSI images was tested.



Figure 5. Overview of the wall painting of case study 2.

The pictures were taken with the same setup (camera, lens and filter). The exposure times varied from 1/60 s for VIS, 1/3 s for IRR and 1/2 s for UVR. Processing of the RAW data is also analogous to the previous steps. Figure 6 shows a compilation of the results. While the UVR image does not show any significant features, the IRR image reveals some details. Especially in the three whitish rose blooms, horizontal and vertical structures show up, which remain hidden in the VIS. The colours used for the rose blooms behave translucent in the NIR and allow viewing underneath the top layer of paint. This phenomenon can also be observed very vaguely at the left of the vase. Therefore, a possibility was needed to highlight the hidden details more and visualise them better. For this purpose, a Principal Component Analysis (PCA) of the images was carried out using the free available software HyperCube.

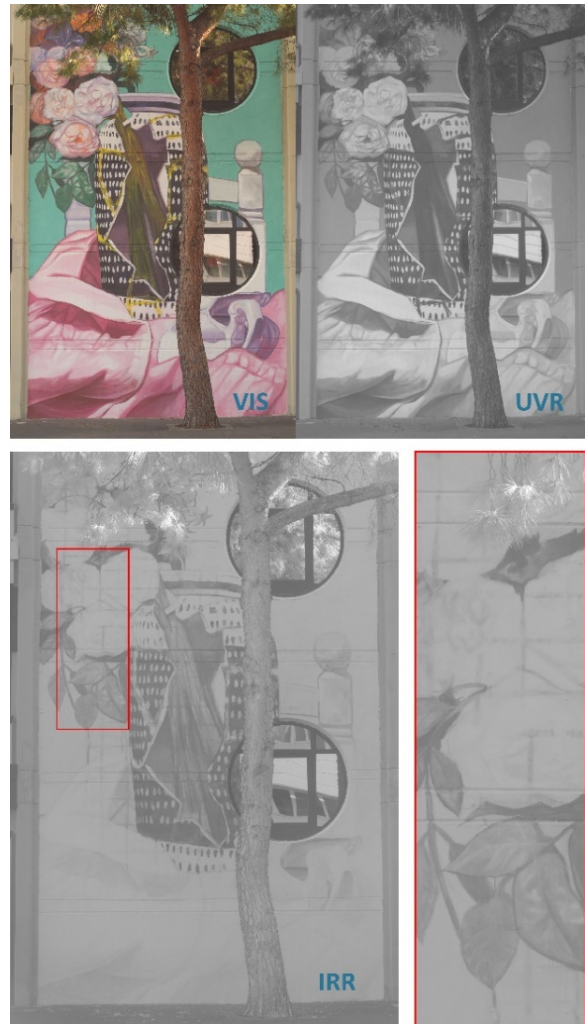


Figure 6. Compilation of the MSI images of case study 2. The IRR shows covered pattern (highlighted in the detail).

PCA is a method for the statistical analysis of data. Applied to image data, it enables an unsupervised extraction of qualitative information of compounds. For example, a standard RGB colour photo can serve as the data basis. The three colour channels represent

different spectral bands (red, green and blue) and are superimposed with pixel accuracy. Varying material characteristics in the different spectral ranges can be compared and analysed pixel by pixel using PCA. Principal Component 1 (PC1) shows the matrix of the maximum variance between the initial data. The values calculated in this way can then be visualised in a greyscale image. Principal Component 2 (PC2) corresponds to a differentiated matrix, where PC1 has been subtracted from the original matrix. In this continuation, any number of PCs can be calculated. Details and differences in the material composition can be filtered and represented in this way in continuous PCs (Domingo *et al.*, 2020; Marini and Amigo, 2020). The advantage of PCA is the comparatively simple evaluation of an unlimited number of spectral bands, as long as the individual image bands are correctly superimposed (Salerno *et al.*, 2014).

Figure 7 shows PC1 to PC5 of the MSI recording of the wall painting. In PC2, the horizontal and vertical structures are already better visible compared to the IRR image. The structure can now be detected below the rose blooms and in parts of the vase. However, visualisation of the variances is limited to 256 grey levels in one PC. That means the total variance of material differences must be represented in these 256 grey values. In the case of the wall painting discussed here, a tree standing in the foreground of the picture significantly influences the differentiated visualisation of the painting. The application of PCA to a partial area of the image allows the use of the entire greyscale for a differentiated representation of the wall painting. In this case, the hidden structures were revealed most clearly in PC4 (Figure 8).

Thanks to PCA, it was possible to detect the horizontal and vertical structures distribution over the entire area of the rose blooms and the vase. They are thus directly related to the detailed central motif and end precisely at its borders. The comparatively simple realised picture components, such as the pink cloth in the lower quarter of the picture, the turquoise background and the back of the chair, on the other hand, do not show any comparable structures. Therefore, it can be assumed that the covered patterns are a preliminary drawing in the sense of a raster. It probably served the artist as orientation for the execution of his work. In consideration of the size of the graffiti, it had to be painted from scaffolding or a hydraulic lift, so such a raster helps immensely in orientation and in keeping proportions and dimensions of the individual elements of the picture.

#### IV. DISCUSSION AND CONCLUSION

MSI is fast, easy-to-execute tool that can be essential for non-destructive and non-contact cultural heritage inspection. Especially in recent years, various research groups have been working on characterising and identifying historical pigments using MSI. Also the

interaction of pigment and binding material is being studied more and more, which strongly influences the spectral properties of the pigments (Cosentino, 2015b; Keller *et al.*, 2019). Many exciting results and new developments can be expected in the coming years.

The case studies presented here to document modern wall paintings in an urban environment showed that it is possible to combine different camera positions and spectral bands using photogrammetry. The field study enabled the correlation of VIS, UVR, UVR-FC, IRR and IRR-FC on a combined high-resolution 3D model. This offers new possibilities for investigation, especially for overall multispectral documentation of large wall paintings and complex, three-dimensional objects.

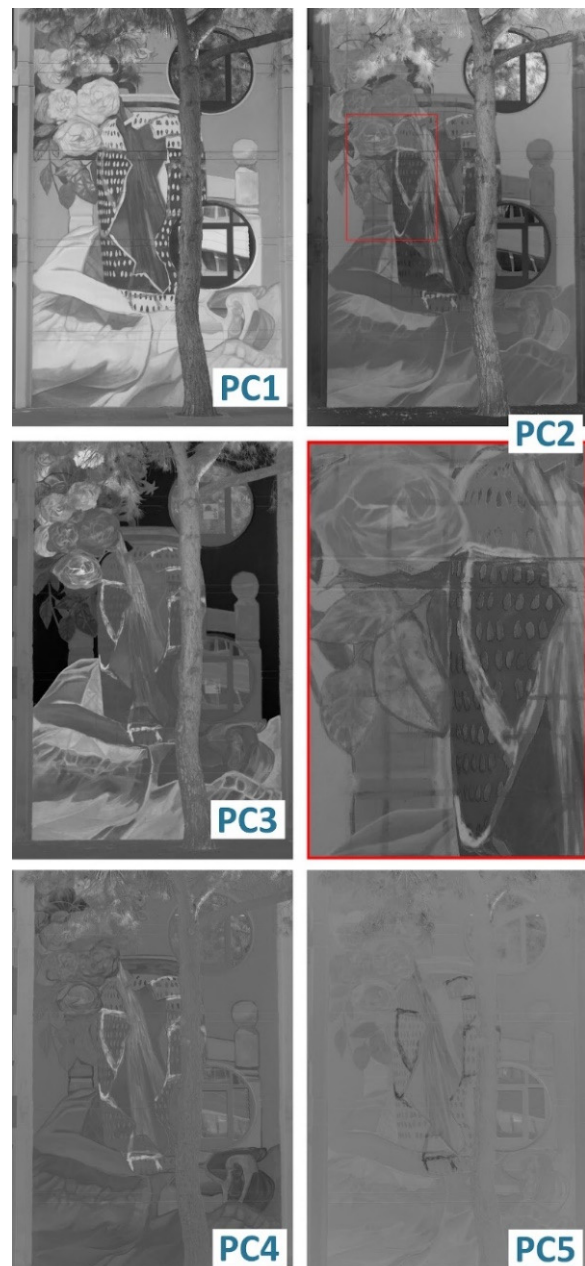


Figure 7. Principal Component Analysis of the wall painting. The image shows PC1 to PC5 analysing the UVR/B/G/R/IRR bands of the MSI. A detail of PC2 is highlighted in red, it shows the covered pattern better than the IRR.



Figure 8. To higher the differentiation a second PCA was processed on a image section without interfering environment (tree, floor, windows). Now PC4 revealed the underdrawn raster entirely.

The advantages of PCA were presented using the example of the second wall painting. For this purpose, a low-cost method consisting of UVR, VIS and IRR was used, and active excitation of the surfaces in specific spectral ranges was dispensed with. This limits the investigation, but it should be considered that the murals are exposed outdoors and in an urban environment. Artificial illumination under ideal conditions without parasitic stray light was impossible or can only be realised with great effort. Nevertheless, thanks to PCA, new findings and insights into the graffiti were obtained. The detection of the covered raster provides information about the artist's working process.

It was shown that MSI could also be used in an urban environment. Despite the resulting limitations of the recording technique, it can provide new insights for

investigating modern wall paintings such as graffiti. In the future, it will be necessary to test the combination of image series on a wider spectral range, integrating different imaging sensors with photogrammetry even at different times. Due to the congruent metric superimposition of different temporal image data, this offers further interesting PCA applications for monitoring cultural heritage.

## V. ACKNOWLEDGEMENTS

This study was carried out within the project "REVIEW – REVEaling hlddEn Wall paintings" and has received funding from the European Union's Horizon 2020 research and innovation programme under the Marie Skłodowska-Curie grant agreement No 101032333.

## References

- Alberghina, M. F., Schiavone, S., Greco, C., Saladino, M. L., Armetta, F., Renda, V., and Caponetti, E. (2019). How many secret details could a systematic multi-analytical study reveal about the mysterious fresco trionfo della morte? *Heritage*, 2(3), pp. 2370–2383. DOI: 10.3390/heritage2030145
- Amigo, J.M. (2020). Hyperspectral and multispectral imaging: setting the scene. *Data Handling in Science and Technology*, 32, pp. 3–16. DOI: 10.1016/B978-0-444-63977-6.00001-8
- Amigo, J. M., and Grassi, S. (2020). Configuration of hyperspectral and multispectral imaging systems. *Data Handling in Science and Technology*, 32, pp. 17–34. DOI: 10.1016/B978-0-444-63977-6.00002-X
- Badea, E., Miu, L., Budrugaec, P., Giurginca, M., Mašić, A., Badea, N., and Della Gatta, G. (2008). Study of deterioration of historical parchments by various thermal analysis techniques complemented by SEM, FTIR, UV-Vis-NIR and unilateral NMR investigations. *Journal of Thermal Analysis and Calorimetry*, 91(1), pp. 17–27. DOI: 10.1007/s10973-007-8513-x
- Bläuer, C., and Keller, A. T. (2020). Mainly red and a hidden blue – Laboratory and MSI investigations on the Carolingian wall paintings in the Chapel of the Holy Cross of Müstair (Switzerland). *Journal of Cultural Heritage*, 42, pp. 72–80. DOI: 10.1016/j.culher.2019.07.024
- Cavallo, G., Aceto, M., Emmenegger, R., Keller, A. T., Lenz, R., Villa, L., Wörz, S., and Cassitti, P. (2020). Preliminary non-invasive study of Carolingian pigments in the churches of St. John at Müstair and St. Benedict at Malles. *Archaeological and Anthropological Sciences*, 12(3). DOI: 10.1007/s12520-020-01024-2
- Cosentino, A. (2014). Identification of pigments by multispectral imaging; a flowchart method. *Heritage Science*, 2014 2:8. DOI: 10.1186/2050-7445-2-8.
- Cosentino, A. (2015a). Panoramic, Macro and Micro Multispectral Imaging: An Affordable System for Mapping Pigments on Artworks. *Journal of Conservation and Museum Studies*, 13(1), pp. 1–17. DOI: 10.5334/jcms.1021224
- Cosentino, A. (2015b). Effects of different binders on technical photography and infrared reflectography of 54 historical pigments. *International Journal of Conservation Science*, 6(3), pp. 287–298.



- Cucci, C., and Casini, A. (2020). Hyperspectral imaging for artworks investigation. *Data Handling in Science and Technology*, 32, pp. 583–604. DOI: 10.1016/B978-0-444-63977-6.00023-7
- Domingo, I., Carrión, B., Blanco, S., and Lerma, J. L. (2015). Evaluating conventional and advanced visible image enhancement solutions to produce digital tracings at el Carche rock art shelter. *Digital Applications in Archaeology and Cultural Heritage*, 2(2–3), pp. 79–88. DOI: 10.1016/j.daach.2015.01.001
- Dyer, J., Verri, G., and Cupitt, J. (2013). Multispectral Imaging in Reflectance and Photo-induced Luminescence modes: A User Manual. British Museum.
- Jones, C., Duffy, C., Gibson, A., and Terras, M. (2020). Understanding multispectral imaging of cultural heritage: Determining best practice in MSI analysis of historical artefacts. *Journal of Cultural Heritage*, 45, pp. 339–350. DOI: 10.1016/j.culher.2020.03.004
- Keller, A. T., Lenz, R., Artesani, A., Mosca, S., Comelli, D., and Nevin, A. (2019). Exploring the Ultraviolet Induced Infrared Luminescence of Titanium White Pigments / Explorando la luminiscencia infrarroja inducida por ultravioleta de pigmentos blancos de titanio. *UV-Vis Luminescence imaging techniques/ Técnicas de imagen de luminiscencia UV-Vis*, Picollo, M., and Stols-Witlox, M. and Fuster-López, L. (Eds.) pp. 201–232. DOI: 10.4995/360.2019.110002
- Keller, A. T., and Lenz, R. (2021). Reflexion, Absorption und Lumineszenz – Strahlendiagnostische Phänomene zu kompositionellen, maltechnischen und materialspezifischen Fragestellungen am Wandbild in der Vorhalle des Bischofstores im Wiener Stephansdom. *Österreichische Zeitschrift für Kunst und Denkmalpflege*, Vol. 1, pp. 153–162.
- Lang, V., and Lenz, R. (2017). „Einiges über die Farbe ...“ Zur Wandmalereitechnik von Adolf Hölzel.“ Landesamt für Denkmalpflege Stuttgart (Eds.): *Mit Religion kann man nicht malen. Adolf Hölzel in Ulm*, Ulm, pp. 74–97.
- Marengo, E., Manfredi, M., Zerbinati, O., Robotti, E., Mazzucco, E., Gosetti, F., Bearman, G., France, F., and Shor, P. (2011). Development of a technique based on multispectral imaging for monitoring the conservation of cultural heritage objects. *Analytica Chimica Acta*, 706(2), pp. 229–237. DOI: 10.1016/j.aca.2011.08.045
- Marini, F., and Amigo, J. M. (2020). Unsupervised exploration of hyperspectral and multispectral images. *Data Handling in Science and Technology*, 32, pp. 93–114. DOI: 10.1016/B978-0-444-63977-6.00006-7
- Mathys, A., Jadinon, R., and Hallot, P. (2019). Exploiting 3D multispectral texture for a better feature identification for cultural heritage. *ISPRS Annals of the Photogrammetry, Remote Sensing and Spatial Information Sciences*, 4(2/W6), pp. 91–97. DOI: 10.5194/isprs-annals-IV-2-W6-91-2019
- Nocerino, E., Rieke-Zapp, D. H., Trinkl, E., Rosenbauer, R., Farella, E. M., Morabito, D., and Remondino, F. (2018). Mapping VIS and UVL imagery on 3D geometry for non-invasive, non-contact analysis of a vase. *International Archives of the Photogrammetry, Remote Sensing and Spatial Information Sciences - ISPRS Archives*, 42(2), pp. 773–780. DOI: 10.5194/isprs-archives-XLII-2-773-2018
- Picollo, M., Stols-Witlox, M., and Fuster-López, L. (2019). *UV-Vis Luminescence imaging techniques/ Técnicas de imagen de luminiscencia UV-Vis*. DOI: 10.4995/360.2019.110002
- Privitera, A., Alberghina, M. F., Privitera, E., and Schiavone, S. (2021). Multispectral imaging and p-xrf for the non-invasive characterization of the anonymous devotional painting ‘maria santissima delle grazie’ from mirabella imbàccari (Sicily, Italy). *Heritage*, 4(3), pp. 2320–2336. DOI: 10.3390/heritage4030131
- Rahrig, M., Drewello, R., and Lazzeri, A. (2018). Opto-Technical Monitoring – a standardized methodology to assess the treatment of historical stone surfaces, *Int. Arch. Photogramm. Remote Sens. Spatial Inf. Sci.*, XLII-2, pp. 945–952. DOI: 10.5194/isprs-archives-XLII-2-945-2018
- Salerno, E., Tonazzini, A., Grifoni, E., Lorenzetti, G., Legnaioli, S., Lezzerini, M., Marras, L., Pagnotta, S., and Palleschi, V. (2014). Analysis of multispectral images in cultural heritage and archaeology. *Journal of Applied and Laser Spectroscopy*, 1(September), pp. 22–27.
- Sferra, S., Ibarra-Castanedo, C., Ambrosini, D., Paoletti, D., Bendada, A., and Maldague, X. (2014). Discovering the defects in paintings using non-destructive testing (NDT) techniques and passing through measurements of deformation. *Journal of Nondestructive Evaluation*, 33(3), pp. 358–383. DOI: 10.1007/s10921-013-0223-7
- Verhoeven, G.J. (2012). Methodes of Visualisation. *Analytical Archeometry, selected Topics*. Edwards, H.G.M.; Vandenabeele, P. (Eds.), pp. 3–48. DOI: 10.1039/9781849732741.
- Webb, E. K. (2015). Reflected infrared imaging revisiting the fundamentals. *Digital Heritage*, pp. 51–54. DOI: 10.1109/DigitalHeritage.2015.7413832
- Webb, E. K. (2017). Reflected Infrared and 3D Imaging for Object Documentation. *Journal of the American Institute for Conservation*, 56(3–4), pp. 211–224. DOI: 10.1080/01971360.2017.1359463
- Webb, E. K., Robson, S., MacDonald, L., Garside, D., and Evans, R. (2018). Spectral and 3D cultural heritage documentation using a modified camera. *International Archives of the Photogrammetry, Remote Sensing and Spatial Information Sciences - ISPRS Archives*, 42(2), pp. 1183–1190. DOI: 10.5194/isprs-archives-XLII-2-1183-2018
- Webb, E. K. (2019). UV-Induced Visible Luminescence for Conservation Documentation/ Luminiscencia visible inducida por UV para la documentación en conservación. Picollo, M., and Stols-Witlox, M. and Fuster-López, L. (Eds.) *UV-Vis Luminescence imaging techniques/ Técnicas de imagen de luminiscencia UV-Vis*, pp. 35–60. DOI: 10.4995/360.2019.110002
- Zainuddin, K., Majid, Z., Ariff, M. F. M., Idris, K. M., Abbas, M. A., and Darwin, N. (2019). 3D modeling for rock art documentation using lightweight multispectral camera. *ISPRS Annals of the Photogrammetry, Remote Sensing and Spatial Information Sciences*, 42(2/W9), pp. 787–793. DOI: 10.5194/isprs-archives-XLII-2-W9-787-2019

**5<sup>th</sup> Joint International Symposium on  
Deformation Monitoring**



**Non-peer-reviewed contributions**

## Deformation monitoring with robotic total stations. Pushing the limits

Josep Raventós, Enrinc Sans

Department of instrumentation and monitoring, BAC Engineering Consultancy Group SL, C/ Avila 138, 3<sup>rd</sup> Floor, Barcelona, Spain, ([jraventos@bacecg.com](mailto:jraventos@bacecg.com); [esans@bacecg.com](mailto:esans@bacecg.com))

**Key words:** *deformation; monitoring; convergences; robotic total station; accuracy*

### ABSTRACT

Deformation monitoring using high accuracy surveying methods are techniques widely demanded and used. Even in these conditions, there are several misunderstandings and misconceptions regarding several topics, such as differences in accuracy between the instrument in laboratory conditions and the system running in real conditions, and variations of accuracy in time and space, among others. The paper provides a case study focused on the construction of a new building above an underground transport hub where a deformation monitoring plan was set up to monitor the existing tunnels and structural elements. The monitoring plan included manual precise levelling for monitoring settlement of several pillars in both the building and the transport hub. It also included three robotic total stations (one in each existing tunnel) to monitor displacements and convergences, specifically in sections previously modelled by the finite elements method. According to several as-built uncertainties of the existing tunnel and transport hub and the fact that the new building loads would be transferred via a shared slab, the threshold limits defined for the convergence control were within the limit of the theoretical accuracy of the system, at  $\pm 1\text{mm}$ . The paper describes the monitoring system setup, the checks for monitoring performance of the system and an evaluation of changes in accuracy of the systems related to environmental conditions, station-target distance and acquisition geometry. Finally, the paper concludes with an analysis of the resulting challenges faced when dealing with low level thresholds.

### I. SCOPE OF THE PROJECT

The scope of the project in which the monitoring system was installed was to construct an eighth floor building above an existing transportation hub. The building had to be constructed over a pre-stressed slab that also played a major role in the structural behavior of the transportation hub. This pre-stressed slab also acted as the structural roof of the transportation hub itself and below this structure three railway tunnels also existed. At the design stage the information regarding the structural connection between the slab and the tunnels, and the tunnels and the ground were not clear, so- as well as a structural investigation- a monitoring plan was established to manage the design uncertainties (Figure 1).

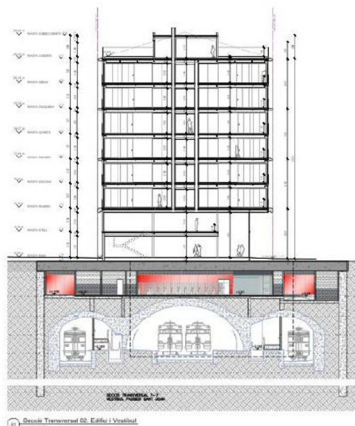


Figure 1. Cross section of the project.

Due to a significant increase in the stress levels on the slab during the construction, a finite element model - FEM - was built in order to assess the stress-strain behavior of the existing structures and the permitted maximum levels of deformation for the hub and the tunnels' structure.

During the first iterations of the FEM a conceptual monitoring plan was defined to address the structural deformation monitoring: fibre optics had to be used for the slab control, precise levelling for pillar control and a robotic total station system for the deformation monitoring of the tunnels.

### II. THE MONITORING PLAN

A monitoring plan was established to assist with the deformation monitoring of both the existing structural form and the future construction.

The monitoring plan was dependent on the results of the FEM, which ran in the design phase to address the deformation analysis. This FEM was then updated during the construction, as a result of the real values obtained by the monitoring. Here is the logistical challenge: to install the instruments as close as possible to the nodes of the model where the deformation is computed and to update them according to the real deformation measured by the instruments.

The scope of the monitoring plan is to define:

- 1) The instrumentation systems.
- 2) The threshold levels in connection with the FEM model.

- 3) The remediation action in the case that threshold limits are reached.
- 4) The coordination and cooperation of different administrations and enterprises involved in the project.

At this stage, the project owner tenders the monitoring services with two different packages, one for the fibre optics and another for the deformation monitoring including precise levelling and robotic total stations.

BAC was awarded with the package of the deformation monitoring, therefore, the fibre optics results are outside the scope of this paper.

The allowed limits of deformation were defined according to the FEM results. As the acceptable deformation was “appearance of cracks” and the uncertainty on the real structural connections between elements is quite high, the limits for the tunnel deformation were defined between 0.75 and 1.5 mm for the convergences between prisms. These values are close- even below- the standard defined accuracy of the robotic total station systems, which increase the challenges faced.

#### A. Design and implementation of the robotic total station (RTS) network

The first step was to design the automated control in the tunnels, with an initial visual inspection of the control area to find suitable locations for the RTS. The location of the RTS should consider the following:

- A visual connection with all the control points
- A position no further than 100 m from all the control points
- Be outside the clearance gauge with the trains and other machines circulating through the tunnels

The first deliverable at this stage were the proposed location plans for the prisms and the RTS. The proposal was consistent with the monitoring plan and approved.

The second stage was the implementation of the system and the compilation of the first readings. The system should be fully operational and stable at least two months before the beginning of the construction activities.

Figure 2 shows a plan of the full system, including the location of the RTS and the reference points. Figure 3 shows the distribution of control points in each tunnel.

All the tunnels have their own particularities, but have one feature in common: one section control is located in the tunnel, one is located in the station and another one in the transition zone between the station and the tunnel. Aside from the geometric considerations and the difficulties of establishing one appropriate line of sight for all the prisms, the environmental conditions of the tunnel (air temperature, humidity and atmospheric pressure) are

more stable, whilst in the transition zone and specially the station there were more significant changes.

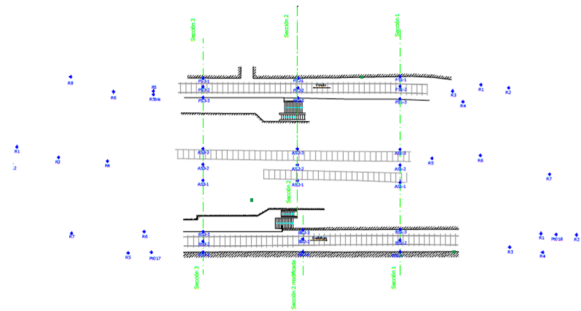


Figure 2. Monitoring area, control and reference points.

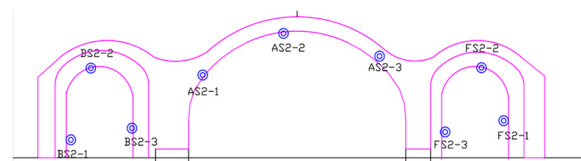


Figure 3. Distribution of monitoring points.

Regarding the line of sight, all the robotic total stations have to be placed in the tunnel section for the sake of security of the instruments. This means in all cases that the section located in the station can be further than 100 m. Additionally, according to the need for a proper distribution of the references (see for example, NWI PRE ISO 18674-9), between 4 to 6 references- half of the total- are further than the limit of 100 m. This means that according to the border conditions of the tunnels, some prisms will have less accuracy than required.

All the robotic total stations used were of the model TOPCON MSAXII and the calculation routine used was that which was implemented within the package of TOPCON monitoring Delta Live and Delta Watch.

The measurement routine was established with one measurement every two hours so that the number of points to be measured per each station was not excessive.

Table 1 shows the geometry of measurement of all the targets- reference and monitoring points- in terms of distance and horizontal and vertical angle from the robotic total station.

The main findings and characteristics of this distribution are:

- Central tunnel:
  - All the control points are close to the total station less than 30 m, but all the references are far away between 37 and 56 m.
  - References are well distributed in terms of horizontal angles but have a worse distribution in terms of vertical angle.
  - Control points are well distributed in terms of horizontal angles but have a worse distribution in terms of vertical angle.

- Lateral-B tunnel:
  - All control points are close enough to the total station maximum around 60 m. Good distance distribution among reference points, with distances between 15 and 70 m.
  - References distribution in terms of horizontal angles are split in two groups, one around 25 and another around 200. Regarding vertical angles, all the points are around 100.
  - All the monitoring points have similar horizontal angles around 20 and vertical angles around 100.
- Lateral- F tunnel:
  - All control points are close enough to the total station maximum around 30 m. Good distance distribution among reference points, with distances between 15 and 63 m.
  - Reference points in terms of horizontal angles are in one single group around values of 300. Regarding vertical angles, all the points are round 100, except for one single point at a value of 300.
  - All the monitoring points have similar horizontal angles around 100 and vertical angles around 100.

**B. Design and implementation of precise levelling network**

As defined in the monitoring plan, the precise levelling network was to be carried out with manual readings and the results to be used as a comparison and calibration for the fibre optic sensors.

The levelling points were to be installed in specific pillars. Some new construction pillars close to the contact with the slab and others that have continuity in the transportation hub level. Also, the upper surface of the existing walls (constructed during the execution of the construction hub) are levelled with the same instruments.

The installed levelling points are those shown in Figure 4.



Figure 4. Levelling control points.

The system requires external references to perform the computation. Those references were installed outside the construction site.

Figure 5 shows results of settlements points to help understand the type of movement measured in the project.

Table 1. Coordinates of control and reference points

Target ID	Coordinates		
	H. Angle [°]	V. Angle [°]	Distance [m]
AR1	196.0106	98.788	45.696
AR2	204.3329	98.9068	45.5921
AR3	198.9278	98.2008	37.2231
AR4	197.7127	97.5916	27.8815
AR5	23.481	104.0164	34.8308
AR6	22.3561	104.0572	44.0438
AR7	12.7493	103.5963	56.474
AS1-1	7.9159	102.3895	27.6962
AS1-2	16.1558	97.0723	27.888
AS1-3	27.4242	102.7751	28.7582
AS2-1	394.4046	107.4128	8.5841
AS2-2	36.1424	91.0596	8.8559
AS2-3	67.1827	103.527	12.5245
AS3-1	208.8988	100.9946	9.1215
AS3-2	177.5896	91.5498	10.3815
AS3-3	156.5435	100.7418	12.9032
BR1	207.8099	106.1259	17.8787
BR2	211.5806	105.9328	24.4881
BR3	216.81	93.7674	11.0199
BR4	222.0319	106.2988	17.2676
BR5	18.6843	102.1682	62.9229
BR6	23.078	103.654	59.4367
BR7	22.2705	102.9023	73.584
BS1-1	17.2692	115.596	10.5811
BS1-2	27.759	93.4013	10.5042
BS1-3	41.6912	101.9613	10.5326
BS2-1	18.4523	107.2776	29.8638
BS2-2	21.2619	97.4655	29.3786
BS2-3	27.086	105.924	28.6305
BS3-1	18.6738	103.3953	47.2741
BS3-2	20.8087	97.9384	46.7211
BS3-3	23.4074	97.5963	47.3293
PT018	209.8563	103.6269	20.614
PT017	18.5985	103.531	58.4337
FR1	296.8986	103.8799	21.5699
FR2	298.4373	102.1154	26.5772
FR3	303.4265	92.9511	16.272
FR4	310.154	106.1325	18.6403
FR5	288.739	296.2545	38.6499
FR5BIS	87.8678	104.4789	38.7959
FR6	289.7147	296.8385	45.7863
FR7	93.8498	97.8119	53.3053
FS1-1	290.8668	111.3271	7.421
FS1-2	307.0931	84.6962	7.5075
FS1-3	325.4728	111.7009	8.2654
FS2-1	94.6325	107.7206	12.4479
FS2-2	87.017	90.4514	12.5364
FS2-3	75.2796	110.7454	13.2156
FS3-1	94.7095	102.6907	29.7767
FS3-2	92.2798	96.0385	30.2484
FS3-3	85.3848	95.1756	30.3254

**III. RESULTS**

As defined in the monitoring plan, deformation monitoring for the tunnels has to be computed and plotted in terms of convergence. Those convergences

have different trigger values per each tunnel, each section and each convergence line, as shortening and elongation results should cause a different behavior in terms of crack appearance.

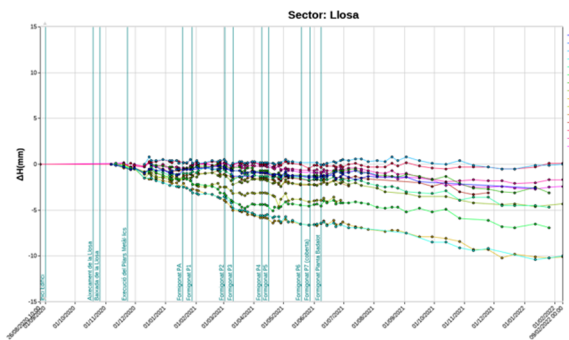


Figure 5. Levelling point results.

Fortunately, the system could be set up and run for almost three months before the construction activities started. This was of great help in order to understand and interpret the stability of the whole system.

From the very beginning all the sections located in the central tunnel showed better stability and better levels of standard deviation.

The most critical sections in terms of the relationship between standard deviation and threshold limit were sections 2 and 3 in the lateral -B tunnel and section 3 in lateral- F tunnel.

As a summary of these initial findings, Figure 6 shows the results of one section of the central tunnel, whilst Figure 7 shows the results of section 2 of the lateral- B tunnel, and Figure 8 shows the results of section 3 in the lateral- F tunnel.

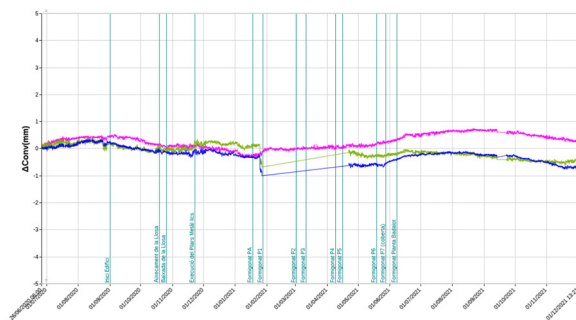


Figure 6. Convergence results. Central tunnel.

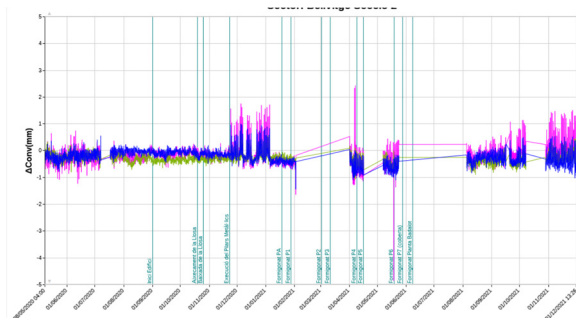


Figure 7. Convergence results. Lateral- B tunnel.

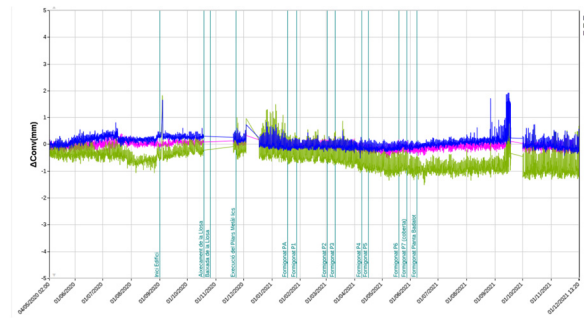


Figure 8. Convergence results. Lateral- F tunnel.

Figures 9 to 11 show the vertical displacement component results of the references for each one of the tunnels. It is clear to see that the central tunnel references are as stable as the monitoring points, with standard deviations between  $\pm 1$ mm. On the other hand, the lateral-F tunnel references show significant differences in the standard deviation values (in the range  $\pm 2.5$ mm). The performance of the Lateral- B tunnel references started well- even better than those located in the central tunnel. However, as the project advanced, the standard deviation levels increased.

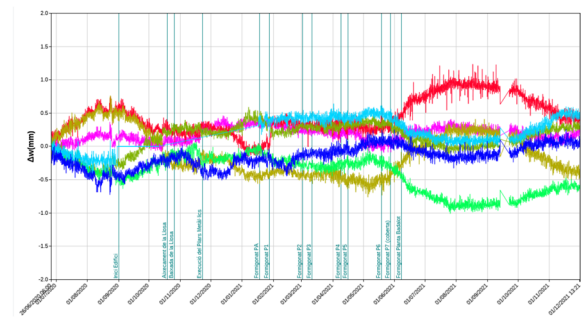


Figure 9. Reference performance. Central tunnel

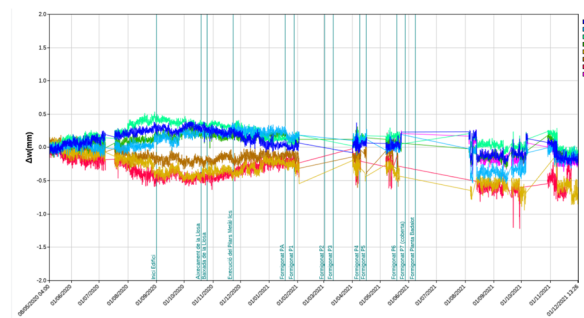


Figure 10. Reference performance. Lateral- B tunnel.

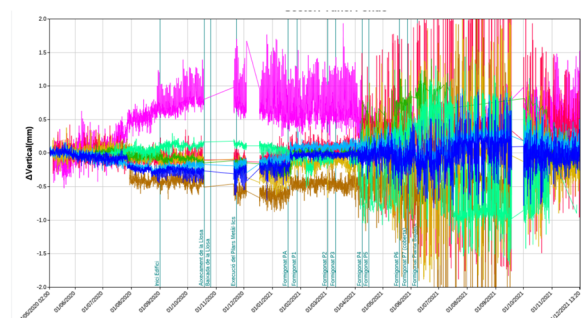


Figure 11. Reference performance. Lateral- F tunnel.

#### IV. CONCLUDING REMARKS

As evidenced above, it is essential to design a deformation monitoring system with a robotic total station based on distances and distribution of RTS, control and reference points, in accordance with ISO 18674/9.

According to the border conditions of the project, the above may not always be possible. In this case, the system should be set up prior to the start of the construction activities to understand the real standard deviation levels of the measurements.

The standard deviation is influenced by environmental changes (see references) particularly related to temperature, density and humidity of the air. These environmental changes are an inherent part of the project, cannot be changed, and should be considered and properly addressed throughout the project.

Finally, the standard deviation of the measurements may be affected by physical obstacles and other visual barriers that can be present in the project. The geometry of acquisition should also be checked throughout the project.

Taking into account the above points, it is clear that the standard deviation of the measurements may change with time in the same project and this needs to be continuously assessed for the success of the project.

#### References

- Rüeger, J (1996), *Electronic distance measurement*. 4<sup>th</sup> Edition. Springer, New York.
- Lackner, S., and Lienhart, W. (2016). Impact of prism type and prism orientation on the accuracy of automated total station measurements. In *Proc. 3<sup>rd</sup> Joint International Symposium on Deformation Monitoring (JISDM)*, Vienna, Austria.
- Lienhart, W (2017). Geotechnical monitoring using total stations and laser scanners: critical aspects and solutions. *Journal of Structural Health Monitoring*, 7, pp. 315-324.

## Current State of Multi-constellation and multi-frequency Precise Point positioning

Fernando Chacón<sup>1</sup>, Antonio Herrera<sup>1</sup>, M. Clara de Lacy<sup>1,2</sup>

<sup>1</sup> Dpto. Ing. Cartográfica, Geodesia y Fotogrametría, Universidad de Jaén, Campus de las Lagunillas, 23071 Jaén, Spain, ([fchacon@ujaen.es](mailto:fchacon@ujaen.es); [aherreraolmo@gmail.com](mailto:aherreraolmo@gmail.com))

<sup>2</sup> Centro de Estudios Avanzados en Ciencias de la Tierra, Energía y Medio Ambiente (CEACTEMA), Universidad de Jaén, Campus de las Lagunillas, 23071 Jaén, Spain, ([mclacy@ujaen.es](mailto:mclacy@ujaen.es))

**Key words:** *precise point positioning; GPS; galileo; multi-GNSS*

### ABSTRACT

Precise Point Positioning is a standalone method to estimate the coordinates of a single GNSS receiver based on undifferenced observations and modelling all the effects present during the observation session by precise products. The reference system of the coordinates estimated will be the same as the satellite orbits used in GNSS data processing. Due to its accuracy, PPP satisfies all most of applications where GPS observations are used. In recent years, the interoperability of new global navigation satellite systems (referred to as multi-GNSS) has driven the combination of observations coming from different satellite constellations. Multi-GNSS consists of the interoperability of at least two satellite constellations with some of their frequencies working in common. In this context, it has been essential to implement effective PPP algorithms to take advantage of the novelties presented by the different satellite navigation systems. As a consequence, some scientific software has been updated to support multi-frequency and multi-constellation GNSS data in PPP mode. Some of them are Bernese 5.2, RTKLIB, goGPS and PCUBE. The last one is being developed by the authors. This program implements two techniques for multi-GNSS data processing. One of them is based on a sequential filter and the other one is based on the Least Squares Approach. The purpose of this work is to study the capability and evaluation of multi-GNSS PPP performance along a whole day comparing the solutions estimated by different GNSS processing software. Special attention will be paid to the benefits introduced by new frequencies and services provided by the European System Galileo.

### I. INTRODUCTION

PPP is a method for obtaining precise positioning using GNSS observations. This approach estimates the coordinates of a single GNSS receiver, modeling all the effects present during the observation session. The reference system of these coordinates will be the same as the satellite orbits used in GNSS data processing. At this moment, this method is a useful tool for estimating station positions due to the fact that its accuracy satisfies the requirements of most applications where GPS observations are used. Currently there are several free online PPP processing resources, all of these support GPS and Glonass dual-frequency observations in static and kinematic mode. However, some of them is no able to process Galileo data. Furthermore, the scientific Bernese software version 5.2 (Dach *et al.*, 2015) has been updated to support dual frequency and multi-constellation GNSS data (GPS, Glonass and Galileo) in PPP mode.

In recent years the interoperability of new global navigation systems (hereafter referred to as multi-GNSS) has driven the combination of observations coming from different satellite constellations. As a result, a remarkable improvement in precision,

reliability and convergence time is expected. Several authors have studied these expected benefits in Precise Point Positioning PPP (Hernández-Pajares *et al.*, 2010; Cai and Gao, 2013; Paziewski and Wielgosz, 2014; Chen *et al.*, 2015; Fan *et al.*, 2017; Liu *et al.*, 2017; 2019; Montenbruck *et al.*, 2017; Pan. Z *et al.*, 2017; Zhao *et al.*, 2017). As a consequence, MGNSS PPP programs have been developed. For example, Moreno *et al.* (2014) developed and implemented PCUBE software; Bahadur and Nohutcu (2018) implemented PPPH program and GAMP software based on RTKLIB was developed by Zhou *et al.* (2018). The improvements achieved in MGNSS PPP are mainly studied using GPS, Glonass and Beidou observations (Liu *et al.*, 2017; Pan *et al.*, 2017; Marques *et al.*, 2018; Pan *et al.*, 2019). The evaluation of Galileo PPP performance throughout a whole day is still rare, (Xia *et al.*, 2019; Zhang *et al.*, 2019) since the Galileo constellation is not yet completed. The Galileo system has provided initial services since 2016. The aim of this paper is to study the possible benefits added by Galileo's initial services and the current GPS constellation in PPP. Not all satellites of the Galileo constellation can be used: E22 is not usable; E20 is unavailable from 2015/05/27 until further notice;



E18 and E14 may be used only for testing purposes. The satellites transmit the signals E1, E6, E5a/b/ab. The current GPS constellation is a mix of old and new satellites. It is composed of four blocks. Blocks IIR and IIR-M are formed of 10 and 7 satellites respectively. Block IIF is formed of 12 satellites and finally three satellites belonging to the GPSIIIA Block were launched in 2018, 2019 and 2020. The last two blocks transmit L1 C/A, L1/L2 P (Y), L2C, L1/L2 M, L1 C/A, L1/L2 P (Y), L2C, L1/L2 M, L5 signals. A significant aspect to consider in July 2020 is the Official U.S. government information about the Global Positioning System (GPS) and related topics (“GPS.gov: New Civil Signals” 2020) which underlines: “until further notice, the L2C and L5 signals are considered pre-operational. A pre-operational signal means the availability and other characteristics of the broadcast signal may not comply with all requirements of the relevant interface specifications and should be employed at the users' own risk”.

In this paper, GPS and Galileo data from ZIM3, MGNS station for one month in 2019 (February 1 to 28, 2019) and for another month in 2021 (November 1 to 30, 2021) are considered. The data sets are processed using different algorithms implemented in the PCUBE program. The reason why the authors use this software is that this program implements different PPP algorithms and its performance was checked with other software such as the online services CSRS-PPP, magicGNSS, and APPS and Bernese (Moreno *et al.*, 2014). One of these algorithms, called MAP3, is able to perform static PPP from multi-frequency and multi-GNSS constellations.

## II. MGNS POSITIONING

MGNS consists of the interoperability of at least two satellite constellations with some of their frequencies working in common, and this is achieved considering the biases due to the presence of different systems and frequencies. Montenbruck *et al.* (2017) defined the term “bias” in the context of GNSS observations: “deviations of the measured value from an idealized reference or a priori model. Biases are commonly treated as additive terms in the functional model of pseudorange and carrier phase observations, and are typically (but not necessarily always) considered as constant values during a given processing arc.” The biases play a very important role when different constellations and signals are involved in GNSS precise point positioning. In this context, the most important ones are: Differential Code Bias (DCB), Inter-system Bias (ISB) and Inter-frequency Bias (IFB).

DCBs represent the variation in travel time for two signals in a constellation, which are independent of ionospheric dispersion but are related to the hardware-dependent group delay differences in a pair of satellite receivers. The term Inter-system bias is the difference of at least two different interoperable GNSS constellation signals. The objective of ISB is to correct

the pseudorange (and carrier phase) model in order to align the measurements of a constellation (*e.g.* Galileo) with that of a reference constellation (*e.g.*, GPS), (Montenbruck *et al.*, 2017). ISBs can be modelled by known values provided by MGEX, available at an internet repository online of two different Data Centers, one being the Crustal Dynamics Data Information System (“CDDIS, products” 2019) and the second one GeoForschungsZentrum Potsdam (“GFZ, products” 2019). They can estimate as additional parameters as well.

## III. GNSS DATA DESCRIPTION AND PROCESSING STRATEGIES

### A. Data set from MGEX

In recent years MGEX or the multi-GNSS Experiment, created by the International GNSS Service (IGS), distributes products and observations coming from multi-GNSS constellations. The analysis centers (ACs) generate the necessary products such as orbits and clocks for the different GNSS constellations. Precise orbit intervals are 5 or 15 minutes and the corrections for the clocks are sampled at 30 seconds or 5 minutes.

MGEX products (orbits and clocks) are computed based on GNSS observations of the MGEX network and, optionally, other proprietary stations. To study the performance of the current Galileo and GPS data in PPP, a GNSS station belonging to MGEX network was selected: ZIM3. The main characteristics of the receiver and antennae of this station are summarized in Table 1. GPS and Galileo data from DOY 32 to 59, 2019 (February 1 to 28, 2019) were processed using precise products from CODE AC. In the same way, we process the dates corresponding to the month of November 2021, DOY 305 to 334 (days 1 to 30).

Table 1. Characteristics of the receivers and antennae involved in the tests

Site	ZIM3
Country	Switzerland
Receiver	TRIMBLE NETR9
Antenna	TRM59800.00
Sat. System	GPS+GLO+GAL+BDS+QZSS+SBAS

Nowadays the Galileo constellation is formed of 28 satellites but not all of them can be used: E22 is not usable; E20 is unavailable from 2015/05/27 until further notice; E18 and E14 could only be used for testing purposes in 2019 but are not available at the date of writing of this document.

A significant aspect to consider in July 2020 is the Official U.S. government information about the Global Positioning System (GPS) and related topics (“GPS.gov: New Civil Signals” 2020) which underlines: “until further notice, the L2C and L5 signals are considered pre-operational. A pre-operational signal means the availability and other characteristics of the broadcast signal may not comply with all requirements of the

relevant interface specifications and should be employed at the users' own risk”.

PCUBE implements different PPP algorithms and its performance was checked with other software such as the online services CSRS-PPP, magicGNSS, and APPS and Bernese (Moreno *et al.*, 2014). One of these algorithms, called MAP3, is able to perform static PPP from multi-frequency and multi-GNSS constellations. To compare the processed daily solution, we subsequently used RTKLib and Bernese 5.2. In order to compare the processed daily solution, we subsequently used RTKLib and Bernese 5.2, including new dates corresponding to the full month of November 2021 (days 1 to 30).

**B. PCUBE software**

PCUBE is a PPP program implemented in MATLAB. This software is able to estimate PPP solutions using two methods: one of them is a sequential filter based on the classical iono-free combination, therefore this algorithm process only dual frequency GNSS data; the other method is named MAP3 and is based on the Least Squares (LS) approach. MAP3 allows us to perform static PPP from multi-frequency and multi-system GNSS observations. The MAP3 algorithm was designed with two parts, and in each part the LS theory is applied. According to Moreno *et al.* (2014). The mathematical formulation used in PCUBE can be seen in (Moreno *et al.*, 2014) and the PCUBE software flowchart is shown in Figure 1.

Table 2 summarizes the main characteristics of the computed solutions. Table 3 summarizes the different models, input files and set-up strategies used in MGNSS PPP. The estimated coordinates were compared with the IGS14 coordinates in the weekly observation period, since they are considered as the “true” coordinates. When GPS + Galileo are processed, ISBs are known from MGEX precise products.

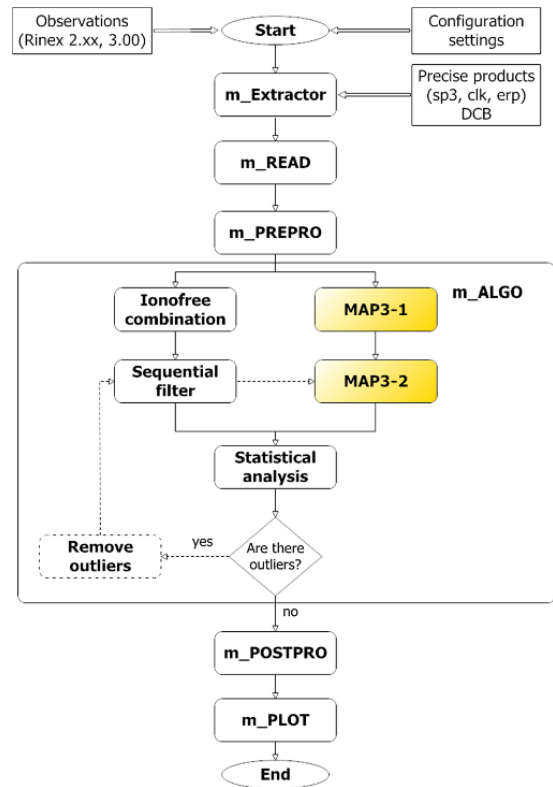


Figure 1. PCUBE software flowchart (Moreno *et al.*, 2014).

Table 2. Main characteristics of the solutions estimated with PCUBE

Solution	Const.	Method	Freq.	Observation
MAP3	GPS + GAL	LSA	3 if L5 available	L1 L2 L5 E1 E5b E5a
MAP3-GPS	GPS	LSA	3 if L5 available	L1 L2 L5
MAP3-GAL	GAL	LSA	3	E1 E5b E5a

Table 3. Models and data processing strategies used

	LSA
Constellations	GPS only, Galileo only, GPS + Galileo
Observations	L1, L2, L5; E1, E5a; E5b
Processing mode	Static
Precise products	Precise ephemeris and clocks from CODE with 5 minutes and 30 seconds sampling rate, respectively (“CDDIS, products” 2019)
Satellite PCO and PCV corrections	IGS absolute antenna model from IGS14.atx
Receiver PCO and PCV corrections	IGS absolute antenna model from IGS14.atx GPS PCO/V L5 are assumed the same with GPS L2 Galileo corrections are assumed the same with GPS
Observables	Undifferenced dual and triple frequency raw observations when 3rd frequency available
Sampling rate	30 and 1 seconds for long and short periods, respectively
Elevation mask	8°
Observation	Elevation dependent weighting
STD observables	0.003 m for phases 0.3 for pseudoranges
Phase ambiguities	Estimated as float for each arc
ISB	Known from precise products from CDDIS (MGEX)
Troposphere modelling	Dry model Saastamoinen and Wet model estimated every two hours
Relativistic effects	Applied (Kouba and Street, 2009)
Phase wind-up correction	Applied (Wu <i>et al.</i> , 1992)
Site displacement	Solid Earth tides and ocean loading applied (Petit and Luzum, 2010)

### C. RTKLIB

RTKLIB is a free software with different GUIs created by Tomoji Takasu (2008). It allows both GNSS data post-processing and real-time positioning (RTK), enabling and disabling different corrections on the processing, modification of parameters to obtain the solution and its presentation. The output file provides the geocentric XYZ coordinates and the covariance matrix of the solution in each epoch, the number of satellites in each epoch and the type of solution.

### D. Bernese

Bernese is a high-precision, scientific GNSS software capable of performing multi-GNSS data processing. Developed at the Astronomical Institute of the University of Bern (AIUB), it has spread through the scientific community over time, used by CODE (Centre for Orbit Determination in Europe) in its international (IGS) and European (EUREF/EPN) activities.

### E. goGPS

goGPS is software created for GNSS raw data processing. Developed to work with low-cost single-frequency GPS receivers, it is adapted to multi-constellation, multi-frequency and multi-track observations. Furthermore, implements multiple algorithms that allow data analysis, and least squares (LS) processing. It can calculate accurate PPP and network adjustments (NET).

## IV. MGNSS PCUBE RESULTS

Table 4 shows the statistics of PPP accuracy of the North, East and Upwards components in terms of RMSE for February 2019 results. The magnitude of the RMSE agrees with those obtained by Hadas et al (2019) when they estimate static PPP coordinates using MGEX data and products at 2019 precision level. From these results, we can observe that Upward RMSE is in general slightly better than 2D. This fact is not normal in GNSS processing, and is probably due to the assimilation of PCO/V used for L5, E5a and E5b and the mismodelling of inter-frequency bias in PCUBE. The positioning error at cm-level is slightly high. Next future, more research will be done processing current data and adding inter-frequency bias model in PCUBE.

## V. MGNSS GOGPS, BERNESE AND RTKLIB RESULTS

Modern data (1-30 november, 2021) coming from the same has been processed using similar modelling options. Tables 4-7 shows the statistics of the PPP accuracy of the North, East and Up components in terms of RMSE processing only Galileo data, only GPS data and GAL+GPS data. In this case for the November 2021 results for GPS; GPS+GAL; GAL respectively.

Table 5 shows the GPS results for each software. It can be seen that goGPS and Bernese are at the same level of results. RTKLIB is slightly worse.

Table 4. ZIM3 positioning results in North (N), East (E) and Upward (U) components in cm. PCUBE

Solution	RMS error [cm]			2D positioning error [cm]	3D positioning error [cm]
	N	E	U		
MAP3 GPS +GAL	1.92	2.55	1.70	3.19	3.62
MAP3-GPS	1.47	1.56	1.28	2.14	2.50
MAP3-GAL	1.96	2.76	1.98	3.38	3.92

Table 5. GPS ZIM3 positioning results in North (N), East (E) and Upward (U) components in cm. GOGPS, BERNESE AND RTKLIB

Solution	RMS error [cm]			2D positioning error [cm]	3D positioning error [cm]
	N	E	U		
GPS					
goGPS	0.15	0.15	0.58	0.21	0.62
Bernese	0.31	0.14	0.53	0.34	0.63
RTKLIB	0.32	0.27	1.18	0.42	1.25

Table 6. GPS+GAL ZIM3 positioning results in North (N), East (E) and Upward (U) components in cm. GOGPS, BERNESE AND RTKLIB

Solution	RMS error [cm]			2D positioning error [cm]	3D positioning error [cm]
	N	E	U		
GPS+GAL					
goGPS	0.24	0.18	0.82	0.31	0.88
Bernese	0.24	0.27	0.91	0.36	0.98
RTKLIB	0.38	0.26	1.24	0.55	1.35

Table 7. GAL ZIM3 positioning results in North (N), East (E) and Upward (U) components in cm. GOGPS, BERNESE AND RTKLIB

Solution	RMS error [cm]			2D positioning error [cm]	3D positioning error [cm]
	N	E	U		
GAL					
goGPS	0.16	0.15	1.13	0.60	1.28
Bernese	0.44	0.17	1.91	0.76	2.05
RTKLIB	N.S	N.S	N.S	N.S	N.S

These tables show accuracy at few mm level is achieved. Next months, PCube will be used with these data set. Comparing only GPS solutions, only Galileo solutions and GPS+GALILEO solutions, we can say the best solution corresponds to the results obtained processing GPS data only.

Table 7 contains the GAL results. In it goGPS is minimally better than Bernese. For RTKLIB there is no estimated solution (N.S.=No Solution). This may be due to the number of unknowns influencing each processing mode of the respective software.

## VI. CONCLUSIONS

In this paper, a first test to analyse the performance of current Galileo and GPS systems in Precise Point Positioning has been carried out. In particular, data coming from ZIM3 will be process with goGPS, Bernese

and RTKLiB. Accuracy at mm level has been achieved with 24 hours' session. The best results are obtained when GPS data only are processed. Next months, the same data set will be processed with PCUBE to compare the results. More research will be done to verify the achieved solutions.

## VII. ACKNOWLEDGEMENTS

This research has been funded by: University of Jaén: Programa Operativo FEDER Andalucía 2014-2020 - Project 1263446 - call made by UJA 2018. POAIUJA 2021-2022 and CECTEMA. Junta de Andalucía: Plan Andaluz de Investigación. Desarrollo e Innovación PAIDI2020 – Project PY20\_00897. Project P07-RNM-03087 and Research Group RNM282. MINECO of Spain: Project CGL2016-78577-P.

## References

- Bahadur, B., and Nohutcu, M. (2018). PPPH: a MATLAB-based software for multi-GNSS precise point positioning analysis. *GPS Solutions*, 22(4), 113.
- BKG, data. (2019). Available in: <ftp://igs.bkg.bund.de/MGEX>, (Aug. 5, 2019).
- CDDIS, data. (2019). Available in: <ftp://cddis.gsfc.nasa.gov/pub/gps/data/campaign/mgex>, (Aug. 5, 2019).
- CDDIS, high rate data. (2019). Available in: <ftp://ftp.cddis.eosdis.nasa.gov/pub/gnss/data/highrate>, (Aug. 5, 2019).
- CDDIS, products. (2019). Available in: <ftp://ftp.cddis.eosdis.nasa.gov/pub/gnss/products/>, (Aug. 5, 2019).
- Cai, C., and Gao, Y. (2013). Modeling and assessment of combined GPS/GLONASS precise point positioning. *GPS Solutions*, 17(2), pp. 223–236.
- Chen, J., Zhang, Y., Wang, J., Yang, S., Dong, D., Wang, J., Qu, W., and Wu, B. (2015). A simplified and unified model of multi-GNSS precise point positioning. *Advances in Space Research*, 55(1), pp. 125–134.
- Dach, R., Fridez, P., Lutz, S., and Walser, P. (2015). Bernese GNSS Software Version 5.2
- Fan, L., Li, M., Wang, C., and Shi, C. (2017). BeiDou satellite's differential code biases estimation based on uncombined precise point positioning with triple-frequency observable. *Advances in Space Research*, 59(3), pp. 804–814.
- GPS.gov: New Civil Signals. (2020). Available in: <https://www.gps.gov/systems/gps/modernization/civilsignals/>, (Feb. 13, 2020).
- GPS.gov: Space Segment. (2020). Available in: <https://www.gps.gov/systems/gps/space/>, (Feb. 13, 2020).
- Hadas, T., Kazmierski, K., and Sośnica, K. (2019). Performance of Galileo-only dual-frequency absolute positioning using the fully serviceable Galileo constellation. *GPS Solutions*, 23(4), 108.
- Hernández-Pajares, M., Juan, J. M., Sanz, J., Ramos-Bosch, P., Rovira-García, A., Salazar, D., Ventura-Traveset, J., López-Echazarreta, C., and Hein, G. (2010). The ESA/UPC GNSS-Lab tool (gLAB): An advanced multipurpose package for GNSS data processing. 2010 5th ESA Workshop on Satellite Navigation Technologies and European Workshop on GNSS Signals and Signal Processing (NAVITEC), IEEE, Netherlands, pp. 1–8.
- Liu, T., Yuan, Y., Zhang, B., Wang, N., Tan, B., and Chen, Y. (2017). Multi-GNSS precise point positioning (MGPPP) using raw observations. *Journal of Geodesy*, 91(3), pp. 253–268.
- Liu, T., Zhang, B., Yuan, Y., Li, Z., and Wang, N. (2019). Multi-GNSS triple-frequency differential code bias (DCB) determination with precise point positioning (PPP). *Journal of Geodesy*, 93(5), pp. 765–784.
- Marques, H. A., Aquino, M., Veetil, S. V., and Monico, J. F. G. (2018). Accuracy assessment of Precise Point Positioning with multi-constellation GNSS data under ionospheric scintillation effects. *Journal of Space Weather and Space Climate*, 8, A15.
- Montenbruck, O., Steigenberger, P., Prange, L., Deng, Z., Zhao, Q., Perosanz, F., Romero, I., Noll, C., Stürze, A., Weber, G., Schmid, R., MacLeod, K., and Schaer, S. (2017). The Multi-GNSS Experiment (MGEX) of the International GNSS Service (IGS) – Achievements, prospects and challenges. *Advances in Space Research*, 59(7), pp. 1671–1697.
- Moreno, B., Rodríguez-Caderot, G., and de Lacy, M. C. (2014). Multifrequency algorithms for precise point positioning: MAP3. *GPS Solutions*.
- Pan, L., Zhang, X., Guo, F., and Liu, J. (2019). GPS inter-frequency clock bias estimation for both uncombined and ionospheric-free combined triple-frequency precise point positioning. *Journal of Geodesy*, 93(4), pp. 473–487.
- Pan, Z., Chai, H., and Kong, Y. (2017). Integrating multi-GNSS to improve the performance of precise point positioning. *Advances in Space Research*, 60(12), pp. 2596–2606.
- Paziewski, J., and Wielgosz, P. (2014). Assessment of GPS + Galileo and multi-frequency Galileo single-epoch precise positioning with network corrections. *GPS Solutions*, 18(4), pp. 571–579.
- Petit, G., and Luzum, B. (2010). (IERS Technical Note; No. 36). (36), 179.
- Xia, F., Ye, S., Xia, P., Zhao, L., Jiang, N., Chen, D., and Hu, G. (2019). Assessing the latest performance of Galileo-only PPP and the contribution of Galileo to Multi-GNSS PPP. *Advances in Space Research*, 63(9), pp. 2784–2795.
- Zhang, R., Tu, R., Liu, J., Hong, J., Fan, L., Zhang, P., and Lu, X. (2019). Performance of Galileo: Global coverage, precise orbit determination, and precise positioning. *Advances in Space Research*, 64(2), pp. 299–313.
- Zhao, L., Ye, S., and Song, J. (2017). Handling the satellite inter-frequency biases in triple-frequency observations. *Advances in Space Research*, 59(8), pp. 2048–2057.
- Zhou, F., Dong, D., Li, W., Jiang, X., Wickert, J., and Schuh, H. (2018). GAMP: An open-source software of multi-GNSS precise point positioning using undifferenced and uncombined observations. *GPS Solutions*, 22(2), 33.
- Zhou, F., Dong, D., Li, P., Li, X., and Schuh, H. (2019). Influence of stochastic modeling for inter-system biases on multi-GNSS undifferenced and uncombined precise point positioning. *GPS Solutions*, 23(3), 59.

## CGPS Crustal velocity field in the Iberian Peninsula

Fernando Chacón<sup>1</sup>, M. Clara de Lacy<sup>1,2</sup>, Manuel Avilés<sup>1</sup>, Antonio J. Gil<sup>1,2</sup>

<sup>1</sup> Dpto. Ing. Cartográfica, Geodesia y Fotogrametría, Universidad de Jaén, Campus de las Lagunillas, 23071 Jaén, Spain, ([fchacon@ujaen.es](mailto:fchacon@ujaen.es); [mclacy@ujaen.es](mailto:mclacy@ujaen.es); [maviles@ujaen.es](mailto:maviles@ujaen.es); [ajgil@ujaen.es](mailto:ajgil@ujaen.es))

<sup>2</sup> Centro de Estudios Avanzados en Ciencias de la Tierra, Energía y Medio Ambiente (CEACTEMA), Universidad de Jaén, Campus de las Lagunillas, 23071 Jaén, Spain

**Key words:** *CGPS station; time series; velocity field*

### ABSTRACT

As part of the research Project “ Geosciences in Iberia: Integrated studies on topography and 4-D evolution” a network of 26 continuous GPS stations, covering the Spanish part of the Iberian Peninsula (22 stations) and Morocco (4 stations) was established. The major objective behind the establishment of this array was to monitor millimetre level deformation of the crust due to African and Eurasian tectonic plates. The locations of the Topo-Iberia sites are in open fields, not on buildings, and founded on bedrock, implying great stability of the concrete pillars and a high quality of observations. We present a velocity field based on the analysis of 1<sup>st</sup> March 2008 up to 31<sup>th</sup> December 2018 data from Topo-Iberia stations along with IGS, EUREF and regional GNSS stations. The data analysis was performed with the Bernese Processing Engine (BPE) of the software Bernese 5.2. At the end of this step, one daily solution in a loosely constrained reference frame is estimated. The daily network solutions is minimally constrained and transformed into the IGB14 frame. The rigid plate motion is statistically inferred using a simple  $\chi^2$  test-statistics to select the coherent subset of sites defining a stable plate. Then, the velocity field is estimated from the IGB14 time series of daily coordinates with the complete covariance matrix using ad hoc software called as NEVE. Velocities were estimated simultaneously, along with annual signals and sporadic offsets at epochs of instrumental changes. Velocity errors are derived from the direct propagation of the daily covariance matrix.

### I. INTRODUCTION

The project “Geosciences in Iberia: Integrated studies of topography and 4-D evolution Topo-Iberia” (Ref.CSD2006-00041) was supported by the Spanish Ministry for the Economy and Competitiveness. Its objective was to understand the interactions in the Iberian Peninsula (SW Europe) between deep, shallow and atmospheric processes, through a multidisciplinary approach linking Geology, Geophysics and Geodesy. As the study area is under a NNW-SSE to NW-SE compression regime, two station alignments (from NE to SW and NW to SE) were built, including continuous CGPS (continuous GPS) stations in Northern Africa. In particular, 26 CGPS stations, covering the Spanish part of the Iberian Peninsula (22 stations) and Morocco (4 stations) was established in 2008 to complement other GPS networks already deployed by different Institutions, EPN (EUREF Permanent Network), IGS (International GNSS Service) and regional governmental agencies to monitor crustal deformation due to Nubia and Eurasian tectonic plates. The new CGPS stations can be seen in Figure 1. Real Instituto y Observatorio de la Armada (ROA), University of Barcelona (UB) and University of Jaen (UJA) played a role of Analysis Centre. A velocity field based on the analysis of 4 years of data (2009- 2012) was published in (Garate *et al.*, 2015). Data analysis was performed by every Analysis Centre, with different approaches. Each group used one of the best known geodetic analysis software packages.

Precise point positioning (PPP) approach with GIPSY-OASIS (Zumberge *et al.*, 1997), developed at Jet Propulsion Laboratory (JPL) was used at San Fernando Naval Observatory (ROA). Geodetic network approach was used by the University of Jaen (UJA) group using Bernese software (Dach *et al.*, 2015) and also by the University of Barcelona (UB) group by using GAMIT (Herring *et al.*, 2008), software developed at the Massachusetts Institute of Technology.

The results put in evidence the maximum horizontal velocities in the Eurasia frame were observed for the stations located on the Africa (*i.e.*, Nubia) tectonic plate in Morocco, where the calculated velocities range from 4.2 to 4.9 mm/year. Within the Iberian Peninsula, maximum velocities were observed in the southern margin, close to the Strait of Gibraltar and the Betic area. Here the velocities reached 3.5 mm/year at ALJI, indicating that the tectonic behaviour of this region is influenced more by the African plate than the Eurasian. The estimated uncertainties for the calculated velocities are below 0.2 mm/year. (Garate *et al.*, 2015).

The objective of the present paper is to continue the previous work carried out by the University of Jaen. In particular, GPS data from the beginning of Topo-Iberia CGPS network to the end of 2018 has been processed and the corresponding crustal deformation velocity field has been estimated.

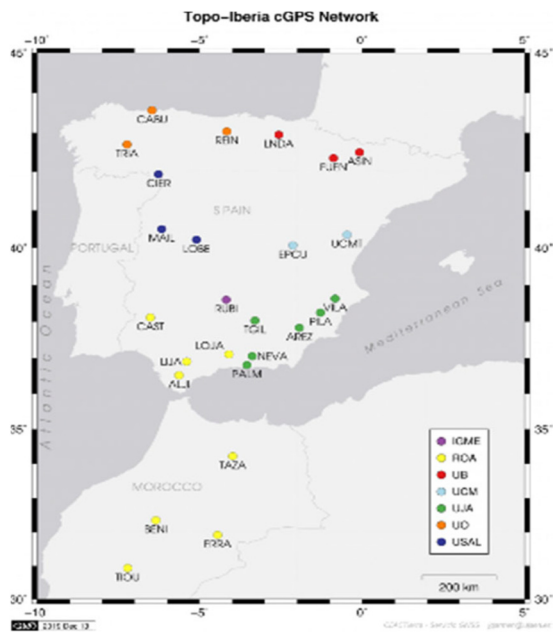


Figure 1. CGPS Topo-Iberia stations.

## II. GPS DATA PROCESSING FROM 2008 TO 2018

Bernese Processing Engine (BPE) has been used to process GPS observations with option shown in Table 1.

In Garate *et al.* (2015) two clusters of GPS data were processed independently. One of them with Topo-Iberia CGPS stations from march 2008 to the end of 2012 and another one containing EUREF/IGS stations all over Europe in the time span 1998-2012. This decision was taken in 2009 to obtain a more stable set of fiducial stations since not many permanent stations covered our study area existed. Nowadays, this problem does not put. One cluster formed by 80 stations were processed. These stations belong to Topo-Iberia CGPS, IGS International GNSS services, EPN (European Permanent Network) and regional networks. It is

important to note that not all Topo-Iberia stations have data covering the whole processing period (2008-2018). Table 2 shows CGPS data considered.

## III. GPS VELOCITY ESTIMATION

From Bernese, one daily solution in a loosely constrained reference frame is estimated. These daily solutions are minimally constrained and transformed into the IGB14 estimating translations and scale parameters. In particular, the realization EPN\_A\_IGB14 was used and 18 core stations contributed to the rigid transformation. These stations were ALME, BELL, BORR, CASC, CREU, ESCO, GAIA, GRAS, GRAZ, HERS, LLIV, LPAL, POTS, RABT, VIGO, VILL, WTZR and YEBE, (Chacón, 2021). One example of the behaviour of the core stations can be seen in Figure 2 where coordinates Time Series of GAIA station along with the residual distribution is shown.

We have estimated the velocity field by using a specific software designed and implemented by the INGV group and called NEVE that manages the complete stochastic model (Devoti *et al.*, 2011; Devoti *et al.*, 2008). The velocities are estimated simultaneously, along with annual signals and sporadic offsets at epochs of instrumental changes (Blewitt. and Lavallée, 2002). The velocity field is estimated from IGB14 time series of daily coordinates with the complete covariance matrix. The velocity errors are derived from the direct propagation of the daily covariance matrix. Figures 3 and 4 shows Up, East and North components Time Series of some CGPS Topo-Iberia station (ALJI, AREZ, ASIN, CAST, EPCU, ERRA, LOJA, NEVA, PALM, PILA, RUBI and TIOU). The noise GPS time series show significant temporal correlations that were taken into account according to (Mao *et al.*, 1999) to get reliable estimates of the velocity uncertainties.

Table 1. Characteristics GPS processing with Bernese 5.2

Mode	Characteristics
Preprocessing	Phases in a baseline by baseline mode using triple-differences.
Basic Observable	Carrier phase. Code only used for receiver clock synchronization.
Elevation angle cut-off	3 degrees + elevation dependent weighting.
Modeled observable	Double-differences, ionosphere-free linear combination.
Data sampling	30 seconds.
Earth geopotential model	JGM3.
Ocean loading model	FES2004.
Ocean tides	OT CSRC.
Atmospheric loading	Not applied.
Solid Earth tides	Applied, IERS. Conventions 96/2000.
Orbits and ERPs	IGS final orbit and ERP Information (Dow <i>et al.</i> , 2009).
Planetary ephemeris	DE2000 from JPL.
Ground and satellite antennae	Absolute antenna phase center corrections based on IGS14 model.
Troposphere	Dry-Niell as a priori model, zenith delay corrections every 2-hours. Horizontal gradient parameter estimated.
Datum definition	Loosely constrained solution (10 m).
Ambiguity	QIF strategy to solve ambiguities for each baseline. Integer ambiguities introduced into final solution.
Satellite clock	Not estimated but eliminated bias by forming double-differences.
Receiver clock	Estimated during the bias pre-processing using code measurements.

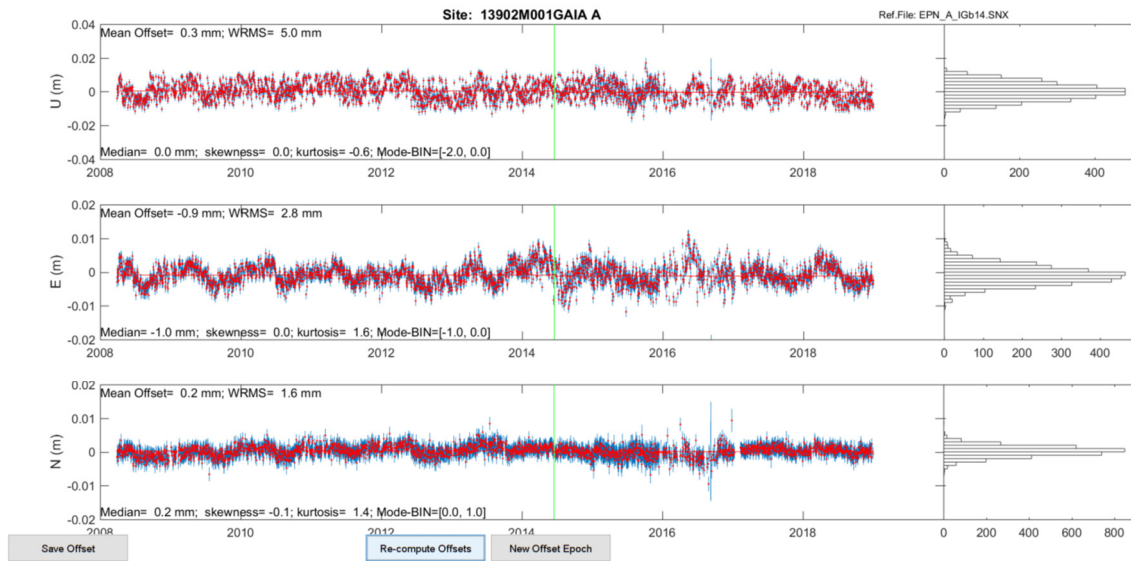


Figure 2. Coordinate Time Series of GAIA (Up, East and North components) along with Helmert transformation residual, Units are meters.

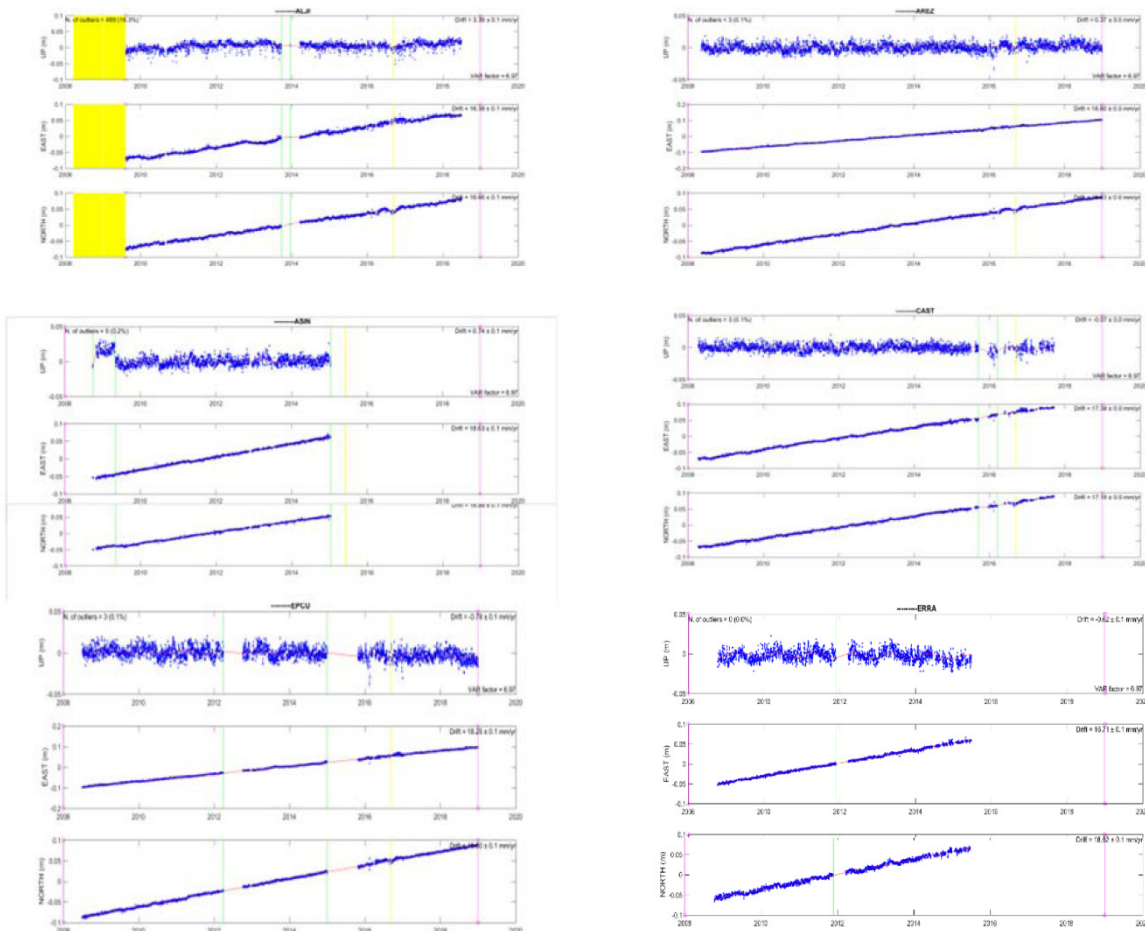


Figure 3. Position time series of the network stations (North and East components in metres). Yellow and green lines are considered as outliers and jumps according to the software applied.

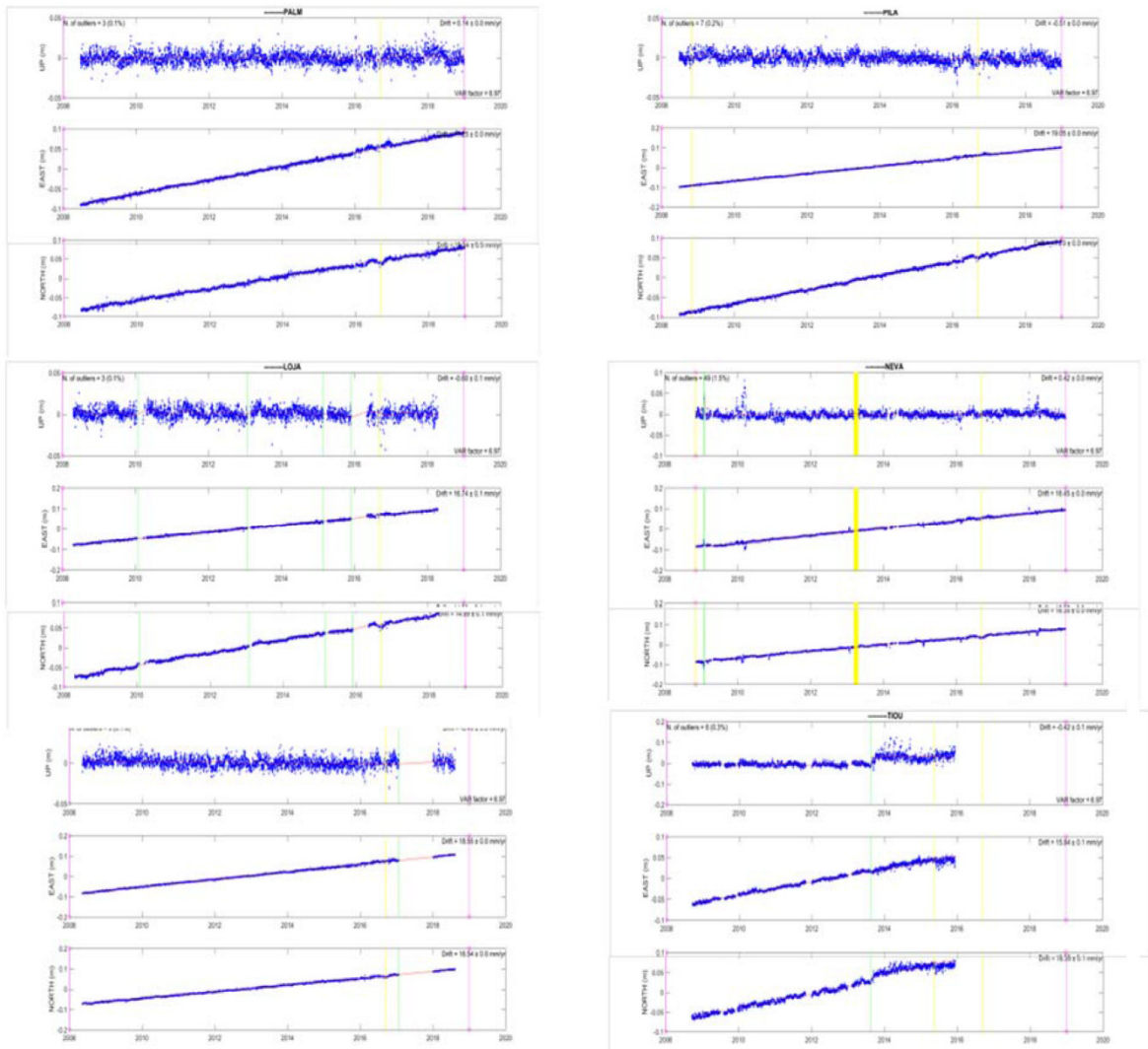


Figure 4. Position time series of the network stations (North and East components in metres). Yellow and green lines are considered as outliers and jumps according to the software applied.



Figure 5. Topo-Iberia velocities in Igb14. (Chacón, 2021).



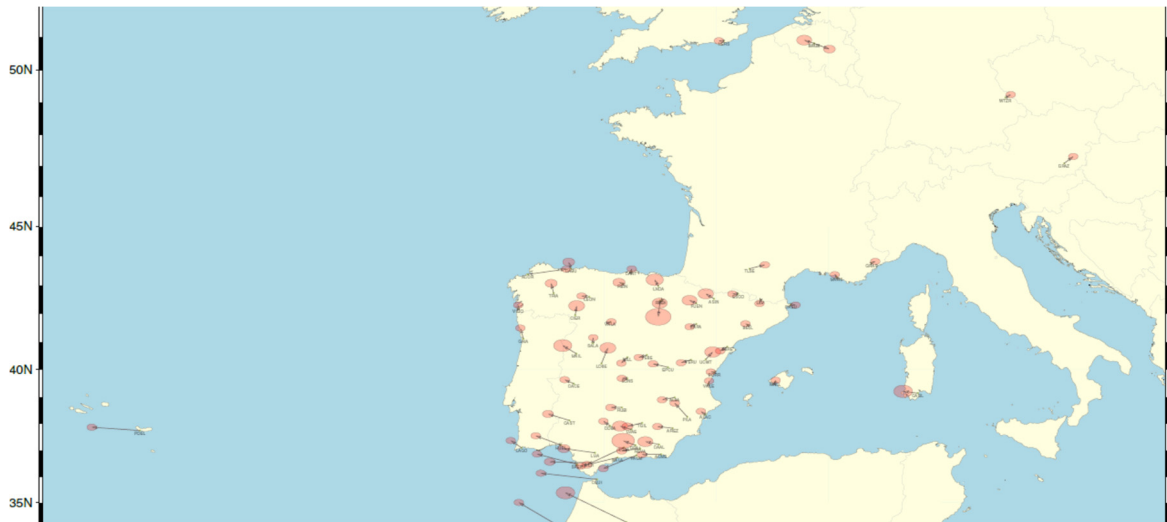


Figure 6. Topo-Iberia velocities with respect to Eurasian fixed plate. (Chacón F, 2021).

Table 2. CGPS Topo-Iberia data set

Station	Data span
ALJI	2008 - 2019
AREZ	2008 - 2019
ASIN	2008 - 2016
BENI	2008 - 2014
CABU	2008 - 2017
CAST	2008 - 2018
CIER	2008 - 2015
EPCU	2008 - 2019
ERRA	2008 - 2016
FUEN	2008 - 2016
LIJA	2008 - 2017
LNDA	2008 - 2015
LOBE	2008 - 2015
LOJA	2008 - 2019
MAIL	2008 - 2015
NEVA	2008 - 2019
PALM	2008 - 2019
PILA	2008 - 2019
REIN	2008 - 2017
RUBI	2008 - 2019
TAZA	2008 - 2015
TGIL	2008 - 2018
TIOU	2008 - 2016
TRIA	2008 - 2017
UCMT	2008 - 2015

Table 3. One example of Topo-Iberia IGb14 velocities in mm/y.

Station	East	North
ACOR	17.07±0.01	17.07±0.02
ALJI	18.78±0.01	16.26±0.01
AREZ	18.79±0.01	16.62±0.01
EPCU	18.25±0.03	16.80±0.03
ERRA	16.70±0.03	18.81±0.03
GAIA	17.80±0.01	17.56±0.02
GRAS	20.69±0.01	16.11±0.01
GRAZ	22.06±0.01	15.72±0.01
LIJA	17.07±0.02	16.96±0.03
LLIV	19.64±0.01	15.98±0.01
MALA	16.77±0.01	15.77±0.01
SFER	16.28±0.01	17.52±0.02
TGIL	18.56±0.01	16.20±0.01
TIOU	15.84±0.02	18.35±0.03
YEBE	18.55±0.01	16.29±0.01

Table 4. One example of Topo-Iberia residual with respect to Eurasian fixed plate in mm/y

Station	East	North
ACOR	3.27±0.41	0.5±0.29
ALJI	-3.36±0.47	0.1±0.33
AREZ	-1.29±0.41	0.1±0.29
EPCU	-1.28±0.42	0.3±0.29
ERRA	-4.23±0.66	2.3±0.46
GAIA	-0.25±0.41	0.96±0.29
GRAS	0.30±0.41	0.14±0.28
GRAZ	0.77±0.41	0.62±0.28
LIJA	-2.62±0.52	0.37±0.36
LLIV	-0.09±0.41	-0.32±0.28
MALA	-3.14±0.41	-0.78±0.28
SFER	-3.38±0.41	0.93±0.29
TGIL	-1.24±0.41	-0.32±0.32
TIOU	-4.87±0.61	1.74±0.43
YEBE	-0.69±0.41	-0.22±0.28

The residual velocities are derived from the absolute IGb14 Eurasia pole and rotation rate that are 62.021155 latitude, -28.467734 longitude and 5.417132 semi-major axis of error ellipse (deg); 0.063221 semi-minor axis of error ellipse (deg); -81.813986 azimuth of semi-major axis (deg).

Figures 5 and 6 shows the velocity field in IGb14 and with respect to Eurasian fixed plate respectively.

The corresponding IGb14 and residual velocities for some stations of Topo-Iberia are shown in Table 3 and 4, respectively.

#### IV. CONCLUSIONS

The obtained results are coherent with those obtained in (Garate *et al.*, 2015). The maximum horizontal velocities in the Eurasia frame are observed for the stations located on the Africa (*i.e.*, Nubia) tectonic plate in Morocco, where the calculated velocities range from 4.2 to 5.2 mm/year. Within the Iberian Peninsula, maximum velocities were observed in the Strait of Gibraltar and the Betic area. The maximum is reached at ALJI and SFER with values equal to -3.4 mm/year at ALJI.

More research will be done about the results obtained at stations as ACOR and TLSE. Currently, GPS data up to 2019 coming from CIER, LOBE, MAIL and TIOU are available for the authors. The results will be updated in the next future.

#### V. ACKNOWLEDGEMENTS

This research has been funded by: University of Jaén: Programa Operativo FEDER Andalucía 2014-2020 - Project 1263446 - call made by UJA 2018. POAIUJA 2021-2022 and CECTEMA. Junta de Andalucía: Plan Andaluz de Investigación. Desarrollo e Innovación PAIDI2020 – Project PY20\_00897. Project P07-RNM-03087 and Research Group RNM282. MINECO of Spain: Project CGL2016-78577-P .

#### References

- Blewitt, G., and Lavallé, D. (2002). Effect of annual signals on geodetic velocity: effect of annual signals on velocity. *Journal of Geophysical Research: Solid Earth*. Vol 107(B7). pp. ETG 9-1-ETG 9-11.
- Chacón, F. (2021). Estudio del campo de velocidades estimado en la Cordillera Bética oriental a partir de campañas GPS no permanentes. Master Thesis.
- Dach, R., Fridez, P., Lutz, S., and Walser, P. (2015). Bernese GNSS Software Version 5.2
- Devoti, R., Esposito, A., Pietrantonio, G., Pisani, A. R., and Riguzzi, F. (2011). Evidence of large scale deformation patterns from GPS data in the Italian subduction boundary. *Earth and Planetary Science Letters*. Vol 311(3-4). pp. 230-241
- Devoti, R., Riguzzi, F., Cuffaro, M., and Doglioni, C. (2008). New GPS constraints on the kinematics of the Apennines subduction. *Earth and Planetary Science Letters*. Vol 273(1-2). pp. 163-174
- Dow, J. M., Neilan, R. E., and Rizos, C. (2009). The International GNSS Service in a changing landscape of Global Navigation Satellite Systems. *Journal of Geodesy*. Vol 83. pp. 191-198.
- Garate, J., Martin-Davila, J., Khazaradze, G., Echeverria, A., Asensio, E., Gil, A. J., de Lacy, M. C., Armenteros, J. A., Ruiz, A. M., Gallastegui, J., Alvarez-Lobato, F., Ayala, C., Rodríguez-Caderot, G., Galindo-Zaldívar, J., Rimi, A., and Harnafi, M. (2015). Topo-Iberia project: CGPS crustal velocity field in the Iberian Peninsula and Morocco. *GPS Solutions*. Vol 19(2). pp. 287-295.
- Herring, T. A., King, R. W., Floyd, M. A., and McClusky, S. C. (2008). *Introduction to GAMIT/GLOBK*.
- Mao, A., Harrison, C. G. A., and Dixon, T. H. (1999). Noise in GPS coordinate time series. *Journal of Geophysical Research: Solid Earth*. Vol 104(B2). pp. 2797-2816.
- Zumberge, J. F., Heflin, M. B., Jefferson, D. C., Watkins, M. M., and Webb, F. H. (1997). Precise point positioning for the efficient and robust analysis of GPS data from large networks. *Journal of Geophysical Research: Solid Earth*. Vol 102(B3). pp. 5005-5017.

## Classical Concepts for Deformation Monitoring - Strategies, Status and Limitations

Wolfgang Niemeier

Institut of Geodesy and Photogrammetry, Technische Universität Braunschweig, Bienroder Weg 81, 38106 Braunschweig, Germany, ([w.niemeier@tu-bs.de](mailto:w.niemeier@tu-bs.de))

**Key words:** *prior information on expected deformations; selection of sensors; geodetic datum; classical congruency test; alternative analysis concepts; kinematic and dynamic models; continuous data*

### ABSTRACT

Since decades the development and improvement of methods for the mathematical and statistical analysis of deformation measurements is a prominent topic within Geodesy, Surveying and Photogrammetry. But I have seen in several projects that the responsible people lose sight of framework conditions for setting-up a reliable monitoring project. Therefore I try to present some basic parameters, starting with a priori knowledge on the behaviour of the monitoring object, the importance of a stable geodetic datum, the possibility always to use most-modern equipment to determine the object geometry, *i.e.* to change the equipment, if necessary. These framework conditions allows us to avoid well-known problems, to overcome existing limitations and to strengthen the potential of our profession in this monitoring area. In the central section the classical concepts and strategies for deformation analysis are outlined, *i.e.* a comprehensive summary of the well-established rigorous and approximate methods are given in theory and with practical examples. Alternative and modern analysis concepts are summarized, but they are presented in the further papers of this mini-symposium. Finally some considerations are made related to kinematic and dynamic models and the transfer from epochal to continuous data in monitoring projects. This paper should serve as introduction to the mini-symposium on “advanced methods for analysis of deformation measurements”.

### I. INTRODUCTION

Deformation Monitoring is an emerging methodology for scientists and practitioners in many areas of Geodesy, Surveying and Photogrammetry. Nowadays for our profession it is necessary to manage monitoring tasks adequately and to fulfill the demands for a lot of different monitoring problems.

Our profession is in open competition with other disciplines in this area and we have to convince contracting bodies or customers that we will solve the problems in an optimal way. To do so several framework conditions have to be fulfilled and our competences have to be on a high level.

#### A. Deformation, displacement, deteriorations and change detection

Following a discussion during the FIG Working Week 2021, it seems to be necessary to clarify some terms, used in relation to deformation studies. We have to differentiate between *deformation*, *displacement*, *deterioration* and *change detection* to avoid any misunderstanding and to be a competent partner for neighboring disciplines.

As depicted in Figure 1 in general one can differentiate between relative and absolute deformations for structures quite simple.

*Relative or intrinsic deformations* are changes of the form of and/or tension within an object, often observed at specific/critical points at the structure. In most cases

here continuous physical sensors are applied, often managed by structural engineers. If the critical sections have open access, optical sensors can be applied, too. As mechanical models of structural engineers often just cover the object itself, these professionals primarily look at this type of information.

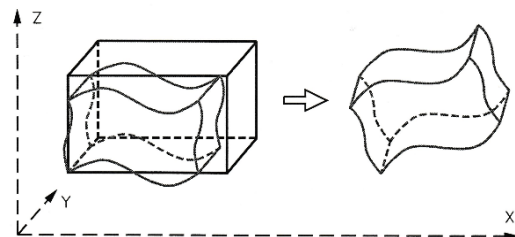


Figure 1. Differentiate between intrinsic deformations and absolute displacements of a body.

The main focus of geodetic sensors is related to *absolute deformations*, *i.e.* to 3D-position changes of an object in relation to its surrounding. If the internal form changes are not in the focus of these studies, one could use the term *absolute displacements*, instead.

Of the selection of points, representing the object, see Section III, allows us to determine relative *and* absolute deformations of the surface of structures.

A third group of displacements are related to building *deterioration*, *e.g.* of historical buildings but also of concrete structures, like bridges and cooling towers, see Figure 2. This flaking of a concrete surface or crushing of edges of masonry or in general material loss

cannot be covered by the classical definition of deformations.



Figure 2. Concrete structures, where deteriorations are critical.

Techniques, based on discrete points, are not suited to determine these deteriorations! Here area-based techniques, like laser scanning or ground based SAR systems have to be applied. Methods to analyze the geometry changes of such objects are not fully developed, yet.

To avoid any misunderstanding, we have to separate the before mentioned effects against *change detection*. In remote sensing the term change detection normally is used as the process of identifying differences in the state of an object or phenomenon by observing it at different times. This process is usually applied to earth observation projects, but can be applied to any structure or building, as well.

In my understanding *change detection* is a *yes-or-no-decision*, which is derived from multitemporal images. In Figure 3 this problem is outlined in a simple way. The pixel-values of two images are subtracted to identify the found differences.



Figure 3. Image Algebra Change Detection: Substraction of pixel-values of two images to identify the differences (FIS, Uni Bonn).

#### B. Point related to area oriented monitoring

The classical paradigm of geodetic monitoring is the approximation of the object under discussion by an adequate number of discrete points, normally realized by well-defined physical marks attached to the surface. Of course, for sensors like total stations, levelling and GNSS the exact relation between the origin of the sensor and these physical marks is necessary.

Within this concept, depicted in Figure 4, the study object is approximated by a quantity of points, which have to be sufficient in number and selected carefully to cover all critical areas, see Section III. For these points the displacements are determined in two or more epochs and then - in a final and really important step -

the deformation pattern of the complete study area has to be derived.

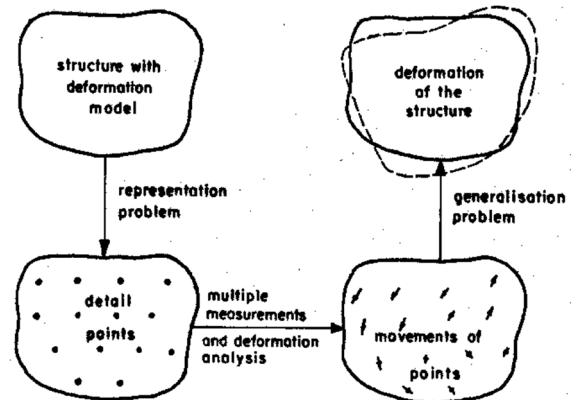


Figure 4. Classical point concept for deformation studies.

Actual developments of theodolite-based so-called *multi stations* make it possible to avoid physical marks. They capture laser scanner data and image data with the same instrument. Both data sets are merged: The scan data are sensitive to distance variations inline of sight, while object movements perpendicular to this viewing direction can be detected by the image data. This allows to define a point not by a manually attached mark, but by structural correspondence at the surface of an object, see Figure 5. The identified point can serve as regular monitoring point in both epochs.

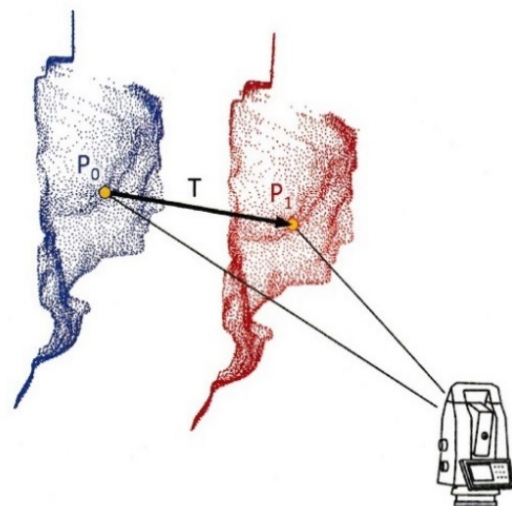


Figure 5. In structure matching of the point cloud between two epochs (blue and red) (Wunderlich et.al, 2020).

Coming to the application of modern sensors, like Laser scanners, InSAR, GBSAR, the surface of an objects is captured by a huge amount of points. But here the surface is scanned in some regular pattern, independent of surface structure and areas of interest, see Figure 6. A defined point, which can be reobserved in a second epoch, does not exist!

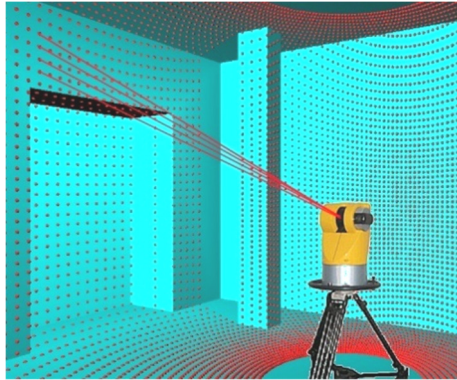


Figure 6. Regular pattern of undefined laser scanning points at a regular surface.

In Section V C concepts are presented to apply classical congruency tests to these area-oriented capturing methods, as well.

## II. MONITORING OBJECTS

In this section the focus is laid on typical monitoring objects resp. problems to identify, why and under which conditions our profession can participate.

### A. Engineering structures

The monitoring of large engineering structures is the classical sample for monitoring in engineering surveying. The classical two-step network set-up for these tasks is given in Figure 7. The advantage of geodetic monitoring is the ability to derive absolute displacements and this requires reference stations outside the structure itself. Typical structures are dams, bridges, tunnels, high rise buildings, harbour cays, but also linear infrastructure objects, like traffic and energy systems.

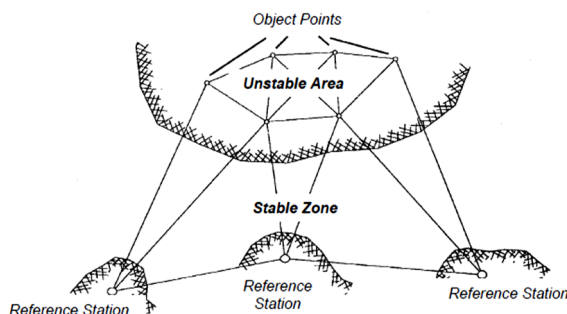


Figure 7. Typical two-step network design with object points to represent the structure and reference stations.

Here a close cooperation with people from civil engineering, structural analysis, rock mechanics and business administration is necessary. The outcome of our monitoring has to have an additional value for the safety and management of the structure.

We have to differentiate between monitoring tasks *during construction*, i.e. for jobs associated with the so-called observation method (EC7) and tasks *after completion of a building*, i.e. to study the behaviour of

structures for years or decades, to guarantee the functionality and safety during the operation phase.

Our classical field are the long-term tasks, and most observation and analysis methods are oriented to these tasks, but due to advanced sensors and almost online processing and analysis we can realize substantial projects for the monitoring during construction, as well.

### B. Sections of the Earth surface

A second group of objects for monitoring are related to local, regional and even larger sections of the earth surface.

Typical monitoring examples are related to natural or artificial slopes, dykes, areas with groundwater withdrawal and mining activities, but as well to tectonic resp. volcanic active areas. In addition, in relation to climate change the study of vertical movements in coastal zones is an important task, too.

For an example as depicted in Figure 8, some a-priori knowledge on the location of the fault is necessary. Then we have to establish a system with sufficient monitoring stations in the surrounding to be able to detect any type of displacement in this area.

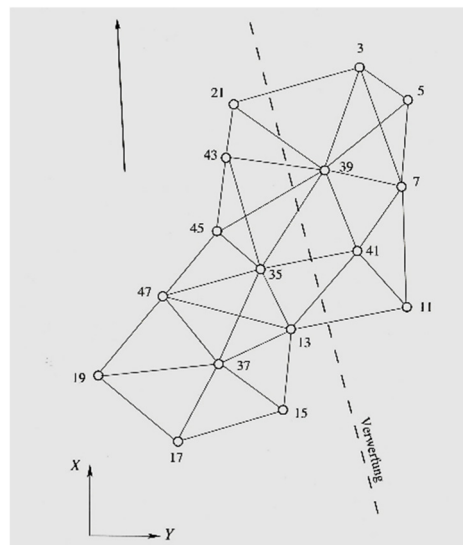


Figure 8. Typical network to monitor specific parts of the earth surface. Sometimes a fracture zone is known.

### C. Industrial objects

A third group of projects for monitoring is related to industrial objects resp. tasks. Typical examples are assembly lines, manufacturing cells, steel beams, quality control of prefabricated industrial parts and radio telescopes.

Each problem requires a specific solution, derived out of the prior information, we have on this problem.

## III. PRIOR INFORMATION

In general the statement hold:

*“No prior information – no adequate monitoring”*

If any professional from Surveying, Geodesy or Photogrammetry is involved in a monitoring project, the first questions during the design phase of a monitoring project are related to the available prior information on the behaviour of an object:

1. What is size/extension of the object?
2. What is sufficient number of monitoring points to approximate the surface or parts of interest?
3. Is separation between deformable body and stable surrounding possible?
4. What is known on expected displacements or internal deformations?
  - Absolute values and critical directions
  - Temporal development of deformations, just as a function of time or of specified external forces?
5. Time to compute the deformation rates: online or offline solutions?

All this information is necessary to set-up a monitoring system, to select the sensors resp. equipment, to design the network with reference to stable areas and to develop the processing and analysis chain.

But often this information is hard to get from the customer. In discussions with civil or structural engineers or with geoscientists, we have to find out, what is known on all the parameters, listed above. Best for this discussion is competence in those areas, *i.e.* at least some knowledge on the thinking and strategies of neighboring disciplines.

Sometimes it helps to set-up more than one monitoring concept, *i.e.* to explain, which effort is required for which results. In any case the prior-knowledge on the monitoring project has to be formulated, to avoid later misunderstandings.

#### IV. SET-UP OF MONITORING SYSTEM

Nowadays we have a huge amount of sensors that can be and are used in monitoring projects. With solid prior information we can select the optimal sensor or combination of sensors to determine geometric changes of the object under discussion. For long-term projects we have to be aware that technology is changing and in some years different sensors exist!

##### A. Network set-up

For most applications the establishment of a monitoring network is the right choice, see Figures 7 and 8. That means, a number of points/stations are positioned on the monitoring object itself, while a number of external reference stations allows to derive the displacements of the object in an almost absolute manner, *i.e.* relative to the outer world. Here well-known aspects from network theory have to be applied, *e.g.* network optimization in respect to precision and reliability. In addition, the sensitivity of a network to be

able to detect the requested displacements, is an important aspect.

##### B. Datum problem

A further problem, often difficult to solve, is the establishment of a *stable geodetic datum*. Most of our sensors give relative information, *i.e.* distances and angles between From- and To- stations or height differences between benchmarks. The same is valid for Laser scanning and GBSAR, the derived information is related to the position of the instrument setup.

For GNSS some people believe that the datum is given by precise ephemeris and by the ITRS and that this is sufficient as basis for a datum. In Niemeier and Tengen (2022) we explain, why it is better to have a group of ground-based stable reference points, instead.

The challenge is to have - in any case - a sufficient number of stable reference stations, as otherwise the derived displacements are no longer reliable.

As example the monitoring network for a dam in Luxembourg is given in Figure 9, where in total 6 reference stations are set-up to guarantee a sufficient network of reference points and by this a stable datum. Of course, the stability of this group of stations has to be analyzed in a rigorous way, see Section VI.

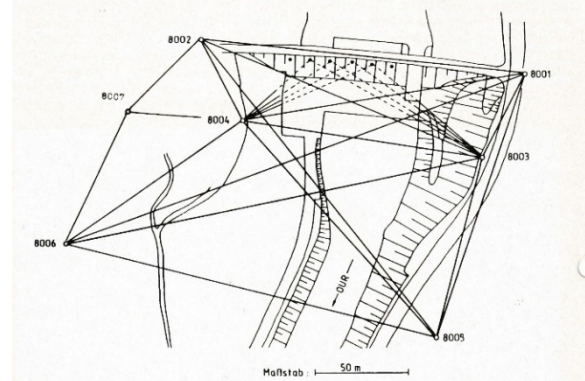


Figure 9. Two-step monitoring network for the Lohmühle dam in Luxembourg.

##### C. Discrete or continuous observations

The adequate *frequency of observation cycles* is responsible for the type of instrument and recording set-up: For taking the observations in epochs/campaigns the normal case is to install instrumental pillars and to position manually the sensors in each campaign via forced centering. The data storage is done by the sensors automatically and after each campaign the processing and analysis of the data is performed.

For permanent installation of sensors and continuous recording the transfer of monitoring data in online modus is the best choice, but not always possible to realize, *e.g.* if power supply is difficult and a radio link is difficult to achieve.

#### D. Prerequisites from practice

Several prerequisites have to be covered by the monitoring approach, before one can claim it to be rigorous and applicable in practice:

- i. The original configuration of points may be different from epoch to epoch, because points are lost and/or added in the course of time.
- ii. For long-lasting monitoring projects the type of geodetic sensors can change: Some decades ago total stations and levelling were the only adequate sensors, later GNSS was included, followed by laser scanning and radar systems. Actually digital images from aircrafts and drones come into play.
- iii. The approach has to be applicable independently of the dimensions of the network, *i.e.* for 1D, 2D or 3D monitoring tasks.
- iv. Nowadays it is often necessary to provide analysis results to the client after each epoch. These results have to be reliable and final, to allow the client to evaluate the stability of the monitoring object.

### V. LONG TERM USABILITY OF MONITORING SYSTEM

#### A. Coordinate approach

As we normally try to apply the most-modern sensors to solve the often sophisticated monitoring tasks, the analysis methodology has to take into account a change of the sensor type and by this in the achievable original or raw information.

This mean that an analysis approach using original observations never could be constructive here, while in specific tasks, esp. in Geophysics, such approaches were used sometimes.

We recommend an intermediate approach based on 1D-, 2D- or 3D-coordinates of stations or surface parameters for area based sensors. Even if some problems occur with this concept, the advantages predominate the shortages by far!

#### B. Datum-Free concept

The next problem has something to do with the effectiveness of geodetic observations to determine form and size of an object. Following Baarda (1968) our observations are very well suited to derive *form and form changes*, but the determination of the absolute size of an object is limited. In elder projects sometimes just one distance observation was made per epoch. Due to limitations of the absolute scale of a distance meter and the atmospheric effects, the determination of absolute size of a network is limited.

To overcome this problem, we recommend always to use the *datum-free approach* (see *e.g.* Niemeier, 2008), *i.e.* to analyze always with maximum number of possible datum parameters and by this to restrict the analysis to form changes. For a pure triangulation the datum defect is 4, in a triangulation or mixed network

we include for distances a scale factor and come up with a datum defect of 4, as well. For GPS-information in 3D-network, being it sets of absolute coordinates or baselines, we would introduce 3 orientation parameters and 1 scale factor.

By this datum-free approach we are able to combine all types of information, coming from traditional or most modern sensors!

#### C. Datum-free concept

As mentioned before, nowadays new sensors and methods for data capture come into consideration, most of them give unstructured, area-based data, as depicted in Figures 6 and 10 for laser scanning.



Figure 10. Segmentation of laser scanner data to define specific surface elements of a bridge (Wunderlich *et al.*, 2016).

One possible solution (Wunderlich *et al.*, 2016) is to use segmentation algorithms for the laser scanner raw data to define specific surface elements and then to approximate these surfaces by parameters.

This allows to use the classical congruency tests to derive significant changes of these surfaces between epochs.

### VI. DATA AND MODEL DRIVEN ANALYSIS

#### A. Data driven analysis

Normally, in our profession we restrict ourselves to the data that are directly available to us, *i.e.* our own observations resp. results. With proper knowledge and processing of our sensor data we come up with precise and reliable results for each new observation epoch.

Any advanced analysis based on just these data has to be restricted to simple models, *e.g.* just linear deformations, which are called kinematic models, see Heunecke *et al.* (2013).

Of course, during the design phase we use knowledge on the possible behavior of the monitoring object to select adequate points, sensors and critical values for displacements.

However, as long as we do not include a geological or physical model on possible displacements, we remain with a data driven analysis.

#### B. Model driven analysis

An extension of this concept is the inclusion of prior information into the analysis approach itself. For most monitored objects some physical model exists.

For engineering structures such a model may consist of knowledge about the behavior during the consolidation phase of a foundation, which normally is given by a consolidation function. Alternatively, a mechanical model for the behavior of a structure may have been derived during the design phase, e.g. a model of the bending of a dam due to the actual water level.

For monitoring of sections of the earth's surface this prior information may consist of knowledge about the existence of active tectonic fissures, the boundary of a landslide effected area or current underground mining activities.

In general, these behavior models do not have the same level of confidence as our geodetic results. They are based on well-founded assumptions or derived from theoretical considerations, but they are not severely tested for a realized project.

Such a model has to contain information on aspects, that are listed in Section III as prior information.

Different methodologies exist to treat prior information. In Section VIII the Dutch concept is outlined to use prior information to setup alternative hypotheses. The validity of these hypotheses can be checked by the adequate tests.

## VII. CLASSICAL CONGRUENCY TEST

### A. Starting information

This standard procedure for deformation analysis was developed by Pelzer (1971), applying the variance analysis method, developed by Scheffé.

This testing method is based on the *coordinate approach*, as introduce in Section V, as it is the most flexible method and allows for a good interpretation of the displacements and geometry of an object.

The coordinate approach requires that, as a first step, for each individual epoch a set of coordinates  $X_i$  and covariance matrices  $\Sigma_{xixi}$  is determined by a least squares adjustment. This set has to include both object points and reference points.

For geodetic professionals it is clear that these adjustments have to be carried out according to adjustment theory and principles, e.g. outliers are detected and by variance-component estimation all is applied properly.

As starting point for this paper we have for a series of epochs  $t_1, t_2, \dots, t_k$  as starting information (Eq. 1):

$$\begin{array}{l} \text{Epoch } t_1: \quad \hat{X}_1, \hat{\sigma}_{01}^2, Q_{x1x1}, f_1 \\ \text{Epoch } t_2: \quad \hat{X}_2, \hat{\sigma}_{02}^2, Q_{x2x2}, f_2 \\ \vdots \\ \text{Epoch } t_k: \quad \hat{X}_k, \hat{\sigma}_{0k}^2, Q_{xkxk}, f_k \end{array} \quad (1)$$

Here the covariance matrices  $\Sigma_{xixi}$  are split up into cofactor matrices  $Q_{xixi}$  and variance factors  $\sigma_{0i}^2$  (Eq. 2):

$$\Sigma_{xixi} = \sigma_{0i}^2 Q_{xixi} \quad (2)$$

This split up allows for testing the *basic hypothesis* of deformation studies: All quantities  $\hat{\sigma}_{0i}^2$ , derived with  $f_i$  degrees of freedom, have to be estimates of the same theoretical variance factor  $\sigma_0^2$ . Additionally, it allows to use theoretical as well as empirical estimates for  $\sigma_0^2$  within the analysis.

As starting point we include **all** points of the monitoring network into the analysis, coordinate estimates for all points have to be considered, leading, in general, to a singular adjustment model and by this to singular cofactor matrices  $Q_{xixi}$ .

For two-step networks the analysis is separated in two steps, as well: At first the group of reference stations is tested on stability, then the group of object points is analysed, where the displacement vectors have to be related just to the subset of stable reference stations.

### B. Global congruency test for two epochs

As a first step one can restrict the statistical analysis to the classical *congruency problem*, i.e. to the question, whether or not statistically significant deviations exist between the geometry of networks in epochs  $t_1$  and  $t_2$ .

The term *congruency test* was introduced by Niemeier (1981), following the general definition that congruency means the quality of correspondence.

Rigorous and approximate approaches for this classical deformation analysis problem can be found in Pelzer (1971; 1985), Niemeier (1979; 1981; 2008), Chrzanowski *et al.* (1981), Heunecke *et al.* (2013), Lösler *et al.* (2017) and elsewhere.

With reference to Figure 11 a rigorous congruency analysis answers the question, whether or not the deviations between the geometric locations of points are caused by real displacements or are just the effect of uncertainties of the observations, i.e. lay within the unavoidable uncertainty level of the networks under consideration; i.e. the level of correspondence is tested.

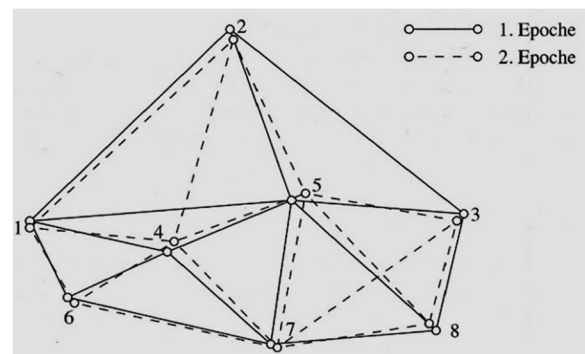


Figure 11. Principle of congruency analysis (Niemeier, 2008).

For simplicity, here we assume that the number of points is identical in all epochs and both epochs are adjusted within the same S-System (see: Baarda, 1968).

The *zero-hypothesis*  $H_0$  of this global congruency test is given by (Eq. 3)



$$H_0: E(\hat{X}_1) = E(\hat{X}_2) , \quad (3)$$

i.e. under  $H_0$  the statistical expectation  $E(\cdot)$  of the coordinate estimates of both epochs are equal.

The common *alternative hypothesis*  $H_A$  is (Eq. 4):

$$H_A: E(\hat{X}_1) \neq E(\hat{X}_2) , \quad (4)$$

what means that there are significant differences between the epochs, if  $H_A$  holds. Normally nothing more is specified for a congruency test.

As a first step for the testing procedure itself the difference vector  $d$  is computed (Eq. 5)

$$d = X_2 - X_1 \quad (5)$$

The corresponding covariance information for this difference vector  $d$  is (Eq. 6):

$$Q_d = Q_{x2x2} + Q_{x1x1} \quad (6)$$

The basic test statistic for this global congruency test is given by the ratio, see Niemeier (2008) (Eq. 7):

$$F = \frac{d^t Q_d^+ d}{\sigma_0^2 h} \quad (7)$$

where the “+” indicates the pseudo-inverse,  $t$  indicates the transposed vector, and  $h$  is the rank of the cofactor matrix  $Q_d$ . Other generalized inverses can be used here, but the pseudoinverse makes it clear that all points are included into the analysis.

**Remark:** In a two-step network at first the group of reference stations is considered. This requires to transfer the datum on this group, see Niemeier (2008).

If this empirical quantity  $F$  exceeds the 95% quantile of the statistical F-distribution with  $h$  and  $\infty$  degrees of freedom, the coordinate estimates between the epochs 1 and 2 differ statistically significantly.

**Remark:** Especially the use of the theoretical variance factor  $\sigma_0^2$  is discussed: Several authors recommend to use a combined empirical estimate  $\hat{\sigma}_0^2$ , instead, to account for the empirical situation more adequately.

### C. Localisation of points with significant movements

The next step of a complete congruency analysis is the *localization* of significant movements for individual points, see Niemeier (2008).

The principle of this *successive elimination approach* is depicted in Figure 12. The concept of the global congruency test is maintained, here applied to a subset of point, where in each step one of the original points is eliminated. In the computational realization, e.g. with the software package PANDA (www.geotec-gmbh.de), this elimination is done by relating the network

geometry successively to each subset of points by datum transformation.

This principle to eliminate in each localization step one individual point, corresponds to the global test in the equation. In Figure 12 this elimination of points 2 and 8 and its corresponding test statistics are depicted. The individual point, that has led to the major reduction, is considered as having significant movements!

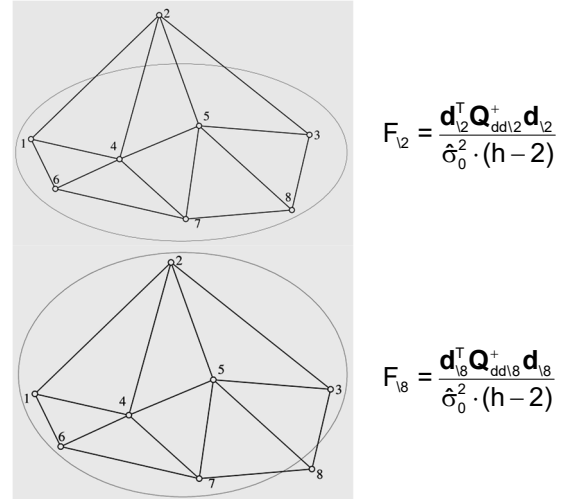


Figure 12. Localisation procedure: Successive elimination of individual points.

**Remark:** Several approaches exist, which can be used for localization of individual points, groups of points or even coordinate components. The here presented method is straightforward and is proven to be statistically correct.

The subset of points, which reduces the primary value of  $F$  in Equation 7 most, is maintained for the next analysis cycle, where the same procedure is applied to the remaining points. If after several cycles the test statistics  $F$  finally falls below the critical value, the procedure stops and all remaining points can be considered as being stable.

## VIII. FURTHER DEVELOPMENTS

### A. Sequential multi-epoch analysis

The starting model for the congruency analysis of  $k$  epochs is given in Niemeier (1979; 1981; 2008) as (Eq. 8):

$$\begin{bmatrix} l_1 \\ l_2 \\ \vdots \\ l_k \end{bmatrix} + \begin{bmatrix} v_1 \\ v_2 \\ \vdots \\ v_k \end{bmatrix} = \begin{bmatrix} A_{11} & 0 & 0 & 0 \\ 0 & A_{22} & 0 & 0 \\ 0 & 0 & \ddots & 0 \\ 0 & 0 & 0 & A_{kk} \end{bmatrix} \begin{bmatrix} \hat{x}_1 \\ \hat{x}_2 \\ \vdots \\ \hat{x}_k \end{bmatrix} \quad (8)$$

This equation considers the normal situation within an adjustment that one has to linearize the functional model, leading to the incremental observation vectors  $l_i$ , the residual vectors  $v_i$ , the design matrices  $A_{ii}$  and the incremental coordinate estimates  $\hat{x}_i$ . Here no functional relations between the epochs are included; each epoch in itself can be adjusted and pre-analyzed.

The corresponding stochastic model is given by (Eq. 9):

$$\Sigma_{uu} = \sigma_0^2 Q_{uu} = \sigma_0^2 \begin{bmatrix} Q_{11} & 0 & 0 & 0 \\ 0 & Q_{22} & 0 & 0 \\ 0 & 0 & \ddots & 0 \\ 0 & 0 & 0 & Q_{kk} \end{bmatrix} \quad (9)$$

In this stochastic model no correlations between the epochs exist, *i.e.* no remaining effects from non-modelled atmospheric conditions are considered. More complete concepts may include these correlations, but this is without the scope of this paper.

A common approach to handle k measuring epochs is repeated application of two-epoch congruency tests. The possible two strategies of Table 1 can be followed.

Table 1. Strategies for a sequential multi-epoch analysis:

Congruency tests for consecutive epochs	Congruency test of each epoch against epoch 1
1 - 2	1 - 2
2 - 3	1 - 3
...	...
k-1 - k	1- k

An important aspect here is the existence of a sufficiently large group of stable reference points during the complete monitoring project. For two-dimensional networks from our practice we consider to have at least 4 stable reference points over all epochs!

#### B. Hypothesis constrained multi-epoch analysis

As mentioned above, one possibility to deal with prior information is to use hypotheses that account for the available displacement models. By this concept it is possible to test several alternative hypotheses, corresponding to various behavior models.

These hypotheses constrain the adjustment model for two or several epochs (Velsink ,2018; Niemeier and Velsinck, 2019).

#### C. Clustering

A promising concept for further analysis is clustering, which allows to identify automatically groups of points with similar behavior. Fletling (2010) has applied this method to the famous simulated test net Delft, given already in Figure 8. Classification was done by using formal criteria of displacement vectors:

- Length
- Azimuth

As result Fleting (2010) could differentiate between 3 clusters, as given in Figure 13. The fault line, assumed to split-up the study area, came out clearly, the lower subset of the left point group was not no obvious in other studies.

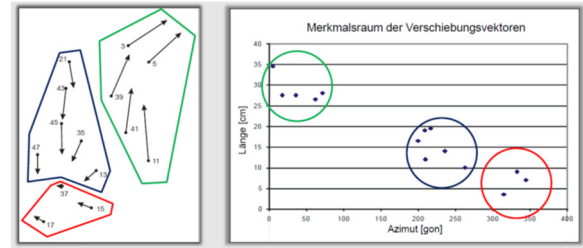


Figure 13. Results of clustering to test network Delft (Figure 8).

#### D. Advanced concepts

During this symposium various general and specific concepts and methods will be presented, that give the state-of-the-art in deformation studies, the details can be found there.

### IX. CONCLUSION

The *global congruency test* is established standard procedure in deformation analysis, as it is applicable for networks with variations in the configuration and changes of sensor types.

It is important to consider the here outlined and discussed prerequisites in any application. Otherwise no reliable results can be achieved.

The analysis of deformation measurements is within the focus of our discipline since decades, but future research and development is necessary to fulfill the requirements of the modern world.

### References

- Baarda W. (1968): A testing procedure for use in geodetic networks. *Neth. Geod. Comm. Vol.2, No. 2*
- Chrzanowski A., Kok J.J., Niemeier W., Pelzer H., Heck B., Baumer R., and Welsch W. (1981). A Comparison of Different Approaches into the Analysis of Deformation Measurements. *XVI. FIG-Kongreß, Montreux, No. 602.3*
- Fletling, R. (2010): Methodische Ansätze zur unscharfen Mustererkennung bei Deformationsmessergebnissen. *Geodätische Schriftenreihe, TU Braunschweig, Heft 27.*
- Heunecke O., Kuhlmann H., Welsch W., Eichhorn A., and Neuner H. (2013): Auswertung geodätischer Überwachungs-messungen. *2nd Edition, Wichmann Verlag, 688 p.*
- Lösler M., Eschelbach C., and Haas R. (2017). Kongruenzanalyse auf der Basis originärer Beobachtungen. *Zeitschrift für Vermessungswesen, 142 Jg., Heft 1, S. , pp. 41-52*
- Niemeier W. (1979). Zur Kongruenz mehrfach beobachteter geodätischer Netze. *Wiss. Arbeiten Geod. Inst. Universität Hannover, Nr. 88, 127 p.*
- Niemeier W. (1981). Statistical Tests for Detecting Movements in Repeatedly Measured Geodetic Networks. *Tectonophysics, vol 71, pp. 335-351*
- Niemeier, W. (2008). Ausgleichsrechnung. Statistische Auswertemethoden, *2nd Edition. de Gruyter, Berlin, 508 p.*
- Niemeier W., and Velsink H. (2019): Strategies and Methods for Multi-Epoch Deformation Analysis based on Geodetic Networks. *4<sup>th</sup> JISDM 2019, Athens*

- Niemeier W., and Tengen D. (2022): Dynamic concepts to handle geodetic networks with continuous data in areas with ground movements. *5<sup>th</sup> JISDM Valencia, 2022*
- Pelzer H. (1971). Zur Analyse geodätischer Deformationsmessungen. *Deutsche Geod. Komm., Series C, Nr. 164*
- Pelzer H. (Editor, 1985). Geodätische Netze II, *Wittwer Verlag, Stuttgart*, 846 p.
- Velsink, H. (2018). Testing Methods for Adjustment Models with Constraints. *J. of Surveying Engineering*. Vol 144, No. 4
- Wunderlich Th., Niemeier W., Wujanz D., Holst C., Neitzel F., and Kuhlmann H. (2016): Areal Deformation Analysis from TLS Point Clouds – The Challenge. *AVN, vol. 123, pp 11-22*
- Wunderlich, Th., Raffl, L.; and Wiedemann, W. (2020): Creating Identities - Two Solutions for Rigorous Deformation Analysis of Areal Observations. *AVN, vol. 127 (2)*

## Deformation Analysis with Feature Voting

Omer Bar, Gilad Even-Tzur

Technion, Geo-Information and Geodesy, Haifa 3200003, Israel, ([omerbar@campus.technion.ac.il](mailto:omerbar@campus.technion.ac.il);  
[eventzur@technion.ac.il](mailto:eventzur@technion.ac.il))

**Key words:** *GNSS; monitor network; deformation; feature voting*

### ABSTRACT

Deformation analysis of GNSS network is usually computed using precise coordinates of the monitoring network points. Coordinates change over time construct a velocity field, which is used to estimate fault model parameters. Estimation process of coordinates is affected by several factors such as measurement errors, datum definition and the measurements datum defect. Points defining the monitoring datum have position accuracies which can increase inaccuracies in velocity estimations and the datum defect could cause biases and instability in computing the velocity field. This research proposes an algorithm of estimating geometric fault parameters using feature voting – addressing changes over time in GNSS vectors. The algorithm selects best solution for specific data-sets using minimal squared-disclosure between data and a tested value set of the fault model parameters. We concentrate on geometric fault models which rely solely on geometry between fault-line and monitoring network points. Geometric fault models are ill-conditioned, combined with low-frequency nature data - numerical instability rises. Vectors were computed with scientific processing software (Bernese), with consistent processing parameters at all epochs. Additionally, several numerical processes were adopted to transform the low-frequency data into usable datasets. Test cases were based upon 8 northern sites in the Israel's continuous operating permanent stations. Simulative data was created from a true solved epoch; then variety of epoch data-sets were introduced to the algorithm to compute pre-defined geometric fault model parameters. Test cases show that simulative data, without and with noises, introduced to the algorithm is suited for estimating model parameters properly.

### I. INTRODUCTION

For the last twenty years researchers use precise GNSS networks to monitor deformation the earth's crust. Investigating the position of control points over time yield insights into the type and nature of crustal movements and help evaluating the deformation model. These monitoring networks consist of control points with precise coordinates measured over time, computed and adjusted independently per epoch. These precise coordinates as a function of time produce a precise velocity field which is used while estimating fault model parameters, using least square adjustment (Even-Tzur, 2001; Vogel and Van Mierlo, 1994; Ostrovsky, 2005; Nocquet *et al.*, 2002).

Precise coordinates are very useful in estimating deformation, they are easily determined by different GNSS techniques, over small or vast areas. Changes in coordinates over time, directly derive the relative deformation between a set of control points internally and relatively to a specific datum. Scientific GNSS processing software, such as GAMIT (Herring *et al.*, 2018) and Bernese (Dach *et al.*, 2015), are frequently operated to compute precise coordinates from GNSS measurements. These scientific software handles a vast amount of error-factors to precisely estimate coordinates. These error-factors are based on known physical phenomena models, and their residuals are being introduced into the computational process.

Precise coordinates and their Variance-Covariance matrix, are affected of numerous error-factors, such as: Measurement-Datum defect, gross measurement errors and random errors. Estimating coordinates of points embeds the Measurement-Datum defect, although it might cause biases in the estimation process. Monitoring network control points and their precise coordinates endure these biases as well - hence there is a need for a stable monitoring-datum. Sometimes obtaining a stable monitoring-datum is not possible to define, for not detecting a subset of monitoring network points that remain relatively fixed over time under a pre-decided significance level. Additionally, errors are gained and inaccuracies rise while relying on un-modeled and un-deducted movements of the monitoring-datum points (Even-Tzur, 2013; Papo and Perlmutter, 1981).

Fault models define surface movements caused by tectonic movement (Cohen, 1999). The models consider numerous factors that causes ground movements, such as – pressure, temperature, soil types and their fraction rates, etc. Geometrical fault models describe the geometric relativity between the fault-line and a point position from it. This relation, for example, can be expressed using some attributes, such as - perpendicular distance from the fault, lock and slip depths, fault slip velocity etc.

These geometrical fault-models are nonlinear ill-conditioned equations. Ill-condition equations show big

errors in output while input consist of small errors. This is a numerical nonstable form of equations, which needs treatment for a stable process of computation (Tikhonov and Arsenin, 1977).

## II. FEATURE VOTING TECHNIQUE

### A. Feature Voting

Feature voting (Boiangiu and Radu, 2003) methodology determines model parameters values while reversing the roles between input data and estimated parameters. For a pre-defined model, for each parameter, numerous values are spanned; each value-set input is tested with the input dataset – if they are compatible (such as residual is under a certain threshold) – a vote is listed for that specific value-set. Usually, tracking the voting is carried out via a voting-matrix, each dimension is logically connected to a parameter and each index to a specific pre-defined value.

Hough transformation, as a common tool for line-extraction from images in Computer Vision, utilizes feature voting technique (Duda and Hart, 1972). Input data are pixels of detected points-of-interest, and its output are the lines detected from them. A line has only two parameters (even after their transformation to the image representation) hence the voting-matrix has only two dimensions. Analyzing all the maxima instances in the voting-matrix, yields the lines detected in the process.

This paper describes detection and analysis of deformation model parameters methodology, while not relying on precise coordinates. Precise vectors (with a time tag) spanning the monitoring network are the methods input, while previous knowledge, such as fault line azimuth, horizontal slip velocity, locking depth etc. - can be added, but not required. Positions are used with a metric precision, only to establish a geometry between input vectors and the fault.

The suggested algorithm compute fault-model parameters adopting feature-voting technique (Fernandes, and Oliveira, 2008), input are vectors computed in several epochs within the monitoring network, with their error estimates. The vectors are computed using a scientific GNSS post-processing software, campaigns processed utilizes same error-models and processing parameters for all epochs; this to ensure same vector solution (or processing type) at all epochs – that sets a single "solution datum" for the vectors. Using vectors from different "solution datums" will cause biases in the parameters values estimation.

Another difficulty is related to the nature of the input dataset (solved vectors), it is a "low frequency" dataset – *i.e.* a small finite amount of vectors to be processed. partially coping with this issue, all vectors in the monitoring networks are being computed - and not only the independent ones. Furthermore, all possible epoch differences are taken into considerations – which as

well enlarges the data size. Hence, more geometrical relations are available for the voting technique.

The vectors error estimates assist in computing the threshold of the matching criteria. For example, an error estimate of 1 cm per direction on all vectors (at all epochs) could yield a velocity of  $\sqrt{2}$  cm over time – or larger. Using this concept, maximal horizontal vector velocity error value can be determined and utilized as the minimal span between tested velocity values.

### B. Modifications for Geometric Fault Models

Feature voting for a geometrical fault model is ambiguous, model equations are point oriented - adaptations are taken to match them to the vector properties. Fault models, and specifically geometrical fault models, describes points velocity affected by a single fault. A vector is a feature assembled between two points, it is necessary to accommodate the model. Furthermore, internal parameters are adapted to cope with internal relativity between the fault-line and the vector points. Point position is replaced with vertical distance to the fault line, hence azimuth and position of the fault are added as needed model parameters.

For example, Equation 1 describes the model of an Infinite long vertical Strike-Slip fault (left locked fault) (Cohen, 1999). This equation describes points velocity with dependency on a function of its geometrical relativity to the fault-line.

$$v_x = \frac{V}{\pi} \tan^{-1} \left( \frac{l}{LD} \right) \quad (1)$$

where  $V$  = the fault slip velocity in mm/year  
 $l$  = perpendicular distance between a point and the fault line  
 $LD$  = Lock depth of the fault-line in kilometers

Perpendicular distance is denoted by the relation between point position and (i) fault-line Azimuth, and (ii) fault locking position.

Fault model equation is modified to meet vectors two nodes – points  $P_1$  and  $P_2$ , as described in Equation 2. The modification is set to the numeric differentiation of the velocities computed on vectors nodes  $v_x^{P_2}$ ;  $v_x^{P_1}$ , with respect to the fault-line parameter value-set, at a single epoch, relying on the original fault model.

$$v_{vector} = v_x^{P_2}(t) - v_x^{P_1}(t) \quad (2)$$

where  $v_x^{P_1}$  = velocity computed on one of the vectors nodes  
 $v_x^{P_2}$  = velocity computed on the second nodes of the vector  
 $t$  = specific epoch time

The velocity for the vectors length is derived from the relative velocity between the two vector nodes.

Multiplication of this vector-velocity in the time span produces the estimated length-change over time (by a set of give values for the fault mode parameters). This methodology is introduced with coordinates that are not precise, and yields computation that corresponds with a specific threshold denoted via cross-validation.

All available vectors with two or more epochs are introduced to the voting process, which enlarges the dataset entering the voting process. Additionally, this helps coping with changes in control points within the monitoring network, for example – a control point is abandoned and a new control point is built instead of it.

### C. Maxima Detection

The voting criteria is described by difference between measured length change in vectors sizes, and the computed change in vector length denoted from a pre-defined fault model and a pre-selected value-set for its parameters. Differences smaller than a selected threshold, denotes a vote to that value-set. All value-sets are being tested for all input vectors, and for each criteria-matching (difference is smaller than the threshold) – the vote is promoted voting-matrix for the selected and tested value-set.

Several maxima can be found in the voting matrix - due to the interval of the parameters values and due to the ill-condition state of the fault model. All votes over a certain significant level (such as vote numeric value is more than 85% of the input vectors), undergo cross-validation computation. The cross-validation is the total squared residuals for each detected maxima value-set, related to all input vectors. For example – in a case of a single fault computation - a maxima value-set is selected with respect to the minimum cross-validation from all detected optional maxima's.

### D. Coping with Low Frequency Data

Input data-set is of low-frequency nature, and the ill-conditioned equation-system is unstable numerically. Enlarging the data-set is possible by replicating input vectors using random noise perturbation with an average of zero – as utilized in Monte-Carlo simulation simulation (Raychaudhuri, 2008). Adding more data with the same trend of the original data, with zero bias and a zero-average random noise, emphasizes the votes for most appropriate value-set and assists in the cross-validation process. Nonetheless, all input is being normalized, to assist overcoming the ill-conditioned state of the fault model.

### E. Initial Values

Initial values can be adopted from other researchers works. Nonetheless, several parameters can be approximated using input data – such as horizontal slip rate, by maximum difference of homological-vectors lengths divided by their time-span. Other parameters should be spread with respect to pre-known physical

attributes – such as, local maximal crust depth for maximal locking depth in a locked fault model.

## III. TEST CASES

Test cases relate to northern area of Israel with eight sites from the Israeli continuous operation reference stations network, assembling the deformation monitoring network for the simulations - gathering a set of 28 vectors. This area, as can be seen in Figure 1, is greatly affected by the Dead-Sea Fault Transform (Reinking *et al.*, 2011). The paper will describe simulations for left Infinite long vertical Strike-Slip fault model. Several simulations resemble the Dead-Sea Fault parameters in the northern Israeli area near the Golan Heights.



Figure 1. Northern Israel with Dead Sea fault simulative fault line (dashed grey) and Survey of Israel CORS sites (blue push-pins).

For the simulations - single epoch was computed with a processing software, and rest of needed measurements epochs were created artificially from it.

### A. Simulative Cases

Synthetic epochs were created by computing the location change to each point, in each epoch, related to the first epoch points coordinates (that was computed using a GNSS processing software) – relying on pre-selected fault model and parameter-values. Since no precise coordinates are in use, each vector was computed a length changes by the position of its end-nodes (point) with respect to the fault-line.

Simulative data cases concluded several stages:

- 1) Two additional epochs without noise added.
- 2) Three additional epochs without noise added.
- 3) Two additional epochs with noise added.
- 4) Three additional epochs with noise added.

The noise added to these test cases is a random normal-distribution and has perturbation nature relatively to the input dataset.

The feature-voting methodology presented returned outputs similar in ratio to the pre-defined fault parameters. Computation process is based on ill-condition equations, hence any tiny truncation and round-off error in the computational process inside the memory - affects the process results. Thus, there is low percentage of absolute accuracy in computed fault parameter values.

Tables 1 and 2 describes the input and outputs of the four cases of the simulations.

Table 1. Simulations results: Known Values

#	Az [°]	Ld [m]	V_Hz [mm/year]	E0 [m]	N0 [m]
1	0.3	12,015	8.2	252,200	760,505
2	0.3	12,015	8.2	252,200	760,505
3	0.3	12,015	8.2	252,200	760,505
4	0.3	12,015	8.2	252,200	760,505

Table 2. Simulations results: Computed Values

#	Az [°]	Ld [m]	V_Hz [mm/year]	E0 [m]	N0 [m]
1	-0.87	11,919	8.1	251,770	747,884
2	0	12,324	8.2	251,902	749,902
3	-0.08	11,900	8.1	251,770	747,885
4	0	12,500	8.3	252,419	775,505

#### B. Discussion and Conclusions

This feature-voting process for evaluating fault parameters has advantages such as (a) changes in the control points of the deformation monitoring network doesn't need any special input manipulation, (b) estimation is not based on precise coordinates – it relies on precise relations between them, (c) copes with gross errors in input – they are eliminated in the voting process while searching for maxima, and (d) geodetic datum and monitoring datum are not set – thus, omitting error-estimates of the coordinates which causes biases in the traditional estimation process of model parameter.

Ill-conditioned state of geometric fault model equations, is taken into consideration in the presented algorithm. Several actions are taken to assist in computing an appropriate value-set for the model parameters such as adding perturbed replicas of the data, normalizing the data and fundamentally use a feature voting technique.

This technique cannot detect rigid body motion, such as full body rotation or translation – due to the fact that there are not internal changes in these cases.

The proposed method can be modified to meet other geometric fault models - such as strike-slip fault models with free slipping or locking in a defined range.

Future research will tackle true data, without constant sites in the input data. Additionally, we will try to describe the estimated error in the output results.

#### IV. ACKNOWLEDGEMENTS

We thank the Survey of Israel in supporting the research and supplying GNSS measurements for it.

#### References

- Boiangiu, C. A., and Radu, I. (2003). Voting-based image segmentation. *The Proceedings of Journal ISOM*, 7.2, pp. 211-220.
- Cohen, S. (1999). Numerical models of crustal deformation in seismic zones. *Advances in Geophysics*, 41, pp. 134-231.
- Dach, R., Lutz, S., Walser, P., and Fridez, P. (2015). *Bernese GNSS Software Version 5.2*. Astronomical Institute, University of Bern. Bern: Bern Open Publishing. DOI: 10.7892/boris.72297
- Duda, R. O., and Hart, P. E. (1972). Use of the Hough Transformation to Detect Lines and Curves in Pictures.. *Communications of the ACM*, 15.1, pp. 11-15
- Even-Tzur, G. (2001). Sensitivity analysis of deformation monitoring networks in the north of Israel. *Israel Journal of Earth Sciences*, 50(1).
- Even-Tzur, G. (2013). Datum Definition for GPS networks. *Survey Review*, 35(277), pp. 475-486.
- Herring, T., King, R., Floyd, M., and McClusky, S. (2018). *GAMIT Reference Manual*. Massachusetts Institute of Technology. Department of Earth, Atmospheric, and Planetary Sciences.
- Fernandes, L. A., and Oliveira, M. M. (2008). Real-time line detection through an improved Hough transform voting scheme. *Pattern recognition*, 41(1), pp. 299-314.
- Nocquet, J. M., Calais, E., And Nicolon, P. (2002). Reference frame activity: Combination of National (RGP) and Regional (REGAL) Permanent Networks Solutions with EUREF-EPN and the ITRF2000. *Proceedings of The EUREF 2002 Symposium*, (pp. 398-404).
- Ostrovsky, E. (2005). *The G1 geodetic-geodynamic network: results of the G1 GPS surveying campaigns in 1996/1997 and 2001/2002*. Survey of Israel, Tel-Aviv, Israel.
- Papo, H., And Perlmutter, A. (1981). Datum definition by free net adjustment. *Bulletin Geodesique*, 55, pp. 218-226.
- Raychaudhuri. (2008). Introduction to Monte Carlo simulation. *WSC '08: Proceedings of the 40th Conference on Winter Simulation*, pp. 91-100. DOI: 10.1109/WSC.2008.4736059.
- Reinking, J., Smit-Philipp, H., and Even-Tzur, G. (2011). Surface deformation along the Carmel Fault System, Israel. *Journal of Geodynamics*, 52, pp. 321-331.
- Tikhonov, A., and Arsenin, V. (1977). *Solutions of Ill-posed Problems*. New York: V. H. Winston and Sons.
- Vogel, M., and Van Mierlo, J. (1994). Deformation analysis of the Kfar-Hanassi network. Haifa: *Perlmutter workshop on dynamic deformation models*, pp. 273-284

## Dynamic monitoring of civil infrastructures with geodetic sensors

Caroline Schönberger, Werner Lienhart, Thomas Moser

Institute of Engineering Geodesy and Measurement Systems, Graz University of Technology, Steyrergasse 30, 8010 Graz, Austria, ([c.schoenberger@tugraz.at](mailto:c.schoenberger@tugraz.at); [werner.lienhart@tugraz.at](mailto:werner.lienhart@tugraz.at); [thomas.moser@tugraz.at](mailto:thomas.moser@tugraz.at))

**Key words:** *dynamic monitoring; global navigation satellite system; robotic total stations, structural health monitoring*

### ABSTRACT

Geodetic sensors are conventionally used for the long-term monitoring of civil structures like bridges, buildings or water dams. With the recorded data the reaction of the structure to slow changing impacts like temperature changes can be observed. However, the reaction due to dynamic impacts like wind loads, traffic loads or earthquakes are usually assessed using non-geodetic sensors like accelerometers. This article discusses how advances in geodetic sensing technology opens up new possibilities. In laboratory tests and on a real footbridge, it is demonstrated that modern total stations and GNSS receivers are well suited for the dynamic monitoring of bridges. It is shown that even small amplitudes in the range of about 1 mm for GNSS and of about 0.2 mm for total stations depending on the distance to the object can be detected.

### I. INTRODUCTION

Monitoring of civil structures can be carried out as static and quasi-static displacement monitoring or by monitoring the dynamic characteristics. For the latter, usually accelerometers are applied on structures to derive its dynamic characteristics induced by wind loads, traffic loads or earthquakes. With advances in geodetic sensing, dynamic responses could also be observed with those sensors (Im *et al.*, 2013).

Global Navigation Satellite Systems (GNSS) are around for more than three decades, and in the recent years dynamic GNSS monitoring for bridges (Moschas and Stiros, 2011), towers (Górski, 2017) and buildings (Yi *et al.*, 2013) where carried out. They show eigenfrequencies below 5 Hz with displacements of 10 – 20 mm.

Advantages of GNSS in structural health monitoring (SHM) are continuous, weather-independent 3D measurements, in real time. Furthermore, no line of sight needs to be established. On the other hand, limitations of accuracy for GNSS measurements are multipath errors, satellite geometry, and a low sampling rate (Shen *et al.*, 2019).

A modern Robotic Total Station (RTS) is able to lock onto a reflector target and follow it automatically (Lienhart *et al.*, 2017). Therefore, a line of sight, as well as a stable total station position are necessary. The inbuilt tilt sensor as well as standard total station features like free stationing allows to monitor the total station position itself.

For deriving the dynamic characteristics, a transformation of the data time series into the frequency domain is needed. Potential approaches are Wavelet Analysis, Fast Fourier Transformation (FFT) or Short Time Fourier Transformation (STFT).

Depending on the data rate, frequencies up to the half of this rate can be derived from this data (Shannon,

1949). Frequencies above this value will be seen as aliasing effect, if they are not filtered out.

This paper will focus on the applicability of GNSS and RTS for dynamic monitoring, its accuracy and limitation, with experiments under controlled laboratory conditions and at a footbridge.

### II. EXPERIMENTS IN LABORATORY SETUP

#### A. GNSS Experiment at rooftop laboratory

The experiment took place at the rooftop laboratory, with very few obstacles to the sky, at TU Graz. A Leica GS18 receiver was setup as a reference on a stable pillar. A Leica GR30 receiver with an AS10 antenna was used as rover. The rover antenna was placed on an APS 400 shaker (Figure 1), which is able to generate controlled oscillations. This experiment covers the vertical acceleration of a frequency range of 1-10 Hz with accelerations from 0.3 to 16 m/s<sup>2</sup>. Both receivers recorded GPS (G), GLONASS (R) and GALILEO (E) signals with a data rate of 20 Hz.



Figure 1. Experiment setup at the rooftop laboratory. Monitoring site with shaker (left), reference site (right).



Additionally, observation data from the Austrian reference network, Austrian Positioning Service (APOS), station GRAZ was used in the analysis. This station is located in around 3 km distance to the laboratory and provides GPS and GLONASS data with 1 Hz.

To compare the results of the GNSS data, the shaker movement was additionally measured very precisely with a laser triangulation sensor (LTS). Its data rate is 312.5 Hz and the data is used as true values.

First, 7.5 minutes of (1) no motion were recorded. Then (2) the shaker was operated in certain frequencies with various amplitude steps, where every frequency-amplitude combination was hold for 50 seconds before starting the next combination. Lastly, (3) a linear sweep from 10 Hz to 0.8 Hz in 2 minutes was carried out.

The data processing chain is shown in Figure 2. The RINEX data of the reference and the rover were processed in postprocessing mode with RTKLIB 2.4.2 (Takasu, 2011) and Leica Infinity 2.4.1 using broadcast ephemeris. On those results an outlier detection using a moving median method (Le Thi, 2021) and a high-pass Chebyshev filter with an edge frequency of 0.05 Hz, to exclude the impact of long-term effects, was applied (Moschas and Stiros, 2011). To transfer the data into the frequency domain an FFT and STFT were carried out.



Figure 2. GNSS data processing chain.

The results in this paper focus on the height component of the data as this is often the most relevant in bridge monitoring.

1) *No Motion*: This data is used to compare combinations of data rate at the reference, used satellite signal, postprocessing program and the use of data from a reference network by comparing its standard deviation.

The data rate of the local reference station was down sampled with GFZRNX (Nischan, 2016) to 1Hz, 5 s and 30 s, which are common intervals for reference network stations and hence possible real time intervals.

A data rate – reference combination was processed with both programs, with only-GPS (G) or GPS and GLONASS (GR) for the APOS reference or GPS, GLONASS and GAL (GRE) for the local reference station.

The standard deviation (STD) of those time series was calculated to quantify the background noise and it is shown in Figure 3.

The best result could be achieved for the local reference with a data rate of 20 Hz and the satellite systems GRE (GRE20Hz). An increased STD could be observed with a reduced reference data rate, especially for multi-GNSS for RTKLIB. For all combinations with a STD of less than 5 mm, RTKLIB results are better.

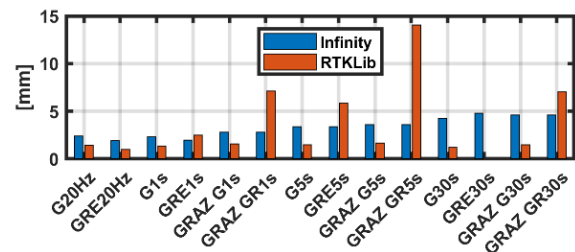


Figure 3. Standard deviation in vertical direction for the time series of no motion.

Calculating an FFT over the GRE20Hz data set, Figure 4, shows noise with a good distribution over the whole frequency domain, and the cut off the low frequencies with the high-pass filter. There is no significant noise on the data recorded by the LTS. Less noise in the RTKLIB results compared to the results from Infinity is clearly visible.

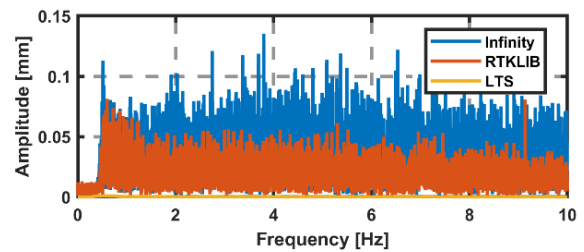


Figure 4. FFT over the no motion part (GRE20Hz) shows noise with a good distribution over the whole frequency domain.

The FFT over the same time period for only GPS and a local reference with a data rate of 5 s (G5s) shows artefacts in the frequency domain, Figure 5. A closer look at a small selection of the time series, Figure 6, show abrupt changes introduced by the reference data rate. The impact of those changes is seen in the frequency domain.

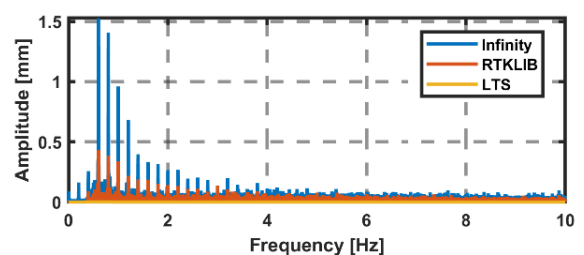


Figure 5. FFT over the no motion part (G5s) shows artefacts in the frequency domain introduced by the reference data rate.

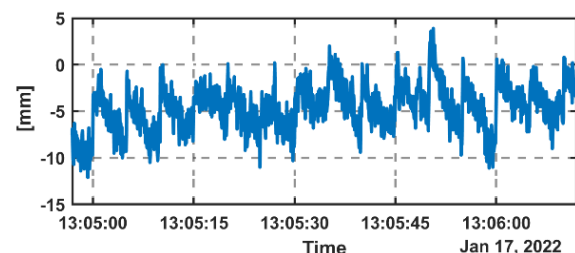


Figure 6. Section of the original time series with a reference data rate of 5 s. Abrupt changes in the data can be seen, which conclude to artefacts in the frequency domain.

Due to the lowest standard deviation in the no motion part and no appearance of unwanted pattern in the frequency domain, the GRE20Hz data set is used for the following research.

2) *Amplitude - frequency steps:* For every frequency-amplitude combination an FFT was calculated. The results of the frequencies: 2 Hz, 5 Hz and 9 Hz are shown in Figure 7, due to a good distribution over the frequency domain.

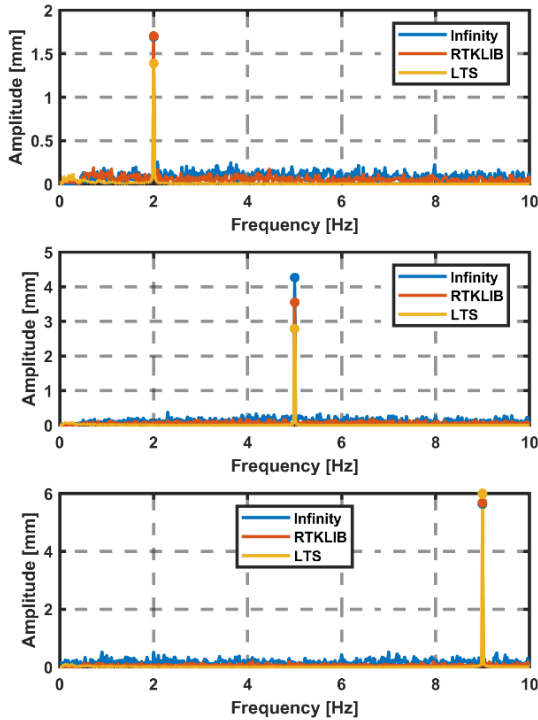


Figure 7. FFTs of GNSS and LTS data over a 50 s period with the frequencies 2 Hz, 5 Hz and 9 Hz.

Calculating the main frequency of the time series works very well for GNSS and LTS measurements. There is a slight difference in the amplitude, especially at 5 Hz. But even amplitudes with less than 2 mm could be calculated well.

3) *Sweep:* Figure 8 shows an FFT over the whole sweep, with the LTS as a reference. All frequencies between 10 Hz and 0.8 Hz could be recorded by the sensors.

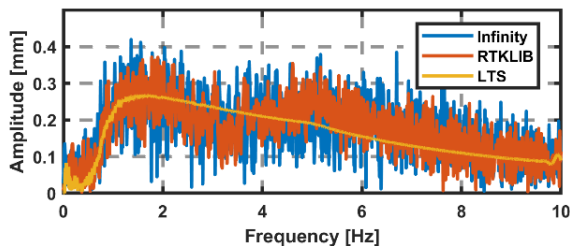


Figure 8. FFT over the whole sweep.

Due to the rapid changes of frequency and amplitude an additional STFT calculated. The block size influences

the time and frequency resolution. A long block, low time resolution, results in a good frequency resolution. For this sweep a block size of 5 s was chosen.

Figure 9 shows a very good frequency calculation for GNSS data for frequencies less than 10 Hz. The amplitude fits the real values well at all frequencies below 2 Hz and over 8 Hz. Between 2 and 8 Hz the amplitude can be too low or too high.

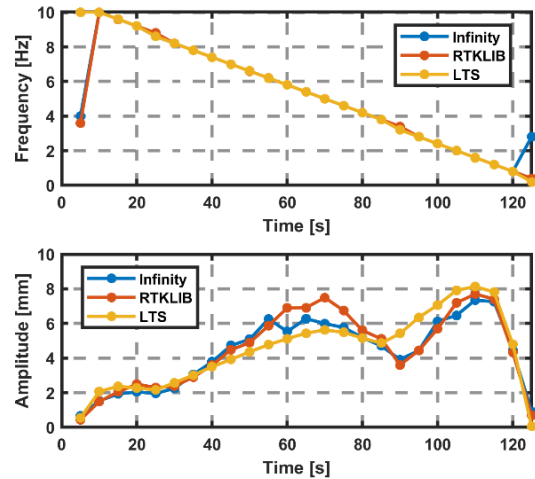


Figure 9. Amplitude and frequency of the sweep over time, calculated with a STFT with block size of 5 s.

### B. Total station experiment at rooftop laboratory

For this study a Leica MS60 was used which is able to carry out dynamic angle measurements with up to 20 Hz and a geometric precision of 3 cc (Leica, 2020).

It is positioned around 25 m from the shaker, on a pillar with a nearly horizontal sighting to the prism, and controlled by a serial GeoCom Interface with Python surrounding. One full static measurement was carried out to receive a reliable slope distance. For the dynamic data gathering only angle measurements are used for more stable time resolution results. The data is processed with MatLab R2018a. For all FFTs the data is filtered through a high - pass filter with a cut-off frequency of 0.5 Hz.

Again, the LTS measurements, but also the data from the acceleration sensors are used as reference data.

1) *No Motion:* Figure 10 shows the time series of a period of time while no active movement occurs. This helps to get an idea of the atmospheric influences on the measurement path.

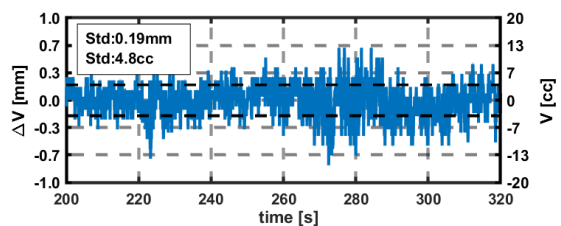


Figure 10. Time series of the RTS while no movement with its standard deviation.

The standard deviation of about 4.8 cc in angle deviation results in an observable movement of about 0.2 mm for the given slope distance of 25.265 m. Smaller movements will be covered by atmospheric noise and therefore are not possible to detect.

2) *Amplitude - frequency steps*: Figure 11 shows FFTs over the same amplitude – frequency combinations as shown in Figure 7.

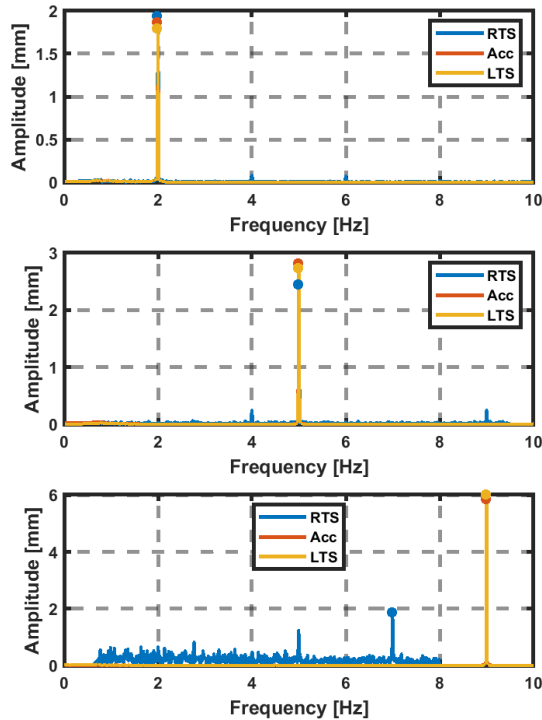


Figure 11. FFTs of RTS, LTS and Acceleration Data over a 50 s period with frequencies 2 Hz, 5 Hz, 9 Hz.

It can be seen, that a frequency of 9 Hz cannot be detected by the RTS. This is due to the fact, that the measurement rate went down to 16 Hz in this time period. Therefore, only frequencies up to 8 Hz can be detected. The drop of the measurement rate seems to be dependent to the ratio of amplitude and frequency of the target. Especially when there are fast direction changes, the RTS has its problems to follow the target. Still, there is a peak at 7 Hz, which is due to the aliasing effect.

Anyways, lower frequencies can be detected flawlessly, as well as the measurement rate goes back up as the movement slows down.

3) *Sweep*: Figure 12 shows an FFT over the whole sweep.

The noise of the RTS is much higher than the noise of other sensors. Still the amplitude and frequency can be detected. Also, the measurement rate stays up to 20 Hz in this experiment, therefore the frequency can be detected up to 10 Hz.

In Figure 13 the time series of the sweep is analysed using a SFTF with a block size of 5 s, equivalent to Figure 9.

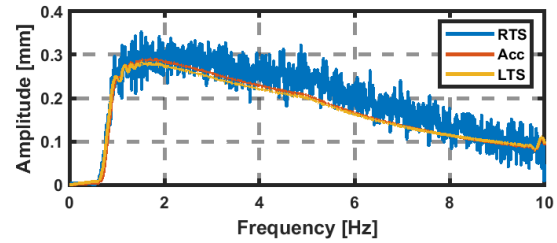


Figure 12. FFT of RTS, LTS and Acceleration Data over the whole sweep.

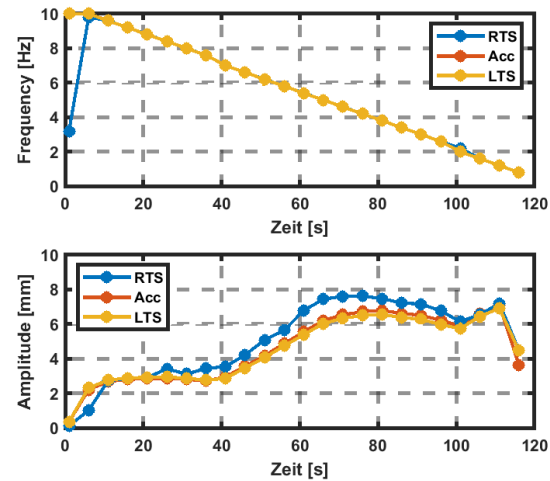


Figure 13. Amplitude and Frequency of the Sweep over time for RTS, LTS and Acceleration sensor, block size 5 s.

The RTS has some problems with following the frequency of 10 Hz, but manages to trace all following frequencies. The amplitude is mostly overshoot by the RTS. This phenomenon increases with increased amplitude, except for very low and very high frequencies. It can be said, that some critical combination of amplitude and frequency can lead to troubles with following the target exactly. This and the drop of the measurement rate at some situations are the main issues of this test.

### III. DYNAMIC MONITORING ON A FOOTBRIDGE

For a real-world test scenario, a nearby public footbridge with a length of around 70 meters was chosen. Different sensorics: GNSS, IMU, accelerometers, prism and image targets were placed on the bridge. The prism was traced by an RTS from a closed by bank and the image target was filmed by a camera from the river bank. Figure 14 shows a schematic representation of the measuring setup and Figure 15 shows a photo taken from the bank.

Around 2 hours of data were recorded including the excitement of the bridge by 15 students jumping over the bridge, 2 people jumping and 1 minutes of no human excitation. The rest was randomly walking people passing by.

#### A. GNSS + IMU

After the very promising results in Section II A, useful results were expected on the footbridge. The Leica

GNSS receiver GR30 with an AS10 Antenna and an IMU (Epson G370N), were mounted in the middle of the bridge, where the highest amplitudes were expected. As a reference a Leica GS18 was located on solid ground. Both receivers recorded GPS, GLONASS and GALILEO signals with a data rate of 20 Hz and the data rate of the IMU was 200 Hz.

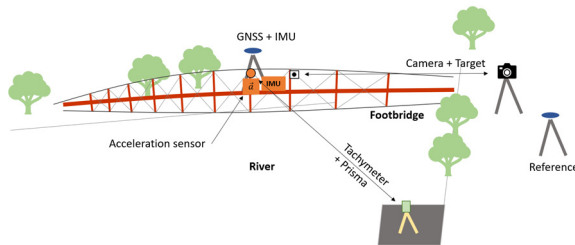


Figure 14. Schematic representation of the measurement setup at a public footbridge in Graz, including GNSS, IMU, RTS, acceleration and camera measurements.



Figure 15. Photo of the measurement setup from the closed by bank, where the RTS was located.

The data processing passed through the same data processing algorithm, as the laboratory experiment.

Figure 16 shows a waterfall plot over the experiment time, where 15 students excited the bridge, with a block size of 5 s, where the frequencies can be found on the ordinate and the amplitudes are color coded. The jumps can be seen clearly with amplitudes of up to 11 mm (bright dots).

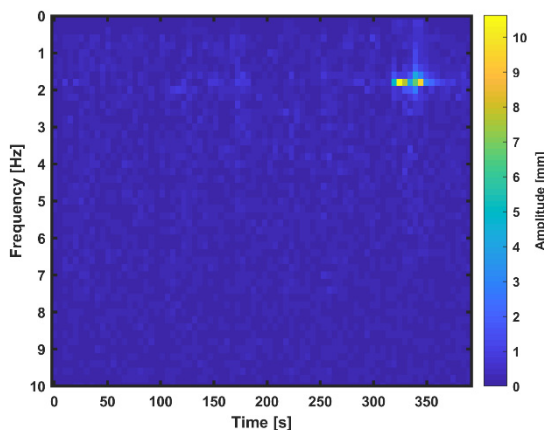


Figure 16. A waterfall diagram over the experiment time of 15 students jumping. The highest amplitudes can be seen around 1.7 Hz, during the time of jumping (320 s - 360 s).

To calculate displacements from the IMU (Z-axis) data, the data was integrated twice. The eigenfrequency of the bridge could be derived via GNSS

data to 1.74 Hz, which is confirmed by the IMU data, with the same result, see Figure 17.

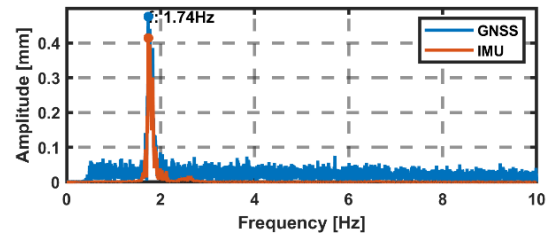


Figure 17. FFT of GNSS and IMU while 15 students jumping on the bridge. For the IMU data a zoom from 1-10 Hz was applied for a better comparison.

Figure 18 shows the amplitudes of the displacement for GNSS and IMU data at the frequency of 1.74 Hz in vertical direction. The jumps can be seen clearly with an amplitude of up to 11 mm.

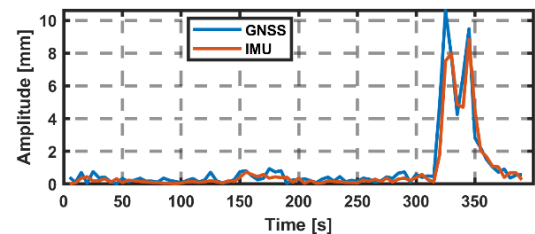


Figure 18. GNSS and IMU Time Series of the amplitude at the derived eigenfrequency of 1.74 Hz.

Both the GNSS and IMU (Z-axis) displacements are very similar and therefore reliable.

Figure 19 shows a waterfall diagram over a 5 minute period where 2 people jumped to excite the bridge. Lower amplitudes compared to the 15 students jumping are expected and it can be seen, that even with amplitudes of around 1 mm the frequencies around 1.7 Hz are dominant. Due to the smaller amplitudes, noise has a bigger impact on the data.

An FFT over this time period still show a main frequency of 1.74 Hz, Figure 20, but the difference between noise and the peak is smaller.

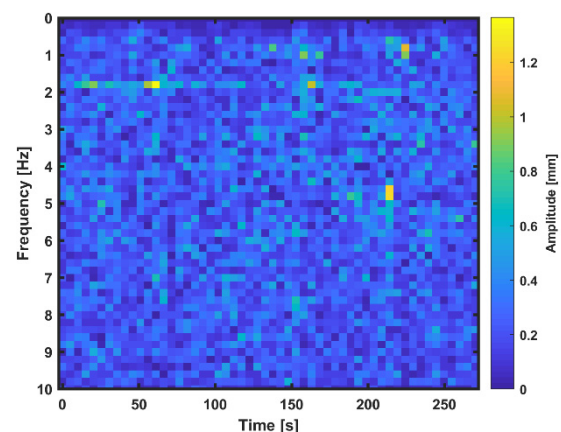


Figure 19. A waterfall diagram over the experiment time of 2 people jumping. Although the amplitudes are below 2 mm, the frequencies around 1.7 Hz are dominant.

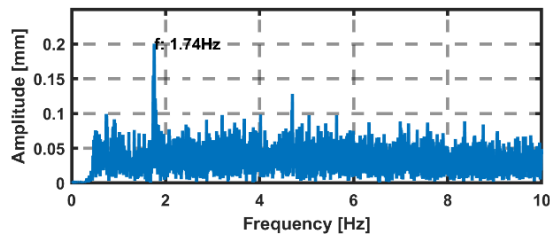


Figure 20. FFT of GNSS while 2 people jumping on the bridge.

Therefore, it can be concluded that even a small excitation, small amplitudes, can be recorded with GNSS and it is a useful technology for dynamic monitoring.

### B. Total Station and acceleration Sensor

In this experiment the RTS is positioned 49.58m from the target which is mounted in the middle of the bridge. In Figure 21 a time series of 90 seconds is shown, where no movement at all occurs on the bridge. The RTS data is compared to the accelerometer data.

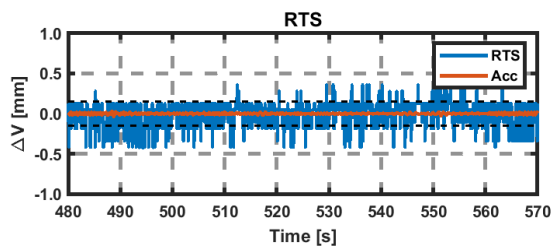


Figure 21. Time series of RTS and acceleration sensor while no movement of the bridge.  $STD_{RTS}$ : 0.15 mm,  $STD_{ACC}$ : 0.01 mm.

The acceleration sensor detects almost no movement at all, while the RTS senses random movement over the same period of time. This can be tied to the resolution of the RTS measurements but also to atmospheric disturbances. Due to the fact of very mild measurement weather, the disturbances are quite low. The standard deviation of 0.15 mm gives an idea of the smallest detectable amplitude.

In Figure 22 the time series of RTS and acceleration data is shown. Again, the event of the students jumping is clearly seen in the figure.

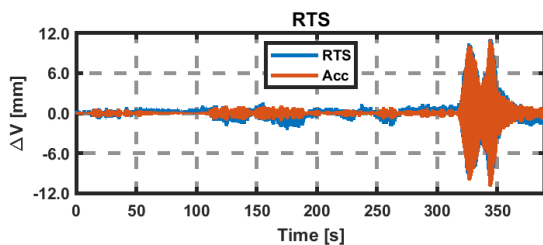


Figure 22. Time Series with event of students jumping (320 s - 360 s).

While the ambient movement of the bridge is very small, a group of people excite the bridge of about 10 mm. Both, ambient and artificial motion can be tracked by the RTS. It has to be said that the

accelerometer data is more flattened because it needs to be integrated twice to derive the movement which acts as a low pass filter.

In Figure 23 the FFTs of the time series above are shown. Both, the RTS and accelerometer, are capable of finding the eigenfrequency of the bridge of 1.74 Hz.

As it was shown, it is possible, to derivate the eigenfrequency from big amplitudes. Figure 24 shows the time series of the data, were the bridge was excited by two people, resulting in lower amplitudes.

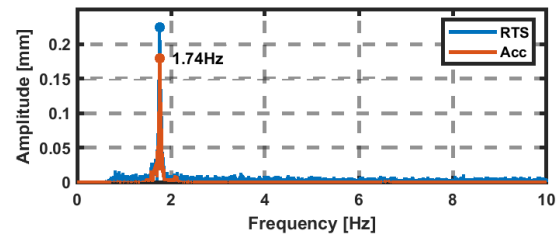


Figure 23. FFT of RTS and Acceleration sensor while 15 students jumping on the bridge.

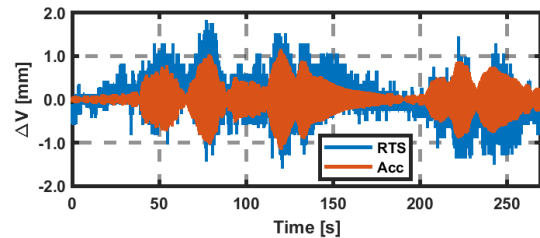


Figure 24. Time series of RTS and acceleration sensor while 2 people jumping on the bridge.

The jumping on the bridge generates amplitudes up to 1 mm. While the filtered acceleration data shows very homogenous movements, the RTS seems to drift a bit over time. This can be bounded to different loadings of the bridge as there were still people crossing the bridge during the experiment. Anyway, it can be seen, that the RTS is capable of following the motion.

In Figure 25 the FFTs of the time series shown above is displayed.

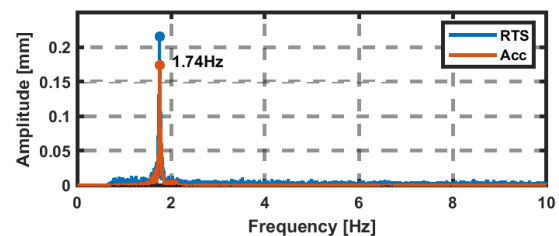


Figure 25. FFT of RTS and Acceleration sensor while two people jumping on the bridge.

Both sensors are capable of finding the eigenfrequency of 1.74 Hz again. Therefore, it can be said that motion significantly higher than the atmospheric disturbances can be detected by the RTS and concluded to the eigenfrequency of an object.

#### IV. CONCLUSION

It is shown in this paper, that GNSS and RTS with a sampling rate of 20 Hz is a useful technology for dynamic monitoring of civil structures, where frequencies of less than 10 Hz are expected.

For GNSS a reference station providing 20 Hz is advantageous, especially for low amplitudes. At lower reference station data rate, artefacts in the frequency domain do occur.

If there is no significant oscillation in the data, the GNSS data noise is equally distributed over the frequency domain. If there is a significant oscillation in the data, the frequency determination was very accurate compared to the LTS data. This was shown in the tests at the laboratory with the shaker but also at the footbridge. This frequency determination worked well for high amplitudes (10 mm) but also for low amplitudes (1 mm). It has to be mentioned that the amplitude calculation differed from the LTS data, especially between 2 Hz and 8 Hz in the range of a few millimetres.

For RTS measurements the standard deviation of no movement is depended on various influences like distance to target, surface and surrounding of the signal path and weather.

The frequency determination was very accurate compared to the acceleration sensor data and LTS data. Unfortunately, the RTS cannot hold its sampling rate at high frequencies (~ 9 Hz) and high amplitudes (~ 6 mm), were it dropped to 16 Hz. Having a closer look at amplitudes at certain frequencies, amplitudes derived from RTS data are tendentially too high. It is shown, that the use of RTS in dynamic observation procedure is possible, but there are some inner and outer influences that need to be considered.

#### V. OUTLOOK

This paper covered the results of accelerations in vertical direction. Further investigations will be carried out in horizontal directions.

#### References

- Górski, P. (2017). Dynamic characteristic of tall industrial chimney estimated from GPS measurement and frequency spe decomposition. *Engineering Structures*, 148, pp. 277-292.
- Im, S. B., Hurlebaus, S., and Kang, Y. J. (2013). Summary review of GPS technology for structural health monitoring. *Journal of Structural Engineering*, 139(10), pp. 1653-1664.
- Le Thi, N., Männel, B., Jarema, M., Seemala, G. K., Heki, K., and Schuh, H. (2021). Selection of an optimal algorithm for outlier detection in GNSS time series. In *EGU General Assembly Conference Abstracts* (pp. EGU21-1598).
- Leica (2020). Data Sheet of Leica MS60
- Lienhart, W., Ehrhart, M., and Grick, M. (2017). High frequent total station measurements for the monitoring of bridge vibrations. *Journal of applied geodesy*, 11(1), pp. 1-8.

Moschas, F., and Stiros, S. (2011). Measurement of the dynamic displacements and of the modal frequencies of a short-span pedestrian bridge using GPS and an accelerometer. *Engineering structures*, 33(1), pp. 10-17.

Nischan, T. (2016): GFZRNX - RINEX GNSS Data Conversion and Manipulation Toolbox. GFZ Data Services. DOI: 10.5880/GFZ.1.1.2016.002

Shannon, C. E. (1949). Communication in the presence of noise. *Proceedings of the IRE*, 37(1), pp. 10-21.

Shen, N., Chen, L., Liu, J., Wang, L., Tao, T., Wu, D., and Chen, R. (2019). A review of global navigation satellite system (GNSS)-based dynamic monitoring technologies for structural health monitoring. *Remote Sensing*, 11(9), 1001.

Takasu, T. (2011). RTKLIB: An open source program package for GNSS positioning.

Yi, J., Zhang, J. W., and Li, Q. S. (2013). Dynamic characteristics and wind-induced responses of a super-tall building during typhoons. *Journal of Wind Engineering and Industrial Aerodynamics*, 121, pp. 116-130.

## Analysis of the Lisbon metropolitan area using the P-SBAS service of the Geohazards Exploitation Platform

Jorge P. Galve<sup>1</sup>, Cristina Reyes-Carmona<sup>1,2</sup>, Anna Barra<sup>3</sup>, Marta Béjar-Pizarro<sup>2</sup>, Oriol Monserrat<sup>3</sup>, Ricardo Garcia Campus<sup>4</sup>, Jose Luis Zezere<sup>4</sup>, Paulo S. de Figueiredo Ferreira<sup>4</sup>, Sara A. Figueira Damaso<sup>4</sup>, Susana I. Magro Siborro<sup>4</sup>, Rosa M. Mateos<sup>2</sup>, José Miguel Azañón<sup>1</sup>

<sup>1</sup> Departamento de Geodinámica, Universidad de Granada, Avenida del Hospicio s/n, 18010 Granada, Spain, ([jpgalve@ugr.es](mailto:jpgalve@ugr.es); [jazanon@ugr.es](mailto:jazanon@ugr.es))

<sup>2</sup> Geohazards InSAR Laboratory and Modelling Group (InSARlab), Geoscience Research Department, Geological Survey of Spain (IGME-CSIC), Calle de Ríos Rosas 23, 28003 Madrid, Spain, ([creyes@igme.es](mailto:creyes@igme.es); [m.bejar@igme.es](mailto:m.bejar@igme.es); [rm.mateos@igme.es](mailto:rm.mateos@igme.es))

<sup>3</sup> Geomatics Division, Centre Tecnològic de Telecomunicacions de Catalunya (CTTC/CERCA), Avinguda Carl Friedrich Gauss 7, 08860 Castelldefels, Spain, ([anna.barra@cttc.cat](mailto:anna.barra@cttc.cat); [omonserrat@cttc.cat](mailto:omonserrat@cttc.cat))

<sup>4</sup> Instituto de Geografia e Ordenamento do Território (IGOT), Universidade de Lisboa, Rua Branca Edmée Marques, Cidade Universitária, 1600-276, Lisboa, Portugal, ([rgarcia@campus.ul.pt](mailto:rgarcia@campus.ul.pt); [zezere@campus.ul.pt](mailto:zezere@campus.ul.pt); [paulo.ferreira@igot.ulisboa.pt](mailto:paulo.ferreira@igot.ulisboa.pt); [saradamaso@campus.ul.pt](mailto:saradamaso@campus.ul.pt); [susanasiborro@campus.ul.pt](mailto:susanasiborro@campus.ul.pt))

**Key words:** *InSAR; GEP; P-SBAS; subsidence; landslide*

### ABSTRACT

Web platforms and cloud computing are revolutionizing the remote sensing methodologies and improve significantly the capacity to analyze the Earth surface. Here, we present the Geohazard Exploitation Platform (GEP) of the European Space Agency (ESA) and, particularly, an application of the P-SBAS service of this platform on the Lisbon metropolitan area. The analysis was developed as part of the project RISKCOAST that deals with coastal hazards, seeking to test diverse methodologies to monitor them. The region of Lisbon is a pilot area of this project because different surficial and coastal processes impact it. To analyze this region, we generated through GEP a deformation map over 3,000 km<sup>2</sup> of the Portuguese coast where 2.8 million people live. Thanks to GEP we generated the map in only 24h. This deformation map serves us to recognize several places with ground instability problems. The main processes identified associated to those unstable terrains were landfill and sediment consolidation, active landslides and local subsidence most probably related to groundwater withdrawal. As far as we know, most of the detected deformations were not registered so far. We also detected deformations of unknown origin. Furthermore, we determined that an area previously affected by ground subsidence in the 90's appears to be currently stable. The mentioned findings show how different processes due to the interaction of human activities and infrastructures with the ground can affect metropolitan areas. In the case of Lisbon metropolitan area, the municipalities can use the obtained information to know and to anticipate future issues regarding building and infrastructure damage. In this sense, this research is an example of how new InSAR technologies such as the modern cloud analytic platforms can serve to identify and monitor surficial processes in an easy way to prevent problems associated to unstable ground.

### 1. INTRODUCTION

Some tools based on web platforms for cloud computing were applied to several coastal areas of the southwestern Europe in the framework of the RISKCOAST project (the Interreg SUDOE Programme; <https://riskcoast.eu/>). These tools are revolutionizing the remote sensing methodologies and improve significantly the capacity to analyze the Earth surface. The mentioned project aims to use tools for processing satellite radar images and deriving Earth surface displacement maps in supporting disaster risk reduction in coastal areas. This objective is focused on the technique of satellite interferometry with the aim of generating maps to detect, characterize and monitor surface movements associated with coastal hazards.

Satellite interferometry, or more specifically, Differential Interferometric SAR (DInSAR) is a powerful tool for the detection and monitoring of ground movements associated with different geological phenomena (Crosetto *et al.*, 2016). Despite being a relatively young technique, its consolidation came at the beginning of this century (Ferretti *et al.*, 2001; Crosetto *et al.*, 2005), it is a versatile, reliable and inexpensive technique for mapping and monitoring subsidence, landslides, infrastructure control and urban areas (Crosetto *et al.*, 2016). Here, we evaluate the operability of a platform that allows this type of analysis to be carried out quickly in the cloud, the platform developed by the European Space Agency (ESA) called Geohazard Exploitation Platform (GEP). At the time of writing (April-2022), this platform has already been put

into service after several years of development and testing, a phase in which several authors of this paper have participated as part of an "Early Adopters" Programme. During this period, we have learned how the platform has been developed and identified its limitations and advantages for supporting decision-making in disaster prevention and management. A first study of the platform's capabilities was described in the article by Galve *et al.* (2017) in the specialized journal "Remote Sensing". This paper adds additional and novel information to that work by including descriptions of new services of the GEP platform, as well as focusing on its benefits for coastal risk analysis.

## II. THE GEOHAZARD EXPLOITATION PLATFORM

Web platforms and related collaborative projects are revolutionizing the way remote sensing data is analyzed. On the other hand, the launch of new radar missions by ESA that offer open-access information allows these platforms to be fed with large amounts of information ready to be analyzed by them. Among the web-based platforms being developed for radar image analysis, the Geohazard Exploitation Platform (GEP) (<https://geohazards-tep.eo.esa.int/#!>) stands out. This platform makes it possible to perform various interferometric analyses with satellite SAR images in the cloud. This platform is a major step towards the widespread use of this technology by a wider community than has developed it so far. Until now, this technology was only applied by a few research teams or specialized companies in the world, and the areas studied in depth were limited to areas of interest for scientist or large companies, especially in the energy sector. With the emergence of platforms such as GEP, it will be easier to extend the users of the technology to members of public institutions, medium-sized or small companies in business sectors where its potential use is not yet known. In this way, land and disaster managers would be one of the target groups of the platform who could develop their own analyses without knowing in depth the mathematics and physics behind the application of this technique. In the GEP platform these analyses are performed through what are called "services". The platform hosts several "services" to identify, monitor and evaluate hazardous processes associated with seismic and volcanic activity, subsidence and landslides, among others.

Today, GEP is a commercial platform that offers a sponsorship programme to develop research projects. Many of the platform's "Early Adopters" maintain their access to the platform free of charge under ESA sponsorship. The access policy and pricing depending on public or commercial use is being defined in a new phase. More information on the platform and its services can be found at the following web address: <http://terradue.github.io/doc-tep-geohazards/overview/index.html#>

## III. STUDY AREA

One of the study areas of the RISKCOAST project is the entire coastline of the Lisbon metropolitan area including the Tagus River estuary and the river basins that flow into this coastline. This area is characterized by some stretches of coast with cliffs and beaches but also show wide sand dune deposits and tidal flats. In this diverse coastal context, it is expected to find different active surface processes also affected by anthropic activities. There were three previous studies using InSAR in the area developed by Catalão *et al.* (2011; 2015) and Oliveira *et al.* (2015). The studies of Catalão *et al.* (2011; 2015) were focused in the subsidence due to the construction of a subway line detected in the Lisbon urban area. These authors processed images from ERS and ENVISAT satellites. For their part, Oliveira *et al.* (2015) analyzed images of the TerraSAR X satellite to monitor the activity of landslides in the surroundings of Lisbon.

## IV. METHODOLOGY

The GEP platform presents a simple interface where algorithms can be run to process satellite radar images and obtain maps of movements on the Earth's surface. The algorithms are implemented in so-called "Services" which can be accessed directly from the main analysis web page. These "Services" containing the acronym "SBAS" have implemented programs to apply the "P-SBAS" algorithm developed by Casu *et al.* (2014) and De Luca *et al.* (2015). These algorithms are widely proven techniques for performing what are known as multi-temporal DInSAR analyses (MTA), *i.e.* analyses over a period of time where a large number of radar images are compared to obtain the time series of movements at each point measured on the Earth's surface. The input data for these algorithms are as follows:

- Set of radar satellite images acquired with the same geometry in the area of interest during the analyzed period.
- Data on the satellite position at the time of acquisition of each image.
- Digital elevation model of the area of interest.

The GEP platform provides access to all available radar images in ESA's archives and processes them directly on ESA's servers using very high-performance computing installations. As a result, users do not need to download all the necessary information, nor do they need to purchase and maintain high-capacity computing power or expensive specialized analysis software.

The DInSAR analysis is performed from the web interface of GEP's so-called "Thematic Apps". These "Thematic Apps" are pages divided into several windows where images, services and parameters for analysis are selected. The steps to follow are simple and can be summarized as follows:



1. Selection of the "Service" in the "Services Window". Once the service has been selected, the window displays a form to be filled in with the necessary parameters to perform the analysis.
2. Selection of the Area of Interest (AOI) in the "Map Window". Using the visualization tools in this window, we can move around the map and draw a rectangle with the area we wish to analyze.
3. Once the rectangle has been drawn, the types of images to be analyzed are selected. This selection is made by dragging the selected images from the "Selection Window" to the "Services Window". The "Services" evaluated can analyze images from the ERS 1/2, ENVISAT and Sentinel-1A/B satellites covering various time periods from the 1990s to the present day.
4. Finally, in the "Services Window", the analysis parameters must be completed and, above all, the stable reference point must be defined, which serves as a basis for determining the unstable areas and for carrying out the displacement measurements based on it. This reference point can also be defined using the "Map Window".

Once the study area, the images to be processed and the analysis parameters have been defined, the service is executed, generating a "Job" which will provide a result in the form of a digital displacement map after 24-48 hours.

The processing is sometimes unsuccessful because of technical errors such as low overlapping of images, wrong choice of reference point or deficiencies in the processing chain. The latter can be corrected by the GEP technical team who identify the problem and reconfigure the service to correct the error. In the case of the first two, a review of the input data can correct the error and result in successful processing.

The results presented in this paper have been developed using images acquired by the Envisat and Sentinel-1A/B satellites. The Envisat data are archived images from that mission from 2003 to 2008. Their images cover areas of approximately 100 x 100 km and have a spatial resolution of 30 x 30 m and a temporal resolution of 35 days, *i.e.* ideally one image of the same location is acquired approximately every month. These images are analyzed from the SBAS Stripmap service. Sentinel-1 data cover areas of 250 x 250 km, acquire an image every 6 days, have a nominal resolution of 4 x 14 m and are completely free of charge. These images are processed by the SBAS-InSAR S-1 TOPS service. Regarding the results provided by GEP, the "SBAS Stripmap" and "SBAS-InSAR S-1 TOPS" services provide displacement rate maps with a spatial resolution of approximately one point every 40-80 m together with the time series of the displacements at each point.

## V. RESULTS

The area covered by the displacement maps obtained with GEP provided a lot of information about imperceptible movement processes occurring around the city of Lisbon. The most recurrent process detected in these maps is the compaction of material extracted in the numerous quarries distributed throughout the region (Figure 1). Compaction or accommodation of near-shore sand dune deposits (Figure 2) and tidal flat deposits (Figure 3) is also common.

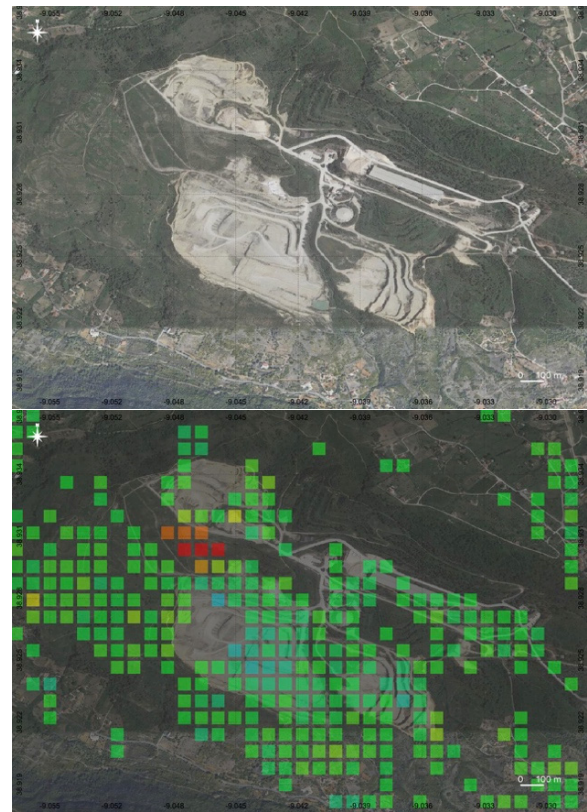


Figure 1. Quarry located in the east of the Lisbon metropolitan area (top) where ground movement velocities in LOS direction of more than 2 cm/year are observed moving away from the satellite (yellow, orange and red pixels in the image on the bottom) linked to the consolidation of fill materials (dumps). The data were obtained through the "SBAS-InSAR S-1 TOPS" service by processing Sentinel-1 ascending orbit images. This applies to the rest of the figures presented in this section from this point onwards.

From the point of view of processes that could generate risk situations or damage to buildings or infrastructures, movements linked to subsidence have been detected in alluvial materials of the Tagus River (Figure 4) and slope instabilities in the relief of hills surrounding the city, which have been the subject of a large number of studies (e.g. Zêzere *et al.*, 2017).

Only one of the sites where ground displacements are detected had clearly evidenced the movement of a landslide already identified (Figure 5), but the rest the instabilities of the area were not known (Figure 6 and 7).

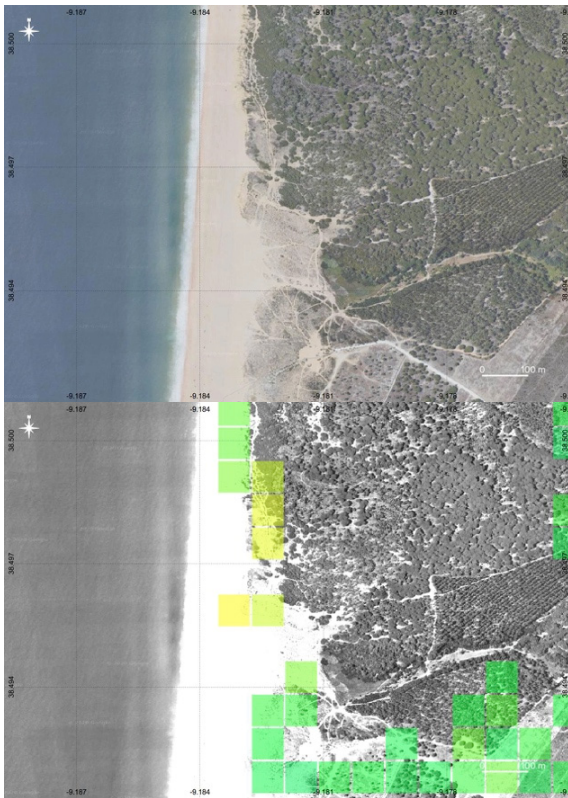


Figure 2. Beach south of Lisbon (top) showing movements with very slow speeds (yellow pixels: 1-1.5 cm/year) possibly linked to the movement of the sand of a coastal dune belt (bottom).

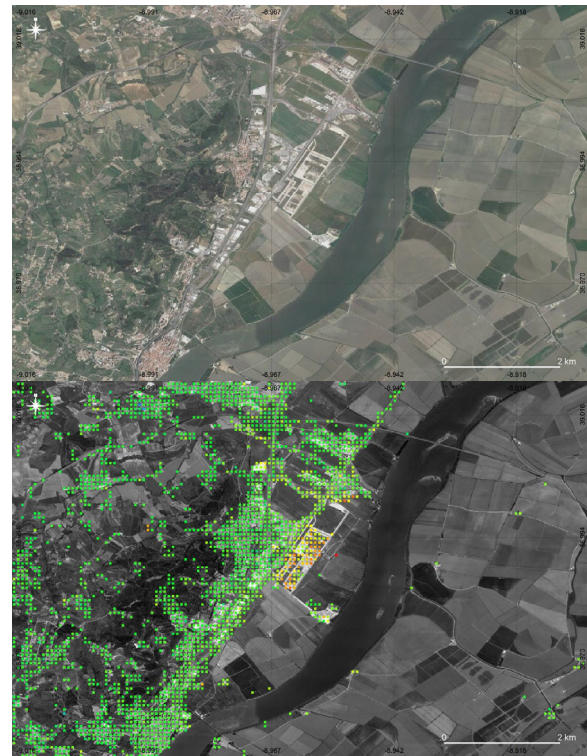


Figure 4. Castanheira do Ribarejo area (Lisbon) along the Tagus river shortly before it flows into the estuary (top). The observed LOS ground velocities are in the range between 1 and 3 cm/year in the direction away from the satellite. It is interpreted as a subsidence zone of unknown origin that coincides with an urbanised area (bottom).



Figure 3. Coastal area on the eastern bank of the Tagus estuary showing a tidal plain occupied by cultivated land (top) A deformation of the terrain in the LOS direction away from the satellite is most likely associated with a subsidence of this terrain (orange pixels: 2-2.5 cm/year) (bottom) linked to the consolidation of the sediment.



Figure 5. Monte Mourão area (358 m). Ground movement velocities in LOS direction of more than 1.5-2 cm/year (yellow and orange pixels) are observed linked to a known active landslide.

The results of GEP have made it possible to locate new areas in the metropolitan region of Lisbon linked to active slope movements.

In the Lisbon urban area, two cases are noteworthy, the instability observed in the area of the "Pedro Arrupe" School located in the north of Lisbon (Figure 8) and the movement of the ground away from the satellite (interpreted as a subsidence) observed in the area where the "Parque das Artes e do desporto" would be located, the high area of a slope facing the IC-16 motorway entering the city (Figure 9).

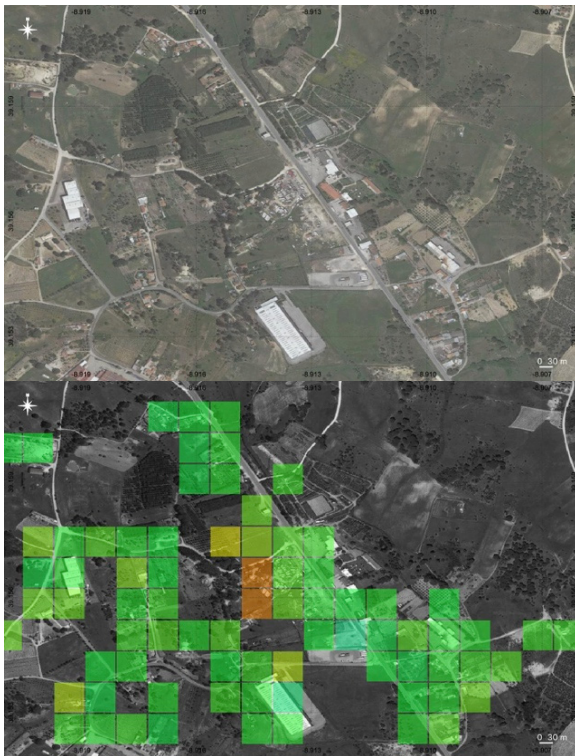


Figure 6. Aveiras de Cima area (top). Ground movement velocities in LOS direction of more than 2 cm/year of unknown origin are observed (bottom).

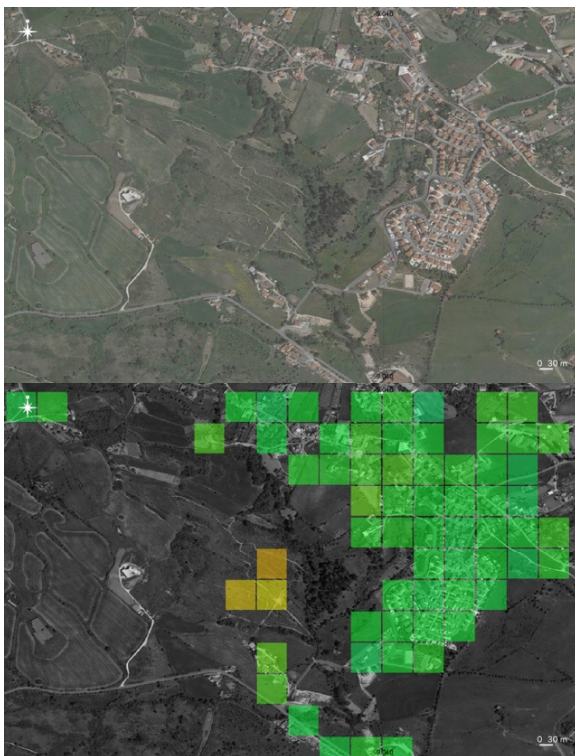


Figure 7. Cotovios area (top). Ground movement velocities in the LOS direction of more than 2 cm/year are observed, possibly linked to a slope movement (bottom).

A remarkable feature of the new analyses with Sentinel-1 images performed in GEP has been to verify that the subsidence zone detected in previous analyses with ERS 1/2 and ENVISAT images at the University of Lisbon Campus (Catalão *et al.*, 2011; 2015) is no longer

active (Figure 10). This subsidence was interpreted by Catalão *et al.* (2015) as a subsidence associated with the extraction of groundwater for the construction of a metro line right in an area where there were layers of fine-grained sands that were consolidated by this cause, added to the urbanisation of the area and the sealing of the soil by this cause. These phenomena may occur again in the future in the city or its metropolitan area, which makes the GEP platform very useful to have a first-order idea of the evaluation of the process.

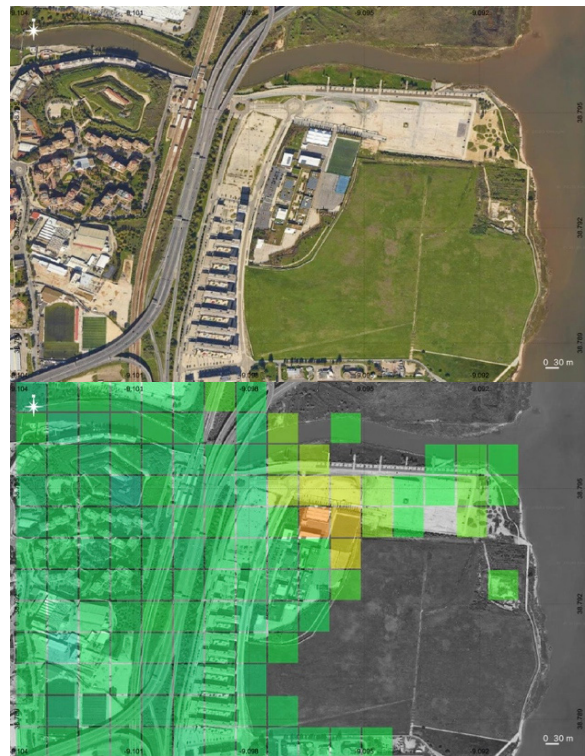


Figure 8. "Pedro Arrupe" School area (Lisbon) (top). Slight ground movements away from the satellite have been detected, possibly associated with a subsidence of unknown origin (bottom).

## VI. DISCUSSION

The GEP results, even with their limitations linked to the resolution of the output data, complement the abundant studies on slope movements and subsidence already carried out in the Lisbon region and provide displacement rates for some movements. This is an achievement in an area where there is a deep knowledge of unstable terrain. Thus, in the Lisbon area, GEP's ability to quickly analyze entire coastal regions and get a preliminary idea of possible unstable areas was demonstrated. In this case, in one day we obtained a displacement map covering a land area of approximately 3,000 km<sup>2</sup> where more than 2.8 million people live. Therefore, a preliminary idea of the general stability of hundreds of kilometers of coastline can be obtained with minimal effort compared to the use of other in-situ monitoring methods.

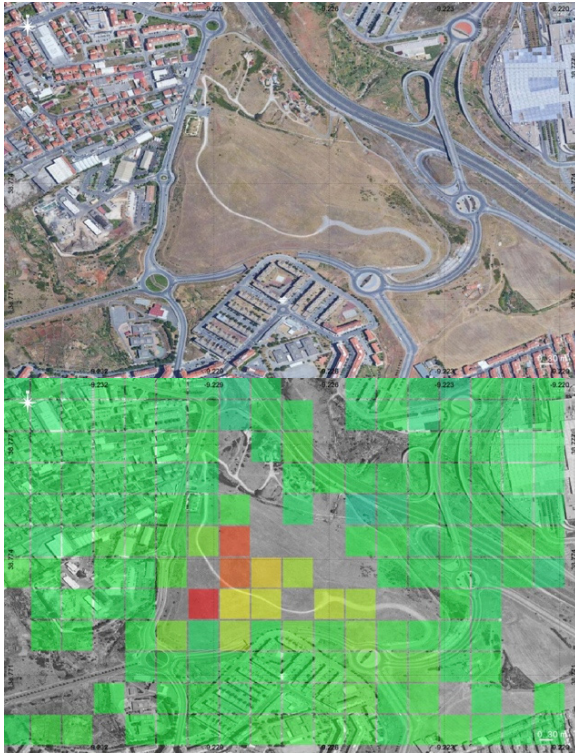


Figure 9. Area of the "Parque das Artes e do desporto" (Lisbon) (top). The area appears to be a large anthropic fill where a slope has been outlined. In the upper area, ground movements away from the satellite of more than 2 cm/year in the LOS direction are observed, possibly related to the consolidation of the fill (bottom).



Figure 10. Area of the University of Lisbon Campus with InSAR data obtained from ERS images (from Catalão *et al.*, 2015) (top). Data obtained from GEP after processing Sentinel-1 images (bottom). The green colour of the pixels indicates stability of the whole area.

From a technical point of view, GEP is a complex tool that, although user-friendly, does not allow control over almost any processing parameters, so it is necessary to contact the technical team when problems arise in the SAR image processing. Furthermore, depending on the availability of images, their quality and the area analysed, it can offer results that are difficult to interpret due to the "noise" that the data may show. In some of the cases presented here, it was necessary to carry out several processing operations with different parameters and images to obtain a reliable result. All these shortcomings are contrasted with the possibility of obtaining results in 24-48 h, which allows several tests to be carried out in a short space of time to obtain several displacement maps.

## VII. CONCLUSIONS

The GEP platform developed by ESA is a useful tool for rapid analyses to locate possible unstable terrain with a continuous movement of a few mm-cm per year. The platform provides unsupervised analysis results, *i.e.* without much modification of the processing parameters to optimize the analysis, but within 24-48 h, which allows a quick and preliminary assessment of the instability situation. In addition, the services mentioned provide time series of displacement, which also helps in the interpretation of the movements and can guide in the identification of the causal factors causing the detected instability. With GEP, a user with basic training can obtain DInSAR data relatively easily, although it is always a preliminary result. At that point, applying the technique is no longer an obstacle and it is the rigorous interpretation of the data that becomes important.

The findings in the Lisbon metropolitan area show how different processes due to the interaction of human activities and infrastructures with the ground can affect urban areas. The municipalities can use the obtained information to know and to anticipate future issues regarding building and infrastructure damage. In this sense, this research is an example of how new InSAR technologies such as the modern cloud analytic platforms can serve to identify and monitor surficial processes in an easy way to prevent problems associated to unstable ground.

## VIII. ACKNOWLEDGEMENTS

The research was supported by the European Regional Development Fund (ERDF) through the project "RISKCOAST" (SOE3/P4/E0868) of the Interreg SUDOE Programme.

## References

- Casu, F., Elefante, S., Imperatore, P., Zinno, I., Manunta, M., De Luca, C. and Lanari, R., (2014). SBAS-DInSAR parallel processing for deformation time-series computation. *IEEE Journal of Selected Topics in Applied Earth Observations and Remote Sensing*, 7(8), pp.3285-3296.

- Catalão, J., Nico, G., Hanssen, R., and Catita, C., (2011). Merging GPS and atmospherically corrected InSAR data to map 3-D terrain displacement velocity. *IEEE Transactions on Geoscience and Remote Sensing*, 49(6), pp.2354-2360.
- Catalão, J., Nico, G., Lollino, P., Conde, V., Lorusso, G., and Silva, C., (2015). Integration of InSAR Analysis and Numerical Modeling for the Assessment of Ground Subsidence in the City of Lisbon, Portugal. *IEEE Journal of Selected Topics in Applied Earth Observations and Remote Sensing*, 9(4), pp.1663-1673.
- Crosetto, M., Crippa, B., and Biescas, E., (2005). Early detection and in-depth analysis of deformation phenomena by radar interferometry. *Engineering Geology*, 79(1-2), pp.81-91.
- Crosetto, M., Monserrat, O., Cuevas-González, M., Devanthéry, N., and Crippa, B., (2016). Persistent scatterer interferometry: A review. *ISPRS Journal of Photogrammetry and Remote Sensing*, 115, pp.78-89.
- De Luca, C., Cuccu, R., Elefante, S., Zinno, I., Manunta, M., Casola, V., Rivolta, G., Lanari, R., and Casu, F., (2015). An on-demand web tool for the unsupervised retrieval of earth's surface deformation from SAR data: The P-SBAS service within the ESA G-POD environment. *Remote Sensing*, 7(11), pp.15630-15650.
- Ferretti, A., Prati, C., and Rocca, F., (2001). Permanent scatterers in SAR interferometry. *IEEE Transactions on geoscience and remote sensing*, 39(1), pp.8-20.
- Galve, J.P., Pérez-Peña, J.V., Azañón, J.M., Closson, D., Caló, F., Reyes-Carmona, C., Jabaloy, A., Ruano, P., Mateos, R.M., Notti, D., and Herrera, G., (2017). Evaluation of the SBAS InSAR service of the European space Agency's Geohazard Exploitation Platform (GEP). *Remote Sensing*, 9(12), p.1291.
- Oliveira, S.C., Zêzere, J.L., Catalão, J., and Nico, G., (2015). The contribution of PSInSAR interferometry to landslide hazard in weak rock-dominated areas. *Landslides*, 12(4), pp.703-719.
- Zêzere, J.L., Pereira, S., Melo, R., Oliveira, S.C. and Garcia, R.A., (2017). Mapping landslide susceptibility using data-driven methods. *Science of the total environment*, 589, pp.250-267..

# Data fusion of MEMS accelerometer and hydrostatic leveling for structural health monitoring – the test rig investigations

Leonhard Pleuger<sup>1</sup>, Mario Haupt<sup>2</sup>, Jens-André Paffenholz<sup>1</sup>

<sup>1</sup> Institute of Geo-Engineering, Clausthal University of Technology, 38678 Clausthal-Zellerfeld, Germany, ([leonhard.pleuger@tu-clausthal.de](mailto:leonhard.pleuger@tu-clausthal.de); [jens-andre.paffenholz@tu-clausthal.de](mailto:jens-andre.paffenholz@tu-clausthal.de))

<sup>2</sup> Glückauf Vermessung GmbH, 99706 Sondershausen, Germany, ([m.haupt@glueckauf-vermessung.de](mailto:m.haupt@glueckauf-vermessung.de))

**Key words:** MEMS accelerometers; hydrostatic leveling; structural health monitoring; deformation measurement; sensor fusion

## ABSTRACT

This paper deals with the data fusion of MEMS accelerometer and hydrostatic leveling to contribute to the structural health monitoring, *e.g.*, of bridge structures. In the past years, researchers derived the deformation and bending line of bridges by profile measurements with terrestrial laser scanners (TLS), by means of MEMS accelerometers and image assisted total station (IATS) also with the aim to obtain the modal parameters (eigenfrequencies and eigenforms). At least the TLS-based approach is not suitable for a long-term monitoring. The approach by using MEMS accelerometers is very promising and allows for a long-term installation. Following the MEMS accelerometer approach, we investigate the data fusion of MEMS accelerometers and hydrostatic leveling, which also allows for a long-term installation of the monitoring system. This approach combines the classical hydrostatic leveling with its data showing long-term stability with the high-frequent data of the MEMS accelerometers. To investigate the data fusion of the abovementioned sensors a test rig is developed to simulate deformations in scaled laboratory environments. The test rig consists of a metal bar with a maximum span width of 3 m, which can be bent by a hydraulic press, and allows for a flexible positioning of both sensors. The scope of the laboratory experiments is the evaluation of different algorithms and methods regarding the data fusion, covering aspects of filtering and calculation of the bending line. Finally, those laboratory experiments should support the understanding and knowledge of the bending line calculations and performance of the used sensors to obtain deformation information with respect to specific load levels.

## I. INTRODUCTION AND MOTIVATION

### A. Introduction

Bridges are an essential part of our modern infrastructure. Following recent statistics (Statista, 2021) of, *e.g.*, German, highway bridges, one can see that a large number of bridge structures is barely acceptable or even worse (Figure 1). Because of their condition many of these bridges face reinforcement action or even replacement. Every construction work is associated with an enormous amount of costs and disturbances for the traffic and the people using the bridge. The goal of the reinforcement cycle is to maximize the bridges' operating time without compromising its structural integrity.

To quantify the structural integrity and the condition of the bridges, *e.g.*, in Germany, they are inspected regularly every six years according to DIN 1076. In addition to that, further inspections are conducted to have a snapshot of the recent situation every three years. By utilizing a monitoring system a high information density of the bridge parameters and their short-term changes can be obtained. This high information density allows a much more accurate prediction of the bridge behavior and therefore an optimal utilization of the load reserves and a prolonged reinforcement cycle. The main drawback of such

monitoring systems seems to be their high costs for installation and operation, so that commonly such monitoring systems are taken into account when the bridge already shows significant damage. More cost-effective systems should be deployed at earlier stages in the bridge life cycle, while those sensor nodes could also support the establishment of digital twins, since real-time data from various sensor nodes is of great importance (Wenner *et al.*, 2021).

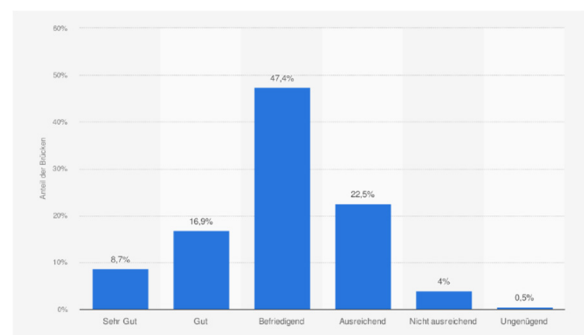


Figure 1. Condition of German highway bridges 2021 (Statista, 2021).

Conventional bridge monitoring systems often consist of classical geotechnical or geodetic sensors. Examples are inclinometers, hydrostatic leveling systems (Haupt and Hesse, 2019), total stations, and

GNSS measurements. These systems monitor different bridge parameters such as modal parameters (eigenfrequencies and eigenforms), bending line, or long-term deformation. The combination of aforementioned classical sensors as well as multiple low-cost or consumer grade sensors, *e.g.*, MEMS accelerometer, are well suited for an efficient acquisition of bridge parameters in the context of structural health monitoring (Omidalizarandi *et al.*, 2019).

### B. Related Work

In the past years, researchers obtained the deformation and bending line of bridges by profile measurements with terrestrial laser scanners (TLS), or they obtained the eigenfrequencies and eigenforms by means of MEMS accelerometers and image assisted total station (IATS).

For instance, (Schill and Eichhorn, 2019) used a profile scanner to derive the vertical deformation of railroad bridges. The authors are calculating the deformation of bridge girders of a railroad bridge both as a bending line and as an oscillation at any point in the axis of the girder. In addition, they were able to obtain the amplitude spectrum of the bridge vibration. (Omidalizarandi, 2020) is determining the modal vibration parameters of a bridge using consumer grade MEMS accelerometers. An image assisted total station (IATS) is used for a 1D coordinate update (1D CUPT). (Štebe *et al.*, 2021) are calculating a 1D vibration trajectory in laboratory experiments using MEMS accelerometers supported by an IATS. Among other algorithms a Kalman filter was used for the data fusion of the acquired data.

For a long-term and extensive usage of these approaches for a bridge monitoring several challenges have to be overcome.

With respect to a cost-effective monitoring system the financial burden of the usage of at least one geodetic sensor (IATS or profile scanner) has to be considered:

- An IATS can only measure one point at a time. The acquisition of several measuring points has to be carried sequentially, which gains an importance to be considered for an increasing number of object points to be measured.
- A profile scanner can only capture deformations in a 2D profile. While increasing the spatial coverage by using classical TLS is an option, one will decrease the temporal resolution.

### C. Motivation of our approach

The aim of our approach is to estimate bridge deformations in particular the vertical deformation to calculate a bending line as well as the oscillation in one point on the bridge girder.

In order to address this task and to avoid the aforementioned challenges due to permanent installations, a different approach will be presented here, which consists of a combination of a precise pressure based hydrostatic leveling and a consumer grade MEMS accelerometer. The combination of these two sensors offers the advantage that the IMU can capture vibrations and frequencies of the bridge girder, while the hydrostatic leveling can provide a 1D coordinate update. As long as the evaluation of the data is done in the local coordinate system of the hydrostatic leveling system no additional external geodetic sensor is required. The hydrostatic leveling allows an acquisition rate of more than 1 Hz. Furthermore, the sensor nodes can be arranged in any arbitrary three-dimensional grid as long as the height differences are within the measurement range of the hydrostatic leveling sensors.

On the one hand, the data analysis is possible in the position domain, *i.e.* metric deformation, where the focus is on the estimation of the bending line and the long-term deformation. On the other hand, the data can be analyzed in the frequency domain with the focus on the eigenfrequencies and eigenforms. The sensor fusion creates a surplus, since the stand-alone sensors either do not have sufficient long-term stability due to drift (accelerometer) or do not have the necessary acquisition rate (hydrostatic leveling).

Possible drawbacks of a combined measurement system are the costly installation of the sensors on the structure or the inertia of the hydrostatic leveling, against dynamic deformations. In addition, the use of consumer grade accelerometers affects the performance of the sensor and the accuracy of the system.

To investigate the potentials of the presented sensor combination the following points will be addressed:

1. Design of a test rig;
2. Evaluation of different data fusion algorithms in a single sensor node;
3. Transfer of the algorithm to additional sensor nodes and calculation of a bending line;
4. Validation of the results with a profile scanner or IATS;
5. Review of the proposed sensor combination and data fusion.

This contribution addresses the points one the design of a test rig and two the evaluation of different data fusion algorithms in a single sensor node.

## II. THE TEST RIG

### A. Design

The goal of the test rig is to simulate at least one span of a bridge supported on two sides. This synthetic bridge is exposed to a load and the deformation resulting from the load measured by the sensor system.

The setup of the experiment can be described with the following principle sketch (Pleuger, 2020), (Figure 2).

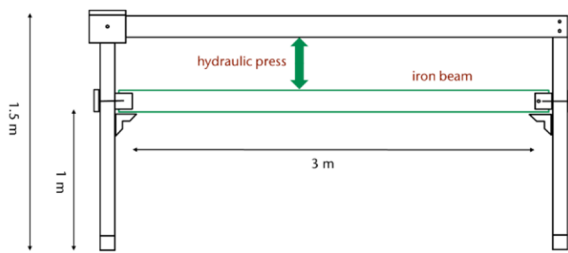


Figure 2. Principle sketch of the test rig with dimensions.

The test rig is a frame in which a beam supported on two sides can be installed. A hydraulic press is installed between the beam and the crossbar of the frame. The beam simulates a bridge girder and the hydraulic press is acting as a permanent load. In addition, an analog dial gauge is mounted next to the sensor node under consideration to validate the measured displacement (Figure 3).

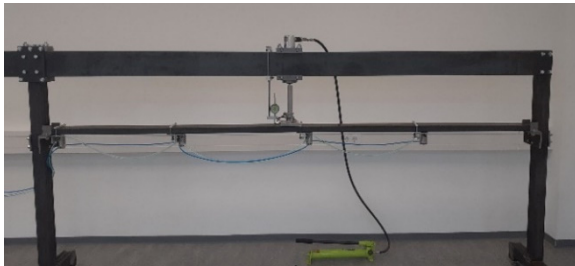


Figure 3. The test rig with applied sensor nodes.

It is possible to shift the force application point of the hydraulic press on the beam. In addition, the design of the stands and supports allows the use of different beams with different cross-sections and lengths with a maximum length of three meters.

The test rig concept is modular and thus it can be rearranged by:

1. Use of other/additional sensors, such as terrestrial laser scanner/profile scanner or IATS.
2. Extension of the synthetic bridge to several spans by installing another stand as a support.
3. Simulation of different (dynamic) loads to describe a bridge crossing more realistically.

#### B. Choice of sensors and sensor application

One selected sensor is the electronic pressure-based hydrostatic leveling system of the type PC-HAS4-500 from the company Position Control (Friedrichsthal, Germany). The measuring range is between 0 mm and 500 mm with an accuracy of max. 0.09 %FS as the sum of nonlinearity, hysteresis and repeatability. The long-term stability is min. 0.09 %FS/a. The units of the hydrostatic leveling system are controlled via an RS-485 interface with ASCII protocol (Position Control, 2022).

The selected accelerometer is part of the IMU chip BNO 055 of the company Bosch. Here, the chip

embedded in the modular system by the company Tinkerforge (Schloß Holte-Stukenbrock, Germany), in particular the IMU brick 2.0, is used. The Tinkerforge python API is used for the sensor control and data logging. The measuring range of the accelerometer is configured to  $\pm 4 g$  resulting in a 14 bit resolution with a maximum acquisition rate of 100 Hz. The non-linearity is specified by the manufacturer as max. 2 %FS and the output noise density is specified as max. 190  $\mu g/Hz$  (Bosch Sensortec, 2016). The suitability of this sensor for bridge monitoring has already been proven by, e.g., (Kemkes *et al.*, 2019).

The sensors are mounted on the test beam in sensor nodes. One sensor node consists of a hydrostatic leveling unit and a MEMS accelerometer, which are firmly connected to the test beam via an aluminum frame (Figure 4).

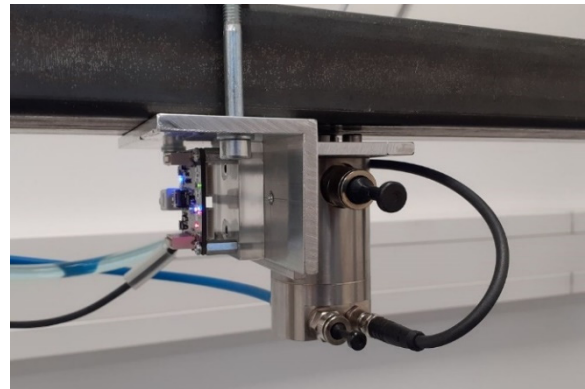


Figure 4. A Sensor node with MEMS accelerometer and hydrostatic levelling - MEMS accelerometer (left) and hydrostatic levelling unit (right); iron beam (top).

To investigate the measurement noise of the sensors, values were recorded over a period of one hour without any external load being applied. The results can be seen in Figure 5 and Figure 6 as the histograms of the captured data.

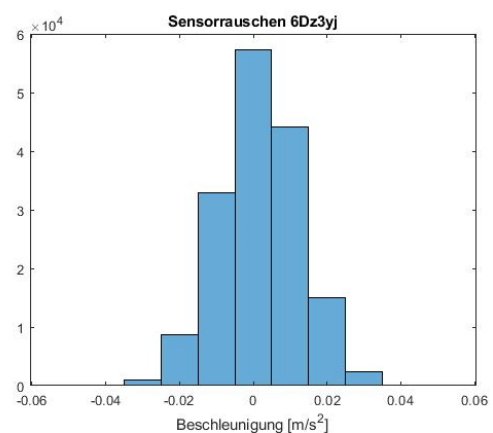


Figure 5. Histogram of the accelerometer (mean centred) for the measured accelerations.

The distribution of the measurements suggests an approximately normal distributed noise. The classes of the accelerometer's histogram were chosen with



respect to the quantification steps of the accelerometer measurement. Table 1 gives an overview of the statistical parameters, which clearly indicate the difference in the sensor performance between hydrostatical leveling and consumer grade accelerometer.

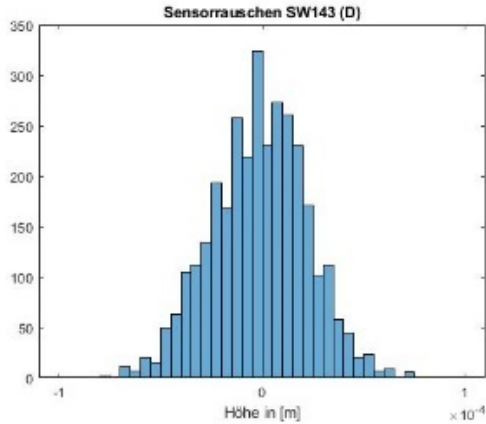


Figure 6. Histogram of the hydrostatic leveling (mean centred) for the measured height differences.

Table 1. Statistical parameters of measurement noise

Parameter	Hydrostatic leveling	IMU
Mean	$-1.55 \cdot 10^{-6} m$	$0.0026 m/s^2$
Median	$-1.02 \cdot 10^{-6} m$	$0.0000 m/s^2$
Standard deviation	$3.33 \cdot 10^{-5} m$	$0.0110 m/s^2$

### C. Experiment

The experiment performed is a static load test in which several load levels are applied. A dynamic load only occurs in the moment of load increase and decrease. The load test is subject to the following sequence:

1. *Initialization of the measurement*
2. *Beam for a few seconds at rest:* Based on the values measured during this time, the external acceleration influences of the accelerometer are subtracted and the deformation of the hydrostatic leveling unit is set to zero.
3. *Application of the load:* After the rest period, the hydraulic press is operated with a hand pump and the beam is loaded. After the pump has been operated for the first time, there is a pause of a few seconds to allow the hydrostatic leveling to adjust. After that, the hand pump is operated according to the same sequence until the desired maximum bending is reached. Each operation of the hand pump corresponds approximately to a deformation of 3 mm at the sensor node under consideration. The load applied by the hydraulic press is to be considered as a static load. No vibrations or overruns are simulated that would occur in a real structure.
4. *Maximum load:* The bridge beam remains in the maximum displacement state for a few seconds.

5. *Unloading:* The beam is unloaded via the hand pump. The beam returns to its initial position. The data acquisition is stopped after a fade-out time.

An example for the captured time series is shown in Figure 7 and Figure 8. The numbers in those figures correspond to the steps in the experiment sequence.

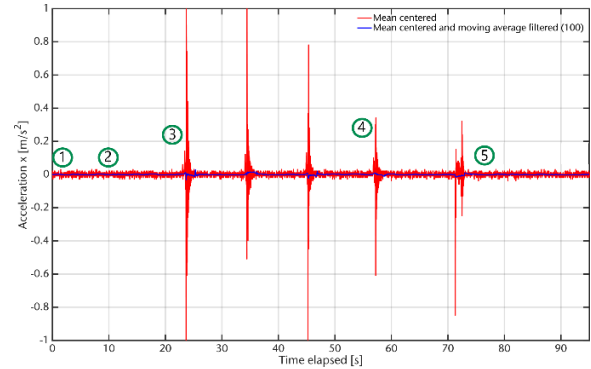


Figure 7. Timeseries of acceleration measurements. The peaks indicate a change of the applied load.

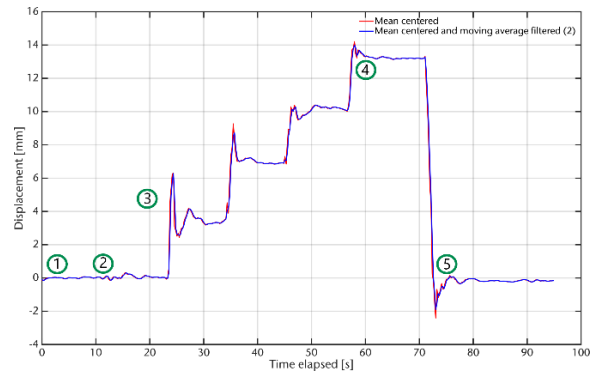


Figure 8. Timeseries of hydrostatic leveling unit measurements.

### III. DATA PROCESSING

The data fusion between acceleration data and height differences, in the following named position data, is done with the help of a Kalman filter. In this paper, two Kalman filter based variants for data fusion are presented. Both variants have the 1D displacement, *i.e.* the vertical deflection, as parameter. The variant A fuses the position data with raw acceleration measurements. A numerical integration of the data is performed using the transition matrix of the filter. The variant B of the filter fuses the position data with the already double integrated acceleration data. Numerical integration is performed separately in selected ambient windows.

A consideration of a individual sensor calibration as well as corrections of temperature and atmospheric pressure is due to the controlled laboratory conditions neglected. The authors are aware of the importance of calibration and environmental parameter corrections which will both be considered in ongoing investigations. Possible approaches are presented by (Kemkes *et al.*, 2019) and (Štebe *et al.*, 2021).

### A. Kalman filter – Basics

The Kalman filter was developed by Rudolf Emil Kalman in 1960. It has a great importance in the evaluation of dynamic time-dependent processes (Kalman, 1960).

The filter consists of a system model and an observation model. In the system model, a state vector  $x_{k+1}$  is predicted for epoch  $k + 1$  using the transition matrix and the state vector of epoch  $x_k$  (Eq. 1):

$$\hat{x}_{k+1}^- = T_{k+1,k} \cdot x_k^- + B_{k+1,k} \cdot u_k + S_{k+1,k} \cdot w_k \quad (1)$$

$u_k$  and  $B_{k+1,k}$  are the variables for the known input vector and its input gain.  $w_k$  and  $S_{k+1,k}$  are the process error vector and its coefficient matrix.

In Equation 1 and the following equations, the superscript minus denotes the predicted value and the superscript plus denotes the filtered value.

The observation model describes the relationship between observations  $y_{k+1}$  and the state vector  $x_{k+1}$  with the measurement matrix  $H_{k+1}$ .  $v_{k+1}$  represents the vector of the measurement error (Eq. 2):

$$y_{k+1} = H_{k+1} \cdot x_{k+1} - v_{k+1} \quad (2)$$

In the filtering step, the system model and the observation model are merged using the Kalman gain  $K_{k+1}$  and the innovation  $i_{k+1}$  (Eqs. 3 and 4):

$$x_{k+1}^+ = x_{k+1}^- + K_{k+1} \cdot i_{k+1} \quad (3)$$

$$i_{k+1} = (y_{k+1} - H_{k+1} \cdot \hat{x}_{k+1}^-) \quad (4)$$

The Kalman gain is calculated by (Eqs. 5 and 6):

$$K_{k+1} = Q_{\hat{x}\hat{x}_{k+1}^-} \cdot H_{k+1}^T \cdot (Q_{ii,k+1})^{-1} \quad (5)$$

$$Q_{ii,k+1} = Q_{yy_{k+1}} + H_{k+1} \cdot Q_{\hat{x}\hat{x}_{k+1}^-} \cdot H_{k+1}^T \quad (6)$$

where  $Q_{\hat{x}\hat{x}_{k+1}^-}$  is the cofactor matrix of the predicted state and  $Q_{yy_{k+1}}$  is the cofactor matrix of the observations. The cofactor matrix of the predicted state is (Eq. 7):

$$Q_{\hat{x}\hat{x}_{k+1}^+} = Q_{\hat{x}\hat{x}_{k+1}^-} - K_{k+1} \cdot Q_{ii,k+1} \cdot K_{k+1}^T \quad (7)$$

Thus, a recursive formulation for the filtered state vector and its associated cofactor matrix is obtained, see, e.g., (Paffenholz, 2012).

### B. Kalman Filter variant A – acceleration and position

Variant A of the Kalman filter was introduced by (Omidalizarandi *et al.*, 2019) and used by (Štebe *et al.*, 2021). Both used an IATS, similar to the hydrostatic leveling, to provide 1D displacement data.

The system model, introduced in Equation 1 is defined as follows, where  $\bar{q} = 0.1$  is the ratio between the system and observation noise and  $\Delta t$  is the acquisition interval (Eq. 8):

$$\begin{bmatrix} z_{k+1} \\ v_{k+1} \\ a_{k+1} \end{bmatrix} = \begin{bmatrix} 1 & \Delta t & \frac{1}{2}\Delta t^2 \\ 0 & 1 & \Delta t \\ 0 & 0 & 1 \end{bmatrix} \cdot \begin{bmatrix} z_k \\ v_k \\ a_k \end{bmatrix} + S_{k+1,k} \cdot w_k \quad (8)$$

$$Q_{\hat{x}\hat{x}_{k+1}} = \begin{bmatrix} \frac{1}{20}\Delta t^5 & \frac{1}{8}\Delta t^4 & \frac{1}{6}\Delta t^3 \\ \frac{1}{8}\Delta t^4 & \frac{1}{3}\Delta t^3 & \frac{1}{2}\Delta t^2 \\ \frac{1}{6}\Delta t^3 & \frac{1}{20}\Delta t^2 & \Delta t \end{bmatrix} \cdot \bar{q}$$

The position data of the hydrostatic leveling and the acceleration data of the IMU are available as observations. Before the data fusion, the accelerations are filtered by a moving average with a filter length of 1 s to reduce the noise. Since the hydrostatic leveling unit collects data at a frequency of 2 Hz and the accelerometer collects data at a frequency of 80 Hz, the observation equation changes depending on which observations are present. When both observations are present, the following expression applies (Eq. 9):

$$\begin{bmatrix} z_{k+1} \\ a_{k+1} \end{bmatrix} = \begin{bmatrix} 1 & 0 & 0 \\ 0 & 0 & 1 \end{bmatrix} \cdot \begin{bmatrix} z_k \\ v_k \\ a_k \end{bmatrix} - v_{k+1} \quad (9)$$

$$Q_{yy_{k+1}} = \begin{bmatrix} \sigma_{HL}^2 & 0 \\ 0 & \sigma_a^2 \end{bmatrix}$$

$\sigma_{HL}$  is the hydrostatic leveling's standard deviation obtained from the experiment sequence 2.  $\sigma_a$  is the standard deviation of the filtered acceleration signal.

If there is only one acceleration, then applies (Eq. 10):

$$\begin{bmatrix} a_{k+1} \end{bmatrix} = \begin{bmatrix} 0 & 0 & 1 \end{bmatrix} \cdot \begin{bmatrix} z_k \\ v_k \\ a_k \end{bmatrix} \quad (10)$$

$$Q_{yy_{k+1}} = [\sigma_a^2]$$

In addition to Kalman filtering, a Rauch Tung Striebel filter is applied to smoothen the time series (Rauch *et al.*, 1965).

### C. Kalman Filter variant B – integration and position

In this variant B, the measured position of the hydrostatic leveling is fused with the dual integrated observations of the acceleration sensors.

*Ambient windows* are used to separate the acceleration time series in blocks with the relevant load signal. Load signals are identified as peaks in the acceleration time series that are greater than five times the calculated standard deviation. The size of the window is set to 0.5 s before the peak and 2 s after the peak (Figure 9).

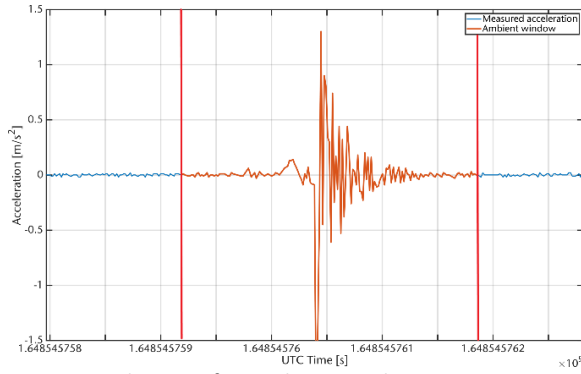


Figure 9. Selection of an ambient window – measurement noise (blue); ambient window raw acceleration (orange); limits of the ambient window (red).

To reduce the sensor drift induced by the numerical integration special integration algorithms have to be utilized. Possible integration methods of this signal would be a zero-phase filter (Štebe *et al.*, 2021), the method of the supporting polynomial (Resnik, 2014), the modeling of the acceleration time series and subsequent integration or the direct modeling of the deformations based on the acceleration (Gindy *et al.*, 2008).

The results shown here were obtained using the zero-phase filter method. Consideration of other integration algorithms and their comparison will be the subject of future work.

The integration algorithm of the zero-phase filter is shown in Figure 10. After each integration, a zero-phase filter is applied to eliminate the low frequency drift. The filter is a sixth order Butterworth filter with a cut off frequency of 0.2 Hz. In addition, a domain correction is applied after the first integration, considering the boundary condition  $v_0 = v_{end}$  (Gindy *et al.*, 2007).

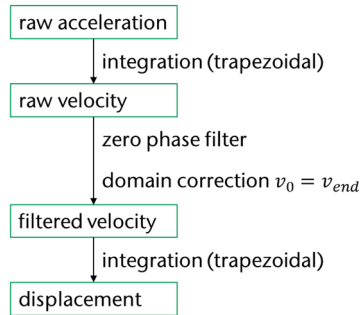


Figure 10. Integration algorithm - zero phase filter.

As a result of the selection of the ambient window and integration, the deformations are available in each of the ambient windows, where each ambient window starts with a deformation of zero (Figure 11).

1) *The data fusion and Kalman filtering:* The system model of this variant of the Kalman filter is defined as follows (Eq. 11):

$$\begin{aligned} [z_{k+1}] &= [1] \cdot [z_k] + S_{k+1,k} \cdot w_k \\ Q_{\hat{x}\hat{x}_{k+1}} &= \bar{q} \end{aligned} \quad (11)$$

The observation model must be adapted depending on which observations are available. A distinction is made between the following cases:

1. No observation (Eq. 12):

$$\begin{aligned} [z_{k+1}] &= [0] \cdot [x_{k+1}] - v_{k+1} \\ Q_{yy_{k+1}} &= [0] \end{aligned} \quad (12)$$

2. Hydrostatic leveling observation (Eq. 13):

$$\begin{aligned} [z_{HL,k+1}] &= [1] \cdot [x_{k+1}] - v_{k+1} \\ Q_{yy_{k+1}} &= [\sigma_{HL}^2] \end{aligned} \quad (13)$$

3. MEMS accelerometer observation (Eq. 14):

$$\begin{aligned} [z_{pseudo,k+1}] &= [1] \cdot [x_{k+1}] - v_{k+1} \\ Q_{yy_{k+1}} &= [\sigma_a^2] \end{aligned} \quad (14)$$

4. Both observations (Eq. 15):

$$\begin{aligned} \begin{bmatrix} z_{HL,k+1} \\ z_{pseudo,k+1} \end{bmatrix} &= \begin{bmatrix} 1 \\ 1 \end{bmatrix} \cdot [x_{k+1}] - v_{k+1} \\ Q_{yy_{k+1}} &= \begin{bmatrix} \sigma_{HL}^2 & 0 \\ 0 & \sigma_a^2 \end{bmatrix} \end{aligned} \quad (15)$$

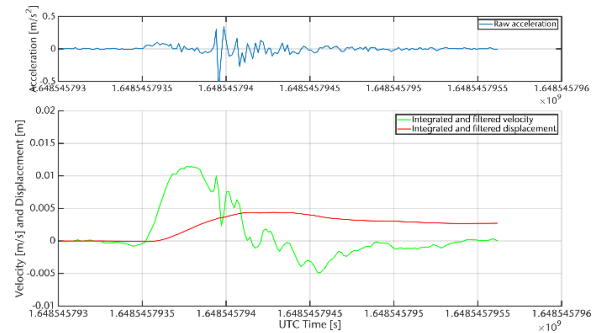


Figure 11. Numerical integration with ZPF Filter - acceleration (blue); velocity (green); displacement (red).

In Equations 14 and 15, the integrated accelerations are considered as a pseudo observation  $z_{pseudo}$ . To avoid accumulations of the integration error, a difference of the integrated accelerations is added to the last filtered state value (Eq. 16):

$$\begin{aligned} z_{integration,k+1} &= z_k + \Delta z_{pseudo} \\ &= z_k + (z_{pseudo,k+1} - z_{pseudo,k}) \end{aligned} \quad (16)$$

#### IV. RESULTS

Figure 12 and Figure 13 show the results of the data fusion using variant A, which has also been used by other researchers in differing scenarios with a combination between IATS and MEMS accelerometer. The input parameters are the mean-filtered acceleration measurements and the position data from the hydrostatic leveling. The variances of the measurement noise are used as cofactors.

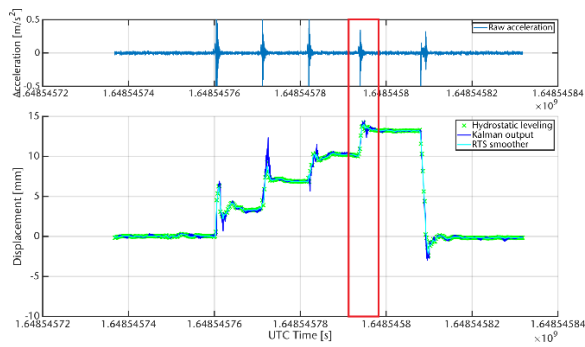


Figure 12. Result Kalman Filter variant A - Fusion of Acceleration with position – hydrostatic leveling (green); Kalman output (blue); RTS Smoother (cyan).

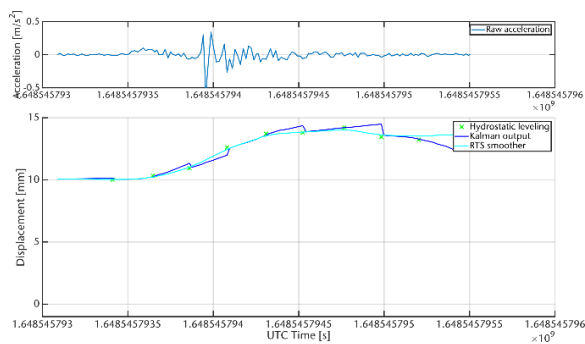


Figure 13. Result Kalman filter variant A – Selection. The Kalman output drifts in one direction until it is updated with a position measurement – hydrostatic leveling (green); Kalman output (blue); RTS Smoother (cyan).

It can be seen that the acquired time series mainly follows the hydrostatic leveling observations. However, especially in the moments of the load application strong oscillations can be seen. On the one hand, this is a result of the drift of the accelerometer, as shown in Figure 13. On the other hand, the oscillations are also caused by vibrations of the water column in the hydrostatic leveling unit, see Figure 12.

The result of the RTS filter strongly approximates the observations of the hydrostatic leveling, because of the standard deviation-based cofactors of the filter.

The results of filter variant B are shown in Figure 14 and Figure 15. It can be seen that the integrated ambient windows describe the deformation adequately in most cases. With the presented filter variant, it is possible to reduce the sensor drift of the MEMS accelerometer in the position domain as well as to significantly reduce the deviations caused by oscillations in the water column in the hydrostatic leveling.

The overall course of the time series is thus smoother and is less influenced by deflections caused by the measuring system, see blue curve in Figure 14.

Even though most of the loading cycles show good results, further investigations on the performance of numerical integration algorithms are necessary to be able to represent different types of deformations (static and dynamic) and different magnitudes of deflections.

Once this is done, the data acquisition can be extended to multiple sensor nodes to calculate a

bending line from the computed deformations. To support this bending line calculation, further measurement quantities of the MEMS IMU should be included, *e.g.*, acceleration in the beam axis, Euler angle or quaternions.

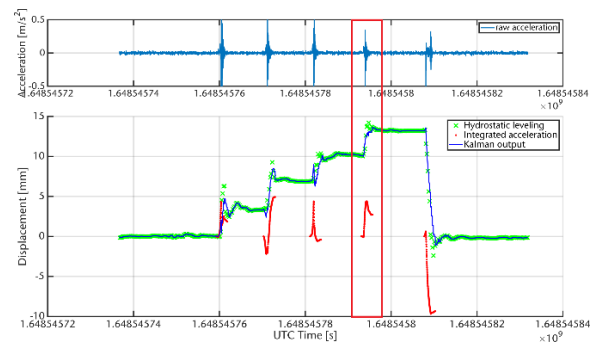


Figure 14. Result Kalman filter variant B – Fusion of integration and position – hydrostatic leveling (green); Kalman output (blue); numerical integration (red).

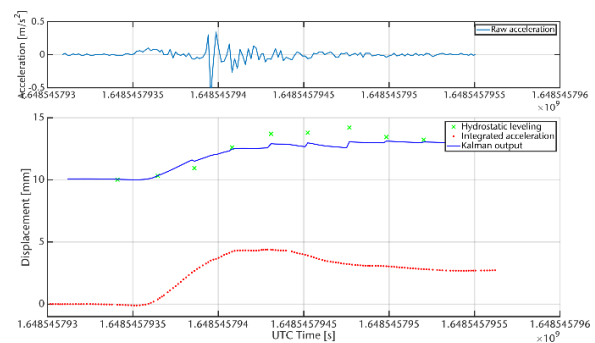


Figure 15. Result Kalman filter variant B – Selection. The Kalman output is updated by but not fully dependent on the position measurement – hydrostatic leveling (green); Kalman output (blue); numerical integration (red).

## V. CONCLUSIONS

In this paper, a sensor fusion between a hydrostatic leveling system and a consumer grade MEMS accelerometer was investigated on a special test rig. The experiment shows that the hydrostatic leveling system provides accurate measurements when static loads are applied. However, the measurements are inaccurate in the moments of dynamic load. A possible approach for the enhancement of the is presented in the addition of a MEMS accelerometer.

Two variants of a Kalman filter were presented for data fusion. Variant A was used in the past by (Omidizarandi, 2020) and (Štebe *et al.*, 2021) under different boundary conditions. Different from this paper, both authors made use an IATS for the 1D CUPT, the types of deformation and load were different, and the objective of (Omidizarandi, 2020) was to determine the modal parameters of the bridge. For this specific load and sensor combination, variant A is less suitable because the hydrostatic leveling provides inaccurate results at times of dynamic loading.

Variant B shows promising results, since the drift of the accelerometer measurements is reduced by the double integration in the ambient window and thus the

dependency on a 1D CUPT is reduced. In particular, when the hydrostatic leveling units provide inaccurate measurements while the double integrated acceleration data can describe the deformation adequately.

The other integration algorithms have to be investigated with respect to their influence on the filter approach. Also under review in future work is the identification of dynamic load periods by means of the acceleration measurements to judge the hydrostatic leveling data in the same period.

In the future, a reference measurement needs to be included that can capture the deformation behavior during dynamic loading in particular, for example a profile scanner.

### References

- Bosch Sensortec (2016). BNO055 Datasheet. Available in: <https://www.bosch-sensortec.com/media/boschsensortec/downloads/datasheets/bst-bno055-ds000.pdf>. Accessed 30 March 2022.
- Gindy, M., Nassif, H.H., and Velde, J. (2007). Bridge Displacement Estimates from Measured Acceleration Records. In: *Transportation Research Record* Vol. 2028(1), pp. 136–145.
- Gindy, M., Vaccaro, R., Nassif, H., and Velde, J. (2008). A State-Space Approach for Deriving Bridge Displacement from Acceleration. In: *Computer-aided Civil Eng* Vol. 23(4), pp. 281–290.
- Haupt, M., and Hesse, C. (2019). Präzise Bauwerksüberwachungsmessung mittels automatischer Druckschlauchwaage – Ein Bericht aus der Praxis. In: *GeoMonitoring* Vol. 7.
- Kalman, R.E. (1960). A New Approach to Linear Filtering and Prediction Problems. In: *ASME–Journal of Basic Engineering* Vol. 82(1), pp. 35–45.
- Kemkes, E., Rüffer, J., Omidalizarandi, M., Diener, D., Paffenholz, J.-A., and Neumann, I. (2019). Ein neues Verfahren zum MEMS-basierten Brückenmonitoring - Zielsetzung und Statusbericht. In: *GeoMonitoring* Vol. 7.
- Omidalizarandi M. (2020). Robust Deformation Monitoring of Bridge Structures Using MEMS Accelerometers and Image-Assisted Total Stations. Dissertation, Hannover.
- Omidalizarandi, M., Neumann, I., Kemkes, E., Kargoll, B., Diener, D., Rüffer, J., and Paffenholz, J.-A. (2019). MEMS based bridge monitoring supported by image-assisted total station. In: *Int. Arch. Photogramm. Remote Sens. Spatial Inf. Sci. XLII-4/W18*, pp. 833–842.
- Paffenholz J.-A. (2012). *Direct geo-referencing of 3D point clouds with 3D positioning sensors*. PhD thesis. DGK, München.
- Pleuger L. (2020). Beschleunigungssensoren aus dem low-cost Segment und Schlauchwaagen im Kontext des Infrastrukturmonitorings. Masterthesis, Clausthal-Zellerfeld.
- Position Control (2022). Technisches Datenblatt Sensor-Typ: PC-HSA4-500. Available in: [https://www.position-control.de/wp-content/uploads/2019/05/Datasheet\\_PC\\_HSD4\\_STANDAR D.pdf](https://www.position-control.de/wp-content/uploads/2019/05/Datasheet_PC_HSD4_STANDAR D.pdf). Accessed 30 March 2022.
- Rauch, H.E., Tung, F., and Striebel, C.T. (1965). Maximum likelihood estimates of linear dynamic systems. In: *AIAA Journal* Vol. 3(8), pp. 1445–1450.
- Resnik, B. (2014). Dynamische Belastungstests von tragenden Konstruktionen mithilfe von Beschleunigungsaufnehmern. In: *Allgemeine Vermessungs-Nachrichten (AVN)* 121(4), pp. 141–148.
- Schill, F., and Eichhorn, A. (2019). Deformation Monitoring of Railway Bridges with a Profile Laser Scanner. In: *zfv* (2/2019), 109–118.
- Statista (2021). Zustand der Brücken an Bundesfernstraßen in Deutschland im Jahr 2021. Bundesanstalt für Straßenwesen. Available in: <https://de.statista.com/statistik/daten/studie/166122/umfrage/zustand-der-strassenbruecken-in-deutschland/>.
- Štebe, G., Krapež, P., Podobnik, J., and Kogoj, D. (2021). Trajectory tracking of an oscillating movement with a low-cost IMU in geodetic surveying applications. In: *Measurement* Vol. 176, pp. 109–207.
- Wenner M., Meyer-Westphal M., Herbrand M., and Ullerich C. (2021). The concept of digital twin to revolutionise infrastructure maintenance: the pilot project smartBRIDGE Hamburg. In: *ITS World Congress* Vol. 27, Hamburg, Germany.

## Rockfall monitoring: comparing several strategies for surveying detached blocks and their volume, from TLS point clouds and GigaPan pictures

Oriol Pedraza<sup>1</sup>, Álvaro P. Aronés<sup>2</sup>, Càrol Puig<sup>2</sup>, Marc Janeras<sup>1</sup>, Josep A. Gili<sup>2</sup>

<sup>1</sup> Institut Cartogràfic i Geològic de Catalunya, Barcelona, Spain, ([oriol.pedraza@icgc.cat](mailto:oriol.pedraza@icgc.cat); [marc.janeras@icgc.cat](mailto:marc.janeras@icgc.cat))

<sup>2</sup> Universitat Politècnica Catalunya, Barcelona, Spain, ([apauloav@hotmail.com](mailto:apauloav@hotmail.com); [carol.puig@upc.edu](mailto:carol.puig@upc.edu); [j.gili@upc.edu](mailto:j.gili@upc.edu))

**Key words:** rockfall; change detection; C2M; M3C2; Terrestrial Laser Scanning; geomatic techniques

### ABSTRACT

Rockfalls are fast slope instabilities frequent in mountainous areas, which cause damage in infrastructures (roads and railways), buildings, vehicles and people. Nowadays, several continuous and discontinuous techniques are available to monitoring the prone areas in order to manage the associated risk. One side task is to detect changes in the source zones (rock cliffs with recurrent events) in order to assess the rockfall activity and calibrate the Magnitude-Frequency curves. Long range and high precision Terrestrial Laser Scanning (TLS) is currently used for this purpose, sometimes in combination with high-resolution pictures taken from UAV or from the ground (with a GigaPan setup, for instance). Some detected changes along time may correspond to precursory displacements while others are due to blocks detached from the cliffs. In our contribution, we present the use of the aforementioned geomatic techniques (TLS and GigaPan) within several algorithms /strategies (Cloud to Cloud, Cloud to Mesh and M3C2) inside some two commercial computer programs and open source program in order to detect and measure the differences along the successive field campaigns. This work has being carried out within the frame of the GeoRisk research project, with field data from the ICGC. In particular, we test the strategies in three sites in the Montserrat Massif (Spain) –Mirador de l'Oliver, Canal dels Aritjols and Mirador dels Apòstols– during four measuring epochs along 2019-2021. The results show that rock volumes as small as 0.001 m<sup>3</sup> can be detected in a regular basis.

### I. INTRODUCTION

Service and transport infrastructures located in mountainous and steep terrain could be exposed to various landslide hazards, including rockfalls. Rockfall is characterized as a fragment or fragments of rock which detach from a cliff face and, subsequently, fall, bounce, and roll as the fragments propagate downslope (Hung *et al.*, 2014). Although their magnitude can be highly variable, rockfalls cause frequent damage due to their intensity and frequency, both temporally and spatially. This poses a major challenge when prioritising the allocation of resources for landslide risk mitigation over large areas.

A clear example is the Montserrat massif (Spain), which constitutes a Natural Park (about 3500 ha) and hosts a monastery with a millenarian history and great tradition in Catalonia. Combining local and foreign tourism, the number of visitors to the monastery area was 2.7 million in 2017, with a further 0.8 million people travelling through the Natural Park for hiking or climbing.

Quantitative rockfall risk analysis (QRA) allows us to assess the different risk scenarios present in infrastructures (Corominas *et al.*, 2005). This quantification is obtained by developing magnitude-frequency relationships from inventory of events, where the cumulative frequency is quoted in spatial and temporal terms (Janeras *et al.*, 2021).

The magnitude-frequency relationships are obtained through known rockfall events. However, some bias on the information on events (mainly the lack of high magnitude and low frequency records) can lead to inaccurate quantification of risk. To partially overcome this situation, in the last decade Terrestrial Laser Scanning (TLS) and/or digital photogrammetry monitoring have complemented this lack of information with site-specific sampling and increased detection capacity (Royán, 2015; Van Veen *et al.*, 2017).

In our contribution, we present the use of the TLS and GigaPan combined with several algorithms/strategies (Cloud to Cloud, Cloud to Mesh, M3C2) in order to detect and measure the differences along the successive field campaigns over the rock cliffs. In particular, we test the techniques in three test sites in the Montserrat Massif (Spain) during four measuring epochs along 2019-2020.

### II. STUDY SITE AND OBJECTIVES

The mountain of Montserrat is located 50 km northwest of the city of Barcelona in Catalonia, in the extreme northeast of Spain (Figure 1). This isolated massif, formed by thick conglomerate layers interspersed by siltstone/sandstone from a late Eocene fan-delta, emerges above the Llobregat river with a total height of 1000 m (from 200 to 1200 m a.s.l.).

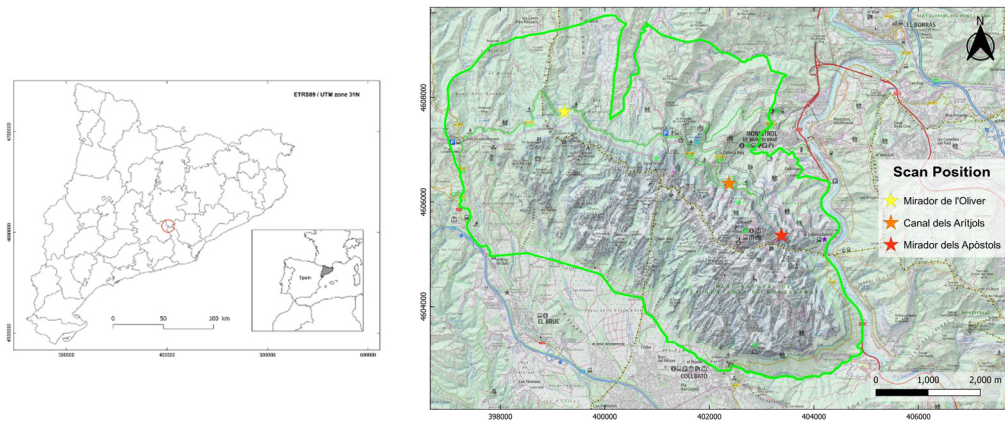


Figure 1. Site map of Montserrat massif, 50 km NW Barcelona city (Catalonia, Spain). The massif ranges between 200 and 1200 m a.s.l. over the Llobregat river at the East. The image shows the three stations where terrestrial laser scanning has been carried out.

Because of the process of sedimentation and the tectonic stresses, the massif is constituted by an intercalation of conglomerate and fine layers of sandstone and siltstone affected by a few joint sets, the prevailing two main near-vertical sets following direction NE-SW and NO-SE, respectively (Alsaker *et al.*, 1996). This configuration gives rise to stepped slopes where vertical cliffs alternate with steep slopes.

The joint systems present and their density, define the blocks susceptible to fall and therefore control the size of the blocks and the magnitude of the rockfalls. From lower to higher volume, it starts with the disaggregation of pebbles from the conglomerate (M3); as the second group (M2) we distinguish the slabs and plates related to physical weathering; and finally, monolithic rock masses delimited by widely spaced joints with very high persistence, (M1) (Janeras *et al.*, 2017).

The main objective of this work is to assess the suitability of the aforementioned geomatic techniques (TLS and GigaPan) to detect and quantify the rockfall events that may occur in three study sites in the period 2019-2021. The sites in this study will be named as follows: [i] Mirador de l'Oliver, [ii] Canal dels Arítjols and [iii] Mirador dels Apòstols. Two of the study sites were located on the BP-1103 road, being the third one close to the Montserrat monastery (Figure 1).

The study was carried out with three TLS point cloud processing software packages, comparing the detected rockfall with the two methods of change detection used.

### III. MONITORING STRATEGY AND SYSTEMS

The Montserrat massif is under progressive surveillance with a wide range of methods, which are described in Janeras *et al.* (2017). From manual and point-based techniques to automatic and continuous systems are in use in the whole area in order to manage the high geological risk over the infrastructures and the visitors. As previously stated, the TLS and the photomonitoring are techniques tested in this study

because they offer a good balance between spatial & time continuity, precision and feasibility. In the following Section A and B, we describe the main characteristics of these techniques as applied in our study.

On the other hand, in the last decade automated and semi-automated workflows have been developed to process the TLS datasets (point clouds), so that professionals can spend more time analysing and interpreting the field net results. Therefore, comparing successive TLS point clouds, the algorithms might detect the changes of the cliff surface, which can be associated as blocks detached from source areas. The volume of these masses are of paramount importance for deriving Magnitude-Frequency relationships.

The present study focuses on testing the most used change detection methods, described in Section C, in order to assess their suitability for the detection of detached blocks in practice.

#### A. Terrestrial laser scanning for rockfall monitoring

LiDAR technology is a remote sensing method used to acquire terrain information in the form of point clouds; a collection of data points in three-dimensional (3D) space. Using a terrestrial laser scanner (TLS) we can rapidly measure the reflected energy of an emitted laser pulse (Girardeau-Montaut *et al.*, 2005), thus acquiring detailed point clouds of terrain with very precise measurements of surface geometry. In the last decade, TLS has become a routine data source for rock slope characterisation and monitoring, especially for its effectiveness in capturing oblique views of vertical rock slopes (Barnhart and Crosby, 2013).

Rockfall detection from the comparison of two-point clouds obtained by LiDAR has been widely used and reported in different articles around the world. In this sense, the Montserrat mountain is not an exception and several authors have carried out their academic work, generating several lines of research started by Abellán (2009) and followed by Royán (2015), Blanch (2016), García (2018), Vinueza (2020), Arones (2021) and Blanco *et al.* (2021).

The technical spec of the TLS sensor and the terrain condition influence the error in the gathered points. According to Jaboyedoff *et al.* (2012) the most relevant sensor parameters are: the laser wavelength; the range measurement method (related to the range precision); the maximum range at select target reflectivity; the laser footprint; and the minimum horizontal and vertical angular increment. The LiDAR equipment is being improved year by year, and as a result, nowadays we are able to capture data faster, at higher densities and precision (Lague *et al.*, 2013).

In the present study, we have used a Leica ScanStation P50 time-of-flight system (Figure 2).



Figure 2. TLS used in the study, Leica ScanStation P50. In the background, the characteristic Montserrat landscape can be appreciated: stepped slopes where vertical conglomerate intercalation of and fine layers of sandstone and siltstone.

The maximum range of Leica P50 depends on the object/terrain reflectivity (Table 1). The precision is remarkable even at these medium/long scanning distances.

Table 1. Leica ScanStation P50 range and precision

TLS System	Max Range	Precision in range	Object Reflectivity
Leica ScanStation P50	270 m 570 m	1.2 mm + 10 ppm 3 mm + 10 ppm	34% 60%

### B. GigaPan

High-resolution panoramic images were generated from a series of pictures captured during each field campaign to aid interpretation of the TLS data. The high-resolution photographs were taken from the scanning position using a Nikon D5300 full frame 24.2 megapixel camera, with a NIKKOR AF-S DX 18-140mm f/3.5-5.6G ED VR - Nikon lens. The camera was mounted on a GigaPan EPIC PRO motorised panoramic head (Figure 3), produced by GigaPan Systems LLC (Lato *et al.*, 2012). The photos were stitched together using GigaPan Stitch software, resulting in a seamless high-resolution panoramic photo of the rock slope (Figure 4).

### C. Methods of Change Detection

Change detection analyses using TLS data are difficult because of (1) the complexity and richness of the point clouds representing the natural environment and (2) because TLS point clouds from different temporal epochs or physical scan positions may not overlap closely enough for accurate point to point comparison (Barnhart and Crosby, 2013). Additionally, the software packages used to process TLS data are often optimized for the built environment and lack analytical tools relevant to natural landscapes.

However, some change detection methods have been successfully used to capture surface changes caused by geomorphic processes, each with their respective advantages and disadvantages. The most commonly used are the following: Cloud-to-Cloud (C2C), Cloud-to-Mesh (C2M), and Multiscale Model-to-Model Cloud Comparison (M3C2). The C2C method compares the points of the first cloud directly with the closest one on the second cloud. In general, the results with C2C are quite noisy, especially when the terrain has some roughness. Therefore, we decide to use and compare the performance of the C2M and M3C2 methods, which are summarized in the next two subsections.

1) *C2M method*: The Cloud to Mesh (C2M) distance comparisons have been used by many authors to detect a change between successive point clouds (Abellán *et al.*, 2009; 2010; Guerin *et al.*, 2014; Vinuesa, 2020). To use the C2M algorithm it is necessary to create a reference (or baseline) mesh, which was built with the point cloud corresponding to the first campaign (July 2019). The algorithm needs at least the following parameters: the size of the triangles for the triangulation of the points and the average distance of the points. The interpolation between the clouds of reference points for the creation of the facets of a triangulated surface model is a complex computational process with irregular surfaces, especially if they have significant roughness. C2M calculates the distance from each point of the second cloud to the nearest point of a facet of a triangulated surface model of the reference cloud (Figure 5A). The accuracy of C2M depends on how well the surface mesh can model the terrain without over interpolating the original geometry of the input point cloud.



Figure 3. GigaPan Epic Pro robotic head with screen and controls equipped with a Nikon D5300 camera.



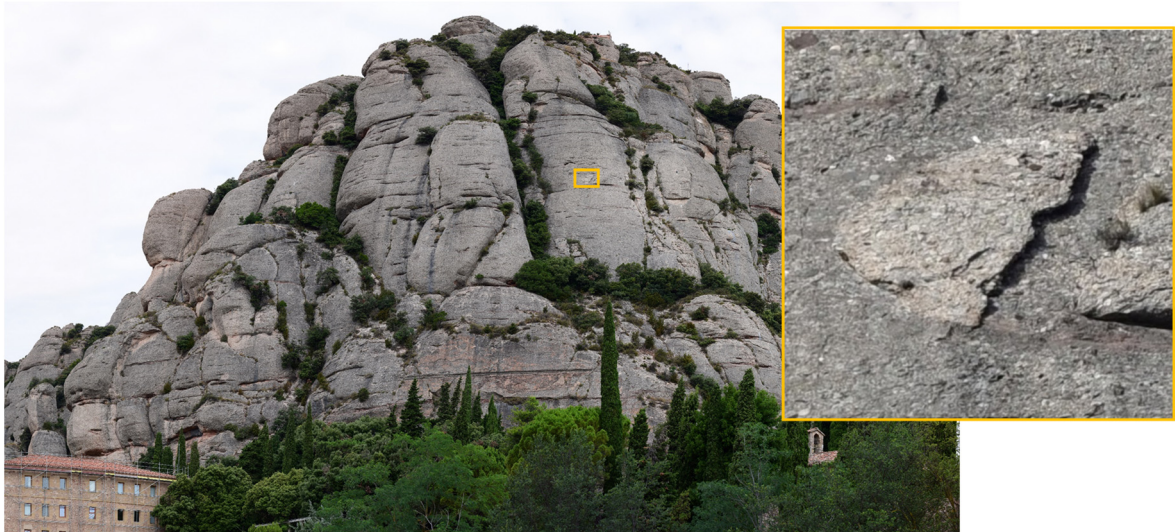


Figure 4. Gigapixel panoramic image, Mirador dels Apòstols. The High Resolution can be appreciated in the right inset.

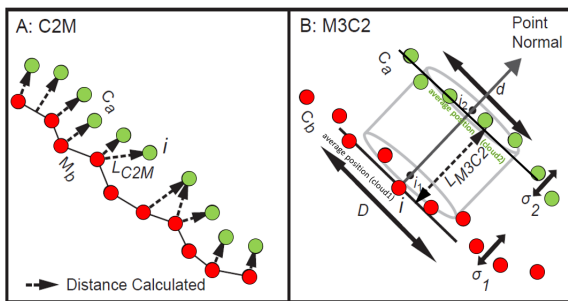


Figure 5. Conceptual diagrams of the C2M and M3C2 techniques. Both A and B are modified from Barnhart *et al.* (2013).

2) *M3C2 Method*: The multiscale model-to-model cloud comparison (M3C2) algorithm created by Lague *et al.* (2013) measures the distance along a local normal vector estimated from each point's neighbourhood, and thus considers local surface orientation in the distance computations. The algorithm projects search cylinders along the local normal vectors to find the locally averaged change between the two clouds. The M3C2 requires two user-defined parameters, which are the normal scale and the projection scale. The normal scale ( $D$ ) is based on the density and roughness of the reference point cloud and is the diameter around each central point to calculate a local normal. The projection scale ( $d$ ) is used to calculate the distance between the two-point clouds and is determined by the defined radius and length of a projection cylinder (Figure 5B). The algorithm operates directly on the point clouds and therefore does not require meshes or grids.

In this study and considering the values reported by Garcia (2018) and Di Francesco *et al.* (2020), the following parameters have been used: the value of 0.25 m has been chosen, since the average distance between the points of the scans is 0.1 m; therefore, between 7 and 8 points of the scan will be used to calculate the normal. This is adequate to avoid too great an influence of the dispersion of points due to the

instrumental error without losing the detail of the real roughness of the surface studied.

#### IV. ACQUIRED DATA

The terrestrial laser scanning was carried out at the three sites described in II, two scans per year, from July 2019 to December 2020. The campaigns or epochs will be named as summarized in Table 2.

Table 2. Campaigns T0-T3

Field date	Name
July 2019	T0 (reference)
December 2019	T1
July 2020	T2
December 2020	T3

The same TLS system was used to collect data at all three sites during the 2-year monitoring period. Each survey consisted of at least one scanning position for each site, with a maximum distance of 375 m and a minimum distance of 75 m from the survey wall.

Figure 6 shows the extent of one of the scan areas. Leica ScanStation P50 scans were parsed using Leica Cyclone REGISTER 360 software.

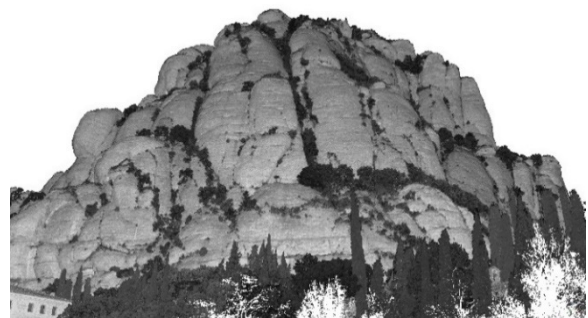


Figure 6. Example of the area covered by July 2019 (T0) scan at the Mirador dels Apòstols.

V. ANALYSIS OF RESULTS. COMPARISON OF METHODS

The rockfall extraction process is depicted in Figure 7. Change detection was conducted to outline active areas due to rockfall.

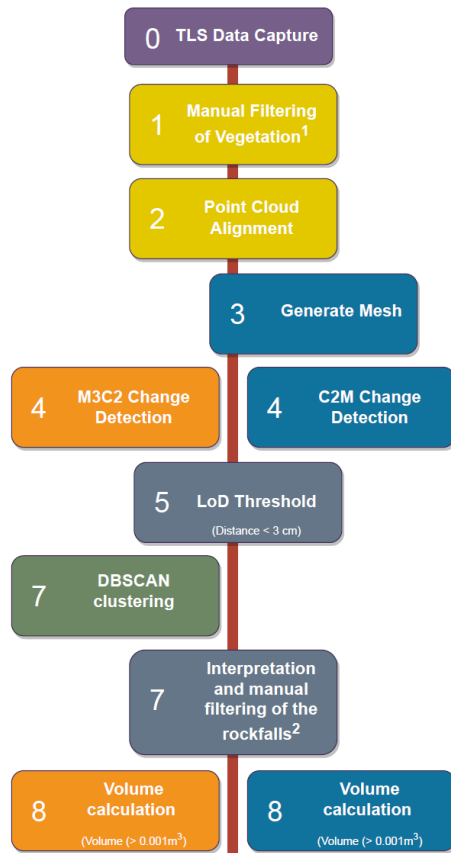


Figure 7. Rockfall detection flowchart.

Point cloud processing has been performed independently with three computer programs: CloudCompare (Girardeau-Montaut, 2021), PointStudio (Maptek, 2021) and Cyclone 3DR (Leica, 2021).

Each software has different tools for the comparison of point clouds and the detection of possible rockfalls (Table 3). Depending on whether point clouds or surfaces are compared, different tools are used.

Table 3. Algorithms in use

Software	Algorithm
Pointstudio (Maptek)	C2M
Cyclone 3DR (Leica)	C2M
CloudCompare	C2M and M3C2

Vegetation was manually removed from the raw point clouds and with the cleaned point clouds aligned to the July 2019 baseline. For the alignment of the clouds, different algorithms are available for each software.

Firstly, with the CloudCompare and Leica Cyclone 3DR software coarse alignment was carried out by manually selecting a minimum of 4 points from the stable areas of the slope with clearly identifiable geometry (Figure 8).

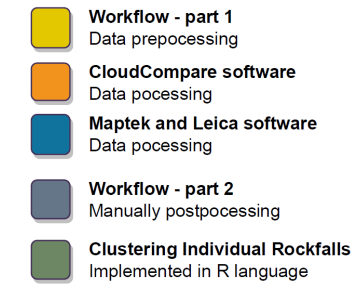


Figure 8. Data processing workflow.

However, with the Maptek PointStudio software, overlapping is achieved by selecting the clouds to be moved, working with the entire point cloud. Once the coarse alignment was done, it was followed by a fine alignment process. In the case of the CloudCompare software, it has the Iterative Closet Points (ICP) algorithm, which is based on aligning the clouds based on a set of strategic points that overlap each other. Similar algorithms are used in Maptek PointStudio and Cyclone 3DR software.

In the three software, records have been obtained in which a root mean square error (RMS) can be observed, with values of, approximately 6 cm. The RMS values of each cloud vary in each software. This variation is because each of them works with a different algorithm to perform the fine alignment process. However, the values are within the same range.

We use both C2M and M3C2 methods for the detection of changes due to rockfall. The change backwards in time highlights the fronts of the changing features. A detection limit threshold was used to extract the fronts and reversals of the loss features. Detection artefacts generated because of random noise within the TLS datasets were manually removed from the point cloud. Finally, false positives were filtered out using (1) a positive-to-negative point ratio threshold and (2) a minimum volume threshold.

The rockfalls detected using the methodology presented in this paper have been summarised in the following Table 4. A total of 8 rockfalls have been detected in the three sector which have been studied. In the Mirador de l'Oliver area, no rockfalls were detected in the period July 2019- December 2020 (T0-T3). In the Canal dels Aritjols area, 1 rockfall was detected in the period July - December 2019 (T0-T1). In the analysis of clouds T1-T2 and T2-T3 no detachments were detected. In the Mirador dels Apòstols area, 7 rockfalls were detected in the period July 2019 - July 2020 (T0-T2). Between T0-T1, there were 3 rockfalls; in the period T1-T2 there were 4 rockfalls and finally in the period T2-T3 no rockfalls were detected.

Table 4. Number of rockfalls --or detached blocks-- per site

Site	T0-T1	T1-T2	T2-T3	Total
Mirador de l'Oliver	0	0	0	0
Canal dels Aritjols	1	0	0	1
Mirador dels Apòstols	3	4	0	7

In the three software used and with the C2M algorithm, the same rockfalls have been detected in each sector (Figure 9 and Table 5). The detection of these rockfalls was carried out manually and corroborated with Gigapixel panoramic images (Figure 10). In the case of the M3C2 algorithm (CloudCompare), similar results were also obtained as can be seen in Figure 9 (right).

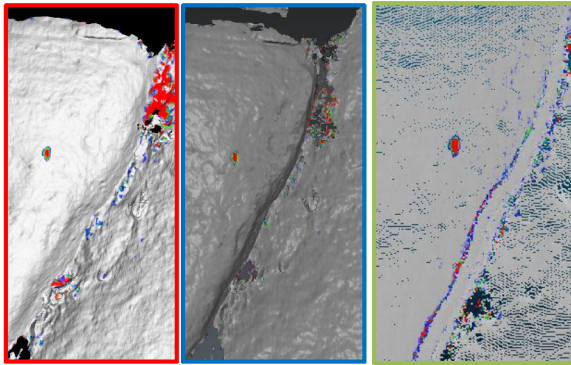


Figure 9. Example of a detached block detected with the three programs: PointStudio- C2M (left); Cyclone- C2M (center); CloudCompare –M3C2 (right).

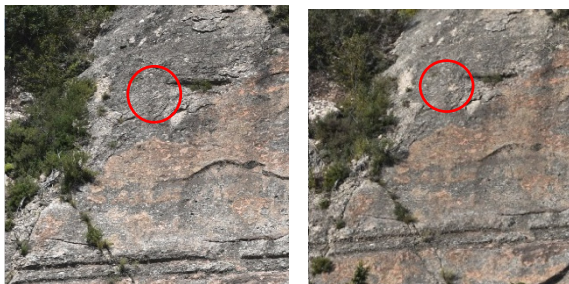


Figure 10. Mirador dels Apòstols site. Comparison between Gigapixel images: T0 campaigns (pre-detachment, left) and T1 campaign (post-detachment, right). In red circle the detected detachment, with a volume of 0.001 m<sup>3</sup>.

Once the rockfalls detected, we computed their volume. Each software has different ways for that. In the case of Mapttek PointStudio, the volume below a surface in relation plane orthogonal to visual TLS at a fixed elevation is calculated. With this method of calculation, it is necessary to analyse each scanned surface independently, the difference between surfaces giving the volume of detached rock (Vinueza, 2020). The Cyclone 3DR obtains the volumes on closed surfaces, so it must be ensured that the meshes containing the rockfall are free of voids that could affect the result. Finally, CloudCompare has the "2.5 D

Volume" volume calculation tool, which can calculate the volume between two clouds through a process of rasterization (gridding) of the point clouds.

The same rock falls have been detected in all three software packages and with both change detection methods, as they have been corroborated by the HR images (Figure 10), and the calculated volumes are relatively similar, even for such small volumes: For instance, the Table 5 shows that the volumes range from 0.001 to 0.055 m<sup>3</sup>, with detachments of less than 0.01 m<sup>3</sup> predominating. The sum of the volumes of all detected rockfalls ranges from 0.078 m<sup>3</sup> to 0.068 m<sup>3</sup>. It is important to mention that these small disparities may be due to differences in the procedure for calculating the volume. For this reason, not having detected any significant rockfall, we state that the instabilities occurring in the study sectors are of low magnitude for the period under consideration.

The Magnitude-Frequency graph corresponding to the 7 rockfalls found in the Mirador dels Apòstols is presented in the Figure 11.

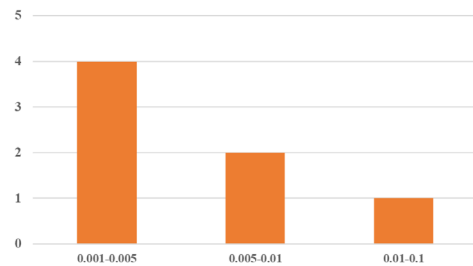


Figure 11. Magnitude-Frequency graph corresponding to the 7 rockfalls detected in the Mirador dels Apòstols.

In addition, satisfactory tests have been carried out with the DBSCAN algorithm to facilitate the detection of rockfalls. As discussed by Tonini and Abellán (2014), an adaptation of the Density-Based Spatial Clustering Algorithm for Noisy applications (DBSCAN) (Ester *et al.*, 1996) was used to cluster individual rockfall events from the unorganised input point cloud. We implemented out the DBSCAN algorithm using R software for statistical computing (R Development Core Team, 2012). R is a free software environment integrating facilities for data manipulation and calculation. The R base can be extended via packages available through the Comprehensive R Archive Network (CRAN).

Table 5. Mirador dels Apòstols, comparison of volumes measured with the C2M method with the three programs

Sector	Volumes measured with Cyclone 3DR [m <sup>3</sup> ]				Volumes measured with Mapttek Pointstudio [m <sup>3</sup> ]				Volumes measured with Cloudcompare [m <sup>3</sup> ]			
	N1-N2	N2-N3	N3-N4	Total	N1-N2	N2-N3	N3-N4	Total	N1-N2	N2-N3	N3-N4	Total
Zona 1	0.008	0.002	0	0.015	0.003	0.001	0	0.005	0.008	0.003	0	0.016
Zona 3	0	0.013	0	0.013	0	0.004	0	0.004	0	0.005	0	0.015
Zona 5	0.005	0.044	0	0.049	0.003	0.055	0	0.058	0.002	0.047	0	0.043
Zona 7	0.001	0	0	0.001	0.001	0	0	0.001	0.002	0	0	0.002
<b>Total</b>	<b>0.014</b>	<b>0.064</b>	<b>0</b>	<b>0.078</b>	<b>0.007</b>	<b>0.061</b>	<b>0</b>	<b>0.068</b>	<b>0.013</b>	<b>0.063</b>	<b>0</b>	<b>0.070</b>

The DBSCAN algorithm looks for sets of positive differences around a given point, according to some search parameters (minimum number of points and search radius) (Figure 12).

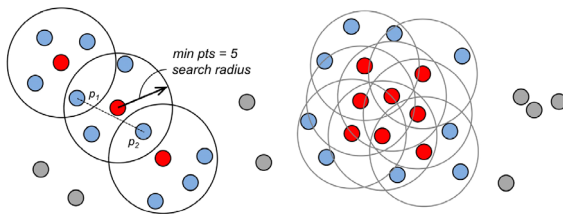


Figure 12. The DBSCAN algorithm there are three types of points as follows: key points (red) are points that satisfy the cluster criteria; border points (blue) do not satisfy the cluster criteria but are within a key point's reach; noise points (grey). From Di Francesco *et al.* (2020).

We started with those proposed in Royán (2015) and Blanch (2016). After a trial-and-error process, using datasets of different characteristics, we concluded that the minimum number of neighbours that the clusters must contain is 15, and the appropriate search radius is 0.01 m in our case.

The clustering process resulted in a point cloud of clustered objects, each with a unique ID. The results were visualised in CloudCompare (Figure 13). Only a small fraction of the clusters corresponds to rockfalls. Most of them are false positives due to the "edge effect" near the limits of the large rock sheets, or related with some remains of vegetation.

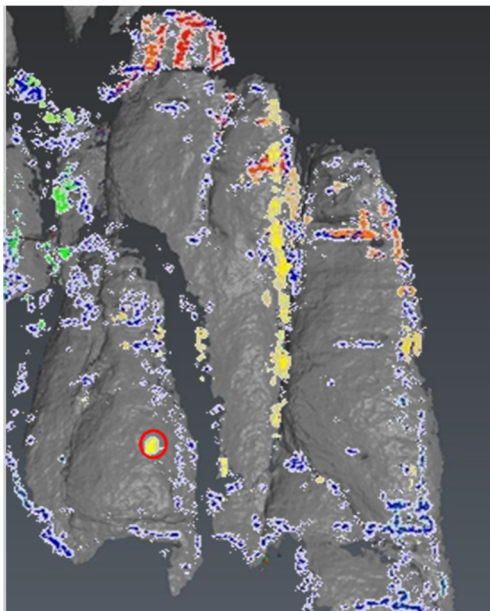


Figure 13. Example of the clusters obtained with DBSCAN. A confirmed rockfall can be appreciated within the red circle, being the rest 'false positives'.

## VI. CONCLUSIONS

Rockfall inventories are essential for capturing rockfall activity and understanding the hazard. The inventories are the basis for the quantitative risk

analysis because the Magnitude-Frequency curves permit the assignment of an annual probability of occurrence for each magnitude.

Our campaigns in Montserrat confirmed that TLS instruments enable a detailed monitoring of the rock cliffs, attaining a new level of accuracy and resolution. Our research shows that CloudCompare, PointStudio and Cyclone (with C2M and/or M3C2 change detection algorithms) offer very similar results for the covered area and period, even for volumes as small as 0.001 m<sup>3</sup>.

We conclude that the same methodology will give satisfactory results in the detection of larger rockfalls, M1 and M2 type, with volumes greater than 0.1 m<sup>3</sup>.

The biggest advantage of CloudCompare is its free licence, greater control of intermediate processes and choice of change detection algorithm, while PointStudio and Cyclone offer more automated processes. Although, according to recent literature, the M3C2 algorithm is more satisfactory and widely used than C2M, in this study we conclude that for complex and irregular surfaces both offer very similar and acceptable results.

In the workflow followed, there are certain tasks that are not automated. Vegetation filtering and rockfall checking on HR images are tedious and time-consuming manual steps. Additional work must be devoted to this automation before TLS monitoring can be truly productive. For instance, for automated rockfall extraction, the improvements may include: the incorporation of the normals (indicative of rock structure, to be used in M3C2); smart routines for clutter and artefact removal; further automation of change detection feature classification; and clustering algorithms capable of separating coalescing rockfall events.

On the other hand, the large number of events collected over years of monitoring will allow the use of Machine Learning techniques to improve the automatic classification of clusters (Blanco *et al.*, 2021).

## VII. ACKNOWLEDGEMENTS

This work is being carried out in the framework of the research project "Advances in rockfall quantitative risk analysis (QRA), incorporating developments in geomatics (GeoRisk)" with reference code PID2019-103974RB-I00, funded by MCIN/AEI/10.13039/501100011033.

## References

- Abellán, A. (2009). *Improvements in our understanding of rockfall phenomenon by Terrestrial Laser Scanning. Emphasis on change detection and its application to spatial prediction.* Universitat de Barcelona - PhD.
- Abellán, A., Calvet, J., Vilaplana, J., and Blanchard, J. (2010). Detection and spatial prediction of rockfalls by means of terrestrial laser scanner monitoring. *Geomorphology*, 119, pp. 162–171.

- Abellán, A., Jaboyedoff, M., Oppikofer, T., and Vilaplana, J. (2009). Detection of millimetric deformation using a terrestrial laser scanner: experiment and application to a rockfall event. *Natural Hazards and Earth System Science*, 9, pp. 365–372. DOI: 10.5194/nhess-9-365-2009
- Alsaker, E., Gabrielsen, R.H., and Roca, E. (1996). The significance of the fracture patterns of Late-Eocene Montserrat fan-delta, Catalan Coastal Ranges (NE Spain). *Tectonophysics*, 266, pp. 465–491.
- Arones, A. (2021). *Monitorización de desprendimientos rocosos en la Montaña de Montserrat mediante técnicas láser. Comparación de alternativas de procesamiento para la detección de bloques desprendidos.* (Trabajo Final de Máster). Universitat Politècnica de Catalunya, Barcelona.
- Barnhart, T.B., and Crosby, B.T. (2013). Comparing Two Methods of Surface Change Detection on an Evolving Thermokarst Using High-Temporal-Frequency Terrestrial Laser Scanning, Selawik River, Alaska. *Remote Sens.*, 5, pp. 2813–2837.
- Blanch, X. (2016). *Anàlisi estructural i detecció de desprendiments rocosos a partir de dades LiDAR a la Muntanya de Montserrat.* (Trabajo Final de Grado). Universitat Politècnica de Catalunya, Barcelona.
- Blanco, L., García-Sellés, D., Pascual, N., Puig, A., Salamó, M., Guinau, M., Gratacos, O., Muñoz, J.A., Janeras, M., and Pedraza O. (2021). Identificación y clasificación de desprendimientos de roca con LiDAR y machine learning en Montserrat y Castellfollit de la Roca (Cataluña). *X Congreso Geológico de España*, 5-7 Julio 2021. Vitoria-Gasteiz. España.
- Corominas, J., Copons, R., Moya, J., Vilaplana, J. M., Altimir, J., and Amigo, J. (2005). Quantitative assessment of the residual risk in a rockfall protected area. *Landslides*, 2, pp. 343–357.
- Di Francesco, P.-M., Bonneau, D., and Hutchinson, J. (2020). The Implications of M3C2 Projection Diameter on 3D Semi-Automated Rockfall Extraction from Sequential Terrestrial Laser Scanning Point Clouds. *Remote sensing*, 12, 27. DOI: 10.3390/rs12111885
- Ester, M., Kriegel, H., Sander, J., and Xu, X. (1996). A Density-Based Algorithm for Discovering Clusters in Large Spatial Databases with Noise. In *Proceedings of the Second International Conference on Knowledge Discovery and Data Mining*, Portland, OR, USA, 2–4 August 1996; Simoudis, E., Fayyad, U., Han, J., Eds.; AAAI Press: Menlo Park, CA, USA, pp. 226–231.
- García, M. (2018). *Millora metodològica per a la detecció i caracterització de desprendiments amb.* Trabajo de Fin de Máster. Universitat de Barcelona, Barcelona.
- Girardeau-Montaut, D., Roux, M., Marc, R., Thibault, G. (2005). Change Detection on Point Cloud Data Acquired with a Ground Laser Scanner. *Int. Arch. Photogramm. Remote Sens. Spat. Inf. Sci.*, 36, pp. 30–35.
- Girardeau-Montaut, D. (2021). CloudCompare, Version 2.11.3 Anoa. Available online: <http://cloudcompare.org> (accessed on 28 December 2021).
- Guerin, A., Hantz, D., Rossetti, J.-P., and Jaboyedoff, M. (2014). Brief Communication: Estimating Rockfall Frequency in a Mountain Limestone Cliff Using Terrestrial Laser Scanner. *Nat. Hazards Earth Syst. Sci. Discuss.*, 2, pp. 123–135.
- Hungr, O., Leroueil, S., Picarelli, L., Article, R. (2014). The Varnes Classification of Landslide Types, an Update. *Landslides*, 11, pp. 167–194.
- Jaboyedoff, M., Oppikofer, T., Abellán, A., Derron, M.H., Loye, A., Metzger, R., and Pedrazzini, A. (2012). Use of LiDAR in Landslide Investigations: A Review. *Nat. Hazards*, 61, pp. 5–28.
- Janeras M., Jara, J.A., Royán, M.J., Vilaplana, J.M., Aguasca, A., Fàbregas, X., Gili, J.A., and Buxó, P. (2017). Multitechnique approach to rockfall monitoring in the Montserrat massif (Catalonia, NE Spain). *Engineering Geology*, 219 (2017) 4–20. DOI: 10.1016/j.enggeo.2016.12.010.
- Janeras, M., Pedraza, O., Lantada, N., Hantz, D., and Palau, J. (2021). TLS - and inventory-based Magnitude - Frequency relationship for rockfall in Montserrat and Castellfollit de la Roca. Conference: *5<sup>th</sup> RSS Rock Slope Stability Symposium*, Chambéry, France.
- Lague, D., Brodu, N., and Leroux, J. (2013). Accurate 3D Comparison of Complex Topography with Terrestrial Laser Scanner: Application to the Rangitikei Canyon (N-Z). *ISPRS J. Photogramm. Remote Sens*, 82, pp. 10–26.
- Lato, M.J., Bevan, G., and Fergusson, M. (2012). Gigapixel Imaging and Photogrammetry: Development of a New Long Range Remote Imaging Technique. *Remote Sens.*, 4, pp. 3006–3021.
- Leica Geosystems AG (2021). Leica ScanStation P50 Product Specifications; Switzerland.
- Leica Cyclone (2021). REGISTER 360-3D Laser Scanning Point Cloud Registration Software. Available online: <https://leica-geosystems.com/products/laser-scanners/software/leica-cyclone/leica-cyclone-register-360> (accessed on 15 November 2021)
- Maptek Pointstudio (2021). Software. Available online: <https://www.maptek.com/products/pointstudio/> (accessed on 15 November 2021)
- Leica Cyclone (2021). 3DR Software. Available online: <https://leica-geosystems.com/es-es/products/laser-scanners/software/leica-cyclone/leica-cyclone-3dr> (accessed on 15 November 2021)
- R Development Core Team (2012). R: A Language and Environment for Statistical Computing. R Foundation for Statistical Computing, Vienna, Austria, <https://www.r-project.org/>
- Royán, M.J. (2015) *Caracterización y predicción de desprendimientos de rocas mediante LiDAR terrestre.* PhD Thesis, Vilaplana (Adv.) Universitat de Barcelona
- Tonini, M., and Abellán, A. (2014). Rockfall Detection from Terrestrial LiDAR Point Clouds: A Clustering Approach Using R. *J. Spat. Inf. Sci.*, 2014, pp. 95–110
- Van Veen, M., Hutchinson, D.J., Kromer, R., Lato, M., and Edwards, T. (2017). Effects of Sampling Interval on the Frequency-Magnitude Relationship of Rockfalls Detected from Terrestrial Laser Scanning Using Semi-Automated Methods. *Landslides*, 14, pp. 1579–1592.
- Vinuesa, J. R. (2020). *Monitoreo de bloques de rocas mediante el uso de láser escáner terrestre (TLS). Estudio de alternativas para la detección de bloques desprendidos.* Trabajo de Fin de Máster. Universitat Politècnica de Catalunya, Barcelona.

## Hydrological-driven landslide in northwestern China measured by InSAR time series analysis

Qianyou Fan<sup>1</sup>, Shuangcheng Zhang<sup>1</sup>, Yufen Niu<sup>2</sup>

<sup>1</sup> College of Geology Engineering and Geomatics, Chang'an University, Xi'an 710054, China, ([1980456976@qq.com](mailto:1980456976@qq.com); [shuangcheng369@chd.edu.cn](mailto:shuangcheng369@chd.edu.cn))

<sup>2</sup> College of Mining and Geomatics Engineering, Hebei University of Engineering, Handan 056038, China, ([niuyufenpippa@163.com](mailto:niuyufenpippa@163.com))

**Key words:** *time-series InSAR; landslide; precipitation; slope stability analysis; two-dimensional deformation*

### ABSTRACT

The Lashagou landslide group is located in the transition zone between the Tibetan Plateau and Loess Plateau and is a typical shallow loess landslide group. Precipitation is a major hydrologic trigger for landslides in the northwestern China. Monitoring landslide movement constitutes a critical and requisite component of landslide hazard mitigation. Multi-track InSAR time series analysis can extract the 3D displacement of landslide, provide an indication of landslide occurrence and extent. In addition, quantifying the interaction between precipitation and landslide initiation and mobility to empirically determine the precipitation threshold associated with landslide movement is crucial for mitigating landslide hazards. In this paper, we highlight the results on mapping landslides over the state of Lashagou landslide group. The deformation rate and time series deformation of the Lashagou landslide group in the line-of-sight (LOS) direction from February 2020 to February 2021 were calculated using ascending and descending Sentinel-1A and Stanford Method for Persistent Scatterers (StaMPS) techniques. Besides, we obtained the two-dimensional deformation of the Lashagou landslide group by combining the slip geometr, LOS deformation, and SAR satellite imaging geometry. The results show that Lashagou landslide group is in the creep deformation stage. We compared the time series deformation of the extracted InSAR with that of the projected GNSS, and find that the measured values of InSAR and GNSS are highly similar in amplitude and deformation trend. In addition, the safety operation of G310 highway under the Lashagou landslide group was evaluated according to the observed deformation. We conclude that concentrated continuous rainfall is the main driver of landslide displacement, and that satellite observations of landslide movement and analysis of hydrological variables have improved our understanding of landslide mechanisms.

### I. INTRODUCTION

Landslide is a natural disaster caused by the shearing movement of the slope under the action of gravity, earthquake and rainfall (Strozzi *et al.*, 2018). It plays an important role in the process of mountain evolution (Shi *et al.*, 2021), and rainfall is one of the most important factors that induce the occurrence and development of landslides (Lu and Kim, 2021). Under the influence of heavy rainfall, surface water infiltration and groundwater runoff cause the groundwater inside the landslide to rise. This increases the pore water pressure, resulting in a significant reduction in soil strength, which is prone to landslide disaster (Zhang *et al.*, 2014). It is important to note that rainfall-induced landslides tend to have a regional cluster effect, which can cause massive damage in a short period of time (Liu *et al.*, 2016). For example, on September 16, 2011, 1162 shallow soil landslides were triggered by heavy rain in Nanjiang County, China (Zhang *et al.*, 2016). The number of rainfall-induced landslides is expected to increase due to the frequent occurrence of extreme rainfall events caused by global climate change (Segoni *et al.*, 2021). Therefore, early identification and

longterm monitoring of rainfall-induced landslides are necessary to mitigate the damage caused by landslides.

Monitoring landslide movement helps people to understand the evolution of landslide morphological characteristics over time and the mechanism by which external forces (such as precipitation and groundwater level changes) control landslide movement (Hu *et al.*, 2019). Moreover, the time series deformation can provide important information for the early warning of landslides (Intrieri *et al.*, 2018), which plays an important role in the management of landslide disasters. Conventional slope monitoring methods can only obtain sparse measurements at a few locations on or within the affected slopes, such as from Global Navigation Satellite System (GNSS), inclinometers, crack gauges, and acoustic sensors (Shi *et al.*, 2018; Song *et al.*, 2021). To overcome this, numerous researchers have sought to utilise the spaceborne Interferometric Synthetic Aperture Radar (InSAR) measurement which can map an entire landslide body continuously at a high spatial resolution (Zhao *et al.*, 2019) and enables the investigation of the spatiotemporal features of multisurface failures (Hu *et al.*, 2020).

A major limitation of InSAR is that the resulting motion measurements are restricted to a one-dimensional line-of-sight (LOS) viewing geometry. However, surface motions generally occur in the three spatial dimensions (*i.e.*, east (E), north (N) and up (U)). This means that the InSAR analysis of a stack of synthetic aperture radar (SAR) images acquired in a single viewing geometry is not able to fully capture the magnitude and direction of surface motions (Fuhrmann and Garthwaite, 2019). As a consequence, these LOS measurements are hard to interpret and communicate to stakeholders unfamiliar with the concept of a 1D viewing geometry. Several methods have been proposed to solve this problem, but the weaknesses of each method cannot be neglected (Ao *et al.*, 2019).

The research object of this paper is the Lashagou landslide group. Based on the Sentinel-1A images of ascending and descending from February 2020 to February 2021, the millimeter-scale LOS deformation is extracted by StaMPS technique. Then, we obtained the 2D-deformation of the Lashagou landslide group by combining the slip geometry, LOS deformation, and SAR satellite imaging geometry. Meanwhile, according to the time series deformation, we found that there is a significant correlation between the accelerated deformation and rainfall of the Lashagou landslide group. Finally, the 2D-dimensional deformation helps us to clarify the magnitude and direction of the landslide deformation, which provides support for the dynamic analysis of the landslide.

## II. STUDY AREA

The study area is located in Linxia City, Gansu Province, which is the transition zone between the Tibetan Plateau and Loess Plateau. The geographical location is shown in Figures 1a and 1b. The geological structure of the study area, affected by the Himalayan orogeny, is a resurrection of old tectonic movement and large scale uneven lifting movement (Cai *et al.*, 2015). There are many valleys in the territory, with an average altitude of 2000 m. The landform types are low mountain valleys and piedmont hills, and the mountainous area accounts for 90% of the total area (Jia *et al.*, 2018).

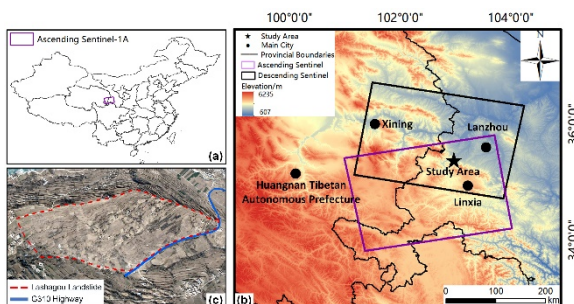


Figure 1. Overview of the study area: a) and b) The location of the study area and the coverage of satellite radar imagery; c) An optical image of the Lashagou landslide group.

The study area has a temperate continental climate, with a stable groundwater level of 11 m and an average annual rainfall of 350-500 mm. The rainfall from May to August accounts for 60%-78% of the annual average rainfall, and it mostly occurs in the form of heavy rain and extreme precipitation events (Wang *et al.*, 2020). Longterm rainfall increases the groundwater level, reduces the mechanical properties of the soil layer, which is prone to landslide disasters.

## III. DATA AND METHODS

### A. SAR Datasets

The SAR images processed are Sentinel-1 Terrain Observation by Progressive Scans (TOPS) data in Interferometric Wide (IW) swath mode with a spatial resolution of about 2.3 m in range and 13.9 m in azimuth. The Sentinel satellite is a satellite constellation consisting of two satellites (Sentinel-1A/B) developed by the European Space Agency (ESA) for the Copernicus Global Observation Program. It uses C-band imaging with a wavelength of 5.6 cm. 29 Sentinel-1 images in the descending track and 32 images in the ascending track from 9 February 2020 to 27 February 2021 with a minimum temporal baseline of 12 days were collected.

According to the principle of maximum overall coherence, the GAMMA software was used to generate interferograms which started with the coregistration of Single Look Complex (SLC) images to a common primary image (31 August 2020 for ascending and 24 September 2020 for descending). The specific acquisition dates and spatiotemporal baseline combinations of the ascending and descending datasets are shown in Figure 2. In this paper, AW3D 30 DEM (ALOS World 3D Digital Surface Model) with a resolution of 30 m is used to eliminate the influence of terrain fluctuations, and high-precision DEM with a resolution of better than 0.2 m obtained by unmanned aerial vehicle (UAV) is used to calculate the slope angle and aspect of the Lashagou landslide group. In addition, this paper obtained the observation data of two GNSS stations (BZ01 and BZ02) located on the Lashagou landslide to verify the InSAR results, and obtained the daily rainfall data of the Linxia meteorological station from 2020 to 2021 for the analysis of factors affecting the landslide stability.

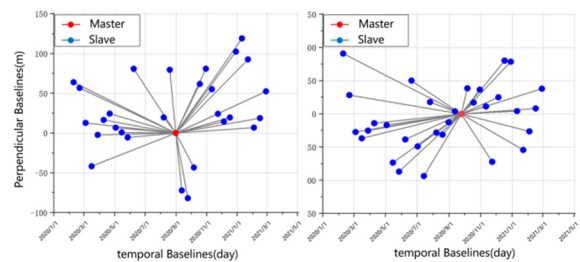


Figure 2. Temporal spatial baseline graph of (a) ascending and (b) descending Sentinel-1A Interferometric Pairs.

## B. StaMPS Processing

A network of interferograms in single look can be generated and geocoded based on the resampled SLC images and a 30 m DEM after the coregistration. The tropospheric delay correction from Generic Atmospheric Correction Online Service (GACOS) for InSAR was then applied to these interferograms (Yu *et al.*, 2017). The interferograms with tropospheric correction were imported into the StaMPS software (Hooper *et al.*, 2012) to perform the PS analysis. Pixels with an amplitude dispersion index lower than 0.45 were selected as the "first-round" coherent pixels. The "second-round" coherent pixels were identified based on the characteristics of their phase noise.

After correcting the look-angle error and squint-angle error, the wrapped phase was unwrapped using a 3D-dimensional phase unwrapping method. Subsequently, spatial correlation errors were removed by high-pass filtering of the unwrapped data over time, followed by low-pass filtering in space. Finally, we obtained the LOS velocity and time series deformation using an SVD (Singular Value Decomposition) method.

## C. Method for 2D-dimensional Deformation

In this paper, the sliding surface is used as the reference surface to observe the movement of the landslide. Under the action of natural forces, the sliding body has a larger terrain drop on the slope of the sliding surface, which is easy to generate a large gravitational potential energy and promote its own displacement. It can be seen that the changes of the slope and aspect of the sliding surface can reflect the overall movement intensity and direction of the landslide, which is just conforms to the law of the landslide movement. Therefore, this paper introduces two terrain factors, the slope and the aspect, to construct the sliding surface coordinates of the landslide movement. It is worth noting that the actual sliding surface of a landslide is often a changing surface. Since the specific shape of the sliding surface cannot be known, a uniform sliding surface is used in this paper to replace the actual sliding surface (Shi, *et al.*, 2020).

Figure 3 shows the geometric relationship between the sliding surface coordinate system and the "North-East-Up" (NEU) coordinate system.  $d_T$ ,  $d_V$ , and  $d_Z$  represent the deformation vectors on the three axes of the sliding surface coordinate system.  $d_N$ ,  $d_E$ , and  $d_U$  represent the deformation vectors on the three axes of the NEU coordinate system, and  $\alpha$  and  $\beta$  represent the slope and aspect of the sliding surface, respectively. According to its geometric relationship, there are deformation projections of  $d_T$  and  $d_Z$  in both the horizontal and vertical directions. Because the slope axis T and the normal axis Z are in the same vertical plane, the deformation projections of  $d_T$  and  $d_Z$  on the horizontal plane should be overlapped, while  $d_V$  perpendicular to the vertical plane, the deformation projection in the vertical direction is zero.  $d_V$  is located

in the horizontal plane, and there are deformation projections in the east-west and north-south directions. From this, the projection relationship matrix of the deformation between the sliding surface coordinate system and the NEU coordinate system can be obtained (Eq. 1):

$$\begin{bmatrix} d_E \\ d_N \\ d_U \end{bmatrix} = \begin{bmatrix} \cos\alpha\sin\beta & -\cos\beta & \sin\alpha\sin\beta \\ \cos\alpha\cos\beta & \sin\beta & \sin\alpha\cos\beta \\ -\sin\alpha & 0 & \cos\alpha \end{bmatrix} \begin{bmatrix} d_T \\ d_V \\ d_Z \end{bmatrix} \quad (1)$$

It is stipulated that the movement towards the satellite is positive, and the movement away from the satellite is negative.

According to the SAR satellite imaging geometry, the surface deformation in the LOS direction ( $d_{LOS}$ ) is the sum of the projection of deformation in the east-west ( $d_E$ ), north-south ( $d_N$ ), and vertical ( $d_U$ ) directions, as shown in Eq. (2):

$$d_{LOS} = [\cos\theta \quad \sin\theta\sin\varphi \quad -\sin\theta\cos\varphi] \begin{bmatrix} d_U \\ d_N \\ d_E \end{bmatrix} \quad (2)$$

where  $\theta$  is the incident angle of the radar satellite  
 $\varphi$  is the heading angle of the radar satellite

In the natural environment, the sliding body usually moves downward along the sliding direction under the force of gravity. In the absence of strong external forces (such as artificial slope changes, etc.), the deformation along the normal direction of the sliding surface is much smaller than the deformation in other directions. Therefore, the deformation along the normal direction  $d_Z$  is regarded as a zero constant in this paper. Combining Equations 1 and 2, the projection relationship matrix of the deformation on the sliding surface coordinate system and the LOS direction of the radar satellite can be obtained, as follows (Eq. 3):

$$\begin{bmatrix} d_T \\ d_V \end{bmatrix} = \begin{bmatrix} a_1 & b_1 \\ a_2 & b_2 \end{bmatrix}^{-1} \begin{bmatrix} d_{LOS}^a \\ d_{LOS}^d \end{bmatrix} \quad (3)$$

where  $a_i = \cos\theta_i * \cos\alpha * \cos\beta + \sin\theta_i * \sin\varphi_i * \cos\alpha * \cos\beta + \sin\theta_i * \cos\varphi_i * \sin\alpha$   
 $b_i = \cos\theta_i * \sin\alpha * \sin\beta + \sin\theta_i * \sin\varphi_i * \sin\alpha * \cos\beta - \sin\theta_i * \cos\varphi_i * \cos\alpha$

## IV. RESULTS AND DISCUSSION

### A. InSAR Monitoring Results

Using the ascending and descending SAR data, the velocity map in the LOS direction of the Lashagou landslide group between 9 February 2020 to 27 February 2021 was calculated. The results are shown in Figure 4, in which Figure 4a is the LOS velocity in the ascending direction, and Figure 4b is the LOS velocity in the descending direction. Note that negative values indicate that the landslide displacement is in the



direction away from the satellite, and positive values indicate that the landslide displacement is in the direction of the satellite. It can be seen from Figure 4 that the deformation of the Lashagou landslide group is mainly distributed in the northern part of Lashagou Village, where the deformation rate of the toe close to the road excavation is faster than that of the crown; thus, the entire landslide moves toward the G310 highway by pulling the crown from the toe. The maximum deformation in the LOS direction of the ascending and descending are -51 mm/yr and 49 mm/yr, respectively. The range and magnitude of the deformation regions calculated in different SAR datasets in the same time period are highly consistent. However, because different SAR satellites have different imaging geometries, and the displacement patterns at different locations of the same landslide may be different, resulting in different deformation features in the southern part of the study area.

respectively. Since the GNSS stations and PS points are not completely coincident, and there are certain errors in both monitoring techniques, the two measurements are not completely consistent. The MAE (Mean Absolute Error) and RMSE (Root Mean Square Error) are shown in Table 1. The maximum MAD and RMSE are 2.64 mm and 2.3 mm, respectively. However, such disparities are notably small in magnitude with respect to the deformation measurements. Therefore, we could conclude that the measurements derived by StaMPS are reliable.

Table 1. Comparison of InSAR and GNSS monitoring results

SAR dataset	GNSS station	Mean absolute error [mm]	Root mean square error [mm]
Ascending	BZ01	2.64	2.30
	BZ02	2.23	1.68
Descending	BZ01	2.51	1.95
	BZ02	2.35	2.00

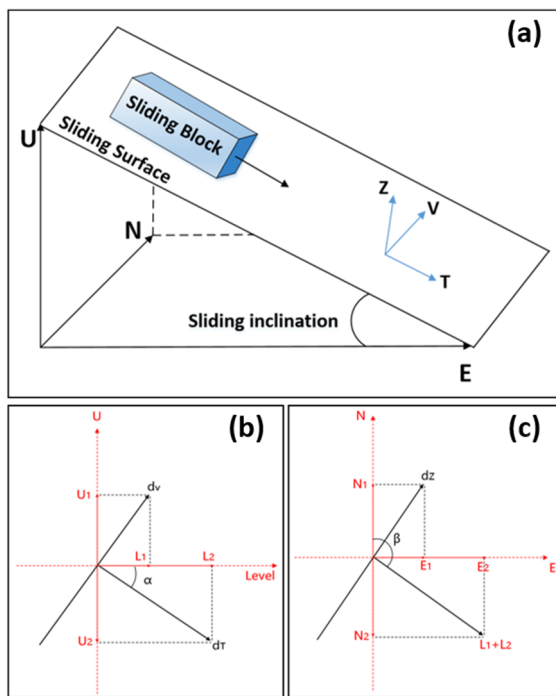


Figure 3. a) The coordinate system of the sliding surface of landslides. b) and c) The geometric relationship between the sliding surface and NEU coordinate system.

The time series deformation measurements of two GNSS stations (BZ01 and BZ02) located at the toe of the Lashagou landslide group were used to verify the accuracy of the InSAR measurements. Their specific locations are indicated by black triangles in Figure 4. In this study, the GNSS deformation observations in the three directions of the NEU are converted to the LOS direction of the radar according to Equation 2. Figure 5 shows the comparison results of the two GNSS stations and the observation values of the adjacent PS points. Figures 5a to 5b are the comparison of ascending InSAR and BZ01, ascending InSAR and BZ02, descending InSAR and BZ01, and descending InSAR and BZ02,

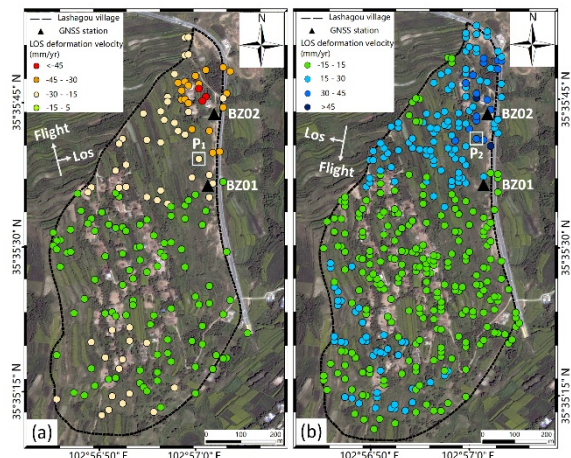


Figure 4. Surface average deformation rate maps in the LOS direction, (a) ascending and (b) descending.

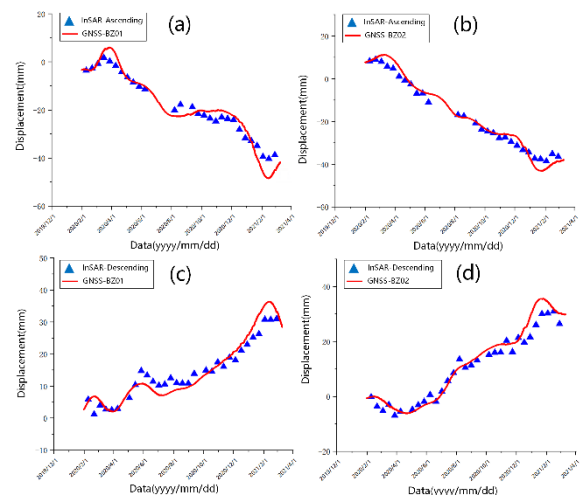


Figure 5. The comparison of LOS time series deformation between InSAR and GNSS.

## B. 2D Displacement Results

In this paper, the LOS velocity in the ascending and descending orbits is used to calculate the two-dimensional deformation velocity of the Lashagou landslide group on the sliding surface according to Equation 3, as shown in Figure 6. Figure 6a shows the deformation velocity along the sliding direction of the landslide on the sliding surface, Figure 6b shows the deformation velocity along the vertical direction on the sliding surface, and Figure 6c shows the two-dimensional deformation velocity on the sliding surface. The red arrows in the figure represent the displacement direction and magnitude of the landslide.

The two-dimensional deformation velocity on the sliding surface clearly shows the magnitude and direction of landslide deformation. Obviously, the deformation along the slope is significantly larger than that in the vertical direction. The maximum sliding deformation rate is 48 mm/yr, and the displacement directions are almost downwards along the slope. The deformation magnitude in the northern part of the landslide group is significantly larger than that in other areas (Figure 6a). The maximum vertical deformation velocity is 49 mm/yr, and the displacement direction varies greatly with the terrain. Obviously, there are two vertical deformation regions in the study area with opposite directions (Figure 6b). In the northern part of the study area, the landslide group moved in the direction of 30° east-north, and the deformation was relatively severe; on the contrary, in the northern part of the study area, the landslide group moved in the direction of 30° south-west, and the deformation was relatively stable. As Figure 6c shows, the maximum two-

dimensional deformation of Lashagou landslide group is 68 mm/yr, and the deformation in the northern area is the most severe. The deformation range is consistent with the deformation characteristics reflected by the InSAR LOS measurements. Therefore, the northern region is the most unstable active block in the Lashagou landslide group, because of the favorable free-face conditions, higher sliding degrees of freedom, and larger sliding force caused by the steep terrain. It is prone to cause overall deformation and failure under the force of external factors, such as rainfall, which seriously threatens the safe operation and driving safety of the G310 highway. Therefore, it is necessary to monitor the deformation trend of the active deformed slope in real time.

## C. Discussion

To analyze the control mechanism of rainfall and freeze-thaw cycles for the Lashagou landslide group, two PS pixels (P1 and P2) and two GNSS stations (BZ01 and BZ02) were selected for time series analysis. Figure 7a is the time series deformation of BZ01 and P2 obtained from the descending LOS deformation results, and Figure 7b is the time series deformation of BZ02 and P1 obtained from the ascending LOS deformation results. Figure 7c illustrates the changes of rainfall during the experiment and the solid blue line is the cumulative rainfall for 30 days. The gray columns indicate freezing periods corresponding to the period from mid-November of each year to mid-February of the following year, and the purple columns indicate freeze-thaw cycle periods corresponding to early November and late February to mid-March each year.

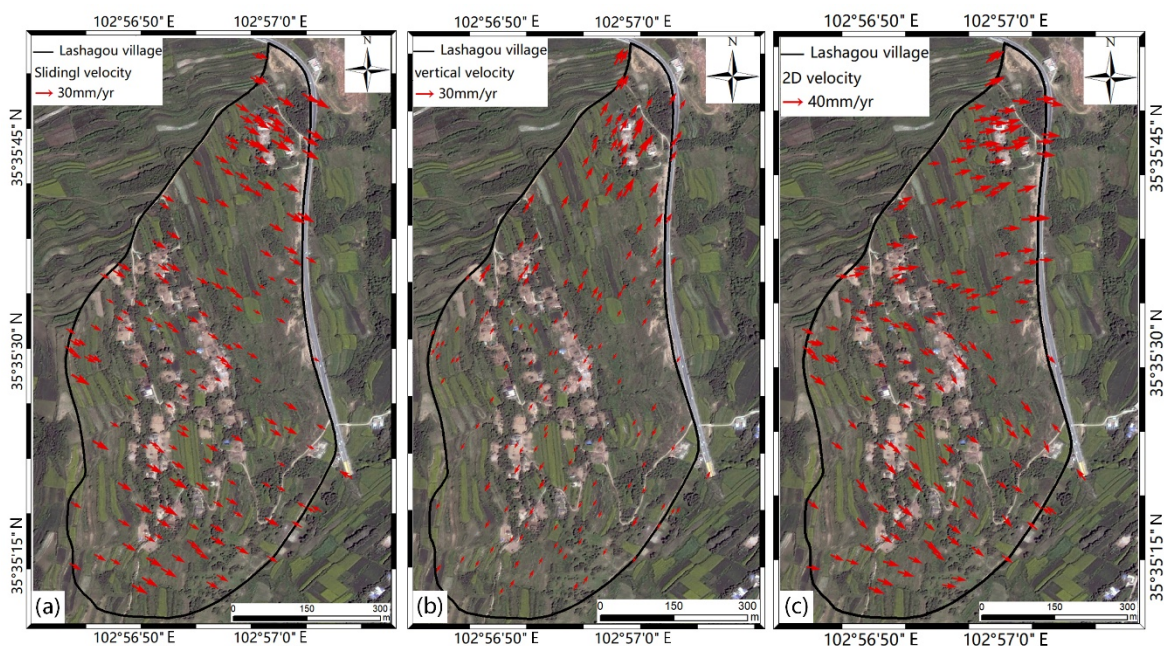


Figure 6. Two-dimensional deformation: a) Deformation along the sliding direction; b) Deformation along the vertical direction; c) Two-dimensional deformation on the sliding surface.

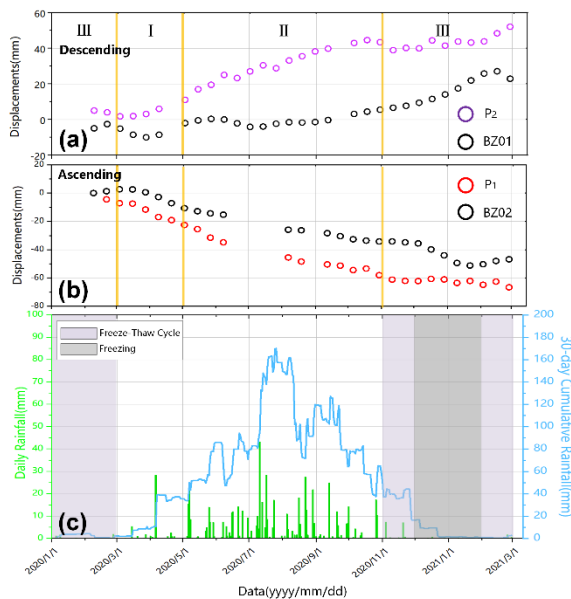


Figure 7. a) and b) Time series deformations of descending and ascending orbits, respectively. c) Relationships among landslide displacements and precipitation.

The landslide displacement is divided into three stages according to the changes of daily rainfall and 30 day cumulative rainfall. In the first stage (March to May), the temperature of the study area rose from about minus 20 °C to above zero, and the surface water changed from solid to liquid (Cai *et al.*, 2015). The rapid snowmelt and surface water infiltration soften the soil near the permeable layer, reduce the shear strength significantly, and form a weak structural surface (Shi, *et al.*, 2020). The release and flow of groundwater may cause different weak discontinuities to connect with each other and gradually penetrate, thus forming sliding zones. The landslide starts to slide along the sliding zone under the forces of gravity and other sliding forces. In the second stage (May to October), the precipitation is concentrated. At this time, rainfall infiltration or the rising groundwater level will lead to an increase in the gravitational potential energy of the landslide and a decrease in the frictional resistance of the sliding zone (Hu *et al.*, 2020), which will cause the landslide to be in a state of continuous accelerated downhill movement in the rainy season. In the third stage (November to February of the following year), the temperature dropped sharply, and the average temperature was negative. During this period, the exposed sliding zone at the free surface of the landslide froze, which increased the shear strength and thus limited the shearing out of the landslide (Zhao *et al.*, 2019). The downhill movement of the slope began to slow until it stabilized. Therefore, the groundwater level changes caused by rainfall and soil freeze-thaw cycles are the main reasons for the continuous deformation of the Lashagou landslide group.

## V. CONCLUSIONS

In this paper, the two-dimensional deformation of the Lashagou landslide group are obtained by using the Sentinel-1A images and the StaMPS method assisted by GACOS. The time series analysis was carried out on the landslide hazard area and the influence of rainfall, human activities and other factors on the stability of the landslide was discussed. The results of the InSAR LOS measurements show that the deformation of the Lashagou landslide group is mainly distributed in the northern area. The deformation rate of the toe close to the road excavation is faster than that of the crown; thus, the entire landslide moves toward the G310 highway by pulling the crown from the toe. Through the comparative analysis with the daily rainfall data, it is found that the groundwater level change caused by rainfall and freeze-thaw cycle are the main reasons for the continuous deformation of the Lashagou landslide group.

The two-dimensional deformation of the sliding surface obtained from the LOS deformation shows that the deformation of the Lashagou landslide group along the sliding direction is generally greater than that of the vertical direction. The two-dimensional deformation of the study area is up to 68 mm/yr, and the persistent deformation in the northern area was caused by the human activities and slop excavation. Compared with the InSAR LOS measurements, the two-dimensional deformation clearly shows the deformation characteristics of the Lashagou landslide group, and the magnitude and direction of landslide deformation in different areas are clearly defined. This helps people better understand landslides and provides important and reliable deformation information for landslide management. This is helpful to improve our understanding of the spatiotemporal evolution of its morphological characteristics and the control mechanism of the influences of internal and external forces on landslide deformation.

## VI. ACKNOWLEDGEMENTS

The authors are thankful for the free using of StaMPS. Sentinel-1 data were provided by ESA.

## References

- Ao, M., Zhang, L., Shi, X.G., Liao, M.S., and Dong, J. (2019). Measurement of the Three-Dimensional Surface Deformation of the Jiaju Landslide Using a Surface-Parallel Flow Model. *Remote Sensing Letters*, Vol. 10, No. 8, pp. 776-785.
- Cai, G.Z., Yang, Z.H., Wang, D.P., Sun, Y.L., and Zhou, S.D. (2015). Cause Analysis and Defense Countermeasures of Geological Hazards in Linxia City, Gansu Province. *Journal of Agricultural Catastrophology*, Vol. 5, No. 4, pp. 32-35.
- Fuhrmann, T., and Garthwaite, M.C. (2019). Resolving Three-Dimensional Surface Motion with InSAR: Constraints from Multi-Geometry Data Fusion. *Remote Sensing*, Vol. 11, No. 3, pp. 241-261.

- Hu, X., Bürgmann, R., Lu, Z., Handwerker, A.L., Wang, T., and Miao, R.Z. (2019). Mobility, Thickness, and Hydraulic Diffusivity of the Slow-Moving Monroe Landslide in California Revealed by L-Band Satellite Radar Interferometry. *Journal of Geophysical Research: Solid Earth*, Vol. 124, No. 7, pp. 7504-7518.
- Hu, X., Bürgmann, R., Schulz, W.H., and Fielding, E.J. (2020). Four-Dimensional Surface Motions of the Slumgullion Landslide and Quantification of Hydrometeorological Forcing. *Nature Communications*, Vol. 11, No. 1.
- Hooper, A., Bekaert, D., Spaans, K., and Arıkan, M. (2012). Recent Advances InSAR Interferometry Time Series Analysis for Measuring Crustal Deformation. *Tectonophysics*, Vol. 514, pp. 1–13.
- Intrieri, E., Raspini, F., Fumagalli, A., Lu, P., Del Conte, S., Farina, P., Allievi, J., Ferretti, A., and Casagli, N. (2018). The Maoxian Landslide as Seen from Space: Detecting Precursors of Failure with Sentinel-1 Data. *Landslides*.
- Jia, C.P., Jin, Z.X., Yang, P., and Tang, Z.L. (2018). Stability Analysis on Landslide in Section K181 + 840 ~ K182 + 040 of Lin-Da Highway. *Journal of Lanzhou Petrochemical Polytechnic*, Vol. 18, No. 3, pp. 26-28.
- Liu, L., Yin, K.L., Wang, J.J., Zhang, J., and Huang, F.M. (2016). Dynamic Evaluation of Regional Landslide Hazard Due to Rainfall: A Case Study in Wanzhou Central District, Three Gorges Reservoir. *Chinese Journal of Rock Mechanics and Engineering*, Vol. 35, No. 3, pp. 558-569.
- Lu, Z., and Kim, J. (2021). A Framework for Studying Hydrology-Driven Landslide Hazards in Northwestern US Using Satellite InSAR, Precipitation and Soil Moisture Observations: Early Results and Future Directions. *GeoHazards*, Vol. 2, pp. 17-40.
- Segoni, S., Gariano, S.L., and Rosi, A. (2021). Preface to the Special Issue "Rainfall Thresholds and Other Approaches for Landslide Prediction and Early Warning". *Water*, Vol. 13, No. 3.
- Shi, X.G., Zhang, L., Zhou C., Li, M.H., and Liao, M.S. (2018). Retrieval of Time Series Three-Dimensional Landslide Surface Displacements from Multi-Angular SAR Observations. *Landslides*.
- Shi, G.L., Chen, Q., Liu, X.W., Yang, Y.H., Xu, Q., and Zhao, J.J. (2020). Deformation Velocity Field in the Aspect Direction of an Ancient Landslide in Taoping Village Derived from Ascending and Descending Sentinel-1a Data. *Journal of Engineering Geology*.
- Shi, X.G., Hu, X., Sitar, N., Kayen, R., Qi, S.W., Jiang, H.G., Wang, X.D., and Zhang, L. (2021). Hydrological Control Shift from River Level to Rainfall in the Reactivated Guobu Slope Besides the Laxiwa Hydropower Station in China. *Remote Sensing of Environment*, Vol. 265.
- Song, C., Yu, C., Li, Z.H., Pazzi, V., Del Soldato, M., Cruz, A., and Urti, S. (2021). Landslide Geometry and Activity in Villa De La Independencia (Bolivia) Revealed by InSAR and Seismic Noise Measurements. *Landslides*.
- Strozzi, T., Klimeš, J., Frey, H., Huggel, C., Wegmüller, U., and Rapre, A.C. (2018). Satellite SAR Interferometry for the Improved Assessment of the State of Activity of Landslides: A Case Study from the Cordilleras of Peru. *Remote Sensing of Environment*, Vol. 217, pp. 111-125.
- Wang, M.H., Zhao, H., Ni, T.X., Chen, L., and Wang, L.C. (2020). Stability Analysis of the Nalesi Ancient Landslide Based on the Discontinuous Layout Optimization. *Northwestern Geology*, Vol. 53, No. 1, pp. 234-242.
- Yu, C., Li, Z.H., and Penna, N.T. (2017). Interferometric Synthetic Aperture Radar Atmospheric Correction Using a GNSS-Based Iterative Tropospheric Decomposition Model. *Remote Sensing of Environment*, Vol. 204, pp. 109-121.
- Zhang, Q., Xu, Q., Yi, J.S., Xu, L., and Ma, Z.G. (2016). Rainfall Infiltration Depth and Formation Mechanism of Slow-Inclination Soil Landslides in Nanjiang. *Chinese Journal of Geotechnical Engineering*, Vol. 38, No. 8, pp. 1447-1455.
- Zhang, S.R., Tan, Y.S., Wang, C., and Yu, M. (2014). Influence of Heavy Rainfall Characteristics on Saturated-Unsaturated Slope Failure. *Chinese Journal of Rock Mechanics and Engineering*, Vol. 33, No. 2, pp. 4102-4112.
- Zhao, C.Y., Liu, X.J., Zhang, Q., Peng, J.B., and Xu, Q. (2019). Research on Loess Landslide Identification, Monitoring and Failure Mode with InSAR Technique in Heifangtai, Gansu. *Geomatics and Information Science of Wuhan University*, Vol. 44, No. 7, pp. 996-1007.

## Soil Moisture Mapping Based on Temperature-Soil Moisture Dryness Index - a case study for the tailing dam in Brumadinho, Brazil

Yu Lan, Jens-André Paffenholz

Institute of Geo-Engineering, Clausthal University of Technology, Germany, ([yu.lan@tu-clausthal.de](mailto:yu.lan@tu-clausthal.de); [jens-andre.paffenholz@tu-clausthal.de](mailto:jens-andre.paffenholz@tu-clausthal.de))

**Key words:** *Soil moisture; Tailing dam; Brumadinho; TMDI; TVDI; ET; Landsat8*

### ABSTRACT

The tailing dam in Brumadinho of Brazil collapsed on 25<sup>th</sup> January 2019, it caused serious casualties and environmental pollution. The monitoring of the tailing dam stability has become an urgent problem. For monitoring, soil moisture is an important parameter, if the soil moisture is too high, it will cause soil liquefaction and then the stability of the tailing dam will decrease. In this study, Landsat 8 data is innovatively used to calculate the Temperature-Soil Moisture Dryness Index (TMDI) for the estimation of soil moisture of the collapsed tailing dam in Brumadinho. The data on 14<sup>th</sup> January 2019 and 30<sup>th</sup> January 2019 are used in order to better understand the soil moisture before and after the collapse of tailing dam. TMDI is calculated based on triangle space of Land Surface Temperature (LST) and Normalized Difference Latent Heat Index (NDLI). This new index TMDI is used for the assessment of the soil moisture and evapotranspiration (ET). The performance of TMDI and Temperature Vegetation Dryness Index (TVDI) are evaluated by the reference evapotranspiration (ET), which is calculated based on the Surface Energy Balance Algorithm for Land (SEBAL). Results of the correlation between TMDI, TVDI and SEBAL-derived ET indicate that TMDI is a better index for estimating soil moisture. The built-up region shows high negative correlation with SEBAL-derived ET. According to the spatial distribution of TMDI and TVDI, in the tailing dam, some parts of the dam body shows high soil moisture which may have the potential risk of soil liquefaction.

### I. INTRODUCTION

Tailing dam in Brumadinho was damaged on 25<sup>th</sup> January 2019, it released mudflow into the local place and even the river, this accident caused great losses. Soil liquefaction may be one of the potential reasons for the loss of stability of the tailing dam. Estimation of soil moisture of an area is very important, not only in agriculture but also in monitoring geological hazard. Remote sensing technology is a good method to monitor the geological hazard, for example, high soil moisture monitoring and deformation detection etc.

For the tailing dam in Brumadinho, based on Landsat data, (Rotta *et al.*, 2020) used the Temperature Vegetation Dryness Index (TVDI) as the indicator to get the soil moisture of the tailing dam. They observed high soil moisture over the Top-of-bench sector of the dam. Besides, they also used Sentinel-1 data to get a time-series of the tailing dam's deformation. They found cumulated displacements between 3<sup>rd</sup> January 2018 and 22<sup>nd</sup> January 2019 (Gama *et al.*, 2020) used Differential Interferometric Synthetic Aperture Radar (DInSAR) to monitor the surface deformation of the tailing dam. They used Small BAseline Subset (SBAS) and Persistent Scatterer Interferometry (PSI) in their analysis. The Digital Surface Model (DSM) was applied to remove the topographic phase component. They found that the maximum displacement was detected along the downstream slope face, they were 39 mm with SBAS and 48 mm with PSI, respectively.

Surface water can absorb the radiation from sun and can convert this kind of energy into latent heat in the form of evapotranspiration (ET). Therefore, surface water has the capability to moderate Land Surface Temperature (LST) (Qiu *et al.*, 2013). If the amount of the surface water is limited, it will induce the constraining of the latent heat transfer, then the LST will easily increase. Based on the correlation between LST and water content, researchers applied the triangle space method to extract the land surface information based on LST and some other indices (Le and Liou, 2021). The most common index researchers used is TVDI, which is based on the triangle space of Normalized Difference Vegetation Index (NDVI) and LST. TVDI is widely used in the agriculture field. TVDI is inversely proportional to soil moisture, which means, the higher the index is, the lower the soil moisture will be. Recently, (Le and Liou, 2021) found the Temperature-Soil Moisture Dryness Index (TMDI), which proved to be a better index in comparison with TVDI. The TMDI is calculated based on the triangle space of Normalized Difference Latent Heat Index (NDLI) and LST. They applied this index to estimate the soil moisture in an alluvial plain located along the southwest coast of Taiwan. In their study, the ET derived from the Surface Energy Balance Algorithm for Land (SEBAL) was used as the reference to evaluate the performance of TMDI and TVDI. They found that TMDI shows sensitivity to the surface soil fluctuation. Besides, they also found that TMDI could perform better than TVDI in

the response to the rapid change of soil moisture. (Le and Liou, 2022) also used TMDI to estimate the soil moisture. The performance of the TMDI was evaluated by the SEBAL-derived ET and verified by the near-surface temperature and in-situ humidity. They found TMDI had negative correlation with the SEBAL-derived ET and positive correlation with the in-situ near-surface air temperature. They also compared TMDI with other indices and they found that TMDI has advantage over other indices especially in the non-vegetation area. They concluded that TMDI was a reliable index for the estimation of soil moisture.

The main content of this paper can be summarized as follows: Section II Study area and data; Section III includes the equations for the TMDI and ET calculation; Section IV includes the results of land use and land cover (LULC) classification, index and LST calculation, the correlation analysis and also the spatial distribution of the soil moisture in the tailing dam; Section V shows the conclusion of the study.

## II. STUDY AREA AND DATA

### A. Study area

The study area is the tailing dam at the Córrego do Feijão iron ore mine shown in Figure 1. It is located in Minas Gerais state of Brazil (20°07'11"S 44°07'17"W).

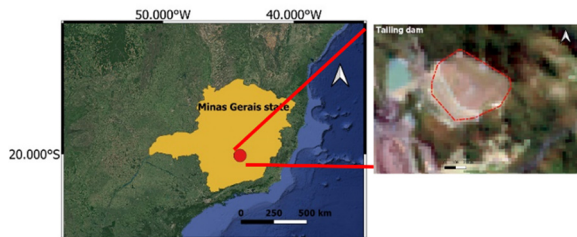


Figure 1. Location of the study area: a) Minas Gerais state (Geofabrik, 2018; Google, n.d.); b) Tailing dam circled in red polygon in Brumadinho generated from Landsat 8 data.

In order to increase the robustness of the calculation of TMDI and TVDI, a larger region, compared to the red polygon in Figure 1b, is clipped for the calculations. The larger region (Figure 2a) includes the whole region of Brumadinho and surrounding areas like Bonfim, Moeda, Rio Manso etc. The tailing dam area is divided into 4 sections (Figure 2b): tailings, dam and the region around the tailings and the region around the dam.

In the tailing dam area shown in Figure 2b, (i) dam is mixed with bare soil and vegetation (grass), (ii) tailings is bare soil with sparse grass, (iii) region around dam is mixed with bare soil and vegetation, (iv) region around tailings is fully covered with vegetation.

The area of each section is shown in the Table 1.

Table 1. Dimension of the Tailing dam

	i	ii	iii	iv
Area (m <sup>2</sup> )	91,807	251,794	182,406	285,541

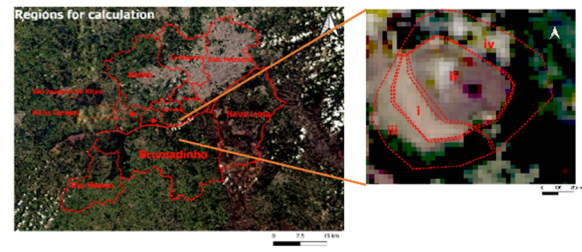


Figure 2. Study area: a) The calculation region of the area; b) Different sections of the tailing dam: (i) dam (ii) tailings (iii) region around dam (iv) region around tailings Both images generated from Landsat 8 data.

### B. Data

Landsat 8 data includes the Operational Land Imager (OLI) and the Thermal Infrared Sensor (TIRS) from the United States Geological Survey (USGS). In this paper, Landsat-8 Collection 2 Level-2 Science Products are used (USGS 2022). The data were captured on 14<sup>th</sup> January 2019 and 30<sup>th</sup> January 2019 and they are used to estimate the soil moisture of the tailing dam in Brumadinho. The first data was captured before collapse of the tailing dam. Which can get the soil moisture 11 days before collapse. The second image was captured 5 days after the collapse of the tailing dam. In this case, the soil in the tailing dam would be exposed, the soil moisture could also be a reference to check if the soil moisture in the tailings was high or not. Information about the data is shown in the Table 2.

Table 2. Data of Landsat 8

Platform	Image date	Sensors	Resolution
Landsat 8	2019/01/14	OLI/TIRS	30 m (OLI)/100 m (TIRS)
Landsat 8	2019/01/30	OLI/TIRS	30 m (OLI)/100 m (TIRS)

In this study, the data from OLI was used to calculate NDVI and NDLI respectively. The data from TIRS is used to calculate LST.

## III. METHODOLOGY

### A. LULC classification

The whole region shown in Figure 2a is located between the mine region and Belo Horizonte, which is the capital of Minas Gerais. This region is composed of vegetation and mine area and parts of built-up area and surface water.

LULC classification for this region was used to classify the whole region into several classes: including vegetation, surface water, bare soil, built-up area and cloud (including the cloud shadow). The open-source software Orfeo toolbox (OTB) 7.4.0 is used for the classification. Based on supervised learning, the Support Vector Machines (SVM) classification algorithm was used for the LULC classification.

### B. Index and LST calculation

TVDI is widely used in the soil moisture estimation. This index is calculated based on NDVI and LST triangle space and it is inversely proportional to the soil moisture. According to the theory from (Le and Liou, 2021), they found another index which could be more sensitive to soil moisture estimation.

TMDI is calculated based on the triangle space of NDLI and LST. The NDLI is proposed for remote sensing of land surface heat flux (Liou *et al.*, 2019), it was proved to be a reliable index to determine the water content's characteristics. Therefore, NDLI in this study is used as the indicator for surface water. This index is calculated based on the Equation 1.

$$NDLI = \frac{(\rho_{Green} - \rho_{Red})}{(\rho_{Green} + \rho_{Red} + \rho_{SWIRI})} \quad (1)$$

where  $\rho_{Green}$  = reflectance of the band 3 (green band)  
 $\rho_{Red}$  = reflectance of the band 4 (red band)  
 $\rho_{SWIRI}$  = reflectance of the band 6 (short-wave infrared band)

Band 10 in TIRS of Landsat 8 is used to calculate LST. According to the instruction of Landsat 8 Collection-2 Level-2 Science Products (USGS 2022). LST can be calculated by the scaling factor shown in the Equation 2.

$$LST = DN_{B10} \cdot 0.00341802 + 149 \quad (2)$$

where  $DN_{B10}$  = digital number of the band 10

### C. NDLI-LST triangle space

According to the theory from (Le and Liou, 2021) and (Le and Liou, 2022), in certain NDLI interval, the given water can absorb the radiation and then change it into latent heat in the form of ET, in this condition, LST can be decreased because of the cooling effect from ET. This can also directly be connected to soil moisture.

Based on this, a linear regression of LST and NDLI can be applied, the triangle space method is used like NDVI-LST triangle space for calculation of TVDI (Zare *et al.*, 2019). In the triangle space of NDLI-LST, the upper limit in the triangle is the dry edge, the lower limit of the triangle is the wet edge. The upper limit and lower limit correspond to the maximum and minimum ET rate (Le and Liou, 2022). With the dry edge and the wet edge, TMDI can be calculated. The equation of TMDI is shown in the Equation 3.

$$TMDI = \frac{(LST - LST_{min})}{(LST_{max} - LST_{min})} \quad (3)$$

where  $LST$  = land surface temperature (K)  
 $LST_{max}$  = maximum LST (K) according to the NDLI along the dry edge

$LST_{min}$  = minimum LST (K) according to the NDLI along the wet edge

The equation of the  $LST_{min}$  and  $LST_{max}$  are shown below (Eqs. 4 and 5).

$$LST_{max} = a_1 + b_1 \cdot NDLI \quad (4)$$

$$LST_{min} = a_2 + b_2 \cdot NDLI \quad (5)$$

where  $a_1, b_1, a_2$  and  $b_2$  = fitting equation coefficients

There is no classification standard for TMDI, but based on the empirical classification from TVDI (Sha *et al.*, 2014), the classification for TMDI is set to the values given in Table 3.

Table 3. Classification standard of TMDI

Extremely humid	Humid	Normal	Slightly dry	Dry
0 to 0.2	0.2 to 0.4	0.4 to 0.6	0.6 to 0.8	0.8 to 1

### D. ET-based evaluation

According to (Le and Liou, 2021), in the NDLI-LST triangle space, LST decreases as the ET increases in a certain amount of water. The variation of LST is because of the cooling effect by ET. Based on this, ET is used as the reference data to evaluate the performance of the TMDI and the TVDI. ET is derived from SEBAL and ET data is available at geeSEBAL (Laipelt *et al.*, 2021). The equation is shown in Equation 6.

$$\lambda ET = R_n - H - G \quad (6)$$

where  $ET$  = evapotranspiration ( $\text{mm H}^{-1}$ )  
 $\lambda$  = latent heat of vaporization ( $\text{MJ/kg}$ )  
 $R_n$  = net radiation ( $\text{Wm}^{-2}$ )  
 $H$  = sensible heat flux ( $\text{Wm}^{-2}$ )  
 $G$  = soil heat flux ( $\text{Wm}^{-2}$ )

## IV. RESULTS AND DISCUSSION

### A. LULC classification

Based on the supervised learning in the OTB 7.4.0, the results of the LULC classification on 14<sup>th</sup> January 2019 and 30<sup>th</sup> January 2019 are shown in Figure 3.

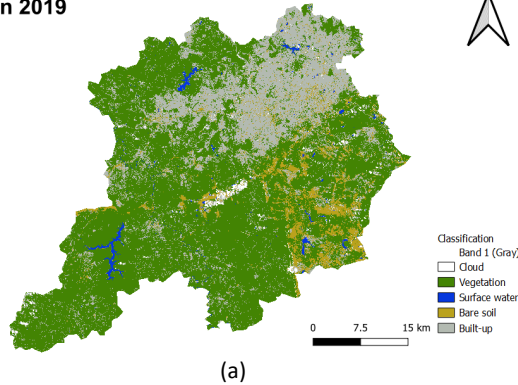
From the results shown above, it is obvious that the vegetation represents a large proportion of the whole study area. Vegetation comprises 67%. The built-up area is 24%. Bare soil occupies about 7% of the whole area and the surface water accounts for 1%.

On 30<sup>th</sup> January 2019, vegetation accounts for 69% of the whole area, bare soil makes up 7%. Built-up occupies 22% while the surface water is 1%.

The accuracy of the LULC classification can be assessed with the Semi-Automatic Classification Plugin (SCP) in QGIS 3.24.1. For the first LULC classification on 14<sup>th</sup> January 2019, in the LULC

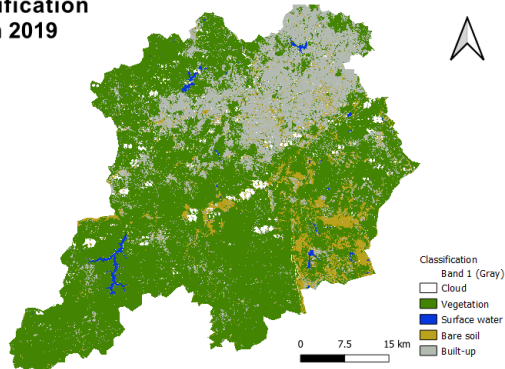
classification result randomly selected fifty samples and tested as well as verified, the overall accuracy is 95.67% and kappa hat classification is 0.91. For the data of 30<sup>th</sup> January 2019, the overall accuracy is 94.11% and kappa hat classification is 0.88.

**Classification**  
14 Jan 2019



(a)

**Classification**  
30 Jan 2019



(b)

Figure 3. Results of LULC classification: a) result on 14<sup>th</sup> January 2019; b): result on 30<sup>th</sup> January 2019.

### B. Index and LST calculation

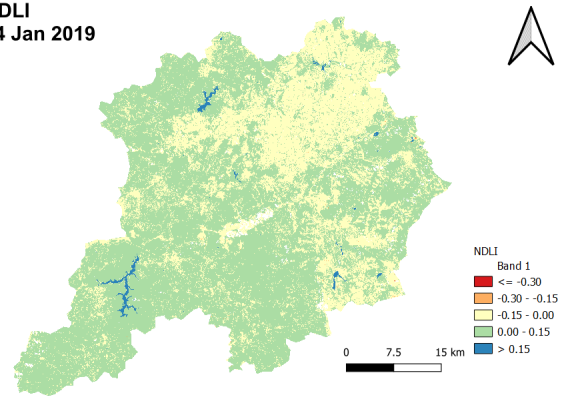
The results of the NDLI and LST are used to generate the NDLI-LST triangle space. The result of the NDLI on 14<sup>th</sup> January 2019 is shown in Figure 4. NDLI ranges from -1 to 1. In the image of NDLI, in order to eliminate the influence from cloud and its shadow, the cloud and its shade are manually erased.

In Figure 4, the results of NDLI on the two dates are shown. For ease of interpretation of the NDLI results, the LULC classification shown in Figure 3 as to be considered. The blank part is the cloud and shadow, which is removed from the image. The built-up area and bare soil show an almost negative NDLI value. The vegetation area shows a relative higher value, from 0 to 0.15, the surface water has an even higher value.

According to the Equation 2, LST can be calculated based on the TIRS (Band 10) of Landsat 8 data collection-2 level-2. The spatial distribution of LST in Kelvin (K) on the two dates is shown in Figure 5. The cloud and its shade are manually erased as well.

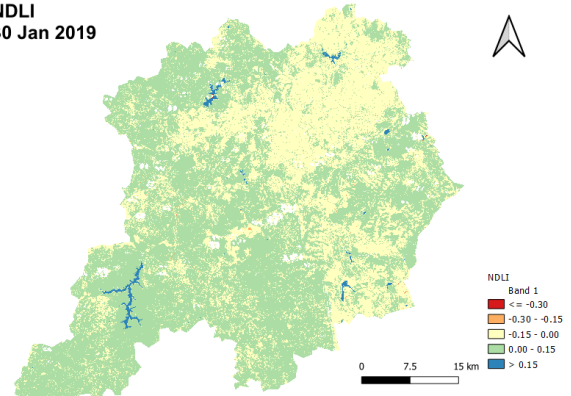
From the results shown above, on 14<sup>th</sup> January 2019 and 30<sup>th</sup> January 2019, high LST values are found in the built-up region and bare soil region. The vegetation region and surface water show relatively low LST values.

**NDLI**  
14 Jan 2019



(a)

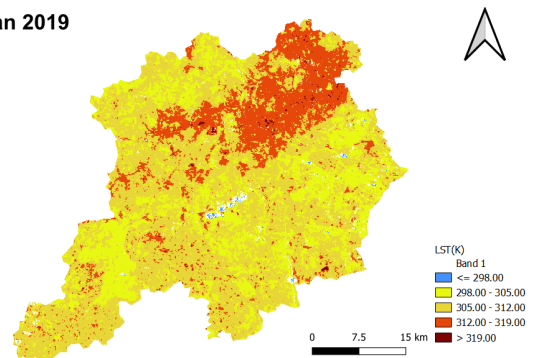
**NDLI**  
30 Jan 2019



(b)

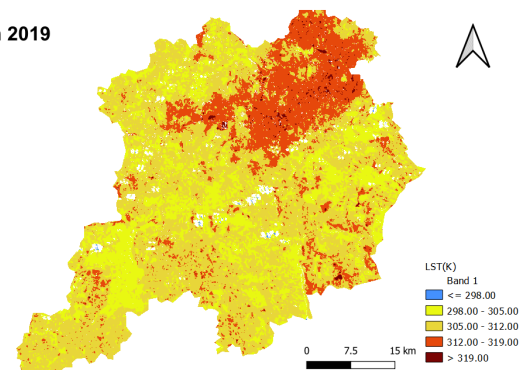
Figure 4. Results of NDLI: a) result on 14<sup>th</sup> Jan 2019; b) result on 30<sup>th</sup> Jan 2019.

**LST**  
14 Jan 2019



(a)

**LST**  
30 Jan 2019



(b)

Figure 5. Results of LST: a) result on 14<sup>th</sup> Jan 2019; b) result on 30<sup>th</sup> Jan 2019.



C. NDLI-LST triangle space

Based on the result of the NDLI and LST, the NDLI-LST triangle space can be generated. According to the Equations 3-5, the results of NDLI-LST triangle space are shown in Figure 6.

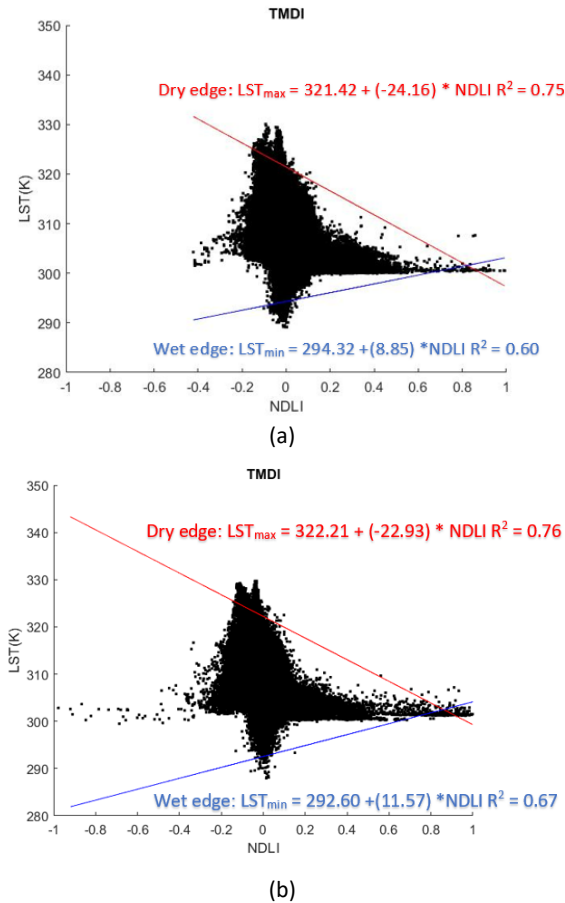


Figure 6. NDLI-LST triangle space: a) NDLI-LST space triangle on 14<sup>th</sup> Jan 2019; b) NDLI-LST triangle space on 30<sup>th</sup> Jan 2019.

In Figure 6, the red line is the dry edge while the blue line is the wet edge. On the dry edge,  $LST_{max}$  shows a negative relation with NDLI.  $R^2$  is 0.75 and 0.76 for the data from 14<sup>th</sup> January 2019 and 30<sup>th</sup> January 2019, respectively. For the wet edge,  $LST_{min}$  shows a positive relation with NDLI. The  $R^2$  is 0.60 and 0.67 on 14<sup>th</sup> January 2019 and 30<sup>th</sup> January 2019, respectively.

With the NDLI-LST triangle space, the results of TMDI can be calculated. According to the Equations 3-5, the results of TMDI are shown in Figure 7.

On 14<sup>th</sup> January 2019 and 30<sup>th</sup> January 2019, the built-up region shows high TMDI values. Because TMDI has negative correlation with soil moisture like TVDI, based on this, it was obvious that the built-up region had low soil moisture. The vegetation region shows relative high soil moisture, especially the vegetation close to surface water has high soil moisture.

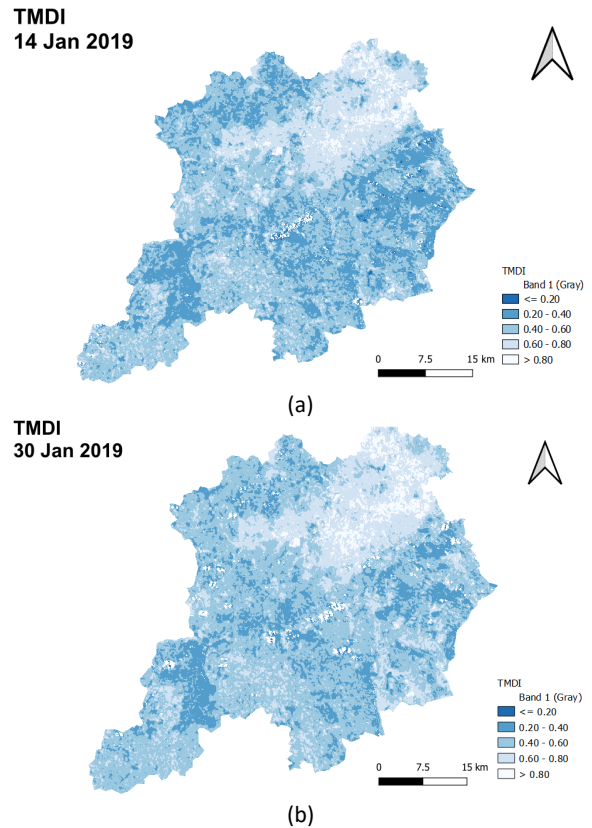


Figure 7. Results of TMDI with the classification schema introduced in Table 3: a) TMDI result from 14<sup>th</sup> Jan 2019; b) TMDI result from 30<sup>th</sup> Jan 2019.

D. ET-based evaluation

ET is derived from SEBAL. Which is used to assess the performance of the TMDI and the TVDI. The images of SEBAL-derived ET are shown in Figure 8.

The vegetation area and the surface water area show relatively high ET while the built-up area and bare soil show low ET.

Based on the LULC classification from Figure 3, the whole region is divided into 5 classes. Cloud and its shadow are excluded. The correlation coefficient between TMDI/TVDI and ET in different LULC classes is shown in the Table 4.

Table 4. Correlation coefficient between TMDI/TVDI and ET in different LULC classes

	14 <sup>th</sup> Jan 2019		30 <sup>th</sup> Jan 2019	
	TMDI	TVDI	TMDI	TVDI
ET (Whole area)	-0.65	-0.57	-0.70	-0.51
ET (Vegetation)	-0.47	-0.43	-0.54	-0.47
ET (Bare soil)	-0.48	-0.49	-0.51	-0.58
ET (Built-up)	-0.72	-0.60	-0.75	-0.64

Overall speaking, TMDI performs better than TVDI based on the correlation coefficient with SEBAL-derived ET. For the whole region, the TMDI shows a negative correlation of -0.65 and -0.70 on those two dates. While the TVDI only shows a negative correlation of -0.57 and -0.51. For different types of LULC, in the built-up area, TMDI and TVDI have higher negative correlation with

SEBAL-derived ET, which have -0.72 and -0.60 on 14<sup>th</sup> January 2019 and -0.75 and -0.64 on 30<sup>th</sup> January 2019, respectively. In vegetation area those two indexes have a lower negative correlation with SEBAL-derived ET. In the vegetation region, the correlation coefficients between ET and TMDI are -0.47 and -0.54 on 14<sup>th</sup> on two dates. The correlation coefficients between ET and TVDI are: -0.43 and -0.47 on those two dates. The spatial distribution of the TMDI and the TVDI in the tailing dam is shown in Figure 9.

tailings even has TMDI below 0.2. Those areas may have possibility to induce soil liquefaction.

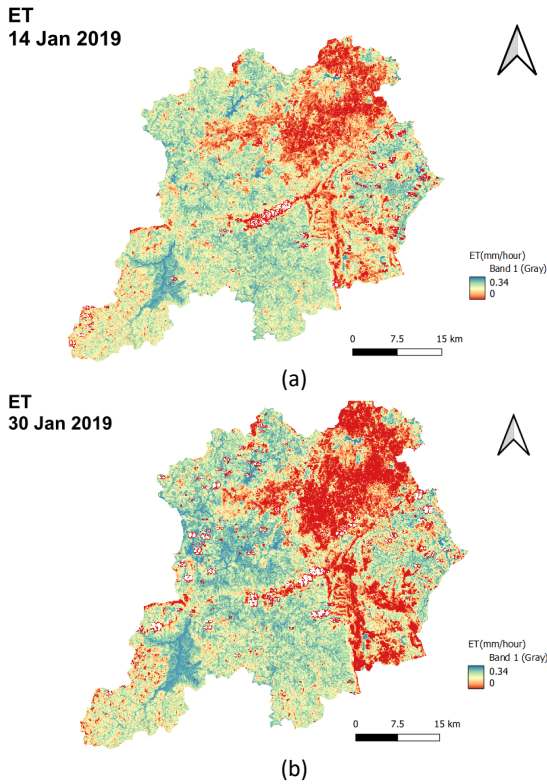


Figure 8. Results of ET combined with the LULC classification results from Figure 3: a) result on 14<sup>th</sup> Jan 2019; b) result on 30<sup>th</sup> Jan 2019.

The mean value of the TMDI and the TVDI in different tailing dam areas are shown in Table 5.

Table 5. Mean value of TVDI and TMDI in the tailing dam region

	14 <sup>th</sup> Jan 2019		30 <sup>th</sup> Jan 2019	
	TMDI	TVDI	TMDI	TVDI
i	0.70	0.65	0.57	0.47
ii	0.56	0.55	0.45	0.39
iii	0.50	0.54	0.52	0.51
iv	0.31	0.37	0.34	0.41

Figure 9a and Figure 9c show the results for 14<sup>th</sup> January 2019, what is before the collapse of the tailing dam in Brumadinho. The border between (ii) tailings and (iv) region around tailings has a high soil moisture content, which is shown by the index ranging from 0.2 to 0.4. (iv) Region around tailings also shows high soil moisture (0.2 to 0.4). In Figure 9a, (iv) Region around

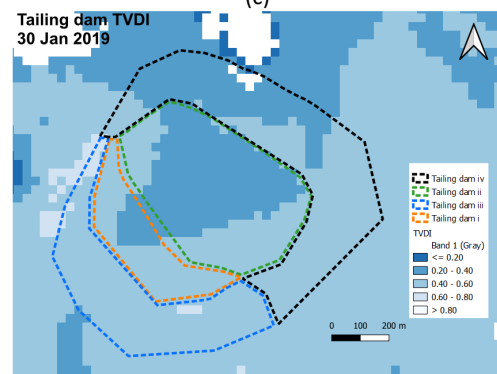
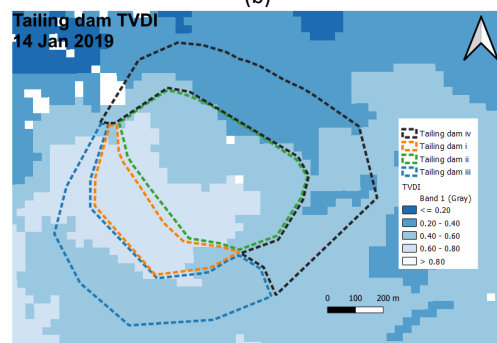
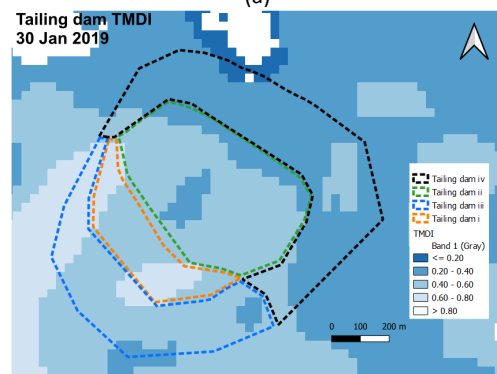
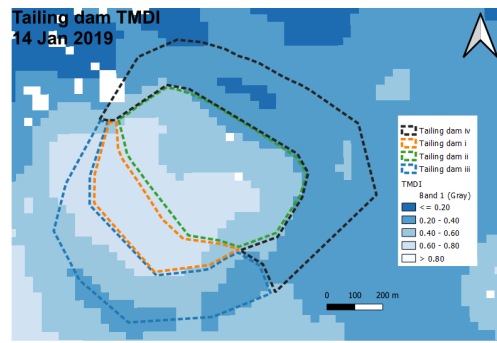


Figure 9. Spatial distribution of the TMDI and the TVDI in the tailing dam area: a) TMDI result on 14<sup>th</sup> Jan 2019; b) TMDI result on 30<sup>th</sup> Jan 2019; c) TVDI result on 14<sup>th</sup> Jan 2019; d) TVDI result on 30<sup>th</sup> Jan 2019.

Figure 9b and Figure 9d show the results for 30<sup>th</sup> January 2019, what is after the collapse of the tailing dam, the internal soil of the tailing dam is already exposed. The soil moisture in region (i) dam is increased according to TVDI and TMDI. The TMDI and the TVDI in

region (ii) tailings reached 0.2 to 0.4. Which can also indirectly verify the soil moisture in this region.

From Table 5 can be seen, that (iv) region around tailings has the highest soil moisture. On 14<sup>th</sup> January 2019 in (iv) region around tailings, the mean TMDI and TVDI are 0.31 and 0.37, respectively. On 30<sup>th</sup> January 2019, mean TMDI and TVDI are 0.34 and 0.41, respectively. After the collapse of the tailing dam, the mean soil moisture in (i) dam and (ii) tailings increases. In (iii) region around dam and (iv) region around tailings a different situation can be seen: in (iii) region around dam based on TVDI the soil moisture increases while based on TMDI the soil moisture decreases. In (iv) region around tailings both the TMDI and the TVDI show a decrease of the soil moisture.

## V. CONCLUSION

This study aims to use a new index, the TMDI to estimate the soil moisture of the tailing dam in Brumadinho, Brazil. Based on the Landsat 8 data on 14<sup>th</sup> January 2019 and 30<sup>th</sup> January 2019, one data is captured before the collapse of the tailing dam while another is captured after the collapse of the tailing dam, the soil moisture and the potential reason of the collapse of the tailing dam can be analyzed. Considering the whole region of Brumadinho and its surrounding areas for the calculation will increase the robustness of the TMDI.

In order to a better understanding, the distribution of land surface characteristics and LULC classification is used to classify the whole study region and divide the study area into five classes. With the sample to verify, the results show a good classification. The overall accuracy on the two dates are 95.67% and 94.11%. By using the OLI and TIRS from Landsat 8 data, NDLI and LST are calculated. The TMDI can be calculated based on the NDLI-LST triangle space. The TMDI is compared with the existing TVDI based on SEBAL-derived ET. The results show, that TMDI has much higher correlation with ET than TVDI, which means this index performs better. In different land type, in the built-up area, the correlation coefficient between ET and TMDI is higher than that in the bare soil and vegetation.

In the spatial distribution of the TMDI and TVDI, the tailing dam is divided into four parts. In the border between (ii) tailings and (iv) region around tailings a relative high soil moisture is presented. Besides, the (iv) region around tailings, which is fully covered with vegetation, also shows high soil moisture. It means that these areas have potential to induce soil liquefaction. In the thermal environment, the TMDI shows importance in the estimation of the soil moisture. It can be a very useful indicator to monitor soil moisture not only in mining field but also in the agriculture and forestry domain.

## References

- Gama, F., Mura, J.C., R. Paradella, G. de Oliveira, (2020). Deformations Prior to the Brumadinho Dam Collapse Revealed by Sentinel-1 InSAR Data Using SBAS and PSI Techniques. In *Remote Sens.* Vol 12, No.21, pp. 3664.
- Geofabrik. (2018). OpenStreetMap Data Extracts. Retrieved March 5th, 2022, from <https://download.geofabrik.de/>
- Google. (n.d.). Google map. Retrieved March 4th, 2022, from <http://www.google.cn/maps/vt?lyrs=s@820&gl=cn&x={x}&y={y}&z={z}>
- Laipelt, L., Kayser, R. H. B., Fleischmann, A. S., Ruhoff, A., Bastiaanssen, W., Erickson, T. A., and Melton, F. (2021). Long-term monitoring of evapotranspiration using the SEBAL algorithm and Google Earth Engine cloud computing. *ISPRS Journal of Photogrammetry and Remote Sensing*, 178, pp. 81-96.
- Le, M. S., and Liou, Y. A. (2021a). Spatio-temporal assessment of surface moisture and evapotranspiration variability using remote sensing techniques. *Remote Sensing*, 13(9), 1667.
- Le, M. S., and Liou, Y. A. (2021b). Temperature-Soil Moisture Dryness Index for Remote Sensing of Surface Soil Moisture Assessment. *IEEE Geoscience and Remote Sensing Letters*, 19, 1-5.
- Liou, Y. A., Le, M. S., and Chien, H. (2018). Normalized difference latent heat index for remote sensing of land surface energy fluxes. *IEEE Transactions on Geoscience and Remote Sensing*, 57(3), pp. 1423-1433.
- Qiu, G. Y., Li, H. Y., Zhang, Q. T., Wan, C. H. E. N., Liang, X. J., and Li, X. Z. (2013). Effects of evapotranspiration on mitigation of urban temperature by vegetation and urban agriculture. *Journal of Integrative Agriculture*, 12(8), pp. 1307-1315.
- Rotta, L. H. S., Alcantara, E., Park, E., Negri, R. G., Lin, Y. N., Bernardo, N., and Souza Filho, C. R. (2020). The 2019 Brumadinho tailings dam collapse: Possible cause and impacts of the worst human and environmental disaster in Brazil. *International Journal of Applied Earth Observation and Geoinformation*, 90, 102119.
- Sha, S., Ni, G., Yaohui, L., Tao, H. A. N., and Yanxia, Z. H. A. O. (2014). Introduction of application of temperature vegetation dryness index in China. *Journal of Arid Meteorology*, 32(1), 128.
- USGS. (2022). EarthExplorer. Retrieved January 05th, 2022, from <https://earthexplorer.usgs.gov/>
- USGS. (2022). Landsat Collection 2 Level-2 Science Products. Retrieved March 01st, 2022, from <https://www.usgs.gov/landsat-missions/landsat-collection-2-level-2-science-products>
- Zare, M., Drastig, K., and Zude-Sasse, M. (2019). Tree water status in apple orchards measured by means of land surface temperature and vegetation index (LST-NDVI) trapezoidal space derived from Landsat 8 satellite images. *Sustainability*, Vol 12, No.1, pp.70.

## Concept for the integration of BIM and GIS data for monitoring land deformation around an ongoing infrastructure project

Szymon Glinka, Tomasz Owerko

Faculty of Mining Surveying and Environmental Engineering, AGH University of Science and Technology, al. Mickiewicza 30, 30-059 Cracow, Poland, ([glinka@agh.edu.pl](mailto:glinka@agh.edu.pl); [owenko@agh.edu.pl](mailto:owenko@agh.edu.pl))

**Key words:** *BIM; GIS; BIM&GIS integration; land deformation; CDE*

### ABSTRACT

The BIM (Building Information Modeling) technology, currently being introduced in many countries, and its integration with GIS (Geographic Information System) data within a single CDE (Common Data Environment) platform may allow a more in-depth monitoring of the investment and faster detection of irregularities related to its implementation. Considered separately, each of the above technologies allows different types of analysis, but the synergy effect created by their integration makes it possible to view the problem in a broader perspective and to make the optimal decision. This issue also concerns the analysis of deformations around the erected object, which can be described by GIS data. On the other hand, the object is currently most often represented by a 3D model in IFC format that has the relevant information. The main aspect of this work is to combine these two types of data and analyze such a solution in terms of investment management support. The final result of the work is a description of a BIM and GIS use case for deformation monitoring and the creation of an algorithm for this task including the exchanged information with reference to OpenBIM standards (data exchange format Industry Foundation Classes - IFC, Information Delivery Manual - IDM). The whole work was also considered with reference to risk management during the project.

### I. INTRODUCTION

Managing a construction project involves many aspects of risk. Emerging new technologies, allowing the digitization of some construction processes, provide opportunities for greater control of risks associated with, for example, ongoing construction work. One of the representatives of this type of risks may be unexpected or expected, but larger than anticipated, deformations of the ground around the implemented investment. By detecting them more quickly and sending information to site managers, it is possible to reduce the costs associated with delayed action on a given risk or to improve site safety. Moreover, by integrating BIM and GIS technology, it is possible to act before risks materialize.

BIM (Building Information Modeling/Management) is a technology increasingly used in the AEC (Architecture Engineering Construction) industry throughout the life cycle of a building. BIM technology is based on a 3D model and the metadata stored within it. It thus creates a database which is defined in a global or local space. This model can be used in any phase of the life cycle (Eastman *et al.*, 2018). The use of this technology supports decision-making processes related to construction investments. This paper focuses primarily on the construction and operational phases of an infrastructure facility.

On the other hand, GIS (Geographic Information System) are systems or databases responsible for operating on geospatial data, located in the global coordinate system (Thurgood and Bethel, 2003). By

using different analytical tools, it is possible to analyze data in terms of many criteria and at different levels of technological advancement. These range from simple operations such as intersecting two layers to the use of complex machine learning algorithms.

By combining BIM and GIS data, synergies are sought (UN-GGIM, WFEO and WGIC, 2020). BIM presents information about the designed or constructed facility, while GIS allows to give context to the model (ISO/TR 23262:2021: GIS (geospatial) / BIM interoperability). This publication focuses on the context concerning the monitoring of an investment through the use of GIS data related to terrain deformation and its recording using a format specific to BIM, namely IFC (Industry Foundation Classes).

A core element of BIM technology, and in particular the idea of openBIM, is the use of an open data exchange format - IFC (ISO - ISO 16739-1:2018 - Industry Foundation Classes (IFC) for data sharing in the construction and facility management industries — Part 1: Data schema) It aims to free itself from native formats and achieve a more efficient exchange of information between stakeholders in the construction process. During research, this schema was used in the proposal of the problem description.

This approach also allows information to be stored and used within a single system, which can be centred on a single CDE - Common Data Environment (ISO - ISO 19650-1:2018) platform. The CDE is the hub for information exchange between stakeholders in BIM-enabled investments. Of course, it is possible to use native formats derived from native software, but this

solution is most often inefficient because stakeholders do not work on identical software, and the exchange of native files causes complications such as loss of geometric or informational data.

The aim of the publication is to present the concept of integrating BIM and GIS for the purpose of monitoring terrain deformation during the construction and operational phases of an infrastructure facility. The main focus is on the description of terrain deformation information recording and information flow in the process.

This publication is conceptual in nature and consists of four parts: the first introduces the topic of BIM and GIS, the second presents the background, the third presents a proposal for the integration process and defines a use case for the integration of BIM and GIS for deformation monitoring, then presents conclusions and plans for future work. The publication does not focus on the characteristics of measurement methods that can be used during the implementation of investments, they are only listed and briefly described with reference to the literature, where it is possible to broaden the knowledge on this subject.

## II. BIM AND GIS INTEGRATION FOR DEFORMATION MONITORING – BACKGROUND

The integration of BIM and GIS technology is a relatively new idea. It emerged with the need for a broader view of the investment. However, due to reasons, different primary applicability of these technologies, some difficulties in their integration exist. The main reasons for these problems are different information records. In GIS, the currently most commonly used open format for exchanging three-dimensional data is CityGML (City Geography Markup Language), while BIM uses the previously mentioned IFC. The detail of the data is also different. GIS usually represents a wide area, but definitely more generalized than in BIM, where the focus falls on a smaller area, but definitely more detailed.

Currently, the integration of BIM and GIS is not fully possible and requires precisely defined requirements for the information to be integrated. The main problems of integration are described among others in (ISO/TR 23262:2021: GIS (geospatial) / BIM interoperability; Liu *et al.* 2017; Song *et al.* 2017).

The GIS data that can support the monitoring of a construction project, and in particular the monitoring of ground deformation, are those acquired from Unmanned Aerial Vehicles (UAVs) and from satellite imagery. This publication is not intended to analyze the measurement methods, so they will only be briefly characterized with reference to the literature. Field measurements using Total Station are difficult to qualify as GIS data, so they are omitted - they are directly geodetic data.

Unmanned Aerial Vehicles allow the use of different types of sensors. The most common are optical and

laser sensors. The use of an appropriate sensor depends mainly on the land coverage of the area subject to analysis. In the case of optical sensors, one must take into account the limitations in penetrating vegetation, so the results obtained may be affected by considerable error. Laser sensors, on the other hand, allow to penetrate vegetation by registering many reflections of a given laser beam (echos). This makes it possible to measure below the vegetation and analyze the reflections from the ground. The use of drones for deformation monitoring in the case of mining areas, *e.g.* (Ćwiakła *et al.*, 2020), is often found in the literature. A collection of UAV applications in civil infrastructure, including those for deformation monitoring are described in (Greenwood *et al.*, 2019).

Another source of data can be satellite data such as InSAR. An example of a system that implements solutions from this field for deformation monitoring purposes is Sille, based on data from the Sentinel-1 mission (Sille). It seems that the application of this type of system for the purpose of deformation monitoring of an infrastructural object can also be applicable, as described among others in (Blasco *et al.*, 2019).

An example of a system that integrates BIM data and geodetic survey data for deformation purposes is Trimble Monitoring (Trimble Monitoring). With this type of system it is possible to visualise and control deformation of an object on an ongoing basis, *e.g.* during the construction phase. However, it is mainly based on measurements with Total Stations and GNSS receivers and therefore mainly single point monitoring is possible.

## III. PROCESS OF INTEGRATION FOR DEFORMATION MONITORING

The process of integration of BiM and GIS technologies should be carried out on the basis of information requirements. The most important elements in BIM technology which define these requirements are:

- IDM - Information Delivery Manual, defines how information should flow throughout the life cycle of an object (or its part)
- IDS - Information Delivery Specification - defines what information should be included in IFC files - assumption of human and machine readability. Currently, this standard is under development and MVD (Model View Definition) is used more often, but it has a lot of limitations.
- OIR/PIR/AIR/EIR - Organizational/Project/Asset/Exchange Information Requirements – accordingly to ISO19650

When used for internal purposes (for example, for a general contractor), integration should take place within the framework of internally defined standards. The process described below relates to a different

scenario, *i.e.* one where the appointing party requires the reporting of ground deformation data for project risk management purposes. The algorithm is shown in the figure below (Figure 1).

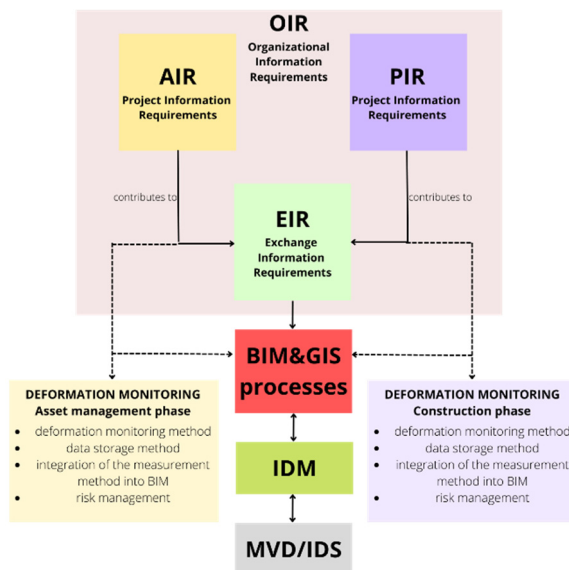


Figure 1. Algorithm for defining Information Requirements for Deformation Monitoring in Construction and Operational (Asset Management) Phase.

The IFC format is used as the basic component for information exchange in BIM technology. In the latest official version, there are difficulties in recording infrastructure information (IFC for infrastructure is expected to be available in 2022 or 2023). However, this does not mean that it is not possible to model components using this format. For this purpose, however, an instance of the IfcBuildingElementProxy class is usually used, which can represent any component not included in the file schema as a separate instance of the class.

The first element of the integration process is the definition of requirements, which was mentioned at the beginning of this section. Considering the integration aspect, the main attention should be paid to the georeferencing of models and unification of coordinate systems used in the project (also for GIS data). The requirements should also include information on the expected resolution of the acquired data and the frequency of its acquisition. The above requirement determines the choice of the measurement method, while the data density - the recording method. The information requirements should also include information about areas that may be particularly susceptible to deformation (places where the contractor or subcontractor should pay special attention).

Another factor is the cyclic measurement of the terrain and the recording of deformation information into an IFC file. For the purposes of this study, three proposals for recording the information were created, as described below.

The first method proposed is to extend the IFC format with classes to record information on terrain deformation. The only classes that currently depict displacement and/or deformation in IFC format (version 4) are IfcStructuralLoadSingleDisplacement and IfcStructuralLoadSingleDisplacementDistortion (IFC Schema Specifications - buildingSMART Technical). These allow the recording of structural displacement due to the application of force. As the focus of this study is on the deformation record relating mainly to the ground surface, this record is not applicable. However, the elements that are possible to use are the attributes of the above classes, shown below in the table (Table 1.).

Table 1. Attributes of the classes responsible for the recording of definitions in the IFC scheme

Attribute name	Type of attribute
Name	IfcLabel
Displacement X	IfcLengthMeasure
Displacement Y	IfcLengthMeasure
Displacement Z	IfcLengthMeasure
RotationalDisplacement RX	IfcPlaneAngleMeasure
RotationalDisplacement RY	IfcPlaneAngleMeasure
RotationalDisplacement RZ	IfcPlaneAngleMeasure

The attributes represent the displacement in each axis and the rotation. The class IfcStructuralLoadSingleDisplacementDistortion can additionally represent deformations using IfcCurvatureMeasure. The above class could serve as a base for writing an object class representing the displacement of control points.

For the first scenario, the information medium would be the IFC model itself, which would write the data using a new type of instance of the IfcControlPoint class. The point would have a property set that would consist of attributes such as those provided in Table 1, and the name of the property set would refer to the date the measurement was taken. In this way it would be possible to store historical and current displacement values.

This type of approach requires editing the IFC class schema, which is a non-trivial and time-consuming process. This solution may also cause difficulties in the exchange of information using the IFC file. To be optimal, the above described class should be implemented in future versions of the format so that it can be used globally. An additional limitation is the ability to store information for single points, so this scenario could only be used for non-densely distributed control points. The advantage of this scenario is that it can be combined with systems that automatically track deformations.

The next two approaches involve acquiring higher density data. The second scenario for recording displacement information concerns the comparison of measurement results from two following ones using an

IFC file. For this purpose it is possible to use the differences between successive records of terrain information. The recording of terrain information in IFC takes place with reference to, depending on the version:

- IFC 2x3 - IfcSite
- IFC 4 - IfcGeographicElement

In the following research, the focus is on IFC version 4.

Terrain geometry can be stored using three classes:

- IfcGeometricCurveSet
- IfcShellBasedSurfaceModel
- IfcTriangulatedFaceSet

A detailed record of the storage capabilities of these classes is shown in the figure below (Figure 2).

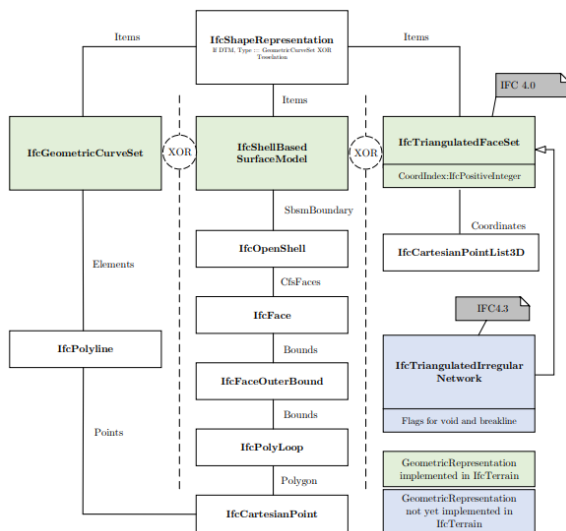


Figure 2. Concepts for Geometric Representation (Clemen *et al.*, 2021).

In this way, the recorded individual measurement effects or differences between measurements can be combined in a single database or CDE platform and analyzed for risks. This analysis can be performed manually or automatically. In this way, GIS data is converted into BIM formats. A limitation of this method is the much larger disk space needed to store the IFC files, resulting from the storage method of the IFC files (schema). For the conversion of elevation data to IFC format, the open-source software IfcTerrain was developed (Clemen *et al.*, 2021).

The third scenario assumes the use of external structures and their spatial integration within the integration of BIM and GIS technologies. Unlike the first two, in which the information carrier was the IFC format, this scenario assumes the use of bypasses, combining both technologies. The publications identified in section two, that present integration problems, show that it is not a simple process. However, properly modelled, using appropriate IT tools, the process allows additional information to be

generated and stored within more efficient structures. Nowadays, database-based solutions are increasingly common, *e.g.* (Wyszomirski and Gotlib, 2020). In this way, it is possible to store information in a structured way. The problem is most often the visualisation of this type of data, as databases need to contain the right methods and class definitions, allowing them to be properly displayed and acted upon within *e.g.* a CDE platform. In the end, they have to be converted into formats characteristic for both technologies (BIM - IFC and GIS - CityGML) anyway. This is most often due to the lack of suitable IT tools for displaying and acting on the data together. Further development of recording techniques can mitigate this problem. An example is the idea of semantic networks, which can serve as a component to draw information from both BIM and GIS and analyze risk within an ongoing construction project (Karan and Irizarry, 2015).

Most importantly, all scenarios described above require a precise definition of information requirements and information flow. The adaptation of the scenario depends on the measurement method used, the frequency of measurement, the object or the deformation predicted.

Finally, the proposed scenarios can be characterised as follows in Table 2.

Table 2. Scenario for the recording of terrain deformation with IFC files

Scenario	Synthetic description
Extension of the IFC format	Adaptation of IFC classes for land deformation monitoring. Recording of displacement information using appropriate classes
Use of IFC files as further results of field measurements	IFC allows information about the terrain to be recorded. Recording consecutive measurements using IFC allows for unified recording and use of the results within one environment. It should be noted, however, that the IFC format is not optimal for recording multiple points
Use of external references	Linking the IFC format to external formats provides the greatest opportunity when considering the area to be analyzed. However, one should bear in mind the limitations resulting from the lack of integration of BIM and GIS technology, which at the moment is not fully coherent

#### IV. DISCUSSION

The concepts described above aim at a more efficient use of deformation data in the construction process, primarily in the execution phase. The flow of information within a single standardized ecosystem, the role of which is played by the Common Data Environment, provides opportunities for greater control and faster recognition of risks.

It seems that the most efficient of the described scenarios to use at present is scenario three, which

allows storage and action on the largest areas. The first scenario requires operating on an IFC file and does not allow dense data to be stored - rather point data of a geodetic rather than GIS nature - but it allows the IFC format to be made more dynamic by providing information to it about the displacement of a control point measured continuously. The second scenario is the easiest technologically but has limitations in the area it can cover - this is due to the method of recording the IFC format.

## V. CONCLUSIONS

The described concept indicates directions for further work that can be undertaken to develop the use case described in the publication. It is planned to further explore the possibility of recording deformations within the integration of BIM and GIS technologies and to automate this process. It is also possible to use machine learning for this purpose, allowing for more efficient tracking. However, it should be remembered that the proposal is mainly aimed at areas where deformations or land displacement may occur (mainly mining areas or sites of mass movements).

Further work is expected to lead to the creation of a software prototype, which will allow the integration of BIM and GIS technologies for the purpose of terrain deformation monitoring. The creation of such a solution, however, requires standardisation in terms of the unification of data recording in both technologies.

## References

- Delgado Blasco, J. M., Fomelis, M., Stewart, C., and Hooper, A. (2019). Measuring urban subsidence in the Rome metropolitan area (Italy) with Sentinel-1 SNAP-StaMPS persistent scatterer interferometry. *Remote Sensing*, 11(2), 129.
- Clemen, C., Schröder, M., Kaiser, T., and Romanschek, E. (2021). ICTERRAIN—a free and open source tool to convert digital terrain models (DTM) to openbim industry foundation classes (IFC). *ISPRS Annals of Photogrammetry, Remote Sensing & Spatial Information Sciences*, 8.
- Ćwiakała, P., Gruszczynski, W., Stoch, T., Puniach, E., Mrocheń, D., Matwij, W., and Wójcik, A. (2020). UAV applications for determination of land deformations caused by underground mining. *Remote Sensing*, 12(11), 1733.
- Eastman, C. M., Eastman, C., Teicholz, P., Sacks, R., and Liston, K. (2011). *BIM handbook: A guide to building information modeling for owners, managers, designers, engineers and contractors*. John Wiley & Sons.
- Greenwood, W. W., Lynch, J. P. and Zekkos, D. (2019). Applications of UAVs in Civil Infrastructure. *Journal of Infrastructure Systems*, 25(2), p. 04019002. DOI: 10.1061/(asce)is.1943-555x.0000464.
- IFC Schema Specifications - buildingSMART Technical (no date). Available at: <https://technical.buildingsmart.org/standards/ifc/ifc-schema-specifications/>
- ISO/TR 23262:2021: GIS (geospatial) / BIM interoperability (no date). Available at: <https://www.iso.org/obp/ui/#iso:std:iso:tr:23262:ed-1:v1:en>
- ISO - ISO 16739-1:2018 - Industry Foundation Classes (IFC) for data sharing in the construction and facility management industries — Part 1: Data schema (no date). Available at: <https://www.iso.org/standard/70303.html>
- ISO - ISO 19650-1:2018 - Organization and digitization of information about buildings and civil engineering works, including building information modelling (BIM) — Information management using building information modelling — Part 1: Concepts and principle (no date). Available at: <https://www.iso.org/standard/68078.html>
- Karan, E. P. and Irizarry, J. (2015). Extending BIM interoperability to preconstruction operations using geospatial analyses and semantic web services. *Automation in Construction*, 53, pp. 1–12. DOI: 10.1016/j.autcon.2015.02.012.
- Liu, X., Wang, X., Wright, G., Cheng, J. C., Li, X., and Liu, R. (2017). A state-of-the-art review on the integration of Building Information Modeling (BIM) and Geographic Information System (GIS). *ISPRS International Journal of Geo-Information*, 6(2), 53.
- SILLE - How does it work (no date). Available at: <https://www.sille.space/en/faq/how-does-it-work>
- Song, Y., Wang, X., Tan, Y., Wu, P., Sutrisna, M., Cheng, J. C., and Hampson, K. (2017). Trends and opportunities of BIM-GIS integration in the architecture, engineering and construction industry: a review from a spatio-temporal statistical perspective. *ISPRS International Journal of Geo-Information*, 6(12), 397.
- Thurgood, J. D. and Bethel, J. S. (2003). Geographic Information Systems. in *Civil Engineering Handbook - Second Edition*, p. 2232.
- Trimble Monitoring (2022). Available at: <https://monitoring.trimble.com/products-and-solutions/transportation-infrastructure>
- UN-GGIM, WFEO and WGIC (2020) White Paper: The value of Integrated Geospatial and Building Information Modelling (BIM) solutions to advance the United Nations Sustainable Development Goals (Agenda 2030) with specific focus on resilient infrastructure. Available at: <http://www.wfeo.org/wfeo-wgic-unggim-white-paper-geospatial-engg-sustainable-development/>.
- Wyszomirski, M. and Gotlib, D. (2020). A unified database solution to process bim and gis data. *Applied Sciences (Switzerland)*, 10(23), pp. 1–19. DOI: 10.3390/app10238518.



## Early detection, permanent monitoring and documentation of critical locations at the surface in mining areas

Alexander Kipp, Andreas Schlienkamp, Anna Ens

RAG Aktiengesellschaft, Im Welterbe 10, 45141 Essen, Germany, ([alexander.kipp@rag.de](mailto:alexander.kipp@rag.de); [andreas.schlienkamp@rag.de](mailto:andreas.schlienkamp@rag.de); [anna.ens@rag.de](mailto:anna.ens@rag.de))

**Key words:** *monitoring; underground mining; remote sensing*

### ABSTRACT

Being responsible for the legacy risks of the underground hard coal mining in Germany, RAG is developing a remote sensing-based monitoring workflow for the early detection and long-term monitoring of ground movements in areas affected by near-surface mining in the southern Ruhr region, Saar region and Ibbenbueren. The workflow to detect surface fractures like sinkholes is based on high resolution airborne imagery and simultaneously recorded ALS data. As a part of RAG's overall concept in the field of multi-sensor monitoring of ground movements this workflow has been steadily improved and will be further on. The complete monitoring area that is covered by the workflow is about 415 km<sup>2</sup>. This paper first outlines the procedure of detecting ground movements by remote sensing. RAG uses an approach with annual simultaneous multispectral image and laser scanning flights. Due to the often small scale phenomena of sinkholes of only a few meters in diameter, a high accuracy of the sensor technology as well as all preceding processes like the determination of control points and reference surfaces is necessary. The process of accuracy assessment is done using continuous GNSS measurements for tie points and the projection centers of the aerial imagery as well as classic photogrammetric stereoscopic measurement. The derivation of geospatial products such as high resolution ortho imagery and digital elevation models will be covered as well as the processing of these datasets to reveal information necessary for risk analysis. The approach is based on the detection of subsidence structures in single date elevation models by pattern recognition as well as the calculation of differences between those datasets. The processing is followed by a step of data enrichment from different mining related data and stored in a specially created database. This enriched data source is provided through a modern GIS application which enables the employees to do the risk analysis and to document their findings. Ongoing research projects are evaluating the future use of artificial intelligence and machine learning to further automate the workflow.

### I. INTRODUCTION

As one of the legal successors of the German coal mining industry, RAG is responsible for monitoring, securing and rehabilitating areas under the influence of pre-industrial near-surface mining. In NRW alone, there are a total of about 31000 old adits.

The area of responsibility of RAG with approx. 7400 shafts and surface openings in North Rhine-Westphalia and Saarland.

This near-surface mining still poses risks today, in some cases hundreds of years later. Sinkholes in which parts of the earth's surface above old shafts and ducts collapse, sometimes spontaneously, can not only cause damage to infrastructure and buildings, but also pose a danger to people.

Since 2013, RAG has been developing a large-scale monitoring system based on remote sensing for the early detection of suspected areas (Figures 1 and 2). Of particular interest here is subsidence in the terrain, some of which are only a few centimeters (Spreckels *et al.*, 2016).

In addition to classic time series analysis of digital terrain models, the monitoring concept enables the analysis of individual time slices using specific

evaluation algorithms. This involves a targeted search for mining-specific terrain types in a data set.



Figure 1. Near surface mining induced sinkhole. Image courtesy, RAG.

The results are then enriched by various attributes and combined with a variety of data available at RAG. The results are stored in a database, that then again enables an analysis over several periods. The database represents a working foundation to employers which specifically work on risk management of post mining areas and assist the decision making about further actions like planning remediation of old shafts.

One of the challenges of this project is the sheer amount of data to be processed. The raw data of the

aerial surveys alone have a size 100 TB per year and the current flight campaign must be compared to former flight campaigns, so a large amount of data storage is needed.



Figure 2. Aerial image detail view of a refurbished sinkhole. Image courtesy, RAG.

#### A. Aerial Imaging and Airborne laserscanning

The basis for this monitoring is provided by high-resolution aerial surveys. These are performed annually outside the vegetation period to obtain the clearest possible view of the ground. Depending on the total area to be covered the UltraCam Falcon or UltraCam Eagle cameras from Vexcel Imaging are used here. The ground sampling distance (GSD) of the image flights is about 3 cm while recording 4 spectral channels: RGB and near infrared. Since 2015, the image flights have been carried out simultaneously with the airborne laser scanner IGI Litemapper 7800 on board, that records the terrain in the form of a 3D point cloud with approx. 10 to 20 points/m<sup>2</sup>, depending on the relief characteristics.

#### B. Ground control points and ALS control planes

Since the ground motions that must be recorded in the study area are about >10 cm, it is necessary to set up a stable configuration of ground control points (GCP) for the accuracy verification of the aerial survey (Figure 3). Since the ground resolution of the images is about 3 cm, the accuracy of the GCP measurements in position and height should be about 1 cm to enable accurate measurements and comparisons for accompanying flight campaigns. Since GCP are measured using GNSS methods in the SAPOS reference network, most of the time those accuracies are not obtained, mainly because of too long base lines to the reference stations and possible individual movement components on the SAPOS stations (Schulz and Schäfer, 2022; Niemeier and Tengen, 2022).

Therefore, RAG has planned and set up its own network of GNSS base stations, around the areas affected by post mining (Spreckels 2022; Spreckels *et al.*, 2020). This network is connected to SAPOS and allows GNSS measurements with much shorter baseline

lengths. This network was set up in 2017 and since then two approaches of measuring were pursued. In both approaches each ground control point is measured twice, with the first approach measuring 60 minutes each and the second approach measuring 15 minutes each. This new network is still in construction. The system is still being tested and a decision which method will be used will be probably made within the next year.



Figure 3. Measurement of ground control points. Image courtesy, RAG.

However, these control points can only be used for aerotriangulation of the acquired images. The airborne laser scanning data are directly referenced on board the aircraft without control points, which leads to an insufficient linkage of the individual flight strips. This results in position and height errors of up to 30 cm at the boundaries of the flight strips. To eliminate such errors, first only the images are triangulated and then a photogrammetric measurement of roof surfaces is performed. These roof areas are finally used as reference areas for ALS data (Figure 4).

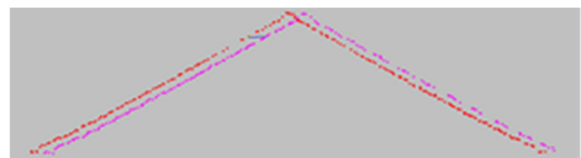


Figure 4. Position and resulting height offset at the edge of the ALS flight strip (Spreckels *et al.*, 2016).

## II. RAG INVESTIGATION AREAS

#### A. Ruhr

In the Ruhr region only areas around the river Ruhr and south of it are part of the monitoring, because only in these areas of the Ruhr near surface took place (Figure 5). Due to the geology the coal seams outcrop here or lie close under the surface.

This region covers about 135 km<sup>2</sup> which leads to about 6000 aerial images captured by the UltraCam Falcon annually and processed in two blocks. The whole area is covered by 104 ground control points.

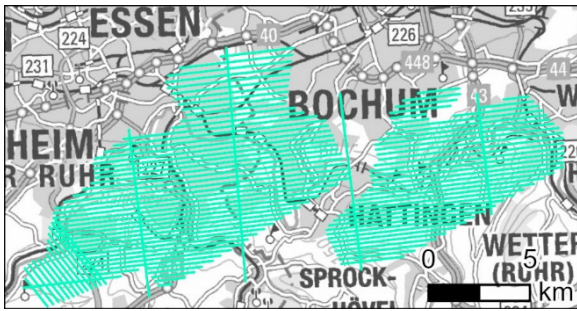


Figure 5. Overview of the monitored areas in the Ruhr Region. Image courtesy BKG, RAG.

### B. Ibbenbüren

Coal mining in the Ibbenbüren region has a history of about 500 years in a relatively small area. Here, coal-bearing layers were partially lifted to the surface by an igneous intrusion.

The aerial survey in this area covers about 55 km<sup>2</sup> which leads to about 1700 aerial images annually and 37 ground control points (Figure 6).

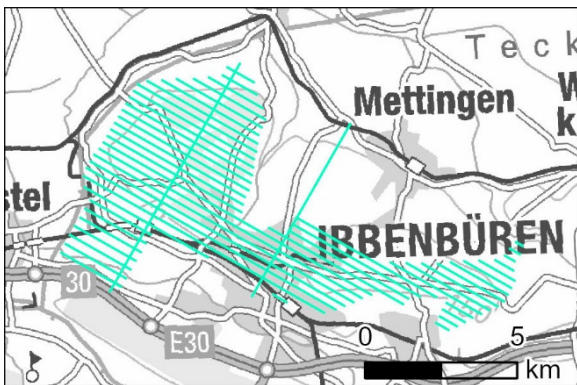


Figure 6. Overview of the monitored areas in Ibbenbüren. Image courtesy BKG, RAG.

### C. Saarland

The monitoring in the Saar region covers an area of about 281 km<sup>2</sup> which leads to about 9500 aerial images captured with an UltraCam Eagle. 225 ground control points are used to assure accuracy (Figure 7).

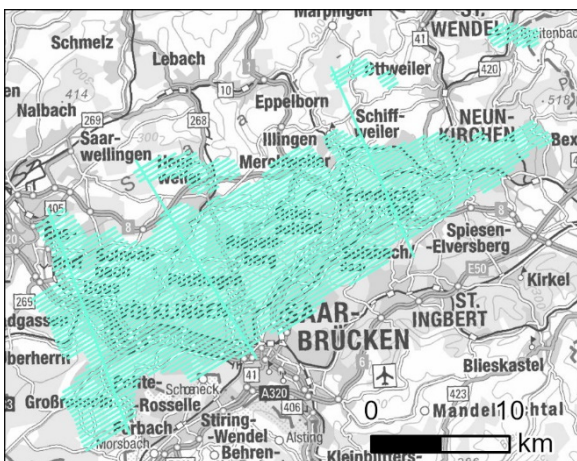


Figure 7. Overview of the monitored areas in the Saar Region. Image courtesy BKG, RAG.

## III. DATA PROCESSING

This chapter will present an overview of the geospatial products derived from the captured remote sensing data as well as their storage and further analysis.

### A. Derived products

As previously mentioned, the main products of the aerial surveys are high resolution aerial images as well as ALS point clouds. The first product derived is a bundle adjusted block of images of each area using Agisoft Metashape. This allows stereoscopic measurements in images pairs from which the control planes (e.g. roofs) for the adjustment of ALS data is retrieved. The images are then mosaicked to a seamless 4 channel orthophoto which allows easy navigation and primarily visual analysis.

The adjusted ALS point are processed using LAStools software. The first processing step includes the classification of ground points from which a sparse digital terrain model is derived for rectification of the orthophoto. Afterwards the point clouds are classified to distinguish between points that represent vegetation and those representing buildings and manmade structures like bridges and powerlines. The final digital terrain model used for further analysis is then calculated using the ground and building points. The buildings are kept in the output data because there are no points recorded under them representing the earth surface.

### B. Depression detection

Based on the high-resolution digital elevation models RAG has developed an ArcGIS Pro workflow which finds mining specific surface structures in a single time slice of those datasets. Typical surface structures of near surface mining are small scale depressions near to shafts or above adits. The workflow is designed in a way that it is only sensitive to depression like structures like mounds that lay underneath the surrounding terrain. The results are in vector format so further analysis can be performed using GIS software (Figure 8).

While the workflow detects numerous features, a filtering is required. Therefore, the resulting data is intersected with multiple RAG datasets such as coal seam outcrops, known locations of shafts and risk areas. The results of this process are then saved into a database and enriched with additional attributes which are calculated on the datasets. These attributes include e.g. the date of first occurrence, the distance to the next shaft, the depth of the depressions, the count of ALS points inside the depression geometry, the diameter and perimeter, the average slope of the depression as well as a shape index that describes the roundness parameters of the depression.

The system recognizes multiple occurrences of depressions in different time slices and links them in the database so that it is possible to monitor changes of

each specific depression over the time. The monitoring capabilities include accessing the height differences of a selected depression to any other time slice it was found in, as well as changes in the perimeter.

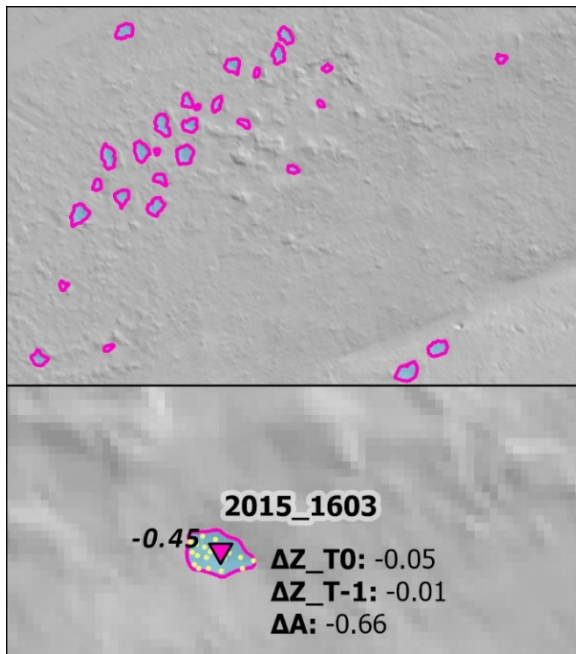


Figure 8. Graphical representation of depressions in the monitoring application. Upper image: view of a cluster of depressions in a forested area. Lower image: Detailed view with additional information.

### C. ABMon-Application

The depression database as well as all the other derived products must be prepared for subsequent work and made available to employers of the risk management in a suitable form.

Therefore, RAG uses many of ArcGIS built in features to build up an application where all the derived products of the aerial survey as well as additional RAG datasets are available in thematic views (Figures 9 and 10). These views may be customized by each user, depending on their specific task. By default, there are four views available, which are linked, so if one map is moved all the others move too. These views include the orthophoto, the shaded relief derived from the digital elevation model, a topographic map as well as old mining plans that were digitized and georeferenced. With this user interface, which can be customized by every employee a broad variety of risk management workflows can be performed. Beside the standard map view there also is the possibility of grouping the data by for example all depressions with certain height differences between time slices. Furthermore, it is also possible to apply filtering based on external data like shafts or risk areas. Another functionality is a time slider through which it is possible Another feature is the time slider, which provides the possibility to visualize changes in the found depressions over time in a simple way. Finally the application offers the possibility to

generate reports which allow the users to simply document their work and share it.

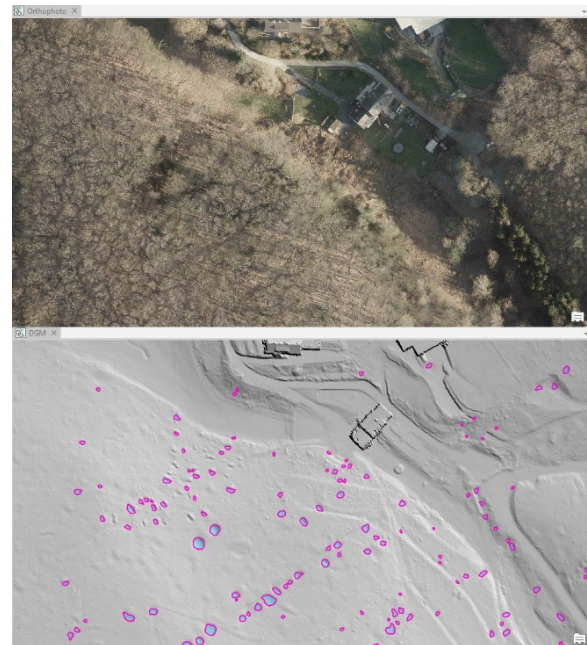


Figure 9. Screenshot of a subsection of the ABMon application. Left image: orthophoto. Right image: shaded relief with detected depressions represented by polygons. Image courtesy: RAG.

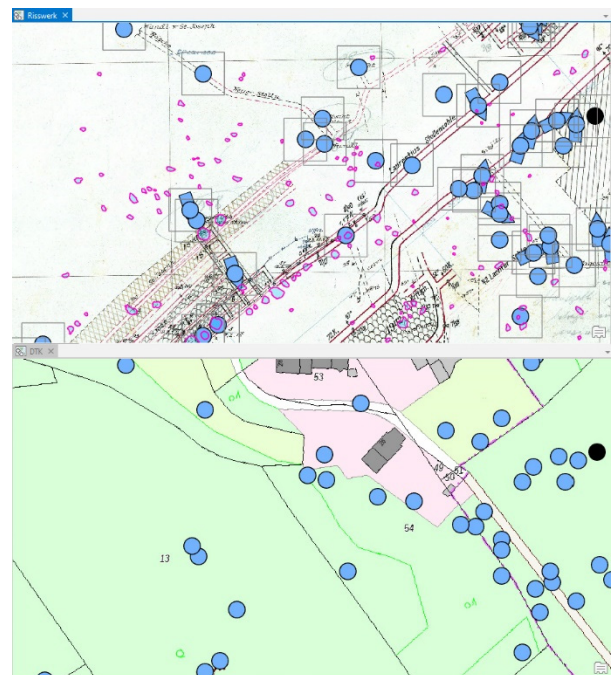


Figure 10. Screenshot of a subsection of the ABMon application. Left image: Mining plan with depressions and locations of know shafts. Right image: Topographic map with location of known shafts. Image courtesy: RAG.

## IV. CONCLUSIONS AND OUTLOOK

While several years of aerial surveys with the goal of detecting ground movements in areas influenced by near surface mining have shown that it is possible to achieve the required accuracies, work is still in progress related to analysis of the derived geospatial products.

With the development of the depression database as well as the monitoring application RAG has taken a step towards dealing with the consequences of near surface mining in a sustainable way. Until now most of the tools rely on standard GIS functionality but the fact that all the recorded and processed data is archived offers the possibility to quickly react to possible future developments of algorithms and advances in geospatial technology.

### References

- Niemeier, W., and Tengen, D. (2022). Dynamic concepts to handle geodetic networks with continuous monitoring data in areas with ground movements. In: *5<sup>th</sup> Joint International Symposium on Deformation Monitoring JISDM 2022*, Valencia, Spain, June 20-22, 2022, these proceedings.
- Schulz, M., and F. Schäfer (2022). GLOMON-Monitoringportal for storage, management, advanced processing and intelligent visualization of GNSS- and other sensors data. In: *5<sup>th</sup> Joint International Symposium on Deformation Monitoring JISDM 2022*, Valencia, Spain, June 20-22, 2022, these proceedings.
- Spreckels, V., A. Schlienkamp, A. Greiwe, and L. Eberhardt (2016). Eignung von ALS, Aero- und UAS-Photogrammetrie zur Früherkennung und Erfassung von Tagesbrüchen. In: *36. Wissenschaftlich-Technische Jahrestagung der DGPF*, Band 25, Bern, Switzerland, June 7-9, 2016, ISSN 0942-2870, pp 97-112.
- Spreckels, V., S. Bechert, A. Schlienkamp, M. Drobniowski, M. Schulz, F. Schäfer, and E. Kemkes, (2020). GNSS, Nivellement und Radar – einheitliche Multisensor-Standorte als Referenzpunkte zur Überwachung von Bodenbewegungen. In: *Tagungsband GeoMonitoring 2020*, Braunschweig, Germany, March 12-13, 2020, pp. 207-231. DOI: 10.15488/9351.
- Spreckels, V. (2022): Multisensor monitoring of ground movements over large areas to conduct the change from the active underground hard coal mining ages to the post-mining era. In: *5<sup>th</sup> Joint International Symposium on Deformation Monitoring JISDM 2022*, Valencia, ESP, June 20-22, 2022, these proceedings.

# Geomonplus – Application for Storage, Allocation, Exchange, and Visualization of Historical and Actual 4d-Position-Data within Mining Areas

Steffen Bechert, Andreas Schlienkamp, Volker Spreckels

RAG Aktiengesellschaft, Im Welterbe 10, 45141 Essen, Germany, ([steffen.bechert@rag.de](mailto:steffen.bechert@rag.de); [andreas.schlienkamp@rag.de](mailto:andreas.schlienkamp@rag.de); [volker.spreckels@rag.de](mailto:volker.spreckels@rag.de))

**Key words:** *ground movement monitoring; spatial data application; time series analysis; web service; data democratizing*

## ABSTRACT

Over decades RAG has collected spatial data from different sensors for the purpose of monitoring and analyzing ground movement caused by underground hard coal mining activities. With monitoring scopes from small objects, like delicate industrial installations surveyed by geometric leveling, to wide area observation by radar satellites, data was stored in several systems. Since there is still ground movement caused by the controlled flooding of former underground mine buildings, RAG will continue surveying the surface and collecting deformation data. To handle and analyse this deformation data and to create a value-adding application RAG cooperated with the company Atos to design Geomonplus. The following main requirements were identified at the start: To store data from different databases with different structures as well as current and future geodetic data sources, the data model needs to have a generic structure. The chosen platform needs to be future-oriented and should be established within RAG. The application also should be integrated into RAG's spatial data infrastructure. The ground movement information needs to find its way into an internal web service to reduce expert's workload and to share insights and expertise. This paper presents the main functions of the newly developed solution for experts as an extension for Esri ArcGIS Pro as well as web service tools for non-experts. Furthermore, some time series examples of leveling data in combination with satellite-based PSI and GNSS evaluations are illustrated. Finally, an outlook on plans to add more time series data such as ground water levels, mine water levels or weather data into the internal web service, is outlined.

## I. INTRODUCTION

### A. Mining Activities of RAG Aktiengesellschaft

When RAG Aktiengesellschaft (hereinafter RAG) was founded as Ruhrkohle AG in 1968 it consolidated the hard coal mining activities of more than twenty mining companies in the Ruhr region and held by far a major part of German hard coal mines. At that time about 186.000 workers were employed at RAG and other Ruhr region mineries (Junker *et al.*, 2019). Companies in other German regions with hard coal deposits like the Saar region and the Tecklenburger Land remained independent until the end of the 1990ies. Then the companies Saarbergwerke AG and Preussag Anthrazit GmbH were also merged with RAG. As a result, RAG became the last German hard coal mining corporation and was operating in three regions in a wide spatial extend (Figure 1):

1. Ruhr, approx. 110 x 40 kilometers
2. Saar, approx. 40 x 25 kilometers
3. Ibbenbueren, approx. 20 x 10 kilometers

These three regions have in common that their mines were operating in deep underground deposits with depths down to 1.500 meters below ground level.

Since state subsidization for coal mining were no longer permitted in the European Union since 2019, the last German mines Bergwerk Prosper-Haniel and

Bergwerk Ibbenbueren stopped their production at the end of 2018.

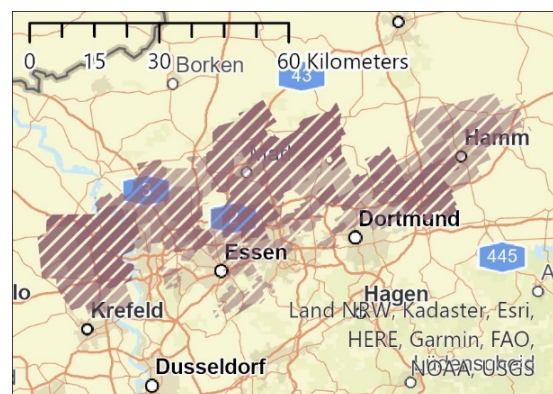


Figure 1. Mining areas in the Ruhr region.

The closure of the last mines was another milestone in a long-planned transition process from a mining corporation to a midsize post-mining company responsible for the mining legacy in the named regions.

### B. Post-Mining Tasks

RAG's post-mining tasks can be divided in two categories, ending and non-ending obligations. Examples for ending obligations are redevelopment of former mining sites and shafts, regulating mining damages or surveying ground movement. Examples for

non-ending obligations are pumping mine water to keep it in a certain secure level or controlling surface water in subsided areas.

To bear the costs of the non-ending obligations the foundation RAG Stiftung was formed from all profitable assets of former RAG Aktiengesellschaft. However, the costs of all ending obligations must be paid by formed reserves. That means RAG cannot act uneconomical and must find ways to improve processes to handle all obligations stable with only about 500 remaining employees.

### C. Deformation Monitoring

In addition to a not insignificant self-interest to preserve its financial and legal goods, RAG must fulfil regulatory requirements and run a system of appropriate geo-monitoring measures to detect ground movement and other incidents (like micro seismic, outgassings, groundwater level, shaft backfilling, et cetera).

Deformation monitoring in areas with active deep underground mining generally means ground subsidence. The hereby induced terrain depressions mainly have a vertical component with its maximum in the centre. However, beside the vertical component of ground movement, a horizontal component arises towards the edges of the depression. This is caused by a sliding into the depression which in turn causes terrain tension and pressing. Depending on the geological composition, the thickness of the mined coalbed and others, active mining provoked ground movement that can have values between centimetres and few decimetres per month in vertical direction. In sum, a few meters to several ten meters can accumulate over years and decades. Whether all or only some of the above deformation components were observed, mainly depends on the affected surface infrastructure.

On the other hand, deformation monitoring in the post-mining era means monitoring of relatively slow and little terrain uplifting. These are caused by the flooding of former underground mines and have values of a few decimetres. With few exceptions the hereby induced horizontal impact and the resulting terrain tension and pressing are so little that they can be neglected. The uplift has values of few centimetre per year at its peak phase and is limited to few decimetres in its maximum. This comes along with higher requirements for the precision of measurements. The occurrence of mining damages to the surface infrastructure is highly unlikely and not yet recognized but nevertheless ground movement observations will be performed until stillstand of the fading uplifts.

### D. Associated Manuscripts

This paper is only one in a series of manuscripts that addresses RAG's efforts to detect and analyse anthropogenically induced ground movement as well as providing data and results. For a better and more comprehensive understanding, the authors recommend articles from Spreckels, V., Kipp, A., Niemeier, W. and Schulz, M..

## II. GEODETIC METHODS AND SENSORS

This chapter gives an overview of typically applied methods to capture deformations and an impression of the data diversity. With one exception (pure position determinations), all methods are performed to observe a specific geometric measurand at a specific location at a specific time, with other words: 4d position data.

### A. Geometric Levelling

Since the vertical component is a major part of ground movement in both active mining and during the flooding of abandoned mines, geometric levelling has been the most important method for deformation monitoring in the past. Despite other technologies like GNSS or satellite-based radar interferometry the geometric levelling is still a frequently used method. This is because geometric levelling is a wide established method with a long history and good precision/effort ratio. Hence, the amount of data observed by this method currently represents the largest part of all used methods.

In this context the high-precision levelling campaigns by the state survey authorities, especially in North Rhine-Westphalia (Geobasis NRW), should not remain unmentioned. The so called Leitnivellements<sup>1</sup> (hereinafter LN) are performed every second year and reach back into the 1960ies in the Ruhr region (see Figure 2). Single official survey points even have a times series that reaches back in the year 1873. Until today the LN play a significant role in deformation monitoring since they are the frame for most levelling's by RAG and others.

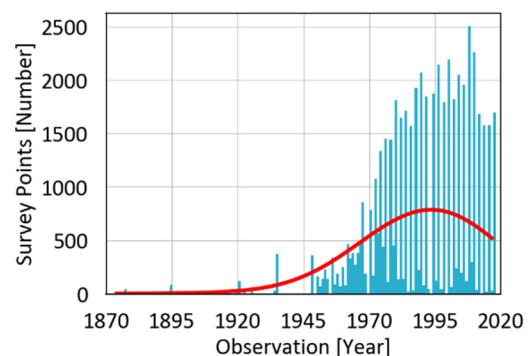


Figure 2. Histogram of officially observed height points in the Ruhr region, showing the beginning of the LN.

<sup>1</sup> Leitnivellements: Leading levelling campaigns

Due to open data offensive by the authorities in North Rheine-Westphalia, this dataset is free for download<sup>2</sup>.

### B. Total Station

Due to relatively high costs, nowadays measurements with total stations come rarely into use. This method is mostly applied in case that the knowledge of vertical movement is not sufficient. This mainly concerns the deformations monitoring of delicate buildings, for example to detect a tilting of parts of a building. Only in single cases and in areas without sufficient GNSS signals traverse lines are surveyed to determine the 3-dimensional coordinates. In contrast, before GNSS was broadly established and mine surveyors were equipped with such instruments the total station measurements were carried out to determine coordinates, for example to measure ground control points for airborne photogrammetry or to determine terrain shifts (Figure 3).

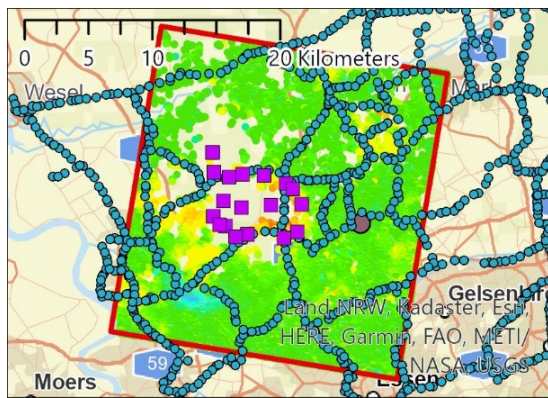


Figure 3. Levelling net, GNSS- and PSI-points from the Geomoplus data base within the map view of ArcGIS Pro.

To survey terrain tension and pressing often tape measurements were carried out.

### C. GNSS

The importance of GNSS at RAG increases more and more. Based on typically achievable precision in RTK-mode GNSS was for example used to survey the areas with maximum subsidence but also to roughly verify the edge of terrain depressions (subsidence trough). With the set-up of several permanent operating GNSS-stations, partly combined with corner reflectors for satellite-based radar interferometry, GNSS becomes an integrator and makes it possible to combine terrestrial and remote sensing methods (Spreckels *et al.*, 2020). Another example: today all reference points for airborne photogrammetry are determined by RTK-GNSS in this network.

### D. Satellite-Based Radar Interferometry

RAG is following the developments of wide area deformation monitoring by satellite-based radar interferometry since 1999 (Spreckels *et al.*, 2001). Over these twenty plus years RAG worked together with scientific institutes as well as with commercial providers. Data from different satellite systems (*e.g.*, Envisat, Radarsat-2, TerraSAR-X, Sentinel-1A/B, and on) were processed and varying evaluation approaches were evolved and applied. This leads to a variety of different data structures which need to be handled.

The latest activities of both state survey authorities, Geobasis NRW<sup>3</sup> (North Rhein-Westphalia) and LVGL<sup>4</sup> (Saarland), to launch web services to provide state-wide ground movement information based on Copernicus Sentinel-1 radar data make it clear that RAG was very foresighted. The web service from Saarland (SaarBoBeKa<sup>5</sup>) is already in service and NRW is planning the same for this year (Riecken *et al.*, 2019), (Engel and Busch, 2018). It must be assumed that in the mid-term this method will be fully established and that it will at least partly replace geometric levelling.

## III. SPATIAL DATA INFRASTRUCTURE

Spatial data is an essential part of many corporate processes within RAG. From the address of a reported mining damage to the information about pipelines in the underground of an ex-mining site or the level of mine water in different mine water retention provinces, spatial data is the basis for a multitude of decisions and activities. Hence it is crucial to provide this information in a reliable manner and obviously a spatial data infrastructure is necessary for this. At RAG this system is called RAG-GDI<sup>6</sup>.

Over the years RAG-GDI has vastly grown. Today it consists of more than 20 servers and several desktop components. Esri products play a significant role for both server and desktop applications. So, the Database Management System ArcSDE is used to administer some of the Oracle Database Server within RAG-GDI, experts work with ArcMap and ArcGIS Pro on their PC's and the ArcGIS API for JavaScript is applied to build up internal and external web services.

The most prominent web service, accessible to all employees, is a RAG internal map centred search engine named Digitale Service Akte (hereinafter DSA). It provides content for over 300 different issues and allows users to carry out tasks such as map exporting (PDF), finding aerial image footage or measurements without further software installations. It is RAG's integration platform to bundle data from diverse expert systems (Kosłowski and Telenga, 2014).

<sup>2</sup> <https://www.opengeodata.nrw.de/produkte/geobasis/rb/fd/>

<sup>3</sup> Bezirksregierung Köln, Abteilung 7

<sup>4</sup> LVGL: Landesamt für Vermessung, Geoinformation und Landentwicklung.

<sup>5</sup> SaarBoBeKa: Saarländisches Bodenbewegungskataster / Saarland's Ground Movement Cadastre:

<https://geoportal.saarland.de/article/Bodenbewegungskataster/>

<sup>6</sup> RAG-GDI: RAG Geo-Daten-Infrastruktur.



## IV. FORMER SYSTEMS, DATA SETS AND SOURCES

## A. Former Systems

Geomonplus (hereinafter GMP) is not a start from scratch. It is more the latest solution to handle survey point data for deformation monitoring purposes. Self-evidently that data was registered even before computer systems existed and stored while computer systems were developed. Hence there are numerous former systems such as:

1. Handwritten table books or paper file cards.
2. Software on mainframe systems.
3. Software on a few decentral Unix server (HVZ).
4. File-based data storage (Excel, CSV, ASCII).
5. ArcMap-AddIn with DB-based storage (GeoMon).

In particular, the Unix server solution HVZ<sup>7</sup> and the ArcMap-AddIn GeoMon had to be considered while developing GMP. The reason for this is that both systems were containing the most relevant data and were providing some indispensable functions (Figure 4).

HVZ was the height register component in a software package<sup>8</sup> which included solutions for most of the geodetic scope of RAG in the Saar region. Levelling measurements *e.g.*, were evaluated in one component (NIV) and then directly brought in to HVZ. The mainly used function of HVZ was the creation of text reports on ground subsidence.

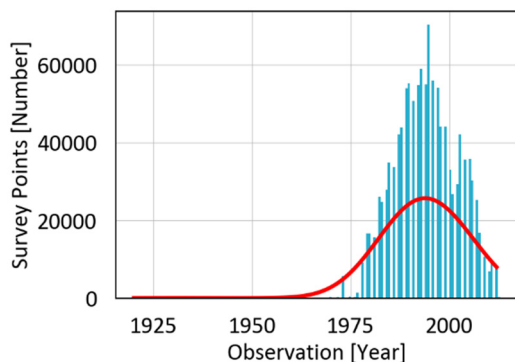


Figure 4. Histogram of observed height points in the Saar region, showing the operational period of HVZ.

GeoMon was the first attempt to set up a GIS-integrated tool to store and analyse time-variant geodetic information of ground movement within RAG. It was designed as an AddIn for ArcMap within the framework of a RAG-R&D project in cooperation with the Technical University of Clausthal (hereinafter TUC) in cooperation with RAG (Kamphans *et al.*, 2008). The main advantages were first the integration of terrestrial geodetic information and satellite-based radar interferometry data in one system and second the direct useability of several other spatial data from the

RAG-GDI. This made it possible to spatially view and evaluate the deformation data together with information about the impacting mining activities in a map. But in the course of use, the import function became more and more outdated and turned out to be disadvantageous, so that less data was imported.

## B. Data Sets and Sources

During the operational period of HVZ more than 1.2 million height observations were stored in a static structured form (Table 1). However, the position data could not be saved and were therefore outsourced in CAD files. Unfortunately, these CAD files had such a diverse layer structure and differing labelling et cetera that the position data could not have been extracted automatically. Moreover, CAD files do not exist for all survey points either. But since position is an essential element of any survey point and is required in GMP (Keyword: 4d position data), over 81,000 points had to be determined. About 36,600 points have been digitized manually. Furthermore, approx. 5,700 points were interpolated between two manually defined points. The remaining approx. 38,700 points could not be determined properly. These points were assigned provisional coordinates (somewhere in France) in the first instance.

Table 1. GMP Data Volume (03/2022)

Source	Data Amount	
	Points	Observations
HVZ <sup>9</sup>	81,435	1,208,830
GeoMon	4,060	5,490
AFIS NRW <sup>10</sup>	27,590	100,192
Import	2,027	5,454

In addition, the system was also used to store length measurements. Since length and height measurements are similar (both 1-dimensional values), this information can easily be integrated.

The amount of data that was imported into the GeoMon database consisted of more than 12,500 unique survey points with overall 64,700 observations, whereof approx. 4,000 points were transferred into GMP. These are 3d determined reference points for the evaluation of airborne photogrammetry campaigns. Most of the remaining points could be neglected because they were either in the HVZ or AFIS NRW inventory.

In addition to the already described data there are different further sources which had not yet been imported. For example, between the beginning of the production phase of GMP in the year 2021 and the de facto shutdown of HVZ and GeoMon in the years 2013 and 2014, FGDB<sup>11</sup> were used as an intermediate

<sup>7</sup> HVZ: Höhenverzeichnis, can be understood as height register.

<sup>8</sup> Designed by Poppenhäger Grips GmbH, since 2005 part of Intergraph, which merged into Hexagon in 2020.

<sup>9</sup> Without virtual points for the storage of length measurements.

<sup>10</sup> AFIS NRW: Amtliches Festpunkt-Informationssystem NRW, Official Reference Point Information System of the Federal State North Rhine-Westphalia (includes the named LN data).

<sup>11</sup> FGDB: File Geodatabase by Esri.

solution. Until today this data has not been imported into GMP. This also applies to an extensive amount of Excel files which have been used over many years. Especially importing Excel files means a lot of manual work. An event-driven approach is the way to go here.

## V. GEOMONPLUS

As the name suggests, GMP was designed with the claim to be an enhancement of GeoMon. It should preserve the advantages of GeoMon (and HVZ) on the one hand and come with crucial improvements on the other hand. To meet this challenge, a group of users, IT experts and scientists came together in the year 2015 and developed initial ideas. The group was made up of members from Atos<sup>12</sup>, TUC and RAG's spatial data department. After the initial specification phase the group was reorganized and continued to operate without TUC. From here on, the development was carried out in tight cooperation with Atos as an agile project using the Scrum<sup>13</sup> method.

GMP consists of different components or layers. Visible to the user are the dialogs or GUI for controlling GMP and displaying information, data, and charts, all in German language. In addition, there is the Oracle-based data base (ArcSDE) with multiple Table and Relationship Classes to store and provide all data (Figure 5). The exception here is radar data, which is stored in FGDB on a network drive due to performance reasons. Finally, scripted interfaces are part of GMP. The applied programming languages are C# for all GMP features and Python for the writing layer (GMP >> Oracle) and scripted interfaces. All dialogs are created with the UI tool kit Windows Presentation Foundation (WPF).

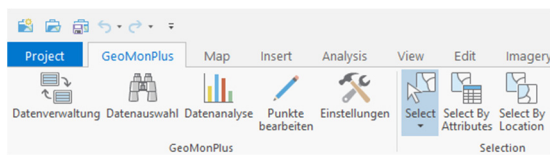


Figure 5. GMP main functions.

### A. Requirements

The following requirements were initially identified and partly adapted to new circumstances.

1) *Generic data model*: As the explanation of the former systems and data sources above show, a generic data model is crucial to integrate a heterogenous data stock. The GMP data model must be able to handle all known former models.

2) *Import interface*: The experience has shown that the Import GUI must be highly flexible and user-friendly and cannot be a bottleneck.

3) *Platform*: GMP must be implemented into the RAG-GDI and based on a future-orientated application. Since GMP is a GIS tool, Esri's ArcGIS Pro was the best choice. Starting with Sprint versions (in the sense of the Scrum method) for ArcGIS Pro version 1.0, the current GMP version is built for ArcGIS Pro 2.7.3.

4) *Interfaces*: One of the most important requirements of GMP is the exchange of data with other internal information systems in order to make the observation results available for a wider range of users.

5) *Geodetic reference system*: Both RAG and the mining authorities in North Rhine-Westphalia and in Saarland remain working with the former official geodetic reference system DHDN with the Gauss Kruger projection. This is due to extensive analogue datasets, such as official mine map inventories. Besides, DHDN (as the bulk) further geodetic reference systems were used over the decades. This leads to the requirements for the geodetic reference system in GMP as follows: First all geometries are basically stored with reference to DHDN<sup>14</sup> / 3-degree Gauss zone 2 and second, further coordinate information with other geodetic reference systems can be attached. This is also true for the vertical reference system. Standard is DHHN2016<sup>15</sup>, further vertical coordinates can be stored for the same point.

### B. Entity relation model and attributes

The presentation of the complete ER model would exceed the scope of this paper by far. However, at least the most important entities and some of their attributes shall be described as follows.

1) *Delivery*: For deformation monitoring, survey points are measured periodically. This usually happens in the context of a definable field campaign, an epoch. In GMP all survey points from one field campaign and epoch are defined as a so-called Delivery. This table holds information about origin, deliverer, purpose, region, epoch, et cetera (Figure 6).

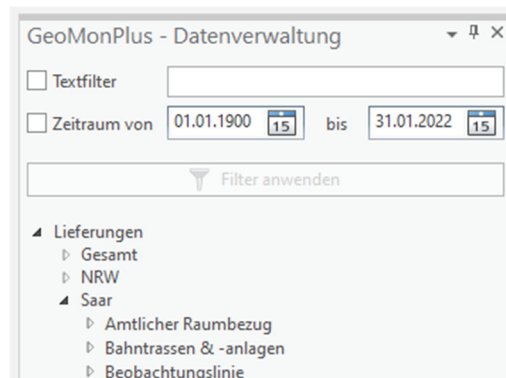


Figure 6. GMP Data Management.

<sup>12</sup> Atos IT-Dienstleistung und Beratung GmbH.

<sup>13</sup> <https://scrumguides.org/docs/scrumguide/v2020/2020-Scrum-Guide-US.pdf>

<sup>14</sup> DHDN: Deutsches Hauptdreiecksnetz, German Main Triangulation Net (EPSG:31466)

<sup>15</sup> DHHN2016: Deutsches Haupthöhennetz 2016, German Main Height Net 2016 (EPSG:7837)

2) *Survey Point*: Contains a representation of each physically existing at least once measured survey point and ties all corresponding point measurements together. Even if the point name differs. This is managed by a position comparison during the import process and allows user interaction in case of wrongly identified corresponding.

3) *Measurements*: As the name suggests all measured coordinates regardless of the geodetic reference system are stored as X, Y, Z in this table. In addition, standard deviation for each coordinate component can be saved. Information concerning the geodetic reference system is held in a related table.

4) *Spatial Reference*: Provides distinct geodetic reference system definition to the related table Measurements as Geodetic Datum, Projection, Vertical Reference System and Vertical Reference Surface.

5) *Display Point*: Every measurement is represented by a point feature and carries the most relevant information like point name, observation date, observation method, point type and a few other. All Display Points are stored with Gauss Kruger coordinates and transformed on the fly in case the ArcGIS Pro Map Frame differs.

6) *Survey Point Group*: Is a construct of Table and Relationship Classes to organize groups of Survey Points divided into epochs. This makes it possible to combine Survey Points from different Deliveries to one grouping without generating redundant data entries. Hereby the same Survey Point can be used in several Concerns.

7) *Observation Line*: Allows it to organize a similar structure as the Survey Point Group does but additionally an order of all containing points is set.

8) *Radar Evaluation*: Every evaluation of satellite-based radar data registered within GMP is represented by a polygon which matches the minimum bounding geometry of all evaluated points (*e.g.*, Persistent Scatterer). This polygon feature carries, like the Display Point, the most relevant information about the evaluation. For example, name of the evaluation, date of the first and last used scene, date of the reference scene and a hyperlink to the corresponding File Geodatabase in which all evaluated points are stored. Information about the source satellite system and the used height model are stored in related tables.

9) *Project*: Is also a structuring entity without its own significant attributes. It makes it possible to tie the above-named objects Survey Point Group, Observation Line and Radar Evaluation.

### C. Main Functions

As in ArcGIS Pro usual, the main functions are embedded as a Tab into the Ribbon at the top of the screen in an own category. The GMP Tab can be customized and more Esri functions can be added. The main functions are from left to right Data Management, Data Selection, Data Analysis, Point Editing and Settings.

1) *Data Management*: This functionality is inspired by the ArcGIS Pro Catalog and gives the users a structured list view on all yet imported data sets as well as access to several further functions such as Survey Point Importing, Adding Items to the Map, Adding Items to a Project, et cetera. It is the central control element of GMP.

The importing of Deliveries into GMP can be conducted by an ASCII interface. Users control this interface by an Import Wizard which supports either fixed ASCII formats or separator formats. In a few steps all required and optional information is queried by the Import Wizard and if present matching points from prior epochs will be linked.

Once imported, Survey Points can be upgraded in several ways. They can be grouped with Survey Points from other Deliveries to a Survey Point Group or to an Observation Line, each with epoch subsets. Survey Point Groups and Observation Lines again can be assigned to Projects. Together with Radar Evaluations these objects build the main data structure within the Data Management tool. To ensure a good user experience the inventory of all items is further structured. Below the main object grouping are further groupings by region and purpose. In case that users still cannot find a desired item, text and time filters can be set.

2) *Data Selection*: This tool enables the users to find GMP content based on attributes, temporal filter, or spatial specifications. This helps if a user is uncertain whether there is data or not to answer a specific question. For example, following query could be defined: Show all survey points from the class levelling point with measurements between 01.01.1990 and 31.12.1990 within the current map extent.

3) *Data Analysis*: To visualise and analyse deformation data from different sensors is the main purpose of GMP. The most important tool is the time series charting (see Figures 7 and 8). The users can either select GMP Display Point in the map and open the Data Analysis dialog by a click on the button in the ribbon or enter the dialog from the context menu of an item within the Data Management.

4) *Point Editing*: This dialog can be used if any changes or corrections on survey points need to be done.

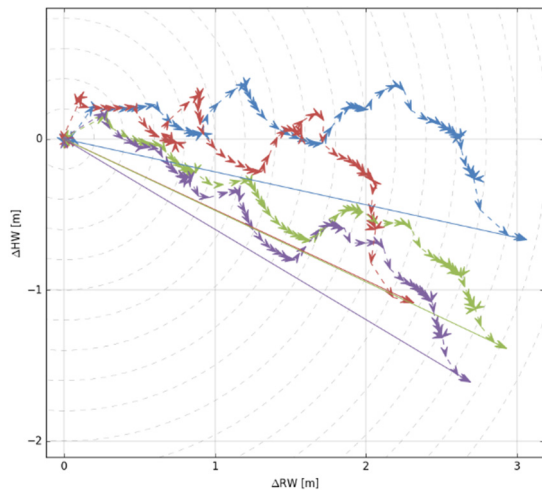


Figure 7. Time series. Detail view on the horizontal displacements of four in Figure 9 highlighted and framed survey point. X:  $\Delta$ Easting, Y:  $\Delta$ Northing in m.

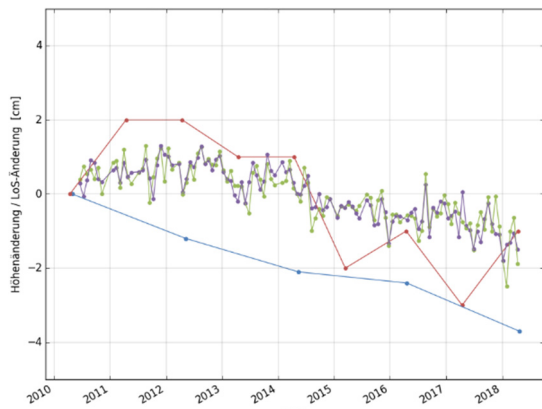


Figure 8. Time series. Comparison of PSI, levelling (blue) and GNSS (red) measurements. X: time in years, Y: height changes / Line-Of-Sight changes in cm.

#### D. Interfaces

Currently there is an automated interface with the DSA as target system. With the help of regularly running transformation scripts, a simplified respectively flat image of selected data is written and provided to the DSA users. In the first step only height measurements are transferred to the DSA. Whether displacement measurements will also be transferred is still in the decision-making process.

At present, an interactive chart<sup>16</sup> is available to DSA users. For example, by using slide controls or the mouse wheel it is possible to change the time or height extend. By hovering the mouse pointer over data points in the chart, information about date and height is displayed. These are merely two examples to indicate the potential of the used charting library.

#### VI. OUTLOOK

The development work on GMP is largely completed, therefore only small improvements are planned for the near future and of course maintenance work like

updating GMP for newer ArcGIS Pro versions. But thanks to the deep integration of Python in ArcGIS Pro (ArcPy), more functions are planned for realization as custom tools within an Esri ArcToolbox. The displacement vectors in Figure 9 are an illustrating example in how external functions can use the GMP data to generate an additional value. Generating vertical bars to display height changes in the printed or PDF maps will be the next custom tool.

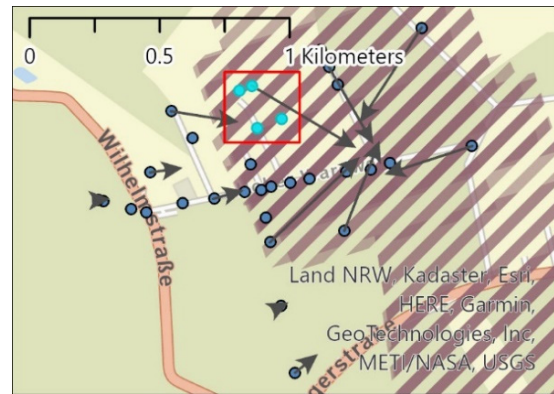


Figure 9. Horizontal displacement caused by underground mining activities in the course of 15 years. Vector scale 1:200.

In addition, a bidirectional interface between GMP and GLOMON<sup>17</sup> (Schulz and Schäfer, 2022) will be realized during 2022. The aim here is to transfer daily determined 3d coordinates from GNSS stations from GLOMON to GMP and then again levelling results from GMP to GLOMON.

Asides from GMP, the development of tools for the analysis of time series in DSA will continue (Figure 10). The enrichment of further non-geometric data like rainfall or air temperature et cetera is currently in the developing stage. A joint representation of time series of two different sensor types in one chart will allow to visualise correlations between effect and phenomenon. Imagine data from a sensor observing the controlled rise of underground mine water level (as the effect) combined with slowly gaining height data of a GNSS sensor (as phenomenon). That provides an easy approach to conclude whether a ground movement is natural or induced.

#### VII. CONCLUSIONS

The knowledge of past and recent ground movement in former mining areas is necessary for RAG to meet its obligations in order to complete the dismantling of abandoned underground mines as well as to be able to assess potential mining damages. To this end, both accurate geodetic observation methods and reliable data management including workflows and storage are vital. With developing GMP, RAG ensures the reliability of the deformation monitoring process for future tasks

<sup>16</sup> The library amCharts 5 is used for the time series charts.

<sup>17</sup> GLOMON: Global Monitoring web service by Allsat GmbH.

and significantly increases the accessibility of the created results.

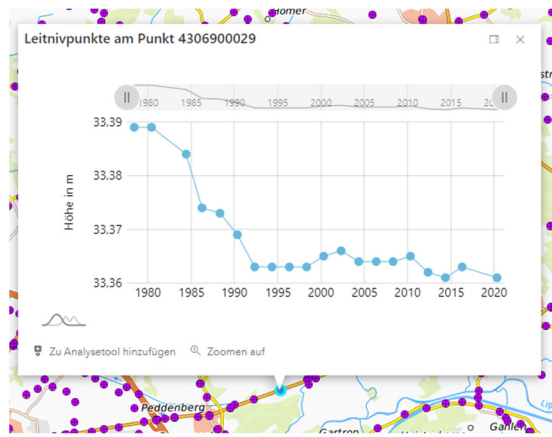


Figure 10. Interactive time series charting in the map of the current DSA version 4.3.

All previously formulated requirements could be met and overall, a versatile tool for deformation monitoring has been created. The additional capabilities of ArcPy make the system even more complete. However, any data-driven application is only as good and comprehensive as its volume. That means, the success of GMP is necessarily linked to the integration of other data. Great efforts will be needed here in the future.

The first times series functions with interactive charts in RAG's internal web service Digitale Service Akte have been met with great acceptance among test users. More data sets and analytics will be added over the next few months and contribute to preserve expertise in a shrinking organization.

#### VIII. ACKNOWLEDGEMENTS

The authors would like to thank everyone who helped to master the challenge of developing a very customized software solution in a technically and expertly demanding environment over a time span of several years, either in the background or in the front.

Very special thanks to the following supporters in alphabetical order: Mr. M. Diehl (Atos), Ms. A. Dietrich (Atos), Mr. U. Grimhardt (RAG), Mr. N. Karrenbauer (Atos), Mr. J. Mühlbach (Atos), Ms. S. Rayado Perez (first TUC, later Atos), Ms. S. Ricken (RAG) and Mr. P. Vosen (RAG). Thank you all very much.

#### References

Engel, T., and W. Busch (2018). Landesweite, radarinterferometrische Bodenbewegungserfassung auf Grundlage von Sentinel-1-Daten – Verfahrensweise und Ergebnisse am Beispiel des Saarlandes. In: *GeoMonitoring 2018: Tagungsband: 1. März bis 2. März 2018 in Clausthal-Zellerfeld*. Busch W (eds), TU Clausthal, Institut für Geotechnik und Markscheidewesen Clausthal-Zellerfeld, pp 11-25.

Junker M., D. Imgenberg, K. Gutberlet, H. Hejney, K. Jaeger, M. Lemke, T. Rehpöhler, M. Schmidt, and H. Witthaus (2019). Vorwort. In: *Technikentwicklung und Forschung bei*

RAG. RAG Aktiengesellschaft, Essen (eds), GeoResources Verlag, König M, Duisburg, pp V.

Riecken, J., B. Krickel, V. Gefeller, and P. Reifenrath (2019). Nutzung der Radarinterferometrie im geodätischen Raumbezug. In: *zfv – Zeitschrift für Geodäsie, Geoinformation und Landmanagement*. Müller J (eds) Vol. 144 Issue 6 (2019), Wißner-Verlag GmbH & Co. KG Augsburg, pp 354-361.

Schulz, M., and F. Schäfer (2022). GLOMON-Monitoringportal for storage, management, advanced processing and intelligent visualization of GNSS- and other sensors data In: *Proceedings of the 5<sup>th</sup> Joint International Symposium on Deformation Monitoring JISDM 2022*, Valencia, Spain, June 20-22, 2022.

Spreckels, V., U. Wegmüller, T. Strozzi, and H.C. Wichlacz (2001). Detection and observation of underground coal mining-induced surface deformation with differential SAR interferometry. In: *Joint Workshop of ISPRS Working Groups 1/2, 1/5 and IV/7, High Resolution Mapping from Space 2001, Sept. 19-21, 2001 Hannover, Germany*. International Society for Photogrammetry and Remote Sensing, Institute for Photogrammetry and Geoinformation University of Hannover, pp 227-234.

Spreckels, V., S. Bechert, A. Schlienkamp, M. Drobniowski, M. Schulz, F. Schäfer, E. Kemkes, J. Rüffer, W. Niemeier, D. Tengen, T. Engel, M. Müller, and P. Schmitt (2020). GNSS, Nivellement und Radar – einheitliche Multisensor-Referenzstationen zur Überwachung von Bodenbewegungen in ehemaligen Bergbaubereichen. In: *GeoMonitoring 2020, Tagung, 12.-13. März in Braunschweig*. Braunschweig, Germany

Kamphans, K., D. Walter, W. Hannemann, W. Busch, V. Spreckels, and P. Vosen (2008). GIS-Einsatz im Monitoring bergbau-bedingter Oberflächenbewegungen. In: *Angewandte Geoinformatik 2008: Beiträge zum 20. AGIT-Symposium in Salzburg*. J Strobl T Blaschke G Griesebener (eds) 1. Edition, H. Wichmann Verlag Heidelberg pp 572-577

Koslowski, T., and K. Telenga, (2014). The Digital Service File (DSA) – The RAG Integration and Information Platform for Spatial Data. In: *Journal of Sustainable Mining*. Smolinski A (eds) Vol. 13 Issue 4 (2014), DOI: 10.7424/jsm140406, pp 28-33.

## Kalman filter for integration of GNSS and InSAR data applied for monitoring of mining deformations

Damian Tondaś<sup>1</sup>, Witold Rohm<sup>1</sup>, Maya Ilieva<sup>1</sup>, Jan Kapłon<sup>1</sup>

<sup>1</sup>Wrocław University of Environmental and Life Sciences, Poland ([damian.tondas@upwr.edu.pl](mailto:damian.tondas@upwr.edu.pl), [witold.rohm@upwr.edu.pl](mailto:witold.rohm@upwr.edu.pl), [maya.ilieva@upwr.edu.pl](mailto:maya.ilieva@upwr.edu.pl), [jan.kaplon@upwr.edu.pl](mailto:jan.kaplon@upwr.edu.pl))

**Key words:** GNSS; InSAR; ground displacements; mining deformations; data integration; GNSS and InSAR fusion; Kalman filter

### ABSTRACT

Ground deformation monitoring can be performed using different measurement methods, e.g., leveling, gravimetry, photogrammetry, laser scanning, satellite navigation systems, Synthetic Aperture Radar (SAR), and others. In the presented study we introduced an original methodology of integration of the Differential Satellite Interferometric SAR (DInSAR) and Global Navigation Satellite Systems (GNSS) data using Kalman filter. However, technical problems related to invalid GNSS receivers functioning and noisy DInSAR results have a great impact on calculations provided only in the forward Kalman filter mode. To reduce the impact of unexpected discontinuity of observations, a backward Kalman filter was also introduced. The applied algorithm was tested in the Upper Silesian coal mining region in Poland. The paper presents the methodology of DInSAR and GNSS integration appropriate for small-scale and non-linear motions.

The verification procedure of the obtained results was performed using an external data source – GNSS campaign measurements. The overall RMS errors reached 18, 16, and 42 mm for the Kalman forward, and 19, 17, and 44 mm for the Kalman backward approaches in North, East, and Up directions, respectively.

### I. INTRODUCTION

Over the years, the capabilities for determining land surface changes have developed significantly and also have found application in areas particularly affected by mining activities. However, none of the available methods for ground deformation monitoring applied separately can provide sufficient spatio-temporal resolution and high accuracy simultaneously. Hence, in this paper, we performed an original methodology for InSAR and GNSS data integration. The developed algorithm can be applied for small-scale non-linear dynamic deformations. To validate the proposed methodology, we used real observations performed in the Upper Silesian mining region in Poland.

The GNSS technology enables permanent monitoring of the surface movements in three-dimensional (3-D) space. Moreover, the evolution of GNSS processing techniques allows to determine positions with millimetre level accuracy and a latency ranging from a few seconds to less than one hour (Branzanti et al., 2013; Tondaś et al., 2020; Hadaś, 2015).

Unfortunately, the spatial range of the GNSS measurements concerns only the location where the geodetic antenna is mounted. Furthermore, to acquire a system for ground monitoring changes across an entire mine area, at least several dozen GNSS receivers are needed (Bian et al., 2014; Tao et al., 2018). Nowadays, to improve the spatial range of GNSS measurements, low-cost receivers are increasingly used. The most important aspect of using low-cost stations is to maintain the quality of the position

determination. Various studies conducted for different types of low-cost receivers indicate sub-millimeter or millimeter differences compared to traditional geodetic GNSS stations (Cina et al., 2015; Hamza et al., 2021).

In contrast to the point-based GNSS technique, the InSAR areal investigations provide a better overview of local terrain changes. Moreover, some SAR products are freely available which significantly reduces the cost of ground deformation monitoring.

Nevertheless, InSAR methods also have some limitations related to (I) temporal resolution (a few days latency in acquiring a new image), (II) limited sensitivity to changes in the northern direction, (III) significant loss of coherence in vegetated areas depending on the radar wavelength, (IV) the impact of local atmospheric conditions brings additional radar signal delay and phase unwrapping problems. Furthermore, deformation can be acquired only in the 1-D line-of-sight (LOS) direction which substantially limits the capabilities to describe the detected surface deformation (Osmanoğlu et al., 2016; Fattahi et al., 2014).

Over past decades a great effort has been made to provide a unified solution for resolving the incomplete information for horizontal InSAR displacements. Hu et al. (2014) provide a systematic review of the methods for mapping 3-D displacements using InSAR measurements pointing out the strengths and weaknesses of each approach. The presented classification was categorized into three groups: (I) combination of multi-pass LOS and azimuth measurements, (II) integration of InSAR and GNSS data,

and (III) prior information assisted approaches. In our study, we refer to the second group of the mentioned methods - the integration of InSAR and GNSS.

Currently, the fusion process involves different approaches and assumptions for linear large-scale displacements or rapid non-linear movements. For instance, Liu et al. (2019) present a concept of linear interpolation and prediction based on the specific spatio-temporal domains. A new type of procedure to integrate InSAR and GNSS results was presented in the study of Boszo et al. (2021). The article shows a method for estimation of 3-D deformation parameters and rates using Sentinel-1 data and GNSS epoch observations converted to the LOS domain. The Kalman filter algorithm was tested on landslide area in Hungary with an assumption for linear velocities. To determine the 3-D deformation parameters, the GNSS data were projected onto the LOS vectors. The presented approach is based only on linear velocities calculated from two GNSS campaigns, thus in the last epoch, the calculated positions were rescaled using the GNSS-derived LOS values.

Based on the presented literature methods, it can be concluded that nowadays the GNSS-InSAR integration is suitable for large-scale linear motions. However, for small-scale non-linear deformations, current integration techniques are not well developed and robust against noise. For our study, we used GNSS observations from permanent ground stations and DInSAR deformation maps derived from Sentinel-1 data. Our algorithm is able to ingest the noisy GNSS NEU coordinates with significant gaps, and time series errors in the DInSAR ascending and descending LOS velocities due to troposphere artifact or improper SAR phase unwrapping. The observation uncertainties are rigorously determined from the parameter estimation process for GNSS data, while for DInSAR results the errors are calculated based on coherence values.

## II. METHODOLOGY

The presented study was conducted for an area affected by underground mining works, for which two groups of data – DInSAR (Sections II.A) and GNSS (Sections II.B) are processed, aiming to achieve comprehensive monitoring of the ongoing ground deformations. A new approach for integration of the data using the Kalman filter is suggested in Section II.C. To verify the obtained results, a quality analysis based on independent data set was performed (Section II.D).

### A. DInSAR processing

In this study, a consecutive cumulative DInSAR manner for surface deformation monitoring is applied, where the second (slave) image of each interferogram is used as a primary (master) image in the next interferometric pair, forming continuous time series. A serious disadvantage is that this approach does not eliminate the contribution of the interferograms with

lower quality. The DInSAR processing is accomplished with the Sentinel Application Platform (SNAP), provided by the European Space Agency (ESA), following the standard procedure. ESA's SAR Sentinel-1 data covering the area of interest acquired in Interferometric Wide swath (IW) mode with VV polarization are used. An external Digital Elevation Model (DEM), namely the 1-sec distribution of the Shuttle Radar Topography Mission (SRTM) Height file (Jarvis et al., 2008), is used for coregistration of the two images of each pair and for subtracting the stable topography component from the wrapped differential interferogram. The Goldstein non adaptive filter (Goldstein et al., 1998) was applied to enhance the two-dimensional phase unwrapping, done with the Statistical-Cost, Network-Flow Algorithm for Phase Unwrapping (SNAPHU, Chen et al., 2000). Finally, the values of the resulted unwrapped interferometric phase are transformed to the metric units.

To determine the error values of a particular pixel, the coherence coefficient was used to measure the phase noise. The phase variance is defined by the probability density functions depended on a multilook levels (Hanssen, 2001). In the presented study, the multilooking level is 1 ( $L = 1$ ) and for single-look data, the phase variance can be expressed as:

$$\sigma_{\phi,L=1}^2 = \frac{\pi^2}{3} - \arcsin\pi(|\gamma|) + \arcsin^2(|\gamma|) - \frac{1}{2} \sum_{k=1}^{\infty} \frac{|\gamma|^{2k}}{k^2} \quad (1)$$

where  $\sigma_{\phi}$  = phase noise  
 $L$  = multilook level  
 $\gamma$  = coherence coefficient  
 $k$  = the index of summation

The final interferometric phase errors in the ascending and descending directions ( $\sigma_{d_{los}}^A, \sigma_{d_{los}}^D$ ) are transformed into metric units:

$$\sigma_{d_{los}} = \frac{\lambda}{4\pi} \sigma_{\phi,L=1} \quad (2)$$

where  $\sigma_{d_{LOS}}$  = InSAR deformation error in LOS  
 $\lambda$  = Sentinel-1 wavelength (~5.55 cm)

The deformation vector measured in the LOS direction can be described by the 3-D components as:

$$d_{los} = [\sin(\theta) \sin(\alpha) - \sin(\theta) \cos(\alpha) \cos(\theta)] \begin{bmatrix} n_s \\ e_s \\ u_s \end{bmatrix} \quad (3)$$

where  $d_{LOS}$  = InSAR deformation in LOS  
 $\theta$  = incidence viewing angle  
 $\alpha$  = azimuth angle of Sentinel-1 satellite  
 $n_s, e_s, u_s$  = the SAR topocentric coordinates

### B. GNSS processing

The coordinates of the permanent GNSS stations were estimated in post-processing mode using a double difference technique. The solution was based on United States' Global Positioning System (GPS), Russian Global

Navigation Satellite System (GLONASS), and ESA's Galileo observations with a daily computational interval. The processing executed in Bernese GNSS software v.5.2 (Dach et al., 2015) was carried out on the Center for Orbit Determination in Europe (CODE, Dach et al., 2018) final precision products. To ensure a stable reference, 14 stations belonging to the International GNSS Service (IGS) network and the European Reference (EUREF) Permanent Network (EPN) were included in post-processing calculations (Figure 1).

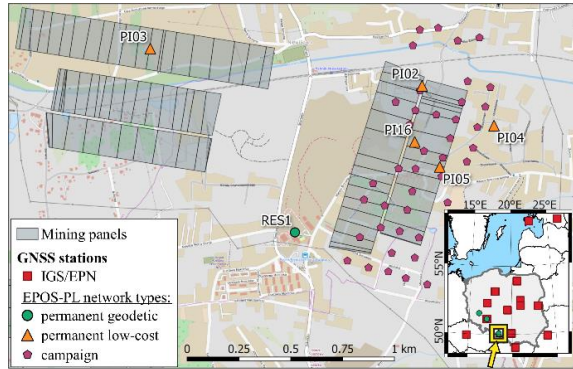


Figure 1. Map of the study area including undergoing mining exploitation panels (grey rectangles), locations of the permanent GNSS stations (green circles and orange triangles), and campaign points (purple pentagons). The map in the bottom right corner shows the locations of IGS/EPN reference stations (red squares)

In addition, independent epoch measurements were also considered in this paper. The GNSS campaign network containing over 100 points over the Upper Silesia region was developed for research purposes by the Military University of Technology in Warsaw (MUT). The MUT team processed the epochs of observations together with the GNSS data from the local network of the Continuously Operating Reference Station (CORS, Mutke et al., 2019).

The results obtained for the permanent and campaign GNSS points were determined in the ITRF2014 reference frame (Altamimi et al., 2016). To ensure consistency with the DInSAR data, which assume unchanging positions concerning the reference points, the ITRF2014 coordinates and uncertainties were transformed to the ETRF2000 frame using the 7-parameters conversion (Altamimi, 2018).

Afterwards, for a better understanding of the local displacements, the geocentric coordinates were converted to the topocentric NEU frame (Tao et al., 2018). The most illustrative way to present the position variation of the GNSS station over time is to take the first computational epoch as the reference value. To avoid the situation of adopting an outlier as an initial value for the permanent stations' time series, the averaged coordinates ( $N_G, E_G, U_G$ ) from the first five computational observations were assumed as reference values. The reference for the positions of the campaigned GNSS points ( $N_C, E_C, U_C$ ) were determined

as the first common epoch with the data from the permanent stations.

### C. DInSAR and GNSS data integration

The DInSAR measurements enable continuous monitoring of large-scale subsidence areas. However, the radar technique affords the observations in ascending and descending LOS directions. Whereas, the GNSS method provides determination of the displacements in 3-D, but only on sites where the antennas were located. Therefore, to perform the integration of small-scale displacements, it was necessary to overlay the DInSAR rasters with the GNSS locations. The information about implemented integration workflow is presented in Figure 2.

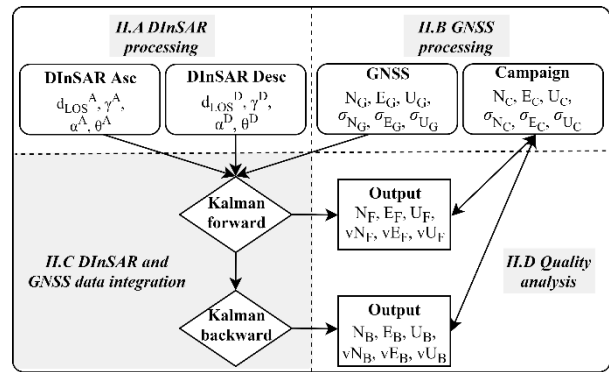


Figure 2. Scheme demonstrating the new method for applying DInSAR and GNSS observations (top part of the graph) in Kalman filter approaches (bottom left part of the graph) including quality analysis (bottom right part of the graph)

The process of integrating DInSAR and GNSS observations is based on the Kalman filter algorithm (Kalman, 1960). To estimate the unknown parameters and uncertainties of the system, the process follows as a recursive two-step procedure. In the first stage, termed as a *time-update*, to predict the parameters in the current epoch ( $t$ ), information about the system from the previous epoch ( $t-1$ ) is used. In the second step, named as a *measurement-update*, the modeled values, as well as the uncertainties, are corrected by the real observations and measurement noise received in the current epoch.

The *time-update* part of the DInSAR-GNSS integration contains the dynamic model for time-varying parameters (Verhagen et al., 2017). The state vector  $\hat{x}$  is based on the three-dimensional values and velocities of ground deformations with a daily interval of calculation ( $\Delta t=1$  day). The computations are conducted in the topocentric reference frame and the initial values ( $\hat{x}_{0|0}$ ) are equal to zero. As the initial values of parameters errors ( $P_{0|0}$ ) the system noise values are taken ( $S_t$ ).

In our approach, the zero mean acceleration model is introduced as the system noise matrix (Teunissen, 2009):



$$S_t = \sigma_0^2 \begin{bmatrix} \frac{1}{4}\Delta t^4 & \frac{1}{2}\Delta t^3 & 0 & 0 & 0 & 0 \\ \frac{1}{2}\Delta t^3 & \Delta t^2 & 0 & 0 & 0 & 0 \\ 0 & 0 & \frac{1}{4}\Delta t^4 & \frac{1}{2}\Delta t^3 & 0 & 0 \\ 0 & 0 & \frac{1}{2}\Delta t^3 & \Delta t^2 & 0 & 0 \\ 0 & 0 & 0 & 0 & \frac{1}{4}\Delta t^4 & \frac{1}{2}\Delta t^3 \\ 0 & 0 & 0 & 0 & \frac{1}{2}\Delta t^3 & \Delta t^2 \end{bmatrix} \quad (6)$$

where  $\sigma_0$  = the level of system noise  
 $\Delta t$  = the interval of calculations

The  $\sigma_0$  parameter was established empirically and the detailed results are presented in Section II.D.

The transition matrix ( $\phi_{t|t-1}$ ) of the dynamic model describes the evolution of the state parameters in time, and can be obtained as a first-order differential equation:

$$\phi_{t|t-1} = \begin{bmatrix} 1 & \Delta t & 0 & 0 & 0 & 0 \\ 0 & 1 & 0 & 0 & 0 & 0 \\ 0 & 0 & 1 & \Delta t & 0 & 0 \\ 0 & 0 & 0 & 1 & 0 & 0 \\ 0 & 0 & 0 & 0 & 1 & \Delta t \\ 0 & 0 & 0 & 0 & 0 & 1 \end{bmatrix} \quad (7)$$

In the *measurement-update* step, to obtain a filtered system state with error variances, the prediction is combined with the actual observations in terms of minimum mean square error.

In the observations vector ( $z_t$ ) the first three elements ( $N_G, E_G, U_G$ ) refer to the topocentric position of the GNSS station received by processing with Bernese Software (Section II.B):

$$z_t = \begin{bmatrix} N_G & E_G & U_G & \frac{d_{LOS}^A}{\Delta T} & \frac{d_{LOS}^D}{\Delta T} \end{bmatrix}^T \quad (11)$$

The two last elements ( $d_{LOS}^A, d_{LOS}^D$ ) are the differential LOS displacements obtained from the DInSAR ascending and descending geometries, respectively (Section II.A). The DInSAR observations were divided by the factor  $\Delta T$ , which is the period of each interferogram, equal to 6, or 12 days in the case of a missing Sentinel-1 image.

In the projection matrix ( $A_t$ ) the number of rows is equal to the number of measurements, while the number of columns determines the number of parameters

$$A_t = \begin{bmatrix} 1 & 0 & 0 & 0 & 0 & 0 \\ 0 & 0 & 1 & 0 & 0 & 0 \\ 0 & 0 & 0 & 0 & 0 & 1 \\ 0 & \sin(\theta^A)\sin(\alpha^A) & 0 & -\sin(\theta^A)\cos(\alpha^A) & 0 & \cos(\theta^A) \\ 0 & \sin(\theta^D)\sin(\alpha^D) & 0 & -\sin(\theta^D)\cos(\alpha^D) & 0 & \cos(\theta^D) \end{bmatrix} \quad (12)$$

The two last rows are related to the conversion of the NEU coordinates into the LOS domain (eq. 3). In the

proposed model, GNSS observations describe displacement values, while the radar observations are considered as velocity measurements. The measurement noise matrix ( $R_t$ ) contains the correlated variances of the GNSS topocentric coordinates ( $\sigma_{N_G}, \sigma_{E_G}, \sigma_{U_G}, \sigma_{NE_G}, \sigma_{NU_G}, \sigma_{EU_G}$ ), whereas estimates calculated from the DInSAR in ascending and descending geometries are assumed to be uncorrelated ( $\sigma_{d_{LOS}^A}, \sigma_{d_{LOS}^D}$ ):

$$R_t = \begin{bmatrix} \sigma_{N_G}^2 & \sigma_{NE_G} & \sigma_{NU_G} & 0 & 0 \\ \sigma_{NE_G} & \sigma_{E_G}^2 & \sigma_{EU_G} & 0 & 0 \\ \sigma_{NU_G} & \sigma_{EU_G} & \sigma_{U_G}^2 & 0 & 0 \\ 0 & 0 & 0 & \sigma_{d_{LOS}^A}^2 & 0 \\ 0 & 0 & 0 & 0 & \sigma_{d_{LOS}^D}^2 \end{bmatrix} \quad (13)$$

The presented Kalman filter algorithm can be applied in a real-time mode and run anytime when a new observation appears. However, this method works only in a forward direction, so the detection and elimination of outliers which potentially occurred in the past is not possible. To get better estimates of the forward results, a backward Kalman filter could be applied (Figure 2).

The Kalman backward algorithm, named also as *smoothing processing*, relies on the forward Kalman filter results, but can also be used parallel to a real-time filter (Verhagen et al., 2017). The backward filter runs recursively with  $t = \{N-1, N-2, \dots, 0\}$ , where  $N$  is the current epoch. The smoothed state values ( $\hat{x}_{t|N}^b$ ) and error variance-covariance matrix ( $P_{t|N}^b$ ).

The Kalman backward filter is mainly used in the post-processing mode. The *smoothing algorithm* cannot run separately – the results from the forward filter are required in every recursion. Finally, the statistical accuracy analysis was performed for the filtered forward ( $N_F, vN_F, E_F, vE_F, U_F, vU_F$ ) and backward ( $N_B, vN_B, E_B, vE_B, U_B, vU_B$ ) state vectors with respect to an external data source (Section II.D).

#### D. Quality analysis

To verify the obtained results, a quality analysis based on independent data set – GNSS campaign data (04.2019, 08.2019, 11.2019, 06.2020, 01.2021) that were realized in a common time span with the DInSAR and GNSS observations, was performed.

Due to the non-identical location of the campaign points with the permanent GNSS sites, the closest possible epoch-based point was selected for the verification. To ensure the co-location of the analysed time series, the offsets between coordinates were calculated. The 3-D shifts were eliminated based on the first common epoch for camping measurement and Kalman backward permanent data sets.

Moreover, to provide the most optimal  $\sigma_0$  value of the Kalman system noise, RMS errors for 4 permanent stations were analysed regarding GNSS epoch measurements.

### III. DEFORMATION IN ACTIVE MINE REGION: CASE STUDY RYDUŁTOWY

The proposed new method of DinSAR-GNSS integration is tested for the area of the "Rydułtowy" mine, located in the south-western part of Upper Silesia in Poland, where the multilevel coal exploitation induces significant ground deformation and high seismicity. The area of interest is located in the immediate vicinity of the coal longwalls panels in the north-eastern part of the "Rydułtowy" mining area. In the expected deformation zones, a considerable number of GNSS receivers were positioned (Figure 1).

In the study area, one permanent geodetic GNSS station (RES1) was placed on the "Ignacy" Historical Mine. The station was not located directly above longwalls panels, however, ground deformations were expected. Five low-cost permanent receivers (PI02, PI03, PI04, PI05, PI16) were mounted to monitor terrain subsidence and lateral displacements during the exploitation of the "Rydułtowy" mine longwalls. The details about equipment and execution of the measurements are presented in Table 1.

Table 1. Classification of GNSS infrastructure deployed in Upper Silesia under the EPOS-PL project.

Name	Receiver	Antennas	Execution of measurements
geodetic RES1	Leica GR30	LEIAR20 LEIM	continuously, beginning 10.08.2018
low-cost PI02-PI05,PI16	Piksi Multi	HXCGPS500 NONE	continuously, beginning 11.02.2019
campaign 42 points	Trimble 5700	TRM39105.00, TRM41249.00	epoch-based, beginning Apr 2018

The beginning of collecting observations was 11.02.2019, however, due to technical problems, the low-cost time series are not complete (maximum break of around 9 months for PI02 station). Moreover, 42 campaign points were distributed over underground coal seams. The results of the measurements were used in the quality analyses. In order to co-locate with the low-cost permanent stations, a cross-reference was done with the nearest points – PI02, PI04, PI05, and PI16.

### IV. RESULTS

The methodology outlined in Section II.C was performed for two low-cost stations (PI16 and PI03 located just above active extraction panels) and one geodetic permanent station RES1 placed in the vicinity of the extraction panels (Figures 3-5). It has to be also noted that the integrated results are available for all six components:  $(N, E, U, vN, vE, vU)$ , therefore each figure contains six panels – the first row is for the

displacements, the second – for the velocities. The analysis of the graphical results is presented in Section IV.A and the details of the obtained residuals for low-cost permanent stations in the vicinity of campaign points are described in Section IV.B.

#### A. Kalman filtering application

The PI16 displacements visible in Figure 3. demonstrate that the epoch and permanent GNSS estimates follow a similar pattern, the North component (left panel) is undulating during the first nine months of the observations and then stabilize around 0.04 m. The East component (middle panel) is demonstrating similar displacement of 0.04 m for the first six months of 2020 and stabilize afterwards. The Up component (right panel) has a similar two-stage displacement cycle. In the first large significant event, lasting for the first nine months of the observations in 2019, introduces a vertical downlift of 0.30 m. During the second stage (the entire 202, the movement is rather slow – up to 0.40 m downlift. The Kalman forward model (green solid line) performs exceptionally well, tracing the estimated PI16 displacements in the North component (top row, left panel) epoch solution (the positive deformation is estimated to be 0.04 m at the last epochs of 03.2021). It is worth to note, that the GNSS permanent station demonstrates a noisy behavior in 06.2020. However, it has no impact on the Kalman filter, which produces stable outputs. Both East and Up components (top row, middle and right panels) forward filter estimates show a strong linear extrapolated trend past 06.2019 until 12.2019.

Velocities (the bottom row) that are taken from the DinSAR observations (dark blue dots in the middle and right panels) show very noisy output. It is interesting to mention, that the fast re-convergence of the Kalman filter fits to the GNSS results, once the GNSS data are available (data gap 06.2019 – 12.2019). The Kalman algorithm derived a good displacements alignment with the epoch solution, except for the last height estimated for 12.2020 (top row, right panel), which shows -0.35 m instead of -0.40 m. Backward Kalman filter as a smoothing solution aligns very well with the GNSS observations in all three components (top row, left, central and right panels), tracing the GNSS permanent solution.

Figure 4 demonstrates the fast changing station PI03, where the Kalman forward model (green solid line) predicts the movements in the North (left panel), East (central panel), and Up (right panel). The overall Kalman forward solution is tracing the GNSS observations, that transpire as a linear extrapolation sections visible in the long GNSS data gaps (06.2019 – 12.2019; 04.2020 – 06.2020). However, it is interesting to observe the quicker return to the tracing data trend in the case of the East component (middle panel), in 10.2019 – two months before the GNSS data reappear in the solution.

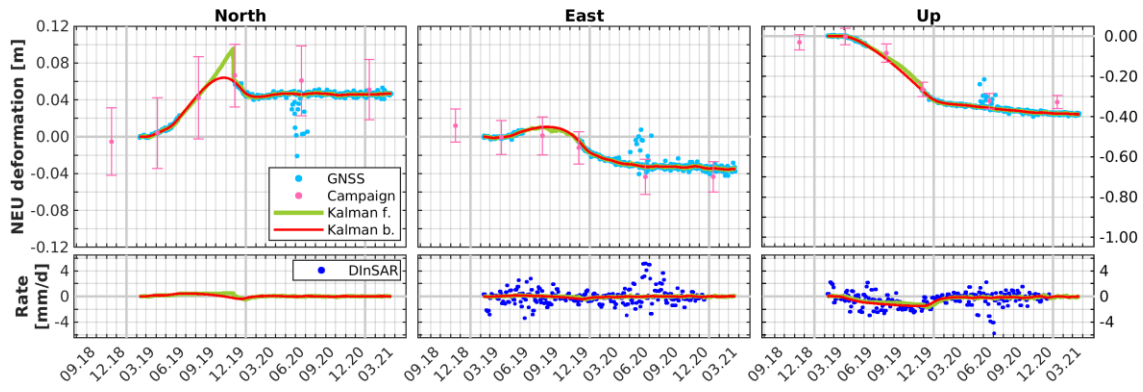


Figure 3. The displacement values (top row) and rates (bottom row) of the PI16 station are determined in the North (left panels), East (middle panels), and Up (right panels) directions. The charts present results of the GNSS permanent data (light blue dots), campaign GNSS measurements (pink dots with error bars), DinSAR data (dark blue dots), forward Kalman filter (green lines), and backward Kalman filter results (red lines).

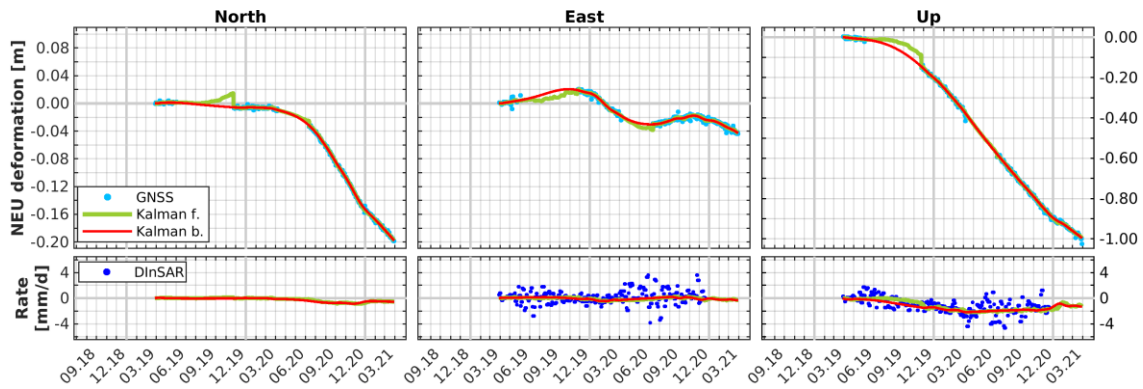


Figure 4. The displacement values (top) and rates (bottom) of the PI03 station are determined in the North (left panels), East (middle panels), and Up (right panels) directions. The legend is the same as in Figure 3

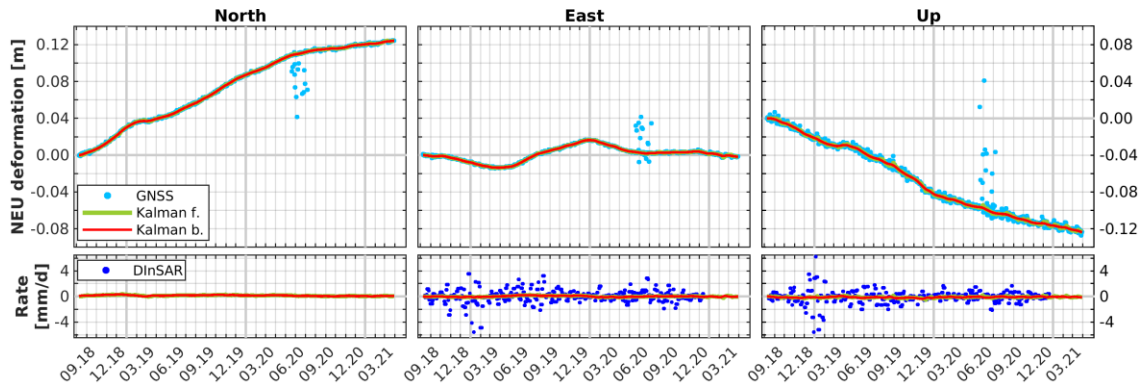


Figure 5. The displacement values (top) and rates (bottom) of the RES1 station are determined in the North (left panels), East (middle panels), and Up (right panels) directions. The legend is the same as in Figure 3

At the same time, the velocity estimated from the DinSAR data is much less noisy than the rest of the time series (bottom row, middle panel). It also has to be noted, that the velocities for the vertical component (bottom row, right panel), show significant negative values from DinSAR with noise low enough to make the trend estimation viable (up to  $2 \frac{mm}{day}$ ). The smoothed solution (backward Kalman filter – the red line), shows no significant jumps or breaks tracing the GNSS estimates very closely.

Figure 5 presents the Kalman filter estimates from DinSAR and GNSS for the RES1 station that is away from the major deformation zone and almost all GNSS data

are available. It is clear that the Kalman filters, both forward and backward, are tracing the GNSS observations curve, while the DinSAR observations for this particular point do not bring any added value. Moreover, evaluating the bottom panels of Figure 5, it is clear to see, that the breaks in 2018 and 2019 brought a lot of noisy data that were difficult to process. Surprisingly, the Up component (right panel), demonstrates sections of different movement velocities aligned well with East component inflection points (03.2019 and 12.2019). The overall quality of the Kalman retrieval at the RES1 station could be taken as a reference for other sites.

Table.2 The North, East, and Up residuals for low-cost permanent stations in the vicinity of campaign points

ID	Dist. to camp. pt. [m]	Max. Up displ. [mm]	Date	North		East		Up	
				Kal. for. [mm]	Kal. back. [mm]	Kal. for. [mm]	Kal. back. [mm]	Kal. for. [mm]	Kal. back. [mm]
PI04	80	-201	04.19	-1	0	3	0	0	0
			08.19	-39	-38	12	15	84	85
			11.19	37	36	-2	-3	24	23
			06.20	2	2	34	34	75	75
			01.21	-34	-34	-20	-20	91	91
PI05	47	-270	04.19	-2	0	0	0	1	0
			08.19	12	19	-12	-12	6	-15
			11.19	4	0	-37	-38	26	20
			06.20	11	12	-5	0	14	7
			01.21	13	23	13	13	-18	-18
PI16	62	-388	04.19	0	0	0	0	1	0
			08.19	3	4	9	9	-22	-31
			11.19	-5	-7	8	7	-7	-8
			06.20	-15	-15	11	11	-33	-34
			01.21	-5	-5	9	9	-56	-56
Overall RMS				18	19	16	17	42	44

### B. Intersecting results

The results presented in the previous sections demonstrate the capabilities of the application of the Kalman filtering in the integration concept for deformation monitoring. The subsequent analysis is based on the residual values for the GNSS permanent sites located in the vicinity of campaign points. The choice of the residual analysis against statistical evaluation is dictated by the small number of low-cost stations (PI04, PI02, PI05, and PI16), and the only 5 overlapping dates between the permanent and campaign points installation. Due to an insufficient number of samples (Chai et al., 2014), the calculation of any statistic based on five values was not robust. However, based on the calculated sets of differences in NEU directions the overall RMS errors were estimated (Table 2).

In Table 2, the discrepancies between the values for the campaign points and low-cost observations do not exceed 0.04 m for the North displacements (columns 5 and 6), however, the uncertainty of the campaign points is also 0.04 m. The overall RMS of the North component for the calculated residuals is 0.018 m and 0.019 m for the Kalman forward and backward approaches, respectively. In the East direction (columns

7 and 8), the discrepancies between the campaign points and the low-cost observations do not exceed 0.09 m, however, the uncertainty of the campaign points is 0.02 m. The RMS Kalman forward and backward filters are equal to 0.016 m and 0.017 m, respectively. There is no visible pattern in the magnitude of the residuals related to the distance to the campaign point (column 2).

The total displacement in the Up direction (column 3) is substantial and reaches -0.388 m (point PI16). The discrepancies between the campaign points and the low-cost observations do not exceed 0.16 m, however, the uncertainty of the campaign points is 0.03 m. The RMS for the Kalman forward and backward approaches are 0.042 m and 0.044 m, respectively. There is no visible pattern related to the maximum displacement (column 3) and the magnitude of residuals, however, the most significant values correspond to the longest distance between these points (column 2). For the PI04 station, the distance to the closest campaign point is 80 m and the three largest residual values are 0.091, 0.084, and 0.075 m for Kalman forward, and 0.091, 0.085, and 0.075 m for Kalman backward.

It is also worth to observe that the Kalman filters provide the solution across all reference epochs regardless of the GNSS missing data (see Figures 3-5).

The provided methodology is able to ingest the noisy GNSS NEU coordinates with significant gaps and the troposphere or unwrapping errors in the DInSAR data. The observation uncertainties are rigorously determined from the parameter estimation of the GNSS data, while for the DInSAR results the errors are calculated based on coherence coefficient values.

To obtain the most reliable Kalman filter results, the optimum noise level resolve of the system was essential (eq. 6). In our study, nine acceleration parameters were analysed with respect to the campaign measurements.

### V. CONCLUSIONS

In the presented study, we introduced an original methodology for integrating DInSAR and GNSS data using the Kalman filter approach. This study concerns the "Rydułtowy" mine, located in the south-western part of Upper Silesia in Poland, where rapid ground deformations are observed. The cross-reference of the data sets is presented for stations PI16, PI03, and RES1. The nearest GNSS campaign sites were used to validate the results of the proposed integration for the permanent stations PI02, PI04, PI05, and PI16.

The lowest RMS error for the Kalman filter was obtained for the acceleration level of  $0.05 \frac{mm}{day^2}$ .

Furthermore, detection and elimination of any potential outliers in the past, using the forward Kalman filter, is not possible. In order to get better integration results, backward Kalman filter was also applied. In comparison to the campaign GNSS results, the overall RMS errors reached 18, 16, 42 mm for Kalman forward and 19, 17, 44 mm for Kalman backward in North, East, Up directions, respectively. The fusion processing may be easily extended by other data sources like, e.g., Permanent Scatterer InSAR, leveling, or LiDAR, to create a framework for multi-sensor ground deformation monitoring system.

## VI. ACKNOWLEDGEMENTS

This study was started in 2016 in the frames of the EPOS-PL project POIR.04.02.00-14-A003/16, and continued in 2021-2022 within the EPOS-PL+ project POIR.04.02.00-00-C005/19-00, that were funded by the Operational Program Smart Growth 2014–2020, Priority IV: Increasing research potential, Action 4.2: Development of modern research infrastructure in the science sector.

The presented investigation was accomplished as part of a scientific internship at Delft University of Technology (TU Delft), Netherlands, conducted within the GATHERS project, funded by the European Union's Horizon 2020 research and innovation programme under grant agreement No 857612. The authors would like to express their gratitude to Freek van Leijen and Hans van der Marel from TU Delft for the valuable guidance and discussions.

## References

- Altamimi, Z.: EUREF Technical Note 1: Relationship and Transformation between the International and the European Terrestrial Reference Systems. EUREF Technical Note 1: Version June 28, 2018 p. 11 (2018)
- Altamimi, Z., Rebischung, P., Métivier, L., Collilieux, X.: ITRF2014: A new release of the International Terrestrial Reference Frame modeling nonlinear station motions. *Journal of Geophysical Research: Solid Earth* (2016)
- Bian, H.F., Zhang, S.B., Zhang, Q.Z., Zheng, N.S.: Monitoring large-area mining subsidence by GNSS based on IGS stations. *Transactions of Nonferrous Metals Society of China (English Edition)* 24(2), 514–519 (2014).
- Bozso, I., Banyai, L., Hooper, A., Szucs, E., Wesztergom, V.: Integration of Sentinel-1 Interferometry and GNSS Networks for Derivation of 3-D Surface Changes. *IEEE Geoscience and Remote Sensing Letters* (2021).
- Branzanti, M., Colosimo, G., Crespi, M., Mazzoni, A.: GPS near-real-time coseismic displacements for the great tohoku-oki earthquake. *IEEE Geoscience and Remote Sensing Letters* 10(2), 372–376 (2013).
- Chai, T., Draxler, R.R.: Root mean square error (RMSE) or mean absolute error (MAE)? -Arguments against avoiding RMSE in the literature. *Geoscientific Model Development* 7(3), 1247–1250 (2014).
- Chen, C.W., Zebker, H.A.: Network approaches to two-dimensional phase unwrapping: Intractability and two new algorithms. *Journal of the Optical Society of America* (2000)
- Cina, A., Piras, M.: Performance of low-cost GNSS receiver for landslides monitoring: test and results. *Geomatics, Natural Hazards and Risk* 6(5-7), 497–514 (2015).
- Dach, R., Lutz, S., Walser, P., Fridez, P.: Bernese GNSS Software version 5.2. User manual. Astronomical Institute, University of Bern (2015).
- Dach, R., Schaer, S., Arnold, D., Prange, L., Sidorov, D., Stebler, P., Villiger, A., Jäggi, A.: CODE final product series for the IGS. Astronomical Institute, University of Bern (2018).
- Fattahi, H., Amelung, F.: InSAR uncertainty due to orbital errors. *Geophysical Journal International* (2014).
- Goldstein, R.M., Werner, C.L.: Radar interferogram filtering for geophysical applications. *Geophysical Research Letters* 25(21), 4035–4038 (1998).
- Hadaś, T.: GNSS-Warp Software for Real-Time Precise Point Positioning. *Artificial Satellites* 50(2), 59–76 (2015).
- Hamza, V., Stopar, B., Sterle, O.: Testing the performance of multi-frequency low-cost gnss receivers and antennas. *Sensors* 21(6), 1–16 (2021).
- Hanssen, R.: Radar interferometry: data interpretation and error analysis. Springer Science & Business Media (2001).
- Hu, J., Li, Z.W., Ding, X.L., Zhu, J.J., Zhang, L., Sun, Q.: Resolving three-dimensional surface displacements from InSAR measurements: A review. *Earth-Science Reviews* (2014).
- Jarvis, A., Reuter, H.I., Nelson, A., Guevara, E.: Hole-filled seamless SRTM data V4, International Centre for Tropical Agriculture (CIAT). Tech. rep. (2008)
- Kalman, R.E.: A New Approach to Linear Filtering and Prediction Problems. *Journal of Basic Engineering* (1960).
- Liu, N., Dai, W., Santerre, R., Hu, J., Shi, Q., Yang, C.: High Spatio-Temporal Resolution Deformation Time Series with the Fusion of InSAR and GNSS Data Using Spatio-Temporal Random Effect Model. *IEEE Transactions on Geoscience and Remote Sensing* 57(1), 364–680 (2019).
- Mutke, G., Kotyrba, A., Lurka, A., Olszewska, D., Dykowski, P., Borkowski, A., Araszkiwicz, A., Barański, A.: Upper Silesian Geophysical Observation System A unit of the EPOS project. *Journal of Sustainable Mining* 18(4), 198–207 (2019).
- Osmanoğlu, B., Sunar, F., Wdowinski, S., Cabral-Cano, E.: Time series analysis of InSAR data: Methods and trends. *ISPRS Journal of Photogrammetry and Remote Sensing* (2016).
- Tao, T., Liu, J., Qu, X., Gao, F.: Real-time monitoring rapid ground subsidence using GNSS and Vondrak filter. *Acta Geophysica* 67(1), 133–140 (2018).
- Teunissen, P.: Dynamic data processing: Recursive least-squares (2009)
- Tondaś, D., Kapłon, J., Rohm, W.: Ultra-fast near real-time estimation of troposphere parameters and coordinates from GPS data. *Measurement* p. 107849 (2020).
- Verhagen, S., Teunissen, P.J.: Least-Squares Estimation and Kalman Filtering. Springer Handbooks pp. 639–660 (2017).

## Multi-epoch deformation analysis with geodetic datum invariance

Hiddo Velsink

HU University of Applied Sciences Utrecht, Padualaan 99, 3584 CH Utrecht, Netherlands, ([hiddo.velsink@hu.nl](mailto:hiddo.velsink@hu.nl))

**Key words:** *geodetic deformation analysis; multiple epochs; geodetic datum; deformation hypothesis testing; least squares; rank deficient covariance matrix; minimal deformation constraints*

### ABSTRACT

Multiple epochs of geodetic deformation observations in 1D, 2D or 3D with their covariance matrices can be adjusted using the least-squares method and tested for deformation hypotheses, using the author's hypothesis constrained multi-epoch analysis method. The method estimates deformations of a subfield relative to points in one or more other subfields. Therefore, the method is invariant for the choice of geodetic datum and does not require stable points. Here it is shown how the geodetic datum is defined at two levels. At the first level position, orientation, size and form of the point field are fixed to enable the use of coordinates (or heights). At the second level the position, orientation, size and form within any epoch interval are fixed, if they cannot be fixed from the observations in the adjustment model. This enables the comparison of epochs that have no predefined points that are stable in the epoch intervals. The stochastic test of the comparison is invariant for the choice of geodetic datum at these two levels. A procedure is described how to find the best deformation hypothesis, taking account of all available statistical information. It is shown that the proposed method is a powerful tool to find the best deformation hypothesis based on geodetic observations and their full stochastic information. It is thus usable for a broad scope of applications of geodetic deformation analysis.

### I. INTRODUCTION

Geodetic deformation analysis considers the problem of identification of deformations in a geodetic point field (Casparly 2000; Heunecke *et al.*, 2013; Velsink 2018b). Usually, several subfields can be distinguished in a point field, for example the subfield of reference points, and the subfield of object points. This last subfield is often not a single field, but can be divided in several subfields, where each subfield can be subject to different forces, resulting in different deformations. In this paper a geodetic point field will be called a geodetic network alternatively.

As an example a bridge over a river is taken. Usually, the movement of the bridge as a whole, relative to the surroundings is of interest. So, reference points are chosen on constructions and houses whose movements are representative of the surroundings. The bridge itself can consist of two abutments and the bridge deck. The movements of these three parts, relative to each other, and the movements of several points on just one part, relative to each other, are of interest. Therefore the object points of the bridge are separated into three subfields. This results in four subfields to be considered in the geodetic deformation analysis of the bridge.

A new method for geodetic deformation analysis of a point field by means of a time series of 1D, 2D or 3D coordinates, or of geodetic measurements, and their covariance matrices, was proposed by Velsink (2016; 2017). The method is called the "hypothesis

constrained multi-epoch analysis method" (Niemeier and Velsink, 2019).

The problem considered in this paper is the geodetic datum invariance at two levels of the hypothesis constrained multi-epoch analysis method. The geodetic datum is here considered to be the coordinate reference system used, including the elements that cannot (or not accurately enough) be derived from the measurements, usually the elements that define the position of the origin, the orientation of the coordinate axes, and the scale. In 3D they comprise seven elements. It is called here the *first level* of the geodetic datum.

In some applications the rates of change in time of these seven elements have to be incorporated into the geodetic datum as well, for example, if a terrestrial reference frame is defined (Altamimi *et al.*, 2002). Likewise, the hypothesis constrained multi-epoch analysis may require an extension of the geodetic datum, which is called here the *second level* of the geodetic datum. In Section VI it will be described, what this second level is, and it will be shown that the hypothesis constrained multi-epoch analysis uses test statistics, which are invariant for the choice of this second level of the geodetic datum.

First, this paper treats in Sections II and III the characteristics of the hypothesis constrained multi-epoch analysis. Subsequently the procedure of deformation tests is shown in Section IV. Then the first and second level of the geodetic datum are treated in

more detail and it is shown that the stochastic tests, used to perform the analysis, are invariant for the second level (Sections V and VI). Finally, an application example is given in Section VII, which shows, how to perform a hypothesis constrained multi-epoch analysis.

## II. HYPOTHESIS CONSTRAINED MULTI-EPOCH ANALYSIS

Niemeier and Velsink (2019) give a concise description of the hypothesis constrained multi-epoch analysis for the case that coordinates and their covariance matrices (regular or singular) are available for  $n$  epochs, where  $n$  can be 2 or more. The model used is called the *coordinates model*, see Figure 1, and is elaborated upon by Velsink (2016). A linearized Gauss-Markov model is used with observations  $\ell$ , residuals  $\mathbf{v}$ , parameters  $\mathbf{p}$  and a coefficient matrix  $\mathbf{A}$  (bold letters indicate matrices or vectors) (Eq. 1):

$$\ell + \mathbf{v} = \mathbf{A}\mathbf{p}. \quad (1)$$

In Figure 1 it is shown that the coordinates model consists of two phases.

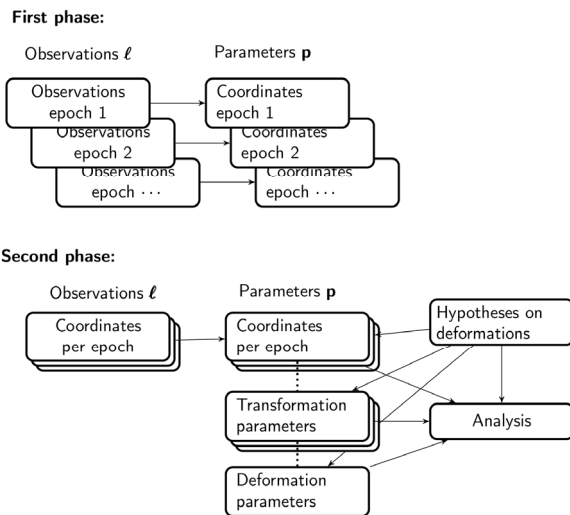


Figure 1. Coordinates model (Velsink 2018b, p. 26).

In the first phase geodetic observations are adjusted for each epoch separately. The results are coordinates for each epoch, including their covariance matrix, which is often singular, because of the geodetic datum used. The second phase takes all coordinates of all epochs, and their covariance matrices, together. Hypotheses on deformations are formulated and tested (this will be treated in Section III A). Figure 1 shows what is contained in the observation vector  $\ell$  and what in the parameter vector  $\mathbf{p}$  in both phases.

If, however, the *measurements* of all  $n$  epochs are available, including their covariance matrices (regular or singular), use can be made of the *measurements model* (Velsink 2017), see Figure 2. The figure shows likewise as Figure 1, what is contained in  $\ell$  and  $\mathbf{p}$ .

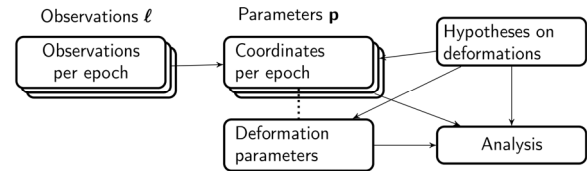


Figure 2. Measurements model (Velsink 2018b, p. 25).

### A. Constraints link epochs

In both models the vector of parameters  $\mathbf{p}$  contains for each epoch the coordinates to be estimated. Therefore, every point has different coordinates for each epoch in which it occurs. If we put all epochs in order of time, an epoch interval for a point is defined here as the time between an epoch where a point appears, and the next epoch, where it appears. For each point, and for each epoch interval, one, two or three *constraints* (for 1D, 2D, and 3D respectively) are formulated, which state, how the point is moving in that epoch interval. If a point does not occur in one or more epochs, one or more of its epoch intervals are longer than for other points.

Usually, the null hypothesis is that points don't move, in which case each constraint is that a coordinate ( $x$ ,  $y$  or  $z$ ) in a certain epoch is equal to the equivalent coordinate of the same point in the next epoch.

### B. Constraints define deformation hypotheses

Both Figure 1 and Figure 2 mention hypotheses on the deformations, which should be incorporated into the Gauss-Markov model. This is done by the constraints, introduced above. If a point is assumed to be moving in a certain epoch interval, for example linearly with a change rate of  $\nabla$ , the  $\nabla$  is added to the parameter vector. How a constraint can be added to the Gauss-Markov model is treated in Section II D.  $\nabla$  may be a vector in itself, for example, if the assumed deformation of one or more points in a certain epoch interval (or even more epoch intervals) is described by a function with more than one parameter.

### C. Geodetic datum – no stable points required

Figure 1 shows that the parameter vector in the coordinates model contains transformation parameters as well. Each epoch interval (from epoch  $i$  to epoch  $i+1$ , where  $i = 1, 2, \dots, n-1$ ) involves a transformation. It takes care of the differences in geodetic datum between the coordinates in the *observation vector* that relate to epoch  $i$  and those that relate to epoch  $i+1$ . This implies that a geodetic datum has to be fixed for one of the epochs, but not for the others. This, in turn, implies that the analysis method does not require any stable points (*i.e.* points that do not move in one or more epoch intervals).

The coordinates in the *parameter vector* are ordered by epoch as well, but they are all defined relative to the same geodetic datum.

The measurements model does not require stable points either. This is, because in this model a geodetic

datum is needed for the parameter vector, but not for the observations in the observation vector, unless coordinates are used as observations. In the latter case transformation parameters have to be added to the parameter vector, which leads to the same situation as in the coordinates model.

#### D. Gauss-Markov model with hard constraints

Usually, the constraints are considered to be hard constraints, *i.e.* they can be added to the observation vector as observations with a standard deviation of zero. This results in a singular covariance matrix of the observations. Most handbooks on adjustment theory only treat the case that the covariance matrix of the Gauss-Markov model is regular (invertible), see *e.g.* Koch (2013, Section 3.2.1). Maybe, this is the reason that some publications state that only an approximate solution is possible, if observations have a standard deviation of zero (Lehmann and Neitzel, 2013; Shi *et al.*, 2017). This, however, is not true. An exact, rigorous solution has been published already more than fifty years ago (Rao and Mitra, 1971, pp. 147-150).

Even if that solution is not used, it is well-known, how a Gauss-Markov model with hard constraints can be solved rigorously by using Lagrange multipliers (Koch 2013, Section 3.2.7), or by reducing the amount of parameters (Wolf 1982; Velsink 2015, p. 401).

Whether the hard constraints are justified, can be tested with a generalized likelihood ratio test (Velsink 2018a). This test can be used to test any deformation hypothesis, which is formulated by means of constraints in the above described coordinates model or measurements model.

### III. ANALYSIS PROCESS

Both the coordinates model of Figure 1 and the measurements model of Figure 2 can be used to perform a geodetic deformation analysis. Both models yield least-squares estimates of the coordinates of all points for all epochs, and the covariance matrix of all these coordinates.

#### A. Testing deformation patterns

However, the estimated coordinates are *not* essential for the deformation analysis! It is the testing of the null hypothesis against alternative hypotheses, which is the core of the analysis. Each alternative hypothesis describes one possible deformation pattern of all points through all epochs. It may be, for example, that a subfield is subject to deformation only during the last few epochs, and that the points of another subfield are moving relative to the other subfields during the first few epochs. The deformations of both subfields constitute one intricate deformation pattern, described in the Gauss-Markov model by several constraints. This deformation pattern is considered one alternative hypothesis and is tested by a generalized likelihood ratio test. To do this, the model of the alternative

hypothesis is written as an extension of Equation 1 (Eq. 2):

$$\ell + v = \mathbf{A}\mathbf{p} + \mathbf{C}\mathbf{V} \quad (2)$$

vector  $\mathbf{V}$  contains the deformation parameters of Figure 1 or 2. Matrix  $\mathbf{C}$  is the corresponding coefficient matrix. The alternative hypothesis is tested against the null hypothesis by using the test statistic (Velsink 2018a) (Eq. 3):

$$F_q = \frac{\mathbf{r}^t \mathbf{C} (\mathbf{C}^t \mathbf{Q}_r \mathbf{C})^{-1} \mathbf{C}^t \mathbf{r}}{q \sigma_0^2}, \quad (3)$$

with  $\mathbf{r}$  the vector of reciprocal residuals, and  $\mathbf{Q}_r$  its cofactor matrix (Velsink, 2018a), which both can be computed during the adjustment of the null hypothesis.  $t$  indicates the transposed of a vector or matrix, and  $q$  is an integer that indicates the degrees of freedom of the test and equals the number of parameters in  $\mathbf{V}$ .  $\sigma_0^2$  is the a priori variance of unit weight, which follows from splitting the covariance matrix of the observations in this factor and the cofactor matrix.

#### B. Hypothesis selection problem

Infinitely many deformation patterns can be formulated for a point field. Many of them can be plausible, considering the physical conditions of the houses, constructions and soil, where the points are located, and the forces that act upon them (*e.g.* earthquakes, landslides, construction works and weather conditions). The approach of the hypothesis constrained multi-epoch analysis method is to test many alternative hypotheses and to find the best one among them. Because different alternative hypotheses can have different degrees of freedom in the generalized likelihood ratio test, the definition of “best” is problematic, and the resulting hypothesis selection problem does not have a unique answer (Velsink 2018b, p. 43). However, a criterion has to be chosen, for example the *test ratio* or the *Akaike information criterion* (Velsink 2018b, p. 43), and applied.

#### C. Adaptation of null hypothesis

When the best alternative hypothesis, according to some criterion of “best”, has been decided upon, this alternative hypothesis becomes the new null hypothesis. The equation of the new null hypothesis is arrived at by writing Equation 2 as (Eq. 4):

$$\ell + v = (\mathbf{A} \quad \mathbf{C}) \begin{pmatrix} \mathbf{p} \\ \mathbf{V} \end{pmatrix} \quad (4)$$

The matrix  $(\mathbf{A} \quad \mathbf{C})$  is the new coefficient matrix and the vector  $\begin{pmatrix} \mathbf{p} \\ \mathbf{V} \end{pmatrix}$  is the new parameter vector.

Testing the adjustment of the adapted null hypothesis should result in an accepted overall model test, which confirms that the alternative hypothesis



yields a good explanation of all measurements in all epochs (or of the coordinates that are derived from those measurements in the separate epoch adjustments).

#### D. Least-squares solution by iteration

Because the used models are linearized ones, both observations  $\ell$  and parameters  $\mathbf{p}$  and  $\mathbf{V}$  are incremental values relative to approximate values. The approximate values have to comply with the nonlinear equivalent of Equation 4. To get the least-squares solution of Equation 4 an iteration process is needed. In each iteration step the estimated increments for both observations and parameters have to be corrected slightly to let the new approximate values comply with the nonlinear equivalent of Equation 4.

These corrections can be computed by least-squares, using the model of condition equations, which is dual to the Gauss-Markov model and has been published first by Gauss (1828). See Velsink (2018a) for this model and its least-squares solution in matrix equations. The adjusted observations of the previous step are the vector of constant terms in this model and the estimated parameters are the observations. After linearization this yields (Eq. 5):

$$\mathbf{t} = (\mathbf{A} \quad \mathbf{C}) \begin{pmatrix} \mathbf{p}_0 \\ \mathbf{V}_0 \end{pmatrix} - \ell_0; E\{\mathbf{t}\} = \mathbf{0}, \quad (5)$$

where  $\ell_0$ ,  $\mathbf{p}_0$  and  $\mathbf{V}_0$  are the approximate values of  $\ell$ ,  $\mathbf{p}$  and  $\mathbf{V}$ . The vector  $\mathbf{t}$  contains the misclosures (computed with the non-linear model) with  $E\{\mathbf{t}\}$  their mathematical expectations. As covariance matrix of the "observations"  $\mathbf{p}_0$  and  $\mathbf{V}_0$  the unit matrix is used. Thus, the values of  $\mathbf{p}_0$  and  $\mathbf{V}_0$  are corrected in this "adjustment within an adjustment" and the corrected values comply with the main nonlinear model.

The constantly improved approximated values of both observations and parameters will usually converge to the least-squares solution of the nonlinear model, that is, to the adjusted observations and the estimated parameters respectively. If not, the initially chosen approximate values are not adequate, or the observations contain gross errors.

#### E. Estimated deformations

The adjustment of the adapted null hypothesis yields least-squares estimates of the deformation parameters  $\mathbf{V}$ . Moreover, the constraints that describe the deformations for each point in each epoch, can be included in the vector of observations as observations with standard deviation zero. In that case, the adjusted observations are the least-squares estimates of the deformations of each  $x$ ,  $y$  or  $z$  coordinate of each point in each epoch.

It is important to note that the estimated deformations of all points are not relative to the first

level of the geodetic datum, but relative to each other, more precisely to points that are held fixed (no deformation) in the model! It may be that such points do not exist. This case will be treated in Section VI A.

#### F. Minimal Detectable Deformations

The hypothesis constrained multi-epoch analysis can be done by the coordinates model or the measurements model. Both models can be adjusted to get a least-squares solution by using a least-squares algorithm that can handle singular covariance matrices, or by using another method to handle hard constraints, see Section II D. Equation 3 can be used to test for deformations. But also formulas are available to compute Minimal Detectable Deformations (MDD) (Velsink 2016; 2017). An MDD of a certain coordinate difference between the coordinates of the same point in an epoch interval gives the deformation in, for example, millimeters that can be detected with a certain probability (chosen beforehand) by a test of a certain alternative hypothesis, described by a matrix  $\mathbf{C}$ .

The MDD's are a powerful tool to describe the ability of a geodetic network to detect deformations (sensitivity analysis). It is an important property of the MDD's that they can be computed before any measurement has been done. Thus, they can be used to formulate *requirements* for deformation networks, and consequently *standards* can be formulated with them.

### IV. PROCEDURE OF DEFORMATION TESTS

To arrive at the treatment of the invariance for changes in the geodetic datum of the hypothesis constrained multi-epoch analysis, first the *procedure* of deformation tests is reviewed.

First, each epoch is adjusted and tested in itself. If the reliability of the geodetic network of an epoch is good enough, and if testing the epoch does not lead to rejection, it is assumed that the epoch model does not contain errors of any significance.

Subsequently the model of all epochs is tested against the most general alternative hypothesis, which is done by the overall model test (Velsink 2018a, p. 6). If this test rejects the null hypothesis, and all epoch tests did not lead to rejection, it may be that still some errors are present in some epoch or epochs, because the combined adjustment of all epochs is more sensitive to errors in individual epochs than the adjustment of just one epoch.

If it is concluded that no errors in any individual epoch are present any more, but the test of all epochs leads to rejection, the conclusion is that deformations are present.

It may be that physical conditions of the earth and of buildings and structures on it are indicative of possible deformations. But even then, other deformations may be present as well. Therefore, all deformation constraints are tested one by one (that is, for each coordinate difference separately) or one point by one

point or both. To get an impression of the number of deformation constraints: with  $n$  epochs,  $d$  dimensions ( $d$  is 1, 2 or 3), and  $k$  points in each epoch (although usually the numbers of points in each epoch differ), there are  $(n - 1)$  epoch intervals and, thus,  $(n - 1) \times d \times k$  deformation constraints. The test of one point by one point means that the  $d$  coordinates of a point in an epoch interval are tested for the alternative hypothesis that this point has moved in that epoch interval, and that no other point has moved in that or any other epoch interval.

The test is performed with the test quantity of Equation 3 and is a  $d$ -dimensional test. The test is repeated for all points in all epoch intervals. Let us call these tests one point by one point the *conventional point tests*. Because the dimension of all conventional point tests is  $d$ , the  $F_q$ 's of all these tests can be directly compared, and give an impression, where deformations might be present. It is not possible to deduce directly from these conventional point tests which points in which epoch intervals are subject to a deformation, let alone determine the character and sizes of these deformations. To accomplish this, more complex alternative hypotheses have to be formulated and tested. This is the hypothesis selection problem, treated earlier in Section III B. It will not be treated fully in this paper. It is sufficient here to conclude that the best alternative hypothesis, and thus the best deformation pattern, is selected.

## V. FIRST LEVEL GEODETIC DATUM

In the introduction (Section I) the first level of geodetic datum invariance has been defined. If a deformation hypothesis is defined by constraints on the parameters of the coordinates model or the measurements model, the hypothesis can be tested with Equation 3. This test is *invariant* for the first level of the geodetic datum (Velsink 2016; 2018a).

### A. Deformation constraints link epochs

As mentioned before, the first level can be defined by fixing the coordinates of some points *in only one epoch*. Let us call these points the datum points and let them be fixed in the *first* epoch. The coordinates of the datum points in the other epochs (which are not part of the datum) are linked to those of the first epoch by deformation constraints.

Usually, the null hypothesis assumes the absence of any deformation. This means that the coordinates of the datum points of the second to  $n$ -th epoch are forced to be equal to the coordinates in the previous epoch by constraints in the coordinates model or measurements model.

### B. Example: just one point moved

Let us suppose that the overall model test rejects the null hypothesis, and that the solution of the model

selection problem is the alternative hypothesis that a point  $S$  is subject to deformation during just one epoch interval, and no other deformation is present. As explained in Section III A, the alternative hypothesis is defined by a matrix  $\mathbf{C}$ . In this case, matrix  $\mathbf{C}$  has  $d$  columns ( $d$  is the dimension: 1, 2 or 3), which contain zeros except for a 1 in the  $d$  rows that correspond to the  $d$  observations that represent the deformation constraints of point  $S$  in that epoch interval.

Let the  $k$ -th observation be the constraint that the  $x$  coordinate of point  $S$  in epoch  $i - 1$  is equal to the  $x$  coordinate of point  $S$  in epoch  $i$ . The observation equation reads (Eq. 6):

$$\ell_k + v_{\ell_k} = -x_{S,i-1} + x_{S,i} + \nabla_{S,i-1,i} \quad (6)$$

The “observed” value of  $\ell_k$  is zero. Its standard deviation is zero as well. When Equation 6 is transferred to the matrices of Equation 4, -1 is inserted in  $\mathbf{A}$  in the column that corresponds to the  $x$  coordinate of point  $S$  in epoch  $i - 1$ , and 1 is inserted in the corresponding column of epoch  $i$ . In matrix  $\mathbf{C}$  1 is inserted in the  $k$ -th row in column 1 (column 2 is for the  $y$  coordinates and column 3 for the  $z$  coordinates).

The parameter  $\nabla_{S,i-1,i}$  only appears in the  $k$ -th observation equation and it ensures that the constraint is *disabled*. It is noteworthy that the addition of parameter  $\nabla_{S,i-1,i}$  in the adjustment model has the same effect as giving the constraint an infinitely large standard deviation (or a weight of zero). Because the constraint remains in the adjustment model, an estimated value will be computed, which is the estimated deformation of the coordinate difference in the epoch interval concerned.

This example serves as an illustration of the way a hypothesis is formulated that just one point in one epoch interval is subject to deformation. The next section contains an example that treats the opposite case, where all points are suspected to be influenced by deformation. It is there that the second level of the geodetic datum plays an important role.

## VI. SECOND LEVEL GEODETIC DATUM

### A. Example: All points move

In professional practice the situation occurs regularly that it is not clear, whether there is any deformation, and that the point by point analysis of Section IV gives an unclear picture, where all points seem to be affected by deformation. In this case it is possible to “disable” all deformation constraints, which is done by adding an additional parameter  $\nabla$  to each deformation constraint, as exemplified by Equation 6. This results in  $n$  separate geodetic networks, when there are  $n$  epochs. Because the relation between all these networks is not defined, it will result in a parameter vector in Equation 4, which cannot be solved in a least-squares sense uniquely.

To get a unique solution (or, equivalently to make the parameters estimable) every epoch interval has to have

at least as many “enabled” deformation constraints as needed to get a unique solution. These minimally needed constraints are here called “minimal deformation constraints” (cf. Pope 1971), and define the **second level of the geodetic datum**. We have seen in Section I that the testing quantity of Equation 3 is invariant for a change of the first level of the geodetic datum. In the sequel the invariance of this test quantity for the second level will be considered.

### B. Form and size

Geodetic deformation analysis is about changes of the form of a geodetic point field, which can clearly be seen in the word *de-form-ation*. It is about size as well, because today our instruments are so good that distances can be measured very precisely and changes of size of a geodetic point field can be determined equally precisely. This means that we are interested in form and size describing elements, and in the changes of these elements. Measurements used for deformation analysis should contain information about form, or about form and size, to be of value. It may be that they contain information about position and orientation relative to the earth, but this is of no value for the deformation analysis, as long as the point field contains all points of relevant objects subject to deformation and of reference objects.

Euclidian or geographic coordinates relative to a reference system contain more than form and size information. They contain information about the position of the origin and the orientation of the coordinate axes relative to the point field under consideration. For this reason coordinates are not suited as form or size elements.

Therefore, it is of importance to know, how form and size elements can be defined in 1D, 2D and 3D. First, form elements in 2D are treated. In the two dimensional Euclidian plane the smallest point field with a form is a triangle (three points). Two triangles have the same form (are *conformal*), when corresponding angles are equal. To fix the form of a triangle, two angles of the triangle are sufficient. Baarda (1966) showed that the form can be defined by two length ratio's as well (cf. Velsink 2018b, pp. 27-28). This means that angles and length ratio's are suited to function as form elements.

In three dimensional Euclidian space the smallest point field with a form that is not in a 2D subspace, is a tetrahedron (four points). To fix the form of a tetrahedron five angles, or length ratio's, or a combination of both are needed (Velsink 2018b, pp. 28-29).

In one dimensional Euclidian space (a straight line) angles are not defined, but length ratio's are. The smallest point field with a meaningful length ratio consists of three points (Velsink 2018b, p. 30).

A size element is a distance between two points. If the form of a point field is defined, the size of it is defined if

one distance between two points within the point field is defined.

With the use of these form and size elements, it is possible to consider the invariance of the test quantity of Equation 3 for a change of the second level of the geodetic datum.

### C. Invariance of test quantity

Let us consider  $n$  epochs in the coordinates model or the measurements model. They can be viewed as  $n$  geodetic networks. Let us assume that the measurements of all these networks contain enough information on the form and size of the network. If the networks are linked by minimal deformation constraints, the form and size of each network are solely determined by the adjusted coordinates or measurements of each network, and not by the deformation constraints.

The test quantity of Equation 3 is invariant for a change in the first level of the geodetic datum. Such a change can be performed, in the case of geodetic deformation analysis, by a similarity or congruency (rigid body) transformation, which leaves the form, or the form and size of a point field unchanged. Therefore, the differences (changes) between the form and size elements of the two epochs of an epoch interval, are left unchanged. This means that the test quantity of Equation 3 is **invariant for a change in the second level of the geodetic datum**, if the second level is defined by minimal deformation constraints.

## VII. APPLICATION

To describe an application of the invariance of the second level of the geodetic datum, a fictitious example from professional practice is presented.

Suppose a building is close to ongoing roadworks and it is monitored for deformations by 3D tacheometry measurements. Initially the consecutive epoch measurements fit well together: the overall model test is accepted. It seems that no deformation occurs. But then the addition of the next epoch leads to rejection of the test and likewise the subsequent epoch. However, the one-by-one tests of Section IV do not give a clear picture. Maybe, a deformation of several parts of the building started, and maybe already during several epochs. It is decided that all epochs up to the last four epochs will be left out of the model and the last four will be analyzed. All deformation constraints between the four epochs are disabled by introducing a bias  $\nabla$ , a different one for each epoch interval and each coordinate. This is realized in the software by specifying a suitable matrix  $\mathbf{C}$ , see Equation 2. This makes the parameter vector  $\mathbf{p}$  not solvable. The software allows the user to specify minimal deformation constraints for each epoch interval by choosing which coordinates are to be fixed. This has the advantage that the adjusted deformation constraints (adjusted from zero to nonzero values) are relative to the fixed coordinates. But

additionally the software offers the possibility *not* to choose a second level of the geodetic datum. In this case, the software uses a generalized matrix inverse to compute the parameter vector  $\mathbf{p}$ . A generalized matrix inverse of a matrix  $\mathbf{M}$  is any matrix  $\mathbf{G}$  that fulfils the Equation 7:

$$\mathbf{M} = \mathbf{MGM}. \quad (7)$$

A special type of generalized matrix inverse, which is unique for  $\mathbf{M}$ , is the pseudo-inverse as defined by Boullion and Odell (1971), also called the Moore-Penrose inverse (Ben-Israel and Greville, 2003). It minimizes the Euclidian norm of  $\mathbf{p}$ , and thus the adjusted deformation constraints, although this has, in view of the mentioned invariance, no significance: any choice of the minimal deformation constraints will give the same test results. Therefore, the software does not use the pseudo-inverse, but the generalized inverse that is calculated the fastest. In MATLAB this can be done by using the matrix left divide (“\”) function to solve the system of normal equations.

The next step is to look at the adjusted deformation constraints, and to identify *deformation patterns* in one or more subfields, during one or more epoch intervals. The result is a collection of possible deformation patterns that might explain the adjusted deformation constraints. Each deformation pattern can consist of several subfields, each of which shows different deformation behavior during different epoch intervals. Each deformation pattern is translated into an alternative hypothesis by specifying a new matrix  $\mathbf{C}$ , and subsequently, after having chosen a level of significance, tested with test statistic (3), which is assumed to have a chi-squared-distribution. This manual process is supported by the software, which has the option to systematically construct many combinations of simple deformation patterns and test them. Research should give more deformation patterns that occur often in professional practice.

Choosing the best alternative hypothesis means solving the hypothesis selection problem as stated in Section III B.

Subsequently all epochs are again added to the model, and the process just described, is repeated for all epochs. Let us assume that it does not lead to noticeably different results, indicating that no deformation was present before the last four epochs.

After determining the best alternative hypothesis, the null hypothesis is adapted (Section III C) to account for the found deformation pattern, and final results are computed. The principal of the roadworks is informed about the deformations.

## VIII. CONCLUSIONS

In this paper the hypothesis constrained multi-epoch analysis method has been explained, and a new result on its use has been derived. It has been shown, how

many epochs of geodetic deformation measurements are included in one adjustment model, for which two options are available, the coordinates model and the measurements model. Deformation hypotheses, or the absence of deformation is introduced in these models by formulating constraints between epochs. The geodetic datum can, thus, be limited to some coordinates in just one epoch. This has the advantage that no stable points are needed to define the geodetic datum.

It has been shown how the least-squares solution of the models is computed with an iterative process of adjustment, which is tested subsequently. If the null hypothesis is rejected, several alternative hypotheses are formulated, which are hypotheses on the deformation pattern.

Each deformation hypothesis can be tested by a test statistic that has a chi-squared distribution and which is invariant for the choice of geodetic datum. One of the deformation hypotheses has to be chosen as the best one. This is the hypothesis selection problem. Subsequently least-squares estimates of the deformations can be computed. It is shown as well, how minimal detectable deformations are determined.

Then a second level of the geodetic datum is defined, which enables the search for possible deformation patterns, when no clear indication is available, what the deformation pattern looks like. The results of the previously mentioned tests are shown to be invariant for this second level.

A fictitious application has been elaborated upon to make it clear what procedure can be used, when the hypothesis constrained multi-epoch analysis method is used.

## References

- Altamimi, Z., Sillard, P., and Boucher, C. (2002). ITRF2000: A new release of the International Terrestrial Reference Frame for earth science applications. *Journal of Geophysical Research: Solid Earth*, 107(B10), ETG-2.
- Baarda, W. (1966). Puntsbepalingsystemen in het platte vlak. Berekening met complexe getallen. Eerste en tweede deel. Veelhoek- en driehoekfiguraties. Heruitgave. Computing Centre of the Delft Geodetic Institute, Delft, stencilled edition.
- Ben-Israel, A., and Greville, T. N. (2003). Generalized inverses: theory and applications. *Springer Science & Business Media*.
- Boullion, T. L., and Odell, P. L. (1971). Generalized inverse matrices. Wiley-interscience.
- Caspary, W. (2000). Concepts of network and deformation analysis, Monograph 11. School of Surveying, The University of New South Wales. Australia, Tech. rep.
- Gauss, C. F. (1828). Supplementum theoriae combinationis observationum erroribus minimis obnoxiae. Henricus Dieterich, Göttingen.
- Heunecke, O., Kuhlmann, H., Welsch, W., Eichhorn, A., and Neuner, H. (2013). Auswertung geodätischer Überwachungsmessungen. Wichmann, second edition.

- Koch, K.-R. (2013). *Parameter Estimation and Hypothesis Testing in Linear Models*. Springer, second edition.
- Lehmann, R., and Neitzel, F. (2013). Testing the compatibility of constraints for parameters of a geodetic adjustment model. *Journal of Geodesy*, 87(6), pp. 555-566.
- Niemeier, W. and Velsink, H. (2019). Strategies and Methods for Multi-Epoch Deformation Analysis based on Geodetic Networks. In *Proceedings of the 4<sup>th</sup> Joint International Symposium on Deformation Monitoring (JISDM 2019)*, Athens, Greece.
- Pope, A. J. (1971). Transformation of Covariance Matrices Due to Changes in Minimal Control. In: AGU Fall Meeting, San Francisco, California, December 9, 1971. *National Ocean Survey Geodetic Research and Development Laboratory*.
- Rao, C. R. and Mitra, S. K. (1971). *Generalized Inverse of Matrices and Its Applications*. Wiley Series in Probability and Mathematical Statistics. Wiley
- Shi, Y., Xu, P., and Peng, J. (2017). A computational complexity analysis of Tienstra's solution to equality-constrained adjustment. *Studia Geophysica et Geodaetica*, 61(4), pp. 601-615.
- Velsink, H. (2015). Extendable linearised adjustment model for deformation analysis. *Survey Review*, Vol 47, No. 345, pp. 397-410.
- Velsink, H. (2016). Time Series Analysis of 3D Coordinates Using Nonstochastic Observations. *Journal of Applied Geodesy*, Vol 10, No. 1, pp. 5-16
- Velsink, H. (2017). Testing deformation hypotheses by constraints on a time series of geodetic observations. *Journal of Applied Geodesy*. Vol 12, No. 1, pp. 77-93.
- Velsink, H. (2018a). Testing Methods for Adjustment Models with Constraints. *Journal of Surveying Engineering*. Vol 144, No. 4 (04018009).
- Velsink, H. (2018b). *The Elements of Deformation Analysis: Blending Geodetic Observations and Deformation Hypotheses*. Doctoral dissertation, Delft University of Technology. DOI: 10.4233/uuid:d7132920-346e-47c6-b754-00dc5672b437
- Wolf, H. (1982). Alternate use of restriction equations in Gauss-Markoff adjustments. In: Blotwijk, M.J.; Brouwer, F.J.J.; van Daalen, D.T.; de Heus, H.M.; Gravesteijn, J.T.; van der Hoek, H.C.; Kok, J.J. and Teunissen, P.J.G., editors, *Forty Years of Thought. Anniversary edition on the occasion of the 65<sup>th</sup> birthday of Professor Baarda*, volume I, pages 194-200.

## Continuous long-term (2016-2021) monitoring of the surface deformations in the Upper Silesian Coal Basin, Poland

Maya Ilieva<sup>1</sup>, Patryk Balak<sup>1</sup>, Paweł Bogusławski<sup>1</sup>, Piotr Polanin<sup>2</sup>, Piotr Gruchlik<sup>2</sup>, Andrzej Kowalski<sup>2</sup>, Damian Tondaś<sup>1</sup>, Krzysztof Stasch<sup>1</sup>, Przemysław Tymków<sup>1</sup>

<sup>1</sup> Institute of Geodesy and Geoinformatics, Wrocław University of Environmental and Life Sciences, Wrocław, Poland, ([maya.ilieva@upwr.edu.pl](mailto:maya.ilieva@upwr.edu.pl); [balakpatryk@gmail.com](mailto:balakpatryk@gmail.com); [pawel.boguslawski@upwr.edu.pl](mailto:pawel.boguslawski@upwr.edu.pl); [damian.tondas@upwr.edu.pl](mailto:damian.tondas@upwr.edu.pl); [krzysztof.stasch@upwr.edu.pl](mailto:krzysztof.stasch@upwr.edu.pl); [przemyslaw.tymkow@upwr.edu.pl](mailto:przemyslaw.tymkow@upwr.edu.pl))

<sup>2</sup> Department of Surface and Structures Protection, Central Mining Institute, Katowice, Poland, ([ppolanin@gig.eu](mailto:ppolanin@gig.eu); [pgruchlik@gig.eu](mailto:pgruchlik@gig.eu); [akowalski@gig.eu](mailto:akowalski@gig.eu))

**Key words:** *DInSAR; mining deformations; subsidence; monitoring; modelling*

### ABSTRACT

The Upper Silesian Coal Basin (USCB), located in Southern Poland, is one of the biggest coal deposits in Europe. It is continuously exploited since 18 century and it is one of the main industrial factors in the regional economy. As a result this is also the second populated region in Poland with 4.5 million inhabitants in the administrative province of Silesia. The extensive extractions of the underground coal resources in USCB trigger significant terrain changes leading to subsidence exceeding 1.5 m per year in some areas. Within the frames of two consecutive phases of the Polish contribution to the European Plate Observing System (EPOS) initiative, namely EPOS-PL and EPOS-PL+, a long-term monitoring over the area of USCB is performed using the advantages of the Differential Synthetic Aperture Radar (DInSAR) technology. C-band radar images acquired by the European Space Agency's Sentinel-1 mission comprising the period between the years of 2016 and 2021 are processed to delineate the range and amplitude of the deformation zones for chosen test sites. The Sentinel-1 constellation provides imagery with revisit time of 6 days, higher than the classical techniques. The standard approach include measurements like levelling, performed 2 to 6 times per year over chosen lines, or measurements with Global Navigation Satellite System (GNSS), while the DInSAR approach gives wider in space and time coverage. The long period of observations gives the opportunity to assess the surface behavior due to the coal underground extractions and to construct more precisely the model of deformations.

### I. INTRODUCTION

The concept for an European infrastructure for integrating and distributing scientific digital data for multidisciplinary solid Earth science rose in the beginning of 21<sup>st</sup> century. In 2010 the European Commission funded the first preparation stage for developing the European Plate Observing System (EPOS; <https://www.epos-eu.org/>). The goal is to create an integrated space for data and services gathered by institutions and scientists from all around Europe, aiming to support the global monitor and study of the solid Earth system. In the following years different European structures initiated the development of regional infrastructures, that later would contribute to the Integrated Core Services (ICS) that will ensure the interoperability of the data and services gathered in the EPOS' so-called Thematic Core Services (TCS).

In 2016, the first phase of the Polish realization of EPOS began with the start of the EPOS-PL project (<https://epos-pl.eu/>). The structure of the project defined several Research Infrastructure Centers (RIC) on state level to provide datasets and services in given research fields, like gravimetry, seismicity, geodesy, etc. As a second level of the EPOS-PL development the first Polish EPOS infrastructures were created in two

polygons were measurements from different observations for monitoring geodynamic processes was integrated. Two polygons from the group of MUSE – Multidisciplinary Upper Silesian Episode, were established in the area of intensive underground coal mining in the Upper Silesian Coal Basin (USCB) in Southern Poland. In the area of MUSE1 and MUSE2 (Figure 1) an in-situ integrated geodetic observation system was built, comprising GNSS permanent stations, campaign GNSS and levelling measurements, also artificial corner reflectors used for calibration of satellite radar measurements. The polygons include also geophysical observation system from seismological, gravimetric and geophysical networks. The collected data are shared as USCB episode in the TCS Anthropogenic hazard platform (<https://tcs.ah-epos.eu>).

Within EPOS-PL project the surface deformations caused by the coal extraction in USCB were, in addition to all other techniques, monitored with the application of the Differential Interferometric Synthetic Aperture Radar (DInSAR) technique. The method is chosen due to the possibility of automation of the processing for delivering of services for regular monitoring of the mine-induced deformations. The character of this deformations is determined by relatively shallow works

– between 400 and 1000 m, with high intensity and considerable volume of extracted underground materials. As a consequence, the observed area suffers from very dynamic ground changes in vertical but also in horizontal directions. The latter is a result of the used mining technique, namely long-wall mining, in which the resources are extracted in multiple layers, panel by panel, usually in 1 or 3-month intervals. The resulted surface deformations has a pattern of multiple distributed smaller patches with non-linear horizontal and vertical development. The horizontal position of the appearing deformation spots follows with several months (6-8 months) the time of the extraction due to the cavity compaction (Ilieva *et al.*, 2019). In the first phase of the Polish EPOS project, namely EPOS-PL, we developed the first concept for an improved DInSAR post-processing (Ilieva *et al.*, 2019) aiming to reduce the effects of the atmosphere artifacts and unwrapping errors. Our tests were made for the area of Bytom mine (Figure 1) where the annual subsidence is estimated in the range around 1.50 m.

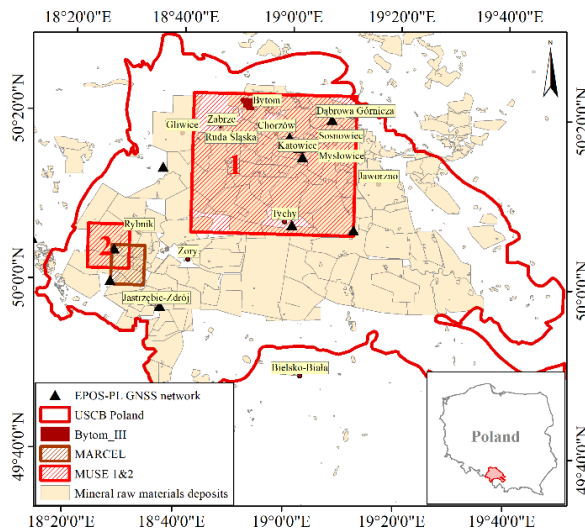


Figure 1. Upper Silesian Coal Basin (USCB) in Southern Poland with the test sites MUSE 1&2 (EPOS-PL) and MARCEL (EPOS-PL+), EPOS-PL permanent GNSS network, and the coverage of the mining deposits.

In the next phase of the study, the second part of the Polish realization of EPOS started in 2020 as EPOS-PL+ project (<https://epos-pl-plus.eu/>). Thanks to the significance of the results for MUSE episodes, an InSAR dedicated center was created - Satellite Data Research Infrastructure Center (CIBDS). In CIBDS we are developing an improved algorithm for post-processing, that will allow robust automation of the DInSAR workflow. The goal is to create a stable service of regular deformation maps that at the next part of the project will also allow the development of prediction models of the expected surface deformations. Such a service will enhance monitoring and decision-making process in the mining industry. We expanded our researches over the test site of MARCEL mine (Figure 1) in USCIB, where we also monitor the stability of two safely pillars. To

validate our DInSAR solution we established dense in-situ network in the area of the pillars and the surroundings where we already performed two campaigns of levelling and GNSS measurements.

## II. IMPROVED DInSAR POST-PROCESSING APPROACH

The Differential Interferometric Synthetic Aperture Radar (DInSAR) is considered as the classical satellite radar approach for monitoring of Earth's surface deformations caused by natural or anthropogenic hazards. Since the first notable results acquired with this technique in the 90s of the 20<sup>th</sup> century (*e.g.* Massonnet *et al.*, 1993) DInSAR method was developed further with several advanced InSAR techniques like Persistent Scattered Interferometry (PSInSAR; Ferretti *et al.*, 2000) and Small Baseline Subsets (SBAS; Berardino *et al.*, 2002). These techniques have the advantage of minimizing the atmospheric errors on the radar signals by creation of a stacks of SAR images, based on the pixels with highest quality in time (highest coherence). On the other hand, they are not capable to keep information in the areas with fast dynamics or with non-linear movement, like in the coal fields of USCIB. This is the reason why in CIBDS we also use the classical DInSAR monitoring. In this method we apply consecutive DInSAR, in which for every next interferometric pair (*e.g.* interferogram *j* in Figure 2) the first SAR image (the primary or master *j* image) is the second (or slave *i* image) of the previous pair – interferogram *i*. In this way we preserve continues time series of differential interferograms. On one hand, this approach has the capability to cancel out the atmospheric influence in one image that would appear with opposite signs in the two common consecutive interferograms. On the other hand, if a longer period of atmospheric perturbation exists in the timeline, it could affect the entire series. Still, despite this disadvantage, the method is valuable with gathering information about the range of subsidence in the center of the subsidence bowls. To estimate the total subsidence in the area of interest we combine the consecutive deformation maps in cumulative solution.

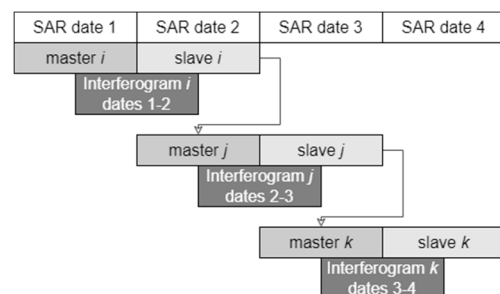


Figure 2. Consecutive DInSAR.

In order to minimize the influences from unstable atmospheric conditions, unwrapping jumps, but also residual orbital ramp and reference uncertainties in the separated interferograms, we propose an improved method for post-processing firstly suggested in EPOS-PL

(Ilieva *et al.*, 2019) and currently under improvement in EPOS-PL+. The method is based on the removal of a oscillating surface from each interferogram (Figure 3), aiming to anchor the entire series of deformation maps to a surface build on common, stable in time, highly coherent points (>0.9).

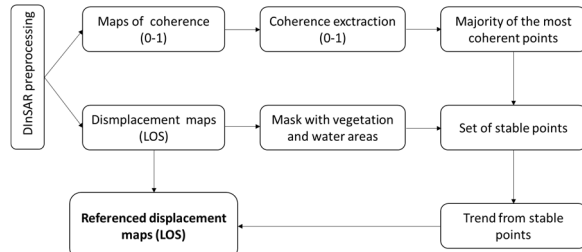


Figure 3. Scheme of the proposed post-processing approach for georeferencing to a surface with common origin.

We extract the most coherent pixels of each interferogram and find which of them keep this quality throughout the entire year. These pixels have a majority for a set of about 60 interferograms in the case of SAR data acquired at 6-days interval that we used – data generated by the SAR sensors mounted on the constellation of two Sentinel-1 (A&B) European Space Agency's (ESA) satellites. This group of points represents the pixels with good reflectivity throughout the entire year, covering all seasonal changes. We also exclude the areas of known deformations. Then we use this set of points to extract the values from displacement maps and based on the latter to construct an interpolated surface that represents to fluctuations from the zero origin. This trend is removed from the corresponding displacement map leading to unification of the datum for the entire set of deformation maps.

At the next step, the automation of the process continues with processing of a new interferogram every time when a new Sentinel-1 image is released by ESA, but not before the corrected orbit file is also available. In this approach it is not necessary to re-processes the entire stack as in the case of some other advanced InSAR methods. The only update is in the check of the stability of the coherence points from the new interferogram in the period of one year prior the last Sentinel-1 acquisition.

As it was mentioned earlier the quality of some deformation maps suffers from the atmospheric perturbation influence. In separate cases this effect is too strong and cannot be eliminated. When it affect short period of time (up to 12 days, or 1 interferogram with low quality) we apply linear interpolation to fill the gap of excluded data, while for minimizing the effect of longer periods of data with lower quality we will integrate machine learning, including Neural Network (NN) approaches. To evaluate the quality and to point out the outliers we do an assessment based on the statistical characteristics of the deformation maps, namely by application of Z-score method for the mean

and standard deviation values of each image. The goal is to improve the smoothness, meaning to minimize the unexpected jumps in the time series generated in the DInSAR deformation maps.

### III. SUBSIDENCE PREDICTION

#### A. Knothe-Budryk theory modelling

In the first EPOS-PL project a collaboration between the two teams from the Institute of Geodesy and Geoinformatics in Wrocław University of Environmental and Life Sciences – responsible for DInSAR processing, and the Department of Surface and Structures Protection, Central Mining Institute who is responsible for subsidence modelling and prediction, started. The standard approach for prediction of mining-induced surface deformation in Poland is to use regular levelling measurements performed along monitoring lines or set of points in 1 to 6 months intervals as main input data in the Knothe-Budryk method (Knothe, 1953, Kowalski, 2015). We started with comparison of these modelled deformation with a one-year (2017) collection of DInSAR deformation maps over a Bytom mine site (Ilieva *et al.*, 2019). This analysis help us to define the need of tuning the modelling parameters and also to perform some test of a solution based on the more dense in time (every 6-days) DInSAR results instead of the levelling measurements performed 2 to 12 times per year (Figure 4).

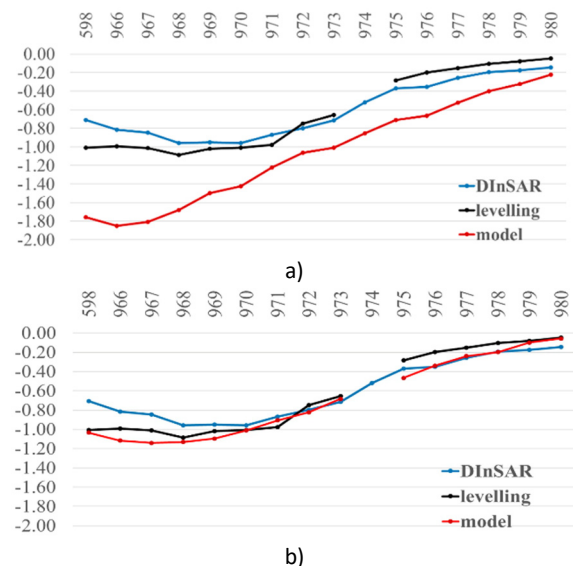


Figure 4. Example of a profile through a subsidence bowl in the area of Bytom mine (USCB) for the period between March and October 2017 (two levelling cycles). The black line present the subsidence measured by levelling, the blue – by DInSAR, red line is the modelled subsidence calculated after Knothe-Budryk theory: a) Based on levelling data; b) Based on DInSAR data.

#### B. Machine Learning approach

Within the second project – EPOS-PL+, we are developing further the concept of using DInSAR surface deformation maps as the input values in the Knothe-



Budryk function for subsidence prediction. We apply a Feedforward neural network (FNN) by creating a set of parameters for each pixel from the deformation maps and from the plans for coal extraction. We used 80 % from the resulted about 300'000 vectors for the set of deformation maps between 2017 and 2021 as training data, while the rest are used for validation and as final testing data (Figure 5).

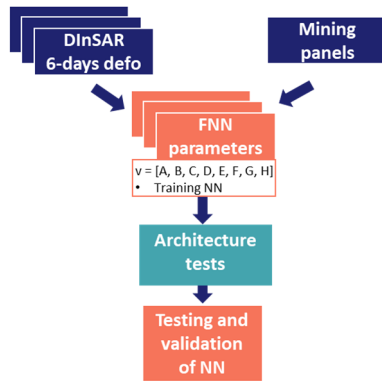


Figure 5. Scheme of the Machine Learning approach under development for subsidence prediction within EPOS-PL+ project.

#### IV. RESULTS

Within the two projects EPOS-PL and EPOS-PL+ we used a set of freely available SAR data provided by ESA on the Sentinel data hub Sentinel-1 A&B radar images (<https://scihub.copernicus.eu/>). At the moment the entire set of the ascending (No 175) and descending (No 051) Sentinel-1 data over USCB for the period 2016-2021 are processed. We used the ESA's platform for processing of Sentinel-1 interferometry – Sentinel Application Platform (SNAP), the Shuttle Radar Topography Mission (SRTM) 1 arc second (30 m resolution) Digital Elevation Model (DEM; Jarvis, 2008) for topographic phase removal, the Goldstein filter (Goldstein and Werner, 1998) for reducing the noise in the wrapped interferograms, and the minimum cost flow (MCF) function for phase unwrapping (Chen and Zebker, 2000). In CIBDS we are developing an automation of the SNAP consecutive processing that can ensure the regular production of deformation maps. We are also developing the automation and improvement of the post-processing approach for correcting the deformation maps described above. Here we present an example of an interferogram over the entire area of MUSE1&2 with the original product, the surface built by interpolation of the LOS displacement values for the locations of the most coherent pixels, and the corrected displacement map – Figure 6.

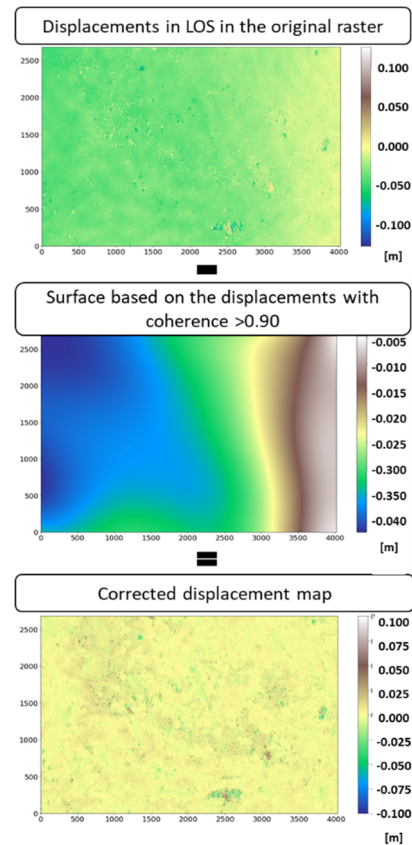


Figure 6. Example for correction of original deformation map as a product of SNAP DInSAR processing (up), the trend surface built from the pixels with stable coherence within 1 year (middle) and corrected displacement map (bottom).

For the needs of EPOS-PL and EPOS-PL+ partners we also produce 3 and 12-month cumulative subsidence maps. Here, the several of the yearly solution for MARCEL test site are presented in Figure 7.

For verifying the results of the DInSAR technique we build a geodetic network of benchmarks in the area of the MARCEL test site, where already two cycles of measurements have been performed (November 2021 and April 2022). Since at the moment of preparation of this report the second cycle of data are just measured but not processed we present the network of the measured levelling lines and an example of the total cumulative 3-years vertical displacements along one of the lines (Figure 8). For the estimation of the vertical component we combined the data from ascending and descending orbit tracks, with assumed north component of the displacement as negligible. After processing of the measurements of the second campaign, we will apply the north component from the GNSS measurements to the 3D decomposition solution.

#### V. CONCLUSIONS

We present an improved method for post-processing of DInSAR deformation maps, based on a trend removal approach aiming to reduce the atmospheric artefacts, the orbital ramp and minimize the unwrapping uncertainties in each deformation map. In addition we perform statistical quality assessment and detection of

the images with lower quality. The goal is to reduce the outliers in the DInSAR time series, that can give, firstly more precise values for the dynamics of non-linear surface displacement in the mining area of USCB, and secondly more reliable data for mining management

and prediction modelling. Within the new phase of the Polish realization of EPOS initiative we, in CIBDS, are developing also a methodology for subsidence prediction based on Neural network approach, using the products of the improved DInSAR processing.

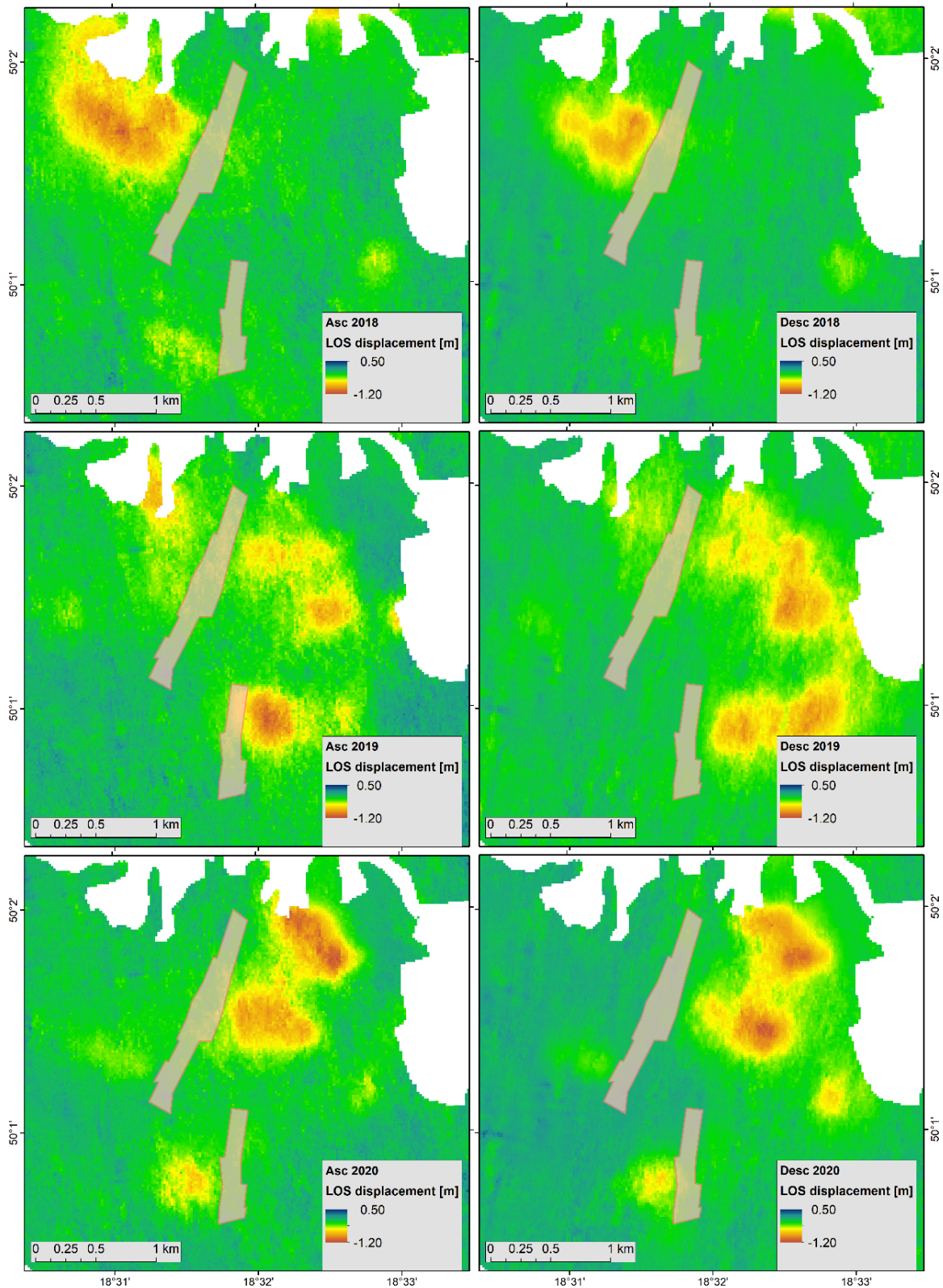


Figure 7. Yearly dynamics of the surface deformations in the area of MARCEL test site in USCB – generated from ascending (“Asc”, left column) No 175 and descending (“Desc”, right column) No 051 Sentinel-1 orbits for the years 2018, 2019 and 2020. The polygons present the location of two underground safety pillars. The Corine Land Cover (version 2018, © European Union, 2018) polygons are used to mask the densely vegetated areas (in white).

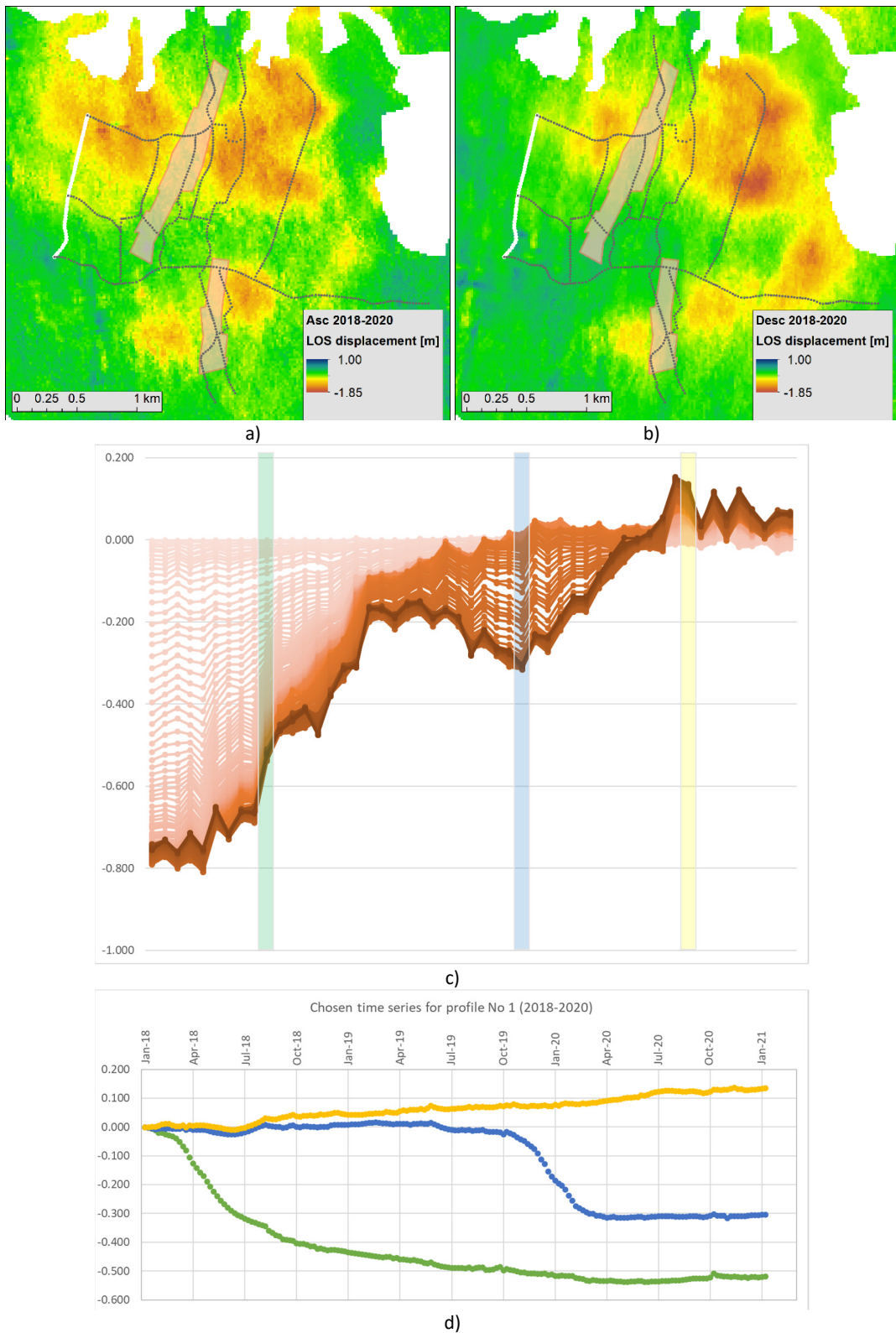


Figure 8. Ascending a) and Descending b) cumulative subsidence for the period 2018-2020 for the area of MARCEL test site with the location of the safety pillars (red polygons) and the levelling network (black dots). The white dots represent the benchmarks from the levelling line used as an example of cross-section through the cumulative DInSAR vertical deformation maps (c), that was estimated as a 3D decomposed solution from the 6-days ascending and descending LOS displacements. d) present the time-series of chosen points – the colours correspond to the point shown with the same colour in the profile above c).

Still we need to accomplish several tasks like the full 3D-decomposition of the deformation maps produced in the LOS, including implementation of the horizontal component from GNSS measurements, defining the

best approach for filling bigger gaps of rejected data with lower quality, and to develop an integration of more external information in the modelling algorithm.

## VI. ACKNOWLEDGEMENTS

The presented investigation is part of the projects EPOS-PL (POIR.04.02.00-14-A003/16) and EPOS-PL+ (POIR.04.02.00-00-C005/19-00), European Plate Observing System, funded by the Operational Programme Smart Growth 2014–2020, Priority IV: Increasing the research potential, Action 4.2: Development of modern research infrastructure of the science sector and co-financed from European Regional Development Fund.

## References

- © European Union, Copernicus Land Monitoring Service, (2018). European Environment Agency (EEA), <https://land.copernicus.eu/pan-european/corine-land-cover/clc2018>
- Berardino, P., Fornaro, G., Lanari, R., and Sansosti, E. (2002). A new algorithm for surface deformation monitoring based on small baseline differential SAR interferograms. *IEEE Transactions on geoscience and remote sensing*, 40(11), pp. 2375-2383. DOI: 10.1109/TGRS.2002.803792
- Chen, C.W., and Zebker, H.A. (2000). Network approaches to two-dimensional phase unwrapping: Intractability and two new algorithms. *Journal of the Optical Society of America A*, 17(3), pp. 401-414. DOI: 10.1364/JOSAA.17.000401
- Ferretti, A., Prati, C., and Rocca, F. (2000). Nonlinear subsidence rate estimation using permanent scatterers in differential SAR interferometry. *IEEE Transactions on geoscience and remote sensing*, 38(5), pp. 2202-2212. DOI: 10.1109/36.868878
- Goldstein, R. M., and Werner, C. L. (1998). Radar interferogram filtering for geophysical applications. *Geophysical Journal International*, 25(21), pp. 4035-4038. DOI: 10.1029/1998GL900033
- Knothe, S. (1953). Wpływ czasu na kształtowanie się niecki osiadania [Influence of time on the formation of subsidence trough]. *Arch. Górnictwa i Hut.*, 1, 51
- Kowalski, A. (2015). Deformacje Powierzchni w Górnośląskim Zagłębiu Węglowym [Surface Deformation in the Upper Silesian Coal Basin]. *Główny Instytut Górnictwa: Katowice, Poland*, ISBN 978-83-61126-93-5
- Ilieva, M., P. Polanin, A. Borkowski, P. Gruchlik, K. Smolak, A. Kowalski, and W. Rohm (2019). Mining Deformation Life Cycle in the Light of InSAR and Deformation Models. *Remote Sensing*, 11, 745
- Jarvis, A., H.I. Reuter, A. Nelson, and E. Guevara (2008). Hole-filled seamless SRTM data V4, International Centre for Tropical Agriculture (CIAT), available from <https://srtm.csi.cgiar.org>
- Massonnet, D., M. Rossi, C. Carmona, F. Adragna, G. Peltzer, K. Feigl, and T. Rabaute (1993). The displacement field of the Landers earthquake mapped by radar interferometry. *Nature*, 364, pp. 138–142

## A discussion on the uses of smart sensory network, cloud-computing, digital twin and artificial intelligence for the monitoring of long-span bridges

Xiaolin Meng<sup>1,2</sup>, Zejun Xiang<sup>3</sup>, Yilin Xie<sup>4</sup>, George Ye<sup>5</sup>, Panagiotis Psimoulis<sup>6</sup>, Qing Wang<sup>2</sup>,  
Ming Yang<sup>7</sup>, Yulong Ge<sup>8</sup>, Shengli Wang<sup>9</sup>, Jian Wang<sup>10</sup>

<sup>1</sup> Beijing University of Technology, Beijing, China, ([mengxl@bjut.edu.cn](mailto:mengxl@bjut.edu.cn))

<sup>2</sup> Southeast University, Nanjing, China, ([w3398a@263.net](mailto:w3398a@263.net))

<sup>3</sup> Chongqing Survey Institute, Chongqing, China, ([xiangzj@cqkcy.com](mailto:xiangzj@cqkcy.com))

<sup>4</sup> Jiangsu Hydraulic Research Institute, Nanjing, China, ([xieyilin1983@gmail.com](mailto:xieyilin1983@gmail.com))

<sup>5</sup> UbiPOS UK Ltd., UK, ([george.ye@ubipos.co.uk](mailto:george.ye@ubipos.co.uk))

<sup>6</sup> The University of Nottingham, UK, ([panagiotis.psimoulis@nottingham.ac.uk](mailto:panagiotis.psimoulis@nottingham.ac.uk))

<sup>7</sup> State Key Laboratory of Media Convergence Production Technology and Systems, China, ([mingyang@nju.edu.cn](mailto:mingyang@nju.edu.cn))

<sup>8</sup> Nanjing Normal University, Nanjing, China, ([geyulong@njinu.edu.cn](mailto:geyulong@njinu.edu.cn))

<sup>9</sup> Shandong University of Science and Technology, Qingdao, China, ([shlwang@sdust.edu.cn](mailto:shlwang@sdust.edu.cn))

<sup>10</sup> Beijing University of Civil Engineering and Architecture, Beijing, China, ([wangjian@bucea.edu.cn](mailto:wangjian@bucea.edu.cn))

**Key words:** *smart sensory network; cloud-computing; digital twin; artificial intelligence; bridge monitoring*

### ABSTRACT

This paper discusses what are the smart sensors that are currently available to be used for real-time monitoring of long-span bridges, how to develop an effective and efficient data strategy for collecting, processing, managing, analysing and visualising data sets from monitored assets to support decision-making, and how to establish a cost-effective and smart sensory network according to the objectives set up through thorough communications with asset owners. Due to high data rates employed and dense monitoring sensors installed the traditional processing technique will not fulfil the monitoring functionalities and is not secure. Cloud-computing technique is widely used in processing and storing big monitoring data sets. Using the experience attained by the authors in the establishment of long bridge monitoring systems in the UK and China this paper will compare the pros and cons of using cloud-computing for long-span bridge monitoring. It will further explore how to use digital twin (DT) and artificial intelligence (AI) for the extraction of relevant information or patterns regarding the health conditions of the assets and visualise this information through the interaction between physical and virtual worlds to realise timely and informed decision-making in managing essential road transport infrastructure.

### I. INTRODUCTION

A very recent statistics carried out by the RAC Foundation reveals that 3,211 bridges in the UK are substandard by the end of 2021, a 3.4% increase compared with those of 2020 (RAC 2021a). In the UK a substandard bridge means those are unable to carry the heaviest vehicles on the road network, including lorries of up to 44 tonnes, and a weight restriction must be applied. As most of 2021 were under the COVID-19 pandemic lockdown in the UK and this rapid structural deterioration must be caused by their natural degradation process. It is estimated the cost to bring these substandard bridges back up to a perfect condition is £1.16 billion and to clean up all the maintenance backlog on 70,944 bridges in the UK would be £5.44 billion (RAC 2021b).

There are much higher bridge inventories both in China and the US. By 2019 China has built more than 878,300 highway bridges and 87% of them are medium and small size bridges. More than 10% of these bridges are categorized as “structurally deficient” which means

that immediate retrofitting is required. Most of the long-span bridges in China (single span > 500 m for a suspension bridge and > 300 m for a cable-stayed bridge) are constructed in the past 30 years and bridges built in the past 10 years usually have a built-in structural health monitoring (SHM) system by the regulations or laws. Zhao *et al.* (2020) give a very comprehensive introduction on the recent research and practice of China in SHM of bridges.

The American Road & Transportation Builders Association (ARTBA) 2022 Report points out that 7% of its total 619,588 highway bridges are “structurally deficient” and 167.5 million daily crossings are on the total 43,578 structurally deficient U.S. bridges in poor conditions (Black 2022). The estimated cost to retrofit all 224,000 bridges that need major repair work or replacement, including the 43,578 structurally deficient bridges, is \$260 billion. Recently, the US has passed its long-awaited Bipartisan Infrastructure Law ([www.whitehouse.gov/bipartisan-infrastructure-law/](http://www.whitehouse.gov/bipartisan-infrastructure-law/)) and it announced to invest \$1tn for clean energy,

internet, its ageing road networks including bridges, etc. Ironically, just before President Biden delivering his first infrastructure speech at “US City of Bridges” Pittsburgh in Pennsylvania on 28 January 2022, a bridge collapsed and injured 10 people. This is an apparent evidence of how serious the shared challenges are for the bridge maintenance and safety around the world.

From 2005 the first author of this paper had participated and then led a series of episodic monitoring campaigns to one of the longest bridges in the UK, the Forth Road Bridge in Scotland (Roberts *et al.*, 2012). With the support mainly from the European Space Agency (ESA) a phased installation of a permanent monitoring system called GeoSHM started from 2014 (Meng *et al.*, 2018a). The Forth Road Bridge was opened to traffic on 4 Sept 1964. The total length of the bridge is 2.5 km with the main span of 1,006 m (Figure 1). It was the world longest bridge outside the US but now it ranks 44. The Forth Road Bridge is essential for the Scottish/UK economy. According to the former bridge master closing one of its four lanes per day will cost £650K. The structural responses are dominated by temperature and traffic loadings and the bridge is susceptible to wind effects which cause excessive lateral movement and predicted over-stress under design wind loading. Regular repairs to the main components were carried out during its service lifetime of 58 years ([www.theforthbridges.org/forth-road-bridge/maintenance](http://www.theforthbridges.org/forth-road-bridge/maintenance)).



Figure 1. The Forth Road Bridge with the Queensferry Crossing as background (from: Edinburgh News).

This paper uses the Forth Road Bridge in Scotland as an SHM example and the experience attained from the SHM systems erected on the bridges in China contributes enormously to the concepts and contents of this paper. The overall focuses of this paper include:

- How to establish a cost-effective and smart sensory network for monitoring long-span bridges.
- How to develop an effective SHM data strategy to handle large quantity of monitoring data from high-rate sensory network.
- Analysis to the pros and cons of cloud-computing technique for an SHM system.

- Discussion on the integrated uses of Digital Twin (DT) and artificial intelligent (AI) for smart monitoring of bridges.

## II. SMART SENSORY NETWORK FOR SHM

The monitoring objectives by the bridge owners, available budget, timeline and most importantly the user demands together govern the overall design and configuration of a structural health monitoring (SHM) system. This requires the SHM developers sit down with bridge owners and listen to their burning pains in managing their assets. Selection of the right sensor types, determination of their optimal placement locations on the structure and design of the data transmission approaches are all essential factors to be considered in the initial stage of setting up a sustainable SHM system. To make this system adaptable to accommodate the changing demands of bridge owners and survive the harsh operational environment smart sensors and the network to connect them into an effective and efficient monitoring system are widely used in the current SHM systems. The smart level of the sensory system depends on the advance of many key impact parameters (KPIs) or affecting factors such as core chipset design, advanced materials and manufacture skill, computing power, wireless or cabled communications such as 5G/6G and fiber optic cables, etc.

In general, the monitoring parameters to be considered in a practical bridge monitoring system include the environmental parameters such as wind speed and its direction, temperature, humidity, rain, snow, ice, etc., the spatial-temporal displacements (four-dimensional, 4D) of the structure such as deflection and deformation, crack, fatigue, corrosion, etc., and the forces on the structure, such as strain and stress and their 4D distributions. Since different bridge owners have their specific monitoring priority agenda and the size and complexity of each individual structure are different therefore the determination of the number and types of the sensors and their placements on the structure is unique. According to Xu and Xia (2012) and Campbell *et al.* (2016) the sensors used to measure these above three types of parameters include loading sensors for wind, earthquake and traffic applied on the structures, the sensors for measuring structural responses such as displacement, strain, stress etc., and the environmental sensors for measuring temperature, humidity, rain, ice, snow, corrosion, solar radiation etc.

Nowadays due to their unique advantages such as higher bandwidth, longer transmission distance, lower latency and stronger security optical fibres are extensively used for large quantity of monitoring data transmission in the bridge SHM systems and various fibre optic sensors are developed to measure strain, temperature, dynamic and static vehicular weight, pressure, image etc. Furthermore, the advance and application of the micro-electromechanical system

(MEMS) sensors makes bridge monitoring more accurate and affordable and hence significantly improve the density of the sensory network on the structure. The use of optical fibres, and fibre optic and MEMS sensors have paved the way for integrating a digital twin (DT), analytic models such as finite element model (FEM) and other advanced data sciences such as big data analytics and machine learning, etc. into daily operation of the SHM systems.

Clearly, bearing this above development trend in mind and considering the affordability of the Forth Road Bridge owner's, GeoSHM was designed as a phased, open and scalable system (Meng *et al.*, 2018a; 2018b). The first phase was to proof the GeoSHM feasibility of fusing the satellite InSAR regional inspection and in-situ point-based monitoring with GNSS positioning and laying an optical fibre-based communication network to form high spatial-temporal monitoring (Meng *et al.*, 2018b; Psimoulis *et al.*, 2017). The demonstration phase of the GeoSHM development was more focused on densifying the existing monitoring footprint and developing a deep learning method to implement effective data mining, interpretation and structural diagnoses (Nguyen *et al.*, 2019). The GeoSHM system consists of the online and offline processing modules which play different roles: the online one for structural condition evaluation and the offline one for health and safety assessment. Figure 2 shows the main components of the GeoSHM sub-systems and how the GeoSHM *in-situ* sensors are linked to the processing centres with the optical fibre network on the bridge and via the TCP/IP protocol through the Internet. The cabled based network has been further upgraded using hybrid communication techniques.

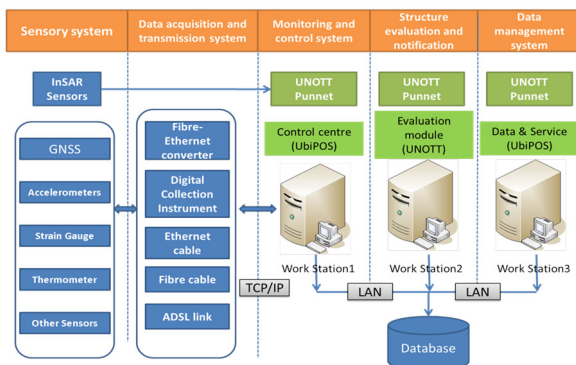


Figure 2. GeoSHM Sub-systems and Data Flow.

In the GeoSHM system, different high-rate sensors are installed at different locations of the structure to gather the digital or analog signals of interest. Figure 3 is a list of the sensors intended to be installed during its demonstration phase. Up to now most sensors have been successfully installed and running on the bridge but due to the pandemic replacing two corroded sensors at two quarter-span locations (SHM8 and SHM9) on the west side of the bridge was delayed. Figure 4 illustrates the current sensor types and locations.

No	Location	Instruments	Fibre Joint Box	Serial to Ethernet Converter ID	Instrument ID
1	Top of the SW tower leg	GNSS	0	N/A	SHM4
		Anemometer	2	0	ANE1
		Accelerometer	2	1	ACC1
1-1	Mid-height of the SW tower leg	Tiltmeter	2	1	TLT1
		Tiltmeter	2	1	TLT2
2	PP87SW (3/8 of the main span)	Accelerometer on cable	2	1	ACC2
3	PP73SW (NAV channel)	Accelerometer on deck	2	1	ACC3
4	PP73SE (NAV channel)	GNSS	2	N/A	SHM8
		Accelerometer	2	1	SHM7
5	PP101W (Mid span)	GNSS	0	N/A	SHM2
		Anemometer	0	0	ANT2
6	PP101E (Mid span)	GNSS	0	N/A	SHM3
		Met Station	0	0	MET1
7	PP73NW (NAV Channel)	Accelerometer	2	1	ACC5
		GNSS	2	N/A	SHM9
8	PP73NE (NAV Channel)	GNSS	2	N/A	SHM6
		Accelerometer	2	1	ACC6
9	PP59NE (1/8 span of the main span)	Accelerometer on cable	2	1	ACC7
		Accelerometer on deck	2	1	ACC8
		GNSS	2	N/A	SHM5
10	Top of the NE tower leg	Anemometer	2	0	ANE3
		Accelerometer	2	1	ACC9
		Tiltmeter	2	1	TLT3
10-1	Mid-height of the NE tower leg	Tiltmeter	2	1	TLT4

Figure 3. A full list of the sensors planned in the Phase Two development of the GeoSHM system.

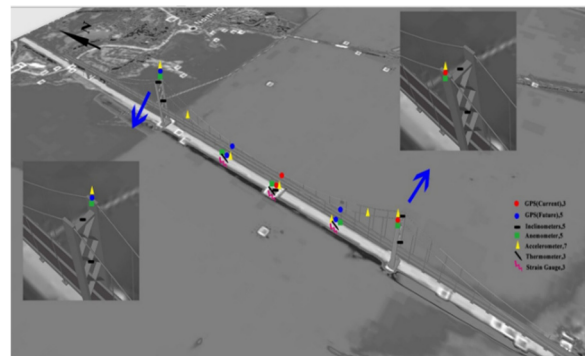


Figure 4. The sensor locations on the Forth Road Bridge.

Traditional sensing systems are mostly cable-based systems with monitoring nodes being installed at essential locations of the structures and these systems are usually sparse and expensive. Great efforts are required to maintain the communication systems since the communication cables are more vulnerable to the environment than the sensors. With wireless communication large quantity of sensors could be installed flexibly and the overall monitoring systems could be more scalable and cost-effective.

Current SHM systems extensively use cable-based communications for data transmission due to the drawbacks in power supply, communication bandwidth, effective ranges and signal interference due to complicated operational environments in wireless based monitoring. Some wireless sensors operate on unlicensed transmission frequency bands such as 2.4 GHz and hence there are output power limitations imposed in different countries. For instance, it is one watt in the US and 0.5 watts in the UK. This affects both data transmission throughput and a valid range.

When the optical fibre connection failed to transmitting data due to the installation challenge and long transmission range limitation for a remote monitoring node in the GeoSHM project wireless communication method was tried and it turned out to be a very reliable and cost-effective solution. Therefore, the communication network used in the GeoSHM project is a combination of optical fibre for most sensory sites and paired long-range Wi-Fi devices for a remote northeast (NE) supporting tower site. The NE

monitoring node is the furthest point in the whole GeoSHM system and consists of a GNSS receiver, an anemometer and a tri-axial accelerometer. Figure 5 is the wireless communication setting-up of SHM5 which sits atop the NE tower of the Forth Road Bridge.



Figure 5. A TP-Link Wi-Fi transceiver point (CPE510) installed atop the NE tower of the Forth Road Bridge.

In this case a pair of TP-Link's Outdoor Wireless Base Station 510 (WPS510) and Access Point 510 (CPE510) are used to receive and transmit monitoring data. CPE510 is linked to the remote sensors of SHM5. WPS510 is installed on the roof of the FRB control centre and linked to the Internet to stream the received data to the GeoSHM server to be processed. The nominal transmission range of these TP-Link devices is 5 km.

Figure 6 is the time series of the SHM5 lateral movement and 100% transmission rate is achieved in a period of three months during the peak of the COVID-19 pandemic which reflects the reliability of wireless communication for SHM.

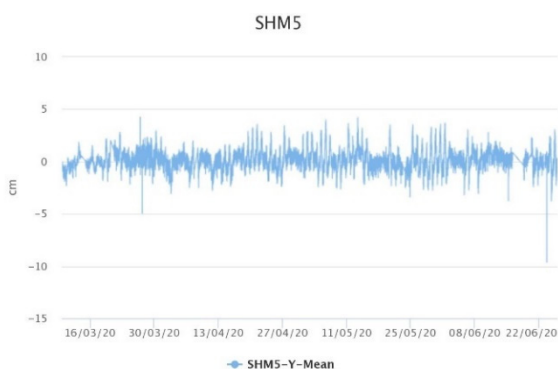


Figure 6. The time series of the lateral movement at SHM5 in three months.

### III. DEVELOPMENT OF AN SHM DATA STRATEGY

Data strategy refers to the tools, processes, and rules that define how to manage, analyse, and act upon data. A data strategy helps different practitioners to make informed decisions based on the available data. It also helps to keep the data safe and compliant. According to Gartner's definition a data strategy is a highly dynamic process employed to support the acquisition,

organization, analysis, and delivery of data in support of business objectives (Maguire 2019).

Using the data-driven approach for the establishment of an SHM system as illustrated in Figure 7 the aim of the development of an SHM data strategy is to provide the bridge owners and operators or service providers with appropriate bridge performance data and derived information to make informed bridge management decisions. The focus of the SHM data strategy should cover the procedures for data pre-processing and cleansing, real time data acquisition, data fusion from different sources, comparisons among real time data, historical ones and those from models, detection of extreme events and identification of system changes. As digital twins, big data analytics, IoT and AI are more and more applied into SHM of large infrastructure efforts should be made in how to seamlessly plug these into an updated SHM data strategy. As an example, the developed GeoSHM data strategy that has been utilized in guiding the development of the GeoSHM system comprises five interlinked components:

1. Data acquisition and pre-processing. All the raw measurements and the corresponding derived time series should be referred to a common spatial-temporal datum such as those defined by the Global Navigation Satellite System (GNSS) and using multi-GNSS including BDS becomes indispensable when a precise spatial-temporal datum is required for life-cycle infrastructure monitoring (Yang *et al.*, 2020). Data acquisition rates and smart triggers for sensor controls should be determined, validated and operational. Also, an appropriate bridge coordinate system (BCS) should be defined, where its X-axis coincides with the main axis of the bridge (longitudinal), Y-axis is perpendicular to the X-axis in the horizontal plane (lateral) and the Z-axis points to the vertical up-direction. All the global, local and body-framed coordinate systems of the monitoring sensors should be linked to the BCS through rigid coordinate transformations. Outliers and gaps in the acquired data sets should be detected and removed before further processing.
2. Data architecture and integration. A data architecture is devised and used to guide data archive and storage process. Immediately after data pre-processing the cleaned data sets will be pushed to the dedicated SHM Cloud. Further data processing including data fusion and mining from summary statistics of whole data sets will be performed on a dedicated processing engine. A heterogeneous database structure is used to store all the data in the same Cloud.
3. Data storage and technology. The GeoSHM users have access to the layered live data stream, historic data, structural health status report and so on, according to their roles which include



bridge masters, engineers, researchers and general public. This part of work is to set data storage and access rules (raw data vs processed ones, and duration in keeping this large quantity of raw measurements) and what kinds of media for storing these data. Solutions are compared against KPIs such as cost, performance, ease to access, etc.

4. Data insight and analysis. Direct comparison of short-term statistics with historical data will be made using statistical control charts. Bridge performance data will be presented on a chart relating maximum displacement (or other variables) to incident loading (traffic, wind, or combined). Live bridge performance data will be presented as a time series with the thresholds which are based on historical data analysis. These will include how to use finite element models, AI and DT to enhance structural health condition assessments.
5. Data governance, privacy. Setting up the rules regarding who is the owner and responsible for the data, who and how can access the data.

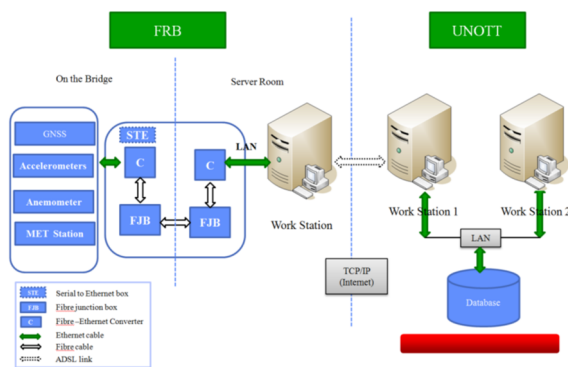


Figure 7. Data storage and technology.

#### IV. CLOUD-COMPUTING TECHNIQUE FOR SHM

As defined by Ray (2018) cloud-computing is the on-demand availability of computer system resources, especially data storage, which is called cloud storage, and computing power, without direct active management of the IT facilities by the users. The advantages and disadvantages about using cloud-computing for an SHM system are listed below.

The advantages in using a cloud-computing platform are:

1. Much lower processing cost. There is no need to purchase expensive hardware equipment, network equipment, and most software systems are also provided by the cloud-computing service providers for free.
2. Scalable computing performance and storage capacity. For the GeoSHM system, less resources need to be purchased at the initial stage, and the computing performance and storage space can

be gradually increased as the amount of data increases in operation.

3. Significantly improved data storage security. Generally, cloud platforms provide corresponding data storage protection or backup strategies which reduces the risk of data loss at the server ends.

The disadvantages in using cloud-computing include:

1. Data security and privacy. Service providers have the opportunity to directly access to the data, which poses potential risks to data security and privacy.
2. Migration of data and services. Transferring large quantity of data/services from an old provider to a new one can be very painful and cumbersome if the SHM user wishes to switch to another provider.

The traditional way to build a structural health monitoring platform starts from purchasing computer workstations and servers, routers, gateways and other hardware equipment, software tools, etc. Due to the lack of maintenance facilities, such as UPS backup power supply, dual network devices, standard air-conditioning room, 24/7 professional maintenance personnel, etc., it may cause data loss because of power failure, network disconnection or even system failure, etc. Data loss statistics with the traditional data storage method in a server at the University of Nottingham (UNOTT) from 2017-2019 is listed in Table 1.

Table 1. Data loss statistics from 2017-2019

Reason	Time frequency	Days of data loss
Network disconnection	5	23
Power failure	6	9
System failure	5	20
<b>Total</b>	<b>16</b>	<b>52</b>

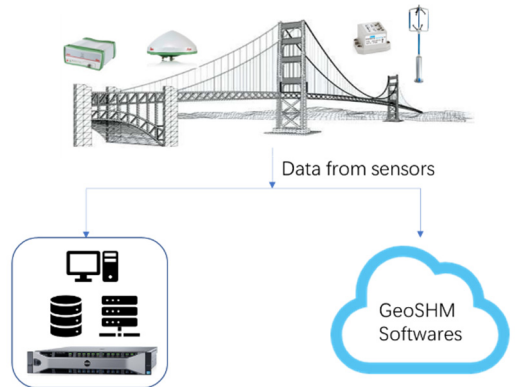
From July 2020, the architecture of the GeoSHM system has been changed and the same data were sent to the Cloud which is located in London and provided by Alibaba Cloud Ltd. Figure 8 is the current hybrid computing architecture of the GeoSHM system. After a period of debugging and optimization, the entire system has been completely transferred to the Alibaba Cloud. There is no data loss caused by the Ali Cloud server.

The Ali Cloud SHM server includes the following three running software modules:

1. The data receiving and management software module. This is used for data receiving, cleaning, and pre-processing and storing relevant statistic data and original observation measurements according to the designed SHM data strategy.
2. Data processing and analysis management software modules. It is used for estimating the SHM parameters and model update driven by AI,

dynamic adjustment of thresholds, real-time health assessment of bridge structures, and warning services.

3. Web-based network client system. It provides real-time data query and statistics, historical data comparison and analysis, real-time health status query and other related SHM functions.



GeoSHM platform in UNOTT Cloud platform in Alibaba  
Figure 8. Hybrid SHM processing platform using Ali Cloud and a local server UNOTT.

## V. DIGITAL TWIN (DT) AND ARTIFICIAL INTELLIGENT (AI) FOR SMART MONITORING OF BRIDGES

In SHM of bridges, a digital twin intends to build a virtual model that uses the real-world heterogeneous data sets gathered from an operational bridge as its input for enhancing asset management process. Once precisely constructed the DT can be used to simulate and predict the possible impacts for certain environmental and loading effects using monitoring data sets as the DT inputs. Linking the DT and artificial intelligence, especially using deep learning and transfer learning, is essential and a current development trend in implementing the smarter, safer and higher-quality infrastructure inspection regime. It is extremely useful while seeking timely, robust, accurate and cost-effective solutions to address much overdue bridge inspections around the world. This new way of inspection includes the integration of smart sensors or other field data acquisition, secured data transmission via cabled and 5G/6G or even LEO satellite broadband comms, building high definition (HD) 3D or 4D models of the assets with DT technique and uses of both AI and analytic models such as FEM to process, analyse and visualise huge monitoring data. Pairing a DT with AI that uses the data from smart sensory system on the structures as its inputs and the high-speed data communications provide great opportunities to conduct instant interaction among the physical world features with the cyber world models to maximize monitoring effects (Liu *et al.*, 2022).

Artificial Neural Networks (ANNs) have been successfully applied in many fields including pattern recognition, connected and autonomous vehicles, civil engineering, public security, etc. (Goodfellow *et al.*,

2016). In the area of SHM, ANNs are one of the most common methods to study the relationship between the bridge responses and loading factors. Bayes is used to determine conditional probability which is the likelihood of an outcome occurring, based on a previous outcome having occurred in similar circumstances. Compared with other AI algorithms Bayes-based Neural Network (BANN) has the following characteristics:

- A single-layer feed-forward neural network.
- Quicker learning process.
- Better generalisation.
- Quantification of uncertainty of predictions.

The last character is extremely important since sensors on the structures bear errors or outliers which are detrimental to the success of structural condition assessment. In the GeoSHM data analytics toolbox, the BANN is employed to generate a non-linear regression model to estimate time-dependent lateral and heaving responses with respect to variation of wind, temperature, and traffic. Inputs and outputs of the regression model are 10-minute average statistics and the use of BANN for monitoring data analysis is described in Figure 9.

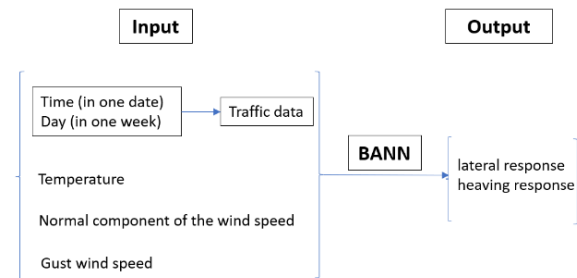


Figure 9. Input and output of the BANN algorithm.

The formula of the Bayesian inference is (Eq. 1):

$$p(\theta|D) = \frac{p(D|\theta) \cdot p(\theta)}{p(D)} \quad (1)$$

where  $p(\theta)$  = prior probability of a parameter  $\theta$  before having seen the data  
 $p(D|\theta)$  = called the likelihood and is the probability of the data  $D$  given  $\theta$   
 $p(\theta|D)$  = posterior probability of  $\theta$  given the data  $D$

Instead of considering a single answer to a question, Bayesian methods allow us to consider an entire distribution of answers which can solve the issues like regularisation (overfitting or not), model selection/comparison and cross-validation data set separation.

Empowered with the BANN, a new rolling assessment and updating approach is developed for the GeoSHM project to detect structural changes of the Forth Road Bridge as shown in Figure 10. The first row in this figure is the time series comparison between the measured

mean lateral movements and those of predicted with the BANN. The second row includes the difference of the two time series in the comparison (called as residual), the upper and lower thresholds determined using at least one year monitoring data (loading and response) and daily mean residual which is used to assess the structural changes. It is apparent that after 13 February 2017 the daily means are either close to or moved out of the set thresholds. Further investigation reveals that on this date the maintenance team had completed the truss end link repair at the north east main span which changed the dynamic characters of the bridge ([www.theforthbridges.org/forth-road-bridge/maintenance/major-projects/truss-end-links-repair](http://www.theforthbridges.org/forth-road-bridge/maintenance/major-projects/truss-end-links-repair)).

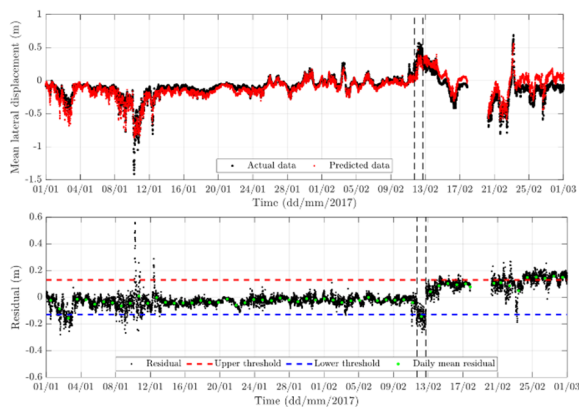


Figure 10. Detection structural changes in the Forth Road Bridge.

## VI. CONCLUSIONS

In this paper the authors discussed four aspects in establishing the structural health monitoring systems of long-span bridges. There is a wide range of smart sensors could be used to monitor loading, response and environmental factors but under the journey to establish digital twins to support timely and informed SHM decision-making both the sensors' quality and density need to be improved. Wireless communication might be a good option when other means of data transmission fail to work, and authors have demonstrated how a long range Wi-Fi could bridge this gap. Large and high-quality monitoring data are the basic requirement for an SHM system and to manage these data a data strategy is essential for building a successful and long lasting SHM. Using the GeoSHM project as an example the authors presented in detail what should be covered in the data strategy development. This paper also analysed the pros and cons of cloud-computing technique for an SHM system and according to the experience of the authors' cloud-computing is a great progress in the SHM system architecture design. Finally, the authors introduced their efforts in successfully using the BANN for the structural change detection of the Forth Road Bridge and discussed the benefits in the integrated uses of Digital Twin (DT) and artificial intelligent (AI) for smart

monitoring of bridges. In summary, integrating smart sensory system, IoT, cloud-computing, DT and AI will greatly benefit the monitoring and inspection work of long-span bridges.

## VII. ACKNOWLEDGEMENTS

The European Space Agency is acknowledged for support the GeoSHM FS and Demo projects, commenced from 2013 until 2019 and in both cases the first author was the overall project leader. The GeoSHM consortium consists of colleague from the University of Nottingham in the UK, UbiPOS UK Ltd, Leica Geosystems Ltd, GFZ in Germany, Geomatic Ventures Ltd and its supporting organisations such as Amey plc, BRDI of China Railway, Bear Scotland, Transport Scotland, AECOM, Geoelectron/Stonex. The first author of this paper has taken the liberty to use some elements from the GeoSHM R&D activities and appreciated all the consortium members consistent contributions in developing this ESA flagship project.

## References

- Black, A. P. (2022). 2022 Bridge Report. *The American Road & Transportation Builders Association*.
- Campbell, R.M., P. Fidler, and P. Vardanega (2016). Bridge Monitoring – A practical guide. *ICE Publishing*, London.
- Goodfellow, I., Y. Bengio, and A. Courville (2016). Deep Learning. *MIT Press*, Cambridge, MA, US.
- Liu, Z., G. Shi, X. Meng, and Z. Sun (2022). Intelligent Control of Building Operation and Maintenance Processes Based on Global Navigation Satellite System and Digital Twins. *Remote Sensing*, Vol. 14, No. 6.
- Maguire, J. (2019). Creating a Data Strategy. *Gartner Research*. [access on 30 May 2022]
- Meng, X., D. T. Nguyen, and X. Yilin (2018a). Design and Implementation of a New System for Large Bridge Monitoring—GeoSHM. *Sensors*, Vol. 18, No. 775.
- Meng, X., R. Xi, and Y. Xie (2018b). Dynamic Characteristic of the Forth Road Bridge Estimated with GeoSHM. *The Journal of Global Positioning Systems*, Vol. 16, No. 4.
- Nguyen, D. T., X. Meng, J. Owen, Y. Xie, P. Psimoulis, and G. Ye (2019). Application of Artificial Neural Network on SHM of Long-span Bridge. In: *Proc of 4<sup>th</sup> Joint International Symposium on Deformation Monitoring (JISDM)*, 15-17 May 2019, Athens, Greece.
- Psimoulis, P., X. Meng, J. Owen, Y. Xie, D. T. Nguyen, and J. Ye (2017). GNSS and Earth Observation for Structural Health Monitoring (GeoSHM) of the Forth Road Bridge. In: *Proc of SMAR 2017 - 4<sup>th</sup> Conference on Smart Monitoring Assessment and Rehabilitation of Civil Structures*, Zurich, 13-15 September 2017.
- RAC (2021a). [www.racfoundation.org/wp-content/uploads/RAC\\_Foundation\\_Bridge\\_Maintenance\\_GB\\_2020.pdf](http://www.racfoundation.org/wp-content/uploads/RAC_Foundation_Bridge_Maintenance_GB_2020.pdf). [access on 29 May 2022]
- RAC (2021b). [www.racfoundation.org/media-centre/number-of-substandard-road-bridges-on-the-rise-again](http://www.racfoundation.org/media-centre/number-of-substandard-road-bridges-on-the-rise-again). [access on 29 May 2022]

- Ray, P. P. (2018). An Introduction to Dew Computing: Definition, Concept and Implications - IEEE Journals & Magazine. *IEEE Access*, Vol. 6, pp. 723–737.
- Roberts, G. W., C. Brown, and X. Meng (2012). Deflection and Frequency Monitoring of the Forth Road Bridge, Scotland, by GPS. In: *Proc. Of the Institution of Civil Engineers Bridge Engineering*, Vol. 165, No. BE2, pp. 105–123.
- Xu, Y., and Y. Xia (2012). Structural Health Monitoring of Long-Span Suspension Bridges. *Spon Press*, London and New York.
- Yang, Y., Y. Mao, and B. Sun (2020). Basic Performance and Future Developments of BeiDou Global Navigation Satellite System. *Satellite Navigation*, Vol. 1, No. 1.
- Zhao, R., K. Zheng, and X. Wei (2020). State-of-the-art and Annual Progress of Bridge Engineering in 2020. *Advances in Bridge Engineering* (2021) Vol. 2, No. 29.

# Multisensor monitoring of ground movements over large areas to conduct the change from the active underground hard coal mining ages to the post-mining era

Volker Spreckels

RAG Aktiengesellschaft, Im Welterbe 10, 45141 Essen, Germany, ([volker.spreckels@rag.de](mailto:volker.spreckels@rag.de))

**Key words:** *Ground movements; geometric monitoring; dynamic network adjustment; levelling; GNSS; InSAR; time series; 4D-database; Double Corner Reflector*

## ABSTRACT

End of 2018 about 300 years of underground deep hard coal mining in Germany came to an end. Under regard to the ordinances of the mining authorities, RAG Aktiengesellschaft (RAG) further on remains responsible for the effects of the former underground mining in the post-mining era (Hager and Wollnik, 2016). The current and future geometric monitoring based on official federal reference networks concerns the tasks to record the fading mining induced subsidence movements and to detect the beginning uplifts to the earth surface resulting from to the controlled, ordinated flooding of the underground mine building. The geometric monitoring of the earth surface had up to now steadily been adapted to the state of the art by the integration of research and development projects (R&D) into day-to-day business, like for GIS, “4D”-databases, terrestrial GNSS surveying, high-end photogrammetry and InSAR remote sensing techniques, following national (DIN) and international standards (CEN, ISO). With the participation of Saarland’s federal ordnance survey, LVGL<sup>1</sup>, the reformation of the traditional, current surveillance networks to a modern Multisensor - Referencestation Network (MSST Network) has been realized in spring 2022 by a GNSS- and InSAR-based ground movement cadastre (SaarBoBeKa). A close cooperation with the companies ALLSAT<sup>2</sup> and GEOTEC<sup>3</sup> led to the development of an innovative time-variant network adjustment method for long time series of GNSS monitoring stations.

## I. INTRODUCTION

During the centuries of underground hard coal mining activities in Germany local subsidence reached amounts of up to 25 meters. For the post-mining regions, the controlled slowly flooding of the underground mine buildings over a time span of several years will lead to some decimeters of uplift in the Ruhr Area, the Ibbenbueren Area and for the Saar Area (Rosner *et al.*, 2014).

Since autumn 2020 RAG and since March 2022 the ordnance survey of the Saarland (LVGL) run a common monitoring system of Multisensor - Referencestations (MSST) see (Spreckels and Engel, 2022).

The MSST combine a Double Corner Reflector (D-CR) for InSAR-monitoring, a GNSS station and levelling points to integrate it to official federal position- and height-reference systems, like LGLV’s innovative and new ground movement cadaster “*Saarlaendisches Bodenbewegungskataster SaarBoBeKa*” (SaarBoBeKa, 2022), see Figure 1.

First works on GNSS-networks started in 2014 when RAG and ALLSAT to set up a GNSS monitoring over one active longwall mining in the Ruhr Area. By and by the MSST-concept developed so that in december 2021 the GNSS- / MSST-monitoring concept of RAG could be realized in the Ibbenbueren Area (Figure 2). In 2022 this

concept will be implemented in the Ruhr Area (Figure 3).

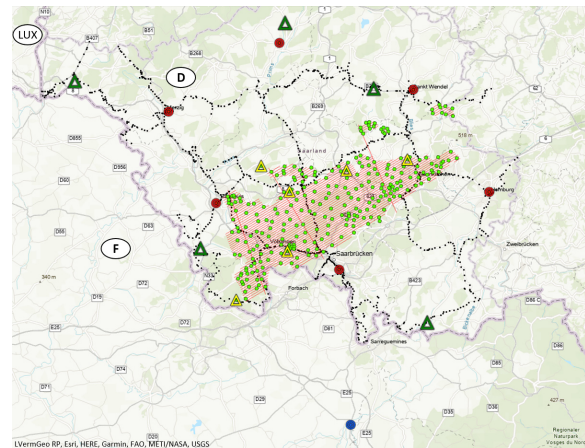


Figure 1. Monitoring concept of LVGL, OBA and RAG in the Saarland: LVGL-MSST (green triangles), RAG-MSST (yellow triangles), SAPOS GNSS stations (red circles), RGP-France GNSS station (blue circle), LN 2019 (black dots), aerial flight strips (red lines), GCP (green dots). Mapped area 90km x 70km. Image courtesy RAG.

MSST will provide robust, high accurate absolute coordinate measurement data within a single station e.g. for levelling, for GNSS measurements of ground

<sup>1</sup> LVGL: Landesamt für Vermessung, Geoinformation und Landentwicklung des Saarlands, Deutschland

<sup>2</sup> ALLSAT: ALLSAT GmbH – Die GNSS Spezialisten. Sokelantstr. 5, 30165 Hannover, Deutschland.

<sup>3</sup> GEOTEC: GEOTEC – Geodaetische Technologien GmbH, Heinrich-Heine-Weg 69, 30880 Laatzen, Deutschland.

control points (GCP) and GNSS-positions of projection centers of aerial flights, for airborne laser scanning (ALS/LIDAR) as well as for UAV data. The D-CR serve as reference points in X-, C- and with large size, for L-band SAR-data of radar satellites.

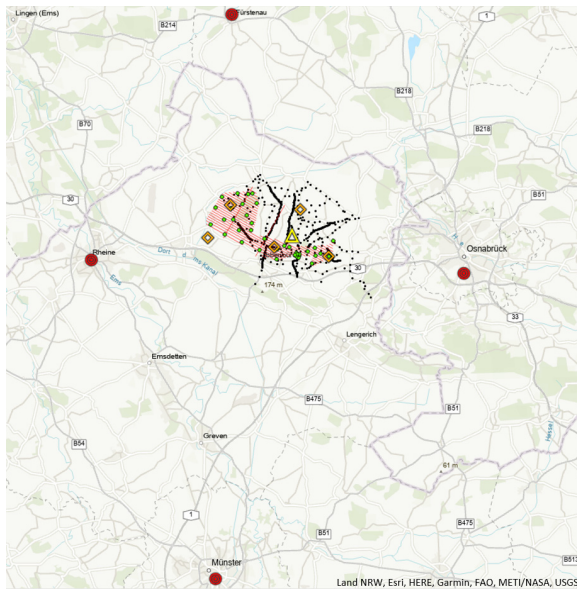


Figure 2. Monitoring concept of RAG for Ibbenbueren. MSST with DCR600 (yellow triangle), GNSS-stations (orange rhomb), SAPOS GNSS-stations (red circles), Levelling Points and LN 2019 (black dots), aerial flight strips (red lines), GCP (green dots). Mapped area 64 km x 65 km. Image courtesy RAG.

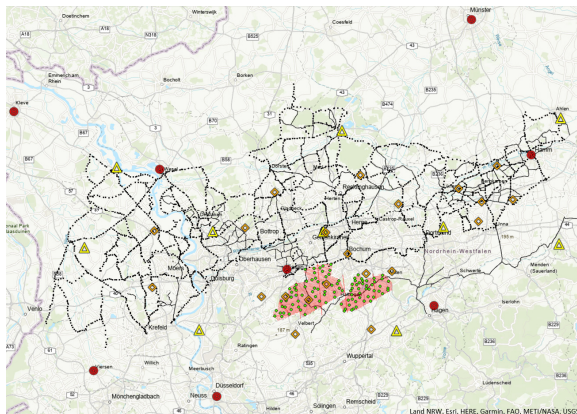


Figure 3. Monitoring concept of RAG in the Ruhr Area. Planned transportable MSST-stations (yellow triangles), GNSS-stations (orange rhomb), SAPOS GNSS-stations (red circles), LN 2020 (black dots), aerial flight strips (red lines), GCP (green dots). Mapped area 145km x 90km. Image courtesy RAG.

For about 150 years terrestrial levelling is the most accurate and precise measurement technique with the longest time series of height measurements in the Ruhr Area. So, leveling still is and will further on be one base for all ordinances of the mining authorities for the geometric monitoring of the earth surface.

In the 1990's GNSS techniques evolved but still do not reach the accuracy of levelling. Current large area surveying methods like aerial photogrammetry and ALS used in RAG's workflows *e.g.* for the early detection of sinkholes are connected to tie points measured by GNSS within the federal reference network of the German *Satellite Positioning Service (SAPOS)*<sup>4</sup>. Since 1999 RAG is using diverse InSAR techniques for the large area monitoring of mining induced ground movements (Strozzi *et al.*, 2001). These methods have a high inner accuracy but do need clearly detectable point-signals in the radar data, like from exactly defined D-CR of MSST, to connect and to combine SAR-data with the other monitoring methods. A short overview will be given in following:

#### A. Levelling

For the active mining regions of the Ruhr Area wide area levelling have been more or less regularly performed from 1873 on, bi-annually since 1948 for the region east of the river Rhine. The design of the levelling network changed over the time, following the active mining areas from the southern old mining regions at the river Ruhr northward towards the river Lippe. In the 1970ies the so called "Leitnivellement" (LN), federal high precision levelling campaigns of the survey authorities, have been implemented in NRW. In 2018 about 1.240 km of high precision levelling had been measured on about 2.300 points for the Ruhr Area (Boje *et al.*, 2008), 200 km of LN in the Saarland and 142 km LN for the Ibbenbueren Area. In future, LN will be performed in 5-year-cycle in NRW from 2025 on (Riecken *et al.*, 2019) and from 2024 on in the Saarland.

#### B. GNSS

In 2004 RAG introduced special transformation parameters for high precision GNSS measurements to harmonize own measurements from former diverse local reference systems in RAG's areas of responsibility (Spreckels 2003). Since 2014 the methods for GCP measurements of aerial image flights have been updated in R&D studies with ALLSAT to an absolute repeat precision of better than  $\pm 1,5$  cm in position and height. For the GNSS time series new time-dependent dynamic network adjustments (DNA) of continuous GNSS monitoring data of reference stations have been developed for the program system PANDA<sup>5</sup> within the R&D project "GNSS-Monitoringnetze" by GEOTEC (Niemeier and Tengen, 2022) and have successfully been implemented into ALLSAT's GNSS-Portal GLOMON<sup>6</sup> (Schulz and Schäfer, 2022).

<sup>4</sup> SAPOS: Satellitenpositionierungsdienst der deutschen Landesvermessung. <https://sapos.de>

<sup>5</sup> PANDA: Programmsystem zur Ausgleichung von geodaetischen Netzen zur Deformationsanalyse. [www.geotec-gmbh.de/en/panda/](http://www.geotec-gmbh.de/en/panda/)

<sup>6</sup> GLOMON: System for GNSS monitoring [www.global-monitoring.de](http://www.global-monitoring.de)

### C. Aerial Photogrammetry

The Over RAG's near surface old mining areas annual aerial flights with onboard combined high-resolution aerial image cameras and ALS are performed since 2015 for the automated detection of sinkholes (Kipp *et al.*, 2022). Due to the flying altitude the cameras reach a ground sampling distance (GSD) of 3 cm to 4 cm and ALS records about 10 points/m<sup>2</sup>. Here a very high repeat precision is needed: 10 cm of deviations on the ground have significantly to be detected between two flight campaigns. So the whole process of: GNSS - GCP measurements, positioning accuracy of the aerial images' projection centers, INS/IMU - navigation data for ALS and the aero-triangulation - has to happen with a cumulated absolute accuracy of better than  $\pm 3$  cm for the whole covariance propagation (Spreckels *et al.*, 2016).

### D. Satellite-based radar interferometry (InSAR)

Since 1999 RAG follows and utilizes the evolving methods of SAR interferometry for the detection of mining induced surface movements. Beginning with Differential SAR interferometry (DInSAR), followed by Persistent Scatterer Interferometry (PSI) and current modern multi-orbit decomposition analyses from ascending and descending orbit data collected by current X-, C- and former L-Band radar satellites. Hereby larger areas than before can be monitored with the meanwhile commonly known potential and the limitations for the detection of surface movements *e.g.* in "Line-of-Sight" (LOS). The LOS measurements can be calculated to surface movements into vertical- and into east-west direction components with decomposition methods (Yin and Busch, 2018).

### E. Multisensor-Referencestations (MSST)

For RAG it is mandatory to relate all measurement data at highest precision to be able to guide standards for the geometric monitoring in the near surface old mining areas and the post-mining regions that could be affected by the rise of the underground mine water level due to the controlled flooding of the former mine buildings. From 2006 on, together with the Institute of Geotechnical Engineering and Mine Surveying at the Clausthal University of Technology (IGMC), RAG installed different kinds of single corner reflectors (CR) over active mining areas in R&D projects for X-, C- and L-band descending orbit satellite data. The changes in position and height had been validated by levelling and static GNSS methods (Walter *et al.*, 2009).

Today, all the above from A. to D. listed measurement methods can be combined in one single station. A D-CR can be tailored in size according to his task as well as the kind of GNSS antennas to be mounted. All D-CR do have special marks and targets even for levelling measurements. From the early discussions to daily practice RAG has designed different prototypes that

have been realized in cooperation with LVGL and Allsat. For one MSST-design a patent is pending (Patent 2021).

The MSST shall serve as a reference for several decades. So, a robust station has been designed, with a solid reinforced concrete foundation of 2 m x 2 m x 2 m, an absolute calibrated chokering antenna and a 1 cm solid stainless steel-plate D-CR. The dimension of the size needs to fulfill the requirements: D-CR of 2 m in diameter with 1 m edge length is suitable for X-, C- and L-band (see Figure 4).



Figure 4. RAG's MSST for Saarland's SaarBoBeKa. Left: reinforced concrete foundation 2m x 2m x 2m, lightning rod, JAVAD RingAnt-G3T GNSS chokering antenna, D-CR  $\varnothing 2,0$ m and levelling points in foundation and D-CR. Right: solar power supply, weather sensors, mobile radio antenna, equipment box. Image courtesy ALLSAT & RAG.

A 2 m D-CR can also be founded on a transportable platform and the GNSS-antenna can be mounted in the center or terrestrial measurement targets in the center and on the flanks of the D-CR (see Figure 5).

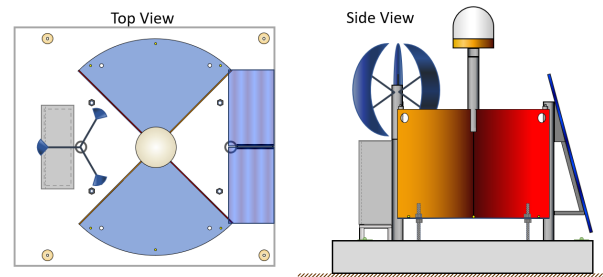


Figure 5. Top view and side view sketches of a fully equipped and self-supplying transportable MSST,  $\varnothing 2,0$ m, to be installed in the Ruhr Area. Image courtesy RAG.

A smaller MSST, the so called DCR600 is now available from ALLSAT. It is a D-CR with 120 cm in diameter, a

centered GNSS antenna, 5/8" adapters for terrestrial targets and it has a mounting for common terrestrial pillars or tripods. It can easily be mounted and de-mounted for temporal projects in smaller regions or for a local object monitoring (see Figures 6 and 7).



Figure 6. DCR600, Ø1,2m with GNSS-Antenna and weather-sensors. Image courtesy ALLSAT & RAG.

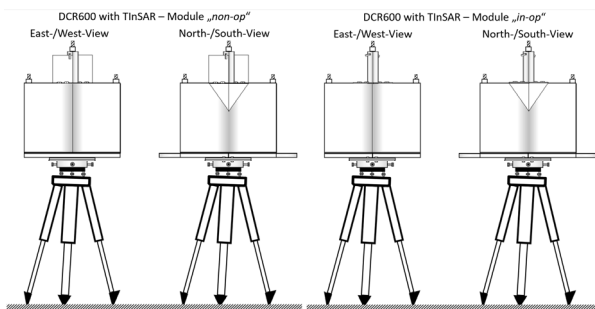


Figure 7. Sketch of the with TInSAR-module extended DCR600. From left to right: TInSAR unit "non-op": east/west view, north/south view, TInSAR unit "in-op": east/west view, north/south view. Image courtesy ALLSAT & RAG.

All MSST can additionally be equipped with weather-sensors. The data transfer can be guided via router to cellular networks or by LAN. The energy supply can be assigned to the power net, solar and/or wind energy.

Several not yet published analyses of LVGL, Allsat and RAG proved that there are no multipath effects from the D-CR to the GNSS antenna.

#### F. Guidance in "4D" – Database: GeoMonPlus (GMP)

In 2005 RAG implemented the first prototype of the GeoMon point-database set up by IGMC within a RAG R&D project (Kamphans *et al.*, 2008). GeoMon has now completely been overworked and brought to the current state of art (Bechert *et al.*, 2022). Herein, the

time stamp of the measurement is one of the essential main data classification criteria.

All the named surveying and remote sensing data can be georeferenced with most possible accuracy via GNSS, D-CR and levelling in one station - and therefore unambiguously guided in databases like GMP.

#### G. Standardization

These days in Germany there are several groups working on manuals and standards for using InSAR techniques in day-to-day business. The German Mine Surveyor Association (DMV)<sup>7</sup> is currently working on a manual how to handle InSAR within the ordinances of the federal mining authorities and the daily work within the frame of the ground movement monitoring.

A working group of the German Adv<sup>8</sup> is currently working on a manual how to handle InSAR within the tasks and ordinances of federal surveying authorities.

At least the German DIN standards working group NA 005-03-02 "Photogrammetry and Remote Sensing" is working on the new DIN standard 18740-9 "InSAR – Radar-Interferometry for ground movement detection" (Spreckels 2022). Here, one focus is set on how international standards are already available and have come into effect, like the standards of ISO/TC 211 "Geographic Information/Geomatics", ISO/TS 19159-3:2018 "Calibration and validation of SAR/InSAR sensors". The aim is, that all these standards can be coordinated with each other.

All of the topics above from A. to F. are parts of the discussions within the named working groups.

## II. GNSS/MSST– CONCEPT IN RAG'S REGIONS

The following chapter will present the current state of the geometric monitoring in the hard coal post-mining regions Saar Area, Ruhr Area and Ibbenbueren.

### A. Saarland

The entire post-mining region of RAG in the Saar Area to be monitored is about 1.500 km<sup>2</sup>. For the near surface old mining regions about 225 steady marked GCP for combined aerial image flights with ALS have annually to be measured. More than 9.600 aerial images are recorded every year for 280 km<sup>2</sup> (see Figure 1).

For InSAR monitoring RAG has installed six MSST with solar and wind energy power supply, equipped with JAVAD RingAnt-G3T GNSS chokering antennas (see Figures 4 and Figure 8). The heavy concrete 2 m x 2 m x 2 m reinforced concrete foundation and the 2 m D-CR bear several levelling points.

LVGL has finished five nearly identical constructed MSST in March 2022, equipped with Leica AR25 chokering GNSS antennas, LAN or LTE connection and plugged to the power net (see Figure 9). LVGL performs

<sup>7</sup> DMV: Deutscher Markscheider Verein, Arbeitskreis „Interferometrie“

<sup>8</sup> Adv: Arbeitsgemeinschaft der Vermessungsverwaltungen Deutschlands – Arbeitskreis 6, Raumbezug.



the InSAR/PSI processing for the whole federal state of the Saarland, provides annually results to OBA and to RAG and publishes the results as open data in SaarBoBeKa (Spreckels and Engel, 2022).



Figure 8. RAG's MSST Stangenmuehle/Fenne, Saarland, LVGL nr. 6707 0 402 00, as to be seen in RAG's orthophoto at 3 cm GSD, aerial flight campaign at noon, April 25<sup>th</sup>, 2021. Mapped area 15 m x 14 m. Image courtesy RAG.



Figure 9. LVGL's MSST Felsberg for Saarland's SAARBOBEKA on a reinforced concrete foundation 2 m x 2 m x 2 m, Leica AR25 GNSS chokering antenna, D-CR Ø2,0m and levelling points in foundation and D-CR. Image courtesy LVGL.

#### B. Ruhr Area

In the Ruhr Area the entire post-mining region in RAG's responsibility to be monitored is about 7.000 km<sup>2</sup>. Here MSST, GNSS, levelling, combined aerophotogrammetry and ALS flight campaigns and InSAR-methods will conduct the geometric surface movement monitoring.

The near surface old mining area is about 300 km<sup>2</sup>, whereof the sinkhole affected old mining area in RAG's responsibility is about 140 km<sup>2</sup>. Here about 100 steadily marked GCP for aerial image flights at 3 cm to 4 cm GSD have to be measured annually, see Figure 3.

For the whole post-mining region RAG will install ten transportable MSST in 2022, equipped with calibrated Leica AR25 GNSS chokering antennas, solar- and wind energy supply (see Figure 5). In total 21 further GNSS-stations with JAVAD RingAnt-G3T GNSS chokering antennas will be constructed, the first of them have been installed from 2014 on.

Here first evaluations concerning the "Dynamic Network Adjustment" (DNA) regarding time-variant approaches have been performed, so that for some SAPOS- and for RAG's GNSS-reference stations individual movement components could be detected with measurement data for more than two years (Niemeier and Tengen, 2022). See section III for more details.

#### C. Ibbenbueren

For the smaller Ibbenbueren near surface old mining area of about 50 km<sup>2</sup> there are 40 steadily marked GCP annually measured for the flight campaign with high resolution arial images and ALS. Since 2021 the entire post-mining area of about 200 km<sup>2</sup> is supplied with one D-CR600 and additional five GNSS-stations, all equipped with Tallysman VP6000 antennas. For this region radar-interferometric multi-orbit decomposition analyses are performed with Sentinel-1A/B radar scenes from 2019 on.

### III. GNSS NETWORKS

For the time of the post-mining era RAG further on operates within three different post-mining regions in Germany. Here the geometric monitoring affords regional reference networks for each area. The height reference is supplied by the elevation cadasters of Geobasis NRW and Saarland's LVGL. For GNSS measurements the German federal SAPOS network defines the reference for the positioning -and height-determination.

All of RAG's GNSS measurements are transmitted to ALLSAT's GLOMON portal and processed for the three post-mining regions.

#### A. Global Monitoring - GLOMON

GLOMON supports the monitoring for the detection of deformations or surface movements using GNSS and other sensors by an automatic processing of GNSS data for results with highest precision and accuracy in the range of a few mm. The SAPOS reference stations are the highest order of federal reference points and can be densified by further GNSS stations or MSST. Like in GMP (Bechert *et al.*, 2022) all 3D coordinates are created for each monitoring station with an exact time stamp, allowing the web-based visualization of time series. Within RAG's R&D project "GNSS-Monitoringnetze" a new innovative concept for the adjustment of time-variant coordinates, the "Dynamic Network Adjustment (DNA)", has been developed by GEOTEC and

implemented in GLOMON (see Schulz and Schäfer, 2022; Niemeier and Tengen, 2022).

### B. The “Dynamic Network Adjustment (DNA)”

Since decades the discrepancy exists that geodesists monitor changes of the earth surface or for large engineering structures. The results are often presented in a suboptimal manner: In most cases, the variations of an object or an area are documented in coordinates for representative points with time stamps or with displacements rates like absolute values or velocities. In our days tightly clocked measurements from sensors deliver continuous data, but there is no complete concept to treat variations continuously within the coordinate approach. One of the new developments is the integration of the program system PANDA from GEOTEC into ALLSAT’s GLOMON portal which supports this innovative time-variant, dynamic network adjustment approach (DNA).

This DNA procedure modifies the approach of stable reference points for geodetic monitoring tasks, which has been valid for decades. The classic approach to such measurements is the assumption of a stable reference frame over a long period of time, based and fixed on a zero measurement. Local measurements are connected to higher-level, supposedly stable reference points, such as the first order SAPOS GNSS reference stations. But even these reference points can be affected by individual movements (see Figure 10).

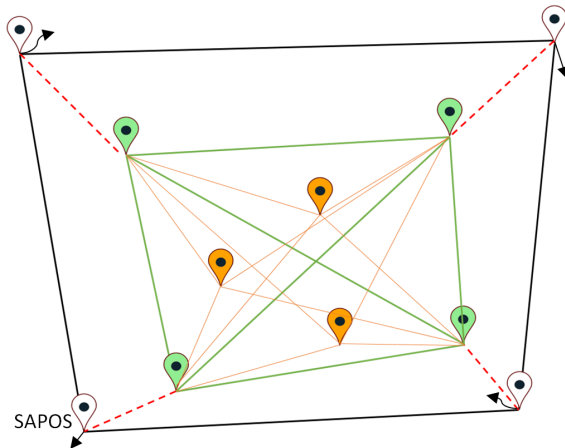


Figure 10. Stability and network hierarchy - first order SAPOS GNSS reference stations (black), GNSS reference stations (green), e.g. GCP for aerial flight campaigns (orange) (Spreckels *et al.*, 2016).

Conventionally regarded, reference points are assumed as stable by definition. But their real movement behavior will directly be projected onto the local measurements like e.g. tie point measurements on ground control points (GCP) for aerial image flight campaigns. To solve this problem in the new DNA approach, all GNSS stations are handed over to a deformation analysis after the post-processing and the network adjustment in order to detect displaced points. Now, the concept of time-invariant reference station

coordinates is reconsidered: this means that reference stations detected as displaced are not fundamentally excluded from the network evaluation, but their movement behavior is described by time-variant coordinates. With the introduction of movement models for reference stations, their movements are no longer projected onto local measurements or monitoring stations (see Figure 11). This information can be used in the areas of interest, e.g. for the optimization of existing movement and deformation models.

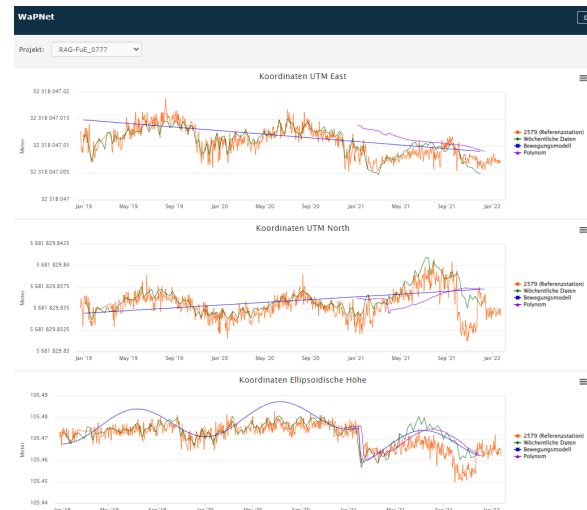


Figure 11. GLOMON time series for the SAPOS GNSS station no. 2579, from 01/2019 to 01/2022. Easting (top), northing (mid) and height (bottom): daily averages (orange). DNA: weekly averages (green), movement model (blue) and derived movement polynomial (purple). Image courtesy RAG & ALLSAT.

In this way, predictions about expected deformations can be made more reliable and can be applied for different specific measurement dates within the process chain of a workflow e.g. including different dates of aerial and UAV image flight campaigns and of their related GCP measurements (see Figures 12 and 13).

The aim of applying an individual movement behavior is to maintain reference points with slight movements as long as possible as reference points.

In case these points will be obtained as reference points, an identical stable and over the time equally balanced reference network configuration will be maintained as long as possible. This is a great advantage for a long-lasting geometric monitoring.

So, the advantage of obtaining the network configuration over a very much longer time is to keep the network parameters stable and robust. The strain and tension and gravity center of a special monitoring network will be kept for the comparison to former and future campaigns related on this network. The loss or change of the one or other reference point will cause more deviation to the network geometry over the time, that we can detect in recent time-invariant network adjustments.

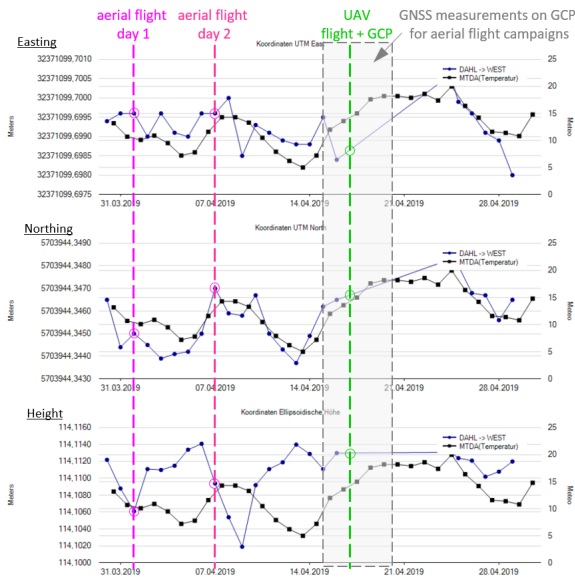


Figure 12. Time series for relative changes in easting (top), northing (mid) and height (bottom) of RAG's GNSS-reference station DAHL, overlain with data-recording dates for aerial image flights and GCP measurements (Spreckels *et al.*, 2016).

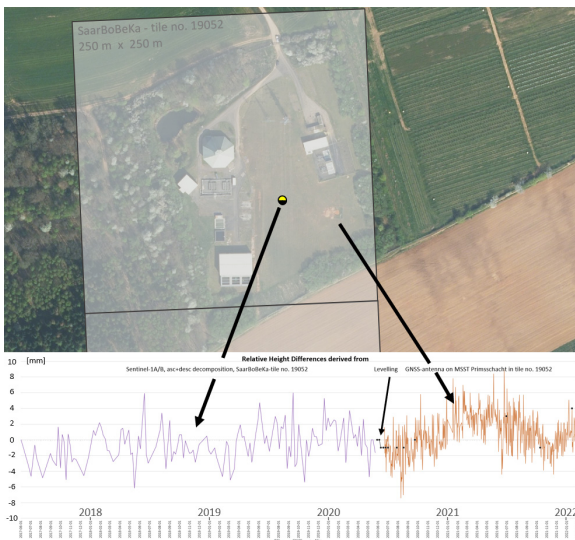


Figure 13. Time series (06/2017-02/2022) for relative vertical movements derived for a 250 m x 250 m tile, SaarBoBeKa - no. 19052, height difference spacing: 2 mm. RAG's levelling measurements (black dots). Decomposition (height component) of Sentinel-1A/B ascending and descending orbit (06/2017-06/2020) by LVGL (purple). GNSS time series (06/2020-02/2022) derived from RAG's MSST station Primsschacht, LVGL no. 6607 0 403 00 (orange). Mapped area 550 m x 330 m. Image courtesy LVGL and RAG.

It has to be taken into account, that the time series for the determination of an individual movement behaviour will take an observation time of at least two to three years for a significant estimation of long-term influences. With this DNA-approach the surveys for RAG's three mining regions are expected to be based on best estimated reference networks for the detection of ground movements and time series analyses. So, a reliable and robust coordinate reference will be established for all of RAG's remote sensing tasks and terrestrial survey of the earth surface as well as for

underground surveys like the 3D data capture of near surface openings (Kipp *et al.*, 2022).

#### IV. CONCLUSION AND OUTLOOK

Further work will focus on the improvement of the time-variant network adjustment with the integration of additional area wide data, like area-wide points *e.g.* from radar-interferometric PSI analyses that are available and soon be comparable to GNSS and levelling in the Saarland from LVGL's SaarBoBeKa (see Figure 13). To adapt all the terrestrial and remote sensing measurement data the needed interfaces between GLOMON and RAG's GMP "4D"-database will be developed as well as the data structure for the guidance of GNSS measurements, levelling, relative movements derived from PSI, on MSST and near GNSS-stations even with the possibility to adapt additional other sensor's data, *e.g.* from weather-sensors, in near future.

#### References

- Bechert, S., A. Schlienckamp, and V. Spreckels (2022). GeoMonPlus – Application for storage, allocation, exchange and visualization of historical and actual 4D-position-data within mining areas. In: *5<sup>th</sup> Joint International Symposium on Deformation Monitoring JISDM 2022*, Valencia, Spain, June 20-22, 2022, these proceedings.
- Boje, R., W. Gstirner, D. Schuler, and M. Spata (2008). Leitnivellements in Bodenbewegungsgebieten des Bergbaus – eine langjährige Kernaufgabe der Landesvermessung in Nordrhein-Westfalen. In: *Nachrichten aus dem öffentlichen Vermessungsdienst Nordrhein-Westfalen (NÖV)*, 3/2008, pp 33-42.
- Hager, S., and F. Wollnik (2016). Mine Surveying and Post-Mining Activities of RAG Aktiengesellschaft / Markscheidewesen und Altbergbau der RAG Aktiengesellschaft. In: *Mining Report Glückauf - Fachzeitschrift für Bergbau, Rohstoffe und Energie*, No. 3, 152. Jahrgang, Verlag Bergbau-Verwaltungsgesellschaft mbH, Herne, ISSN 2195-6529, June 2016, pp 224-232.
- Kamphans, K., D. Walter, W. Hanneman, W. Busch, V. Spreckels, and P. Vosen (2008). GIS-Einsatz im Monitoring bergbaubedingter Oberflächenbewegungen. In: *20. AGIT-Symposium Angewandte Geoinformatik, Salzburg, Austria*, Wichmann Verlag, ISBN 978-3-87907-464-8, July 2-4, 2008, pp 572-577.
- Kipp, A., A. Schlienckamp, and A. Ens (2022). Early detection, permanent monitoring and documentation of critical locations at the surface in mining areas. In: *5<sup>th</sup> Joint International Symposium on Deformation Monitoring JISDM 2022*, Valencia, Spain, June 20-22, 2022, these proceedings.
- Niemeier, W., and Tengen, D. (2022). Dynamic concepts to handle geodetic networks with continuous monitoring data in areas with ground movements. In: *5<sup>th</sup> Joint International Symposium on Deformation Monitoring JISDM 2022*, Valencia, Spain, June 20-22, 2022, these proceedings.
- Patent (2021). Referenzstation zur Nutzung in der großflächigen Bestimmung der Bewegung der Erdoberfläche in SAR-Anwendungen. Allsat GmbH, Hannover Germany, Spreckels, V. & M. Schulz. *Patent*

- application*, Deutsches Patent- und Markenamt, December 20, 2021, Az. 10 2021 131 933.1
- Riecken, J., B. Krickel, V. Gefeller, and P. Reifenrath (2019). Nutzung der Radarinterferometrie im geodaetischen Raumbezug. In: *Zeitschrift für Geodäsie, Geo-Information und Landmanagement (zfv)*, Vol. 144, issue 6, 2019, Wißner Verlag, DOI: 10.12902/zfv-0281-2019, pp 354-361.
- Rosner, P., M. Heitfeld, V. Spreckels, and P. Vosen (2014). Auswirkungen von Geländehebungen im Zuge des Grubenwasseranstiegs im Ruhrrevier. In: RuhrGeo Tag 2014, Bochum, Germany, March 27, 2014, pp 153-177.
- SaarBoBeKa (2022). Bodenbewegungskataster Saarland. URL:<https://geoportal.saarland.de/article/Bodenbewegungskataster/>. Last access: 2022-03-22.
- Schulz, M., and F. Schäfer (2022). GLOMON-Monitoringportal for storage, management, advanced processing and intelligent visualization of GNSS- and other sensors data. In: *5<sup>th</sup> Joint International Symposium on Deformation Monitoring JISDM 2022*, Valencia, Spain, June 20-22, 2022, these proceedings.
- Spreckels, V. (2003). Subsidence determination by different sensor types using standardized transformation parameters. In: *Joint ISPRS/EARSel Workshop "High Resolution Mapping from Space 2003"*, Oct. 6-8, 2003, Hannover, Germany, 6 pages.
- Spreckels, V. (2022). Status of the new German DIN standards project „InSAR – Radarinterferometry for the detection of ground movements“. In: *5<sup>th</sup> Joint International Symposium on Deformation Monitoring JISDM 2022*, Valencia, Spain, June 20-22, 2022, these proceedings.
- Spreckels, V., A. Schlienkamp, A. Greiwe, and L. Eberhardt (2016). Eignung von ALS, Aero- und UAS-Photogrammetrie zur Früherkennung und Erfassung von Tagesbrüchen. In: *36. Wissenschaftlich-Technische Jahrestagung der DGPF*, Band 25, Bern, Switzerland, June 7-9, 2016, ISSN 0942-2870, pp 97-112.
- Spreckels, V., and T. Engel (2022). Set-up and application of multisensor-referencestations (MSST) for levelling, GNSS and InSAR in the former mining regions Saarland and Ruhrgebiet within Germany. In: *5<sup>th</sup> Joint International Symposium on Deformation Monitoring JISDM 2022*, Valencia, Spain, June 20-22, 2022, these proceedings.
- Strozzi, T., U. Wegmueller, L. Tosi, G. Bitelli, and V. Spreckels (2001). Land Subsidence Monitoring with Differential SAR Interferometry. In: *Photogrammetric Engineering & Remote Sensing (PE&RS)*, Vol. 67, issue. 11, November 2001, pp 1261-1270.
- Walter, D., U. Wegmueller, V. Spreckels, D. Hannemann, and W. Busch (2009). Interferometric monitoring of an active underground mining field with high-resolution SAR sensors. In: *ISPRS Hannover Workshop 2009 - "High-Resolution Earth Imaging for Geospatial Information"*, Hannover, Germany, June 2-5, 2009, 6 pages.
- Yin, X., and W. Busch, (2018). Nutzung der Sentinel-1 Aufnahmekonfigurationen zur Ableitung von Bodenbewegungskomponenten im Rahmen eines radarinterferometrischen Bodenbewegungsmonitorings. In: *Tagungsband GeoMonitoring 2018*, Clausthal-Zellerfeld, Germany, March 1.-2., 2018, pp. 119-138. ISBN: 978-3-86948-627-7.

# Set-up and application of multisensor-reference stations (MSST) for levelling, GNSS and InSAR in the former mining regions Saarland and Ruhrgebiet within Germany

Volker Spreckels<sup>1</sup>, Thomas Engel<sup>2</sup>

<sup>1</sup> RAG Aktiengesellschaft, Im Welterbe 10, 45141 Essen, Germany, ([volker.spreckels@rag.de](mailto:volker.spreckels@rag.de))

<sup>2</sup> State Office for Survey, Geoinformation and Land Consolidation Saarland (LVGL), Von der Heydt 22, 66115 Saarbrücken, Germany, ([t.engel@lvgl.saarland.de](mailto:t.engel@lvgl.saarland.de))

**Key words:** *ground movement cadastre; SaarBoBeKa; geometric monitoring; levelling; GNSS; InSAR; persistent scatterer; double corner reflector*

## ABSTRACT

In 2017 the Mining Authorities *Oberbergamt des Saarlands* (OBA), the *State Office for Survey, Geoinformation and Land Consolidation Saarland* (LVGL) of the German federal state Saarland and the former mining company *RAG Aktiengesellschaft* (RAG) planned and set up a project to realize a modern network of so called multisensor-reference stations (MSST) for the monitoring of ground movements in post-mining and tectonically active regions. The MSST will serve as reference for the combined GNSS, Levelling and InSAR-based “*Bodenbewegungskataster Saarland (SaarBoBeKa)*”, the ground movement cadaster of LVGL. A MSST consists of a solid heavy double corner reflector (D-CR) suitable for X-, C- and L-Band ascending and descending orbit data, a calibrated permanent registering GNSS chocking antenna and levelling points, all founded in a heavy reinforced concrete block. Additional components are weather-sensors and data transmission units. The MSST will be included into the German SAPOS GNSS framework and height measurements to official levelling points are attached to the German Height Reference System DHHN2016. LVGL operates a network of five MSST, RAG added six MSST distributed over the mining affected area. All LVGL stations are prepared to serve as stations of the German SAPOS GNSS framework and for this have to be supplied by the power network and the data transfer has to be done by LAN or LTE. All of RAG’s MSST are powered by solar-cells and a small wind energy converter. The data transfer is performed by mobile communication to the GLOMON portal of ALLSAT. In GLOMON the RAG measurements are calculated by the program WapNet and sent to LVGL to be integrated in SaarBoBeKa. For the mining district of the Ruhr Area in the federal state of North Rhine-Westphalia (NRW) RAG is currently planning to construct and operate 10 MSST in 2022. The status of the MSST projects are presented.

## I. INTRODUCTION

In Germany several centuries of near surface and underground mining activities led to changes and impacts to the earth surface of several meters in position and height. Subsidence troughs and discontinuous movement behavior led to damages to the infrastructure and to the environment that had to be compensated and regulated. The active mining ended in the Saar Area in the year 2012 and in NRW in 2018, so that the mining induced ground movements meanwhile nearly completely faded away.

Now that the hard coal production has expired, RAG is still accountable for the mining legacies. These are long-term liabilities like polder measures, mine water management and groundwater purification as well as classical legacies, e. g. reclamation and environmental protection, the processing of mining damage as well as post-mining activities (Hager and Wollnik, 2016). One part of the post-mining activities is the geometric monitoring of surface openings, near-surface old mining areas and the surveillance of the earth surface whilst the ordinance, controlled partial flooding of the

former mine buildings (Spreckels *et al.*, 2018; 2020; Rudolph *et al.*, 2020).

For the three main hard coal mining regions in Germany, the Ibbenbueren Area, the Ruhr Area and the Saar Area up to now the classical precision levelling is still the official and most resilient survey method by ordinance of the federal mining- and survey-authorities.

During the past four decades GNSS-methods and since about two decades modern satellite based interferometric radar methods (InSAR) developed from research status to the use in day-to-day business. Now the connection between terrestrial high precision point and line measurements to area-wide distributed point determination is possible by targets that can be determined in each surveying method:

- Levelling points build the bridge to the official federal state height reference systems;
- GNSS-measurements are integrated into federal GNSS-reference networks for height and position;

- InSAR results can be referenced to the federal height and position networks by using multisensor-reference stations (MSST).

Following these requirements, a MSST consists of the components:

- Permanent GNSS-station;
- Double corner reflector (D-CR);
- Levelling points in the D-CR and founding;
- Additional needed sensors.

## II. SURVEILLANCE AREAS

For all mining regions a nearly indissoluble mixture of each other overlapping and interfering effects over the time appeared and have to be monitored in the post-mining era. The coal mining in the Ruhr area is supposed to start around the 13<sup>th</sup> century, for the Saar Area in the 15<sup>th</sup> century and in Ibbenbueren in the 16<sup>th</sup> century.

So overlaying effects like tectonics, active and post-mining activities, mine-water- and ground water management, large construction projects, climate change, water withdrawal, erosion, washout and possible sinkhole development characterize these regions.

### A. Saarland

In the year 2017 Saarland's federal mining authority OBA and federal survey authority LVGL agreed together with RAG upon a common development of an MSST-based network within the official reference networks for building up an InSAR-based ground motion cadaster, SaarBoBeKa.

The monitoring technique ordained by OBA up to then only included precision levelling over the more local areas of responsibility of mine sites. For the regional post-mining influences that are expected by the flooding of the underground hard coal mining buildings (Rosner *et al.*, 2014) an area-based monitoring backed on MSST and a thinned out precision levelling to a 5-year-cycle was ordained that started in 2019. The northern parts of the Saarland are affected by recent tectonic effects caused by the still active underground volcanism due to the Eifel plume located in 45 km to 400 km depth below the earth surface.

### B. NRW: Ruhr area and Ibbenbueren

In NRW the large area precision levelling, so called "Leitnivellement" (LN), first installed in 1873, will still be the common standard measurement technique but it will be thinned out to a 5-year-cycle from 2025 on. The ordinance survey Geobasis NRW is looking for operating the planned InSAR-based "Bodenbewegungskatster NRW" in 2022 (Riecken *et al.*, 2019).

For the Ruhr Area the challenge is the wide-spread region that had been under excavation for several centuries.

Even Ibbenbueren has a long mining history since the 16<sup>th</sup> century as a local mining region with specific tectonic structures (Goerke-Mallet, 2000).

## III. MULTISENSOR REFERENCE STATIONS (MSST)

For the three surveillance areas different kinds of MSST are realized or planned. The MSST shall serve as reference station for several decades and have to be specially designed for their monitoring purpose – simple, robust, durable, low maintenance, suitable for all radar sensors and orbits, easy to build and handle, and, as far as possible, forward looking to be prepared for coming sensors and techniques.

The current design has been chosen in consideration of the long operation time: the foundation is easy to build, the D-CR can easily be strictly aligned in east-west direction and equipped with different additional sensors.

The decision for non-adjustable CR is due to the experience in the Ruhr- and the Saar Area with the high expenditure of time and personnel for the re-orientation of CR to different satellite's orbits, as well for ascending and for descending orbits, see Figure 1 in Spreckels *et al.* (2008).



Figure 1. LVGL's MSST Hellendorf for Saarland's SaarBoBeKa on a deep and solid grounded reinforced concrete foundation 2 m x 2 m x 2 m, Leica AR25 GNSS chokering antenna, D-CR Ø2,0m and levelling points in foundation. Image courtesy LVGL.

The dimensions for the diameter of the D-CR and the steel plates had been calculated in analogy to optical reflectors taking into account the effective reflection area and the deviation of the reflector center (Joeckel and Stober, 1995) according to different radar satellite orbits's incidence and azimuth angles.

Additionally the experience with CR in the analyses of X-, C- and L-band radar sensor data within RAG's R&D projects since 2005 and even the mean lifespan of about ten to fifteen years for adjustable CR made of perforated sheet rounded up the final D-CR design: the D-CR consist of 1 cm solid stainless steel plates at a

diameter of 2 m and 1 m edge length. Measurement marks in the D-CR and the foundation allow to adapt and survey the D-CR in position and height. The reinforced concrete foundation contains measurement marks and is able to carry pillars or masts for permanent GNSS stations.

#### A. Saarland

In the Saarland the MSST of LVGL are part of the official federal geodetic reference system and in following special requirements are given (Figure 2). The MSST shall serve as a reference network for some decades and have to fulfill long life requirements. Since March 2022 LVGL operates five MSST for InSAR monitoring. The MSST are equipped with calibrated Leica AR25 chokering GNSS antennas, LAN connection and plugged to the power net. The heavy 2 m x 2 m x 2 m reinforced concrete foundation has been connected to the solid ground by concrete pillars where needed. The founding and the solid 2 m D-CR of 1 cm stainless steel plates bear several levelling points (see Figure 1).

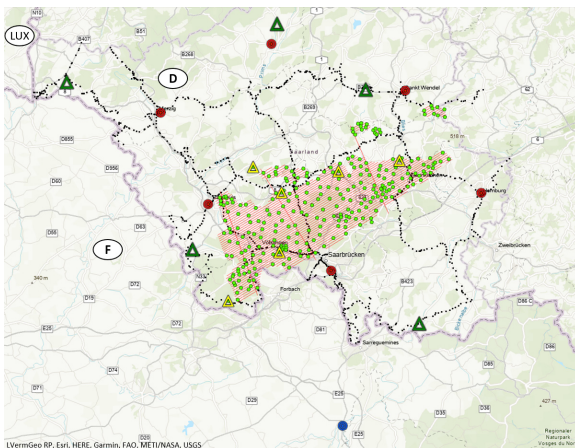


Figure 2. Monitoring concept of LVGL, OBA and RAG in the Saarland: LVGL-MSST (green triangles), RAG-MSST (yellow triangles), SAPOS GNSS stations (red circles), RGP-France GNSS station (blue circle), LN 2019 (black dots), aerial flight strips (red lines), GCP (green dots). Mapped area ~ 90 km x 70 km. Image courtesy RAG.

For the geometric monitoring of RAG's mining effected area six MSST operate since summer/autumn 2020. All MSST are equipped with weather-sensors, solar & wind energy power supply and with JAVAD RingAnt-G3T GNSS chokering antennas. The 2 m x 2 m x 2 m reinforced concrete foundation had been set as a solid block into the ground. The founding and the 2 m - D-CR, identical to LVGL, bear several levelling points (see Figure 3).

#### B. Ruhr area NRW

The Ruhr Area, like Ibbenbueren, see shapter C, lies in NRW where no official ordination of the mining authorities for an InSAR-based ground movement monitoring is given. But Geobasis NRW is working on

the InSAR-based *Bodenbewegungskataster NRW* that is expected in 2022. So, for this large spread monitoring region the MSST have to fulfill long life requirements but they will not be parts of the official point reference in NRW (Figure 4).



Figure 3. RAG's MSST Primsschacht for Saarland's SaarBoBeKa. From left to right: wind & solar power supply, equipment box, reinforced concrete foundation block at size 2 m x 2 m x 2 m, D-CR Ø2,0 m, JAVAD RingAnt-G3T GNSS chokering antenna. Image courtesy ALLSAT.

The solid D-CR at a diameter of 2 m and 1 m edge length is identical to the Saarland D-CR. In contrast to the MSST used in the Saarland no heavy foundation is necessary and the D-CR can be founded on a transportable reinforced concrete plate where all needed equipment can be mounted. The advantages of this design are, that in a case of need, this platform can be hooked up and transported to some other place. Currently the static for the construction of the concrete platform of 2,3 m to 2,2 m is computed. Figure 5 shows sketches of the fully equipped transportable MSST.

In agreement with *Geobasis NRW* these MSST will operate with calibrated Leica AR 25 GNSS chokering antennas that are used on NRW's SAPOS GNSS stations.

#### C. Ibbenbüren, NRW

The geometric monitoring for the small Ibbenbueren area is done by standard precision levelling attached to the LN but even here no official ordination for an InSAR-based ground movement monitoring is given. RAG performs the geometric monitoring with five GNSS stations and a smaller type of MSST that is suitable for X- and C-band radar data. The DCR600 is commercially available by ALLSAT. It is a D-CR with 120 cm in diameter, a centered GNSS antenna and four 5/8" adapters for terrestrial targets. Weather-sensors complete the equipment. It has a mounting *e.g.* for terrestrial pillars or tripods and a special roof mount. The DCR600 is designed for a flexible use in smaller regions or for a local object monitoring (see Figure 6).

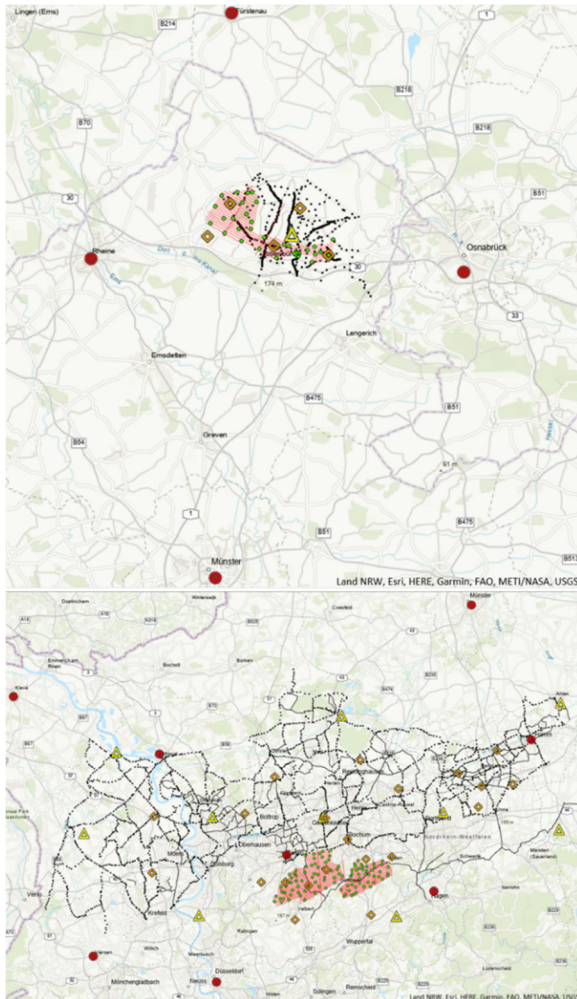


Figure 4. Monitoring concept of RAG in NRW. Ibbenbüener (top) and Ruhr Area (bottom): MSST-stations (yellow triangles), GNSS-stations (orange rhomb), SAPOS GNSS-stations (red circles), LN (black dots), aerial flight strips (red lines), GCP (green dots). Mapped area: ~ 64 km x 65 km (Ibb.) and ~ 145 km x 90 km (Ruhr). Image courtesy RAG.

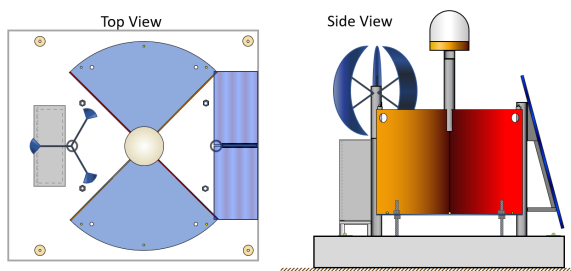


Figure 5. Top view (left) and side view sketches of a fully equipped and self-supplying transportable MSST, Ø2,0 m, to be installed in the Ruhr Area. Image courtesy RAG.

#### IV. GERMAN GROUND MOTION CADASTER

The availability of the free Sentinel-1A/B radar satellite data since 2014 pushed the development and applications for InSAR-based methods from research status into daily practice. The “*BodenBewegungsdienst Deutschland*” (BBD) is a Germany-wide InSAR-based ground motion service set up in 2019 by the Federal Institute for Geoscience and Natural Resources (BGR)

and the German Aerospace Center (DLR) (BGR, 2019). But: the BBD has no sovereign, governing character.



Figure 6. DCR600, Ø1,2 m with GNSS-Antenna and targets. View from west (left) and south (right). Image courtesy ALLSAT & RAG.

The first operational and ordinative ground motion cadaster in Germany is LVGL’s “*Saarlaendisches Bodenbewegungskataster SaarBoBeKa*” (SaarBoBeKa 2022), operating since March 2022.

The launch of the “*Bodenbewegungskataster NRW*” is scheduled in 2022 by Geobasis NRW.

#### A. SaarBoBeKa

SaarBoBeKa has been discussed since 2017 and was realized in 2022 with the participation of Saarland’s authorities “Ministerium für Umwelt und Verbraucherschutz”, the “Oberbergamt des Saarlands” (OBA) and LVGL. The already in Section III presented MSST and levelling serve as the geometric geometric reference (see Figure 7). SaarBoBeKa provides a dense-meshed area-wide ground motion cadaster for changes to the earth surface in the Saarland based on interferometric data from Sentinel-1A/B radar satellites of the European Space Agency (ESA) within the *European Union’s Earth observation programme “Copernicus”*.

For this ground motion cadaster official, quality-assured and annually updated ground movements are derived and made publicly available as a web service. The process chain of the complete workflow can be seen in Figure 8.

The data and privacy protection has been guaranteed by generalizing the pointwise by persistent scatterer interferometry (PSI) derived information to 250 m x 250 m cells. For all persistent scatterer (PS) of each tile the relative movements will be averaged and presented in one geometric centered point element that can be chosen for the visualization of the ground motion time series. (see Figure 9).

To derive quality assured and reliable relative changes in height and in east-west – direction the InSAR-analyses of Sentinel-1A/B satellite data taken from ascending and descending orbits have been combined and processed in a decomposition approach (Yin and Busch, 20018). Whilst the postprocessing and quality assessment a data cleansing by blunder and



outlier detection is performed for PS with *e.g.* high standard deviations in “Line-of-Sight” direction (LOS) and a trend analysis with best-fitting polynoms is performed for each PSI time-series (Busch and Linke, 2014).

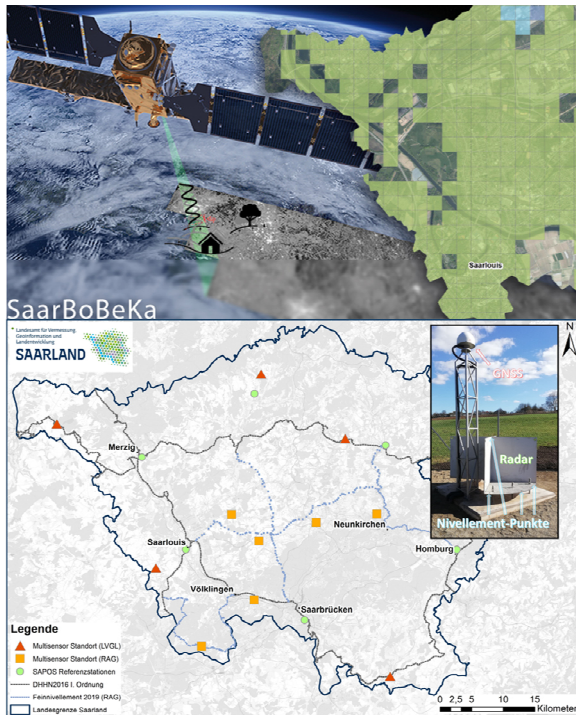


Figure 7. MSST and levelling lines as geometric reference for SaarBoBeKa.

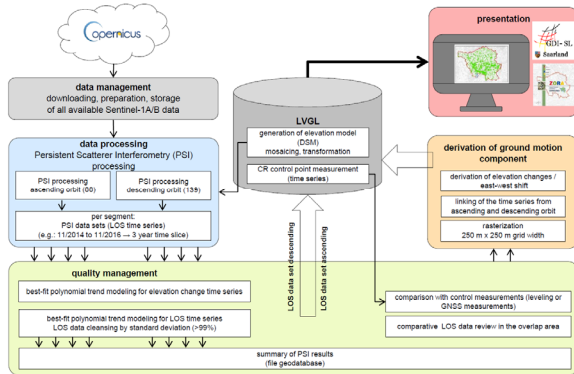


Figure 8. Process chain of the SaarBoBeKa-workflow.

For an early detection of possible ground movements an annual update is intended and if needed half-yearly updates can be processed and published.

The annual processing will be done with the radar data for a time span of three years so that the each other following analyses will have an overlapping time span of two years. By this, an optimum of dense PS will be saved for area-wide PSI- and decomposition results (Evers *et al.*, 2020; Gefeller *et al.*, 2016).

The link between geodetic and radar-interferometric data are the MSST that are used for the validation and verification of the InSAR results compared to geodetic measurements with the aim to transfer this high geometric quality from points into the area for an accurate and controlled ground motion service in

position and height. Figure 10 gives an impression how future comparison in MSST can happen: here the time series of the relative vertical InSAR-related movements of the SaarBoBeKa 250 m x 250 m tile no. 19052 from June 2017 to June 2020 and the GNSS-height measurements on RAG’s MSST Primsschacht from July 2020 to February 2022 are presented together with levelling RAG performed to the MSST foundation. Unfortunately, the current measurements do not overlap but the spread of both the sensors movement behavior is at the same extent and fit to the levelling.

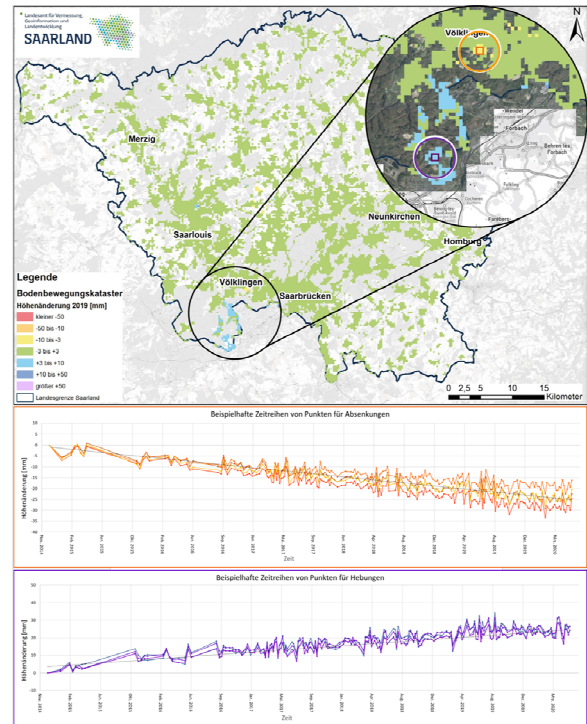


Figure 9. SaarBoBeKa: 250 m x 250 m tiles with colour-coded movement classification (top), time series of a cell showing subsidence (mid) and a cell showing uplift (bottom), Dec. 2014 – June 2020. Image courtesy LVGL.

Farther, LVGL’s MSST comply the requirements for a German SAPOS GNSS station and for this these ground bound MSST will be integrated into the SAPOS framework to additionally improve the position services for GNSS users.

### B. Bodenbewegungskataster NRW

Different to LVGL, Geobasis NRW will back the geodetic reference of the “Bodenbewegungskataster NRW” only their SAPOS GNSS stations and on the very long and for large areas available time-series of the “Leitnivellement” (LN) in NRW.

The use of MSST for the whole federal state NRW, like in the Saarland, would lead to the installation of more than 100 MSST, what is technically and financially regarded not feasible.

## V. CONCLUSION AND OUTLOOK

The development of InSAR-techniques for the geometric monitoring of the earth surface has come to daily practice and now face the demands of classic geodetic reference networks. Since more than 20 years RAG accompanies the InSAR developments first in R&D project and since several years more and more in day-to-day business. Due to the ordinances of the authorities all the results have to be mounted into the federal German reference networks for height and position. For the German federal state Saarland RAG's monitoring workflow has been developed in cooperation with the mining and survey authorities and now is completely based on the official SaarBoBeKa.

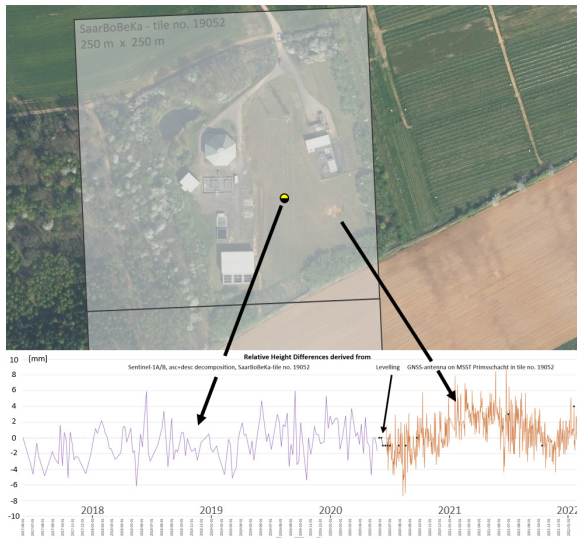


Figure 10. Time series (06/2017-02/2022) for relative vertical movements derived for a 250 m x 250 m tile, SaarBoBeKa - nr. 19052, height difference spacing: 2 mm. RAG's levelling measurements (black dots). Decomposition (height component) of Sentinel-1A/B ascending and descending orbit (06/2017-06/2020) by LVGL (purple). GNSS time series (06/2020-02/2022) derived from RAG's MSST station Primsschacht, LVGL nr. 6607 0 403 00, Saarland (orange). Mapped area  $\sim$  550 m x 330 m. Image courtesy LVGL and RAG.

In NRW a slightly different kind of reference for the ground motion cadaster than in the Saarland will be operated. Consequently, RAG realizes the SaarBoBeKa workflow in the NRW post-mining regions in a comparable manner and installs an own high accurate MSST- and GNSS-station based network mounted within the SAPOS and LN networks. This network will contain 10 MSST and 30 GNSS stations for the Ruhr area. For Ibbenbueren five GNSS stations and one MSST have already been installed in 2021.

In RAG's latest R&D projects GEOTEC (Niemeier and Tengen, 2022) developed the "Dynamic Network Adjustment" (DNA) approach that is implemented in ALLSAT's GLOMON portal (Schulz and Schäfer, 2022). The current analyses show that RAG is able to check either the own networks and even the federal geodetic reference framework in position and height.

Accordingly, the high demands of the authorities for the geometric monitoring can be faced and put into practice for RAG's post-mining era – and areas.

## References

- BGR (2019). BodenBewegungsdienst Deutschland. URL: <https://bodenbewegungsdienst.bgr.de/mapapps/resource/s/apps/bbd/index.html?lang=de>. Last access 2022-03-22.
- Busch, W., and J. Linke (2014). Räumliche Höhenänderungsanalyse auf Grundlage einer automatisierten Ausgleichung massenhaft vorliegender PSI-Zeitreihen mittels Orthogonaler Polynome. In: *Allgemeine Vermessungs-Nachrichten*, AVN, issue 7, 2008, Wichmann Verlag, Heidelberg, pp. 298-210, ISSN 0002-5968.
- Evers, M., H. Hammer, A. Thiele, and K. Schulz (2020). Strategies for PS processing of large Sentinel-1 datasets. In: *Proceedings of ISPRS - International Archives of the Photogrammetry, Remote Sensing and Spatial Information Sciences*, virtual event, Aug. 31. – Sept. 2., pp. 99-106. DOI:10.5194/isprs-archives-XLIII-B1-2020-99-2020.
- Joeckel, R., and M. Stober (1995). Elektronische Entfernung- und Richtungsmessung. Konrad Wittwer Verlag, 1999, 325 pages. ISBN: 3-87919-150-6.
- Gefeller, V., T. Engel, and W. Busch (2016). Automatisierte Zusammenfügung von sich zeitlich überlappenden PSI-Zeitreihen für Langzeit-Bodenbewegungsmonitoring. In: *GeoMonitoring 2016*, Braunschweig, Germany, March 3.-4., 2016, pp 119-136. ISBN: 978-3-926146-26-7.
- Goerke-Mallet, P. (2000). Untersuchungen zu raumbedeutsamen Entwicklungen im Steinkohlenrevier Ibbenbueren unter besonderer Berücksichtigung der Wechselwirkungen von Bergbau und Hydrologie. Dissertation, RWTH Aachen, 2000, 226 pages. ISBN-13: 987-3-89653-801-2.
- Hager, S., and F. Wollnik (2016). Mine Surveying and Post-Mining Activities of RAG Aktiengesellschaft / Markscheidewesen und Altbergbau der RAG Aktiengesellschaft. In: *Mining Report Glückauf - Fachzeitschrift für Bergbau, Rohstoffe und Energie*, No. 3, 152. Jahrgang, Verlag Bergbau-Verwaltungsgesellschaft mbH, Herne, ISSN 2195-6529, June 2016, pp 224-232.
- Niemeier, W., and Tengen, D. (2022). Dynamic concepts to handle geodetic networks with continuous monitoring data in areas with ground movements. In: *5<sup>th</sup> Joint International Symposium on Deformation Monitoring JISDM 2022*, Valencia, Spain, June 20-22, 2022, these proceedings.
- Riecken, J., B. Krickel, V. Gefeller, and P. Reifenrath (2019). Nutzung der Radarinterferometrie im geodätischen Raumbezug. In: *Zeitschrift für Geodäsie, Geo-Information und Landmanagement (zfv)*, Vol. 144, issue 6, 2019, pp 354-361. DOI: 10.12902/zfv-0281-2019
- Rosner, P., M. Heitfeld, V. Spreckels, and P. Vosen (2014). Auswirkungen von Geländehebungen im Zuge des Grubenwasseranstiegs im Ruhrrevier. In: *RuhrGeo Tag 2014*, Bochum, Germany, March 27, 2014, pp 153-177.
- Rudolph, T., P. Goerke-Mallet, A. Janzen, A. Mueterthies, K. Pakzad, S. Teuwsen, C.-H. Yang, V. Spreckels, and L. Vehling (2020). Bergbaumonitoring im südlichen Ruhrgebiet. In: *Tagungsband GeoMonitoring 2020*, Braunschweig,

- Germany, March 12-13, 2020, pp. 163-177.  
DOI: 10.15488/9348.
- SaarBoBeKa (2022). Bodenbewegungskataster Saarland.  
URL:<https://geoportal.saarland.de/article/Bodenbewegungskataster/>. Last access: 2022-03-22.
- Schulz, M., and F. Schäfer (2022). GLOMON-Monitoringportal for storage, management, advanced processing and intelligent visualization of GNSS- and other sensors data. In: *5<sup>th</sup> Joint International Symposium on Deformation Monitoring JISDM 2022*, Valencia, ESP, June 20-22, 2022, these proceedings.
- Spreckels, V., D. Walter, U. Wegmueller, J. Deutschmann, and W. Busch (2008). Nutzung der Radarinterferometrie im Steinkohlenbergbau. In: *Allgemeine Vermessungs-Nachrichten*, AVN, issue 7, 2008, Wichmann Verlag, Heidelberg, pp. 253-261, ISSN 0002-5968.
- Spreckels, V., S. Bechert, A. Schlienkamp, M. Drobniowski, M. Schulz, and F. Schäfer (2018). GNSS, Nivellement und Radar – einheitliche Multisensor-Standorte als Referenzpunkte zur Überwachung von Bodenbewegungen. In: *Tagungsband GeoMonitoring 2018*, Clausthal-Zellerfeld, Germany, March 1.-2., 2018, pp. 241-257. ISBN: 978-3-86948-627-7.
- Spreckels, V., S. Bechert, A. Schlienkamp, M. Drobniowski, M. Schulz, F. Schäfer, and E. Kemkes, (2020). GNSS, Nivellement und Radar – einheitliche Multisensor-Standorte als Referenzpunkte zur Überwachung von Bodenbewegungen. In: *Tagungsband GeoMonitoring 2020*, Braunschweig, Germany, March 12-13, 2020, pp. 207-231. DOI: 10.15488/9351.
- Yin, X., and W. Busch. 2018. Nutzung der Sentinel-1 Aufnahmekonfigurationen zur Ableitung von Bodenbewegungskomponenten im Rahmen eines radarinterferometrischen Bodenbewegungsmonitorings. In: *Tagungsband GeoMonitoring 2018*, Clausthal-Zellerfeld, Germany, March 1.-2., 2018, pp. 119-138. ISBN: 978-3-86948-627-7.

## Status of the new German DIN standards project “InSAR–Radarinterferometry for the detection of ground movements”

Volker Spreckels

Chairman of DIN NA 005-03-02 AA – Photogrammetry and Remote Sensing, Germany, ([volker.spreckels@rag.de](mailto:volker.spreckels@rag.de))

**Key words:** *DIN; standards; InSAR; SAR; interferometry; ground movements*

### ABSTRACT

The German DIN institute for standards works on the new standards project DIN 18740-9 “InSAR – radar interferometry for the detection of ground movements”. Due to the increasing availability of radar satellite data and applications the need for clear and comparable terms and definitions, validated methods and processing as well as ground reference data has been committed to DIN. First meetings with representatives and experts from universities, research and development, public authorities, associations and industries have taken place and it had been commonly agreed to set up this new standard project. A close alignment with international developments of CEN and ISO is intended. The current work of the standards committee DIN NA 005 “DIN-Normenausschuss Bauwesen (NABau)” - NA 005-03 FB “Fachbereich Geodäsie, Geoinformation” - NA 005-03-02 AA “Photogrammetrie und Fernerkundung” will be presented.

### I. INTRODUCTION

Due to the increasing number of radar satellites and data archives modern advanced interferometric SAR techniques (InSAR) found their way into day-to-day practice. The detection and monitoring of ground movements is of great interest for the corporate and public sector.

Nation-wide analysis had been made by private companies for several countries like the UK, The Netherlands and Germany (TerraMotion, 2022), but the georeferencing and ground movement validation is not definitely clear.

From the official side some nation-wide InSAR surveys are present like for Italy (Costantini *et al.*, 2017), The Netherlands (Netherlands Geodetic Commission, 2018), Norway (NGU, 2018) and Germany (BGR, 2019). This Germany-wide available “*BodenBewegungsdienst Deutschland (BBD)*” set up by the *Federal Institute for Geosciences and Natural Resources (BGR)* and the *German Aerospace Center (DLR)* meanwhile coexist with official German ground motion services (Figure 1). An already operating service is the “*Saarländisches Bodenbewegungskataster (SaarBoBeKa)*” (SaarBoBeKa, 2022) a German federal state service of the “*Landesamt für Vermessung, Geoinformation und Landentwicklung (LVGL)*”. LVGL realized SaarBoBeKa in 2022 in cooperation with Saarlands mining authorities “*Oberbergamt des Saarlands (OBA)*” and the former German hard coal mining company “*RAG Aktiengesellschaft (RAG)*” (Spreckels and Engel, 2022) (Figure 2).

Even in 2022 the “*Bodenbewegungskataster NRW*” from the survey authorities “*Geobasis NRW*” is awaited for the German federal state of North Rhine-Westphalia (Riecken *et al.*, 2019).

For Europe the “*European Ground Motion Service (EU-GMS)*” (Frei, 2017) is under development as an element of the “*Copernicus Land Monitoring Service, CLMS*” (CLMS, 2016).

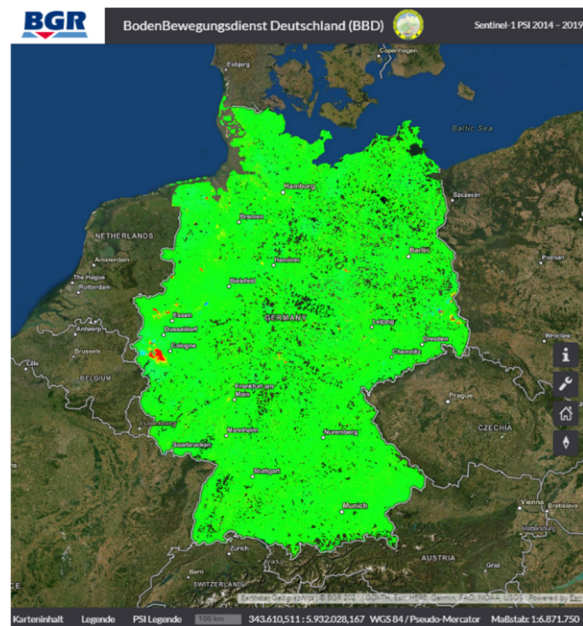


Figure 1. The Germany-wide available, free accessible “*BodenBewegungsdienst Deutschland (BBD)*”, based on Sentinel-1A/B Persistent Scatterer Interferometry (PSI) for ascending and descending orbits. Image courtesy BGR.

### II. INSAR - METHODS

On FRINGE 2003 the “*European Space Agency (ESA)*” approved to support the validation of the following different InSAR methods: *Permanent Scatterer<sup>TM</sup> Interferometry - PSI* (Ferretti *et al.*, 1999; 2000; 2001), *Small Baseline Subset Algorithm - SBAS* (Berardino *et al.*, 2002), *Interferometric Point Target Analysis - IPTA* (Werner *et al.*, 2003) as well as other developments

from *e.g.* (Hanssen *et al.*, 2005; Adam *et al.*, 2003; Kampes and Adam, 2005).

211 will be sought for a close coordination between DIN and ISO.

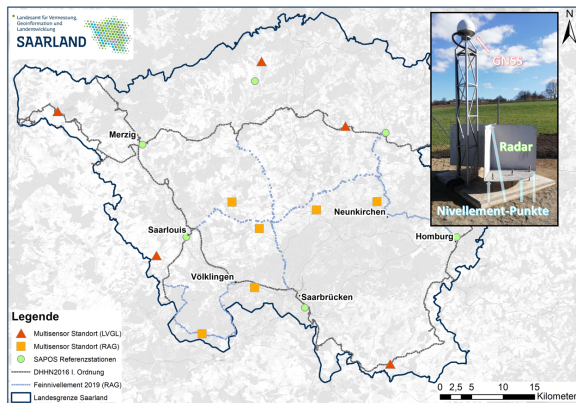


Figure 2. LVGL's ground motion service "SaarBoBeKa", based on combined levelling / GNSS- / double corner reflector stations (MSST) and Sentinel-1A/B Persistent Scatterer Interferometry (PSI) for ascending and descending orbits. LVGL-MSST: red triangles; RAG-MSST: orange squares; SAPOS GNSS Reference stations: green circles. Levelling lines: light grey (LVGL) and light blue (RAG). Image courtesy LVGL.

Another SBAS based development is the "Intermittent Small Baseline Subset" - ISBAS (Lanari *et al.*, 2007).

At this point we see that it is necessary to evaluate this bandwidth of manifold InSAR surveys *e.g.* provided by corporate services as well as services from federal states, from countries or from Europe-wide analyses. The basics, the potentials and the limitations of these diverse, sometimes open to the public results have definitely to be determined to avoid misinterpretation.

Some initiatives have already worked on the evaluation and validation of InSAR-results.

### III. INTERNATIONAL / EUROPEAN INITIATIVES

The *Terrafirma* project as part of the "Global Monitoring for Environment and Security Program" (GMES) had been set up by ESA with the aim to provide a Europe-wide ground motion hazard information service (Terrafirma, 2005-2015) (Figure 3). A "Product Validation" and a "Process Validation" were established to examine and demonstrate the reliability and accuracy of PSI-methods for ground motion surveys in comparison to ground truth reference data (Hanssen *et al.*, 2008; Crosetto *et al.*, 2009) and for a quality management (Adam and Parizzi, 2008; Adam *et al.*, 2009) (Figure 4).

The standards of the "International Organization for Standardization" (ISO) is working on InSAR standards. Here, the Technical Committee ISO/TC 211 "Geographic Information/Geomatics", ISO/TS 19159-3:2018 "Calibration and validation of SAR/InSAR sensors" has, up to now, primarily set the focus on the sensors, for their calibration and validation. The contact to ISO/TC

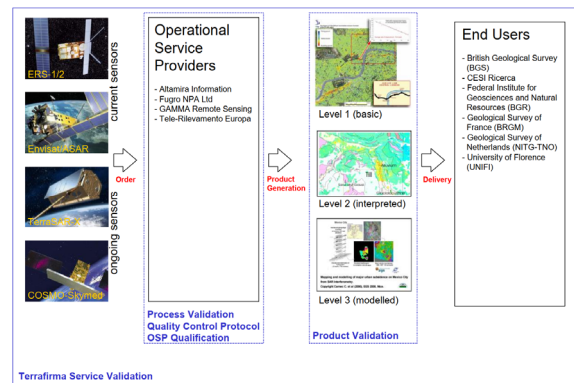


Figure 3. Validation components of the Terra Firma Services: "Process Validation" and "Product Validation" (Figure 1 in Adam *et al.*, 2010).

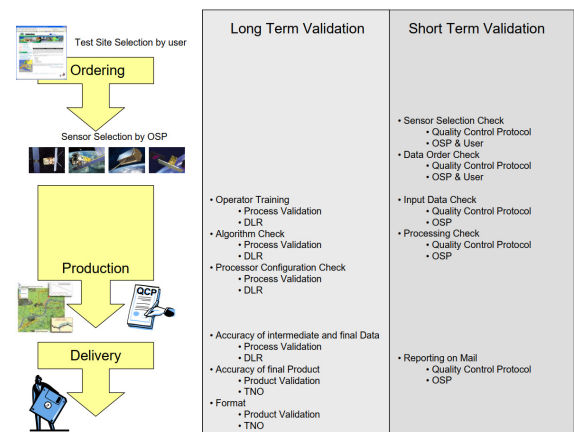


Figure 4. Service elements (yellow) for Level 1 basic products and Long Term / Short Term Validation. (Figure 3 in Adam *et al.*, 2010).

### IV. NATIONAL INITIATIVES

National initiatives dealing with the application of InSAR analyses in day-to-day business are only known to the author for Germany. If other national initiatives are planned, in progress or have been finished, the author will be pleased for a small note or a feedback to the according drafts.

One German initiative was published in 2013, set up by the "German Mine Surveyor Association" (DMV)<sup>1</sup>. DMV published guidelines for the "Deployment of satellite-based radar-interferometric methods for the detection of mining induced ground movements" (DMV, 2013). The aim was to handle InSAR techniques within the ordinances of the federal mining authorities related to the daily work of the companies within the frame of the ground movement monitoring. These guidelines are currently under revision and will be updated to the latest state of the art in 2022.

Furthermore the "Working group of the German Survey Authorities" (AdV)<sup>2</sup> is busy working on a guide

<sup>1</sup> DMV: Deutscher Markscheider Verein e.V., Arbeitskreis „Interferometrie“

<sup>2</sup> AdV: Arbeitsgemeinschaft der Vermessungsverwaltungen Deutschlands – Arbeitskreis 6, Raumbezug.

for the “*Use of radar-interferometry in the geodetic spatial reference*” to handle InSAR within the tasks of federal surveying authorities (Riecken and Krickel, 2019).

It is clear to be seen that national and even international standards are necessary to lay the framework for associations, agencies, organizations, data- / service provider and customer as an appropriate means to issue rules and guidelines for producer- and consumer-protection. Here, special attention is paid to the georeferencing of ascending and descending orbit - InSAR-analyses and the validation of movements detected in Line-of-Sight (LOS), as well as the calculated movement components in height and east-west direction against GNSS- and terrestrial ground truth measurements.

## V. STANDARDIZATION

Already since 2015 a standard for InSAR has been discussed at the DIN working committee NA 005-03-03 “*Photogrammetrie und Fernerkundung*” for the standards series 18740 (Baltrusch and Reulke, 2017).

The main topics are

- Terminology.
- InSAR techniques.
- Sensors, processors, algorithms.
- Corrections (atmosphere, topography, ...)
- Data availability (free, commercial).
- Requirements on processors and data.
- Application scopes.
- Precise geolocalisation and georeferencing.
- Accuracy requirements for georeferencing.
- e.g. with corner reflectors and other sensors.
- Data formats, data provision.
- Cartographic presentation.

In 2017 DIN organized a workshop with presentations held by universities, providers and customers. The need for regulations had been expressed so that the working committee began to look for possible and interested members to be consulted for an active participation. In 2019 a working group had been established but due to the Covid-19 pandemic the activities lost a bit of their momentum. In 2022 the partly reorganized working group will focus on the listed topics in sub-workgroups and plans to publish a draft to the end of the year 2023.

Over the years lots of new techniques and developments have been observed for their potential or market maturity and for their possible importance for the standardization works. New developments for InSAR processing came to market like multi-orbit high resolution SAR interferometry, the decomposition to height- and east-west-movement components from ascending and descending orbit data. An important topic is the correct and accurate georeferencing of InSAR-results. The experience with corner reflectors (CR), double corner reflectors (D-CR) and additional

measurement equipment like GNSS and levelling measures will definitely be considered closer.

At the moment different types of double corner reflector stations are realized in Germany:

The German “*Federal Agency for Cartography and Geodesy*” (BKG) installs platforms at the “*Integriertes Geodätisches Referenznetz Deutschland (GREF)*” stations on a deep founded 2 m concrete ring. Two separate trihedral, perforated sheet - CR and a multi-use pillar in the middle are installed on one carrier frame (Friedländer and Liebsch 2019). Levelling points build the connection to the German Height Reference System “*Deutsches Haupthöhennetz 2016 (DHHN2016)*”. BKG has already installed 3 D-CR at in total 23 stations as to be seen in Figure 5. An accompanying installation of *Compact Active Transponder (CAT)* is planned.



Figure 5. BKG's station Bremgarten. Image courtesy Bundesamt für Geodäsie und Kartographie (BKG).

The survey authority of the German Saarland (LVGL) use solid stainless steel D-CR founded in down to the solid ground set reinforced concrete blocks. These blocks contain the D-CR and a permanent GNSS station on a lattice mast. Levelling points are set in the D-CR and the concrete block to build the connection to the German Height Reference System “*Deutsches Haupthöhennetz 2016 (DHHN2016)*”, see Figure 6. Five of these “*Multisensor-Reference Stations (MSST)*” have been installed in 2021 and operate since March 2022 (Spreckels and Engel, 2022).

The former German hard coal mining company RAG uses nearly the same LVGL configuration. RAG put the D-CR and the GNSS station on a 2 m x 2 m x 2 m reinforced concrete block and uses a self-sufficient solar- / wind power supply, see Figure 7 (Schulz and Schäfer, 2022; Spreckels and Engel, 2022; Spreckels, 2022).

In the Netherlands a network of patented, combined GNSS and D-CR stations, the so called “*Integrated Geodetic Reference Stations*” (IGRS), see Figure 8, has been installed in parts of The Netherlands (Hanssen et al., 2018).



Figure 6. LVGL's MSST Felsberg. Image courtesy LVGL.



Figure 7. RAG's MSST Primsschacht (left) and solar & wind power supply on RAG's MSST Lauterbachschacht (right). Image courtesy ALLSAT & RAG.



Figure 8. The Netherlands: Integrated Geodetic Reference Station (IGRS). Patented D-CR and GNSS-platform (Hanssen *et al.*, 2018, page 3).

The practical experience of BKG, LVGL and RAG will be considered and accordingly implemented into the work of the DIN committee. It is furthermore intended

to establish contact to foreign expertise and to keep a close contact to ISO/TC 211 so that the national and international activities will pull together and not oppose each other.

And, thought before, even future developments will be taken into account like MDA's planned particular CHORUS mission presented end of 2021 (MDA, 2021). Here a collaborative multi-sensor constellation of X- and C-band satellites is foreseen. The satellites move on inclined orbits that allow data recording up to maximum latitudes at 62,5° by ruling out the polar regions (Bamford, 2022).

## VI. CONCLUSION AND OUTLOOK

The DIN standards committee DIN NA 005-03-02 AA "Photogrammetrie und Fernerkundung" is working on the standards series DIN 18740-9 "InSAR – radar interferometry for the detection of ground movements". The working group consists of experts from federal agencies, survey authorities and companies. Additional expertise will be obtained by workshops held together with the members of the remote sensing community in a close exchange of experience.

In 2022 the working group will focus on the topics listed in Section V in different sub-workgroups with the aim to publish a draft of the standard to the end of the year 2023.

Even a close contact to ISO/TC 211 is wanted as well as to foreign experts and groups that we friendly invite to get in contact with us.

## References

- Adam, N., B. Kampes, M. Eineder, J. Worawattamateekul, and M. Kirchner (2003). The development of a scientific permanent scatterer system. In: *Proceedings of the Joint ISPRS/EARSeL Workshop "High Resolution Mapping from Space 2003"*, Hannover, Germany, Oct. 6-8, 2003, 6 pages.
- Adam, N., and A. Parizzi (2008). TerraFirma Quality Control Protocol for Level 1 Products, TerraFirma Project Document, issue 1.5, 61 pages.
- Adam, N., A. Parizzi., M. Eineder, and M. Crosetto (2009). Practical persistent scatterer processing validation in the course of the TerraFirma project. In: *Journal of Applied Geophysics*, Vol. 69, issue 1, pp 59-65. DOI: 10.1016/j.jappgeo.2009.07.02
- Adam, N., A. Parizzi., and B. Kampes (2010). TerraFirma Service Validation Protocol C5. ESA GMES TerraFirma Technical Note V.37, ESRIN/Contract no. 17059/03/I-IW, 139 pages.
- Berardino, P., G. Fornaro, R. Lanari, and E. Sansosti (2002). A new algorithm for surface deformation monitoring based on small baseline differential SAR interferograms. In: *IEEE Transactions on Geoscience and Remote Sensing*, Vol. 40, Issue 11, Nov. 2002, pp 2375 - 2383. DOI: 10.1109/TGRS.2002.803792
- Baltrusch, S., and R. Reulke (2017). DIN-Normungsarbeit in der Photogrammetrie und Fernerkundung – Stand und Perspektiven. In: 37. *Wissenschaftlich-Technische*

- Jahrestagung der DGPF*, Würzburg, Germany, March 7-10, 2017, pp 280-287.
- Bamford, C. (2022). MDA presents details on CHORUS constellation capabilities. In: SpaceQ, March 7<sup>th</sup>, 2022. URL: <https://spaceq.ca/mda-presents-details-on-chorus-constellation-capabilities/>. Last access 2022-03-23.
- BGR (2019). BodenBewegungsdienst Deutschland. URL: <https://bodenbewegungsdienst.bgr.de/mapapps/resource/s/apps/bbd/index.html?lang=de>. Last access 2022-03-22.
- CLMS (2016). Copernicus Land Monitoring Service. URL: [https://www.copernicus.eu/sites/default/files/documents/Copernicus\\_LandMonitoring\\_13Feb2017.pdf](https://www.copernicus.eu/sites/default/files/documents/Copernicus_LandMonitoring_13Feb2017.pdf). Last access: 2022-03-22.
- Costantini, M., A. Ferretti, F., Minati, S. Falco, F. Trillo, D. Colombo, F. Novali, F. Malvarosa, C. Mammone, F. Vecchioli, A. Rucci, A. Fumagalli, J. Allievi, M. G. Ciminelli, and S. Costabile (2017). Analysis of surface deformations over the whole Italian territory by interferometric processing of ERS, Envisat and COSMO-SkyMed radar data. In: *Remote Sensing of Environment*, 202, August 2017, pp 250-275, DOI: 10.1016/j.rse.2017.07.017.
- Crosetto, M., O. Monserrat, A. Jungner, and B. Crippa (2009). Persistent Scatterer Interferometry: potential and limits. In: *ISPRS Hannover Workshop 2009 "High-Resolution Earth Imaging for Geospatial Information"*, ISPRS Archives – Volume XXXVIII-1-4-7/W5. Hannover, Germany, June 2-5, 2009, 6 pages.
- DMV (2013). Deutscher Markscheider-Verein e. V. Grundsätze zum Einsatz von satellitengestützten Verfahren der Radarinterferometrie zur Erfassung von Höhenänderungen. September 16, 2013. URL: [https://www.dmv-ev.de/images/stories/uploads/DMV\\_Radarinterferometrie\\_Grundsaeetze\\_2013\\_09\\_16.pdf](https://www.dmv-ev.de/images/stories/uploads/DMV_Radarinterferometrie_Grundsaeetze_2013_09_16.pdf). Last access 2022-03-22.
- Ferretti, A., C. Prati, and F. Rocca (1999). Permanent scatterers in SAR interferometry. In: *IEEE 1999 International Geoscience and Remote Sensing Symposium, IGARSS'99*, Hamburg, Germany, June 28. - July 2, 1999, pp 1528 - 1530. DOI: 10.1109/IGARSS.1999.772008
- Ferretti, A., Prati, C., and Rocca, F. (2000). Nonlinear subsidence rate estimation using permanent scatterers in differential SAR interferometry. In: *IEEE Transactions on Geoscience and Remote Sensing*, Vol. 38, issue 5, Sept. 2000, pp 2202–2212, DOI: 10.1109/36.868878
- Ferretti, A., Prati, C., and Rocca, F., (2001). Permanent scatterers in SAR interferometry. In: *IEEE Transactions on Geoscience and Remote Sensing*, Vol. 39, issue 1, Jan. 2001, pp 8 - 20, DOI: 10.1109/36.898661
- Frei, M. (2017). European Ground Motion Service (EU-GMS) - A proposed Copernicus service element. Sept. 21, 2017, 24 pages. URL: <https://land.copernicus.eu/user-corner/technical-library/egms-white-paper>. Last access: 2022-03-22.
- Friedländer, S., and G. Liebsch (2019). Monitoring geodätischer Infrastruktur – Das Potential der SAR-Interferometrie für das Vermessungswesen. Presentation, DIN Normungsausschuß Photogrammetrie und Fernerkundung, Berlin, October 8, 2019.
- Hanssen, R. F., F. van Leijen, G. Ketelaar, P. S. Marinkovic, and S. Gehlot (2005). PSIC4: PSI-processing over a validation test site. applicability report. TU Delft Technical Report, ESA Contract Nr. 18707/04/I-LG, Feb. 2005.
- Hanssen, R. F., F. J. van Leijen, G. J. van Zwieten, C. Bremmer S. Dortland, and M. Kleuskens (2008). Validation of existing processing chains in TerraFirma stage 2; Product validation: validation in the Amsterdam and Alkmaar area, In: *GMES TerraFirma Report*, ESRIN/contract No. 19366/05/I-E, 1-85, May 28, 2008, 85 pages.
- Hanssen, R. F., H. van der Marel, F. J. van Leijen, and J. Kamphuis (2018). Integrated Geodetic Reference Station (IGRS) – A new device for datum connection in the observation space. Presentation, EUREF 2018 Symposium, Amsterdam, The Netherlands, May 31, 2018, 2008, 85 pages. URL: <http://www.euref.eu/symposia/2018Amsterdam/03-08-Hanssen.pdf>, 36 pages. Last access: 2022-03-28.
- Kampes, B., and N. Adam (2005). The STUN algorithm for persistent scatterer interferometry. In: *Proceedings of FRINGE 2005*, SP-610, Frascati, Italy, Nov. 28 – Dec. 2, 2005, pp 1-14. ISBN: 92-9092-921-9
- Lanari R., F. Casu, M. Manzo, G. Zeni, P. Berardino, A. Pepe, and M. Manunta (2007). An Overview of the Small Baseline Subset Algorithm: A DInSAR Technique for Surface Deformation Analysis. In: *Pure and Applied Geophysics* Vol. 164, pp. 637-661, Birkhäuser Verlag, Basel, 2007. DOI: 10.1007/s00024-007-0192-9
- MDA (2021). CHORUS constellation. URL: <https://mda.space/en/article/mda-announces-chorus-name-of-its-commercial-earth-observation-mission>. Last access: 2022-03-23.
- Netherlands Geodetic Commission (2018). The Netherlands Bodemdalingskaart. URL: <https://bodemdalingkaart.nl/portal/index>. Last access: 2022-03-22.
- NGU (2018). The Norwegian Ground Motion Service. URL: <https://insar.ngu.no/>. Last access: 2022-03-22.
- Ricken, J., and Krickel, B. (2019). Bodenbewegungsmonitoring im Raumbezug / Geodetic Spatial Reference: The Monitoring of Ground Movements. In: *Allgemeine Vermessungs-Nachrichten (AVN)*, Vol. 126, issue 8-9, 2019. pp 225–231.
- Riecken, J., B. Krickel, V. Gefeller, and P. Reifenrath (2019). Nutzung der Radarinterferometrie im geodätischen Raumbezug. In: *Zeitschrift für Geodäsie, Geo-Information und Landmanagement (zfv)*, Vol. 144, issue 6, 2019, pp 354-361. DOI: 10.12902/zfv-0281-2019
- SaarBoBeKa (2022). Bodenbewegungskataster Saarland. URL: <https://geoportal.saarland.de/article/Bodenbewegungskataster/>. Last access: 2022-03-22.
- Schulz, M., and F. Schäfer (2022). GLOMON-Monitoringportal for storage, management, advanced processing and intelligent visualization of GNSS- and other sensors data. In: *5<sup>th</sup> Joint International Symposium on Deformation Monitoring JISDM 2022*, Valencia, ESP, June 20-22, 2022, these proceedings.
- Spreckels, V., and T. Engel (2022). Set-up and application of multisensor-referencstations (MSST) for levelling, GNSS and InSAR in the former mining regions Saarland and Ruhrgebiet within Germany. In: *5<sup>th</sup> Joint International Symposium on Deformation Monitoring JISDM 2022*, Valencia, ESP, June 20-22, 2022, these proceedings.
- Spreckels, V. (2022). Multisensor monitoring of ground movements over large areas to conduct the change from the active underground hard coal mining ages to the post-



mining era. In: *5<sup>th</sup> Joint International Symposium on Deformation Monitoring JISDM 2022*, Valencia, ESP, June 20-22, 2022, these proceedings.

Terrafirma (2005–2015). Terrafirma GMES Products. URL: <http://www.europe-geology.eu/terrafirma/#mapobj>. Last access: 2022-03-23.

TerraMotion (2022). Land Motion Surveys. URL: <https://www.terramotion.co.uk/national-motion-surveys>. Last access: 2022-03-23.

Werner C., U. Wegmüller, T. Strozzi, and A. Wiesmann (2003). Interferometric point target analysis for deformation mapping. In: *Proceedings of IGARSS 2003, International Geoscience and Remote Sensing Symposium*, Toulouse, France, July 21-25, 2003, 3 pages. DOI: 10.1109/IGARSS.2003.1295516

## Low-cost GNSS RTK receiver in structure monitoring under demanding conditions

Przemysław Kuras, Daniel Janos, Łukasz Ortyl

Information Technology in Civil Engineering Research Group, AGH University of Science and Technology, 30-059 Cracow, Poland, ([kuras@agh.edu.pl](mailto:kuras@agh.edu.pl); [janos@agh.edu.pl](mailto:janos@agh.edu.pl); [ortyl@agh.edu.pl](mailto:ortyl@agh.edu.pl))

**Key words:** *low-cost GNSS receiver; u-blox ZED-F9P; network RTK; comparison; positioning accuracy*

### ABSTRACT

Low-cost GNSS receivers are becoming increasingly popular in monitoring applications. Especially dual-frequency receivers, acquiring signals of all available satellite systems, offer great possibilities. The main goal of this study is to evaluate the accuracy of a position determined using low-cost receiver in different field conditions. The u-blox ZED-F9P receiver was used for testing, with the satellite signal supplied by either a dedicated u-blox ANN-MB-00 low-cost patch antenna or the Leica AS10 high-precision geodetic one. A professional Leica GS18T geodetic receiver was used to acquire reference satellite data. The tests were conducted in two ways. In the first one, the position was determined by low-cost and professional receivers in a typical RTK Network measurement, with a stationary antenna and various field conditions. Reference observations were made using the precise total station. The second test was carried out to check the positioning quality of the u-blox ZED-F9P receiver on the move to recognize its applicability in the automotive industry. A suitable route was proposed, for which reference data was provided by robotic total station and the 360-degree prism, coaxially mounted with the tested patch antenna. Conducted tests showed the advantage of the u-blox ZED-F9P over professional geodetic equipment. As a result, it is concluded that this receiver equipped with a geodetic-grade antenna provides high-quality positioning. In most cases of the partially obscured horizon, precise coordinates were obtained, making the ZED-F9P a valuable alternative to the high-end geodetic receivers in monitoring applications.

### I. INTRODUCTION

The diversity of satellite positioning techniques developed over several decades provides sufficient accuracy for many monitoring cases. However, in recent years there has been a significant progress in this field through the increasing availability of low-cost receivers. Among them, especially dual-frequency receivers, available on the market for a short time, have become the subject of a growing number of studies, both in terms of determining the position using the static (Wiśniewski *et al.*, 2013) and kinematic (Takasu and Yasuda, 2009) methods.

A few years ago, the ZED-F9P low-cost dual-frequency GNSS receiver, manufactured by the Swiss company u-blox, appeared on the market. Wielgocka *et al.* (2021) tested the ZED-F9P receiver for positioning accuracy using different methods. In static mode, they obtained RMSE (Root Mean Square Error) values of 11, 17 and 15 mm for north, east and up components, respectively, based on differences from reference data. In contrast, in RTK mode, they found that the manufacturer's parameters were not met and were 20 mm and 53 mm (both RMSE) for horizontal and vertical components, respectively, for a baseline shorter than 0.5 km. In addition, it was noted that the main source of height error was the use of low-cost antennas. Further tests for this receiver were performed by Hamza *et al.* (2021), who used low-cost

antennas from various manufacturers to determine position using the static method. Their results allowed them to conclude that low-cost instruments give a coordinate accuracy of a few millimeters, but their precision is four times worse than that of geodetic receivers (based on adjustment of the established geodetic network). A detailed study on the influence of patch antenna was carried out by Kriemeyer *et al.* (2020) by comparing with geodetic-grade antennas, with and without consideration of antenna relative calibrations.

A critical component of the low-cost receivers is the patch antenna, due to the noticeable degradation in positioning accuracy. For this reason, they have been tested using high-precision geodetic antennas. Thus, Tsakiri *et al.* (2017) verified the accuracy of single-frequency u-blox receivers. The results obtained were comparable to geodetic receivers - not exceeding 0.005 m ( $2\sigma$ ) in all components (for a baseline shorter than 0.5 km) and 0.02 m (for up to 18 km long baseline). Even better results were obtained by Poluzzi *et al.* (2019), obtaining RMSEs below 2 mm and about 5 mm for the horizontal (Hz) and vertical (V) components, respectively, based on 1-hour static observations. Besides, they estimated the accuracy of the real-time solution as 4 mm (Hz) and 8 mm (V) RMSE. A similar RTK mode study was performed by Semler *et al.* (2019), comparing the ZED-F9P results with a professional geodetic receiver. They obtained a 3D position standard

deviation value of 7 mm, which they considered excellent for low-cost GNSS equipment compared to a value of 13 mm obtained with a high-end receiver.

It is worth noting that the tests mentioned above were usually conducted under favorable field conditions, with a large number of available satellites and an open horizon. However, terrain obstacles are a significant handicap in many practical cases, so it seems reasonable to perform tests under such conditions. The tests carried out in this paper take into account different terrain situations, ranging from an open-sky environment, through a horizon obscured from different directions, to the case of an urban canyon.

Furthermore, in testing the accuracy of the devices, it is crucial to provide reliable reference values. Most comparisons utilize results obtained with different GNSS receivers, equipped with various antennas (patch and geodetic), using other positioning methods. In this paper, satellite observations are compared with total station measurements, which provide higher accuracy and are less dependent on random factors such as satellite availability or multipath effect.

The motivation for undertaking the research was to verify the accuracy of low-cost dual-frequency GNSS receiver operating in RTK mode in relation to high-precision observations. An essential element of our work was to create diverse field conditions in which low-cost receivers can be used, such as during vehicle positioning.

Furthermore, expecting worse results for low-cost receivers, a mid-cost solution was conducted in the tests. A high-precision geodetic antenna was combined with a low-cost receiver. Despite the higher cost of the antenna, this combination is still a cost-effective alternative to high-end geodetic equipment in situations where high positioning accuracy is required.

## II. TESTED DEVICES

The u-blox ZED-F9P is a 2-frequency, 4-system GNSS receiver - it receives GPS (L1C/A, L2C), GLONASS (L1OF, L2OF), Galileo (E1B/C, E5b) and BeiDou (B1I, B2I) signals. It offers RTK and RTN operation with high frequency (up to 20 Hz) and accuracy ( $\pm 1$  cm + 1 ppm). In conditions of good satellite visibility, the receiver quickly resolves its position (cold start < 24 s, reacquisition < 2 s). Also, anti-jamming and anti-spoofing algorithms are implemented into the receiver, allowing by the assumption to discard unwanted signals. It has a wide operating temperature range, low power consumption, light weight and a large number of physical I/O and communication capabilities. The parameters of this device declared by the manufacturer, its price, and programming libraries available on the Internet, provide great opportunities for using this receiver. In the presented work the C099-F9P application board was used for testing.

Since the C099-F9P is an application board with the receiver itself, an active GNSS antenna must be

connected to it. The manufacturer includes a patch antenna (model ANN-MB-00), which should provide the required accuracy in conditions with good visibility of satellites. It is small (its dimensions are only 60.0 x 82.0 x 22.5 mm) and weather-proof (protection level IP67).

To reduce the number of reflections from other objects and/or the environment reaching the antenna, when mounting the above antenna, it should be ensured that it is placed on a plate made of a well conductive metal (so-called ground plane). For the following tests, a special 4 mm thick disc with a diameter of 200 mm and a bracket for it were self-made of aluminum. The assembly is shown in Figure 1. The whole set provides a coaxial mounting with the second antenna and the Leica GS18T receiver, allowing straightforward interpretation of the results later in the tests.



Figure 1. The u-blox ANN-MB-00 antenna with self-made aluminum ground plane.

To check the performance of the ANN-MB-00 antenna in multipath reduction, measurements were additionally performed with a professional surveying antenna Leica AS10, which was applied in another similar tests (Garrido-Carretero *et al.*, 2019; Xue *et al.*, 2021).

## III. STATIONARY EXPERIMENT

### A. Experimental setup

The details of the conducted experiment have been presented by Janos and Kuras (2021). Measurement stations were planned at locations with different horizon exposure conditions (Figure 2), so that the test would be reliable and different results could be obtained. Measurements were made in May, when trees gather leaves and constitute a barrier for a satellite signal. Pt 1 had a perfect exposure of the horizon, Pts 2-4 had the horizon covered only from one side, Pt 5 had in addition tree branches directly above it, Pt 6 was surrounded by trees and a nearby hill, while Pt 7 was located in an "urban canyon".

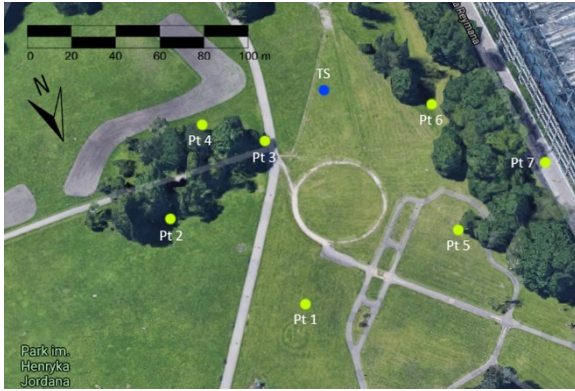


Figure 2. Measurement site for stationary test.

The reference coordinates were measured with the Leica MS50 precision total station (angle accuracy 1", distance accuracy  $\pm 1 \text{ mm} + 1.5 \text{ ppm}$ ) in combination with the Leica GPR1 surveying prism. The total station was referenced to 2 points, the coordinates of which had previously been determined using a static GNSS technique. The session lasted 45 minutes. The observation data were collected with Leica GS16 geodetic receivers (GPS + GLONASS) and calculated with commercial software. The final accuracy of the reference points is estimated to be a maximum of  $\sigma_{2D} = \pm 2.4 \text{ mm}$  and  $\sigma_H = \pm 2.6 \text{ mm}$ . For further considerations, the obtained coordinates are considered constant and error-free.

The measurements with both receivers – Leica GS18T and u-blox ZED-F9P – were performed in RTK Network mode. In this mode Leica declares a slightly higher measurement accuracy of its receiver due to the distance to the base. To obtain consistent results, in both cases, RTCM corrections to the observations were provided by the same CORS network (Leica SmartNet Poland).

The measurement at the station consisted of at least five measurement series (the exception was station Pt 7) for each hardware configuration. Measurements in successive configurations (Leica GS18T, u-blox ZED-F9P + Leica AS10, u-blox ZED-F9P + ANN-MB-00) were performed alternately to ensure that each receiver had the most similar measurement conditions (access to the same satellites). The scheme of one measurement series on the station was as follows:

- Receiver initialization - maximum 30 seconds.
- Measurement - 30 seconds.
- Change of antenna/receiver.

The collected observations in one 30-second measurement were averaged. After completing the measurement at the station, at least five separate (averaged) measurements of each antenna were obtained and taken for further analysis.

## B. Results

The test of the ZED-F9P receiver started with measurements under good satellite visibility conditions. The Pt 1 measurement station had no

significant obstacles around it. The next measurement stations were located in places with one side of the horizon obscured by tall trees. Those sides were the southern, eastern, and northern for Pt 2, Pt 3 and Pt 4 stations, respectively. The subsequent measurement stations were located in even more demanding conditions. Point Pt 5 was planned with the horizon obscured from the west (by trees and a football stadium). Additionally, the tripod was set up directly under the tree branches. The Pt 6 station, on the other hand, was located in the surroundings of trees, less dense, however, on all sides. Additionally, on the southern side the horizon was limited by a nearby mound and on the western side by the football stadium.

The last station was located in difficult measuring conditions for GNSS technology. On the west side the horizon was directly limited by a building, while on the east side by a line of tall trees - the tripod was set up along an alley running between a park and a large football stadium. It is worth mentioning the problems that were encountered during the measurements. As many as 8 series of measurements were performed on this station. The Leica GS18T receiver had a fixed solution only in half of the series. The ZED-F9P receiver with the Leica AS10 antenna had even fewer fixed solutions - only 3. The same receiver, but with the ANN-MB-00 antenna, had fixed solutions in 4 series. Unfortunately, the result of one of them differed considerably from the reference coordinates - by as much as 13 meters on the vertical coordinate. This measurement was removed from further considerations, nevertheless the result is still not satisfactory.

The results are summarized for different hardware configurations and for all measurement stations. Table 1 contains the differences of the measured coordinates in relation to the reference values, averaged from the five measurement series. Similarly, Table 2 contains standard deviations calculated based on the five measurement series.

The following values were used to compare the results: the summed coordinate differences (Eq. 1) and the mean standard deviation (Eq. 2):

$$\text{sum}_{XYH} = |d_X| + |d_Y| + |d_Z| \quad (1)$$

where  $d_X, d_Y, d_Z$  = differences from reference values

$$\text{MSD} = \sqrt{(\sigma_X^2 + \sigma_Y^2 + \sigma_Z^2)/3} \quad (2)$$

where  $\sigma_X, \sigma_Y, \sigma_Z$  = standard deviations of coordinates

An increasing trend of  $\text{sum}_{XYH}$  values can be seen in Figure 3. Surprisingly, better results were obtained at station Pt 6 than at the station Pt 1 with a fully open horizon. It can be assumed that despite many obstacles on the horizon from different sides, there were also free gaps that made it possible to create a good-quality

angular resection of signals coming from the satellites of all constellations.

Table 1. Differences from the reference values [mm]

Rec.		Pt1	Pt2	Pt3	Pt4	Pt5	Pt6	Pt7
GS18T	X	-10	-6	0	-1	18	4	-4
	Y	2	7	27	11	-24	-8	1
	H	19	5	14	5	31	-4	-32
ZED+AS10	X	-7	-6	-4	3	15	-4	-64
	Y	-2	1	20	10	-26	-9	-33
	H	11	6	11	-1	9	-10	38
ZED+ANN-MB-00	X	-9	-9	-11	8	13	-2	21
	Y	0	0	20	8	-26	-10	69
	H	27	14	30	4	35	9	237

Table 2. Std. deviations based on measurement series [mm]

Rec.		Pt1	Pt2	Pt3	Pt4	Pt5	Pt6	Pt7
GS18T	X	8	9	9	7	5	21	29
	Y	6	13	9	6	15	25	47
	H	14	12	34	29	20	38	57
ZED+AS10	X	8	9	6	14	18	11	75
	Y	14	6	10	8	9	16	106
	H	21	29	23	31	32	31	15
ZED+ANN-MB-00	X	10	16	9	5	11	18	110
	Y	6	7	10	6	17	22	147
	H	17	16	30	36	42	31	392

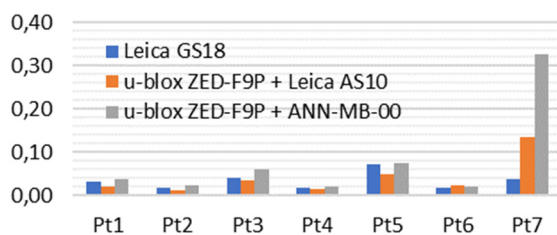


Figure 3. Values of  $sum_{xyH}$  [m] on each station point.

Considering the conditions at all measurement stations, it can be concluded that both receivers performed well. The u-blox ZED-F9P, equipped with the Leica AS10 antenna, had a slight advantage in the clear areas, while its rival excelled in the very demanding "urban canyon" type conditions at the last station.

In Figure 4 the increasing tendency of the  $MSD$  values can be clearly seen. It is a result of measurement difficulties at subsequent stations (more and more obscured horizon, access to less satellites of a given constellation, as well as more reflected signals and interferences). This proves a good choice of successive measurement stations in order to increase the difficulty of measurement.

#### IV. EXPERIMENT IN MOTION

##### A. Experimental setup

The second experiment consists in checking the quality of the calculated position of the antenna being in motion (in contrast to the static tests carried out by Janos and Kuras (2021)) determined by the GNSS

receiver u-blox ZED-F9P. To ensure the highest possible accuracy of the reference data, a total station measurement was performed simultaneously. To facilitate the processing of the measurement data, a 360° prism was mounted coaxially with the GNSS antenna. The plan was implemented by mounting a surveying pole to the fork and handlebars of the bicycle (Figure 5). The aforementioned prism and antenna were mounted on the pole. Acquisition of both GNSS and total station data was done continuously at a frequency of about 10 Hz and about 7 Hz, respectively. Measurement data from the ZED-F9P was sent to the tablet via a USB cable and saved via an application written for this purpose. The Leica MS50 instrument collected the observations on board. With the system thus assembled, two passes were made, in opposite directions of travel.

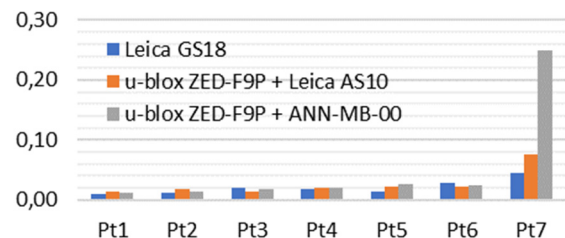


Figure 4. Values of  $MSD$  [m] on each station point.

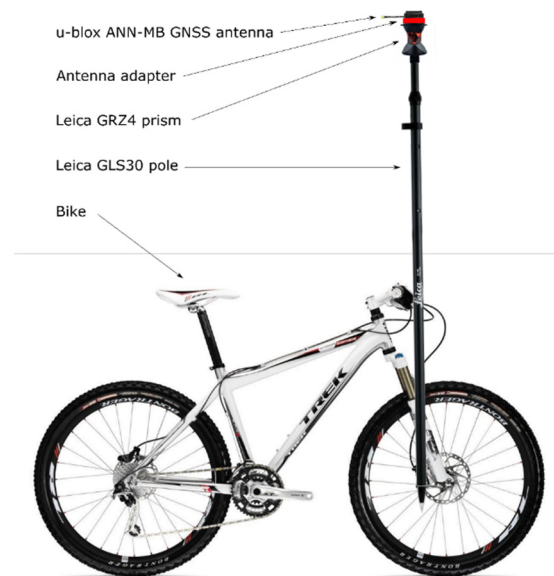


Figure 5. Measuring equipment on a bicycle.

The measurements were made in a city park - in an area with varied satellite visibility. The rides were made through alleys leading both through open spaces, half-obscured, and with the horizon completely obscured by bushes and trees. Layout of the survey points on the satellite images background are presented in Figure 6. The obstacles can be clearly seen. The measurement campaign was performed in May when trees already have been covered with leaves and together with their branches represent a real obstacle for the GNSS satellite signal.



Figure 6. Measurement site for the experiment in motion with markings of positioning quality.

### B. Preliminary results

The reference data was determined based on two control points occupied by geodetic GNSS receivers in 45-minute static session. Then the reference observations were acquired using the Leica MS50 robotic total station set up on the control points.

To compare coordinates obtained from two devices (total station and low-cost receiver), a special script has been written, which performs spline interpolation by reference points and calculation of distances from measurement points to this spline.

Two rides, in opposite directions of travel, were made in a city park to check the repeatability of the results. Graphs illustrating the preliminary experimental results are presented in Figure 7.

Figure 6 illustrates the results of the rides. It is noticeable where the receiver had a limited horizon and where it had problems with the fixed solution. The location of the total station is also marked. Efforts were made to have it as central as possible to the whole survey, because of the better distribution of the positioning error, caused by the increasing influence of the measurement error in horizontal and vertical angles, as well as distance. It can also be seen why in some places on the route GNSS measurements are missing - then the total station's line-of-sight was interrupted by bushes, trees or other objects. However, the ride through sensitive places - bushes obscuring the horizon from the east, as well as tall trees located in the centre of the sketch, was captured. Hence, the given

location of the total station was considered to be the most favourable.

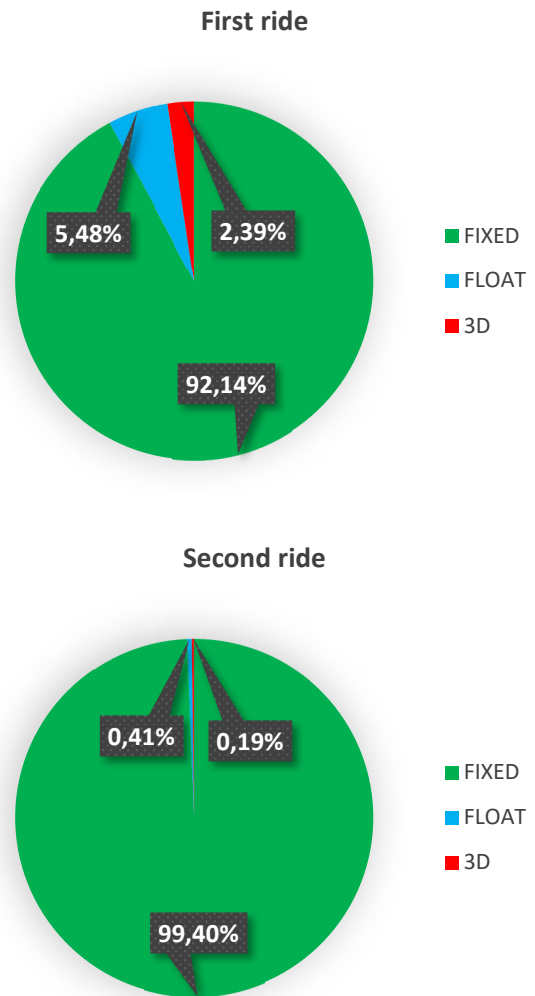


Figure 7. Pie charts showing the quality of GNSS positioning for the first and second test rides, respectively.

The receiver copes very well with positioning an antenna that is in motion. This happens both in places with a fully exposed horizon and those obscured from one of the sides. This is evidenced particularly by the results of the second ride (99.40% of fixed solutions). The first ride was more challenging - the route led through a place with a fully obscured horizon, hence the lower percentage of the highest precision measurements (92.14%).

The preliminary results indicate a high quality of positioning under demanding field conditions, however, a comparison with the observations collected by the total station will be the subject of further detailed analysis.

It is worth noting that the reference coordinates were determined at a different time, with a different satellite constellation, which also ensures the independence of the results obtained.

As expected, the receiver lost the fixed solution in places where the horizon is completely covered by tree crowns. Despite this, the accuracy of position

determination did not drop drastically. However, these results may not be reliable due to the definitely low number of float positions. It is also not a satisfactory value, e.g. for precise monitoring of buildings or standard geodetic measurements. On the other hand, changes in the conditions of GNSS satellite signal reception and loss of good positioning quality are signalled correctly.

The 3D quality solutions look not bad either. The receiver, while moving, jumps quickly from areas with good satellite visibility to areas with poor signal quality (and vice versa). Due to the lack of such information in the technical documentation of the device, it can only be supposed that some algorithms are used to predict the movement of the receiver and maintain the accuracy of its position. The duration of the float and 3D quality position was short, so the results may not be completely reliable, and it would be necessary to conduct additional research on this aspect only.

## V. CONCLUSIONS

In stationary test the u-blox ZED-F9P receiver performs well for a GNSS receiver in this price range. The ANN-MB-00 antenna is suitable for precise measurements and provides centimeter accuracy, but only in conditions with sufficient horizon exposure.

The ZED-F9P configuration with the ANN-MB-00 antenna provides an excellent relation of positioning quality to price, as well as size, weight or power consumption. This makes the u-blox a very versatile receiver and can be used in many industries, such as autonomous vehicles, building monitoring, surveying, robotics and marine.

In the case of positioning in more demanding conditions and/or with greater accuracy, a replacement for the patch antenna with a model of the survey-grade type would be worth considering. In the test the Leica AS10 antenna has significantly improved the measurement performance of the u-blox ZED-F9P, with smaller PCV (Phase Centre Variations) and more efficient multipath reduction. This configuration turned out to be better than a professional geodetic receiver in most field cases. It can be assumed as promising outcome, considering the price gap between both devices.

The u-blox ZED-F9P performs well also in mobile GNSS surveys. It achieves the fixed solution type in the conditions of limited horizon visibility. In order to assess the positioning accuracy, a detailed comparison with the observations collected by the total station will be performed in further work.

Thanks to its small size, low power requirements, and the multitude of ways to communicate and exchange data with the device, the u-blox ZED-F9P receiver is a very good option for all kinds of applications where high GNSS positioning accuracy is needed. Based on the comprehensive static tests, this receiver can be

successfully applied in the projects requiring accuracy of approximately  $\pm 2$  cm.

## VI. ACKNOWLEDGEMENTS

This research was partially funded by AGH University of Science and Technology subsidy no. 16.16.150.545.

## References

- Garrido-Carretero, M.S., M.C. de Lacy-Pérez de los Cobos, M.J. Borque-Arancón, A.M. Ruiz-Armenteros, R. Moreno-Guerrero, and A.J. Gil-Cruz (2019). Low-cost GNSS receiver in RTK positioning under the standard ISO-17123-8: A feasible option in geomatics. *Measurement*, Vol. 137
- Hamza, V., B. Stopar, and O. Sterle (2021). Testing the Performance of Multi-Frequency Low-Cost GNSS Receivers and Antennas. *Sensors*, Vol. 21, No. 6
- Janos, D., and P. Kuras (2021). Evaluation of Low-Cost GNSS Receiver under Demanding Conditions in RTK Network Mode. *Sensors*, Vol. 21, No. 16
- Kriemeyer, A., H. van der Marel, N. van de Giesen, and M.-C. ten Veldhuis (2020). High Quality Zenith Tropospheric Delay Estimation Using a Low-Cost Dual-Frequency Receiver and Relative Antenna Calibration. *Remote Sensing*, Vol. 12, No. 9
- Poluzzi, L., L. Tavasci, F. Corsini, M. Barbarella, and S. Gandolfi (2019). Low-cost GNSS sensors for monitoring applications. *Applied Geomatics*, Vol. 12
- Semler, Q., L. Mangin, A. Moussaoui, and E. Semin (2019). Development of a low-cost centimetric GNSS positioning solution for Android applications. *The International Archives of the Photogrammetry, Remote Sensing and Spatial Information Science*, Vol. XLII-2/W17
- Takasu, T., and A. Yasuda (2009). Development of the low-cost RTK-GPS receiver with an open source program package RTKLIB. In *Proc. of the International Symposium on GPS/GNSS*, Jeju, Korea.
- Tsakiri, M., A. Sioulis, and G. Piniotis (2017). Compliance of low-cost, single-frequency GNSS receivers to standards consistent with ISO for control surveying. *International Journal of Metrology and Quality Engineering*, Vol. 8, No. 11
- Wielgocka, N., T. Hadas, A. Kaczmarek, and G. Marut (2021). Feasibility of Using Low-Cost Dual-Frequency GNSS Receivers for Land Surveying. *Sensors*, Vol. 21, No. 6
- Wiśniewski, B., K. Bruniecki, and M. Moszyński (2013). Evaluation of RTKLIB's Positioning Accuracy Using low-cost GNSS Receiver and ASG-EUPOS. *TransNav: International Journal on Marine Navigation and Safety of Sea Transportation*, Vol. 7, No. 1
- Xue, C., P. Psimoulis, Q. Zhang, and X. Meng (2021). Analysis of the performance of closely spaced low-cost multi-GNSS receivers. *Applied Geomatics*, Vol. 13

## Experimental assessment of the accuracy of a Ground-Based Radar Interferometer in a fully controlled laboratory environment

George Piniotis, Vassilis Gikas

National Technical University of Athens, School of Rural, Surveying and Geoinformatics Engineering, Zographos, 15780, Athens, Greece, ([piniotis@survey.ntua.gr](mailto:piniotis@survey.ntua.gr); [vgikas@central.ntua.gr](mailto:vgikas@central.ntua.gr))

**Key words:** *ground based radar interferometer; laser tracker; shake table; displacement accuracy; vibration; frequency*

### ABSTRACT

Ground Based Radar Interferometry (GBRI) counts almost twenty years of maturity. Ever since its infancy, GBRI has been extensively used in structural health monitoring, thanks to its high sampling rate (up to 200 Hz) and remote, ultra-high displacement observation accuracy (claimed to be of the order of  $\pm 0.01$  mm in lab. conditions) at multi-point locations on a structure. Nevertheless, despite the fact that GBRI has already been extensively used for bridge monitoring projects, the published results of the comparisons derived between GBRI and other technologies (*e.g.*, accelerometers, seismometers and Laser Doppler Vibrometers) are usually limited to real structures cases at operational conditions; and therefore, an exhaustive assessment of the inherent quality measures of GBRI observables is still missing. This paper presents the results obtained from an exhaustive investigation of the performance capabilities of a GBRI sensor (IBIS-S sensor, IDS Radar<sup>®</sup>), in terms of precision (repeatability) and accuracy (trueness) at fully controlled, lab conditions. Dynamic displacements of a sinusoidal form were produced using an automatically operated portable shake table and on-purpose built software. Testing scenarios cover a frequency range corresponding to structural modal frequencies (up to 20 Hz) and an amplitude range of  $10^{-5}$  to  $10^{-2}$  m. The measurements of a Laser Tracker sensor serve as a benchmark against which the results of the GBRI unit are assessed, in terms of displacement accuracy and frequency estimation correctness.

### I. INTRODUCTION

Systematic recording of oscillations in large-scale structures provides critical information regarding their dynamic behavior, and ultimately, the assessment of their structural integrity. This process is performed in the context of structural integrity monitoring (Structural Health Monitoring, SHM) (Farrar and Worden, 2013). Also, monitoring the actual dynamic response of structures contributes to an improvement of their design parameters for future use (Calvi *et al.*, 2008), as well as to the improvement of preventive maintenance strategies (Staszewski *et al.*, 2004). The study of dynamic response of structures is based on physical quantities such as displacement, velocity, acceleration, tension, inclination and strain. Among them, measures of displacement surpass other parameters in structural integrity monitoring studies, as structural modal frequencies do not usually exceed 20 Hertz (Hz). For the extraction of the dynamic characteristics of structures (modal frequencies, modal shapes, damping coefficient, etc.) methodologies such as Operational Modal Analysis (OMA) (Zhang and Brincker, 2005) are used. They rely on vibrations referred only to environmental and operational excitation such as wind, temperature variation and road traffic. Contrarily, Experimental Modal Analysis (EMA) (Cunha *et al.*, 2006) entail structural oscillation measurements resulting from controlled excitations. A

key challenge of OMA techniques relates to the fact that the dynamic response of structures under functional / environmental excitations is extremely low, with an oscillation amplitude ranging from a few centimeters, for more flexible structures (Rodelspelger *et al.*, 2010) down to and below a millimeter, for the most rigid ones (Gikas *et al.*, 2019). This feature dictates using extremely high performance displacement sensors (in terms of sensitivity, accuracy, precision, sampling rate, etc.) to depict the actual structure kinematics and their frequency content. In addition, the same quality characteristics necessitate for detecting structural defects (Farrar and Worden, 2013) through tracking local variations in the dynamic response, associated to minor changes in the pattern of oscillations (Rezvani *et al.*, 2018). However, despite the substantial advantages, measuring dynamic displacements in SHM applications is still a cumbersome and specialized task (Dong *et al.*, 2019). Many technologies allow the direct measurement of displacements at individual points of a structure with high accuracy (of the order of a few millimeters or better), but none of them has been established in practice, as a benchmark for monitoring the structural integrity of structures. These technologies include: digital levels (Owerko *et al.*, 2012), extensometers (Ziaei *et al.*, 2017), robotic total stations (Psimoulis and Stiros, 2007), differential methods of GNSS (Moschas, 2014), accelerometers (Bartoli *et al.*, 2008), Linear Variable



Differential Transformers (LVDTs) (Song *et al.*, 2007), Digital Image Correlation (DIC) (Piniotis *et al.*, 2016) and Laser Doppler Vibrometers (Gocal *et al.*, 2013). Ground Based Radar Interferometry (GBRI) is a non-destructive technology for monitoring vibrations of structures, such as bridges, buildings, high structures, etc. GBRI provides remote displacement measurements with high sampling rate (up to 200 Hz) and extremely high accuracy (better than  $\pm 0.1$  mm), which is claimed to be of the order of  $\pm 0.01$ mm in laboratory conditions. In the past, several studies have examined the performance of GBRI technology against alternative technologies in applications of structural response monitoring. However, the published studies to the best of the authors knowledge, are limited to comparisons of displacement time series in project-scale structural measurement scenarios. These studies do not account for critical parameters in data collection such as sensor installation strategies, data sampling or synchronization issues with other sensors and do not consider for methodological issues concerned with data processing and analysis. The objectives of this work are: (i) the experimental testing and performance assessment of a real aperture ground based radar interferometer (IBIS-S radar; Ingeneria Dei Sistemi, IDS) in dynamic monitoring (oscillations) in controlled laboratory conditions, and by extension, (ii) to demonstrate the potential (capabilities and limitations) of the GBRI technology.

#### A. GBRI technology in dynamic monitoring of structures

Monitoring structural behavior and condition of structures aims at evaluating their performance against operating loads, detecting potential damages, and overly assessing their structural integrity (Technical Chamber of North Greece, 2009; Farrar and Worden, 2013). Benefits include the improvement of their safe operational level, through early warnings in case of damage or failure, the reduction of maintenance costs, through preventive interventions, and the increase of structural efficiency, as a result of reducing downtime for maintenance work.

In this context, GBRI technology has been used in monitoring buildings (Luzi *et al.*, 2017), bridges (Bartoli *et al.*, 2008; Gentile, 2010; Piniotis *et al.*, 2016), masonry towers (Pieraccini *et al.*, 2013), industrial chimneys (Rodelspelger *et al.*, 2010; Piniotis *et al.*, 2013), suspension cables of cable-stayed bridges (Piniotis *et al.*, 2016), wind turbines (Pieraccini, 2013), cable masts (Gentile and Ubertini, 2012) and lighting pylons (Kuras *et al.*, al. 2009).

#### B. Previous related work

Evaluation of IBIS-S radar performance in structural monitoring applications has been previously performed against accelerometer sensors (Bartoli *et al.*, 2008), velocity sensors (Gentile, 2010), seismometers

(Negulescu *et al.*, 2013), inductive gauge (Beben, 2011) thermal camera (Stabile *et al.*, 2012), video recording system (Kohut *et al.*, 2012), laser interferometer and Laser Doppler Vibrometer (Gocal *et al.*, 2013). In the latter, the static-semi-static performance of GBRI technology was studied, through thoroughly designed experimental tests demonstrating an accuracy of  $\pm 0.1$  mm. Gocal *et al.* (2013) also compared the dynamic displacement measurements of the IBIS-S radar with the corresponding measurements of a Laser Doppler Vibrometer, in real conditions of monitoring a tram crossing bridge, confirming an accuracy better than  $\pm 0.1$ mm. A thorough examination of the relevant literature reveals that, in most studies, the evaluation of the IBIS-S radar system is performed in real structures through comparative presentation of measured displacement, velocity or acceleration time series against other sensors' data, and in some cases frequency domain diagrams, providing no further quantitative or qualitative investigation.

## II. INSTRUMENTATION AND EXPERIMENTAL SCENARIOS

### A. Experimental design requirements

This research aims to evaluate the GBRI displacement measurements in terms of precision (repeatability) and reliability (correctness) in laboratory conditions, under controlled dynamic oscillation scenarios, with oscillation characteristics corresponding to the dynamic characteristics of large-scale structures. More specifically, evaluation of the sensor under examination (IBIS-S, IDS) relies on comparisons between the radar measured displacements against those of a Laser Tracker sensor, while producing oscillations via a portable shake table of one degree of freedom.

In order to ensure that the research goals were achieved, the following prerequisites should be met:

- Conducting of the experiments in a suitable laboratory space, that can drastically reduce the presence of unwanted signals (electromagnetic interference, reflected signals, etc.) and additionally ensure the operational stability of the measurement systems and the absence of external environmental conditions (*e.g.* wind).
- Design of observation scenarios with emphasis on the oscillation characteristics of large-scale structures, in which, the oscillation amplitude decreases as the oscillation frequency increases. More specifically, oscillation amplitudes from  $\mu\text{m}$  (response proportional to rigid structures) to a few cm (response proportional to flexible structures) were selected. The range of the oscillation frequencies is representative of the modal frequencies that most structures demonstrate (up to 20 Hz).
- Adequate sampling frequency of measurement systems for the correct representation of displacement time series. According to ISO 4866:

2010 (Kuras, 2015), the sampling frequency in oscillation measurements must be at least five times higher than the highest oscillation frequency value, in order to reliably represent the motion event.

- Satisfy specific, preselected dynamic oscillation characteristics (amplitude and frequency) for each experimental scenario.
- Ensure sufficient amount of measurements to ensure the necessary analysis in determining the response frequency.
- Strict alignment of the IBIS-S radar line of sight (LOS) with the motion axis of the shake table so that the observables of both systems are directly comparable.
- Accurate synchronization of recording systems, required for the automation of data processing.

### B. Test site and instrumentation

Data collection took place in the anechoic chamber of the Laboratory of Wireless and Long Distance Communications of the School of Electrical and Computer Engineering, NTUA (Figure 1). The chamber is used for laboratory testing of electromagnetic radiation equipment, as it effectively neutralizes or reduces reflected waves (Chronopoulos, 2017). It is a specially designed cage, insulated from external radiation sources and lined up with suitable tiles for the absorption of unwanted electromagnetic signals.



Figure 1. The anechoic chamber of the Laboratory of Wireless and Long Distance Communications, of the School of Electrical and Computer Engineering, NTUA.

The device used for oscillation generation consists of two parts, the electrodynamic power generator (shake table) ELECTRO-SEIS® Shaker 400 by APS Dynamics and the amplifier APS EP-124. The shake table allows for a

maximum oscillation amplitude of  $\pm 8$  cm and a frequency range from 0.01 Hz to 200 Hz (APS 400 Data sheet & manual). The APS EP-124 unit amplifies the incoming electrical signal and supplies the shake table with the appropriate electrical power. The amplitude of the shake table oscillation is altered by controlling its power supply through the amplifier. During the experimental process, the shake table was set to sinusoidal oscillation at pre-determined values of oscillation amplitude and frequency for each observation scenario. To control the oscillation frequencies and monitor the corresponding amplitude, an on purpose built PC software was developed in Labview programming language. The 6211-USB (National Instruments®) digitizer was used to connect and "drive" the shake table from a PC.

In order to cross check the shake table motion performance, a velocity measuring sensor, namely a Laser Doppler Vibrometer/LDV (VibroMet 500V) was used. The LDV sensor was set to measure the velocity of a metallic target that was fixed suitably on the moving shake table platform.

Since the motion of the shake table was set to be sinusoidal at a specific, unique frequency ( $f$ ) for every scenario, the conversion of velocity data to displacements was straightforward, through their division by the term  $(2 \times \pi \times f)$ . This was accomplished by the in house built Labview software routine, in real time, after having collected and digitized the raw velocity data. With this process, the peak to peak amplitude of the shake table's oscillation was displayed in real time on the PC screen, enabling the adjustment of the default nominal oscillation amplitude for each experimental scenario, by the appropriate tuning of the shake table's power supply through the amplifier.

The evaluation of the performance of the IBIS-S radar was performed by comparing its results with those of the Faro® Laser Tracker Vantage sensor. The Laser Tracker system is a portable device capable of computing the 3D coordinates of the system's target (Spherical Mount Reflector, SMR), through extremely accurate measurements of the zenith angle, the horizontal angle and the radial distance to the target. It uses the Absolute Distance Meter (ADM) phase shift technology to measure distances, while it utilizes a built-in meteorological station for their correction. The accuracy of the instrument, according to standard ASME B89.4.19-2006, is expressed in the form of the maximum permissible error (Maximum Permissible Error, MPE), which is  $\pm 16 \mu\text{m} + 0.8 \mu\text{m} / \text{m}$  for distances and  $\pm 20 \mu\text{m} + 5 \mu\text{m} / \text{m}$  for angle measurements (FARO Laser Tracker Vantage Manual). According to Faro®, the standard performance of the sensor corresponds to accuracy that is half the value of the aforementioned Maximum Permissible Errors (MPE). The system has an effective range of 0 m - 80 m and is used for static as well as dynamic measurements, due to its high sampling frequency (1000 Hz).

C. Instrumentation setup

The experiment regards measuring the harmonic oscillations performed by the shake table at specific pair values of nominal frequency and amplitude. For this purpose, a passive GBRI system target (metallic cone), a Laser Tracker system SMR target and an LDV metallic target were properly fixed on the moving surface of the shake table (Figure 2).

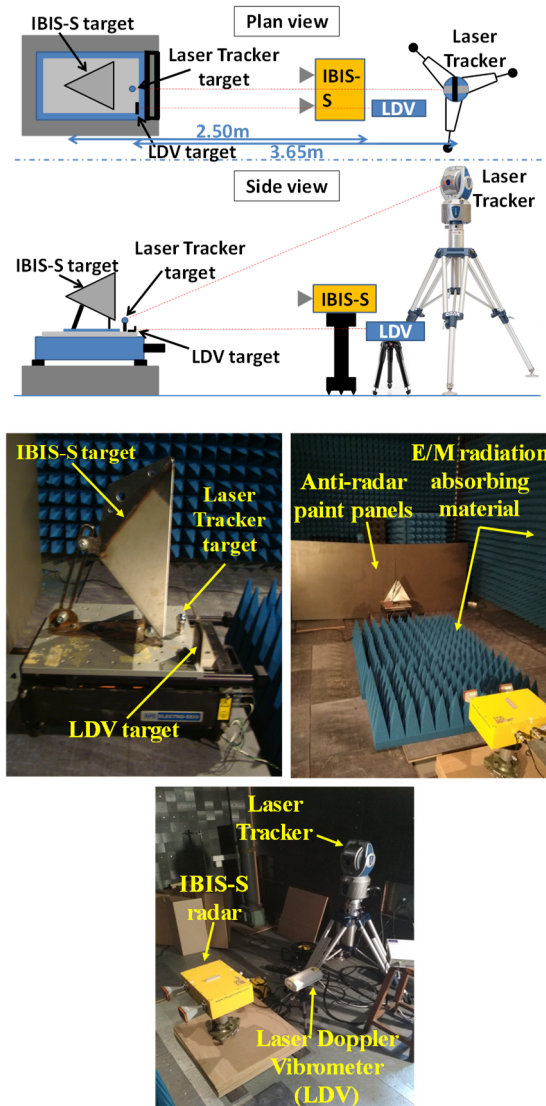


Figure 2. Instrumentation setup.

Then, the measuring systems were placed so that their lines of sight were parallel to the motion axis of the shake table. To ensure adequate accuracy in the alignment, the Laser Tracker was used in the setting out process.

This setup allowed for a direct comparison of the shake table’s oscillation amplitude as resulted from the two observation systems (*i.e.*, the radar IBIS-S and the Laser Tracker).

Prior to experimental testing, in order to determine the noise level of the radar sensor in the anechoic chamber, a series of measurements were performed with the shake table being stationary.

The scope of this investigation was to determine the signal amplitude attributed to noise due to various sources of error; for instance, signal interference, signal reflections and building microtremors, or other unusual patterns, suggesting problems in observational conditions. As shown in Figure 3, the estimated noise level is extremely low, as the apparent displacement is of the order of 3 μm maximum (standard deviation of ± 0.8 μm).

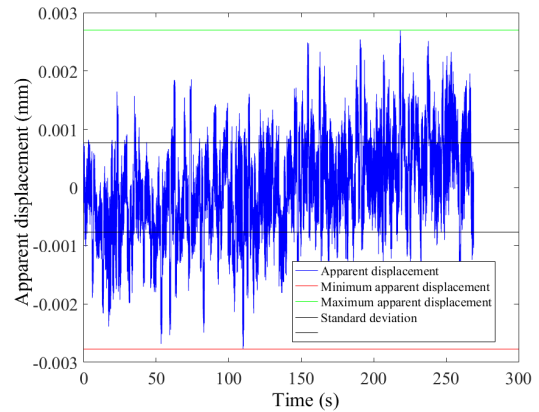


Figure 3. Apparent displacement with stationary shake table.

In addition, the results of the measurement series of the stationary radar target are presented in a Box & Whisker plot (Figure 4). All observation scenarios exhibit a mean noise value of less than 10 μm (maximum mean value: 8 μm) and maximum standard deviation ± 2.6 μm. This value is considered negligible, confirming the ideal experimental conditions and emphasizing the high precision (repeatability) of the IBIS-S radar, which proves to be better than ± 0.01 mm in laboratory conditions.

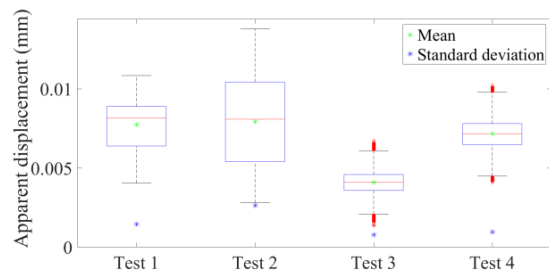


Figure 4. Apparent displacements' Box & Whisker plot.

D. Experimental scenarios

The sampling frequency for both recording systems was set at 200 Hz (ten times the maximum oscillation frequency of the shake table) to ensure dense representation of the vibration events. Scenarios of low oscillation frequencies (1 Hz – 5 Hz) paired with oscillation amplitudes ranging from 0.5 mm to 20 mm, whilst scenarios at higher frequencies (10 Hz - 20 Hz) paired with signal amplitudes spanning from 0.05 mm to 0.75 mm. In total, 25 experimental scenarios were performed, summarized in Table 1.

Table 1. Experimental scenarios. F= frequency;  
A= Amplitude

	f (Hz) @ A (mm)
1	@ (5, 10, 15, 20)
2	@ (1, 5, 10, 15)
5	@ (0.5, 1, 5)
10	@ (0.05, 0.1, 0.5, 0.75)
15	@ (0.05, 0.1, 0.25, 0.3)
20	@ (0.05, 0.075, 0.1, 0.1, 0.1, 0.2)

Since data synchronization was not possible via an absolute (*e.g.* GNSS) or relative (*e.g.* triggering) time source, synchronization was accomplished via two excitation events using the cross-correlation method. Both events were realized through appropriate modifications in the shake table's Labview "driving" software, to perform instant "start" and "stop" operation.

### III. DATA PROCESSING AND RESULTS' ANALYSIS

Considering raw data processing, custom software was developed in Matlab® programming language to implement the following tasks:

- Compute the time difference between the signals of the two measurement systems through cross-correlation.
- Visualize the synchronization outcome of the cross-correlation event via plotting the time series of the synchronized signals.
- Generate the Power Spectral Density (PSD) diagrams for each dataset and derive the oscillation frequency value.
- Compute the oscillation amplitude for both systems' signals via calculating half of the difference between the local maximum and local minimum, for each oscillation period and store the matrix of oscillation amplitudes.
- Compute the differences in the oscillation amplitude for both measurement systems.
- Create the histogram of the oscillation amplitude differences for each experimental scenario.

#### A. Time domain analysis

Detailed examination of the synchronized time series data of the two systems (Laser Tracker and GBRI) confirmed the ultra-high degree of coincidence of the results.

Figure 5 shows the oscillation time series obtained for both systems for two representative trials – *i.e.*, a low ( $f=1$  Hz,  $A=10$  mm) and a high frequency ( $f=20$  Hz,  $A = 0.1$  mm).

Statistical analysis of the oscillation amplitude differences (not shown here), reveal a strong normal distribution pattern. However, the most prominent findings result from the analysis of the Empirical Cumulative Distribution Function (ECDF) diagrams organized according to their nominal frequency.

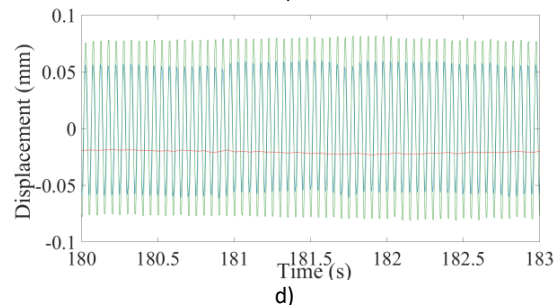
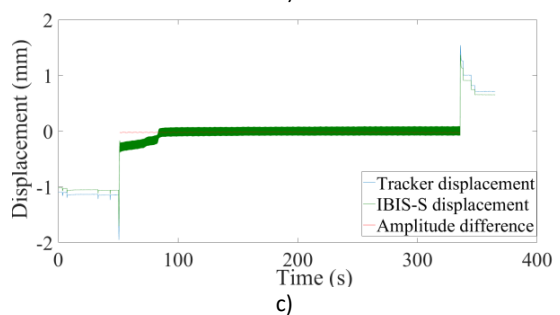
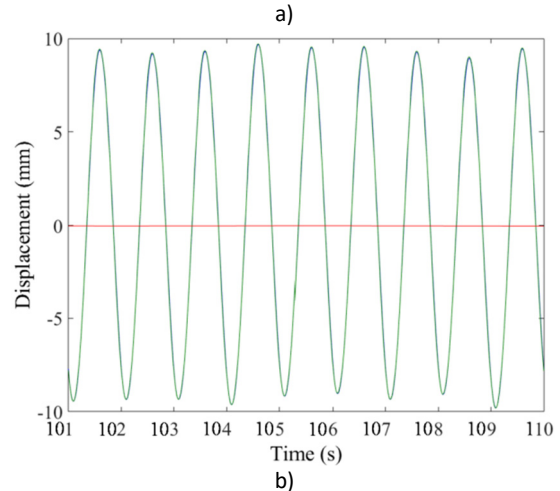
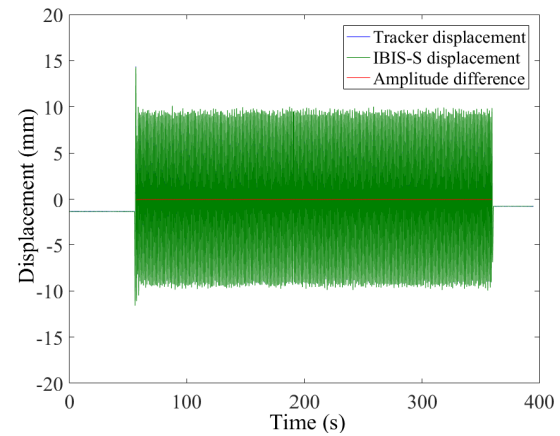


Figure 5. a) and b) Oscillation time series and zoomed in instances obtained from both systems, for low frequency ( $f=1$  Hz,  $A=10$  mm); c) and d) high frequency ( $f=20$  Hz,  $A = 0.1$  mm).

Analysis of the ECDF diagrams (Figure 6) suggests that the trueness (deviation from nominal value) of IBIS-S system is substantially better than  $\pm 0.1$  mm, in laboratory conditions. Except from two test scenarios all values of amplitude differences range from -0.10 mm to 0.02 mm. The ECDF curves demonstrate a highly steep slope, suggesting that the vast majority of

observed amplitudes follow closely their nominal values.

In addition, it is apparent that as the oscillation amplitude increases, for scenarios performed at the same nominal oscillation frequency, the slope of the ECDF curve decreases, indicating an increase in variability.

This phenomenon probably reflects a small error in the alignment between the line of sight of IBIS-S radar and the actual direction of oscillation, also affected by the small difference in the targets' location that becomes clear for largest oscillation widths (see Box and Whisker plot in Figure 7).

### B. Frequency domain analysis

For the evaluation of the IBIS-S system in the frequency domain, power spectral density diagrams were built on a linear scale for the two sensors. For each sensor and experimental scenario, the nominal oscillation frequency of the shaker is dominant, *i.e.* the resulting frequency values for each observation scenario coincide with each other and with the corresponding nominal frequency of the shake table. This demonstrates the excellent performance of the IBIS-S system in determining frequencies. Also, the power spectral density diagrams were examined on a logarithmic scale. In this form, in addition to the dominant motion frequency, low value frequencies and harmonics of the nominal frequency are also evident, as a result of the imperfect sinusoidal motion of the shake table. In particular, since the shake table was not

operated in a closed loop (no feedback sensor was used), and thus, its electrical control power was not corrected in real time, its motion was not perfectly sinusoidal. However, for the needs of the present work, the creation of a "perfect" sinusoidal motion is not required, as the research goal is to compare the measured signals from two measuring systems while monitoring the same phenomenon, *i.e.* the shake table movement.

## IV. CONCLUDING REMARKS

This paper offers a systematic attempt to evaluate the accuracy (precision and trueness) and potential of a Ground Based Radar Interferometer/GBRI (IBIS-S, IDS) in laboratory conditions. The experimental process utilizes a shake table to generate oscillations of known characteristics in a controlled laboratory environment and a Laser Tracker system as a means of evaluating the GBRI system. As the interest of this study is focused on monitoring the dynamic behavior of large-scale structures, the oscillation characteristics (frequency and amplitude) are selected to represent corresponding modal frequencies and amplitudes.

Statistical analysis of the experimental results shows that the precision (repeatability) of the system is  $\pm 0.01$  mm or better and its accuracy (reliability) better than  $\pm 0.1$  mm. Additionally, the extremely high sensitivity of the system in the determination of oscillation frequencies up to 20 Hz and amplitudes of less than 1 mm is proven.

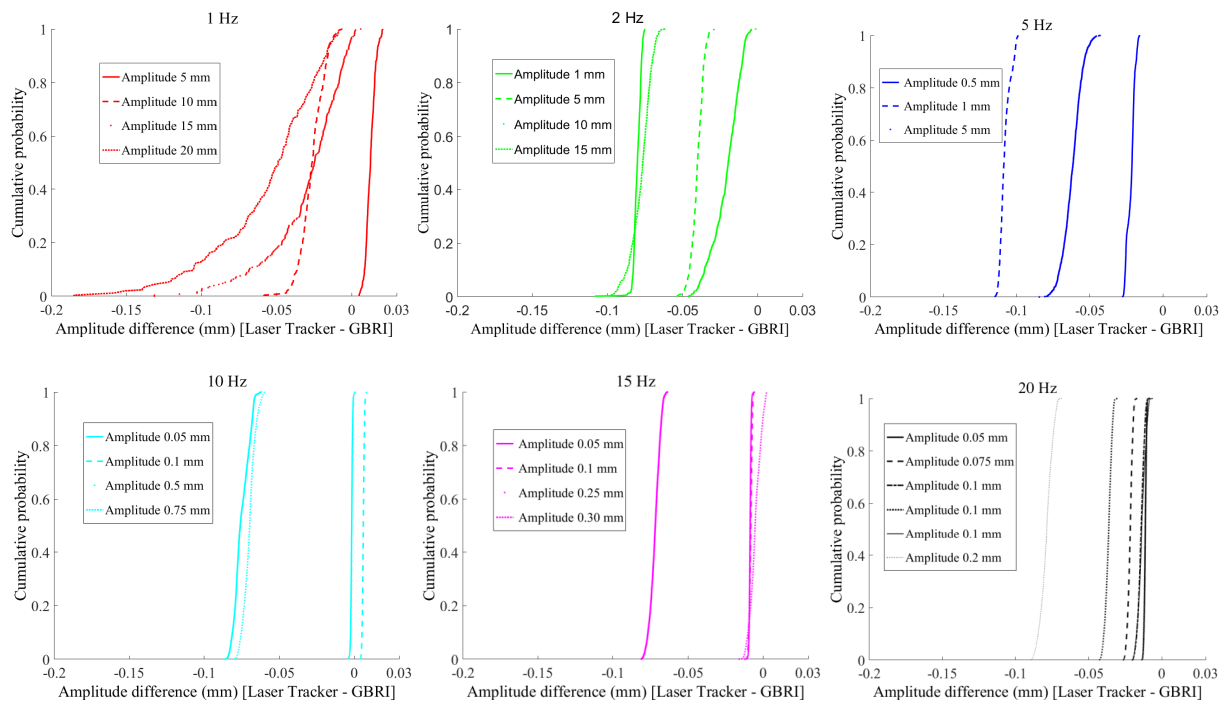


Figure 6. Empirical Cumulative Distribution Function (ECDF) diagrams, organized according to nominal frequency.

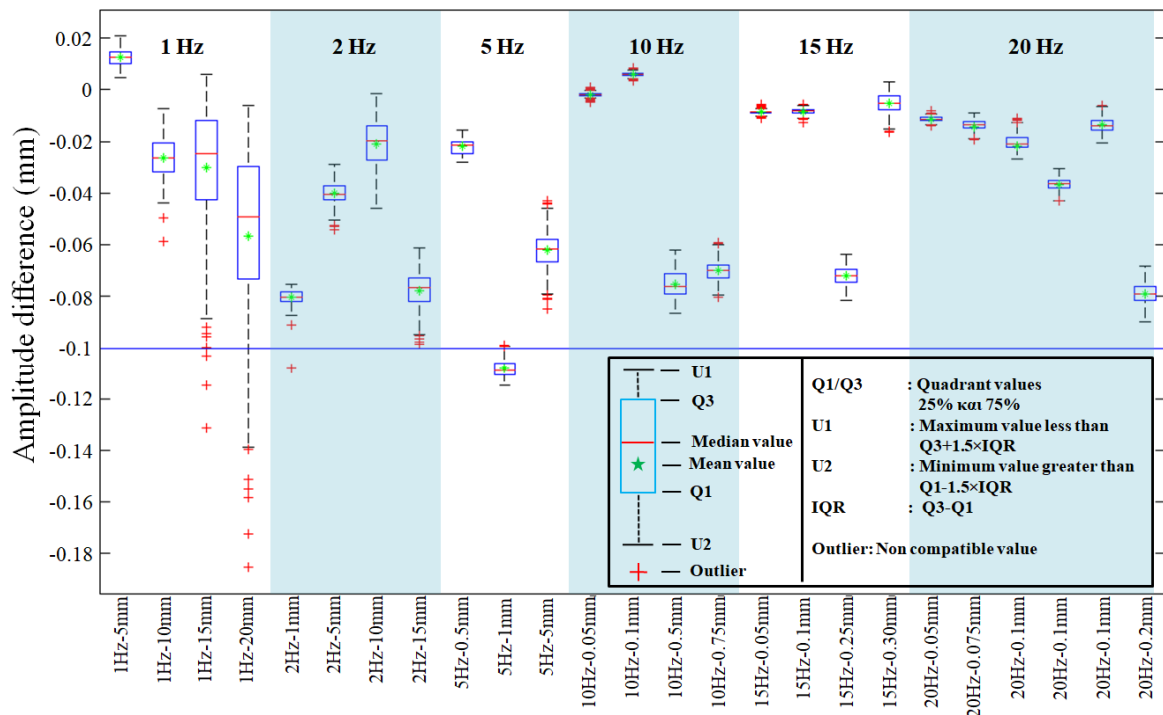


Figure 7. Box and Whisker plot of all experimental scenarios.

## V. ACKNOWLEDGEMENTS

For the realization of the present research, specialized equipment from various NTUA Laboratories were used. The authors express their gratitude to Professors M. Kattis and M. Sakellariou (Laboratory of Structural Engineering & Technical Works, SRSGE NTUA) for the shake table disposal, Professor I. Antoniadis (Laboratory of Dynamics and Structures, SME NTUA) for the disposal of the LDV sensor, Professor Ch. Kapsalis (Wireless and Long Distance Communications Laboratory, ECE NTUA) for the disposal of the anechoic chamber and Professor A. Papagiannis (Department of Physics, SAMPS NTUA) for the disposal of the laser protective glasses for the LDV sensor.

## References

- APS 400 Data sheet & manual.
- Bartoli, G., Facchini, L., Pieraccini, M., Fratini, M., and Atzeni, C., (2008). Experimental utilization of interferometric radar techniques for structural monitoring, *Structural Control and Health Monitoring*; Volume 15, pp 283–298, Published online in *Wiley InterScience*, DOI: 10.1002/stc.252.
- Beben, D., (2011). Application of the interferometric radar for dynamic tests of corrugated steel plate (CSP) culvert, *NDT&E International*, Volume 44, pp 405-412.
- Calvi, G.M., Priestley, M.J.N., and Kowalsky, M.J., (2008). Displacement-Based Seismic Design of Structures, 3<sup>rd</sup> Greek Conference Earthquake Engineering & Technical Seismology, 5–7 November, Athens-Greece.
- Chronopoulos P., (2017). *Study of the Impact of an Anechoic Chamber on the Modeling of Very Low Frequency Electric Sources Using Image Theory*, Thesis, Supervisor: Professor Ch. Kapsalis-NTUA, Wireless and Long Distance Communications Laboratory, ECE NTUA, Athens-Greece.
- Cunha, A., Caetano, E., Magalhães, F., and Moutinho, C., (2006). From input–output to output-only modal identification of civil engineering structure, SAMCO Final report.
- Dong, C.-Z., Celik, O., and Catbas, N., (2019). Marker-free monitoring of the grand stand structures and modal identification using computer vision methods, *Structural Health Monitoring*, Volume 18, Issue 5-6.
- FARO Laser Tracker Vantage Manual.
- Farrar, C.R., and Worden, K., (2013). *Structural Health Monitoring - A machine learning perspective*, Wiley.
- Gentile, C., (2010). Radar-based measurement of deflections on bridges and large structures, *European Journal of Environmental and Civil Engineering*, April 2010, DOI: 10.1080/19648189.2010.9693238.
- Gentile, C., and Ubertini, F., (2012). Radar-based Dynamic Testing and System Identification of a Guyed Mast, *AIP Conference Proceedings*, Volume 1457, Issue 1.
- Gikas, V., Mpimis, A., Piniotis, G., Perakis, H., Papadimitriou, F., Drimeris, K., and Sotiriou, P., (2019). Long-term Monitoring of a Multi-span Beam Bridge Using a Network of Digital Inclinometers: First Results and Perspectives, 4<sup>th</sup> Joint International Symposium on Deformation Monitoring, 15-17 May, Athens, Greece.
- Gocal, J., Ortyl, L., Owerko, T., Kuras, P., Kocierz, R., Cwiakala, P., Puniach, E., Sukta, O., and Balut, A., (2013). Determination of displacements and vibrations of engineering structures using ground-based radar interferometry, ISBN: 978-83-7464-645-1, Wydawnictwa AGH.
- IBIS-S Acquisition Software Manual.
- Kohut, P., Holak, K., Uhl, T., Ortyl, L., Owerko, T., Kuras, P., and Kocierz R., (2012). Monitoring of a civil structure's state based on noncontact measurements, *Structural Health Monitoring*, Volume 12, pp 411-429.

- Kuras, P., (2015). Surveying techniques in vibration measurement, EVACES 2015, *6<sup>th</sup> International Conference on Experimental Vibration Analysis for Civil Engineering Structures*, October 19-21, Dübendorf (Zürich), Switzerland.
- Kuras, P., Owerko, T., and Strach, M, (2009). Application of interferometric radar to examination of engineering objects vibration, *Reports on Geodesy*, pp 209-216, January 2009, Krakow, Poland.
- Luzi, G., Crosetto, M. and Fernández, E., (2017). Radar Interferometry for Monitoring the Vibration Characteristics of Buildings and Civil Structures: Recent Case Studies in Spain, *Sensors*, 24 March, Switzerland.
- Moschas, T., (2014). Measurement of high frequency oscillations with GPS of 100 Hz sampling rate, Doctoral dissertation, Laboratory of Geodesy and Geodetic Applications, Department of Civil Engineering, University of Patras, February 2014, Patras-Greece.
- Negulescu, C., Luzi, G., Crosetto, M., Raucoules, D., Roull, A., Monfort, D., Pujades, L., Colas, B., and Dewez, T., (2013). Comparison of seismometer and radar measurements for the modal identification of civil engineering structures, *Engineering Structures*, Volume 51, pp 10-22.
- Owerko, T., Ortyl, L., Kocierz, R., Kuras, P., and Salamak, M., (2012). Investigation of displacements of road bridges under test loads using radar interferometry – Case study, Conference: Bridge maintenance, safety, management, resilience and sustainability. *Proceedings of the Sixth International IABMAS Conference*, 8-12 July, Stresa, Lake Maggiore, Italy.
- Pieraccini, M., Dei, D., Mecatti, D., Parrini, F., (2013). Dynamic Testing of Historic Towers Using an Interferometric Radar from an Unstable Measurement Position, *Journal of Nondestructive Evaluation*, 32, pp. 398–404, published online: 24 July, DOI: 10.1007/s10921-013-0193-9.
- Pieraccini, M., (2013). Monitoring of Civil Infrastructures by Interferometric Radar: A Review, Hindawi Publishing Corporation, *The Scientific World Journal*, Volume 2013, Article ID 786961, DOI: 10.1155/2013/786961.
- Piniotis, G., Mpimis, A., and Gikas, V., (2013). Dynamic Testing and Output-Only Modal Analysis of a Bypass-Stack During Extreme Operating Conditions, Winning conference paper, *2<sup>nd</sup> Joint International Symposium on Deformation Monitoring*, September 2013, Nottingham, UK.
- Piniotis, G., Gikas, V., Mpimis, T., and Perrakis, H., (2016). Deck and Cable Dynamic Testing of a Single-span Bridge Using Radar Interferometry and Videometry Measurements, *Journal of Applied Geodesy*, Published online: 31 Mar 2016, DOI: 10.1515/jag-2015-0030.
- Psimoulis, P.A., and Stiros, S.C., (2007). Measurement of deflections and of oscillation frequencies of engineering structures using Robotic Theodolites (RTS), *Engineering Structures*, Volume 29, pp 3312-3324.
- Rezvani, K., Maia, N.M.M., and Sabour, M.H., (2018). A Comparison of some methods for Structural Damage Detection, *Scientia Iranica B*, Volume 25, pp 1312-1322.
- Rodelsperger, S., Laufer, G., Gerstenecker, C. and Becker, M., (2010). Monitoring of displacements with ground-based microwave interferometry: IBIS-S and IBIS-L, *Journal of Applied Geodesy*, Published online: 15 Jun 2010, DOI: 10.1515/jag.2010.005.
- Song, G., Gu, H., Mo, Y.L., Hsu, T. T. C., and Dhonde H., (2007). Concrete structural health monitoring using embedded piezoceramic transducers, *Smart Materials and Structures*, Volume 16, pp 959–968.
- Stabile, T.A., Perrone, A., Gallipoli, M.R., Giocoli, A., Pignatti, S., Palombo, A., and Pascucci, S., (2012). Joint application of non-invasive techniques to characterize the dynamic behavior of engineering structures, *15 WCEE Conference*, Lisbon, Portugal.
- Staszewski, W., Boller, C., and Tomlinson, G. R., (2004). *Health Monitoring of Aerospace structures*, Wiley.
- Technical Chamber of North Greece, (2009). Monitoring of the structural condition of important projects for complete maintenance, Conclusion of Chambers' working group, June 2009, Thessaloniki-Greece.
- Zhang, L., and Brincker, R., (2005). An overview of operational modal analysis: Major development and issues, *Proceedings of the 1st international operational modal analysis conference*, pp 179–190, Aalborg University, Copenhagen.
- Ziaei, A., Ahangari, K., Moarefvand, P., and Mirzabozorg, H.O., (2017). Extensometers results correction in concrete dams: A case study in RCC Zhavah Dam, *Structural Monitoring and Maintenance*, Volume 4, pp 17-31.

# Steel bridge structural damage detection using Ground-Based Radar Interferometry vibration measurements and deep learning Convolutional Neural Networks

George Piniotis, Vassilis Gikas

National Technical University of Athens, School of Rural, Surveying and Geoinformatics Engineering, Zographos, 15780, Athens, Greece, ([piniotis@survey.ntua.gr](mailto:piniotis@survey.ntua.gr); [vgikas@central.ntua.gr](mailto:vgikas@central.ntua.gr))

**Key words:** *bridge structural health monitoring; ground based radar interferometry; bailey type steel bridge; continuous wavelet transform; deep learning convolutional neural networks*

## ABSTRACT

This paper introduces a new, data-driven, vibration-based, damage detection strategy realized on an on-purpose built, *Bailey* type, steel bridge model (6.12 m x 1.80 m, scale 1:2.5) as part of the research work undertaken in the School of Rural, Surveying and Geoinformatics Engineering, NTUA, Greece. Vibrations of the bridge model in a “healthy” and damaged condition were recorded using a Ground-Based Radar Interferometer (GBRI). Structural damage was deliberately induced on the bridge model by removing a number of carefully selected structural parts, whilst bridge excitation was achieved using a vibration generation apparatus. This system employs an in-house built in trolley system capable of realizing preset dynamic load scenarios. The damage detection approach developed relies on the transformation of GBRI vibration measurements to Continuous Wavelet Transform (CWT) scalogram images. The latter are then used to apply alternate pattern recognition techniques; particularly, a class of pre-trained Deep Learning Convolutional Neural Networks (CNNs) through the application of Transfer Learning technique. The classification results of the bridge health status reach an accuracy of the order of 90%, suggesting the effectiveness and the high potential of the proposed approach.

## I. INTRODUCTION

Non-Destructive Structural Health Monitoring (ND-SHM) methods measure the response of a bridge structure against static or dynamic loads of a controlled or an arbitrary character. In recent years, they have attracted a great deal of attention, as a result of the non-invasiveness and constantly evolving technology in the field. In contrast to static loading excitation, methods that rely on the measured response of structures under dynamic loading are much easier to implement, as they do not require the operational shutdown of the bridge, making them widely used in the last decade. Their principle of operation relies on the assumption that a structural damage of any kind induces changes in the structural parameters, (*i.e.*, stiffness, mass or energy damping), which, in turn, alter the dynamic response of the structure (Farrar and Worden, 2013). ND-SHM methods are classified into parametric ones, which are based on Finite Element Models (FEM) (Model-based); and non-parametric ones that rely only on response-measurements of a structure (Data-based). The latter, are also known as vibration-based inspection methods that rely in the measurement of the response (displacement, speed, acceleration, elongation, etc.) of a structure during its oscillation, using appropriate sensors. However, as there are no sensors that can directly measure structural damage, it is necessary to transform raw oscillation measurements into suitable

features/indicators, which in turn, are sensitive to structural damage. These features are compared against the corresponding features extracted from Finite Element analytical Models (FEM) or against features produced from oscillation measurements previously obtained, and if the comparison yields a statistically significant difference, the presence of a structural defect might be possible. Otherwise, the structure is considered to be in a “healthy” structural condition.

The transformation of raw measured oscillation data to meaningful, damage-sensitive features is a hard task that requires a great deal of user intervention, along with specialized user skills. However, in the last decade, new methods emerged; for instance, techniques of Deep Learning Neural Networks that seem to overcome such prerequisites and pave the way towards the automation of Structural Health Monitoring data analysis techniques.

Deep Learning Neural Networks or Deep Neural Networks (DNNs) allow the automatic extraction of appropriate features directly from data, without user intervention. The name of the Artificial Deep Learning Neural Networks is a consequence of their complex architecture, which is based on multiple layers of non-linear transformations. Neural networks of this class, in order to model a high degree of data abstraction, (Provos, 2015), build up complex, high-level, abstract representations of primary data, resulting from a series



of increasingly simpler representations of this data, with each representation corresponding to their different feature characteristics (Helm *et al.*, 2020). In effect, moving from the simplest to the most complex layer of representation, an increase in the understanding of the underlying problem characteristics is progressively achieved. In this way, deep neural networks allow computers to "learn" from empirical knowledge and perceive the world, based on a hierarchical structure of concepts, with each concept being defined by its relation to a number of simpler concepts. The types of Deep Neural Networks widely used are Convolutional Neural Networks (CNNs) and Recurrent Deep Neural Networks (RNNs).

In the present study, taking advantage of the Transfer Learning technique, pretrained Convolutional Neural Networks (CNNs), which have shown excellent results in the field of pattern recognition in images (Jarret *et al.*, 2009; Krizhevsky *et al.*, 2012) are used. Prior to implementation, these models were adjusted suitably to accommodate the characteristics of the Bailey type steel bridge used in this study.

#### A. Convolutional Neural Networks (CNNs) – Transfer Learning technique

The name Convolutional Neural Networks (CNNs) stems from the mathematical operation of convolution, which takes place at one layer of their structure, at least. The purpose of CNNs is to learn abstract features of input data that usually refer to images. Their structure is based on the sequence of convolutional layers (which also use a non-linear activation function, usually RELU) and pooling layers. The last network layers consist of neural networks of the classic "shallow" form of Multi-Layer Perceptrons (MLPs), in which the classification process takes place. A convolutional neural network (CNN) is a type of artificial neural network primarily designed and used in image recognition to process pixel data.

Transfer Learning is a machine learning technique, which is based on the generalization of experience (Zhuang *et al.*, 2021). It allows the re-use of knowledge acquired during the solution of a problem, known as the "source domain", to solve a different but similar problem, the field of which is called the "target domain" (Azimi and Pekcan, 2019) (Figure 1). In practice, this operation asks for an appropriate adjustment of the most recently computed classification layers whilst the latter still retains the same layer architecture. A taxonomy of the alternative approaches of this technique are given in Zhuang *et al.* (2021).

The great asset of the Transfer Learning technique resides in the ability to face situations of excessive lack of training data (Pan and Yang, 2010). Specifically, the size of neural networks and the amount of training data proved to share an almost linear relationship (Tan *et al.*, 2018). In addition, if a set of predetermined parameters are used (layer weights, etc), the time periods required

for network training are significantly shorter than the corresponding time required for the training of Neural Networks developed from scratch. Finally, the Transfer Learning technique makes possible for new users of Neural Networks to successfully use existing networks of award-winning architectures.

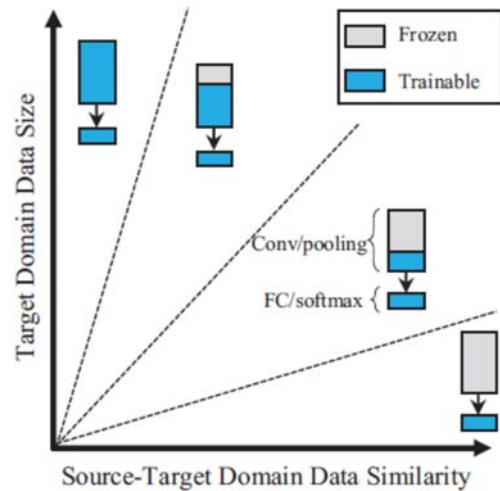


Figure 1. Different Transfer Learning Strategies (Azimi and Pekcan, 2019).

#### B. Related work – CNNs in Structural Health Monitoring (SHM)

It has been only since 2017 that Deep Learning Neural Networks are in use in SHM vibration inspection studies aiming at detecting, locating and determining the type of a damage in civil engineering structures. The work by Azimi *et al.* (2020) offers a thorough review on the use of Deep Learning Neural Networks in SHM applications. It provides a taxonomy of research findings concerned with the use of Deep Neural Networks: (i) in vibration based inspection methods, and (ii) in visual inspection methods which are further categorized in crack detection applications and structural components identification / change detection.

From this analysis it is apparent that the majority of the research effort resides on the use of oscillation measurements obtained from acceleration sensors. The most common type of structures examined in the literature are bridges of different types. In all SHM studies, the use of alternative Deep Learning Neural Network architectures is proposed. Only three research studies rely on oscillation measurements that pertain to physical models of real structures, which have been constructed according to regulations (Khodabandehlou *et al.*, 2018; Zhang and Wang, 2019). In the remaining studies, oscillation measurements have been used obtained in laboratory constructions that resemble real structures; however, they do not comply with any design standard or with the similitude law.

## II. THE PROPOSED APPROACH

### A. Research objective

The aim of this study is to investigate the potential of damage detection in bridge structures using oscillation measurements from a Real Aperture – Ground Based Radar Interferometer (RAR-GBRI) sensor; in particular, the IBIS-S radar system produced by the Italian company IDS (Ingeneria Dei Sistemi). In this regard, a set of experimental trials were undertaken in a laboratory conditions, subject to controlled excitation on a bridge model, both in intact condition and under intentionally induced structural damages. The type of structure chosen was the *Bailey* bridge type, which is widely used in Greece, both for normal connection needs and after emergencies as a result of natural disasters.

The main reason for choosing a laboratory space for testing was in order to avoid the influence of external environmental conditions; especially, temperature variations. Clearly, temperature changes have an extremely large effect on structural behavior, which can mask the corresponding effect of a structural damage.

For a successful outcome of the trials, special attention is required for the artificial stimulation of the laboratory structure, so that it resembles bridge operational stimuli, *e.g.* the scenario of a passing vehicle. In addition, due to the use of indoor space and taking into account the mode of radar operation, it was necessary to take precautions to limit the multipath effect of its signals.

Regarding the conditions that the damage detection methodology should meet, the use of Deep Learning Neural Networks was decided, so that the extraction of classification features, which would be further used in pattern recognition, was conducted automatically, without user intervention.

### B. Design and construction of a scaled Bailey type steel bridge

In order to meet the needs of this study, a physical model of a single-truss / single-storey (one truss made of five panels and one storey at each girder) *Bailey* type steel bridge (American M2 type) was designed by the PhD Candidate Mr. Vassilios Papavassiliou, Lab. of Metal Constructions, NTUA School of Civil Engineering and manufactured (Figure 2) by him and the first author. The model structure corresponds to a 50-foot *Bailey* bridge in a scale @ (1:2.5), with dimensions 6.125 m x 1.815 m. The design was performed using Finite Element Modeling (FEM) in SAP2000 software.

The design and setting up of the bridge model fully adheres the similitude theory, and therefore, it is possible to generalize the results of this research to real *Bailey* type bridges. Consequently, a constant ratio (1: 2.5) was maintained in the dimensions and cross-sections of the model, in relation to a corresponding real size 50-foot opening bridge. In addition, in order to achieve a mass correspondence factor, and therefore,

similarity in the developed accelerations, sandbags were placed on the deck of the model, thus appropriately changing its weight (ballast). The construction of the bridge model was followed by experimental measurements of its oscillation, which were compared with the numerical results from the Finite Element Model (FEM). The results of the comparisons indicated further changes in the structure. Thus, the sway braces, which were originally implemented by wires, were finally replaced by steel bars, whereas the way of attaching the transoms to the lower parts of the girder panels was also changed.

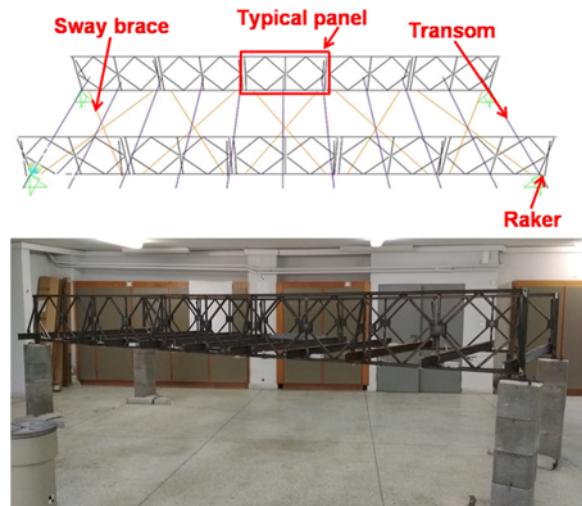


Figure 2. Bailey bridge FEM (up) and constructed model (down).

### C. Measurement environment and experimental equipment

The physical model of the *Bailey* bridge was placed in the metrology sector, in the basement of the School of Rural and Surveying Engineering of NTUA. This room ensures stable temperature conditions, especially in summer months. During the experiments the temperature was constant, of a value of 24° Celsius. In order to reduce multipath reflections of the radar signal, a special barrier surface (Figure 3), was constructed using suitable tiles that absorb reflected electromagnetic signals.



Figure 3. Special barrier surface for the absorption of reflected electromagnetic signals.

This barrier surface was placed perpendicular to the Line of Sight (LOS) of the radar sensor.

The apparatus used for the excitation of the bridge model consists of two parts; namely, the electrodynamic power generator (excitation unit) Modal 110 exciter (MB Dynamics Inc<sup>®</sup>) and the amplifier unit that accompanies it. The electrodynamic power generator has a frequency output range from DC up to 5000 Hz, a maximum oscillation range of  $\pm 1.9$  cm, a maximum power output of 500 Newtons and weighs 25 kg. The amp unit is responsible for the amplification of the incoming electrical signal and for supplying the excitation unit with the appropriate electrical power. The unit's moving part range of motion is controlled by thoroughly adjusting its power supply through the amplifier.

A dedicated set of software routines were developed in LabVIEW graphical programming environment to control the excitation unit's movement, while a National Instruments<sup>®</sup> 6211-USB data acquisition card was used to connect and "drive" the unit from a PC system. In order to excite the bridge model in the most possible realistic manner, the excitation unit was forced to a controlled motion with a "white noise" signal, due to its resemblance with standard functional bridge excitation, such as vehicle crossings.

An iron mass, weighing 2.5 kgr, was placed on top of the excitation unit, so as to create sufficient excitation on the bridge, taking advantage of the inertia effect. In addition, with the aim of realizing the diversity of the bridge excitation, a suitable electric vehicle was constructed, on which the excitation unit was placed, while iron rails were distributed on the bridge deck, for forcing the movement of the vehicle along them (Figure 4).



Figure 4. The electric vehicle with the excitation unit placed on it. Its movement was forced along the iron rails shown.

Using this excitation configuration it was possible to load the bridge in two modes; firstly, through holding the vehicle stationary at many different predefined locations in the bridge deck, with the excitation unit in operation at each one of them. Secondly, with

continuous vehicle bridge deck crossings, while the excitation unit was inactive. Unfortunately, vehicle bridge deck crossings affected GBRI displacement data, making them impossible to be further processed.

#### D. Experimental setup and observational scenarios

Experimental planning involves measuring the oscillation of individual points along the bridge deck, using the GBRI unit for a number of predefined scenarios with the bridge in "healthy" state/condition, as well as with the bridge artificially damaged. On the north side of the bridge deck, three passive GBRI targets (metal cones) were properly fixed. Subsequently, the GBRI was placed under the bridge, as shown in Figure 5, while the absorbing barrier surface was placed in the background to reduce multipath effects (Figure 5).



Figure 5. Experimental setup.

The radar system was put into operation at a sampling frequency of 200 Hz and acquired oscillation data for a 10 min period for each trial and for each one of the following bridge conditions (Figure 6): (i) bridge in "healthy" state condition, (ii) bridge with a raker element removal, and (iii) bridge with a sway brace element removal.

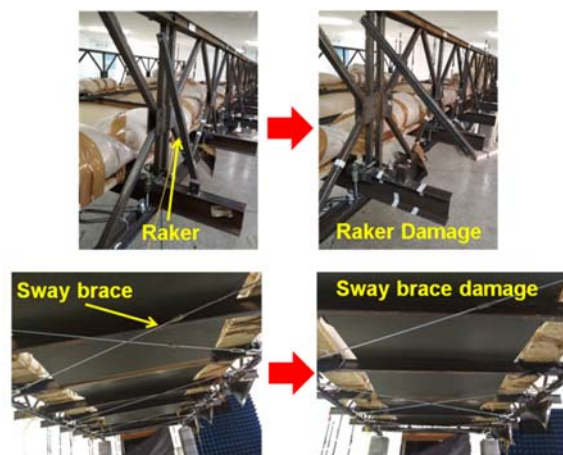


Figure 6. Artificial damages induced to the Bailey type bridge.

In total, 33 trials were performed for each of the three bridge structural states. In every test trial the excitation unit featured white noise characteristics to resemble an excitation pattern of passing vehicles.

It is pointed out that in order to avoid biases in the data, the order of the experimental scenarios was mixed and the position of the oscillation generator, as well as the intensity of the excitation itself, varied from

scenario to scenario. In addition, all experimental scenarios for structural state (ii) and (iii) were applied deliberately at various locations along the bridge deck. In the sequel, the GBRI measurements were processed using the dedicated IBIS DV software and finally the vertical displacement time series of each reflective cone were computed for each of the experimental scenarios. Thus, a total of: 33 (experimental scenarios) x 3 (structural states) x 3 (reflective cones) have resulted in 297 displacement cases, lasting 10 minutes each.

#### E. Data pre-processing and transformation

Prior to processing the GBRI displacement data via the pre-trained Deep Learning Neural Network strategy discussed previously, the raw data have undergone through a number of pre-processing and transformation steps. For this purpose a dedicated set of software routines was developed in Matlab<sup>®</sup> programming language to implement the following steps (Figure 7):

- Signal noise removal (filtering): In order to remove the unwanted displacement signal noise, a band pass, 8<sup>th</sup> class Butterworth digital filter was applied using a frequency band from 1 Hertz to 40 Hertz (Hz). These cut-off frequencies have been selected based on the FEM analysis of the model structure, according to which its modal frequencies lie in the frequency band from 5 to 30 Hz.
- Outlier detection: Detection of outliers and replacement using linear interpolation on their neighboring values. The criterion for locating outliers was defined as: 3 x mean absolute deviation (Median Absolute Deviation).
- Data standardization: Subtraction of the data average value and division by their standard error.
- Data normalization: The standardized data were normalized in the range of 0 to 1 using the formula (Eq. 1):

$$\bar{d}(t) = \frac{d(t) - \min(d)}{\max(d) - \min(d)} \quad (1)$$

where,  $\bar{d}(t)$  is the normalized displacement value,  $d(t)$  is the corresponding standardized displacement value,  $\min(d)$  refers to the minimum standardized displacement value and,  $\max(d)$  is the maximum standardized displacement value.

- Conversion of the pre-processed displacement signal to images using the Continuous Wavelet Transform (CWT): Following extensive investigation of the alternative techniques used for converting a time series dataset to an image representation, we concluded on the CWT technique as it suits for the study and analysis of signals with abrupt changes. By virtue of the CWT

technique characteristics, the pre-processed time series data were represented simultaneously in the time and frequency domain, using the Morse (3, 60) analytical wavelet. The 2D plots generated correspond to the time and frequency values of a point displacement respectively. In these plots, the frequency intensity is depicted using a color scale. These images constituted the input data of the pre-trained GoogleNet, ResNet-18 and ResNet-50 type Deep Neural Networks.

In order to determine the most efficient representation of a signal time series into an image formulation, the pre-processed datasets were converted into scalogram images of Continuous Waveform Transform images for periods of 10, 15, 20, 30, 60 seconds and 10 minutes. Analysis revealed that the optimal time for building a scalogram was 15 sec. Therefore, 40 Continuous Wavelet Transform images were generated for every 10-min test trial scenario; namely, 3960 images (= 40 images x 33 scenarios x 3 targets) for each one of the *Bailey* bridge model structural states (*i.e.*, "healthy", raker damage, sway brace damage), equals to a total of 11880 images. The constructed images have a resolution of 656 x 875 pixels, which was then changed to 224 x 224 pixels, so that they could be successfully inputted into the pre-trained Deep Neural Networks.

#### III. DAMAGE DETECTION THROUGH SUPERVISED LEARNING

Following the pre-processing of the raw displacement signal and its conversion into RGB images, the latter were fed into the pre-trained Deep Learning Neural Networks; specifically, the *GoogleNet*, ResNet-18 and ResNet-50. These Networks rely on award winning layer architectures, since they have won the first place in the annual ImageNet Large Scale Visual Recognition Challenge (ILS).

The aforementioned Networks were used without any change in their layer structure, except from the last layers. More specifically, the last output layer contains three neurons that correspond to the three categories of the bridge structural state adopted in this study (*i.e.*, the "healthy" state, raker damage state and the sway brace damage state). The learning rate was set to 0.001, so that the change of layer weights was not "aggressive". Following a random separation of the data, 80% of the data volume was used for training the networks, while the remaining 20% was used for testing. The accuracy achieved was 87.1% for *ResNet-18* and 91.4% for *GoogleNet*, respectively. In addition, in order to investigate the effect of the existence of more layers in the Deep Learning Neural Networks architecture on their performance, the *ResNet-50* Deep Neural Network was used. The latter consists of 50 layers, so its performance could be directly compared with the performance of ResNet-18, bearing 18 layers. The average accuracy of the *ResNet-50* network proved

to be the highest one, reaching a percentage of 92.3%, for the same input data used in *GoogleNet* and *ResNet-18*. Comparing to the performance of the *ResNet-18* it can be concluded that through adding 32 convolutional layers, an increase of about 5% in the classification accuracy was achieved. Table 1 depicts the classification performance metrics *i.e.* the accuracy (A), precision (P), sensitivity or Recall (Sen.), specificity (Spec.) and F-score (F), for each one of the Deep NNs, in percentages (%).

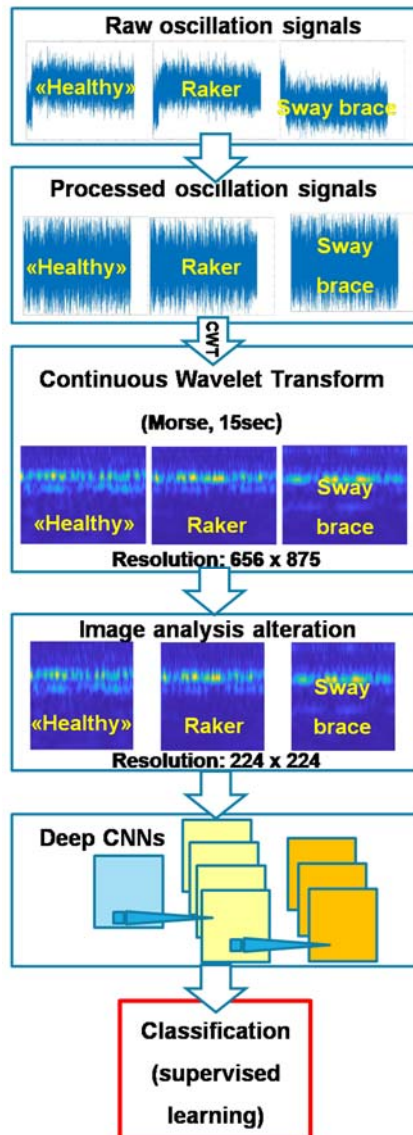


Figure 7. Methodological approach.

For all Deep Neural Networks used, the classification performance metrics are excellent, revealing their effectiveness for all bridge structural states, healthy and damaged.

In order to validate the results in the most affirmative way and to avoid over-fitting phenomena, in addition to the random division of data to training (80%) and testing (20%) images we enforced the k-fold cross validation method. Using this method, the data are randomly divided into k-sections (k-folds) and then, the algorithm is trained considering k-1 sections. In total, k neural network trainings are performed, omitting a different part of data each time, and finally the average of the accuracy results of the resulting k networks is calculated (Azimi and Pekcan, 2019). In the present study, the use of five-fold cross-validation was used, leading to an average classification accuracy of 90.4% for *ResNet-18*, 93.5% for *GoogleNet*, and 94.1% for *ResNet-50*, suggesting the suitability and effectiveness of the proposed method. Figure 8 shows the confusion matrices resulting for *ResNet-50* Deep Neural Network, when applying the five-fold cross-validation method.

#### IV. CONCLUDING REMARKS AND FUTURE WORK

This paper introduces a new, data-driven, vibration-based, damage detection strategy applied on a laboratory *Bailey* type, steel bridge physical model (scale 1:2.5), built dedicatedly for fulfilling the goals of ongoing Structural Health Monitoring research work. Bridge oscillations were measured using a Ground Based Radar Interferometer (GBRI). Towards structural “health” condition identification the bridge physical model is excited using a “white noise” vibration generation apparatus, based on an on purpose built trolley, variously positioned on the bridge deck, to realize the monitoring scenarios, while structural damage is artificially induced by removing specifically selected structural parts, namely bridge rakers and sway braces.

The presented approach adopts state of the art pattern recognition techniques, namely Deep Learning Neural Networks (NNs) and particularly, the award-winning Deep NNs (*GoogleNet*, *ResNet-18* and *ResNet-50*), taking advantage of the Transfer Learning technique, after appropriately having transformed GBRI vibration measurements to Continuous Wavelet Transform (CWT) scalogram images.

The structural condition identification results demonstrate that the proposed strategy framework reaches an average identification accuracy of 94.1% (*ResNet-50*) when applying the five-fold cross-validation method, confirming its effectiveness and promising potential.

Table 1. Classification performance metrics in percentages (%) for each one of the Deep NNs used

	GoogleNet					ResNet-18					ResNet-50				
	A	P	Sen.	Spec.	F	A	P	Sen.	Spec.	F	A	P	Sen.	Spec.	F
Healthy	94.1	91.2	91.3	95.6	91.2	91.3	87.8	85.7	94.1	89.5	95.5	94.5	91.9	97.3	93.2
Raker damage	94.6	91.2	92.7	95.5	91.9	91.0	85.2	88.3	92.4	86.7	94.3	89.5	93.9	94.5	91.6
Sway brace damage	94.0	91.8	90.2	96.0	90.7	91.9	88.3	87.2	94.2	87.7	94.8	93.2	91.2	96.7	92.2

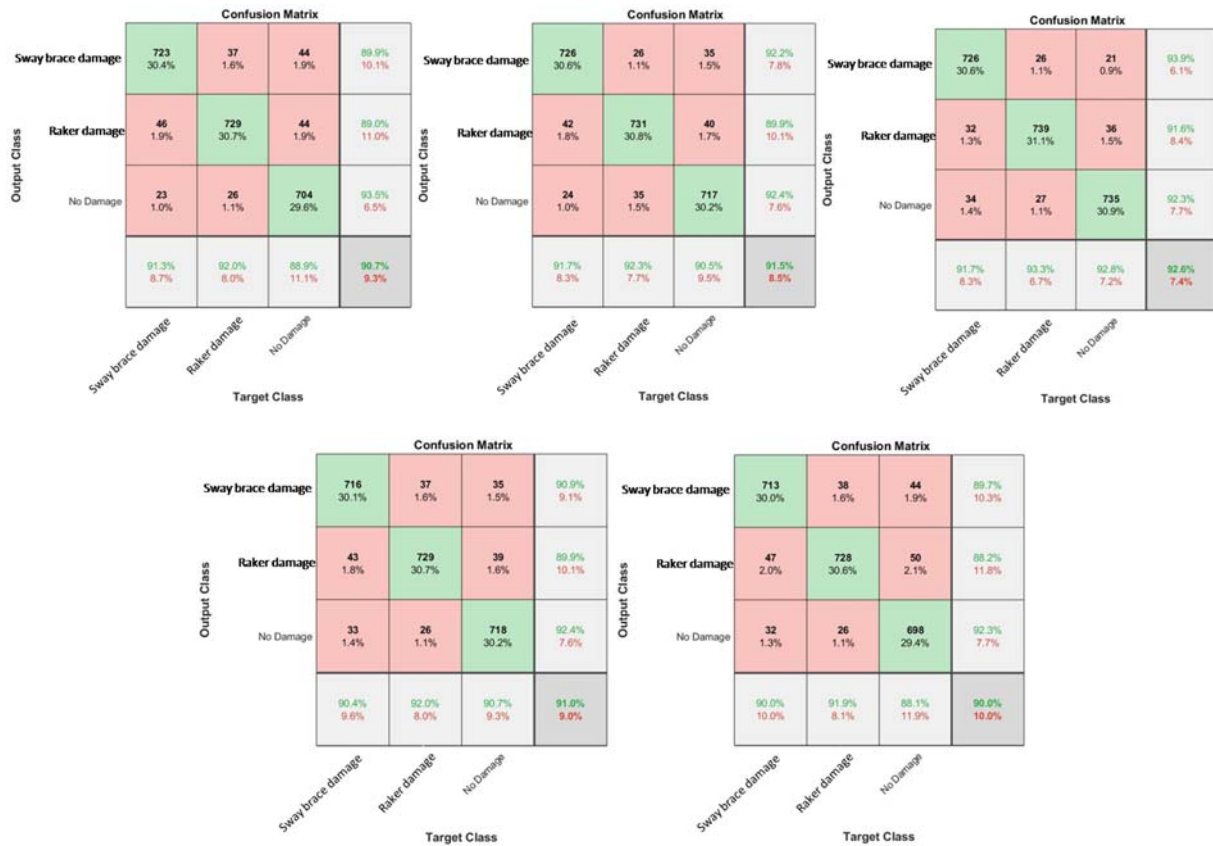


Figure 8. Confusion matrices resulting from the application of the five-fold cross-validation method for ResNet-50 Deep Neural Network.

In the future, the focus will be placed in detecting and locating potential damages on the structure. Also, the authors will focus on the implementation of Deep Neural Networks in an unsupervised learning frame, so as to apply them on real structures, in which data from damaged structural conditions are unavailable.

#### V. ACKNOWLEDGEMENTS

The authors express their gratitude to Mr Vassilios Papavasiliou (Civil Engineer, MSc, PhD candidate in the Laboratory of Steel Structures, School of Civil Engineering, NTUA), who designed the physical model of the Bailey type steel bridge and subsequently constructed it along with the first author. They also express their gratitude to Professor Ch. Gantes (Laboratory of Steel Structures, School of Civil Engineering, NTUA) and X. Lignos (member of Laboratory of Steel Structures Teaching Staff, School of Civil Engineering, NTUA) for permitting the use of their Laboratory equipment for the Bailey type steel bridge construction.

#### References

Azimi M., Eslamlou A.D., and Pekcan G., (2020). Data-Driven Structural Health Monitoring and Damage Detection through Deep Learning: State-of-the-Art Review, *Sensors*, DOI: 10.3390/s20102778.

Azimi M., and Pekcan G., (2019). Structural health monitoring using extremely compressed data through deep learning,

*Computer-Aided Civil and Infrastructure Engineering*, vol. 35, Issue 6, pp 597–614, DOI: 10.1111/mice.12517.

Farrar C.R., and Worden K., (2013). *Structural Health Monitoring - A machine learning perspective*, Wiley.

Helm J.M., Swiergosz A.M., and Haerberle H.S. (2020). Machine Learning and Artificial Intelligence: Definitions, Applications, and Future Directions. *Curr Rev Musculoskelet Med* 13, pp. 69–76. DOI: 10.1007/s12178-020-09600-8.

Jarrett K., Kavukcuoglu K., Ranzato M. and LeCun Y., (2009). What is the best multi-stage architecture for object recognition?, *2009 IEEE 12<sup>th</sup> International Conference on Computer Vision*, pp. 2146-2153, DOI: 10.1109/ICCV.2009.5459469.

Khodabandehlou H., Pekcan G., and Fadali M.S., (2018). Vibration-based structural condition assessment using convolution neural networks, *Structural Control Health Monitoring*, DOI: 10.1002/stc.2308.

Krizhevsky A., Sutskever I., and Hinton G.E., (2012). Imagenet classification with deep convolutional neural networks, in: *Advances in Neural Information Processing Systems*, pp. 1097–1105.

Pan J. S. and Yang Q., (2010). A Survey on Transfer Learning, "in *IEEE Transactions on Knowledge and Data Engineering*, vol. 22, no. 10, pp. 1345-1359, October, DOI: 10.1109/TKDE.2009.191.

Provos A., (2015). Implementation of a MATLAB library for rapid research and prototyping of new methods of training Deep Convolutional Neural Networks using CAFFE, Thesis, Supervisor: Professor Delopoulos A., Aristotle University of Thessaloniki, Laboratory of Data Processing and Computing, Department of Electrical and Computer Engineering, Thessaloniki, Greece.

- Tan C., Sun F., Kong T., Zhang W., Yang C., and Liu C., (2018). A Survey on Deep Transfer Learning, Artificial Neural Networks and Machine Learning - ICANN 2018 - 27th International Conference on Artificial Neural Networks, Rhodes, Greece, October 4-7, 2018, Proceedings, Part III. Volume 11141 of Lecture Notes in *Computer Science*, pp. 270-279, Springer.
- Zhang T., and Wang Y., (2019). Deep learning algorithms for structural condition identification with limited monitoring data, *International Conference on Smart Infrastructure and Construction 2019* (ICSIC), DOI: 10.1680/icsic.64669.421.
- Zhuang F., Qi Z., Duan K., Xi D., Zhu Y., Zhu H., Xiong H., and He Q., (2021). A Comprehensive Survey on Transfer Learning. *Proceedings of the IEEE*, 109(1), pp. 43-76, DOI: 10.1109/JPROC.2020.3004555.